PROCEEDINGS VOL II

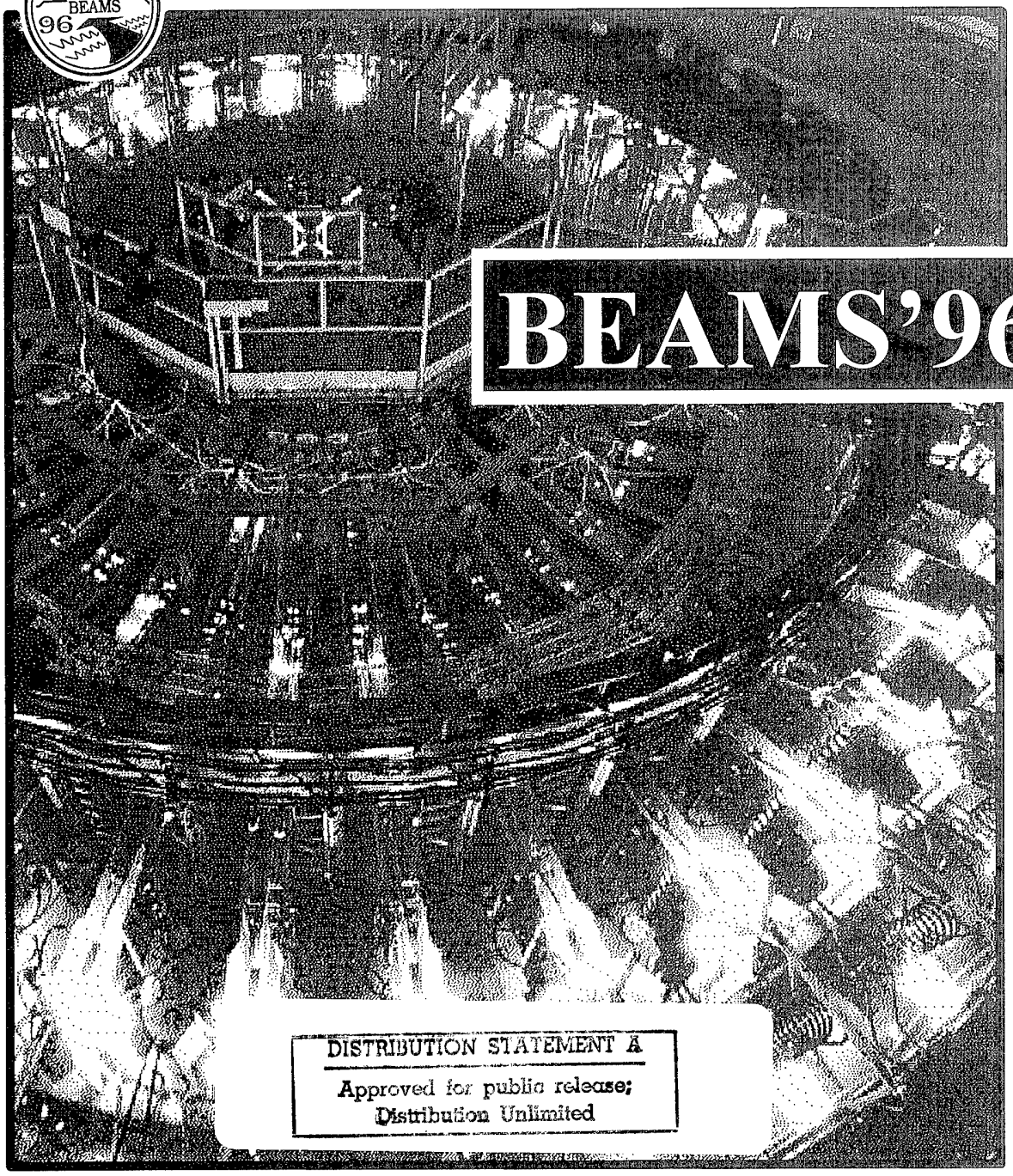

BEAMS'96

DISTRIBUTION STATEMENT A
Approved for public release;
Distribution Unlimited

11th International Conference on High Power Particle Beams
Prague, Czech Republic
June 10-14, 1996

19961212 084

DISCLAIMER NOTICE

THIS DOCUMENT IS BEST QUALITY AVAILABLE. THE COPY FURNISHED TO DTIC CONTAINED A SIGNIFICANT NUMBER OF PAGES WHICH DO NOT REPRODUCE LEGIBLY.

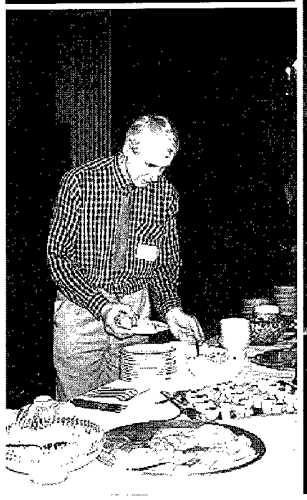

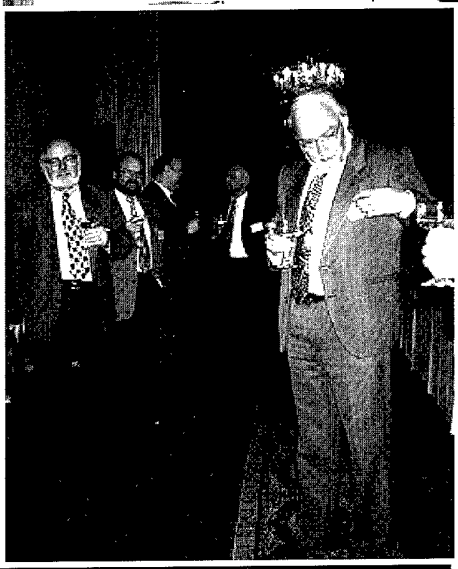

BEAMS'96

Proceedings of the
11th International Conference on High Power Particle Beams

Prague, Czech Republic
June 10-14, 1996

Edited by

Karel Jungwirth and Jiří Ullschmied
Institute of Plasma Physics, Prague

Volume II

DISTRIBUTION STATEMENT A
Approved for public release;
Distribution Unlimited

Published by

Committees of the 11th International Conference
on High Power Particle Beams
Institute of Plasma Physics
Academy of Sciences of the Czech Republic
Za Slovankou 3
182 00 Prague 8
Czech Republic

Proceedings of the 11th International Conference
on High Power Particle Beams - Vol. II
First Edition, 1996

ISBN 80-902250-4-7 (Vol.2)
ISBN 80-902250-2-0 (set)
ISBN 80-902250-3-9 (Vol.1)

Printed by Tiskárna „K", Ltd., Sokolovská 45, 18600 Prague 8, Czech Republic
Cover designed by Jiří Ullschmied

TABLE OF CONTENTS

VOLUME I

Opening Addresses (K. Jungwirth, P. Šunka) ..... **VII**

PAPER INDEX ..... **i-xvi**

Invited Papers O-0
(J. Quintenz - SNL; V. Chernyshev - VNIIEF Arzamas;
B. Goel - FZK, K. Yatsui - LBT Nagaoka) **1**

Invited Papers O-1
(ICF, Accelerators, B&P Diagnostics) **37**

Invited Papers O-2
(Ion Beams, Ion Diodes) **72**

Invited Papers O-3
(PP Technology, POS, BDTT) **121**

Invited Papers O-4
(Liners, Z-pinches, Plasma Foci) **140**

Invited Papers O-5
(Electron Beam Physics, B-P Systems) **182**

Invited Papers O-6
(HP Microwaves, FELs) **206**

Invited Papers O-7
(Industrial Applications of Beams and PP) **249**

Invited Papers O-8
(Radiation Sources) **276**

Contributed Papers P-1
(B-P Interaction, Electron Beam Physics, FELs, H-P Microwaves) **319**

Contributed Papers P-2
(Capillary Discharges, H-C Discharges, Laser Plasma Discharges,
Imploding Liners, Plasma Foci, Pseudosparks) **501**

AUTHOR INDEX

VOLUME II

PAPER INDEX ..... **i-xvi**

Contributed Papers P-2 - continuation
(Radiation Sources, Z-Pinches) **649**

Contributed Papers P-3
(Accelerator Related Topics, Electron Beam Applications, Ion Beam
Applications, PP-Applications, BDTT, Explosive Generators, Pulsed
Power Technology) **781**

Contributed Papers P-4
(Astrophysics, B-P Physics, ICF, Ion Beam Physics, Ion Diodes,
Ion Rings, Ion Sources, POS, SOS, Targets) **1027**

Panel Discussion
(G. Cooperstein, H. Bluhm, H. Karow, J. Quintenz,
D. Ryutov, G. Mesyats, V. Smirnov, R. Sudan) **1273**

Closing Ceremony
(K. Jungwirth, J. Shiloh, J. Quintenz) **1287**

BEAMS Statistics (J. Ullschmied) **1289**

From the BEAMS Pre-history **1290**

LIST OF PARTICIPANTS **1293**

AUTHOR INDEX

PAPER INDEX - Volume I

Invited Papers

O-0-1 • **Progress in Pulsed Power Fusion**, Quintenz, J.P., Adams, R.G., Bailley, J.E., Bloomquist, D.D., Chandler, G.A., Coats, R.S., Cook, D.L., Cuneo, M.E., Deeney, C., Derzon, M.S., Desjarlais, M.P., Dukart, R.J., Filuk, A.B., Haill, T.A., Hanson, D.L., Johnson, D.J., Kiefer, M.L., Leeper, R.J., Lockner, P.R., Marder, B.M., Matzen, M.K., Mc.Daniel, D.H., McGuire, E.J., Mehlhorn, T.A., Mendel, C.W., Menge, P.R., Renk, T.J., Rosenthal, S.E., Ruiz, C.L., Sanford, T.W.L., Seamen, J.F., Seidel, D.B., Slutz, S.A., Spielman, R.B., Stygar, W.A., Sweeney, M.A., Tisone, G.C. 1

O-0-2 • **High Power Explosive Magnetic Energy Sources for Thermonuclear and Physical Applications**, Chernyshev, V.K. 7

O-0-3 • **Status of Equation of State for Aluminium in the Light of Beam-Target Interaction Experiments at KALIF**, Goel, B., Hoebel, W., Marten, H., Vorobiev, O.Yu., Lomonosov, I.V., Gryaznov, V.K. 23

O-0-4 • **Pulse-Power Technology and Its Application at LBT, Nagaoka**, Yatsui, K., Masuda, W., Grigoriu, C., Masugata, K., Jiang, W., Imada, G., Imanari, K., Sonegawa, T., Chishiro, E. 27

O-1-1 • **Pulsed Power Driven Hohlraum Research at Sandia National Laboratories**, Leeper, R.J., Alberts, T.E., Allshouse, G.A., Aubert, J.H., Baca, P., Baca, P.M., Bailey, J.E., Barber, T.L., Breeze, S.P., Carlson, A.L., Chandler, G.A., Cook, D., Derzon, M.S., Douglas, M.R., Dukart, R.J., Fehl, D.L., Gilliland, T., Hebron, D.E., Hurst, M.J., Jobe, D.O., Johnson, D.J., Kellogg, J.W., Matzen, M.K., Martinez, C., Mehlhorn, T.A., McDaniel, D.H., McGuire, E.J., McGurn, J.S., McNamara, W.F., Moats, A.R., Muron, D.J., Nash, T.J., Noack, D.D., Olsen, R.W., Olson, R.E., Porter, J.L., Quintenz, J.P., Ruggles, L.E., Ruiz, C.L., Sawyer, P.S., Seamen, J.F., Spielman, R.B., Stark, M.A., Torres, J.A., VanDevalde, D.M., Vargas, M., Wenger, D.F., Zagar, D.M. 37

O-1-2 • **Determination of the Time Dependent Magnetic Field Distribution in Pulsed-Power Systems**, Maron, Y., Arad., R., Davara, G., Gregorian, L., Krasik, E.Ya., Kroupp, E., Sarfaty, M., Shpitalnik, R., Weingarten, A. 41

O-1-3 • **Spectroscopic Techniques for Measuring Ion Diode Space-Charge Distributions and Ion Source Properties**, Filuk, A.B., Bailey, J.E., Adams, R.G., Carlson, A.L., Ching, C.H., Desjarlais, M.P., Lake, P., McGuire, E.J., Mehlhorn, T.A., Pointon, T.D., Maron, Y., Stambulchik, E. 48

O-1-4 • **Recent Experiments towards Production and Diagnostics of Nitrogen Ion Beam for Medium-Mass Ion Beam ICF**, Kasuya, K., Yasuike, K., Miyamoto, S., Nakai, S., Kamiya, T., Funatsu, M., Okayama, H., Nishigori, K., Sunami, H., Wu, C., Ido, D., Adachi, T., Watanabe, M., Ebine, T., Niimi, G. 52

O-1-5 • **Status of Magnetically-Insulated Power Transmission Theory**, Mendel Jr., C.W. 56

O-1-6 • **The Proof-of-Concept Experiment for the Spiral Line Induction Accelerator**, Putnam, S.D., Bailey, V.L., Smith, J., Lidestri, J., Thomas, J., Lackner, H., Nishimoto, H. 60

O-1-7 • **The State of Development of an Intense Resonance Electron-Ion Accelerator Based on Doppler Effect**, Yegorov, A.M., Ivanov, B.I., Butenko, V.I., Ognivenko, V.V., Onishchenko, I.N., Prishchepov, V.P. 64

O-1-8 • **Ion Beam Neutralization with Ferroelectrically Generated Electron Beams**, Herleb, U., Riege, H. 68

O-2-1 • **Target Experiments with High-Power Proton Beams**, Baumung, K., Bluhm, H., Hoppe, P., Kanel, G.I., Razorenov, S.V., Rusch, D., Singer, J., Stoltz, O., Utkin, A.V. 72

O-2-2 • **Field-Reversed Ion Ring Configurations for Fusion**, Sudan, R.N., Greenly, J.B., Hammer, D.A., Omelchenko, Yu.A., Podulka, W.J. 81

O-2-3 • **Plasma Lens Focusing and Plasma Channel Transport for Heavy Ion Fusion**, Tauschwitz, A., Yu, S.S., Bangerter, R.O., Barnard, J.J., Eylon, S., Fessenden, T.J., Kwan, J., Leemans, W., Peters, C., Reginato, L., Sharp, W.M. 91

O-2-4 • **Formation of an Intense Proton Beam of Microsecond Duration**, Engelko, V., Giese, H., Schalk, S. 95

O-2-5 • **Uniform Current Density and Divergence Control in High-Power Extraction Ion Diodes**, Desjarlais, M.P., Coats, R.S., Lockner, T.R., Pointon, T.D., Johnson, D.J., Slutz, S.A., Lemke, R.W., Cuneo, M.E., Mehlhorn, T.A. 101

O-2-6 • **Anode Plasma Dynamics on an Extraction Applied-B Ion Diode: Effects on Divergence, Ion Species and Parasitic Load**, Greenly, J.B., Appartaim, R.K., Olson, J.C. 111

O-2-8 • **Light Ion Beam Transport Research at NRL**, Hinshelwood, D.D., Boller, J.R., Cooperstein, G., Fisher, R.C., Greenly, J.M., Jones, T.G., Mosher, D., Neri, J.M., Noonan, W.A., Oliver, B.V., Olson, C.J., Ottinger, P.F., Rose, D.V., Stephanakis, S.J., Welch, D.R., Young, F.C... 115

O-3-1 • **The DECADE Performance Assessment Program**, Weber, B.V., Ottinger, P.F., Commisso, R.J., Goyer, J.R., Kortbawi, D., Thompson, J., Rowley, J.E., Filios, P., Babineau, M.A. 121

O-3-2 • **Microsecond Plasma Opening Switch Experiments on GIT-4**, Bystrickii, V.M., Kim, A.A., Kokshenev, V.A., Koval'chuk, B.M., Lisitsyn, I.V., Sinebryukhov, A.A., Sinebryukhov, V.A. 127

O-3-4 • **A 3-MA Compact-Toroid-Plasma-Flow-Switched Plasma Focus Demonstration Experiment on SHIVA STAR**, Kiuttu, G.F., Graham, J.D., Degnan, J.H., Brzosko, J.S., Coffey, S.K., Gale, D.G., Holmberg, C.D., Kreh, B.B., Meyers, J.W., Outten, C.A., Ruden, E.L., Ware, K.D. 131

O-3-5 • **New Solid State Opening Switches for Repetitive Pulsed Power Technology**, Lyabutin, S.K., Mesyats, G.A., Rukin, S.N., Slovikovskii, B.G., Turov, A.M. 135

O-3-7 • **Beam Driven Transmutation Technology**, Bowman, C.D. 139

O-4-1 • **ANGARA-5-1 Program Development on Superfast Liner Implosion for ICF Physics Study and Basic Research**, Branitski, A.V., Grabovski, E.V., Fedulov, M.V., Frolov, I.N., Kuznetsov, D.V., Mishenski, V.O., Nedoseev, S.L., Oleinik, G.M., Otochin, A.A., Pichugin, V.E., Smirnov, V.P., Volkov, G.S., Zaitsev, V.I., Zajivikhin, V.V., Zakharov, S.V., Zurin, M.V., Velikhov, E.P., Dyabilin, K.E., Fortov, V.E., Lebedev, M.E., Danilenko, K.V., Zakharov, S.V., Gerusov, A.V., Razinkova, T.J., Sasorov, P.V., Nikiforov, A.F., Nikiforov, V.G., Krukovkii, A.Yu. 140

O-4-2 • **X-Ray Power Increase from Symmetrized Wire-Array Z-Pinch Implosions**, Sanford, T.W.L., Nash, T.J., Allshouse, G.O., Marder, B.M., Nash, T.J., Mock, R.C., Douglas, M.R., Spielman, R.B., Seamen, J.F., McGurn, J.S., Jobe, D., Gilliland, T.L., Vargas, M., Struve, K.W., Stygar, W.A., Hammer, J.H., DeGroot, J.S., Eddleman, J.L., Whitney, K.G., Thornhill, J.W., Pulsifer, P.E., Apruzese, J.P., Mosher, D., Peterson, D.L., Maron, Y. 146

O-4-3 • **PBFA Z: A 20-MA Z-Pinch Driver for Plasma Radiation Sources**, Spielman, R.B., Breeze, S.F., Deeney, C., Douglas, M.R., Long, F., Martin, T.H., Matzen, M.K., McDaniel, D.H., McGurn, J.S., Nash, T.J., Porter, J.L., Ruggles, L.E., Sanford, T.W.L., Seamen, J.F., Stygar, W.A., Torres, J.A., Zagar, D.M., Jobe, D.O., Peterson, D.L., Shoup, R.W., Struve, K.W., Mostrom, M., Corcoran, P., Smith, I. 150

O-4-4 • **S-300, New Pulsed Power Installation in Kurchatov Institute, Investigation of the Stable Liner Implosion**, Chernenko, A.S., Gorbulin, Yu.M., Kalinin, Yu.G., Kingsep, A.S., Koba, Yu.V., Korolev, V.D., Mizhiritskii, V.I., Rudakov, L.I. 154

O-4-5 • **Test of EMG-720 High Explosive Magneto-Cumulative Generator**, Popkov, N.F., Pikar', A.S., Ryaslov, E.A., Kargin, V.I., Mironychev, P.V., Nazarenko, S.T., Pavlov, V.S., Makartsev, G.F., Gurin, V.E., Korolev, P.V., Kataev, V.N., Nudikov, V.N., Russkov, A.S., Semyonov, S.I., Chernyshev, V.V., Vorontzov, V.I., Saratov, A.F., Logunov, G.I., Degnan, J.H., Kiuttu, G.F., Coffey, S.K., Summa, W.J., Ware, K.D. 158

O-4-6 • **Mechanism of Hot Spots Formation in Magnetic Z-Pinch**, Kubeš, P., Koláček, K., Krejčí, A., Kravárik, J., Paduch, M., Tomaszewski, K. 162

O-4-8 • **Ion Beams from High-Current PF Facilities**, Sadowski, M. 169

O-4-9 • **Pinches and Micropinches in the SPEED 2 Plasma Focus**, Roewekamp, P., Decker, G., Kies, W., Lucas, B., Schmitz, F., Ziethen, G., Simanovskii, D.M., Bobashev, S.V. 173

O-4-10• **Generation of Rotation and Shear Flow in an Imploding Liner**, Hammer, J.H., Ryutov, D.D. 177

O-5-1 • **First Results on the GOL-3-II Facility**, Agafonov, M.A., Arzhannikov, A.V., Astrelin, V.T., Bobylev, A.V., Burdakov, A.V., Chagin, M.N., Denisenko, P.V., Deulin, Yu.I., Khilchenko, A.D., Koidan, V.S., Konyukhov, V.V., Kvashnin, A.N., Lee, O.A., Makarov, A,G., Mekler, K.I., Melnikov, P.I., Nikolaev, V.S., Perin, S.S., Postupaev, V.V., Razilov, R.V., Rovenskikh, A.F., Semenov, E.P., Sinitsky, S.L., Tarasov, A.V., Vdovin, S.V., Zotkin, R.P. 181

O-5-2 • **Multi-Kiloampere, Electron-Beam Generation Using Metal Photo-Cathodes Driven by ArF and KrF Lasers**, Carlson, R.L., Moya, S.S., Ridlon, R.N., Seitz, G.J., Shurter, R.P. 187

O-5-3 • **Numerical Simulation of the High Explosive Magnetic Cumulative Generator EMG-720**, Deryugin, Yu.N., Zelenskii, D.K., Kazakova, I.F., Kargin, V.I., Mironychev, P.V., Pikar', A.S., Popkov, N.F., Ryaslov, E.A., Ryzhackova, E.G. 191

O-5-4 • **Studies of Collective Processes in REB-Plasma Systems**, Masuzaki, M. 195

O-6-1 • **New Developments in Relativistic Klystron Amplifiers**, Friedman, M., Colombant, D., Fernsler, R., Hubbard, R., Lampe, M., Serlin, V., Slinker, S. 205

O-6-2 • **Powerful FEM-Generator Driven by Microsecond Sheet Beam**, Agafonov, M.A., Arzhannikov, A.V., Ginzburg, N.S., Peskov, N.Yu., Sinitsky, S.L., Tarasov, A.V. 212

O-6-3 • **Pulse Shortening in High Power Microwave Sources**, Benford, J., Price, D., Benford, G. 216

O-6-4 • **Generation Efficiency and Radiation Stability of Multiwave Cerenkov Generators**, Deichuly, M.F., Koshelev, V.I., Petkun, A.A. 220

O-6-5 • **High-Power Broad-Band Tunable Microwave Oscillator, Driven by REB in Plasma**, Kuzelev, M.V., Loza, O.T., Ponomarev, A.V., Rukhadze, A.A., Strelkov, P.S., Shkvarunets, A.G., Ulyanov, D.K. 224

O-6-6 • **Beam-Plasma Generators of Stochastic Microwave Oscillations Using for Plasma Heating in Fusion and Plasma-Chemistry Devices and Ionospheric Investigations**, Mitin, L.A., Perevodchikov, V.I., Shapiro, A.L., Zavyalov, M.A., Bliokh, Yu.P., Fainberg, Ya.B. 228

O-6-7 • **Design and Cold-Testing of Two 100 MW Gyroklystron Amplifiers for Collider Applications**, Lawson, W., Cheng, J., Castle, M., Saraph, G., Anderson, J., Hogan, B., Granatstein, V.L., Reiser, M. 237

O-6-8 • **First Experimental Observation of Cyclotron Superradiance**, Ginzburg, N.S., Zotova, I.V., Sergeev, A.S., Konoplev, I.V., Shpak, V.G., Yalandin, M.I., Shunailov, S.A., Ulmaskulov, M.R. .. 241

O-6-9 • **High-Efficiency FEL with Bragg Resonator Driven by Linear Induction Accelerator**, Ginzburg, N.S., Kaminski, A.A., Kaminski, A.K., Peskov, N.Yu., Sedykh, S.N., Sergeev, A.P., Sergeev, A.S. 244

O-7-1 • **Plasma Technology for Treatment of Waste**, Cohn, D. 248

O-7-2 • **Pulsed Power Systems for Commercial Treatment of Materials Using Short Pulse, Intense Ion Beams**, Neau, E., Schneider, L.X., Reed, K.W. 254

O-7-3 • **Application of Low-Energy High-Current Electron Beams for Surface Modification of Materials**, Proskurovsky, D.I., Rotshtein, V.P., Ozur, G.E. 258

O-7-5 • **Progress Toward a Microsecond Duration, Repetitively Pulsed, Intense-Ion Beam**, Davis, H.A., Olson, J.C., Reass, W.A., Coates, D.M., Hunt, J.W., Schleinitz, H.M., Lovberg, R.H., Greenly, J.B. 262

O-7-6 • **Pulsed Electron Beam Facility GESA for Surface Treatment of Materials**, Mueller, G., Schumacher, G., Strauss, D., Engelko, V., Andreev, A., Komarov, O., Schegolikhin, N. 266

O-7-7 • **Laser Sources of Multiply Charged Heavy Ions**, Rohlena, K., Králíková, B., Krása, J., Láska, L., Mašek, K., Mocek, T., Pfeifer, M., Skála, J., Straka, P., Farny, J., Parys, P., Wolovski, J., Woryna, E., Mróz, W., Golubev, A., Sharkov, B., Shumshurov, A., Collier, J., Haseroth, H., Langbein, K. 270

O-7-8 • **Large-Scale Plasma Source Ion Implantation and Deposition Experiments**, Rej, D.J., Faehl, R.J., Henins, I., Mašek, K., Nastasi, M., Scheuer, J.T., Walter, K.C., Wood, B.P. 274

O-8-1 • **SYRINX - a Research Program for the Pulsed Power Radiation Facility**, Etlicher, B., Chuvatin, A.S., Choi, P., Frescaline, L., Aranchuk, L., Cassany, B., Avrillaud, G., Frolov, V., Rouille, C., Auvray, P., Semushin, S., Dumitrescu-Zoita, C., Leon, J.F., Kovack, F., Monjaux, P., Lassalle, F., Bayol, F., Johan, A., Kovalchuk, B., Kim, A. 275

O-8-2 • **Inductive-Energy Power Flow for X-Ray Sources**, Ware, K.D., Filios, P.G., Gullickson, R.L., Hebert, M.P., Rowley, J.E., Schneider, R.F., Summa, W.J., Vitkovitsky, I.M. 283

O-8-3 • **Excitation of Intense Shock Waves by Soft X-Radiation**, Branitski, A.V., Fortov, V.E., Danilenko, K.N., Dyabilin, K.S., Grabovskii, E.V., Vorobiev, O.Yu., Lebedev, M.E., Smirnov, V.P., Zakharov, A.E., Persiansev, I.V. 291

O-8-4 • **Plasma X-Ray Sources Powered by Megajoule Magnetocumulative Generators**, Popkov, N.F., Averchenkov, V.Ya., Pikar', A.S., Ryaslov, E.A., Kargin, V.I., Lazarev, S.A., Borovkov, V.V., Nazarenko, S.T., Makartsev, G.F. 295

O-8-5 • **RS-20-Type Repetitive Generator with Planar Configuration of Plasma Opening Switch**, Agalakov, V.P., Barinov, N.U., Belenki, G.S., Dolgachev, G.I., Zakatov, L.P., Qiu, A.C., Shen, Zh.K., Sun, F.J., Wang, X.H., Xu, R., Zeng, J.T. 300

O-8-6 • **Studies on Pulsed Hollow Cathode Capillary Discharges**, Choi, P., Dumitrescu-Zoita, C., Larour, J., Rous, J., Favre, M., Zambra, M., Moreno, J., Chuaqui, H., Wyndham, E., Wong, C.S. ... 304

O-8-7 • **Powerful Accelerators for Bremsstrahlung and Electron Beams Generation on the Basis of Inductive Energy-Storage Elements**, Diyankov, Vl.S., Kovalev, V.P., Kormilitsin, A.I., Lavrentiev, B.N. 308

Contributed Papers P-1

P-1-2 • **Experimental Study of Collective Processes in REB**, Bogdanov, L.Yu., Sominski, G.G. 318

P-1-4 • **Theoretical Aspects of the Electronical Devices Operating Due to Interaction between Annular Electron Beams and the Azimuthal Surface Waves**, Girka, V.O., Girka, I.O. 322

P-1-6 • **Spectrum of Plasma Electrons Observed in Strong Langmuir Turbulence Driven by REB**, Vyacheslavov, L.N., Gurko, V.F., Kandaurov, I.V., Kruglyakov, E.P., Meshkov, O.I., Sanin, A.L., Zharov, V.F. 326

P-1-9 • **Energy and Angular Spreads of Beam Electrons and Microwave Radiation Due to Strong Beam-Plasma Turbulence**, Koguchi, H., Masuzaki, M., Yoshikawa, M., Takahata, S., Toda, K., Ando, R., Kamada, K. 330

P-1-10 • **Macroscopic Symptoms of Collapse in REB-Plasma Interaction Experiments in Strong Magnetic Field**, Burmasov, V.S., Kandaurov, I.V., Kruglyakov, E.P., Meshkov, O.I., Sanin, A.L., Vyacheslavov, L.N. 334

P-1-12 • **Broadband mm Radiation from Beam Driven Strong Turbulence**, Masuzaki, M., Yoshida, H., Ando, R., Kamada, K., Ikeda, A., Lee, C.Y., Kawada, M. 338

P-1-16 • **Spectroscopic Measurements of Turbulent HF Fields at the REBEX Machine**, Ullschmied, J., Šimek, M., Koláček, K., Řípa, M. 342

P-1-19 • **High Power Microwave Emission and Diagnostics of Microsecond Electron Beams**, Gilgenbach, R., Hochman, J.M., Jayness, R., Rintamaki, J.I., Lau, Y.Y., Luginsland, J., Lash, J.S., Spencer, T.A. 346

P-1-20 • **Multi-Stage Autoacceleration of an Intense Relativistic Electron Beam**, Kamada, K., Hasegawa, D., Igarashi, H., Kusunoki, T., Lee, C.Y., Koguchi, H., Ando, R., Masuzaki, M. 350

P-1-21 • **Transport Control of Intense Electron Beam Using Undulator Guide**, Mori, M., Nishiyama, S., Kawata, S., Hanamori, S., Naito, K., Kato, S., Kawakita, Y., Hakoda, M. 354

P-1-23 • **Generation and Transportation of Low-Energy, High-Current Electron Beams**, Ozur, G.E., Proskurovsky, D.I., Nazarov, D.S. 358

P-1-25 • **Focusing and Guiding Intense Electron Beams by a Superconductor Tube**, Roth, P. 362

P-1-26 • **Reduction of Angular Spread at Nonadiabatic Electron Motion in Magnetically Insulated Diode**, Arzhannikov, A.V., Sinitsky, St.L. 366

P-1-27 • **Experimental Study of a High-Power TWT Electron Beam**, Arkhipov, A.V., Sominski, G.G. 370

P-1-28 • **Modelling of Electron Stream Discharge**, Vrba, P. 374

P-1-29 • **Chaotic Dynamics of Electron Beam with Virtual Cathode in the Bounded System**, Anfinogentov, V.G. 380

P-1-32 • **Effective Code for Numerical Simulation of the Helical Relativistic Electron Beam**, Lygin, V.K., Manuilov, V.N., Tsimring, Sh.E. 384

P-1-33 • **Electron, Ion, and Atomic Beams Interaction with Solid High-Molecular Dielectrics**, Milyavskii, V.V., Skvortsov, V.A. 388

P-1-39 • **An Experimental Study on Cyclotron-Cherenkov Radiation**, Lee, C.Y., Masuzaki, M., Yoshida, H., Toyosugi, N., Kamada, K., Ando, R. 392

P-1-40 • **Harmonic Millimeter Radiation from a Microwave FEL Amplifier**, Liu, Y.-H., Marshall, T.C. 396

P-1-43 • **High-Harmonic Relativistic Gyrotron as an Alternative to FEL**, Bratman, Vl.L., Kalynov, Yu.K., Kolganov, N.G., Manuilov, V.N., Ofitserov, M.M., Samsonov, S.V., Volkov, A.B. 400

P-1-45 • **Electromagnetic Properties of Corrugated and Smooth Waveguides Filled with Radially Inhomogeneous Plasma**, Shkvarunets, A., Kobayashi, S., Weaver, J., Carmel, Y., Rodgers, J., Granatstein, V.L., Destler, W.W. 404

P-1-46 • **A 2-Gigawatt, 1- Microsecond, Microwave Source**, Caryotakis, G., Jongewaard, E., Phillips, R., Scheitrum, G., Tantawi, S., Luhmann Jr., N.C. 405

P-1-53 • **High-Selectivity Resonator for Powerful Microwave Sources**, Abubakirov, E.B., Fuchs, M.I., Kovalev, N.F. 409

P-1-57 • **Experimental Investigations of Beam Potential Depression Effect in Gyrotrons**, Kuftin, A.N., Zapevalov, V.E. 413

P-1-58 • **Study of Space Charge Oscillations in Gyrotron**, Louksha, O.I., Sominski, G.G. 417

P-1-59 • **Co-operative High-Power Radiation of Two Beams at the Dual Vircator Complex**, Magda, I.I., Prokopenko, Yu.V. 421

P-1-61 • **Coaxial Plasma Filled Structures**, Onishchenko, I.N., Balakirev, V.A., Korostelev, A.M., Markov, P.I., Sidorenko, D.Yu., Sotnikov, G.V. 425

P-1-64 • **Beam-Plasma Processes Relevant to High-Power Wide-Band Plasma-Filled Microwave Sources**, Zavyalov, M.A., Mitin, L.A., Perevodchikov, V.I., Shapiro, A.L. 429

P-1-65 • **Dependence of Microwave Generation on Beam-Plasma System Length**, Krasilnikov, M.A., Kuzelev, M.V., Rukhadze, A.A. 430

P-1-66 • **Approaches to Achieving High Efficiency, Long Pulse, Vacuum Backward Wave Oscillator Operation**, Schamiloglu, E., Gahl, J.M., Grabowski, C.T., Abdallah, C.T. 433

P-1-67 • **Observations of Electron Bunching in the Micro-Pulse Electron Gun**, Shiloh, J., Mako, F., Peter, W., ... 437

P-1-68 • **Wide-Bandwidth High-Power Travelling Wave Tube Amplifiers: Comparison of Dielectric and Periodic Slow-Wave Structures**, Shlapakovskii, A. S. 441

P-1-69 • **Reflex Triode with Resonant Cavity as a Load for Inductive Storage**, Didenko, A.N., Gorbachev, K.V., Kogutnitskii, A.E., Mikhailov, V.M., Nesterov, E.V., Roschupkin, S.A., Shumilin, V.P., Stroganov, V.A. 445

P-1-70 • **Experimental Studies of a Generation Delay Time in Reflex Triode with Inductive Storage**, Didenko, A.N., Fortov, V.E., Gorbachev, K.V., Nesterov, E.V., Roschupkin, S.A., Shumilin, V.P., Stroganov, V.A. 449

P-1-73 • **Virtual Cathode Driven by Short Pulse Electron Gun**, Spassovski, I.P., Cho, S.O., Lee, J., Lee, B.-Ch., Jeong, Y.-U., Messina, G., Yovchev, I.G., Nikolov, N.A. 453

P-1-74 • **Accelerator for High Power Microwave Generation**, Chernykh, E.V., Fortov, V.E., Gorbachev, K.V., Nesterov, E.V., Stroganov, V.A., Shumilin, V.P. 457

P-1-75 • **Pulsed Power Microwave Calorimeter**, Lisichkin, A.L., Nesterov, E.V., Shumilin, V.P., Stroganov, V.A. 461

P-1-76 • **Air Breakdown Induced by a High-Power Short-Pulse Microwave**, Wakisaka, T., Yatsuzuka, M., Nobuhara, S. 465

P-1-77 • **Coaxial Vircator Source Development**, Woolverton, K., Kristiansen, M., Hatfield, L.L. 469

P-1-78 • **A 70 Ghz High-Power Repetitive Backward Oscillator with a Permanent-Magnet-Based Electron-Optical System**, Shpak, V.G., Shunailov, S.A., Ulmaskulov, M.R., Yalandin, M.I., Ermakov, A.E., Zhakov, S.V., Gass, V.G., Korobeinikov, A.Yu. 473

P-1-79 • **High Power Microwave Oscillator: Vircator-Klystron**, Jiang, W., Masugata, K., Yatsui, K. .. 477

P-1-80 • **Effect of Plasma Formation on Electron Pinching and Microwave Emission in Virtual Cathode Oscillator**, Yatsuzuka, M., Nakayama, M., Nobuhara, S., Young, D., Ishihara, O. 481

P-1-84 • **Formation and Diagnostic of Helical Gyrotron Electron Beams**, Andronov, A.N., Ilyin, V.N., Khmara, V.A., Kuftin, A.N., Lygin, V.K., Louksha, O.I., Manuilov, V.N., Postnikova, A.S., Robozerov, S.V., Sominsky, G.G., Tsimring, Sh.E., Zapevalov, V.E. 485

P-1-85 • **Multi-Frequency Microwave Pulses Production in a Vircator**, Zherlitsyn, A.G., Lyakshev, A.N., Melnikov, G.V. 489

P-1-86 • **Research of the Generation of Microsecond Microwave Irradiation in Vircator**, Zherlitsyn, A.G., Kotlyarevskii, G.I., Lyakshev, A.N., Tstvetkov, V.I. 492

P-1-87 • **Generation of Ultrashort Microwave Pulses Based on Cyclotron Superradiance Effect**, Ginzburg, N.S., Zotova, I.V., Sergeev, A.S. 496

Contributed Papers P-2

P-2-1 • **Dynamics of Capillary Discharge Driven by Fast Pulse Power Generator**, Hosokai, T., Nakajima, M., Aoki, T., Horioka, K., Ogawa, M. 501

P-2-4 • **Time Resolved Observations of Plasma Evolution in the Hollow Cathode Region of a Transient Hollow Discharge**, Favre, M., Zambra, M., Moreno, J., Chuaqui, F., Wyndham, E., Choi, P. 505

P-2-5 • **Improvement on the Physical Description of the Boundary Conditions between the Hollow Cathode Region and the A-K Gap in a Transient Hollow Cathode Discharge**, Kaufman, Y., Choi, P. 509

P-2-6 • **Investigation of Ectons Dynamics in Laser-Induced Breakdowns**, Skvortsov, V.A., Vogel, N.I. 513

P-2-7 • **The Generation of High-Power Charge Particle Micro Beams and Its Interaction with Condensed Matter**, Vogel, N.I., Skvortsov, V.A. 518

P-2-8 • **The Rayleigh-Taylor Instability and the K-Shell Radiation Yield for Imploding Liners**, Baksht, R.B., Datsko, I.M., Labetsky, A.Yu., Rousskikh, A.G., Fedyunin, A.V. 522

P-2-9 • **Investigation of Energy and Current Concentration in Composite Z-Pinch through Its Soft X-Ray Emission on ANGARA-5-1**, Branitski, A.V., Grabovski, E.V., Zakharov, S.V., Zurin, M.V., Oleinik, G.M., Smirnov, V.P., Frolov, I.N., Borisov, V.V., Slavnov, Yu.K., Usov, Yu.K. 526

P-2-10 • **Measurements of Soft X-Ray Power and Spectral Features on ANGARA-5-1**, Branitski, A.V., Oleinik, G.M. 530

P-2-11 • **Investigation of Layered Z-Pinches on ANGARA-5-1**, Branitski, A.V., Grabovski, E.V., Zakharov, S.V., Zurin, M.V., Nedoseev, S.L., Oleinik, G.M., Smirnov, V.P., Frolov, I.N. 548

P-2-12 • **Some Features of Liners Convergence Accelerated with the Help of Powerful EMGs**, Grinevich, B.E., Chernyshev, V.K., Buzin, V.N., Petrukhin, A.A., Zharinov, E.I. 538

P-2-17 • **Investigation of Superfast Composite Pinch with Unstable External Liner on ANGARA-5-1**, Branitski, A.V., Grabovski, E.V., Fedulov, M.V., Frolov, I.N., Kuznetsov, D.V., Medovshikov, S.F., Mishenski, V.O., Nedoseev, S.L., Oleinik, G.M., Pichugin, V.E., Sasorov, P.V., Smirnov, V.P., Zaitsev, V.I., Zakharov, S.V., Zurin, M.V. 542

P-2-18 • **New Concentrator of 5 MA on ANGARA-5-1 for Liner Implosion**, Grabovski, E.V., Nedoseev, S.L., Oleinik, G.M., Pichugin, V.E., Smirnov, V.P., Zajivikhin, V.V. 546

P-2-19 • **Liner-Converter Experiment on AMBIORIX**, Gasque, A.M., Grua, P., Romary, P., Sajer, J.M., Friart, D., Zenhter, P., Jacquet, L., Pornet, J., Dan'ko, S., Gorbulin, Yu., Kalinin, Yu.G., Kingsep, A. 550

P-2-20 • **Generation of Rotation and Shear Flow in an Imploding Liner**, Hammer, J.H., Ryutov, D.D. 554

P-2-25 • **Liner-Wall Interaction During the Magnetic Implosion**, Chernyshev, V.K., Zharinov, E.I., Mokhov, V.N., Garanin, S.F., Grinevich, B.Ye., Kudelkin, I.D., Buzin, V.N., Ionov, A.I., Sokolova, O.V., Zimakov, S.D., Yegorychev, B.T., Yerichev, V.N., Shaidullin, V.Sh., Degnan, J.H., Hussey, T.W., Kiuttu, G.F. 558

P-2-28 • **Electrical Characteristics of a Small Plasma Focus Device**, Choi, P., Favre, M., Silva, P., Chuaqui, H., Wyndham, E. 566

P-2-29 • **Studies of Current Sheath Evolution in a Small Plasma Focus Device**, Silva, P., Favre, M., Chuaqui, H., Wyndham, E., Choi, P. 570

P-2-30 • **Characteristics of a Small Plasma Focus Device**, Favre, M., Silva, P., Chuaqui, H., Wyndham, E., Choi, P., Dumitrescu-Zoita, C. 574

P-2-32 • **Influence of Stub Anode on Plasma Motion and Neutron Yield in a 18-kJ Plasma Focus**, Lu, M., Yang, T., Han, M., Yang, S. 578

P-2-33 • **Computer Simulation of a Plasma Focus Device Driven by a Magnetic Pulser**, Georgescu, N., Zoita, V., Larour, J.. 582

P-2-34 • **Highly Ionized Copper Contribution to the Soft X-Ray Emission in a Plasma Focus Device**, Zoita, V., Patran, A., Larour, J. 587

P-2-35 • **Magnetic Pulse Compression Circuits for Plasma Devices**, Georgescu, N., Zoita, V., Presura, R. 591

P-2-36 • **Soft X-Ray Spectroscopic Investigation a of a Plasma Focus Operated in Pure Neon**, Presura, R., Zoita, V., Paraschiv, I. 595

P-2-37 • **Working Gas Effects on the X-Ray Emission of a Plasma Focus Device**, Cengher, M., Presura, R., Zoita, V. 599

P-2-38 • **Pseudospark Switches (PSS) for Pulsed Power Applications**, Heine, F., Prucker, U., Frank, K., Goertler, A., Schwandner, A., Tkotz, R., Hoffman, D.H.H., Christiansen, J. 603

P-2-41 • **Nanosecond Breakdown of Liquid Dielectrics**, Mankowski, J., Kristiansen, M., Hatfield, L. ... 607

P-2-42 • **The EMP Excitation of Radiation by the Pulsed Relativistic Electron Beam**, Balakirev, V.A., Sidel'nikov, G.L. 611

P-2-43 • **High Power Pulsed Neutron Source for Electronuclear Installation**, Korenev, S.A., Puzynin, I.V., Samoilov, V.N., Sissakian, A.N. 615

P-2-44 • **Intensive Neutron Source Based on Powerful Electron Linear Accelerator LIA-30 and Pulsed Nuclear Reactor FR-1**, Bossamykin, V.S., Koshelev, A.S., Gerasimov, A.I., Gordeev, V.S., Grishin, A.V., Averchenkov, V.Ya., Lazarev, S.A., Maslov, G.N., Odintsov, Yu.M. 619

P-2-45 • **Monte Carlo Simulation of High-Flux 14 MeV Neutron Source Based on Muon Catalyzed Fusion Using a High-Power 50 MW Deuteron Beam**, Vecchi, M., Karmanov, F.I., Latysheva, L.N., Pshenichnov, I.A. 623

P-2-47 • **The NIKE Electron Beam-Pumped KrF Laser Amplifiers**, Serlin, V., Sethian, J.D., Pawley, C.J., Obenschein, S.P., Gerber, K.A., Deniz, A.V., Lehecka, T., Webster, W. 627

P-2-48 • **AIRIX at CESTA**, Anthouard, P., Bardy, J., Bonnafond, C., Delsart, P., Devin, A., Eyharts, P., Eyl, P., Guilhelm, D., Labrouche, J., Launspach, J., De Mascureau, J., Merle, E., Picon, J.C., Roques, A., Thevenot, M., Villate, D., Voisin, L. 628

P-2-50 • **Space Power Distribution of Soft X-Ray Source ANGARA-5-1**, Dyabilin, K.S., Fortov, V.E., Grabovskii, E.V., Lebedev, M.E., Smirnov, V.P. 632

P-2-51 • **Dielectric-Filled Radiofrequency Linacs**, Faehl, R.J., Keinigs, R.K., Pogue, E.W. 636

P-2-52 • **Operation of LIA-30 Linear Induction Accelerator in the Mode of Generation of Two Bremsstrahlung Pulses**, Bossamykin, V.S., Gerasimov, A.I., Gordeev, V.S., Grishin, A.V., Gritsina, V.P., Tarasov, A.D., Fedotkin, A.S., Lazarev, S.A., Averchenkov, V.Ya. 640

P-2-53 • **X-Ray Radiation Source Based on a Plasma Filled Diode**, Popkov, N.F., Kargin, V.I., Ryaslov, E.A., Pikar', A.S. 644

PAPER INDEX - Volume II

Contributed Papers P-2 - continuation from Volume I

P-2-54 • **Ironless Betatrons - Short Radiation Pulse Generators for Roentgenography of Fast-Going Processes**, Pavlovskii, A.P., Zenkov, D.I., Kuropatkin, Yu.P., Mironenko, V.D., Suvorov, V.N. ... 649

P-2-55 • **Determination of the Effective Impulse Time Duration of Interaction of Soft X-Radiation with Matter**, Dyabilin, K.S., Fortov, V.E., Grabovskii, E.V., Lebedev, M.E., Smirnov, V.P. 653

P-2-56 • **"INTERRAD" - Inductive Terawatt X-Ray Generator (project)**, Popkov, N.F., Pikar', A.S., Kargin, V.I., Ryaslov, E.A., Lyubomirskii, A.G. 656

P-2-57 • **New Bifocal Pinch Experiment SPEED-3**, Raacke, J., Berntien, U., Decker, G., Kies, W., Roewekamp. P. 659

P-2-58 • **Plasma Flow Discharge Researches at the PIRIT-2000 Facility**, Popkov, N.F., Ryaslov, E.A., Kargin, V.I., Pikar', A.S., Vorontsov, V.I., Kotel'nikov, D.V., Melkozerov, A.V. 663

P-2-59 • **A 10 TW Pulsed Energy Complex 'PIRIT-2000' for Investigation of Short-Wave Radiation**, Popkov, N.F., Ryaslov, E.A., Kargin, V.I., Pikar', A.S., Vorontsov, V.I., Kotel'nikov, D.V., Melkozerov, A.V. 667

P-2-62 • **Focusing of Megaampere Electron Beam in Gas Cell for Production of Flash X-Ray Source**, Zinchenko, Vl., Chlenov, A.M., Shijan, V.D. 671

P-2-63 • **Optimization of the Linear Induction Accelerator Construction for Maximizing the Bremsstrahlung Output**, Zinchenko, Vl., Toulisov, E.V., Chlenov, A.M., Shijan, V.D. 675

P-2-64 • **Space and Time Resolved Observations of Hot Spots Dynamics in a Vacuum Spark Discharge**, Chuaqui, H., Favre, M., Saavedra, R., Wyndham, E., Choi, P., Dumitrescu-Zoita, C., Soto, L. 679

P-2-65 • **Imaging of Exploding Wire Plasmas by High-Luminosity Monochromatic X-Ray Backlighting Using an X-Pinch Radiation Source**, Pikuz, S.A., Shelkovenko, T.A., Romanova, V.M., Hammer, D.A., Faenov, A.Ya., Pikuz, T.A. 683

P-2-90 • **Electron Beam Effects on the Spectroscopy of Satellite Lines in Aluminum X-Pinch Experiments**, Abdallah Jr., J., Faenov, A.Yu., Hammer, D.A., Pikuz, S.A., Csanak, G., Clark, R.E.H., Romanova, V.M., Shelkovenko, T.A. 687

P-2-66 • **Research of Generation Mechanism of Plasma Points in Z-Pinch**, Afonin, V.I., Garafov, A.M., Kovalev, V.P., Lazarchuk, V.P., Ostashev, V.I., Petrov, S.I., Potarov, A.V. 691

P-2-67 • **On the Ionization-Temperature Instability Role in Z-Pinch Hot Spots Generating**, Afonin, V.I., Diyankov, O.V., Glazyrin, I.V., Koshelev, S.V. 697

P-2-92 • **About Possible Mechanism of Generation of Plasma Points in Plasma of Multicharged Ions of Fast Z-Pinch**, Afonin, V.I., Voronov, B.F., Zakharov, A.E., Murugov, V.M., Ponomarev, S.V., Senikh, A.V. 701

P-2-68 • **Supression of Rayleigh-Taylor Instability in Z-Pinch Loads with Tailored Density Profiles**, Cochran, F.L., Velikovich, A.L., Davis, J. 705

P-2-69 • **Limitations on the K-Shell X-Ray Conversion Efficiency of a Krypton Z-Pinch Plasma**, Davis, J., Giuliani Jr., J.L., Rogerson, J., Thornhill, J.W. 709

P-2-70 • **2.5 D Numerical Method for MHD Equation with Magnetic Diffusion in Arbitrary Moving Coordinate System for Z-Pinch Plasma Simulation**, Diyankov, O.V., Glazyrin, I.V., Koshelev, S.V. 713

P-2-71 • **Numerical Modelling of MHD Instabilities in Z-Pinch Hot Spot**, Glazyrin, I.V., Diyankov, O.V., Karlykhanov, N.G., Koshelev, S.V. 717

P-2-72 • **Sheath Broadening in Imploding Z-Pinches Due to Large-Bandwidth Rayleigh-Taylor Instability**, Hammer, J.H., Eddleman, J.L., Tabak, M., Toor, A., Zimmerman, G.B., De Groot, J.S. 721

P-2-73 • **Numerical Analysis of Cold Core Formation During Wire Electroexplosion**, Karlykhanov, N.G., Glazyrin, I.V., Diyankov, O.V. 725

P-2-74 • **On the Necessary Modification of Z-Pinch MHD-Models**, Kingsep, A., Rudakov, L. 729

P-2-75 • **X-ray Spectroscopic Characterization of Hot Spots in Neon Z-Pinch**, Renner, O., Krouský, E., Krejčí, A., Pfeifer, M., Foerster, E. 733

P-2-76 • **Diagnostics of Low Energy Carbon Fibre Z-Pinch**, Kubeš, P., Kravárik, J., Skladnik-Sadowska, E., Baranowski, J., Paduch, M., Tomaszewski, K., Gogolewski, P. 737

P-2-77 • **Concept and Elementary Theory of a Sandwich Liner**, Linhart, J.G., Chittenden, J.P. 741

P-2-78 • **Optimized Debris Stoppers for Z-Pinches**, Gondarenko, N.A., Pereira, N.R. 745

P-2-79 • **PRS and POS/PRS Coupling Experiments on HAWK**, Peterson, G.G., Apruzese, J.P., Commisso, R.J., Fisher, A., Kellogg, J.C., Mosher, D., Stephanakis, S.J., Thornhill, J.W., Weber, B.V., Young, F.C. 749

P-2-80 • **X-Ray Emission from a High-Atomic-Number Z-Pinch Plasma Created from Compact Wire Arrays**, Sanford, T.W.L., Mosher, D., De Groot, J.S., Hammer, J.H., Marder, B.M., Maxon, S., Nash, T.J., Spielman, R.B., Springer, P.T., Struve, K.W., Thoe, R.S., Welch, D.R., Alley, W.E., Bruns, C., Eddleman, J.L., Emic, J., Gilliland, T.L., Hernandez, J., Jobe, D., McGurn, J.S., Mock, R.C., Seamen, J.F., Vargas, M., Zimmerman, G.B. 753

P-2-81 • **Numerical Simulation of PRS Yields for a Pulsed Power DECADE-QUAD Generator**, Giuliani, J.L., Schneider, R.(2), Rogerson, J., Davis, J. 757

P-2-82 • **Optimization of Gas Target Production for Z-Pinch Implosions**, Semushin, S., Etlicher, B., Rouille, C. 758

P-2-83 • **Space and Time Resolved Observations of Plasma Dynamics in a Compressional Gas-Embedded Z-Pinch**, Soto, L., Chuaqui, H., Favre, M., Saavedra, R., Wyndham, E., Aliaga-Rossel, R., Mitchell, I. 762

P-2-84 • **Computer Modelling of a Small Neon Gas-Puff Pinch**, Ullschmied, J. 766

P-2-86 • **Hydrosimulations of Z-Pinch**, Benattar, R., Ney, P. 771

P-2-87 • **Numerical Modelling of High-Temperature Plasma in a Strong Magnetic Field at RFNC-VNIIEF**, Diyankov, O.V., Glazyrin, I.V., Karlykhanov, N.G., Zubov, A.D. 775

P-2-88 • **Current Instability of "Snow Plough"**, Rudakov, L.I., Sevastianov, A.A. 779

P-2-89 • **Radiation from Turbulent Intense Z-Pinches**, Rudakov, L.I., Sudan, R.N. 780

Contributed Papers P-3

P-3-2 • **Particle Acceleration by Inverse-Weibel Instability**, Kawata, S. 781

P-3-3 • **High Current Pulsed Ion Inductor Accelerator for Destruction of Radioactive Wastes**, Korenev, S.A., Puzynin, I.V., Samoilov, V.N., Sissakian, A.N. 785

P-3-4 • **Processes in a Dense Long-Pulse Electron Beam Focused on a Solid Target**, Arkhipov, A.V., Sominski, G.G. 789

P-3-6 • **Application of an Intense Long Pulse Electron Beam for Investigation of ITER Divertor Material Erosion**, Engelko, V., Andreev, A., Komarov, O., Kovalev, V., Lyublin, B. 793

P-3-7 • **Electron-Beam Sustained Glow Discharge in a N2+CO Gas Mixture at Cryogenic Temperature**, Azharonok, V.V., Filatova, I.I., Chubrik, N.I., Shimanovich, V.D., Gurashvili, V.A., Kuzmin, V.N., Turkin, N.G., Vaselenok, A.A. 797

P-3-8 • **Processing of Metals by Powerful Electron Beams**, Gofman, Yu.I. 801

P-3-9 • **Use of Charged Particles Beams for Research of Mechanical Behaviour of Thermonuclear Reactor First Wall Candidate-Materials**, Gofman, Yu.I. 805

P-3-11 • **Modification of Material Surfaces by the Pulsed Electron Beam Facility "GESA"**, Mueller, G., Schumacher, G., Strauss, D., Engelko, V., Andreev, A., Kovalev, V. 809

P-3-12 • **Modification of Titanium Alloy Parts Properties by Intensive Current Electron Beam**, Nochovnaya, N.A., Shulov, V.A., Proskurovsky, D.I., Rothstein, V.P. 813

P-3-17 • **High Power Pulse Electron Beam Modification and Ion Implantation of Hg(1-X)CdXTe Crystals**, Voitsekhovskii, A.V., Remnev, G.E., Opekunov, M.S., Kokhanenko, A.P., Korotaev, A.G., Denisov, Yu.A., Oucherenko, D.A. 817

P-3-18 • **Influence of Pulsed Electron and Ion Beams of Energy on the Structural and Mechanical Properties of Metals**, Romanov, I.G., Tsareva, I.N., Romanova, G.M. 821

P-3-19 • **SO2, NOx and H2S Oxidation by Simultaneous Application of Electron Beam and Electric Field in Humid Air**, Salnikov, L.I., Nichipor, H., Radjuk, E., Chmielewski, A.G., Zimek, Z. 824

P-3-21 • **Research of Action of a Pulsing Frequent Electron Beam on Micro-organisms in Water Solutions**, Sokovnin, S.Yu., Kotov, Yu.A., Mesyats, G.A. 828

P-3-22 • **About Transport Current Change in High-Temperature Superconducting Real Wires and Tapes as a Result of Electron Irradiation**, Davlatjan, T.A., Kalachnikov, V.V., Kruglov, V.S., Tokarev, A.S. 832

P-3-23 • **Influence of Electron Irradiation on Current Distribution Process in Granulated High-Temperature Superconducting Real Wires and Tapes**, Davlatjan, T.A., Kalachnikov, V.V., Kruglov, V.S., Tokarev, A.S. 836

P-3-92 • **Mass-Transport in W-Cu System under High Energy Electron Irradiation**, Bondarenko, G.G., Tikhonov, A.N., Shlenov, Yu.V., Yakunkin, M.M. 840

P-3-25 • **Influence of Carbon and Nitrogen Ions on the Structure and Properties of Carbon Fibers**, Gavrilov, N.W., Emlin, D.R., Ligachev, A.E., Ligacheva, E.A., Nochovnaya, N.A., Karpova, I.G. . 844

P-3-26 • **Metal Surface Characterization by Intense Pulsed Ion Beam Irradiation**, Hashimoto, Y., Yatsuzuka, M., Uchida, H., Yamasaki, T. 848

P-3-28 • **Ion Beam Treatment of PE and PTFE and their Adhesion Abilities**, Klyachkin, Yu., Kondyurin, A. 852

P-3-29 • **Structure of Polymer Surface after Pulse Ion Beam Treatment**, Klyachkin, Yu., Kondyurin, A., Tereshatova, E., Yakusheva, D. 853

P-3-31 • **The Use of Pulsed Power Ion/Electron Beams for Studying of Units of Electronuclear Reactor**, Korenev, S.A., Korenev, A.S., Puzynin, I.V., Samoilov, V.N., Sissakian, A.N. 854

P-3-33 • **Pulsed Metal-Ion Beams for Modifications of Solids**, Langner, J., Piekoszewski, J., Stanislawski, J. 860

P-3-37 • **Chain of Phase Transitions in Metals Subjected to Heavy Inert Gas Ion Bombardment**, Panesh, A.M., Lozovskii, A.D. 864

P-3-39 • **The Nuclear Interaction Analysis Methods for Diagnostics of High Power Ion Beam Technologies**, Ryzhkov, V.A., Grushin, I.I., Remnev, G.E. 869

P-3-40 • **The Deposition of Thin Metal Films at High-Intensity Pulsed-Ion-Beam Influence on the Metals**, Remnev, G.E., Zakoutaev, A.N., Grushin, I.I., Matvienko, V.M., Potyomkin, A.V., Ryzhkov, V.A., Ivanov, Yu.F., Chernikov, E.V. 873

P-3-41 • **The Application of High Power Ion Beams in Aircraft Engine Building for Recontruction of Refractory Alloy Parts**, Shulov, V.A., Nochovnaya, N.A., Remnev, G.E. 878

P-3-42 • **Modelling of Ion Beam Surface Treatment**, Stinnett, R.W., Maenchen, J.E, Renk, T.J., Struve, K.W., Campbell, M.M. 882

P-3-43 • **Short-Pulsed-Electric Degradation of Aquaeous Organics**, Bystritskii, Vit.M., Gonzales, A., Olson, T., Puchkarev, V., Rosocha, l., Wessel, F., Yankelevich, Y. 886

P-3-44 • **Thermal Imaging Experiment on ANACONDA Ion Beam Generator**, Jiang, W., Yatsui, K., Olson, C.J., Davis, H.A. 890

P-3-45 • **Preparation of Thin Films by Ablation with the ANACONDA Ion Beam Generator**, Yatsui, K., Jiang, W., Davis, H.A., Olson, C.J., Waganaar, W.J., Rej, D. 894

P-3-46 • **Study of YBCO Thin Films Deposited by Intense Pulsed Light Ion Beam Evaporation**, Grigoriu, C., Chamdani, E.P.A., Miu, D., Masugata, K., Yatsui, K. 898

P-3-93 • **High Power Ion Beam Influence to Stainless Steels**, Remnev, G.E., Struts, V.K. 902

P-3-47 • **Energy Characteristics of the Process of Air Scrubbing from Hydrocarbon Contaminants in a Barrier-Discharge Reactor**, Bugaev, S.P., Kuvshinov, V.A., Sochugov, N.S., Khryapov, P.A. 905

P-3-48 • **Compact Repetitive Generators for Medical X-Ray Diagnostics**, Filatov, A.L., Korzhenevskii, S.R., Kotov, Yu.A., Mesyats, G.A., Motovilov, V.A., Scotnikov, V.A. 909

P-3-50 • **Compact High-Current, Subnanosecond Electron Accelerator**, Shpak, V.G., Shunailov, S.A., Ulmaskulov, M.R., Yalandin, M.I., Pegel, I.V., Tarakanov, V.P. 913

P-3-51 • **Nuclear Reactions Cross Section Measurement Using Z-Pinch Technology**, Bulgakov, T., Bystritskii, Vit.M., Mesyats, G.A., Sinebryukhov, V.A., Sinebryukhov, A.A., Bystrickii, V., Grebenyuk, V., Parzhitskii, S., Sabirov, B., Stolupin, V., Luchinsky, A., Chaikovski, S., Mahrin, V., Ratakhin, N., Sorokin, S., Gula, A., Filipowicz, M., Wozniak, J. 917

P-3-52 • **About Using of Ion Accelerators in Accelerator Driven Systems**, Chigrinov, S., Kievitskaya, A., Petlytski, V., Rutkovskaia, K. 921

P-3-58 • **The Experimental Investigation of Explosive Opening Switch**, Zhang, J., Zhong, H., Li, Ch., Liu, Y., Cheng, D., Peng, X. 924

P-3-59 • **High Power, Repetitive Stacked Blumlein Pulse Generators**, Davanloo, F., Borovina, D.L., Korioth, J.L., Krause, R.K., Collins, C.B., Agee, F.J., Kingsley, L.E. 928

P-3-62 • **Inductive Line Energy Storage Generator**, Choi, P. 932

P-3-66 • **Schemes of High-Power Pulsed Generators with Inductive Storages on Stepped Lines**, Gordeev, V.S., Bossamykin, V.S. 938

P-3-67 • **The Nanosecond Generator RG-1 with Near-Rectangular Pulse**, Bulan, V.V., Grabovski, E.V., Gribov, A.N., Luzhnov, V.G. 942

P-3-68 • **Protection of Control and Monitoring Equipment from Electromagnetic Noise in the 67 MJ, 50 kV Capacitor Bank**, Galakhov, I.V., Gasheev, A.S., Grusin, I.A., Gudov, S.N., Kuz'michev, Yu.P., Murugov, V.M., Osin, V.A., Pankratov, V.I., Pegoev, I.N. 946

P-3-69 • **Diagnostics of the 67 MJ, 50 kV Pulsed Power Capacitor Bank**, Galakhov, I.V., Gasheev, A.S., Grusin, I.A., Gudov, S.N., Murugov, V.M., Osin, V.A., Pankratov, V.I., Pegoev, I.N. 950

P-3-70 • **PFN-Marx Pulsers for HPM Testing Application**, Kekez, M.M. 954

P-3-71 • **Controlled Multiple Channel Switch**, Kormilitsyn, A.I., Diyankov, V.S. 958

P-3-72 • **Energy Concentration on S-300 Pulsed Power Generator**, Bakshaev, Yu.L., Chernenko, A.S., Korolev, V.D., Mishiritskiy, V.I., Zazhivikhin, V.V. 962

P-3-73 • **High-Voltage Nanosecond Generator with Pulse Repetition Rate of 1,000 p.p.s.**, Gubanov, V.P., Korovin, S.D., Stepchenko, A.S. 965

P-3-74 • **High-Voltage Many-Pulses Generator with Inductive Energy Store and Fuse**, Kovalev, V.P., Diyankov, V.S., Kormilitsyn, A.I., Lavrentyev, B.N. 969

P-3-75 • **Functioning of High-Tc Bulk Superconductor Lenses (Supertrons) for Intense Electron Beams**, Matsuzawa, H., Matsushita, A., Ueda, Y., Matsubara, H., Suganomata, S. 973

P-3-76 • **Synchronization of 67 MJ, 50 kV Pulsed Power Capacitor Banks Operation**, Besuglov, V.G., Galakhov, I.V., Gasheev, A.S., Grusin, I.A., Gudov, S.N., Kirillov, G.A., Murugov, V.M., Osin, V.A., Petrakov, V.N. 977

P-4-82 • **High-Power Semiconductor RSD-Based Switch**, Bezuglov, V.G., Galakhov, I.V., Grusin, I.A., Zolotovsky, V.I., Gudov, S.N., Logutenko, S.L., Murugov, V.M., Osin, V.A., Petrakov, V.N., Grekhov, I.V., Korotkov, S.V., Kovtun, V.I., Martynenko, V.A., Chumakov, G.D. 981

P-3-77 • **Nanosecond Electron Beams Compact Generator**, Konkin, D.V., Nagovitsin, A.Yu., Pavlov, S.S., Popkov, N.F. 985

P-3-79 • **Design and Analysis of the PBFA-Z Vacuum Insulator Stack**, Shoup, R.W., Long, F., Martin, T.H., Stygar, W.A., Ives, H., Spielman, R.B., Struve, K.W., Mostrom, M., Corcoran, P., Smith, I. 989

P-3-80 • **Characterization of Diamond Film and Bare Metal Photocathodes as a Function of Temperature and Surface Preparation**, Shurter, R.P., Moir, D.C., Devlin, D.J. 993

P-3-81 • **Development Status of Triggered Vacuum Switches at All-Russian Electrotechnical Institute and Prospects of Its Applications**, Alfverov, D.F., Vozdvijenskii, V.A., Sidorov, V.A. . 999

P-3-82 • **DECADE Design and Testing Status**, Sincerny, P., Childers, K., Goyer, J., Kortbawi, D., Roth, I., Stallings, C., Dempsey, J., Schlitt, L. 1003

P-3-83 • **Explosive Opening Switches with Controlled Time of Current Rising in the Load**, Chernyshev, V.K., Volkov, G.I., Ivanov, V.A., Pak, S.V., Skobelev, A.N. 1008

P-3-84 • **Development of Highly Repetitive Pulse Power System Using Amorphous Metallic Cores**, Masugata, K., Yatsui, K. 1010

P-3-85 • **Printed Board Dipole Trim Magnet Design for 20 MeV LIA**, Liu, Ch., Zhu, W., Zhang, K., Zhang, W., Yu, H. 1014

P-3-86 • **Halo Formation in RMS Matched Intense Ion Beams**, Chen, Ch., Fink, Y., Davidson, R.C., Qian, Q. 1018

P-3-87 • **Equivalent Circuit Modeling of Space Charge Dominated Magnetically Insulated Transmission Lines**, Hiraoka, K., Nakajima, M., Horioka, K. 1022

Contributed Papers P-4

P-4-1 • **High-Voltage Space Tether for Particle Scattering in Earth's Radiation Belts**, Danilov, V.V., Mirnov, V.V., Ucer, D. 1027

P-4-2 • **Electron Beams in Large Coronal Loops**, Karlický, M., Aurass, H., Mann, G. 1031

P-4-4 • **Relativistic Electron Beam Dynamics in the Pulsar Magnetosphere**, Chedia, O.V., Kahniashvili, T.A., Machabeli, G.Z., Nanobashvili, I.S. 1035

P-4-6 • **Energetic High Current Density Electron/Ion Beam Generation in Plasma Opening Switches**, Krasik, Ya.E., Arad, R., Weingarten, A., Maron, Y. 1039

P-4-7 • **CO Laser Interferometer for REB-Plasma Experiments**, Burmasov, V.S., Kruglyakov, E.P. .. 1046

P-4-9 • **Measurements of the Initial Density Distribution of Gas Puff Liners by Using Rayleigh Scattering**, Kalinin, Yu.G., Shashkov, A.Yu. 1050

P-4-10 • **Refractive Index Gradient Diagnostics: Analysis of Different Optical Systems and Application to the COBRA Ion Diode**, Knyazev, B.A., Greenly, J.B., Hammer, D.A., Krastelev, E.G., Cuneo, M.E. 1054

P-4-11 • **Spectroscopic Determination of the Magnetic Field Distribution in a Gas-Puff Z-Pinch Plasma**, Gregorian, L., Davara, G., Kroupp, E., Maron, Y. 1058

P-4-12 • **Spectroscopic Investigations of the Implosion Dynamics of a Gas-Puff Z-Pinch Plasma**, Davara, G., Gregorian, L., Kroupp, E., Peter, B., Fisher, V., Maron, Y. 1063

P-4-14 • **Application of Charge Coupled Devices as Spatially-Resolved Detectors for X-Ray Spectrograph**, Attelan-Langlet, S., Etlicher, B., Mishenski, V.O., Paspazian, Yu.V., Smirnov, V.P., Volkov, G.S., Zaitsev, V.I. 1064

P-4-15 • **CR-39 Nuclear Track Detector Application for the Diagnostics of Low Energy High Power Ion Beams**, Opekounov, M.S., Pechenkin, S.A., Remnev, G.E., Ivonin, I.V. 1068

P-4-16 • **Voltmeter with Compton Electrons**, Pereira, N.R., Gorbics, S.G., Weidenheimer, D.M. 1071

P-4-17 • **The Role of Electron Beams and New Excitation Channels and for Dielectronic Satellites in Dense Plasmas**, Rosmej, F.B., Bryunetkin, B.A., Faenov, A.Ya., Skobelev, I.Yu., Kalashnikov, M.P., Nickles, P.V., Schnuerer, M. 1075

P-4-18 • **Visualisation of the High-Current E-Beams on Solid Surfaces**, Solomonov, V.I., Osipov, V.V., Mikhailov, S.G., Lipchak, A.I. 1076

P-4-21 • **Characteristics of Charge Coupled Devices over X-Ray Spectral Band**, Mishenski, V.O., Volkov, G.S., Zaitsev, V.I., Zazhivikhin, V.V. 1080

P-4-24 • **Study of Plasma in MAGO Chamber by Own Neutron Radiation**, Burenkov, O.M., Garanin, S.F., Demin, A.N., Dudin, I.F., Korchagin, V.P., Morozov, I.V., Mokhov, V.N., Pavlovsky, E.S., Chernyshev, V.K., Yakubov, V.B. 1084

P-4-25 • **Focused Proton Beams Propagating in Reactor of Fusion Power Plant**, Niu, K. 1091

P-4-26 • **Energy Loss of Heavy Ion Beams in Plasma**, Okada, T., Hotta, T. 1095

P-4-27 • **Stable Propagation of Light-Ion Beam in Inertial Confinement Fusion**, Okada, T., Murakami, H. 1099

P-2-91 • **The Interaction Physics of the Fast Ignitor Concept**, Deutsch, C., Furukawa, H., Mima, K., Murakami, M., Nishihara, K. 1103

P-4-32 • **Investigation of the Composition of an Ion Beam Produced Using a Multi Arc Ion Source**, Engelko, V., Giese, H., Mischin, M., Schalk, S., Tsibin, O.Y. 1107

P-4-33 • **Measurement of Extent of Intense Ion Beam Charge Neutralization**, Engelko, V., Giese, H., Schalk, S. 1111

P-4-97 • **Charge Neutralization of Small Ion Beam Clumps**, Welch, D.R., Olson, C.L., Hanson, D.L. .. 1115

P-4-35 • **Ne Beam-Kr Target Interaction**, Fortov, V.E., Kostin, V.V., Vorob'ev, V.S., Kulish, M.I., Mintsev, V.B., Hoffman, D. 1119

P-4-39 • **Recent Results from Experimental and Numerical Investigations of the Selfmagnetically B_θ-Insulated Ion Diode**, Bauer, W., Hoppé, P., Bachmann, H., Bluhm, H., Buth, L., Massier, H., Rusch, D., Stein, E., Stoltz, O., Vaeth, W., Westermann, T. 1123

P-4-40 • **Ion Diode Diagnostics to Resolve Beam Quality Issues**, Bluhm, H., Arzhannikov, A., Buth, L., Hoppé, P., Licht, V., Matveenko, A., Rusch, D., Stoltz, O., Singer, J., Singleton, C., Tauschwitz, A., Vaeth, W., Yoo, S. 1127

P-4-42 • **Electron Inertia Effects for an Electron Fluid Model by the Applied-B Ion Diode**, Gordeev, A.V., Levchenko, S.V. 1131

P-4-43 • **The Vortex-Like Self-Consistent Electron Fluid Model by the Applied-B Ion Diode: Equilibrium and Instability**, Gordeev, A.V. 1135

P-4-44 • **Electron Sheath Collapse in an Applied-B Ion Diode**, Grechikha, A.V. 1139

P-4-45 • **Ion Diode Optics: Measurement of Divergence and Aiming of Beams for Transport to Light-Ion ICF Targets**, Krastelev, E.G., Knyazev, B.A., Lindholm, F., Hammer, D.A., Kusse, B.R., Greenly, J.B. 1143

P-4-46 • **Modification of Diode Characteristics by Electron Back-Scatter from High-Atomic-Number Anodes**, Mosher, D., Cooperstein, G., Rose, D.V., Swanekamp, S.B. 1147

P-4-47 • **Experimental Observations of Effects of Electron Backscattering from High-Atomic-Number Anodes in Large-Aspect-Ratio, Electron Beam Diodes**, Cooperstein, G., Mosher, D., Stephanakis, S.J., Swanekamp, S.B., Weber, B.V., Young, F.C. 1151

P-4-48 • **Self-Pinch Focusing Experiments Performed on the KALIF Accelerator Using the Bappl Diode**, Hoppé, P., Nakagawa, Y., Bauer, W., Bluhm, H., Buth, L., Guth, H., Hellmann, A., Massier, H., Rusch, D., Stoltz, O., Tauschwitz, A., Vaeth, W. 1155

P-4-49 • **Ion Diode Simulation with a Finite-Volume PIC Approach for the Numerical Solution of the Maxwell-Lorentz System**, Munz, C.-D., Schneider, R.(1), Stein, E., Voss, U., Westermann, T., Krauss, M. 1159

P-4-50 • **Characteristics of Magnetically Insulated Diode in a Multi-Shot Operation**, Chishiro, E., Masugata, K., Yatsui, K. 1163

P-4-51 • **Evaluation of the Effect of Anode Groove Pitch to Ion Beam Focusibility on Spherical Plasma Focus Diode**, Imanari, K., Jiang, W., Masugata, K., Yatsui, K. 1167

P-4-52 • **The Cornell Field-Reversed Ion Ring Experiment FIREX: Experimental Design and First Results**, Podulka, W.J., Greenly, J.B., Anderson, D.E., Glidden, S.C., Hammer, D.A., Omelchenko, Yu.A., Sudan, R.N. 1171

P-4-53 • **3-D Studies of the Formation and Stability of Strong Ion Rings**, Omelchenko, Yu.A., Sudan, R.N. 1175

P-4-57 • **High Current Ion Injectors for Long-Pulse Induction Accelerators**, Hasegawa, J., Nakai, H., Iwasaki, H., Nakajima, M., Horioka, K., Kawasaki, S. 1179

P-4-61 • **Microstructured Liquid Metal Electron and Ion Sources (MILMES/MILMIS)**, Mitterauer, J. 1183

P-4-93 • **Generation of High Intensity and High Power Metal Ions by Vacuum Arc TAMEK Sources**, Tolopa, A.M. 1187

P-4-96 • **Experiments on Ion Space-Charge Neutralization with Pulsed Electron Beams**, Herleb, U., Riege, H. 1191

P-4-99 • **Photo-Resonance Anode Plasma Production by a KrF Laser**, Knyazev, B.A., Melnikov, P.I., Doroshkin, A.A., Matveenko, A.N., Bluhm, H. 1195

P-4-63 • **Interaction of a Fast Magnetic Field with Non-Magnetized Plasma for the Plasma Opening Switch Case**, Chuvatin, A.S., Rudakov, L.I., Etlicher, B. 1199

P-4-64 • **Experimental Characteristics of GIT-8 Plasma Opening Switch**, Chuvatin, A.S., Rouille, C., Etlicher, B., Bayol, F., Morell, A., Kim, A., Loginov, S.V., Kokshenev, V.A., Koval'chuk, B.M. 1203

P-4-65 • **Anomalous Resistivity in the Plasma Opening Switch**, Dolgachev, G.I., Zakatov, L.P., Kalinin, Yu.G., Kingsep, A.S., Nitishinski, M.S., Ushakov, A.G. 1207

P-4-67 • **Investigation of a Strip-Line Long-Conduction-Time Plasma Opening Switch on MAG-1'**, Frolov, V., Chuvatin, A.S., Semushin, S., Etlicher, B. 1211

P-4-68 • **Theoretical Modelling of the Magnetic Field-Penetration in a Plasma Opening Switch Experiment**, Gomberoff, K., Shpitalnik, R.R., Weingarten, A., Krasik, Ya.E., Maron, Y. 1215

P-4-69 • **Spectroscopic Investigation of the Time Dependent Magnetic Field Distribution in a Plasma Opening Switch**, Shpitalnik, R.R., Weingarten A., Gomberoff, K., Krasik, Ya.E., Arad, R., Sarfaty, M., Maron, Y. 1216

P-4-71 • **Experimental Investigation of the Ion Current Distribution in Microsecond Plasma Opening Switch**, Bystrickii, Vit.M., Grigor'ev, S.V., Kharlov, A.V., Sinebryukhov, A.A. 1217

P-4-72 • **Experimental Investigation of the Material Surface Modification in Microsecond Plasma Opening Switch**, Bystrickii, Vit.M., Grigor'ev, S.V., Kharlov, A.V., Sinebryukhov, A.A., Burkov, P.V., Grigoryev, V.P., Koval, T. 1221

P-4-73 • **Effect of Anomalous Resistivity on the Dynamics of Plasma Switching**, Kingsep, A., Munier, A. 1225

P-4-74 • **Energetic Ion Emission in a Positive Polarity Nanosecond Plasma Opening Switch**, Sarfaty, M., Krasik, Ya.E., Weingarten, A., Fruchtman, A., Maron, Y. 1229

P-4-79 • **Preliminary Studies on a Plasma Focus Opening Switch**, Wong, C.S., Choi, P., Moo, S.P., Singh, J.P. 1233

P-4-80 • **Two Dimensional Hall MHD Modeling of a Plasma Opening Switch with Density Inhomogeneities**, Zabaidullin, O., Chuvatin, A.S., Etlicher, B. 1237

P-4-81 • **Theoretical Model of the SOS Effect**, Darznek, S.A., Mesyats, G.A., Rukin, S.N., Tsiranov, S.N. 1241

P-4-85 • **Inhomogeneous Mixing Effect of D and T Fuels on ICF Pellet Implosion**, Kawata, S., Kurawaki, K., Tuyuki, A., Hirota, K. 1245

P-4-86 • **Large-Size Pellet in Ion-Beam ICF**, Kawata, S., Kurawaki, K., Tuyuki, A., Hirota, K. 1249

P-4-87 • **Slowing Down of an Ablatively Accelerated Foil after Impact on a Stationary Target**, Marten, H., Goel, B., Hoebel, W. 1253

P-4-88 • **Temperature Diagnostics of KALIF Targets by Soft X-Ray Spectroscopy**, Meisel, G., Bluhm, H., Buth, L., Hoppe, P., Huetner, R., Rusch, D., Saenger, E., Schoen, T., Singer, J., Stoltz, O. 1257

P-4-89 • **Stability of Burning Wave in Practical Size of Target**, Niu, K. 1261

P-4-90 • **Plasma-Beam Interaction Experiment at TIT**, Ogawa, M., Neuner, U., Endou, T., Yamauchi, S., Nakajima, M., Horioka, K., Oguri, Y. 1265

P-4-92 • **Theoretical and Experimental Investigation of REB Interaction with Aerogel Targets**, Efremov, V.P., Fortov, V.E., Demidov, B.A., Ivonin, I.A., Vorobiev, O.Yu., Keeler, N. 1269

Note

Missing code numbers belong to the pre-registered papers not presented at the conference. In a very few cases the full texts of papers were not available even two months after the deadline and, therefore, just the abstracts have been included in the Proceedings.

CONTRIBUTED PAPERS P-2

continuation from Volume I

Capillary Discharges

Hollow Cathode Discharges

Laser Plasma

Imploding Liners

Plasma Foci

Pseudosparks

Radiation Sources

Z-Pinches

IRONLESS BETATRONS - SHORT RADIATION PULSE GENERATORS FOR ROENTGENOGRAPHY OF FAST-GOING PROCESSES

A.I.Pavlovskii, D.I.Zenkov, Ju.P.Kuropatkin, V.D.Mironenko, V.N.Suvorov

All Russia Scientific Research Institute of Experimental Physics
607190, Sarov (Arzamas-16), Nizhni Novgorod Region, Russia

INTRODUCTION

Pulsed roentgenography technique plays an important role in high-pressure physics researches employing shock waves, explosion energy magnetic cumulation, as well as in gasdynamics study of explosive facilities and other fields of investigations. Characteristics of a radiation generator and an image recorder which should meet high demands of explosive tests determine the technique capabilities. The required high spatial and temporal resolution limits the radiation pulse duration, irradiator dimensions and define the spectrum content of radiation used and the experiment geometry.

In 1955 it was suggested (A.I.Pavlovskii) to study fast-going processes in massive objects with a comparatively hard bremsstrahlung radiation, ironless circular induction electron accelerators - betatrons - being the sources of such radiation. High-current ironless betatrons of record power, to 100 MeV [1], were constructed and for nearly thirty years are employed in various researches of fast-going processes.

The high-current betatron concept was based on the maximizing of stable acceleration region extension $I_{lim} \sim (\Delta r/r_0)^2$ as well as the injection energy $I_{lim} \sim \beta^2\gamma^3$ at a relatively small orbit radius. This caused the study of different ways of betatron field formation in the absolutely ironless systems and extensive investigations of annular electron beam shaping and accelerating processes at maximal currents. The injection parameter effects on the current captured in acceleration [2], various types of injectors and beam input systems were studied. An injector of nearly 2 MeV energy with a thermocathode was created. Also, the feasibility of toroidal focusing fields application and space charge compensation were studied. It allowed to realizate a radiation generator of then record characteristics. However, the level achieved happened to be lower then the expected one at such injection energy, so the present investigations were undertaken.

CURRENT INCREASE INVESTIGATIONS IN IRONLESS BETATRONS

In the electromagnet design employed for high-current ironless betatrons a betatron magnetic field with a large area of stable acceleration $\Delta r/r_0 \approx 0.7$ and $\Delta z/r_0 \approx 0.6$ is formed by a system of current-carrying coils shown in fig.1(a). It comprises two groups of plane helical coils contributing mostly into betatron field and a central solenoid which couples these coils and generates the accelerating

magnetic flux. This ironless electromagnet provided electron acceleration to 100 MeV energy. In this case the maximal magnetic field was 14 kG on the equilibrium orbit of r_0=23.4 cm radius.

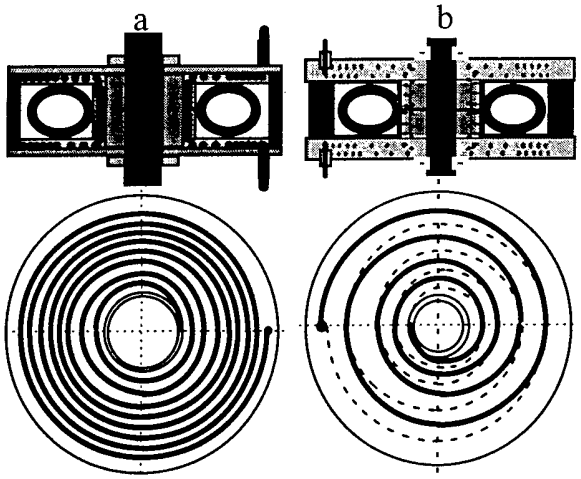

Fig. 1. Schematic diagram of the electromagnets

The magnetic field produced by a ironless electromagnet differs from an ideal betatron field in 1% azimuthal asymmetry, a slight slope of the equilibrium orbit plane and nearly 5% azimuthal constituent of a magnetic field. A priori, estimation of these disturbance effect on the accelerating current did not seem possible. For this purpose the electromagnet was designed which current-carrying coil system consists of two coil group symmetrical in relation to the middle plane (fig.1(b)). Each group of coils has two layers of plane helixes and a two-layered central solenoid coupling them. Application of two-layered plane helixes and the solenoid provided a good azimuthal symmetry and eliminated the azimuthal constituent of the field. The influence of magnetic field structure variations was checked via the comparison of betatron radiation output with various electromagnets. The betatron radiation output with a new electromagnet happened to be approximately thrice as much. The effect of the magnetic field azimuthal constituent was studied separately. The experiments where conducted with the betatron with a new electromagnet where a special winding produced the azimuthal field of varying value. A noticeable drop in the betatron radiation output was marked at 5% increase in the azimuthal field (fig.2). The effect of magnetic field structure variation turned out to be stronger then one might expect.

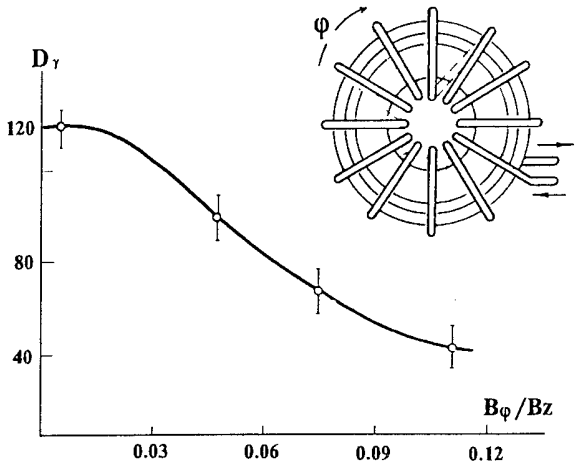

Fig. 2. Intensity dependence on azimuthal field magnitude.

As it was mentioned, a substantial current increase in the betatrons at the expense of injection energy increase proved to be a very complicated feasibility problem. In search for its optimal solution the investigations in nanosecond injection pulse range where undertaken. The self-emission cathode applied in the injector diode helped to study the dependence of betatron radiation output on the injection pulse duration (fig.3). When the injection lasts less than two revolutions (6 ns), this dependence trajectory testifies for the

determinant influence on the electron capture efficiency in interaction collective effects acceleration. These investigations were conducted at 300 keV injection energy. At injection energy increase the deficit in the injected current was marked that resulted in a considerable lowering of injection efficiency. The required current dependence on the injection energy U^3, the diode current grows with voltage increase $U^{3/2}$.

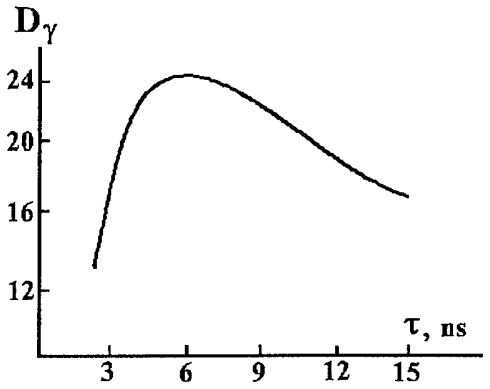

Fig. 3. Intensity dependence on the injection pulse duration.

The problem of good-quality high-current electron beam production remains unsolved. Under these conditions to advance in the high injection energy region it was obligatory to increase the efficiency of electron capture for acceleration. As a rule, this value is 5%, not more. We managed to succeed in this at the expense of the local disturbance in betatron field attenuating in time of 5-10 revolutions of an electron. At the optimal ratios of disturbing and betatron fields, of winding geometry creating field disturbance and its attenuation velocity, the multi-revolution capture of electrons into acceleration is realized. The dependence of the current circulating in the betatron on the injection energy was studied with the optimized facility of magnetic field local disturbance. An injection pulse lasts for 4-6 (20-30 ns) electron revolutions on the orbit. Fig.4 presents the results obtained. It is evident that the discovered method of efficiency increase for electron capture into acceleration allowed us to bring the experimental dependence closer to the calculated one. The maximal circulating electron current was 280±30 A and nowadays it is record for circular accelerators. We should note that these results were achieved with

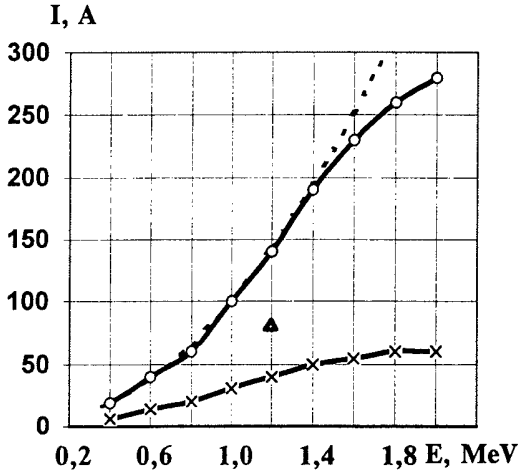

Fig. 4. Beam current dependence on the injection electron energy.
×- betatron-prototype; Δ- modernized betatron, self-captured; O- modernized betatron, captured with field disturbance.

a porcelain accelerating chambers having a relatively high conducting cover which resistance was 2-50 Ohm.

PULSED HIGH-CURRENT BETATRON APPLICATIONS

High-current ironless betatrons created helped in rational solution of the problem of the roentgenographic study of fast-going processes in massive objects. We realized the possibility of x-raying the

investigation object in different directions or imaging several phases in one experiment when some radiation generators are employed. High probability of getting information from a single explosive experiment is rendered by reliable operation of the accelerator and special devices. When studying the processes which last lesser then the acceleration period, this device estimates current capture into acceleration, and if it appears to be noticeably different from it nominal the detonation of an investigated

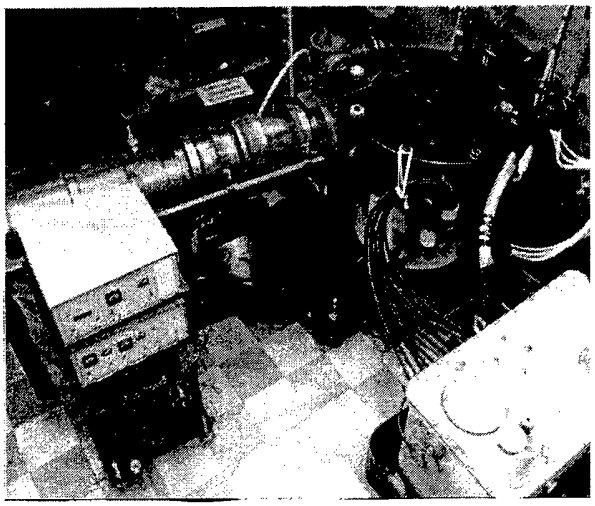

Fig.5. Ironless high-current 65 MeV betatron.

object is blocked. Fig.5 shows the picture of pulsed high-current ironless 65 MeV betatron with 23.4 cm radius of the equilibrium orbit. The radiation pulse duration is 40 ns, focus dimensions 2×4 mm^2. This radiation generator was employed in the researches of magnetic cumulation of explosion energy and some other. More powerful generators are used for x-raying of extremely thick heavy materials. The investigation results cited here, which made possible the substantial increase of current in the betatron, give new opportunities in researches of fast-operating processes. The table lists almost ultimate characteristics of high-current ironless betatrons - generators of radiation for fast-going process studies.

Accelerated electron energy, MeV	100
Number of the accelerated particles per pulse	$1 0^{13}$
Circulating current in the orbit, A	300
Radiation dose in a meter from the target, roentgen	250
Radiation pulse duration at 0.5 amplitude: -short pulse, ns -long pulse, μs	 40-300 1-10
Synchronization accuracy with the investigated process, ns	50
Irradiator dimensions, mm	2×5
Maximal thickness of a lead test x-rayed per pulse in a meter from the target, mm	265

In conclusion it should be noted that the possibilities of current increase in circular induction accelerators are not yet complete. The results obtained give grounds for a hope to achieve kiloampere circulating currents in the ironless betatrons.

[1] A.I.Pavlovskii, G.D.Kuleshov, Ju.A.Zisin, A.I.Gerasimov, :Doklady Akad. Nauk SSSR, V.160 No1 (1965) p.68
[2] A.I.Pavlovskii, G.D.Kuleshov, A.I.Gerasimov, A.P.Klementiev, V.O.Kuznetsov, V.A.Tananakin and A.D.Tarasov, :Journal of Technical Physics, V.47 No2 (1977)p.371

DETERMINATION OF THE EFFECTIVE IMPULSE TIME DURATION OF INTERACTION OF SOFT X - RADIATION WITH MATTER.

K. S. Dyabilin, V. E. Fortov, E. V. Grabovskij,
M. E. Lebedev, V. P. Smirnov

High Energy Density Research Center, Izhorskaya 13/19, Moscow 127412, Russia
Troitsk Institute of Innovative and Fusion Research, Troitsk, 142092, Russia

It is known that under the interaction of the pulsed power with the matter the ablation occurs. From one side this ablation leads to the shock wave formation in the condensed matter from an other leads to the screening of the power and decreasing of its interaction with target. We suggest a new method of determination of the effective time of interaction of the powerfull radiation with condensed matter. This method based on known method of determination of sound velocity in compressed matted described in [1].

Description of the method.

Let us consider that powerfull radiation strikes the condensed matter fig. 1. This radiation absorbed in the near surface layer (1) of the condensed composite target (metal (1,2) + indicator matter(3)). At fig. 2 the x-t diagram of the hydrodynamic process in condensed target is presented. The shock wave (1) was formed at time moment t_1 and propagated into the target. This shock wave pass to another co-called "indicator" matter (this matter is a transparent matter with well known equation of state; under compression the indicator matter emitted light, the dependence of emitted light and pressure should be well known too) and velocity of the shock wave changed (2), the dotted line in this figure presents the motion of the boundary between the surface layer and indicator matter. During the time the ablation of the target will cause the absorption out of target (time moment t_2). (Of cause this moment is not sharp.) So the pressure on the target surface decreased and the rarefaction wave (3) appeared which was expanded through the matter being compressed before. The velocity of rarefaction wave is more than that of the shock wave. At the some distance x_2 the rarefaction wave achieved the shock wave and amplitude of shock wave decreased substantially. At this moment (t_2) the intensity of luminescence of indicator also decreased. Measurements of the velocity of the shock wave and the time of the achievement of rarefaction of the shock wave (both were measured by optical method) allowed to determine the real time of the radiation with target interaction.

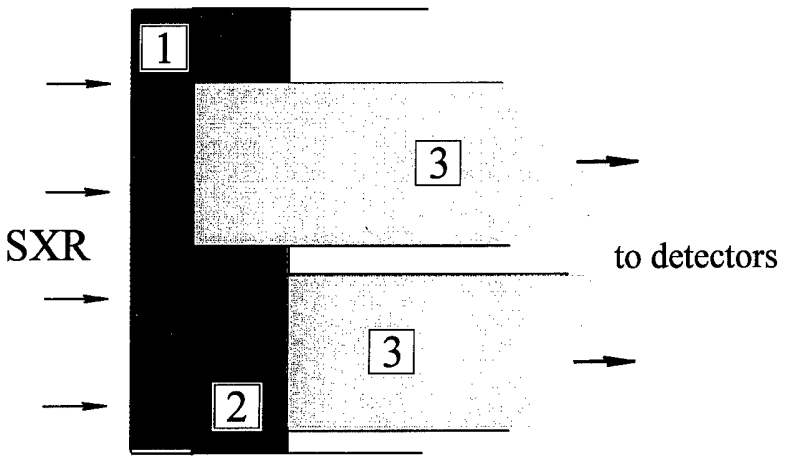

Figure 1. Target. 1,2 - absorbed layers; 3 - indicator layers

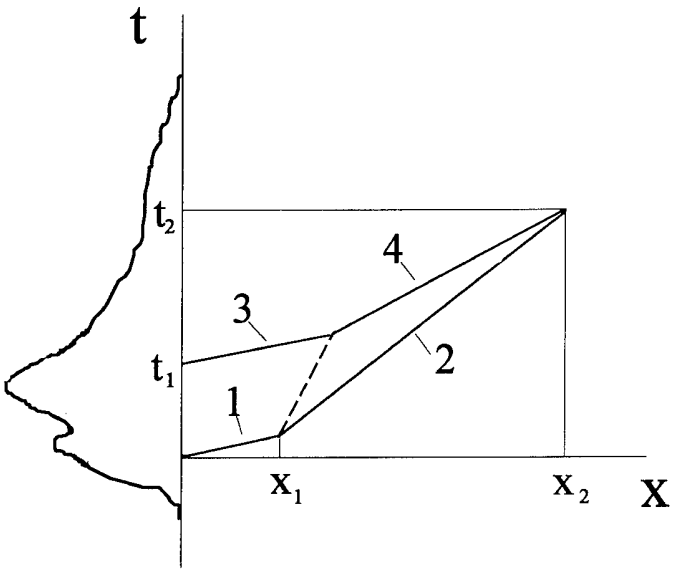

Figure 2. X-t diagram of the process. Left - impulse of radiation.; 1 - shock wave in absorbed layer; 2 - shock wave in indicator layer; 3 - rarefaction wave in absorbed layer; 4 - rarefaction wave in indicator layer

Experiment

The experiments were carried out at the "ANGARA-5-1" installation. The SXR power level was about 1-2 TW/cm^2 with the pulse duration about 30 ns. The shock pressure of Pb target about 300 GPa was achieved. [2].

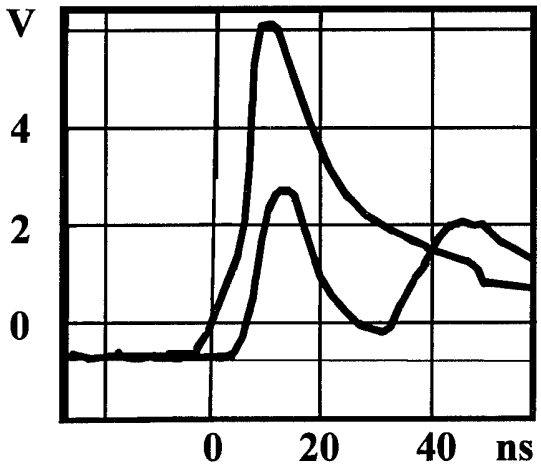

Fig. 3 Oscilogram traces from photodiodes. Records: up for up indicator layer, down - for down indicator layer (see fig. 1)

The target (4 mm in diameter) consists of 16 μm Al layer (poz. 1 on fig. 1), 88 μm Pb layer (poz. 2) and fused quartz indicator layers 400 μm in diameter (poz. 3). Radiation was coupled out of the experimental apparatus by means of optical-fiber communication links. The optical radiation from the fibers was detected by photodiodes with time resolution less than 1 ns. Typical oscilogram is presented on fig. 3.

In this experiments we estimate the effective interaction time of the powerful soft x radiation with the condensed matter as about 20 ns. In future we plan to perform analogues experiments with different indicator layers and materials.

References:

1. Ya. B. Zel'dovich and Yu. P. Raizer, *Physics of Shock Waves and High Temperature Hydrodynamic Phenomena*, (Academic Press, New York, 1966).
2. E. Grabovskij et al., *JETP Lett.* **60** (1994) 3.

P-2-56

INTERRAD- INDUCTIVE TERAWATT X-RAY GENERATOR

(Project)

N.F. Popkov, A.S. Pikar', V.I. Kargin, E.A. Ryaslov, A.G. Lyubomirskii

All-Russian Research Institute of Experimental Physics (VNIIEF), Sarov, Nizhniy Novgorod Region, 607190, Russia.

Abstract.

There are given the results of the development and experimental research of explosive electron beam accelerator circuits powered by magneto-cumulative generators forming the current pulse, using explosive plasma opening switches.

The conceptual lay-out of inductive terawatt X-ray generators powered by EMGs is proposed. The calculation results of the terawatt X-ray generator including the load placed in a special bunker are represented in the present paper. There are analyzed the losses at the stage of the HE energy conversion into that of the magnetic fields, those occured in transmission along the high-voltage cable line, as well as the processes developing in plasma opening switches.

Introduction.

For several years in VNIIEF there have been designed and researched the X-radiation sources of " PIRIT " type. During this time several electro-physical facilities are developed, implemented and introduced into practice, provided the energy storage in the range of 40 kJ-2 MJ. In principle, "PIRIT" facilities are based on the use of the inductive energy storages and current pulse formation, employing opening switches. Inductive storages as compared to the capacitive ones possess a higher parameter of the stored energy density and, moreover, MCGs may be effectively applied to energize them, provided the generated energy makes dozens and hundreds of megajoules.

Application of new and more capacitant energy sources, i.e. magneto-cumulative generators (MGSs) and explosive current opening switches leads to a considerable deminishing of the sizes, weight and cost of the facilities intended to generate powerful X-radiation fluxes.

In the course of the work carrying out the authors studies various X-ray generator lay-outs. Among those there were generators with the H-pressed discharge, Z-pinches and generators including inductive accelerators, those with the formation line and those of a direct action incorporating inductive storages [2-5].

Earlier, there were reported the research results of the X-ray generator development based on the direct-action accelerators. In all the designs considered the multi-turn MCGs were used ensuring the 10-15 MA current pulses output at the voltage of several dozens of volts. To coordinate the diode impedance with that of the energy source, we used the current enhancing transformer and the especially developed for this purpose helical opening switch with the explosive plasma opening element. L474, L475 and L476 electron beam generators with the power supply unit energy storage of 200-500 kJ were developed [6].

The developed technology was successfully used to create comparatively simple research X-ray generators with the energy storage of several megajoules based on Z-pinches, capillary Z-pinches etc.

Based on the obtained experimental results the authors developed the concept of the placed in a special bunker stationary facility powered by explosive magneto-cumulative generators (EMG).

INTERRAD Facility Project

Inductive storages have some certain advantages over the capacitive ones. One of the superior properties is that inductive storages possess a comparative by low inductiveness facilitating the energy storaging. Due to this small inductiveness number, there may be implemented the lay-out with the magnetic flux transmission by the cable line into a series of independent storages equipped with the opening elements. These elements further commutate the circuit so that the fluxes are summated and the voltage is increased. This lay-out is implemented in the powerful inductive terawatt X-ray generator Project called "INTERRAD".

The facility consists off the following units:

- EMG-720 generators placed at the side fields;
- Energy transport cable line;
- Set of inductive storages (inductors) with explosive plasma opening switches;
- High-voltage vacuum energy transmission line;
- Vacuum chamber of the plasma erosion opening switch (PEOS);
- High-current and high-voltage diode;
- Radiation output vacuum channels.

The INTERRAD is represented in Fig. 1. There were performed the calculations modeling the processes of energy generation, transformation and delivery to the INTERRAD facility vacuum diode, provided the MCGs energy supply is 100 MJ. The calculation results are shown in Fig. 2.

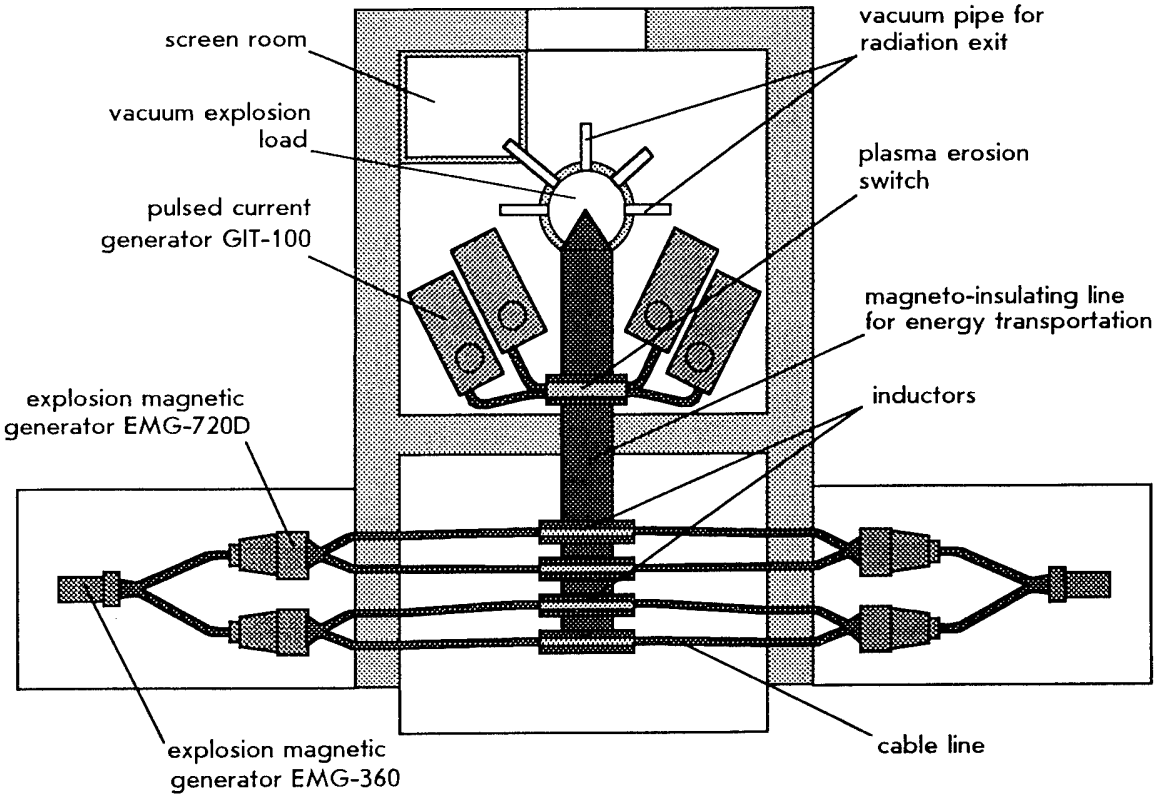

Fig. 1 INTERRAD basic units arrangement.

In the calculations there were accounted the energy losses in MCGs, cable line, current commutation using the plasma explosive and plasma flow opening switches.

The plasma erosion opening switch (PEOS) calculations were conducted, following the model of the carbon plasma erosion, taking into account the electron component magnetization by the current of the storage's own magnetic flux; as well as its own magnetic field pressure on the PEOS plasma surface and plasma acceleration in the course of powering.

Primarily, the connected in parallel cascade helical EMG-720 are powered by the stationary capacitor bank with the energy storage of 1.2 MJ. The energy increased up to 100 MJ is fed to 8 torroidal inductive storages by the 5 m. long cable line for the characteristic time of 25 μs. Then, at the plasma opening switches' operation during 2 μs the magnetic flux is delivered to the vacuum energy transport line with the inductiveness of 300 nH.

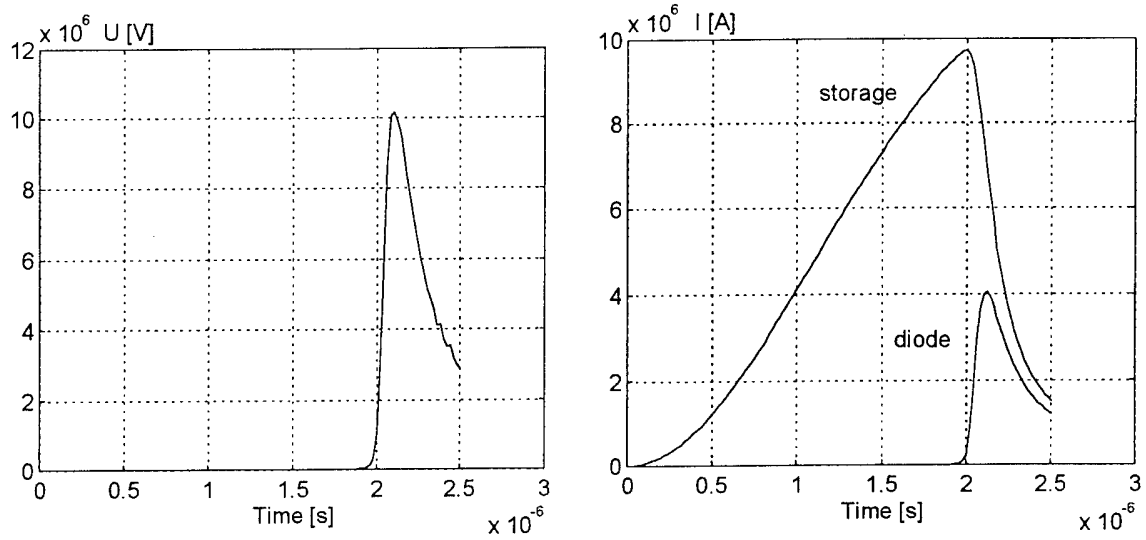

Fig.2. Calculation results of PEOS voltage and respective currents vacuum inductive storage and diode.

In the 2nd cascade the vacuum inductive storage current is growing up to the amplitude of 10 MA and is commutated by PEOS to the high-voltage electron diode at the voltage of 10 MV. In case of the current circuit brake the inductive storage current is reduced down to 5 MA and for 100 ns the current is increased up to 4 MA in the high-current vacuum diode.

The present INTERRAD project of the inductive terawatt X-ray generator demonstrate new capabilities of powerful stationary electro-physical facilities. Moreover, using "PIRIT" technology, not only traditional capacitive storage lay-outs may be improved but, also, new design are possible to be implemented.

[1]. A.I.Pavlovskii, N.F.Popkov et al, "Optimization Study for Characteristics of Pulsed Energy Sources with Plasma Switch" см. [4], pp.208.

[2]. A.I.Pavlovskii, N.F.Popkov et al, "Two-stage System for Short Current Pulse Formation" in Megagauss Fields and Pulsed Power Systems, V.M.Titov and G.A.Shvetsov, Eds. (Nova Science Publishers, New York, 1989), pp.393.

[3]. A.I.Pavlovskii, N.F.Popkov et al, "Investigations of High-current Discharges Supplied from Magnetic Cumulation Generators" см. [2], pp.679.

[4]. A.I.Pavlovskii, N.F.Popkov et al, "Powerful Pulsed Energy Source for Plasma Physics Research" in Megagauss Magnetic Field Generation and Related Topics, Book abstracts, 8-11 Nov. 1992, Albuquerque, New Mexico (USA) pp.208.

[5]. A.I.Pavlovskii, N.F.Popkov et al, "MC-Generator Current Contour Break by Explosive-Driven Plasma Switch" см. [2], pp.503.

[6]. Pavlovskii A.I., Popkov N.F., Kargin V.I., Pikar A.S., Ryaslov E.A. Magnetic Cumulation Generator As a Power Source to Accelerate Intense Electron Fluxes. - Megagauss Fields and Pulsed Power Systems, 1990, pp. 449-452.

NEW BIFOCAL PINCH EXPERIMENT SPEED 3

J. Raacke, U. Berntien, G. Decker, W. Kies, P. Röwekamp

Heinrich-Heine-Universität Düsseldorf, Inst. für Experimentalphysik
Universitätsstr. 1, 40225 Düsseldorf, Germany

Introduction

Intense sources in the spectral range of VUV- to SXR-radiation ($\lambda = 200 \ldots 0.05$ nm) are used for e.g. micro lithography or X-ray microscopy. These applications require intense short radiation pulses emitted in small spectral channels from a spot-like source.
For technical applications a compact and transportable design in combination with easy maintenance is also desired.
Pinch plasmas emitting intense line radiation in the XUV- and SXR-range are under consideration and investigated as possible sources. In recent years in Düsseldorf such plasmas were created with the high performance driver SPEED 2 operated in a Mather-type plasma focus configuration [1].

Set-up of SPEED 3

As a step towards practical application of pinch plasmas the compact plasma focus SPEED 3 was designed. It consists of a bifocal configuration with plane insulators, a very short accelerator and a hollow inner electrode (see fig. 1).

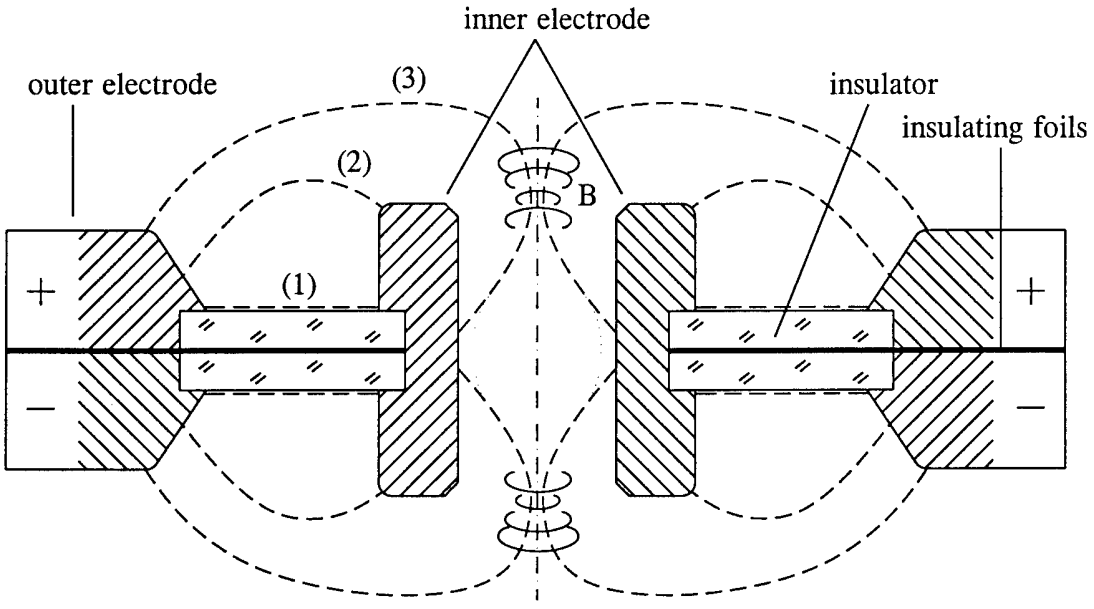

Figure 1: Plasma focus SPEED 3 and discharge phases

Eight parallel two-stage-marx-modules are used as drivers. They are arranged in a regular octagon around the discharge chamber and determine the size of the system (height 65 cm, diameter 130 cm). These modules are switched by fast triggerd (50 kV pulse) spark gaps with a jitter of less than 2 ns and connected by parallel plate transmission lines to the outer electrodes in the discharge chamber. Due to the compact design and therefore short transmission lines simultaneous switching is crucial for symmetric current drive and discharge efficiency.
Typical and maximum data of the driver are shown in table 1.

	typ.	max.	
bank energy:	5.4	12.5	kJ
bank voltage:	66	100	kV
short circuit curent:	0.83	1.25	MA
capacitance:	2.5		μF
inductance:	16		nH
current rise time:	0.3		μs
current rise rate:	4.2	6.3	kA/ns
jitter of spark gaps:	< 2		ns

Table 1: Typical and maximum data of SPEED 3

Both sides of the discharge chamber contain a plasma focus with an outer ring electrode, plane insulator and inner electrode. This set-up results in two foci near both ends of the hollow inner electrode. The hole reduces the plasma wall contact during the pinch phase and therefore the erosion of electrode material and the production of undesired hard X-rays. The use of plane insulators keeps the system inductance low and favours high current efficiency. Since high power discharges cause problems of sheath formation, a metal foil was initially used in order to predetermine the electric potential on the insulator surface. The description of the discharge history is generally divided into three phases (see fig. 1). During the first $70 - 100$ ns after the triggering the plasma sheaths are formed by sliding discharges on the insulator surfaces. Then the sheaths take off and are accelerated along and towards the axis by $\vec{j} \times \vec{B}$-forces (second phase). In the compression and pinch phase hot plasma columns are formed at both ends of the inner electrode.

Diagnostics

The electrical signals U and dI/dt are used to characterize the development of the discharge and the pinch quality . The current derivative is detected with tiny coils, placed close to the parallel plate transmission lines. Four different positions for these probes have been used to control the symmetry of the current drive. The voltage is capacitively divided and registered by digital storage oscilloscope together with various other signals: a scintillator-multiplier combination detects hard X-rays and neutrons (in discharges with deuterium), the pulses of which are separated due to their different time of flight. In the visible spectral range three framing cameras with 10 ns exposure time are used at radial and axial positions to image the sheath shape and pinch formation. With a fast photodiode the temporal development of the visible emission is registered.

For the XUV- and SXR-range a pinhole camera (time integrating), a 4-frame MCP-camera (exposure time 5 ns) and a streak camera can be used, if line radiation in this spectral range ($\lambda < 20$ nm) is emitted from pinch plasmas of heavy gases (e.g. Ne, Ar). Up to now efficient pinch formation only takes place in pure deuterium or hydrogen. Signals of an efficient discharge in deuterium and a series of framing camera pictures of discharges in a deuterium-argon mixture are shown in figure 2 and 3.

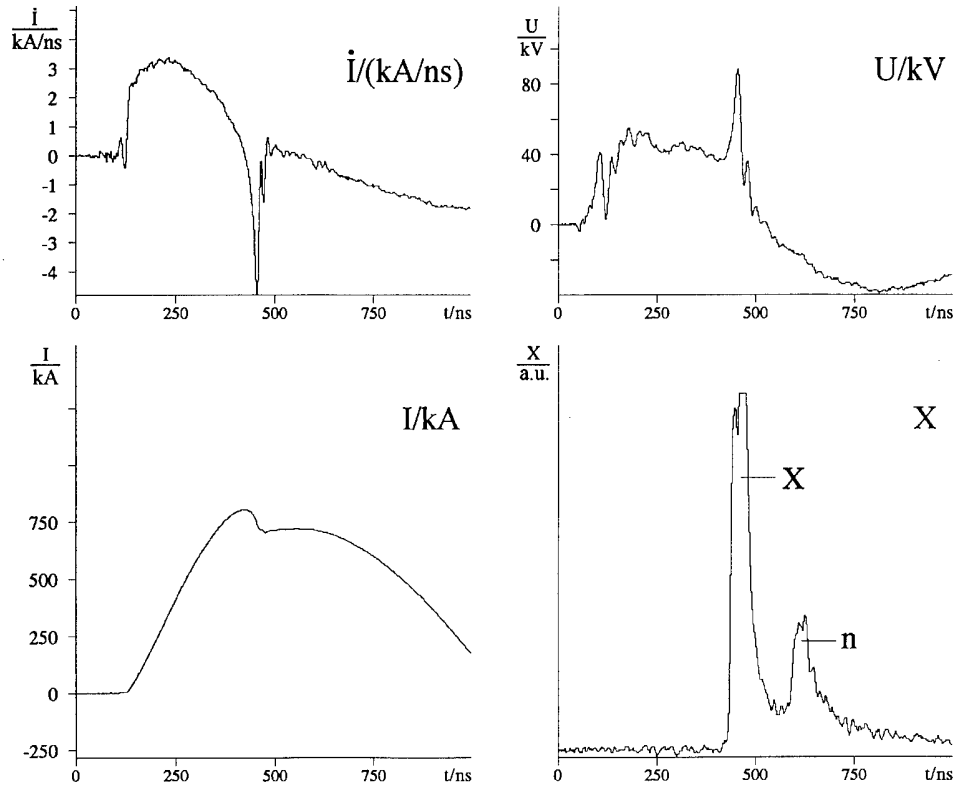

Figure 2: Electrical signals of an efficient discharge

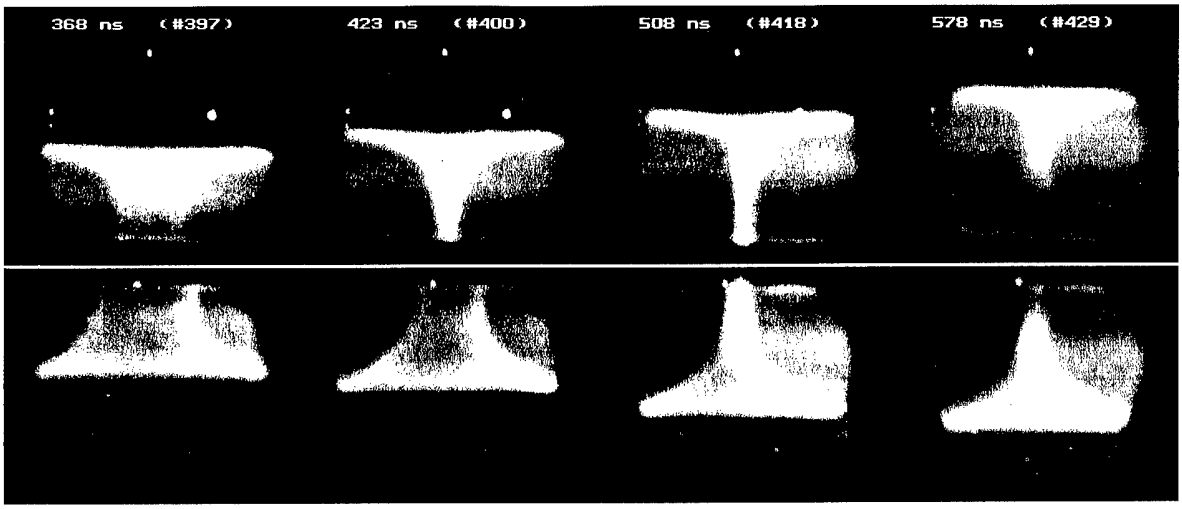

Figure 3: Framing camera pictures (10 ns exposure)

Experimental results

The experiments performed up to now almost exclusively deal with discharge initiation, sheath and pinch formation. The influence of the insulator on sheath and pinch formation and the discharge reproducibility is known to be of great importance. Efficient sheath and pinch formation is achieved using pure deuterium or hydrogen as filling gases. As observed in SPEED 2 small admixtures of heavy gases cause sheath break-up and filamentation. In contrast to systems with cylindrical insulators the polarity effect [2] is considerably reduced in SPEED 3. The potential control within the plane insulators has almost no effect on the sheath formation and was therefore replaced by a grounded copper plate (thickness 10 mm) separating both sides of the set-up. While the sheath velocities in deuterium in axial and radial directions exceed $1.5 \cdot 10^5$ m/s, the axial velocity in a deuterium-argon mixture is reduced by a factor of 3.
A pinch of about 1.5 cm in length is formed on both ends of the inner electrode. The time difference of about 40 ns between the maximum compression of the two pinches is caused by a slower sheath formation in that part, where the outer electrode is positive (polarity effect). Up to now the complete sheath detachment inside of the hollow inner electrode during the pinch phase was not observed.
Special attention was put on the influence of the insulator surface. Efficient pinch formation with new and unconditioned glass insulators was achieved after a few cleaning discharges. But after about 15 efficient discharges the insulator surfaces show severe damages (microscopic cracks) preventing further proper sheath formation. The deposition of copper cristallites onto the surface known as a sign of a well conditioned surface does almost not take place. First tests with Al_2O_3-coated (thin layer: 300 nm, sputtered) insulators reveal an improved behaviour, though the coating is damaged within a few discharges.

Outlook

The grounded mid-plate enables two new measures: Heavy gases can be injected through a small channel directly into the pinch region. This could avoid the problems already observed with static admixtures. In two additional thin tubes micro-pickup coils can be inserted in the inner electrode to detect the current and a sheath detachment.
The conditioning problem of glass unsulators is presumably overcome by alumina coating or by using pure alumina discs. This material is superior to glass insulators especially in high power experiments with respect to sheath formation and reproducibility of the discharges.

References

[1] J. M. Bayley, G. Decker, W. Kies, M. Mälzig, F. Müller, P. Röwekamp, J. Westheide and Yu. V. Sidelnikov: *Observation of the soft X-ray production in the SPEED 2 plasma focus.* J. Appl. Phys. 69 (2), pp. 613–617, 1991.

[2] J. W. Mather: *Dense plasma focus.* Methods of Experimental Physics 9B, p. 187, 1971.

PLASMA FLOW DISCHARGE RESEARCHES AT THE PIRIT-2000 FACILITY

N.F.Popkov, E.A.Ryaslov, V.I.Kargin, A.S.Pikar', V.I.Vorontsov, D.V.Kotel'nikov, A.V.Melkozerov
VNIIEF, Sarov, Russia, E-mail: popkov_3001@spd.rfnc.nnov.su

INTRODUCTION

The effective use of capacitor storages with store more than 1 MJ as plasma load driver is possible to use devices of formation of a rapidly increasing current pulses. To them plasma opening switches [1] concern. By use such opening switches of current pulses in a microsecond range of powering duration the drift of plasma to the load very strongly grows. It results in low density of a switch current and to increase of installation dimensions [2]. The group of the Phillips laboratory researchers used the plasma flow switch for switching megaampere currents with high magnetic field magnitudes on installation SHIVA-STAR [3]. The duration of a closed condition of the plasma flow switch reaches 3-5 μs.

During of the capacitor store discharge on PFD plasma shell it is accelerated in the load. When PFD is moving with large speed about edge central coaxial phase of sharp switching on the load comes. The authors investigated the plasma flow switch of a current on facility PIRIT-2000 at currents about 5 MA and powering duration about 1.5 μs. Plasma erosion switch with linear density of a current about 10 kA/cm was used earlier for the formation of facility current.

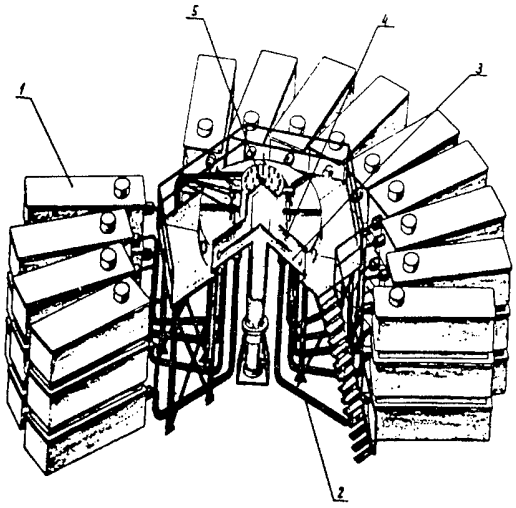

Fig. 1. The Scheme of "PIRIT-2000" Arrangement.

1. PIRIT-2000 FACILITY

PIRIT-2000 [4] is a fast operating capacitor bank having the capacitance of 17 μF and the output voltage up to 500 kV. It is comprised by 54 standard capacitive modules of 40 kJ each, connected by semi-rigid high voltage cable KVI-500 introduced into the vacuum chamber where the load is embedded. Total energy stored in the capacitive storage reaches 2 MJ. Fig. 1 shows the facility set-up. PIRIT-2000 consists of following functional systems: initial module energy capacitive storage 1, high voltage cable line 2, vacuum chamber with cable collector 3 and load 5. In the current experiments the load is of the coaxial gun for PFD powering in vacuum. PIRIT's initial capacitive store possesses the inductance of 15 nH and is comprised by 54 modules being the pulsed voltage generators [5]. The module's shock capacitance is 0.32 μF, inductance - 0.75 μH and the output voltage - up to 500 kV. The cable collector feeds an energy vacuum into the vacuum volume through the lower plane of the chamber. The collector is formed by the high voltage vacuum termination of each KVI-500 cable. For the powering of plasma guns generating PFD plasma, the bank of 8 μF, 100 kV is used.

The internal diameter of the external tube of the PFD chamber is 20.6 cm and vacuum gap between the external and internal vessels is 3 cm. For obtaining of the initial plasma PFD at the external tube, there are uniformly installed 40 plasma guns. The track of the PFD acceleration was chosen to be 20 cm long from the plasma gun location. In this place there are located eight copper blades short - circuiting the load electrodes. At the external tube of the coaxial chamber there are deployed magnetic probes and optical sensors registering the PFD light and magnetic field distribution both in time and along the plasma acceleration track. Along one line there are installed from 4 to 8 magnetic field and optic sensors.

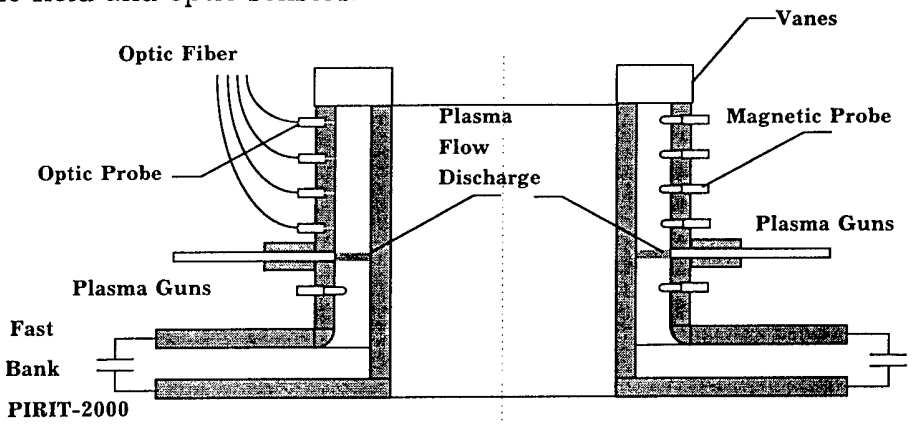

Fig. 2. Schematic Design of Coaxial Plasma Chamber for Powering of PFD.

2. EXPERIMENTAL DIAGNOSTIC

For studying magnetic field distribution, shell's velocity in the process of PFD acceleration, its initial parameters we employed the following methods: point magnetic probes; fiber - optical sensors with the multi - channel registration system; Langmuir unitary probes; Faraday collimated cylinders for ion plasma current registration; as well as sectioned Rogovsky coils.

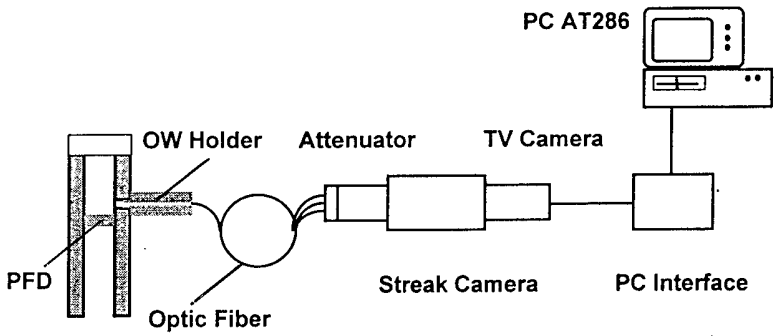

Fig. 3. Measurement Lay Out When Applying Optical Method.

Probes were situated in the holes in the external coaxial tube, protruding 6 mm inside the discharge gap of the coaxial chamber. To define the liner flying velocity there was employed the method of measuring the time interval between the light flashes. The experimental lay out was chosen based on the assumption that during the current shell passing the light registrator, there would be recorded a considerable increase of the radiation brightness in comparison with the background. The measurement lay out is shown in Fig. 3.

Concentration of plasma injected into the coaxial plasma chamber gap was determined, using Langmuir probes. The value of plasma density at the cathode made n_e=6 10^{15} cm^{-3} in 2.5 μs after the injection.

3. EXPERIMENTAL RESULTS

In our experiments the PFD plasma is generated as a result of operation of 40 plasma guns powered from a separate capacitor bank. The working energy resource of the facility being equal to 1-2 MJ and voltage of the capacitive storage being high, the load current rise period is provided to be not less than 1.5 μs. According to preliminary 1-D simulations, to provide for the acceleration trace of 10-20 cm be covered for 1-1.5 μs, the shell mass should be in the range of 1-5 mg. The drawback of PFD plasma production, using plasma guns, is the considerable initial thickness of the annular shell along the axis of the coaxial chamber. It may reach 5-10 cm, depending on the delay between the guns' battery operation and that of the capacitive storage of PIRIT-2000 facility. The facility configuration, allowed for obtaining in the load of the maximum current of 5.8 MA during 1.5 μs without plasma gun's operation. Two-ten μs after the operation of plasma guns the capacitive storage of PIRIT-2000 facility was initiated. At the time less than 2 μs the formation of PFD was not observed.

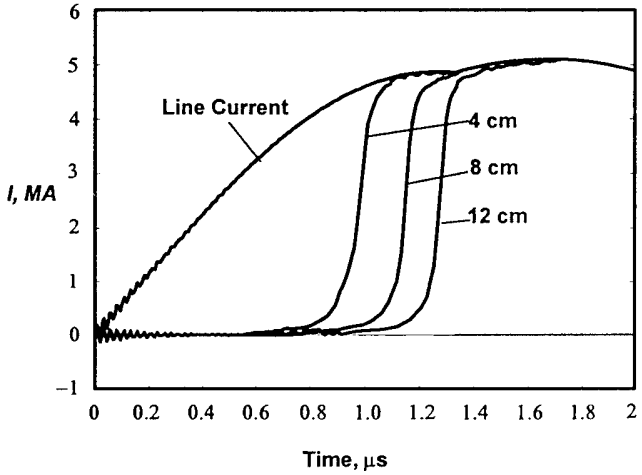

Fig. 4. Disk Line Current Pulses and Magnetic Field Probe's Signals.

Main working pulses were obtained when the delay was 4-6 μs. In Fig. 4 there are shown the signals of magnetic probes installed on the track of PFD plasma acceleration, as well as those from the current sensors situated at the disk line output and upstream the plasma guns. Signals of magnetic field sensors showed that the current shell had quite a considerable thickness.. It makes 3 cm at distance 6 cm, 2 cm - for probe № 3, and is reduced up to 1.5 cm - for probe № 4. The latter was positioned at the distance of 12 cm from the place of plasma injection and registered the (0.1-0.9) rise time t_r less than 100 ns. The distance between probes 3 and 4 was covered by the current shell for 200 ns, the corresponding average velocity being 20 cm/μs. Though, the signals of all the sensors showed a slow rise up to 0.1 U for the time (2-3)t_r. This proves that magnetic field penetrates quite far through plasma (for 5 and even 10 cm), at least at the anode of the coaxial load.

In Fig. 5 there is given the photo of the glow of the light guides used for determination of the movement velocity of the glowing PFD plasma current layer. Generally, the picture registered allows to derive the velocity number. This makes 20-30 cm/μs at the distance between optical sensors 3 and 4, though with the accuracy of about 50%. It was unexpected that the light pulse rise time proved to be 2-5 times more than that of the appropriate magnetic probe signal. Possibly, the glow is connected with either a deep penetrating current channel carrying up to 10% of the circuit current for reflection of the

light radiation of the main current channel from plasma shell (in case of "nontransparant" plasma).

Another unexpected behavior of the light pulses lies in the prolonged glow of plasma after passing of the glowing shell. In this moment magnetic probes show a full current transmission to the direction of the load (within the limits of error probable), but the plasma glow remains. Magnetic field in the gap between the coaxial chamber electrodes reaches 150 kOe at the maximum current. This is enough to magnetize electrons. So, most probably, the glow is caused by near wall plasma (both on the cathode and anode).

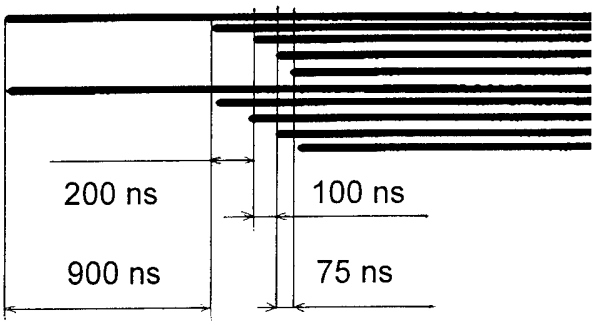

Fig. 5. Signals of optical probes.

The experiments proved that, varying the operation delay in the range of 2-10 μs, the PFD load current rise time increases up to 150-200 ns, if the delay is more than 6 μs, the prepulse increment being the most intense. The same result was obtained earlier, when researching plasma opening switches [2]. Reduction of the delay from 6 to 2 μs leads to the less current in the coaxial plasma chamber. Load current rise time does not change, but the prepulse duration drops down up to the rise time.

CONCLUSION

In the experiments was used plasma flow discharge for formation of a pulse of a current of installation PIRIT - 2000. PFD current amplitude reached 5 MA at the level of Marx generator's charging voltage of 70 kV. Load current rise time reached 100 ns, the load being in all the experiments short-circuited and situated at the distance of 20 cm from plasma guns. Magnetic field magnitude of the plasma switch 150 kOe is achieved, that 15 times is higher, than for plasma erosion switch [2]. In the experiments there were employed two methods: magnetic probes positioned on the track of PFD propagation and the optical method facilitating PFD light registration through the row of holes in the external electrode of the coaxial working chamber. Data retrieved, using magnetic probes helped to derive the PFD current shell propagation velocity (up to 20±5 cm/μs) at the distance of 12 cm on its way to the load. The optical method facilitated determination of the velocity of the current shell glow front.

[1] C. W. Mendel, Jr. and S. A. Goldstein, "A fast-opening switch for use in REB diode experiments" J. Appl. Phys. 1977, vol 52, p 1004-1009.

[2] A. I Pavlovskii, N. F. Popkov, E. A. Ryaslov, A. S. Pikar, V. I. Kargin et al. "Characteristic optimization of pulsed energy sources with plasma switches" in Megagauss magnetic field generation and pulsed power application, Ed. by M.Cowan and R.B.Spielman, Nova Science Publishers, NY, 1994, p. 757.

[3] W. L. Baker, G. Bird, I. S. Buff et al. "Multi-megaampere plasma flow switch driven liner implosions. " in "Megagauss Fields & Pulsed Power Systems" edited by V. M. Titov and G. A. Shvetsov Nova Science Publishers, New York, 1990. pp. 653-662

[4] A.I. Pavlovskii, N.F. Popkov, E.A. Ryaslov, et all "Powerful pulsed energy sources for plasma physics investigations" in [2] p. 429.

[5] V.S. Bossamykin, A. I. Gerasimov, A.I. Pavlovskii et all, "System of 500 kV Marx generators for LIA-30 radial line charging", 9-th IEEE Int. Pulse Power Conference, Albuquerque, NM (USA) 21-23 June 1993, Springfield, VA, NTIS, 1993, v. 1 pp. 993-995

A 10 TW PULSED ENERGY COMPLEX PIRIT-2000 FOR INVESTIGATION OF SHORT-WAVE RADIATION

N.F. Popkov, E.A. Ryaslov, V.I. Kargin, A.S. Pikar', V.I. Vorontsov, D.V. Kotel'nikov, A.V. Melkozerov

VNIIEF, Sarov, Russia, E-mail: popkov_3001@spd.rfnc.nnov.su

INTRODUCTION

Other the past several years abroad program of research on the plasma physics of high-energy densities has been conducted at VNIIEF. Some facilities were designed with a wide range of achievable currents and various storage energies to allow the study of a wide class of physical processes in plasma switches and plasma irradiating discharges and to improve measurement techniques.

The results of experiments with PIRIT-2000 on the investigation of a plasma pulsed X-ray source are presented here [1, 2]. The facility is designed on the basis of the scheme with a primary module capacitive energy storage feeding a vacuum inductive storage. The formation of a rapidly increasing current pulse and its commutation on a load are executed by a plasma opening switch. The possibility of using vacuum diodes and different types of plasma loads for the generation of high-power X-ray radiation fluxes exists.

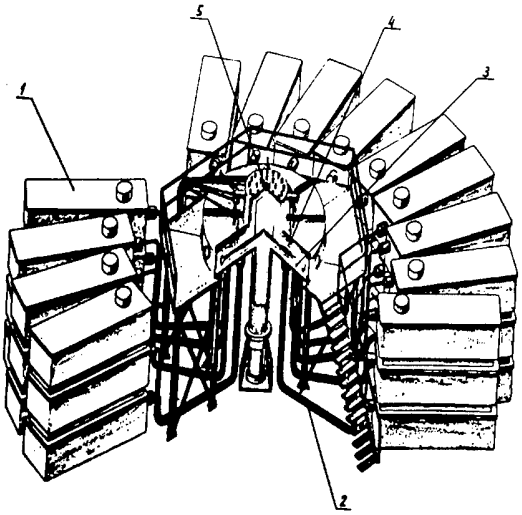

FIG. 1 The scheme of PIRIT-2000 arrangement.

1. FACILITY DESCRIPTION

The facility PIRIT-2000 refers to the class of machines with inductive capacitive storage of energy and its space-time formation. The arrangement of this facility is presented in Fig 1. A vacuum chamber is placed in the center and the modules of primary energy storage are arranged around it in three stories. The primary storage with maximum energy store up to 2 MJ consists of 54

modules; its inductance is 13 nH. The GIN-500 pulsed voltage generator as a storage module is a 0.75 μH, 0.32 μF five-stage Marx generator that stores up to 40 kJ at 100 kV charge to deliver up to 200 kA in 1-1.3 μs to a load [3].

Each pulsed voltage generator is connected to the collector of the inductive storage by a KVI-500 high voltage, high current cable. The inductance of the facility cable line is 5 nH.

The inductive storage is a vacuum disc line with the inductance of 15 nH, composed of a high voltage disc electrode 3 m in diameter and a grounded vacuum chamber body. The energy supply is executed through the lower chamber plane by a vacuum cable collector. The facility collector is formed of a high-voltage vacuum termination of each KVI-500 cable. On a higher level of the chamber there are axially arranged up to 120 plasma injectors connected by coaxial cables up to three GIT-100 pulsed current generators (each is 40 kJ, 100 kV capacitor bank). The plasma injector is made by terminating a piece of semirigid coaxial cable with flush the center conductor [2]

2. RESULTS OF INVESTIGATIONS ON CURRENT PULSE FORMATION

The investigations were carried out sequentially on the facilities of 18, 36 and 54 modules. First, the characteristics of the plasma opening switch of the facilities when they take inductive and ohmic loads were investigated [2]. The formation of the inductively stored current pulse on PIRIT facilities with the help of a plasma switch was investigated for storage energies of 40, 120, 320 kJ and 1, 2 MJ. The current pulse amplitude of the inductive storage varied from 200 kA up to 10 MA, the intensity of the electric field from 50 to 150 kV/cm and the magnetic field amplitude from 5 to 30 kA/cm.

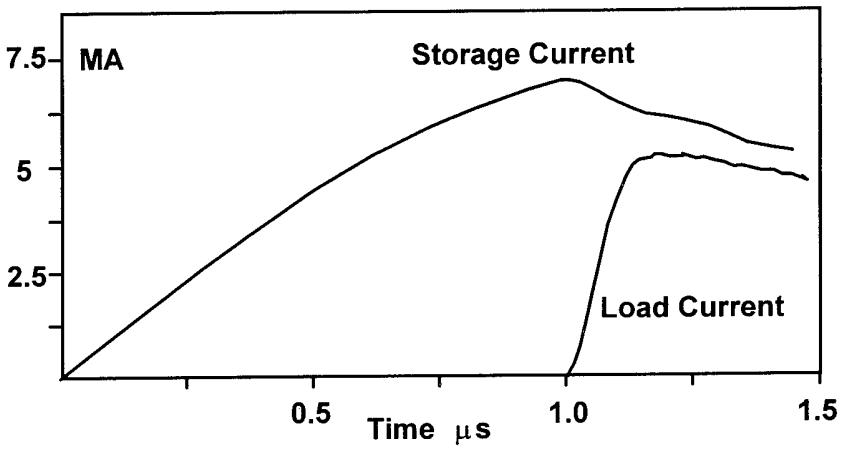

FIG. 2 Characteristic current pulses of PIRIT-2000

On a one-module facility the current rise time for the inductive load was as high as 20 ns; i.e., 50-fold pulse sharpening took place. When using the second stage of the plasma opening switch we managed to reduce the current-rise time to 10 ns. When the vacuum diode was used as a load, the voltage amplitude of the pulse obtained was 2 MV and the beam current was 150 kA; i.e., the 4-fold increase of voltage over the generator (GIN-500) voltage was achieved. With the help of a plasma opening switch, a current of 5 MA amplitude, 150 ns front and 10 TW power was formed in the inductive load from the primary current pulse with the amplitude of 7 MA (T/4=1.3 μs) on the facility PIRIT-2000

(Fig. 2). Vacuum and plasma diodes as well as plasma Z-discharges are used in PIRIT facilities as irradiating loads.

3. EXPERIMENTS WITH PLASMA DIODE ON PIRIT-2000 FACILITY

The experiments on X-ray radiation generation with maximum storage energy up to 1 MJ and load current up to 5 MA were carried out with plasma load on the facility PIRIT-2000. The cathode diameter was 15 cm and the anode-cathode gap - 5 cm. The cathode was made of a thin-walled tube, its end being closed by a metallic grid. Six plasma guns, injecting plasma to the cathode are placed on the anode.

The X-ray dose measurement was executed with the help of thermoluminescent dosimeters. Registration of X-ray radiation in a wide spectral range was implemented with the help of PIN-diodes and X-ray diodes. The integral radiation output of plasma loads was measured by a thermocouple foil calorimeter [4]. To determine the electron temperature of plasma we used the method of absorbing filters in the region of soft X-ray radiation. In the course of experiments the operation modes of plasma diode were studied by means of changing the parameter of plasma, injected into the diode.

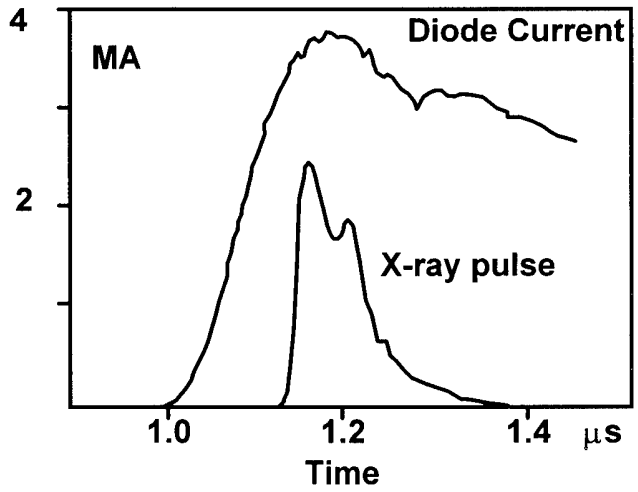

FIG. 3 Diode current and the X-ray pulse for PIRIT-2000.

The current amplitude in the load was 4 MA, with a rise time of 150 ns. The peak integral output of X-radiation energy, measured by an open thermocouple calorimeter, was as high as 100 kJ with an energy storage of 1 MJ. Figure 3 presents the current pulses of plasma load as well as the signal from the X-ray detector. The measurements by the thermocouple calorimeter behind the filters of 10 μm Al and 10 μm Ni give 40 kJ and 10 kJ absorbed X-ray energy; this makes it possible to judge on the spectrum of the X-ray radiation. Figure 4 shows a typical spectrum roughly unfolded from X-ray diode data with different filters.

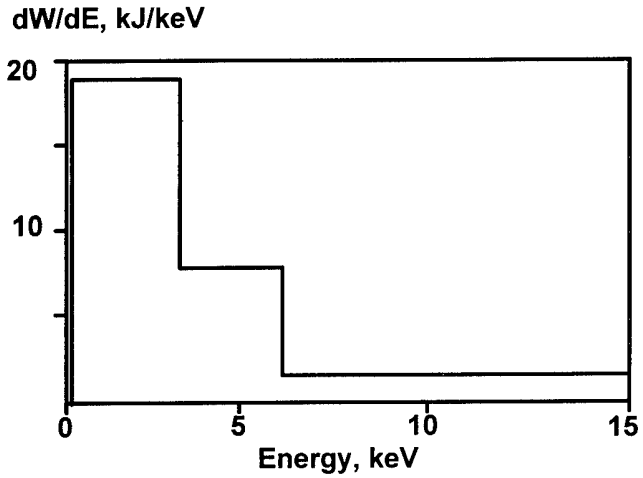

FIG. 4 X-ray spectrum unfolded from an array of filtered X-ray diode detectors.

CONCLUSION

The results of experiments on a plasma X-radiation source in the PIRIT-2000 facility are presented in this paper. The facility is designed with module capacitive energy storage, energizing a vacuum inductive storage. The formation of a rapidly growing current pulse as well as its commutation on a load was carried out by a plasma opening switch. A vacuum diode as well as various types of plasma loads can be used for the generation of a high-power X-ray flux. The energy store of a primary 54 modules capacitive storage is up to 2 MJ, its inductance is 15 nH and its output voltage is 500 kV. The current amplitude in the plasma load was 4 MA with the 150 ns rise time.

The maximum integral energy output of X-ray radiation, measured by an open thermocouple calorimeter, was as high as 100 kJ, while the storage energy was 1 MJ. The plasma load usage at the 4 MA current ensured the 100 kJ generation in X-ray radiation and the density of the X-ray radiation flux at a distance of 1 m from the source was as much as 0.8 J/cm^2, while near the source it was 10 J/cm^2. The PIRIT facilities can be applied for different radiation technologies, namely sterilization, X-ray lithography and chemical production.

[1] A.I. Pavlovskii, N.F. Popkov, E.A. Ryaslov, et all "Powerful pulsed energy sources for plasma physics investigations" in Megagauss magnetic field generation and pulsed power application, Ed. by M.Cowan and R.B.Spielman, Nova Science Publishers, NY, 1994, p. 429.

[2] A.I. Pavlovskii, N.F. Popkov, E.A. Ryaslov, et all "Characteristic optimization of pulsed energy sources with plasma switches" in Megagauss magnetic field generation and pulsed power application, Ed. by M.Cowan and R.B.Spielman, Nova Science Publishers, NY, 1994, p. 757.

[3] V.S. Bossamykin, A.I. Gerasimov, A.I. Pavlovskii et all, "System of 500 kV Marx generators for LIA-30 radial line charging", 9-th IEEE Int. Pulse Power Conference, Albuquerque, NM (USA) 21-23 June 1993, Springfield, VA, NTIS, 1993, v. 1 pp. 993-995

[4] Suchkov V. P. et al "Foil adiabatic calorimeter" PTE, No 5, p. 58-61 (1987).

FOCUSING OF MEGAAMPER ELECTRON BEAM IN GAS CELL FOR PRODUCTION OF FLASH X-RAY SOURCE

V.F.Zinchenko, A.M.Chlenov, V.D.Shijan

Research Institute of Scientific Instruments
RF Atomic Energy Ministry
Turaevo 140061 Lytkarino, Moscow region, Russia

Abstract

One of the important problems to be solved in development of the intense source of flash X-rays is a choice of the optimum construction of a high-current diode at the exit of an electron accelerator.

In this report, the results of numerical investigations of megaamper relativistic electron beam (REB) generation and focusing in a compound diode are discussed. The diode consists of a vacuum field-emission annular cathode, a planar anode and a gas cell inserted between the anode foil and a target.

Introduction

Use of high-current REB with electron energy limited by 1 MeV is one of the most preferable ways to generate intense flash of hard Roentgen radiation (HRR). When solving this problem, it is necessary to study some features of REB generation and focusing with the following parameters:

peak beam current, I_{max} = 1 MA;

electron energy, E_e = 0.5...0.7 MeV;

pulse duration, t_p = 50...100 ns.

For these REB parameters, its own electromagnetic field significantly influence on electron trajectories in the diode region. Therefore, a possible way to control REB transport in the diode and, consequently, to obtain an optimal radial and angular distribution of electron flow at the target (converter) is bound up with studying the utilization of REB intrinsic fields.

The interaction of focused REB with the target damaged by thermal explosion has been examined in refs. [1,2]. The magnetic stopping of REB in the target leads to decreasing the optimal thickness of the target and increasing the HRR output unlike of the case of "cold" target.

In ref.[3], a construction of the diode having an additional grounded foil between the cathode and the anode has been considered. This construction allows to focus megaamper electron beam with electron energy of ~ 1 MeV on a small region at the central axis. However, when electron energy decreases up to 0.5...0.7 MeV, the focusing efficiency of beam within this arrangement falls because the operation mode of the diode becomes similar to that of a reflex triode. Therefore, there is need to provide effective charge neutralization of the beam in the focusing region. This problem can be solved by employing a drift chamber filled in with neutral gas and inserted between the anode and the target.

Possibilities of using a gas cell for transport and focusing of REB with electron energy of ` 20 MeV were discussed in reports [4,5]. The present work deals with studying the focusing of weakly relativistic electron beam with megaamper current on a gas cell to generate intense flash of HRR.

Modeling

At present, the following physical model of electron beam penetration into neutral gas is generally accepted. REB injected into a gas cell rapidly ionizes molecules of gas, creating the highly collisional plasma that composes of mobile electrons and immobile ions. In process of redistribution of plasma particle charge, the beam neutralization is reached for the time $\tau_e=(4\pi\sigma)^{-1}$, where σ is the plasma conductivity. Furthermore, when the beam propagates through the plasma, it induces electromagnetic fields that resulted in generating plasma reverse current I_p and hence to full or partial current neutralization of the beam. Since the plasma reverse current damps during the magnetic decay time

$$\tau_m = \frac{4\pi\sigma R^2}{c^2},$$

(where R is the radius of a plasma channel, c is the light velocity), it becomes possible to transport the beams with the current greater than the Alfven one up to a significant distance.

Obviously, the dynamics of REB injected into gas has complicated dependence on many factors and defys simple analytic description.

More accurately the influence of different characteristics of REB and a gas cell on beam dynamics in gas has been studied using numerical simulation of beam transport through a gas cell by "particle-in-cell" method.

Admitting the axial symmetry availability, the equations of electron motion in the gas cell are written in the form:

$$\begin{aligned}
\frac{dP_r}{dt} &= -eE_r + \frac{e}{cm}\cdot\frac{P_z\cdot H\varphi}{\gamma} \\
\frac{dP_z}{dt} &= -eE_z - \frac{e}{cm}\cdot\frac{P_r\cdot H\varphi}{\gamma} \qquad (1) \\
\frac{dr}{dt} &= V_r, \quad \frac{dz}{dt} = V_z
\end{aligned}$$

where e and m are the charge and the rest mass of electron, respectively, P_r and P_z are the components of momentum.

Induced electric and magnetic fields are defined by solving the Maxwell equation system:

$$\begin{aligned}
\frac{\delta E_r}{\delta t} &= -c\cdot\frac{\delta H\varphi}{\delta z} - 4\pi\sigma E_r - 4\pi j_{br}, \\
\frac{\delta E_z}{\delta t} &= \frac{c}{r}\cdot\frac{\delta(rH\varphi)}{\delta r} - 4\pi\sigma E_z - 4\pi j_{bz}, \qquad (2) \\
\frac{\delta H\varphi}{\delta t} &= -c\cdot\left(\frac{\delta E_r}{\delta Z} - \frac{\delta E_z}{\delta r}\right),
\end{aligned}$$

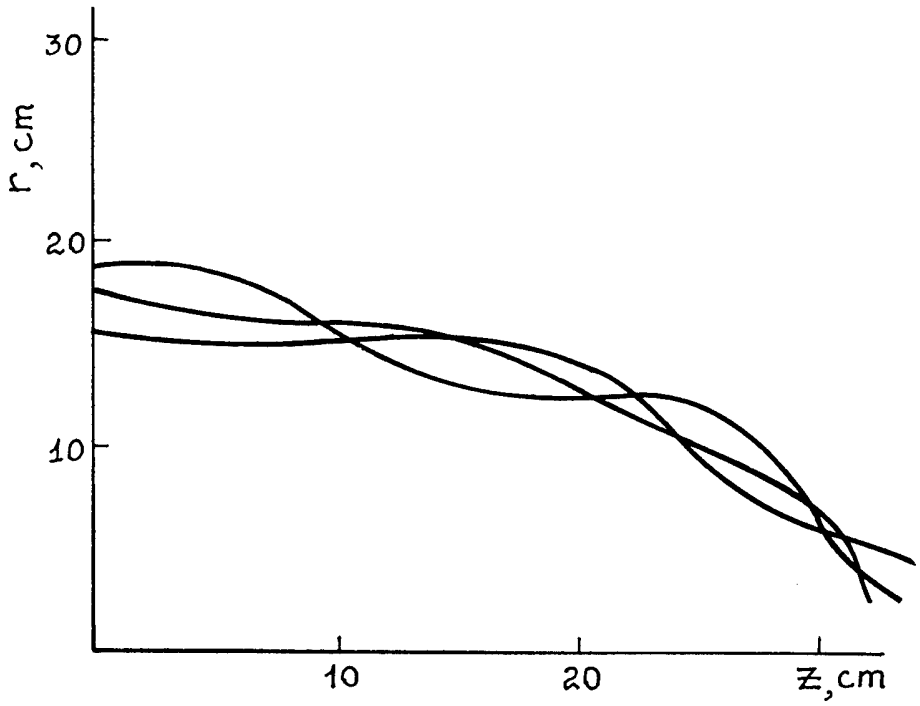

Figure 1. Typical trajectories of electrons in a gas cell (N_2) at pressure 1 Torr for beam parameter I_{max}=1 MA, E_e=0.7 MeV

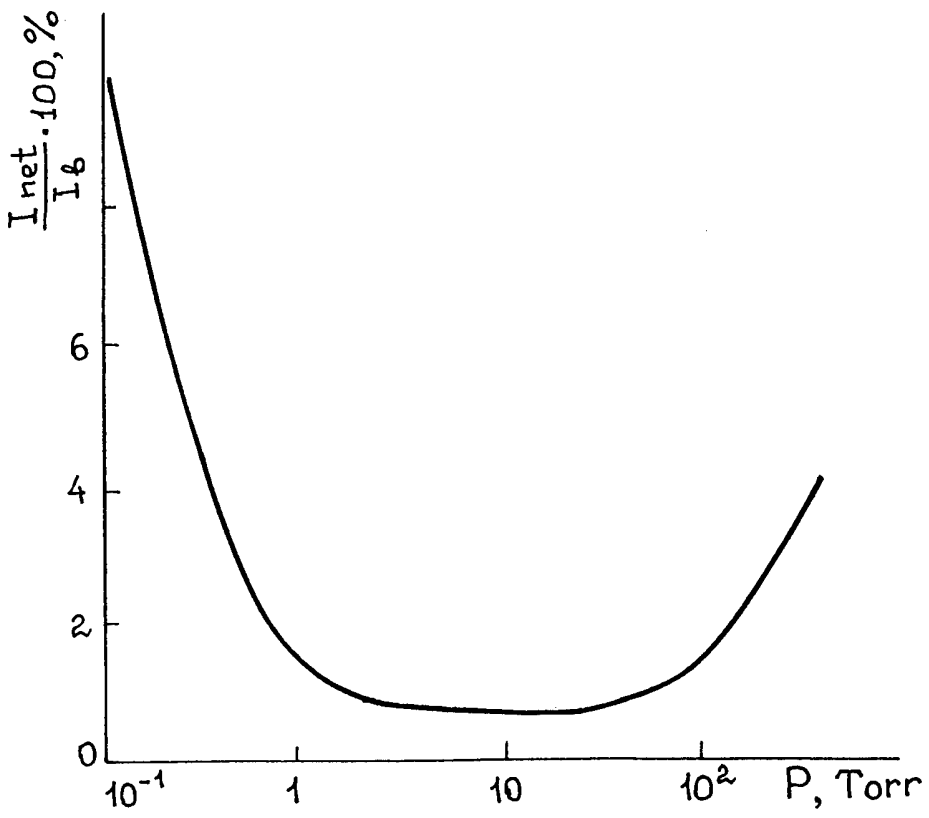

Figure 2. The net current as a function of gas pressure

where j_{br} and j_{bz} are the components of beam current.

Presenting the current pulse $I_b(t)$, injected into the gas cell, in the form of a certain number of macro-particles, we then integrate numerically equations (1, 2) over a chosen time and space grid. The gas conductivity variation with time is defined by numerical integration of the equation

$$\frac{d\sigma}{dt} = kj_b + \eta\sigma - \alpha\sigma^2, \text{ where } k=2*10^7 \text{ (in CGS units), } \alpha, \eta \text{ are}$$

the kinetic coefficients, depending on gas consistency.

A series of transport calculations for the annular REB with peak current = 1 MA, electron energy of 0.5...0.7 Mev, pulse duration of 50 ns, initial radius of beam r_0 = 0.2 m, injected into the gas cell with gas pressure of 10^{-1} to 10^3 Torr has been carried out. The obtained results show that at optimal pressure = 1 Torr, electron trajectories in the cell are similar to ballistic ones (Fig. 1). Maximum conductivity σ_{max} reaches 10^{12} s^{-1}. The main part of REB energy, as calculated, is focused on a limited region at the central axis with a radius of 2...3 cm. In Fig.2 the dependence of net current in the gas cell on gas pressure is also presented.

As the modeling shows, due to high conductivity of plasma in the gas cell during the transport of the REB's main part, a plasma compact channel is formed where the beam with its magnetic field is frozen. The electrons, deviating from a certain mean trajectory, perform relatively small oscillations. about this trajectory.

Summary

As the results of the modeling show, under optimum conditions in a gas cell inserted between the anode of a high-current diode and the target-converter, the annular megaamper REB with the initial radius r_0 = 0.2 m is focused on a small area of the target (r = 2...3 cm) without significant losses of the total beam energy.

[1] Zinchenko, V.F., Timofeyev, V.V., Shijan, V.D.: Proc. 8th Int. Conf. on High-Power Particle Beams, Novosibirsk (1990), 769

[2] Zinchenko, V.F., Timofeyev, V.V., Shijan, V.D.: Phizika Plazmy (rus), 18 (1992), 1296

[3] Zinchenko, V.F., Timofeyev, V.V., Shijan, V.D.: Proc. 9th Int. Conf. on High - Power Particle Beams, Washington (1992)

[4] Sandford, T.W.L., Poukey, J.W., Mock, R.C., Welch, D.R.: J. Appl. Phys., 71 (1992), 472

[5] Sandford, T.W.L., Halbleib, J.A., McAtee, W.H., Welch, D.R.: J. Apl. Phys., 70 (1991),1778

OPTIMIZATION OF THE LINEAR INDUCTION ACCELERATOR CONSTRUCTION FOR MAXIMIZING THE BREMSSTRAHLUNG OUTPUT

V.F.Zinchenko, E.V.Tulisov, A.M.Chlenov
V.D.Shijan

Research Institute of Scientific Instruments
RF Atomic Energy Ministry
Turaevo, Lytkarino, Moscow region, 140061, Russia

Abstract

The results of experimental and theoretical optimization of the linear induction accelerator (LIA) construction are presented. The major aim of these investigations was to maximize the bremsstrahlung output near the target face.

The work was carried out in two stages:

1) modernization of the injector module and

2) focusing of relativistic electron beam (REB) produced at the exit of the accelerating system (AS) in the increasing axial magnetic field.

Besides, the methods of diagnostics of angular and energetic parameters of REB based on measurements of radiation dose fields behind the target are described.

Introduction

The high current electron accelerator LIA-10 is a linear induction accelerator in radial lines with successive sectional structure of the accelerating system. A detail description of its construction is given in references [1] - [3]. The accelerator of this type is used in RISI for generation of intense pulses of bremsstrahlung. At present time the following accelerator's parameters are realized:

- peak current of REB, I_{max} = 30 kA;
- effective electron energy, $E_{e',max}$ = 10 MeV;
- FWHM, $t_{1/2}$ = 10 ns
- peak dose rate, $P_{max} = 10^{12}$ rad(Si)/s .

Lately, complex investigations bound up with optimization of the LIA-10 construction have been carried out with the aim of increasing the generated bremsstrahlung output. In this paper, the results of the optimization of the accelerator injector are presented.

According to the original design of LIA-10, its injector consists of 4 separate sections of inductors (accelerating modules). The voltage induced by accelerating modules (AM's) is summed at a tapered cathode. A thin annular electron beam is generated in the foiless diod (Fig.1) with magnetic isolation in axial field. The

beam is then accelerated as it propagates through the 12 AM's operating during the pulse generation in consistance with a chosen temporal programme. A peak current of REB at the exit of the injector is 40 kA with an electron energy being 2.5 MeV.

The main purpose of this study is to investigate the possibilities of increasing the energy and current of REB injected into AS for decreasing the losses of REB in AS and increasing the bremsstrahlung output. Some of the problems in optimization of the injector construction can be solved, including a choice of cathode-anode gap geometry at the exit of the injector and an optimum number of AM's in the injector; dynamics of beam generation in the injector's diode and timed operation sequence of the AM's forming the injector and the LIA-10 AS.

Numerical Simulation and Experimental Results

Because numerical simulation must be followed by experiments, a simple calculation model of high current REB generation in the accelerator injector has been developed. Let's consider an ideal geometry of an injector used in the modeling (See Fig.1). The voltage induced by AM's is summed by the tapered cathode and applied to the cathode-anode gap. While separate AM induces an accelerating voltage pulse $V_0(t)$, then an electric field strength $E_z^{(i)}(z,t)$ induced by i-th AM can be expressed as:

$$E_z^{(i)}(z,t)=V_0(t)/l_0,\quad z_i \leqslant z \leqslant z_{i+1} \qquad (1)$$
$$z_{i+1}=z_i+l_0,\quad l_0=0.4\ \text{m}$$

A shape of the accelerating voltage pulse was determined by using special experiments.

For the mathematical description of temporal behavior of current and voltage pulses in the injector diode, so called telegraph equations were used:

$$R^*J = -\frac{1}{C^*}\frac{\delta \text{æ}}{\delta z} - \frac{1}{c^2} L^* \frac{\delta J}{\delta t} + E_{ind} \qquad (2)$$
$$\frac{\delta \text{æ}}{\delta t} = -\frac{\delta J}{\delta z}$$

where J(z,t) is the current, running through the tapered cathode, L^*, R^*, C^* are the self-induction, resistance and capacity per unit length of cathode, respectively; $E_{ind}(z,t)$ is the electric field strength induced by the injector forming AM's (1).

Boundary conditions for equation set (2) at the cathode tip ($z=L_k$), taking into account the operating features of the cathode under explosion emission conditions, can be described as follows:

$$J(L_k,t) = 0, \quad E_c \leqslant E_{th}$$
$$\left.\frac{\delta J}{\delta z}\right|_{z=L_k} = 0, \quad E_c > E_{th} \qquad (3)$$

where E_c is the macroscopic electric field strength near the cathode tip. E_{th} is the starting threshold of the electron explosion emission from the cathode.

By solving the equation set (2) at the boundary conditions (3), we obtain distribution J(z,t) in the cathode length. A voltage applied to the diode gap is estimated from:

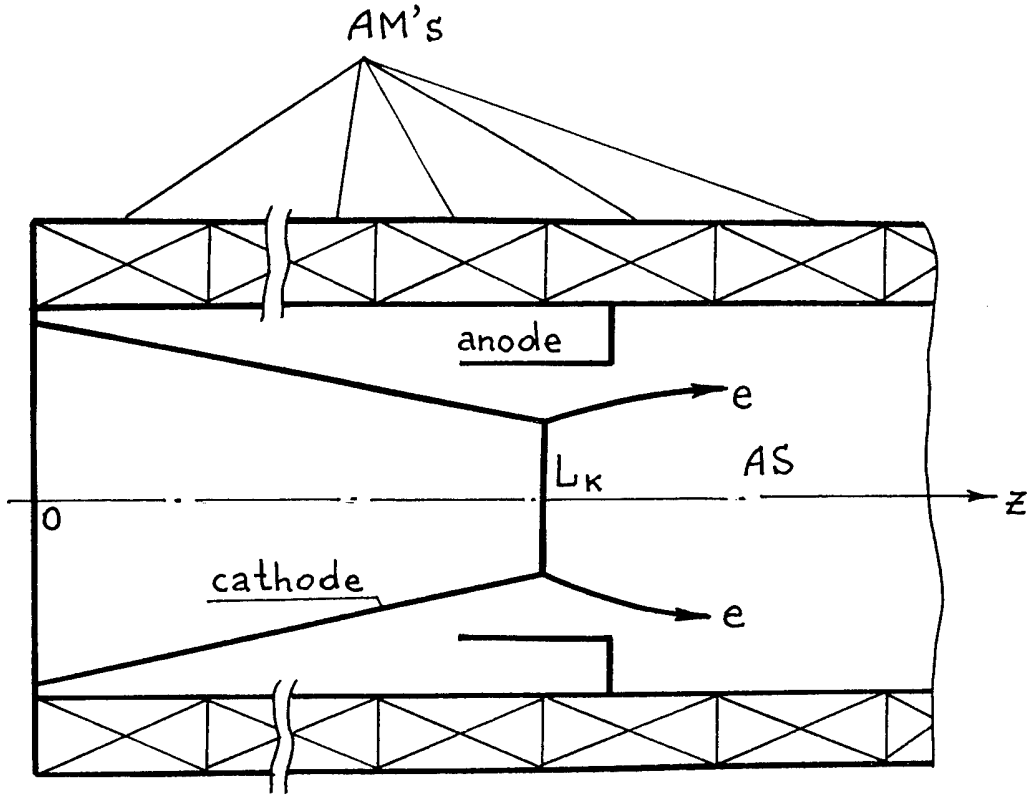

Figure 1. Schematic of the LIA-10 injector

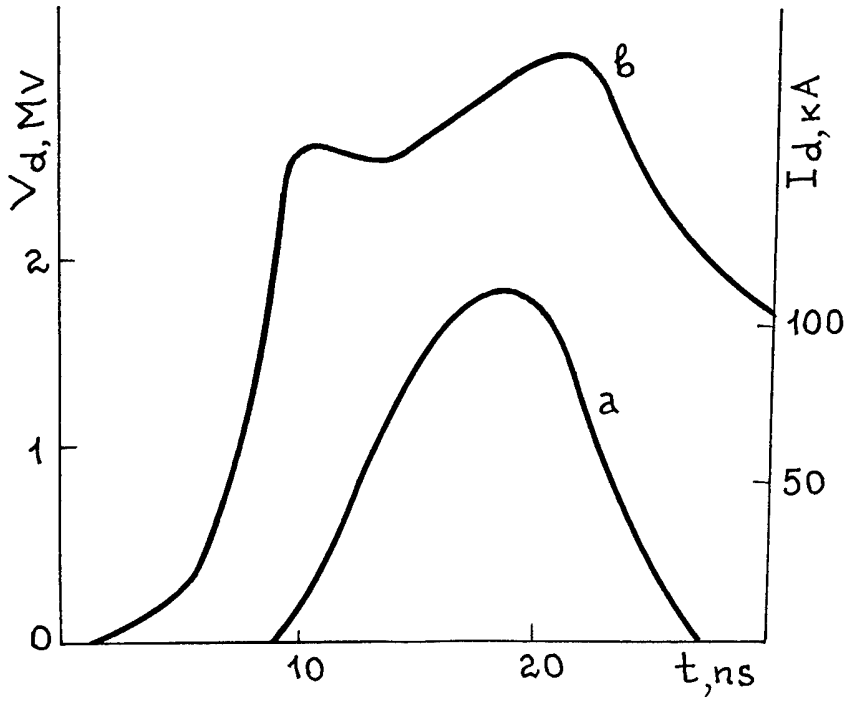

Figure 2. Current (a) and voltage (b) pulse at the exit of the injector formed by 7 AM's

$$V_d(t)=\int_{Z_{min}}^{L_k}(-R^{*}J-\frac{1}{c^2}L^{*}\frac{\delta J}{\delta t}+E_{ind})dZ \qquad (4)$$

A magnitude of E_{th} was only one of unknown parameters of the calculation model. Its value was obtained by comparison of experimental and calculation results on REB current amplitude and a value of temporal shift of voltage and current pulses at the exit of the 4 AM's injector (original version of LIA-10). The optimal value (E_{th}=800 kV/cm) agrees quite well with known experimental results obtained for explosion cathodes [4].

Using the above model, complex of calculations to optimize parameters of the modified LIA-10's injector was performed. Typical shapes of current and voltage pulses at the exit of the injector are presented in Figure 2.

The additional calculation of REB propagation through AS showed that the following REB parameters at the exit of AS are realized: peak current I_{max}=120 kA, electron energy E_e=10 MeV, FWHM $t_{1/2}$=10 ns, beam mean radius r_b=5 cm. After REB focusing in the increasing axial magnetic field (B_z=4 T), a magnitude of peak dose rate at the face of the target reaches $5*10^{12}$ rad(Si)/s.

To control additionally the AS operation, a method for determination of electron energy (E_e) as well as angle of electron incidence on the target (Θ_e) has been developed. The method is based on measuring the characteristics of dose field downstream the target. It was shown, using Monte Carlo electron -photon transport code, that the relative dose profile at the central or displaced (~15...20 cm) axis of REB weakly dependes on electron energy and is defined only by an angle Θ_e. While knowing Θ_e, electron energy is estimated from comparison of calculated and experimental dose values related to a single electron at a certain point downstream the target.

Using integral thermoluminescent dosimeters (LiF, CaF_2), we obtain mean values (Θ_e) and (E_e) for a REB pulse. On the other hand, by employing dynamical detertors, it is possible to get distributions $\Theta_e(t)$ and $E_e(t)$ during the pulse.

Conclusion

Thus, the calculational and experimental methods presented in this study allow to determine correctly basic characteristics of LIA-10 REB in process of the accelerator construction optimization as well as during the accelerator operation.

[1] Pavlovskii, A.I., Bosamykin, V.S.,: Atomnaja Energija, **37** (1970) 228.

[2] Pavlovskii, A.I., Bosamykin, V.S., Gerasimov, A.I., : Dokl. Acad. Nauk SSSR, **222** (1975) 817.

[3] Pavlovskii, A.I., Bosamykin, V.S., Gerasimov, A.I., : Dokl. Acad. Nauk SSSR, **250** (1980) 1118.

[4] Rudakov, L.I., : Generazija i fokusirovka silnotochnykh electronnykh puchkov (in russ.), Moscow, Energoatomizdat, 1990.

SPACE AND TIME RESOLVED OBSERVATIONS OF HOT SPOT DYNAMICS IN A VACUUM SPARK DISCHARGE

H. Chuaqui, M. Favre, R. Saavedra, E. Wyndham, P. Choi*, C. Dumitrescu-Zoita* and L.Soto**

Facultad de Física, Universidad Católica de Chile, Casilla 306, Santiago 22, Chile
**LPMI, Ecole Polytechnique, Palaiseau 91128, France*
***Comisión Chilena de Energía Nuclear, Casilla 188-D, Santiago, Chile*

ABSTRACT

Experimental observations of the plasma formations in a Vacuum Spark discharge are presented. A low power Nd:YAG laser pulse incident onto a Titanium cathode initiates the discharge. The evolution of the Titanium plasma electron density and temperature is followed both in the visible and the soft X-ray part of the spectrum. The former uses a novel micro holographic interferometric technique permitting a spatial resolution better than 20 μm. The probing beam is a 6 ns frequency doubled Nd:YAG laser. The latter emission is resolved using a number of different methods. The spatial information is derived from a 1 ns multi framing camera X-ray camera which projects the plasma image using four different slit wire pinhole images and six pinhole images, each aperture being filtered differently. The temporal evolution of the emission of each discharge is followed using several Silicon PIN diodes. The x-ray spectrum is deconvolved from the filter and detector response and interpreted using a collisional radiative package. The hot spots are seen to form in a submilimetre pinch stemming from the incident laser focus which has a life time of about 20 ns. The hot spots are much shorter events, reaching substantially higher densities, but involve only part of the line density of the pinch column.

INTRODUCTION

The Vacuum Spark is a small scale device which allows the achievement of plasma conditions leading to radiative collapse on a nanosecond time scale [1]. Most of the work on Vacuum Spark has been performed using low inductance capacitor banks to drive the discharge, although interesting results have been obtained using pulse power driving techniques [2,3]. In a previous experiment we have used a low inductance coaxial line feed by a Marx generator to power the discharge. Short circuiting of the line switching gap allows the Vacuum Spark to be driven in the hybrid regime [4]. Under these conditions, a pre ionising laser plasma, resulting from the application of a short laser pulse focused onto the cathode, is produced at a time when there is a field of over 100 V/cm across the discharge electrodes. It has been found that in this mode of operation a relatively low laser energy is sufficient to generate adequate initial conditions to achieve radiative collapse [5]. In this work we report on the time and space evolution of a Vacuum Spark Titanium plasma. The electron density and temperature is followed both in the visible and the soft X-ray part of the spectrum. The plasma electron density dynamics is followed using a novel micro holographic interferometric technique permitting a spatial resolution better than 20 μm [6]. Hot spots are seen to form in a submillimetre pinch stemming from the incident laser focus which has a life time of about 20

ns. The hotspots are found to be short events, reaching substantially high densities within a nanosecond of their initiation, but which involve only part of the line density of the pinch column.

EXPERIMENTAL APPARATUS

The Vacuum Spark is operated in the hybrid mode. It is driven by a 1.5 Ohm coaxial pulse forming line with a maximum current of 140 kA in a 120 ns pulse. A 0.4 J, 8 ns Nd:YAG laser pulse is focused through the cylindrical anode onto the cathode. Both cathode and anode are made of Titanium. Further details on the experimental set-up have been published elsewhere [4,5]. The micro holographic interferometric technique, based on the Mach-Zehnder Interferometer, is used to study the plasma electron density and is complemented with simultaneous results from image plane interferometric holograms. The probing beam is a 6 ns frequency doubled Nd:YAG laser. A visible streak camera is used to follow the axial evolution of the discharge plasma. The X-ray emission is resolved by a number of different methods. The spatial information is derived from a 3 ns multi framing X-ray camera in which the plasma projects a set of images using four different slit wire images [7] and six pinhole images, each image obtained through different filter. The temporal evolution of the emission of each discharge is followed using several Silicon PIN photodiodes and with absolute XUV Silicon photodiodes. The soft X-ray emission is quantified for different regions of this highly reproducible discharge.

EXPERIMENTAL RESULTS

Figure 1 shows an axial optical streak of the Vacuum Spark plasma, covering a period of 300 ns, from the time when the laser strikes the cathode until a time shortly after the peak of the discharge current. The very short lived formation of the hot spot plasma column is seen just before peak current. There is a clear tendency for the hot spot formation of the plasma points to propagate from the cathode towards the anode. Position of the plasma points is found to be highly reproducible if the discharge is operated in the hybrid mode. Characteristic electric and X-ray emission signals are shown in figure 2. The voltage is ramped up, as is characteristic in the hybrid mode, and the initiating laser is fired at 1.4 μs. PIN diodes 1 and 3 see the whole discharge region, whereas, PIN 2, 4 and 5 see only the half of the discharge volume which is closer to the cathode. For ~70 ns since the application of the laser, the impedance is high and electron beam induced emission from the anode is observed, until breakdown takes place at 1.5 μs. For the next ~150 ns, the cathode region is seen to emit at energies above 1 keV, as shown by PIN-5. Close to peak current burst of x-ray pulses are emitted, as indicated by PIN-3 and PIN-4. At this time

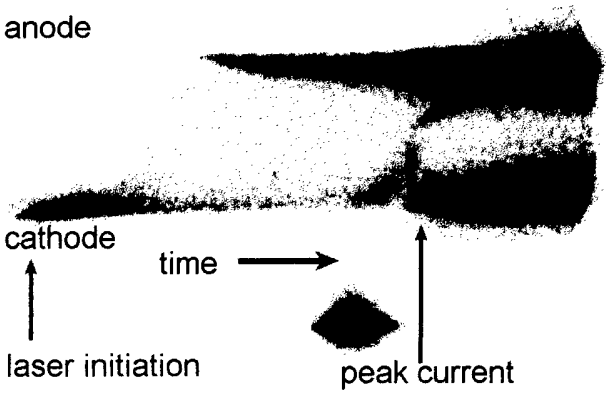

Figure 1: axial streak of the Vacuum Spark plasma.

emission seen by PIN-5 does not greatly increase. On comparing signals from PIN-2 and PIN-3, the fact that PIN-2 sees only the cathode region and PIN-3 the whole discharge volume, indicates that the plasma emitting regions, hot spots, propagate from the cathode towards the midpoint of the discharge. The relative amplitude of the different PIN diode signals also indicates that successive hot spots are of decreasing characteristic temperature.

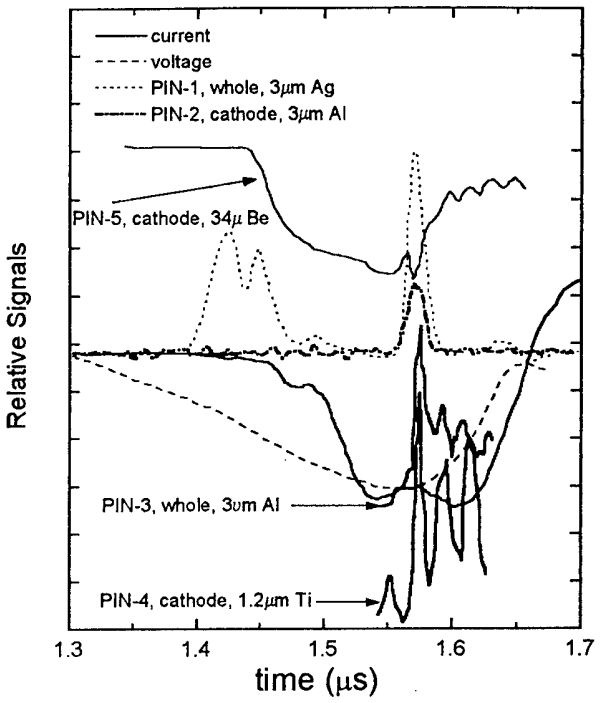

Figure 2: characteristic electric and x-ray signals.

A series of x-ray frames is shown in figure 3. The timing of each frame is relative to the maximum of the signal in PIN-2, in Fig. 2. The frames correspond to the slit-wire pin hole camera configuration. Exposure time is 1 ns. The upper series was obtained with a 5 μm Al filter, and the lower one, with a 1 μm Ti filter. At each time, both filtered images correspond to the same shot. It is clear that brighter hot spots form first near the cathode, whereas at later times they tend to form further away from the cathode and are of much less intensity. This observations are in full agreement with the PIN diode x-ray signals shown in Fig. 2.

Micro holographic interferograms of the plasma column at the time of plasma point formation have been obtained with a 6 ns laser. A typical example is shown in figure 4. The duration of the laser pulse is too long to freeze plasma point formation in the sub-nanosecond time scale, but does show the larger scale plasma distribution. In particular, the interferogram shows a

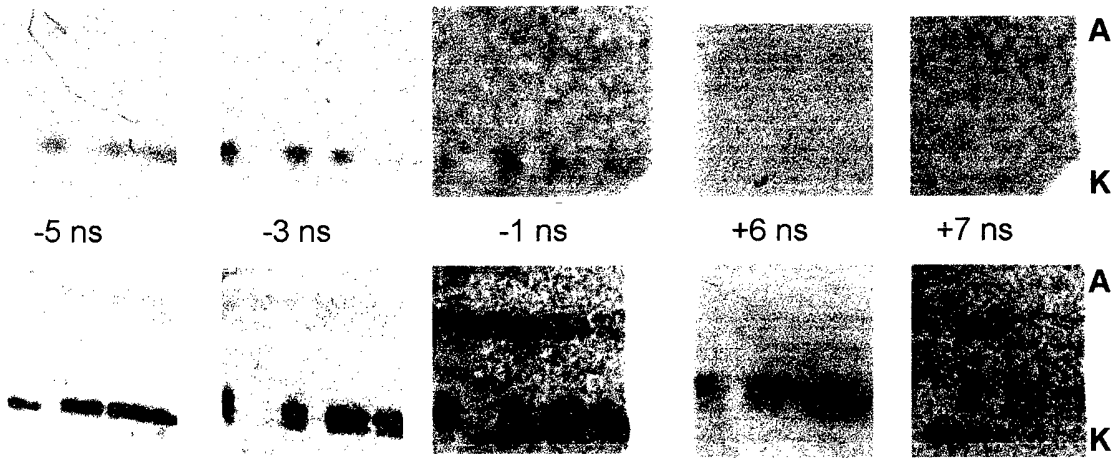

Figure 3: series of X-ray slit-wire framing camera photographs.

dense down spreading anode plasma and the initial plasma column stemming from the laser focus point.

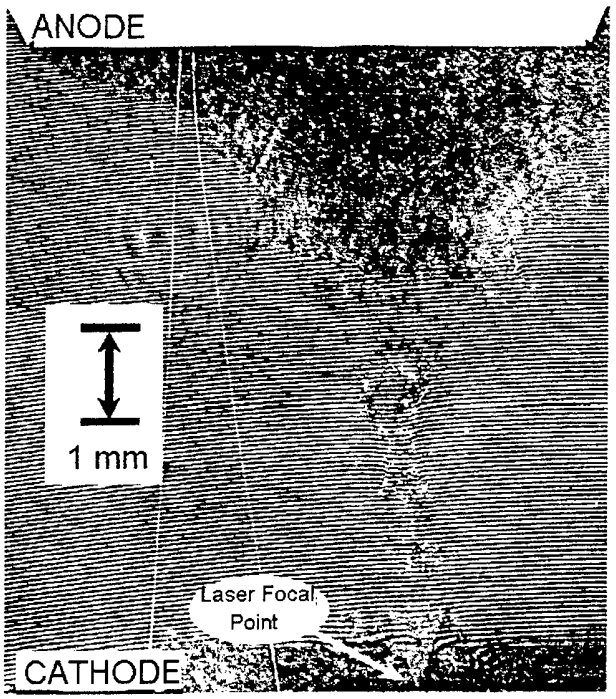

Figure 4: Micro Holographic Interferogram of the plasma column at the time of Plasma Points formation.

DISCUSSION AND CONCLUSIONS

The present results show that plasma formation in the Vacuum Spark evolve rapidly once a dense plasma has formed on the cathode, at the laser focal point. A plasma column stems from this focal point and plasma points, hot spots, form on a nanosecond time scale, propagating to the axial midpoint of the discharge, where the anode blow off meets the column. Plasma temperature can be obtained from the measured emission ratios observed with different filter combinations. The X-ray emission can be modelled using a CRE code [8] and when the detector response (film, photocathode, PIN diode) is convolved with the modelled emission, a good measure of the plasma temperature is obtained. In this case, the cathode bright spot is found to have a temperature of approximately 750 eV, whereas the temperature of the hot spots is about 400 eV in the first hot spot at 1 mm from the cathode, and 250 eV in the second, at 2.5 mm from the cathode. If a third hot spot forms at 3.5 mm, its temperature is ~150 eV. The anode blow off plasma has a higher temperature for longer than both the cathode bright spot and the ensuing plasma column. This temperature might be slightly over 1 keV.

The combination of these two new diagnostics, the Micro Holografic Interferometer and the Slit-Wire Camera, allows fine scale plasma structures to be resolved, both in density and temperature. Further work is presently under way to study in finer detail the hot spots dynamic.

ACKNOWLEDGEMENTS

This work has been funded by FONDECYT and CEC ISC. R. Saavedra acknowledges a postgraduate studies scholarship awarded by CONICYT.

REFERENCES

[1] K.N Koshelev and N.R. Pereira, J. Appl. Phys. **69**, R21, 1991.
[2] S.M. Zakharov et al., Sov. J. Plasma Phys. **10**, p. 303, 1984.
[3] H. Chuaqui et al., Phys. Fluids B **5**, p. 4244, 1993.
[4] E. Wyndham et al., J. Appl. Phys. **71**, p. 4164, 1993.
[5] H. Chuaqui et al., Phys. Plasmas **2**, p. 3910, 1995.
[6] L. Soto et al., submitted to Rev. Sci Instrum.
[7] H. Chuaqui et al., *Proc. 1994 ICPP* (Foz do Iguazu, Brasil), 1994, p. 29.
[8] R.W. Lee et al., JQSRT **32**, 1984.

Imaging of Exploding Wire Plasmas by High-luminosity Monochromatic X-ray Backlighting Using an X-pinch Radiation Source.

S.A. Pikuz, T.A. Shelkovenko and V.M. Romanova
P.N. Lebedev Physical Institute, Russian Academy of Sciences,
Leninsky Prospect 53, Moscow, Russia
D.A. Hammer
Laboratory of Plasma Studies and School of Electrical Engineering,
Cornell University, Ithaca, New York 14853, USA
A.Ya. Faenov and T.A. Pikuz
Multicharged Ions Spectral Data Center of VNIIFTRI,
Mendeleevo, Moscow Region, 141570, Russia

Abstract

A new diagnostic method for dense plasmas, monochromatic x-ray backlighting, is described. In this method, shadow images of a bright, dense plasma can be obtained with high spatial resolution using monochromatic radiation from a separate plasma, permitting a major reduction in the required backlighting source power. The object plasma is imaged utilizing spherically bent mica crystals as x-ray optical elements. Images of test objects obtained using x-ray radiation having different photon energies are presented. Shadow images of exploding Al wire plasmas in the $1s^2$-1s3p line radiation of He-like Al XII are also shown. Spatial resolution as fine as 4 μm is demonstrated. The scheme described here is useful for backlighting extended high density plasmas, and could be a less costly alternative to using X-ray lasers for such purposes.

X-ray backlighting of high density plasmas[1,2] is one of the most effective target diagnostic methods in the inertial confinement fusion research program. It has also been used to investigate high density pinch discharges[3].

Here we describe a new approach to imaging dense plasmas, monochromatic X-ray backlighting, along with initial experimental results obtained with it. Shadow images of bright object-plasmas are obtained with high spatial resolution using a single spectral line from a separate plasma. This method substantially reduces the requirements on the backlighter source radiation power relative to that of the object-plasma. Moreover the field of view in this scheme as tested was a few cm by a few mm. To accomplish this, we used a mica crystal that has been accurately bent to form a spherical reflecting surface as a lens to form the X-ray shadow image, thereby providing the high spectral selectivity to the focused radiation that is central to this diagnostic technique. The principle of monochromatic X-ray backlighting was published elsewhere[4]. A schematic diagram of the method is shown in Fig. 1, and combinations of different films and filters used in various experiments are shown in Fig. 2a.

Experimental tests of monochromatic backlighting were performed using the XP pulser at Cornell University operating at about 350 kA peak current in a 100 ns pulse and the BIN generator at the Lebedev Institute with a current of 250 kA in a 100 ns pulse. X-pinch plasmas, produced by the explosion of crossed wires in the vacuum diodes of the two pulsers, were used as the source of x-ray radiation. One of the main tasks of these experiments was to obtain a shadow image of a test object with the best possible spatial resolution using radiation with different wavelengths. The radiation from different types of wires, from Al to W, was used,

covering a wide range of x-ray energies from near 1 to several keV. The diagnostic system geometry was adjusted before a pulse to be set for different spectral lines using spherical mica crystals having radii of 186 and 100 mm.

Since mica is a natural crystal, actual samples can have different values of the crystal lattice spacing d. Because we must work with Bragg angles θ near normal in the formula $2d\sin\theta = m\lambda$, we must know d with high accuracy, where λ is the wavelength of the radiation and m is the order of reflection. In order to determine d to the required accuracy, the crystal was set up in a spectrograph with an extended $1s^2$-1s3p He-like Al (exploding wire) source, as illustrated in Fig. 3a. With a spherical crystal, there is actually a "Rowland sphere," and the form of the spectral line from the extended source on the Rowland sphere is an arc of a circle, as shown in Fig. 3b. The radius of this circle, r, can be measured very accurately and is related to the crystal quantity d according to $r = m\lambda R/2d$, where R is the crystal radius. Notice that if neither d nor λ are accurately known, an accurate measurement of r will determine the ratio λ/d, giving the quantity actually needed to set up a backlighter for another plasma, namely the angle θ in the expression $2d\sin\theta = m\lambda$. An X-ray microscope[5,6] and Cauchois spectrograph[6,7] were used to determine the size and shape of the backlighter source (see Fig. 4).

In order to determine the actual spatial resolution of the backlighter diagnostic, images of metal grids, thin wires having 37.5 and 12.5 μm diameter, and 8 μm diameter glass fibers were obtained using several different x-ray spectral lines. The spatial resolution was estimated using the grid or wire sharpness. Clear images of the wires and glass fibers can be seen with a field of view (5-7) mm $\times$ (10-13) mm in Fig. 5. It should be noticed that the glass fibers were transparent to shorter wavelength radiation, e.g. H-like Ti radiation. Thus, the 30 μm diameter glass shell in which an 8 μm diameter Cu wire was contained is not visible in the fourth image in Fig. 5. The best spatial resolution, 4 μm, was obtained using the mica crystal with R = 100 mm, as shown in Fig. 6.

The ability of the mica crystals to reflect radiation in many orders of reflection (m values) may enable us to image a test object in several spectral lines. In order to separate the spectral information we used a combination of different filters and two films as detectors. In this case, the front film was an additional filter for the back film. The data on film sensitivity and the absorption of radiation by these films were taken from Henke's work[8,9]. In these experiments, 100 μm thick Be foil and combinations of Al and Ti filters were used (see Figs. 2a and 5). The curves of photon detection efficiency using different filter and film combinations are shown in Fig. 2b. The detection efficiency is defined as the product of absorption in the filter divided by the film sensitivity.

As a particular example, we discuss X-pinches from Ta and W wires as backlighter sources. Two DEF films were used to obtain images. For both Ta and W the system geometry was tuned to the L_α line of Ta (wavelength $\lambda = 1.534$Å, angle of incidence $\theta = 83°$, m = 13) and the images of test objects are shown in Fig. 5. Although there is no line with a wavelength of 1.534 Å in the spectrum of W, M-shell radiation with wavelengths 3.98 Å and 4.94 Å is reflected by the crystal in 5th and 4th orders, respectively, and can be used to obtain an image. These wavelengths are in the M-shell radiation of Ta as well as W ions. Therefore, in the case of the X-pinch from W wires, the image of the object was obtained using M-shell line radiation. The fact that there was no image on the second film in the W test verifies this point. By contrast, using the Ta backlighter, an image was obtained on the back film from the L_α line and on the front film from the M-shell radiation simultaneously. (We used filter combinations of Be, Ti, and Al foils, as shown in Fig. 5, to understand which radiation was responsible for creating the image. From the curves of detector efficiency it is clear that the image of the grid with the filters from Al and Be foils was created using the radiation with $\lambda = 1.533$Å. All images were investigated by this method.)

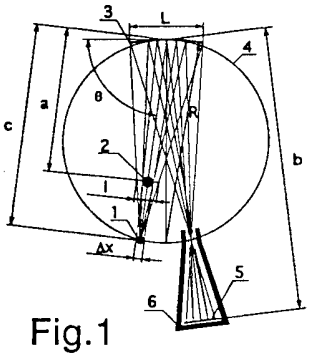

Fig.1

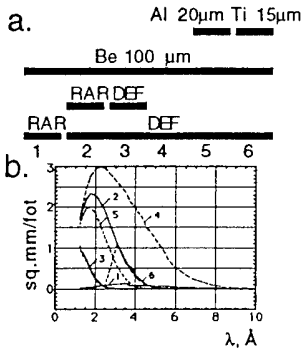

Fig.2

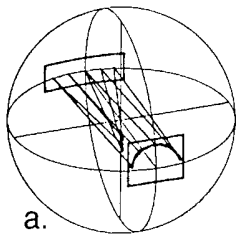

Fig.3

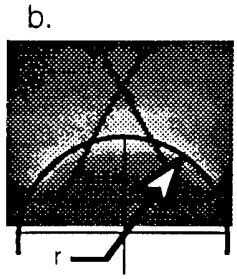

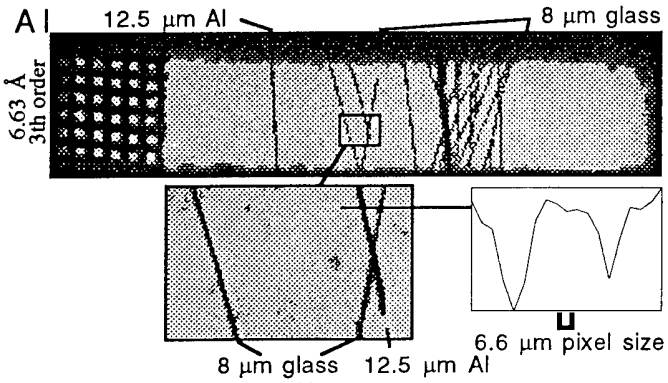

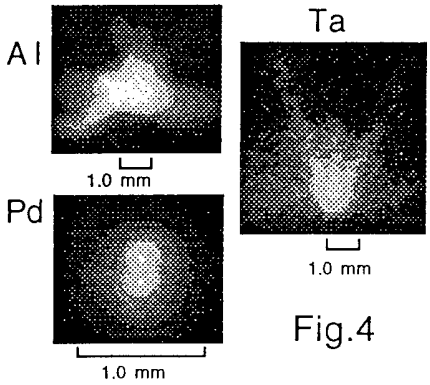

Fig.4

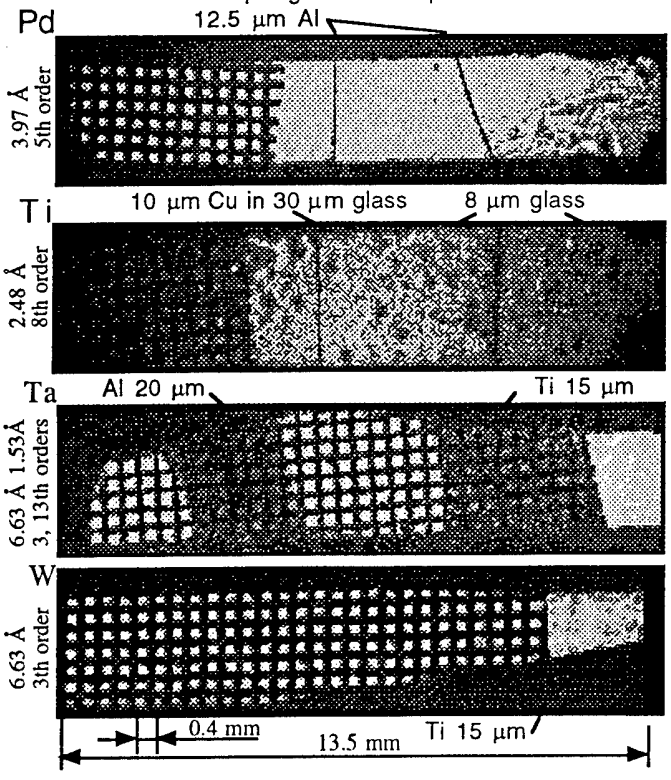

Fig.5

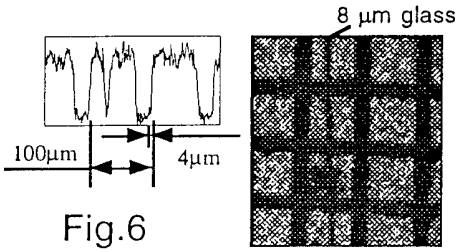

Fig.6

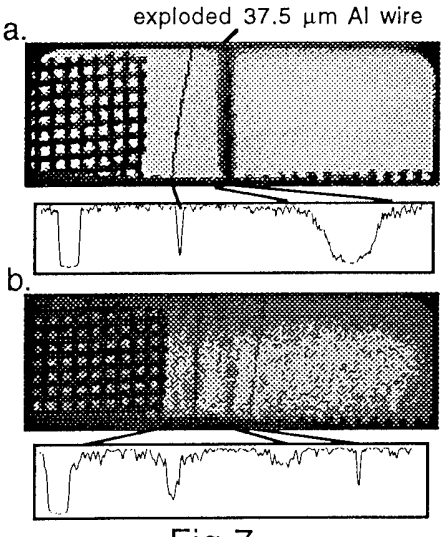

Fig.7

As a demonstration of the possibility of using the diagnostic method described here to investigate a dense plasma, experiments with an exploding Al wire were performed. For the backlighting X-pinch, two 37.5 μm Al wires were used. An angle of incidence of $\theta = 86$ degrees at the crystal was suitable for the $1s^2$-1s3p line of He-like Al with a wavelength of 6.6343 Å. An exploding thin Al wire was placed in the main discharge circuit parallel to the X-pinch return current rods[4] in each pulse in these experiments. Only a small portion of the main current, a few kA peak, passed through this wire. This current is equivalent to the current flowing through a wire at an early stage of a high-current Z-pinch[10]. Shadowgrams of the exploding Al wires which were initially 37.5 μm and 15 μm diameter are shown in Fig. 7. A stainless steel wire grid with wire thickness 200 μm and an Al wire the same size as the exploding one but which carried no current were used for focus control and tuning.

The x-ray backlighting method tested in the experiments described here can be an alternative to using a short wavelength laser for probing a plasma under many conditions. The spatial resolution obtained with this method is better than that which can be obtained by other methods.

REFERENCES

[1.] M.H. Key, R.G. Evans, and D.J. Nicholos, Rutherford Lab. Report RAL-78-020, p. 21 (1978).

[2.] D.T. Attwood, IEEE J. Quantum Electronics **QE-14**, p. 909 (1978).

[3.] D.H. Kalantar and D.A. Hammer, Phys. Rev. Lett. **71**, 3806 (1993).

[4.] S.A. Pikuz, T.A. Shelkovenko, V.M. Romanova, et al., JETP Lett. **61**, 638 (1995).

[5.] S.A. Pikuz, B.A. Brunetkin, G.V. Ivanenkov, et al., JQSRT **51**, 291-302 (1994).

[6.] I.Yu. Skobelev, S.A. Pikuz, A.Ya. Faenov, et al., JETP **81**, 692-718 (1995).

[7.] A.Ya. Faenov, S.A. Pikuz, T.A. Pikuz, V.M. Romanova, T.A. Shelkovenko, X-ray Science and Technology **5**, 323-340 (1995).

[8.] B.L. Henke, F.G. Fujiwara, M.A. Tester, C.H. Dittmore, M.A. Palmer, J. Opt. Soc. Am. **B1**, 828-849 (1984).

[9.] B. L. Henke, J. Y. Uejio, G. F. Stone, C. H. Dittmore, F. G. Fujiwara, J. Opt. Soc. Am. **B3**, 1540-1550 (1986).

[10.] A. Bartnik, G.V. Ivanenkov, L. Karpinsky, S.A. Pikuz, T.A. Shelkovenko, Fizika Plazmy **16**, 1482 (1990).

FIGURE CAPTIONS

Fig. 1 Schematic diagram of the backlighting method. 1-Radiation source, 2-object under study, 3-crystal, 4-Rowland circle, 5-detector, 6-shield.

Fig. 2 a-Filter and film combinations, b-curves of detector efficiency.

Fig. 3 Diagram (a) and results (b) of experiments for determining the d of mica crystals.

Fig. 4 Images of backlighting sources.

Fig. 5 Shadow images of test objects.

Fig. 6 Shadow images and densitogram of a stainless steel grid and an 8 μm diameter glass fiber in $1s^2$-1s3p line radiation of Al XII ions.

Fig. 7 Shadow images and densitograms of a stainless steel grid and exploding wires with 37.5 (a) and 15 μm (b) initial diameter in $1s^2$-1s3p line radiation of Al XII ions. Wires which carried no current are also imaged.

Electron Beam Effects on the Spectroscopy of Satellite Lines in Aluminum X–Pinch Experiments

J. Abdallah, Jr.[1], A. Ya. Faenov[2], D. A. Hammer[3], S. A. Pikuz[4], G. Csanak[1], R. E. H. Clark[1], V. M. Romanova[4], and T. A. Shelkovenko[4]

[1]*Los Alamos National Laboratory, Los Alamos, New Mexico 87545*
[2]*MISDC, NPO "VNIIFTRI", Mendeleevo, Moscow region, 141570 Russia*
[3]*Cornell University, Ithaca, New York*
[4]*P. N. Lebedev Physical Institute, Moscow, Russia*

Abstract

Aluminum wire X–pinch experiments performed at the Cornell University XP pulsed power generator and at the Lebedev Institute BIN generator show detailed high resolution spectra for satellilte lines of Li–like, Be–like, B–like, and C–like ions. These lines, which correspond to transitions originating from autoionizing levels, are observed in the direction of the anode with respect to the bright X–pinch cross point. The intensities of these satellites are much smaller or absent in the direction of the cathode. Such transitions are caused by collisions of ions with energetic electrons (5–15 keV) which are created by the inductive voltage drop between the cross point and the anode. A collisional–radiative model was constructed using a non–Maxwellian electron energy distribution consisting of a thermal Maxwellian part plus a Gaussian part to represent the high energy electron beam. The shapes of the observed satellite structures are consistent with the calculated spectrum for electron temperatures between 30–100 eV, and beam densities of about 10^{-7} times the plasma electron density.

The purpose of the present work is to study in detail the spectroscopy of satellite lines which are observed in X–pinch produced plasmas. Satellite emission lines are observed from the Li–like, Be–like, B–like, and C–like ion stages of aluminum. The transitions correspond to the radiative $2p \rightarrow 1s$ decay of autoionizing levels having a $1s$ shell vacancy. The satellite lines are observed only toward the anode side of the x-pinch cross point. The upper levels are populated mainly by electron impact excitation and ionization of $1s$ shell electrons in relatively cold regions of plasma and by dielectronic recombination to a lesser extent. The high energy electrons which are required to stimulate such transitions are produced by the inductive voltage drop from the cross-point to the anode, in effect forming an electron beam. This explains why the satellite lines are much less intense or absent on the cathode side of the hot spot (see below). Dielectronic recombination due to thermal electrons is also important for determining the spectral line structures.

The experiments were performed using the XP pulser at Cornell University operating at about 350 kA peak current in a 100 ns pulse and the BIN generator at Lebedev Institute with a current of 250 kA in a 100 ns pulse.

High temperature and high density X–pinch plasmas were created during the explosion process which occurs when two or more crossed wires are placed between the output

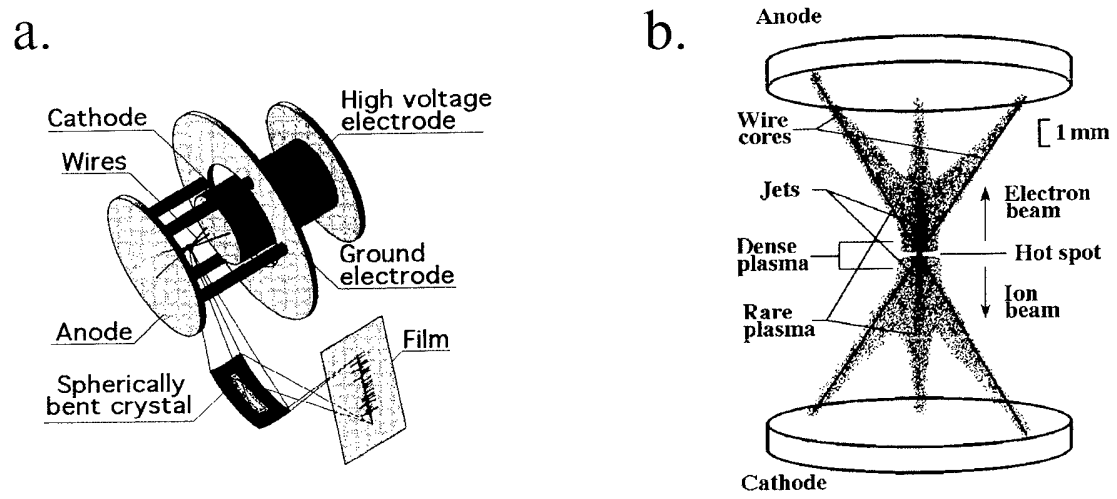

Figure 1: a) Schematic diagram of the X-pinch experiment including an x-ray spectrograph; b) Schematic diagram of the plasma regions formed in the X–pinch.

electrodes of the pulser diode (Fig. 1). The plasmas created were studied using various diagnostics in different spectral ranges. The spectra of highly charged ions in the x-ray region were obtained using the Focusing Spherical spectrograph with one dimensional Spatial Resolution (FSSR–1D)[1,2]. This spectrograph is constructed with mica crystals curved on a 100 mm spherical surface. The spatial resolution in these experiments was better than 50 microns. However, in principle, 10 microns can be achieved. The spectral resolution of the spectrograph $\lambda/\Delta\lambda$ exceeds 3000 and does not depend on the size of the plasma[3]. This is the most important feature for recording the radiation emitted by the diffuse plasma surrounding the x-pinch bright spot.

A spectrogram obtained with the XP–pulser using crossed aluminum wires is shown in Fig. 2. Note that the spectrum is resolved in one spatial dimension and integrated in time. Densitograms of this spectrum are shown on both sides of the wire cross point. The strong asymmetry of the line radiation relative to the cross point is obvious. The resonance and intercombination lines of He–like Al ions were recorded on both sides of the cross point in the second order of the mica crystal reflection. Strong satellite lines corresponding to transitions in Li–like through C–like aluminum were observed in the anode direction and were only weakly observed or absent in the cathode direction. Lines corresponding to $np \rightarrow 1s$ transitions in H–like Al ions were also observed (not shown) in the cathode direction. These lines were recorded in the third order of the mica crystal reflection. The presence of lines belonging to H–like aluminum make it possible to measure the wavelengths of satellite lines with an accuracy of 3–5 mA. The spectra were recorded on KODAK DEF film and the images were digitized using an OPTRONICS PHOTOSCAN densitometer with a 12.5 micron pixel size.

The population densities of the atomic levels were deduced from non-equilibrium steady-state kinetics calculations and were used as input for the spectral simulations. The rate coefficients, used in the evaluation of the rate equations, were computed with a non-equilibrium electron energy distribution. In general, the rate coefficient for a process involving a collision of a single electron with an ion in initial state i which induces a transitions to a final state j is given by[4]

$$r_{ij} = \int F(E) v(E) \sigma_{ij} dE, \tag{1}$$

where E is the electron energy, $F(E)$ is the electron energy distribution function, v is the associated velocity $(2E/m)^{1/2}$, m is the electron mass, and σ_{ij} is the cross section. Eq.

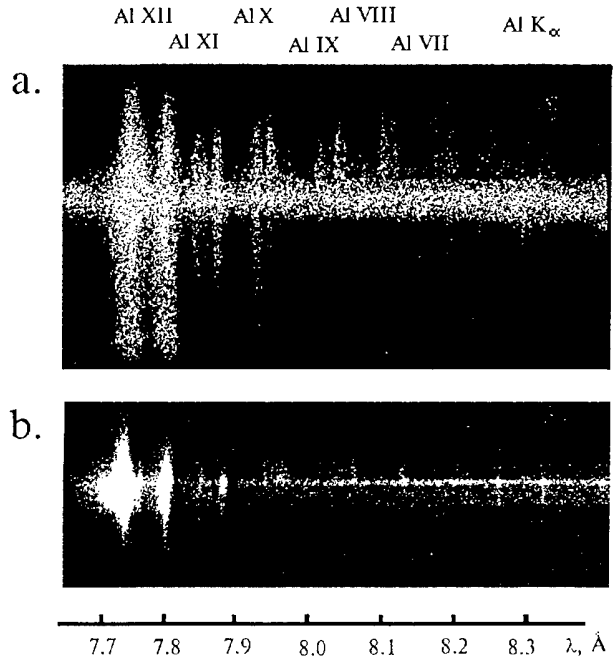

Figure 2: A FSSR–1D spectrum from an aluminum plasma produced by crossed wires in the XP–pulser (a) and in the BIN–generator (b).

1 corresponds to a weighted average of the cross section for a particular distribution of electron energy. All integrals presented in this section are evaluated on the interval $0 \leq E \leq \infty$. For an X–pinch plasma in the direction of the anode the effect of both thermal electrons and beam electrons must be incorporated into the electron energy distribution function. For the present application the function

$$F = (1 - f)F_0(E, T) + fG(E, E_0, \Gamma) \tag{2}$$

was chosen. In Eq. 2 f is the beam fraction, which is the fraction of the total free electron density involved in the beam, F_0 is the Maxwellian function which represents the thermal electrons, and G is the Gaussian function chosen to represent the beam electrons. The Maxwellian function is given by the usual relationship

$$F_0(E, T) = \frac{2}{\pi^{1/2}} \frac{E^{1/2} e^{-E/kT}}{(kT)^{3/2}}, \tag{3}$$

where kT corresponds to the temperature of the distribution in units of energy, and k is the Boltzmann constant. The Gaussian function is given by

$$G(E, E_0, \Gamma) = gE^{1/2} e^{-(E-E_0)^2/(2\Gamma^2)} \tag{4}$$

where E_0 is the center of the Gaussian, Γ is its width, and g is a normalization constant. The functions F, F_0, and G are normalized such that

$$\int F dE = \int F_0 dE = \int G dE = 1. \tag{5}$$

See Ref. 5 which uses a similar method for including the effects of high energy electrons.

A detailed fine structure atomic model for the He–like through C–like ionization stages of aluminum was calculated using the Los Alamos suite of atomic physics codes[6,7]. The

full effects of intermediate coupling and configuration interaction were included. The level structure corresponding to the configurations $1s^2(2s2p)^w$, $1s^2(2s2p)^{w-1}3l$, $1s^1(2s2p)^{(w+1)}$, and $1s^1(2s2p)^w3l$ was calculated for the Li–like through C–like ion stages.

The spectra were constructed using Lorentz line shapes with widths approximating the experimental resolution. Since satellite lines are generally weak and optically thin, and the plasma density is low, optical depth effects have been neglected. Figure 3a shows a comparison of a calculated spectrum with $kT = 40$ eV and $f = 10^{-7}$ with the experiment in the spectral range appropriate for B–like satellite lines. The figure also includes the C–like contribution. Several features in the spectra are not accounted for by the simulations. Figure 3b shows comparison of experimental and calculated spectra for the Be–like stage of ionization. The calculated spectrum corresponds to a temperature of 60 eV and $f = 10^{-7}$. The calculated spectrum is in excellent agreement with experiment. Figure 3c is comparison of experimental and calculated spectra for the Li–like stage of ionization. The calculated spectrum corresponds to an electron temperature of 80 eV and $f = 3 \times 10^{-7}$. Note that there seems to be a slight inconsistency between the calculated wavelengths and the calibration of the experimental measurement. However, the overall agreement between theory and experiment is quite good. The study shows that these structures can be reproduced by calculations with electron beam fractions $f \sim 10^{-7}$, in agreement with experimental estimates. The calculations also suggest that a temperature gradient from approximately 30 to 80 eV is formed in the plasma.

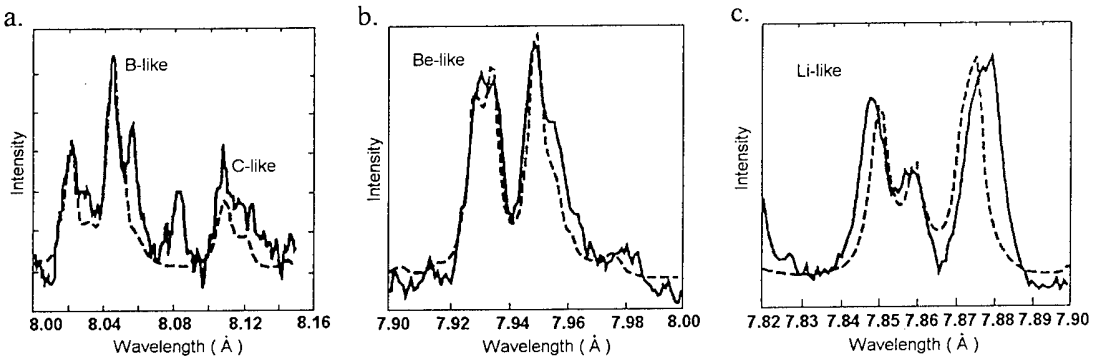

Figure 3: A comparison of the calculated spectrum (dashed line) with experiment (solid line).

References

[1] A.Ya. Faenov, Yu.A. Agafonov, B.A. Bryunetkin, V.M. Dyakin, A.I. Erko, G.V. Ivanenkov, A.R. Mingaleev, S.A. Pikuz, T.A. Pikuz, V.M. Romanova, and T.A. Shelkovenko, Proceedings of the International Society for Optical Engineering Meeting SPIE–93, San Diego CA, July 1993, 2015, p. 64.

[2] A.Ya. Faenov, Yu.A. Agafonov, S.A. Pikuz, A.I. Erko, B.A. Bryunetkin, V.M.Dyakin, G.V. Ivanenkov, A.R. Mingaleev, T.A. Pikuz, V.M. Romanova, and T.A. Shelkovenko, Physica Scripta 50, 333 (1994)

[3] V.A. Boiko, A.V. Vinogradov, S.A. Pikuz, I.Yu. Skobelev, and A.Ya. Faenov, Journal of Soviet Laser Research 6, 105 (1985)

[4] Ya.B. Zel'dovich and Yu.P. Raizer, Physics of Shock Waves and High Temperature Hydrodynamic Phenomena, Academic Press, New York and London (1966)

[5] F.B. Rosmej, JQSRT 51, 319 (1994)

[6] J. Abdallah, Jr. and R.E.H. Clark, Los Alamos National Laboratory reports, LA-11436-M, I-V (1988)

[7] J. Abdallah, Jr., R.E.H. Clark, J.M. Peek, and C.J. Fontes, JQSRT 51, 1 (1994)

Research of Generation Mechanism of Plasma Points in Z-pinch

V.I.Afonin, A.M.Gafarov, V.P.Kovalev,

V.P.Lazarchuk*, V.I.Ostashev, S.I.Petrov*, A.V.Potapov

Russian Federal Nuclear Center - All-Russia Research Institute of Technical Physics

456770 Snejinsk, Chelyabinsk region, p.o. box 245, Russia

** Russian Federal Nuclear Center - All-Russia Research Institute of Experimental Physics.*

607200 Sarov, Nizhniy Novgorod region, Russia

1. Introduction

Fast Z-pinches, formed at explosion of single thin wires by a powerful pulse of current, are by a subject of intensive experimental researches already more than twenty years /1,2/. The interest to these researches is associate with formation in pinching process of a plasma column, so-called "hot" points - high-temperature dense objects, intensively radiating in a soft x-ray region. The analysis of x-ray spectra shows, that electron temperature **Te** in "hot" points can reach about several keV, density $n_e \geq 10^{22}$ cm^{-3}. Such high specific parameters of plasma present doubtless interest for researches in the field of physics of high energy density , x-ray spectroscopy of multicharge ions.

At present the significant progress in understanding of physical processes, responsible for heating of plasma in "hot" points is achieved. The model of radiation compression stated in detail in /3/, originally developed for plasma of low inductance vacuum spark, can be applied with success to the affined phenomena - "hot" points in fast Z-pinch. This model shows, that the energy losses of plasma in line emission of multicharge ions play a significant role in process of micropinching. The estimations of plasma parameters , based on model of radiation compression, are in a good agreement with experimental data.

In present work the results of experimental investigations of "hot" points, formed at explosion of thin Al-wires, are reported. The experiments are accomplished on the fast high current generator SIGNAL /4/, which was modernized with the purpose of increase of load current. The measurements of x-ray emission from "hot" plasma points are allowed to estimate their parameters.

2. The experimental installation and methods of diagnostics

The high current pulse generator SIGNAL represents the inductive energy storage. The switching of current in load is carried out by plasma opening switch over characteristic time about 50 ns. The recently completed modernization of the SIGNAL installation has allowed to raise amplitude of current in a load up to 210 kA. As a load, the wires from aluminium by a diameter 20..30 microns and length of 8 mm were set in diode of the SIGNAL generator.

The time-integrated images of a plasma column in soft x-ray radiation were registered by pinhole chamber with diaphragms by a diameter 15 and 30 micron.

X-ray streak camera was used for investigation of the space-time characteristics of Z-pinch x-rays emission. 1D-image of Z-pinch is formed on the streak-tube photocatode by a slot-hole diaphragm, oriented normally to the wire axis. The sweep direction is also normal to the wire axis.

In the conducted experiments the time resolution was about 0.9 ns, the space one along axis of Z-pinch - 0.2 mm.

The continuous spectrum of x-ray radiation of "hot" points in the range of photon energies $h\nu$ =3..7 keV was measured by a method of "grey" filters. The space resolution of this diagnostic, which is structurally similar to a pinhole chamber, is about 0.2 mm, that permits to separate spectra of different "hot" points in majority of cases. The registration of radiation, past through filters was carried out on a x-ray film of a UFSh-O type. The film was previously calibrated on static x-ray source in the range of photon energies $h\nu$ =4..9 keV.

Crystal spectrographs with flat crystals of gypsum (2d =15.2 Å) and potassium asid phthalate KAP (2d =26.5 Å) registered the line emission of hydrogen- and helium-like ions of aluminium. The space resolution along pinch axis was provided by slots of 0.1..0.2 mm width , placed before crystals and oriented in crystal dispersion plane. A spectral range of the spectrograph with gypsum crystal is $h\nu$ =1.5..1.9 keV, the one of the spectrograph with KAP crystal - $h\nu$ =1.5..2.2 keV.

3. Experimental results

The characteristic pinhole images of an exploding Al-wire are shown on fig. 1. The top image is recorded with diaphragm of 30 micrometers diameter, filter - Mylar 5 μm.

The pipe-like form of Z-pinch x-rays image is obvious. The pinhole image demonstrates a quite high degree of uniformity of plasma column compression on the whole its length, except for some necks, which are developed at further pinching into "hot" plasma points. The diameter of a main plasma column, measured on pinhole image for several experiments, is within the limits of 140..250 micrometers.

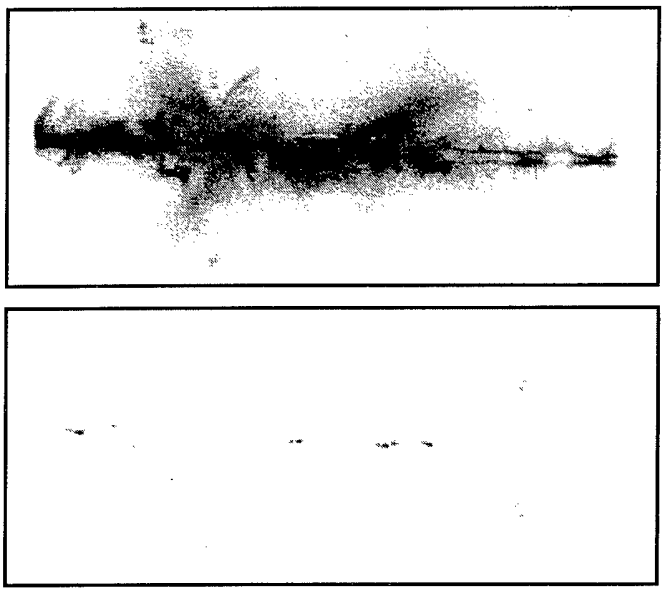

Fig. 2. Pinhole images of exploding Al-wire.
Top image - diaphragm 30 μm, filter - Mylar 5 μm;
Bottom image - diaphragm 15 μm, filter - Mylar 15 μm.

The bottom image on fig. 2 is formed by the diaphragm of 15 micrometer diameter with mylar filter 15 micrometer thichness. On this image the emission only from particular "hot" points is observed. The size of these points in direction perpendicular to the axis of the wire are evaluated in 10..30 μm. Usually in experiments there is observed from five up to fifteen "hot" points, laying on axis of Z-pinch. Sometimes, however, on pinhole images there are the luminous objects, located on significant distance from an axis of pinch. Their sizes, as a rule, are much more, and reach hundreds micrometers.

On the fig. 2 the results of registration of Z-pinch "hot points" with help of x-ray streak camera are submitted. On the drawings there are shown:

- working photochronogramm;
- down - space integrated x-ray pulse form;
- right from photochronogramm - time integrated Z-pinch emission along length;
- right top corner - Z-pinch pinhole image;
- right bottom corner - spectral sensitivity of the channel and parameters of elements of the x-ray optical circuit, involved in the experiment.

Results of data processing of x-ray photochronography show, that the bursts of radiation with $h\nu \geq 1.5$ keV from particular "hot" points begin in about 30..50 ns after switching of a current in load. The bursts in different "hot" points occur at different time, the characteristic time of their life is several nanoseconds.

The typical sample of x-ray line spectrum of H- and He-like ions of aluminium , is demonstrated on fig. 3. The electron temperature, determined on the ratios of resonant lines He_α and Ly_α, and also their dielectron satellites, has appeared equal 0.4 keV. It should be noted, that for majority of the registered x-ray line spectra $Te \leq 0.5$ keV. On the other hand the values Te, determined on continuum fall-down, usually lie within the limits 0.5..0.9 keV and have rather significant dispersion for different "hot" points even in one pulse. This seeming contradiction may be explained if we suppose very significant temperature gradients within the region of "hot" point.

The value of plasma density we were estimated from the lowering of ionisation potential of multicharged ions and disappearance of thear highly exited energy levels in dense plasma. For the spectrum on fig.3 the plasma density were within the limits $\rho=0.25..0.5$ g/cm^3 (corresponding electron density $n_e \cong 10^{23}$ cm^{-3}). It should be noted, howerer, that such high plasma density must cause very considerable spreading of lines, corresponding to transitions from highly exited energy levels (about 7...10 eV for levels with n=5). At the same time experimental spectra give a slightly lesser values. A one possible reason for such disagreement may be a significant density gradients in "hot" plasma points.

A preliminary calculations of x-ray line spectra from "hot" points with help one-dimensional radiation hydrodynamic code SS-9 /5/ , confirm this assumption. This simulations give adequate description for experimental spectra if the model of "hot" point consisting of a "hot" dense core and low dense corona is used.

The more careful and accurate analysis of x-ray spectra will be conducted in near future.

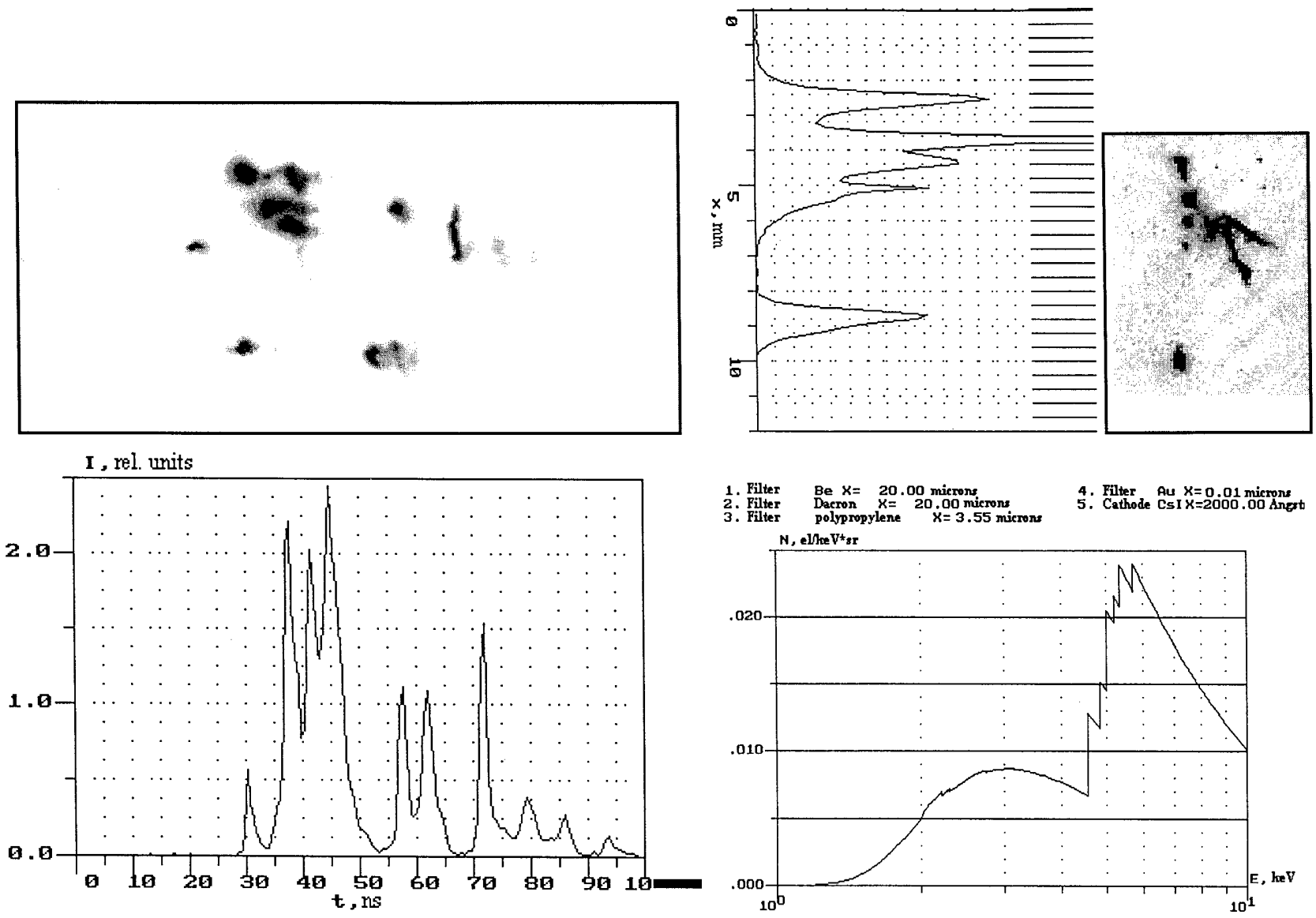

Fig. 2. Spatial-time picture of soft x-ray emission of exploding wire

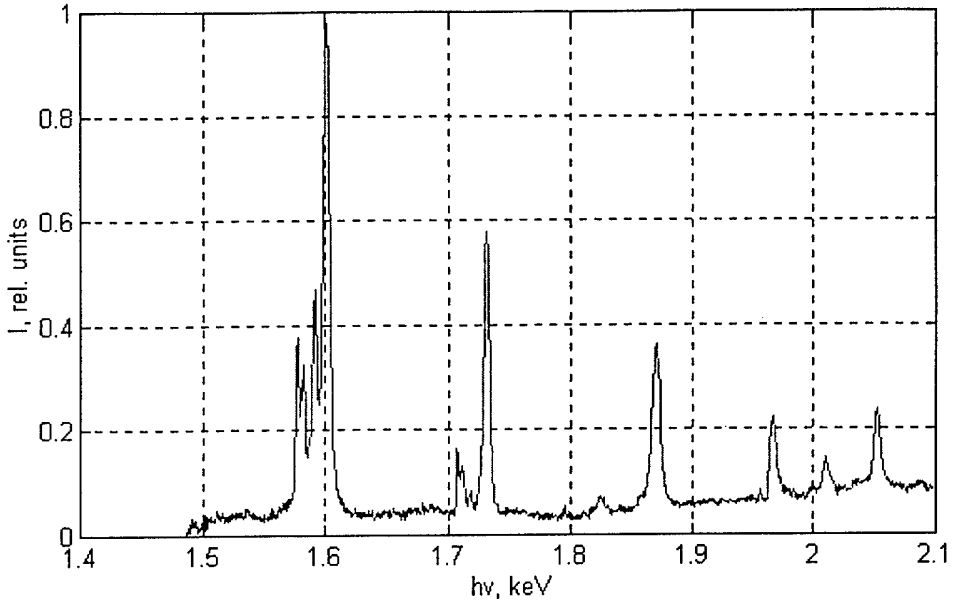

Fig. 3. Line spectrum of H- and He-like aluminium ions of "hot" points of exploding wire. Spectrograph with potassium asid phthalate crystal.

4.Discussion of experimental results

Most completely the experimental data on "hot" plasma points can be interpreted in model of radiation compression /3/, in which the equilibrium state of a pinch - in our case of a plasma point - is reached at change of a radiation mode from volume to surface, though quasi equilibrium is possible in optically thin plasma /6/.

In the model /6/ the electron density $\mathbf{n_e}$ (cm^{-3}) and the neck radius **r** (cm) are given by expressions:

$$\mathbf{n_e} \cong 1.26\times10^{22}\times T^{3/2}\times J^2\times(U/T)/\exp(U/T),$$

$$\mathbf{r} \cong 0.28\times T^{-5/4}\{\exp(U/T)/(U/T)\}^{1/2},$$

where:

T is electron temperature, eV;

U is ionization potential of an ion with mean charge Z;

J is Piza-Braginsky's critical current, MA.

In its turn the critical current with accounting for radiation losses from plasma is determined by an equation

$$J\cong 0.27\times(\Lambda/k)^{1/2},$$

where

Λ is coulomb logarithm, accepted equal to 10;

$k=1+U/T+1.7\times10^{7}\times\exp(-\Delta E/T)\times m/(Z^2\times T)$ is radiation factor, taking into account the contribution of photorecombination and line emission in radiation losses;

m is number of equivalent electrons of an ion Z in state with main quantum number **n**;

$\Delta E\cong(2n+1)/(n+1)^2\times U$ is energy of excitation of state **n** of an ion Z.

As the plasma at $T\cong$ 400...900 eV contains basically H- and He-like ions of aluminium, for this interval of temperatures it is possible to find at Z=11

J=(0.20..0.11) MA; r=(10 ...1)$\times 10^{-4}$ cm; n_e=(1.1..9.3)$\times 10^{23}$ cm^{-3},

and at Z=12

J=(0.26..0.18) MA; r=(10 ...1)$\times 10^{-4}$ cm; n_e=(1.1..22)$\times 10^{23}$ cm^{-3}.

Taking into account, that in the discussed experiments the maximum value of a current did not surpass 0.25 MA, it is possible to conclude, that quasi equilibrium of neck plasma is reached already at value of a current in pinch, equal to critical $J \cong 0.20$ MA and $T \cong 400$ eV, at which its cross size makes ~20 microns and the electron density is ~10^{23}cm^{-3}, what is in a quite good agreement with experimental data.

With increase of a current in pinch, growth of temperature and density of neck plasma, its cross size decreases . As it is seen from indicated estimations, at this the value of critical current, necessary for a quasi equilibrium mode, decreases, and there can be, that $J<I$, where I- the current in pinch.

Hence, it is possible to conclude, that during development of neck there are the extrusion of a current from it on pinch periphery, the interception of a current by its corona, that is experimentally shown in work /7/.

Acknowledgments:

The authors express gratitude to operational staff of the SIGNAL installation and employees of the diagnostics group for technical maintenance of experiments. We thank also V.Yu.Politov carrying out the analysis of x-ray spectra and fruitful discussions.

The work is conducted at financial support of ISTC within the framework of project 009.

5. References

1. Burkhalter P.G., Davis J.D., Rauch T., Clark W., Dahlbacka G., Shneider R. J.Appl. Phys., 1979, 50, 705.

2. Zakharov S.M., Ivanenkov G.V., Kolomensky A.A., Pikuz S.A., Samokhin A.I., Plasma Physics, 1983, v 9, issue 3, pp 469 - 476.

3. Koshelev K.N., Sidelnikov Yu.V. et al.//Spectroscopy of multicharge ions in hot plasma/ edit. Saphronova U.N.; Moscow, Nauka, 1991.

4. Diyankov V.S., Kovalev V.P. et al. VIII All-Union symposium on high current electronics. The theses of the reports, part III, p.48. Sverdlovsk, 1990.

5. Cochubei Yu. K., Gasparyan P.D., et.al. Problems of Theoretical and Applied Physics , 1993 , v.2 , p. 65.

6. Afonin V.I. Plasma Physics, v.20, № 3, 1994.

7. Sarkisov G.S., Etlisher B. et al. JETPh, v.108, issue 4(10), 1995.

ON THE IONIZATION-TEMPERATURE INSTABILITY ROLE IN Z-PINCH HOT SPOTS GENERATING

Vasiliy I. Afonin, Oleg V. Diyankov, Igor V. Glazyrin, Serge V. Koshelev

Russian Federal Nuclear Center – All-Russian Research Institute of Technical Physics (RFNC - VNIITF)
P.O.Box 245, Snezhinsk, Chelyabinsk Region, 456770 Russia

Abstract

This paper is devoted to the investigation of instability evolution, generated neither by initial Z-pinch outer boundary perturbation, but by perturbation in initial temperature [1].

Treatment of this process was developed numerically, using 2D MHD code MAG [2, 3]

Obtained results show, that nevertheless higher modes appear, they didn't become the leading modes.

Introduction

Nowadays the idea, that the process of hot spot generation is the consequence of the initial perturbation of Z-pinch boundary evolution, is generally accepted.

But in some experiments the phenomena of plasma stratification along Z-pinch axis was found. In the paper [1] the condition of this phenomena appearance has been analyzed and the hypothesis, that this phenomena is caused by axial perturbations, appeared because of Ionization-temperature instability, has been discussed.

The present paper is devoted to the numerical investigation of this hypothesis.

Brief description of numerical experiments

A number of calculations with varying initial values of variables has been performed. Because the hypothesis is connected with instability development in single wire the correspondent initial data has been used: generator current of 200 kA was taken and assumed to be constant. Initial radius of wire was taken to 10μm (close to usial experimental data). By 1D MHD code ERA [4] the calculations of initial time of electroexplosion have been conducted. It has been obtained that the radius of expanded wire is about 0.3 cm.

By 2D MHD code MAG several cases of wire compression have been analyzed:

1. It has been supposed that wire before compression is homogeneous
2. Cold core existing is taken into account. Therefore the density profile was set to $\rho(r) = \rho_o \cdot r_o/r$ and temperature $T(r) = T_o \cdot r/r_o$
3. Initial density and temperature distribution at the time of maximum expansion was taken from ERA code

The perturbation in temperature was taken in the following cases:

- in the form of sine wave per z-direction and damped exponential as far as penetration into the plasma.

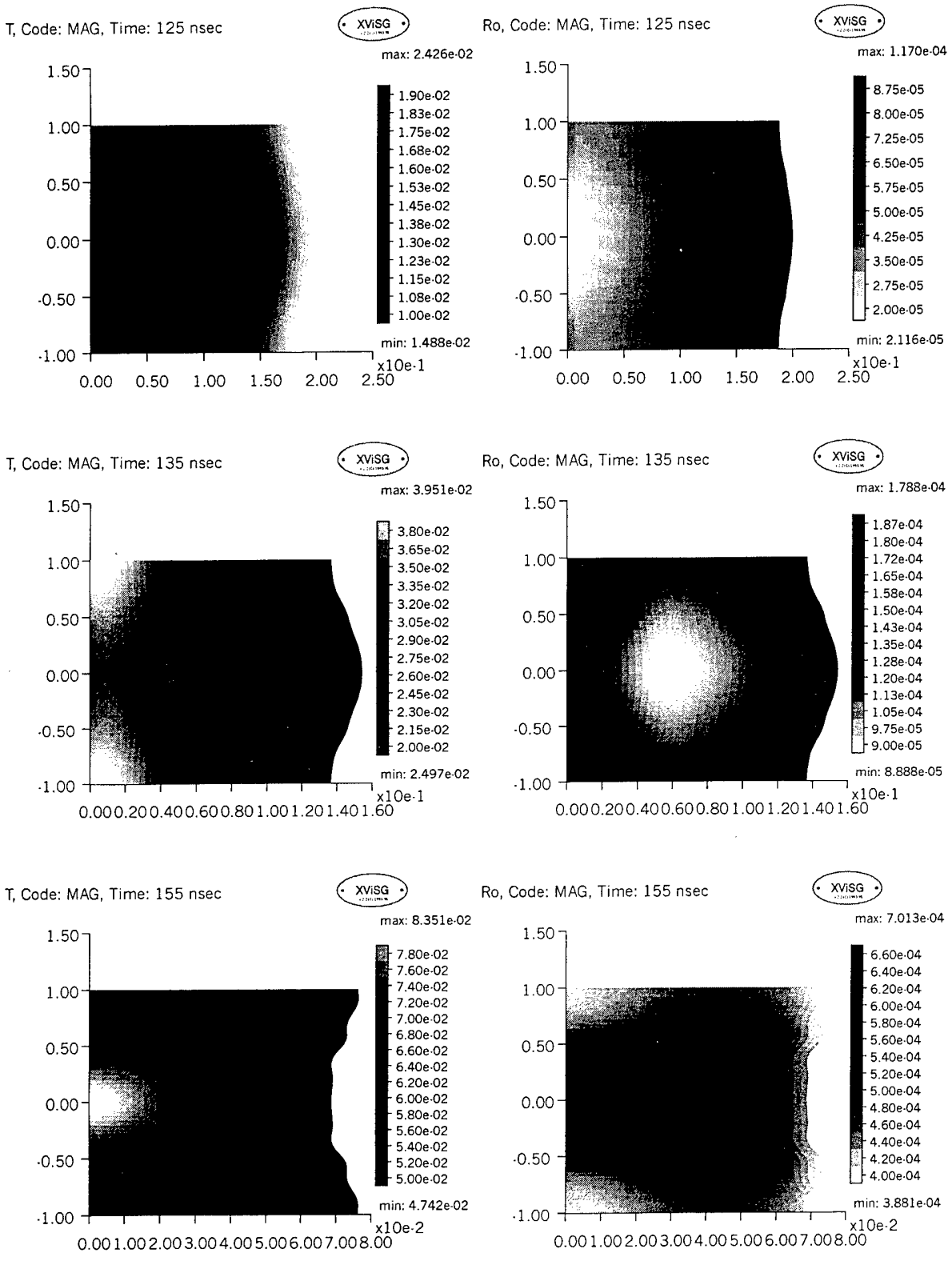

Fig. 1

Ionization - Temperature Instability Development.
Left - Temperature (keV), Right - Density (g/cm^3).
Corresponding times: 125, 135 and 155 nsec.

- composition of different modes. One mode was taken to be leading (k=1) and next modes (k=2,3,4,...) were added to the leading mode.

For all cases the dynamics of processes is coincided in common (see Fig.1). The instability is developing due to different pressure of plasma, cavity reaches the axis (Fig.1, upper pictures), reflected from axis, produces two shock waves propagating in opposite directions. These shock waves are met at other place and new hot spot is appeared (Fig.1, lower pictures). The processes is repeated again. During current period the plasma is oscillated several times.

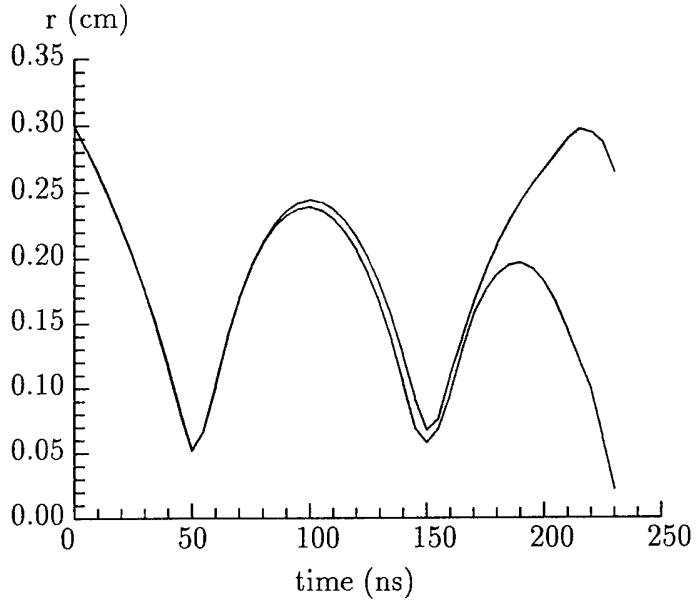

Figure 2: Minimum and maximum radii of Z-pinch outer boundary vs time

In Fig.2 one can see the graph of minimum and maximum radii of Z-pinch outer boundary versus time. It characterizes the process of instability growing. At the initial time difference between them is very little, after Z-pinch was compressed for the first time it almost hasn't grown. The main growing of instability occurs during the third compressing.

The time dependence of modes amplitude vs. time is shown in Fig.3. The first mode is the main one, the other modes are growing in time, but the second mode is growing much faster then the other modes. It can be interpreted as the modes saturation processes.

Conclusion

Some calculations have been conducted for the hypothesis analysis of ionization-temperature instability development in Z-pinch. One can concluded that obtained plasma column oscillation and axial motion could explain the hot spot motion alone the axis for these parameters of wire compression. The calculated mechanism of modes saturation could help in analysis of observed experimental data when some hot spots are degenerated and new ones are arisen but in smaller quantity.

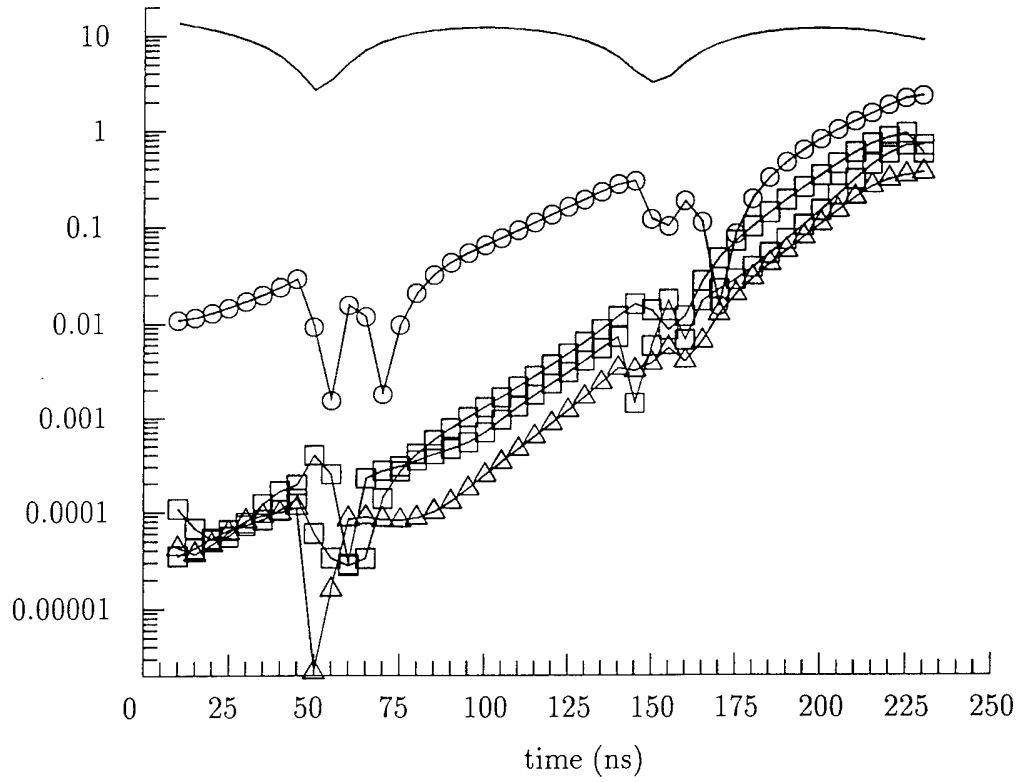

Figure 3: Modes amplitude vs. time. Without sign – main mode, circles – second mode, squares – third one, triangles – fourth one

Acknowledgment

The authors are grateful to Igor Krasnogorov and Rouslan Kotov for their helpful assistance in preparing this paper.
This work is supported by ISTC, Projects #009

References

[1] Afonin,V.I., Plasma Physics, **21** (1995) 267 (in Russian).

[2] Diyankov,O.V. and Terekhoff,S.A. in *Dense Z-pinches*, ed. by M.Haines and A.Knight, AIP Conference Proceedings **299**, New York, (1994), p.121.

[3] Glazyrin,I.V., Diyankov,O.V., Kotov,R.A., Koshelev,S.V., High School News, Physics, Tomsk Univ., **12**, (1995), 23 (in Russian).

[4] Karlykhanov,N.G., Glazyrin,I.V., Diyankov,O.V., Numerical analysis of cold core formation during wire electroexplosion, this Conference Proc.

ABOUT POSSIBLE MECHANISM OF GENERATION OF PLASMA POINTS IN PLASMA OF MULTICHARGE IONS OF FAST Z-PINCH

V.I.Afonin, B.F.Voronov**, A.E.Zakharov**, V.M.Murugov*, S.V.Ponomarev, A.V.Senikh*

Russian Federal Nuclear Center - All-Russia Research Institute of Technical Physics
456770 Snejinsk, Chelyabinsk region, Russia

**Russian Federal Nuclear Center - All-Russia Research Institute of Experimental Physics*
607200 Sarov, Nizhniy Novgorod region, Russia

***Research Institute of Impulse Devices*
115304 Moscow, 9 Luganskaya St.

Summary

The results of streak camera research in visible and x-ray ranges of wavelengths of explosion of thin aluminium wires on high current generator with amplitude value ~ 200 kA and width of rise front ~ 50 ns are discussed.

Introduction

Despite long-term intensive researches of fast Z-pinches, the interest to them is not abated up to present time. At this one of the most interesting phenomena in plasma of such pinches is generation of "hot" plasma points (PP) with extremely high values of density and temperature.

Now the accepted one is the apprehension about decisive role of MGD[1]-instability in generation of PP in high current pinches [1], according to which PP is the belts of a plasma string, developed from the perturbation of its border. However in work [2] the condition of genesis of small-scale axial non-uniformity in electronic density and temperature of a uniform string of equilibrium plasma of multicharge ions of Z-pinch were considered in linear approximation and the assumption is stated that these perturbation can serve initial for development of belt instability.

In this work the preliminary results of research of development of ionization-thermal instability into the belt one are presented.

Experimental results

The experiments on explosion of aluminium wires were conducted on the high current generator SIGNAL with inductive energy accumulator [3], which after modernization provided in load amplitude value of current up to $I \cong 210$ kA with rise front 50 ns and voltage up to 250 kV. As load of the generator aluminium wires with diameter 20..30 μm, length 0.8 cm and high initial symmetry were used; the variation of a diameter of a wire on whole length did not exceed 1 %.

For registration of a space-time picture of emission of a plasma string (PS) in optical range of wavelengths the streak camera SFER-6 with time resolution 0.1 ns and space resolution 0.1 mm was used. Dynamics of "hot" PP of a plasma string in quantums with energy more than 1 keV was investigated by a technique on the basis of x-ray streak camera RFR with time resolution 0.9 ns and space resolution 0.2 mm.

Measuring channel both techniques included streak camera in mode of slot-hole sweep and slot-hole chamber, building the image of PS on the photocathode of streak camera. The registration of the 2D image from streak camera screen was made on photographic film.

[1]MGD stands for Magnet Gas Dynamics

In the Fig. 1 the characteristic working photochronogram of evolution of PS in visible radiation, and in the Fig. 2 the emission of PS at various moment of time is presented. Makes oneself conspicuous the fact, that already at initial stage of explosion of a target the small-scale non-uniformity of PS emission is observed. In process of time the space scale of non-uniformity grows up to $\lambda \sim 0.12..0.15$ cm.

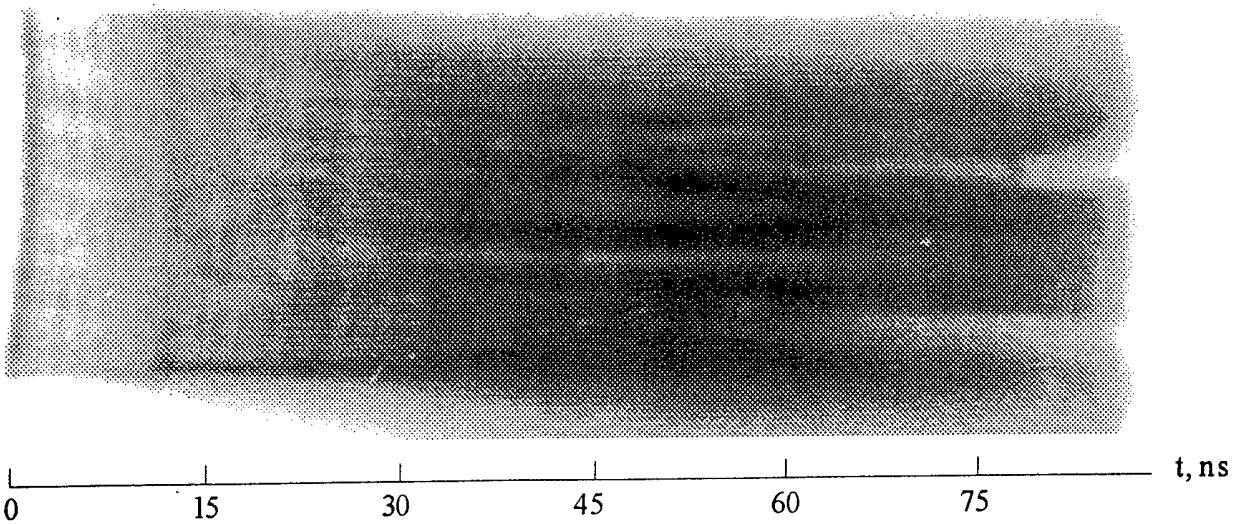

Fig. 1. The working photochronogram of explosion of Al-wire at optical range of wavelength

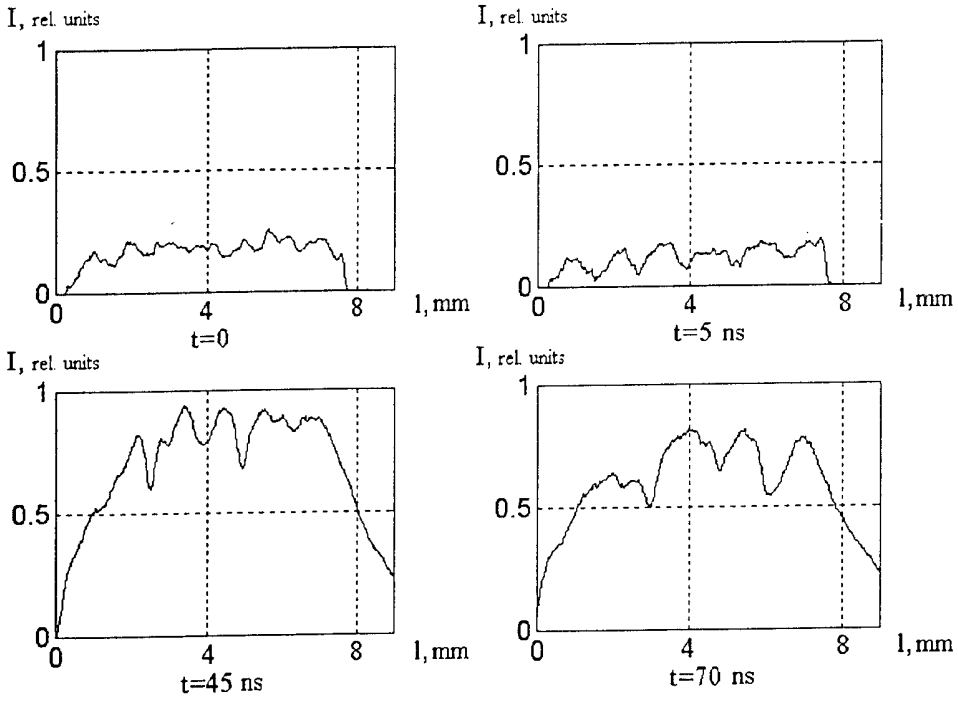

Fig. 2. Emission of plasma string (in relative units) at different points of time t.

The characteristic x-ray photochronogram of Z-pinch dynamics is shown in Fig. 3. The sweep duration makes 100 ns, the beginning of the sweep lags behind moment of occurrence of emission in optical range of wave lengths by 7±3 ns. Results of processing of the photo-chronogram show, that the bursts of radiation with energy of quantums $h\nu > 1$ keV from particular PP begin after 30..50 ns from moment of explosion of the liner. The bursts in

different PP occur at different time, the characteristic times of PP life make several ns. From the submitted photochronogram it is visible, that characteristic space scale of PS non-uniformity to the moment of emergence and subsequent evolution of PP makes 0.1..0.15 cm.

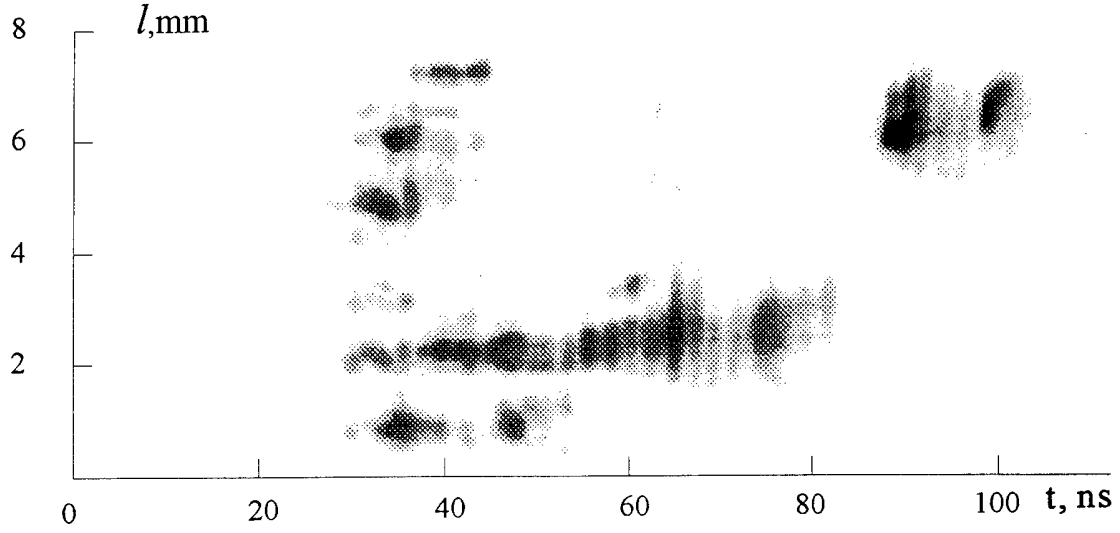

Fig. 3 The characteristic x-ray photochronogram of explosion of Al-wires

Discussion of experimental results

We shall consider electroexplosion of conductor, assuming uniformity of its properties and one of the formed plasma both along length and on cross-section.

Let at the moment of time $t = 0$ through the conductor, described in radius r_o (cm), density ρ (g/cm^3), length l (cm), conductivity σ (cm$^{-1}\cdot\Omega^{-1}$) and nuclear weight A, the current I begins to flow with increase rate β (A/s), and β=const. At $r_o < \delta$, where δ is the skin depth, it is possible to believe, that the input of energy in conductor occurs evenly on the whole volume, what has a place for the conditions of the conducted experiments. After sublimation of conductor its conductivity decreases and the skin depth increases. Therefore we shall assume, that energy input in products of explosion occurs also evenly in volume. Neglecting expansion of products of explosion of conductor at the sublimation stage, we shall evaluate parameters of PS to the moment of its maximum expansion, characterizing the plasma by some average (on time of heating and mass) temperature T (eV), average charge of ions Z and counting, that PS border moves into vacuum with threefold speed of a sound. The beginning of collapse t_c will be tallied with a condition of equality of pressure of plasma and the pressure of self magnetic field of current in PS. Then, using condition of conservation of mass, it is possible to find characteristic time of expansion in the form:

$$T_c \cong 2.5\cdot10^{7}\cdot(r_o/\beta)\cdot[T\cdot\rho/A\cdot(Z+1)]^{1/2}.$$

In turn the temperature of plasma to the moment of time t_c is determined by joule heating of PS with Spitzer conductivity:

$$T \cong 5.7\cdot10^{-5}\cdot[A^3/\rho\cdot(Z+1)]^{1/6}\cdot(\beta/r_o)^{1/3},$$

and average charge of ions at conditions of corona balance of plasma can be found from equation [3]:

$$U/T \cong (2n\xi/\mu)^{1/3}\cdot(10^4/T)^{2/3},$$

where n is the main quantum number of a shell, ξ is the number of electrons and μ is the number of vacancies in the shell n, U is potential of ionization of an ion Z.

At last, the radius of expansion is from formula:

$$r \cong 5{,}4 \cdot 10^9 \cdot (\rho^{1/3}/A^{1/2}) \cdot (Z+1)^{5/6} \cdot (r_o/\beta)^{2/3}.$$

For characteristic parameters of the discharge of the SIGNAL installation $\beta \cong \cong 4 \cdot 10^{12}$ A/a, $\tau_\phi \cong 50$ ns) it is possible to find in case Al-targets with r_o = 10..16 μm at Z=6 parameters of plasma: $T \cong 28..24$ eV, $t_c \cong 28..42$ ns, $r \cong 0.3..0.42$ cm.

For obtaining of final estimations we shall use work [4], according to which in close experiments (by parameters of the current generator and targets) at electroexplosion of wire the "cold" dense nucleus and the hot plasma corona was observed during long time, and approximately 3% of initial mass of a target passed into corona. It is equivalent to that initial density of a target in our estimations should be replaced $\rho \rightarrow 0.03\ \rho$. With allowance for these the estimations will become: $T \cong 51..44$ eV, $t_c \cong 7..10$ ns, $r \cong 0.09..0.125$ cm. Accordingly the density of plasma will make $\rho \cong (1..1.3) \cdot 10^{-5}$ g/cm^3.

Using these results, it is possible to evaluate and characteristic scale of perturbations to the moment of maximum expansion of PS, proceeding from ideas about development of ionization-thermal instability in plasma of multicharge ions of Z-pinch [2]. Really, according to [2] the condition of development of this type of instability is the condition:

$$K \geq Z\, \rho \xi \cdot 10^{10}/(T^2 \cdot A^{1/2}),$$

where ξ is the number of equivalent electrons in state with main quantum number n, K is the wave number. From here for characteristic ρ, ξ, T, A we shall obtain characteristic scale of perturbations at the beginning of compression of PS:

$$\lambda \leq \lambda_{max} \cong 0.16..0.1 \text{ cm}.$$

With compression of PS by magnetic field of current, the formed axial perturbations in temperature can serve initial for formation on their basis magnet hydrodynamic instabilities. At this from whole spectrum of initial perturbations with $\lambda \leq \lambda_{max}$ only that can be developed in "hot" PP, for which $\lambda \geq x \cong r$, where x is radial distance, passed by a thermal or shock wave, r is radius of maximum expansion of PS. As it is easy to see, in case more short-wave perturbation there will be the overlapping of thermal waves on large radiuses from axis of PS due to thermoconductivity, so that to the axis of system the practically cylindrical shock (thermal) wave will approach, not forming PP on the axis. It is possible to conclude, that PP will be formed by such perturbations, for which $\lambda \geq r$.

For our estimations of λ and r we have $\lambda \geq 0.09..0.125$ cm. Hence, on whole length of a plasma string l = 0.8 cm there can be formed about 5..8 "hot" PP at convergence along thermal perturbations shock waves to the axis of system, that is in fair agreement with the submitted experimental results.

Thus, the submitted in work photochronograms and analysis of process of electro-explosion of aluminium targets specify to significant role of ionization-thermal instability of plasma of multicharge ions of Z-pinch in mechanism of generation of "hot" plasma points, which can become decisive for targets with high initial symmetry. Just these perturbations, instead of perturbations in geometry of a plasma string, can be initial for development of belt instability.

The work is fulfilled within the framework of project #009-95 of International ScienceTechnology Center.

References

[1] Yankov V. V. Plasma Physics, 1991, v 17, p 521.
[2] Afonin V.I. Plasma Physics, 1995, v 21, p 267.
[3] Diyankov V.S., Kovalev V.P. et al. VIII All-Union symposium on high current electronics. The theses of the reports, part III, p.48. Sverdlovsk, 1990.
[4] Sarkisov G.S., Etlicher B., Atelan S., Ruie K. JETPh Letters, 1995, v 61, p 547

SUPPRESSION OF RAYLEIGH-TAYLOR INSTABILITY IN Z-PINCH LOADS WITH TAILORED DENSITY PROFILES

F. L. Cochran
Berkeley Research Associates, Inc., P.O. Box 852, Springfield VA 22152, USA
A. L. Velikovich
Berkeley Scholars, Inc., P.O. Box 852, Springfield, VA 22152, USA
J. Davis
Naval Research Laboratory, Washington, D. C. 20375, USA

Abstract

A load structure with tailored density profile which delays the onset of the Rayleigh-Taylor instability development in imploding Z-pinches by inverting acceleration of the magnetic field/plasma interface is proposed and studied numerically. This approach makes it possible to start gas-puff implosions from large radii (like 8 cm) and produce significant K-shell yield with current pulse duration of 250 ns and longer.

In plasma radiation sources, Z-pinch loads are imploded to convert implosion kinetic energy to soft x-ray radiation [1]. Conventional load configurations are wire arrays and cylindrical annular gas puffs. These loads are imploded by the magnetic pressure which is produced by the axial current. At stagnation, the plasma's kinetic energy is thermalized and can be further converted to K-shell radiation.

Rayleigh-Taylor instability of a pinch plasma accelerated by the magnetic field is a major factor limiting PRS radiative performance. Since the linear growth rate of the RT instability is $\Gamma = \sqrt{gk}$, the distance L traveled by the plasma shell during the implosion is related to the ratio A of final to initial perturbation amplitudes according to $L = (\ln A)^2 \lambda / 4\pi$ (here, g is the inward acceleration, $\lambda = 2\pi/k$ is the perturbation wavelength). The distance L available for acceleration is therefore limited by the RT instability: e.g., for a wavelength $\lambda = 0.5$ cm and amplification A below 1000, L must be less than 2 cm. Having started from a larger radius, a plasma shell would not arrive at the axis in one piece [4], and hence, would be an inefficient radiator.

To produce a K-shell yield at stagnation, the plasma has to be accelerated to high velocities - hundreds to thousand km/s. The limitation on initial radius translates into severe requirements on the design of the pulsed power machine driving the implosion. Suppression of the RT instability imposing this limitation would make it possible to implode PRS with larger radii and longer implosion times. This means that there is a considerable potential for improving radiative performance of existing machines and that new parameter ranges will be open for the next generation of machines.

The RT instability could be mitigated by so-called snowplow mechanism [2] responsible for enhanced efficiency of double puff Z-pinch loads [3]. This mechanism employs superstability of the shock wave driven into the load by magnetic pressure. Although exponential growth of the RT instability at the magnetic field/plasma interface, once it starts, is not suppressed by the snowplow mechanism, the stagnating front part of the load is perturbed much less than in the case of a thin shell. For this reason, as predicted in Ref. 4, large diameter uniform-fill loads can be good radiators. Recent experiments [5] have confirmed the viability of uniform fill loads.

Here, we demonstrate that exponential RT growth could be fully suppressed as long as a shock wave propagates into a load with an appropriately tailored density profile.

E/ω thus being an adiabatic invariant of the motion ("number of quanta"). Recalling that $E = M|g|l\xi^2/2$ and $\omega = \sqrt{|g|/l}$, where M, l, and ξ are mass, length, and amplitude of oscillations of the pendulum, respectively, we find that $\langle\xi\rangle^2|g|^{1/2} = \text{inv}$, and hence, the mean-square amplitude $\langle\xi\rangle$ grows as $|g|^{-1/4}$.

Small-amplitude, single-mode perturbations on the surface of an incompressible fluid in a time-dependent gravitational field are described by the same equation as a pendulum, with l replaced by $k^{-1} = \lambda/2\pi$. Solutions of this equation describe gravitation waves running across the surface, whose amplitudes, in the limit $t \to \infty$, follow the above law $\langle\xi\rangle \propto |g|^{-1/4}$. For the case of a load with a tailored density profile, a similar, relatively slow, non-exponential perturbation growth is predicted.

Numerical simulation results presented below have been obtained with the same two-dimensional magnetohydrodynamic code PRISM (which stands for Plasma Radiating Imploding Source Model) as used in Ref. 4 and in previous simulations of X-pinch and Z-pinch implosions [6, 7]. The physical model incorporated into this code includes electrical resistivity, separate energy equations for ions and electrons which include their respective thermal conductivities, and lookup tables for equation of state properties and radiative power. A "local" approximation or single zone opacity and transport scheme is used for the radiation. Argon was the only material considered in the simulations discussed here. Initial perturbations were seeded as small random density variations. The axial length of the computation field was 0.333 cm.

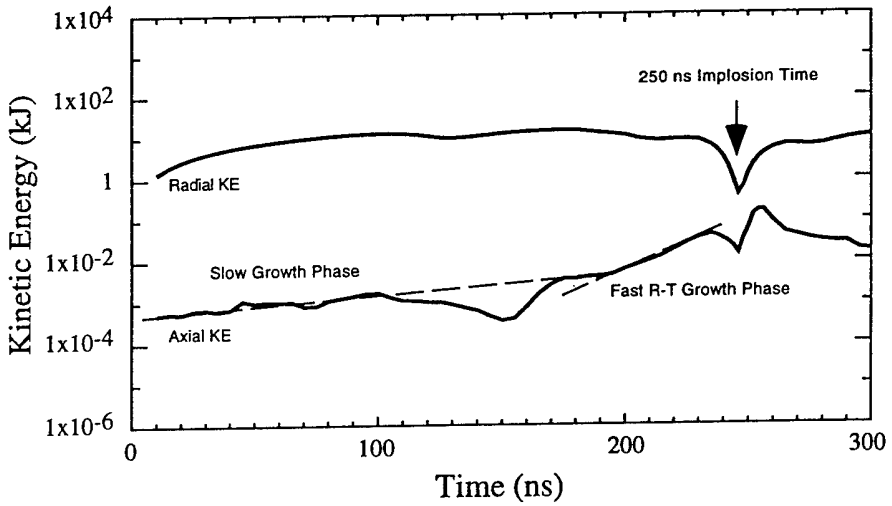

Figure 2. Radial and axial kinetic energies vs. time for a load a with a tailored density profile imploded with a constant current. Stagnation occurs at $t = 250$ ns.

Figures 2 and 3 illustrate the numerical results obtained for constant current $I = 5$ MA and the initial density of the load shown in Fig. 1(b), with a line density of 300 μg/cm. The usable portion of the imploding plasma's kinetic energy is its radial kinetic energy KE_r, whereas its axial kinetic energy KE_z is an integral measure of perturbation growth. While the shock wave propagates from 8 cm to 2 cm, compressing and accelerating the load mass, the acceleration of magnetic field/plasma interface is inverted. Thus the perturbations run across the back surface of the load as waves with slowly growing amplitudes. During the slow growth phase, which lasts about 190 ns, KE_z behaves exactly as expected, see Fig. 2. Small-amplitude waves running across

Therefore, radii of the structured loads and the corresponding implosion times could be increased to a greater extent than is possible even for uniform-fill loads, without sacrificing the implosion quality.

The idea of this approach is very simple. Let magnetic pressure drive a shock wave into a stratified plasma layer with increasing density. This causes the shock wave to slow down. Since the magnetic field/plasma interface also slows down, the effective gravity vector **g** is directed from the magnetic field (massless fluid) to the plasma [Fig. 1(a)]. Once there is no light fluid supporting a heavy fluid in a gravitational field, there is no reason for exponential growth of perturbations of the interface - rather, they would oscillate. Although magnetic pressure continues to perform work, accelerating an increasing plasma mass, the interface feels a deceleration, and this is all that counts.

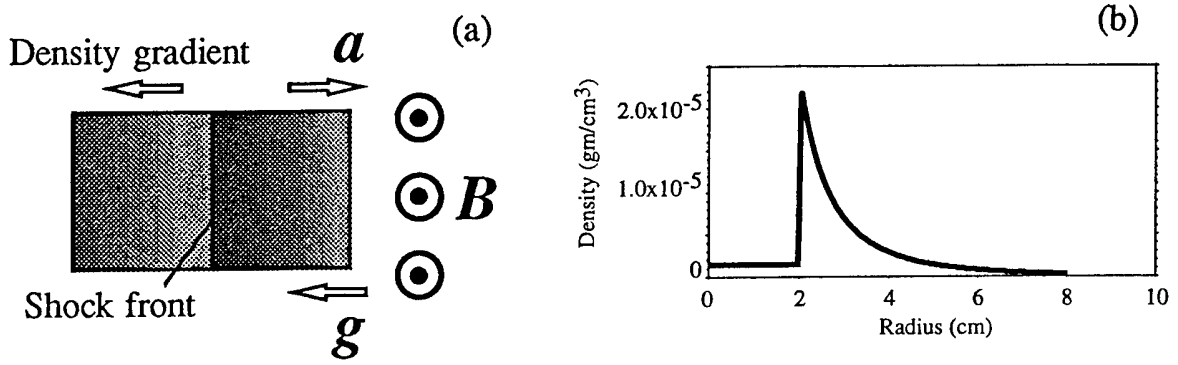

Figure 1. (a) Plasma acceleration inverted by the tailored density profile. (b) The $1/r^3$ initial density profile used in the simulation.

As an elementary example, consider a snowplow model of a Z-pinch imploding a plasma density profile of the form $\rho = \rho_0(r/R_0)^{-s}$ truncated at $r = R_0$, with $s > 2$, by constant current I. This model assumes that the plasma is collected in an infinitely thin shell whose radius is given by $R(t)$. Then the equation of motion is

$$\frac{d}{dt}\,\mu\frac{dR}{dt} = -\frac{I^2}{c^2 R}, \tag{1}$$

where $\mu = 2\pi\int_R^\infty \rho(r)rdr$ is the line mass collected by the shell. Solving Eq. (1), we find the effective gravity acceleration experienced by the shell:

$$g = -\frac{d^2R}{dt^2} \propto -(s-2)\left(\frac{R}{R_0}\right)^{s-3}\left[1 + C\left(\frac{R}{R_0}\right)^{s-2}\right] < 0, \tag{2}$$

where C is an arbitrary positive integration constant.

Since the acceleration g in Eq. (2) is negative, that is, directed from magnetic field to plasma, we expect oscillations instead of exponential perturbation growth. It does not mean, however, that perturbations do not grow. As seen from Eq (2), for $s \geq 3$, $|g|$ decreases with time. Consider a pendulum oscillating in a decreasing gravitational field. Going down to the equilibrium position, the pendulum is accelerated by a stronger field than that decelerating it after it passes the equilibrium point on the way up. The amplitude of its oscillations is thus increased. We can evaluate its growth, supposing the gravitational field to vary at a sufficiently slow rate, the energy-to-frequency ratio

the back surface are discernible in Fig. 3(a). As shown in Fig. 3(a), the plasma shell remains almost cylindrical during the slow growth stage. Although only the $m = 0$ modes are simulated here, the same - and for the same reason - must be true for all perturbation modes and all wavelengths. Similar behavior is found for any current waveform, once the density profile has been appropriately tailored.

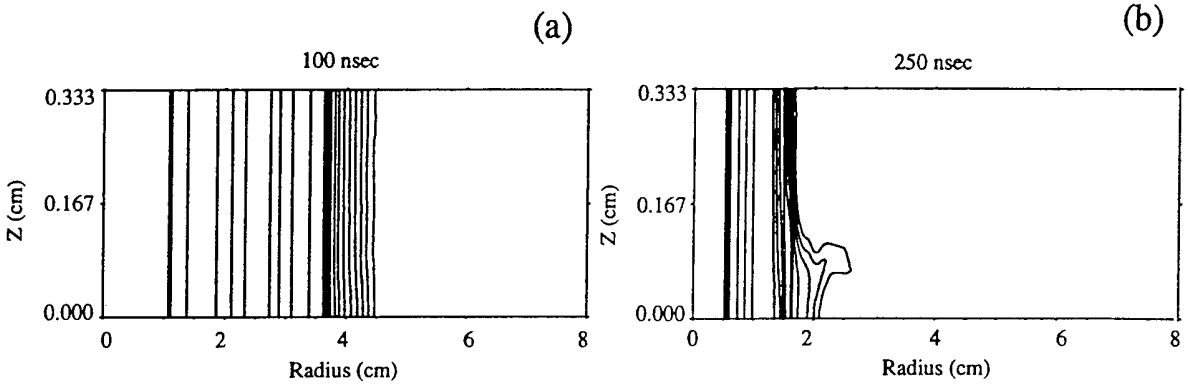

Figure 3. Density contours corresponding to slow growth phase, $t = 100$ ns (a) and rapid growth phase, $t = 250$ ns (b) in Fig. 2.

When the shock wave reaches the inner, high-density part of the load, and the reflected rarefaction wave transmits decreased pressure to the back surface, its acceleration is inverted again, with the result that the classical RT exponential growth starts to distort the shell at the back surface. If, as in this simulation, the inner surface is sufficiently close to the axis, the central regions of the implosion could remain relatively unaffected by the instability, as seen in Fig. 3(b).

Suppression of the RT instability by inverting acceleration is a robust, purely hydrodynamic effect. Formally, there are no limitations on its efficiency, and one can demonstrate the feasibility of implosions generating K-shell yield with arbitrarily large outer radii of the loads and arbitrarily long current pulses. In fact, the density in the outer layers of the load should not be too small - otherwise, a diode regime, beam generation would take place instead of an implosion. The lower limits on the density of the load and on the level of the gas pre-ionization have yet to be established. A practical method of tailoring initial density profiles (with specially designed gas puff nozzles, or otherwise) should also be developed. One can hardly doubt , however, that efforts and costs required for this development would be minimal compared with those involved in building and operating major pulsed power facilities.

[1] N.R. Pereira and J. Davis, J. Appl. Phys. **64** R 1 (1988).
[2] S.M. Gol'berg and A. L. Velikovich, Phys. Fluids B **5**, 1164 (1993).
[3] R. B. Baksht, A. V. Luchinsky, and A. V. Fedyunin, Sov. Phys. - Tech. Phys. **37**, 1118 (1992).
[4] F. L. Cochran, J. Davis, and A. L. Velikovich, Phys. Plasmas **2**, 2765 (1995).
[5] R. B. Spielman *et al.*, Bull. Am. Phys. Soc. **40**, 1845 (1995).
[6] F. L. Cochran and J. Davis, Phys. Fluids B **2**, 1238 (1990).
[7] C. Deeney *et al.*, Phys. Fluids B **5**, 992 (1993).

LIMITATIONS ON THE K-SHELL X-RAY CONVERSION EFFICIENCY OF A KRYPTON Z-PINCH PLASMA

J. Davis, J.L. Giuliani, Jr., J. Rogerson, and J.W. Thornhill

Radiation Hydrodynamics Branch

Plasma Physics Division

Naval Research Laboratory

Washington, D.C. 20375

ABSTRACT

The radiative behavior and its influence on the energy redistribution of a dynamically imploding current driven krypton gas puff plasma is investigated. Time dependent radiation magnetohydrodynamic numerical simulations self-consistently driven by a circuit equation are carried out for loads that remain stable to the Rayleigh-Taylor instability. The circuit driving the load is represented by a superclass pulsed power generator with peak short circuit currents of between 60 and 100 mega-amperes. The loads are configured either as thin annular cylindrical shells or uniform cylindrical fills. The results suggest a class of load designs leading to higher density on axis that may produce enhanced K-shell yields.

I. INTRODUCTION

Over the years steady progress has been made toward enhancing the kilovolt radiation conversion efficiency from pulsed power driven imploding z-pinch plasmas. In general, most of the higher kilovolt yields are due primarily to higher currents and improved understanding of power flow/load coupling, load physics, and load design. However, higher currents alone do not always account for all the increases. For example, an array of magnesium coated aluminum wires produced almost twice as much K-shell radiation than either pure magnesium or aluminum wire arrays on the same pulsed power driver.[1] Higher current into a properly designed load should generate higher magnetic fields leading to greater kinetic energy of run-in resulting in a higher compression ratio heating the plasma to temperatures that produce an abundance of harder kilovolt radiation. The challenge is to design loads that optimize kilovolt yields while minimizing anticipated shortcomings due to poor choices in the initial conditions such as mass loading, initial radius of individual wires as well as array radius, circuit design so that peak current occurs at load assembly, pure vs. mixed element, etc.

The purpose of the present investigation is to evaluate and assess the effects on the implosion dynamics and radiative behavior introduced by using separate electron and ion temperatures and a time dependent Collisional Radiative ionization model.

II. Model

The dynamics of z-pinch plasmas generally exhibit three (and sometimes four) distinct and sometimes overlapping stages. The first stage is the initial heating and

expansion phase establishing the conditions for stage two. In the second stage, so long as the current discharge continues, the implosion is driven by the **JxB** forces. The third stage is characterized by the plasma reassembling on axis converting kinetic energy of run-in to thermal energy. The plasma rapidly heats and ionizes to ionization stages not generally accessible during the implosion phase. During this third stage the newly formed hot dense plasma emits an intense kilovolt x-ray pulse. On occasion, a final and fourth stage develops when the current is large enough to maintain plasma confinement, additional heating and compression occurs accompanied by additional x-ray production.

The numerical simulations presented here to characterize the dynamics of a radially imploding Z-pinch plasma are based on a one-dimensional two temperature multi-zone non-LTE-radiation-magnetohydrodynamic model, DZAPP, with a transmission line circuit model for the driving generator.[2] The system of equations used to simulate the radiation magnetohydrodynamics of the implosion selfconsistently driven by a circuit was presented in an earlier paper and will not be duplicated here.[3] The equations have been expanded to include the effects of separate electron and ion temperatures and a time dependent nonLTE collisional radiative model to describe the dynamics of the manifold of atomic states.

The current profile used in the simulations was generated from a voltage waveform driving a circuit equation representative of a number of Decade-like modules which produces peak short circuit currents of 60, 80, and 100 mega-amperes. Obviously, the current that actually drives the load is significantly less.

Results

Numerical simulations have been carried out to determine the radiative performance of a z-pinch krypton gas puff plasma configured as either a thin annular shell or a uniform fill. The radiative yields are determined as a function of mass and length for fixed radii for load lengths $2 \geq \ell \geq 5$ cm. The choice of the loads' outer radius was determined from earlier results of a 2-D MHD Rayleigh-Taylor stability analysis suggesting that the largest radius for a stable shell is about 3 cm while it is about 7 cm for a uniform fill.[4] Recent preliminary studies of structured load designs suggest that by profiling the initial density it may be possible to go beyond 7 cm radius and maintain plasma stability.

For a uniform fill krypton gas puff load with an outer radius of 5 cm and a length of 3 cm driven by a peak short circuit current of 60 mega-amperes, a comparison is made of the radiation emitted from a one and two temperature 1-D MHD model in Collisional Radiative Equilibrium (CRE) and a two temperature plasma description with a Time dependent Collisional Radiative (CRT) model. The K-shell yield (includes all radiative contributions above 10 keV) as a function of mass is shown in Figs. 1. The curves are labeled A, B, and C and refer to one and two temperature CRE and two temperature CRT models, respectively. An immediate conclusion is that the driving current is insufficient to heat the plasma to K-shell temperatures, partly because of the enormous radiative cooling in the 0-5 keV regime. The difference between the 1 and 2 temperature CRE results (curves A and B) is a direct consequence of the hot ions. At stagnation the hot ions carry off kinetic energy that would otherwise, in a one temperature scenario, be converted into K-shell radiation, leaving behind a less dense core plasma. That is, in the one temperature approximation more energy couples into the core producing higher densities and since the radiation is proportional to N_i^2, the total yield in the one temperature scenario continues to increase until the plasma becomes to massive to be compressionally heated to efficiently radiate in the L- and K-shells. In addition, in the two temperature CRE case the electrons

must first equilibrate with the hot ions and only then can they re-excite the ions possibly producing radiation. After stagnation the plasma cools by radiation and expansion, producing a cooler residual plasma that redistributes the radiation to lower energy photons in the L- and lower- sub-shells.

The third curve labeled C on Fig. 1 represents the results from a fully time dependent simulation (CRT). This is important, particularly as the Z of the load increases, because it takes time to ionize up into the higher ionization stages. One can take a kind of asymptotic view that the total time it takes to radiate from the K-shell is the sum of the times it takes for the ions and electrons to equilibrate plus the ionization to the K-shell plus the excitation to populate excited state manifold plus the radiative decay of the K-shell excited state manifold. The cumulative sum of these times must be short in comparison to the post stagnation time it takes to cool due to expansion if there is to be sufficient time to radiate efficiently from the K-shell. The time dependent two temperature CRT K-shell yield is shown on Fig. 3 as curve C. Including time dependence reduces the K-shell yield by a factor of about 10 below the 2 temperature CRE results.

The variation of load current with length was investigated for the 60 MA case for the two temperature CRT simulation for a 3 cm 10 mgm shell and 5 cm 5 mgm uniform fill. The dotted portions of the curves represent extrapolations to smaller lengths. The variation of the peak load current with length is substantial both for the shell and uniform fill. For example, for the shell configuration the peak load current driving a 3 cm. long load is about 30 MA compared to 25 MA for a 5 cm. long load, a 17% decrease. The results indicate that for shorter loads higher peak load currents are achievable. The K-shell yield is shown as a function of load length in Fig. 2.

Figures 3 compares the K-shell yield as a function of mass between a 3 cm shell and a 5 cm uniform fill for a 60 MA driver. The load length is 3 cm in each case. The K-shell yield of the shell is consistently higher than the uniform fill by at least a factor of 2 over the chosen parameter space. Finally, Figure 4 compares the K-shell yields for a 7 cm uniform fill of 3 cm length driven by peak short circuit currents of 60, 80, and 100 MA. As mentioned earlier the total yields (L- and M- shell) are impressive and have not changed much from our earlier simulations. The K-shell yields are considerably lower by orders of magnitude from our earlier calculations and exhibits improvement as the peak current increases from 60 to 100 MA.

Conclusions

The results presented here clearly demonstrate the necessity of including separate electron and ion temperatures as well as time-dependent ionization dynamics in order to predict reliable K-shell yields, particularly for krypton and higher atomic numbered material loads. The limited but systematic survey conducted here both for shells and uniform fills show that as one moves from the 1-temperature to the 2-temperature CRE simulations the K-shell yield falls by about an order of magnitude. The 2-temperature time-dependent CRT K-shell simulations, over the same range of parameter space, are reduced even further to values between 1 to 10's of kJ. For the K-shell thin shells still radiatively out perform uniform fills at the same radius. However, the utility of the uniform fills, and structured loads in general, is that they can stable implode at larger radii and can compete radiatively with stable shells. It is also worth noting that the yields are a consequence of machine design and that by treating the generator and load as an integrated system can result in higher K-shell yields.

1. C. Deeney, P.D. LePell, et. al. Phys. Rev. E 51, 4823(1995).
2. D.D. Hinshelwood NRL Memo Rept 5185 (1983). See National Technical Information Service Document # 135024. Copies may be ordered from the National Technical Information Service, Springfield, Virginia 22161.
3. J. Davis, J.L. Giuliani, Jr., and M. Mulbrandon, Phys. of Plasmas 2, 1766(1995).
4. F. Cochran, J. Davis, and A. Velikovich, Phys.of Plasmas 2, 2765(1995).

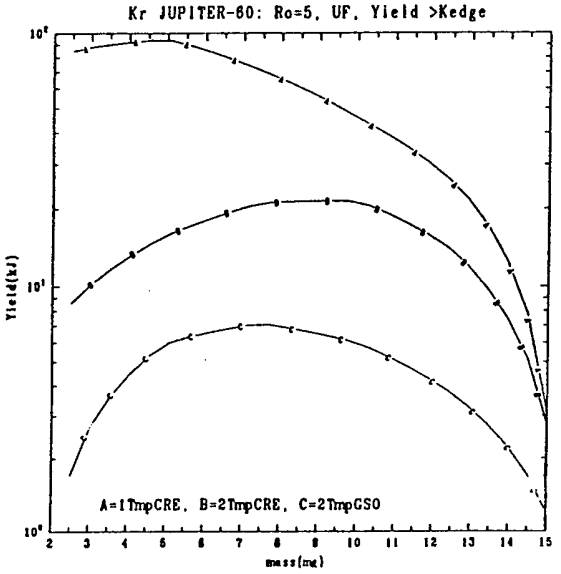

K-shell yield as a function of load mass for a uniform fill of 5 cm radius and current of 60 MA for a 1 a.nd 2 temperature CRE model and a 2 temperature GSO time dependent equation of state.

Figure 1

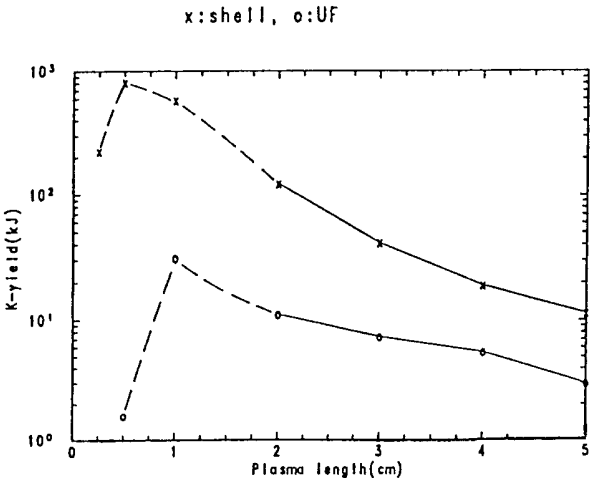

Variation of K-shell yield as a function of load length for a shell and uniform fill for a 60 MA driver.

Figure 2

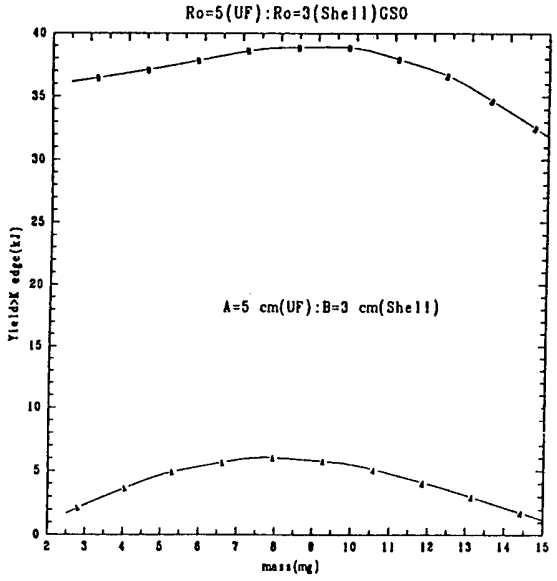

K-shell yield as a function of load mass for a 3 cm shell and a 5 cm uniform fill for a 60 MA driver.

Figure 3

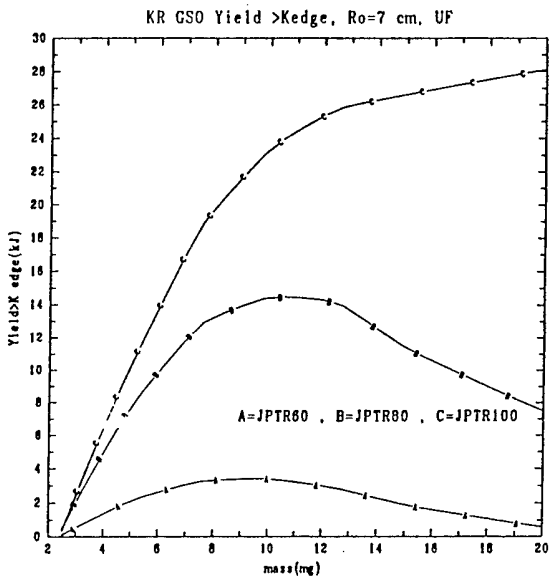

K-shell yield as a function of load mass for a 7 cm uniform fill driven with a 60, 80, 100 MA driver.

Figure 4

2.5D NUMERICAL METHOD FOR MHD EQUATION WITH MAGNETIC DIFFUSION IN ARBITRARY MOVING COORDINATE SYSTEM FOR Z-PINCH PLASMA SIMULATION

Oleg V. Diyankov, Igor V. Glazyrin, Serge V. Koshelev

Russian Federal Nuclear Center – All-Russian Research Institute of Technical Physics (RFNC - VNIITF)
P.O.Box 245, Snezhinsk, Chelyabinsk Region, 456770 Russia

Introduction

There is a great variety of approaches in code constructing, which are used now for plasma flows in Megagauss magnetic fields simulation. Among them one can find Lagrangian, Eulerian, Lagrange-Eulerian codes.

In this paper the code MAG [1, 2] for plasma modeling in arbitrary moving coordinate system and its present stage of development are presented. Using of arbitrary moving coordinate system allows to simulate flows with large deformations inside the flow region, conserving the correct description of conditions on its weakly deformated boundaries.

Model

The system of equations used in MAG code is Braginskii [3] model for one-temperature case (only electron temperature is taken into account)

$$\begin{aligned}
\frac{\partial \rho}{\partial t} + div(\rho \cdot \mathbf{u}) &= 0 \\
\rho \cdot \left(\frac{\partial \mathbf{u}}{\partial t} + (\mathbf{u} \cdot \mathbf{grad})\mathbf{u}\right) + \mathbf{grad}p &= -\frac{1}{4\pi} \cdot [\mathbf{B} \times \mathbf{rotB}] \\
\rho \cdot \left(\frac{\partial \mathcal{E}}{\partial t} + (\mathbf{u} \cdot \mathbf{grad})\mathcal{E}\right) + p \cdot div\mathbf{u} + div\mathbf{q} &= \rho \cdot Q_{ext} + \mathbf{j} \cdot \mathbf{E} \\
\frac{\partial \mathbf{B}}{\partial t} &= -c \cdot \mathbf{rotE} \\
\mathbf{E} &= \frac{\mathbf{j}}{\sigma} - \frac{1}{c} \cdot [\mathbf{u} \times \mathbf{B}] \\
div\mathbf{B} &= 0 \\
\mathbf{j} &= \frac{c}{4\pi} \cdot \mathbf{rotB} - \frac{c\, m_p}{e} \cdot \frac{A_i}{Z\, \rho} \cdot \nabla p \\
\mathbf{q} &= -æ \cdot \mathbf{grad}T
\end{aligned} \tag{1}$$

All variables are generally accepted.

The heat conductivity, electrical conductivity coefficients and average ion charge were calculated using the tables, which had been proposed in the paper [4].

Brief description of the numeric method

The initial MHD system has been written in Cartesian and cylindrical coordinate systems, then the dependence on the third variable has been eliminated. After this it was written in moving coordinate system. The received in such manner system describes 2D plasma flows with three components of dependent vector variables: mass velocity and magnetic field. This system has been splitted into two systems: hyperbolic and parabolic. The explicit TVD-type difference scheme has been used for hyperbolic system

and implicit Kershaw-type scheme has been used for parabolic one. The linear solver has been constructed on the basis of ICCG method.

The received hyperbolic system is solving in a moving coordinate system. There are five algorithms for coordinate system moving:

- the Lagrange one;
- the Euler one;
- a local algorithm (new coordinates of a site are determined by the coordinates of four neighbour sites);
- an algebraic algorithm (coordinates of inner mesh sites are determined by the coordinates of the boundary sites);
- an algorithm of mesh constructing, using the solution of Poisson equation.

These algorithms allow to perform modeling of wide range of MHD flows:

- Plate expansion under laser radiation
- Plasma – wall interaction in tokamak
- Z-pinch instability developing

Some examples of numerical modeling

In this paper we would like to give three examples of modeling, which could be performed using the presented method.

The *first one* is the modelling of laser beam interaction with thin aluminium plate. The modeling was performed in plane and axial symmetry. Initially plate of 50 micrometers thickness with density of 2.7g/cm^3 was heated by laser beam. The energy was absorbed in the density range from $3 \cdot 10^{-4}\text{g/cm}^3$ to $3 \cdot 10^{-3}\text{g/cm}^3$. The plate was expanding, and in the middle of the expanded area the hot area of plasma has been produced.

The problem was modelled, taking into account spontaneous magnetic field (the term $\frac{cm_p}{e} \cdot \frac{A_i}{Z\rho} \cdot \nabla p$ in the equation (1) is responsible for this field). The magnetized electrical conductivity and heat conductivity coefficients were taken into account.

Results are presented in Fig.1. One can easily see, that while taking into account spontaneous magnetic field, maximum temperature in plasma fakel is 1.5 times larger than without its accounting.

Second one is a problem of modeling of plasma – wall interaction in tokamak. This modeling was performed taking into account external magnetic field, and without magnetic field. In Fig.2. one can see the results of this modeling. In Fig.3 the graph of evaporated wall mass with respect to the angle for two cases is presented.

The *third one* is the compressing of initially perturbed gas puff Z-pinch by the φ component of magnetic field. The initial conditions are: 1.4 cm gas puff with density of $8 \cdot 10^{-6}\text{g/cm}^3$ and temperature of 10^{-2}eV was compressed by magnetic field, produced by linearly growing to 1.6 MA for the time of 100 ns current. In the second calculation pinch was initially rotated (initial value of mass velocity was: $u_\varphi = 10^5$ cm/sec).

One can see stabilizing of plasma with respect to rotation.

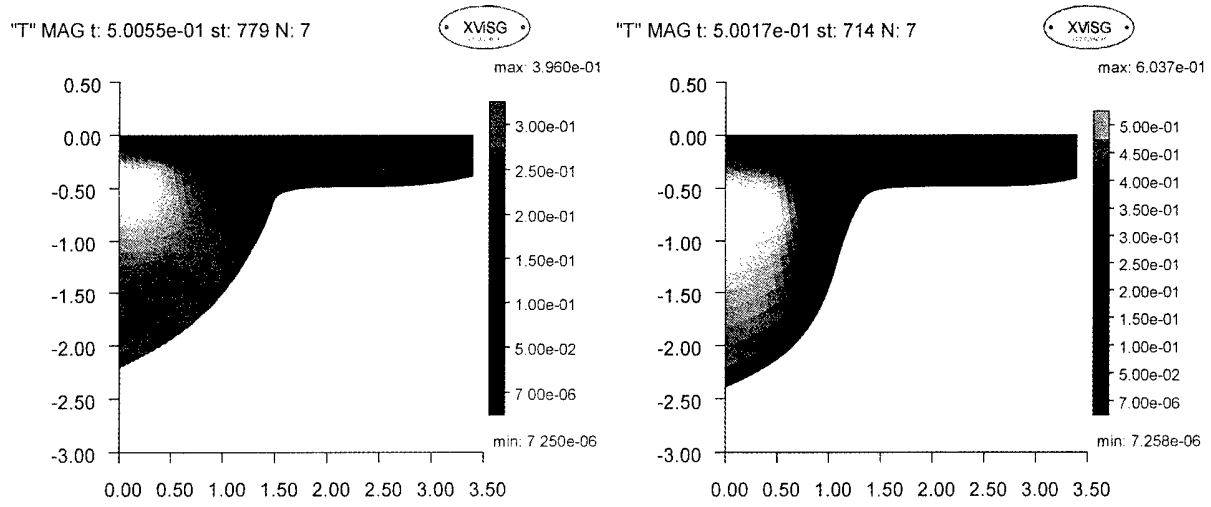

Fig 1. Temperature's map. Left - w /o magnetic field, right - with the field.

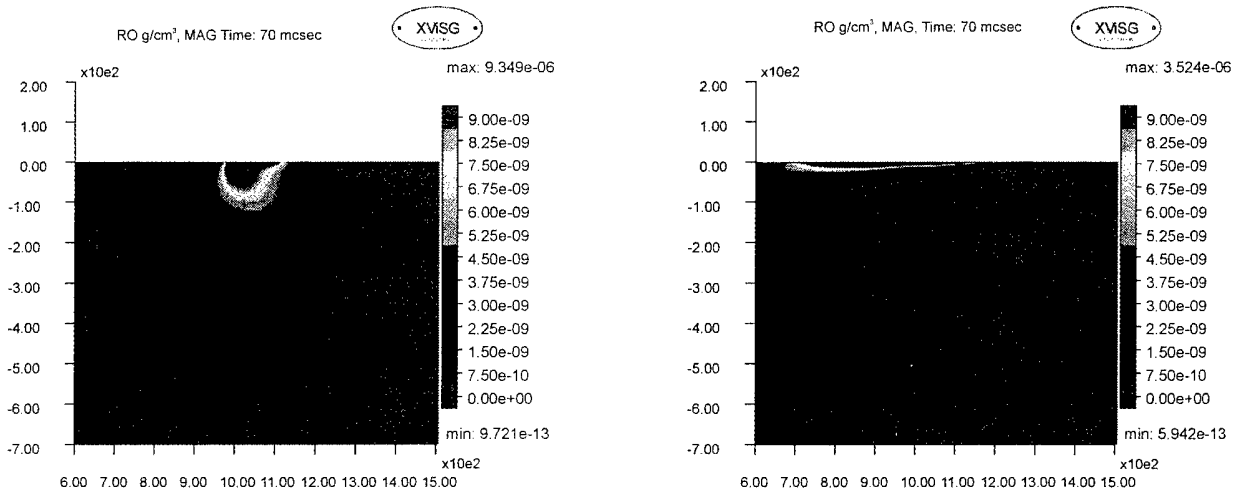

Fig 2. Density's maps, angle of beam 40. Left - w /o magnetic field, right - with the field.

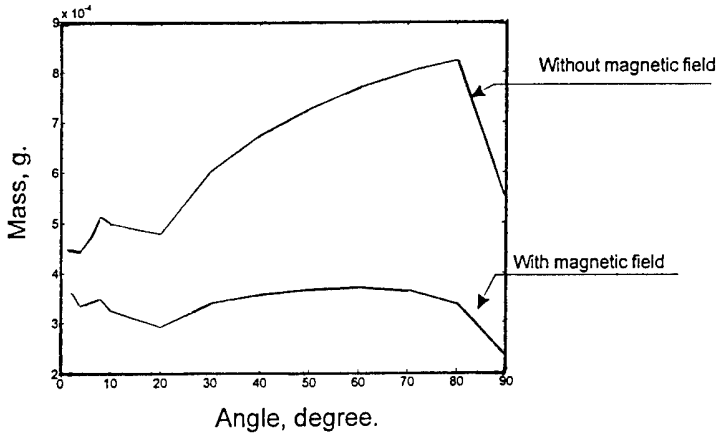

Fig. 3 Evaporated mass vs. angle of beam

Conclusion

Presented in this paper MAG code is now fastly been developing. Now the authors are working on the radiation transport accounting. We plan to implement in the nearest future two-temperature MHD model.

Acknowledgment

The authors are grateful to Serge Terekhoff, who has initiated the work on the MAG code. We are grateful to Vladimir Lykov for his permanent attention to this work. We are glad to thank Rouslan Kotov and Igor Krasnogorov for their help in preparing this work.
This work is supported by ISTC, Projects #009 and #107

References

[1] Diyankov,O.V. and Terekhoff,S.A. in *Dense Z-pinches*, ed. by M.Haines and A.Knight, AIP Conference Proceedings **299**, New York, (1994), p.121.

[2] Glazyrin,I.V., Diyankov,O.V., Kotov,R.A., Koshelev,S.V., High School News, Physics, Tomsk Univ., **12**, (1995), 23 (in Russian).

[3] Braginskii,S.L., *Review of Plasma Physics*, ed. by M.A.Leontovich (Consultant Bureau, New York), **1** (1965) 205.

[4] Ermakov,V.V., Kalitkin,N.N., Tables of electrical conductivity and electron heat conductivity coeffitients for plasmas of 11th matters, Preprint of Appl. Math. Inst., Moscow (1978) (in Russian).

NUMERICAL MODELLING OF MHD INSTABILITIES IN Z-PINCH HOT SPOT

Igor V. Glazyrin, Oleg V. Diyankov, Nikolay G. Karlykhanov, Serge V. Koshelev

Russian Federal Nuclear Center – All-Russian Research Institute of Technical Physics (RFNC - VNIITF)
P.O.Box 245, Snezhinsk, Chelyabinsk Region, 456770 Russia

Abstract

The focus of the work is on the study of some physical mechanisms connected with Rayleigh-Taylor-type MHD instabilities development. We compare our numerical results with experimental data obtained at High Current Electronics Institute (HCEI, Tomsk) [1]. Dependence of liner stability and radiation output vs. mass of liner, its initial radius, cascade scheme has been investigated in Tomsk. In our paper we try to explain by 1D and 2D MHD modelling the obtained experimental data and to analyze the role of main scales determining the liner implosion: magnetic field penetration into the body of plasma, heat-conductivity, radiation transfer. Some phenomena are investigated: shock wave motion, ionization, axial plasma motion and others. For double gas puff the collision of outer cascade with inner plasma is investigated in detail.

Introduction

Presently an essential efforts went into the description of the problem of the MHD instability of the gas puff implosion. The Rayleigh-Taylor (RT) instabilities are the first obstacle to obtain homogeneous plasma column. The RT instability problem has not been solved up to now. In papers [2, 3] it is supposed that multilayer gas puff has an internal property of suppressing MHD instability.

In this paper the MHD model is used to analyze processes of RT instability. There are several mechanisms which could be studied by MHD and play an essential role in liner implosion: thermal wave from plasma current heating, radiating effects cooling plasma, structure of observed shock wave, etc.

The numerical modelling is carried out by 1D MHD code ERA [4] and 2D MHD code MAG [5]. Radiation effects in MAG code are treated in optically thin plasma approximation (bremsstrahlung loses of energy). ERA allows to take into account radiation transfer in continuum and line spectrum. That permits to specify the results of 2D calculations.

Different Liner Configurations

A series of calculations were carried out for GIT-4 parameters: current with an amplitude of 1.6 MA with front duration of 100 ns [1]. Then current assumed to be constant. Several cases are considered for Argon load:

1. one-cascade puff; m = 31 μg/cm (only 1D); r_0 = 1.4 cm;
2. one-cascade puff; m = 61 (1D) and 50 μg/cm (2D); r_0 = 1.4 cm;
3. one-cascade puff; m = 154 (1D) and 250 μg/cm (2D); r_0 = 1.4 cm;
4. one-cascade puff; m = 61 (1D) and 50 μg/cm (2D); r_0 = 4 cm;
5. double puff; inner cascade: m_{in} = 61 (1D) and 50 μg/cm (2D); r_{in} = 1.4 cm; mass between inner and outer cascades m_{inter} = 20 (1D) and 9 μg/cm (2D) 1.4 cm $\leq r_{inter}$ <3.96 cm (1D) and 3.5 cm (2D); outer cacsade: m_{out} = 10 (1D) and 15 μg/cm (2D); r_{out} = 4 cm.

K-shell radiation yield obtained by ERA code for these cases is slightly correlated with Oreshkin's results presented in paper [1]: there is a maximum of the yield for single-cascade gas puff with 50 μg/cm and initial radius of 1.4 cm (case 2). It is interesting to note that the effects of temperatures of electrons and ions distinction play an important role for light liner (case 1). 1D and 2D results are summarized in Table 1. In 1D results the heavy liner is compressed very late and due to constant current could not expand. Therefore the 1D results of the case are incorrect.

Table 1: Summarized results for different cases. CR – compressed ratio as it is looked in a pinhole picture (the result has been obtained by corresponding computer code), TOI – time of implosion (ns), TASW – temperature after shock wave (eV), TAMC – temperature at maximum compression (eV), MFDL – magnetic field diffusion length (mm) at the beginning of implosion (for double gas puff second digit is the MFDL in inner cascade)

Case	CR	TOI	TASW	TAMC	MFDL
1	9	110	80	800	1.5
2	14	120	60	1750	2.5
3	10	230	40	1650	5.5
4	8	210	100	600	2
5	15	290	20	2300	3.5 (1.5)

Hot Spot Formation in Light and Heavy Liners

Using 2D code MAG the instability development was studied. For the investigation one need to set the source of nonhomogeneous. It has been supposed that small region ($\sim$50% in z-direction and $\sim$5% in r-direction) near upper boundary has smaller density ($\sim 5 \div 10\%$)

The study showed the difference in dynamics of light and heavy liners implosion (see Fig.1). For light liner the surface modes of RT instability are dominated and for heavy one the surface mode is transformed to the instability developing inside plasma (volumetric mode). This phenomena is connected with the penetration of magnetic field which is higher for heavy liner. The heat conductivity is lower due to lower temperature and higher density.

Calculated dynamics of hot spot formation in the case of light liner is quite ordinary (Fig.1, upper two pictures): the shock wave propagates to the axis and heat wave propagates ahead shock wave due to high heat conductivity. As a result small hot spot is formed. This hot spot – hot dense region radiates intensive without significant absorption.

The hot spot formation for heavy liner is more complicated (Fig.1, middle and lower pictures): because of the magnetic field penetration the strong shock wave runs away from the plasma edge (Fig.1, middle pictures) and then reaches the axis. As a result hot spot is formed (Fig.1, lower pictures) but it is not so hot and dense comparing to the case of light liner. This can be interpreted in the following way. First, only a small part of liner mass is involved into the spot formation, second, shock wave is not so intensive (has lower velocity), third, an axial motion of plasma is significantly higher. Plasma radiates in heavy liner from two regions: 1) hot spot and 2) hot region near plasma edge. The radiation from hot spot is absorbed effectively in cold dense neighbors regions. It could be the possible explanation of decreasing of radiation output in heavy liners. Hot region

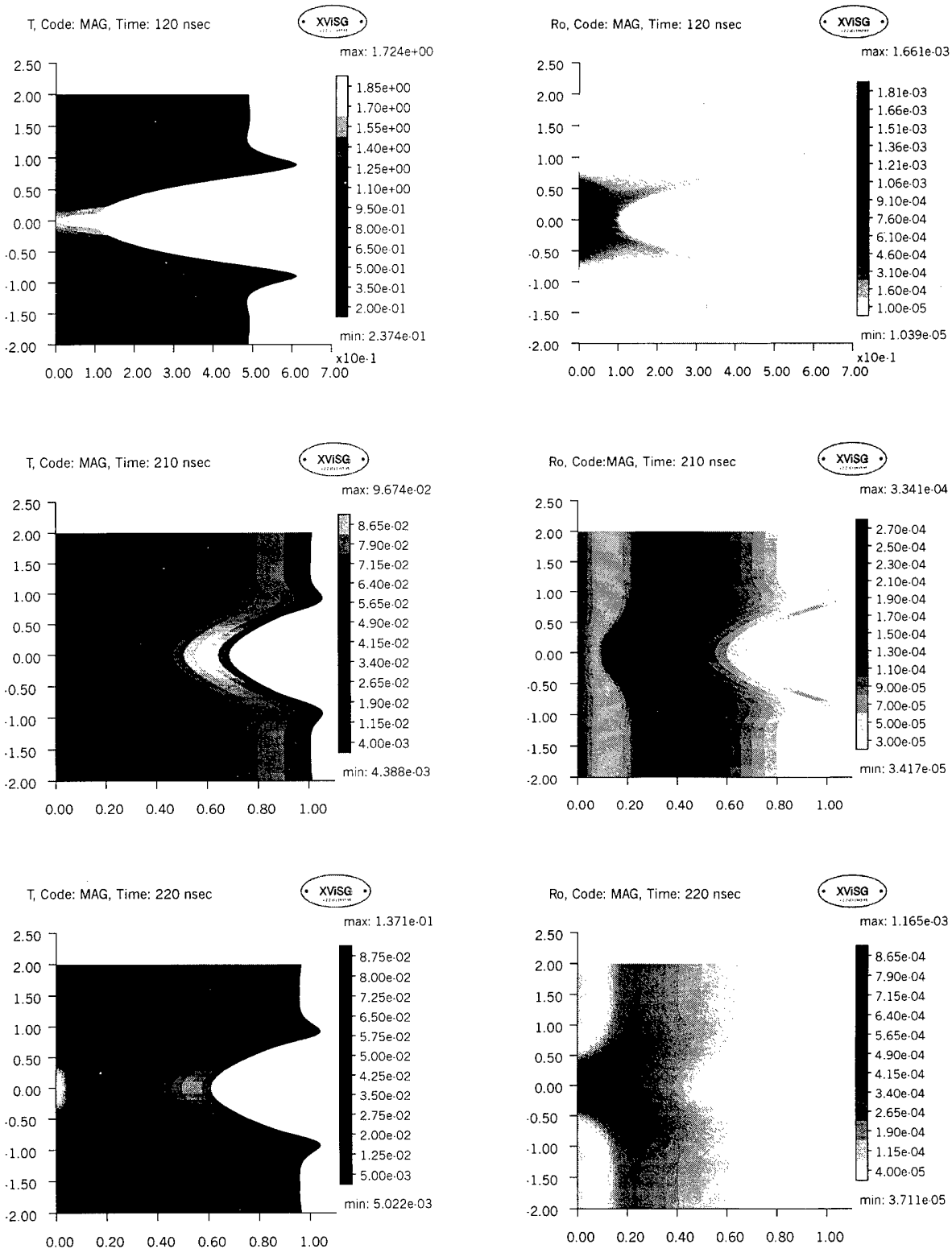

Fig. 1 One-cascade liner.
Left - Temperature (keV), Right - Density (g/cm^3).
Upper - Light Liner (50 μg/cm).
Middle and Lower Heavy Liner (250 μg/cm).

near plasma edge is formed due to Joule heating. Because of low density the radiation yield is not great. The final stage of hot spot formation is connected with two shock waves propagation in opposite direction.

Double Gas Puff Dynamics

The goal of multilayer liner using is instability suppression. It is supposed that a collision between outer accelerated layer and inner one (which is keeping without motion up to the time when magnetic field reaches inner liner due to diffusion) can provide the suppression. The outer liner in Tomsk experiment has lower mass and is a subject of instability. The calculated mechanism of instability suppression during shell collision is the next: the cavity of pertubated outer shell reached inner shell and then the hot region is formed (temperature increases from 98 eV up to 195 eV). Then heat wave is moving fast mainly alone the edge of inner shell and heats the upper edge of inner shell. At the moment the magnetic field continues to press the liner and therefore more uniform (in z-direction) shock wave propagates to the axis.

We estimated only the experimental data of outer-to-inner mass ratio $\eta = m_{outer}/m_{inner} < 0.3$. One need to investigate other range of η.

Spontaneous Magnetic Field Influence

To investigate the effect of spontaneous magnetic field influence on hot spot formation the term $\frac{cm_p}{e} \cdot \frac{A_i}{Z\rho^2} \cdot [\nabla\rho \times \nabla p]$ has been added to the equation of magnetic field diffusion. Results of calculation with and without this term differ slightly. Temperature increases from 1.72 keV to 1.89 keV at maximum compression, but the symmetry of implosion is disrupted. The influence for other data will be studied.

Conclusion

In a future we plan to investigate the role of Hall effect in the frame of Electron MHD, develop 2D radiation transfer code, two-temperature model, develop hybrid code (MHD+PIC) to study the effects of fast particles motion.

Acknowledgment

Authors would like to thank I.Krasnogorov for his help in transport coefficient addition to MAG code. We are grateful to V.Rot'ko for his help in preparing the paper.
This work is supported by ISTC, Projects #009 and #076

References

[1] Baksht,R.B., Datsko,I.M., Kim,A.A. et al., Proc. of 4th Int. Conf. "Zabakhin Scientific Talks" ZST'95, Snezhinsk, Chelyabinsk Region, Russia, (1995).

[2] Branitskii,A.V., Vikharev,V.D., Grabovskii,E.V., et al., Proc. of 8th Int. Conf. on High Power Part. Beams, BEAMS'90, Novosibirsk, **1** (1990), 437.

[3] Baksht,R.B., et al., ZhTF, **38**, No.11 (1992), 949 (in Russian).

[4] Glazyrin,I.V., Karlykhanov,N.G., Kondrat'ev,A.A., et al., AIP Conf. Proc., Dense Z-pinches, **299** (1994) 139.

[5] Diyankov,O.V., Glazyrin,I.V., Koshelev,S.V., 2.5D numerical method for MHD equation with magnetic diffusion in arbitrary moving coordinate system for Z-pinch plasma simulation, this Conference Proc.

Sheath Broadening in Imploding Z-pinches due to Large-bandwidth Rayleigh-Taylor Instability

James H. Hammer, James L. Eddleman, Max Tabak, Arthur Toor and George B. Zimmerman

Lawrence Livermore National Laboratory, P.O. Box 808, Livermore, California, 94550, USA

John S. De Groot

University of California, Davis, California, 95616, USA

Abstract

The magnetic Rayleigh-Taylor (RT) instability has been predicted[1] and observed[2] to cause break-up of the plasma sheath in imploding z-pinches. In this work we show that, for the type of density profile encountered in strongly-radiating pinches, instability at very short wavelengths grows to the non-linear stage and seeds progressively longer wavelengths. The result is a self-similar broadening of the sheath as found for mix layers in fluid RT unstable systems[3].

Introduction

The development of RT instability in imploding pinches is intimately tied to the evolution of the density profile, as can easily be seen from the expression for the growth rate of localized modes , $\gamma = \sqrt{\vec{g} \cdot \nabla \ln \rho}$ where g is acceleration and ρ is the density. From this it is apparent that the steepness of the density profile (where the acceleration and gradient are in the same direction) controls the severity of the instability. For annular pinches with radially-inward acceleration, the unstable region is in the outer portion of the plasma sheath where the density decreases with radius.

If the imploding plasma sheath remains at low pressure ($P << B^2/8\pi$) due to radiative cooling and if, for the moment, we ignore the effects of instability, the density profile will develop a sharp outer edge[1]. This behavior has been found in 1D radiation-MHD simulations of pinches and can be understood on simple physical grounds. Consider a time during the implosion at which the current has diffused through the edge plasma, and assume constant resistivity for simplicity. The current density in the edge will then be roughly uniform. If the scales we are considering are small compared to the pinch radius, the edge region will also have nearly uniform magnetic field (or a field that increases with radius). The JxB force density will then be roughly uniform, or radially increasing in this region. If the pressure is low, then the plasma responds to the JxB force by accelerating, with much greater acceleration in the low density portions of the plasma. The differential acceleration leads to steepening of an initially-diffuse profile, with the process continuing until the profile is so steep that, even though the pressure is low, the pressure gradient is of order the JxB force. We can relax the constant resistivity assumption, which increases the effect for plasma liners, i.e., low density plasma will ohmically heat faster and radiatively cool more slowly, so it will tend to become hotter, and in the Spitzer regime, a better conductor. The low density plasma will then carry more current and undergo even greater differential acceleration. At sufficiently low density, the plasma may not behave Spitzer-like due to anomalous resistance (e.g. from lower-hybrid drift instability), and the steepening effect will be relaxed. In the following, we neglect this effect, i.e., assume it occurs at negligibly small density.

Within a few Alfven transit times for the edge (<< implosion time, typically), a state is reached where the density falls to zero on a spatial scale $\delta = c_s^2/g$ where c_s = sound speed. For imploding loads approximately a centimeter in radius driven by the Saturn accelerator at Sandia National Laboratory[4], g is of order 10^{15} cm/sec^2 so $\delta \sim 10\ \mu m \times (ZT_e+T_i)/A = 75\ \mu m$

for a sheath with $T_e = T_i = 50$ eV, Z=5, A=40. For annular loads, the total sheath thickness is given by the resistive skin depth which is about a millimeter for the Saturn case, so the sheath tends to a profile with an outer edge an order of magnitude sharper. Recent linear theory has shown that these profiles are unstable to a surface mode that is not stabilized by resistivity[2]. There is also a simple physical picture for the absence of resistive stabilization. Consider a sharp boundary plasma sheath undergoing magnetic acceleration. If the sheath is very resistive, the current is initially uniformly distributed, however if we perturb the surface of the sheath the current density is necessarily higher where the surface curves inward and lower in the outwardly curved regions to satisfy current conservation. The higher current density region experiences greater JxB force and so drives even further inward with the converse true for the low current density region. The growth rate turns out to be the same as if the plasma were a perfect conductor. The surface modes can therefore become unstable at short wavelengths, $\lambda = 2\pi/k$ << magnetic skin depth and even $\lambda \ll \delta$, with growth rate $\gamma=(kg)^{1/2}$. At very short wavelengths the mode may be stabilized by viscosity or finite gyroradius effects. For the example parameters above, and at a typical Saturn accelerating field strength of 4×10^6 Gauss, the ion gyroradius is $r_i = 2.3$ μm. Finite gyroradius effects can enter when $kr_i \sim 1$, or at wavelengths of 10 - 15 μm. Viscosity limits are of similar magnitude. Modes with $\lambda = 15$ μm will exponentiate of order 100 times during the implosion, indicating strong nonlinearity should develop.

Simulations

We have done 2D MHD simulations to study the nonlinear development of the modes, starting with a sheath in hydrodynamic equilibrium with uniform, steady acceleration and resistive equilibrium (uniform current density). The curvature of the sheath is neglected for simplicity. The model profiles are given by:

$$T = const.$$

$$\rho(x) = \rho_0\left(1+\frac{\delta}{\Delta}-\frac{x}{\Delta}-\left(1+\frac{\delta}{\Delta}\right)e^{-\frac{x}{\delta}}\right)$$

$$B = B_0\left(1-\frac{x}{\Delta}\right)$$

$$\Delta = \frac{B_0^2}{4\pi\rho_0 g} \qquad x = r_{sheath} - r$$

These profiles become invalid at $x = \Delta$, reflecting the fact that sheath solutions are inherently time dependent. They are useful, however, for studying modes with wavelengths short compared to Δ since we can vary the resistivity without affecting the unperturbed profile and mode growth occurs more rapidly than the rate of change of Δ for a time-dependent sheath solution. A square 70 x 70 mesh is used with reflecting boundary conditions in z. The code takes a Lagrangian step and the mesh is rezoned to the initial mesh each cycle, so the calculation is effectively Eulerian. The linear growth of short wavelength surface modes is observed with growth rate independent of resistivity, in agreement with the analytic theory[2]. The temperature and resistivity are held fixed, with the dimensionless resistivity appearing in linear theory, $\mu = \left(\eta c^2/4\pi\right) g/c_s v_A^2$, set to a range of values ($v_A = B_0/\sqrt{4\pi\rho_0}$). Typically $\mu \sim 1$ for Saturn implosions, so we have done simulations with $\mu = 0.1, 1.0, 10.$ to cover the relevant range. The value of $\delta/\Delta = 0.1$ was held fixed for all simulations, and the equilibrium is initially perturbed with a random velocity perturbation of peak magnitude $10^{-3}c_S$.

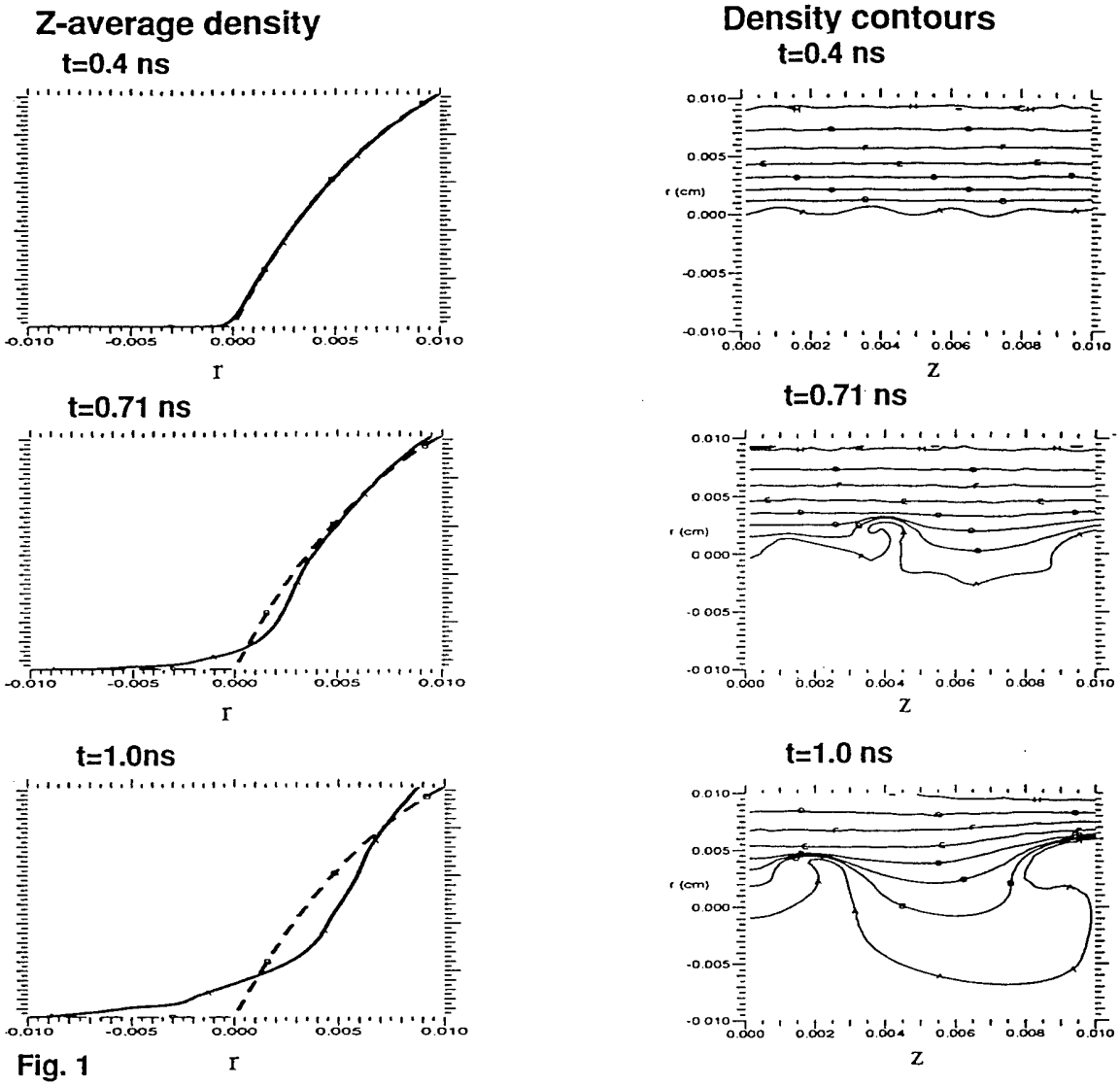
Z-average density
t=0.4 ns
r
t=0.71 ns
r
t=1.0ns
r
Density contours
t=0.4 ns
z
t=0.71 ns
z
t=1.0 ns
z

Fig. 1

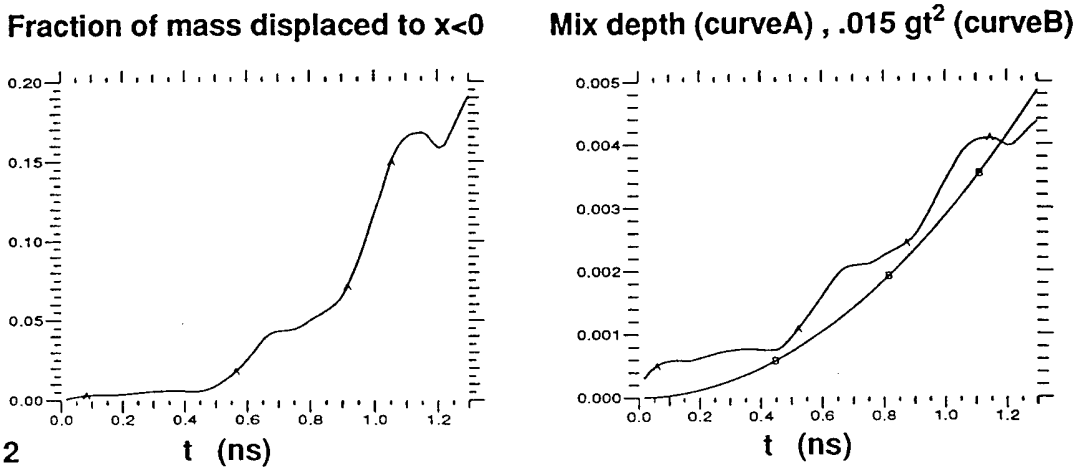
Fraction of mass displaced to x<0
t (ns)
Mix depth (curveA) , .015 gt² (curveB)
t (ns)

Fig. 2

The non-linear development is analogous to fluid RT behavior[3]. Short wavelength modes saturate when the amplitude is a fraction of the wavelength, and drive longer wavelength modes. These, in turn, drive even longer wavelengths until the scale is of order the size of the simulation. The characteristic perturbation scale and depth of the "mix layer" where plasma and accelerating magnetic field become intermixed is roughly proportional to gt^2, with little memory of initial conditions. Variation of the resistivity over 2 orders of magnitude about the typical value for Saturn had small effect on the scaling. Figure 1 shows results for the case with μ=1.

In Fig. 2, the "mix depth" is plotted for the case μ=1. The mix depth is defined (for numerical convenience) as the distance one would have to "dig" into the unperturbed profile in order to produce the mass displaced to $x<0$ by the turbulent flow. Comparison with the z-averaged profiles indicates that significant deviations from the original profile extend about a factor 1.7 times the mix depth defined in this way. With this multiplier, the mix penetration depth for the light fluid (vacuum magnetic field) into the heavy fluid (plasma) scales as .026 gt^2, in comparison with .042 gt^2 found for 2D simulations of classically RT unstable, sharp boundary fluids[3]. Calculations with μ= 0.1 and 10. give the same value for the mix penetration depth to accuracy similar to that shown in Fig. 2. It will be important to extend these calculations to the case where the simulation domain and mix region extend to scales larger than the sheath edge scale height, δ. Given that at long scales the system more closely resembles the classically unstable, sharp-boundary case, it seems likely that the penetration depth scaling as gt^2 will persist.

Conclusions

The 2D resistive magnetohydrodynamic calculations reported here show that density profiles expected for imploding, radiating pinches are unstable to RT modes at very short wavelengths. The short wavelengths grow to nonlinear amplitudes at early times, then stimulate longer wavelength modes resulting in self-similar growth of a mix region between plasma and the accelerating field. The behavior is similar to that of classically-unstable fluids and appears to be insensitive to the resistivity.

Since the implosion distance also scales as gt^2, one might expect the turbulently-broadened sheath width at the time of stagnation to scale proportional the initial pinch radius, e.g. sheath width ~ stagnation radius ~ 0.1 x initial radius. One complicating factor occurs when the RT growth is sufficiently large that low density "bubbles" break completely through the sheath and rapidly implode to the axis. In general, simulations including the complete geometry, self-consistent circuit, energy, magnetic field and radiation transport are required to account for the bubble-breaking and other complexities. The present work may provide a guide for establishing physically-reasonable initial perturbation levels for more complete calculations. Such calculations usually lack the resolution to follow the turbulent cascade from microscopic scales early in time to the macroscopic scale flows that are well resolved .

[1] T.W. Hussey, N.F. Roderick, and D.A. Kloc, J. Appl. Phys. **51**, (1980) 1452.
[2] J.H. Hammer, et.al., Phys. Plasmas **3**, (1996) 2063.
[3] D.L. Youngs, Physica **12D**, (1984) 32.
[4] J.H. Hammer, S. Maxon, M. Tabak, K. Estabrook, J. L. Eddleman, C.W. Hartman, A. Toor , G. B. Zimmerman and J.S. De Groot, Bull. Am. Phys. Soc. **39**, (1994) 1605.

* This work was performed under the auspices of the U.S. Department of Energy by Lawrence Livermore National Laboratory under Contract No. W-7405-ENG-48.

NUMERICAL ANALYSIS OF COLD CORE FORMATION DURING WIRE ELECTROEXPLOSION

Nikolay G. Karlykhanov, Igor V. Glazyrin, Oleg V. Diyankov

Russian Federal Nuclear Center – All-Russian Research Institute of Technical Physics (RFNC - VNIITF)
P.O.Box 245, Snezhinsk, Chelyabinsk Region, 456770 Russia

Abstract

It has been shown experimentally that wire explosion is connected with cold core formation and leads to a complex profile of magnetic field [1, 2]. The focus of the paper is the attempt to analyze this phenomena by numerical modelling. A series of calculations has been carried out using 1D radiation Lagrangian MHD code ERA [3]. The model has been developed and the influence of different terms including into the model has been analyzed.

Task Statement and 1D Model

All presented results have been obtained by ERA code. The equations describing ERA two-temperature MHD model are published in papers [3, 4] include two-temperature MHD, radiation transport equations for lines and continua, ionization state variations, a host of tables for EOS, transport coefficients etc.

The current driving the wire explosion has the triangle form with front duration of 50 ns, decay duration of 150 ns and maximum amplitude of 210 kA. These parameters are close to experiments on wire implosion with small generator using. Initial diameter of aluminum wire was chosen 20 μm.

Three different cases have been considered (refer to phenomena determining the model):

1. Microturbulence effects were not taking into account
2. Accounting microturbulence effects and anomalous transport coefficients due to ion-acoustic and lower-hybrid-drift microinstabilities development
3. Previous case plus accounting of mixing of ion components including neutral atoms

Magnetic Field Profile

Results of calculation in the frame of model corresponding to the first case show that magnetic field is concentrated in very thin skin layer and prevent the expansion of plasma on wire. Maximum of expansion for this case is about 150μm. It is in contrast with existing experimental data on wire explosion. Accounting of anomalous transport decreasing the electrical conductivity in a coronal region and leads to the increasing of the magnetic field penetration depth. Therefore plasma expands up to 3$\div$5 mm. Because of anomalous effects the conductivity in coronal region is much smaller that in core. Growing current generates the magnetic field which penetrates into the core and freezes into the central part of wire. This field prevents imploding inner region of wire. After 50 ns current begins to fall and boundary condition for magnetic field determinates the complex profile

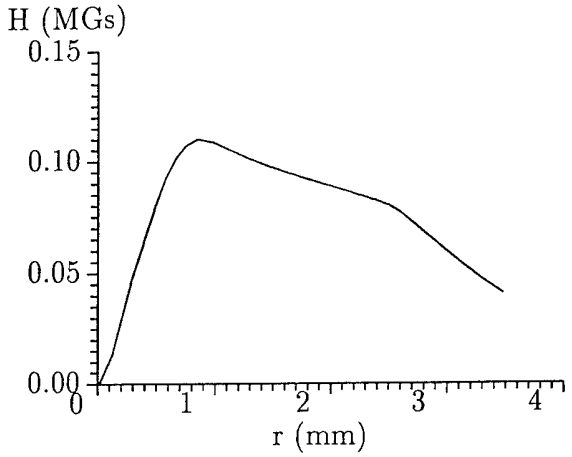

Figure 1: Magnetic field profile

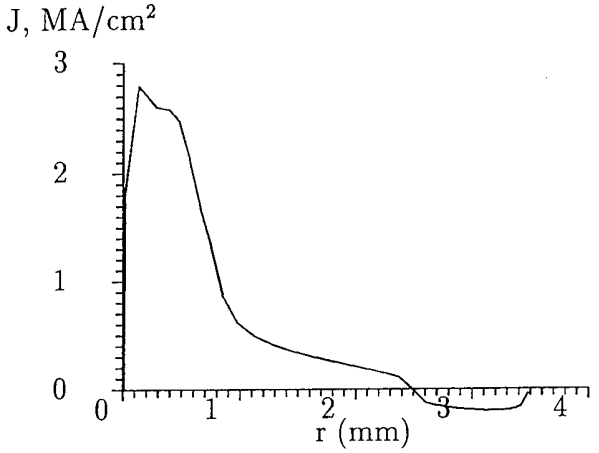

Figure 2: Density of current profile

of magnetic field as it is shown in Fig.1. In the coronal region the current flowing in opposite direction appeares (see Fig.2)

Cold Core Formation

Long existence of cold core could be explained by the formation of weakly ionized steam region. The steam region prevents heating of central core by radiation and electron heat conductivity ("screening" effect). Corresponding results are shown in Fig.3. They have been obtained taking into account of mixing with neutral atoms and without it. Second case (without neutrals) has been realized by supposing that minimal charge could not be smaller that 1.

In Fig.4 one can see the evaporated portion of wire mass vs. time for these two cases. The bound of evaporated matter has been calculated in suggestion of steam density of $\rho = 10^{-2}\mathrm{g/cm^3}$.

Radiation play an essential role in wire dynamics (radiation loses is about $60 \div 80\%$ from realized energy on wire). Line radiation is about 30% from total yield (plus bremmstrahlung and recombination radiation). Mainly the coronal region radiates and it deter-

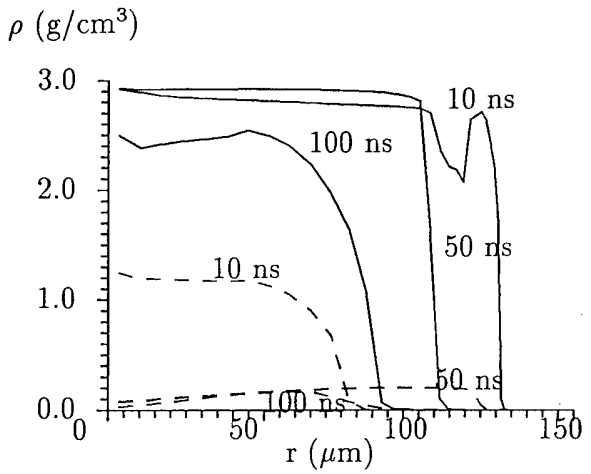

Figure 3: Cold core formation. Solid line – accounting of mixing of ion components including neutral atoms, dashed line – without accounting

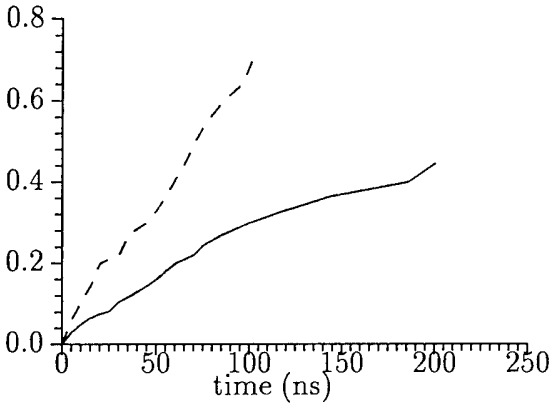

Figure 4: Portion of evaporated mass vs. time. Solid line – with accounting of mixing, dashed – without one

mins the temperature of this region.

Conclusion

It has been found that cold core formation is connected with 1) microturbulence effects consideration; 2) accounting of mixing of ion components including neutral atoms; 3) frozen magnetic field in the stage of pinch swelling 4) "Screening" effect by weakly ionized steam region.

One needs to continue the investigation and to analyze these processes by 2D code for real hot spot forming. It is interesting to study this phenomena in the frame of Electron MHD [5].

Acknowledgment

We are grateful to M.Timakova for her help in preparing the paper.
This work is supported by ISTC, Projects #009 and #076

References

[1] Sarkisov,G.S., Etlicher,B., Attelan,S., Rouille,C., Pisma v ZhETF **61** (1995) 547 (in Russian).

[2] Sarkisov,G.S., Etlicher,B., Yan'kov,V.V., et.al, ZhETF **108**, issue 4(10) (1995) 1355 (in Russian).

[3] Glazyrin,I.V., Karlykhanov,N.G., Kondrat'ev,A.A., et al., AIP Conf. Proc., Dense Z-pinches, **299** (1994) 139.

[4] Barysheva,N.M., Zuev,A.I., Karlykhanov,N.G., et.al, Zh. Vych. Mat. i Mat. Fiz., **22**, (1982) 401 (in Russian).

[5] Kingsep,A.S., Chukbar,K.V., Yan'kov,V.V. *Plasma theory questions*, Moscow: Energoatomizdat, **16** (1987) (in Russian).

ON THE NECESSARY MODIFICATIONS OF Z–PINCH MHD–MODELS

A.Kingsep, L.Rudakov
Russian Research Center "Kurchatov Institute",
123182, Moscow, Russia

Abstract. Numerical modelling of fast Z-pinch dynamics which allows for effects of electron magnetohydrodynamics (EMHD) is discussed; of these, the most important manifestation proves to be nonlinear convective penetration of field (current) into the plasma of Z-pinch. This highly nontrivial dynamics can be modeled using a relatively simple modification of of the diffusion equation for magnetic field. Two models of this type are suggested — for a one-scale pinch and for a thin liner. As a consequence, this opens possibility of numerical modelling of processes that involve the effects of EMHD on the basis of reliable, simple and well-operating MHD codes.

Introduction. In this paper, we consider some features of current /field penetration into the plasma of pulsed systems. To study these plasmas, the MHD numerical models are the most popular based on both the field frozen in a substance and diffusion of the field which is governed by a conventional equation. However, in a broad range of parameters, to wit,

$$V_{Te}, V_{Ae} \gg j/ne \gg V_A, c_S, \tag{1}$$

$$\omega_{Be}, \omega_{pe} \gg \tau^{-1} \gg \omega_{Bi}, \omega_{pi}, \tag{2}$$

$$c/\omega_{pe}, \rho_{Be} \ll a \ll c/\omega_{pi}, \rho_{Bi}, \tag{3}$$

not conventional MHD but electron magnetohydrodynamics (EMHD) [1,2] is valid. Here, a and τ are space and time scales of the problem, respectively; all the other terms are conventional. One of the important EMHD results is that nondiffusive penetration of a magnetic field into a weekly inhomogeneous plasma should occur. It was shown that this process could be described by the equation

$$\partial \mathbf{B}/\partial t + (c/8\pi e)[\nabla B^2, \nabla n^{-1}] = (c^2/4\pi\sigma)\nabla^2 \mathbf{B}, \tag{4}$$

which, in turn, converts to the Burgers' equation and then can be exactly integrated. As a consequence, it turns out that the magnetic field, depending on the topology of the $(\mathbf{B}, \nabla B^2, \nabla n)$ triplet, can either be locked in a boundary layer of finite thickness or penetrate into the plasma as a nonlinear travelling wave [10]:

$$B(z,t) = B_0\{1 - tanh[(z - ut)/\Delta]\} \tag{5}$$

where $u = (cB_0/8\pi e)|\partial n^{-1}/\partial x|$ and $\Delta = (4ec/\sigma B_0)|\partial n^{-1}/\partial x|^{-1}$. Just this result has been thoroughly confirmed in both simulations [3–5] and experiment [6–9]. Under close examination, however, the problem of an excessive coincidence

of experiment and theory arises. The field penetrates too readily into plasma, meanwhile, it is only one of two existing solutions of (4). Under the unfavorable orientation of the basic triplet mentioned above, the other solution corresponds to the field locking in the narrow vicinity of the plasma boundary. In particular, it can be seen from the paper [11] (see also [8]), where the sign of the gradient was not quite defined in the penetration region and the validity of (1)–(3) is dubious.

Thus, our goal is 1) to propose the proper explanation of the experimental data and 2) to suggest the model of penetration which can be introduced into the MHD–codes.

Enhanced field diffusion. As one can see, in the window of parameters specified by the inequalities (1)–(3), the field (current) dynamics proves to be rather complicated. Only for a regular density gradient does the physical scenario appear more or less clear. However, in the general case, a random profile of density seems to be more realistic, and this profile stimulates accordingly the random dynamics of field penetration. This idea in principle corresponds to the results of [4] where an attempt was enterprised, of the EMHD modelling of the fast Z–pinch, and the picture reminding multiple "tongues" of the penetrating magnetic field (or current loops) were observed. Unfortunately, too long simulations were necessary to complete this work.

Let the density be $n = n(x)$ where x is the coordinate along the boundary. Instead of the diffusion equation, we have [cf.(4)]:

$$\frac{\partial B}{\partial t} + B(\mathbf{u}\nabla)B = D_0\nabla^2 B, \quad \mathbf{u} = \frac{c}{4\pi e}[\mathbf{e}_y, \nabla\frac{1}{n}]. \tag{6}$$

Then we substitute $B = B(z) + \delta B(x,y)$, $\delta B \ll B$ into (6) and average this equation over x : $\partial B/\partial t + (c/4\pi e)(\partial B/\partial z) < \delta B \cdot \partial n^{-1}/\partial x >= 0$. Next, we multiply (6) by $\int^x (n^{-1}(x') - < n^{-1} >)dx'$ and also average over x:

$$\frac{c}{4\pi e} B\frac{\partial B}{\partial z} < \int^x (n^{-1}(x') - < n^{-1} >)dx' \frac{\partial}{\partial x} n^{-1} >= D_0 < \delta B \frac{\partial}{\partial x} n^{-1} > .$$

Finally, we get (see also [1]):

$$\partial_t B = D_1 \partial_z B^2 \partial_z B, \tag{7}$$

where $\partial_q \equiv \partial/\partial q$ and $D_1 = (c/4\pi e)^2(4\pi\sigma/c^2) < (n^{-1} - < n^{-1} >)^2 >$. Taking into account that for small B the diffusion coefficient must tend to $c^2/4\pi\sigma$, we may propose the resulting formula (first obtained by Chukbar and Yan'kov as exact result in a model problem [1]):

$$D_{eff} = D_0[1 + \mu(\omega_{Be}\tau_{ei})^2], \tag{8}$$

where $\mu =< (\delta n/n)^2 >$, $0 \leq \mu \leq 1/2$. In the numerical codes, this factor has to be introduced as indefinite one and subsequently determined from the

comparison with experimental data. In the limit of essential EMHD behavior, $\omega_{Be}\tau_{ei} \gg 1$, Eq.(7) may be represented in a form:

$$\partial_\tau B = \partial_z(B^2\partial_z B), \quad \tau = \mu\tau_{ei}t/4\pi nm.$$

The scaling substitution is possible: $B = \tau^b\beta(\psi)$; $\psi = z/\tau^c$. Then,

$$b\beta(\psi) - c\psi\partial_\psi\beta = \partial_\psi\partial_\psi\beta^3 \quad \text{and} \quad 2(b-c)+1 = 0.$$

Exact solution is obtainable for the case of constant frozen–in flux, i.e., of zero total current:

$$\beta = [\alpha(\psi_0^2 - \psi^2)]^{1/2}, \tag{9}$$

where $\alpha = \pi nm/\mu\tau_{ei}$ and the quantity ψ_0 just determines the total frozen–in magnetic flux. If we are interested in more realistic case, that is a constant field B_0 at the boundary, it follows that $b = 0, c = 1/2$. The resulting equation can be solved numerically. Nevertheless, its solution can be readily shown to be similar to (9), that is, it has the shape of the front analogous to the shock wave: $d\beta/d\psi \gg 1$ at $\psi \longrightarrow \psi_0 - 0$.

One–scale Z–pinch. Features peculiar to the diffusion regime can hardly be restricted to such a 1–d modulation, at least, as concerned the one–scale Z–pinch. Let us assume the random density perturbation in the $\{r, z\}$ geometry, of the order of δn and with a typical space scale $a \sim< n/|\nabla n| >$. Then taking into account that typical velocity of the field penetration [see (5)], $u \sim cB_0/4\pi nea$, we can introduce, in accordance with conventional formula, the efficient diffusion coefficient in a very simple form:

$$D_{eff} = [= \frac{\lambda u}{3} =] = \frac{\varepsilon cB}{4\pi ne}, \tag{10}$$

where $\varepsilon \propto< \delta n/n >$. Like μ in (8), it has to be subsequently determined from the comparison with experimental data. To provide the proper matching to the conventional MHD, we have to add $D_0 = c^2/4\pi\sigma$ to the RHS of Eq.(10). The same result, in a more precise form, could be obtained on the base of the percolation theory, to wit, $D_0 + (\varepsilon cB/4\pi ne)(\omega_{Be}\tau_{ei})^{-3/13}$ in the case of steady chaotic perturbation, and $D_0 + (\varepsilon cB/4\pi ne)(u/a\Omega)^{-3/10}$ in the case of the randomly oscillating perturbations, with a, Ω be typical space scale and frequency. One readily can see that both exact formulas are very close to (10), moreover, to realize these solutions "perfect chaos" is necessary, that is rather strong assumption. Thus, efficient diffusive coefficient (10) seems to be quite reasonable approach. It is interesting to note that it depends on very few parameters, like, e.g., Bohm coefficient, hence, it also may be introduced on the base of many different models.

Thin liner. If we consider a thin imploding shell, 1-d perturbation seems to be more probable than in the case of the one– scale Z–pinch. Nonetheless, let us summarize both additional terms in the efficient field diffusion:

$$D_{eff} = D_0[1 + \mu_1(\omega_{Be}\tau_{ei}) + \mu_2(\omega_{Be}\tau_{ei})^2]. \tag{11}$$

Note that compact liner is normally good-radiating (but H- or He-liner), therefore, it remains cool while implosion, $T = \text{const}$, hence, $(\omega_{Be}\tau_{ei}) \propto B/n$. Next, we add the condition of the compact acceleration:

$$g = \text{const} \quad \Longrightarrow \quad \rho g = \partial_r \frac{B^2}{8\pi} \longrightarrow \frac{B}{n} \propto (\partial_r B)^{-1}.$$

This estimate should be substituted into (11) thus resulting in

$$\partial_t B = \partial_r D_0 [1 + \frac{\chi_1}{\partial_r B} + \frac{\chi_2}{(\partial_r B)^2}] \partial_r B.$$

(We have used the property of the shell being thin which makes the geometry to be quasi-plane). One readily can see that the second term in brackets in the RHS vanishes, as a result, efficient diffusion may be successfully modeled by Eq.(8).

These models, (8) for the liner and (10) for a "thick" Z-pinch, may be used within the frames of relatively simple and well-operating MHD codes, instead of unwieldy PIC calculations. Thereby we can take into account some important EMHD manifestations.

The work was supported by the Russian Foundation for Basic Research (grant 96-02-16258).

[1] Kingsep,A.S., Chukbar,K.V., Yan'kov,V.V.: Reviews of Plasma Physics, B.B.Kadomtsev, Ed., Consultants Bureau, **16**, NY, (1990)
[2] Gordeev,A.V., Kingsep,A.S., Rudakov,L.I.: Phys.Reports, **243** (1994), 215
[3] Mason,R.J., Auer,P., Sudan,R.N., et al. : Proc. 8-th IEEE Pulsed Power Conf., San Diego, Calif., Cat. No 91 Ch 3052-8, (1991), 529
[4] Lindemuth,I. : Nonlinear Plasma Phys. Summer School, St.Petersburg, (1993)
[5] Mason,R.J., Auer,P., Sudan,R.N. : LA-UR-92-1409, LASL (1992); Phys Fluids B, (1993)
[6] Bystritskii,V.M., Krasik,Ya.E., et al : IEEE Trans. Plasma Sci., **19**, (1988), 107
[7] Maron,Y., Sarid,E., Zahavi,P. : Phys.Rev.A, **39**, (1989), 5842
[8] Commisso,R.J., Goodrich,P.J., Grossmann,J.M. : Phys.Fluids B, **4(7)**, (1992), 2368
[9] Chuvatin,A.S. : PhD Thesis; Paris, Ecole Polytechnique, (1993)
[10] Kingsep,A.S., Mokhov,Yu.V., Chukbar,K.V. : Fiz.Plazmy [Sov.Journ. Plasma Phys.], **10**, (1984), 854
[11] Hinshelwood,D., Weber,B., et al : Phys.Rev.Lett., **68**, (1992), 3567

X-RAY SPECTROSCOPIC CHARACTERIZATION OF HOT SPOTS IN NEON Z-PINCH

O. Renner[1], E. Krouský[1], A. Krejčí[2], M. Pfeifer[1], E. Förster[3]

[1]*Inst. of Physics, Acad. Sci. CR, Na Slovance 2, 180 40 Prague 8, Czech Republic*
[2]*Inst. of Plasma Physics, Acad. Sci. CR, Za Slovankou 3, 182 00 Prague 8, Czech Republic*
[3]*MPG Research Unit X-ray Optics, Max-Wien-Platz 1, 07743 Jena, Germany*

Abstract

Hot spots created in neon gas-puff Z-pinch were studied by precise spectroscopic methods. The macroscopic plasma parameters were found using the contour method and independently confirmed by a detailed comparison of the measured and synthetic spectra. Two groups of hot spots with substantially different electron densities and temperatures were observed, their parameters are discussed with respect to possible photopumping experiments.

Introduction

Neon plasma in a gas-puff z-pinch is being extensively studied as a lasing medium of a resonant photopumping x-ray laser scheme [1]. The measurements of the plasma conditions, mainly its temperature and density, are motivated by an effort to determine a distribution of different ions and populations of their ground and excited electronic states. Optimum parameters for the neon-lasant plasmas (T_e = 50 - 100 eV, n_e = 10^{18} - 10^{19} cm^{-3}, plasma column diameter less than 1 mm) are relatively easily achieved in long-living bulk plasmas [2]. The period of hot spot occurrence corresponds to considerably higher temperatures and densities; the knowledge of their characteristics is, however, important for understanding the second plasma implosion [3] and decay. The origin of these small diameter, short-living plasma formations is discussed in the accompanying paper [4]. The hot spots produce strong emission in the photon energy range of about 1 keV, thus information on their macroscopic parameters can be provided by K-shell spectroscopy. Here we present the results of spectroscopic experiments done at the IPP Z-pinch apparatus and provide their detailed interpretation.

Experimental

A schematic diagram of the experimental arrangement is shown in Fig. 1. The plasma was generated in a low energy Z-pinch device (4.3 kJ, 150 kA, risetime 1.1 μs). The radiative characteristics were studied using different diagnostic tools - filtered x-ray diode providing survey information on broad-band x-ray emission and a lifetime of the hot spots (ranging from units to several tens of ns), x-ray pinhole camera, and absolutely calibrated flat-crystal spectrograph with spectral resolution $\lambda/\Delta\lambda \approx 1200$ and a limited spatial resolution along the discharge axis. The slightly demagnified pinhole camera images indicate that the plasma emission is significantly inhomogeneous - the hot spots of an average size 30 - 100 μm are localized close to the gas-puff axis and spaced at irregular intervals. The time-integrated spectra were recorded on x-ray film Kodak DEF, microdensitometered and converted to intensity scale using a calibration curve. The contributions from hot spots formed at different axial positions were distinguished and correlated with corresponding pinhole images. This allows the realistic size-dependent escape factors to be estimated.

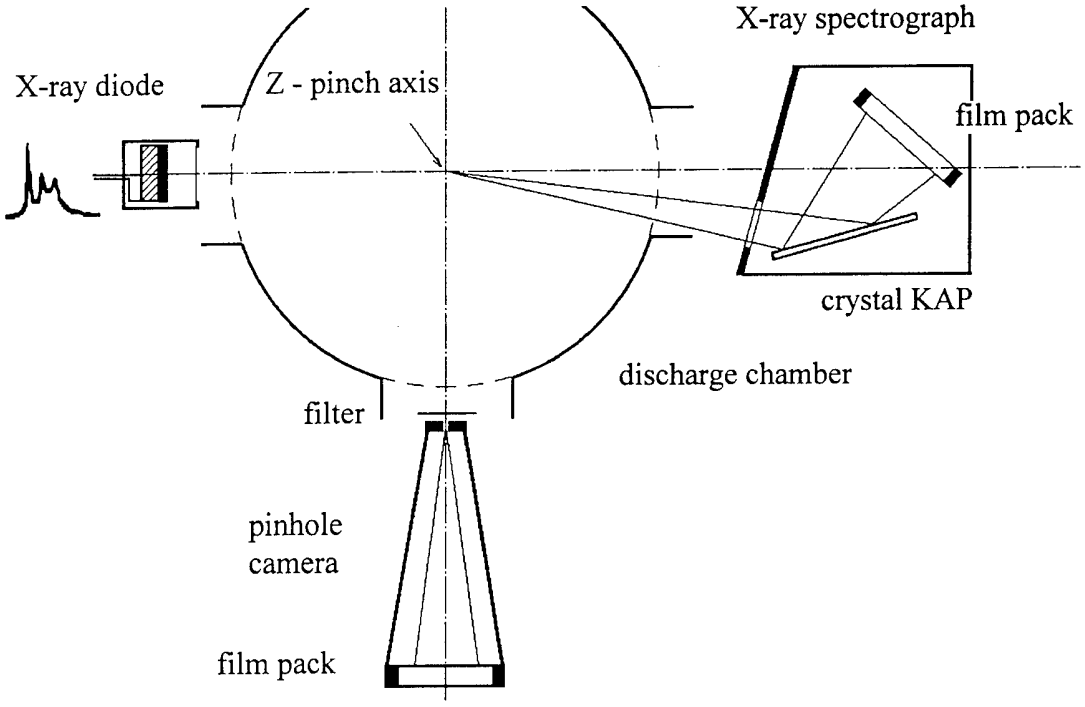

Fig. 1.

Results and discussion

An example of the spectra detected is shown in Fig. 2. The observed relative widths (FWHM) of the spectral line profiles are within $(2.2 - 4.2) \times 10^{-3}$. The absolute radiative energy corresponding to line emission in the spectral range 900 - 1100 eV was typically 1×10^{-2} J to full solid angle. The spectra could not be evaluated by using a standard diagnostic technique based on relative intensities of dielectronic satellites - contrary to observations [1,5], at given plasma parameters the emission is dominated by resonance lines and the satellite intensities do not fit with the dynamic range of the detector. Thus to estimate the macroscopic plasma parameters from K-shell emission, an approach suggested by Coulter et al. [6] was followed.

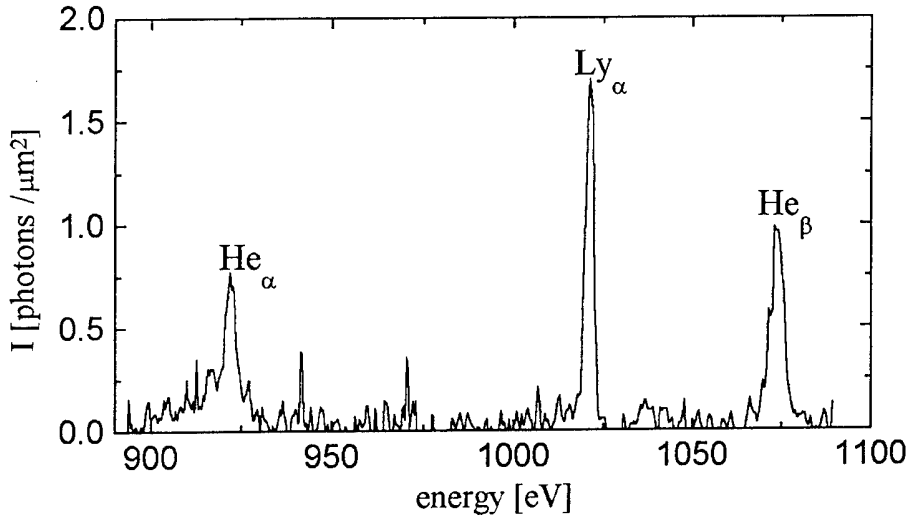

Fig. 2.

In the electron density-temperature space, the contours corresponding to the observed intensity ratios of Ne He_α, Ly_α and He_β lines were calculated by using a computer code RATION [7]. This package solves the system of steady state non-LTE rate equations to calculate populations of H- to Li-like ions and provides selected diagnostic line ratios and synthetic spectra as a function of the plasma density, size and temperature. The effect of opacity is approximated by escape factors, the code includes line broadening mechanisms (Doppler and Stark contributions) and provides a mechanism for modifying the spectral profiles by an instrumental smearing function. The validity of this collisional radiative model is restricted to plasmas with small temperature and density gradients, which need not be fulfilled at Z-pinches. The diagnostic data were provided at the intersection of the contours computed for all possible combinations of the above mentioned transitions, thus partly overcoming difficulties connected with non-unique determination of electron density and temperature from an individual intensity ratio.

The spectra with dominant Ly_α emission (like that shown in Fig. 2) correspond to hot spots with electron temperature $T_e \geq 400$ eV and electron density $n_e = (1 - 2) \times 10^{22}$ cm^{-3}. The majority of the observed spots is characterized by $T_e = 150 - 200$ eV and $n_e \approx 1 \times 10^{21}$ cm^{-3} (see Fig. 3). These results were cross-checked by detailed comparison of the spectral line profiles of the experimental and the computer-generated [7] spectra. The comparison of the measured (solid line) and the synthetic (dashed line) spectrum presented in Fig. 3 indicates a satisfactory agreement between experiment and theory. The spectrum is dominated by the Ne He_α line, which is characteristic for lower electron temperatures. The observed line profiles are slightly broader than the theoretical ones; the fit might be improved by assuming higher n_e but then the satellite structure would be overestimated.

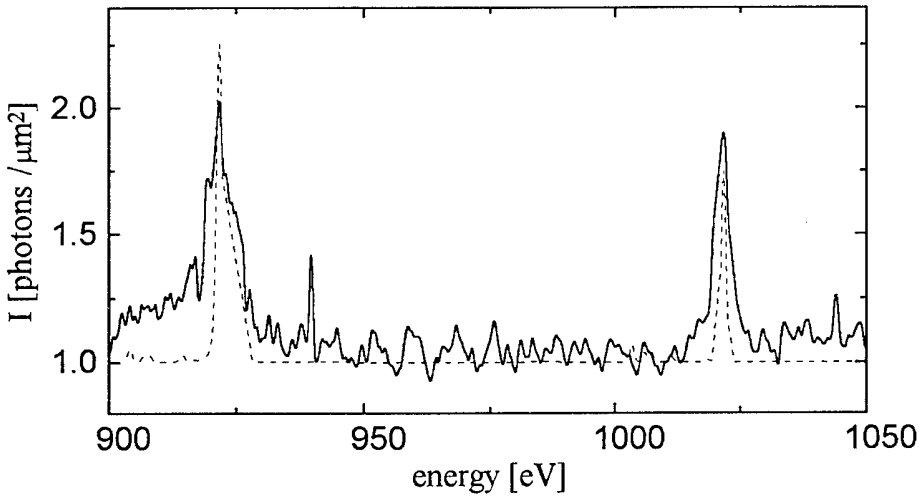

Fig. 3.

The electron densities found at higher-parameter hot spots were confirmed by a detailed analysis of the spectral line profile. At $n_e \leq 10^{24}$ cm^{-3}, the width of the Ly_α lines are rather insensitive to n_e [8], thus the questioned values were found from the He_β line broadening. The measured (solid line) and the synthetic Stark-broadened (dashed line) profiles are compared in Fig. 4, the best fit is obtained for $n_e = 1.8 \times 10^{22}$ cm^{-3}. The agreement between the values found by these two independent methods is very good.

The measured values of T_e and n_e were used to determine the ion population and the distribution of the ground and excited states of photopumped Ne IX; for $T_e = 150$ eV and $n_e = 1 \times 10^{21}$ cm^{-3} the difference in populations of ground and excited states is given by a factor

of 200 and slightly less for higher n_e; as discussed above, the validity of these calculations is limited by the assumptions of the steady-state collisional-radiative equilibrium model used. As to the environment for sodium-neon photopumping experiments, hot spots are too small, too dense and possibly too non-uniform for successful application.

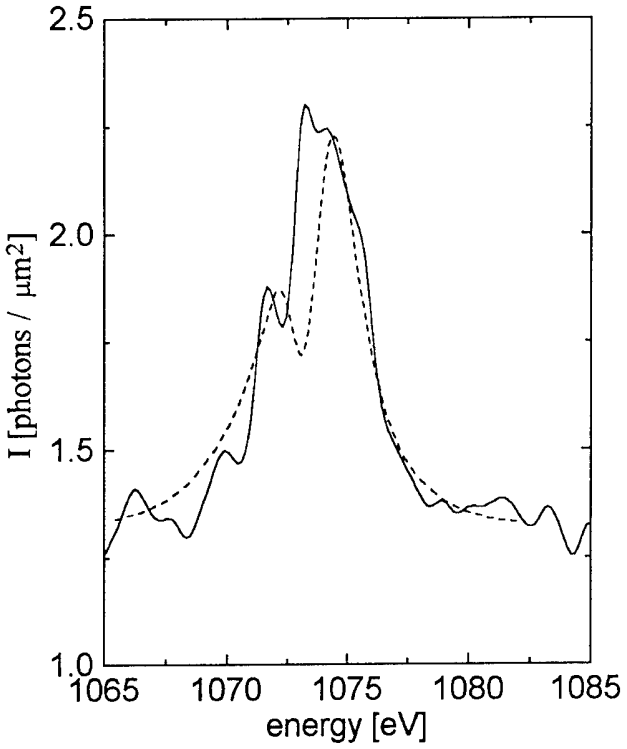

Fig. 4.

Conclusion

To conclude, the characteristics of the hot spots created in neon gas-puff Z-pinch were investigated by precise spectroscopic methods. The values of electron density and temperature found by the contour method were confirmed by comparison of the measured and synthetic spectra and by a detailed analysis of the Stark-broadened spectral line profiles. Two groups of hot spots with substantially different n_e and T_e were observed. The parameters of hot spots are too high to provide an appropriate medium for Na/Ne photopumping experiments. The knowledge of these parameters is important for mapping the time history of Z-pinches.

Acknowledgment

This work was supported in part by the Grant Agency of the Czech Republic under Grant No. 202/93/1023.

[1] Young F.C., Welch B.L. and Griem H.R.: 3rd Int. Conf. on Dense Z-Pinches, AIP Conf. Proc. **229**, London 1993, p. 437.
[2] Krejčí A. , Rauš J., Pifl V., Golubev A.V., Platonov Yu.Ya., Krouský E. and Renner O: IEEE Trans. on Plasma Science **16** (1993), 584.
[3] Welch B.L., Young F.C. and Griem H.R.: J. Appl. Phys. **74** (1993), 2260.
[4] Kubeš P., Kravárik J., Koláček K., Krejčí A., Paduch M. and Tomaszewski K.: this conference.
[5] Nave G., Challis C.D., Dangor A.E. and Lunney G.: J. Appl. Phys. **65** (1989), 3385.
[6] Coulter M.C., Whitney K.G. and Thornhill J.W.: J. Quant. Spectrosc. Radiat. Transfer **44** (1990), 443.
[7] Lee R.W., Whitten B.L. and Stout R.E.: J. Quant. Spectrosc. Radiat. Transfer **32** (1984), 91.
[8] Lee R.W.: J. Appl. Phys. **58** (1985), 612.

DIAGNOSTICS OF LOW ENERGY CARBON FIBRE Z-PINCH

P. Kubeš[1], J. Kravárik[1], E.Skladnik-Sadowska[2], J.Baranowski[2], M. Paduch[3], K. Tomaszewski[3], P. Gogolewski[3]

[1]*FEE, Czech Techn. Univ., Technická 2, 166 27 Prague 6, Czech Republic*

[2]*INS 05-400 Swierk n. Warsaw, Poland*

[3]*Institute of Plasma Physics and Laser Microfusion, P.O.Box 49, 00-908 Warsaw 49, Poland*

In this paper there are presented results of measurements of X-rays, fast electrons, ions and schlieren pictures an exploding carbon fibre of 6μm in diameter, located between tips of the conical electrodes within a small 0.5 kJ Z-pinch facility. Thin fibres are often used as the load in Z-pinch experiments due to high initial cylindrical symmetry for a simple source of X-ray emission from low- and high-energy facilities [1]. In our experiments a strongly asymmetric source of XUV radiation and relatively long X-ray emission was observed.

Small energy of a capacitor enables the development of 60kA current (during 1000ns) between two conical electrodes (with 10° top angle) under the pressure $2x10^{-3}$Pa. The distance between the electrodes is 8mm. The carbon fibre is located between the electrodes with a special holder.

The Schlieren method was used for the visualization of a pinch column. The YAG neodym laser generating pulses of about 4ns length used as a source of diagnostic beams. X-rays were detected with two scintillator photomultiplier detectors positioned side-on and end-on at distance of 30cm from Z-pinch. Soft X-rays were detected with NE 102 scintillator of 20μm and/or 2mm in thickness, which were covered with aluminum foils of 1.5 or 3μm in thickness. The XUV signals were detected by two fast silicon p-i-n diodes filtered by 750 nm Al foil in axial and radial directions to the fibre axis. Fast electrons and ions were detected by means of on Faraday cups located in different radial positions at distances 28 and 68cm from the fibre and perpendicularly to the discharge axis (in the main symmetry plan).

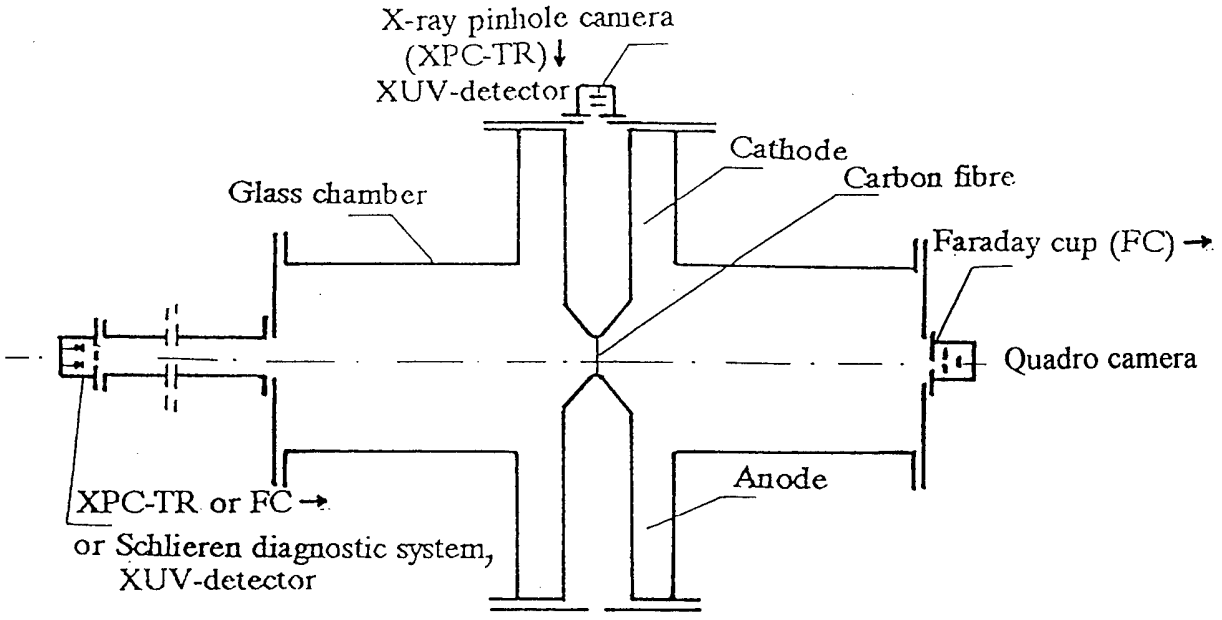

Fig.1. Schematic diagram of the Z-pinch (with carbon fibre) device equipped on the Faraday cups (FC) and X-ray time-resolved pinhole cameras (XPC-TR).

Simplified scheme of the measuring system has been presented in Fig.1. All the current wave-forms, timing, X-rays, ions and electrons signals were registered with HP multi-channel digital oscilloscope.

For Z-pinch discharges performed with a carbon fibre was carried out a series of X-ray measurements using different sets of Al-foil filters and NE-102A scintillator. The intensive emission of X-rays was observed at on energy level of above 500eV. Fig.2 presents the time correlation of soft and hard X-rays in comparison with dI/dt wave forms, as registered for three shots. The soft X-ray emission of energy within 0.5-1.5keV interval appears 500-700ns after the breakdown. This radiation correlates with the current maximum during 700-1200ns. On the bottom picture there is shown a signal correlated with a laser pulse, which corresponded to the enclosed Schlieren picture.

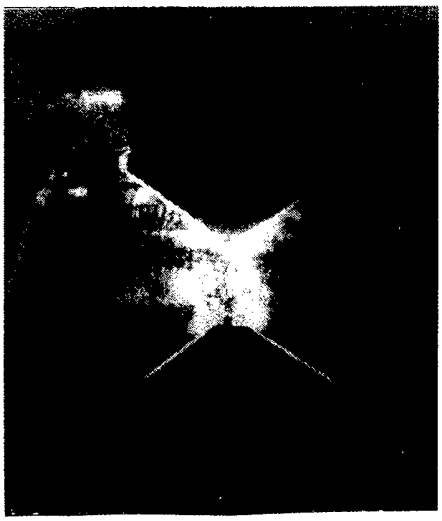

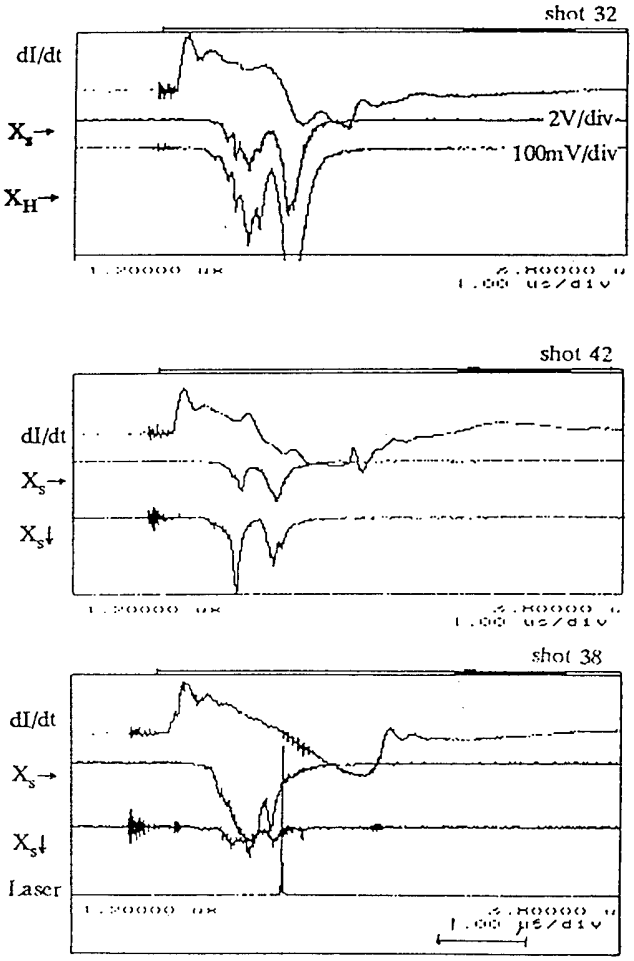

Fig.2. The X-ray signals (X_H, X_S) in comparison with current derivative (dI/dt) waveforms, as obtained from three shots. On the left-Schlieren picture corresponding to the laser pulse.

Measurements of ion- and electron-components were performed perpendicularly to the z-axis, i.e. there were measured perpendicular components of carbon-ions and electron motion. The measurements carried out simultaneously of two different distances

made possible to determine absolute values of transversal energy of ions and electrons. Some examples of typical ion- and electron-signals in comparison with corresponding dI/dt and soft X-ray traces, have been presented in Figs.3 and 4.

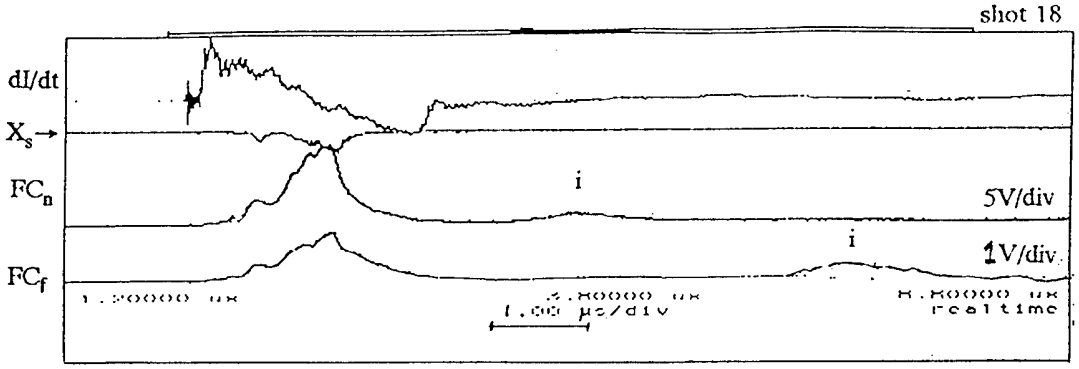

Fig.3. Ion signals obtained from Faraday cups at different distances: 28cm (FC_n), and 68cm (FC_f), in the time correlation with dI/dt and X-ray (X_s→) signals.

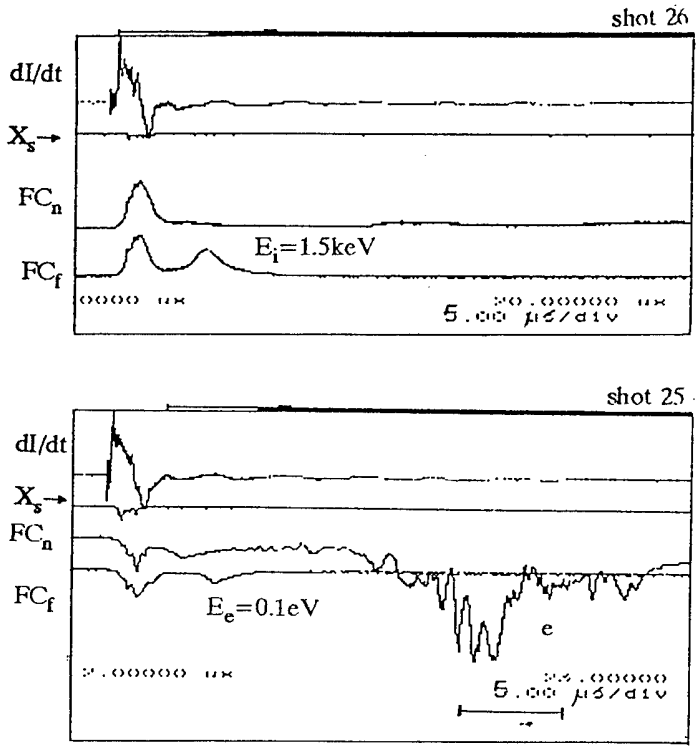

Fig.4. Comparison of time-resolved ion signals (FC_n and FC_f - upper picture) with electron signals (FC_n and FC_f - lower picture) in correlation with soft X-rays (X_s) and dI/dt trace.

The observed ion signals demonstrate the appearance of two (sometimes even three) separate pulses of different energy. Basing on time of flight differential measurements it has been estimated that the two ion pulses, correspond to 1.5keV, and 12eV ions, respectively. Also electron signals, as measured with an inverted polarity of the Faraday collectors, show at least two separate groups of electrons, which correspond to about 10eV and 0.1eV, respectively. The measuring method applied has not enable measurements of electrons of energy above 20eV, although such electrons could also be

emitted. It should be noted that velocity of 1.5keV carbon ions and that of 0.1eV electrons is almost the same what suggest that the electrons are dragged by ions clusters.

The last diagnostics results have shown the generation of the short (10-20ns) XUV pulse in the direction of the fibre axis before disintegration of the pinch column during 100-300ns after breakdown. The radiation is strongly asymmetric and its axial intensity is more than 100 times higher than the radial intensity.

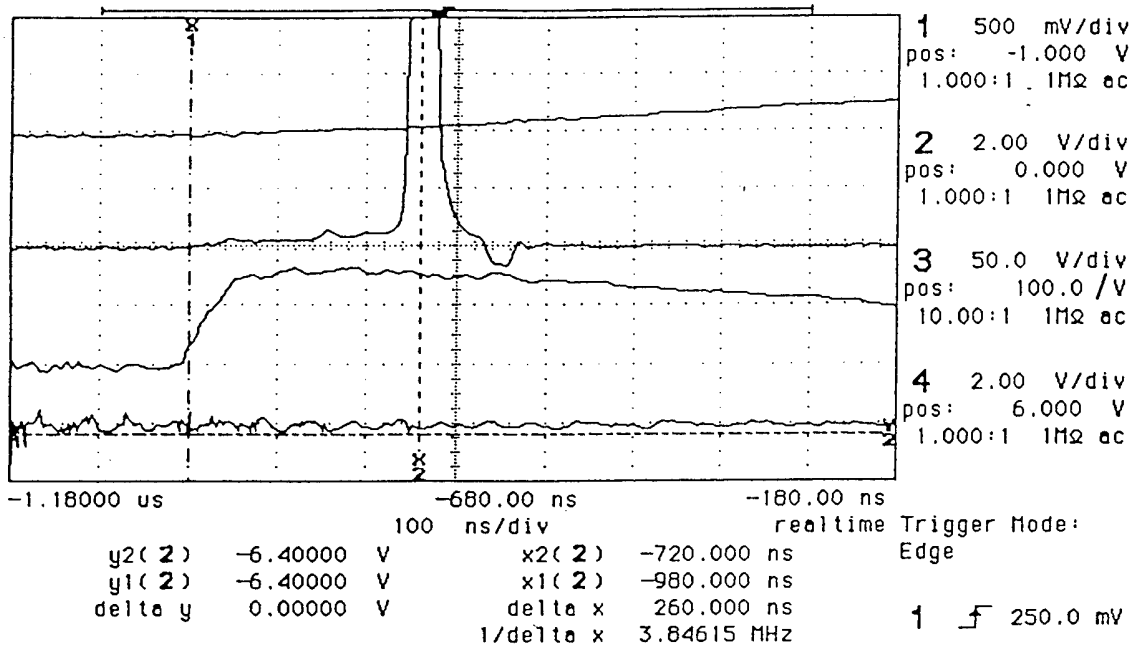

Fig.5. Shot 144.
Trace 1: current (Rorowski coil), trace 2: PIN diode signal in z-ais direction (distance 25 cm), trace 3: current derivative, trace 4: PIN diode signal in radial direction (distance 25 cm).

To learn more about the ion emission from Z-pinch with carbon fibres experiments it is necessary to perform studies with Faraday cup parallel to accelerations axis. Measurements of X-rays spectrum in the time should be very interesting.

Acknowledgments:

This research has been supported by grant GACR No. 202-95-0178 „Stable Structures in Magnetic Pinches"

References

[1] M.Sadowski, A.Szydłowski, J.Baranowski, P.Kubes and J.Kravarik: Study of Ions and Electrons Emitted Axially from Low-Energy Z-Pinch Discharges in Nitrogen and Argon, Proc. 17th Symposium on Plasma Physics and Tech. (Praha 95).

[2] P.Kubes, J.Kravarik, K.Hakr, J.Pilach, J.Baranowski, M.Sadowski, A.Szydłowski: Time-Resolved Diagnostics of Fast Ions in Low Energy Z-Pinch with Conical Electrodes, Proc. 17th Symposium on Plasma Physics and Tech. (Praha 95).

CONCEPT AND ELEMENTARY THEORY OF A SANDWICH LINER

[1]J.G. Linhart, [2]J.P. Chittenden,
[1]Dip. di Fisica, University of Ferrara, [2]Plasma Physics, Imperial College, London

Abstract

A system is described in which a cylindrical liner L is imploded by a Z-pinch. The liner is insulated form the driving magnetic field by a plasma layer created by exploding a thin foil separated from L by foam. The results of this analysis are compared with a one-dimensional numerical simulation of the system.

Introductions

In order that a projectile driven by a magnetic pressure does not explode as a result of Joule's heat deposited in it, one must interpose between the main body of the projectile and the magnetic piston a plasma layer which transmits the $B^2/8\pi$ pressure and carries the currents induced by the B-field [1,2,3].

Thus has been achieved in experiments in which a snowplough (SP) in a coaxial discharge implodes on a thin cylindrical liner [3,4]. Unfortunately the SP is not always aximuthally and axially symmetric and there can be several current sheaths and restrikes at the insulator, especially at high voltages. In order to avoid these drawbacks it has been suggested that the plasma cushion can be generated by exploding a thin metal foil F situated outside a cylindrical liner L [5] and separated from it by a thin layer of an insulatin material, such as foam [6] . (Fig. 1)

We shall first analyse the implosion of such a sandwich liner by a Z-pinch. The results of this simple analysis will be then compared with one-dimensional numerical simulation of the system.

The implosion of a sandwich liner

Let us assume that the current I_z generating the pinch field B_φ is given by $I = I_m \cdot \sin \omega t$, that both F and L are aluminium foils and that the foam has a specific density of approx. $2 \cdot 10^{-2}$ g/cm^3 [6,7].

It is obvious that the plasma cushion separating L from B_φ must be produced well before $t_m = \frac{\pi}{2\omega}$ (the time of the current maximum I_m) and therefore, the time t_{ex} of explosion of F must be a small fraction of t_m . Assuming that for $t < t_{ex}$ all the current I flows in F we have [8,9]

$$t_{ex} = \left[12\pi^2 g \left(\frac{r_0 \delta_0}{\omega I_m} \right)^2 \right]^{1/3} , \text{ where (for Al at NTP) } g \sim 1{,}1 \cdot 10^9 \qquad (1)$$

The explansion of the exploded foil resembles initially a free expansion with a speed

$$V_{th} \sim \sqrt{\frac{(\alpha+1)\, kT_{Al}}{M_{Al}}} , \qquad (2)$$

where α is the mean degree of ionisation and T_{Al} the temperature of the Al plasma. This expansion will be slowed down and eventually stopped by the growing B_φ field.

It would be desirable - in order to imitate the good feature of the plasma drive [4]- that the liner L should not feel the $B^2/8\pi$ pressure until the current I reaches a large enough value for efficient propulsion. This could be accomplished if the pressure p_{Al} were transmitted across the foam layer at such a low speed V_f that the front of this pressure wave arrived at the liner L only when $I << I_m$. The speed V_f can be expressed as

$$V_f = \sqrt{\gamma_f \frac{p_{Al}}{\rho_f}} . \qquad (3)$$

The polytropic coefficient γ_f of foam will be nearly 1 and we shall assume that $\rho_f \cong 2\cdot 10^{-2}$ g/cm^3 and $p_{Al} \sim \frac{B^2}{8\pi}$. This is not true for $t < t'$, however, at that time the value of p_{Al} is small. We will have, therefore,

$$V_f \sim \frac{B}{\sqrt{8\pi\rho f}} \cong 0{,}28 \cdot \frac{I}{r_0} \quad . \tag{3}$$

Putting $I = I_m \sin \omega t$, the distance travelled by the p_{Al} pressure wave in the foam will be smaller than

$$s = 0{,}28 \frac{I_m}{\omega \cdot r_0}(1 - \cos \omega t) \tag{4}$$

and indicates the foam thickness to be used.

The time t_s required for the pressure wave to reach L is given by

$$t_s = 0{,}637 \left[\cos^{-1}\left(1 - \frac{s}{s_m}\right)\right] t_m \quad , \tag{4}$$

where $s_m = 0{,}28 \frac{I_m}{r_0 \omega}$. For the parameters of Ex. 2 we obtain $s_m = 0{,}28$ (cm) and if $s = 0{,}1$(cm) then $t_s = 0{,}32$ (μsec). In reality the pressure wave will be preceded by a radiation heat wave [10] and consequently t_s will be shorter than indicated by eq. (7.a).

By inserting a foam layer between F and L, we are not only aiming at delaying the propulsion of L until a large I is reached. The most important feature of the plasma drive is not to vaporise L during the implosion. We require, therefore, that after the arrival of the pressure or heat wave at L the density n_L remains at its solid state value n_s in spite of the T_L being much higher than the NTP value for vaporisation of Al. Let us try to understand this situation using the following simple model. (Fig. 2)

The surface current density $i = \frac{B_\varphi}{0{,}4\pi}$ dissipates Joule heat $\dot{w}_J$ in a shell of thickness δ_e. This is mainly radiated away ($\dot{w}_r$), however, a small portion $\dot{q}$ reaches L through heat conduction across the plasma slab (thickness $\delta >> \delta_e$). The solution of this problem determines T_L and using then equation (8) we get n_L. The equations governing this situation are (assuming a pressure equilibrium)

$$\dot{w}_J = i^2 \rho_e \delta_e^{-1}\, 10^7 \qquad \dot{w}_r = \sigma_{SB} T^4 [1 - \exp(-2\kappa_0 \delta_r)], \qquad i^2 = \frac{1+\alpha}{2\pi} 10^2\, nkT \tag{5}$$

being the equations describing the exploded F layer, where δ_e follows from equation (2), δ_r is the thickness of the high temperature layer, $\kappa_0 \cong 10^{-25} \langle n^2 \rangle \cdot T^{-7/2}$ and $\rho_e \cong 0{,}3 \cdot 10^{-5} \frac{1-\alpha}{\alpha} \sqrt{T}$, with $\alpha = \frac{n_e}{n_n + n_i}$ the degree of ionisation.

The heat flux towards L is described by

$$\dot{q} = 2 \cdot 10^{-5} T^{5/2} \cdot \frac{\partial T}{\partial r} \quad . \tag{5}$$

As a first approximation we shall assume that $\dot{w}_r >> \dot{q}$ and that $\delta_e \sim \delta_r \sim \delta' \approx \frac{n_s}{n} \delta_0$. We get from 5 a,b,c, eliminating i^2, that

$$T = 0{,}3 \cdot 10^6 \left[\frac{1-\alpha^2}{\alpha} \left(\frac{\delta_0}{\delta'}\right)^2 \delta_0^{-1} F^{-1}\right]^{0{,}4} \quad , \tag{6}$$

where $F^{-1} = 1 - \exp(-2\kappa_0 \delta') \sim 1$ in most of our cases. But δ'/δ_0 follows from (5c)

$$\frac{\delta_0}{\delta'} = 0{,}9 \cdot 10^{-8} \cdot \frac{1}{T(1+\alpha)} i^2$$

and finally

$$T = 0{,}576 \left[\frac{1-\alpha}{(1+\alpha)\,\alpha \cdot \delta_0 F}\right]^{0{,}222} \cdot i^2 \quad , \quad \text{where } i = \frac{I}{2\pi r_0} . \tag{6}$$

Ex: $\alpha = 0{,}1$, $\delta_0 = 10^{-4}$, $r_0 = 1$, $I = C \cdot 10^6 (\mathrm{A})$, we get $T = 3{,}2 \cdot 10^5 \cdot C^{0{,}888}$, for $C = 1$ one has $T = 28\,(\mathrm{eV})$.

Equation (5d) assuming a plane geometry, can be integrated for $\dot{q} = \text{const}$ along the distance δ_f and provided $T_L << T$, we get for the energy transferred to L

$$Q = \frac{4}{7} 10^{-5} \int_0^t \frac{T^{7/2}}{\delta_f} dt \quad ,$$

where δ_f will be given by $\delta_f = 0{,}9 \cdot 10^{-8} d \frac{i^2}{T_f (1+\alpha)}$, $T_f = \epsilon T$, $\epsilon < 1$. Using (6a) we get

$$Q = 1{,}31 \cdot 10^{-14} \left(\frac{1-\alpha}{\alpha}\right)^{0{,}55} \frac{i_m^{4{,}22}}{\omega (1+\alpha)^{1{,}55} \delta_0^{0{,}55} \epsilon d} \int_0^{\omega t} (\sin \omega t)^{4{,}22} \, \mathrm{d}(\omega t) \; . \qquad (7)$$

If the L layer does not loose energy then the T_L at $\omega t = \pi/2$ reaches a value

$$T_L = \frac{2}{\alpha''} (1+\alpha)^{-1} \frac{Q_{\max}}{N_L k} \quad ,$$

where N_L is the number of atoms of L per cm^2 of its surface, α'' the number of degrees of freedom and α' the degree of ionisation. As the integral in (7) at $\omega t = \pi/2$ is approximately equal to 0.6, we obtain for the maximum T_L

$$T_L \sim 180 \, \alpha''^{-1} \left(\frac{1-\alpha}{\alpha}\right)^{0{,}55} (1+\alpha)^{-1{,}55} \frac{i_m^{4{,}22}}{\omega \delta_0^{0{,}55} N_L \cdot \varepsilon \cdot d} (1+\alpha')^{-1} \quad . \qquad (8)$$

Ex: $\alpha = 0{,}1$, $\alpha' = 0{,}1$, $\omega = 2{,}10^6$, $\delta_0 = 10^{-4}$, $i_m = 10^6$, $N_L = 5 \cdot 10^{19}$, $\omega d = 0{,}1$, $\alpha'' = 6$ then $T_L \cong 2{,}5(\mathrm{eV})$.

The thickness δ_L of L follows from (the solid $\delta(r) = \delta \frac{r_0}{r}$)

$$\frac{\delta_L}{\delta(r)} = 1{,}1 \cdot 10^8 \frac{T_L (1+\alpha')}{i^2} \cdot \frac{r}{r_0} \quad . \qquad (9)$$

at $r_0 / r = 2$, $i = i_m$ the previous example gives $\delta_L / \delta = 1{,}7$.

Our analysis is inaccurate in many respects. It ignores the heat conduction due to radiation transport, the fact that during t_s the liner is not heated at all, etc. However, some of these approximations tend to cancel each other, others should not introduce large errors. From equs. (8) and (9) it seems that our liner will not remain solid; it will vaporise and will be partially ionised, but it will not expand too much and consequently the ρ_L will be high - perhaps of the order of $1(\mathrm{g/cm^3})$.

Following the arrival of the pressure wave on L, the liner will be driven by $B^2/8\pi$. Assuming for a while that $t_s + t_{ex} << t_m$, the dynamics of the liner will follow the equation

$$\ddot{r} = -10^{-2} \frac{I^2}{r \cdot M} \quad , \qquad (10)$$

where M is the mass per cm length of the sandwich.

In order that collapse of L be synchronised with t_m we require that

$$M \cong 10^{-2} \left(\frac{I_m}{r_0 \omega}\right)^2 \quad . \qquad (11)$$

For the parameters used in our previous examples, we obtain $M = 0{,}01\,(\mathrm{g \cdot cm})$ and consequently $\delta \leq 3\,(\mu\mathrm{m})$.

From all these approximate considerations one would expect our sandwich liner to behave as sketched in figure 3 .

Numerical simulation of the collapse of a sandwich liner

The approximate analysis presented in section 1 provides a basis for the understanding of the sandwich implosion. We have tried to obtain a more precise picture by

means of a numerical simulation. The initial situation for our computation is that of an already exploded foil F, the foam is represented by a carbon gas at a temperature of 1 (eV) and the liner L by high density Al gas. We wish to find out whether, at the end of the implosion (e.g. $r = r_0/10$) , the thickness δ_L of L remains as small as indicated by eq.(11) or whether L has exploded and also if the B_φ remains mainly outside of F. The physical model is that of MHD with appropriate diffusion coefficients.

From plots of the radial mass density contours $\rho(r)$ for several instants during the sandwich implosion as well as the current density distribution, it is evident that the $\langle q \rangle$ corresponding to L increases sharply as $r \to r_0/10$ and that the $i(r)$ distribution is blocked by the F plasma. We can conclude, therefore, that the L does not expand and the B_φ-flux diffused across the sandwich amounts to a few % of the total flux.

The temperature of the F layer is seen to grow from about 5 (eV) to 50 (eV), agreeing well with the formula (6a). The T_L is up to 500 (nsec) below 7 (eV) as predicted by eq. (8). The final $\langle \rho_L \rangle$ (at $I_r = I_m$) is approximately 0,1 g / cm^3, again not too far from the estimate of equation (9).

Conclusion

The acceleration of solid liners to speeds in excess of 1 cm/μsec by means of a Z-pinch could be facilitated by employing a sandwich composed of thin foil-foam-thick foil rather than a pure plasma drive. A similar concept of separating the hot and cold region is encountered in pellet implosions driven by a laser driver. The exloded foil corresponds to the already exploded ablator, the foam to the rest of it [10]. Although in early experiments [5] the explosion of a cylindrical foil in a Z-pinch geometry appears to occur uniformly over the entire surface of the foil, new experiments with foils in a sandwich configuration will be necessary before the assumptions made in this paper can be considered applicable.

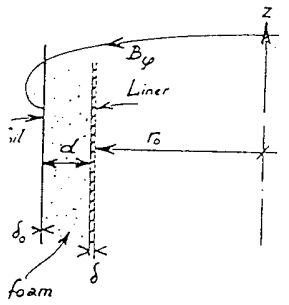

Fig.1

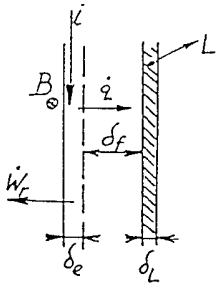

Fig.2

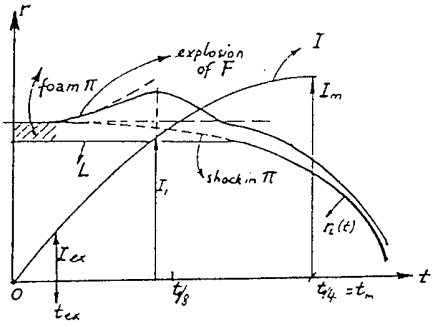

Fig.3.

References

1. Physics of high energy densities, Proc. E. Fermi School, p.151 (Varenna 1969).
2. J.G. Linhart, IEEE Trans. Plasma Sci. 16, 43 (1988).
3. L. Bilbao et al., Kerntechnik 57, 330 (1992).
4. A. Bortolotti et al. Proc. 3rd Int. Conf. Z-pinches, p. 372 (1993, AIP Press N.Y.).
5. G. Schenk and J.G. Linhart, Exploding Wires 3, 223 (Plenum Press, N.Y. 1964).
6. J. Falconer et al., J. Vac. Sci. Technol. A48, 968 (1990).
   M. Takagi et al., J. Vac. Sci. Technol. A49, 820 (1991).
7. S. Stern et al. Proc. 3rd Int. Conf. Z-pinches, p. 509 (1993, AIP Press, N.Y.).
8. Exploding Wires, 1, p. 83 and p. 97 (1961).
9. E.C. Cnare, JAP 37, 543 (1961).
10. M. Dunne et al. Phys. Rev. Lett. 75 3858 (1995).

OPTIMIZED DEBRIS STOPPERS FOR Z-PINCHES

N. A. Gondarenko and N. R. Pereira

Berkeley Research Associates, PO Box 852, Springfield, VA 22152 USA

Abstract

A pulse power generator discharging through an array of wires or a gas cylinder creates a pulse of useful soft x-rays, which is usually followed by deleterious byproducts such as plasma, hot gases and droplets of metal from evaporated electrodes. Separating the extraneous material from the x-rays is done with a debris shield. This paper discusses optimization of such shields.

Introduction

Ideally, a debris shield stops all the debris while transmitting most of the desirable x-rays. Whether debris stops in a shield depends in a complicated way on the debris properties, material shield strength at the initial temperature, but certainly demands a minimum mass per unit area. As an example, about 3 mg/cm^2 plastic proved sufficient in one case. However, x-ray transmission also depends directly on mass per unit area, multiplied by the mass absorption coefficient μ/ρ. Soft x-rays are strongly absorbed (or $\mu/\rho \gg 1$ cm^2/g), so that for minimal absorption the mass per unit area must remain small, the opposite of what is needed for stopping debris. Worse, strong x-ray absorption implies that a substantial fraction of the x-ray energy goes toward heating the shield, which could easily evaporate. In this case the evaporated material must be stopped by timely closure of a secondary valve. For both survivable and sacrificial debris shields optimization is clearly essential.

For a survivable debris shield the material and allowable thickness depend strongly on the x-ray energy. Soft x-ray absorption decreases with photon energy $h\nu$ as $1/(h\nu)^3$, and increases with atomic number Z roughly as Z^4. This puts a high premium on debris shields with low atomic numbers. For the very softest photons below about 1 keV, solid deuterium [1] is the best choice, while lithium or lithium compounds (e.g., LiH) become suitable for slightly harder x-rays $\gtrsim$ 1.3 keV. For still harder x-rays one can use beryllium, boron or alloys thereof, and eventually plastics for the hardest photons. If the debris shield must cover an extended area any of these materials may be reinforced by fibers of carbon or other superstrong materials. These can be woven into a fine mesh, whose rapid heat conduction to the cooler surrounding shield might prevent x-ray evaporation.

Each photon $h\nu$ is transmitted with an efficiency $T(h\nu) = \exp[-(\mu/\rho) \times \rho d]$, where ρd is the mass per unit area, ρ is the density, and d the thickness. For a spectrum of photons as typically produced by z-pinches,[2] a suitable definition of x-ray transmission efficiency $T_c(h\nu)$ is to count only the x-rays above a cutoff energy $\mathcal{E}_c = h\nu_c$. Then the transmission efficiency is

$$T_c(\mathcal{E}_c; s) = \int_{\mathcal{E}_c}^{\infty} d(h\nu) T(h\nu) s_c(h\nu), \tag{1}$$

where the x-ray energy spectrum $s_c(h\nu)$ is normalized through $\int_{\mathcal{E}_c}^{\infty} d(h\nu) s(h\nu) = 1$, and the subscript $_c$ refers to the cutoff.

For many pinches the cutoff excludes little energy. Figure 1 shows the energy in a computed spectrum for an aluminum pinch [3] (solid line) and a 1 keV blackbody (dashed). Both spectra are normalized to unity over their full range $0 < h\nu < \infty$. A

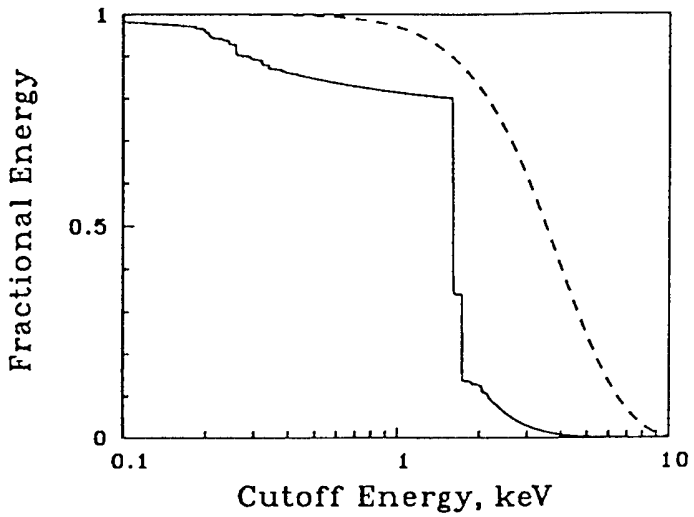

Figure 1. Energy in spectrum as function of cutoff $\mathcal{E}_c$

low cutoff $\mathcal{E}_c \simeq 0.5$ keV excludes about 15% of the pinch energy while a 3× higher cutoff $\mathcal{E}_c \simeq 1.5$ keV excludes only 5% more, up to about 1/5 of the available x-rays. For this aluminum spectrum the k-lines at 1.6-1.7 keV carry from 50% to 75% of the energy. In contrast, cutting off the 1 keV black body spectrum at 1.5 keV excludes less than about 10% of the energy.

The debris shield's allowable thickness is a function of cutoff energy and spectrum. As an example, the open circles in Figure 2 show the thickness of lithium that transmits 85% of the x-rays from an aluminum pinch. As expected from the lack of photons in the softer part of the spectrum, below the k-lines the allowable thickness is approximately constant, about 3 mg/cm^2. This is comparable to the debris penetration thickness. For higher cutoff energy at the two k-lines the allowable thickness jumps to 5 mg/cm^2 and 10 mg/cm,^{2} after which the thickness increases gradually. For larger cutoffs $\mathcal{E}_c \gtrsim 1.7$ keV the thickness approaches that for a 1 keV black body (solid diamonds). This and similar curves for other black body temperatures can be expressed analytically.

The closed circles in Figure 2 represent the corresponding thickness for beryllium. The two materials show a virtually identical dependence of thickness on cutoff energy $\mathcal{E}_c$. The reason is that the x-ray attenuation coefficients μ/ρ of low atomic number materials vary with photon energy $h\nu$ in a universal manner. In the photoelectric regime, which dominates attenuation of soft x-rays,

$$\frac{\mu}{\rho} = \frac{aG(Z)}{H(h\nu)},$$

where $G(Z) \simeq Z^n$ with $n \simeq 4$, and $H(h\nu) \simeq (h\nu)^\alpha$ with $\alpha \simeq 3$. In reality the function $H(h\nu)$ depends slightly on atomic number, $H(h\nu) = H_Z(h\nu)$, but this will be ignored because any dependence on Z invalidates the arguments below.

For a foil with thickness d and atomic number Z the transmission is

$$T_c(\mathcal{E}_c; s) = \int_{\mathcal{E}_c}^{\infty} dx \ \exp[-(G\rho d)a/H(x)]s(x) / \int_{\mathcal{E}_c}^{\infty} dx \ s(x).$$

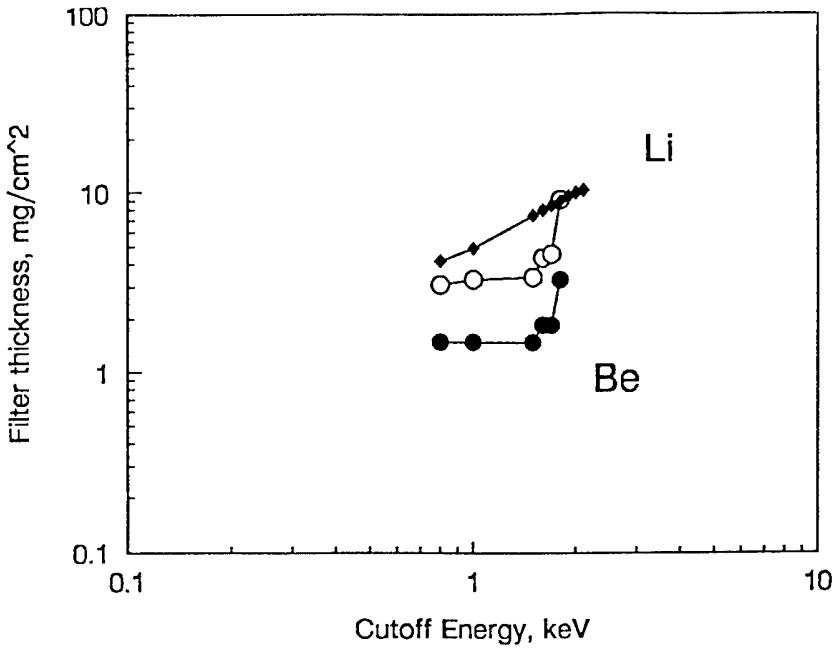

Figure 2. Thickness for 85% transmission versus cutoff $\mathcal{E}_c$.

In this formula the functional dependence on photon energy $x = h\nu$ is called out explicitly: it enters through the spectrum $s(x)$ and the argument of the exponent, $[-(G(Z)\rho d)a/H(x)]$. The properties of the material, the atomic number and the density, appear only in the factor $[G(Z)\rho d]$ that multiplies the universal function of photon energy $a/H(x)$.

The different foil materials have the same transmission as long as the spectrum is the same and the factor $G(Z)\rho d$ is the same. For this to happen the mass per unit area ρd must scale inversely proportional to $G(Z) \simeq Z^4$, i.e.,

$$\rho d \propto \frac{1}{G(Z)} \propto Z^{-4}.$$

Once the allowable thickness is computed for the spectrum of interest and a single material, for another material it can be scaled from the transmission at a single photon energy, e.g., the k-lines. On this basis, the allowable mass per unit area for a beryllium shield is then $(3/4)^4 \simeq 0.316$ of that for lithium: plastic must be 5 times thinner still. In the other direction, hydrogen or deuterium can be the thickest: over 90% of the x-rays at 1 keV go through 3 mm deuterium.[1]

The shape of the allowable thickness as function of cutoff energy depends solely on the energy spectrum. An increase in cutoff energy from $\mathcal{E}_c$ to $\mathcal{E}_c + \delta\mathcal{E}_c$ brings with it an increase in thickness from d to $d + \delta d$. The acceptable transmission $T_c(\mathcal{E}_c, d)$ at cutoff energy $\mathcal{E}_c$ is defined by Eq. (1), and variation of this formula gives

$$\frac{\partial d}{\partial \mathcal{E}_c} = \frac{s(\mathcal{E}_c)\,[T(\mathcal{E}_c, d) - T_c(\mathcal{E}_c, d)]}{\int_{\mathcal{E}_c}^{\infty} dx(-\partial T(x,d)/\partial d)s(x)}.$$

The integrand in the denominator is positive, and the transmission at the cutoff energy $T(\mathcal{E}_c, d)$ is always less than the allowable transmission as function of the cutoff energy

$T_c(\mathcal{E}_c, d)$. Therefore the allowable thickness d increases with cutoff energy. The spectrum determines the slope, with an extremely rapid rise at the k-lines.

For a sacrificial debris shield, when the x-ray fluence is so large that the debris shield evaporates, separation between x-rays and debris needs a fast closing valve behind the shield. There is an optimum position R_o for such a shield, as is easily seen as follows. A debris shield at distance R from the pinch receives a dose $D \propto 1/R^2$. Dose is energy per mass, and without allowance for energy lost in melting or evaporation the dose D is also proportional to temperature, and $T \propto 1/R^2$. The debris shield's backside evaporates. The velocity of the evaporate v_e is proportional to $\sqrt{T}$, whence $v_e \propto 1/R$. At a constant velocity v_e the material reaches a second valve, located at R_2 from the pinch, after a time $t_2 = (R_2 - R)/v_e \propto (RR_2 - R^2)$. This time is zero when the debris shield is right in front of the valve, $R \lesssim R_2$, or at the pinch, $R \gtrsim 0$. The largest closing time comes from placing the shield halfway between pinch and valve, at the optimum position $R_o = R_2/2$. Then the valve's closure time is maximum, and with a given closing velocity v_c the opening in the valve can be the largest.

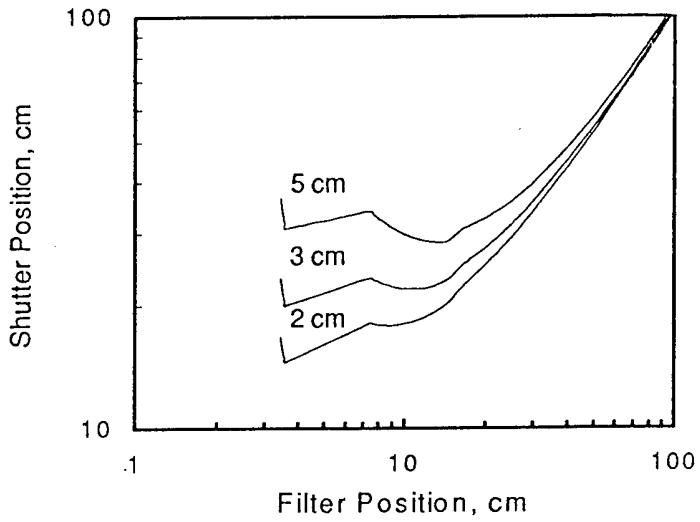

Figure 3. Minimum distance between pinch and second valve versus shield position.

A more quantitative result needs explicit consideration of the thermodynamic properties of the shield material. As an example, Figure 3 shows the minimum position of the shutter R_2 as function of shield position R, for different openings in the shutter and a 1 km/s closure velocity. The debris shield is lithium precooled to 77 K, exposed to a 40 kJ aluminum pinch. The optimum shield position is from 8 to 15 cm, somewhere in the middle between the pinch and the valve at 18 to 30 cm. At the optimum position the lithium is just melted but not yet vaporized: the phase transitions are seen by the knicks in the curve.

In conclusion, we would like to thank Dr. A. L. Velikovich for useful discussions.

[1.] N. R. Pereira and J. D. Sethian, private communication, 1994.
[2.] N. R. Pereira and J. Davis, *X-rays from z-pinches on relativistic electron beam generators,* J. Appl. Phys. **64**, R1 (1988).
[3.] R. Clark, private communication, 1995.

PRS AND POS/PRS COUPLING EXPERIMENTS ON HAWK*

G.G. Peterson†, J.P. Apruzese, R.J. Commisso, A. Fisher, J.C. Kellogg,
D. Mosher, S.J. Stephanakis, J.W. Thornhill, B.V. Weber, and F.C. Young

Plasma Physics Division, Naval Research Laboratory, Washington DC, 20375, USA

Experiments are being conducted on Hawk to investigate the electrical coupling of a plasma opening switch (POS) to a neon plasma radiation source (PRS) and to evaluate the k-shell x-ray yield scaling of implosions with different initial radii, mass, and implosion times. Understanding the coupling and scaling is important for optimizing the performance of more-powerful inductive-storage generators that rely on POS technology.

Inductive-store pulsed-power generators have been the focus of considerable research over the past few years as a promising technology for the next generation of high-power PRS drivers.[1-4] Advantages of inductive stores over traditional water line machines include lower cost of manufacturing and operation, smaller size, and suppression of prepulse. The main pulsed-power research problem pertaining to the PRS application of this technology is realization of a POS that can conduct multimegampere currents for a microsecond, and then efficiently transfer current to a load on a 100- to 300-ns time scale.

The present Hawk research addresses the technical issues associated with driving PRS loads with opening-switch technology, including: transfer of current to the load during implosion, the effect of switch-to-load spacing on PRS performance, and the scaling of implosion quality and x-radiation with initial load radius and implosion time. Successful larger-radius PRS operation would permit efficient excitation of higher-energy x-rays[5, 6], while longer-implosion times would relax performance requirements on the POS[2 - 4].

In the direct-drive mode, the Hawk Marx bank feeds a coaxial vacuum line which delivers 700 kA to a PRS load in 1.3 μs. Employing a 1-μs conduction-time POS, the load current rises to 500-600 kA in 100 ns, and then remains essentially constant until the PRS implodes. This constant-current behavior, characteristic of inductive PRS drivers,[7] is ideal for studying load-mass and load-radius variations, as the associated variations in implosion time do not substantially change the implosion kinetic energy.

Experiments were performed with the configuration shown in Fig. 1. The gas-puff nozzle was mounted on the anode 54-cm downstream of the POS plasma guns. Neon gas is used in these experiments as its k-shell is efficiently excited for this implosion energy. The rise time of the gas density exiting the nozzle was 70 μs and the machine was fired 90 μs after gas first appeared. Within this time, the neon travels about 7 cm axially and doesn't interfere with transmission-line power flow. Conical-annular nozzles of 1-, 1.75-, and 2.5-cm radius, 10-degree inward tilt, 0.1-mm throat gap, and 0.9-mm exit width were used. The nozzle material was a Te-Cu alloy, which required refurbishment every two shots. Nozzles of a W-Ni-Cu alloy are now being tested which show no wear after 18 consecutive shots. The cathode consisted of an annular knife-edge tube of the same radius as the nozzle exit. The cathode was press fitted into a vaned holder attached to the end of the 10-cm-diameter center conductor of the vacuum line. Diagnostics include transmission-line and load B-dot current monitors, a capacitive voltage monitor, vacuum-emission x-ray diodes (XRDs), a photo-conducting diode (PCD), a time-integrated pinhole camera, and a KAP crystal spectrometer.

The POS plasma was injected through an 8-cm rod section of the anode using 12 cable guns placed symmetrically in azimuth. The Marx bank was discharged 2.5 μs after firing the plasma guns. The POS consistently delivered over 500 kA of the conducted 600-kA current

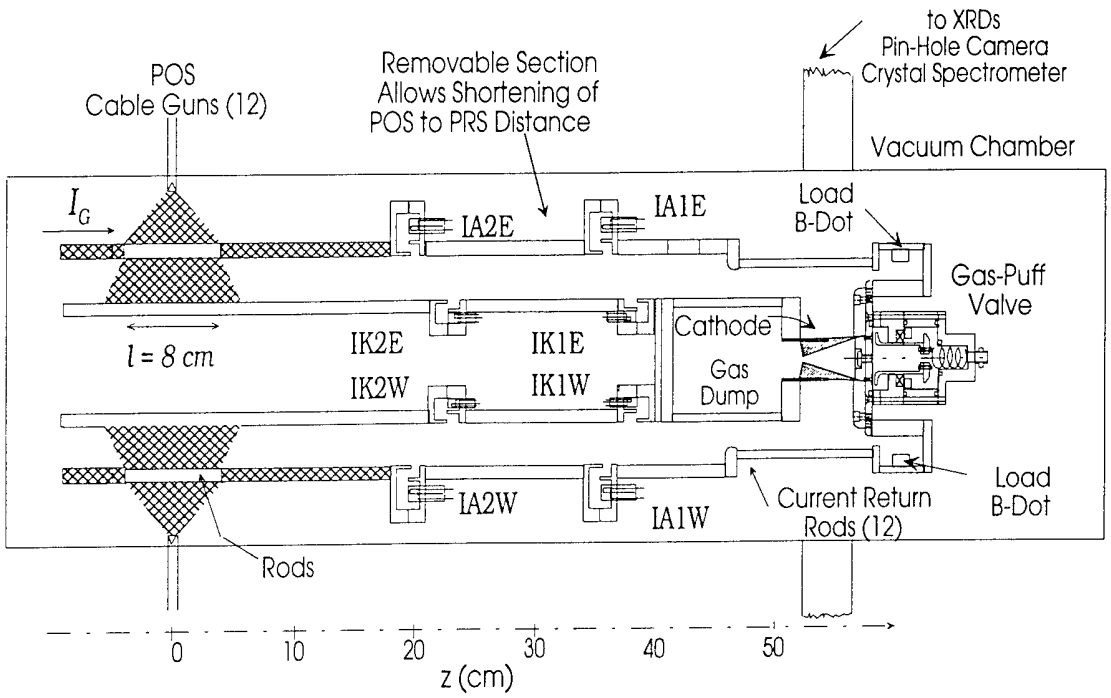

Fig. 1. The Hawk front end showing the POS, vacuum feed, current monitors, and gas-puff load.

to the PRS load. The conduction time averaged 900 ns with about 70-ns jitter. POS voltage varied from 300 to 600 kV and load current rise time varied from 75 to 150 ns (Fig. 2). Comparison of anode and cathode current monitors in the vacuum feed indicate little or no vacuum electron flow throughout the discharge. The measured load current wave forms are consistent with power flow calculations employing an opening switch model and a slug-model for the PRS implosion in the Bertha transmission-line code.

With load currents of 500-550 kA, about 700 J/cm of kinetic energy is delivered to the final pinch. The imploded mass m and kinetic energy K are calculated for each shot from the cathode current trace by an iterative process that matches the timing of the radiation spike to the slug-model implosion time. The calculated masses are consistent with those inferred from nozzle pressures and measured with interferometry.

POS-driven PRS shots with the 1.0- and 1.75-cm nozzles were fired for the range of masses shown in Table 1. All shots were fired with 2-2.3 cm A-K gaps (load lengths). The 2.5-cm radius nozzle was fired only at 15 μg/cm. Typical implosion times were 110-150 ns for the 1-cm nozzle, and 190-250 ns for the 1.75-cm nozzle. Direct drive shots were fired using the 1.75-cm radius nozzle. The experiments show that the use of a POS to shorten the current rise time is an effective

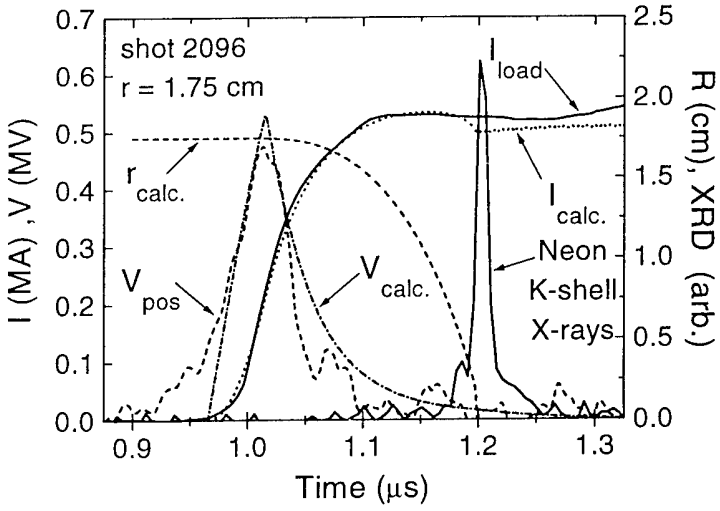

Fig. 2. Comparison of measured and modeled electrical characteristics. Also shown is the slug-model radius and XRD signal.

Nozzle Radius (cm)	Mass Range m (μg/cm)	K-shell Yield Y (J/cm)	Implosion Times (ns)	Number of shots
1.0	9-28	200	107-204	19
1.75	8-80	150	190-250	35
2.5	15	70	265	1
Direct Drive	60-130	65	830-890	9

Table 1. Shot summary for the Hawk neon PRS experiment.

way to drive PRS implosions. The POS-driven implosions produced up to 200 J/cm ± 20% of neon k-shell x-rays with x-ray pulse widths of 5-15 ns, as measured with an Al-filtered XRD. The best 1-cm-radius shots produced yields 1.5 times larger than those at 1.75-cm. More data with the 2.5-cm nozzle are needed to draw firm conclusions, but yields are about 1/3 of the 1-cm-radius yields. Direct drive shots on Hawk required greater than 700 ns implosion times to achieve the same final load currents as the POS-driven shots. Consequently, the direct drive shots were over-massed. The direct drive shots had reduced implosion quality and x-ray yields less than half of the best mass-optimized POS-driven shots at the same 1.75-cm radius.

Figure 3 plots the measured k-line x-ray yield as a function of specific kinetic energy K/m for the 1- and 1.75-cm shots. An error of about ±20% should be applied to the plotted points due to differences between the two Al-filtered XRD measurements. One systematic error, to be corrected by future spectral measurements, is due to an assumed 1:1 energy ratio between the neon Ly-α to He-α lines. A Cu-filtered XRD was fielded on one of the mass-optimized 1-cm-radius shots to measure the ratio. The measured ratio of 2:1 and yield correspond to a 350-eV plasma with 80% of the load mass contributing to the x-radiation. Applying this ratio to the Al-filtered XRD response suggests that the highest plotted yields should be reduced by about 1/3. The yields in Table 1 include this correction.

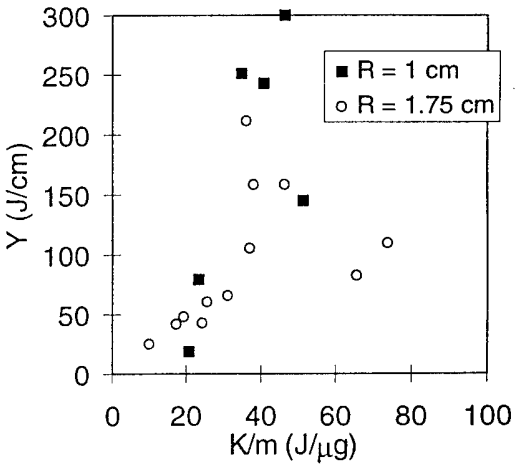

Fig. 3. Experimental k-line yield vs. specific kinetic energy.

Although the yields are larger for the smaller-radius nozzles, Fig. 3 shows that the optimum load mass is the same for the different nozzles, demonstrating that optimal yield depends only on K/m. This dependence, predicted by simple analyses,[5, 6] is most easily demonstrated with an inductive driver such as Hawk because the current, and therefore K, depend weakly on the radius- and mass-dependent implosion time. On a water-line PRS driver, the current during implosion depends strongly on implosion time. Differences in peak yield for the two radius cases suggest differences in implosion quality, due perhaps to improved azimuthal symmetry and stability at small-radius.

The predicted radiated k-line energy is estimated for each shot from the calculated m and K values using the Whitney-Giuliani[5] and Two-Level[6] models. These two calculations are usually in good agreement. Figure 4 compares the data of Fig. 3 to the average of the two model yields. On average, a 15:1 compression ratio is required to make the calculated radiation yield consistent with that measured. The four highest experimental yields are brought into better agreement with the rest of the data and analysis by applying the above 1/3

reduction for a 2:1 line ratio. This high-quality implosion is confirmed by the x-ray pinhole images of Fig. 5. The image diameters are consistent with the 1.3- to 2.3-mm stagnation diameters associated with a 15:1 compression for the two nozzle radii. Further confirmation is provided by the measured 5- to 15-ns fwhm radiation-pulse widths. A simple model can estimate the radiation half-width by assuming inertial confinement of the stagnated-plasma at either the slug-model final implosion velocity or, comparably, the sound speed determined from the Two-Level model temperature.[6] Either velocity divided into the above stagnated-plasma diameters yields characteristic pulse widths consistent with measurements.

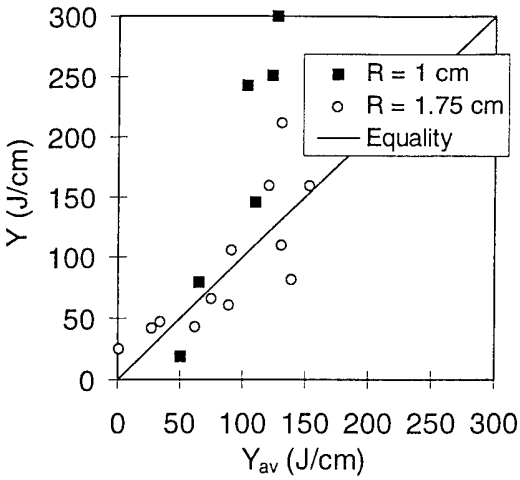

Fig. 4. Comparison of experimental yield (Y) with an average of the Two-Level and Whitney-Giuliani models (Y_{av}).

The 1.75-cm image of Fig. 5 shows weaker and more-diffuse radiation from the 0.5-cm region of plasma adjacent to the nozzle. This effect, seen also in other gas-puff PRS experiments, may be associated with the thin-shell gas distribution close to the nozzle. Thin shells are more susceptible to Raleigh-Taylor instabilities than the more filled-in distributions further from the nozzle, and disruptions due to the instability will be greater for larger-radius implosions.

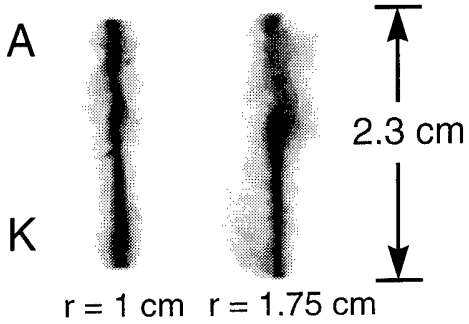

Fig. 5. Time-integrated pinhole photos for 1-cm and 1.75-cm radius loads.

In summary, the Hawk inductive-storage generator has proved to be an excellent test-bed for the study of POS-driven PRS implosions. Fast and efficient current transfer from the POS to the load has produced the optimum neon k-shell yields predicted by simple analyses. The characteristic weak dependence of implosion kinetic energy on load conditions is ideal for systematically studying variations in load radius and mass. Experiments are continuing in order to: complete measurements with the 2.5-cm-radius nozzle, determine the x-ray spectrum as a function of K/m, and study the effects of varying the POS-to-PRS separation and plasma length.

* Research supported by the United States Defense Nuclear Agency.
† NRL/NRC Research Associate

[1] S. J. Stephanakis et al., Appl. Phys. Lett. **48**, 829 (1986).
[2] R.J. Commisso et al., Phys. Fluids B **4**, 2368 (1992).
[3] C. Deeney et al., J. Appl. Phys. **72**, 1297 (1992).
[4] B.V. Weber et al., Phys. Plasmas **2**, 3893 (1995).
[5] K.G. Whitney et al., Phys. Plasmas **2**, 2590 (1995).
[6] D. Mosher, N. Qi, and M. Krishnan, NRL Pulsed Power Physics Technote,. **94-25** (1994)
[7] D. Mosher and R.J. Commisso, J. Radiation Effects, Research & Engng. **11**, 113(1993).

X-RAY EMISSION FROM A HIGH-ATOMIC-NUMBER Z-PINCH PLASMA CREATED FROM COMPACT WIRE ARRAYS*

T. W. L. Sanford,[1] D. Mosher,[2] J. S. De Groot,[3] J. Hammer,[4] B. M. Marder,[1] S. Maxon,[4] T. J. Nash,[1] R. B. Spielman,[1] P. T. Springer,[4] K. Struve,[5] R. S. Thoe,[4] D. R. Welch,[5] W. E. Alley,[4] C. Bruns,[4] J. L. Eddleman,[4] J. Emic,[4] T. L. Gilliland,[1] J. Hernandez,[4] D. Jobe,[1] J. S. McGurn,[1] R. C. Mock,[1] J. F. Seamen,[1] M. Vargas,[1] and G. B. Zimmerman[4]

[1]*Sandia National Laboratories, Albuquerque, NM 87185*
[2]*Naval Research Laboratory, Washington, DC 20375*
[3]*University of California, Davis, CA 95616*
[4]*Lawrence Livermore National Laboratory, Livermore, CA 94550*
[5]*Mission Research Corporation, Albuquerque, NM 87106*

Thermal and nonthermal x-ray emission from the implosion of compact tungsten wire arrays in 5-MA Saturn discharges is reported. The timing of multiple implosions and the thermal x-ray spectra (1 to 10 keV) agree with 2D radiation-hydrocode simulations. Nonthermal x-ray emission (10 to 100 keV) correlates with pinch spots distributed along the z-axis. The similarities of the measured nonthermal spectrum, yield, and pinch-spot emission with those of 0.8-MA, single-exploded-wire discharges on Gamble-II suggest a common nonthermal-production mechanism. Nonthemal x-ray yields are lower than expected from current scaling of Gamble II results, suggesting that implosion geometries are not as efficient as single-wire geometries for nonthermal x-ray production. The instabilities, azimuthal asymmetries, and inferred multiple implosions that accompany the implosion geometry lead to larger, more irregular pinch spots, a likely reason for reduced nonthermal efficiency. A model for nonthermal-electron acceleration across magnetic fields in highly-collisional, high-atomic-number plasmas combined with 1D hydrocode simulations of Saturn compact loads predicts weak nonthermal x-ray emission.

Intense bursts of warm x rays (10 to 100 keV) are desired for the study of in-depth material effects induced by nuclear radiation. The plasma radiation source (PRS) provides an excellent source of keV thermal x rays when the imploding plasma stagnates on the axis of symmetry, and its radial kinetic energy is converted into internal energy and radiation.[1] However, thermal radiation production from the PRS, of which Saturn is the highest-current example, drops rapidly for photon energies exceeding a few keV due to the low masses required for high temperature, and the growth of instabilities.[1] The need for x-radiation sources in the 5- to 100-keV regime between existing PRS and bremsstrahlung sources motivated the present work.

High-atomic-number z-discharge plasmas created by passing 0.8 MA through single wires on the Gamble-II generator demonstrated matched-load behavior,[2] efficient conversion of coupled electrical energy to XUV radiation, about 10% conversion to keV thermal x-ray lines and continuum,[3] and more importantly for the present work, about 0.25% conversion to non-thermal, bremsstrahlung-like lines and continuum in the 5- to 100-keV regime[4]. This and other pinch plasmas have nonthermal x-ray emission correlated with the formation of tight, x-ray-bright pinch spots.[5] The Gamble-II experiments demonstrated a Z^2 atomic-number scaling for the nonthermal radiation yield and suggested an I^2 current scaling. These scalings motivated the present Saturn experiment[6] to measure and model the x-radiation from tungsten z-pinches at order-of-magnitude higher currents than Gamble II. Saturn compact arrays were configured to resemble the nonthermal Gamble-II loads in a low-inductance geometry for efficient coupling.

The radius of the wire array was chosen such that implosions occurred early with respect to the time of nominal peak current, enabling a sausage-unstable z-pinch to form pinch spots[7] during the peak current-portion of the pulse. The array mass was chosen to recover similar values of $E/n \sim I/(m/L)$ as in Gamble II, where E is an inductive electric field, n is ion density, I is current, m and L are load mass and length.[6] Gamble-II tungsten-wire loads with strong nonthermal emission had I/(m/L) values of about 2 MA/(mg/cm).[4] Aluminum, copper, and tungsten loads of 0.5 to 8 mg were studied. For this mass scaling, a 4-mm-diameter array was

the lowest-inductance configuration that satisfied the early-implosion requirement. This small annular radius also insured that a small-radius pinch, similar to the Gamble-II single-wire pinches, would form. Compared to conventional PRS loads,[1] the Saturn compact pinch has an order-of-magnitude higher mass confined in a region of order-of-magnitude smaller radius and is therefore much denser and brighter.

Six B-dot probes measured the current in the MITL adjacent the insulator stack, and two B-dot probes measured the current in the radial feed adjacent to the load They were bench calibrated and intercalibrated with piezoelectric stress gauges to an accuracy of 5%. Typically, peak load currents were 5.5 MA. This current level was lower than usual for Saturn because of early implosion and the higher inductance of the compact-array. MITL currents were typically 1 MA higher, indicating significant electron-beam losses that were evidenced by strong bremsstrahlung and damage in the load region.

The temporal and spatial characteristics of the radiation were sampled by detectors at 35° from the normal to the symmetry axis so that each viewed 1.5 cm of the 2-cm plasma length. A nickel bolometer, filtered diamond photoconducting detectors (PCDs), and a filtered fluorescer array (FFA) measured the radiation output as a function of time in broad photon-energy bins ranging from 0 to ~350 keV.[6] A fast-framing x-ray pinhole camera measured the spatial distribution of the radiation in 1-to-4-keV and 4-to-10-keV energy bands in five, 3-ns frames with 5-ns dwell times. A KAP crystal spectrometer measured the time-integrated x-ray spectrum from 0.8 to 3 keV with 1-eV resolution. Owing to the broad band response of the detectors and uncertainties in x-ray spectra, the uncertainty in the measured radiation output from a PCD or FFA is about a factor of two.

Figure 1 compares the radiation measured in the bolometer (response centered at 0.4 keV), a 1-keV PCD, and a 140-keV PCD for 4-mg Al and W compact-array loads. The 140-keV channel shows a broad electron-beam-bremsstrahlung signature on top of which nonthermal radiation spikes from the plasma are visible for the tungsten load. Though x-ray yields in the sub-keV and keV regimes were comparable for Al, Cu, and W, higher-energy, nonthermal yields were consistent with the Z^2 scaling observed in Gamble-II experiments. Tungsten x-ray yields in the 10- to 100-keV regime were comparable to those measured on Gamble II at lower currents, resulting in a yield efficiency of about (0.05 ± 0.03)%.

X-radiation at all energies is characterized by multiple radiation peaks. The period between peaks grows from about 10 ns to about 40 ns as the mass is increased from 1 to 8 mg. The multiple-peak behavior is interpreted as an oscillation of plasma radius predicted by analysis[8] and radiation-MHD (RMHD) code simulations.[9] Inertia causes kinetic pressure to exceed magnetic pressure at peak compression so that the plasma expands against the magnetic field. As the plasma expands and cools, magnetic pressure again exceeds the kinetic pressure and the plasma is recompressed. The process continues until the driving

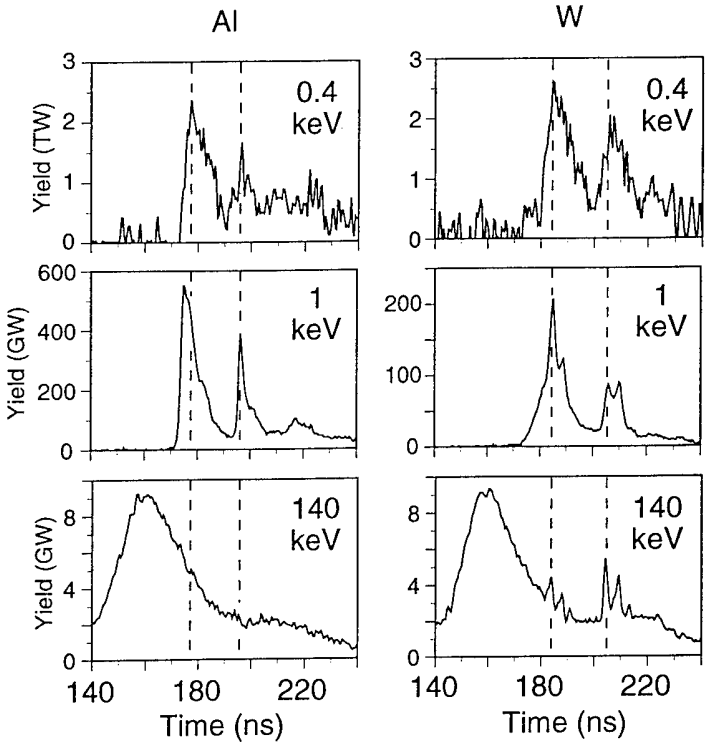

Fig. 1. Comparison of radiation measured in the bolometer (0.4 keV), 1-keV PCD, and 140-keV PCD for 4-mg Al and W loads.

current pulse decays, excess internal energy is radiated away, or instabilities terminate the oscillations. Quantitative agreement between experiment and RMHD results for the variation of bounce period with mass indicates that the current measured by the load monitors indeed flows through the plasma.

Additional support for the load-current measurements is provided by the measured variation of implosion time with load mass in Fig. 2. The circuit-model code Zork with a slug-model imploding load calculates current histories and implosion times that agree with the load monitors and x-ray diagnostics.[6] The dashed line corresponds to the implosion time for a linearly-increasing current fitted to the Saturn waveform.[6]

Figure 3 compares power-law fits to the time-integrated x-ray spectrum measured by the various diagnostics with that calculated by RMHD for a 4-mg W load. The short dashed lines show the uncertainties in the x-ray measurements. Little spectral difference is measured over masses of 1 to 4 mg. The spectrum shows a clear change in slope at about 10 keV separating thermal and nonthermal regimes. Comparison of the measured spectrum with RMHD shows that photon energies $h\nu > 12$ keV are associated with nonthermal processes not accounted for in the simulation. The slope of the measured spectrum in the 10- to 100-keV range is consistent with that measured in the Gamble-II experiment[4]: both spectra vary like $(h\nu)^{-1.4}$. This similarity indicates similar nonthermal-electron spectra in the two experiments, thereby suggesting a common nonthermal-production mechanism. However, the Gamble-II nonthermal efficiency was about three times higher than Saturn's, suggesting that an implosion geometry does not produce nonthermal x rays as efficiently as single-wire discharges. Instabilities, azimuthal asymmetries, and inferred multiple implosions that accompany the implosion geometry lead to larger, more irregular pinch spots, a likely reason for reduced nonthermal efficiency.

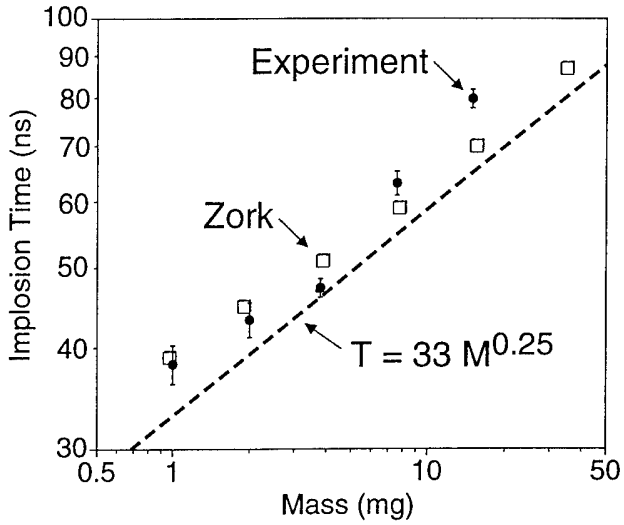

Fig. 2. Variation of measured and calculated implosion time with load mass.

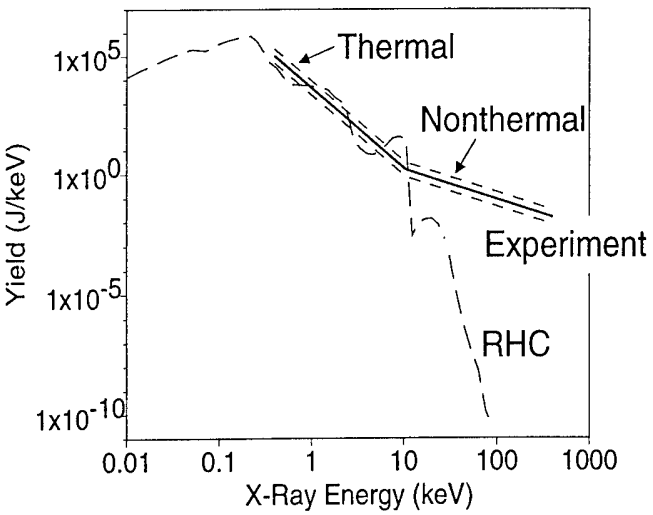

Fig. 3. Comparison of experimental power-law spectrum with that calculated by RMHD for a 4-mg tungsten load.

A fluid model for nonthermal electron acceleration in dense, high-atomic-number (high-Z) z-pinches has been developed and benchmarked against the electromagnetic, Monte-Carlo code IPROP.[6,10] In such plasmas, electrons (with initial energies in excess of a minimum value K_0) gain energy from the electric field (in excess of a critical field E_c) by cross-field scattering collisions until they reach energy K_f, an energy high enough to make them collisionless on the cyclotron-frequency time-

$$E_c(V/cm) = 3\times10^{-5}\varepsilon^{1/2}\Omega_c^{2/3}\Omega_s^{1/3}$$

$$K_0(eV) = 6\varepsilon^{1/2}\Omega_s / E$$

$$K_f(eV) = 6\times10^{14}E^2/\varepsilon\Omega_c^2$$

scale. Here, ε = 1/(Z+2), Ω_c is the electron cyclotron frequency, and Ω_s is the elastic scattering frequency for a 250-keV electron. For electric fields lower than E_c or initial electron energies below K_0, no energy gain above thermal levels is predicted. When the magnetic field approaches zero, only the K_0 equation, essentially the Dreicer runaway condition, is significant. High energies are achieved for high-Z because the scattering rate is about Z-times the energy loss rate. The particle-in-cell MHD code TIP, used to study the time-evolution of density, temperature, and electromagnetic-field radial profiles in compact-array pinches[6], calculates that peak electric fields and temperatures are at least an order-of-magnitude less than the minimum required values E_c and K_0. Therefore, strong nonthermal-electron acceleration is not predicted, in support of Saturn experimental observations.

*This work was supported by the U.S. DOE under Contract DE-AC04-94AL85000.

[1] N. R. Pereira and J. Davis, *J. Appl. Phys.* **64**, R1 (1988).
[2] D. Mosher, et al., *Ann. N. Y. Acad. Sci.* **25**, 632 (1975).
[3] C. M. Dozier, et al., *J. Phys.* **B10**, L73 (1977).
[4] D. J. Johnson, S. J. Stephanakis, and D. Mosher, NRL Memo Rep. 3207, 1976.
[5] C. Deeney, PhD. Thesis, Blackett Laboratory, Imperial College, London SW7, UK (April 1988).
[6] T. W. L. Sanford, D. Mosher, et al., Sandia Report SAND96-0222, UC-706, March 1996.
[7] D. Mosher and D. Colombant, *Phys. Rev. Lett.* **68**, 2600 (1992).
[8] D. Mosher and D. Colombant, *Dense Z-Pinches*, N. R. Pereira, J. Davis, and N. Rostoker, eds., *AIP Conf. Proc.* **195** (AIP, New York, 1989), p. 191.
[9] J. H. Hammer, et al., *Phys. Plasmas* **3**, 2063 (1996).
[10] D. R. Welch, C. L. Olson and T. W. L. Sanford, *Phys. Plasmas* **1**, 768 (1994).

NUMERICAL SIMULATIONS OF PRS YIELDS FOR A PULSED POWER DECADE-QUAD GENERATOR[†]

J. Giuliani, Jr., R Schneider[*]. J. Rogerson, and J. Davis

Radiation Hydrodynamics Branch
Plasma Physics Division
Naval Research Laboratory, Washington, DC 20375, USA

[*]*Simulation and Test Division, Defense Nuclear Agency, Alexandria, VA 22310, USA*

Abstract

A systems study of the power flow coupling between the multi-modular, inductive energy store DECADE-QUAD generator and an imploding z-pinch load is investigated and discussed. An end-to-end numerical simulation for the transmission line generator, the plasma opening switch, and the dynamic load is applied to predict the inductive notch of the load current, the kinetic energy coupling, and the radiation yield arising from argon puff gas implosions. Predicted load performance is evaluated using a 1-D non-LTE radiation transport treatment self consistently coupled to the MHD model and circuit power flow. The loads are configured as shells, uniform fills, and structured density profiles. The latter profiles are chosen for their stability during run-in as determined by 2-D MHD numerical simulations. Various models of the switch behavior are studied and their impact on the load dynamics. The radiative performance from an argon puff gas will be determined as a function of switch model, mass loading, and initial pinch radius.

[†]Research supported by the Defense Nuclear Agency

(The full text has not been supplied.)

P-2-82

OPTIMIZATION OF GAS TARGET PRODUCTION FOR Z-PINCH IMPLOSIONS

S.Semushin, B.Etlicher, C.Rouillé,

Laboratoire de Physique des Milieux Ionises, Laboratoire du C.N.R.S., Ecole polytechnique, 91128, Palaiseau, France

Abstract. Optimization of shell parameters for further imploding in a Z-pinch has been done. The nozzle shape was selected with the help of two dimensional gas dynamics computer simulation. During the optimization the influence of the electrode configuration was taken into account. Two types of nozzle are presented. The advanced construction with three gaseous shells may use different gases. The other one is based on aluminium vapor jet. The designs were tested by interferometry. Resulting mass distributions are analyzed by real experiment and by means of 2D MHD computer simulations. New nozzles provides smaller zippering, higher radiation power and more reproductive results.

Introduction

The aim of this study was in the increasing of generator energy contribution to compressing substance. The optimization of such complicated nonlinear system requires the deep understanding of physical processes. The numerical simulations give the full picture of the flow and by this reason allow to find the solution in an acceptable time.

The determination of nozzle profile, which gives the stationary homogeneous output flow with highest possible exit velocity, is a classical aerodynamical problem with well known solutions. Such direct approach is not effective in case of gas-puff nozzles. Simple estimations show, that due to the design limitations it is very difficult to get Mach number higher than 4-5, what gives the jet spreading angle at least 15°-20°. This is not sufficient. Other problems is specific for powerful current generators. Stationary or quasi stationary regime requires big delay of the main shot after the opening of the valve. This delay becomes especially great for longer high Mach nozzles. Due to high gas leakage into the interelectrode space, the vacuum is aggravated, and in result, the implosion results are unstable and bad vacuum can even lead to shortcut of the main current.

For further optimization we use the nozzles with nonhomogeneous exit flow. In such kind of nozzles the gas after the throat expands intensively in the transverse direction, though this expansion slows down with the longitudinal distance. Flow interaction with walls at the final part of the nozzle produce a skew shock wave, which allows to concentrate a larger fraction of mass near the axis. Analogous type of nozzles has been used for gas target production at [1] in laser experiments. The effect of this approach is local, it gives smaller jet divergence only in the interelectrode region. Further from the nozzle the jet divergence is even increased because of the fall of the exit mean Mach number, but this region is already out of our interest.

Moreover, we apply the same principle not only to the simple central jet (as in [1]), but also to the annular hollow jets, which compose complex multishell liner.

Two nozzle designs are presented here. Three shell system is produced by the complex nozzle and is intended for powerful generators. Its supplying system enables independent regulation of the mass in each shell and the use of different gases in these shells. Other nozzle uses aluminium vapor and is optimized for GAEL generator [2].

The results of gas dynamical simulations were tested by optical methods. The resulting efficiency of the design is estimated as by the experiment, as by two dimensional MHD simulations. Such exhaustive use of simulations on all stages provide comprehensive analysis of the considered processes.

Numerical methods

For modeling of transient processes of start up flow from the gas puff nozzles a conservative form of Euler equations is used. Gas was considered like compressible and ideal. The

computations were made by the homogeneous conservative difference algorithm, realized in multidimensional gas dynamics simulation code AEOL [3]. The main distinction of the algorithm is in the use of rectangular grids without fitting between the boundary and the mesh. This approach allows to change the shape of the object easily.

For MHD simulations a new adaptive mesh refinement method (AMR) [4] was used. In adaptive mesh refinement approach the points can be added to a fixed mesh, where it is necessary, and can be deleted, where they become unnecessary. This economies computer resources. AMR method, proposed in [4], was developed specially for the simulation of the essentially nonlinear problems, and it can be used not only for traditional gas dynamics computations, but also for complicated and strongly non stationary problems of hot plasma dynamics. This method is very effective, the time of run for Z-pinch simulation is only 10-30 minutes on a middle range workstation.

One fluid two component model of fully ionized plasma with modified Spitzer conductivity was chosen for this simulations. These modifications correct the conductivity value for low density regions.

Design of three shell nozzle

On GIT-4 installation for Z-pinch experiments on gas-puff and plasma-on-wire configurations two split nozzle had been used. Despite the flow from the outer nozzle is preionized, but in the experiments it has no influence on compression. After computer simulation it was found that the outer shell produces insignificant mass.

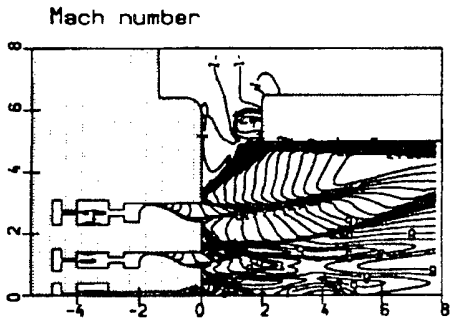

Fig.1 Flow from new nozzle , t=300 ms. Mach number contours.

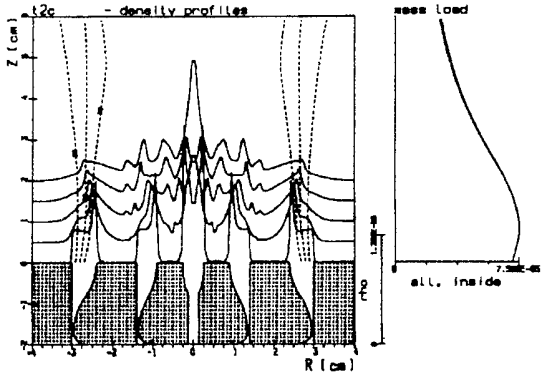

Fig.2 Mass distributions for different Z, t=300 μs. Doted lines limit the areas with 70-80-90 percents of mass in cross section

For further experiments it was necessary to design another nozzle system, which can provide complex multi layer gas target. Wire can be installed at the axis of the system. The gas shell may consist from up to 3 gas layers, with possibility of different gases in each part of the shell. External shell diameter is 60 mm, main shell diameter - 28 mm, the thickness is about a few millimeters In the central part.a simple 5 mm jet may be added.

The smaller is the divergence and spreading of shells - the better. But this ideal configuration is impossible because of different limitations in design. To decrease the jets spreading it is necessary to enlarge the jet exit Mach number. Two shell system requires two annular splits configuration. In this case it is very difficult to increase exit Mach number of jets, because the expansion ratio is proportional to the difference between the throat and the exit split widths. The width of the throat is limited by 0.5-1 mm, because such mechanical precision can be supported in normal exploitation conditions. The output width is limited by 5-6 mm. This limits the Mach number by values 4-5, and the divergence of the jet stays still big. It is necessary to undertake other measures. These may be inclined nozzles, or concave-convex nozzle profiles, which have been successfully used in [1]. Here they are used for annular jets. All these measures give local effect in axial direction, but is is necessary to form good gas shells only for 2 cm distance between cathode and anode.

Three gas system with possibility of separate regulation of pressure and mass load of each shell requires complex supplying system, which must provide also good angular homogeneity of all the shell. It makes this system rather complicated, because it is necessary to fix in space a few nested coaxial cylinders. Two annular valves would be too heavy to work fast. So, multi piston valve system was selected. It consists from 6 valves/holes inside toroidal plenum chamber in external shell, 3 - for intermediate shell and from 1 valve/hole cylindrical chamber. The pistons of all valves are moved synchronically. The number of valves is limited, in other case the system will be very heavy and slow. Because of low number of holes between plenum and vacuum, it was necessary to introduce stilling chambers. The number of holes from stilling chamber to the nozzles (12 and 6) is twice as the number of valves, and these holes are shifted angularly with respect to valves, to gives the equal path for different gas jets.

Careful optimization of the principally different nozzle configurations have been done. The resulting nozzle profiles and the flow (Mach number contours) can be seen on Fig.1. In 2D simulations the sets of holes was transformed to annular channels with equivalent areas. The recommended time of shot is about 300 μs after the the opening of the valves. Flow regime is not yet stationary, but the suitable density distribution is already formed. This small delay also strictly limits the dangerous penetration of gas into the vacuum chamber.

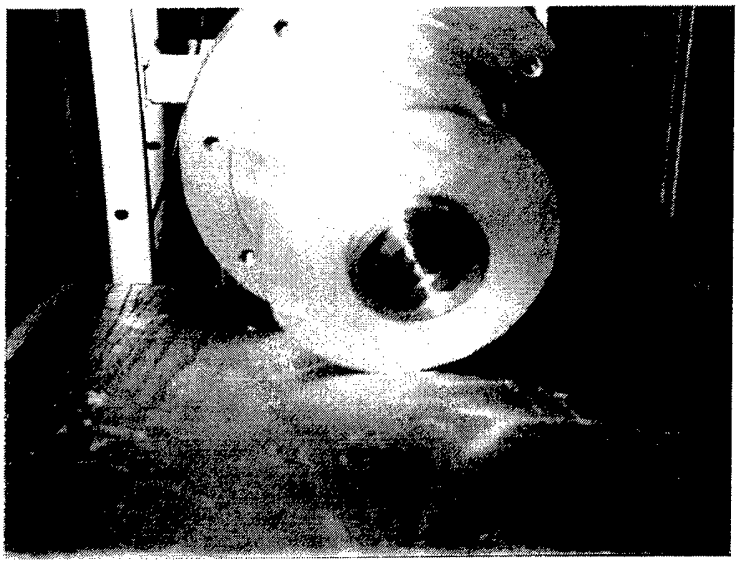

Fig.3 Front view of the nozzle system.

The mass load of each shell or jet is proportional to its plenum pressure and can be varied independently. The simulations show, that the mutual influence of shells during such regulation does not change the principal features of the flow.

The resulting mass distribution is given on Fig.2 for same plenum pressure in all chambers of 0.5 atm for argon. In this case the mass load is about 80 μg/cm. Jet divergence is small. Axial mass load variation at 2 cm length is within a few percents.

This nozzle has other advantage: the high density gradients on the external side of the outer shell. During discharge this will provide easy formation of a thin current layer, and, consequently, efficient start of pinch compression.

The external sight of nozzle system is at Fig.3. Time resolved interferometry and other optical diagnostics confirmed all results of gas dynamical simulations.

MHD simulation of Z-pinch compression.

The behavior of such complex mass distribution during Z-pinch compression was estimated numerically. The results of simulations for generator parameters of GIT-4 are presented on Fig.4. The distributions of density, gas pressure and magnetic filed are presented for the moment of maximal current (1 MA). From this figure it can be also seen how the mesh is adopted to the solution.

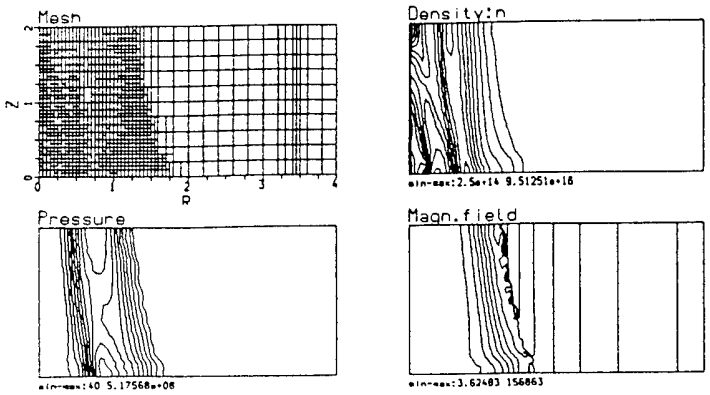

Fig.4 MHD simulation of gas-puff implosion on GIT-4, t=150 ns

The initial density field was taken from gas dynamics simulations for plenum pressure in external shell four times smaller than for internal. Because of too high mass the compression is not very deep, but homogeneous. Zippering effect is absolutely negligible, and no instabilities arise.

Aluminium vapor nozzle optimization

Among different methods of gas-puff creation for Z-pinch compression a metal vapor jet looks attractive. On GAEL installation (2.3 Ohm, 250 kA, 60 ns) [1] the vapor is produced in the explosion of an aluminium foil by an additional source of current. Gas dynamics simulation usually starts up from the moment when all aluminium foil is vaporized after the preliminary discharge.

In the standard nozzle the jet spreading was high. In our case annular nozzle is inapplicable because simulation results show that in such design the nozzle throat gap must be about 0.1 mm. It is difficult to support such mechanical precision in normal exploitation conditions.

In the case of a single hole-type nozzle the cross section area is increased as the radius squared. This gives higher exit to throat areas ratio and, therefore, higher Mach number in comparison with the annular geometry of the nozzle. In our case the central tube has a diameter of about 2 mm and the exit hole diameter is limited from above by 5 mm. This yields the Mach number of about 4.

Jet radius was minimized by simulations. In the experiment the new nozzle shows better Z-pinch performance with respect to the old configuration.

Conclusions

In this paper, on the basis of the gas dynamics computer simulation, the gas-puff preparation is investigated and improved for the concrete installations. Non traditional method of gas-puff nozzle design, which is proposed here, enables serious improvements.The resulting configurations of the nozzles were estimated by MHD simulations of Z-pinch compression.

In experiments the elaborated systems provide higher radiation output and more reproductive results.

[1] R.Brückner Etude de l'Ionisation Laser de Jets de Gaz haute Densité. Thèse de Docteur en Sciences, Université d'Orleans, Janvier 1994.
[2] Wessel F.J., Etlicher B. and Choi P., Phys. Rev. Lett. **69** (1992), 3181.
[3] Gerasimov B.P., Karagichev A.B.,. Semushin S.A, Sov. Phys. Dokl., **31** (1986), 391-393.
[4] Semushin S.A., Adaptive Mesh Refinement approach for MHD and gas dynamical problems.Preprint LPMI, Ecole Polytechnique, 1996.

P-2-83

SPACE AND TIME RESOLVED OBSERVATIONS OF PLASMA DYNAMICS IN A COMPRESSIONAL GAS EMBEDDED Z-PINCH

L. Soto[1], H. Chuaqui[2], M. Favre[2], R. Saavedra[2], E. Wyndham[2], R. Aliaga-Rossel[3], I. Mitchell[3]

[1] *Comisión Chilena de Energía Nuclear, Casilla 188-D, Santiago, Chile.*
[2] *Facultad de Física, Pontificia Universidad Católica de Chile, Casilla 306, Santiago 22, Chile*
[3] *The Blackett Laboratory, Imperial College, London SW7 2BZ, U. K.*

Recent experiments in a gas embedded compressional Z-pinch are presented. The experiments have been carried out in H_2 at 1/3 *atm*, using a pulse power generator capable of delivering a $dI/dt > 10^{12}$ *A/s*. The pinch is initiated by a focused laser pulse, which is coaxial with a cylindrical DC microdischarge. This configuration results in double column pinch at early times, which at current rise evolves into a gas embedded compressional Z-pinch. Diagnostics used are Rogowskii coil, single frame holographic interferometry and holographic shadowgraphy, visible streak camera images from which, current, density, line density, pinch radius and plasma motion are obtained. The pinch is characterized by a maximum on axis density which is much higher than the expected value from filling pressure, with a Bennett temperature of 40 *eV* at 130 *kA*.. Results shown confirm the high degree of compression achievable with the composite preionization scheme.

INTRODUCTION

The study of various Z-pinch configurations has provided some understanding of the relevant mechanisms leading to instabilities. Disruption of the discharge by these instabilities severely limit the maximum temperature and density. A number of experiments have been carried out in Z-pinches using our small pulse power generator(GEPOPU). Experimental results obtained show that generally in gas embedded Z-pinches, after an initial expansion, $m = 1$ instabilities leading to a helix develop, eventually disrupting the plasma column. The development of these instabilities happens during tens of nanoseconds.

Recently a new configuration of a gas embedded Z-pinch has been reported [1], a double column pinch in that it is possible to obtain a gas embedded *compressional* Z-pinch. This configuration exhibits axial compression up to twice the expected value from filling pressure, and some 20 times the density obtained in a conventional laser initiated Z-pinch. In previous work we have compared the behavior in three gas embedded Z-pinch configurations under different preionization conditions: laser initiated, needle Z-pinch, and a composite Z-pinch, performed in the same generator. Anomalous stability has been observed in the needle Z-pinch and compressional gas embedded Z-pinch. It is conjectured that the stability observed is explained by resitive effects and finite Larmor radius effects[2,3]. In the present work new experimental results in the gas embedded compressional Z-pinch in H_2 at 1/3 atm are presented.

EXPERIMENTAL APPARATUS

The experiments were carried out on GEPOPU, a generator capable of delivering currents up to 200 *kA* to a 1.5 Ω impedance load for 120 *ns*. The value of *dI/dt* of the current ramp was approximately $2 \cdot 10^{12}$ *A/s*. A DC microdischarge is established between two stainless steel conical hollow electrodes with 2 *mm* diameter, separated by 10 *mm*. A few nanoseconds

before the application of the main voltage from the driver, a pulsed Nd-YAG laser (20 *ns*, 200 *mJ* at 1.06 μm) is focused through the anode onto the cathode. As the main voltage is applied, the laser generated plasma acts as an electron source to provide preionization on a central plasma column. Initially this conduction channel is highly resistive. The combined preionization scheme produces two parallel concentric conductive paths.

A Nd-YAG frequency doubled 6 *ns* laser pulse was used for optical diagnostics to obtain simultaneous single shot image-plane holographic interferometry and holographic shadowgraphy. Visible streak camera provides radial and axial plasma motion. In this way the evolution of the electron density profile, $n_e(r)$, the electron line density, N, and the external Z-pinch radius, a, are obtained with good temporal and spatial resolution. The total current, $I(t)$, and the external voltage, $V(t)$, were also measured with a Rogowskii coil and a capacitive divider. A maximum voltage of 200 *kV* was used.

RESULTS AND DISCUSSION

In previous work [1] we have obtained a sequence of eight interferometric frames with a 10 *ns* separation between frames from the same discharge. This diagnostics has good temporal resolution but limited spatial resolution[4]. From these holographic multiframe interferograms it became apparent that the electron density at the centre is an increasing function of time, during the initial 110 *ns*. However, the low spatial resolution of the interferograms provided deconvolution of the density profile which resulted in large error margin in the line density estimates. Simultaneous single frame holographic interferogram and shadowgram presented here, confirm earlier results and provide quantitative information about electron density profile and a significantly better measurement of the line density.

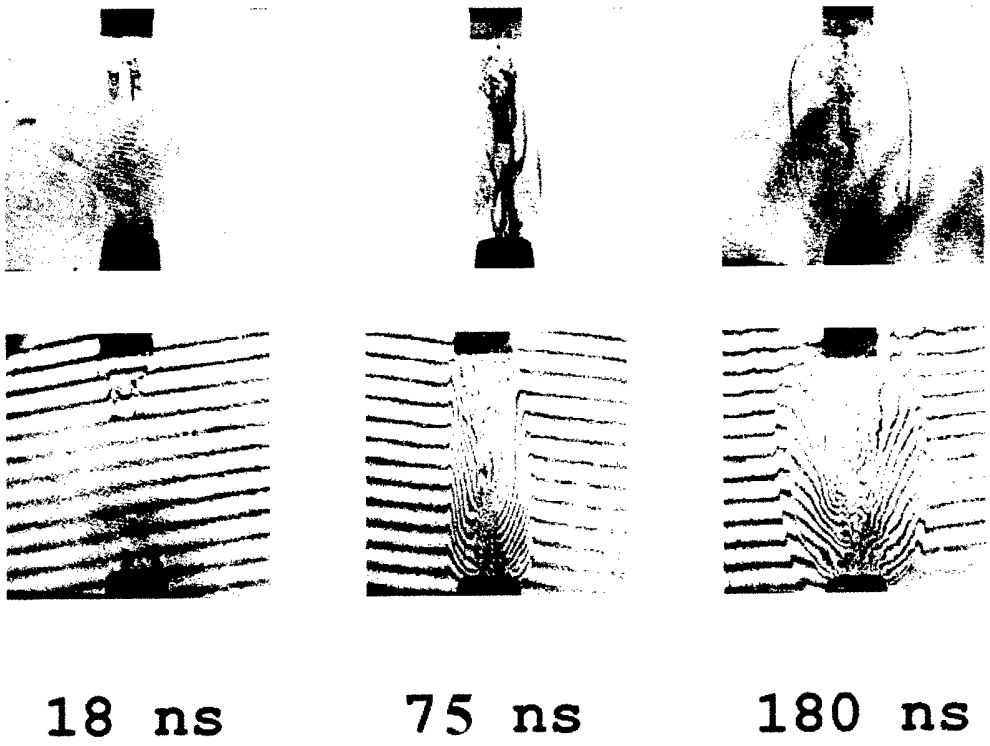

Figure 1 Sequence of simultaneous holographic shadowgrams (top) and interferograms (bottom) obtained on three separate shots.

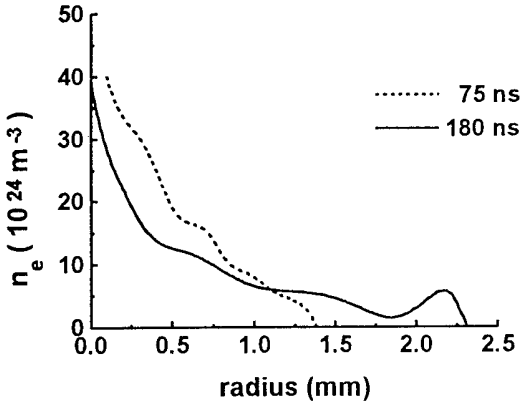

Figure 2 Density profiles obtained from interferograms shown in Fig. 1. At early times the density is not measurerable in the interferogram.

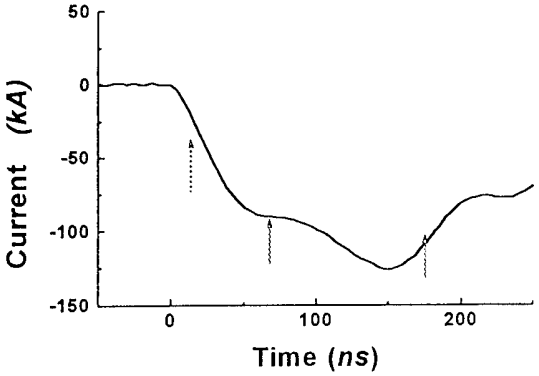

Figure 3 Typical current trace, arrows show the corresponding times for the interferograms shown in Fig. 1.

In figure 1 shadowgrams and interferograms are shown for three different times. Figure 2 shows the corresponding Abel inversions which provide electron density as a function of radius. A typical current trace, with arrows showing the times for the interferograms, is shown in figure 3. At 18 *ns* ionization at the pinch edge is observed, whereas no fringe deviation is apparent near the axis. This indicates that the axial electron density is smaller than $1.2x10^{23}$ m^{-3}, being larger than $4x10^{25}m^{-3}$ at 75 *ns* after the current start. From the corresponding shadowgram it can be seen that the refractivity is high at the pinch centre, which is in agreement with the fact that no fringes are visible at the centre of the interferogram. At later times, 180 *ns*, near the peak current of 130 *kA*, the electron density at the centre is $3.8x10^{25}$ m^{-3}. The line density under these conditions is of the order of $5x10^{19}$ m^{-1}, which is significantly higher than reported previously. This difference is due to a higher electron density at the pinch centre and a much better defined plasma edge density profile. The Bennett temperature can thus be estimated at only 40 *eV*, which is consistent with the negative results obtained with soft X-ray diagnostics used to measure temperature.

From axial streak photographs it is observed that the initial laser spark at the centre has independent dynamics, which is consisten with a metallic laser spark in expansion. The spark remains near the electrode. This observations agree with previous inteferometric results[1] which show that the maximum spark size is 2 *mm* at 50 *ns*. From radial streak photographs, as shown in figure 4, an initial 10 *ns* fast expansion phase is observed, followed by about 50 *ns* expansion of the central channel of $2x10^4$ *m/s*. The expansion of the internal wall of the annular plasma is of the same order, whereas the externel wall has a slower expanding velocity of $6x10^3$ *m/s*. A direct comparison with either a laser initiated gas embedded Z-pinch, needle Z-pinch (both with_single axial current channel), or annular initial microdischarge only, does produce a significantly different behaviour. The reduced expanding rate of the external wall in the composite pinch compared with the microdischarge only case, is presumably due to the presence of the central current channel. The fact that the laser initiation does make a difference is an indirect evidence that there is a significant fraction of the current flowing near the axis. At the end of this phase the two initial plasmas coalesce into one with an apparent internal structure, a brigther central region which is maintained during the following 110 *ns*. At the end of this phase the maximum current is achieved (130 *kA*). This interpretation is consistent with

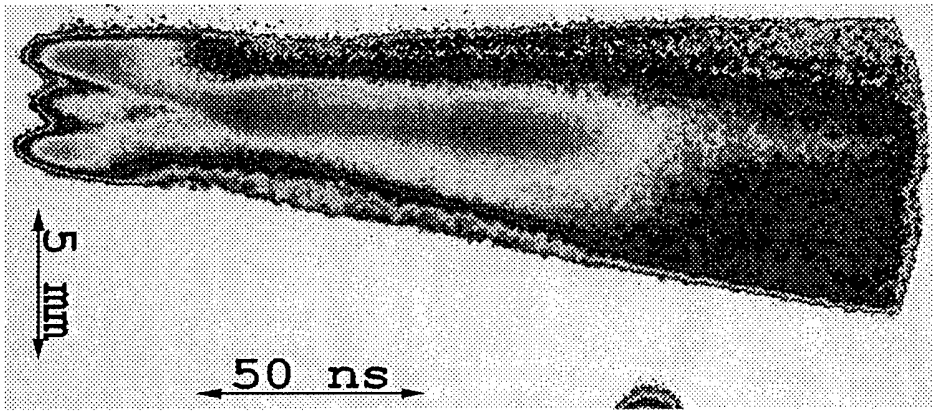

Figure 4 Radial streak photograph in which the different expansion rates are observed, having separate coaxial initial current channels coalescing at later times.

the holographic observations. Densities achieved in the composite pinch are significantly higher than those observed in a laser initiated gas embedded pinch. The results shown here confirm that in the composite pinch radial compression is obtained. This is the only gas embedded pinch in which this behaviour has been observed so far.

Results obtained with the present configuration suggest that by controlling the initial preionization conditions it migth be possible to improve the stability properties of a gas embedded Z-pinch. Future work being considered includes experiments with smaller intial radius for the annulus, lower background pressure and up to 1.2 *MA* peak current in the LLAMPUDKEÑ generator[5].

ACKNOWLEDGEMENTS

This work has been partially funded by FONDECYT, grants 1950048, 1960555 and 2960008, European Commission ISC grant nr. CI1*CT92-0053, and Imperial College (MAGPIE project). R. Saavedra holds a CONICYT scholarship.

REFERENCES

[1] L. Soto, H. Chuaqui, M. Favre, and E. Wyndham, Phys Rev. Lett. **72**, 2891 (1994).

[2] H. Chuaqui, L. Soto, M. Favre, E. S. Wyndham, and M. Skowronek, in Proc. III International Conference of Dense Z-pinches, London (1993), p 27.

[3] L. Soto, H. Chuaqui, M. Favre and E. Wyndham., 1994 *Proc. 1994 Int. Conf. on Plasma Physics,* **V. 1,** Contributed Papers, 216 (Iguazu Falls, Brazil)

[4] L. Soto, H. Chuaqui and M. Skowronek, App. Optics, **34**, 7831 (1995).

[5] H. Chuaqui, E. Wyndham, C. Friedli and M. Favre, "LLAMPÜDKEÑ: a High Current, Low Impedance Pulse Power Generator for Dense Plasma Research", submitted to Laser and Particle Beams.

P-2-84

COMPUTER MODELING OF A SMALL NEON GAS-PUFF Z-PINCH

Jiří Ullschmied

Institute of Plasma Physics, Czech Academy of Sciences
P.O. Box 17, 182 00 Prague 8, Czech Republic

Abstract

The macroscopic dynamics of a cylindrical gas-puff pinch and conditions of radiation plasma collapse are studied by using a one-dimensional ('mechanical') computer model. Besides the Joule plasma heating, compressional heating, magnetic field freezing in a plasma and recombination losses also the real temperature- and density-dependencies of radiation plasma loss are taken into account. The results of calculations are compared with experimental data taken from a small neon-puff z-pinch experiment operated at IPP Prague.

Introduction

Pronounced radial oscillations of the beam-heated magnetized plasma column and quasi periodical bounces of the z-pinch plasma bulk radius are often observed in relativistic electron beam-plasma experiments with short-pulse beams and in small gas-puff pinches [1,2]. These oscillatory movements are in fact the forced macroscopic oscillations of an elastic hot-plasma body driven by fast changes of the radial pressure balance. In gas-puff Z-pinches, the driving force F_{ext} of plasma oscillations is the external magnetic pressure produced by the driving current I(t), and the counter force is the plasma kinetic pressure (+ eventually the pressure of a magnetic field frozen in a plasma at early pinch stages). The pinch dynamics can be studied by using the one-dimensional analytical model (see [3-6]) based on energy, momentum and particle conservation laws, in which a long cylindrical plasma body is characterized by the (reduced) mass per unit length $M^*=M/2$, by the time-dependent radius $R(t)$, and by the (averaged over the plasma cross section) temperature $T(t)$ and density $N=N(t)$.

Model equations

Providing that the total number of particles per unit plasma length remains conserved during the investigated process), the radial plasma dynamics may be described by three coupled balance equations for three time-dependent functions only - $R(t)$, $N(t)$ and T(t) - with the initial values R_o, N_o, T_o : the particle balance equation

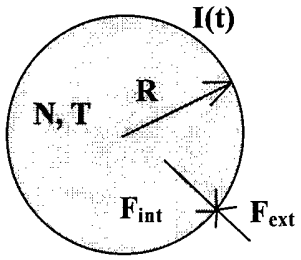

$$N \cdot R^2 = N_o \cdot R_o^2,$$

the momentum balance differential equation

$$M^* \cdot \frac{d^2R}{dt^2} + c_{visc} \frac{1}{R} \frac{dR}{dt} = F_{int} - F_{ext},$$

and the energy balance differential equation

$$\frac{d}{dt}(W_{kin} + Q_{int}) = P_{heating} - P_{loss},$$

where $F_{int} = F_{thermal} + (F_{frozen\ B})$ and $F_{ext} = F_{driving\ I}$ are the internal forces and external (driving) forces, respectively, c_{visc} characterizes the viscous damping, and

$$F_{thermal} = NTS, \qquad F_{frozen\ B} = \frac{\mu_o I_{st}^2}{8\pi R} \qquad F_{driving\ I} = \frac{\mu_o I(t)^2}{4\pi R},$$

$I(t)$ is the time-dependent driving current, I_{st} some start skin-off current value. $P_{heating}$ is the

heating power, $P_{heating} = P_{Joule} + P_{compr}$, and $P_{loss} = P_{rec} + P_{radiation}$ the loss power, where

$$P_{Joule} = \frac{1}{\sigma}\frac{I^2}{\pi R^2} \qquad P_{compr} \sim M^* \frac{1}{R}\left(\frac{dR}{dt}\right)^2 \qquad P_{rec} = \beta T$$

and the the kinetic and thermal plasma energies W_{kin} and Q_{int} are defined as

$$W_{kin} = \frac{M^*}{2}\left(\frac{dR}{dt}\right)^2 \qquad \text{and} \qquad Q_{int} = 2\pi N_o \cdot R_o \cdot \frac{T}{R}.$$

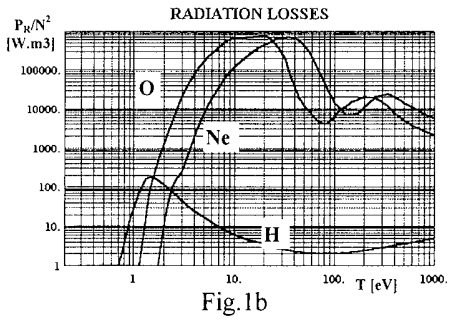

Fig.1b

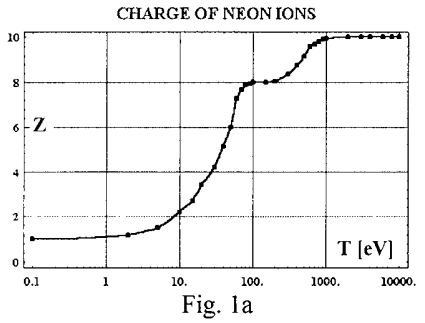

Fig. 1a

The radiation loss temperature-dependence

$$P_{radiation} \sim f_{approx}(T) \cdot N_o^2 \cdot R_o$$

is introduced through the interpolating functions (Fig. 1a) constructed on the base of the plasma radiation data for hydrogen, oxygen and neon published e.g. in [7-9].

Another approximation function is used for the temperature dependence of the neon ion charge $Z = Z(T)$ - see Fig.1b. In such a case the substitution $N \rightarrow N(1+Z\{T\})$ was used.

Though such an approach results in restricting the investigated plasma movement to homogenous expansion (compression) only, all plasma mixing processes (instabilities, turbulence) being necessarily neglected, it proved to be useful at studying the influence on the global plasma dynamics of a number of energy transfer processes. On the first place the influence of radiation losses on the pinch dynamics was studied.

Pinch dynamics without radiation losses

The simplest case of undamped plasma bouncing at a constant driving current and negligible losses may be handled analytically. For a constant fully skinned-out driving current I_o, the period of oscillations is (in the first approximation) proportional to the square root of M^*/I_o^2, and the minimum plasma radius is proportional to $N_o T_o R_o^3/I_o^2$. The time of the first plasma compression does not differ much from the time of singularity of the solution for an infinitely thin hollow plasma cylinder of equivalent mass (zero counter force) - c.f the gray line in Fig. 2a.

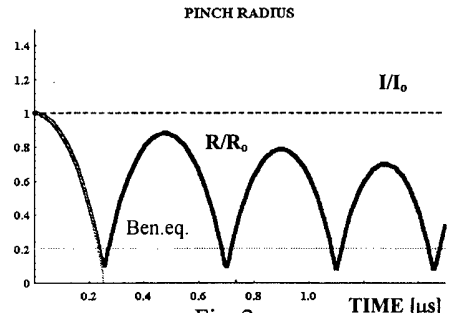

Fig. 2a

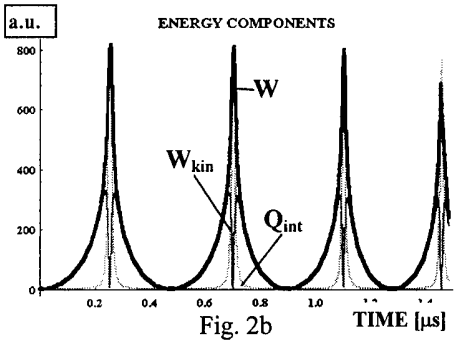

Fig. 2b

In all other cases Wolfram's Mathematica was used for solving the balance equations numerically. When neglecting completely the Joule heating and radiation losses, the plasma radius oscillates around the Bennet equilibrium. The full curve in Fig.2a shows the bouncing calculated for a constant driving current and small recombination losses only. The time dependencies the total energy W, and of the kinetic and thermal energy components are depicted in Fig. 2b.

The dynamics of the pinch radius calculated for a sinusoidal driving current with I_{max}=160 kA and no radiation losses is shown in Fig. 3a, and the corresponding dependence of the plasma temperature in Fig. 3b.

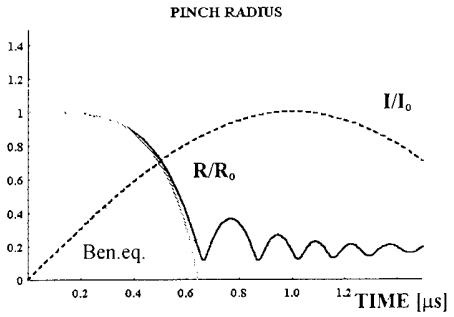

Fig. 3a

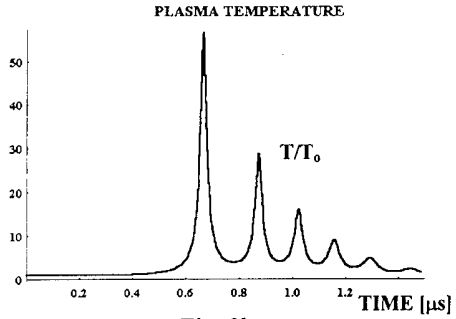

Fig. 3b

Pinch dynamics without radiation losses

As soon as the radiation losses are taken into account, neither the Joule, nor the compressional heating (even when taking into account the frozen-in magnetic field) manages to stop the radiation collapse (the solution has a singularity with $R \rightarrow 0$). Radiation collapse can be avoided e.g. by assuming that the plasma column gradually becomes optically thick, so that at the moment of maximum compression the radiation comes from a thin surface layer only, the thickness of which proportional to the current plasma radius. The pinching then stops at the radius, at which the energy input and output become balanced (around R/R_o = 0.1, $T/T_o \approx 15$ - see the full lines in Figs.4a, b).

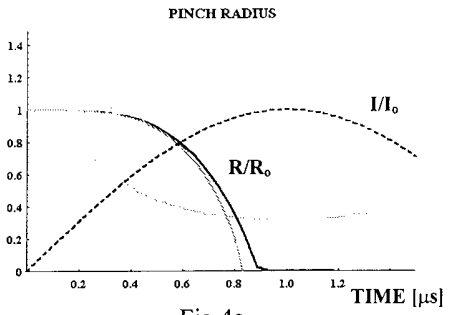

Fig.4a

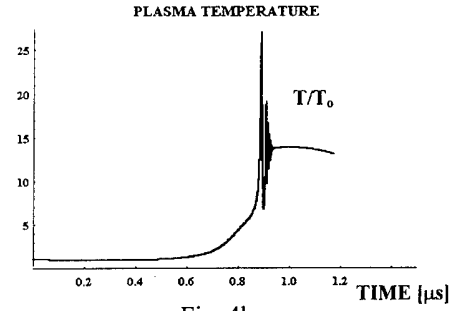

Fig. 4b

Most of the calculations were tailored to the small IPP neon gas-puff pinch (I_{max}=160 kA, $N_o=10^{17}$ cm^{-3}, R_o=1 cm, T_o=1 eV) - [12]. The calculated minimum plasma radius $R_{min} \approx 0.6$ mm, the maximum temperature of the plasma bulk $T_{max} \approx 60$ eV, and the maximum plasma density $N_{max} \approx 2.5 \cdot 10^{19}$ cm^{-3} at the main plasma compression stage agree remarkably well with the experimentally obtained values.

Radiated power

Also the calculated time dependence of the radiated XUV power resembles well the experimental one. The simulated curves make it possible to explain all the main features of the observed XUV signals, namely the repeated bouncing observed at non-optimum pinch parameters, and pronounced splitting of the radiation peak corresponding to the first plasma compression - see Fig. 5. The computed time

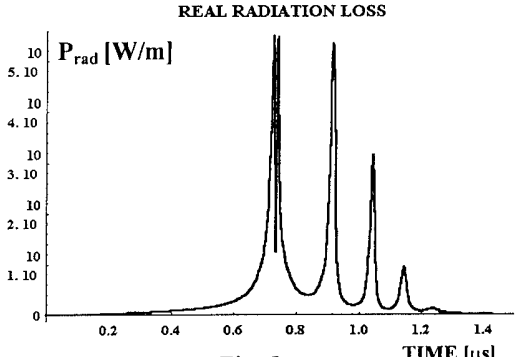

Fig. 5

dependences of the radiation losses agree qualitatively well with the measured XUV signals even at the times after the first plasma compression. In particular, in non-optimum pinch regimes the split broad first radiation peak is followed by several narrower spikes with a comparable or lower amplitude.

At the optimum pinching, however, strong MHD instabilities developing during the first compression (witnessed e.g. by the occurrence of hot spots [10]) result in and a partial or even total current disruption, some part of the current being expelled to the peripheral discharge regions.

The disruption process was simulated in a model way by changing the time dependence of the driving current *I(t)* several tens of ns after the maximum pinching. The temporal dependence of the radiated power after the maximum plasma compression on a longer time scale is determined by the time delay and by the speed of the current disruption. At a fast current disruption the radiation signal turns to a single split peak. If the current disruption is only temporal (see Fig. 6a) another much narrower radiation peak may occur several hundred ns after the first compression, as shown in Fig. 6b. At a slower but irreversible current disruption (see Fig 7a) the radiation signal decay becomes slower - Fig. 7b. In both these cases the calculated XUV signal shapes coincide remarkably well with those observed in a real experiment, as illustrated by Fig. 6c and 7c (cf. also [11]).

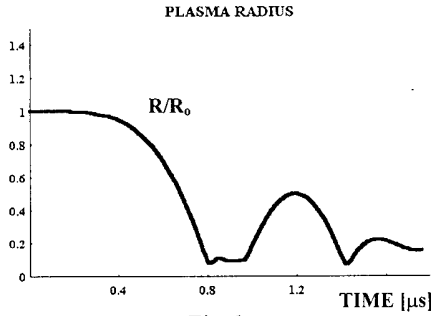

Fig.6a

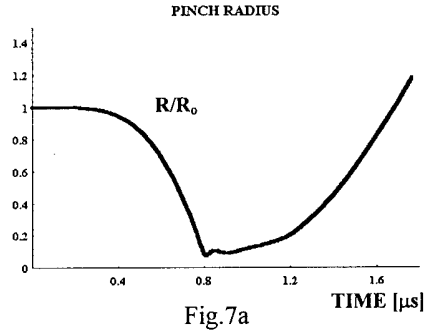

Fig.7a

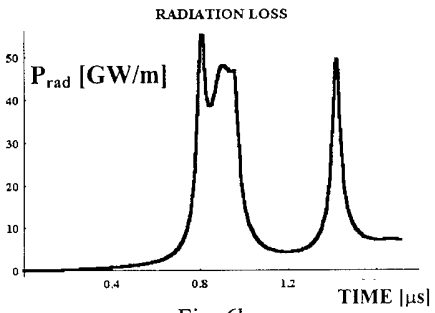

Fig. 6b

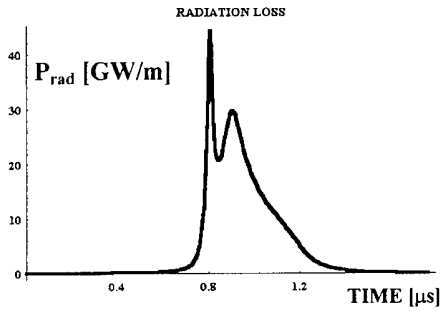

Fig. 7b

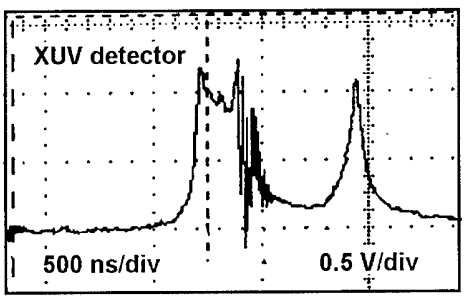

Fig. 6c
XUV diode signal at a fast current disruption

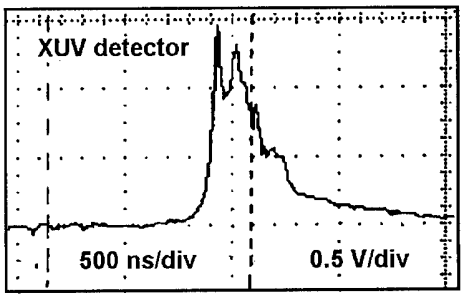

Fig. 7c
XUV diode signal at a slow current disruption

Conclusion

The performed computations of a Z-pinch dynamics show that neither the Joule heating, nor the internal kinetic and magnetic (due to partially frozen driving magnetic field) pressures can stop the plasma radiation collapse, if full radiation losses are taken into account.

Contrary, if the radiation losses are artificially reduced even the 1-D model gives realistic time dependencies of both plasma radius and temperature, and the values of the minimum plasma radius and maximum plasma temperature at the stage of the first plasma compression agree well with those obtained by using several independent methods of plasma diagnostics. The simulated curves make it possible to explain all the main features of the observed XUV signals, namely the repeated bouncing observed at non-optimum pinch parameters, and pronounced splitting of the radiation peak corresponding to the first plasma compression.

Experimental XUV signals in non-optimum pinching regimes witness, we believe, full or partial (reversible) disruption of the driving current occurring at the time of maximum plasma compression.

This work has was supported in part by the Grant Agency of the Czech Academy of Sciences under contracts No 14358 and A1043504

References:

[1] Krejčí , A. et al: Proc. 17th Symp. Plasma Ph. & Techn., Prague 1995, p. 107

[2] Krejčí, A.: Czech. J. Phys. *40* (1990) 182

[3] Jungwirth, K., Ullschmied, J.: IPPCZ-244 (1981) 144

[4] Mosher, D.: Proc. AIP Conf. on Dense Z-Pinches, Laguna Beach 1989, p. 191, 262

[5] Mosher, D., Colombant, D.: Phys.Rev.Letters *68* (1992) 2600

[6] Miyamoto, T., et al: Proc. AIP Conf. on Dense Z-Pinches, Laguna Beach 1989, p. 447

[7] Breton, C., de Michelis, C., Mattioli, M.: Jour. Quant. Spectr. Rad., *19* (1978) 367

[8] Cox, P.D., Tucker, W.H.: The Astrophys. Journal, *157* (1969) 1157

[9] Drawin, W.H. in: At. and Mol. Data for Fusion, IAEA Vienna-199 (1977) 217

[10] Krejčí, A., Krouský, E., Renner, O.: Czech J. Phys. *40* (1990) 1244

[11] Krejčí, A. et al.: Proc. BEAMS'94, May 25-29, Washington D.C., Vol. III, p. 2020

Hydrosimulations of Z-Pinch

R. Benattar & P. Ney
Laboratoire de Physique des Milieux Ionisés
Ecole Polytechnique, 91128 Palaiseau- France

Abstract

Simulations on gas puff and plasma on wire for different configurations are presented. The code is a 1D cylindrical lagrangian code including radiative transfer. Different models of opacities calculations in LTE and non LTE can be used.

We vary the mass and the size of the plasma, the atomic number Z of the material, the current and the magnetic field.

We can get from the simulations the time evolution of the radial distribution of different values such as the electron and ion densities, the electron and ion temperatures, the current and the magnetic field, the mass density, the pressure ....

Emission spectra and their evolution are presented for different kinds of plasmas.

1.- **The code FILM** [1],[2]

The hypothesis are:

- 1D Lagragian cylindrical geometry
- Radial motion of the plasma
- Quasi neutrality ($Zn_i - n_e << n_e$)

We solve 7 Equations :

- The mass conservation
- The momentum conservation for ions and electrons
- The energy transport for ions and electrons
- 2 Maxwell's Equations : Faraday's law and Ampere's theorem
- Ohm's law in order to eliminate the electric field

We use the Sesame Equations of states and calculate the transport coefficients

The Code calculates function of radius and time :

- the mass density,
- the radial velocity,
- the electronic and ionic temperatures,
- the azimutal magnetic field,
- the current density.

A package of radiative transfer can be added to the hydrodynamics which modify the previous values and allows to get the emission spectrum.

2.- **Model of Radiative Transfer**

From the equation of transfer, the radiative energy deposited by unit time and unit mass at the optical depth r is :

$$E(x) = 2\pi cons \int_0^{\infty} I(h\nu) k(h\nu, r) \exp\left(-\int_0^{x} k(h\nu, r)\rho(r)dr \right) d(h\nu)$$

We calculate the radiative energy balance inside each cell at each time step taken into account the right E_d and the left E_g radiative energy coming from all the other cells after attenuation, the self emission of the cell E^* and the self absorption of the cell.

We add this energy amount (>0 or <0) to the energy delivered by the magnetic field in order to deduce the temperature at the current time step.

The EOS tables loaded gives the other variables.

The equations of energy balance are :

$$E_d(t,cel) = 2\pi cons \sum_{f=1}^{ns} \sum_{m=cel}^{nc-1} j(f,t,m+1)k(f,t,cel)\exp\left\{-\sum_{i=cel}^{m} k(f,t,i)\rho(i)dr\right\}d(h\nu)$$

$$E_g(t,cel) = 2\pi cons \sum_{f=1}^{ns} \sum_{m=2}^{cel} j(f,t,m-1)k(f,t,cel)\exp\left\{-\sum_{i=ce}^{m} k(f,t,i)\rho(i)dr\right\}d(h\nu)$$

$$E^*(t,cel) = 4\pi cons \sum_{f=1}^{ns} j(f,t,cel)k(f,t,cel)\exp\{-k(f,t,cel)\rho(cel)dr\}d(h\nu)$$

The calculated emitted spectrum in kev/kev/cm2

$$Spectre(f) = 2\pi cons \sum_{t=1}^{nt} \sum_{cel}^{nc} j(f,t,cel)\exp\left\{-\sum_{i=cl}^{nc} k(f,t,i)\rho(t,i)dr\right\}\tau$$

k is the spectral opacity of the material of the cell and **j** the emissivity for the current temperature and density. τ is the time during which the spectrum is calculated.

The opacities and emissivities are calculated using different versions of the screened hydrogenic model [3],[4]:

- Average Atom LTE
- Average Atom LTE with l-splitting
- Collisional radiative non-LTE stationary
- Collisional radiative non-LTE stationary with l-splitting

The calculations of opacities and emissivities are done for a wide range of mass density and temperature.

At low temperature and high density the right calculation of the e-i collision frequency is included in the f-f contribution.

3.- **Results of simulations**

We have run the code for two different structured pinches and two generators. The results are done without and with radiative transfer.

3.1.- GAEL simulation

Figures 1 and 2 show the radial time evolution of the electron density of a plasma on wire made of an aluminium wire 12.5 μm diameter surrounded by a low density ($6.2\ 10^{-4}$ g/cm^2) aluminium gas 1.5 mm radius with a total mass of 29.5 μg and the time evolution of the current of the generator which is coupled to the plasma.

Figures 3 and 4 show the same evolution of the electron density and the current but adding to the simulation the radiative transfer. When radiative transfer is activated the plasma expands very fast by comparison of the case when it is not active when the pinch can repeats before the current of the generator is turned off.

3.2.- Powerful generator.

The generator is not coupled to the plasma and it delivers a linear ramp of current varying from zero to 16 MA in 140 ns.

Figures 5 and 6 shows as previously the evolution of the electron density and the current. Figures 7 and 8 the same evolution but with radiative transfer activated.

The internal wire 12.5 μm diameter is made of nickel. It is surrounded by two parabolic profiles of argon gas reaching a radius of 20 mm.

The current decreases when the pinch occurs. It decreases more when the radiative transfer is activated.

The time dependence of the density profile versus radius expands in the same manner as previously.

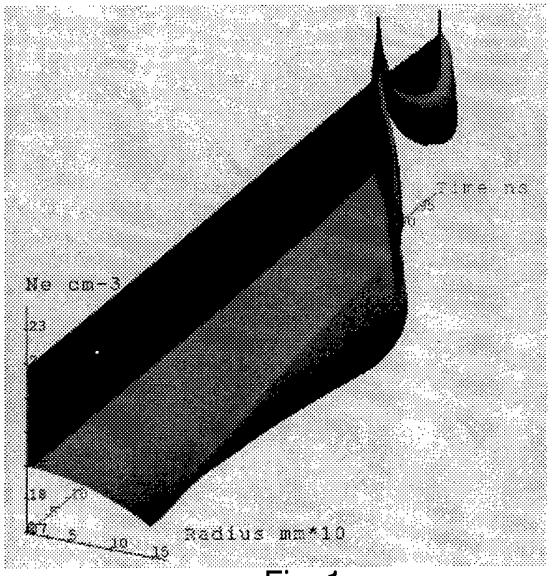

Fig. 1

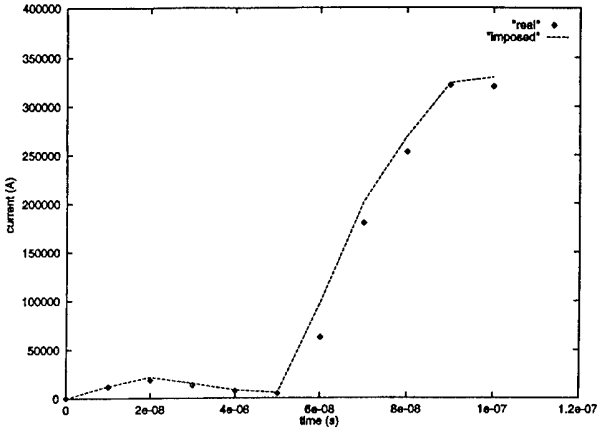

Fig. 2

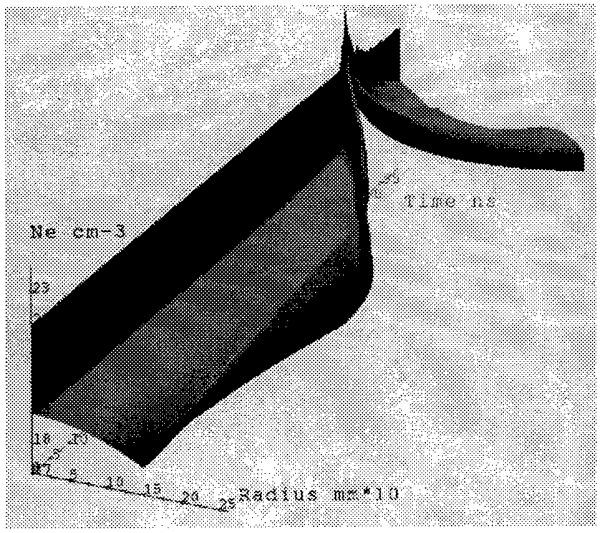

Fig. 3

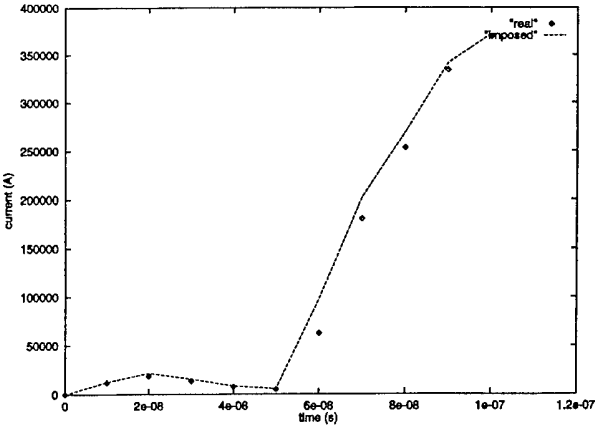

Fig. 4

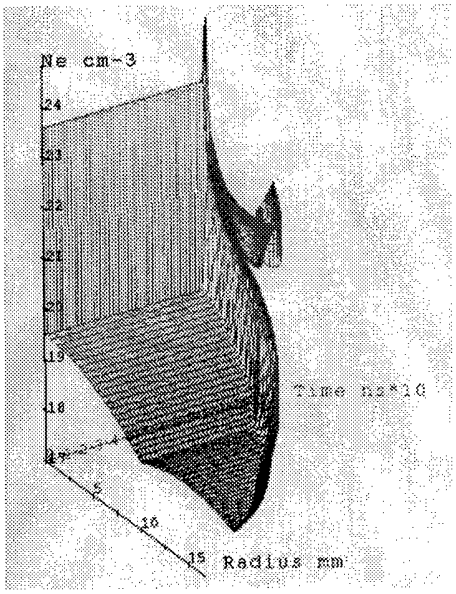

Fig. 5

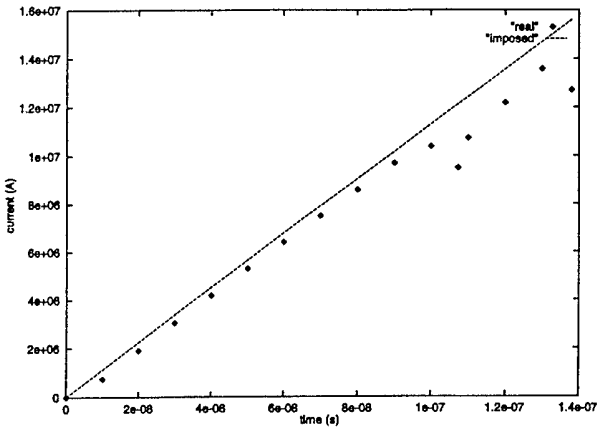

Fig. 6

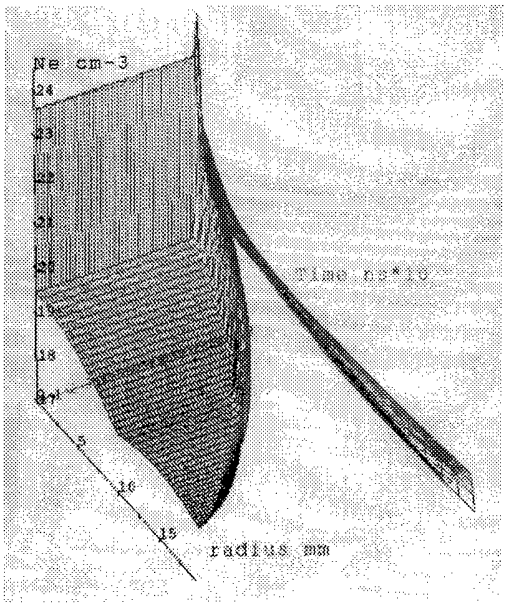

Fig. 7

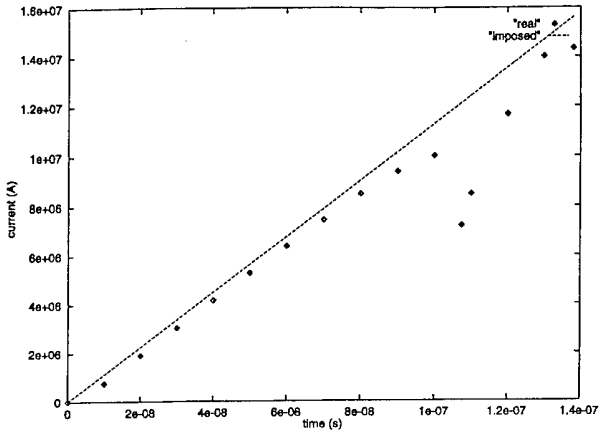

Fig. 8

4.- **Conclusion**

In the case where there is no transfer the plasma can pinch an other time when the current continue to increase.

The evolution of the plasma is totally different when the radiative transfer is on. In this case the preheating of the plasma by the radiation makes the wire to explodes.

The decreasing of the current is also much important at the pinch time in this case.

References

[1] J. Virmont Rapport Greco Ecole Polytechnique unpublished (1982)
[2] M. Gazaix Rapport PMI 1542 Ecole Polytechnique unpublished (1985)
[3] R. Benattar, C Galos & P. Ney J.Q.S.R.T 54, 53, (1995)
[4] R. Benattar, C Galos & P. Ney J. of X-Ray Sc & Tech 5, 249, (1995)

NUMERICAL MODELLING OF HIGH-TEMPERATURE PLASMA IN A STRONG MAGNETIC FIELD AT RFNC-VNIITF

Oleg V. Diyankov, I.V. Glazyrin, N.G. Karlykhanov, A.D. Zubov

Russian Federal Nuclear Center- All Russian Scientific Research Institute of Technical Physics (RFNC-VNIITF)
P. O. Box 245, 456770, Snezhinsk, Chelyabinsk Region, Russia

Abstract

Review of code development at RFNC-VNIITF for numerical modelling of high-temperature plasma in a strong magnetic field is presented. Three codes are described: 1D MHD ERA code and 2D MHD codes: MAG and TIGR-M.

ERA is 1D two-temperature Radiation Lagrangian MHD Code. ERA includes magnetic field diffusion; electron and ion heat conduction with heat flux inhibition; superthermal particles creation mechanism and transport equations for particles. Radiation effects can be treated in different cases: three temperature model; multigroup diffusion model; multigroup nonstationary kinetic model; multigroup nonstationary kinetic model with quasidiffusion approximation. A detailed configuration atomic model has been employed to calculate the line opacity, Doppler effect and ionic state variation. The state populations are calculated using a set of time-dependent atomic rate equations for electron collisional excitation and de-excitation, dielectronic and radiative recombination, photoexcitation and others processes. The ionization state of plasma is calculated self-consistently with line and continuum radiation transport. There are a number of tables which contain the characteristics of elements: state equations and different kinetic transport coefficients. Equations of state taking into account the energy of ionization are used for electron and ion pressure and internal energy calculations. In the Code the relevant Braginskii magnetized transport coefficients are used. The microturbulence effects due to current-drive microinstabilities are also included into the Code.

2D resistive MHD Code MAG for plasma modelling in arbitrary moving coordinate system is developed for the case of three components of velocity and three components of magnetic field. The Code is build on the basis of TVD scheme in Lagrangian form. This approach allows to simulate flows with large deformations inside the flow region, conserving the correct description of conditions on its weakly deformed boundaries. The code is modified to include Hall term in the equation for magnetic field evolution. The Code is using the same set of equations of state and magnetized transport coefficients as ERA code excluding radiation effects and superthermal particles transport.

In TIGR-M Code the Eulerian-Lagrangian description of motion with special velocity vector decomposition in moving coordinate basis is used. There are two particular cases of magnetic fields configuration in the Code: 1) two components of velocity and two components of magnetic field lying in the same plane as velocity vector does; 2) two components of velocity and one component of magnetic field which is normal to velocity vector. One coordinate lines family coinciding with interface is Lagrangian one, the other is an Eulerian one (that is a set of straight lines). For realization of implicit finite difference technique the method of splitting according to physical processes and space variables is taken. The following types of problems can be solved with the Codes:

- a set of magnetically related problems which fall in the dynamics of flow of heat-conducting gases in complex systems, taking into account stratified structures consisting from different materials;
- inertial confinement fusion investigations, particularly to study effects in plasma liner implosion and laser-fusion target;
- MHD instabilities development in Z-pinch and its suppression by an axial magnetic field.
- plasma-wall interaction in the tokamak ITER and others.

Work is supported partially by ISTC, Projects #009 and #107.

P-2-88

Current instability of "Snow plough"

L.I.Rudakov, A.A.Sevastianov

Russian Research Center "Kurchatov Institute"
Moscow, Russia

The hollow cylindrical liner collapsing to the axis as a result of compression by the magnetic field of the current passing though it is one of the basic schemes for the generation of bright X-pulse. The main factor deteriorating the efficiency of this scheme is widely believed to be an instability of the Reyleigh-Teylor type. The analysis of data obtained in the experiments with liners on the installations "Module-A5", "Saturn" and "Angara-5" [1, 2, 3] shows substantial discrepancy with the supposed Rayleigh-Taylor scenario of liner shell disruption. First of all this discrepancy can be seen in the fact that the stratification appears at the very beginning of acceleration phase, when liner is actually at its initial position. Besides, much attention must be paid to the fact that modulation scale along the axis increases with time, the rate of this process being to high for it to be explained by nonlinear dynamics of mass redistribution along the axis. All the above mentioned considerations lead us to the conclusion that in this case we deal with a current dynamics, which nevertheless — as can be seen in the experiments — could give rise to the fall-through of the current into the internal regions of the liner, thereby determining future behaviour of mass. In the experiments on the installation "Modul-A5" it was observed the exact correlation between the process of stratification and occurrence of the lighting kernal in the region near the axis (Fig.1 a,b).

We have chosen a model of compact acceleration of highly radiative liner shell [1], in which we disregard the kinetic pressure of plasma with respect to the pressure of the magnetic field and suggest that all parts of the shell have exactly the same acceleration g:

$$g = \frac{Z_{eff}}{nM_pA}\frac{\partial}{\partial r}\frac{B^2}{8\pi}, \qquad (1)$$

here n – electron density, M_p – proton mass, and constants Z_{eff} and A – the charge and the atomic weight of ions, respectively.

Only slow relative motion of different parts of the liner is allowed, their relative speed being much less then the characteristics speed of the shell as a whole gt. To reach the stage of compact acceleration the liner should first collapse to the

dimensions of skin layer $\delta_s \sim \sqrt{(c^2/4\pi\sigma)t}$. Therefore for this approach to be valid it is necessary that $R \gg \delta_S$. In the same approximation we also disregard cylindrical geometry effects. As long as we are going to restrict our consideration to the purely current instabilities, we will not take into account plasma movement along the liner axis, which is valid if $\partial/\partial z \ll 1/\delta_s$.

If at the beginning of compression liner mass is widely distributed along the radius, the subject of our considerations is the creation of plasma layer raked up to the skin depth scale. In this case the acceleration is a function of time. This is a "snow plough" model. As long as only processes with a characteristic time scale of about δ_S/v_o will be considered in the following, we can disregard the "slow" evolution of liner acceleration with time $g(t)$.

Taking into account everything mentioned above we will use two-fluid MHD in the following form [1]:

$$n\frac{\partial}{\partial t}\frac{B}{n} + nv\frac{\partial}{\partial r}\frac{B}{n} - \left(\frac{\mathbf{j}}{e}\cdot\nabla\right)\frac{B}{n} = \frac{c^2}{4\pi\sigma}\frac{\partial^2 B}{\partial r^2}; \tag{2}$$

$$n = \frac{Z_{eff}}{gM_pA}\frac{\partial}{\partial r}\frac{B^2}{8\pi}. \tag{3}$$

Discontinuity condition together with (3) gives immediately ion speed:

$$v = -\frac{\partial B/\partial t}{\partial B/\partial r}, \tag{4}$$

Substituting into (2) $\mathbf{j} = (c/4\pi)\mathrm{rot}\mathbf{B}$, (3) and (4) one can obtain a single equation for the magnetic field. Normalizing $[r] = \delta_o$, $[t] = t_{\mathrm{diff}}$, $[z] = (B_o\sigma/nec)\cdot[r] \equiv (\omega_{Be}\tau_e)\cdot\delta_o$, $[B] = B_o$, here δ_o — liner depth at the moment when we start our consideration of its two-dimensional evolution and $t_{diff} = \delta_s^2(c^2/4\pi\sigma)^{-1}$. We can write down this final equation as follows:

$$B\frac{\partial}{\partial r}\left(\frac{\partial B/\partial t}{\partial B/\partial r}\right) - \frac{\partial}{\partial r}\left(\frac{\partial B/\partial z}{\partial B/\partial r}\right) + \frac{\partial^2 B}{\partial r^2} = 0. \tag{5}$$

Introducing new variables in a way as it has been done in [1] $\tau = t$, $\ell = z$, $B = B(r,z,t)$, and defining $\psi \equiv \partial B/\partial r$, we can rewrite equation (5) as follows:

$$B\frac{\partial\psi^2}{\partial\tau} - \frac{\partial\psi^2}{\partial\ell} + \psi^2\frac{\partial\psi^2}{\partial B} = 0, \tag{6}$$

with the general solution described implicitly by

$$F\left(\psi^2,\quad 2\psi^2(\tau-\tau_o) - B^2,\quad \psi^2(\ell-\ell_o) + B\right) = 0, \tag{7}$$

here $F(\ldots)$ - could be any function, and τ_o & ℓ_o - arbitrary constants.

Besides of trivial $\psi^2 = \text{const}$ there is a bit more complicated but still one dimensional diffusive solution, that can be readily obtained from (7):

$$\psi^2_{\text{diff}} = \frac{B^2}{2\tau} \quad or \quad B \sim \exp\left(\frac{r}{\sqrt{2\tau}}\right). \tag{8}$$

As a next step we can try to construct solutions with a modulation along the axis. Keeping in mind the future application to the treatment of experimental results, it is reasonable to represent the solutions in the form of a small disturbance to the diffusion solution (8):

$$2\psi^2\tau = B^2 + 2\tau_o\psi^2\left\{\exp\left(\frac{\gamma}{\psi^2}\sin^2\left(\frac{\psi^2\ell + B}{\psi^2 + \psi_o^2}\right)\right) - 1\right\}, \tag{9}$$

here τ_o, γ, ψ_o^2 - small constants. The partial solution (9) is build up of characteristics (7) in this way in order to garantee the compactness of the initial disturbance all over the area of possible values of B и ℓ, but at the same time to reveal exponential growth of the amplitude at the linear stage.

Equation (7) suggests a good opportunity to construct solutions with the features necessary for experiment treatment, in particular, solutions describing the fall-through of the magnetic field inside the liner interior. In this case the condition $B = 0$ at the internal plasma boundary must be replaced by the condition $\psi = 0$, for the acceleration to be finite. But at $\psi \to 0$ there is a degeneration of characteristics(7). This problem can be avoided if we create the following combination of old characteristics: $\xi = \tau + \ell B + \psi^2\ell^2/2$. As long as ξ tends to $\tau + \ell B$ with the time, the desirable dependence of the field on the internal plasma boundary can be introduced — for example in the equation (9) — by means of a corresponding function $B_1(\xi)$:

$$2\psi^2\tau = B^2 - B_1^2(\xi) + 2\tau_o\psi^2\left\{\exp\left(\frac{\gamma}{\psi^2}\sin^2\left(\frac{\psi^2\ell + B - B_1(\xi)}{\psi^2 + \psi_o^2}\right)\right) - 1\right\}, \tag{10}$$

The complete freedom of the choice of the function $B_1(\xi)$ is virtual, in reality the evolution of the field inside in determined by a selfconsistent dynamics of liner and circuit. Therefore here we can only visualize this process on a simple model function $B_1(\xi)$ $B_1(\xi) = 1 - \text{ch}^{-1}(\alpha\xi)$. When using such a choice B_1 is always between 0 and 1 (normalized to the external field) and tends to 1 with time. The characteristic time of magnetic field penetration inside is α^{-1}. Therefore for the phases of liner evolution —

1) collapsing to the regime of a compact acceleration, diffusion of the liner shell;

2) occurrence and evolution of modulation along the liner axis;

3) penetration of the field through the liner shell

— to be easily distinguished the following hierarchy of time scales is needed (normalized to diffusion time): $\alpha \ll \gamma \ll 1$.

Fig.1 c) displays the dependence $\psi^2(B,\ell)$ reconstructed on a computer from equation (9) for $\tau = 10$, $\tau_o = 1$, $\psi_o^2 = 0.1$, $\gamma = 0.01$ in the region, in which the solution is unique. Color intensity is proportional to the value of ψ^2. Though modulation scale increases in the internal regions of plasma, we can suggest that the modulation which is observed in experiments corresponds to the regions of maximal irradiation (maximal ψ^2) on the plasma boundary. The number of strats is constant for some time, later it starts decreasing reversed proportional to the time.

References

[1] L.I. Rudakov. *Proc. of the 2-nd Int. Conf. Dense Z-pinches, Laguna Beach, California 1989. AIP Conf. Proc. N 195, editors N.Pereira, J.Devis and N.Rostoker. N.Y. 1989, P.290.*

[2] R.B.Spielman, R.J.Dukart, D.L.Hanson et al. *ibid., P.3.*

[3] V.P.Smirnov et al. *Proc. of the 3-d Int. Conf. on Dense Z-pinches, London, UK, No 299. editors M.Haines and A.Knight, N.Y. 1993, P.580.*

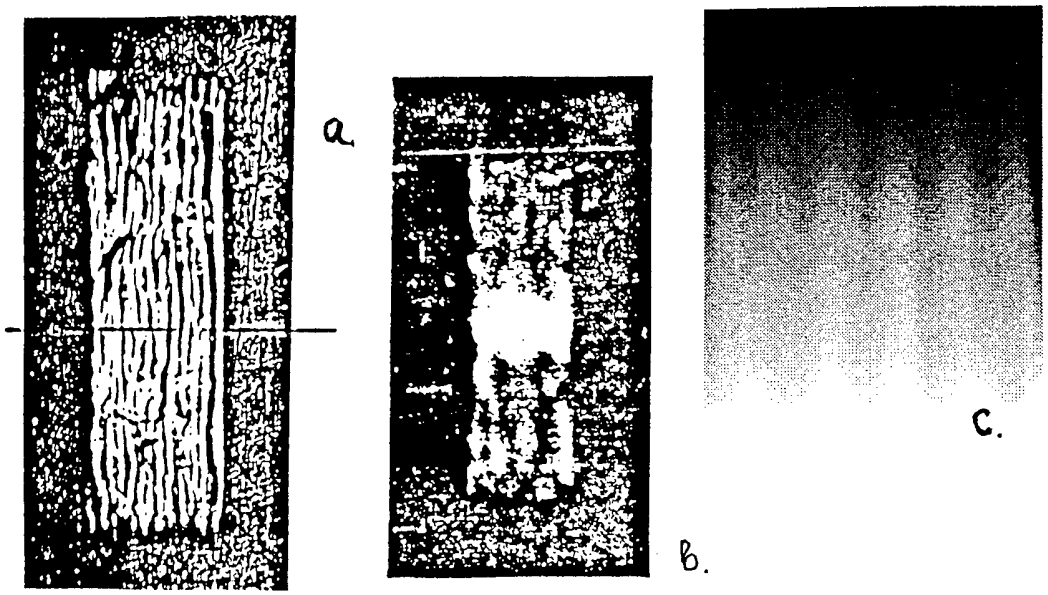

Fig.1. Observed (a,b) and calculated (c) stratification of a plasma shell.

P-2-89

RADIATION FROM TURBULENT INTENSE Z-PINCHES

L.I. Rudakov

RRC Kurchatov Institute
123182 Moscow, Russia

R.N. Sudan

Laboratory of Plasma Studies, Cornell University
Ithaca, NY 14853, USA

Abstract

The main goal of this paper is to develop a model of the processes that lead to the final turbulent state of the pinch. In this state the implosive pressure due to the current equals the counterpressure of the turbulent components of the magnetic field B_r, B_θ and B_z and velocity v_r, v_θ, v_z within the pinch. Thin loops of toroidal magnetic field are created at the pinch surface due to the Rayleigh-Taylor instability which as they collapse into the plasma are distorted and tangled by the turbulent plasma motion into complicated shapes.

In this model we propose that the bulk of the energy in the loops drives shocks and turbulent eddies in the fluid. During the final stage of the collapse of the rings the remaining loop magnetic energy will dissipate in Joule heating as a result of magnetic reconnection and annihilation. The kinetic energy in turbulent motions transfers from the large to small scales where viscous dissipation converts it to heat. On the other hand the stretching and twisting of the magnetic loops acts to reduce turbulent motion. After some time the input of loops due to the surface instability must decrease because their volume density becomes too large and the resistance to their movement increases. As a result the power input, the rate of plasma heating and radiation from the pinch drop.

In contradiction to the conventional non-turbulent laminar model of radiative collapse where the compression tends to infinity, in our model there is a counter-pressure from the ensemble of compactly packed magnetic loops. For this reason plasma compression is limited and the radiatively cooled plasma is forced into the regions between the loops. Only the plasma frozen in the interior of the magnetic loops remains hot because it radiates poorly because of its low density.

This final state, in which the dissipated power and radiation from the plasma are strongly decreased, is predicted to be the new state of "cold turbulent pinch".

(The full text will be published elsewhere.)

CONTRIBUTED PAPERS P-3

Accelerator-Related Topics

Electron Beam Applications

Ion Beam Applications

Pulsed Power Applications

BDTT

Explosive Generators

Pulsed Power Technology

PARTICLE ACCELERATION BY INVERSE-WEIBEL INSTABILITY

S. Kawata

Department of Electrical Engineering, Nagaoka University of Technology, Nagaoka 940-21, Japan
e-mail: kawata@voscc.nagaokaut.ac.jp

Abstract

A high demagnetization rate $\partial B/\partial t$ can be obtained through fast decoupling of a magnetic field from an electric circuit which generates the magnetic field. Nowadays fast decoupling is possible by present switching technologies. A high particle-acceleration gradient can be obtained in an inductive acceleration system compared with that in a conventional induction accelerator. Based on this new proposal, inductive ion and electron accelerations are investigated numerically. The mechanism presented in this paper may be considered as pseudo-inverse Weibel instability.

Introduction

A number of new particle acceleration mechanisms have been studied and proposed [1,2] in order to break through the limitation of the acceleration gradient for current accelerators. In a conventional induction accelerator [3], in which a cylindrically symmetric azimuthal magnetic field B_θ is used for the generation of an inductive acceleration field, the acceleration field is also limited, and the denagnetization rate $\partial B_\theta/\partial t$ is determined by an electric circuit structure and a magnetic core material; typically $\partial B_\theta/\partial t \simeq$ a few T/μs. [3] Here t denotes the time. Using the Maxwell equation, one can easily obtain the relation of $V = \Delta B_\theta S/\tau$, where V is an acceleration-voltage increase for a time duration τ, ΔB_θ a change in B_θ, and S the area through which B_θ penetrates perpendicularly. (3) Therefore one of the important points for attaining a high acceleration gradient is to obtain a short τ. We propose to use a magnetic field which is decoupled from the electric circuit by fast opening-switch technology, and to use the demagnetization process to obtain a large acceleration field. Based on this new proposal, inductive ion and electron accelerations are investigated numerically.

Nowadays, fast switching technologies are firmly established and available. For example, 1) a plasma opening switch provides a switching time of $\leq 5\sim10$ns. [4] 2) Another available tool is an intense high-power laser. Based on the fast opening-switch technologies, it is possible to decouple a magnetic field in the short switching time from an electric circuit that generates the static magnetic field. Consequently we may have a high acceleration gradient compared to that of a conventional induction accelerator.

Inductive Acceleration Mechanism

In order to demonstrate the generation of the large acceleration field, we perform a simple estimation and a particle simulation for ion or electron acceleration in the system (Fig.1). First, the static magnetic field, sustained by electric currents, is applied in an acceleration vacuum. Then the currents are terminated abruptly by the fast opening

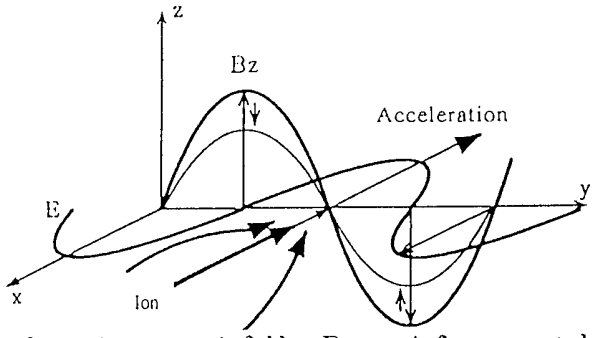

Fig. 1 A static spatially alternating magnetic field B z is first generated and is abruptly decoupled from the electric circuit which generates Bz. During the demagnetization phase a high acceleration field E is induced. Ions are accelerated by E and focused by Bz.

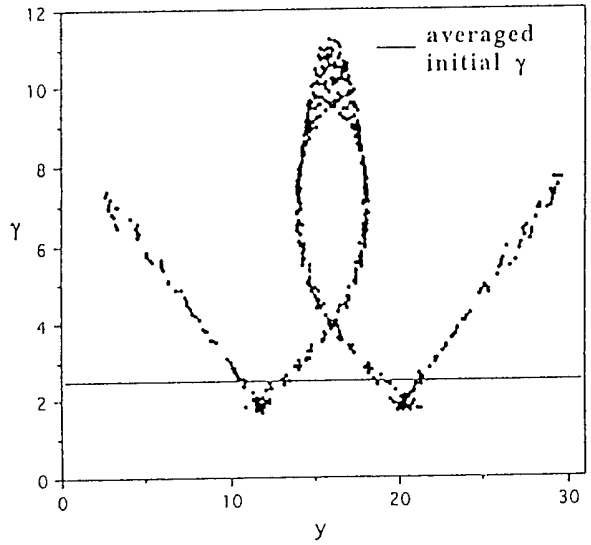

Fig. 2 A particle map by particle (PIC) simulation. The electron relativistic factor γ versus y at the maximum acceleration time. The initial electron speed is 0.9c on average, the beam initial temperature is 10 eV, and the maximum γ=11.5. A fraction of the electrons is accelerated well.

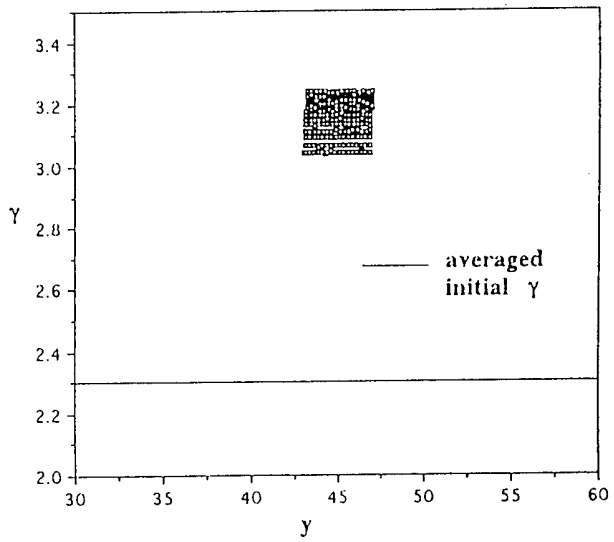

Fig.3 An ion map by particle simulation. The ion relativistic factor γ versus y at the maximum acceleration time. The initial ion speed is 0.9c on average, the beam initial temperature is 10 eV, and the maximum γ=3.24. The ions are accelerated well.

switch described above. In this paper we assume that the switching time is small compared with a characteristic time of the change in the magnetic field, based on the discussions presented above. Our analyses are performed immediately after the static magnetic field is decoupled and free from the circuit. For simplicity a spatially alternating magnetic field B_z, whose wave number is k, is employed instead of B_θ without loss of generality. The magnetic field B_z in an acceleration area induces an inductive electric acceleration field.

The magnetic field energy is converted to the energy of the inductive electric field E:

$$\frac{\partial E}{\partial t} = c\frac{\partial B_z}{\partial y}, \tag{1}$$

$$\frac{\partial B_z}{\partial t} = c\frac{\partial E}{\partial y}. \tag{2}$$

Incoming beam charged particles are accelerated by the inductive field E in the acceleration area. In addition to the acceleration, the magnetic field focuses the beam.

It is assumed that the static magnetic field is $B_z = B_0 sin(ky)$ and $E = 0$ at the time $t = 0$. As a solution [5] which satisfies these initial conditions, we obtain

$$B_z = B_0 sin(ky)cos(\omega t), \tag{3}$$

$$E = B_0 cos(ky)sin(\omega t), \tag{4}$$

$$\omega = \pm kc. \tag{5}$$

During the first period ($0 < t < \pi/|\omega|$), ions/electrons can be accelerated by this mechanism. We use this acceleration phase. The maximum acceleration field is B_0, and

$$\frac{\partial B_z}{\partial t} = -B_0 \omega sin(ky)sin(\omega t). \tag{6}$$

Therefore $|\partial B_z/\partial t| = B_0\omega = B_0 kc$, and the changing time τ in B_z is $1/(kc)$. For efficient acceleration, $\pi/(kc)$ should be comparable to or larger than the switching time duration mentioned above. When the wave number k is 1/3, $|\partial B_z/\partial t| \simeq 10^{10} B_0(Tesla)$ Tesla/s, which is rather large compared with that in a conventional induction accelerator.

On the other hand, the mechanism presented in this paper may be considered as pseudo-inverse process of the Weibel instability. [6,7] In the Weibel instability an anisotropic-plasma energy is converted to magnetic field energy: a magnetic field perturbation, whose wave number is k, causes a filamentation of the electron particle stream in a direction perpendicular to both k and B_z. The filamentation enhances the perturbation of B_z. During the growth of B_z an inductive electric field decelerates the electrons. Consequently the electron energy is converted to the magnetic field energy in the Weibel instability. In our mechanism, we use a pseudo-inverse process of the Weibel instability, although the acceleration takes place in a vacuum. The magnetic energy is converted to electron energy through the energy of the inductive electric field, which accelerates electrons.

Numerical Simulation for Inverse-Weibel-Instability Acceleration

A 2.5-dimensional (x, y, v_x, v_y, v_z) particle (PIC) simulation is also performed with the following initial and boundary conditions: a sinusoidal magnetic field ($B_0 sin(ky)$) is applied in the entire computation space domain (2.5cm in x and 5cm in y), where the

amplitude B_0 is 1Tesla. In both the x and y directions, 32 space grids are employed in the computation. The wavelength $2\pi/k$ is 5cm in the simulation. An electron beam, whose size is 3.12mm in width (along the x axis) and 5cm along the y axis, moves in the $+x$ direction and an average speed of $0.9c$ and a temperature of 10eV, and is located initially at the left side of the computational area. A cyclic boundary condition is used in both the x and y directions. The computations are performed until electrons pass through the computation space in the x direction. Figure 2 shows an electron map in the y-γ space at the end of the computation for the electron beam number density n of 10^{12} /cm^3. Here γ shows the relativistic factor. Figure 2 shows that some electrons are accelerated well by this mechanism. The maximum electron γ is 11.5, and the initial one is 2.30. For this particular case, the acceleration gradient is about 183MeV/m, which is a reasonable value, because the theoretical acceleration gradient from eq.(3) is $E = B_0 = 300$MeV at maxinum.

Ions are also accelerated well in this system with the following example parameter values: the computational space area is 0.5 m in the x direction and 1.0m in the y direction. The wavelength $2\pi/k$ is 1 m in the simulation. B_0 is 10 Tesla. An ion beam, whose size is 12.5 cm in width (along the x axis) and 25 cm along the y axis, moves in the $-x$ direction with an average speed of $0.9c$ and a temperature of 10eV, and is located initially at the right side and the center in y of the computational area. Figure 3 shows an ion map in the y-γ space at the end of the computation for the ion beam number density n of 10^9 /cm^3. Figure 3 shows that some ions are accelerated well. The maximum ion γ is 3.24, and the initial one is 2.30. For this particular case, the acceleration gradient is about 1.76 GeV/m.

Conclusions

We proposed a new method to obtain a high $\partial B/\partial t$ for an inductive charged-particle acceleration. The magnetic field, which is free from the electric circuit, induces a large acceleration field. The acceleration-gradient value itself is determined by the magnitude of the magnetic field employed and the wave number k. Our results showed that a high acceleration gradient can be obtained, compared with those of conventional accelerators. The present fast switching technologies make this method possible.

[1] Tajima, T. and Dawson, J.M., *Phys.Rev.Lett.* **43**, (1979)267.

[2] Kawata, S. , Maruyama, T., Watanabe, H. and Takahashi, I., *Phys. Rev. Lett.* **22**, (1991)2072, and references therein.

[3] Barnard, J.J. et al., *Laurence Livermore National Lab. Report*, **UCRL-LR-108095** (1991).

[4] Cooperstein, G. and Ottinger, P.F. (ed.), *IEEE Trans. Plasma Sci.* **PS-15**, No.6, (1987).

[5] If we use a cylindrically-symmetric system and an azimuthal magnetic field $B_\theta = B_0 j_1(\omega r/c)cos(\omega t)$ as a more practical example instead of B_z, we obtain $E = B_0 j_0(\omega r/c)\ sin(\omega t)$. Here j_n is the Bessel function of the first kind of integral order n, and r the radius. In this example the essential points of our results described in the text do not change.

[6] Kawata, S., *Jpn. J. Appl. Phys.* **34**, (1995)L523.

[7] Weibel, E.S., *Phys. Rev. Lett.* **2**, (1959)83.

HIGH CURRENT PULSED ION INDUCTOR ACCELERATOR FOR DESTRUCTION OF RADIOACTIVE WASTERS

S.A. Korenev, I.V. Puzynin, V.N. Samoilov, A.N. Sissakian.

Joint Institute for Nuclear Research,
141980, Dubna, Moscow region, Russia

Abstract. The project of high current pulsed linear ion this report. Accelerator consists of ion injector, system of separation on the charge and kinetic energy of ions, inductor inductor accelerator for applications is considered in the accelerating system, system of out put ion beam to air. Ion source with explosive ion emission uses as injector of accelerator, which can produce all kind of ions. System of separation includes pulsed magnetic system. Inductor accelerating structure including the inductors on the basis amorphous iron with inside magnetic elements for transport of pulsed high current ion beams.

INTRODUCTION

The high current ion beams are used for surface modification of different materials. The requests of many technologies consist in the increasing of kinetic energy of ion beam. The destruction of radioactive wasters presents large interest and in this case is necessary increasing of kinetic energy by ion beams. The linear inductor ion accelerator can be used. The research linear inductor ion accelerators [1,2] allow to design these machines. However, two tasks (injector and window for out put ion beam from vacuum chamber to air) is limited progress in the this field.

The project of linear ion inductor accelerator for different application is considered in the this report. The new type of injector on the basis of ion source with explosive ion emission and new construction of windows for out put ion beams is suggested in the proposal.

THE GENERAL STRUCTURE OF ACCELERATOR

The general block-diagram of linear ion inductor accelerator is given in Fig.1. Accelerator consists of ion injector, separation system, linear inductor accelerating system, system of out put ion beams from vacuum chamber to air.

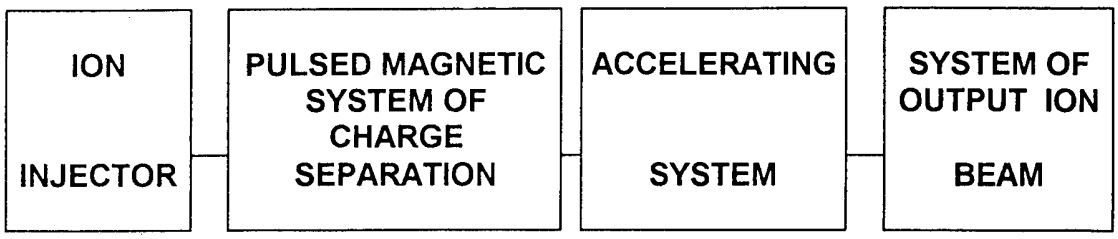

Fig.1. The general block-diagram of ion inductor accelerator

The ion injector on the basis of ion source with explosive ion emission allows to production of different kind of ion beams. Pulsed magnetic separation system separates ion beams on the charge and kinetic energy. The properties of explosive ion emission lead to separation of ion beams on these parameters.For supply pulsed magnetic will be use pulsed high current generator on the basis of LC- line with tyratron commutator. Inductor accelerating system on the basis of amorphous iron allows to receive stored energy for accelerating ion beams and gradient of electrical field 20 kV/cm [2]. The system for out put ion beam from vacuum chamber has Ti or Be foils with special coatings.

The main parameters of linear inductor accelerator for application has got next parameters:

- kinetic energy 20 - 50 MeV;
- pulsed beam current 1 - 200 A;
- pulse beam duration 100 nsec;
- repetition 5 - 50 Hz;
- kind of ion beams: all conducting materials
- length 50 - 75 m.

ION INJECTOR

A detailed discussion of pulsed explosive emission is reviewed in detail in refs. [3] only the main principles are considered here. A plasma (emitter of ions) is formed on the surface of the anode (on the plasma initiator) and then to extract ions from by applying a single positive voltage pulse. The main mechanism for maintaining the anode plasma is follows. Initially there ia a condition of auto-emission from the heating by ion current of points, micro-heterogeneities on the surface of anode, and electron emission from cathode. The atoms in the vapor are ionized and form an anode plasma which is the emitter of ions so that an ion beam can be extraction from this plasma, and the effects promote the formation of a stable vacuum discharge.

For operation of a planar ion source on the bases of explosive ion emission, the intensity of the electric field E in the diode must exceed the threshold E needed for forming the anode plasma:

$$E = KU/d > 10^7 \text{ V/cm}, \qquad (1)$$

where: U is the voltage applied to the diode, K is the amplification factor of the electrical field on the initiator determining its geometry, and d is the distance between anode and cathode.

For supply of ion source we are used pulsed high voltage generator by Arkad'ev-Marx type with next parameters:

- voltage 300 - 700 kV;
- pulse duration 300 - 500 nsec;
- repetition 1-5 Hz;
- stored energy 10 - 50 J.

Also as a high voltage generator can be used inductor accelerating section.

Ion source consists of vacuum chamber, high voltage insulator, anode electrode with initiator of anode plasma, extractor electrode and beam current measurement system on the basis of current transformer (Rogovsky transformer), see Fig.2.

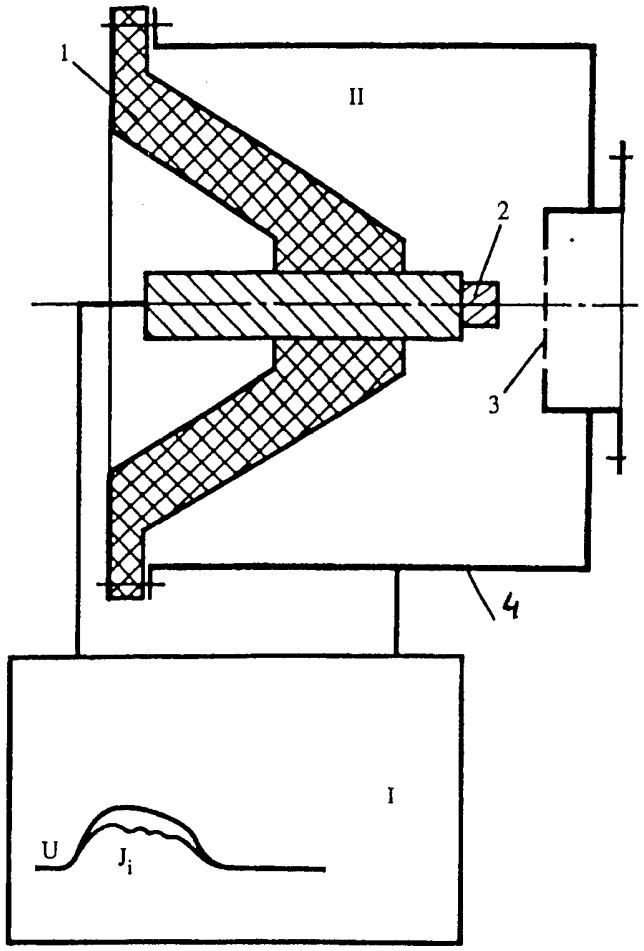

Fig.2. Block-diagram of an ion injector: I - Arkad'ev-Marx generator; II - ion source: 1 - high voltage insulator; 2 - anode plasma initiator; 3 - extractor; 4 - vacuum chambe

The kind of ion beams determine by materials of initiator of anode plasma. This ion source can be use for production of different ions of conductivity materials: metals, ceramics. For example, the emission characteristics of ion source is shown in Fig.3.

FOIL'S WINDOW FOR OUT PUT ION BEAM

The diamond-like coatings with both sides onto Be or Ti foil allow increasing life-time to 10 times in the comparison with clean foil.

CONCLUSION

This proposal has primary test of few units.

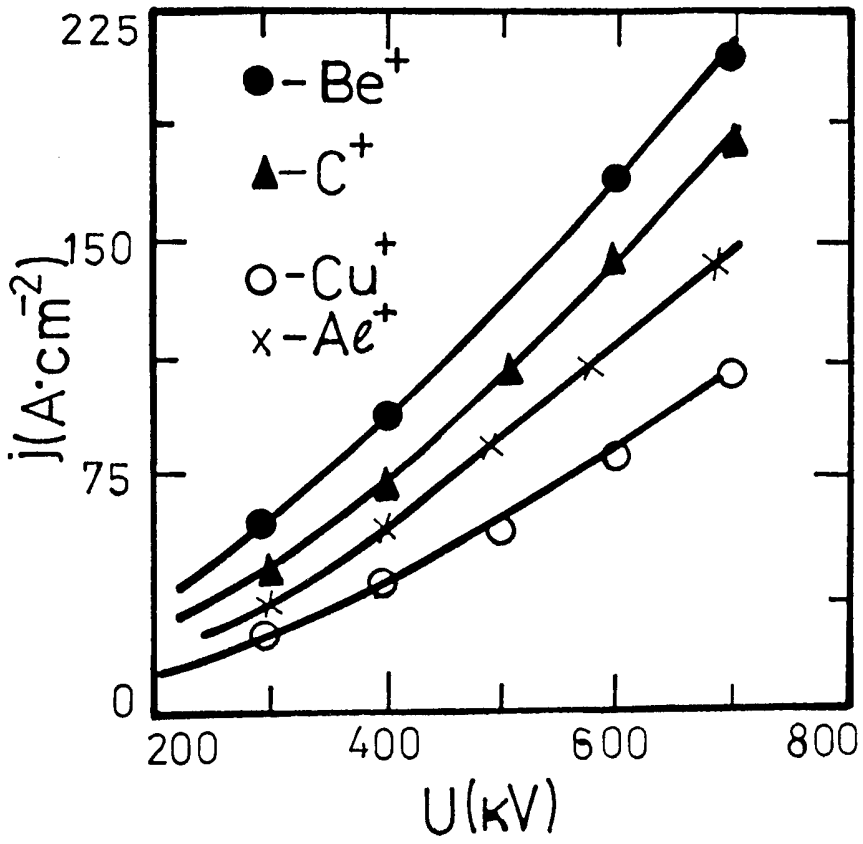

Fig.3. Emission characteristics of ion source for few kind of ion beams.

REFERENCE

[1] Keefe D. Proton Accelerator Conference, Proc. (1976), pp. 127-132.
[2] Vahrushin Yu.P., Anatsky A.I. Linear inductor accelerators. Moscow, tomizdat, (1978).
[3] Korenev S. Nuclear Instruments and Methods in Physics Research B80/81 (1993), pp. 242 - 247.

PROCESSES IN A DENSE LONG-PULSE ELECTRON BEAM FOCUSED ON A SOLID TARGET.

A.V.Arkhipov, G.G.Sominski

St.Petersburg Technical University,
29, Polytekhnicheskaja ul., St.Petersburg, 195251, Russia

Recently a number of applications appeared where a long- pulse (duration more then 0.1 ms) electron beam had to be focused on a solid surface to obtain energy density 1 kJ/cm^2 or more [1,2]. It is well known that in these conditions a jet of partially ionized sputtered target matter propagates into the beam and shields, to some extent, the surface from the energy flux. But the self-consistent process is too complicated to obtain reliable values of jet parameters, shielding efficiency and surface etching rate otherwise then experimentally.

We investigated such processes in a special experimental setup (see also [1]). Its schematic layout is presented in Fig.1. Electron beam energy and current were varied over a broad range - 10..40 keV and 0.1..4.5 A correspondingly. The beam was formed in a Pierce gun and after additional two-stage magnetic compression struck a graphite target in less then 1 mm^2 spot. Thus power density up to 20 MW/cm^2 was available. Instead of focusing the beam upon the target it was possible also to disperse it over a large- area collector, which was useful for selecting target- caused phenomena among others. Due to multi-stage compression system and long (~1 m) drift tube the electron gun was rather effectively protected from plasma influence and usually current pulse duration (up to 5 ms) was not limited by gun gap breakdown.

In our experiments in single-pulse regime was obtained the following set of beam parameters and signals: voltage on the gun gap; currents of cathode, target and electrodes forming a transportation channel (TC); signals of X-ray gauges located near

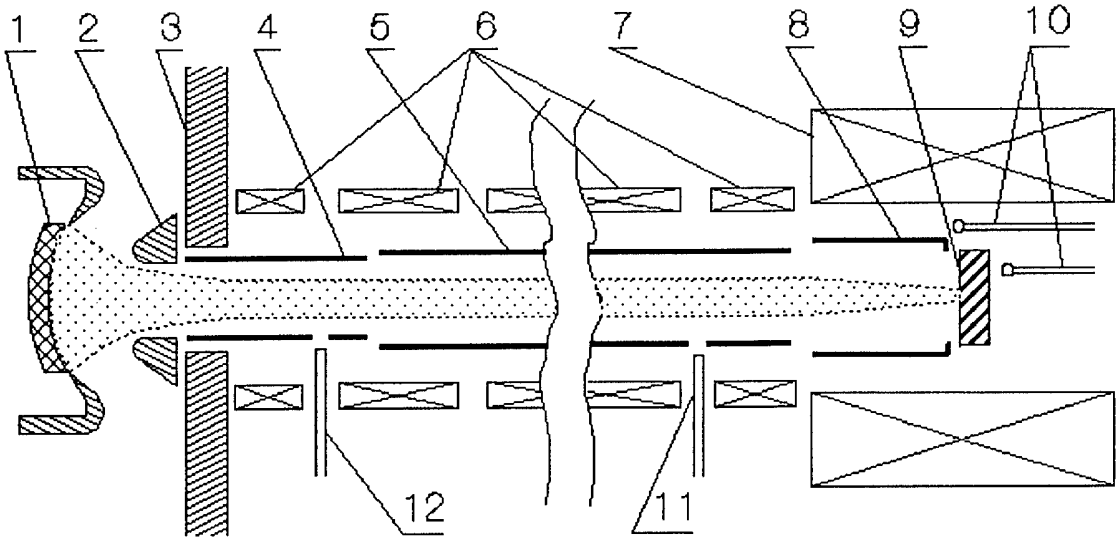

Fig.1. Diagram of the experimental device.
1 - thermionic cathode; 2 - anode; 3 - shield; 4 - section of TC inside the magnetic shield; 5 - drift tube; 6,7 - solenoids; 8 - large-area collector; 9 - target; 10 - X-ray gauges; 11,12 - light guides.

the target, which we connect with a flow of fast electrons on the target surface; light radiation of plasma from different parts of transportation channel.

In shots with comparatively small current (less then 0.5 A) all current was divided between two electrodes - the target I_t (or the collector, if the target solenoid was not connected) and a section of TC situated inside the magnetic shield (4 in fig.1) I_e. The proportion between these two currents depended on the magnetic field magnitude and distribution, so we attribute I_e to electrons reflected by one of magnetic mirrors.

But for larger beam currents the evolution changed considerably and three stages were traceable in oscillograms (Fig.2). In the first period the character of processes in the beam was the same as for small current (this stage is marked with sign "I" in the Fig.2). The duration of this stage depended on beam current and magnetic field parameters and thus on current distribution over the system electrodes.

Later (stage II in Fig.2) a current appeared on the main part of the drift tube (5 in Fig.1). The sign of the current shows its ion nature. Simultaneously a dip in the target current and a rise in the magnetic shield electrode currents were observed. But signals of X-ray gauges didn't confirm the fall of fast electron flow to the target. And during this stage (and the next stages too) electrode currents could be easily redistributed among the electrodes by application to them small (about 50 V) voltages. So we think that the current signals after the stage I were strongly affected by the flows of secondary particles and did not reflect reliably the current of primary electrons.

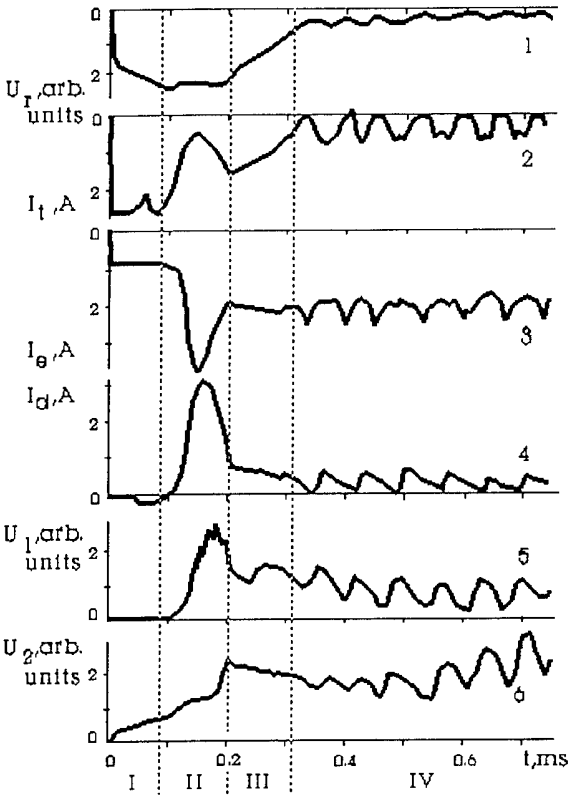

Fig.2. A set of oscillograms obtained in a 30 kV, 3.5A current pulse with the beam focused on the target.
1 - X-ray gauge signal; 2 - target current; 3 - current to the TC section inside the magnetic shield; 4 - drift tube current; 5 and 6 - signals of light recievers connected to light guides 11 and 12 correspondingly.

There are a number of possible sources of secondary charged particles (electrons and ions) in the beam system: ionization of residual gas and sputtered matter, plasma generation on bombarded surfaces, secondary electron and electron-induced ion emission, etc. On our esteems, full beam neutralization even with only residual gas ions had to occur at our vacuum conditions (~10^{-6} Torr) in less then 100 μs, independently on the beam current. But in experiment the difference between the cases of large and small current was qualitative. And we attribute the difference to the interaction of the beam with bombarded electrodes - generation of dense collector plasma and intense sputtering with ionization of sputtered matter. Dense target plasma formation and propagation through the transportation channel during the stage II was observed (in the case of focused beam) in the signals of light receivers (U1 and U2 in Fig.2). If the beam was not focused on the target, the light in the target part of TC was not

observed which indicates that in this case dense target plasma didn't form. But defocusing of the beam had not altered the character of the stage II processes. So we are inclined to consider that in the defocused beam the current evolution during the stage II was determined, at least in the defocused beam, by the influence of the plasma born on the magnetic shield electrode 4. The fact of plasma generation on this electrode was confirmed by the traces of etching found later on its surface. Another reason for this conclusion is that the "quiet" stage I was the shorter the greater was the magnitude of magnetic field in the TC and thus the greater was the current to magnetic shield electrode.

The mechanism of influence of this plasma on the processes in the beam is not yet clear. The plasma could act here simply as a more intensive (compared with gas ionization) source of secondary particles. It would result in the rise of the beam potential that will push ions in radial direction onto the drift tube. (The positive potential with magnitude of a few Volts would be enough for ions to overcome the magnetic field).

The other possibility is in effect of the plasma formation on electron optics of the system. Magnetic field lines in the region were the TC passes the magnetic shield come onto the surface of electrode 4 (Fig.1). But slow secondary electrons moving along the lines could be repelled by electrostatic field of the Pierce gun beam cross-over situated in the same region. Thus the electrons would be left in the beam and would hold ions there. The ion accumulation in the cross-over, in its turn, could be ineffective due to the gun gap field drawing action. Thus ions and secondary electrons both would accumulate in the beam until dense plasma would affect the field distribution and allow slow electrons to reach the electrode 4. Thereafter the stored plasma would decay with slow electrons moving along magnetic lines to the magnetic shield electrode and ions moving in transverse direction to all the TC parts. Thus in this hypothetical model the burst of secondary currents on various electrodes observed during the stage II finds its explanation.

The typical value of the stage II duration was about 100 μs. If the beam was dispersed over the large-area collector then after the end of this stage signals usually stabilized and this stability lasted for all the rest of the beam current pulse. Magnitudes of the signals here differed from their initial values because of contribution of the secondary flows. But in the cases of the beam current exceeding 2A a low-frequency (~20 kHz) modulation of all signals was observed (it can be traced in Fig.2 during the stage IV also). In [5] this modulation is described in detail.

For the case of the beam with considerable current focused in a small spot on the target one more phenomenon was observed. The flow of primary electrons to the target fell in value up to 10 times (stage III in Fig.2). It was registered in current and X-ray signals both. This fall we attribute to the shielding of the target by the dense target plasma and sputtered matter. The studies of one-shot beam prints on a graphite target had shown that the print forms depended on the duration of the current pulse. If the pulse was interrupted while plasma processes were not yet fully developed the print was solid (Fig.3a) and the target etching rate was about 10^{-5}g/J or less. But if the pulse was turned off later (during the stage IV), the beam print shape became annular and its radius and the etching rate value considerably increased (Fig.3b).

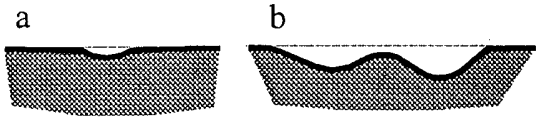

Fig.3. Forms of single-shot beam prints obtained in short (a) and long (b) current pulses.

Thus in this paper the results obtained in experiments with a dense medium-energy electron beam in regime of long single pulses are presented. When the beam was focused on a target, power density up to 20 MW/cm^2 was available. Specific processes caused by dense flows of secondary particles and plasma were observed and studied. Rather effective target shielding occurred when density of energy dose on the target reached the value of about 1 kJ/cm^2. The target plasma and sputtered matter, that caused the shielding, affected the beam structure also.

[1] Bazylev B., Landman L., Wurz H.: Proc. of Conf. on Phys. and Technol of Plasma, Minsk,1994, Pt.2, p.451-452.
[2] Milora S.L.: J. of Vac. Sci., 7 (1989), p.925-937.
[3] Arkhipov A.V., Sominskii G.G.: Tech. Phis. Lett., 20 (1994), p.431-432.
[4] S.P.Bougaev, V.I.Kanavets, V.I.Koshelev, V.A.Cherepenin. Relativistic Microwave Multiwave Oscillators, Novosibirsk, "Nauka", 1991 [in Russian].
[5]. Arkhipov A.V., Bogdanov L.Yu. at el.: Izv. Vyssh. Uchebn. Zaved. Appl. Non-Linear Dynamics. 3 (1995), Pt.1-N.4, Pt.2-N5. [in Russian].

APPLICATION OF AN INTENSE LONG PULSE ELECTRON BEAM FOR INVESTIGATION OF ITER DIVERTOR MATERIAL EROSION

V.Engelko, A.Andreev, O.Komarov, V.Kovalev, B.Luyblin
Efremov Institute of Electrophysical Apparatus, St.Petersburg, 189631, Russia
H Würz
Forschungszentrum Karlsruhe GmbH, INR, P.O.3640, Karlsruhe, D-76021, Germany

To test ITER divertor candidate materials and to check the physical models for simulation of the divertor material erosion under plasma disruption conditions the measurements of target plasma dynamic and material erosion have to be performed. The energy fluxes with pulse duration ≥ 100 μs and power densities ≥ 5 MW/cm^2 are required. The paper describes the facility ELDIS producing an electron beam which parameters are close to required ones. The facility consist of three main parts: vacuum diode with multipoint explosive emission cathode, accelerating tube, and magnetic compression channel. Kinetic energy of electrons is 60-140 keV, maximum power density at the target 5 MW/cm^2, pulse duration - up to 60 μs, beam diameter at the target - 1.2 cm, magnetic field induction at the target - up to 4 T. The results of the measurements and calculation of electron. beam parameters and some results of the target plasma dynamics and target erosion investigation are given

Introduction

One important task of the ITER research activity is the study of divertor components erosion under plasma disruption and instability conditions. At the Efremov Institute, St.Petersburg, the disruption erosion of divertor materials is investigated applying the electron beam facility ELDIS as a source of the energy flux. A powerful electron beam is a rather convenient instrument for such investigations because its parameters can be determined with high accuracy and can be controlled. To perform experiments under clear conditions not only integral beam parameters should be known but also angle distribution of electrons because it influences significantly on the density of the energy deposition into the target. The paper describes the facility and presents results of the measurements and calculation of beam parameters and some results of investigation of the beam-target interaction.

The ELDIS facility was build and the disruption simulation experiments are carried out in collaboration between the Forschungszentrum Karlsruhe, Germany and Efremov Institute, St.Petersburg, Russia.

Description of the facility

The scheme of the ELDIS facility is shown in Fig.1. It consists of the following main components: the vacuum diode with a multipoint explosive emission cathode (1), the accelerating tube (2); the compressing channel (3), the target chamber (4). The use of the accelerating tube allows to vary kinetic energy of electrons in the range of 60-140 keV. Pulse duration is controlled with the step of 1 μs. The power density at the target is increased by compressing of the beam downstream increasing magnetic field. Magnetic induction at the target position is 4T. This value is close to typical magnetic induction in the ITER divertor region.

The ELDIS facility is equipped with the diagnostic apparatus to monitor the parameters of both the electron beam (accelerating voltage, beam current, current density, radial distribution of beam power density at a target, angular distribution of beam electrons, power density temporal dynamics in a time) and the target plasma (density, temperature, expansion velocity). Target material erosion is measured by means of samples weighing before and after irradiation and also with the help of microprofilometer.

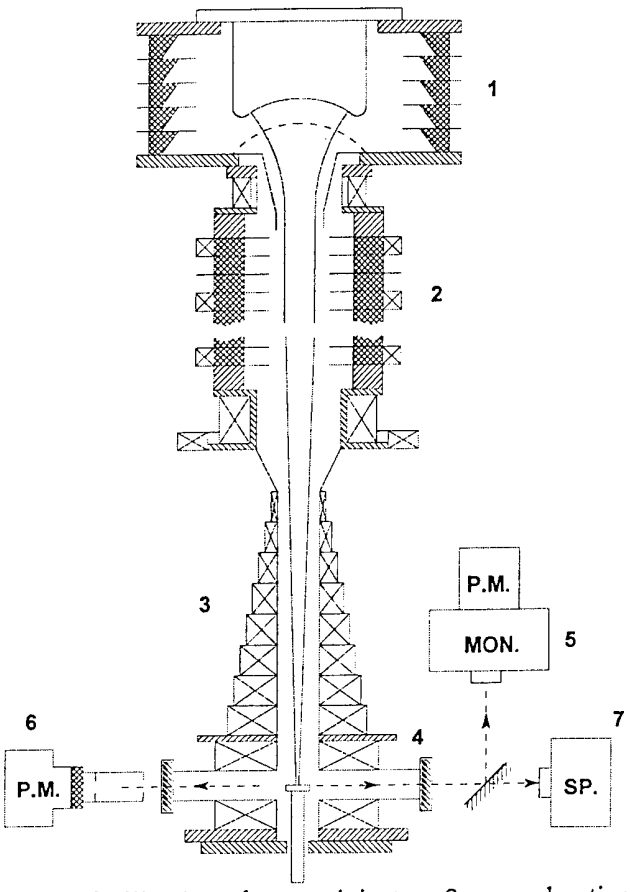

Fig.1. Scheme of the ELDIS facility:1 - electron injector; 2 - accelerating tube; 3 - compressing channel; 4 - target chamber; 5 - monochromator with photomultiplier; 6 - photomultiplier with interference filter; 7 - spectrograph.

Beam parameters

The peculiarity of the ELDIS facility is that because of use of multipoint cathode the beam is formed consisting of electrons rotating around magnetic force lines. In the course of the beam compression the transverse energy of electrons $W_\perp$ increases in accordance with adiabatic invariant $W_\perp/B$=const. This leads to decrease of the incident angles of electrons and therefore to decrease of the effective range (half width of the distribution of the energy deposition) of electrons in a target matter. So, because of transformation of the big part of electron kinetic energy into transverse motion one can expect that the density of the energy deposition into the target will be increased.

In order to determine the distribution of the energy deposition it necessary to know the angle distribution of electrons. It was calculated numerically with the help of the code POISSON-2 [1]. Fig.2 shows the examples of the calculated angle distributions.

The results of calculations were verified by means of the measurement of the dependence of the current to the target on target position in the compressing channel and measurement of the penetration of electrons trough the collimators with certain diameter and length being varied [2]. Both the current to the target and penetration of electrons depend strongly on the angle distribution of electrons.

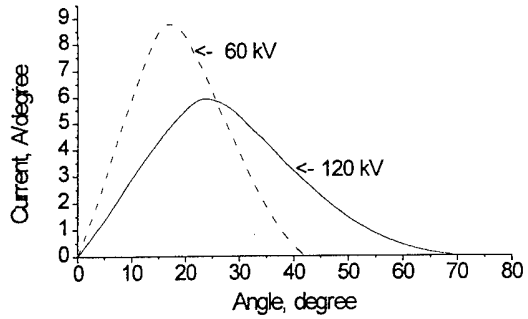

Fig.2. Calculated angle distribution of electrons at kinetic energy of 60 keV and 120 keV.

Comparison the results of measurements and calculations showed that the method of the angle distribution calculation is correct.

Beam power density at the target was determined by means of the measurement of the currents density distribution and also from the dependence of the diameter of the melted zone on the metal target on pulse duration. The radial distribution of the power density determined by means of the second method is shown in Fig.3. Maximum value of the power density near the beam axis is 5 MW/cm^2.

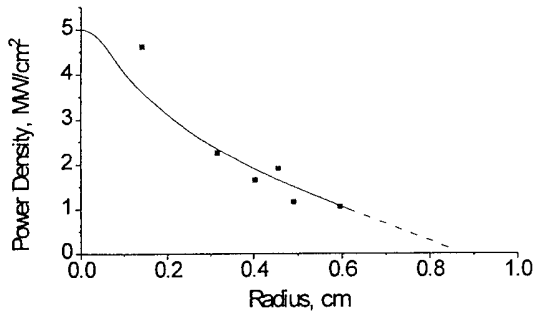

Fig.3. Radial distribution of power density on the target. Points represent experimental data.

Using the angle distribution and power density one can calculate the distribution of the energy deposition into the target. Results of such calculations performed by means of Monte-Carlo method are shown in Fig.4. The energy deposition distribution depends on electric and magnetic fields configuration in the cathode region, accelerating voltage, density of the cathode points. Maximum density of the energy deposition - around 50 kJ/g - is achieved when accelerating voltage is 60 keV and the density of the cathode points is 4 cm^{-2}.

Beam interaction with target

The beam-target interaction was investigated for the following target materials: three types of graphite based materials - RG-Ti-91, UAM-92-5D and UAM-93+0.1%B; cooper and tungsten. The following results were obtained.

The energy threshold for target plasma emergence is equal to 30 J/cm^2 for Cu, 65 J/cm^2 for C and 56 J/cm^2 for W. Plasma electron temperature is low: 0.7-0.8 eV for Cu and 0.5-0.6 eV for C. Density of the target plasma is approximately the same - (2-4*10^{16} cm^{-3}) for all materials investigated. Most likely the extent of ionisation does not exceed 10%. The beam-target interaction process takes place without a marked shielding effect.

The erosion rates for investigated materials are the following: RG-Ti-91 5μm (1.8 mg/cm^2); UAM-93+0.1%B - 12 μm (2.28 mg/cm^2); UAM-92-5D - 17 μm (1.8 mg/cm^2) ; W - 0.4 μm (0.75 mg/cm^2).

The comparison between the calculated distribution of the volumetric energy deposition with measured depth of the crater on the target allows to determine the threshold energy density, at which the target material starts to distruct. For the tested graphite-based material the threshold energy density was found to be around 10 kJ/g. This value is considerably less than that for graphite sublimation (59kJ/g for one-atom sublimation mode and ~ 30 kJ/g for three-atom mode). Thus, erosion of the graphite targets can not be explain by surface evaporation only. It is likely to be connected with the volumetric destruction when the energy density exceeds 10-12 kJ/g. Note, that similar result was obtained in [3].

A low threshold of the specific energy density leading to graphite destruction changes the notion of the factors affecting the divertor erosion.

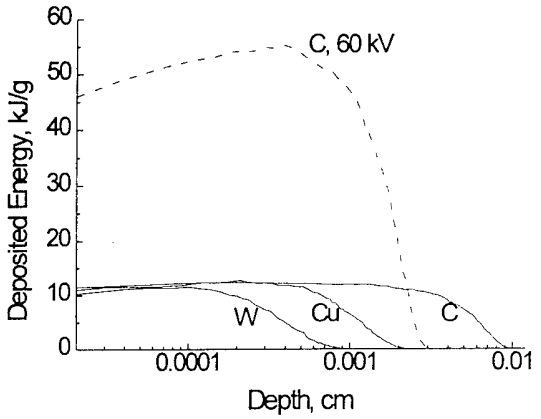

Fig.4. Distribution of the deposited energy into the different targets (W, Cu, C) for electron kinetic energy of 120 keV and into the graphite target for electron kinetic energy of 60 keV.

In particular, the role of high-energy plasma electrons increases because of a low screening of such electrons by shielding layer. At the plasma temperature of 10 keV electrons with an energy higher than 60 keV convey to the divertor surface about 5MJ/cm^2. Such energy density can cause an essential erosion of graphite - 20-30 μm per pulse at the distraction threshold of around 10 kJ/g.

Comparison of the expected energy deposition into divertor material by high-energy plasma electrons with one produced by the ELDIS facility shows that this facility can simulate the energy load caused by such electrons at the plasma electron temperature ~ 10 keV.

References

[1] **V.T.Astrelin, V.Ya.Ivanov**. Computer code for calculation of characteristics of intense relativistic particle beams // *Avtometriya* (USSR), 1980, No.3, PP.92-99 (in Russian).

[2] **Arzhannikov A.V., Koydan V.S., Loginov S.V.** Determination of the angle spread of magnetised relativistic electron beam from its passing through micro-holes // *Equipment and Technics of Experiment* (USSR). 1983, No.4. PP.36-38, (in Russian).

[3] **V.Engelko, A.Andreev, T.Burtseva, O.Komarov, V.Kovalev, B.Ljublin, H.Würz**. Investigation of the candidate divertor materials erosion at the powerful electron beam // (to be published in *Fusion Materials*).

[4] **V.T.Astrelin** at al, Proc. 18th Symp. on Fusion Technology, Karlsruhe, Germany. 1994. P.371 (Elsevier, Amsterdam, 1995).

ELECTRON-BEAM SUSTAINED GLOW DISCHARGE IN A N_2+CO GAS MIXTURE AT CRYOGENIC TEMPERATURE

V.V.Azharonok, I.I.Filatova, N.I.Chubrik, V.D.Shimanovich, V.A.Gurashvili*, V.N.Kuzmin*, N.G.Turkin*, A.A.Vaselenok*

Institute of Molecular and Atomic Physics of Belarus Academy of Sciences, F.Scaryna Avenue 70, Minsk, 220072, Belarus
**Troitsk Institute of Innovative and Thermonuclear Investigations, Troitsk, Moscow Region, 142052, Russia*

Abstract

A quasi-continuum electron-beam sustained glow discharge in a flow of N_2+CO gas mixture at cryogenic temperature was studied by the emission spectroscopy methods. Effective values of electron-ion recombination and rate of electron adhesion to electronegative molecules ($Fe(CO)_5$, $Ni(CO)_4$, H_2O) present in the discharge have been determined in dependence of reduced electric field strength E/N.

Introduction

A non-self-sustained glow discharge in a flow of molecular gases ionized by a high power electron beam is widely used to excite active medium of plasmachemical reactors and powerful CO-lasers due to the high degree of the vibrational excitation of molecules in the discharge plasma. Degree of vibrational non- equilibrium of the discharge plasma depends in many respects on plasma's neutral component temperature T_g as well as on free electron loss processes as a result of electron-ion recombination and electron adhesion to electronegative molecules. An influence of impurities of O_2, H_2O, C_3F_6 molecules on plasma conductivity in CO-laser was studied at T_g=100 K [1]. Electron adhesion processes to $Fe(CO)_5$, $Ni(CO)_4$ molecules was considered at T_g=300 K [2].

The present work is devoted to investigations of gas temperature T_g fields in a non-self-sustained glow discharge in a flow of N_2:CO= 10:1 mixture at cryogenic temperature and to studies of the processes determining discharge plasma vibrational non-equilibrium.

Experiment

The experimental apparatus have been described in detail in our previous publication [3]. The discharge was operated in a discharge chamber with an equipotential netted anode and a segmented cathode disposed at an angle of 6° to each other. A distance between electrodes L at the chamber entrance was equal to 5 mm. The gas mixture was pre-ionized by electron beam with energy E_e of 100 keV. Values of total pressure and speed of the mixture pumped through the discharge chamber were equal to 60 Torr and 100 m/s, correspondingly. Gas

temperature T_g of the mixture at the chamber's entrance was maintained at 100 K. The discharge duration was varied in the range of 0.2-20 s.

Emission spectra were registered in the range of $\Delta\lambda$=200-700 nm with spectral resolutions of 0.1, 2.4 nm and a spatial resolution of ~0.1 mm. To measure gas temperature, a method was used [3] of registering the unresolved rotation structure of an electronic-vibrational bands of diatomic molecules. As pirometric bands, those of the 2+ system of N_2 and 1- system of N_2^+ were used.

Effective values of electron-ion recombination β_{ei} and rate of electron adhesion ν_e have been determined in the range of reduced electric field strength variation $E/N=(0.8 - 1.2) \cdot 10^{-16}$ V cm^2 using the balance equation

$$q_e = \nu_e \cdot n_e + \beta_e \cdot n_+ \cdot n_e$$

(under condition of $n_- << n_e$), where q_e is the measured value of the rate of working medium ionization by the electron beam; n_-, n_+ and n_e are the concentrations of negative ions, positive ions and electrons, correspondingly.

Results and discussion

The N_2+CO plasma spectrum in the investigated wavelength range $\Delta\lambda$ includes mainly molecular bands of N_2 second positive, N_2^+ first negative, CN violet, C_2 Svan systems, NO β-system and FeI, NiI atomic lines. The most likely mechanisms of NO, CN and C_2 molecule formation in plasma are the interactions between vibrationally excited N_2(X,V"), CO(X,V") molecules and products of their dissociation leading to degradation of N_2+CO mixture. Presence of FeI and NiI atoms in plasma testifies that in the discharge the decomposing takes place of $Fe(CO)_5$ and $Ni(CO)_4$ molecules which are usually formed in metal balloons at CO pressure of approximately 100 atm.

Axial distributions of radiation plasma intensity and gas temperature T_g are ingomogeneous (fig. 1, 2). The temperature T_g values are equal to 670 K near the

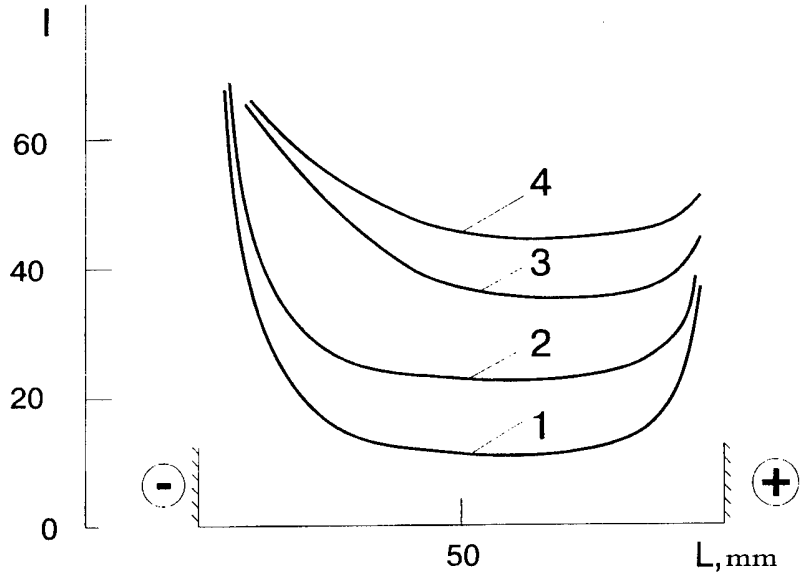

Fig. 1. The emission intensity of the non-self-sustained discharge N_2+CO plasma along the electrode gap: molecular bands of N_2 (1); N_2^+ (2); C_2 (3), CN (4)

cathode, 500 K near the anode and 120 K in the center of the electrode gap (fig.2). In the vicinity of electrodes the discharge energy goes mainly to excitation of electronic states of N_2, N_2^+, CN, C_2 molecules (fig.1).

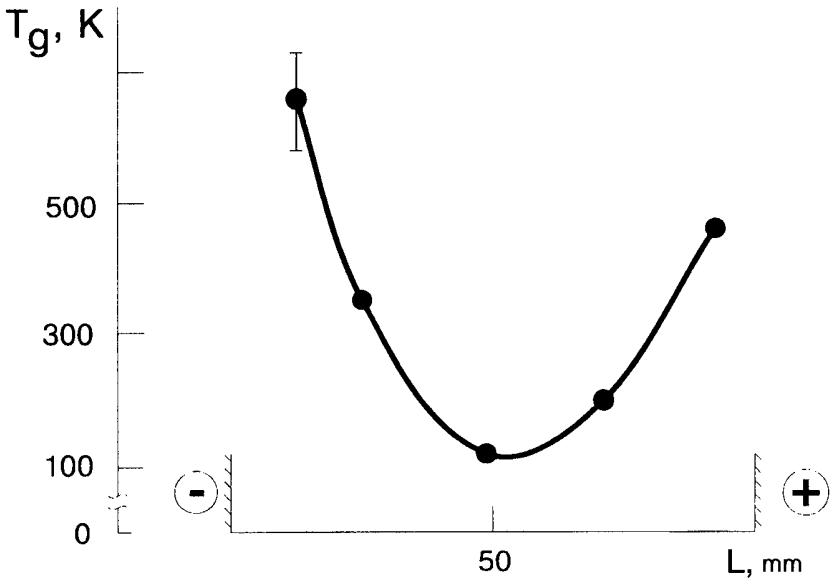

Fig. 2. The N_2+CO plasma's neutral component temperature T_g distribution along the electrode gap

The molecules can be deactivated by quenching at intermolecular collisions followed by essential heat releasing. In the central zone of the electrode gap the main portion of the discharge energy is utilized to excite vibrational levels of N_2 and CO molecules ground state ($X^1\Sigma$). Therefore, the radiation intensity of N_2, N_2^+ molecules is lower in the center of the electrode gap rather then near electrodes. By contrast with it the radiation intensity of CN and C_2 molecules does not practically change along L. This is due to high efficiency of quasi-resonant energy exchange between vibrationally excited $N_2(X,V''>9)$, $CO(X,V''>10)$ molecules and $C_2(X, V''=0)$, $CN(X, V''=0)$ molecules being in the ground electronic state [4, 5]:

$$CO(X,V''\geq 10) + C_2 \rightarrow CO(X,V'') + C_2(d^3\pi),$$
$$CO(X,V''\geq 10) + CN \rightarrow CO(X,V'') + CN(B^2\Sigma),$$
$$N_2(X,V''\geq 12) + CN \rightarrow N_2\ (X,V'') + CN(B^2\Sigma).$$

Evaluations of energy defects between $N_2(X,V'')$ and $C_2(d^3\pi, V')$ have allowed us to establish that the following mechanism of quasi-resonant excitation of $C_2(d^3\pi)$ molecules is possible in the discharge in the N_2+CO mixture:

$$N_2(X,V''\geq 9) + C_2 \rightarrow N_2\ (X,V'') + C_2(d^3\pi).$$

Inhomogenety of molecular bands radiation intensity and gas temperature T_g gradient along the electrode gap can lead to rise of the discharge instability and to an exchange of environment optical properties in the direction of electric current. In the case of discharge duration increasing (20 s) a widening of the near-anode zone to the discharge center has been observed. Simultaneously the

stratification of the discharge along the electrode gap near the anode took place. There were three characteristic zones of plasma radiation intensity with dimensions of ~5 mm each. The discharge stratification was accompanied by modulation of electric current and voltage with a frequency of ~0.25 Hz. The most probable cause of the discharge stratification is the local reduction of the plasma conductivity resulting from processes of losing free electrons due to electron adhesion to electronegative molecules of impurities ($Fe(CO)_5$, $Ni(CO)_4$, H_2O) present in discharge and molecules of NO formed in plasma.

The table presents the β_{ei} and ν_e values measured at T_g =120 K in the N_2+CO mixture previously purified from the impurities down to the level of P^*/P~1 ppm, where P^* is a partial pressure of the impurities.

P^*/P, ppm	1			>50
$E/N \cdot 10^{-16}$, V·cm^2	0.6	0.7	0.8	0.8
$\nu_e \cdot 10^4$, s^{-1}	1.5	1.3	1.2	300
$\beta_{ei} \cdot 10^{-8}$, cm$^2 \cdot$ s^{-1}	0.6	0.7	0.8	60

For comparison the data of free electron lose rates in non-purified (P^*/P > 50 ppm) cryogenic mixture are given. At T_g=120 K the value of β_{ei} is the order of magnitude higher than that at T_g=300 K [2]. Purification of the mixture (from $Fe(CO)_5$, $Ni(CO)_4$ impurities) makes electron adhesion rate two orders of magnitude lower and allows specific energy contribution into discharge to be W/G=300-350 J/g at electron beam current density of j_e=(7-12) μA/cm^2. To achieve the same values of W/G for non-purified mixture the value of j_e=2 mA/cm^2 is required.

Conclusion

Processes of quasi-resonant energy exchange between CO and N_2 molecules and CN, C_2 radicals formed in the electron-beam sustained glow discharge in a flow of CO+N_2 mixture at cryogenic temperature play a vital role in the reduction of the vibronic excitation degree of the mixture.

Presence of electronegative molecules $Fe(CO)_5$, $Ni(CO)_4$ in the discharge plasma and the gradient of the plasma's neutral component temperature (ΔT_g ~ 550 K) along the electrode gap lead to the decrease of plasma conductivity and to the discharge stratification in the near-anode zone where the discharge sustained electron beam enters the discharge chamber.

[1] Shashkov V.M., Shchekotov E.Yu.: Rep. of AS USSR, **306** (1989) 1397 (in Russian).
[2] Center R.E.: J. Appl. Phys., **44** (1973) 3538.
[3] Azharonok V.V., Gurashvili V.A., Kusmin V.N. at all.: Plasma Phys. Rep., **19** (1993) 469.
[4] Grigor'yants G.M., Dymshits B.M., Ionih Yu.Z.: Optics and Spectroscopy, **65** (1988) 766 (in Russian).
[5] Taieb G., Leday F.: Canad. J. Phys., **48** (1970) 1956.

PROCESSING OF METALS BY POWERFUL ELECTRON BEAMS

Yu.I. Gofman

Kharkov State University, 4 Svobody sq., Kharkov 310077, Ukraine

Abstract

Treatment of metals by powerful relativistic electron beams is discussed. The quenching effects, recrystallisation, aging and other structural and phase transformations can be achieved depending on regime of irradiation. In principle, it permits to get also structural states of metal, which are impossible to get by conventional methods of heat treatment. Irradiation was found to decrease the recrystallisation threshold. Electric steel with unique magnetocontrasting structure, which decrease of electromagnetic loss, compositions "metal-glue-metal" based on low-carbon steel with high vibration absorption properties were obtained using irradiation, for example.

Introduction

One of the most actual problems in industry is the transition from conventional technologies to most efficient economical and ecological technologies based on progress in modern science and engineering. One of this perspective technologies is powerful relativistic electron beams treatment (PREBT) [1-4]. Effectiveness of this treatment method is connected with the deep penetration of relativistic electrons into a metal, unlike conventional methods of heat treatments, where heating is realized only on the surface. Electron beams energy in modern commercial technological accelerators have value up to one or several MeV and materials is no radioactive after such irradiation. These accelerators are of safe, reliable and easy-to-handle, completely suitable for industrial applications. Practical advantage is that the treatment can be conducted in air or, if it necessary, in a protective medium. Power of the electron beam have value from some kW up to 100 kW and at power ratings exceeding 3 - 4 kW, electron accelerators have a higher costeffectiness, than lasers [5].

Experimental methods

The investigation of recrystallization processes, aging and other structural and phase transformation in conducted after irradiation with 1.2 and 4.5 MeV electrons and included X-ray, metallographic, electric resistance, internal friction and microhardness studies. The effect of process temperature and electron flux on the relative microhardness after PREBT and model annealing which simulated the temperature conditions during irradiation is studies. Details of experimental described in [1-3].

Results and discussion

The dependence of relative variation of microhardness - reverse temperature (in Arrhenius coordinates) for constructional low - carbon steel strongly differ in irradiated steel and steel after conventional heat treatment (Fig.1) [4]. It is evident that PREBT is more effective in reducing the microhardness, and the effect depends from radiation dose. It confirm that specific radiation effect exist at this treatment. The results of metallographic studies correlate well with the microhardness data and provide a clear pattern of the recrystallization processes [1]: irradiation was found to decrease the recrystallisation threshold, its temperature range decreases and recrystallization occur at a higher rate.

Same results, which were described above , were obtained on electric steel [1]. Formation in electric steel unique magnetocontrasting structure, which consist of alternating zone of dynamo and transformer steel carry out by PREBT [6], besides. It obtain, if to include in process of production electric steel after second cold rolling short-term PREBT of zone in which must be isotropic structure, Application such type of steel lead to significance decrease of electromagnetic loss in transformers.

The improvement results was obtained for quenching processes by PREBT [1,7]. The high levels of hardness, wear resistance and ductility for tool steel produced by irradiation treatment are attributed to the dispersity of carbides increased that enhancing more intensive stopping of dislocations [1,8]. The radiation treatment can also be used for enhancing the properties of surface layers through alloying [1,9]. The alloying additives can be introduced directly during irradiation, or applied beforehand as a surface coat. After irradiation the increase of surface hardness was evidenced to a depth of 1,5 mm. The practice of surface hardening of such components of metallurgical units as rolls and related components becomes widespread recently. Speeded up aging of aluminum alloys and unusual phenomenon - decay its unsaturating solid solution observe under PREBT, besides [3].

Vibration- and sound-proof compositions "metal-glue-metal" for advanced drawing based on low-carbon steel with were obtained using scanning irradiation [2]. Study of amplitude-dependent internal friction show very high damping decrement for same composition (Fig.2). Such material is necessary for motor-car construction and building.

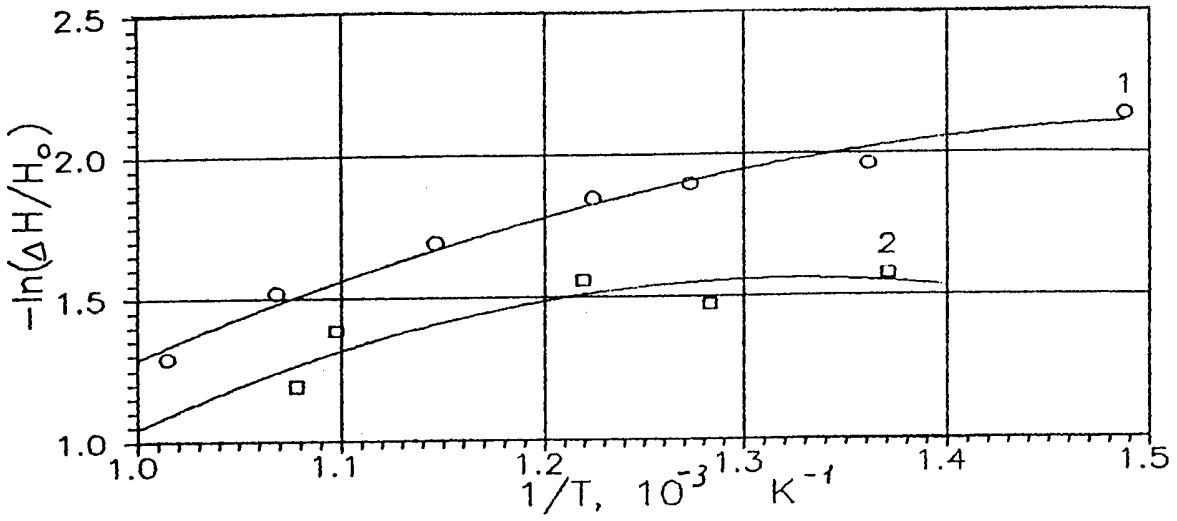

Fig.1. Effect of treatment on relative variation of microhardness of low-carbon steel: model heat-treatment (1); beam treatment (2).

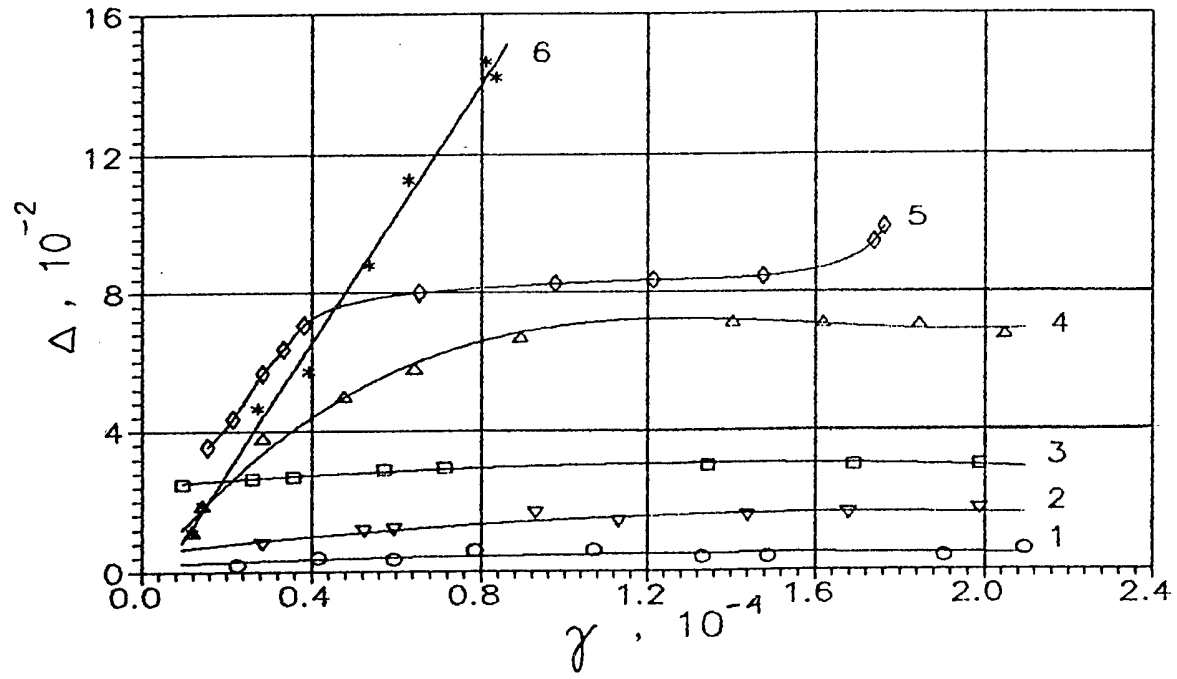

Fig.2. Dependence of damping decrement on the strain amplitude for low-carbon steel (1) and its laminated compositions with interlayers of adhesives: Moment-1 (2); BF-2 (3); EPC (4); cyacrine (5); PVA (6).

Conclusions

PREBT results show is the significant improvement of the performance characteristics of the irradiated metals and its products. The physical nature effects of PREBT may be connect with part of unstable Frenkel pairs [10]. The effect of PREBT described above clearly demonstrates the promise of this technology in industry for creation or modification of the large variety of metal and composite materials and manufacture of his products and the branch of application beam-heat treatment continued to extend.

[1] Yu.I. Gofman, :Russian Metallurgy. Metally, **3** (1993) 99.

[2] I.V. Frantsenyuk, L.I. Frantsenyuk, Yu.I. Gofman et. al., :Physics and Chemistry of Materials Treatment, **3** (1991) 319.

[3] Yu.I. Gofman, A.I. Kirdin, T.A. Kovalenko et al., :Russian Metallurgy. Metally, **6** (1994) 64.

[4] I.V. Frantsenyuk, L.I. Frantsenyuk, Yu.I. Gofman et.al., :Voprosy Atomnoi Nauki i Tekhniki. Ser. Fizika Radiatsionykh Povrezhdeniy i Radiatsionnoe Materialovedenie, **1/2** (1992), 39 (in Russian).

[5] I.L. Pobol, :Itogi Nauki i Tekhniki. Ser. Metallovedenie i Termicheskaya obrabotka, **24** (1990) 99 (in Russian).

[6] Yu.I. Gofman, I.V. Mizik, A.I. Kirdin, :Abstr . 3 Interbranch Conf. "Radiatizionnaya Fizika Tviordogo Tela", Sevastopol, (1993) 55 (in Russian).

[7] E.S. Machurin, G.I. Alekseev, A.G. Farobin et al., :Fizika i Khimiya Obrabotki Materialov, **5** (1986) 26 (in Russian).

[8] A.E. Braginskaya, V.N. Manin, A.V. Makedonskiy et al. :Fizika i Khimiya Obrabotki Materialov, **1** (1983) 8 (in Russian).

[9] G.V. Kraev, I.M. Poletika, L.V. Meita et. al. :Izvestiya Sibirskogo Otdeleniya Akademii Nauk SSSR, **4** (1989) 119 (in Russian).

[10] Yu.I. Gofman, A.I. Kirdin, O.G. Oleynik, :Russian Metallurgy. Metally, **6** (1995) 153.

USE OF CHARGED PARTICLE BEAMS FOR RESEARCH OF MECHANICAL BEHAVIOUR OF THERMONUCLEAR REACTOR FIRST WALL CANDIDATE - MATERIALS

Yu.I. Gofman

Kharkov State University, 4 Svobody sq., Kharkov 310077, Ukraine

Abstract

Systematic analysis of radiation creep experiments at cyclic irradiation have been provided, in first. Peculiarities of radiation defects generation in metals at various charged particle bombardment are analyzed. Original method which connect radiation creep and stress relaxation is described. Stress relaxation in aluminum under 100 MeV carbon ions bombardment and Al-Mg-Sc alloy under 5 MeV electron bombardment have been investigated. Effects cyclic irradiation is obtained. It is show that radiation creep under cyclic irradiation may be described of "climb plus glide" mechanism.

Introduction

Use of charged particle beams for research of radiation creep is one of the promising directions in study of mechanical behaviour of first wall of thermonuclear reactor materials. It makes possible to carry out experiments directly during irradiation in a wide range of the energy spectrum and the spatial distribution of the radiation defects and to carry out experiments in the conditions which can be controlled more efficiently in comparison with the reactor tests. On principle, can be obtained new physical information on the nature of radiation effects in such experiments in comparison with postradiation tests.

Radiation defects generation by various charged particles

Various charged particles are used for investigations of radiation creep: electrons, protons, deuterons, alpha-particles, ions [1]. It is also planned to carry out these experiments on more powerful accelerators [2]. Ions and electrons have different ionization losses and, consequently, the released energy in the irradiating specimen differs and defect generation sections also differs. It can be shown [1] that for a thin target, in which the energy loss of the particle is relatively small, the following equation for released energy on one defect is

$$\vartheta = \frac{A\, dE/dx}{N_o \rho_o \sigma_d}$$

where N_o is Avogadros number, A is the atomic weight, ρ_o is the density of the examined material, dE/dx is the ionization losses of bombarding charged particle, σ_d is the displacement generation cross-section.

Table 1 data for which were partially taken from [1,3] gives several parameters characterizing processes of radiation damage by carbon ions and electrons and its paths in Al.

Table 1. Parameters of radiation damage and path of carbon ions and electrons in Al

Particle	Energy, MeV	Ionization energy losses, MeV/cm	Displacement generation cross-section, b	Released energy on defect, MeV	Path, cm
e^-	5	4.2	12	5.8	1.1
C^{12}	100	3900	240000	0.27	0.015

Experimental method

Hard requirements are imposed on experimental equipment for carrying out mechanical tests during irradiation. Analysis of design features of these plant which was carried out in [2] and showed that it must consist of working cell; system for diagnostic and monitoring of beam; loading system; force measuring system; strain measuring system; system for temperature monitoring and unit for remotely operated control over experimental plant and recording of experimental data.

First-hand measurement or supershort elongiation on beam is very difficult problem. And the original experimental methods of radiation creep measurements is proposed [4]: radiation creep rate is determinated from the radiation stress relaxation curve. The stress relaxation tests were made under irradiation after preliminary load within elastic region. It can be showed [4] that radiation creep rate is

$$\dot{\varepsilon}_r = \Delta\sigma_r(t) \Big/ M \cdot t$$

where $\Delta\sigma_r$ is stress relaxation at time t, M is stiffness of the "sample-apparatus" system.

Stress relaxation in aluminum during 100 MeV carbon ions bombardment [1] and in Al-2%Mg with small addition of Sc during 5 MeV electrons bombardment [5] slightly above room temperature and stresses near yield point was investigated. Irradiation was not only stationary, but cyclic, yet, that take place in thermonuclear reactor. Aluminum and its alloys are considered thermonuclear reactor first wall candidate-materials [5].

The results and discussion

The radiation creep rate may be described as

$$\dot{\varepsilon}_r = K \cdot G \cdot \sigma$$

where K is module of radiation creep and radiation damage rate $G = \Phi \cdot \sigma_d$, where Φ is flux of particles and σ_d is displacement generation cross-section, σ is aplied stress.

Modules of radiation creep in stationary and cyclic carbon ions irradiation with period T = 9 s is adduced in table 2.

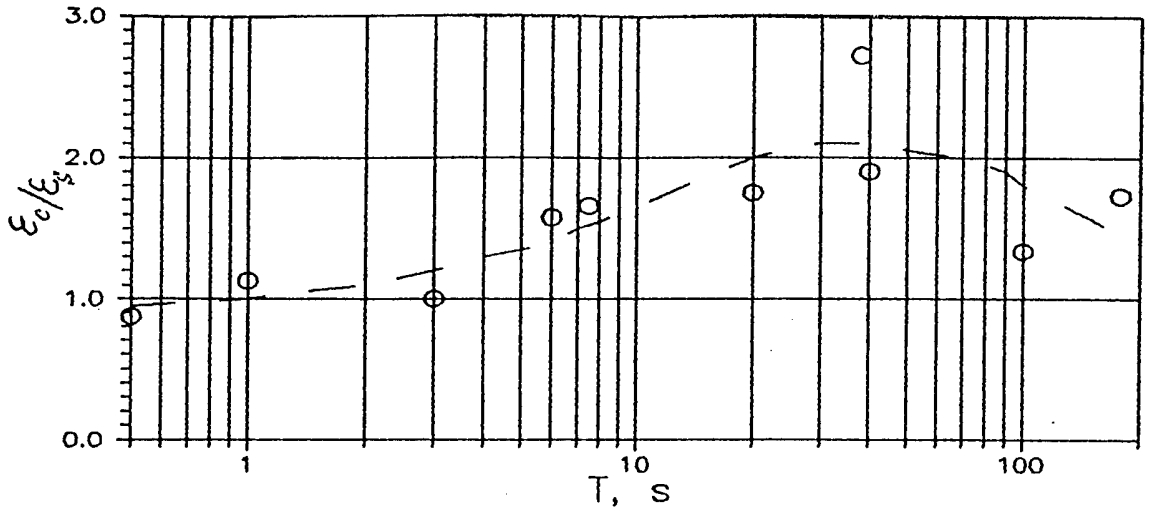

Fig.1. Dependence of radiation creep deformation ratio during cyclic (duty factor η = 0,5) and stationary electron irradiation on cycling period.

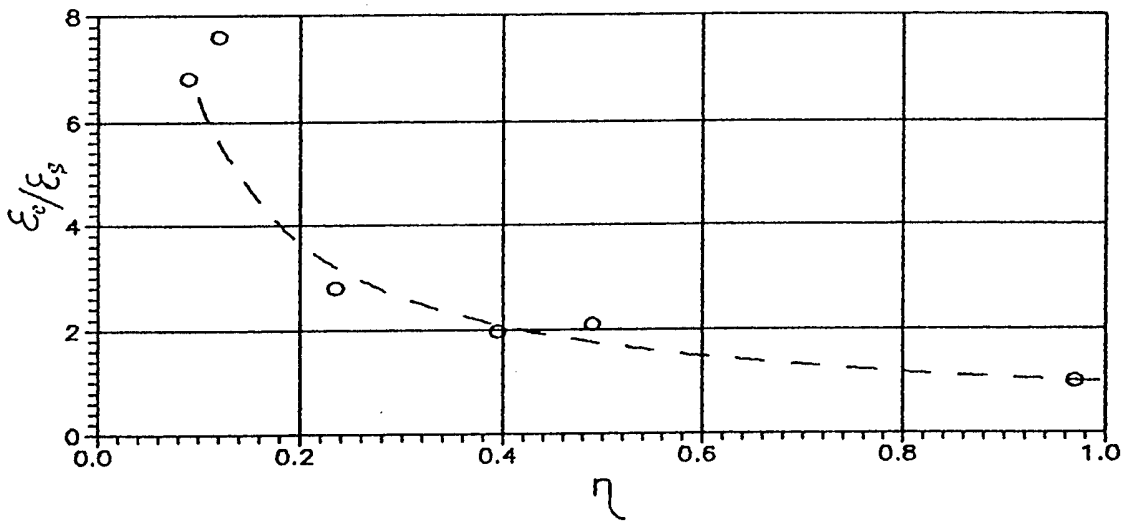

Fig.2. Dependence of radiation creep deformation ratio during cyclic (period T=40 s) and stationary electron irradiation on cycling duty factor.

Table 2. Modules of radiation creep at carbon ions irradiation.

Types of irradiation	Modules of radiation creep, (dpa* • MPa)$^{-1}$
Stationary	0.09
Cyclic	0.23

* dpa is displacement per atom

It may be seen that cyclic irradiation more than doubles radiation creep rate.

Dependence of accumulating during irradiation deformation on Al-Mg-Sc alloy reduce on integral flux of electrons on period of radiation cycling and its duty factor (radiation "on - off" time ratio) is shown at figure 1 and 2, accordingly.

It is shown that when cycling the irradiation, the creep accelerates in times corresponding with the dynamic preference time which is connected with outstripping interstitial flux in comparison with vacancies flux on sinks at unstationary radiation condition. Time of this outstripping - the dynamic preference time is [1,5]

$$t_d = (\rho_o \cdot D_v)^{-1}$$

where ρ_o is density of sinks, D_v is coefficient of vacancies diffusion.
And for diffusion parameters of aluminum [1,5] and dislocation density $\rho_d = 10^8$-10^9 cm^{-2} may be obtained t_d = 100-10 s, accordingly, that agree with irradiation period during which the radiation creep acceleration were observed for both ions and electrons irradiation.
It is very interesting that "radiation creep rate - frequency irradiation cycling" dependence have quasiresonant character. The decreasing character dependence of radiation creep rate on radiation duty factor indicates that the radiation creep mechanism is the "climb plus gliding" [6].

Conclusion

Systematic investigation of radiation creep at cyclic irradiation is provide on base of original method of radiation creep rate determination. Effect of dynamic preference is confirmed and is determined that controlling mechanism of radiation creep is "climb plus gliding".

[1] Yu.I. Gofman, I.I. Zalubovskiy, S.A. Pis'menetskiy, :Physics and Chemistry of Materials Treatment, **25** (1991) 14.
[2] Yu.I. Gofman, :Programma eksperimental'nyh issledovaniy na mezonnoy fabrike IYaI AN SSSR. Proc. 5 All-Union Simp., Moscow (1987) 370 (in Russian).
[3]. International Commission on Radiation Units and Measurements, Radiation Dosimetry: Electron Beams with Energies between 1 and 50 MeV, Report **35**, Bethseda (1984).
[4] V.D. Afanas'ev, E.D. Vorob'iov, Yu. I. Gofman et al., :Soobscheniya OIYaI, Dubna, **18-83-791** (1983) (in Russian).
[5]. I.V. Al'tovskiy, V.D. Afanas'ev, Yu.I. Gofman et al., :Voprosy Atomnoy Nauki i Tekhniki, ser. Fizika Radiatsionnyh Povrezshdeniy i Radiatsionnoe Materialovedenie, **3** (1990) 55 (in Russian).
[6]. E.P. Simonen, : J. Nucl. Mater., **113** (1980) 282.

MODIFICATION OF MATERIAL SURFACES BY THE PULSED ELECTRON BEAM FACILITY „GESA"

G. Müller, G. Schumacher, D. Strauß
Forschungszentrum Karlsruhe GmbH, Institut für Neutronenphysik und Reaktortechnik,
Postfach 3640, D-76021 Karlsruhe, (Germany)

V. Engelko, A. Andreev, V. Kavaljov
D.V. Efremov Institute, 189631 St. Peterburg (Russia)

Abstract

Pulsed heat treatment is a modern and ecologically sound technique of surface modification. The special feature of pulsed heat treatment is the possibility of applying high heating and cooling rates is. Fast cooling rates (as much as 10^7 K/s) of the heated layer cause a change in its physical properties; metastable phases with amorphous and nanocrystalline structures are formed. For investigation of the modifications of material properties by pulsed electron beams a new powerful electron beam facility GESA was developed and manufactured [1]. It produces an electron beam with a kinetic energy of 50 - 150 keV, a max. beam current of 500 A, a beam diameter of 6 - 10 cm and a pulse duration of 5 - 40 µs. All marked beam parameters (energy, current density, pulse duration) are controlled.

The paper presents the results of investigation focused on the transformation of the micro-structure, alloy formation and high temperature corrosion behavior of the Superalloy MCrAlY treated by an electron beam. Further the improvement of tribological properties by pulsed heat treatment of tappets used in car engines, consisting of a 16MnCr5 steel, are described.

1 INTRODUCTION

The possibility of applying high heating and cooling rates to material surfaces is the special feature of pulsed heat treatment. Fast cooling rates (as much as 10^7 K/s) of the heated layer cause a change in its physical properties (change of microstructure, improved wear and corrosion resistance, and increased microhardness) [2,3].

Proper adjustment of the energy supplied in the pulsed mode is crucial for successful surface treatment to generate the desired modifications. The decisive parameters are the energy of the electrons, the current density and the pulse duration. It is necessary that these three parameters can be set ad lib and independent of each other.

The GESA facility produces an electron beam with a kinetic energy of 50 - 150 keV; maximum beam current of 500 A; beam diameter 6 - 10 cm and pulse duration of 5 - 40 µs. All beam parameters mentioned (energy, current density, pulse duration) are controllable.

The influence of the pulsed electron beam treatment performed by the GESA facility on the micro-structure, alloy formation and high temperature oxidation behaviour of the Superalloy MCrAlY was investigated. MCrAlY type coatings are widely used for oxidation protection on gas turbine blades at high temperature (>900°C), with M being Ni and/or Co [4]. An improvement of the corrosion resistance of these coatings would allow higher combustion temperatures leading to enhanced efficiency of gas turbines and increased life time.

Hardening of car engine tappets consisting of 16MnCr5 steel has also been investigated with the goal to improve the tribological properties.

2 RESULTS AND DISCUSSION

2.1 CONTROLLED MELT AND RESOLIDIFICATION OF HIGH TEMPERATURE SUPERALLOY MCRALY

The specimens consisting of Inconel 738 were coated by low pressure plasma sprayed (LPPS) MCrAlY with 35% Co, 28% Ni, 20,5% Cr, 16% Al and 0,5%Y. The coating thickness was 200 µm which is one order of magnitude higher than the electron range used in the experiments. Therefore only the MCrAlY-coating is involved in the pulsed heat treatment.

The beam parameters are the following: electron energy E=120 keV, current density j=8 A/cm² and pulse duration τ=30 µs.

By solving numerically the heat equation using the energy deposition profile and thermal properties of MCrAlY at given parameters, the maximum cooling rate and resolidification velocity were obtained to be $2{,}5 \cdot 10^6$ K/s and 0,3 m/s.

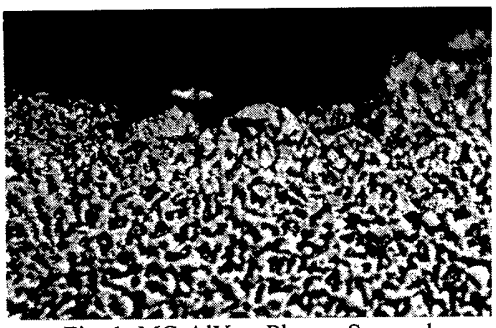

Fig. 1: MCrAlY as Plasma Sprayed

Fig.2: MCrAlY after Electron Beam Treatment

After treatment the irradiated zone was examined metallographically by SEM. Fig. 1 and Fig. 2 show the micrographs of cross section before and after irradiation. After electron beam treatment a glassy surface layer with a thickness of approximately 20 µm can be observed. The original two phase structure changed into a single phase structure in the melting zone. This modified layer was not affected by etching, while the two-phase structure shows deep corrosion traces. Further the surface roughness induced by the LPPS process is reduced significantly. The hardness of the single phase layer increased from 440 HV to 1200 HV.

2.2 HIGH TEMPERATURE OXIDATION TEST AT 1000°C IN AIR

The specimens for investigation of high temperature corrosion behaviour were treated under isothermal conditions at 1000°C up to 9600 hours in air. During the experiment the specimens were frequently examined metallurgically by SEM to monitor the formation of the Al_2O_3- and Cr_2O_3-oxide layer. This layer acts as a barrier against oxidation in the high temperature region.

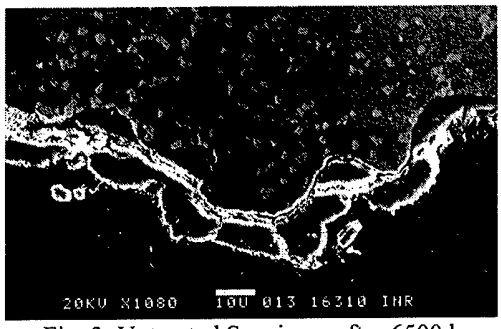

Fig. 3: Untreated Specimen after 6500 h

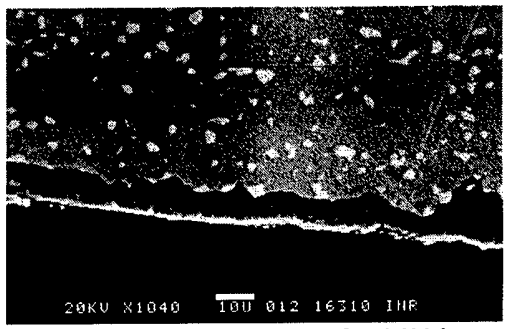

Fig. 4: Treated Specimen after 9600 h

In the untreated specimen after 6500 h exposure the oxide layer is traversed by micro-fissures. This leads to spallation of parts

of the oxide layer, that must be built up again by Al out of the MCrAlY (Fig 3.). The periodical occurrence of this oxide loss is responsible for the limited life time of the protective coating.

In contrast, the treated specimen shows a homogeneous dense Al_2O_3 layer on the top of the melting zone even after 9600 h oxidation test (Fig. 4). The homogeneous single phase surface structure suppresses micro-stresses and the so initiated crack formation.

2.3 *Pulsed Heat Treatment of Tappets*

Tappets serve as the intermediate component between camshaft and valve of a car engine (Fig. 5) and consist of a carburized 16MnCr5 steel. The material loss by friction does not allow a precise function during the engines life time. The experimental goal is the improvement of tribological behaviour by modifying the tappet's surface using pulsed electron beams.

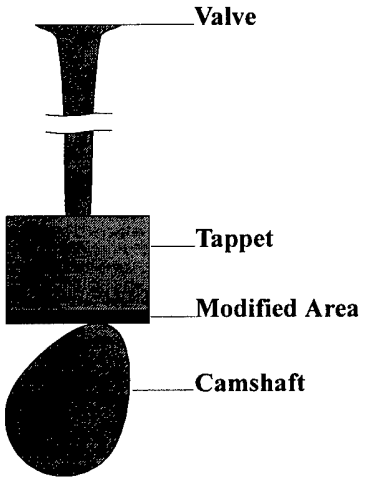

Fig. 5: Tappet, Camshaft and Valve

The beam parameters are E=100 keV, j=6 A/cm^2 and τ=25 µs.

In Fig. 6 the materials hardness with and without electron beam treatment is shown as a function of the depth in the specimens cross section. The hardness (Vickers, 25 p) within the melting zone increases from 1200 HV to 1300 HV. At the interface to the bulk material the hardness declines and approximates the untreated tappets values.

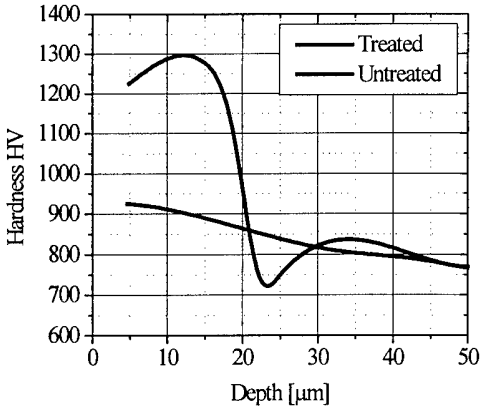

Fig. 6: Hardness of Treated and Untreated Tappet

In SEM studies grain sizes of about 300 nm were found in the melting zone. The reason for the decline of hardness under the untreated tappets value between 20 and 25 µm could be a tempering effect that leads to a fine bainitic structure. Investigations of this effect are in progress.

To compare the wear resistance of treated and untreated surfaces a car engine test was performed. The rippled surface formed during the treatment through boiling required polishing before installing the tappet. The material loss during 18 runs (2h per run) at different revolutions were measured in situ by the radioactive tracer method (RTM) [5]. Tab. 1 shows an increase of the tappets wear resistance by a factor of 4,3. Even the non-treated camshaft lost less material in combination with a modified tappet by a factor 2,3.

	Treated Tappet	Untreated Tappet	Ratio
Tappet	0,87 mg	3,79 mg	**4,3**
Camshaft	0,88 mg	2,04 mg	**2,3**

Tab. 1: Total Wear of Treated and Untreated Tappets after the Test Runs of the Engine

3 CONCLUSIONS

Pulsed electron beam treatment has proved a powerful tool for surface property improvement; in particular for the enhancement of wear and corrosion resistance.

1. Treated test specimens exhibit the formation of homogeneous surface layers with an increase in hardness between 40% and a factor of three.

2. The high temperature corrosion resistance of the Superalloy MCrAlY can be improved by electron beam treatment. The stable protective oxide layer suppresses material loss by spallation as observed on the untreated coating.

3. The wear resistance of tappets can be significantly (x4,3) increased by pulsed electron beam treatment as shown by an RTM test. Even its friction partner, the camshaft, shows a reduced material loss by a factor of 2,3.

4 REFERENCES

[1] G. Müller, G. Schumacher, D. Strauß, V. Engelko, A. Andreev, O. Kamarov and K. Shigalichin, BEAMS 96, in press.

[2] V. Engelko, A. Lazarenko and O. Pechersky, BEAMS 92, Washington, D.C., May 25-29, 1992, Vol. III, pp. 1935-1941.

[3] Yu.F. Ivanov, I.S. Kashinskaya, S.V. Lykov, A.B. Markov, E.M. Oks and V.P. Rothstein, BEAMS 94, San Diego, CA, June 20-24, 1994, Vol. II, pp. 857-860.

[4] R.J. Hecht, G.W. Goward and R.C. Elam, US Patent 3 928 026 1975.

[5] P. Fehsenfeld, A. Kleinrahm, E. Bollmann, KfK-Nachr. Jahrg. 18 4/86, pp. 224-234

MODIFICATION OF TITANIUM ALLOY PARTS PROPERTIES BY INTENSIVE CURRENT ELECTRON BEAMS

N. A. Nochovnaya , V. A. Shulov , D. I. Proskurovski , V. P. Rotshtein

Moscow Aviation Institute, 4, Volokolamskoye shosse, Moscow, 125871, Russia

Abstract

The influence of irradiation regimes by low energy intensive current electron beams of microsecond duration on chemical composition and phase-structural state of titanium alloy parts surface layers. It is shown that this treatment enables: to purify surface of details from the oxygen and carbon impurities; to improve the element distributions homogeneity in a depth; to decrease roughness of surface up to 0.05-0.07 μm; to modify the phase composition and structure of material in surface layer up to 10 μm thickness. In addition, the fatigue life can be increased in 80 times.

Introduction

Lately the concentrated fluxes of energy often have been used for modification of metal material parts surface properties. The perspective method of this treatment is irradiation of details by low energy intensive current electron beam (LEICEB) of microsecond duration. The usage of LEICEB allows to modify surface microrelief, chemical composition and phase-structural state of near surface areas and so alter service properties of machine parts purposely. But up to the present, as a rule, only the iron contented materials have been studied. The similar complex investigations of titanium alloys have been carried out. It increases the nomenclature of details which can be irradiated by LEICEB with purpose of service characteristics improving. In this connection the main objectives of the present research were complex study of chemical composition and structure of refractory alloy parts near surface layers after LEICEB treatment and determination of its effect on fatigue strength and microhardness.

Experimental

The aircraft engine compressor blades and samples manufactured from VT8M, VT6, VT9, VT18U, VT25U-titanium alloys by mechanical treatment of

rods were used as targets. The irradiation of targets has been carried out under the following values of parameters: energy of electron-E=20-30 keV; pulse duration-τ=0.7-2.5 μs; energy density-w=2.5-5 J cm^{-2}; number of pulses-n=1-100. According to calculated data these regimes ensure melting of surface layer material. After irradiation the blades and samples have been studied by means of Auger electron spectroscopy, X-ray diffraction analysis, scanning electron microscopy and microscopic metallography. Moreover, microhardness (H_μ) and roughness (R_a) of target surfaces have been measured. The part of the samples and blades have been annealed in vacuum (~10^{-3} Pa) at temperature 500-550 ^{0}C during 2 hours. The total set of researches has been repeated after annealing. High cyclical fatigue tests have been carried out using the test bench under the following conditions: frequency-f=3 kHz; temperature-500 ^{0}C; air; load- σ=360 MPa. The latter corresponds to the 2×10^7 cycles base of the production blades.

Results

It is shown (Fig. 1) that hard etched layer with 5-10 μm thickness is formed during high speed quenching from melt.

Figure 1. Microstructure of compressor blades surface layer after LEICEB treatment (w=5 J cm^{-2}, n=40, τ=2.5 μs): a- VT25U; b- VT9.

Microstructure of this layer can be modified from globular structure to columnar one. Some results of initial and irradiated samples surface layer state investigation are presented in Fig. 1-3 and Table 1. It follows from these data that as a result of rapid crystallization from melt the following processes take place:

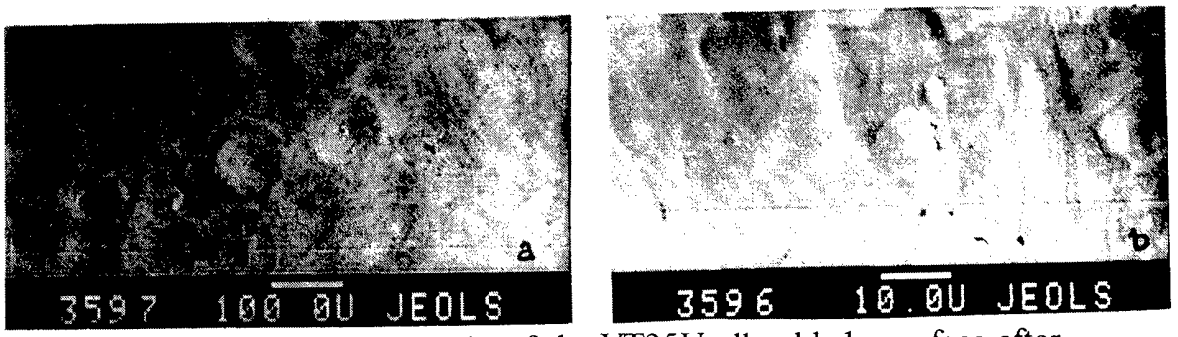

Figure 2. SEM-micrographs of the VT25U alloy blades surface after irradiation (w=5 J cm^{-2}, τ=2.5 μs): a- n=5; b- n=40.

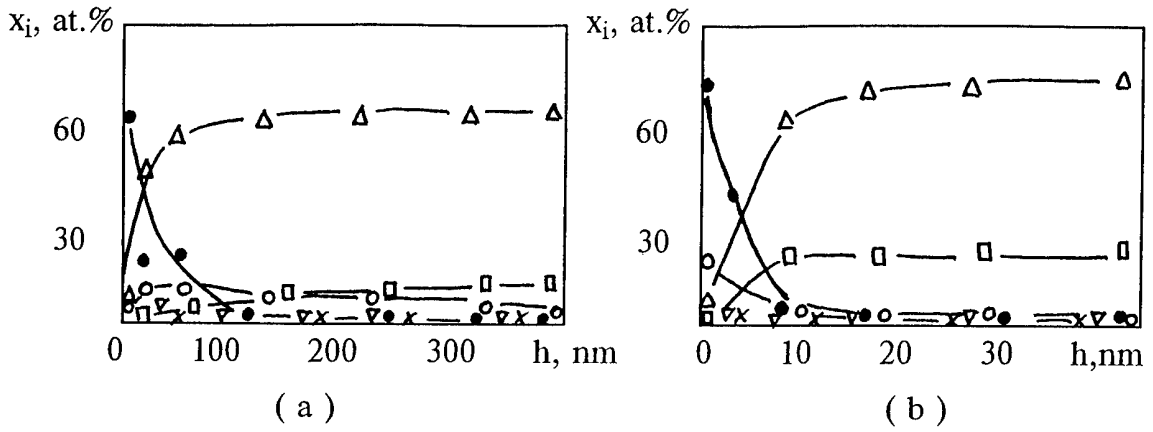

Figure 3. The element distributions in the VT9 alloy blades surface layer before (a) and after (b) irradiation (w=5 J cm^{-2}; n=40): Δ-Ti; •-C; o-O; □-Al; ∇-Zr; ×-Mo.

(i) considerable alterations of chemical composition in a 200 nm thickness surface layer (purification from the C, O - impurities and a increase of the Al concentration up to 15-20 at.%); (ii) modification of phase composition in the 10 μm thickness surface layer (it follows from Table 1 that almost total decay of β-phase and the formation of 30-40%-α"- phase are observed as the result of LEICEB treatment); (iii) formation of tensile residual stresses in the same layer (this is displayed as X-ray lines displacement to greater angles and decrease of the microhardness values); (iv) a lot of microdefects (craters 5-100 μm in a diameter and 0.5-2 μm in a depth) is formed during irradiation at low pulse number. The rise of the pulse number leads to decrease of craters distribution density and they are practically absent on the surface at n>40 (Fig.2b). In this case the surface roughness was equal to 0.05-0.07 μm. It allows to conclude that LEICEB treatment has a good perspective for the microrelief smoothing and the formation of the surface without the stress concentrators (craters).

At the same time the columnar grain structure formation in the crystallized near surface area of the blades is undesirable for the practical applications. Since the columnar grain structure is formed at great number of pulses and at high value of energy density (w≥5 J cm^{-2}, n≥40) the gentle regimes of treatment (w=2-3 J cm^{-2}) can be recommended for the modification of titanium alloy parts properties (with the conservation of great number of pulses). The latter is necessary for decrease of crater formation probability. At last the final heat treatment of the

irradiated blades must be carried out to stabilized the structure in surface layers and to improve the service properties.

Alloy	n, pulses	Heat treatment	m_α, mas. %	m_β, mas. %	$m_{\alpha''}$, mas. %	$\Gamma_{1/2}(110)$, grad	H_μ, HV 0.05
VT6	-	-	93.4-93.0	6.6-7.0	0	0.4-0.425	370±30
VT6	1	-	97.2-97.0	2.8-3.0	0	0.62-0.65	230±30
VT6	100	-	100	0	0	0.67-0.72	290±20
VT6	100	+	100	0	0	0.41-0.43	400±20
VT8M	-	-	92.9-92.2	7.1-7.8	0	0.37-0.38	380±20
VT8M	10	-	66.0-64.0	0	34.0-36.0	0.70-0.71	230±20
VT8M	100	-	63.0-61.0	0	37.0-39.0	0.75-0.76	250±20
VT8M	100	+	97.8-97.2	2.2-2.8	0	0.35-0.36	390±20
VT9	-	-	93.0-92.0	7.0-8.0	0	0.50-0.54	420±30
VT9	10	-	68.0-66.0	0	32.0-34.0	0.75-0.76	290±20
VT9	10	+	95.0-96.0	5.0-4.0	0	0.60-0.62	330±20

Table 1. The influence of irradiation ($w=2.5$ J cm^{-2}, $\tau=2.5$ μs) on microhardness, phase composition and a half-width of X-ray (110)-line ($Cu_{K\alpha}$ - irradiation).

Conclusion

The results of VT18U alloy samples fatigue tests allow to conclude that fatigue long life can be increased in 80 times by means of LEICEB(at $w=2.5$ J cm^{-2}, $n>40$ pulses) and final annealing ($N_{VT18U}=2\times10^7$ cycles; $N_{VT18U,\ ir.}=8\times10^8$ cycles). Thus, intensive current electron beams have a good perspective to be introduced in aircraft engine building for titanium alloy parts service properties modification.

HIGH POWER PULSE ELECTRON BEAM MODIFICATION AND ION IMPLANTATION OF $Hg_{1-x}Cd_xTe$ CRYSTALS.

A.V. Voitsekhovskii, * G.E. Remnev,* M.S. Opekunov,
A.P. Kokhanenko, A.G. Korotaev, Yu.A. Denisov, D.A. Oucherenko

** Nuclear Physics Institute of Tomsk Polytechnic University, Lenin ave. 2A, Tomsk, 634050, Tomsk State University, Department of Radiophysics, Lenin ave. 36,Tomsk, 634050, Russia*

Abstract

$Hg_{1-x}Cd_xTe$ (MCT) samples (x= 0.21 - 0.22) are irradiated by pulse electron beams under the doze 10^{13}-10^{17} cm^{-2}. Electron beams have the next parameters: 500 keV energy electron (30-40 A/cm^2 electron current density, 60-80ns current pulse); 200 keV energy electron (8-10 A/cm^2 electron current density, 100-200 ns current pulse). Electroconductivity and recombination of modified samples are investigated by Hall effect and photoconductivity methods. For 200 keV electron energy beam irradiation the n-type surface regions have been obtained under threshold mechanisms of donor defect generation. For 500 keV electron energy beam irradiation the maximum value of charge carrier lifetimes occur in p- to n-type conductivity conversion range for the initial p-type crystals due to the conductivity compensation.

MCT samples (x= 0.21 - 0.22) are implanted by Al ions under the dose 10^{12}-10^{16} cm^{-2}. Ion beams have the next parameters: (1-10) A/cm^2 ion current density; (100-200) ns current pulse; (150-450) keV Al ion (Al^+,Al^{++},Al^{+++}). The ion distribution and doping profiles were investigated by PIGE and Hall effect methods. The comparison between MCT samples after power pulse ion implantation and after standard ion implantation demonstrate difference in ion distribution, doping profiles and defect formation radiation mechanisms.

Introduction

As a rule, irradiation by easy particles as electrons with energy more than 1 MeV, possessing the lengths of run comparable with the cross sizes of opto- and microelectronic devices, is applied for volume radiating doping of semi-conductor materials. The temperature of irradiation is 300 K. It corresponds to conditions of ion implantion, but considerably exceeds the working temperature (77-150 K) of devices, based on narrow-gap semiconductors, to which MCT (x= 0.21- 0.22) is concerned [3, 4].

The properties of layers formed by ion implantion of narrow-gap MCT are determined, first of all, by radiating infringements. Formed n^+ layer does not depend from the type of conductivity of a material or nuclear number of implantant [1]. However, the characteristics of electrical structures depend on conditions of ion irradiation [2].

In given work the pulse accelerators of ions "MUK" and "TEMP-2"[6,7], were used as a sources of electron and ion. Its work in the mode of accelerating of electrons and ions (energy - 150-500 кеV) and ensure the current density up to 100 A/cm^{-2} at a duration of pulses 50 - 200 ns. The purpose of this work is adaptation of modes of powerful pulse sources of electrons and ions for semiconductor technology: reception of MCT with given parameters and unhomogeneous structures n^+-n, p-n types. The traditional methods of measurement of electrical, recombinational and photoelectrical (at excitation on a length of a wave 10.6 μm)

characteristics were used for valuation of efficiency of influence the electron irradiation on semiconductor material.

Electron Beam Modification

As a result of irradiation the MCT crystals with x=0.22 on "MUK" accelerator [6] in an interval of dozes $(0.5 - 5.0)\cdot10^{16}cm^{-2}$, the concentration of electrons in n - type samples (starting $n=2.0\cdot10^{14}$ cm^{-3} at T = 77 K) increased in 20-30 times, but electron mobility changed slightly and was $(1\text{-}2)\cdot10^{5}cm^{2}V^{-1}s^{-1}$. More essential changes were observed at p-type samples in an interval of used irradiation dozes. The contribution of an electron component of conductivity increased at surface layer (up to 5-10 μm) down to p-n conversion of the type of conductivity. We consider that the main results of given experiments are:

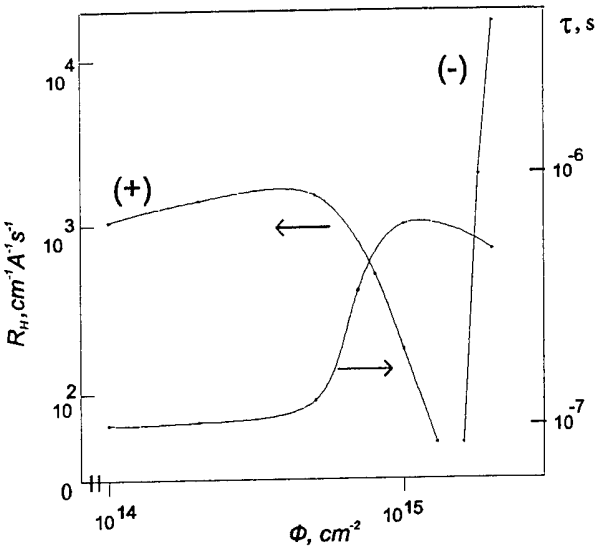

Fig.1 Hall coefficient (R_H) and lifetime versus irradiation doze for p-type samples MCT

1. Introduction of radiating donor defects at the expense of effect of mechanism of prethreshold defect generation at high energy pulse irradiation of electrons with energy up to 200 keV.

2. Formation of non-uniform distribution concentration of the type n^{+}-n(p) structures on depth for the samples with 30-50 μm thickness.

3. An absence of introduced by irradiation centers of recombination and centers of electron dissipation.

It was followed to wait more uniform distribution of parameters of irradiated samples on depth for case of irradiation the MCT crystals on the "TEMP-2" accelerator [7] (dozes up to $2.0\cdot10^{16}$ cm^{-2} at energy up to 500 кеV), since the process of radiating mechanism of defect generation should not test difficulties, connected with a deficit of energy of electron for beating atoms from units of a lattice.

The doze dependence of lifetime of photocarrier from fig. 1 show, that in the area p-n conversion of a type of conductivity the heaviest significance of a lifetime in irradiating material will be realized. It will be agreed with the results of account for the mechanism of recombination through local centers, which parameters are determined by temperature dependencies of lifetime [5].

Ion Implantation

After irradiation the profile of implant ions analyzed by PIGE method with using resonance reaction $^{27}Al(p, \gamma)^{28}Si$ with energy of analyzing protons 991,8 keV (fig.2)[8]. Surface electron concentration Ns, being the integral electron concentration through all implantant layer, determinated by measurements of a Hall coefficient by a Van-der-Pauw method in the assumption of the small contribution of non-irradiated part of a semiconductor in conductivity. The results of measurements of integrated electrophysical parameters of MCT after irradiation by the Al ions show, that electron concentration after irradiation in n - type MCT is increased, and the conversion of conductivity occurs in p - type samples already at

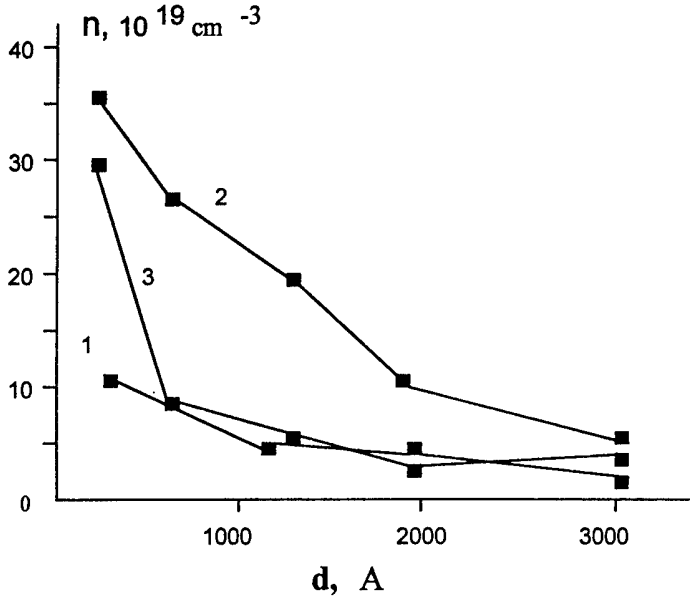

Fig.2 Distribution profiles of Al in MCT.
(1-1000 pulse; 2-2000 pulse; 3-3000 pulse).

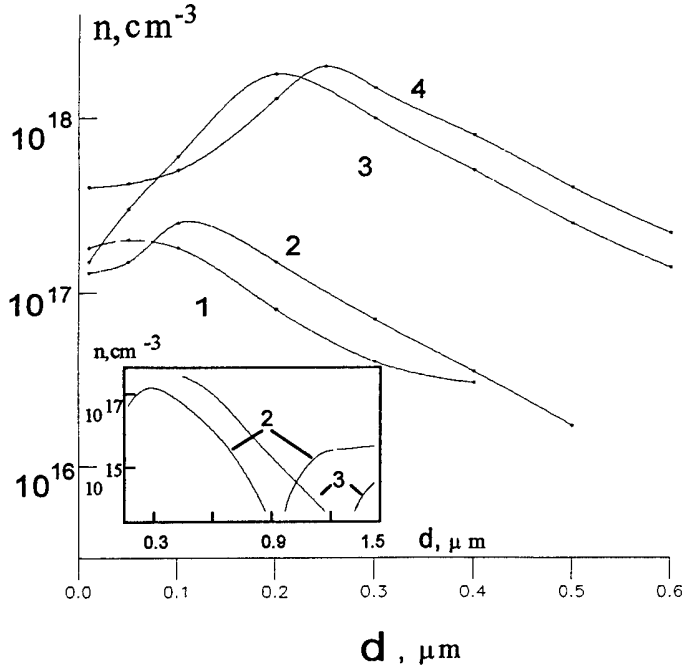

Fig. 3. Space distributions of concentration of charge carriers after implantation of the ions Al in n- (curve 1,4) and p-(2,3) MCT. An irradiation doze Φ (cm^{-2}): 1,2-10^{12}; 3,4-10^{13}. The complete profiles of distribution of charge carriers for p- MCT are represented on an insert.

minimum doze of irradiation $\Phi=10^{12}$ cm^{-2}. Thus, high power ion beams give the same picture, as usual ion sources, namely: the electrical properties of MCT after irradiation by ions are determined by radiating defects of a donor type. Appreciable decrease of electron mobility is marked in initially n-type samples, that is connected with formation of extended defects of crystal structure, formed by implantation [1]. The absence of evident doze dependencies of electrophysical parameters of MCT is explained, as appear, by that the minimum doze of irradiation $\Phi=10^{12}$ cm^{-2}, received in our experiments, corresponds with well known [1] saturation doze (Φ_{sat}) for implantation of heavy ions in MCT. The analysis of profiles of electron concentration n(d), indicated on fig. 3 has shown, that practically all laws, typical for ion implantation in MCT [1], take place and at high power pulse irradiation for dozes $(1\text{-}20)\cdot10^{14}$ cm^{-2}. N-type conductivity arrange in a layer of a semiconductor, exceeding the depth of average projection run R_p of ions data energy (3000 Å).

With increasing the irradiation doze the maximum of electron distribution is shifted deep into a semiconductor (see fig. 2). The concentration in a maximum of distribution for a doze $1\cdot10^{13}cm^{-2}$ is $n_{max}=2.0\cdot10^{16}cm^{-3}$, that corresponds to significance of saturation, connected with " fixing " a Fermi level at a level of radiating defects. Thus the profiles n (d) coincide practically in samples , having starting a various type of conductivity. There are some difference from case of standard modes of ion implantation : the significance of n_{max} on the order less than the significance of saturation $2\cdot10^{18}$ cm^{-3} at irradiation doze $\Phi=1\cdot10^{12}$ cm^{-2}, which (n_{sat}) is reached practically for all investigated ions at such irradiation doze [1].

Conclusion.

The results show an opportunity of application of high energy pulse beams of electrons for directed changes of electrical and recombinational parameters of narrow-gap semiconductors, that are a main material for optical electronic devices. Results of experimental researches show, that irradiation of MCT crystals by ion beams permit to form n^+-n and n-p structures deep into samples 0.5-1.0 μm at irradiation dozes $(1 - 10)\cdot 10^{12}$ cm^{-2}. The further increasing of irradiation doze means the deep penetration (up to 10 μm) of electric profiles deep into samples and the formation a high concentration of extended defects of a radiating origin in region ~R_p of implanted ions, influencing on processes of transport of charge carriers.

[1]. Voitsekhovskii,A. V., Lilenko,Yu. V., Shastov,K.V., Et al.: Phys.St.Sol. (B), **118** (1989) 285

[2]. Voitsekhovskii,A. V., Et al : 3 All-Union conference " Ion-beam modification of semiconductors and other materials of microelectronics " Novosibirsk (1991) 2

[3]. Voitsekhovskii,A.V., Et al. : Sol. Stat. Communs., **31** (1979) 2 105

[4]. Voitsekhovskii,A.V., Et al. : Radiation Eff., **66** (1982) 1-2 78

[5]. Voitsekhovskii,A.V., Kokhanenko,A.P., Petrov,A.S., : Physica Stat. Sol. (A), **90** (1985) 1 241

[6]. Remnev G.E., Isakov I.F., Opekunov M.S., Matvienko V.M., Luconin S.U., Vasilyev S.U., Furman E.G. : BEAMS`94 , Book of Abstracts, P3-46, 1994.

[7]. I.F.Isakov, V.N.Kolodii, M.S.Opekunov., Et al.: Vacuum, v.42, No.1/2,1991,pp.159-162.

[8]. Ryzhkov V.A., Opekunov M.S., Remnev G.E., Et al.: Book of Abstracts *10-th Confer. on the Chemistry of Big-Purity Substances.* Nizhnii Novgorod, Russia, June 1995.: 1995, p.151-152.

INFLUENCE OF ELECTRON AND ION BEAMS OF ENERGY ON THE STRUCTURAL AND MECHANICAL PROPERTIES OF METALS

I.G. Romanov, I.N. Tsareva, G.M. Romanova

Mechanical Engineering Research Institute
Russian Academy of Science, 603024 Nizhny Novgorod, Russia

As it was ascertained in works [1-2] plastic deformation processes by ion implantation begin to proceed already at doses 10^{14}-10^{15} cm^{-2}, and the radiation-peening of material occurs. However, all the experiments about which it was reported earlier were accomplished on quasi-continuous accelerators, and thin metallic films and foils were used as targets. The application of the ion treatment for property modification of different materials permits to reveal new effects by interaction of charged particles with a solid body, which are not observed at traditional radiation regimes.

Copper and α-iron notable for their elastic-plastic properties were chosen as investigated materials. Tests were carried out at massive annealed samples with a polished surface (12-th class of roughness). Radiation by small doses $E = 2 \cdot 10^{14} - 2 \cdot 10^{15}$ cm^{-2} of ion C^+ was conducted on the impulse accelerator „Muk" with energy 100 keV at ion current density 5 A/cm^2 and pulse duration $\tau = 100$ ns.

This accelerator permits also to conduct the electron treatment. Pulse electron radiation was accomplished at energy 100 A/cm^2 and pulse duration 50 ns. The distance from the electron emitting source up to the target, which presented steel P6M5, was changed during the conducted experiments.

The metallografic analysis and Bragg-Brentano radiography with Mo-K_α-radiation were used for registration of structural changes initiated by ion and electron treatment. Crystal lattice microdeformation values were determined from physical broadening of diffraction lines (111), (222), of copper and (011), (022) of iron by the approximation method. Measurements of the cross metallographic specimen microhardness at load 0,3-0,5 N and friction coefficient of sphere penetrator slip from steel IIIX-15 at variable load 0.3-1 N were carried out. After the ion radiation the X-ray-structural analysis did not reveal any changes in a phase composition of testing materials.

But on copper diffractograms already at doses $2 \cdot 10^{14}$ cm^{-2} it was observed a considerable increase of relative intensity of lines (200), (222), (400) and a decrease of intensity of lines (220), (420), testifying to the appearance of a primary grain orientation. The dose increase up to $2 \cdot 10^{15}$ cm^{-2} is accompanied by a texture degree relaxation. Visible increase in intensity of lines (011), (022) and decrease in intensity if reflexes (002), (013) are observed at dose $2 \cdot 10^{15}$ cm^{-2}. Texture appearance confirms the proceeding of plastic deformation processes under the action of accelerated ions mainly in the slip system planes (fcc-Cu:{111}<110>, bcc-Fe: {110}<111>). After radiation the metallographic analysis did not reveal any changes in the average grain size. The plastic deformation intergrain mechanism is considered to be probable because of a polycrystal grain turn as a result of the stress influence caused by radiation. The X-ray line physical broadening analysis showed the presence of microstresses (Cu: $\varepsilon = 6{,}68 \cdot 10^{-4}$; α-Fe: $\varepsilon = 6{,}83 \cdot 10^{-4}$) at doses preceding the plastic deformation dose, while in the initial annealed samples stresses of the II sort were absent. The average dislocation density in grains at that time was increased by a factor of 10^{-2}

and made up $(2\text{-}3)\cdot10^{10}$ cm^{-2}. Thus, the pulse ion C^+ treatment in the range of small doses is accompanied by the course of plastic deformation in massive e materials and leads to a considerable dislocation density increase.

In the described experiment changes in the diffraction picture, obtained at sounding of layers with thickness up to 10 μm, take place at depths which exceed the ion path in a solid body by a factor of 10^2 (Cu-C^+: R_P = 105 nm, α-Fe-C^+: R_p = 112 nm) . The question about the reasons of the long-range interaction effected by ion radiation remains still debatable.

In the course of discussion of the discovered structural changes the following factors must be taken into consideration: the influence of temperature patterns, static stresses connected with impurity atoms and welding radiation defects, dynamic stresses caused by acoustic wave propagation (AW) by ion implantation.

Solution of the heat conduction equation [3] for radiation in consideration of chosen radiation regimes showed that the target heating by ion beam bombardment was negligible (T_{max} = 320 K). Therefore the structural changes by ion bombardment of this kind cannot be explained by thermal effects. According to the conducted estimation [4] stresses caused by implanted impurity atoms may exceed the material yield point and initiate the plastic deformation. However, the fields of these stresses appear to be prevailing in thin surface layers with thickness comparable with the ion path. But they are not long-range because they decrease inversely proportionally to the cube of distance from the surface and scarcely can provoke the texture depths up to 10 μm. In our opinion, acoustic wave pressures may be the initial cause of a long-range effect. Theoretical calculations carried out in accordance with the model proposed in the work [5] showed that the pressure amplitude (by j = 5 A/cm^2) of the resultant primary in the layers to 100 μm reaches 760 MPa for Cu and 980 MPa for α-Fe, that is considerably higher than the material yield point (Cu: G = 68 MPa, α-Fe: G = 200 MPa). Furthermore, the acoustic ware pressure in copper with lower yield point is higher than in α-Fe. Therefore, the texture appears in Cu at lower radiation doses.

After electron radiation the X-ray structural analysis of steel P6M5 revealed the following: The distance decrease between the Source and the target from 5 cm up to 10 cm provoked the increase of diffraction peaks of carbides Fe_3C and Fe_3W_3C and the appearance of peaks γ-Fe. The strong heating of samples be the subsequent distance reduction up to 2.5 cm stimulated the decay of carbides, dissolution of carbon in α-Fe and thus the considerable growth of austenite. Parallel with above mentioned structural changes by electron radiation the substantial increase of peaks γ-Fe was observed. This testifies the proceeding of plastic deformation processes. It must be noted that the electron beam provoked the fusion and the increase of surface roughness.

Microhardness measurements of C^+ ion irradiated copper and iron samples revealed the zone with increased mechanical properties 200 μm in depth (Fig.1). We ascertained the considerable dislocation density increase in grain on depths of 10 μm. Electron-microscopic researches, conducted by some authors [6], showed changes in the dislocation structure after ion radiation in the layer of 100-200 μm. Analogous effects apparently take place also in this experiment providing metal hardening according to the dislocation mechanism.

After electron radiation the zone with increased mechanical properties was also observed. The microhardness increases from 350 kg/mm^2 up to 500-550 kg/mm^2 at depths 100-200 μm is conditioned not only by the thermoelastic excitation of waves, but also by the efficiency pulse during evaporation). In this case the amplitude of compression pulse may exceed the ferrite yield point, provoking the plastic deformation and thus the increase of dislocation density.

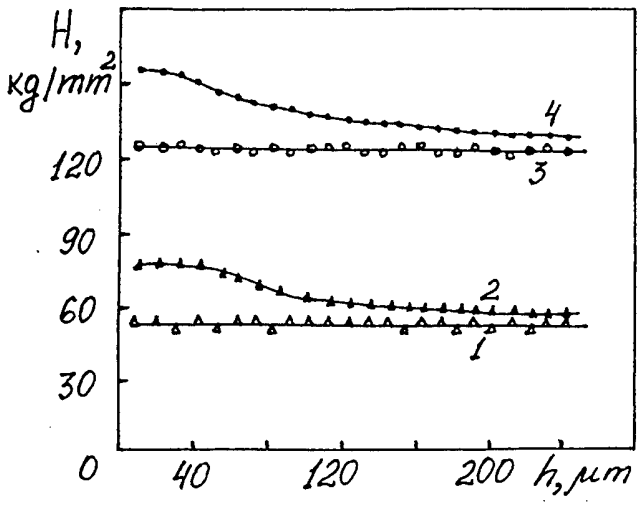

Fig. 1
Microhardness distribution in depth for Cu and α-Fe before and after pulse irradiation by C^+ ions (E =100 keV) by dose 10^{15} cm^{-2}:
1 - non-irradiated Cu, 2 - irradiated Cu,
3 - non-irradiated α-Fe, 4 - irradiated α-Fe.

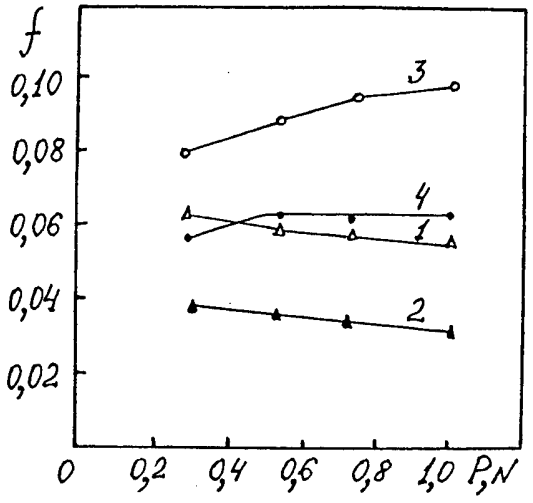

Fig. 2
Friction coefficient dependence on load for copper and iron before and after pulse irradiation by C^+ ions (E = 100 keV):
1 - non-irradiated Cu, 2 - P = $2 \cdot 10^{14}$ cm^{-2},
3 - non-irradiated α-Fe, 4 - P = $2 \cdot 10^{14}$ cm^{-2}.

After the ion treatment changes in test material friction properties were observed. The samples irradiated by doses corresponding to plastic deformation doses possessed the lowest friction coefficient (Fig. 2). By the following dose increase the tendency to the reset of initial values was exhibited. The improvement of friction properties is conditioned, on one hand, by the increase of irradiated target hardness. On the other hand, the appearance of the texture favourably orientated with respect to the shift during the ion influence may promote the decrease of tangential stresses in the contact zone, ensuring the friction loss decrease. Electron irradiation caused the friction coefficient increase at all the test loads, that was connected with the roughness parameter increase during the surface fusion.

References

[1] A.P. Pavlov, D.I. Tetel'baum, E.V. Kuril'chik, I.G. Romanov; Reports of Academy of Sciences, 1990, V.311, N3, P.606.

[2] E.V. Kuril'chik, P.V. Pavlov, A.P. Pavlov, D.I. Tetel'baum; Surface, 1992, N4, P.102.

[3] I.G. Romanov, A.P. Pavlov, I.N. Tsareva et al.; Izvestiya of the Russian Academy of Sciences, 1992, V.56, N7, P.2.

[4] I.G. Romanov; Materials Science Forum, 1992, V. 97-99, P. 533.

[5] P.V. Pavlov, Y.A. Semin, V.D. Scupov, D.I. Tetel'baum; Physics and technology of semiconductors, 1988, V. 20, N3, P.1503.

[6] A.N. Didenko, E.V. Kozlov, Y.P. Charkeev; Surface, 1988, N3, P.120.

P-3-19

SO_2, NO_x AND H_2S OXIDATION BY SIMULTANEOUS APPLICATION OF ELECTRON BEAM AND ELECTRIC FIELD IN HUMID AIR

L.I.Salnikov[1], H.Nichipor[1], E.Radjuk[1], A.G.Chmielewski[2], Z.Zimek[2]

1/ Institute of Radiation Physics and Chemistry Problems of the Academy of Sciences Rep. of Belarus, Minsk-Sosny, 220109, Rep. of Belarus
2/ Institute of Nuclear Chemistry and Technology, Dorodna 16, 03 195 Warsaw, Poland

Abstract

The theoretical model of SO_2, NO and H_2S oxidation in humid air by electron beam with the electric field presence was developed. Data established by our simulation calculations using this model show that SO_2 and H_2S molecules through SO_2 are being converted effectively into H_2SO_4 in result chain process.

Introduction

The rate of SO_2 and H_2S oxidation in irradiated humid air can be increased by an electric field simultaneous application. At the same time the energy cost of those molecules removal is significantly decreased what is related to the chain reaction which takes place in such conditions as it was described by Nichipor et al [1]. It was found that with the electric field presence a dissociative attachment of the electrons with the O_2 molecules is very efficient what leads to the chain described by the following reaction cycle:

$$O_2 + e^- \rightarrow O^- + O \quad (1)$$
$$O^- + O_2 + M \rightarrow O_3^- + M \quad (2)$$
$$SO_2 + O_3^- \rightarrow SO_3^- + O_2 \quad (3)$$
$$SO_3^- + H_2O \rightarrow H_2SO_4 + e^- \quad (4)$$

The influence of electric field on the kinetics of NO and SO_2 removal is related to an increase of e^- concentration due to the chain process (1)-(4) and an increase OH, HO_2 radicals concentrations.

The aim of the present work is to simulate the homogeneous gas phase chemistry of the electron beam process in the gas mixture $H_2O + O_2 + N_2 + SO_2 + NO + H_2S$ with the electric field presence.

Model of calculation

The applied model of calculation was described by Nichipor et al [2-3]. Primary process of ionization and dissociative excitation under the accelerated electrons influence have been taken into account in the process of humid air mixture radiolysis with the addition of different initial SO_2, NO and H_2S concentrations. The electrons which appeared in the gas mixture under electron beam influence are energized by electric field. The energy which was transmitted to electrons by electric field helps them to participate actively in chemical processes. The rate constants of the most important processes of the used model have been modified in respect of electric field.

All known process of positive and negative ions and neutral molecules were taken into account in humid air radiolysis with additives SO_2, NO and H_2S.

The chemical model includes 57 different species and 236 reactions.

The integration of the complete system of first order ordinary differential equations was performed by use of the computer code KINETIC employing a Gear algorithm especially suited for stiff systems.

Result and discussion

The first step was the calculation of the final SO_2, NO and H_2S concentrations as a function of dose with the electric field presence (E/N= 0^{-15} • cm^2). The mixture containing N_2 (68%), O_2 (20%), H_2O (12%), NO (0 - 500 ppm), SO_2 (250 - 1000 ppm), H_2S (0 - 1000 ppm) at T = 340 K, p = 1 atm, j = 0,32 mA/cm^2 were taken into consideration. Through this simulation study it was shown that the oxidizing reaction

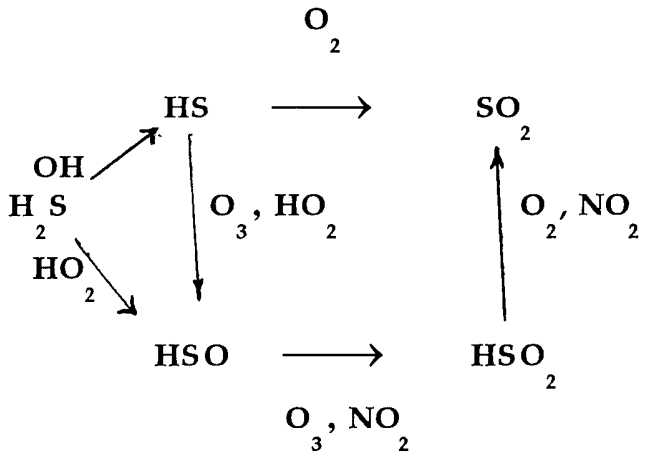

giving SO_2 as an intermediate substance go simultaneously with NO and SO_2 conversion reactions

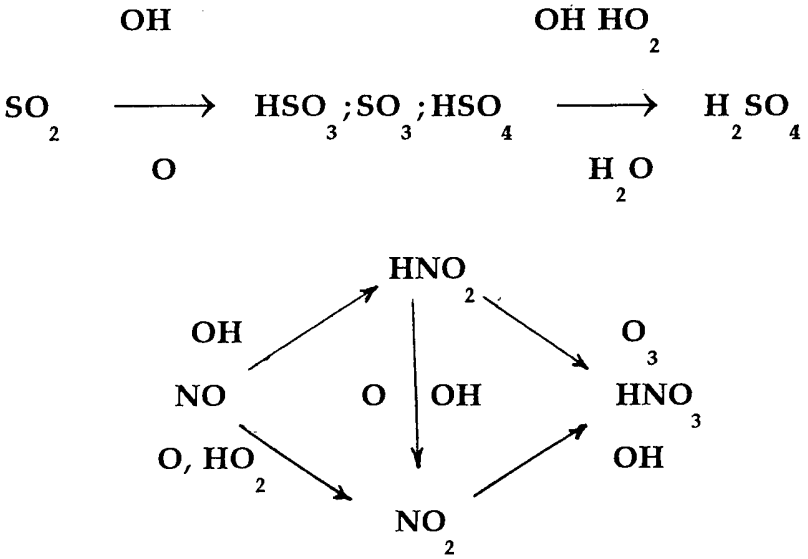

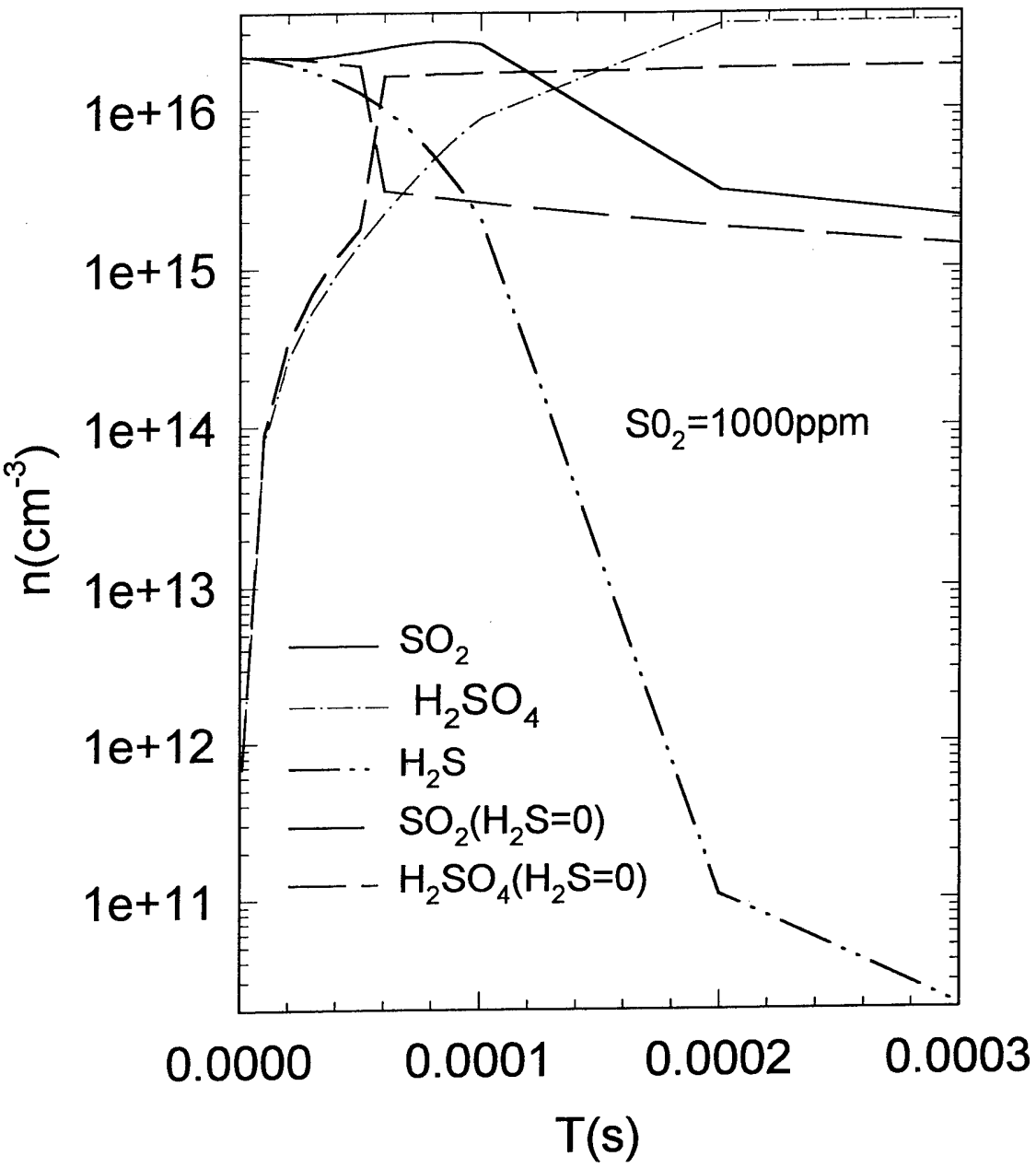

Fig.1. The results of calculations of irradiated humid gas mixture with presence of electric field

Typical results of SO_2, NO and H_2S removal as a function of absorbed dose with the electric field presence are shown in Fig.1. It was established that chain process (1)-(4) lead to the O and OH, HO_2 radicals concentrations increasing and due to this fact the H_2S to SO_2 conversion was accelerated and the SO_2 conversion into H_2SO_4 was accelerated too. This results in more efficient decomposition of additives to compare with similar reactions without electric field given by Nichipor et al [3].

The influence of the H_2S conversion into SO_2 on the chain process (1)-(4) is more effective when initial SO_2 concentration is low according to model calculations. When H_2S particles are present and initial SO_2 concentration is higher, the stable level of the H_2SO_4 concentration can be reached faster.

Conclusions

As it was demonstrated above the model calculations of humid air radiolysis with NO_x, SO_2 and H_2S additives under electric field influence shows that SO_2 and H_2S molecules through SO_2 are being converted effectively into H_2SO_4 in result of chain process. That chain process with H_2S molecules presence are more intense due to energy transfer from electric field. The total SO_2 and H_2S conversion into the H_2SO_4 molecules is performed in time $\tau = 2 \bullet 10^{-4} s$, that is 2 times longer than conversion SO_2 into H_2SO_4 without H_2S addition.

1. Nichipor H., Radjuk E., Chmielewski A.G., Zimek Z., Lysov G.W. :
J.Advanced Oxidat.Techn., (1996) - in print
2. Nichipor H., Radjuk E., Chmielewski A.G., Zimek Z., Lysov G.W. : Radiat.Phys.Chem., **46** (1995) pp.1115-1118.
3. Nichipor H.V., Dashouk E.M., Yatsko S.N. : Radiat.Phys.Chem. , **46** (1995) pp.1111 -1114.

P-3-21

Research of action of a pulsing frequent electron beam on microorganisms in water solutions

S.Yu. Sokovnin, Yu.A. Kotov and G.A. Mesyats

Institute electrophysics, Ural Branch, RAS , 34, Komsomolskaya, St., Ekaterinburg, Russia, 620219

Abstract

Action nanosecond high-current electron beam (HCEB) on microorganisms in water solutions is investigated.

It is experimentally found, that the disinfection doze nanosecond HCEB for a mix from Coli-fomes, Salmonella enteritidies, Staphlococuc aureus with initial concentration micro-organisms on billion 1/ml of each kind in a physiological solution, makes 4 kGy, thus the absorption doze on a surface chamber by thickness of 1,5 mm was 20 kGy.

Effect of abnormal influence of hashing of a tight packed water solution on wreck microorganisms is established at irradiation HCEB, which cannot be explained as by alignment of a doze on volume a chamber, as diffusion of a oxygen. It permits to lower a disinfection doze at processing of a water HCEB.

Introduction

Environmental contamination calls for disinfection of natural and waste water. The method most universally employed at present is the chemical decontamination of water, which consists of either chlorination or ozonization. However, chlorination is responsible for toxic organic chlorine compounds forming in water, while ozone treatment gives rise to both biologically decomposable organic matter and complicated organic compounds. A general drawback of chemical disinfection is that microorganisms residing within suspended particles cannot be affected.

An alternative solution is radiation treatment, owing to its universal destroying action on various kinds of biological entities. To disinfect water, use has been made of both gamma radiation of isotopes and electrons accelerated by a 0.3 to 1 Mev continuous-action accelerator. Irrespective of the type of radiation, the radiation sterilization dose is not over 4 kGy for waste water and does not exceed 1 kGy for natural water.

With the recent advent of solid-state-switching pulsed repetitive electron accelerators [2], whose advantages include a longer service life, a relatively smaller size, and a lower cost (in comparison with continuous-action accelerators), a currently central problem is to investigate the biological effect of a high-current electron beam (HCEB) on aqueous solutions. Available data on surface sterilization by pulsed nanosecond HCEBs [3] have shown the application of such beams to be highly efficient.

Experiment

In the experiments we used airtight stainless steel cells 1.5 mm deep, where the initial concentration of microorganisms in the physiological solution ranged between 10^5 and 10^9 1/ml. The sanitary microbiological analysis was performed by the method of sowing o n diagnostic culture media.

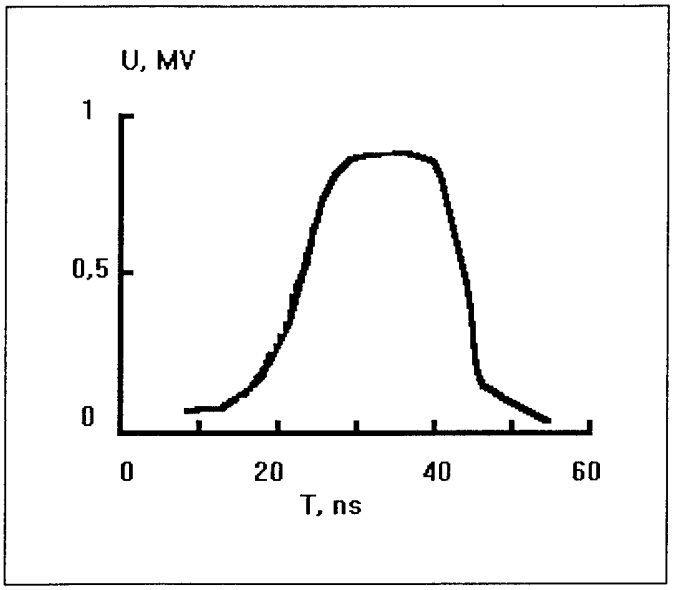

Fig. 1. Voltage pulse oscillogram of the "Ruslan"

Cells containing microorganism were irradiated at room temperature, by means of a pulsed repetitive "Ruslan" accelerator [4] having an electron energy of 700 keV, an electron beam current of 5000 A, a half-height pulse duration of 26 ns, a pulse repetition frequency of 1 to 10 pps, and a beam area of 60*10 cm^2. The accelerator voltage oscillogram are presented in Figs 1.

Plastic film detectors were used to measure the absorbed dose of the HCEB. The field of the absorbed dose in water was measured in irradiation depth. For results of the experiments and for the calculated absorbed dose distribution for mono-energetic elec trons refer to Fig. 2.

The value of the absorbed dose on wall of the absorbed dose on the rear (remote) wall of the cell bath is taken to be the sterilizing value as it is lowest in the entire volume of the cell.

Table. Irradiation results

N	D_o, kGy	N_0, 1/ml	n_0	n_1	n_2	n_3	n_4	Hashing
1	12.8	10^9	503	332	61	5	no gr.	no
2	12.8	10^7	248	62	2	no gr.	no gr.	no
3	12.8	10^5	3	no gr.	no gr.	no gr.	no gr.	no
4	11.1	10^9	711	200	39	2	no gr.	no
5	11.1	10^9	55	8	1	no gr.	no gr.	yes
6	9.8	10^9	2048	211	42	2	no gr.	no
7	9.8	10^9	15	1	no gr.	no gr.	no gr.	yes

Note: N_0 - is the initial concentration of microorganisms; n_i the number of colonies per milliliter after irradiation, with i = 1, 2 ... being the order of breeding of the irradiated culture when transplanted onto a culture medium; D_o - the absorbed dose on the surface of the cell; no gr. -stands for the absence of the growth of microorganisms.

We carried out experiments on equal-dose irradiation of cells with different initial con-cen-trations of microorganisms and investigated the effect that agitating the solution in the process of irradiation has on the destruction of microorganisms. The solution was stirred by shaking the cells as they were irradiated. Results of the experiments are consolidated in a table.

Discussion

It has been found experimentally that the sterilizing dose of the nanosecond HCEB for a mixture with an initial concentration of microorganisms of 10^9 l/ml of each species in the physiological solution is 4 kGy with the absorbed surface dose being 20 kGy.

Results of experiments on the irradiation by approximately equal doses of microorganisms with different initial concentrations have shown (see table) that the number of microorganisms that have survived is determined by the absorbed dose and is independent of the initial concentration. This is inconsistent with data [5] obtained for gamma radiation and electron beams of accelerators with directly current and shows that increasing the concentration of microorga-nisms raises their radiation resistance.

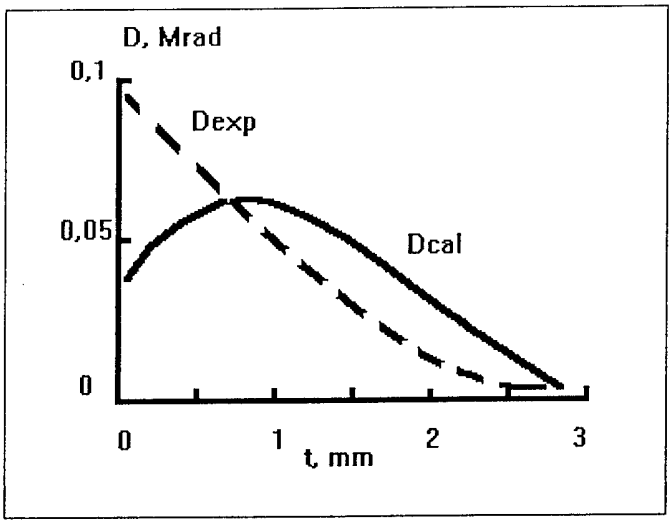

Fig. 2. Dose distribution in water.

Agitating the solution in the process of irradiation has been found to have a dramatic effect on the destruction of microorganisms. Thus shaking the cell one time with half a dose leads to the surviving microorganisms decreasing in number by more than an order of magnitude (see table, Nos 4 and 5). With the cell shaken three times with every quarter of the full dose, the number of microorganisms that have survived decreases by two orders of magnitude (Nos 6 and 7). This strong effect of agitation cannot be attributed to only the equalization of the dose in the volume of the cell, because the difference between the dose on the surface and the dose on the rear wall of the cell (1.5 mm deep) is less than one order of magnitude (Fig. 2). Ref. [5] provides data to the effect that shaking the suspension in the presence of oxygen lowers the radiation resistance of microorganisms. In our case, however, the cell is sealed, and the possibility of oxygen diffusing into the suspension is absent.

Earlier [3] a three-fold reduction of lethal doses for various kinds of microorganisms was found to take place when an HCEB was used for surface sterilization. In our case, a still more dramatic decrease in lethal doses may be expected if we assume that secondary factors, which arise as the HCEB decelerates and which are capable of penetrating more deep than electrons (X-ray, microwave and ultraviolet radiation, shock wave, etc.) are responsible for this effect.

Thus it may be concluded that when irradiating water from natural water sources with a characteristic contamination at a level of 10^7 l/ml, a dose on the order of 2.5 kGy will be needed to produce potable water. Allowing for the fact that active agitation can be arranged in the process of irradiation, the required value of the dose on the rear wall can be set at a level of 1 to 1.5 kGy. However, when water is stirred violently, the question of the ratio of the doses on the surface and on the rear wall becomes nontrivial and invites investigations.

To check up on the results obtained, water of the Verkh-Issetski pond (drinking water supplysource in Ekaterinburg) was exposed to irradiation. A 50 mcm thick polyethylene

film wasused to seal cells (p = 2 mm). When in the act of being irradiated, the cells were repeatedly shaken. The absorbed dose on the surface and that on the rear wall were 14 and 1.3 kGy, respectively. The water exposed to irradiation turned out to be sterile, whereas the check sample index was 70 000.

The absorbed dose of 1.3 kGy corresponds to a consumption of 0.62 kW h (with the transmission-of-power-to-beam efficiency being 75%) required for cleaning 1 m^3 of water, a requirement which correlates with the power consumption in the event of ozonization.

References

1. Shubin V.N., Sharanin Y.I., Brusentsova S.A. et al. / Radiation Disinfection of Waste and Natural Water, M.: Energoatomizdat, 1985, 64 p.
2. Kotov Yu. A., Mesyats G.A., Rukin S.N. and Filatov A.L./ DAN, v.330 (1993), , p.p. 15-17.
3. Vasiliev N.V., Gorn A.K., Kachushina G.G. et al. /DAN, v. 253 (1980), p.p. 1120-1122.
4. Kotov Yu.A., Mesyats G.A., Rukin S.N.et al./ 9th IEEE Pulsed Power Conf., 1994, Albuquerque, New Mexico, USA, v. 1, p.p. 134-139.
5. Tumanyan M.A. and Kaushanski D.A./ Radiation Sterilization, M.:Meditsina, 1974, 304 p.

ABOUT TRANSPORT CURRENT CHANGE IN HIGH-TEMPERATURE SUPERCONDUCTING REAL WIRES AND TAPES AS A RESULT OF ELECTRON IRRADIATION.

Davlatjan T.A., Kalashnikov V.V., Kruglov V.S., Tokarev A.S.
Institute of Superconductivity and Solid State Physics, RRC "Kurchatov Institute", Kurchatov sq., Moscow, 123182, Russia

It is shown, that an influence of electron irradiation on a transport current capability of real high-temperature superconducting wires and tapes based on BiSrCaCuO has the ambiguous nature and depends on conditions of synthesis, phase structure, as well as kind of a studied sample (ceramics, wire or tape).

The research was conducted on real wires and tapes with different phase structure: "2212" and "2223" and also had various technologies of manufacturing: melt-textured growth (I) or oxide-powder in silver tube (II). Samples irradiation was conducted by fast electrons with energy 4-10 MeV on air with control of sample temperature in irradiation process. The critical current was determined on voltage-current characteristics of studied real superconducting wires and tapes.

The received results on electron irradiation influence on critical current are submitted on fig. 1-2 at in different magnetic fields. For some samples at measurements in own magnetic field it is possible to measure the appreciable increasing of critical current at small irradiation dozes. For other these dependencies are the same as doze dependencies, received while usual lowertemperature superconductors irradiation. For

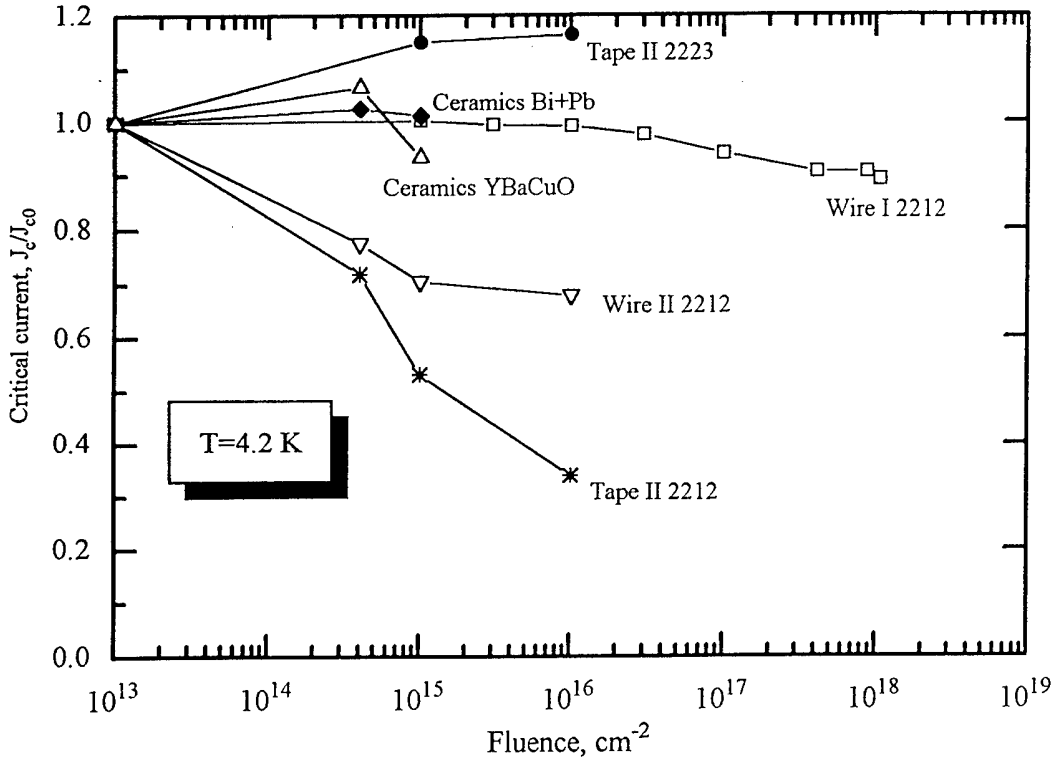

Fig.1. Dependence of samples critical current on fluence at B=0 T

all given above tapes and wires at dozes higher $1*10^{16}$ cm^{-2} the transition to subsequent stabilization of critical current size is observed. At external magnetic field the nature of dependencies of critical current with electron irradiation doze has some changes.

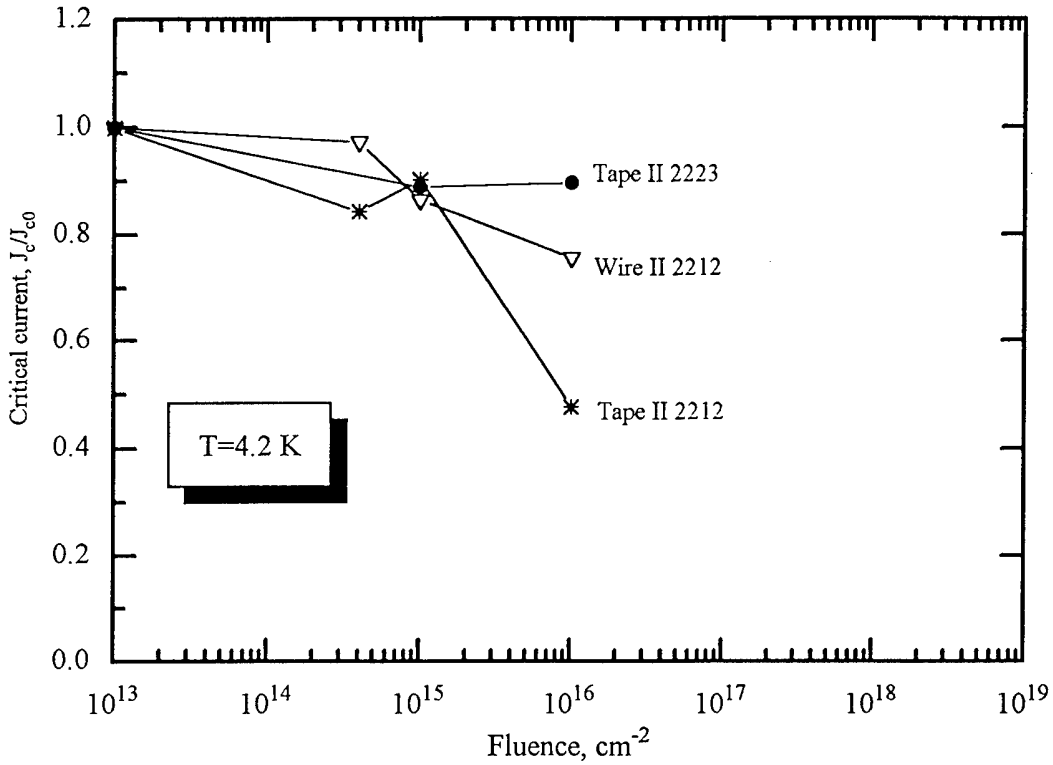

Fig.2. Dependence of samples critical current on fluence at B=5 T

In the field of small external magnetic fields to 0.3T investigated samples show the strong dependence of critical current from value of applied magnetic field (Fig.3-4). In this field of external magnetic fields at some samples the so called "peak - effect" is observed and in irradiation process the value of "peak - effect" for Bi-wires and tapes varies: so at tape Tape II-2212 it appears as a result of electron irradiation, while at tape Tape II-2223 it thus disappears.

In granulated samples such as Ba-Sr-Ca-Cu-O the transport current is determined by intergrane and ihtragrane currents, which depend as from properties of grain, as from intergrane boundary properties. And main factor affecting the transport current change are radiation-stimulated diffusion processes. For phases Bi- 2212 and 2223 it is possible to say about absence of considerable changes of grain, i.e. possible processes then at such irradiation dozes happen on the grain surface and are reduced to intergrane boundaries properties changing and weak connection transformation as a result of atoms displacement [1-5].

Observable distinction in transport current behaviour for superconducting wires and tapes is directly connected with intragrain boundery properties, determined by conditions of sample synthesis for given phase structure and tape manufacturing technology. While electron irradiation directly on intragrain boundary the formations of new phases are concentrated, as well as changing of weak connection happens, that improves connection between superconducting grains. At the same time for wires and tape decrease of transport current is observed, where the main role already is played by

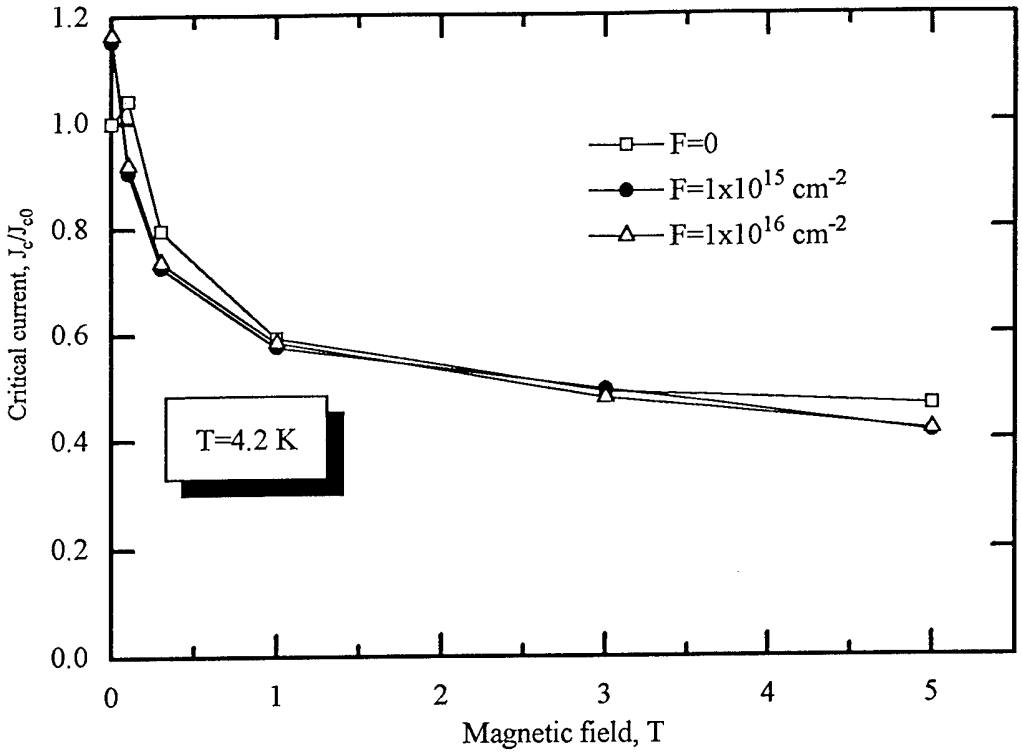

Fig.3. Dependence of critical current for Tape II 2223

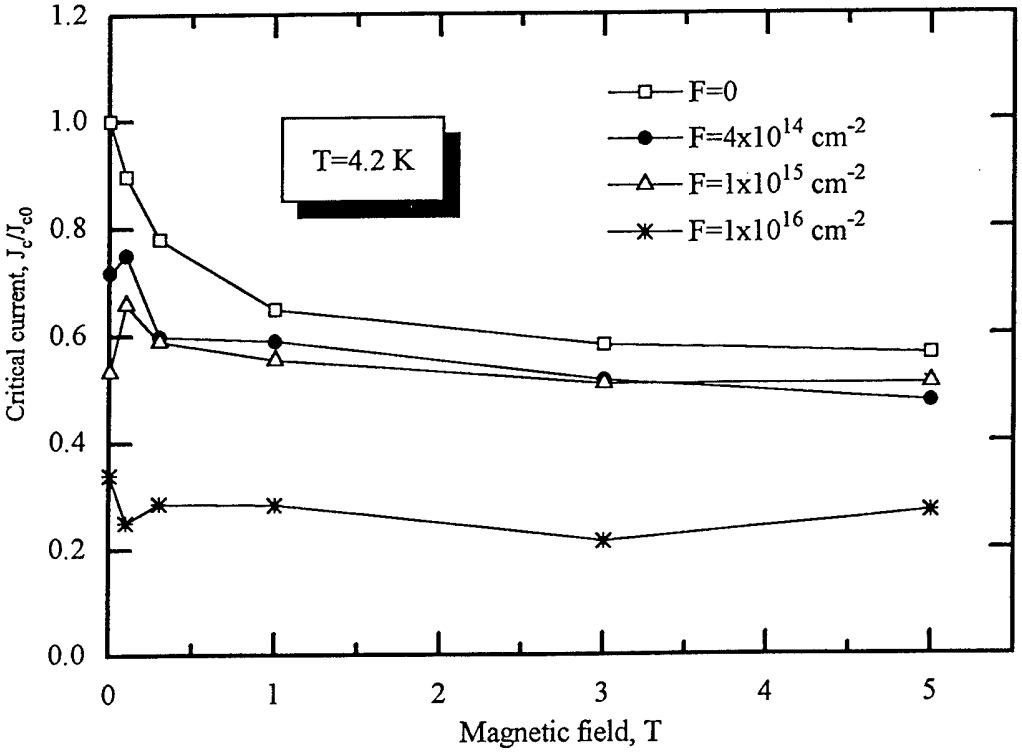

Fig.4. Dependence of critical current for Tape II 2212

chemical structure changes on intragrain boundary because of diffusion processes from grain volumes , localization of impurities there and formation of no-superconducting amorphous intragrain interlayer. The adduced results testify about considerable role of oxygen radiation-stimulated diffusion in HTSC-materials, at least in near-surface area of their grains, as well as about various nature of fast electrons interaction with Bi- and Y-ceramics.

References:

[1]. B.B.Boiko and et.al. -Phys.Stat.Sol.(a),1989, v.113,p.K235.
[2]. G.J.Clark and et.al.- Appl.Phys.Lett.,1987,v.51, N18,p.1462.
[3]. M.A.Kirk and et.al. - Physica C,1989,v.162-164,p.532.
[4]. Blatter G., et al - Vortices in High Temperature Superconductors. 1993. Zurich.
[5]. Daeumling M., et al - Nature, 1990, v.346, p.332.

INFLUENCE OF ELECTRON IRRADIATION ON CURRENT DISTRIBUTION PROCESS IN GRANULATED HIGH-TEMPERATURE SUPERCONDUCTING REAL WIRES AND TAPES.

Davlatjan T.A., Kalashnikov V.V., Kruglov V.S., Tokarev A.S.
Institute of Superconductivity and Solid State Physics, RRC "Kurchatov Institute", Kurchatov sq., Moscow, 123182, Russia

It is known, that electron irradiation by small dozes of granulated samples BiSrCaCuO, do not result in appreciable changes of superconducting properties directly of grain as a result of radiation damages, changes the condition of intergranulated contact in studied samples. It is shown, that if at thermomechanical stresses the resistance of intergranular contact grows, fast electron irradiation causes as increasing and reduction of this resistance.

The behaviour of real wires and tapes on the basis of high-temperature superconductors BiSrCaCuO current characteristics is in general determined by granular macrostructure and intragrain connections in these superconductors. In the same time the nature of intragrain connections depends on technological sample history, different external effects and constructive features of wire. The voltage-current characteristics of such wires and tapes has some peculiarities (Fig.1). Among them it is

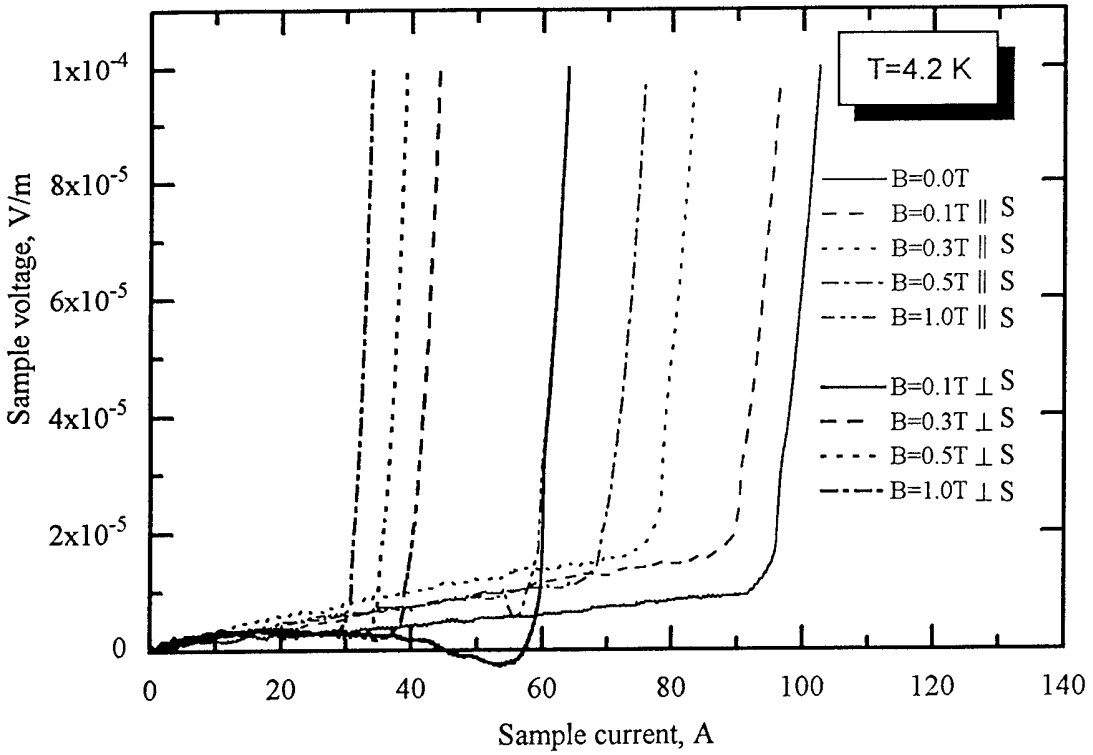

Fig.1. Voltage-current characteristics of samp. Tape-I(2223) before the electron irradiation at the different external magnetic field at the different orientation

possible to note the availability in beginning of voltage-current characteristics of "primary resisting dependency" of electric field intensity from current value, passing

through sample and is connected with (analogous to multifilamentary cables on the NbTi base) current transfer process.

The external magnetic field besides it results in reduction of critical current and voltage-current characteristics displacement into the side of lower currents in the sample, it also influence on the sample resistivity. The change of current transfer nature can testify about strong change of current ways between grains as a result of mutual orientations of external magnetic fields changes, current in sample and directly sample, possessing definite geometry. And it permits to say about unhomogeneity of intragrain layers properties.

At thermocycle temperature no-stabilised samples from high-temperature superconducting wires and tapes the change of primary voltage-current characteristics resistivity, connected with arising thermomechanical stresses is observed. These stresses as a result worsen intragrain contacts, change the conditions of current transfer between grains and leads to increasing of primary resistivity on voltage-current characteristics (Fig.2). Temperature annealing of samples results in these stresses relaxation and, as a result, - in partial or total restoration of intragrain contacts, that as a result improves by this superconducting grain connections in the sample and reduces this resistivity.

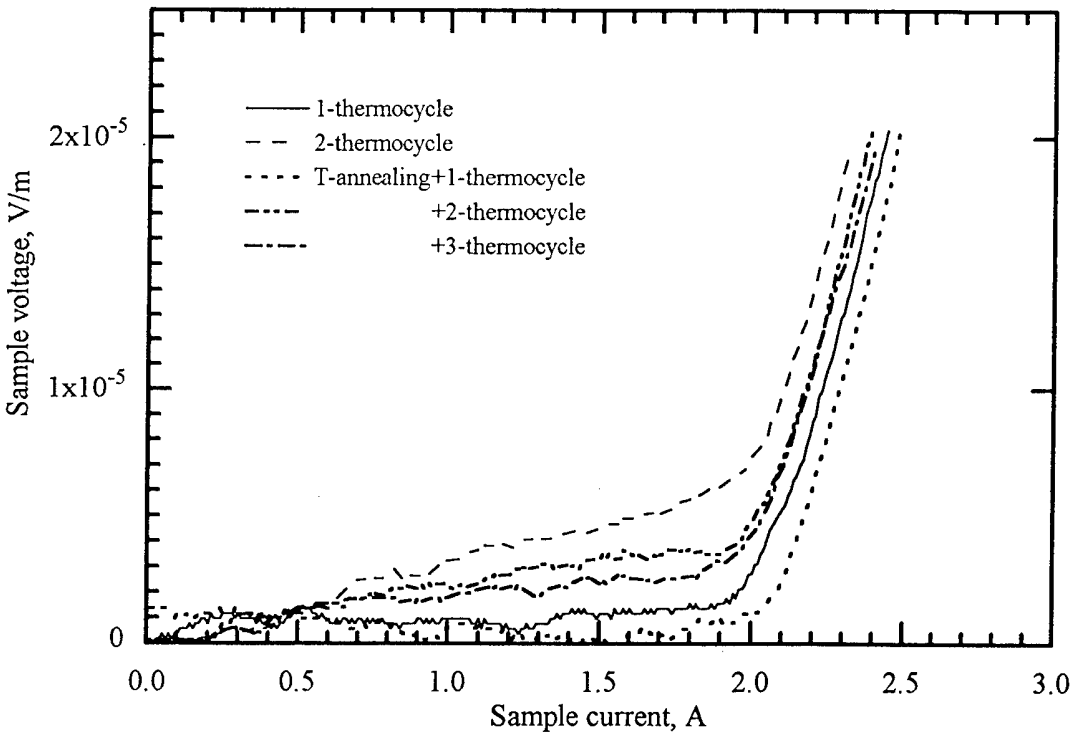

Fig.2. Voltage-current characteristics after thermocycle and annealing

Small dozes electron irradiation of granulated samples BiSrCaCuO, doing not result in appreciable changes of grain superconducting properties as a result of radiation damages, changes the condition of intragrain contact. If at thermomechanical stresses the resistance of intragrain contact grows, the fast electrons irradiation can change the nature of current transfer, leading as to increase, as to reduction of intragrain contact resistance. So for wires the reduction of primary resistivity after some definite irradiation doze (Fig.3) is observed. Further irradiation results in subsequent

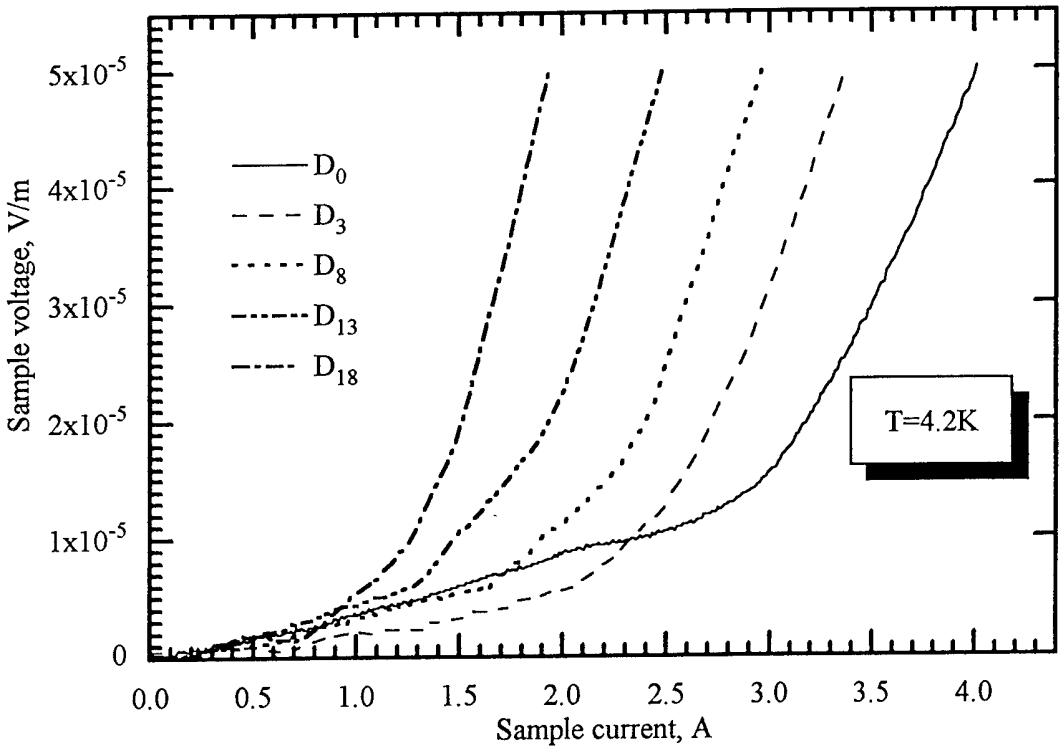

Fig.3. Voltage-current characteristics of Wire-I (2212) after electron irradiation

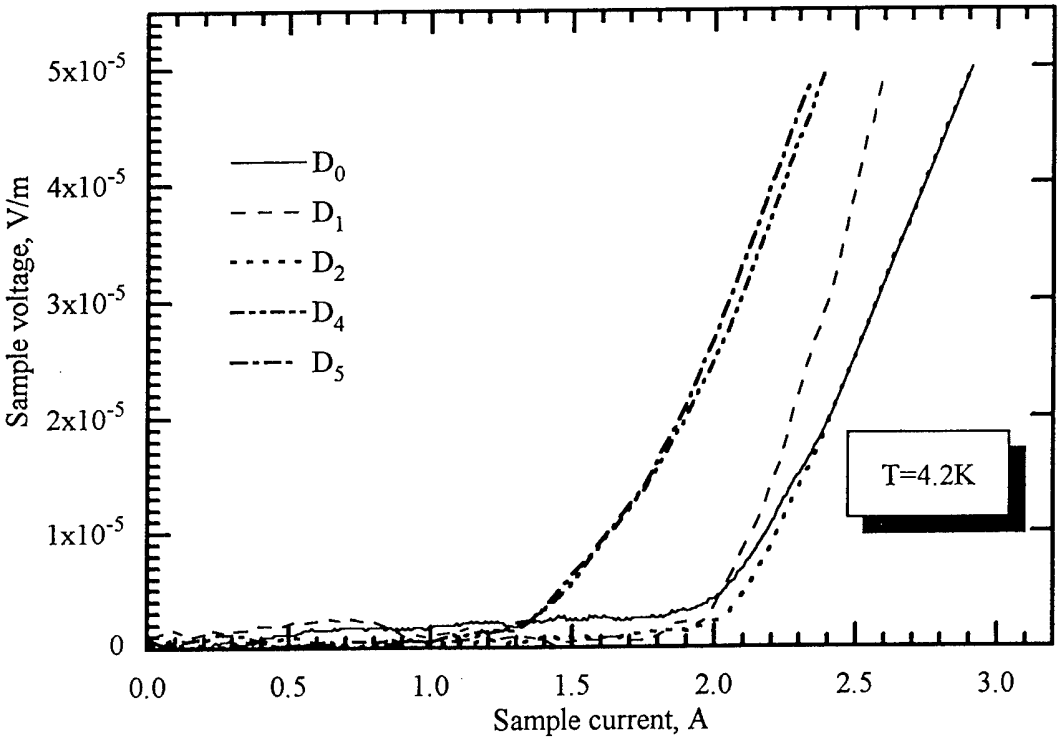

Fig.4. Voltage-current characteristics of Tape-I (2212) after electron irradiation

increase of this resistivity. In the same time for tapes the reduction is characteristic already after first irradiation dozes and then practically does not change (Fig.4).

The analysis of results at different orientation of sample and current direction in it concerning to direction of external magnetic field, has shown, that the changes of current transfer condition are connected with non-uniform changes of grain surface properties, for example, while electron irradiation, as well as at intragrain connection deterioration is observed the increasing of primary voltage-current characteristics resistivity in current transfer process. Subsequent temperature annealing results in restoration of these connections and resistivity reduction. This resistivity has unmonotonous dependency from external magnetic field. The current transfer process at different temperatures passes in different planes.

Thus the received results permit to say about complicated processes, passing on intragrain border or in near-surface grain layer and resulting in anisotropic changing of their properties. For real wires and tapes on the base of granule HTSC voltage-current characteristics primary resistivity may be the main characteristic of current transfer process in such samples, as far as it directly connected with intragrain borders condition.

Mass-transport in W-Cu system under high energy electron irradiation.

G.G.Bondarenko , A.N.Tikhonov , Yu. V.Shlenov , M.M.Yakunkin
Moscow State Institute of Electronics and Mathematics
Bolshoy Vuzovskiy per., 3/12, Moscow, 109028, Russia

Abstract

The research of the mass-transport effect was conducted for the system "W-Cu", the components of which were non-dissolved both in the solid and in the liquid conditions. It has been shown that under the electron irradiation the mutual solution copper and tungsten took place on the passing zone and reaches 30% for both tungsten and copper. The depth of the mutual penetration was 8-10 mm. The possible mechanisms of this effect are dissussed.

One of the interest problems of mass-transport theory in the solids is connected with the explanation of the anomal atom's mobility under the action of the electron beams with the energy $E \geq 1$ MeV.

Therefore it's assumed the effect can lead to the rise of new-technologies, which are the alternative one's based on using high energy ion beams. By analogy to the ion alloying [1] the effect of the electron stimulated mass-transport was called "electron alloying".

Till the present time the electron alloying's research was carried out for the systems, which had the mutual solubility of the components. Therefore it was a problem to explain this effect: it was either connected with unknown mechanism of mass-transport, or it was the classic thermo-active process with great defect's numbers created by the irradiation. That's why in our experiment the effect was researched in the W-Cu system, the components of which were nonsolubility between themselves in the solid and liquid state.

The specimens were produced by means of the diffusion welding. They consisted of the copper layer of 5 mm thickness and plaquer tungsten layer of 0,1 mm thickness. The specimens were in the special plant, which provided constant specimens temperature by 297 K.

The accelerator "UELV-10-10" with the exit electron beam power till 10 kW was used for irradiation.

The irradiation was performed in the vacuum through the tungsten layer with the following conditions:
electron energy - 10 MeV;
current density - from 1 $\mu A/cm^2$ up to 15 $\mu A/cm^2$;
total dose of irradiation - $(1.2\text{-}17.1)\cdot 10^{17}$ e/cm^2;
duration of irradiation - 5 hours;
specific power of the electron beam was not more than 50 W/cm^2.

Then both the etalon and irradiational specimens were cut by means of the electrodischarge machine and the metallografic polishes were used. The

concentration alteration of elements in the transitional zone before and after irradiation was defined by the EMA method on the microanalisator "Camebax". At first the quality estimation was carried out with the record of the intensivity of X-rays' radiation change (fig.1). Precise concentrational alterations of elements were calculated by means of the program for research of the concentration profile in the transitional zone (fig.2).

The quality research of the W-distribution in the contact zone W-Cu after welding showed the absence of solubility on the interphase in the etalon specimen. But the mutual diffusion of the components was observed after the irradiation (fig.1). The depth of the penetration increased with the irradiation dose increasing. The quantitative determination of copper and tungsten concentration profiles in the transitional zone showed that the great mutual solibility (up to 30 percent) copper and tungsten was observed on the interphase.

Fig.1. Contact zone W-Cu after the irradiation. (the view of the concentration curves).

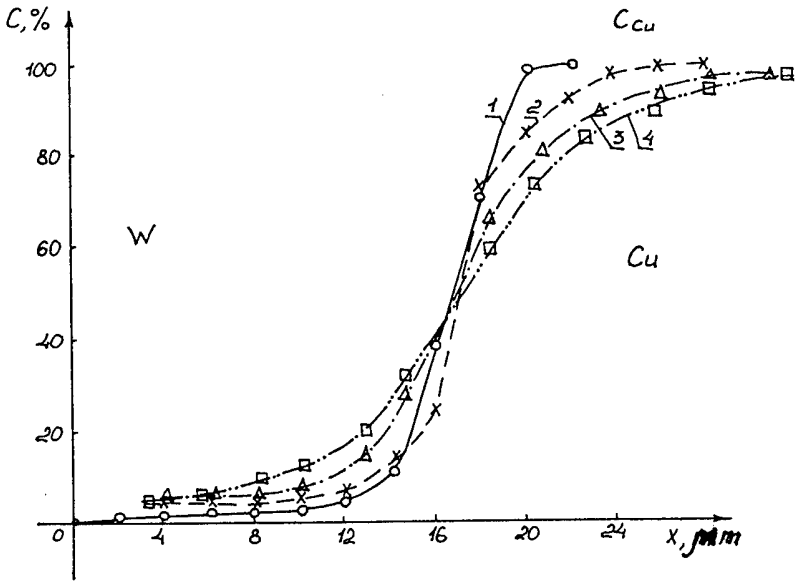

Fig.2. Concentration of copper in the Cu-W system before (curve N1) and after (curves 2,3,4) irradiation.
2 - $1{,}2 \cdot 10^{17}$ e/cm^2
3 - $10 \cdot 10^{17}$ e/cm^2
4 - $17{,}1 \cdot 10^{17}$ e/cm^2

The effect of the saturation, when the view of the concentration curses was not depend of fluence was observed at dose 10^{19} e/cm^2. The penetration deep of components was rised up to 15 μm .

The observed effect is phenomenal one's because it's imposible to get the alloys of such composition by means of only famous ways. As the metals are nonsolubility in each other not only in solid but in liquid state it's unlikely that the heating of the contact border by means of the exchange of energy between the bombarded electrons can lead to the visible increasing electron's mobility in the diffussion zone.The other possible mechanism of the "gigantic electron stimulated diffussion" is connected with the exiton "softening" spacing near the defect. But it didn't find the wide discussion in scientific literature.

Let's examine the way according which the masstransport in the system is controlled by the defect formation on the interphase of diffusion components. For that it's necessary to propose the existence of only a small mutual solubility of the components. The value of the interstitials migration in the crystal is higher versus the vacancies one, and the significant number of the intersttial atoms escape to sinks in the diffusion zone. These sinks are dislocasions, dislocation loops, micropores in the diffussion zone. We can propose that the interstitial atoms don't take part in the diffussion mass transport. If to believe that the atoms in the crystal are moving on vacancy mechanism, then the diffusion process depends on the vacancy existence and their mobility.

Then the diffussion coefficient will be

$D=D_{term}+D_p$, where

D_p - coefficient of the radiation stimulated diffusion;

D_p can be express over the diffusion coefficient of vacancies D_v and their superequilibrium concentration C^v_p is created by irradiation in the transitional layer.

$D_p = C^v_p \cdot D_v = (\Delta n/N) \cdot D_v$, where

Δn - supersaturated numbers of the vacancies created by irradiation;

N - numbers of atoms in the unit of the volume.

If the speed of vacancy formation on the interphase W- Cu is constant, then Dp must be:

$D_p = \Phi \sigma_d \nu D_v \tau_v$, where

τ_v - duration of the vacancy life;

Φ - the electron flux;

σ_d - the cross section of the displacement of atoms under electron irradiation;

ν - the cascade function;

The experimental and theoretical results are in bad agreement. Theoretical values are much decreased in spite of $D_v = 10^{-3}$ cm^2/s was extremally large in ouw theoretical estimate. The cause of it is either

nonsufficient basis ground of the simplified suppositions (for example, about the constant rate of the vacancy generation by the radiation) or the existence other mechanism of mass transport in this system.

It is unlikely too that the energy of electron beam is sufficiently for the formation of local melting regions in crystal. Such regions are connected with the exitement their effective temperature and can arise in solid under the more heavy particle irradiation.

Thus the fenomena of electron-stimulated mass-transport not the simple explanation in the flames of the real notius about the interaction between the relativistic electron beam with solids and classic explanation of the diffusion process.

Therefore it's possible to propose the existence of the unknown mechanism of the mass-transport.

References

1. Vade T. at al. // Proc. 6th Symposium Ion Source and Ion Assisted Technology// Tokyo, Pergamon Press, 1982, p.433.

P-3-25

INFLUENCE OF CARBON AND NITROGEN IONS ON THE STRUCTURE AND PROPERTIES OF CARBON FIBERS.

Gavrilov N.W., Emlin D.R., Ligachev A.E. , Ligacheva E.A.(a), Nochovnaja N.A.(b), Karpova I.G.(b).

Institute of Electrophysics, UD RAS;
Moscow Aviation Technology Institute (a);
All-Russian Institute of Aviation Materials, Moscow(b).

Introduction

Ion irradiation of carbon fibers with the prupose of directed modification of their properties - perspective area as scientific researches and practical application. Irradiation of fibers by ions of non-metals (carbon, nitrogen and oxygen) and metals can change surface and chemical structure of fibre (especially after the implantation in a fibre of ions of metals). It turn let us to hope, that by means of ion irradiation it is possible to change physico-chemical properties of carbon fibers and probably even to design with the help of a method of ion irradiation the composite materials.

In the present research results of experimental researches of physico-chemical and mechanical properties of a carbon fiber, subjected to the irradiation by ions of carbon and nitrogen by energy 30 keV are brought.

Experimental

Carbon fibers produced from polyacrylonitrile (PAN) precursor were used in our experiments.

Carbon fiber were irradiated by carbon and nitrogen pulse ion beams (energy - 30 keV, current densities per pulse - 3 - 9 $^{mA}/cm^2$, pulse length ~ 1ms; the ion source shows stable operation with pulse repetition rate of up to 50 s^{-1}).

To estimate the structural parameter of the investigated carbon fibers (d_{002} - the distance between planes of the crystalline lattice) X-ray diffraction was used.

Research of strength of a carbon fibre was conducted on a filament fibre (the length - 10 mm). Diameter of the filament fibre was measured in three different points with the help of optical microscope. For the speamens subjected to one kind of the irradiation was carried out 25 - 30 measurements of filament fibre.

The measurement of size contact angle of wetting is an important method of research of processes of interaction on border of a surface solid - liquid.

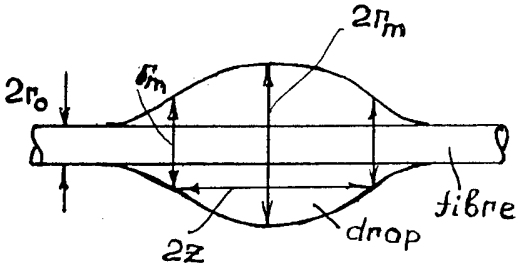

Fig.1 Circuit of wetting of an individual fibre by a liquid

The small sizes of a drop and the insignificant extent of perimeter of wetting provides an opportunity of a fast establishment of balance after drawing of a drop on a sting and simultaneously reduce to the minimum gisteresis phenomenon of wetting. Besides it is in this case possible to give up the gravitational forces and therefore to simplify the settlement formulas. Carbon fibre by diameter 4 - 7 microns fixed in a special framework. On fibre we are putting 5 - 7 drops of a liquid (gliserin or olein acid).

After that the framework is located under lense of the optical microscope and the drops of a liquid on a fibre are photographed. We have measured the following parameters of a drop in any scale on a projection of the image (Fig.1): a diameter of a carbon fibre $2r_0$, ecvatorial diameter of a drop $2r_m$ and distance 2z between points meridial curve, in which the width of a drop makes half of its diameter. After that we have calculated meanings of parameters, $x_m=r_m/r_0$ and $y_m=z/r_m$ on which with the help of the special tables found size contact angle of wetting or the meaning contact angle of wetting.

Results and Discussion

Topography of the Surface of Carbon Fibre

The changing topography of carbon fibre surface are taking place after implantation of ions of the carbon and nitrogen $10^{18}cm^{-2}$. The longitudinal lines and hollow appear on the surface of the fibre. The surface become ribbed and this ribs are situated along the axis of the fibre. The roughness of the surface fibre is increasing and the middle height of this roughness is 0,05 - 0,15 μm.

During the growth of doze of C^+ to $1 \cdot 10^{19}cm^{-2}$ the topography of the surface of carbon fibre doesn't change in practice. On the other hand after implantation of N^+ the roughness of the surface of the fibre are changing seldomly and on some samples of the fibre it reaches 0,4 - 0,5 μm. Such type of the roughness which is forming on the surface of the carbon fibre after implantation is connected with irradiated ions in the near-surface layer of the fibre and with the ability of chemical interraction of nitrogen with carbon which can bring us to the creation of different chemical phase.

The structure and strength of the carbon fibre

As a result of the irradiation by the carbon ions with growth of the ion's doze there is some increase of the meaning of inner surface length which is d_{002} = 0,348nm (the nonirradiate carbon fibre d_{002}=0,342nm). The afterwards increasing of dose of the irradiated ions don't has a real influence on the magnitude of the d_{002}. (Fig.2). After the irradiation by the nitrogen ions the magnitude d_{002} (with dose $2 \cdot 10^{18}$ N^+cm^{-2}) achieves the maximum meaning, which is d_{002}=0,351nm.

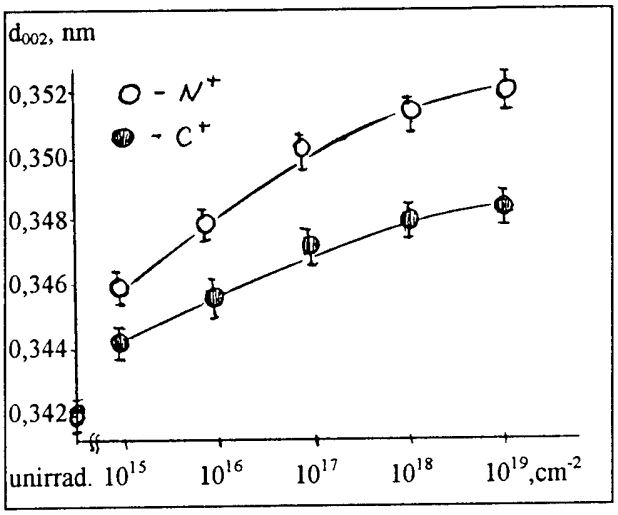

Fig.2. Influense of ion irradiation on d_{002} - parameter.

Increasing of doze of ions to $1 \cdot 10^{19} cm^{-2}$ don't bring the real changing of the researching parameter. The strength of fibre don't touched by the ion irradiation is 1800 MPa. After the irradiation into the carbon fibre of ions of carbon ($10^{14} cm^{-2}$) it's tensile strength increase on 10% and it is 1970 MPa. (Fig.3.) With growth of the doze of irradiated ions to the $10^{16} cm^{-2}$ the strength of the fibre decreasing to the 18% and achieves it's minimum value 1650 Mpa. The rest of the increasing of doze of the irradiated ions bring us to the increasing of the strength of fibre the 2400 Mpa with $1 \cdot 10^{18} cm^{-2}$. It is known, that tensile strength depends very much from the design of the structure of the carbon fibre.

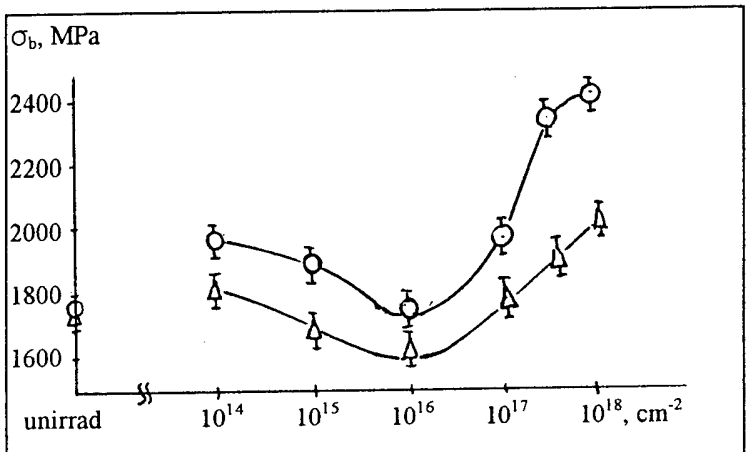

Fig.3. Tensile strength of carbon fibre after ion irradiation. (o - C^+; Δ- N^+)

The growth strength of the carbon fibre. The growth of strength of the carbon fibre in the interval of the dozes of the irradiated ions (C^+, N^+, 10^{14}-$10^{18} cm^{-2}$) can be understand as the increasing d_{002}. The analogue results was received in the work [1] during the research of the influence of the neutron irradiation on the mechanical properteis of the carbon fibre. Now we don't have clear understanding of this phenomenon and need deeper research.

Wetting of irradiated carbon fibre

The research of the influence of ion irradiation of carbon and nitrogen on the magnitude of contact angle of the surface fibre was conducted with the help of organic liquids - glitserin and olein acid. It was find out that the growth of doze of the irradiated ions has nonunique influence on the magnitude of the contact angle. (Fig.4.) With the minimum doze of the irradiated ions $10^{14} cm^{-2}$ the magnitude of the contact angle of wetting is increasing (from 37^0 to 40^0 for the olein acid and from 30^0 to 60^0 for the glitserin). With the increasing of the doze of the irradiated ions the contact angle of wetting is decreasing for the both types of liquids and reach it's minimum value with the ion doze - $10^{16} cm^{-2}$. During the rest of the increasing of the doze of the irradiated ions to

the $10^{19}cm^{-2}$ the magnitude of the contact angle of wetting is increasing and reaches the magnitude 44^0 (for the glitserin) and 42^0 (for the olein acid).

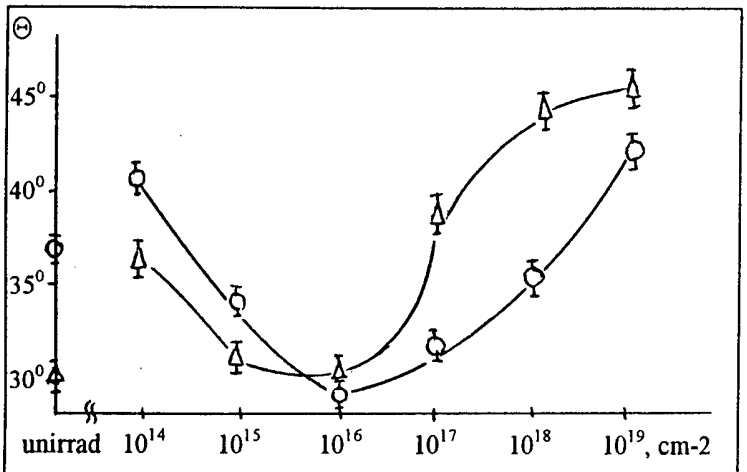

Fig.4. The influence of C^+ on the magnitude of the contact angle Θ during the wetting of the carbon fibre glitserin (O) and olein acid (Δ).

Changing of the contact angle of the surface fibre (after irradiation by N^+) have the analogue character. Also thinking about the fact that the surface tension of the glitserin and olein acid are distinguished at least 2 times and draw up 63 $^{MJ}/m^2$ and 32,5 $^{MJ}/m^2$ and the magnitude of contact angles of wetting in dependition of the implantation dozes is very close to each other. We can make a conclusion that the magnitude of the contact angles depends of the topography of surface fibre, of the near-surface layer fibre and of the "activity" of the surface of the irradiated carbon fibre.

With the increasing of the doze of irradiated ions the extent of the influence each of these three facts is different and that's why the dependence of the contact angle of wetting of doze has difficult nature.

Conclusions

1. It was settled that after irradiation of carbon fibre by the carbon and nitrogen ions (10^{17} - 10^{18} cm^{-2}) there comes the change of topography of it's surface.
2. With the doze of carbon ions $10^{16}cm^{-2}$ there come about at the same time the decreasing of the carbon strength and of magnitude of the contact angle of wetting.

Finansial support of this research was provided by Los-Alamos National Laboratory (contract N 1629Q0014-35).

References

1. Ligacheva E.A., Kostikov V.I., Skripchenko G.B. - Vlijanie neitronnogo obluchenija na structuru i svoistva uglerodnih volokon (The influence of neutron irradiation on structure and property of carbon fibres). Fisica i himija obrabotki materialov, 1979, N4, pp. 14 - 18.

P-3-26

METAL SURFACE CHARACTERIZATION BY INTENSE PULSED ION BEAM IRRADIATION

Yoshiyuki HASHIMOTO,* Mitsuyasu YATSUZUKA,** Hitoshi UCHIDA**
and Tohru YAMASAKI**

*Kobe City College of Technology,
8-3 Gakuen-Higashimachi Nishiku, Kobe, Hyogo 651-21, Japan
**Himeji Institute of Technology,
2167 Shosha, Himeji, Hyogo 671-22, Japan

Abstract

Matal surface characterization by irradiation of an intense pulsed ion beam (IPIB) with power density of 34MW/cm^2 and pulse width of 30ns has been studied experimentally. The IPIB irradiation leads to the nanostructured phase on the titanium surface. The IPIB irradiation to $Ni_{65}Cr_{15}P_{16}B_4$ alloy results in amorphous structure on the surface within 0.66μm in depth. The cooling rate is calculated to be 2×10^9 °C/s which is sufficiently larger than the critical cooling rate for amorphous formation of nickel alloys.

Introduction

Recently, intense pulse ion beams (IPIBs) with a high power density (~GW/cm^2) and a short pulse duration (~10ns) have attracted as a new heat-source instead of a laser in a material development field. Since ion ranges are extremely shorter than electron ones, the beam energy is deposited to a surface layer, typically, within a few μm. As a result, a target surface is heated above melting point in a short time of several nanosecond, and is immediately followed by rapid cooling. Solidification of metals at the rapid cooling rate results in production of non-equilibrium microstructures such as amorphous and/or nanocrystalline phases[1-4]. In this paper, the formation of an amorphous layer on the $Ni_{65}Cr_{15}P_{16}B_4$ alloy and the production of nanocrystalline phase on a titanium surface are successfully demonstrated.

Experimental Setup

Figure 1 shows a schematic drawing of experimental setup. An IPIB was generated by an inverse pinch ion diode (IPD)[5,6] with the pulsed power generator "HARIMA-II" (400kV, 3Ω and 50ns) at Himeji Institute of Technology. The IPD consisted with a ring anode (diameter:50mm) and an annular cathode (diameter:16mm). A Teflon plate (thickness:2mm) was attached to the anode surface as an ion source. The anode-cathode gap length was 3mm. A target material for IPIB irradiation was located at the focal point 120mm from anode.

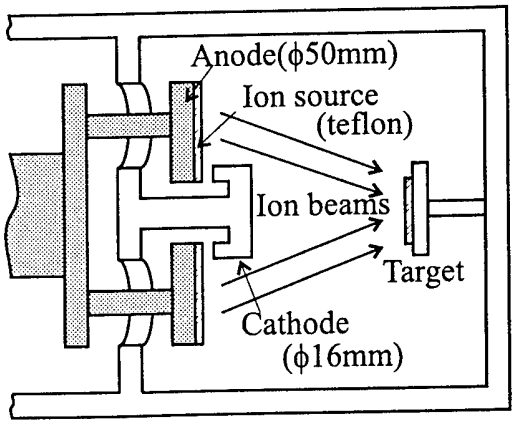

Fig. 1 Experimental setup of an inverse pinch ion diode and a target.

The maximum diode voltage and pulse width were 180kV and 30ns, respectively. The typical diameter and current density of the IPIB were 30mm and 180A/cm^2 at the focal point, respectively. Figure 2 shows the time evolution of beam power density obtained from the results of diode voltage and current density. The power density is not constant in time and has the largest value of 37MW/cm^2. The total beam energy is estimated to be 1.02J/cm^2 by integrating the power density with respect to time. We assume the ideal rectangular beam with the same total beam energy as 1.02J/cm^2 estimated above. Supposing that the pulse duration equals to the FWHM value of 30ns in Fig.2, we obtain the uniform power density of 34MW/cm^2. The dominant ion spices were found to be the carbon (53%) and the fluorine (47%) using the Thomson-parabola ion spectrometer.

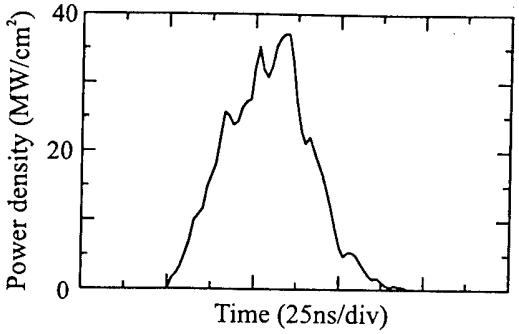

Fig. 2 The time evolution of beam power density.

Surface Characterization by IPIB Irradiation

The IPIB was irradiated to a titanium target for surface modification. The titanium target was polished with the emery paper (#1000) and annealed in a vacuum. The target was irradiated with the IPIB of 5 shots for the more uniform irradiation. Figure 3 shows the X-ray diffraction patterns of (a) irradiated and (b) non-irradiated titanium. Here, the incident angle of X-ray α is 2° which corresponds to the maximum diffraction depth of 0.85μm from the surface. The X-ray diffraction peaks of IPIB-irradiated titanium are broaden compared with that of non-irradiated titanium. The width of X-ray diffraction peaks are similar to that of amorphous phase. The width B of X-ray diffraction peak is dependent on the grain size d in Scherrer's formula as follows[7)]

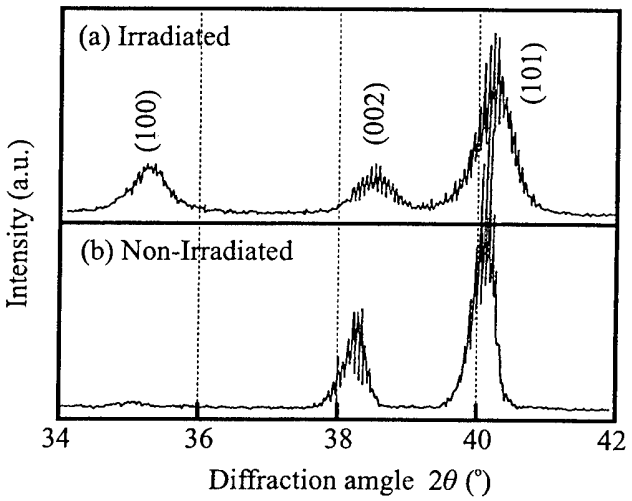

Fig.3 X-ray diffraction patterns of (a) irradiated and (b) non-irradiated titanium.

$$d = 0.9\lambda / B \cos\theta_B, \tag{1}$$

where λ is the wavelength of X-ray and θ_B is Bragg angle. Substituting the present conditions in Fig. 3 to eq.(1), the grain size of non-irradiated titanium was calculated to be approximately 32nm. On the other hand, the grain size of IPIB-irradiated titanium was calculated to be approximately 11nm. These results demonstrate the formation of nanostructured titanium surface by IPIB irradiation.

Next, the IPIB was irradiated to a $Ni_{65}Cr_{15}P_{16}B_4$ alloy for an amorphous layer formation. Figure 4 shows a HR-TEM micrograph and the corresponding selected area diffraction pattern of the IPIB-irradiated $Ni_{65}Cr_{15}P_{16}B_4$ alloy. Randomly oriented lattice fringes as well as a halo diffraction pattern are observed in the entire field of the micrograph except in some small area. These results indicate the formation of a homogeneous amorphous layer by IPIB irradiation.

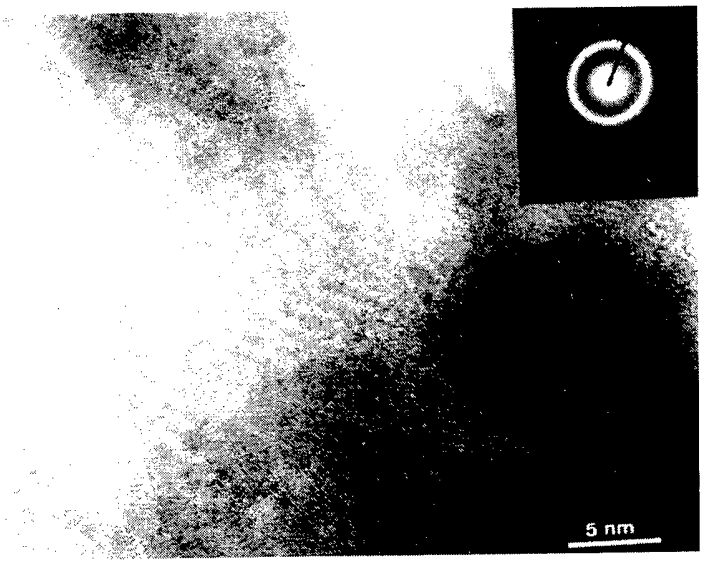

Fig.4 HR-TEM micrograph and selected area diffraction of IPIB-irradiated $Ni_{65}Cr_{15}P_{16}B_4$ alloy.

Time Evolution of Target Temperature

The time evolution of surface temperature and the cooling rate are estimated from the solution of the differential equation for heat conduction under the present conditions. Assuming an ideal rectangular beam with constant power p and pulse duration τ, the temperature rise of the target surface is written as

$$T(z,t) = \frac{2p}{K}\sqrt{\kappa t}\ \mathrm{ierfc}\left[\frac{z}{2\sqrt{\kappa t}}\right] \quad \text{for } 0 < t < \tau \tag{2}$$

and

$$T(z,t) = \frac{2p\sqrt{\kappa}}{K}\left[\sqrt{t}\ \mathrm{ierfc}\frac{z}{2\sqrt{\kappa t}} - \sqrt{t-\tau}\ \mathrm{ierfc}\frac{z}{2\sqrt{\kappa(t-\tau)}}\right] \quad \text{for } t > \tau, \tag{3}$$

where $\mathrm{ierfc}x = \frac{1}{\sqrt{\pi}}e^{-x^2} - x\mathrm{erfc}x, \mathrm{erfc}x = 1 - \frac{2}{\sqrt{\pi}}\int_0^x e^{-y^2}dy$, κ is the thermal diffusion rate, K is the thermal conductivity, z is depth from the surface and the radiation loss from the surface is ignored.

Substituting the present parameters (p=34MW/cm^2 and τ=30ns) into eqs.(2) and (3), we obtain the time evolution of temperature rise on titanium surface as shown in Fig. 5, where the effect of the latent heat for fusion and vaporization are considered. The titanium surface of z=0~4μm is heated up to its melting point of 1,660°C in a very short time of several nanosecond, and is immediately followed by rapid cooling. The

cooling rate from the melting point to the phase transition point (880°C) is found to be $dT/dt = 1\times10^9$ °C/s. This rapid cooling causes to production of the nanostructured phase on the titanium surface.

By similar procedure mentioned above, the cooling rate of nickel after IPIB irradiation is estimated. The cooling rate from the melting point (1,453°C for nickel) to the glass transition point (417°C for the $Ni_{65}Cr_{15}P_{16}B_4$ alloy) is found to be $dT/dt=2\times 10^9$ °C/s. The estimated cooling rate is larger than the critical cooling rate ($10^5 \sim 10^6$ °C/s) for amorphous layer formation of nickel alloys.

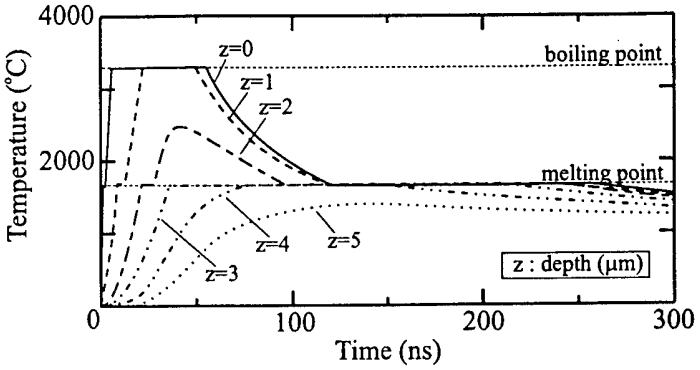

Fig.5 Temperature rise of the titanium surface for IPIB irradiation of 34 MW/cm^2 and 30 ns.

Conclusion

A mixed carbon and fluorine IPIB with the power density of 34 MW/cm^2 and the pulse width of 30 ns was irradiated to the target materials. The IPIB leads to the nanostructured phase on the titanium surface. The IPIB irradiation heats the titanium surface up to its boiling point of 3,287 °C. The cooling rate from the its melting point to the phase transition point is calculated to be 1×10^9 °C/s. The IPIB irradiation to $Ni_{65}Cr_{15}P_{16}B_4$ alloy results in amorphous structure on the surface within 0.66 μm in depth. The cooling rate from the melting point to the glass transition point is estimated to be 2×10^9 °C/s, which is sufficiently larger than the critical cooling rate for amorphous formation of nickel alloys.

Acknowledgment

A part of this work was supported by the Sasakawa Scientific Research Grant from the Japan Science Society.

[1] G. E. Remnev and V. A. Shulov : Laser & Particle Beams **11** (1993) 707.

[2] E. L. Neau : IEEE Trans. on Plasma Science **22** (1994) 2.

[3] M. Yatsuzuka, T. Yamasaki, H. Uchida and Y. Hashimoto: Appl. Phys. Lett., **67** (1995) 206.

[4] M. Yatsuzuka, Y. Hashimoto T. Yamasaki and H. Uchida: Jpn. J. Appl. Phys., **35** (1996) 1857.

[5] Y. Hashimoto, M. Sato, M. Yatsuzuka and S. Nobuhara : Jpn. J. Appl. Phys. **31** (1992) 1922.

[6] Y. Hashimoto, M. Yatsuzuka and S. Nobuhara : Jpn. J. Appl. Phys. **32** (1993) 4838.

[7] B. D. Cullity: "*Elements of X-ray Diffraction*", (Addison-Wesley Pub., 1978) p.101.

P-3-28

ION BEAM TREATMENT OF PE AND PTFE AND THEIR ADHESION ABILITIES

Yu. Klyachkin and A. Kondyurin

Institute of Technical Chemistry, Russian Academy of Sciences
13 Lenin St., Perm 614000, Russia

Abstract

Ion beam treatment of polymer materials leads to sharp change of surface structure. Therefore, exploitation characteristics of polymers are changed including a good adhesion ability to dispersed metals and active adhesives. In this work the results of adhesion characteristic study of polyethylene (PE) and polytetrafluorethylene (PTFE) after ion beam treatment have been presented.

Polymers were treated by nitrogen ion beam with energy of 30 keV and pulse current density of 5 mA/cm^2. After treatment changes of surface energy and chemical activity of polymer surface were observed. At low treatment dose a sharp change of interface structure in adhesion joint with epoxy and polyurethane adhesives was observed. United polymer network on boundary between treated polymer and adhesive occurred. Adhesion joint durability increased by two orders in joints of PE and by 15 times in joints of PTFE. Modified polymers retain their adhesion abilities at ageing and cleaning with using of solvents.

Low optimum dose for achievement of maximal adhesion and high current density at pulse regime of treatment permit to propose a new technological method of surface modification of inert polymers.

(The full text will be published elsewhere.)

STRUCTURE OF POLYMER SURFACE AFTER PULSE ION BEAM TREATMENT

Yu. Klyachkin, A. Kondyurin, E. Tereshatova, D. Yakusheva

Institute of Technical Chemistry, Russian Academy of Sciences
13 Lenin St., Perm 614000, Russia

Abstract

Appearance of new exploitation properties of polymers after ion beam treatment is connected with changes of structure, which take place in surface layer under the action of ion beam. This changes is connected with high dissipated energy of moving ion in polymer surface layer in comparison with binding energy and ionizing potential of atoms. Therefore, a study of influence of high current density of ion beam on changes of structure is interesting for modification of surface layer of polymer. High density of dissipated energy in thin surface layer limits a current density due to a low thermoconductivity and thermostability of polymers. The pulse regime of treatment permits to increase of current density to 10-15 mA/cm^2 without heating of treated polymer.

In this work the studies of polyethylene, polypropylene, polyisoprene, polystyrene, polytetrafluorethylene, polyurethane after action of ion beam with energy of 10-30 keV at 1-12 mA/cm^2 current density in pulse regime are presented. Usage of spectral methods (IR ATR, Raman, UV-transmissions and reflections, XPS), methods of surface energy measurement and other modern methods is shown the effectiveness of pulse regime. Influence of air oxygen to oxidizing processes in surface layer of polymer after ion beam treatment was considered. Lamellar structure model of surface layer was proposed.

(The full text will be published elsewhere.)

P-3-31

THE USE OF PULSED POWER ION/ELECTRON BEAMS FOR STUDYING OF UNITS OF ELECTRONUCLEAR REACTOR

S.A.Korenev, A.S.Korenev, I.V.Puzynin, V.N.Samoilov, A.N.Sissakian

Joint Institute for Nuclear Research,
141980, Dubna, Moscow region, Russia

Abstract. The questions of using power pulsed ion beams for studying some units of model's electronuclear installation are considered in this report. It allows to analyze the question of heating loads on the targets, entering and output windows for beams of charge particles. The methods of increasing a life-time of these windows on the basis thin foils with help of surface modification of materials by high current pulsed ion beams are considered.

INTRODUCTION

A new method of production of electric power based on the ideas proposed by C. Rubbia [1] has been practical interest. In this case the questions of stable work units of the pilot installation for test of electronuclear method for production of electropower is very important. The general scheme of this installation includes a proton accelerator, target unit and a device for transformation of beam energy to electropower [2]. Among a lots of the units the window for entering the beam to the target is haughty.

Investigations on using the pulsed high power electron/ion beam technologies for surface modification of materials [3,4] allow to find application for study of two questions of electronuclear rector:

1. heating loads for different materials for this reactor;
2. increasing life-time of window for proton beam.

The main questions of using the pulsed high current electron/ion beams for several units of the electronuclear installation are considered in the this report.

THE MAIN PRINCIPLE OF PULSED POWER ELECTRON/ION BEAM TECHNOLOGIES

STUDY OF HEATING LOADS ON THE MATERIALS OF ELECTRONUCLEAR INSTALLATION

Pulsed electron or ion beam is a pulsed energy source. This energy separates in the solid state at the during interaction of beam with irradiated sample. For example, for beam current I = 200 A, pulse length t = 250 ns, kinetic energy E= U = 500 KeV (kV), energy for one pulse is W = I U t= 200 5 10(5) 250 10(-9) = 25J. For beam current 1000 A this energy is 50 J. This is high energy for pulse on the small depth penetration determined kinetic energy. This energy enough for different processes in solid state.

In the dependence of beam kind (electron or ion) we can see special peculiarities, which consist in the next.

Electron pulsed beam (Fig.1a):

- small size of electrons;
- small ionization losses;
- the depth of penetration for kinetic energy 100 - 1000 keV for many materials consists of 10 - 500 mm;
- adiabatic heating processes of interaction by pulsed electron beam with solid state;
- electron beam mixing.

Ion pulsed beam (Fig.1b):

- large size of ions in comparison with electrons;
- large ionization losses;
- small depth of penetration with comparison with this parameter for electron beam, for example for kinetic energy 100 - 1000keV depth of penetration is about 0.05 - 1.0 mm;
- adiabatic heating processes of interaction by pulsed ion beam with solid state;
- synthesis of components of samples;
- ion beam mixing;
- ion spray of irradiated samples;
- long distance effects.

The properties of these beams allow to use these technologies for test experiments with materials for electronuclear reactor.

The pulse length of electron beam t for rapid thermal processes, especially for complex materials, when necessary have stable stoichoimethric relationship must satisfy next condition:

$$t << t(p) = 2h^2\rho c / \lambda, \qquad (1)$$

where: t(p) - heating constant of sample;
h - depth of penetration;
ρ, c, λ - density, heat capacity and heat conductivity of irradiated materials.

In this case we have step distribution of temperature in their radiated sample. The last means, that energy release of electron beam can be on the depth penetration, which determined kinetic energy of electrons. The temperature T in an irradiated sample on electron rate depth can be calculated from formula :

$$T = 2Wt / h\,\rho S, \qquad (2)$$

where W- electron beam power density;
S- irradiated square.

For pulsed ion beams we have another situation and for calculation of heating of sample we must use next formula:

$$T = 2Wt^{0,5} / (3.14\,\lambda\,\rho\,c)^{0,5} \qquad (3).$$

More detail description of main principles of beams pulsed technologies can find in the [3,4].

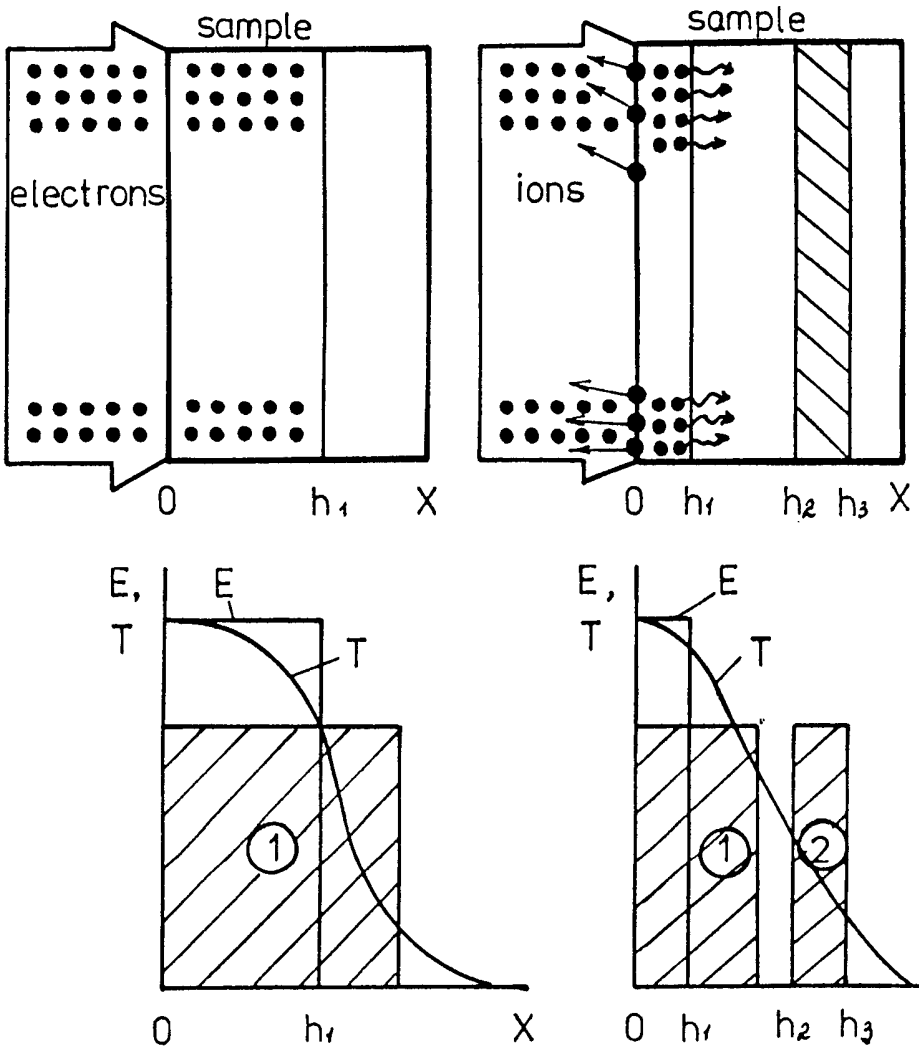

Fig. 1a. Pulsed electron beam.

Fig.2. Pulsed ion beam

MODIFICATION AND DEPOSITION OF FILMS AND COATINGS ON THE FOILS WINDOWS

The surface modification of materials consists in the ion/electron mixing, surface melting and other surface effects which can make better properties of these materials for its using for different units, which can work in the intensive loads and conditions. Also for increasing life-time of window's foils for intense proton beams can be used foils with special films and coatings. For receiving effect of increasing life-time of foils necessary have films or coatings with more stable heating and corrosion properties.

The main problems of this method is very good adhesion films with substrate. An electron or ion mixing in the ion diode with explosive ion emission [5] allows to decide this problem.

EQUIPMENT

The source consists of the high voltage pulsed generator, vacuum high voltage diode with vacuum system, diagnostic system and vacuum chamber for irradiation of samples and for substrates - foils for windows of target units.

The pulsed high voltage generator has got next main parameters:

- voltage 100- 700 kV;
- pulse duration 300 - 1000 nsec;
- stored energy 100 - 500 J;

- repetition 1-5 Hz.

High voltage vacuum diode consists of stainless steel vacuum chamber , high voltage insulator made from capralon, an anode with anode plasma initiator, a extractor electrode and diagnostics devices. Beam current measurements are carried out with an integrating Rogowski transformer and Faraday cup, and a high resistance divider is used for measurements of pulsed voltage.

The main emission characteristics of source for electron and ion regimes are given in Fig. 2,3.

The mode of operation can be changed from ion beam to electron beam.

This is done by changing the polarity of the voltage on the output side of the pulsed high voltage generator.

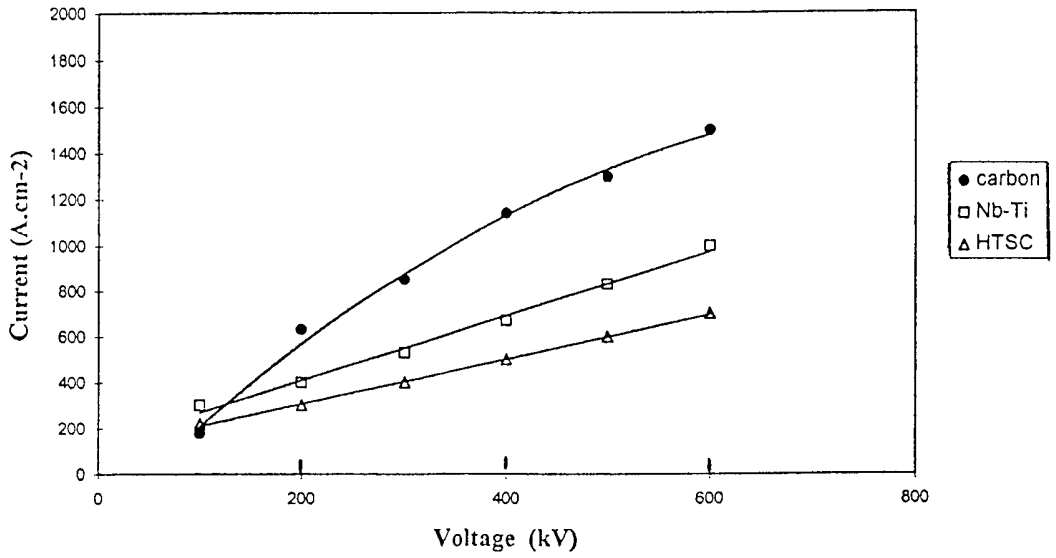

Fig.2. Emission characteristics of source in an electron regime.

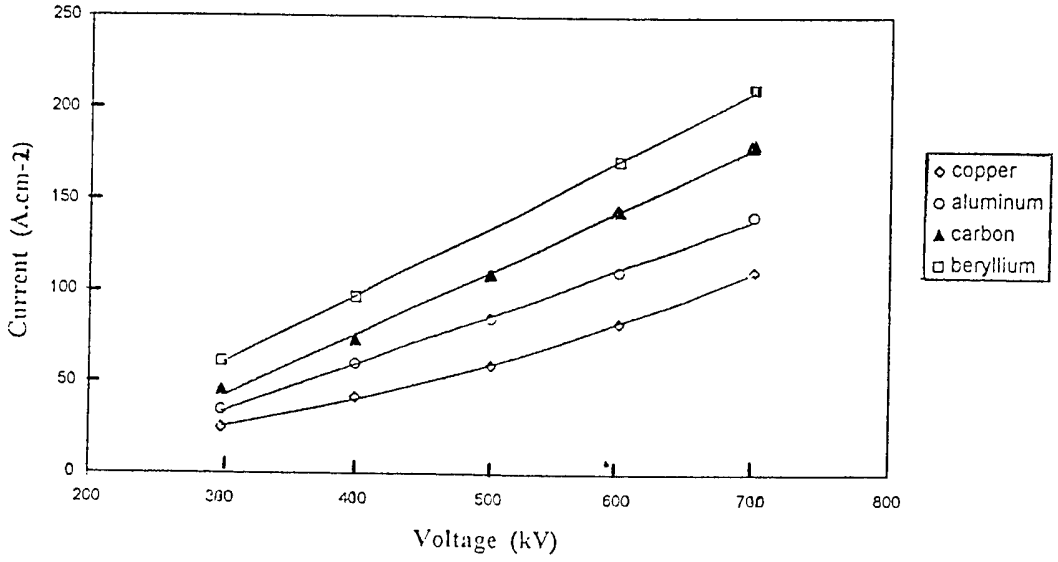

Fig.3. Emission characteristics of source in ion regime.

This ion source uses for deposition of films or coatings with ion/electron mixing.

FOIL'S WINDOWS FOR BEAM

The special technology for preparation of output foils for charge particle beams was elaborated on the basis of carbon films on the Al and Be foils. It concerns with problem of increasing a life-time. For proton beam of this reactor better use carbon coating thickness about 30-50 mkm on the Be foil of thickness 0.5 - 3 mm. The technology consists of first deposition of carbon or diamond-like films or coatings with ion mixing on the Be or Al foil from both sides and after electron mixing for more long depth of mixing of C and substrate. The typical foil's window is given in Fig. 4.

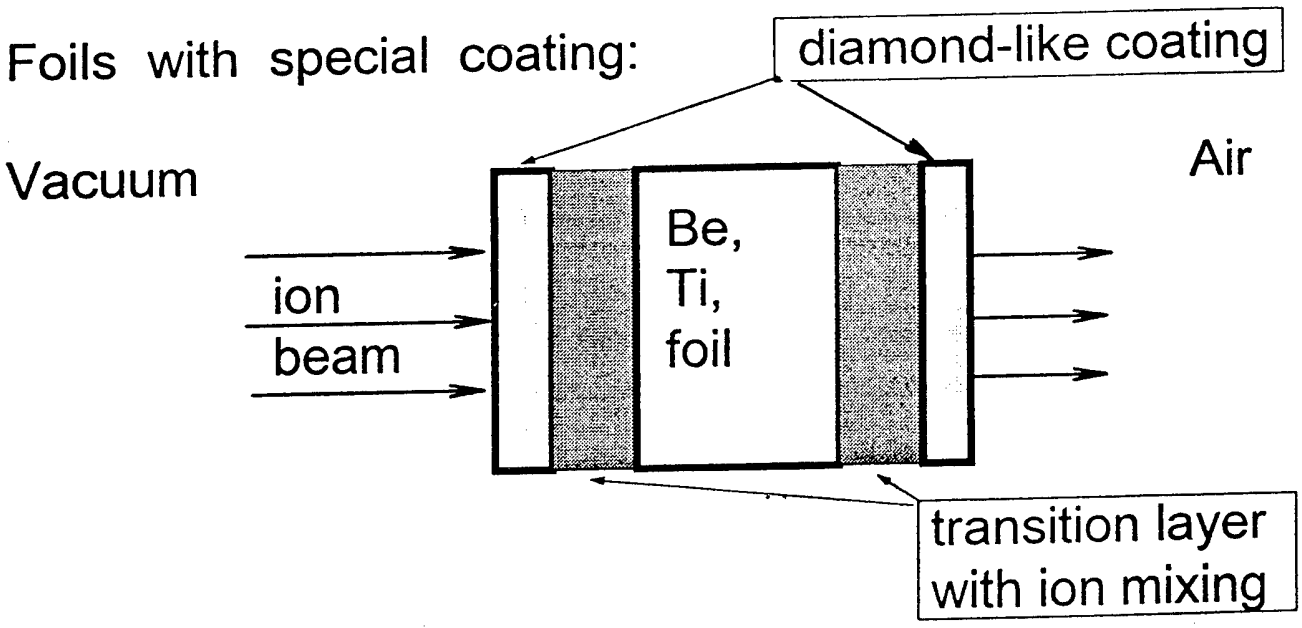

Fig.4. Typical foil's window with additional coatings.

Test experiments with high power pulsed electron beams show increasing life-time to 10 times with comparison with clean Be and Ti foils.

The measurements of oxidation resistance acids show stable characteristics at the during 8 hours.

CONCLUSION

1. New method for test of materials of electronuclear reactor is suggested.
2. New method of increasing life-time of foil's window is suggested and is tested.
3. Surface modification of materials by pulsed high current ion/electron beams can be used for preparation of materials for electronuclear reactor and similar systems.

REFERENCE

[1] Carmine F., Geles C., Klapisch R., Revol J.P., Roche Ch., Rubio J.A., Rubbia C. "An Energy Amplifier for Cleaner and Inexhaustible Nuclear Energy Production Driven by Particle Beam Accelerator" CERN/AT/93-47(ET) (1993)
[2] Barashenkov. Preprint of JINR, No P2-1101, 1977.
[3] Korenev S. Proc.3rd International Conf. "Energy Pulse and Particle Beam Modification of Materials" (EPM'89), Drezden, Germany, (1989), pp. 448-451. .
[4] Korenev S. Nuclear Instruments and Methods in Physics Research B80/81 (1993), pp. 242-247.
[5]Korenev S., Perry A. X Intern. School on Vacuum Ion and Electron Technology, Sozopol, Bulgaria, (1994), p.25, Vacuum , (1996) (in pres).

P-3-33

PULSED METAL-ION BEAMS FOR MODIFICATIONS OF SOLIDS

J.Langner, J.Piekoszewski, J.Stanisławski

Soltan Institute for Nuclear Studies

05-400 Otwock-Świerk n.Warsaw, Poland.

Introduction

The modification of surface properties of materials with high-intensity pulsed ion beams has been studied for over a decade [1,2]. The transient heat generation by HIPIB in a near surface region may cause variety of the processes, e.g. crystalline defects annealing, mixing, glazing, quenching etc. [3,4]. For the modification of a material surface particularly interesting conditions are created in a case when the transient heat transfer is connected with the mass transport into a substrate during the same pulse. A high temperature of the surface region (up to the melting point and above) and the transient nature of the heat evolution create unique conditions for the interaction between host and deposited materials, during which various metastable phases and alloys can be formed. Such conditions can be obtained within IONOTRON-type generators which were developed at SINS for the investigations of controlled thermonuclear fusion [5]. Intense ion-plasma beams generated by those facilities have energy densities ranging from 1 to 10 J/cm^2 and pulse length within a microsecond range. These beams are capable to melt a near-surface layer of any material and to dope with doses of the order of 10^{14} to $5x10^{17}$ atoms/cm^2.

In our previous experiments, which were carried out in the 80s for the modifiacation of various materials, there were used only ions formed from the working gas (H_2, N_2, BF_3, Ar etc.) which was injected into the interelectrode region. In recent experiments a plasma stream consists partly ions of thr working gas and partly those of metal ions. In this case it is possible to introduce any metal ions (e.g. Al, Ti, Cu, W, Co etc.) into a thin surface layer of any substrate and to form the coating with very good adhesion.

IONOTRON- facility for surface modification

In IONOTRON, schematiclly presented in Fig.1, the ion beam is formed in a low-pressure, high-density plasma discharge initiated between two concentric cylindrical sets of rods, allowing a free passage of particles through the electrode region. A fast electromagnetic

valve introduces a portion of the working gas into the interelectrode region. With some delay (τ) after a moment of the valve opening, when the gas density attains the desired distribution in this region, a voltage from the charged condenser bank is applied to the electrodes. The parameters of the power supply system, the electrode dimensions and the initial gas conditions are selected in such a way that the final stage of the discharge is accompanied by a strong drift of electrons along the electrode rods. A suppression of the electron current allows an effective acceleration of ions in the interelctrode radial electric field.

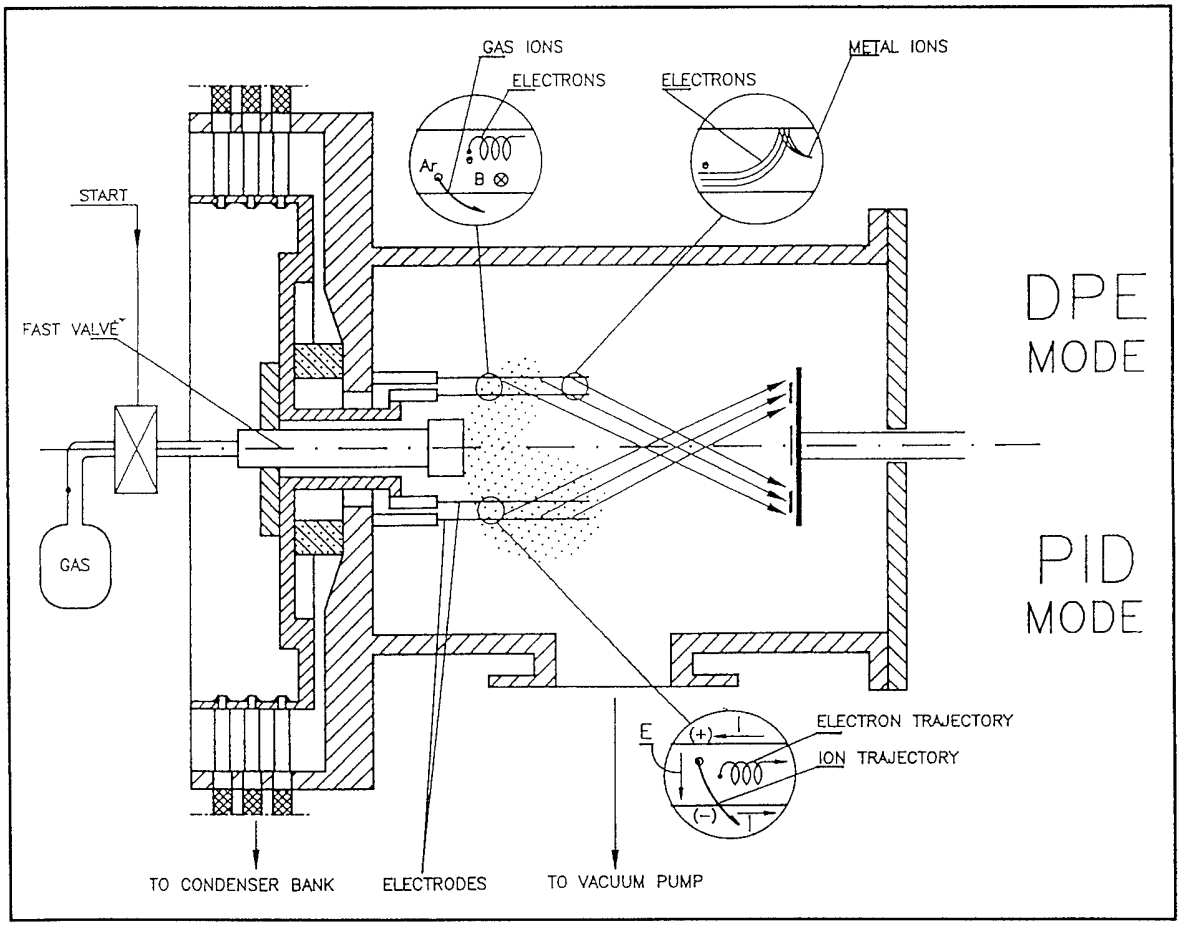

Fig.1 Schemes of the IONOTRON device operating in different modes(DPE or PID).

Depending on the time delay (τ) two operating modes are possible. In PID (Pulse Implantation Doping) mode, (τ) is long enough for the working gas to fill up completely the interelectrode region. Then the discharge produces a high intensity (up to tens kA) short duration (about 1 μs) plasma pulse, containing ions of the working gas only.

Such a technique has been used for the doping semiconductors (p-n, n-p silicon junctions formation), for introducing of high doses of nitrogen into steels, glazing of the ceramics etc.

In the second mode, referred to as DPE (Deposition by Pulse Erosion), delay (τ) is relatively short and the working gas (expanding from the valve) does not reach the electrode ends. Under such conditions axial electron currents flowing to the electrode ends induce the local melting and evaporation of an electrode material and the metal ions are present within the plasma stream. In our recent experiments different metal (Mo,Ti, Al, Cu, Ni) rods as the electrode material were used . The effectiveness of DPE process as well as the range of delay times (τ) in which the process is most effective, depend on the type of the working gas. It has been checked that the most effective deposition can be obtained for argon gas and there is no deposition in the case of hydrogen gas. This can be easily understood in view of the known fact that velocity of the gas molecules propagation in vacuum depends on the atomic number of these molecules, and in the case of hydrogen the working gas fills the whole interelectrode space even at the shortest delay times used.

Fig.2 presents the mass increment of 1H18N9T stainless steel thin disk located at a distance of 20 cm from ends of the electrodes, as a function of (τ) for argon and nitrogen at Al deposition.

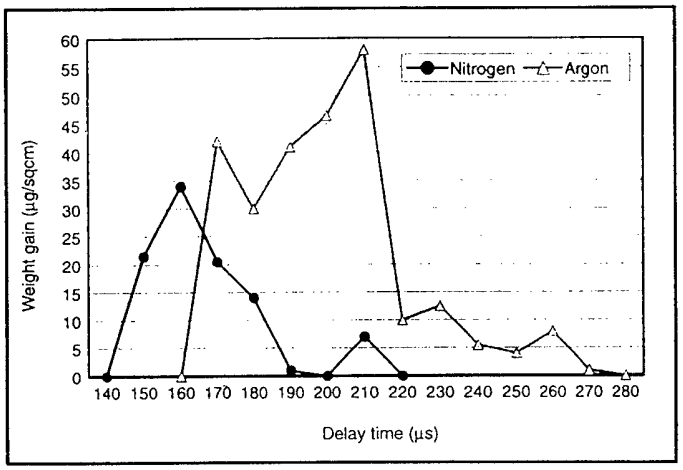

Fig.2 Weight gain vs. delay time in DPE process

The practical limitation of this method for the producing of metal-ion beams come out from the fact that few metallic electrodes are available in a suitable form (e.g. chromium rods are not commercially available).

In order to eliminate this limitation and to extend of the possibilities of the IONOTRON generator a separate metallic pulsed plasma source (based on the metal vapour vacuum arc) was installed in IONOTRON device (inside the ring type fast gas valve). The source was supplied from a high-current generator via a separating transformer. The arc current reached 120kA and the pulse width was 100 µs. Depending on the choice of operation conditions in this combined system , it is possible to form pulses containing both, gas and metal ions.

Metal-ion processing

The DPE experiments performed so far have included the formation of nickel and aluminium coatings on copper (Ni/Cu and Al/Cu), aluminium coatings on AISI 316L and 1H18N9T stainless steels, titanium and molibdenium coatings on AISI 321 stainless steel as well as on ceramic substrate. As it was shown in Paper[6] (see Fig 3), the atoms of the deposited material penetrate the substrate to a depth exeeding 3 μm. This is the result of the diffusive mixing in the molten substrate layer. In term of the surface concentrations, the thickness of the deposited layers may exeed 10^{18} atoms/cm^2. Adhesion tests have revealed extremely strong bonding of the layers with substrate.

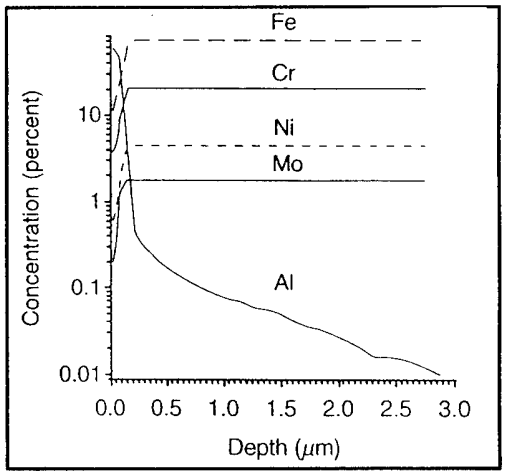

Fig. 3 The SNMS profiles of Al/AISI 316L structure.

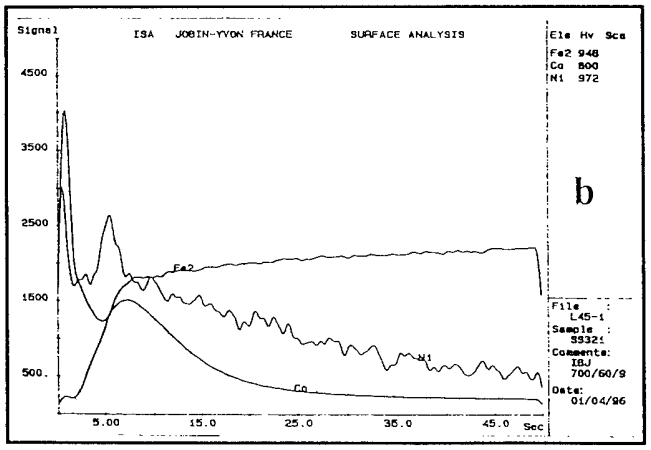

The investigations on the formation of coatings by combined metod are at the preliminery stage of development. First results on the deposition and mixing of Co, Ti, W and Cr were presented on SMMIB'95 [7] and Intern. Workshop Tomsk'96. Fig. 4 show GDS elemental profile of the cobalt/AISI s/s structure.

Fig.4 GDS profile of Co/AISI s/s structure.

References

[1] J.E.E. Baglin, R.T. Hodgson et al.: Nucl. Instr. and Meth. 191 (1981) 169.

[2] J. Piekoszewski, M. Gryziński, J. Langner, Z. Werner: phys. status solidi (a) 67 (1981) K163.

[3] J. Piekoszewski, J. Langner: Nucl. Instr. and Meth. B53 (1991) 148.

[4] A. D. Pogrebniak, G. E. Remnev et al.: Nucl. Instr. and Meth. B36 (1989) 286.

[5] M. Gryziński: INR Reports 711 and 715, 1966.

[6] J. Langner, J. Piekoszewski , C. Pochrybniak, F. Rosatelli, S. Rizzo, A. Miotello, L. Guzman, P. Lazzeri: Surface and Coatings Technology 59 (1993) 281.

[7] J.Langner, J.Stanisławski, J.Piekoszewski: Surface and Coatings Technology (in print).

P-3-37

CHAIN OF PHASE TRANSITIONS IN METALS SUBJECTED TO HEAVY INERT GAS ION BOMBARDMENT

A.M. Panesh, A.D. Lozovskii

Karpov Institute of Physical Chemistry
Vorontzovo Pole St. 10, Moscow 103064, Russia

The totality of new phenomena taking place on heavy inert gas (Ar, Kr, Xe) ion bombardment of metals was under study in this work. Such phenomena are: grains creation in metals, their crystallization, melting and anomalous thermal desorption bound to these. We suggest that all of these phenomena originate from the presence of mutually interacting complexes made of heavy inert gas atoms and vacancies in such metals. A model of one of phase transitions in irradiated metal layer is proposed.

Crystal grains of heavy inert gas were observed during study of the interaction of heavy inert gas ion (Ar^+, Kr^+, Xe^+) beams having energies 10-100 keV with single crystals of metals [1-7]. Grains in a metal are well shown in figures in [1-7], and their crystallinity can be deduced from definite reflexes at microdiffraction pattern. Grains with sizes of about 2-4 nm and density of $2 \cdot 10^{18}$ cm^{-3} can be seen at room temperature with the help of transition electron microscopy (TEM) and microdiffraction methods. These methods allow to evaluate parameters of crystal lattices of grains.

Main parameters of grains appearing as depend on ion beam type and irradiated metal parameters were obtained experimentally. It was mentioned that the crystal grains with sizes of about 1-4 nm appear at fluences in the range of 10^{16}-10^{17} ion $\cdot cm^{-2}$. For example on irradiation of nickel with Kr^+ ions Kr containing grain has diameter that equals 2.0 nm [8]. Grain crystal structure (fcc) is the same as that of metal (Ni), lattice parameter a=0.50 nm. Melting temperature of the grain T=575 K.

Crystal structure kind is fully depends on that of irradiated metal. For example grains of krypton have fcc, vcc or hdp structures in different metals and Kr crystal obtained after gas cooling has only fcc structure. It is worth mention that lattice parameter of grain differs from that of correspondent noble gas (after crystallization from liquid phase) considerably. For example on irradiation of nickel with Kr^+ ions grain appears having a=0.50 nm, while the lattice parameter of krypton crystal created from gas is 0.564 nm. In general it is worth mention that lattice parameter of grain is smaller than that of crystal obtained after crystallization from liquid phase. Moreover, lattice parameter of grain of heavy inert gas depends on metal. For example: Xe in Al matrix has a=0.60 nm; Xe in Ni matrix has a=0.52 nm [9]. Ordinary crystals have only fixed values of lattice parameters.

Some authors [3, 6, 10] have established that the heating of irradiated samples up to (600-900) K leads to vanishing of crystal grain diffraction reflexes, and those reflexes appear again on sample cooling. So crystal grain melting is observed and this phase transition can go in opposite direction. Correspondent melting temperatures of grains are not bound to that of ordinary noble gas crystals. So all the totality of experimental data is a witness that both parameters and behaviour of the created grains of heavy inert gas depend firstly on metal matrix.

Existing models of such crystal grains creation in single crystals of metals subjected to heavy inert gas ion bombardment are not complete enough. In order to explain the fact of their creation most of authors (see for example [11, 12]) tries to draw an analogy with helium bubbles in irradiated metals and makes such series of proposals:

1. Grains are made of only noble gas atoms.

2. Crystal lattice type of a grain does not affect its properties.

3. Such grain parameters as density n and pressure p obey to Ronchi and Simon extrapolating equations [11, 12]. Those equations describe the behaviour of macroscopic volumes of noble gases.

4. The properties of metals with grains (among them surface tension coefficient, Poisson coefficient and so on) do not differ from that of not irradiated metals. Above that some parameters experimentally obtained for macroscopic volumes of metals with dislocation-like structural defects are used for estimations and calculations.

5. The only phase transition - equilibrium phase transition of the first type (crystallization-melting) is considered. It is suggested that it is equivalent to the correspondent phase transition for condensed noble gas.

All of authors used the following standard procedure:

1. Size, structure type, lattice parameters and melting temperature can be evaluated with the help of TEM and microdiffraction methods. *2*. The crystalline noble gas atom density is deduced from its lattice parameters and structure type. *3*. This density datum is used for the determination of pressure in grains on the basis of Ronchi extrapolating equation in spite of the metal crystal structure. *4*. The equilibrium Laplace pressure in grains is deduced from grain radius and surface tension coefficient of the non irradiated metal. *5*. Pressure that corresponds to the experimental value of the noble gas melting temperature is calculated on the basis of empirical Simon equation. This equation describes melting curve of heavy inert gas macroscopic volume with P-T variables. *6*. Calculated pressure values lie in the range of tens kbar. This range is narrow enough, so one makes the conclusion about good concord between this model and experiment.

It is a pity that the following proposals made on the basis of this disagree with experimental facts:

1. There is not any proof that the grains are made of only noble gas atoms. Moreover were it like this grain could not appear: diffusion energy of noble gas atoms equals (even for the lightest of them - Ar) 7 eV in Ni [13]. It makes the migration of noble gas atoms impossible in the experimental range of temperatures, especially on irradiation with middle range ion energies (10^5) eV at T=300 K.

2. Grain crystal structure type is the same as that of matrix. It is natural to wait that it is the matrix that considerably determinates grain properties (among others by means of matrix structure).

3. Being purely empirical Ronchi and Simon equations does not contain any information about small volumes of noble gases (100-1000 atoms) having crystal lattice type differing from that of condensed noble gases.

4. Metal properties considerably depend on the existence of defects in crystal structure and their concentration for both extent and point ones [14]. Moreover it was shown that surface tension coefficient in metal containing argon-vacancy complexes does not bound to that in non defective metal.

5. There is not any proof that the observed phase transitions are equilibrium. Moreover on the middle energy (about 10^5 keV) ion beam irradiation their appearance process misses liquid phase (it is not seen experimentally).

6. Finally one can observe grains with different sizes (2-3 times scatter) for the same experimental conditions. It is evident that the equilibrium pressure in such grains must vary. It should lead to considerable varying of melting temperature with grain size. This in turn means the absence of phase transition point in considered system, process of melting taking place over wide range of temperature. Nothing like this is observed in experiments. Therefore phase

transitions in irradiated metals do not look like that in macroscopic volumes of compressed noble gases.

So phase transition of the first kind: crystallization-melting is observed in metals subjected to heavy noble gas ion bombardment. Its specific feature is taking place in unordinary system:

- it is not phase transition in metal;
- it is not phase transition in noble gas (structure and lattice parameter of grains are different for the same gas but different matrices and so on);
- it is not phase precipitation in submission solution of AB kind (A - metal atom, B - noble gas atom), because of that noble gas atoms in submission state are almost immobile (especially on the middle energy ion beam irradiation at T=300 K), it does not allows them to create new phase as the nearest neighbours.

In order to elucidate nature of these phenomena experiments on interaction of heavy noble gas ions with metals at elevated temperatures and in other energy range (about 1 keV). Theoretical approach to be developed must take in account both implanted atoms and another defects of crystal structure. Theoretical consideration of these phenomena will be published later.

Low energy ion beam has some preference in the investigation of ion beam interaction with metals: 1. There is no cascades of atom-atom collisions on slowing down of such beam particles in metal. 2. Low depth of penetration gives an opportunity to use such method as thermal desorption spectroscopy (TDMS) having high sensitivity. 3. Direct answer are to have been got: whether pressure is high in grains of noble gases.

TDMS method have been chosen as the main one for the investigation of low energy (<1 keV) argon (Ar^+) ion beam interaction with metals (Ni, Co). It was caused by the following:

1. Method of thermal desorption is enough sensitive to changes of implanted gas atom state. 2. Path length for low energy ions is short: (10-20) Ă. 3. Comparatively small changes of implanted gas atom state bound to structural reorganization lead to instant desorption of particles situating near surface. 4. Change of temperature (thermal desorption method) allows to alternate simultaneously both matrix state and that of implanted atoms that is to study phase transitions.

Interesting results were obtained on the study of thermal desorption of argon implanted in cobalt Co(111) at low energy (E=0.6 keV). During heating of cobalt single crystal it changes its structure at T=690 K: hdp Co(001) transforms into fcc Co(111). Reverse transition can be seen during cooling at T=640 K, that is hysteresis takes place. It is natural to assume that such structural phase transition affects the state of implanted atoms in metal. In order to study the influence of structural phase transition hdp to fcc in cobalt on Ar atom thermal desorption the following sequence of operations was made:

To begin with sample was heated up to temperature higher then that of the phase transition hdp to fcc and then was cooled down to 650 K, that is cobalt has fcc phase. It was followed by irradiation and cooling of irradiated cobalt. During cooling we registered spectrum of reverse argon atom thermal desorption, that is gas flow was measured during temperature decrease. The spectrum shows evidence that after irradiation in fcc phase during cobalt heating in the moment of phase transition to hdp Co anomalous thermal desorption is observed: jump like raise of Ar atom desorption rate, that looks like the desorption energy being negative. The appearance of anomalous desorption peak of preliminary implanted Ar atoms caused by structural phase transition in Co can be explained as an evidence of movement activation energy of argon-vacancy complexes caused by structural reorganization of neighbourhood for that complex. The effect of anomalous desorption of noble gas atoms bound to structural phase transition in irradiated layer have been observed for single crystals Zr and Ti, too. The discovered

phenomenon of anomalous desorption served as a good tool for the first kind phase transition diagnostics in metal-noble gas system.

It is known that implanted atom states depend on main parameters of ion irradiation: energy and fluence. Studying TDMS spectra change with these parameters one can make conclusions about changes of implanted atom states in subsurface irradiated metal layer. If fluence is considerable enough the interaction between structural defects of irradiated substance (vacancies, admixture atoms, own interstitials and so on) has substantial influence on implanted atom states. That is why primary stage of implanted atom state investigation for Ar in subsurface irradiated layers of Ni(100) and Ni(110) single crystals was carried out for low fluences. Correspondent TDMS spectra consideration has shown that there is a number of Ar states in nickel, part of them being bound to the very surface and part - being distant from the surface. The latter can be considered as clusters with integer amounts of vacancies and argon atoms. Fluence raise results in raise of cluster complexity.

Thermal desorption spectra of Ar from Ni(100) (Ar^+ fluence is fixed) at different temperatures show that as temperature during irradiation raises the last high temperature peak maximum moves to higher temperatures. This is an evidence that binding energy increases and in general cluster (responsible for this peak appearance) becomes larger. Besides that raise of temperature during irradiation simplifies TDMS spectra towards to its drastic change at T=870 K. Now the only peak exists in thermal desorption spectra. Its narrowness means that this peak describes the decay of the only state and high maximum temperature indicates high binding energy. The appearance of this peak in TDMS spectra has bright threshold character changing both irradiation temperature and fluence. Experiments have shown that for the system described above this peak formation takes place at fluences $>8 \cdot 10^{16}$ cm^{-2}.

Study of distribution of implanted argon in metal for the same experimental conditions show that the characteristic depth of Ar distribution at the irradiation temperatures T=(300-850) K correlates with the path length for Ar^+ energy E=0.6 keV. The scene changes drastically at the irradiation temperature T=870 K: seam depth is considerably larger than the depth of penetration. It is about 150 Å. Besides that at the above mentioned temperature argon atom distribution in the metal is close to uniform up to 150 Å. The results obtained during study of the reverse thermal desorption from irradiated nickel is not less interesting: anomalous thermal desorption section was observed that is desorption rate increases during decrease of temperature.

This phenomenon can be seen at very narrow irradiation temperature range T=(870-900) K fluence being $>8 \cdot 10^{16}$ cm^{-2}. That is anomalous thermal desorption emergence has threshold character and lies in the same range of parameters as the emergence of high temperature peak in ordinary TDMS spectrum. The samples showing anomalous part in thermal desorption spectra (about T=860 K) were studied with TEM and microdiffraction methods. Analysis of irradiated nickel samples gave evidence that there appear grains having mean diameter 3 nm and volume density $1.6 \cdot 10^{24}$ m^{-3} in subsurface layer for the following ion irradiation conditions: T=870 K, E=0.6 keV, $d=8 \cdot 10^{16}$ cm^{-2}. Let us mention that crystal grains was not observed for samples whose TDMS spectra have not anomalous thermal desorption section.

During heating of Ni (Co) samples containing crystal grains up to 860 K (850 K) grains can still be registrated by TEM, but reflexes of crystal vanish in microdiffraction pictures. So the melting of crystal grains was observed at T=860 K (850 K). Crystal grains can not be seen also in properly irradiated samples subjected to heating up to T=1450 K: thermal desorption evacuates almost all argon from metal at T=1350 K.

Generalized thermal desorption spectra from Ni and Co are constructed by addition of direct and reverse TDMS spectra of Ar. If irradiation temperature equals 870 K, then two thermal desorption peaks can be obtained: high temperature (1350 K) and that with participance

of anomalous thermal desorption (850-860 K). Besides of these peaks there is a peak with participance of anomalous thermal desorption situating about T=640 K (temperature of structural phase transition fcc to hdp in Co) in reverse TDMS spectrum of Ar from Co. It is natural to assume that the peaks with anomalous thermal desorption sections correspond to some other phase transition. But this temperature range has only one phase transition - crystallization of grain.

The observed peak reorganization in TDMS spectrum with the increase of irradiation fluence and temperature and the emergence of high temperature (T=1350 K) narrow peak in TDMS spectrum with reaching of critical fluence and temperature show evidence that collective mode emerges and therefore there is critical phenomenon of phase transition type in this range of the system parameters.

Further experimental investigation of noble gas grain creation over a wide range of temperatures and irradiation fluences will allow to construct phase diagram of this phenomenon and to study grain properties for different conditions [15-27].

References

[1] Desoyer J.C., Templier C., Delafond J., Garem H.// Nucl. Instr. and Meth. 1987, V.B19/20. P.450
[2] Hashimoto I., Yorikawa H., Mitsuyta H., Yamaguchi H., Takaishi K.// Jour. Nucl. Mat. 1987, V.149, P 69
[3] Hashimoto I., Yorikawa H., Mitsuyta H., Yamaguchi H., Takaishi K.// Jour. Nucl. Mat. 1987, V.149, P100
[4] Andersen H.H., Bohr J., Johansen A., Johnson E.// Phys. Rev. Lett. 1987, V.59, P 1589
[5] Cox R.J., Goodhew P.J., Evans J.H.// Acta Metall. 1987, V.35, P.2497
[6] Eiichi Yagi, Masaya Iwaki, Koki Tanaka// Nucl. Instr. and Meth. in Phys. Res. 1988. V.B33, P.724
[7] Jager W., Merkle K.L.// Phil. Mag.A. 1988, V.57, P.497
[8] Evans J.H., Mazey D.J.// J. Phys.F: Met. Phys. 1985, V.15, P.L1
[9] Donnelly S.E., Rossouw C.J.// Science. 1985, V.230, P.1273
[10] Yamaguchi H., Hashimoto I., Mitsuya H., Nakamura K., Yagi E.// J. Nucl. Mater. 1989, V.161, P.164
[11] Ronchi C.// J. Nucl. Mater. 1981, V.96, P.314
[12] Klein M.L., Venables J.A. (eds.). - Acad. Press, New York. 1977, V.2, P.692
[13] Melius C.F., Wilson W.D., Bisson C.L.// Rad. Eff. 1980. V.153, P.111
[14]. Kosevich A.M. Physical Mechanics of Real Crystals, Kiev: Naukova dumka, 1981, P 174-285.
[15] Kuzminov D.B., Panesh A.M., Simonov A.P.// Lett. to Rus. J. of Technical Phys. 1986, V.12, #10, P.610
[16] Kuzminov D.B., Gerchikov M.Y., Panesh A.M., Simonov A.P. //Rus. J. Surface. Physics, Chemistry, Mechanics. 1987, #8, P.113
[17] Kuzminov D.B., Gerchikov M.Y., Panesh A.M., Simonov A.P. //Rus. J. Phys. Chem. 1988. V.62, #7, P.1980
[18] Kuzminov D.B., Chernikov V.N., Gerchikov M.Y., Panesh A.M., Simonov A.P.// Lett. to Rus. J. of Technical Phys. 1988, V.14, #21, P.1952
[19] Kuzminov D.B., Volkov A.A., Gerchikov M.Y., Panesh A.M., Simonov A.P.// Rus. J. Surface. Physics, Chemistry, Mechanics. 1988, #10, P.126
[20] Devjatko Y.N., Panesh A.M., Storojenko V.A., Tronin V.N.// Lett. to Rus. J. of Technical Phys. 1989, V.15, #22, P.87
[21] Kuzminov D.B., Chernikov V.N., Gerchikov M.Y., Panesh A.M., Simonov A.P. //Radiation Effects Express 1989, V.2, P.159-164
[22] Devjatko Y.N., Panesh A.M., Tronin V.N.// Rus. J. Phys. Chem. 1989, V.63, #10, P.2841
[23] Panesh A.M. //Izvestiya Akademii nauk SSSR, seriya fizicheskaya. 1990, V.54, #7, P.1404-1410
[24] Panesh A.M., Timofeev A.B. // Rus. J. Phys. Chem. 1988. V.62, #2, P.501
[25] Gerchikov M.Y., Panesh A.M., Simonov A.P.//Rus. J. Surface. Physics, Chem., Mechan. 1988, #6, P.101
[26] Gerchikov M.Y., Panesh A.M., Simonov A.P.//Rus. J. Surface. Physics, Chem., Mechan. 1985, #8, P.147
[27] Gerchikov M.Y., Panesh A.M.// Rus. J. Phys. Chem. 1988, V.62, #10, P.2829

THE NUCLEAR INTERACTION ANALYSIS METHODS FOR DIAGNOSTICS OF HIGH POWER ION BEAM TECHNOLOGIES

V.A.Ryzhkov, I.I.Grushin, G.E.Remnev

Nuclear Physics Institute, 2a Lenina, Tomsk, 634050, Russia

Abstract

The complex of Nuclear Interaction Analysis Methods including a charged particle activation analysis (CPAA and HIAA), a spectrometry of ion induced gamma-emission (PIGE and HIIGE) , characteristic X-ray emission (PIXE) and Rutherford Backscattering Spectrometry (RBS) have been used for diagnostics of the High Power Ion Beam (HPIB) assisted technologies. Accelerated ion beams from electrostatic generator EG-2.5 and cyclotron U-120 were used for realization of the techniques. The complex allows to solve a lot of problems of elemental and isotopic analysis. First, it is a determination of micro- and macrocomponents of modified materials; second, a determination of surface density of thin films, multilayers and coatings, total surface gaseous contamination and amounts of the elements implanted in specimens; third, a measurement of concentration depth profiles of the elements. Experiments shown that the preferable application of nuclear analysis methods allows to avoid the considerable errors arising when the concentration depth profiles of elements are measured by SIMS or AES in studies of mass transfer processes induced by HPIBs.

Introduction

A diagnostics application efficiency mostly depends on reliability of applied analysis method not on it's cost. So, right choice of the diagnostic method is very important step to achieve a good result in HPIB studies. Generally an elemental diagnostics of HPIB technologies is connected with analysis of surface and near-surface layers of solid. The necessity of certification of applied materials adds some of bulk analysis methods. The correct realization of surface diagnostics is complicated one because the considerable surface modification under HPIB exposure is observed.

As a rule, so-called atomic methods are used for elemental and isotopic diagnostics of HPIB technologies. The AES and SIMS methods are taken to be more cheap and simple than nuclear methods. But in situations where large numbers of similar samples are being routinely analyzed via nuclear methods, the cost per sample may therefore compare favorably with atomic methods. Furthermore, as it will be mentioned below, the values of main analytical characteristics of atomic methods (ionization coefficients and sputtering factors) are considerably changed under HPIB surface modification and so incorrect results are obtained by AES and/or SIMS-diagnostics. Nuclear methods' result independence on level of HPIB exposure shows reliability and advantage of these methods for elemental and isotopical HPIB diagnostics.

Experimental results

1. The techniques of micro- and macro-characterization of materials

Energy-disperse XRF-method (with photon excitation of ^{55}Fe and ^{109}Cd) is used for the routine material characterization of sputtered targets and substrates with the detection limits of elements with z>13 about 1÷100 ppm. CPAA, HIAA, PIGE and HIIGE techniques are used for determination of light elements. So the data obtained by CPAA via nuclear reactions $^{12}C(d,n)^{13}N$, $^{14}N(p,\alpha)^{11}C$, $^{16}O(p,\alpha)^{13}N$, $^{23}Na(d,p)^{24}Na$, $^{41}K(\alpha,n)^{44}Sc$ and $^{40}Ca(\alpha,p)^{43}Sc$ were used for selection of high-purity (HP) materials of sputtered targets (graphite, Nb, Mo, W, Al, leucosapphire Al_2O_3, ZnS, Zn) and substrates (Si, GaAs, CdTe). Detection limits were about 10^{-7}, $3\cdot10^{-7}$ и 10^{-6} % weight for C,N and O, respectively [1].

HIAA and HIIGE measurements were carried out on the cyclotron ion beams of ^{12}C, ^{14}N and ^{16}O with energy 0.75÷1.75 MeV/amu. It was shown that the utilization of ^{12}C, ^{14}N and ^{16}O ion activation with energy about 1 MeV/amu allow to determine less than the nanogram amounts of D, Li, Be and B without nuclear interferences from the gaseous elements (C,N,O) those contents into the near-surface layers of solid are characterized as abnormally high. HIAA deuterium determination via nuclear reaction $^{2}H(^{12}C,n)^{13}N$ is most sensitive and selective. The HI-IGE detection limits in HP niobium matrix were about 1÷3 ng/cm^2 for D, Li, Be and B, 0.3 μg/cm^2 for F and 5÷15 μg/cm^2 for C, N and O. The technique are available for coupling with ERDA, HI-RBS and HI-IXE, too.

Nuclear reactions such as the (p,p'γ) and (p,αγ) are used by PIGE techniques for instrumental determination of Li, B, F and Na traces with the detection limits up to 0.1 ppm. All of the above mentioned methods can be used for checking of stoichiometric and isotopic ratio with standard relative deviation (SRD) no more than 0.005[2]. Usually SRD is no more than 0.2 in determinations of the impurities.

2. The techniques for determination of surface contents of elements

XRF analysis by X-ray excitation of ^{109}Cd and measuring of characteristic X-rays of elements with Si(Li)-detector was used for determination of surface density of ZnS, Nb, W, Au, Pb films with $\Delta h \approx$(0.2-100)nm prepared by HPIB assisted sputtering upon the mylar, Al- and Cu-foils as the substrates. The angular distributions of the sputtered products are measured by the XRF-technique with SRD equaled 0.01-0.3 for thickest and thinnest layers of sputtered product, respectively. To measure an angular distribution of C (graphite), Al, Si and Al_2O_3 (leucosapphire) the autoradiography technique based on the 3 MeV-deuteron activation is developing now.

Instrumental CPAA technique was developed to study the gaseous contamination of thin tungsten and gold films deposited upon HP AsGa plates by the HPIB sputtering of HP tungsten and gold targets. The specimens were irradiated in helium atmosphere by 3 MeV deuterons from cyclotron and then the ^{13}N- and ^{15}O-activity formed from the nuclear reactions $^{12}C(d,n)^{13}N$ and $^{14}N(d,n)^{15}O$ was detected by γ-γ-coincidence spectrometer. The interference free detection limits were about 3÷5 ng/cm^2.

The CPAA technique via $^{12}C(d,n)^{13}N$ coupled with optical ellipsometry allowed to determine the density of diamond-like carbon films produced by the

HPIB sputtering of HP graphite. Nuclear reaction $^{27}Al(d,n)^{28}Al$ was used for determination of total doze of Al^{n+} ions in $Hg_{1-x}Cd_xTe$ ($x=0.21\div0.22$) through the short-pulsed implantation.

The instrumental HIAA and HIIGE measurements via nuclear reactions $^{9}Be(^{14}N,\alpha n)^{18}F$, $^{9}Be(^{14}N,d\gamma)^{21}Ne$ and $^{9}Be(^{14}N,2\alpha\gamma)^{15}N$ were used for determination of total doze of beryllium ($2{,}0\cdot10^{17}$ at/cm^2) implanted into niobium for producing of the reference samples on environmental measurements [3]. The detection limits were about $(1\div5)\cdot10^{15}$ at/cm^2.

3. Concentration depth profiling techniques

Two non-destructive depth profiling methods are used in our institute: PIGE — for light elements and RBS — for medium and heavy ones. The main analytical characteristics of the both methods are similar: the depth resolution is about 10÷100 nm and detection limit is about $10^{18}\div10^{19}$ at/cm^3.

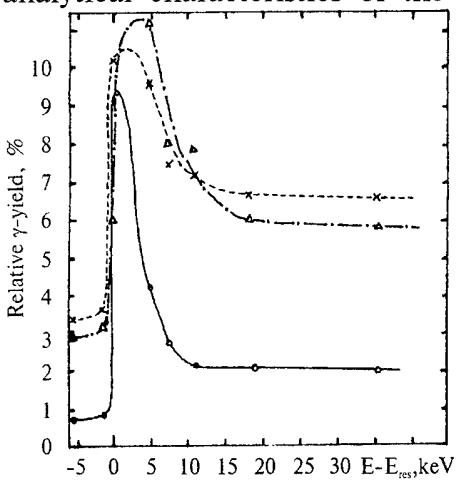

Fig. 1 PIGE profiling of thin films and drop fractions after short-pulsed implantation of Al^{n+} into MCT

The PIGE techniques are based on application of narrow isolated resonances in excitation function of (p,γ)-, (p,p')- and (p,αγ)-reactions. By scanning on proton energy they localize resonance at the required depth from the specimen surface. Gamma-spectrometry with a large NaI scintillation detector and Ge(Li)-detector was used for the characteristic γ-rays account. Usually we use a relative variant of analysis with thin Al, CaF_2, AlN, C and LiF films as references. The most probable characteristics of applied nuclear reactions are presented in the table.

Table

Material of specimen	Maximal analyzed depth, μm	Analyzed element	Detection limit, at/cm^3	Depth resolution, nm	Nuclear reaction	Resonant energy, E_{res}, keV
Si	4	*Al*	10^{18}	3	$^{27}Al(p,\gamma)^{28}Si$	992
TiN	2	*F*	10^{16}	30	$^{19}F(p,\alpha\gamma)^{16}O$	872
TiN	2	*N*	10^{19}	3	$^{15}N(p,\alpha\gamma)^{12}C$	429
TiN	0.5	*C*	10^{19}	3	$^{13}C(p,\gamma)^{14}N$	1748
Si	2	*Li*	10^{18}	80	$^{7}Li(p,\gamma)^{8}Be$	441

To analyze a short-pulsed ion implantation of Al^{n+} into semiconductor materials (Si, MCT), mixing of thin multilayer Al-, Al-Si, Al-C-structures and ion beam assisted preparation of TiN films on steel, the concentration depth profiles of Al and N were determined by the resonant nuclear reactions $^{27}Al(p,\gamma)^{28}Si$ and $^{15}N(p,\alpha\gamma)^{12}C$. The depth resolutions were about 30nm and 50nm, and detection limits were about 10^{19} and 10^{20} at/cm^3 for Al and N, respectively, in our recent measurements. Fig.1 shows that the technique allows to determine simultaneously

a thickness of thin film and a diameter's distribution of drop fraction (with average diameter about 3÷8 μm) formed on surface of samples by short-pulsed ion implantation (accelerator "MUK").

4. A comparison of atomic (SIMS,AES) and nuclear (PIGE) methods of concentration depth profiling in studies of HPIB-technologies

The Al depth profiles after HPIB exposure (accelerator "TEMP-1") were measured by PIGE, SIMS and AES at the same examined specimens. As it is shown at fig.2, the SIMS and AES methods decreased the concentration values and penetration depth of aluminum at 2-3 times compare to the nuclear method's data. We suppose that the differences are connected with the separate sputtering of filling specimen's substance and nanocrystal Al_xCu_y- or Al_xFe_y-phases formed by HPIB surface modification. Obviously the separate sputtering can lead to considerable errors in AES and SIMS depth profile measurements.

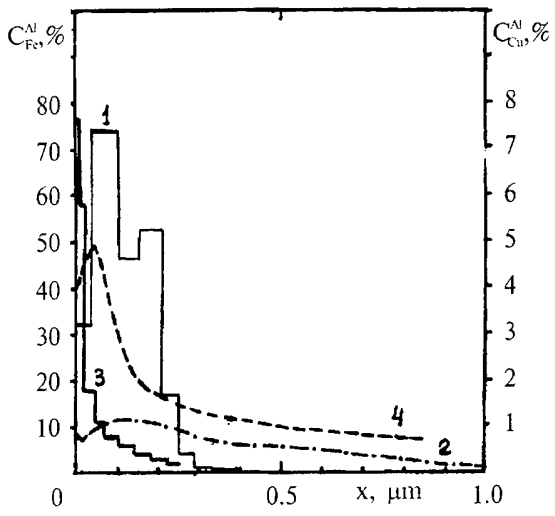

Fig. 2. Depth profiles of Al in Cu and Fe after HPIB-treatment. Initial Al film with depth about 400nm after 1 pulse HPIB with current intensity 40 A/cm^2 .
Fe-plate: 1 - PIGE, 2 - SIMS;
Cu-plate: 3 - PIGE, 4- AES

Furthermore the experimental data of majority of papers connected with elemental depth profiles measured by AES or SIMS on HPIB studies demonstrate that the maximal penetration depth of an implanted element is considerably exceed the one's projective range. We think these effects are not connected with the long range effect but only with the errors of atomic depth profiling methods. The problem is very important for a correct realization of the HPIB diagnostics and it needs in further investigation.

Conclusion

The described complex of Nuclear Interaction Analysis Methods allows to work out all of problems for the elemental HPIB diagnostics. In comparison with AES and SIMS, the NIAMs are more reliable methods of the HPIB diagnostics because they have best accuracy in caring out of the quantitative analysis and depth profiling.

References:

1. Ryzhkov V.A., Oblivantsev A.N., Rybasov A.G. Unification of the techniques of activation analysis on the charged particles during the determination of traces of the gas-forming elements in high-purity solid materials// High-purity substances (Russia) 1995. N 6. P.49-53.
2. Ryzhkov V.A., Kabyshev A.V., Lopatin V.V. Activation determination of micro and macro components in boron and aluminum nitrides using cyclotron ion beams // J.of Anal. Chem.(Russia), 1991.V.46.N 6. P.1181-1187.
3. Ryzhkov V.A., Kompaniets A.A., Ryabchikov A.I. Activation determination of implanted beryllium in reference samples.// J.of Anal.Chem.(Russia) 1992. V.47. N4. P.673-677.

THE DEPOSITION OF THIN METAL FILMS AT THE HIGH-INTENSITY PULSED-ION-BEAM INFLUENCE ON THE METALS

G.E.Remnev, A.N.Zakoutayev, I.I.Grushin, V.M.Matvienko, A.V.Potyomkin, V.A.Ryzhkov
Nuclear Physics Institute, Tomsk Polytechnic University, Tomsk, Russia

Yu.F.Ivanov
Construction Academy, Tomsk

E.V.Chernikov
Siberian Physical Technical Institute, Tomsk.

Abstract

The high-intensity pulsed ion beam with parameters: ion energy 350-500 keV, ion current density at a target > 200 A/cm^2, pulse duration 60 ns) was used for the metallic deposition. Film deposition rate was 0.6-4.0 mm/s. Transmission electron microscopy/ transmission electron diffraction investigations of the copper target-film system have been performed. Impurity content in the film have been determined using X-ray fluorescence analysis and secondary ion mass spectrometry. The angular distributions of the ablated plasma have been measured.

Introduction

The high-intensity pulsed ion beam (HIPIB)/solid interaction results in the generation of an ablated plasma (10^{19}-10^{20} cm^{-3}, 0.2-2 eV) which can be used to advantage for the deposition of thin films [1]. The deposition process is analogous to pulsed laser deposition, but operates with higher total energy incident on a target allowing accelerated deposition rates or larger area coverage. The paper deals with the results of investigation on the deposition of metallic films, their structure and impurity content.

Experimental procedure

The basic experimental arrangement required for producing films by High-Intensity Pulsed-Ion Beam Deposition (HIPIBD) has been described in Ref. 6. Briefly, the study was carried out on TEMP-2 accelerator (ion energy 350-500 keV, ion current density at a target > 200 A/cm^2, power density (0.7-1.5) 10^8 W/cm^2, pulse duration 60 ns, pulse repetition rate 8-10 min^{-1}) [2].

Metallic deposition.

Transmission electron microscopy (TEM) and transmission electron diffraction (TED) investigations presented in Ref. 3, 4, 5, 6 showed that the metal films grown by the HIPIBD are polycrystalline formations containing both microparticles of the droplet fraction and microblisters (Fig.1a). The parameters (average sizes, linear density, volume fraction) of these structural formations depend on some conditions, including melting (evaporation) point, degree of cristallinity of a substrate, the quantity of pulses of the deposition, the number of depositing pulse, the diode-target-substrate geometry, as well as the structural and phase state of a target. Fig. 1b-g illustrates the results of analysis of the last factor influence. It has been

found that the influence of the high-intensity pulsed-ion beam (HIPIB) on the copper target is accompanied by changing the defect structure and phase composition of the metal.
(i) Carbon particulates with the cubic crystalline lattice (a(FCL)=0.421nm) (Fig. 1 b-d) are observed on the target surface, with increasing the number of pulses of the HIPIB action the particulates' average sizes and their volume fraction increase. It was noted that on the target surface the particulates are the volume formations, frequently having a facetting, and in the near-surface layer (~0.5 μm layer thickness) the particulates are very thin disks (Fig. 1b).
(ii) Spherical particulates of the copper oxides are observed on the target surface. Their average sizes increase with increasing the number of pulses, but their linear density decrease. The near-surface layer has the gradiental defect structure: the nanocrystalline surface layer ($\bar{d}_{cr}$=20 nm), the submicron near-surface layer ($\bar{d}_{cr}$ =300 nm, Fig. 1e,f). Crystallite sizes of this layer increase with increasing the number of pulses of the HIPIB action. The HIPIB influence on the metal is accompanied by changing the relief of the sample polished face (Fig. 1 f, g). It has been found that both a wave length and a degree of the relief periodicity depend on the number of pulses of HIPIB, metals, as well as the state of a metal that can be either a polycrystal (Fig. 1g) or a monocrystal (Fig. 1h).

Impurity content measurements in films.

The super-high rate of the film deposition by HIPIBD allows to produce films with the low impurity content, especially with impurities of light gaseous elements, such as C, N. O, constantly being in residual atmosphere (P=$5\cdot10^{-5}$ Torr). We have carried out a number of experiments dealing with the sputtering of high-purity (999.9) W and Au targets. The initial high-purity targets were certificated by the charged particle activation analysis (CPAA) method [7]. The films were deposited on high-purity AsGa plates with the content of C, N and O less 10^{-5} %. A thickness of the deposited films was determined by X-ray fluorescence analysis method with the excitation by photon radiation ^{109}Cd and the registration of the characteristic X-ray radiation of elements by Si(Li)-detector. For instrumental CPAA determination of C and N both in the films and on the AsGa substrates surface we used the irradiation by deuterons of a cyclotron with the energy of ~3.1 MeV in He-atmosphere and subsequence determination of induced activity of analytical radionuclides ^{13}N and ^{15}O with periods of half-decay 9.965 min and 2.04 min, respectively. The table presents the total content (surface density q) and the relative content (f_0) of C and N in the W films, a background (surface contents in AsGa substrates: q_C(AsGa)=0.8 μg/cm^2 and q_N(AsGa)=0.3 μg/cm^2) being taken into consideration. The content of C and N in gold films was lower than a limit of determination $q_{min} \approx 0.3\ q_C(AsGa) \approx 0.3\ q_N(AsGa)$. Quantitative estimates of the film impurity content were made using the secondary ion mass spectrometry also.

Table. Impurity contents of C and N in the W films.

The number of pulses	q_W, μg/cm^2	q_C, μg/cm^2	f_C, wt. %	q_N, μg/cm^2	f_N, wt. %
30*	0.45	2.3	0.51	0.77	0.17
100**	1.1	11.8	1.1	0.97	0.09
100***	1.3	9.7	0.75	0.62	0.05

* without preliminary sputtering of the target surface and without nitrogenous trop;
** with preliminary sputtering of the target surface and without nitrogenous trop;
*** with preliminary sputtering of the target surface and with nitrogenous trop.

The performed investigation allows to conclude the following:
(i) The content of C in the W films is an order of magnitude higher than the content of N, but the C total quantity is proportional to the number of pulses, that indicates the contamination of the films by gases of residual atmosphere of the work chamber during the deposition process.
(ii) The preliminary sputtering of the W target surface decreases a level of the N contamination of the produced films by two or three times and doesn't influence a level of the contamination caused by the C-containing compounds that determining a degree of vacuum in the work chamber.
(iii) The luck of detectable quantities of C and N in gold films indicates the chemical nature of the gas contamination in the W films.
(iv) The contamination of the films occurs during breaks between pulses after the deposition of the ablated plasma plume onto a substrate.
Thus, we have presented a possibility to produce high-purity films of noble metals (Au, Ag, platinoids) from the ablated plasma at sputtering initial high-purity targets by HIPIB. Pure films of chemically active metals may be produced if to improve a vacuum in the work chamber.

The angular distribution of the ablated plasma.

The HIPIB with the following parameters: 350 keV ion energy, 250 A/cm^2 current density at a target, $8.75 \cdot 10^7$ W/cm^2 power density at target, 60 ns pulse duration, 5.25 J/cm^2 fluence at target, was used in the experiments. A diagram of the experimental system for angular measurements is shown schematically in Fig. 2a. All the targets were tablet-shaped with S=1 cm^2. Energy-disperse X-ray fluorescence analysis via X-ray excitation of ^{109}Cd and measuring of characteristic X-rays of elements by Si(Li)-detector was used for determination of surface density of ZnS, Nb, W, Au, Pb films with a thickness of 0.2-400 nm for studying the angular distributions of the sputtered products. Standard relative deviation of the XRF results was 0.01-0.3 for the thickest and thinnest layers of the sputtered products, respectively. To measure an angular distribution of C (graphite), Al, Si and Al_2O_3 (leucosapphire) the autoradiography technique based on the 3 MeV-deuteron activation is developing now. The plume of the ablated plasma is cone-shaped and characterized by a highly forward peaked distribution, $\exp(-n|\theta|)$ with $3 < n < 4.5$, where θ is measured with respect to the target normal (Fig. 2a, b). This is in contrast to what one expects from a purely thermal evaporation characterized by a $\cos(\theta)$ distribution.

Conclusion

The joint, TEM/TED investigations of the copper target-film system have been performed. The modifying influence of HIPIB on the structure and phase composition of the target has been determined, a connection between the structure of the target and that of the film being revealed. The angular distribution has an exponential behavior, and the exponential parameter for investigated materials is ranged from 3 to 4.5 depending on the sort of materials. The influence of pressure of residual atmosphere to concentration of elements, which form gases, is investigated.

Acknowledgment

This work is supported by the contract 1631 Q0014-35 between University of California, Los Alamos National Laboratory and Tomsk Nuclear Physics Institute for Materials Processing with Intense Ion Beams.

References

[1] H. A. Davis, G. E. Remnev, R. W. Stinnet and K. Yatsui, *MRS Bulletin*, 1996 (in press).
[2] G. E. Remnev, I. F. Isakov, G. E. Kotlyarevsky et al., in *Proc. of 9th Intern. Conf. on Surface Modification of Metals by Ion Beams*, San Sebastian, Spain, 1995 (to be published).
[3] A. N. Zakoutayev, G. E. Remnev, Yu. F. Ivanov, M. S. Arteyev, V. M. Matvienko, and A. V. Potyomkin, in *Film Synthesis and Growth Using Energetic Beams*, edited by H. A. Atwater, J. T. Dickinson, D. H. Lowndess, and A. Polman (Mater. Res. Soc. Proc. **388**, Pittsburgh, PA, 1995), pp. 388-393.
[4] Yu. F. Ivanov, G. E. Remnev, A. N. Zakoutayev, V. M. Matvienko, A. V. Potyomkin , in *Proc. of IV Conf. on Modification of Structural Materials by Charged Particle Beams,* Tomsk, 1996, pp. 442-444.
[5] Yu. F. Ivanov, G. E. Remnev, A. N. Zakoutayev, V. M. Matvienko, A. V. Potyomkin , submitted to *Sov. Tech. Phys. Letters* (1996).
[6] Yu. F. Ivanov, V. M. Matvienko, A. V. Potyomkin, G. E. Remnev, A. N. Zakoutayev, in *Ion-Solid Interactions for Materials Modification and Processing,* edited by D. B. Poker, D. Ila, Y-S. Cheng, L. R. Harriott, and T. W. Sigmon (Mater. Res. Soc. Proc. **396**, Pittsburgh, PA, 1996)
[7] Ryzhkov V. A., Oblivantsev A. N., Rybasov A. G., *High-purity substances* (Russia), 1995, No. **6**, pp. 49-53.

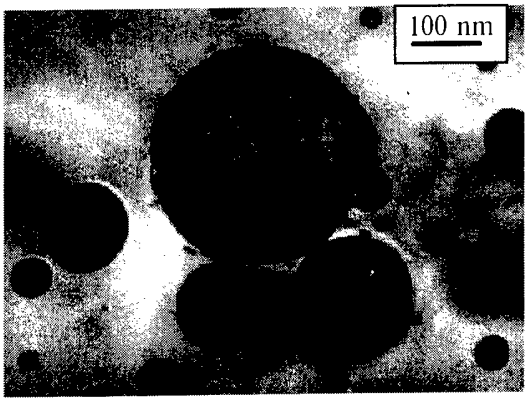

(a)

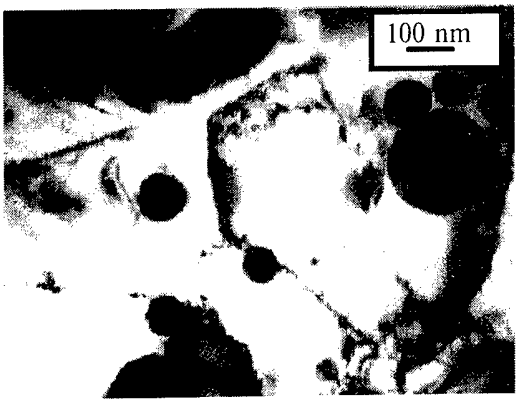

(b)

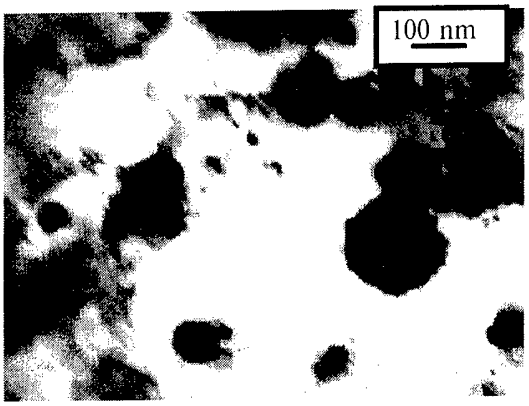

(c)

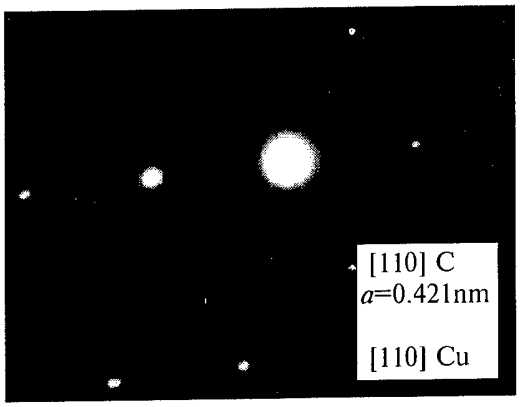

(d)

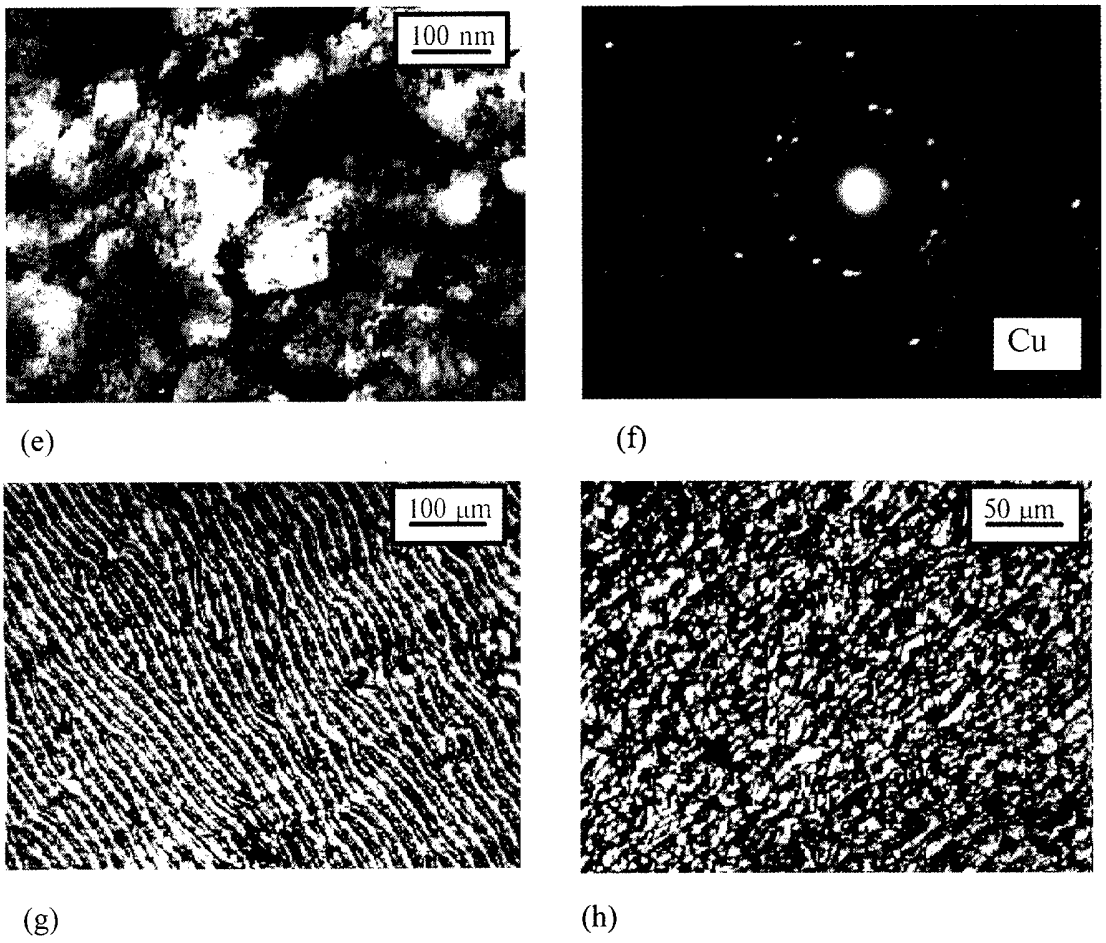

Fig. 1, (a, b, c, e) TEM, (d, f) TED and (g, h) optical images of the structure of both (a) the Cu film and (b, d) the Cu target obtained at sputtering both (a-f) a polycrystal and (g) a monocrystal.

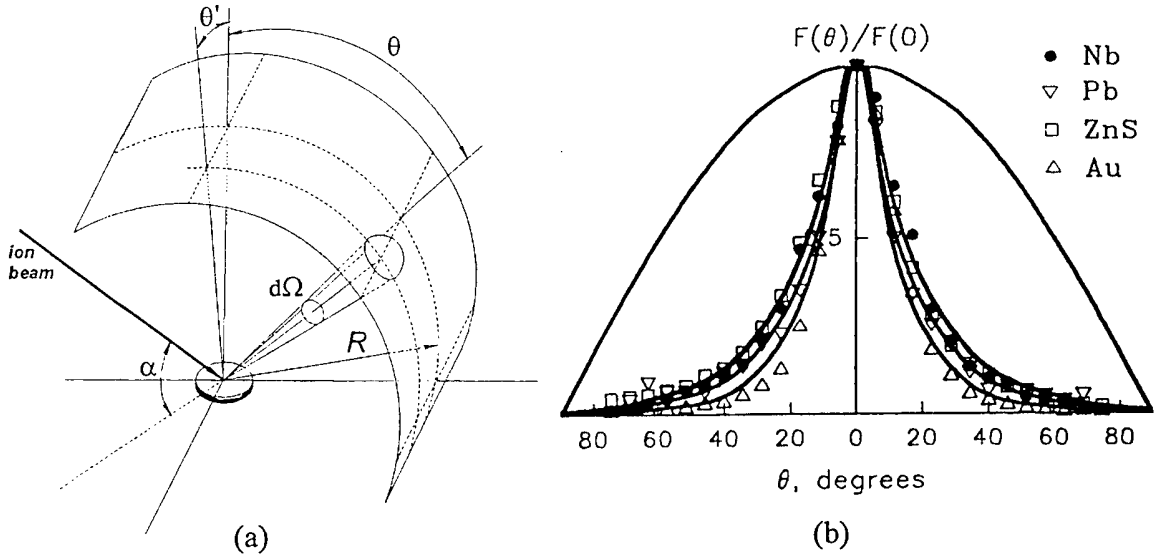

Fig. 2, (a) Schematic diagram of the angular measurements; (b) Angular distributions of the ablated plasma (Nb ~ exp (-3.1| θ |), Pb ~ exp(-3.4| θ |), ZnS ~ exp(-3.0| θ |), Au ~ exp(-4.3| θ |), a cos (θ) distribution is presented for comparison).

P-3-41

THE APPLICATION OF HIGH POWER ION BEAMS IN AIRCRAFT ENGINE BUILDING FOR RECONSTRUCTION OF REFRACTORY ALLOY PARTS

V. A. Shulov, N. A. Nochovnaya, G. E. Remnev

Moscow Aviation Institute, 4, Volokolamskoye shosse, Moscow, 125871, Russia

Abstract

The influence of high power pulsed ion beam irradiation and final heat treatment on physical and chemical state of refractory alloys (VT25U, VT9, GS26) blades surface layers were investigated after their operation in gas turbine engine. It is shown that ion beam treatment allows to reconstruct and recovery service properties of these parts.

Introduction

The irradiation by high concentration fluxes of energy (high power pulsed ion beam /HPPIB/ treatment especially [1, 2]) is one of the most advanced methods for surface processing of turbo machine parts. HPPIB application allows to improve service properties of these details dramatically [3, 4]. Furthermore, HPPIB irradiation can be used for reconstruction of compressor blades passed operation [5]. In this connection the main aim of the present research is the elaboration of technological fundamentals of gas turbine engine blades reconstruction and their service properties recovery by HPPIB treatment.

Experimental

The compressor and turbine blades (with ZrN and NiCrAlY coatings) manufactured from the VT25U, VT9 and GS26-refractory alloys (Russian aviation alloys) were chose as objects of investigation. These parts passed operation in gas turbine during 800 (titanium alloys) and 600 (GS26) hours. The coating thickness on the surface of the blades was equal to 15 μm (ZrN) and 100 μm (NiCrAlY) accordingly. Moreover, the VT25U, VT9-titanium alloy blades without coating have been studied after the 800-hour operation in gas turbine engine. The surface state of these parts has been determined by means of Auger electron spectroscopy, X-ray diffraction analysis, scanning electron microscopy, optical metallography,

measurements of roughness and microhardness. The irradiation of targets has been carried out using the TEMP-and VERA-accelerators [3] at the following values of ion beam parameters: ion energy - E=300-500 keV; ion current density in pulse - j=60-600 A cm^{-2}; pulse duration - τ= 50-100 ns; area of beam cross section - S=30-200 cm^{-2}. The total set of the blades surface state investigations has been repeated after irradiation. At last new coatings have been deposited on the purified surface of the blades by the plasma-vacuum deposition method and their fatigue strength and oxidation resistance have been determined.

Results

Some results of these researches are presented in Fig. 1,2 and Table 1. It is shown that the HPPIB treatment enables:
(i) to melt material of surface layers with thickness of h=0.4-3 μm at j>60 A cm^{-2}
(ii) to eradicate the surface microdefects (microcracks, furrows and etc.) at low values of ion current density (j≈60 A cm^{-2}) and a great number of pulses (n>15)
(iii) to remove material of surface layers with thickness of h=0.4-1 μm during pulse at j>120 A cm^{-2} (titanium alloys, ZrN-coating) and j>200 A cm^{-2} (nickel alloy, NiCrAlY-coating).

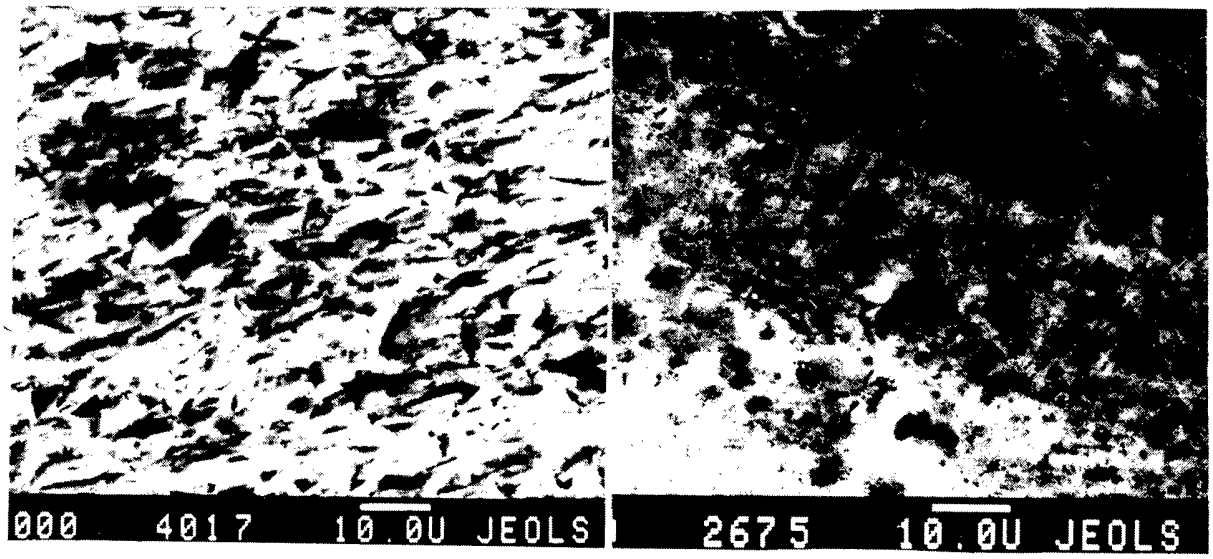

a b

Figure 1. SEM-micrographes of the VT9(a) and VT25U(b) alloys blade surface after the 800-hour operation: a- degraded ZrN-coating; b- oxidized surface treated by ion beam (E=300 keV; j=150 A cm^{-2}; n=3 pulses).

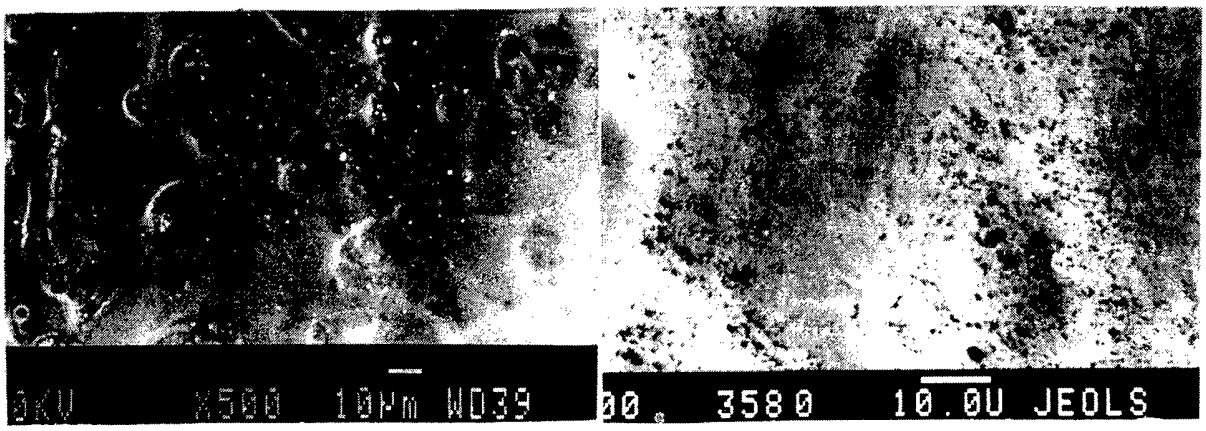

a b

Figure 2. SEM-micrographs of GS26 alloy blades surface after the 600-hour operation and HPPIB treatment: a - E=500 keV, j=600 A cm^{-2} , n=120 pulses; b - E=500+300 keV, j=600+60 A cm^{-2}, n=120+20 pulses.

Alloy	Coating	E, keV	j, A cm^{-2}	n, pulses	R_a,±0.0 2μm	Hμ,±30 HV 0.2	σ_{-1}, ±10 MPa	h_0, ±5 μm
VT25U	-	-	-	-	0.19	640	360	80
VT25U	-	300	120	20	0.18	320	200	100
VT25U	-	300	120	20	-	-	-	-
		300	60	15	0.10	290	350	60
VT9	ZrN	-	-	-	0.85	960	300	40
VT9	ZrN	300	150	25	0.20	450	310	65
VT9	ZrN	300	150	25	-	-	-	-
		300	60	10	0.09	310	360	35
GS26*	NiCrAlY	-	-	-	>2.0	860	240	60
GS26*	NiCrAlY	500	600	120	0,30	420	180	80
GS26*	NiCrAlY	500	600	120	-	-	-	-
		300	60	20	0.12	650	300	20

Table 1. The results of the blade tests: σ_{-1} - fatigue strength ($N=2\times10^7$ cycles; f=80 Hz; T=20°C); h_0 - thickness of oxidized layer (*- the tests have been carried out with the samples) after high temperature exposure in air during 800 hours (Ti-alloys) and 500 hours ($T_{VT25U,\ VT9}$ =550°C; T_{GS26} =1000°C).

The crater formation phenomenon and the simple Lengmyur's evaporation form the foundation of gas-dynamic removal process of damaged surface layer and coating. The blade surface irradiated at high values of ion current density held a great amount of craters. Crater diameter and their depth were equal to 5-100 and 0.5-1 μm correspondingly. The latter can lead to a crack net formation and as a result to a decrease of service properties of the blades reconstructed by HPPIB. In this connection it is proposed to irradiate these damaged blades by the HPPIB at low values of ion current density ($j \approx 60$ A cm^{-2}) for melting of the original formed craters sharp edges or to carry out mechanical polishing before new coating deposition. Since the surface layer material "disstrengthening" takes place during termalization of ions than the blades passed the HPPIB irradiation would be annealed in vacuum at operation temperature before or after deposition of new coating.

The results of comparative tests (Table 1) are shown that fatigue and corrosion properties of the blades reconstructed by HPPIB were up to standard of these properties of initial parts.

Conclusion

The test results of refractory alloy blades treated by high power ion beams allow to conclude that these beams can be used for the removal of oxidized surface layers and protective coatings damaged during operation in gas turbine engine. It is proposed to carry out the two-stage ion beam irradiation:

1) for removal of surface layers and coatings damaged during operation (at high values of ion current density, $j>200$ A cm^{-2});

2) for smoothing of surface microreleif (at low values of ion current density, $j=60\pm10$ A cm^{-2}).

References

[1] Yatsui K.: J. Laser and Particle Beams, 7(1989)733.

[2] Pogrebnjak A.D.: J. Phys. State Solids, 117(1990)17.

[3] Remnev G.E. and Shulov V.A.: J. Laser and Particle Beams, 11(1993)707.

[4] Shulov V.A., Remnev G.E. and Nochvnaya N.A.: J. Surface (Russia), 5(1993)127.

[5] Shulov V.A., Remnev G.E. and Nochvnaya N.A.: J. Aviation Industry (Russia), 2(1992)12.

P-3-42

MODELING OF ION BEAM SURFACE TREATMENT

R. W. Stinnett, Quantum Manufacturing Technologies , Inc.
3701 Hawkins St. NE
Albuquerque, NM

J. E. Maenchen and T. J. Renk, Sandia National Laboratories
Albuquerque, NM 87185

K. W. Struve, Mission Research Corporation
Albuquerque, NM

M. M. Campbell, PASTDCO
1248 Princeton NE
Albuquerque, NM 87106

Abstract

The use of intense pulsed ion beams is providing a new capability for surface engineering based on rapid thermal processing of the top few microns of metal, ceramic, and glass surfaces. The Ion Beam Surface Treatment (IBEST) process has been shown to produce enhancements in the hardness, corrosion, wear, and fatigue properties of surfaces by rapid melt and resolidification. We have created a new code called IBMOD that enables the modeling of intense ion beam deposition and the resulting rapid thermal cycling of surfaces. This code has been used to model the effect of treatment of aluminum, iron, and titanium using different ion species and pulse durations.

1. Introduction

The emerging capability to produce high average power (5-100 kW) pulsed ion beams at 0.1-1 MeV energies is enabling the development of a new, commercial scale thermal surface treatment technology called Ion Beam Surface Treatment[1] (IBEST). IBEST uses high energy pulsed (0.03-1μs) ion beams to directly deposit energy in the top 0.1-10 micrometers of the surface of materials, including metals, ceramics, and glass. This is illustrated in Figure 1. The depth of treatment is controllable by varying the ion energy and species. Efficient deposition of the energy in a thin surface layer allows melting of the layer with relatively small energies (typically 1-10 J/cm^2) and allows rapid cooling and resolidification of the melted layer by thermal diffusion into the underlying substrate. Typical cooling rates (>1x10^9 K/sec) are sufficient to cause amorphous and fine grain layer formation and the production of new microstructures including nano-crystalline and metastable phases. IBEST has been used to melt and resolidify metals, glass and ceramics for a variety of possible industrial applications. Experiments have shown that surfaces treated by this rapid quenching technique can have significantly improved properties that depend on the specific material but include corrosion, wear, and hardness and the production of smooth and crack-free surfaces.

Because the effects of IBEST on materials are based on rapid thermal cycling, the capability to model this thermal cycling is crucial to the understanding and application of IBEST to different materials and geometries. We have developed a new code called IBMOD that is specifically designed to model IBEST processing. IBMOD calculates the deposition of ions in materials and follows the resulting temperature variation with time and one dimensional spatial resolution. It provides the capability to use different pulse shapes and durations, multiple ion species, time varying ion energies, varying beam incidence angles, and temperature-dependent materials properties.

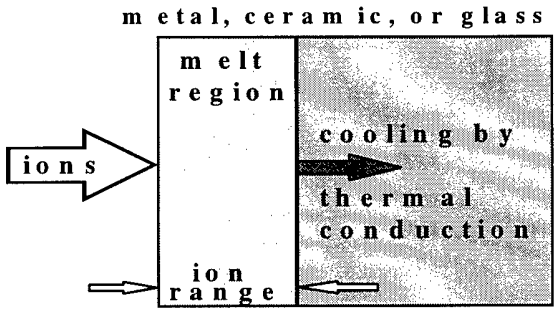

Figure 1. The Ion Beam Surface Treatment process uses short (<1μs), intense pulses of ions to melt surfaces. This melting is followed by rapid resolidification at 10^9K/s.

2. IBMOD Code Description

IBMOD has been developed jointly by Quantum Manufacturing Technologies and Sandia National Laboratories under a Cooperative Research And Development Agreement. It builds on the RANGE code developed several years ago by Sandia for DOE and DoD. IBMOD combines energy deposition based on the Anderson and Ziegler formulations[2] with thermal relaxation using a 1-D fully implicit, finite difference algorithm[3] that has been modified to include a time-varying source, variable spatial zoning, temperature dependent specific heat and thermal conductivity and melting/resolidification phase transitions. The stopping powers used in IBMOD includes zeroth order corrections to the electron energy loss to account for straggling.

Because of the short time scale characteristic of IBEST, IBMOD allows superheating of the liquid surface layer above the equilibrium vapor temperature. The temperature is clamped when it reaches the ablation temperature[4], given by $T_{ablation}= 0.1H_v/R$, where H_v is the heat of vaporization and R is the universal gas constant. IBMOD can model deposition using user-specified ion species as well as ion energy and current density profiles. Multiple ion species with different time histories can be used. It is also possible to model two layers of different materials.

Temperature dependent data for over 30 materials including elements, alloys, ceramics, glasses, and polymers is already available in IBMOD. Calculations indicate the inclusion of temperature dependent specific heat and thermal conductivity data is important for accurate IBEST modeling and typically changes calculated peak temperatures by 15-30%.

3. Modeling Results

In order to explore the modeling capability of IBMOD we have used the simple but representative ion voltage and current waveforms shown in Tables 1 and 2. The energy density delivered to the surface in either case is 4.0 J/cm^2. Different energy densities were obtained by scaling the incident current densities. The results of aluminum surface treatment with hydrogen ions and carbon ions, using pulse lengths of 180 ns and 1000 ns are shown in Figures 2,3, and 4.

Table 1. Ion voltage and current density waveforms used for the 180 ns, 4J/cm^2 case.

Time - ns	Voltage-kV	Current Density-A/cm2
0	400	58.5
180	300	70.0
181	0	0

Table 2. Ion voltage and current density waveforms used for the 1000 ns, 4 J/cm^2 case.

Time - ns	Voltage-kV	Current Density-A/cm2
0	400	10.5
1000	300	12.6
1001	0	0

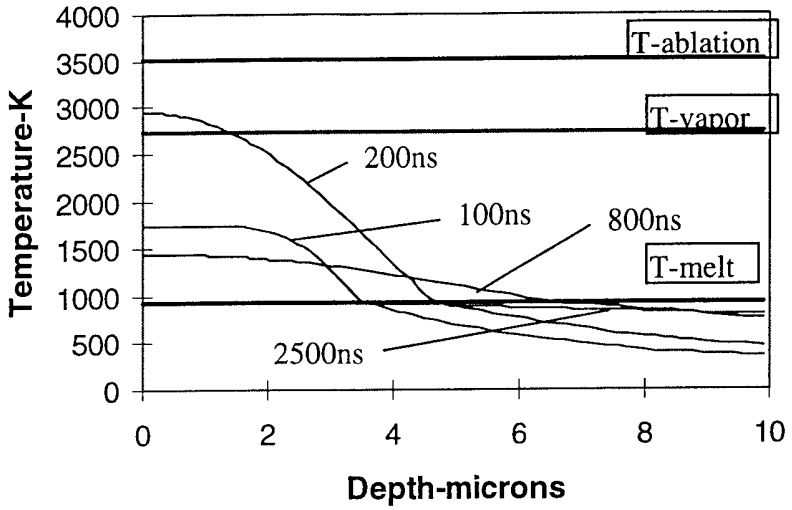

Figure 2. Temperature as a function of time and depth in an aluminum sample treated using a 4 J/cm^2 proton beam as described in table 1. The treatment level was chosen to not significantly exceed the vapor temperature for aluminum.

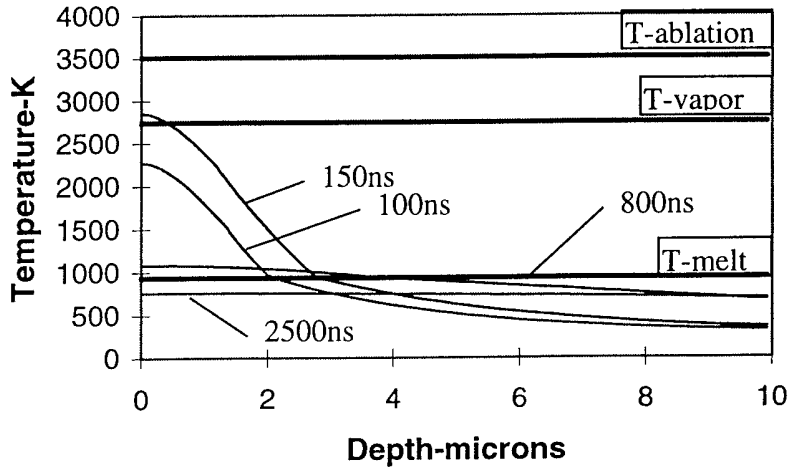

Figure 3. Temperature as a function of time and depth in an aluminum sample treated using a 2.8 J/cm^2 carbon (+1) ion beam with the waveshape described in table 1 but with current densities scaled down by 30% to limit the peak temperature to that shown in Figure 2.

Although the metrics for optimum IBEST processing are still being determined, it is likely that optimum treatment will result from the energy efficient achievement of the maximum temperature possible over the maximum depth obtainable without ablating the surface. Figure 2 predicts that a temperature of 2500-3000K in a 2 micron depth of aluminum can be achieved using a 4J/cm^2, 180 ns pulse of 300-400 kV protons. The total melt depth is 6.5 microns.

Figure 3 shows that the use of carbon ions instead of protons causes the energy to be deposited nearer the surface, resulting in a more surface-peaked temperature profile and limits the amount of energy that can be deposited without significantly exceeding the vapor temperature to 2.8 J/cm^2. This reduces the depth that can be heated to 2500-3000K to less than 1 micron. The total melt depth is 4 microns. Because of the short time scale for IBEST, the maximum temperature achievable without significant surface vaporization lies somewhere between the vapor and ablation temperatures.

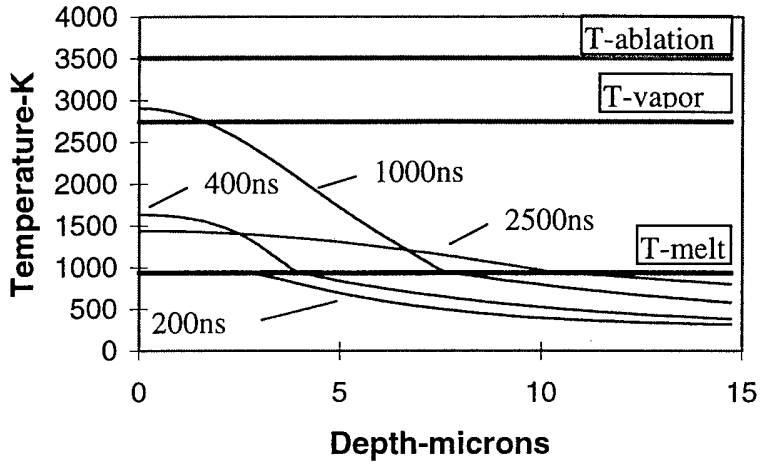

Figure 4. Temperature as a function of time and depth in an aluminum sample treated using a 6.8 J/cm^2 proton beam with the waveshape described in table 2 but with current densities scaled up by 70% to achieve the same peak temperature as the cases shown in Figures 2 and 3. Note that the depth scale here is different from those in Figures 2 and 3.

The use of a 1000 ns long proton pulse, as shown in Figure 4, requires 70% more energy to achieve 2500-3000K temperature over a 2 micron depth because of the increased effect of thermal conduction. The greater energy does, however, result in a 10 micron melt depth. The increased melt depth may be an advantage in extending the depth of the surface property enhancement.

Discussion

These calculations illustrate the effects of different ion species and pulse lengths on the treatment of aluminum. Calculations for iron and titanium show similar effects. Process development and optimization for a variety of materials is now being done on Sandia National Laboratories' RHEPP-1 facility. IBMOD has successfully modeled observed melt depths in initial tests with aluminum and steel. It will be extensively used in the future to correlate time and depth resolved temperature profiles with experimentally measured enhancements in surface properties. Additional tests are planned to further verify the ability of IBMOD to accurately model a range of treatment parameters and materials of interest in surface engineering applications.

The new modeling capability provided by IBMOD will be an essential tool in understanding and developing optimum IBEST processing parameters for a range of materials and applications.

References

1. R. W. Stinnett, R.G. Buchheit, F.A. Greulich, C.R. Hills, A.C. Kilgo, D. C. McIntyre, J. B. Greenly, M. O. Thompson, G. P. Johnston, abd D. J. Rej, "Thermal Surface Treatment Using Intense, Pulsed Ion Beams," Mat. Res. Soc. Symp. Proc. Vol. 316, p521-532.
2. H.H. Andersen and J. F. Ziegler, The Stopping and Ranges of Ions in Matter, V.3,V.5, Pergamon Press, 1979, 1980.
3. R.D. Richtmeyer and K. W. Morton, Difference Methods for Initial Value Problems, 2nd Ed., Wiley, 1967
4. S. I. Anisimov, Ya. A. Imas, G. S. Romanov, Yu. V. Khodyko, Action of High Power Radiation on Metals, Moscow, Nanka, 1970

Short-Pulsed-Electric Degradation of Aqueous Organics

V. M. Bystritskii, A. Gonzales, T. Olson
V. Puchkarev[a], L. Rosocha[b], F. Wessel, Y. Yankelevich[c]

University of California, Department of Physics and Astronomy
Irvine, CA, 92717-4575

Abstract

We describe the degradation of aqueous organic solutions (specifically, aromatic chlorinated compounds), based on short pulsed corona/streamer discharge in a water-air aerosol. The aerosol (droplet diameter: 10-100 μm) is injected into a discharge reactor with a repetitively pulsed voltage of 40-60 kV, 50-150 ns, 10^2-10^3 Hz. The relatively large water dielectric constant and high degree of atomization result in efficient degradation of the organic molecules, including paranitrophenol, di-chlorophenol and per-chloro-ethylene. The specific energy cost for degradation of one organic molecule is in the range of 40-100 eV/mol (calculated from the energy input in the discharge), and depends upon system operating parameters and the organic-species concentration.

Introduction

20th century technology has produced a remarkable increase in the standard of living of the world's population. Nevertheless, an insidious byproduct is toxic pollution of the global environment, especially in the natural reservoirs of air, water, and soil, by chemically stable halogenated-aromatic compounds .

In the case of flue- and toxic-gas remediation a promising technique involves the use of a non-thermal plasma (NTP)[1,2], with tens eV secondary electron energies, generated by direct electron-impact dissociation and ionization of the pollutant. However, for bulk-aqueous processing NTP techniques are not as efficient, due to the formation of highly conductive breakdown channels, and the requirement for primary electron energies of the order of a MeV and pulsed fields of several hundred kV/cm.

Described here our approach degrades an air-water aerosol (droplet diameter 10-100 microns) by a repetitive (0.01-1 kHz), short-pulse (10-100 ns), medium-voltage (10-60 kV) discharge which generates ionizing streamers and a swarm of supra-thermal electrons (Te = 1-100 eV). The main advantages are:

- absence of bulk-discharge heating,
- increased air-liquid surface area exposed to reactive components,
- efficient ionization of the volume element.

Earlier NTP procession of an aerosol mixture involved microsecond-to-millisecond spark discharge pulselengths.[3,4] The approach suffered from considerable resistive energy losses due to the media heating and non-optimized formation of the water/air spray, which significantly decreased the effectiveness of the treatment.

Experimental Apparatus

A schematic of the experimental device is illustrated in Fig. 1. The reactor vessel is fabricated from Lucite tubing (25-cm diameter, 150-cm length), with a set of intermeshed horizontal electrodes located in the middle of the chamber. An atomizer is mounted at the top of vessel that injects air-pressurized water under pump action (throughput 1-5 gallon/hr). A collector at the bottom of the system accumulates processed water that falls through the central portion of the reactor, separate from that which condenses on the chamber walls.

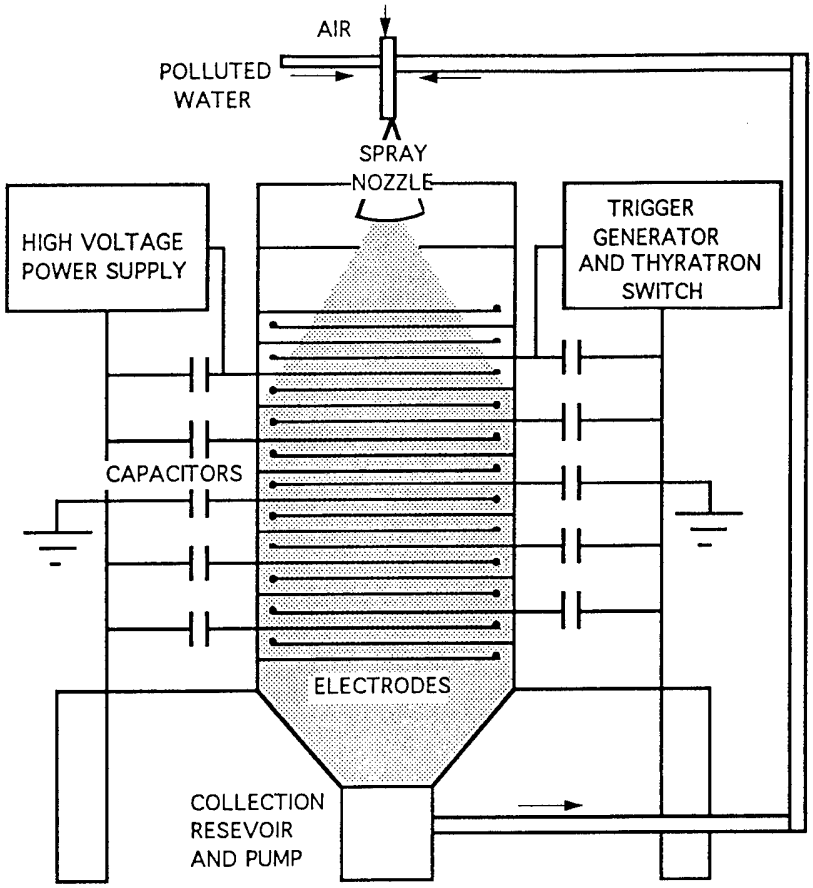

Figure 1. Illustration of the reactor.

The high-voltage pulse-modulator consists of a dc power supply, inductive choke, hydrogen thyratron trigger generator, thyratron bias supply, capacitors/pulse-forming cables. When the thyratron shorts the capacitors/pulse forming line cables to ground a high voltage pulse is applied across the discharge electrodes of the reactor with an amplitude twice the charging voltage. The pulse duration and impedance is controlled by the cable length and parallel number. The current through the chamber was measured by active resistor shunt of 10^{-1} Ohm, placed in series with pulse forming network.

Analysis of the initial and final concentrations of the processed organics and composition of the intermediates was "off-line" using several techniques: UV spectra-photometry for chemical-concentration analysis, pyrolytic analysis for total organic carbon (TOC) concentration, gas-chromatography with mass spectroscopy (GC/MS) for identification of chemical intermediates, specific-ion-electrode argentometric method to measure the released chloride (Cl-) concentration in halogenated organics.

Results and Analysis

The reactor was initially operated with aerosol flow of aqueous para-nitrophenol at voltages between 50 to 60 kV for high (0.5-1.0 kHz) and low frequency (< 0.2 kHz), respectively. Table 1 displays the results for a given set of operational parameters with concentrations of 10^{-4} and 5 10^{-4} M/l. A useful figure of merit is the specific-energy cost required to degrade one molecule of pollutant. The relevant equation is:

$$S_C = \frac{IV_o \tau v T}{(C_{in} - C_{fin}) N_{Av} V}$$

where V_o is the applied voltage, I is the average discharge current (including the displacement current, i.e., $I = I_{tot} - I_{dis}$, $I_{dis} = CdV/dt$), τ is the pulse duration, ν is the discharge, pulse-repetition rate, T is the processing time, C_{in}, C_{fin} are the initial and final molar concentrations (in moles/liter) respectively, N_{Av} is the Avogadro number, and V is the processed volume. I_{tot} was measured by a 0.1 Ω resistive shunt connected in series with the pulse-forming line; the displacement current is estimated to be I_{dis} = (50-100) A, since the reactor electrodes present a capacitance of the order of 100 pF and $dV/dt = (0.5\text{-}1)10^{12}$ V/s.

Table 1. PNP degradation parameters, units, and data.

C_{in}	V	V_o	I	t	n	T	C_{fin}	S_c	TOC_{in}	TOC_{fin}
Mol/l	l	kV	A	ns	Hz	s	Mol/l	eV/mol	mg/l	mg/l
10^{-4}	0.5	40/2	20	80	30	600	$<10^{-6}$	104	6.0	4.4
510^{-4}	0.5	40/2	20	80	50	600	3.610^{-6}	76	29.7	25.5

The results of scaling studies with PNP are displayed in Fig. 2, starting with a PNP concentration of 800 ppm, a pulsed voltage of 50 kV, and a frequency of 300 Hz. For these data nearly 40% of PNP is degraded in 4 cycles and the specific-energy cost is a favorable 40 eV/molecule measured for process cycle 1, when the decrease in concentration per cycle is largest. For comparison, competing degradation technologies report specific-energy costs of the order of several hundred, suggesting much higher energy efficiency for the present approach. Note that the TOC also decreased markedly over the 12 processing cycles. GC/MS data suggests the formation of intermediates with higher molecular weights than that PNP (possibly due to polymerization).

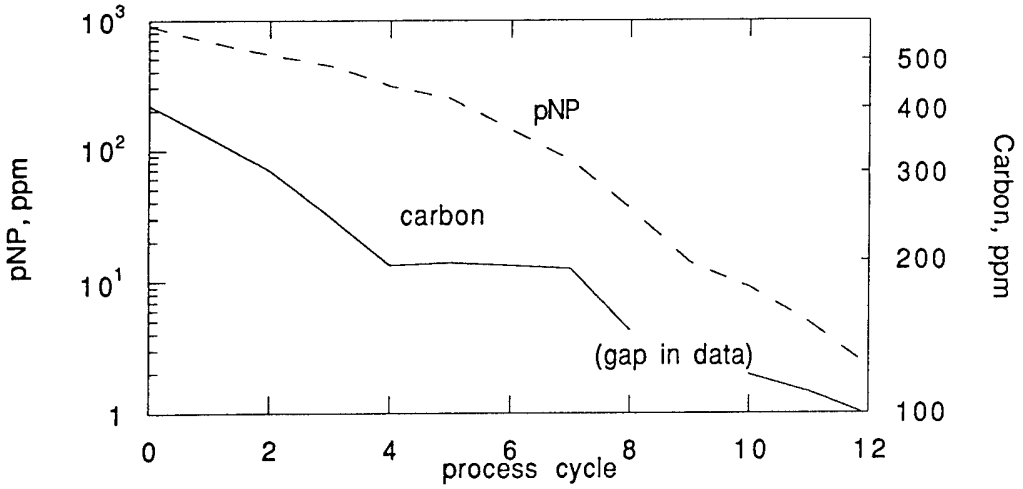

Figure 2. pNP and carbon concentrations vs. sample re-processing cycles.

Several tests using dichlorophenol (DCP) involved concentrations of 1000 ppm, 300 Hz pulse repetition frequency, and a voltage of 50 kV. Chlorine that was chemically liberated was dissolved in water, as HCl with a removal rate approximately 10% per cycle and a maximum for the number of cycles studied of 62%, as illustrated in Fig. 1; for these conditions the figure of merit is estimated to be 40-60 eV/molecule, which is a factor of 2 better than reported elsewhere.[5] Since there was no trend toward saturation, the technique demonstrates the potential for multi-cycle re-processing of halogenated organics.
Initial experiments using 100 ppm of 0.5l of perchloroethylene (PCE) solution also demonstrated efficient de-chlorination, when 16-78% of the chlorine ions were removed after

one to four cycles, respectively, and each cycle took 5 minutes of processing. The respective figure of merit parameter is, Sc ~ 60 eV/mol.

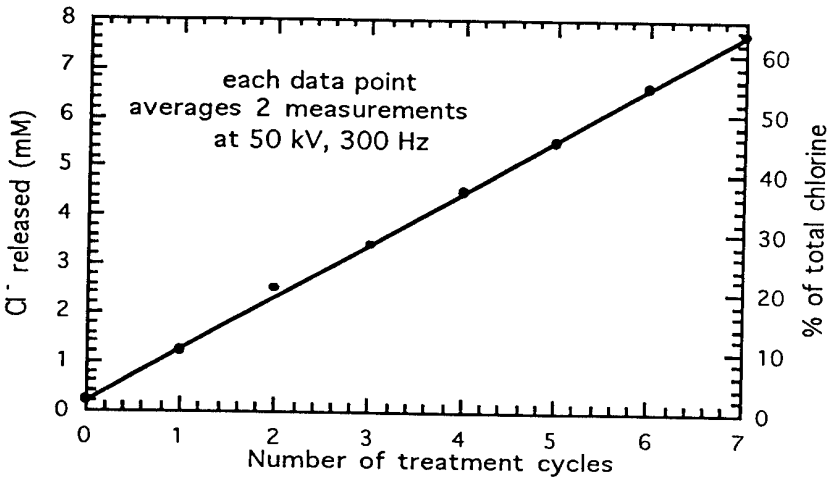

Figure 3. Chlorine removal from 1000 ppm dichlorophenol

Summary

We have demonstrated a means to degrade an aerosol mixture of various organics (PNP, DCP, PCE) using a medium voltage, repetitive, short pulsed discharge. The technique provides high electrical efficiency for applications involving water borne pollution. Future studies are planned to identify intermediate by-products and to optimize the operating parameters which lead to a higher degree of final mineralization.

Aknowledgments

We thank T. Wood and D. Yee for providing DCP and PCE samples and their analysis after the treatment. This work was supported by the Los Alamos National Laboratories LACOR Program and Notre Dame consulting agreement.

[a.] University of Southern California, Los Angeles, CA 94007
[b.] Los Alamos National Laboratory, Los Alamos, NM 87545
[c.] On leave from Institute of High Voltage, Tomsk, Russia, 634050

References

1. NATO ASI Series, v. G34, Part A, B. Non thermal Plasma Techniques for Pollution Control, Springer-Verlag, Berlin, Heidelberg, 1993.
2. Book of Abstracts Second International Symposium on Advanced Oxidation Technologies, San Francisco, CA, Feb 28-March 1 (1996).
3. Ryazanov, N., et al., Book of Abstracts, VII All-Union Conference of Pulsed Power Applications for Industry, (in Russian), Nikolaev (1988).
4. V. Bystritskii, V., I Lisitsyn, Ryazanov, N., Sinebryukhov, A., Yankelevich, E.,, Proc. 10-th Intl. Conf. on High Power Particle Beams, San Diego, CA (1994) p. 849.
5. D.M. Willberg, P. Lang, et al., Electrohydraulic discharge treatment of hazardous Wastes, Proc. 2nd Intl. Symp. on Advanced Oxidation Technologies, San-Francisco, February 28-March 1, 1996, p. 123.

P-3-44

THERMAL IMAGING EXPERIMENTS ON ANACONDA ION BEAM GENERATOR

Weihua Jiang and Kiyoshi Yatsui
Laboratory of Beam Technology, Nagaoka University of Technology
Nagaoka, Niigata 940-21, Japan

Joseph C. Olson and Harold A. Davis
Los Alamos National Laboratory, Los Alamos, NM 87545, USA

The thermal imaging technique was used in two experimental measurements. First, the ion intensity distribution on the anode surface was observed from different angles by using a multi-pinhole camera. Second, the plume from a target intercepting the beam was visualized by observing the distribution of temperature increase on a thin plate hit by the plume.

The thermal imaging technique[1] for ion beam diagnostics was developed by Los Alamos National Laboratory (LANL). It uses an infrared camera to obtain the two-dimensional distribution of temperature variation of the measured surface where the ion beam energy is deposited. In previous experiments, this technique was used to measure the ion beam energy-density distribution on a certain cross-sectional plane of the beam. In the experiments reported in this paper, we have measured 1) the relative ion beam brightness distribution on the anode surface observed from different angles and 2) the distribution of energy deposition of the target plume generated by the ion beam on a witness plate that is hit by the plume. The experiments were carried out by using the intense ion beam (400 keV, 30 kA, 1 μs) generated by ANACONDA, an ion beam generator located at LANL.

1. Measurement of ion beam intensity distribution

Figure 1 shows the experimental setup for ion beam diagnostics. The ion beam is generated by a focus type B_r diode. A pinhole plate is located at the focal point of

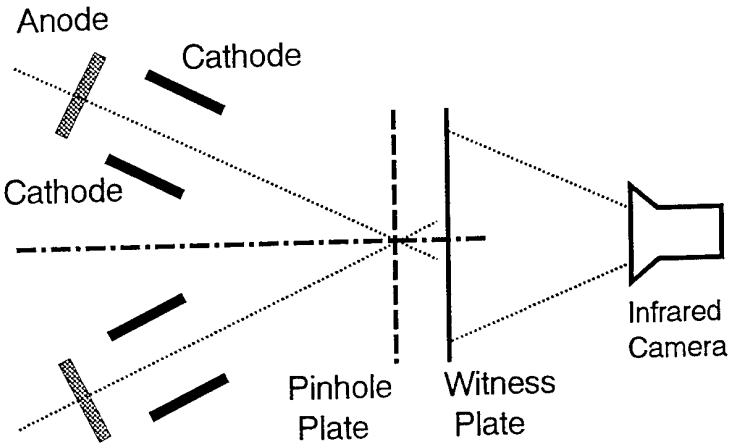

Fig. 1 Experimental setup for ion beam diagnostics.

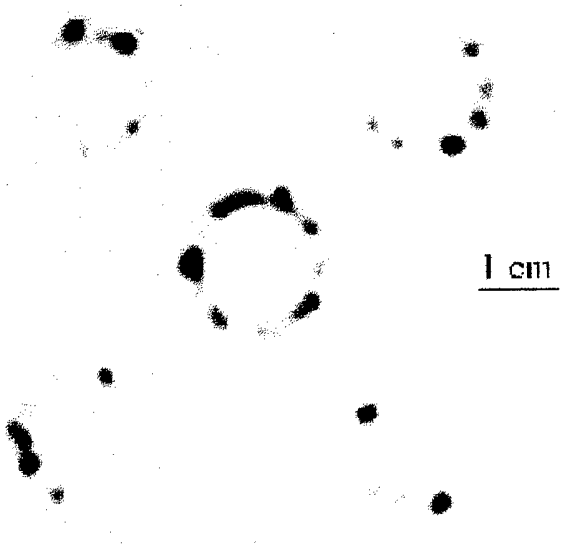

Fig. 2 Photograph of infrared emission from the witness plate, obtained with experimental setup of Fig. 1.

the ion beam, which is about 40 cm from the anode surface. Behind the pinhole plate, separated by 25 mm, there is a titanium witness plate with 0.08 mm in thickness. The temperature distribution of the witness plate is monitored by an infrared camera.

Figure 2 shows a typical infrared photograph of the witness plate obtained after the ion beam shot. For this shot, there were 5 pinholes 2 mm in diameter with one on the axis and the other four uniformly distributed on a circle of radius 3.8 cm. In Fig. 2, we can see five circles, one from each pinhole (some are incomplete), that are the pinhole images of the annular anode. Since the blackness in Fig. 2 is proportional to the temperature increase on the witness plate, the images provide the time-integrated distributions of ion beam energy on the anode surface, observed from different angles.

From Fig.2, we have obtained two conclusions. First, the ion beam emission on the anode surface is not uniform. The intensity of ion beam emission depends strongly on the location at the anode. Second, the spatial distribution of the ion beam intensity on the anode surface depends strongly on the position of observation. The

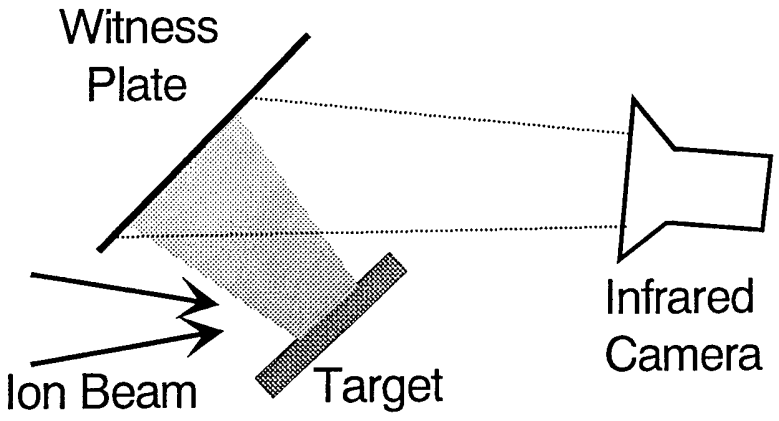

Fig. 3 Experimental setup for target plume diagnostics.

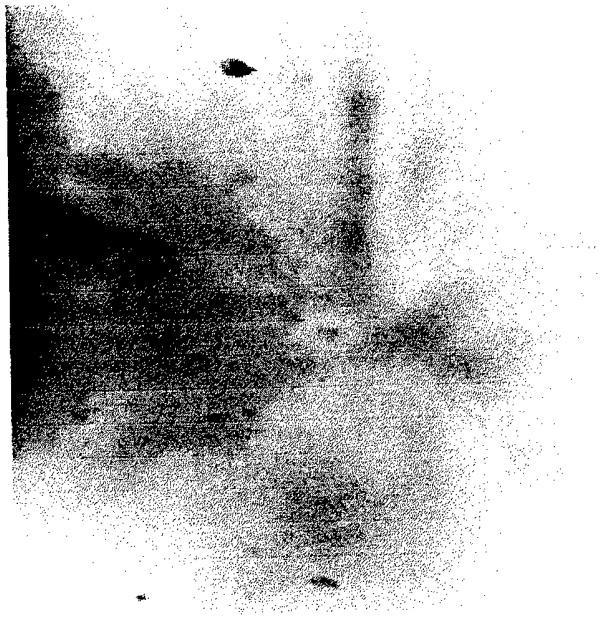

Fig. 4 Photograph of infrared emission from the witness plate, obtained with the experimental setup of Fig. 3.

image obtained at the center looks more uniform than the other four. The metal supports of the inner cathode cause three breaks on each circular image.

By comparing the images obtained from different shots, we have found that the distribution of ion beam intensity, obtained at the each angle, changes shot to shot. Therefore, the distribution of ion beam intensity on the anode surface is not caused by any asymmetry on the anode surface due to roughness or damage.

2. Measurement of target plume produced by the ion beam

When an intense ion beam strikes a target, some of the target surface material is evaporated or ionized due to the energy deposition of the ion beam. This target material then expands in the vacuum forming a plume containing plasma and hot gas. When this plume hit a solid substrate, some of the material cools and condenses on the substrate forming a thin film. If this plume flows through low pressure gas instead, the plume material combines to form very fine solid particles. These processes have been used for thin film deposition and nano-sized power production.[2,3]

To visualize the target plume, we have used the thermal imaging technique. Figure 3 shows the experimental setup of thermal imaging measurement of the target plume. The witness plate, a titanium plate with 0.08 mm in thickness, is located in front of the target. The temperature distribution of the witness plate is monitored by the infrared camera.

Figure 4 shows a typical infrared photograph of the witness plate obtained after the ion beam shot. For this shot, the target was a titanium disk with 5 cm diameter and the witness plate was set 12.7 cm from, and parallel to, the target. The temperature increase obtained from Fig. 4 is shown in Fig. 5.

The temperature shown in Fig. 5 is not the instantaneous temperature rise on the surface of the witness plate when it is hit by the plume. It is the temperature distribution when thermal equilibrium is reach in the direction of plate thickness, but before significant thermal conduction occurs in the direction along the plate surface. Therefore it shows the distribution of energy absorption from the plume by the witness plate.

By integrating the temperature increase

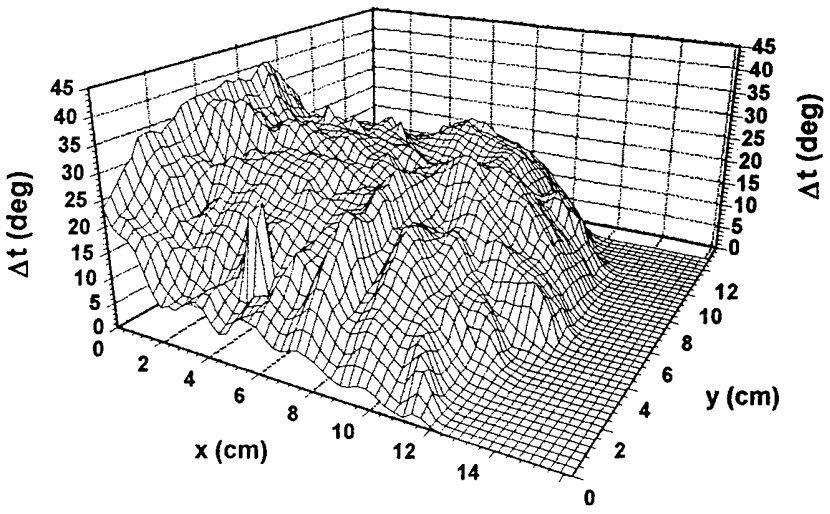

Fig. 5 Distribution of temperature increase obtained from Fig. 4.

given by Fig. 5, we have obtained the total energy of ~ 17.8 J, which is the energy absorbed by the witness plate from the plume.

We have observed the dependence of the maximum temperature increase on the distance between the target and the witness plate. Figure 6 shows the results. For each distance, we have taken the data from five shots. In Fig. 6, the circles show the average values and the error bars show the maximums and the minimums. It is seen that the temperature increase decreases with target-substrate distance, which is in agreement with the data obtained previously by another method.[4]

References

[1] H. A. Davis, R. R. Bartsch, D. J. Rej, and W. J. Waganaar, Proc. 10th Int'l. Conf. on High Power Particle Beams, II, (1994) 668.

[2] K. Yatsui, X. D. Kang. T. Sonegawa, T. Matsuoka, K. Masugata, Y. Shimotori, T. Satoh, S. Furuuchi, Y. Ohuchi, T. Takeshita, and H. Yamamoto, Phys. Plasmas, 1 (1994) 1730.

[3] K. Yatsui, C. Grigoriu, H. Kubo, K. Masugata, and Y. Shimotori, Appl. Phys. Lett., 67 (1995) 1214.

[4] J. C. Olson, M. O. Thompson, H. A. Davis, D. J. Rej, W. J. Waganaar, and D. R. Tallant, Mat. Res. Soc. Symp. Proc., 388, (1995) 171.

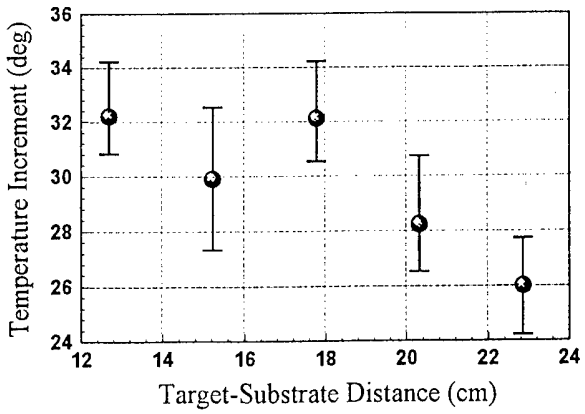

Fig. 6 Dependence of maximum temperature increase on target-substrate distance.

P-3-45

PREPARATION OF THIN FILMS BY ABLATION WITH ANACONDA ION BEAM GENERATOR

K. Yatsui and W. Jiang
Laboratory of Beam Technology, Nagaoka University of Technology, Nagaoka, Niigata 940-21, Japan

H. A. Davis, J. C. Olson, W. J. Waganaar, and D. Rej
Los Alamos National Laboratory, Los Alamos, NM 87545, USA

Thin films of silicon carbide are produced by using the technology of ion beam evaporation. Various analytical methods are used to analyze film thickness, film composition and crystallizability for samples obtained with different target-substrate distances.

1. Introduction

The technologies relating to intense, pulsed, charge particle beams, largely supported by inertial confinement fusion programs, have been developed for several decades. In recent years, it has been realized that these technologies are also applicable in industrial fields.[1] For example, the ion beam evaporation (IBE) is an efficient and economical method for preparation of both thin films and nanosize powders.[2-4]

The IBE is a technology that evaporates the target material by irradiating a target surface with an intense, pulsed ion beam. Due to the large ion stopping power in solids,

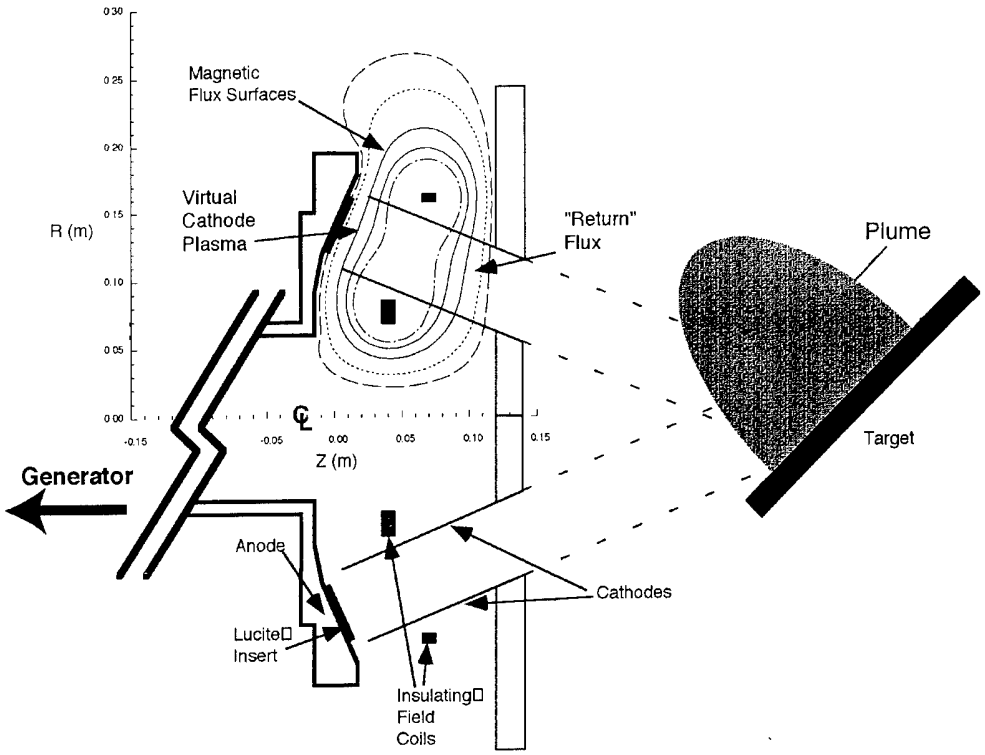

Fig. 1 Configuration of ANACONDA ion beam diode.

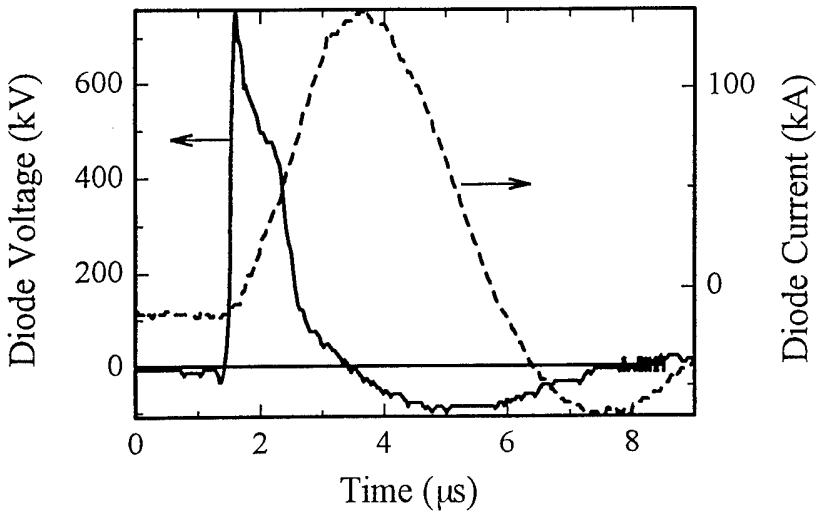

Fig.2 Typical waveforms of diode voltage and diode current

in solids, very high energy density can be obtained in a small target volume close to the surface. This volume of target material is instantly evaporated and ionized expanding from the target surface into vacuum. When a substrate is located facing the target surface, the expanding material strikes the substrate and cools on the substrate surface resulting in a very thin film.

ANACONDA is an intense ion beam generator developed by Los Alamos National Laboratory for research on the application of ion beams to material processing. We have used the ion beam generated by ANACONDA (400 keV, 30 kA, 1 μs) to evaporate SiC target and to deposit the evaporated material on a silicon substrate. The deposited film was analyzed by using profilometry, Rutherford Backward Scattering (RBS) and X-Ray Diffraction (XRD) for film thickness, film composition and crystallizability, respectively.

2. Experimental setup

Figure 1 shows the configuration of the ANACONDA ion beam diode, which is an extraction type B_r diode. The ion beam is extracted from the annular anode and focused onto the target. Typical waveforms of the diode voltage and current are shown in Fig. 2. The ions are mostly carbon and oxygen with a small proton component. The ion beam intensity obtained at the focus point has a FWHM of 6 to 8 cm.

The target is a sintered SiC disk with 5 cm diameter. It is located at the focus of the ion beam at an angle of 45 degrees to the axis.

A silicon substrate is located in front of and parallel to the target with a separation variable from 11.5 to 18 cm. The film samples on the substrate were obtained by firing 40 shots of ion beam on the target without breaking the vacuum.

3. Results of analyses

In order to obtain the thickness of the film, a portion of substrate is masked during film deposition giving a sharp edge to the film. Figure 3 shows this edge obtained by using a profilometor. Figure 3(a) and 3(b) show the samples obtained with target-substrate distances of 11.5 cm and 18 cm, respectively. From Fig.3, the film thicknesses are ~ 0.8 μm and ~ 0.3 μm for the target-substrate distances of 11.5 cm and 18 cm, corresponding to deposition rates of 20

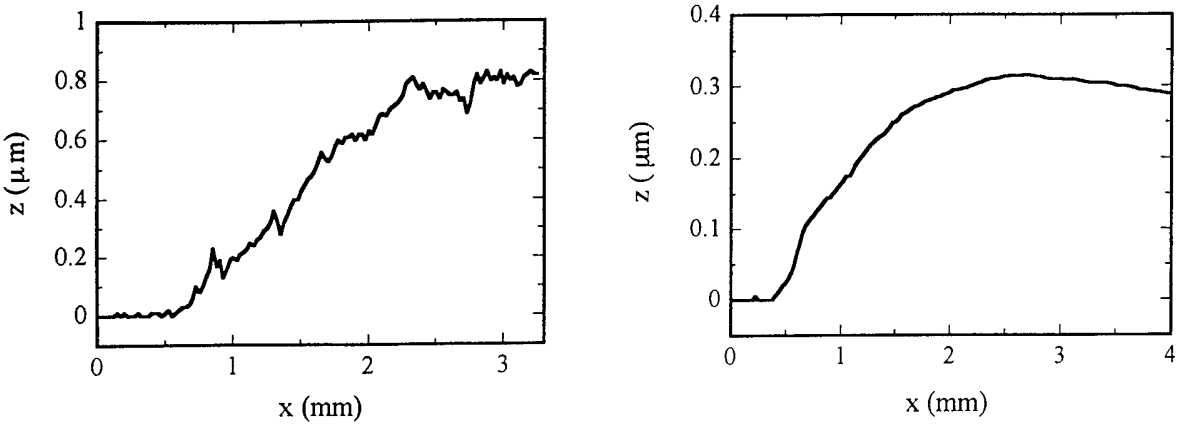

Fig. 3 Profile of the film surface showing film thickness, for films obtained with target-substrate distance of (a) 11.5 cm and (b) 18 cm, respectively.

nm/shot and 7.5 nm/shot, respectively.

Table 1 shows the film compositions obtained by using RBS. Although the ratio of Si:C in the target is 1:1, it is found to be 1:2 in the film obtained with target-substrate distance of 11.5 cm and about 1:3 in that obtained with target-substrate distance of 18 cm. In addition, some oxygen are obtained in the latter film. Extra carbon and oxygen may come from anode material deposited on the target. The anode is made of Lucite containing carbon, oxygen and hydrogen.

The sample obtained with target-substrate distance of 11.5 cm was analyzed by using XRD. Figure 4 shows the major peaks obtained by the XRD. It is seen from Fig. 4 that, except for the peaks of the substrate material, the observed diffraction peaks are mainly given by β-SiC, indicating that the thin film has cubic silicon carbide structure.

Table 1 Film composition obtained by RBS.

target-substrate distance	Si (%)	C (%)	O (%)
11.5 cm	33	66	0
18 cm	21	62	17

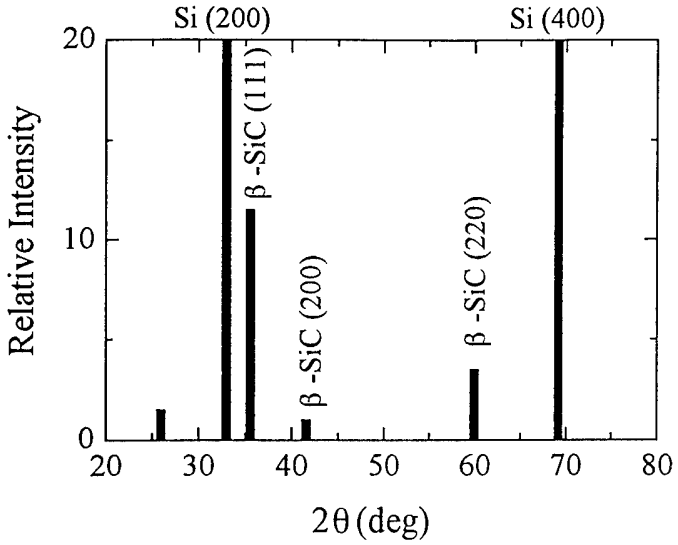

Fig. 4 XRD peaks of the SiC film on silicon substrate obtained with target-substrate distance of 11.5 cm.

References

[1] K. Yatsui, Laser and Particle Beams, **7** (1989) 733.

[2] Y. Shimotori, M. Yokoyama, H. Isobe, S. Harada, K. Masugata, and K. Yatsui, J. Appl. Phys., **63** (1988) 968.

[3] K. Yatsui, X. D. Kang. T. Sonegawa, T. Matsuoka, K. Masugata, Y. Shimotori, T. Satoh, S. Furuuchi, Y. Ohuchi, T. Takeshita, and H. Yamamoto, Phys. Plasmas, **1** (1994) 1730.

[4] K. Yatsui, C. Grigoriu, H. Kubo, K. Masugata, and Y. Shimotori, Appl. Phys. Lett., **67** (1995) 1214.

STUDY OF YBCO THIN FILMS DEPOSITED BY INTENSE PULSED LIGHT ION BEAM EVAPORATION

Constantin Grigoriu, E.P.Achmad Chamdani, Dana Miu, Katsumi Masugata and Kiyoshi Yatsui

Laboratory of Beam Technology
Nagaoka University of Technology
Nagaoka, Niigata 940-21, Japan

Introduction

The present report describes deposition of $YBa_2Cu_3O_{7-x}$ (YBCO) thin films by intense pulsed ion beam evaporation (IBE). Standard deposition configuration (front side deposition, IBE/FS), is compared with a new proposed one, back side deposition (IBE/BS). This method has proven valuable for improving the film morphologies and stoichiometry.

Figure 1 schematically illustrates the two geometrical configurations. In standard IBE/FS method, the deposition takes place on the frontal side of the substrate, while in the IBE/BS method, the substrate is placed on the reverse side of the holder, film being deposited due to diffusion process.

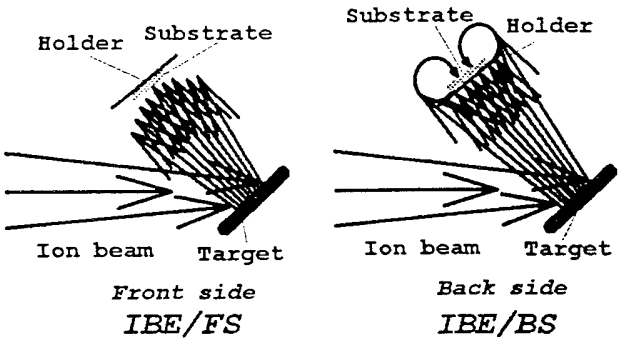

Fig. 1 IBE/FS and IBE/BS deposition configurations.

Experimental

Experiments currently underway at Beam Technology Lab. utilize a light ion beam generator ETIGO-II [1,2]. The relevant experimental characteristics are presented in Table I.

Following deposition, the layers were amorphous; therefore they were annealed in flowing oxygen.

The microstructure of the samples was examined by atomic force microscope (AFM), X-ray diffraction analysis (XRD) and Rutherford backscattering spectroscopy (RBS).

Table I. Ion beam characteristics and main experimental arrangement characteristics.

Diode voltage	Diode current	Pulse width	Ion current density	Fluence at target	Power density at target	Beam composition
1.1 MV	80 kA	70 ns	0.5 kA/cm^2	~30 J/ cm^2	~0.4 GW/ cm^2	90% protons

Target	Substrate	Deposition in vacuum	Target-substrate distance	Beam-target angle	Beam area on target
$YBa_2Cu_3O_{7-x}$	Si(100); MgO(100); $SrLaGaO_4$(100)	3×10^{-2} Pa	60 mm	45^0	~5 cm^2

Results

Firstly, the films deposited by IBE/FS are not satisfactorily, with relatively poor morphologies. In general, the surface of the film have some irregularities, the surface is pretty rough, and also, one can be found droplets with diameters above 1.5 μm. The poor roughness is attributed to liquid droplets ejected from the target. The films deposited by the new method, IBE/BS, exhibit an improved roughness, with no droplets. For comparison, in Fig. 2 are shown two micrographs obtained by atomic force microscopy:
(a) for a film deposited by IBE/FS, one shot and (b) for a film deposited by IBE/BS, one shot.

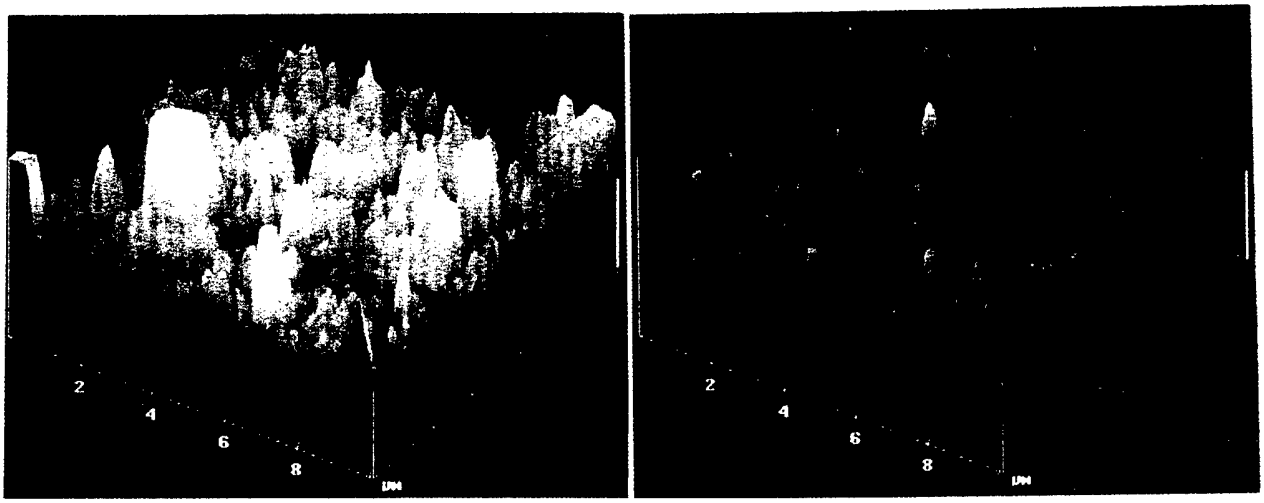

(a) (b)

Fig. 2 AFM micrographs of YBCO films deposited in vacuum, on MgO (100), one shot, substrate temperature 700 ^{0}C, annealed films: (a) by IBE/FS, (b) by IBE/BS;(x, y 2000 nm/div; z 300 nm/div).

Roughness calculated as arithmetical average of the surface deviation from the mean plane R_a, and root mean square average R_{ms}, is about five times better for the IBE/BS case; (for IBE/FS, R_a =55.47 nm and R_{ms} = 84.23nm; for IBE/BS R_a =10.35 nm and R_{ms} =17.93 nm).

In the case of the IBE/FS we measured a deposition rate in vacuum, of 300~400 nm/shot, for a beam energy density of 30 J/cm^2, power density of 0.4 GW/cm^2 and a target-substrate distance of 6 cm. In the case of IBE/BS deposition, the rate was around 30 nm/shot, that is, an order of magnitude lower. If we compare with other methods (for example laser ablation), the deposition rate is still much higher, so IBE/BS remains an attractive method.

Concerning crystallinity, we investigated the XRD patterns of the films.

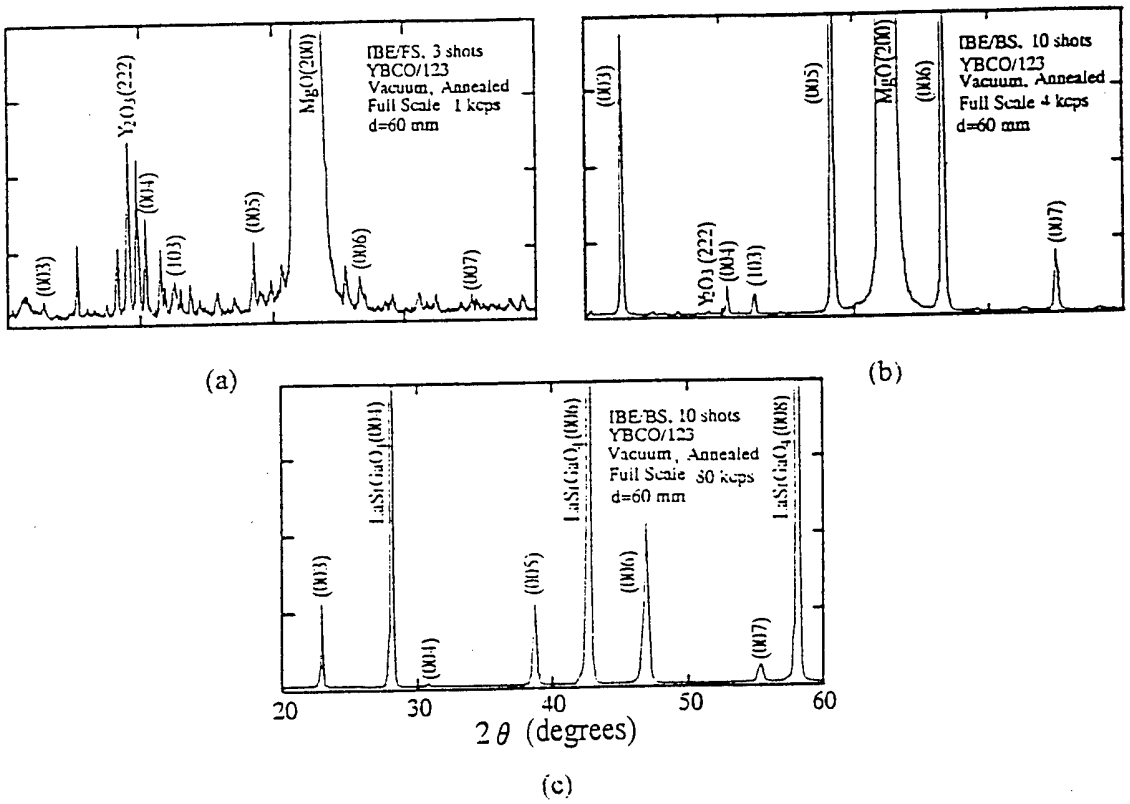

Fig. 3 XRD patterns for films deposited by IBE/FS on MgO, full scale 1 kcps, (a); by IBE/BS on MgO, full scale 4 kcps, (b); by IBE/BS on $LaSrGaO_4$, full scale 80 kcps (c).

In the case of the films deposited by IBE/FS, multiple shots, 1:2:3 target, the X-ray-diffraction patterns were inadequate, with many extra-peaks of unidentified phases, that can be associated with the deviation from the film optimal stoichiometry. As an example, in Fig. 3 (a) is shown the XRD pattern of a film deposited in vacuum, by IBE/FS, 3 shots, on MgO.

The similar results have been obtained for Si substrate.

The films deposited by IBE/FS one shot, exhibit an improved XRD pattern with pronounced intensity (00*l*) lines, indicating a structure with the c–axis oriented perpendicular to the substrate.

By the indirect deposition method, IBE/BS, the films have been successfully deposited, for multishot deposited films too. Figure 3 (b), (c) presents XRD patterns for IBE/BS deposited films on MgO, and $LaSrGaO_4$ substrate. We see a strong c axis $\perp$ orientation to substrate surface, for the films deposited by IBE/BS in comparison with IBE/FS.

As can be observed from Fig. 3 (c), the films deposited on $LaSrGaO_4$ substrate have a significant improved crystallinity in comparison with MgO (for $LaSrGaO_4$ substrate, XRD pattern is 80 kcps, in comparison with 4 kcps for MgO). This is due to the small lattice mismatch between YBCO and $LaSrGaO_4$ (YBCO a=0.382 nm, b=0.389 nm; MgO a=0.42 nm ; $LaSrGaO_4$ a=0.384 nm). Also, because $LaSrGaO_4$ shows no phase transformation below 1520 ^{0}C unlike 850~900 ^{0}C for MgO, the deposition and annealing processes, do not perturb the interface substrate-film.

In order to elucidate the film stoichiometry we have investigated composition by RBS. The analysis reveals two important aspects:

1) Films deposited especially by IBE/FS are off-stoichiometrically, depleted in yttrium and copper, (in comparison with initial target). This can be explained by the fact that the plume that impinges the substrate, consisting of huge amount of very energetic particles, produces a strong bombardment of the previous layer. Consequently, it is possible to occur a selective reevaporation. Also, annealing process could contribute in some measure. We have to point out that in one of our previous works [3], we studied the composition of the films deposited by IBE/FS, multishot, by electron probe microanalysis method (EPMA). That analysis shown that the films are depleted in Ba and Cu. Concerning to this ambiguity, our opinion is that RBS method is more proper and accurate for analysis of YBCO thin films, because EPMA is a method very sensitive to elemental standards required for comparison and correction (they have to be in the same form as the sample, etc.). In future we must clear up this aspect, by a third different analysis method.
2) RBS results, demonstrated that in case of Si and MgO, IBE/FS, multishot deposition, appears a strong interdiffusion process between layer and substrate. In the case of IBE/BS the interdiffusion process is significantly decreased because IBE/BS method avoids strong bombardment of the film by high energetic particles.

References

[1] Y.Shimotori, M.Yokoyama, H.Isobe, S.Harada, K.Masugata and K.Yatsui: J. Appl. Phys. **63**, (1988) 968.

[2] Y.Shimotori, M.Yokoyama, S.Harada, K.Masugata and K.Yatsui, Jpn. J. Appl. Phys. **28**, (1989) 468.

[3] X.D.Kang, K.Masugata and K.Yatsui: Jpn. J. Appl. Phys. **33**, Pt. 1, (1994) 1155.

[4] K.Yatsui, X.D.Kang, T.Sonegawa, T.Matsuoka, K.Masugata, Y.Shimotori, T.Satoh, S.Furuuchi, Y.Ohuchi, T.Takeshita, and H.Yamamoto: Phys. of Plasmas **1**, Pt. 2, (1994) 1730.

[5] K.Yatsui, A.Tokuchi, H.Tanak, H.Ishizuka, A.Kawai, E.Sai, K.Masugata, M.Ito and M.Matsui, Laser Particle Beams **3**, 119 (1985).

[6] A.Tokuchi, N.Nakamura, T.Kunimatsu, N.Ninomiya, M.Den, A.Araki, K.Masugata, and K.Yatsui, *Proceedings of the 2nd International Topical Symposium on Inertial Confinement Fusion Research by High-Power Particle Beams*, edited by K.Yatsui (Nagaoka University of Technology, Nagaoka, Japan, 1986), p. 430.

[7] C.Grigoriu, E.P.Achmad Chamdani, T.Sonegawa, K.Masugata, and K.Yatsui, *Proceedings on New Applications of Pulsed High-Energy Density Plasmas*, edited by K.Yatsui (Nagoya, Japan 1995), NIFS-PROC-23, Nat. Inst. for Fusion Science p. 10.

P-3-93

HIGH POWER ION BEAM INFLUENCE TO STAINLESS STEELS

G.E.Remnev, V.K.Struts

Nuclear Physics institute, Lenin Street 2a, Tomsk 634050, Russia

Abstract

The influence of pulsed high power carbon ion beams on stainless chromium-nickel steels is investigated. The morphology, microhardness and wear resistance of the samples' surface after the irradiation treatment are studied.

Introduction

The irradiation of metals and alloys, in particular - stainless steels, by pulsed high power ion beams (PHPIB) leads to the change of microstructure and phase composition of material undersurface layers, which is caused by high rate of energy input (up to 10^{13} J/cm^3·sec) and cooling rate (up to 10^{10} K/sec). It allows to change operational characteristics of tools, made of these materials, in a proper way [1-3]. The establishment of the dependencies of physical processes in alloys under PHPIB irradiation needs in theoretical and experimental research.

Experimental and Discussion

The work presents results of the research of 316, 304 austenite chromium-nickel stainless steels, 15-5 PH austenite-ferrite steel and 440A chromium ferrite steel, modified by PHPIB (the names of steels are given according to the Russian Standard). The Table 1 presents the chemical composition of these steels.

Table 1. The chemical composition of the steels (%).

Steel	C	Cr	Cu	Mn	Mo	Ni	P	S	Si
316	0.045	16.25	0.36	1.63	2.17	10.15	0.025	0.013	0.69
304	0.044	18.35	0.16	1.46	0.34	8.56	0.026	0.003	0.51
15-5 PH	0.07	14.7	3.5	1.0	-	4.5	0.04	0.03	1.0
440A	0.65	16.64	-	0.4	0.08	-	0.019	0.018	0.36

The samples were irradiated by carbon ion (70%) and proton (30%) beam with energy of E=300 keV, pulse duration τ=50 nsec. Ion current density was changed in the range of j=60 - 140 A/cm^2, number of pulses was n=1, ..., 3.

Before the irradiation, the polished samples had an average roughness of the surface of n_a=0.3 μm. The irradiation of the samples by ion beam with density of j=60-70 A/cm^2 leads to melting of the tracks of diamond particle on the sample surface and to the formation of craters with 20 μm diameter and 0.5 μm depth. The higher number of pulses, the higher number of craters and their size: the diameter increases up to 30 μm, the depth - up to 0.7 μm (fig. 1). The irradiation of chromium-nickel alloys by PHPIB with 100 A/cm^2 current density leads to the formation of crater-like meltings with linear size of 50 μm and depth more than 1.5 μm. The increasing of ion current density up to 140 A/cm^2 leads to the formation of sell structure

on the surface with crater-like formations of the same dimensions as size of craters for the current density of j=100 A/cm^2.

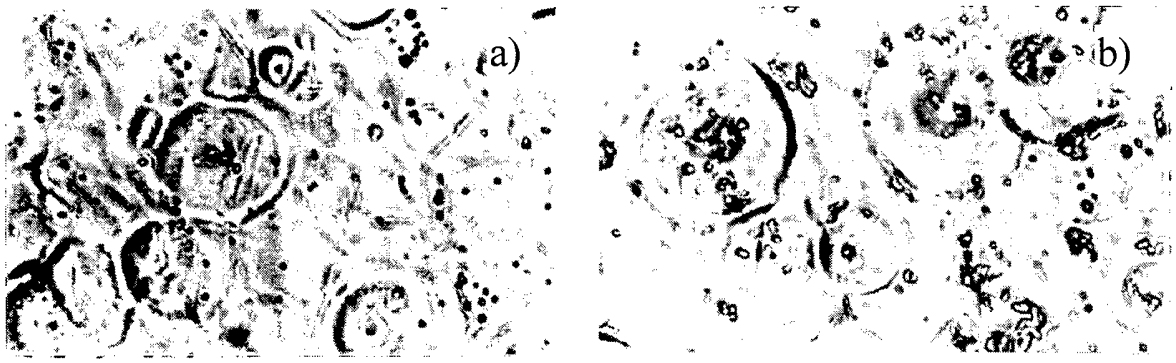

Fig. 1. Microphotography picture of 316 Steel after irradiation (x300): a) j=160 A/cm^2, n=1 pulse; b) j=60 A/cm^2, n=3 pulses.

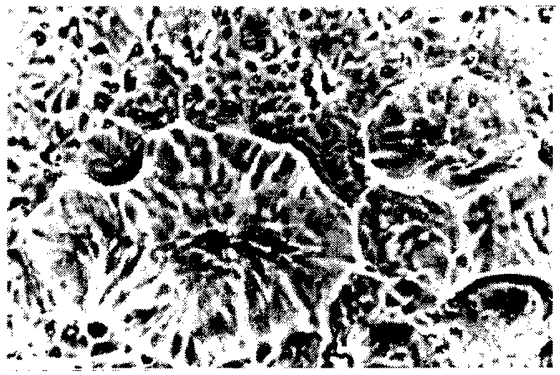

Fig. 2. Microphotography picture of 440A Steel after irradiation (x300): j=100 A/cm^2, n=1 pulse.

The surface morphology of 440A chromium steel differs from morphology of chromium-nickel alloys for the higher ion current densities (j=140 A/cm^2): the chromium-nickel alloys form round plate craters, but 440A chromium steel form the craters with radial relief structure (fig. 2).

The Table 2 presents the microhardness values of the samples H_v for different regimes of irradiation. The load on the diamond indentor was 0.098 N.

The table shows that PHPIB irradiation leads to the decrease of microhardness even for the small values of the current density, which does not lead to the full melting of the surface. It can be conditioned by the removing of results of plastic deformation at the sample polishing. The further decreasing of microhardness, when the ion current density increases up to 100 A/cm^2, n=1 pulse, can be explained by the fact, that the heating of the samples up to 1050-1100° C leads to the chromium carbide solution in austenite, and rapid cooling of irradiated undersurface layer fixes the state of the solid solution and decrease of carbide extraction. Beside that, the re-crystallization processes take place at the hardening process, which remove the stresses, formed at the sample polishing. For the most cases, the increase of the number of pulses with the same current density leads to the increasing of microhardness.

Table 2. The steels' microhardness H_v (GPa)

Steel	j=0	j=60 A/cm^2 n=1	j=60 A/cm^2 n=3	j=100A/cm^2 n=1	j=100A/cm^2 n=3	j=140A/cm^2 n=1
316	2.87	2.01	1.83	1.78	1.91	2.41
304	2.81	2.13	2.44	2.33	2.46	2.65
15-5 PH	4.13	2.95	2.97	2.95	3.02	2.61
440A	2.76	2.50	2.72	2.31	2.12	2.27

It is obvious that the considerable part of the different metal carbides, which is dissolving in austenite at the high temperatures after the first ion current pulse, is extracted from the solid solution after the repeated heating of the samples (after the next ion current pulses). The carbides are extracted on the grain boundaries, and it leads to the reducing of the steel plasticity. The increasing of microhardness with increase of ion current densities ($j \geq 140$ A/cm^2) can be explained by the formation of shock waves, which blow up the plastic deformation of alloy undersurface layer.

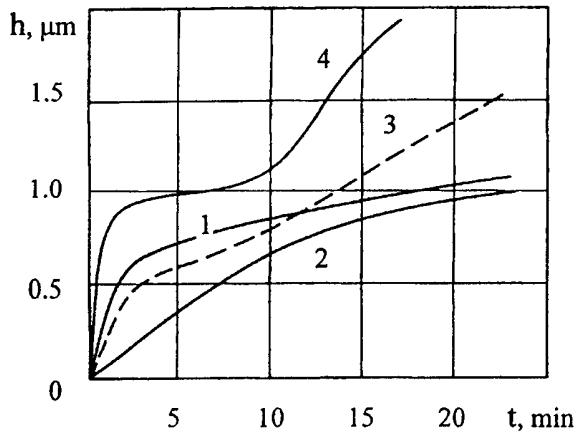

Fig. 3. Wear resistance (track depth *h*) depending on time of indentor moving for 316 Steel: 1) j=0, 2) j=60 A/cm^2, n=1 pulse, 3) j=60 A/cm^2, n=3 pulses, 4) j=100 A/cm^2, n=1 pulse.

The fig. 3 presents the results of 316 Steel investigation on the wear resistance by "needle-disk" method with the different irradiation conditions: 1 - j=0 (before irradiation), 2- j=60 A/cm^2, n=1 pulse, 3- j=60 A/cm^2, n=3 pulses, 4 - j=100 A/cm^2, n=1 pulse. The load on the diamond indentor was 0.098 N, the indentor velocity was 0.86 m/sec. The reducing of wear resistance of the samples irradiated by 100 A/cm^2 PHPIB is caused by the increasing of plasticity and reducing of microhardness. The increase of the wear resistance treated by beams with small current density is very unexpected result. The reducing of friction factor, measured with these irradiation regimes, corresponds to the increasing of the sample wear resistance.

Conclusion

The irradiation of stainless steels by pulsed high power ion beams with ion current densities of 100 A/cm^2 leads to the increase of the plasticity and decrease of the microhardness. The increasing of the number of pulses leads to the increase of microhardness, because carbides are extracted from solid solution, the increasing of current densities up to $j \geq 140$ A/cm^2 leads to the increase of the microhardness, because shock waves are formed. The wear resistance of 316 Steel increases under average regimes of irradiation.

The authors would like to acknowledge Sandia National Laboratories, USA for the support of the work.

References

1. V.M.Bystritskii, S.V.Grigor'ev, A.A.Sinebrjukhov, G.E.Remnev, V.K.Struts. Proc. of the 9-th International Pulsed Power Conference. Albuquerque, New Mexico, 1993.
2. E.E.Bloom, J.O.Steigler. Phase Transformation During Irradiation. Editet by F.V.Nolfi (Rus.transl. 1989), p.255.
3. B.A.Kalin, V.I.Polsky, V.L.Yakushin. Proc. of 1-st Conference on Modification of Structural Material Properties by Charged Particle Beams, Tomsk, 1988, p.53.

Energy Characteristics of the Process of Air Scrubbing from Hydrocarbon Contaminants in a Barrier-Discharge Reactor

S.P. Bugaev, V.A. Kuvshinov*, N.S. Sochugov, and P.A. Khryapov

Institute of High Current Electronics, RAS
*Institute of Petroleum Chemistry, RAS,
4, Akademichesky Ave., Tomsk, 634055, Russia

Abstract

The electrical and chemical characteristics of the air scrubbing, with the use of a barrier discharge, from impurities of xylene being a typical organic contaminant have been investigated. Based on the interrelation between the electrical and chemical characteristics, an approach to the optimization of the cleaning process has been proposed that allows a severalfold reduction of the energy input.

Introduction

Contamination of the air with gaseous hydrocarbons or organic liquid vapors is an inevitable attribute of many chemical engineering processes. In the recent years, the studies of the processes of profound oxidative destruction of organic contaminants which are based on the nonthermal selective activation of oxygen and hydrocarbon molecules have actively been carried out [1-3]. In view of this, the use of gas-discharge reactors with a low-temperature nonequilibrium plasma at atmospheric pressure is attractive. A number of works have been performed to study the process of air scrubbing from organic contaminants in various types of electrical discharge, e.g. a barrier discharge [1], a pulsed corona [2], a gliding discharge [3].

The present report describes an experimental study of some electrophysical and chemical engineering aspects of the air scrubbing in the plasma of a barrier discharge from xylene being a typical organic contaminant in the vent wastes of many enterprises using organic solvents.

Experimental equipment and technique

The experiment on scrubbing the air from a xylene mixture was performed with the use of a flow-through gas-discharge reactor of coaxial design. The flow rate of gas pumping through the reactor could be varied in a range from 0.01 to 1 m^3/h, concentration of xylene could be varied in a range from 0.08 to 4 g/m^3. The discharge was initiated by high voltage pulses with a base width of 70 μs. The peak voltage was varied from zero to 10 kV and the pulse repetition rate from 0.05 to 3 kHz. The power deposited in the discharge was varied from zero to 50 W by varying the pulse peak voltage and repetition rate. The xylene percentage in the air stream before and after scrubbing was measured using the flame ionization detector of a chromatograph (type 3700).

Results and discussion

The results of experiments on the scrubbing of air from a xylene impurity in the barrier-discharge reactor operating in the steady-state flow-through mode are presented in Fig. 1 as a dependence of the degree of cleaning X on the average energy density W ($kW \cdot h/m^3$). The average energy density is the ratio of the discharge power U (kW) to the flow rate Q (m^3/h) of the air :

$$W = U/Q.$$

The degree of cleaning is the ratio of the xylene concentrations in the air, C_0 and C_m (g/m^3), at the reactor inlet and outlet, respectively, to the xylene concentration at the inlet:

$$X = (C_0 - C_m)/ C_0.$$

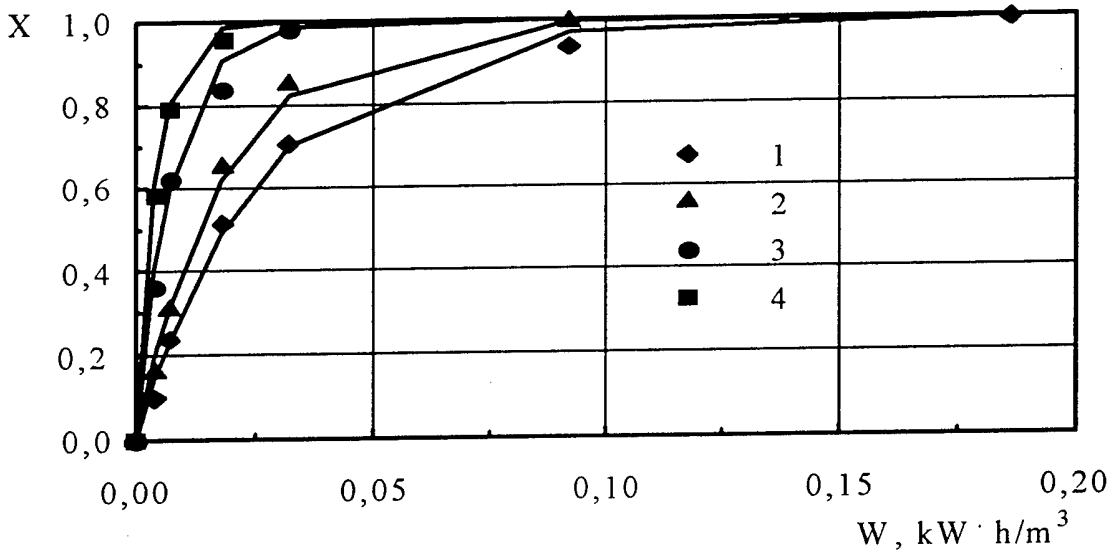

Fig.1 Effect of the average energy density W on the degree of cleaning X of air from xylene. Q=0.2 m^3/h. C_0= 1.98 (1), 1.34 (2), 0.5 (3), and 0.24 g/m^3 (4).

Fig. 1 shows the effect of the average energy density on the degree of cleaning for a fixed flow rate of the air and a varied initial content of xylene. The degree of cleaning therewith decreased with increasing the initial concentration of xylene for the average energy density being unchanged.

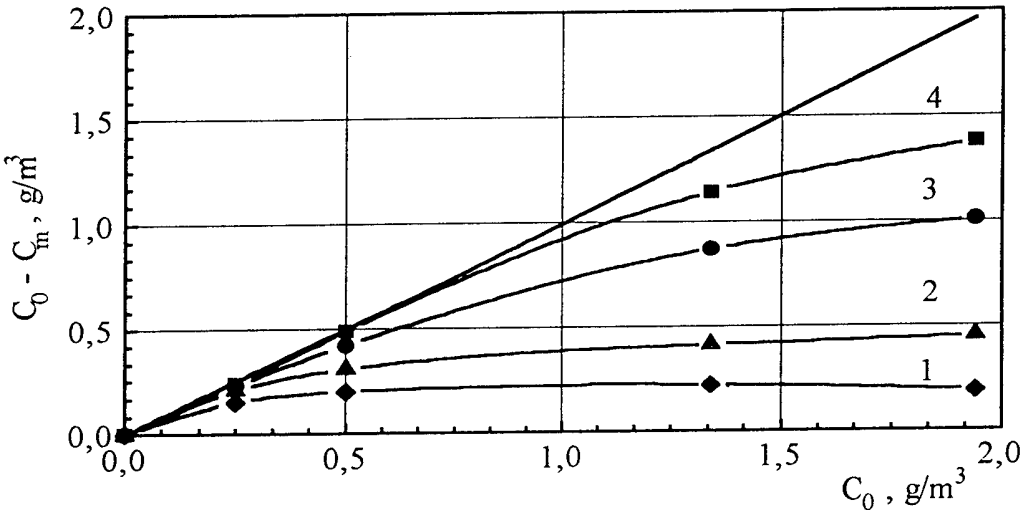

Fig.2 Fall of xylene concentration in air (C_0-C_m) as a function of initial concentration C_0 for W = 0.0035 (1), 0.007 (2), 0.018 (3), and 0.032 kW·h/m^3 (4).

The solid lines in Fig. 2 present the fall of the xylene concentration $\Delta C = C_0 - C_m$ as a function of the initial concentration C_0 for various average energy densities. The straight line shows the limit that is achieved with complete oxidation of xylene and corresponds to a hypothetical infinite average energy density. The curves in Fig. 2 show saturation, and for each average energy density W there exists a limiting value of the fall in xylene concentration ΔC_{max} achievable at large values of the initial concentration C_0. From the experimental data it follows that $\Delta C_{max} = kW$, where $k = 63$ g/kW·h is the coefficient of proportionality and the value $1/k = 0.016$ kW·h/g has the meaning of minimum possible expenditures of energy for combustion of a unit mass of xylene in the reactor having the given construction. The behavior of the experimentally obtained curves can be described, e.g., by an equation of the form

$$\Delta C = kW[1 - \exp(-1.2\, C_0/kW)], \quad (1)$$

Equation (1) can be simplified for two limiting cases, where the exponential term tends to zero or to unity. The former case corresponds to the saturated portion of the dependence $\Delta C(C_0)$, and equation (1) takes the form

$$\Delta C = \Delta C_{max} = kW. \quad (2)$$

In this case, the air is scrubbed from xylene incompletely; however, the energy cost for the combustion of a unit mass of xylene is low and equal to $1/k$. When the exponential term in equation (1) tends to unity, it can be expanded into a series and restricted by two first terms. Equation (1) will then take the form

$$\Delta C = C_0 \quad (3)$$

which corresponds to the case of complete cleaning of the air. Equation (1) can be reduced to the form of equation (3) if the condition $C_0/kW << 1$ is fulfilled. We may put $C_0/kW \approx 0.1$; equation (1) will then be written as

$$\Delta C \approx 0.1kW. \quad (4)$$

It is obvious that the expressions (2) and (3) are the linear interpolation of different portions of the experimental curve $\Delta C(C_0)$ and the expression (4) is an approximate one allowing to relate the values ΔC and W far from the saturation of the dependence $\Delta C(C_0)$. Comparison of expressions (2) and (4) shows that the average energy density necessary for the oxidation of unit mass of xylene in the saturation region of the dependence $\Delta C(C_0)$ is an order of magnitude lower than that corresponding to the conditions of profound scrubbing of the air ($\Delta C \approx C_0$). Complete scrubbing of the air from xylene vapor, i.e., the fulfilment of the condition $\Delta C = C_0$ for a given average energy density is attainable only for the initial concentrations of xylene being much lower than the highest possible value of fall in xylene concentration ΔC_{max}.

More efficient use of atomic oxygen, a reduction of the energy cost of the scrubbing process and complete cleaning of air from an organic impurity can be attained in a multicell plasma chemical reactor where the average energy density delivered to each cell provides for the fulfilment of the condition

$$C_{n-1} - C_n \approx (C_{n-1} - C_n)_{max} << C_{n-1},$$

where C_{n-1} and C_n are the respective concentrations of the impurity at the inlet and outlet of the n-th cell. The average energy density in the reactor should decrease with increasing cell number n. For a barrier-discharge plasma chemical reactor having a coaxial design, its decrease in average energy density can be achieved, e.g., through a stepwise or gradual increase in the spacing of the air gap (decreasing the diameter of the inner electrode). The possibility to decrease the energy cost of the scrubbing when using a multicell reactor can be demonstrated by the experimental data (Fig. 2). E.g., when the average energy density in the reactor is 0.032 kW·h/m^3 (curve 4, Fig. 2) , a high degree of cleaning is achieved for initial xylene concentration no higher than 0.6-0.7 g/m^3. At the same time, the same degree of cleaning at the initial concentration equal to 0.6-0.7 g/m^3 can be achieved at the series connection of 3-4 analogous reactors with average energy density equal to 0.0034 kW·h/m^3 (curve 1, Fig. 3). In each of these reactors no more than 0.2 gram of xylene per one m^3 of air will be exposed to oxidation but summary energy cost will not exceed 0.0102-0.0136 kW·h/m^3 that is 2.3-3 times lower than the value obtained at a onecell cleaning. Minimum achievable energy cost of cleaning is determined by the coefficient k in the equations (1-4) and for the above-cited conditions it will be 0.016 kW·h/m^3 .

Conclusion

The use of a barrier discharge for scrubbing air from organic contaminants is competitive with conventional methods of cleaning at an impurity density not exceeding 0.5 g/m^3. The advantages of the proposed cleaning method are its immunity to catalytic poisons and inertialessness and the possibility of operation with low-calorie contaminants. Application of a multicell reactor allows to decrease essentially the energy cost of cleaning and to avoid the secondary air contamination by the redundant ozone.

[1] W.H. McCulla, L.A. Rosocha, W.S. Neely, E.J. Clothiaux, M.J. Kushner, and M.J. Rood, : *First INEL Plasma Applications to Waste Treatment Workshop Idano Falls.* 1 (1991).
[2] M.G. Glothaus, R.K. Hatcherson, R.A. Korzekwa *et al.*, :*Proc. 9th Pulse Power Conf.* 180 (1991). p.180.
[3] A. Czernichowski and H. Lesueur, :*Proc. 10th Intern. Symp. on Plasma Chemistry.* v.**3**, (1991), p. 3-2.

COMPACT REPETITIVE GENERATORS FOR MEDICAL X RAY DIAGNOSTICS

A.L. Filatov, S.R. Korzhenevskii, Y.A. Kotov, G.A. Mesyats, V.A. Motovilov, and V.A. Scotnikov.

Electrophysics Institute, Russian Academy Sciences,
34, Komsomolskaya St. , Ekaterinburg, 620219, Russia

Abstract

In the article opportunities of application of pulsed generators as medical diagnostics apparatus are considered. Distinctive features of developed generators are the small dimensions, weight and low consumed energy. These qualities permit to used them as portable X-ray apparatus.

The apparatus can work as in radiographic and X-ray copy mode. Results of reception of the X-ray image of objects are indicated:
On a X-ray film;
On a screen of TV-set;
On a display on a personal computer.

The main experiments were conducted on a generator with the following characteristics: output voltage ranging between 30 - 120 kV, current amplitude up to 200 A, a FWHM of 15 - 25 ns, and a pulsed repetition rate up to 1000 pps. The generator is powered by a 220- V 50- Hz supply line. The power consumption is 2.3 J per pulse. The generator is a 150 mm in diameter and 480 mm high oil - filed metal-made casing, with the total volume amounting to 10 l, and weights 15 kg.

Introduction

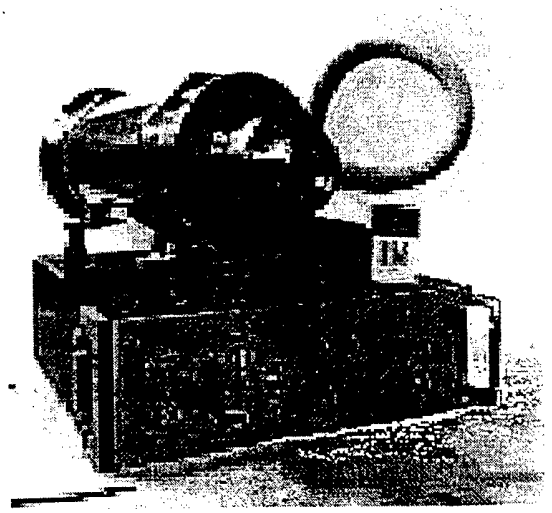

Fig.1. Disign of the generator, the power control console and the vacuum pump.

It is possible to allocate two main requirements to X-ray medical generators:
1. High quality of image;
2. Low irradiation doze.

Besides there is also a number of lower level parameters: the cost-effective, friendly for a archiving, consumer energy and other. We present results that show our generators being compatible and superior to the existing generators.

Approach

The quality of the image is determined by the geometrical resolution of details of penetrated object and resolution on density of materials or in other words, X-ray focus and energy of quantum. Our nanosecond pulsed power X-ray generator used diodes with a needle anode. Thus, X-ray focus is determined by a diameter of a

needle's. There is not problematic achievement of focus of 0.5 mm or smaller, that is very high result for medical X-ray diagnostic apparatus. A contrast of the image of objects with close densities is determined by energy of quantum. Therefore our generators provides the same image contrast as any conventional generators. It is necessary to note that by the used of a digital registration of a X-ray image its quality depends on a level of an equipment and programs of image processing.

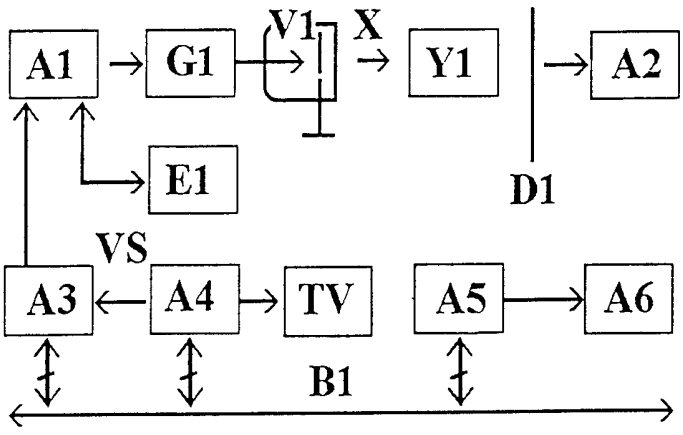

Fig.2. A system of registration and processing of X-ray image by nanosecond pulsed generator.
A1 - generator of start pulses; G1 - nanosecond pulsed power generator; V1 - vacuum tube; X - x -ray; Y1 - researched object; D1 - roentgen lulinescence screen; A2 - CCD camera; E1 - management and control equipment; A3 - synchronization device; A4 - videocatcher; TV - TV monitor; A5 - videoadaptwer VGA; A6 - monitor VGA; B1 - bus ISA.

An irradiation doze depends on a system sensitivity to transform and transfer the image. Many types of medical apparatus require a constant X-ray control. For reduction of an irradiation doze with an image intensifier (a factor of amplification of 10^3 - 10^4) usually is used. For nanosecond pulsed X-ray generator, it is expediently to use a system of image stopping. In this case it is possible to choose a mode of shift shots on a screen with a frequency 1 shot per second (or any other). Thus, the irradiation doze can be reduced in 50 times. In this case one has only to synchronise the generator operation with the TV-image reading. Such an optimisation will significantly reduce an irradiation doze. Because of this effect, all DC X-ray sources produce at "train" on a screen when moving objects are analysing. For our pulsed generators this effect will be avoided.

On the other parameters (cost, dimensions, the consumed electric power etc.) nanosecond pulsed generators have also better characteristics.

Equipment

The electrical circuit of a generator and description of its work are considered in [1]. The nanosecond generator with a control block and vacuum pump are shown in Fig. 1. The generator parameters: output voltage ranging between 30 - 120 kV, current amplitude up to 200 A, a FWHM of 15 - 25 ns, and a pulsed repetition rate up to 1000 pps. The generator is powered by a 220-V 50-Hz supply line. The power consumption is 2.3 J per pulse. The generator is a 150 mm in diameter and 480 mm high oil - filed metal-made casing, with the total volume amounting to 10 l, and weights 15 kg.

The block diagram of the registration system and processing of X-ray images is shown in Fig. 2. The system control is realised by PC (the mode of operations - quantity of pulses in a bunch, duration of the bunch and shots pulses of CCD are shown in Fig. 3). The image of irradiation object is registered on a screen of TV - monitor and monitor of a computer. Both

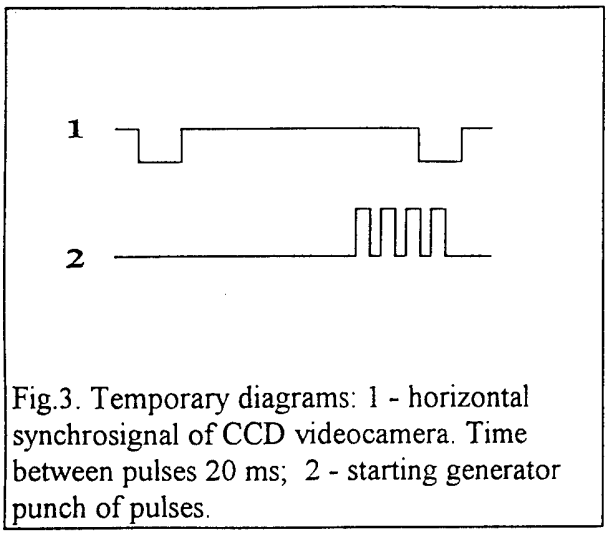

Fig.3. Temporary diagrams: 1 - horizontal synchrosignal of CCD videocamera. Time between pulses 20 ms; 2 - starting generator punch of pulses.

images can be saved and stored in the data base. For initial processing of the image the mathematical methods to agree a target range of visualisation devices (TV set, graphic PC monitor) with maximum quantity of gradation of transformed video signal were used. On second stages digital filter is used for construction of sharp borders. This method allows to discover graphic features of the objects with insignificant differences in brightness.

We used the most simple system of registration (Fig. 2) . Roentgen luminescence screen (ZnS CdS - Ag) and television camera. CCD - video camera trade mark HS - 135 with the sensitivity 0.2 Lx was used. Such system of registration did not used in modern technology. Nevertheless result of experiments are quiet encouraging.

Results

The purpose of experiments was optimisation of work of all circuit to improve qualitative image of various penetrating objects. Modified parameters were: quantitative of pulses in a series, duration of a seers and the time between a series and horizontal synchrosignal. The exposition doze was measured by TLD dosimeter.

Fig.4. X-ray computer image of a hand. Irradiation skin doze was 3.3 - 6 mRh.

In Fig. 4 we present the image of the hand which was done after the improvement of our system. Irradiation skin doze was 3.3 - 6 mRh. According to [2], for X-ray picture of chest a crate doze in 1.5 time lager, and for stomach - 30 times. For our generator it corresponds to doze of 10 mRh and 200 mRh. The spatial resolution was as high as 80 μm.

Discussion

At the present time there is manufactured CCD - video cameras with sensitivity 50μLx, that is 4000 times greater then the one used in the experiment. This may improve considerably the quantity of an image. There is a reservation (5-10 times), by using power and qualitative optics. There were manufactured more contrast TV monitors< specially intended for X-ray copy. There is also a significant reservation to decrease an exposition doze in 1000 times.

Conclusion

Using nanosecond pulsed X-ray generators with a modern equipment of visualisation of the X-ray image and computer control make it possible to reduce considerably exposed

dozes of a patient and a doctor. Even during continuous operations (20 min) the irradiation surface doze will not exceed 1 Rh, and for obtaining one shot on the screen of a TV set monitor exposition dozes will be of the order of 1 μRh.

Therefore, an X-ray image intensifier which is very expensive and not reliable was excluded from the registration system. Estimation shows that to realised the high-sensitivity X-ray system will require expenses at a level of ~ $ 80,000.

Reference

1. Kotov Yu. A., Mesyats G.A., Korzhenevskii S.R. et al. " Compact repetitive electron beams and X-ray generator. Part 2: a hand-carried X-ray apparatus". in Proc. 10-th IEEE International Pulsed Power Conference, July 10-13, 1995, NM, USA.

2. Rentgenotekhnika: handbook/ in 2 vol. ed. by Kluev V.V. - Moscow: Mashinostroenie, 1980. - vol. 2. (in Russian).

COMPACT HIGH-CURRENT, SUBNANOSECOND ELECTRON ACCELERATOR

V.G. Shpak*, S.A. Shunailov*, M.R. Ulmaskulov*, M.I. Yalandin*
I.V.Pegel**, V.P.Tarakanov***

* *Institute of Electrophysics, Russian Academy of Sciences*
34, Komsomolskaya Str., Ekaterinburg, 620049, Russia

** *High-Current Electronics Institute, Russian Academy of Sciences*
4, Academitchesky Av., Tomsk, 634055, Russia

*** *High-Temperature Institute, Russian Academy of Sciences*
13/19 Izhorskaya Str., Moscow, 127412, Russia

Abstract

A compact subnanosecond, high-current electron accelerator producing an annular electron beam of duration up to 300 - 400 ps, energy ~ 250 keV, and current up to 1 kA has been developed to study transient processes in pulsed power microwave devices. The measuring and recording techniques used to experimentally investigate the dynamics of the beam current pulse and the transformation of the electron energy during the transportation of the beam in a longitudinal magnetic field are described. The experimental data obtained are compared with the predictions of a numerical simulation.

High-current electron accelerators operating with explosive electron emission cathodes allow electron beams with durations of 10^{-10} - 10^{-9} s and ultimate (over 10^4 - 10^5 A/cm^2) current densities to be generated in miniature vacuum diodes [1]. Such beams, being single dense bunches several centimeters in length, are used for example in the sources of high-power wideband ($\Delta f \sim 1/t$) electromagnetic pulses with microwave carriers [2]. Using a short beam one can investigate the transient processes in microwave devices, in the case when the stray reflections and the feedback are "delayed".

The technique used to produce a subnanosecond pulse of accelerating voltage [1] predetermines the irregularity of the pulse waveform and, hence, of the axial energy structure of the beam. Therefore, a subnanosecond high-current beam is too complex to describe analytically. At the same time, the now available instrumentation and oscillographic equipment allow an experimental study of the dynamics of a single electron bunch in real time. It is possible to simulate numerically the non-steady-state processes in the vacuum diode of an accelerator and in the beam drift region. We used for the simulation an axially symmetric version of a 2,5 D and 3 D completely electromagnetic code (KARAT) [3]. The goals of this work were: (i) to design a compact subnanosecond high-current electron accelerator; (ii) to study experimentally the transformation of the current pulse and the conversion of the electron energy during the transportation of a magnetized electron bunch in an extended drift chamber; and (iii) to compare the experimental data with the predictions of the numerical simulation.

The subnanosecond high-current electron accelerator is based on the type RADAN 303B compact generator [4], a pulse peaker [5], and magnetically insulated coaxial diode with an explosive-emission cathode (Fig. 1). At the output of the chopper a subnanosecond pulse was formed (Fig. 2) that was transmitted through a nonuniform stepwise line and then arrived at the vacuum diode to produce at the cathode an accelerating voltage of amplitude up to 250 kV. The risetime of the accelerating pulse was twice as much as the falltime [5]. The explosive-emission tubular graphite cathode of diameter 4 mm was in the region of a uniform magnetic field (12 kOe) created by a pulsed solenoid. Also placed in the field of this solenoid was a cylindrical drift chamber, of diameter 10 mm and length 30 cm, separated from the cathode by the anode unit. Here collimators were mounted whose length was over the characteristic cyclotron step of the beam magnetized electrons. By varying the collimators, it

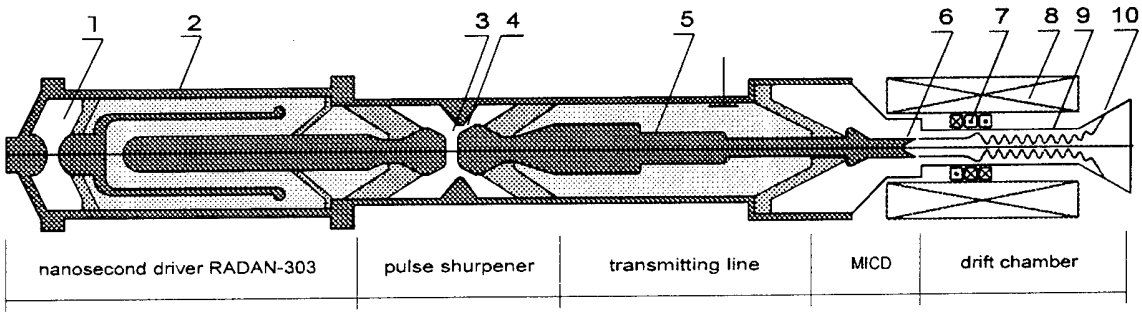

Fig.1. Subnanosecond electron accelerator. 1, 3, 4 - gas spark gaps; 2 - double pulse-forming line; 5 - 50-80-Ω mating transformer; 6 - cathode; 7 - colliding coils; 8 - solenoid; 9 - drift chamber; 10 - beam collector.

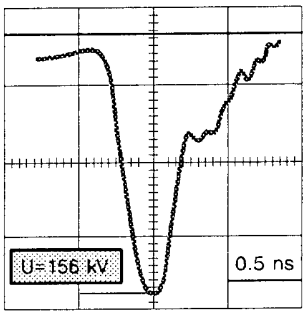

Fig.2. High voltage pulse waveform at the 50-ohm output of subnanosecond modulator .

was possible to reduce the beam current by more than an order of magnitude. With this neither the accelerating pulse amplitude nor the geometry of the cathode-anode gap was varied. The residual pressure in the drift chamber was ~ 10^{-2} Torr. The electron current in the drift chamber was measured by a Faraday cup placed at the end of a 6 - Ω coaxial line whose output was connected to a strip line. The transducer allowed an observation of the processes in their "pure form" when any reflections, inevitable in this type of device, were shifted from the front of the legitimate signal by more than 1.5 ns. The temporal resolution was on a level of 150 - 200 ps which was limited by the bandwidth of the delay line of the oscilloscope. The cross-sectional structure of the subnanosecond electron beam was fixed within a pulse by imprints left by the beam on a dozimetric film that was placed on a movable collector at various points of the drift chamber. A block of several films shot by the beam allowed an evaluation of the maximum electron energy.

The accelerating pulse had a highly irregular waveform with no flat top (Fig.2). Therefore, the space charge of the fast electrons emitted at the peak accelerating voltage added to the acceleration of the leading low-energy electron fractions at the inlet of the drift chamber. As a result, for a short bunch at the drift chamber inlet, a longitudinal crossover region appeared. In such a region, the current pulse amplitude of an electron bunch is a maximum and the risetime of the current pulse should be shorter than the risetime of the accelerating pulse. The crossover was indicated in the experiment (Fig. 3) as a maximum of the dependence I(z) near the drift chamber inlet for various values of current. Increasing the transportation length of the bunch decreased the current pulse amplitude (Fig. 4a). This was accompanied by a consistent spread in the bunch duration. Most probably, the current reached its maximum in the crossover at risetimes shorter than the response of the measuring system (~ 200 ps) and so its measured value was somewhat underestimated. This in particular accounts for the spread in the amplitudes and fall rates of the peak beam current obtained in the experiment (Fig. 4a) and predicted by the numerical simulation of the bunch dynamics in the drift chamber (Fig. 4b).

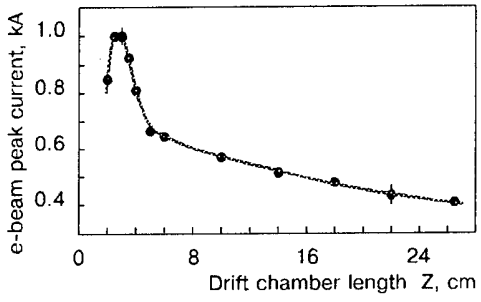

Fig. 3. Drop of e-beam peak current with increasing the drift chamber length.

Both the experiment and the numerical simulation have demonstrated that the subnanosecond beam current strongly reduced (by a factor of five to ten and more) by the collimator acquired a double-hump waveform (Fig. 4c). There occurred a collimation of the electrons emitted from the surface of the cylindrical cathode at accelerating potentials exceeding some value. Electrons with small radii of cyclotron orbits, emitted mainly during the risetime

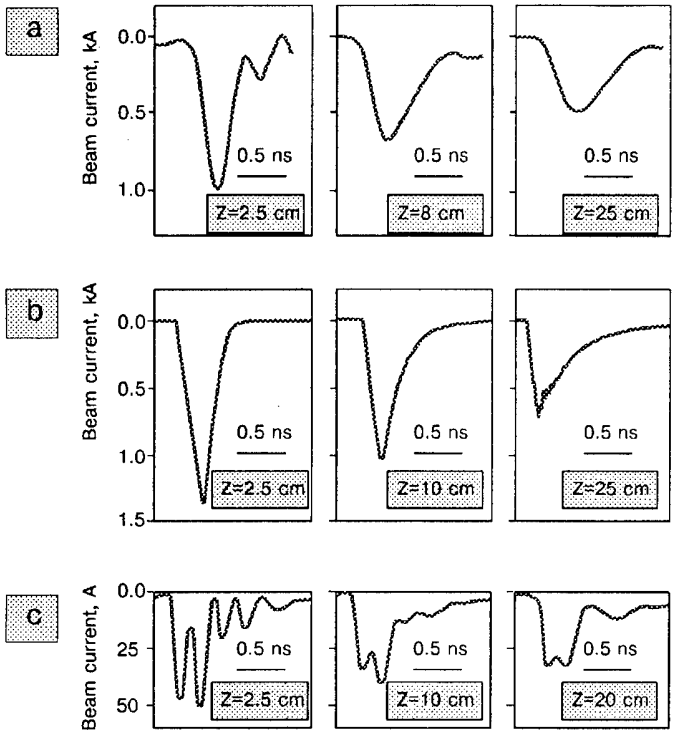

Fig. 4. Current amplitude drop and temporal dispersion of a noncollimated subnanosecond annular e-bunch, obtained experimentally (a); the same traces simulated numerically (b); the behaviour of strongly collimated e-bunch observed in experiments (c). All measurements and calculations were done for various axial points (Z) in the drift chamber.

and falltime of the subnanosecond accelerating pulse, got into the drift chamber. The middle, high-energy, part of the pulse was cut off most efficiently. That is, the cylindrical collimator served not only simply to reduce the number of particles having high transverse velocities but also "filtered" high-energy particles. Note that the pronounced dip in the current pulse testifies to the fact that a substantial part of the fast electrons are emitted from the cylindrical cathode surface adjacent to the sharp edge. The spinning in crossed electric and magnetic fields is most efficient when emission centers are formed in this region. The reduction of the interhump dip (see Fig. 4c) can be accounted for by the fact that the fastest electrons from the second current burst gradually come up the slow tail of the first one.

The current pulse transformation was also studied experimentally under the conditions where the beam electrons at the drift chamber inlet were imparted with a high transverse velocity using a set of oppositely connected coils (kicker) producing a strong radial disturbance of the guide magnetic field. The pitch-factor of the beam electrons in this case could reach values over unity. For the electrons that had passed through the field of the kicker, the value of the pitch-factor depended on the conditions at the inlet into the nonuniform magnetic field region, namely, on the energy of a particle, its radial position, and the initial value of the pitch-factor. Correspondingly, with the total energy of each electron remaining unchanged, the spread in the longitudinal velocities of the beam electrons increased substantially. With the axial field of the solenoid ~12 kOe and the transverse field of the kicker within the undisturbed beam radius ~ 1 kOe, the low-energy electron fractions (<150 keV) were cut off by the magnetic plug. Thus, the system enhancing the transverse oscillator velocity played the role of a magnetic separator that cut off electrons having energies below a certain energy. As a result, the beam having passed through the kicker carried a reduced charge, while the peak current of the beam in its transportation was much more abrupted than for a straightforward beam, and the dynamic dispersion of the bunch (spreading in time) became more significant (Fig. 5). These factors are important, for instance, in analyzing the operating modes on electron hyporesonance microwave devices with a short beam and, in particular, in developing criteria for the evaluation of their efficiency.

During the transportation of a beam carrying a current (I ~ 1kA, j ~ 10^4 A/cm^2) an additional (up to ~ 1.5-fold) acceleration of some part of electrons took place that depended on the drift length (Fig. 6a). These data have been obtained on analyzing the depth to which the dozimetric films were shot. The mechanism for this additional acceleration might be the self-acceleration of some electrons in the field of the space-charge wave generated in the dense electron flow. The numerical simulation has confirmed these results and has shown that the z-component of the electric field wave may reach values of some tens of kilovolts per centimeter and that the most high-energy electron fraction is localized at the beam front. The experiment and the numerical simulation have also shown that the energy increment for the additionally accelerated electrons depends on the beam current at the drift chamber inlet (Fig.

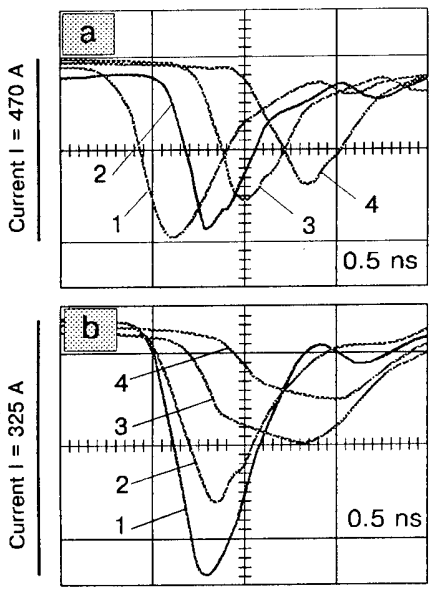

Fig. 5. Traces of the beam current obtained at different distances from the kicker's impacting coils (a: 2.5 cm; b: 23 cm) with an intense artificial enhancement of the transverse velocity. Axial field = 12 KOe. Transverse field of the impact coil: 1 - 0 kOe; 2 - 0.75 kOe; 3 - 0.9 kOe; 4 - 1.25 kOe. Injected current: 500 A (a; b).

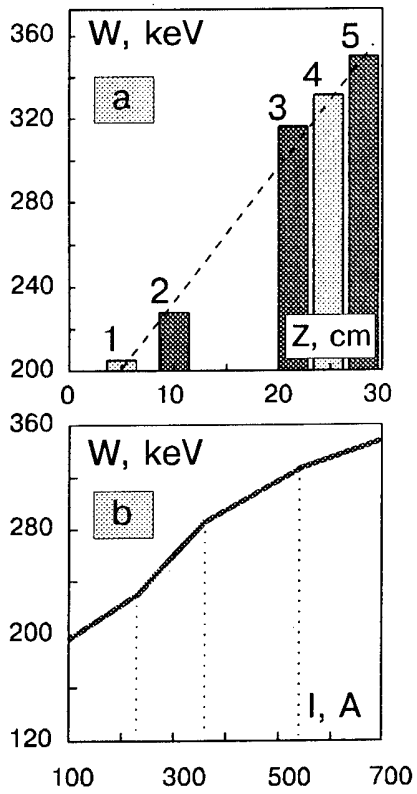

6b). This is quite clear since the amplitudes of the space-charge wave fields should be determined by the electron flux density.

Thus, the dynamics of a straightforward magnetized high-current electron beam of subnanosecond duration has been studied by a numerical simulation and experimentally. The experiment and the simulation have given a good fit of the results and have demonstrated that in transporting a subnanosecond bunch in a drift chamber it is possible to attain a substantial additional acceleration (self-acceleration) of some part of the beam electrons. The degree of acceleration depends on the beam current. Strong collimation of a short magnetized annular beam emitted by an explosive-emission cathode transforms the current pulse and changes substantially its energy structure.

References

[1]. B.M.Kovalchuk, G.A.Mesyats, V.G.Shpak, "Generation of Powerful Subnanosecond Pulses," Proc. Int. Pulsed Power Conf., 1D5 , Lubbok, TX, 1976.

[2]. N.S.Ginzburg, I.V.Konoplev, I.V.Zotova, et. all., "First Experimental Observation of Cyclotron Superradiance', See this Issue.

[3]. V.P.Tarakanov, User's Manual for Code KARAT, Berkeley Research Associates, Inc., VA, USA, 1992

[4]. V.G.Shpak , S.A.Shunailov, M.I.Yalandin, A.N.Dyad'kov, "The RADAN SEF-303A, a small high-current pulsed power supply" IET, 1993, 36, №1, pp.106-111.

[5]. G.A.Mesyats, V.G.Shpak, S.A.Shunailov, M.I.Yalandin, "Desk-top subnanosecond pulser research, development and applications", Proceedings of SPIE International Symposium: Intense Microwave Pulses, Vol.2154, pp. 262-268, Los Angeles, CA, 1994.

Fig. 6. (a) - increase in maximum electron energy with increasing beam drift length: 1,4 - experiment; 2,3,5, - numerical simulation. (b) - increase in maximum electron energy versus peak beam current (numerical simulation).

NUCLEAR REACTIONS CROSS SECTION MEASUREMENT USING Z-PINCH TECHNOLOGY

T.Bulgakov[1], Vit.Bystritskii[1], G.Mesyats[1], A.Sinebryukhov[1], V.Sinebryukhov[1], V.Bystritsky[2], V.Grebenyuk[2], S.Parzhitskii[2], B.Sabirov[2], V.Stolupin[2], A.Luchinsky[3], S.Chaikovsky[3], V.Mahrin[3], N.Ratakhin[3], S.Sorokin[3], A.Gula[4], M.Filipowicz[4], J.Wozniak[4]

[1]*Institute of Electrophysics RAS, Academy ave.4, Tomsk 634055, RUSSIA*
[2]*Joint Institute for Nuclear Research, Dubna, 141980, RUSSIA*
[3]*High Current Electronics Institute RAS, Academy ave.4, Tomsk 634055, RUSSIA*
[4]*Institute of Physics and Nuclear Techniques, 30-059 Krakow, Poland*

ABSTRACT

Direct experimental estimate of the upper limit of the $d + d \rightarrow {}^3He + n$ cross-section at deuteron energies below the keV region is obtained for the first time. The experiment was performed at the Pulsed Ion Beam Accelerator of the High-Current Electronics Institute in Tomsk, using high intensity, radially converging deutron beams, generated during implosion of liner plasma. A two-jet liner made of $17\%D_2 + 83\%N_2$ gas, was used, with the inner jet serving as a target. The dd-fusion neutrons were registered by time-of-flight scintillator spectrometers and BF_3 detectors of thermal neutrons placed in polyethylene moderator. The upper limit obtained for the $d + d \rightarrow {}^3He + n$ cross-section for deuteron energy 440 eV is $\sigma < 2 \cdot 10^{-34} cm^2$ at 90% confidence level. The result demonstrates that liner implosion technique can be used in the investigations of nuclear reactions between light nuclei at infra low energies, previously not accessible in experiments with classical beam accelerators.

INTRODUCTION

The investigation of nuclear fusion of light nuclei in the sub-keV region may provide important knowledge about strong interactions in this energy region, such as verification of their fundamental symmetries (charge symmetry, parity, etc.). At present, only data on np, nd and nHe scattering lengths in different spin states exist; while their proton counterparts, scattering phases and probabilities are missing. Several other problems are of a significant interest too, like existence of weakly bound states or resonances in few body hadronic systems and the contribution of meson exchange currents in the radiative capture $p + d \rightarrow {}^3He + \gamma$ [1]. The characteristics of nuclear reactions in the sub-keV region are also needed for answering a number of questions in astrophysics. For example, in the analysis of abundance of light nuclei in stars and the Galaxy, the extrapolated values of the cross-sections for nuclear reactions are used, which require assumptions about absence of resonances or any anomalies in the scattering amplitudes in the low-energy region [2]. The measured values of the cross-sections between p, d and t nucleis did not exceeded of 10^{-31} cm^2 [3].

Investigation of these reactions at lower energies using classical accelerators is difficult, if not impossible, because the beam intensities are too low to measure cross-sections of the order $10^{-32} - 10^{-45} cm^2$ as they are predicted by the theoretical estimates [4].

In Refs. [5] a method of measuring nuclear cross-sections at ultra-low energies was proposed, using high-intensity, radially converging ions beams generated during plasma

liner implosion. At energies under consideration, the number of particles per pulse is then of the order of 10^{20}, which may enable one to substantially decrease the lower limit of energies at which the cross-sections are measured, and reach values in the range $10^{-38} - 10^{-42}$ cm^2.

The goal of this work was to measure the cross-section of neutron yielding *dd*-reaction at average deuteron energy of about 440 eV using the Z-pinch approach.

METHOD OF MEASUREMENT

The liner is formed as a hollow-cylinder gas jet by ultrasonic deuterium gas puff injected into vacuum through annular Laval nozzle with electromagnetic valve. Subsequently, a high-voltage ionizing pulse is applied to the liner, and the deuterons are accelerated towards the axis by the magnetic field of the liner's electric current. In the final stages of compression the ions collide with sub-keV energies in the axis region. In such process the energy fluctuations of the accelerated deuterons in the final stage of compression amount to about 20%.

There are several difficulties inherent in the proposed method. The main one is due to plasma instabilities in the final stage of liner compression which lead to appearance of deuterons with energies up to several hundreds keV. Because at 20-300 keV the corresponding cross-sections are of the order of $10^{-28} - 10^{-30}$ cm^2, the background of such events may be comparable with the signals ¿from reactions in the investigated energy range. There are two possibilities to overcome this difficulty. The first possibility is to stabilize the liner by external axial magnetic field, as described in [6]. The second one is based on inserting a solid-state rod of a finite diameter co-axially with the liner [7]. In this way maximum compression is not achieved (compression factors less than 10) and plasma instabilities do not develop. If the rod contains deuterium (eg. deuterized poliethylene) it can serve as a target at the same time.

Alternatively, one can inject a thin annular stream of gas containing deuterium along the rod surface. In this method the rod provides only a limitation of the inner diameter of the final compression zone and the material it is made of, is not critical. This approach has been used in the present experiment.

THE EXPERIMENT

The experiment was performed in the Institute of High Current Electronics of the Siberian Branch of the Russian Academy of Sciences using the high-current nanosecond ion accelerator with the characteristic parameters: $I_{max} = 750$ kA, $U_{max} = 700$ kV and current pulse duration $\tau = 60$ ns. The experimental set-up included a high-power, high-current nanosecond generator, a load unit, and a registration system of *dd*-reaction products. The inner gas jet of the two-jet liner served as a target. The *dd*-fusion neutron detection system consisted of: (a) time-of-flight scintillator spectrometers (4 units), and (b) thermal neutron detectors filled with BF_3 placed in polyethylene moderator (6 detectors). The scintillator detectors were $100 \times 100 \times 750$ mm parallelepipeds, viewed by two photomultipliers XP-2020. The diagnostics set-up for controlling liner acceleration included: a soft X-ray detector, photoelectron recorder with image intensifier and a dB/dt probe.

With this experimental set-up the cross-section for *dd*-fusion neutron channel is given by:

$$\sigma_{dd} = \frac{N_n}{I_d n_t d\varepsilon_n} \qquad (1)$$

where N_n is the number of registered neutrons, I_d is the total number of accelerated liner deuterons hitting the target, n_t is deuteron target density, d is deuteron range in the target and ε_n is neutron registration efficiency. The value of I_d is determined by the energy characteristics of the generator, the efficiency of the generator-to-liner energy transfer and the final liner velocity. In the zero-dimensional model of liner compression I_d can be determined using the expression for the specific liner mass, per unit length

$$M = 2 \times 10^{10} I^2 \ln(R/r)/v^2 \qquad (2)$$

where I is accelerator current in MA, v is liner velocity at the final compression stage (in cm/s), and R, r are initial and final liner radii, respectively.

The investigation was preceded by a methodical experiment aimed at testing the performance of the nuclear registration equipment exposed to intensive γ-ray radiation and strong electric and magnetic fields arising from the operation of the high-current accelerator. For this purpose, two different liner gases were used: helium and deuterium. The time of maximum implosion was 60-100 ns for both liners. In the absence of high voltage at the photomultipliers the noise level did not exceed 10 mV.

In the next stage, the X-ray load of neutron detectors from the intensive bremsstrahlung in the liner was investigated. During the shot (discharge of the accelerator) the signal from the unscreened neutron scintillation detector had the amplitude of about 20 V and was about 40 ns long. As could be expected, the time of appearance of the signal corresponded to helium liner compression stage. Subsequently, the detector was surrounded by a 5 cm layer of lead, which practically eliminated the X-ray load. This enabled us to strictly identify signals from dd-fusion neutrons (for the deuterium liner). In order to suppress the X-ray background in the thermal neutron detectors a 1.2 cm layer of lead was used.

Further investigation of liner compression dynamics allowed us to choose the working conditions such that the yield of dd-fusion products due to Z-pinch instabilities was significantly below the sensitivity threshold of the detection system. For this purpose a two-jet system was used with 17%D_2 +83%N_2 gas mixture as a liner. The outer jet constituted a hollow gas cylinder with an outer diameter of 27 mm and thickness of 3 mm. The inner nozzle formed a gas puff with an outer diameter of 13 mm around a stainless steel rod, 9 mm in diameter, placed coaxially with the liner.

The liner mass was 33 μg, which corresponded to the total number of $2.8 \cdot 10^{17}$ deuterons in one shot. The average deuteron energy was $< E_d >= 440$ eV (the average energies in the individual shots ranged between 300 eV and 620 eV). The total target mass was 102 μg, which corresponded to 9.1×10^{17} deuterons. The total neutron registration efficiency was 2.1×10^{-3} and the neutron registration threshold of the scintillation detectors 0.25 MeVee (in light — equivalent electron energy units). In course of the experiment the spectrometers were periodically calibrated, using the standard γ-sources ^{60}Co and ^{137}Cs. Additionally, check-outs of the registration equipment were done after every five shots, on average, with the 17%D_2 + 83%N_2 mixture by making a shot with pure deuterium and the coaxial rod removed. In such shots intensive neutron fluxes were observed ($10^6 - 10^7$ neutrons per pulse), originating from the high energy deuterons due to liner instabilities.

The actual experimental sample consisted of 52 shots with the two-jet 17%D_2 + 83%N_2 gas liner and the limiting rod inserted. One neutron was observed during all run. In this way, we have obtained the upper limit $\sigma < 2 \cdot 10^{-34}$ cm^2 for the $d + d \rightarrow {}^3He + n$ cross-section at average deuteron energy of 440 eV with 90% confidence level.

SUMMARY

A direct experimental estimate of the upper limit for the $d + d \rightarrow {}^3He + n$ cross-section at sub-keV deuteron energies was obtained for the first time. The estimate obtained for $< E_d >= 440$ eV $\sigma < 2 \cdot 10^{-33}$ cm^2 shows that the proposed method of investigation of strong interactions can provide more constrained information. The presently obtained upper limit is still significantly higher than the theoretical estimates. However, realistic possibilities exist to bring this limit down by several orders of magnitude.

The work was supported by the International Science Fund (grant no. RGN000), the Russian Fund for Fundamental Research (grant no. 95-02-05689) and by the grant received from the Plenipotentiary of the Polish Government for corporation with JINR in Dubna. The authors express their gratitude to Dr. V.B.Brudanin, Profs A.Hrynkiewicz and J.Niewodniczański for their support in the present investigations, Prof. V.B.Belyaev and O.I.Kartavtsev for useful discussions.

REFERENCES

[1] C.Barghlolz, Astr. J., **233**, 1979, L161-L171; Nucl. Phys., **A474**, 1987, 1
[2] C.Rolfs, Proc. Intern. School of Phys. "Enrico Fermi", Course C.3, Villa Monastero, 23 June - 3 July 1987, edited by P.Kienle, R.A.Ricci and A.Rubbino, North Holland, 1989, 417
[3] G.M.Griffiths, M.Lal, C.D.Scarfe, Can. J. Phys., **42**, 1963, 724
[4] V.B.Belyaev, V.M.Bystritsky, A.A.Sinebryukhov et al., Preprint JINR **D15-95-378**, Dubna, 1995, submitted to NIM
[5] Vit.M.Bystritskii, A.A.Sinebryukhov, Viach.M.Bystritsky et al., 10-th IEEE International Pulsed Power Conference, Abstract Book, P2-67, Albuquerque, New Mexico, July 10-13, 1995, USA
[6] S.A.Sorokin, A.A.Chachaturyan, S.A.Chaikovskii, Fiz.Plazmy **17**, 12 1991, 1453
[7] R.B.Baksht, Zh.Tech.Fiz. **59**, 1989, 57

ABOUT USING OF ION ACCELERATORS IN ACCELERATOR DRIVEN SYSTEMS

S. Chigrinov, A. Kievitskaia, V. Petlevski, C. Rutkovskaia

Radiation Physics & Chemistry Problems Institute, Academy of Sciences of Belarus
Minsk-Sosny, 220109, Belarus

The problem of the development of nuclear power engineering has gained renewed interest through studies on different options to satisfy a huge need in the energv of the future. Nuclear power characterised by a high concentration of energy per unit of fuel mass can meet this demands. One of promising nuclear power installations is **the Accelerator Driven Systems (ADS)** based on using of high energy accelerators and subcritical target/blanket system. **ADS** can be used [1]:

- **to produce thermal (electric) power;**
- **to produce tritium for fusion reactors;**
- **to transmute long-lived radioactive wastes;**
- **to incinerate weapon and commercial plutonium**

ADS are the safety and reliability of operating ones as the subcritical systems, satisfy the principles of nuclear non-proliferation and anti-terrorism.

The process of interaction of high energy particles with the matter is an extremely complicated process involving the participation of a large number of various particles [2,3]. The projectile particle interacts with nucleus through the series of inelastic and elastic collisions what is called internuclear cascade (in the matter it is called intranuclear one). Fast nucleons are emitted from the nucleus and then high energy fission, evaporation of **n, p, d, ^{3}He, ^{4}He, γ-quantum** takes place in de-excitation process from the nucleus. The charged particles lost their energy for ionization processes and the main multiplying component becomes the neutrons. It is known that the number of neutrons in the nuclear reactors is limited (≈ 2.7 per one fission). In the **ADS** it is possible to receive much more per one particle of the beam. Fig.1 shows as atomic weight of accelerated particle increases the number of neutrons and their energy (Fig. 2) rises too. Thus, larger number of neutrons will be created in

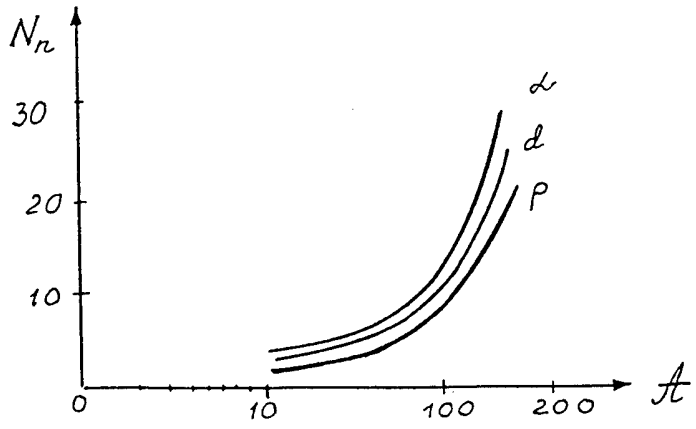

Fig. 1

The dependence of the number of secondary neutrons (per one particle of a beam) N_n from atomic weight of nuclei-target A for p, d, and ^{4}He beams with 1 GeV/nucleon energy

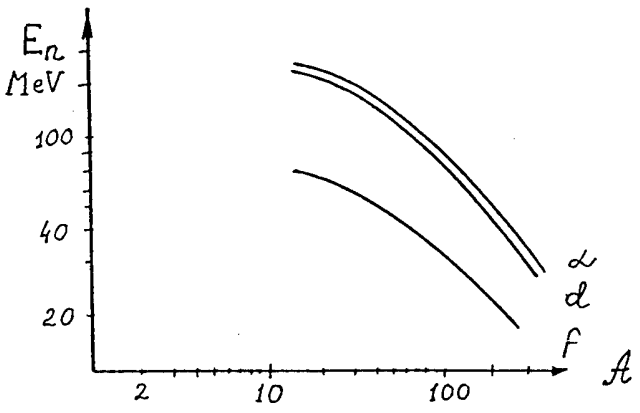

Fig.2

The dependence of the average neutron energy E_n from atomic weight of nuclei-target A for p, d, and ^{4}He beams with 1 GeV/nucleon energy

next collisions that is the energy cost of electronuclear neutrons will be smaller then for proton beam. As can be seen from Fig. 3, the relative ionization loses are smaller for deuterons and α-particles than for protons [4]. Therefore, using of light nuclei (**d** or **^{4}He**) could improve neutronics of Accelerator Driven Systems.

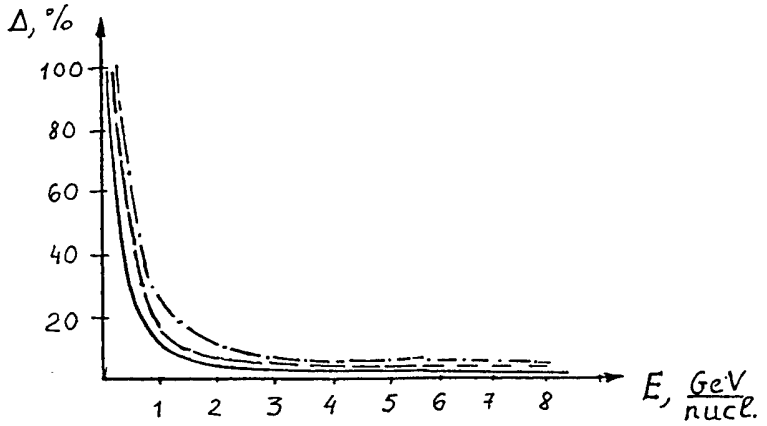

Fig.3

The relative ionization loses of the energy in Pb:

——- d, - - - - - α-particles, - · - · - · - · - p-beams.

Physical analysis of the potential of Accelerator Driven Systems we demonstrate on the **Accelerator Molten Salt Breeder (AMSB)** consisting of high energy accelerator (proton, deuterium and ^{4}He nuclei) and molten salt fluoride target/blanket (R = 4.5 m and D = 6 m), heat exchanger and power generator. It is used the fuel composition **LiF - BeF_2 - ThF_4 (64-18-19 mol. %)**. The calculations of the physical characteristics of **AMSB** were carried out by the method developed in the works [2,3]. It is assumed that the beam power is constant and equal 300 MW, i.e. per one nucleon of projectile nuclei with 1 GeV energy. In the Table are shown the results of the calculations. As can be seen, the replacement of proton beam to **d-beam** permits to increase neutron generation to ≈ **24 %** and ^{4}He-beam increases it to ≈ **14 %**. These neutrons have higher average energy in comparison of neutrons produced by proton beam. It could be necessarily noted that using of deuteron beam leads to the same increasing of the number of generated neutrons as addition of 0.5 mol.% $^{233}UF_4$ in the fuel

composition **LiF - BeF_2 - ThF_4 (64-18-18)** and using of α-particles instead of protons is analogous to addition of **1 mol.%** of $^{233}UF_4$. Amount of unloading ^{233}U rises from ≈ **480 kg/year** to ≈ 570 kg/year for d-beam and ≈ **590 kg/year** for ^4He. At the same time the thermal power generated in the target/blanket increases by ≈ 1,2 - 1,3 times for d- and α-particle beams in comparison of proton beam.

Table 1. The neutronic characteristics of AMSB versus the kind of the beam

The characteristic	**p**	**d**	**^4He**
The particle energy, GeV/nucleon	1	1	1
The beam power, MW(th)	300	300	300
The number of second neutrons per 1 particle of beam, N_n	26.2	64.7	118.6
The average energy of second neutrons, E_n MeV	17.7	24.3	28.2
Multiplication factor; k_{eff} beginning/1 year	0.026 0.346	0.026 0.404	0.026 0.567
Production rate of ^{233}U, kg/year	480	570	590
Thermal power (the average for 1 year), MW (th)	330	400	420

Conclusion

The prospects of using of light nuclei accelerators (d- and α-particles beams in **Accelerator Driven Molten Salt Breeder** for the production of ^{233}U and thermal power is shown without a discussion of the problems of their construction and design. The replacement of the proton beam by deuterium or α-particles ones allows to reduce the energy cost of one neutron from **11.5 MeV** up to **9.3 - 10 MeV**, to increase the number of neutrons per one particle of the beam and their average energy. It leads to gain of fissile nuclei and thermal power production in **AMSB** by ≈ 1.2 - 1.3 times.

References

[1] C. Bowman et al. / Nuclear Energy Generation and Waste Transmutation Using an Accelerator-Driven Intense Thermal Neutron Source, Rep. LANL UR-91-2601, 1991.

[2] S. Chigrinov, K. Gudima, A. Kievitskaia, V. Petlytski / Hyperfine Interactions - 77 (1993) 149-159.

[3] S. Chigrinov, A. Kievitskaia, C. Rutkovskaia, V. Petlytski and K. Furukawa / Proceedings of 7th Int. conf. on Emerging Nuclear Energy Systems, Sept. 20-24, 1993. Makuhari, Chiba, Japan. p.434.

[4] G. Vorobiev, K.Tolstov / Preprint JINR P1-85-351 - Dubna 1985, 4p.

P-3-58

THE EXPERIMENTAL INVESTIGATION OF EXPLOSIVE OPENING SWITCH

Zhang Jiande, Zhong Huihuang, Li Chuanlu, Liu Yonggui, Cheng Dongqun, Peng Xianyang

Dept. of Applied Physics, National University of Defense Technology
Changsha, 410073, China

Abstract

The explosive opening switch (EOS) used in explosive-driven magnetic-flux compression generator (EMCG) circuits is investigated. It is shown that (1) under certain conditions, the EOS voltage is hardly dependent on the sizes of the explosive and aluminium foil used in EOS; (2) with the explosive coated by an insulator pipe, the opening effect of EOS is better; (3) by use of EOS, a pulse with 5 kA current, 100 kV voltage and 250 ns risetime has been transferred into a resistance load.

Introduction

Explosive-driven Magnetic-flux Compression Generators (EMCG) provide for the generation of large amount of energy compactly stored in a magnetic field. Opening switches for use in EMCG circuits allow the energy to be used for applications requiring higher power than that can be developed by the EMCG themselves. For use in EMCG circuits, Explosive Opening Switches (EOS) offer some important advantages. Explosive-driven opening switches operate on command, can be made to conduct for extremely long time, and have energy available for the opening process that can be large, compared to the electrical energy of the circuit [1]. So more and more attention has been attracted to the investigation of EOS.

In this paper, the experiment of a type of EOS is described. These switches ate well suited to EMCG circuits and can transfer considerable pulsed power into a resistance load.

Experiments and Results

1 EOS Structure

EOS investigation was carried out by use of the model, the design of which is given in Fig. 1. The system of explosive charge (1) initiation ensured nonsimultaneity of the detonation front outlet on the surface of aluminium foil (2) not exceeding 0. 05 μs. The ribbed barrier (3) was made of Teflon with the rifling parameters 2 x 2 x 21. The switches were powered from the condenser bank and EMCG in different experiments, respectively.

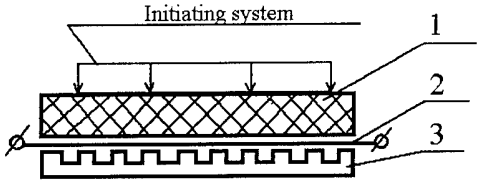

1 - Cylindric explosive charge
2 - Aluminium foil
3 - Ribbed barrier

Fig. 1 EOS structure

2 Changing Size Experiment

In order to investigate the effect of different sizes of explosive and aluminium foil on EOS opening, the 'Changing Size Experiment' was carried out.

The principle circuit of the experiment is shown in Fig. 2. The scheme operates in the following way. As soon as the current in the storage inductance L achieves the maximum, the EOS is activated, then the current is interrupted and the high voltage is produced.

The current and voltage were measured with Rogowski coil and voltage divider, respectively.

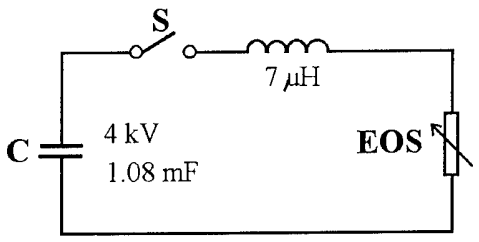

Fig. 2 The principle circuit of the 'Changing Size Experiment'

Fig. 3 gives the current and voltage waveform of EOS with the aluminium foil of thickness d = 0.1 mm, width a = 36 mm and the cylindric explosive of diameter d = 50 mm. This Fig. indicates that; at the quarter period of the LCR discharge (204 μs) the discharge current reaches maximum I_o = 39. 8 kA, and the EOS starts to be activated, then the voltage pulse with the magnitude V_s = 44 kV and the risetime τ_r = 1.96 μs is produced.

Changing the aluminium foil thickness to δ = 0.3 mm, we get the current and voltage waveform as shown in Fig. 9. This Fig. shows that the current I_o = 40 kA, the voltage V_s = 42 kV and the voltage risetime τ_r =1.5 μs.

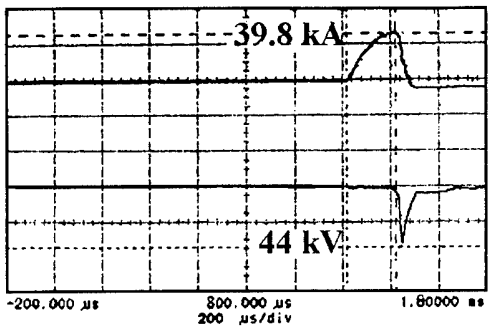

Fig. 3 The current (above) and voltage (below) waveform of EOS with b=0.1 mm, a=36mm and d=50 mm

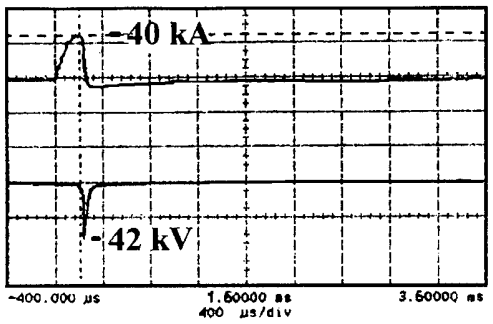

Fig. 4 The current (above) and voltage (below) waveform of EOS with b=0.3 mm a=36mm and d=50 mm

Comparing Fig. 4 with Fig. 3, we find that the change of the foil thickness under the same experiment conditions has little effect on EOS voltage and voltage risetime.

Keeping δ the same as that in Fig. 3 and changing the cylindric explosive diameter to d = 100 mm, we get the voltage waveform as shown in Fig. 5.

This Fig. shows V_s =90 kV and τ_r =1.55 µs, and implies that the change of the cylindric explosive diameter has little effect on EOS opening.

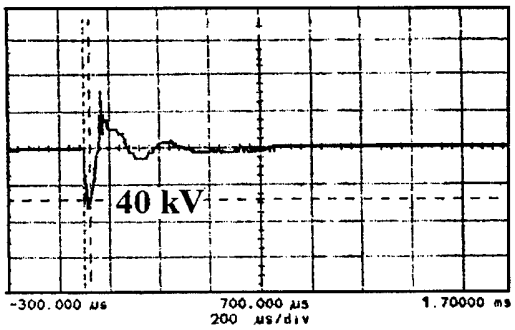

Fig. 5 The voltage waveform of EOS with δ=0.1 mm, a=36 mm and d=100 mm

3 Insulator Pipe Experiment

When the EOS was powered from an EMCG, an experiment on the EOS was made with the explosive coated by a polyvinyl chloride (PVC) insulator pipe.

The experiment principle circuit is shown in Fig. 6, where L_g(t) is the variable inductance of EMCG, L the storage inductance in EMCG circuit.

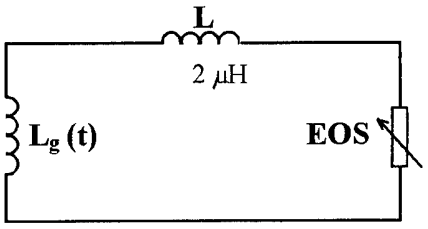

Fig. 6 The principle circuit of the' Insulator Pipe Experiment'

Fig. 7 gives the current and voltage of EOS with δ = 0.1 mm, a = 36 mm aluminium foil and d = 50 mm explosive coated by a PVC pipe of thickness - 8 mm and height - 87 mm.

This Fig. indicates that when EMCG completes operation and the L_g(t) approaches zero, the current reaches maximum I_o = 23 kA, and EOS starts to open. Then the voltage with V_s = 100 kV and τ_r =1.05 µs is obtained.

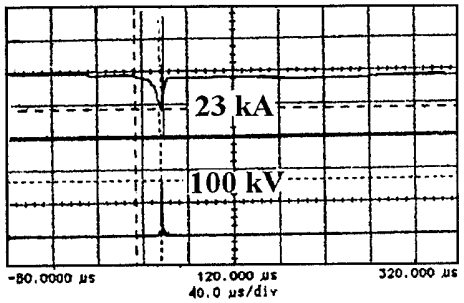

Fig. 7 The current (above) and voltage (below) of EOS with a PVC pipe

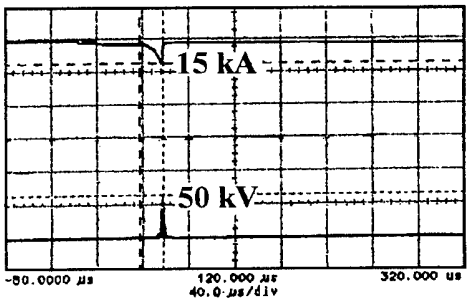

Fig. 8 The current (above) and voltage (below) of EOS without a PVC pipe

Fig. 8 shows the current and voltage waveform of EOS without a PVC pipe. The Fig. gives I_o = 15 kA, V_s = 50 kV and τ_r =1.5 µs.

In order to compare the EOS effects with and without PVC pipe conveniently, the EOS resistance R_s is defined as $V_s/0.6l\ I_o$ [2]. From Fig. 7 with PVC pipe, R_s = 7. 12 Ω and $dR_s/dt = R_s/\tau_r$ = 6.78 Ω/μs. And from Fig. 8 without PVC pipe, R_s = 5.46 Ω and dR_s/dt = 3.64 Ω/μs.

The comparison indicates that the opening effect of EOS with PVC coating pipe is better than that without PVC coating pipe. The possible reason is that when EOS operates without PVC coating pipe, there exists the effect of rare wave on EOS.

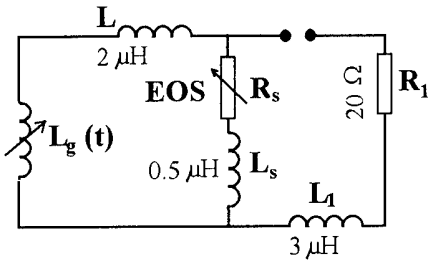

Fig. 9 The principle circuit of 'Resistance Load Experiment'

4 Resistance Load Experiment

Based on the 'Insulator Pipe Experiment' , the EOS experiment was carried out with a spark closing switch and a resistance load as shown in Fig. 9, where L_g(t) and L were mentioned above, R_s and R_l, are the resistances of EOS and load, L_s and L_l are the spray inductances of connecting cable of EOS and load , respectively.

The current and voltage waveform of EOS with the same parameters as Fig. 7 is given in Fig. 10. From this Fig., the I_o = 33 kA, V_s =120 kV and r, = 554 ns.

Fig. 11 gives the current and voltage of the load. The Fig. shows the V_l =100 kV, I_l =5 kA, and τ_r =250 ns (voltage tisetime)

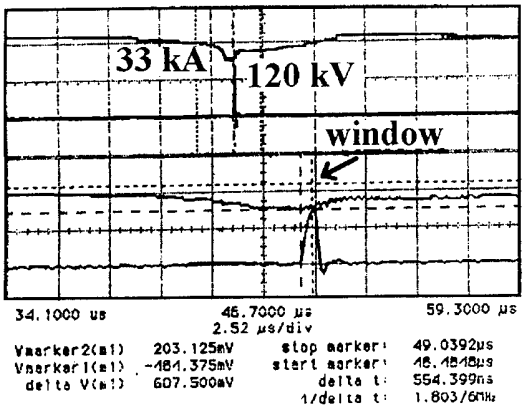

Fig. 10 The current (above) and voltage (below) waveform of EOS in the 'Resistance Load Experiment'

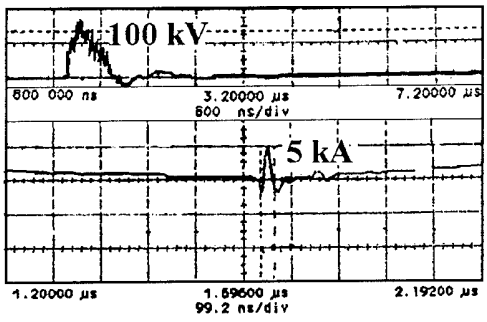

Fig. 11 The current (below) and voltage (above) of the resistance load.

Analysis and Discussion

1 Electric Exploding and Breakdown Strength

From the results of 'Changing Size Experiment' , it is found that the EOS opening effect has little relation to the aluminium thickness and the explosive diameter. The phenomena imply that (1) the electric exploding does not affect the EOS opening and (2) the explosive products have high enough breakdown strength.

According to Ref. [3], when the cross section of the foil

$$A \approx A_o = K I_o \tau_{eq}^{1/2} \qquad (1)$$

the electric exploding will greatly affect switches opening, where τ_{eq} is 'equivalent action time scale', I_o the current in circuit before the start of interruption, $K = 4.5 \cdot 10^{-9}$ (corresponding to aluminium) a constant.

In our experiment, we can get A_o = 1.087 mm^2, and A = 3.6 mm^2 (Fig. 3), 10.8 mm^2 (Fig. 4), respectively. It is evident that $A >> A_o$, hence the electric exploding offers little effect on EOS opening.

Pavlovskii estimated the breakdown strength for the explosive products to be E_b =100 kV/cm [4]. In our experiment, the maximum electric field strength in EOS was only E_s = 10 kV/cm. So the breakdown did not happen and EOS opening effect was not affected by the change of the explosive diameter.

2 EOS Resistance and Rise Ratio

From the experiment circuit shown in Fig. 9, we can get the equivalent circuit similar to 'transformer T equivalent' as shown in Fig. 12.

For convenience, we designate

$$L_1 = L_s + L$$
$$L_2 = L_s + L \quad (2)$$
$$M \equiv L$$

and define the equivalent coupling coefficient

$$K_{eq} = M / \sqrt{L_1 L_2} \quad (3)$$

the equivalent turn ratio

$$N_{eq} = \sqrt{L_1 / L_2} \quad (4)$$

According to Ref. [2], the maximum of resistance load current

$$I_1, = 0.61\, I_o\, K_{eq} / N_{eq}\, (1+r)\, Q \quad (5)$$

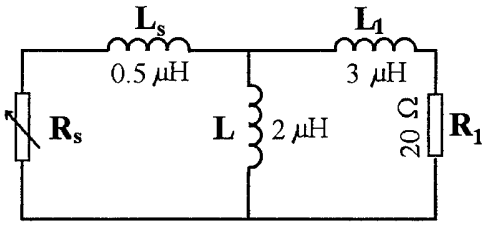

Fig. 12 The T equivalent circuit of 'Resistance Load Experiment'

where r is the dimensionless ratio of load resistance to maximum switch resistance scaled by the equivalent turns ratio

$$r = R_1 / R_s N_{eq}^2 \quad (6)$$

$$Q = \sqrt{1 - 4r(1 - K_{eq}^2) / (1+r)^2} \quad (7)$$

From the experimental parameters and results I_o = 33 kA, I_l = 5 kA, L_s = 0.5 μH, L_1 = 3 μH, L =2 μH, R_1 = 20 Ω, we can get K_{eq} = 0.56, N_{eq} = 2 and the maximum switch resistance $R_s \approx R_1 / N_{eq}^2$ = 5 Ω.

It is well-known that the switch resistance before the start of interruption

$$R_o = \rho \cdot \frac{l}{\delta x a} \quad (8)$$

where p is the aluminium resistivity, L, δ, and a are the length, thickness and width of the broken aluminium foil.

In the experiment, $\rho = 2.5 \cdot 10^{-5}$ Ω·mm, δ = 0.1 mm, a =36 mm, l = 50 mm, we can get

$$R_o = 0.347\ \text{m}\Omega \quad (9)$$

Therefore the switch resistance rise ratio (defined as $M_f = R_s / R_o$)

$$M_f = 1.4 \cdot 10^4 \quad (10)$$

These results are in good agreement with Ref. [5].

Conclusion

According to the experimental results and discussion above, we can conclude that

(1) under certain conditions, the EOS voltage is hardly dependent on the sizes of the explosive and aluminium foil used in EOS

(2) with the explosive coated by an insulator pipe, the opening effect of EOS is better, the possible reason is that the effect of the tare wave on the EOS is deleted;

(3) by use of EOS, a pulse with 5 kA current, 100 kV voltage and 250 ns risetime has been transferred into a 20 Ω resistance load. This result implies that 5 Ω EOS resistance and 10^4 order resistance rise ratio have been obtained.

References

[1] J. H. Goforth, et. al., 'Multi-megampere Current Interruption from Explosive Deformation of Conductors', Los Alamos National Laboratory

[2] R. E. Reinovsky, et. al., High Voltage Power Condition Systems Powered by Flux Compression Generators' Los Alamos National Laboratory

[3] Ch. Maisonnier, et. al, 'Rapid Transfer of Magnetic Energy by Means of Exploding Foils' , Rev. Sci. Instrum. Vol. 37 (1960) 1380

[4] Pavlovskii, A. I. , et. al., 'Magnetoimplosive Generators for Rapid-Risetime Megampere Pulse' , Sov. Tech Phys. Lett. , Vol. 3, No. 177, p.320

[5] U. K. Chernyshev. et. al. 'Study of Basic Regularities of Formation of Multi-MA-Current Pulses with Short Risetime by EMG Circuit Interruption' , I. V. Kurchatov Institute of Atomic Energy, USSR

P-3-59

HIGH POWER, REPETITIVE STACKED BLUMLEIN PULSE GENERATORS

F. Davanloo, D.L. Borovina, J.L. Korioth, R.K. Krause and C.B. Collins

Center for Quantum Electronics, University of Texas at Dallas
P.O. Box 830688, Richardson, TX 75083-0688

F.J. Agee

U.S. Air Force Phillips Laboratory, WSR
Kirtland AFB, NM 87117-6008

L.E. Kingsley

U.S. Army CECOM, S&TCD
Ft. Monmouth, NJ 07703-5203

Abstract

The repetitive stacked Blumlein pulse power generators developed at the University of Texas at Dallas (UTD) consist of several triaxial Blumleins stacked in series at one end. The lines are charged in parallel and synchronously commuted with a single switch at the other end. In this way, relatively low charging voltages are multiplied to give a high discharge voltage across an arbitrary load. Extensive characterization of these novel pulsers have been performed over the past few years. Results indicate that they are capable of producing high power waveforms with risetimes and repetition rates in the range of 0.5-50 ns and 1-300 Hz, respectively, using a conventional thyratron, spark gap, or photoconductive switch. In this report we review the progress in the development and use of stacked Blumlein pulse generators. The technology and the characteristics of these novel pulsers driving flash x-ray diodes are discussed.

Blumlein Pulsers

Design and construction of the pulse forming system for the Blumlein generators were given elsewhere [1-4]. Briefly, a single Blumlein pulse generator consisted of two critical subassemblies: (1) a single Blumlein pulse forming line, and (2) a commutation system capable of operation at high repetition rates. The basic organization is shown schematically in Fig. 1(a). The Blumleins were constructed from copper plates, potted with epoxy on outer surfaces to reduce corona, and separated by laminated layered Kapton (polyimide) dielectrics. Scaling of these devices was studied by the construction of several separate systems with different lengths, capacitances, and impedances. All Blumleins had a smooth taper which increased from the load diode end to the thyratron switching end as seen in Fig. 1(a).

In operation, the middle conductor was charged to a positive high voltage which would be varied to 75 kV, and commutation was effected by a hydrogen thyratron. Several hydrogen thyratrons with different voltage hold off characteristics were used. This resulted in peak voltages available at the load which spanned the range from 5 to 100 kV. To access voltages far above 100 kV, a stacked Blumlein pulse generator was designed and constructed [2-4]. It consisted of three separate but integrated subassemblies: (1) the switching assembly, (2) pulse forming Blumleins, and (3) the pulse stacking module. The basic organization for the second prototype stack Blumlein pulse generator with twelve Blumlein lines is shown in Fig. 1(b).

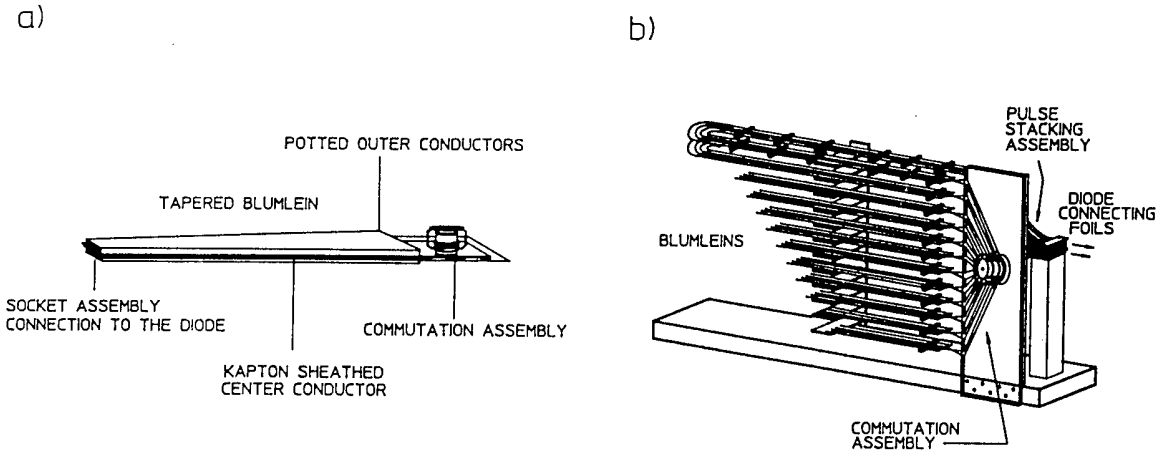

Fig. 1 Schematic drawings of the high repetition rate, Blumlein pulse power generators.

Extensive characterization of this prototype pulse generator has been performed in our laboratory [3-4]. Distortions of the propagated pulses were minimized by directly connecting the lines to the thyratron as seen in Fig. 1(b). The use of a single switching element allowed the device to be operated at repetition rates to 200 Hz.

The pulse forming lines were constructed from 3.7 m long sections of copper plate. They were 3.2 mm thick and 2.5 cm wide with rounded edges. Two 2.3 mm thick Kapton insulator plates were placed along the length between the copper conductors. These dielectric sheets were 15.2 cm wide to prevent electrical breakdown between copper lines. This assembly was held together by Delrin presses which were installed and tightened around the lines at 30 cm intervals. Two of these sections were set on each shelf and a carefully fabricated u-turn was used to connect them together. In this way, twelve Blumleins, each with a length of 8.2 m, were placed on the shelves, one above the other. At one end, these lines were connected to the vertical thyratron assembly, and at the other end, the lines were stacked in series behind the thyratron mounting assembly, as seen in Fig. 1(b). The Kapton insulators were constructed from thirteen 0.127 mm thick Kapton sheets. They were laminated together with a high dielectric epoxy. The thickness of these boards varied by less than 10% over their entire length. This construction procedure resulted in an impedance of 40 Ω for each Blumlein. Copper foils were connected to the ends of the lines and angled together, along with the dielectric, to stack directly on top of one another. The lines were then connected in series for about 10 cm. A load then was connected to the stacked assembly.

Flash X-ray Generation

Blumlein pulse power sources developed at the University of Texas at Dallas were mainly used to drive x-ray diode loads. The diodes were designed and constructed in two configurations for low and high voltage pulsing of our Blumlein devices. Figure 2, schematically presents the diode configuration for use with the single Blumlein pulsers. A diode with transmission geometry electrodes was used with the stacked Blumlein pulsers as seen in Fig. 3. Reasonable matching of these heads to the pulse generators allowed production of high power x-ray pulses with durations as short as 10 ns.

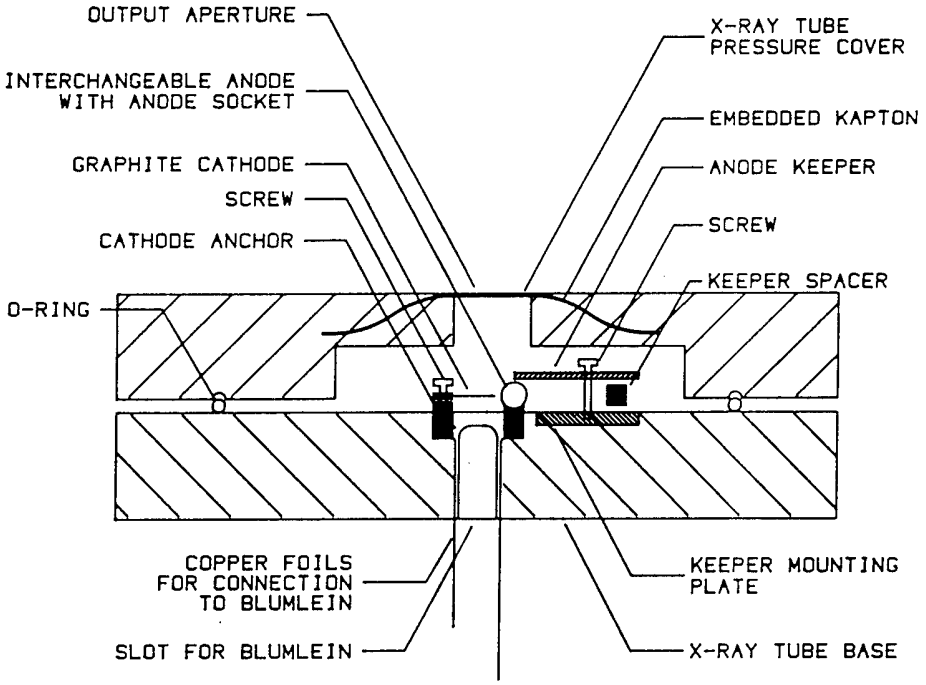

Figure 2. Schematic drawing of a cross section of the x-ray diode used with the single Blumlein pulsers.

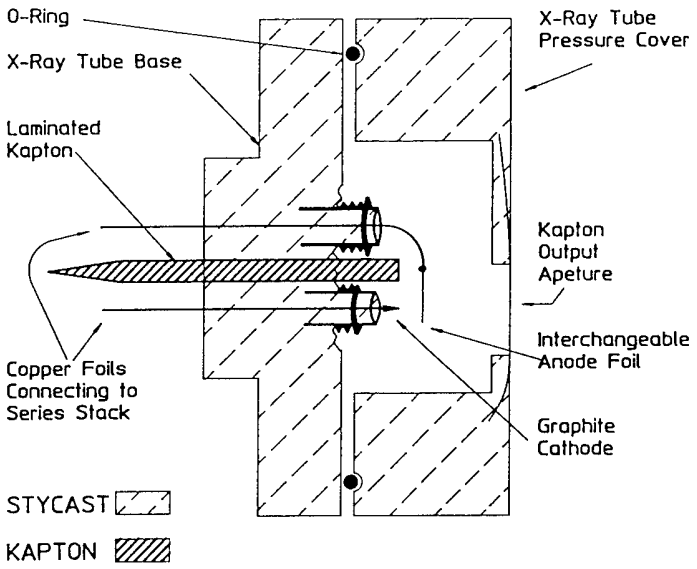

Figure 3. Schematic drawing of a cross section of the x-ray diode used with the stacked Blumlein pulsers.

Methods of x-ray spectroscopy inapplicable for single shot systems were used to record the spectral content of the output. Figure 3 shows a typical spectral distribution of fluxes emitted from x-ray diodes matched to the single line and stacked Blumlein pulse generators. A cylindrical anode and a bladelike graphite cathode were used in the diodes matched to the single line pulse generators as seen in Fig. 2 [1]. With this type of diode geometry, about one-third of the pulse energy appeared in the x-ray lines of the anode material as seen in Fig. 4(a). The remainder was distributed over a fairly broad band of the

true continua [2,3]. With the stacked Blumlein device and the diode configuration of Fig. 3, a spectrum was accumulated at 45 kV of charging as shown in Fig. 4(b). It was a true continuum, peaking at intensities of 5 x 10^9 photons/keV/shot and contained useful intensities of x-rays of up to 350 keV. Spectral measurements at 70 kV of charging voltage indicated that the output peaked at an intensity above 5 x 10^{10} photons/keV/shot, and photons were produced with an end point energy in excess of 450 keV.

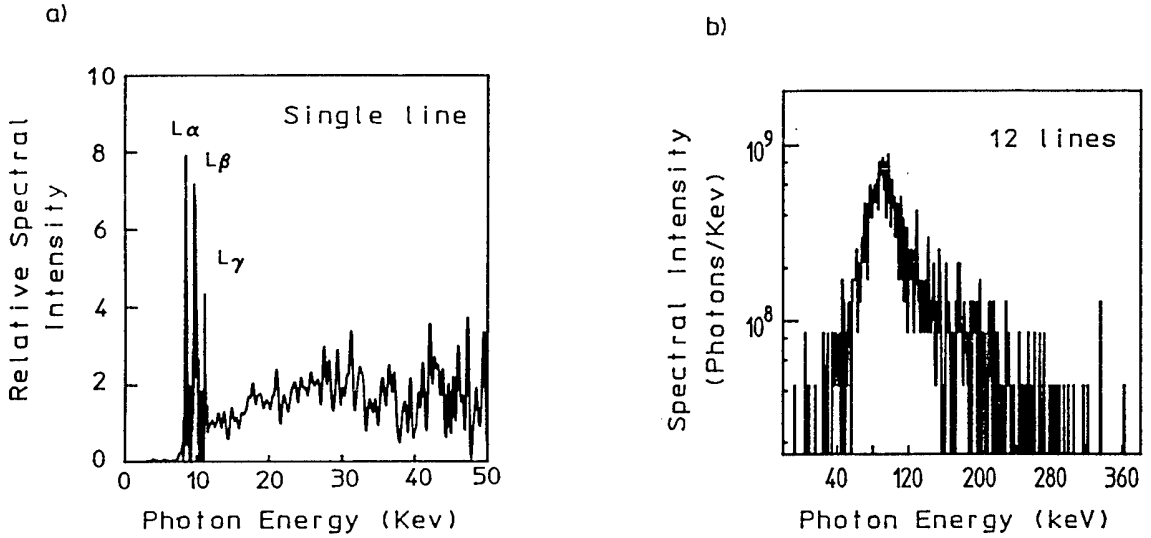

Fig. 4 Typical spectral distribution of x-ray fluxes emitted from a tungsten anode. (a) Spectrum obtained from a diode matched to the single Blumlein pulse generator. (b) Spectrum obtained from a diode matched to the stacked Blumlein pulse generator.

Conclusion

Flash x-ray systems powered by the Blumlein pulse generators have been used to excite the fluorescence from high-pressure rare gas plasmas [5]. The deposition of hundreds of millirads of x-rays in nanosecond pulses into tens of atmospheres of argon gas has resulted in a strong excitation of the VUV spectra that depends upon the generation of highly ionized precursors [5]. Our own application concerns the use of these flash x-ray devices to excite nuclear transitions where the ultimate signal to noise ratio will depend only upon the total radiation that can be delivered to an extended absorber in a working period. While Blumlein pulse sources have been mainly used to generate x-ray pulses, the diode can be replaced with a proper load for a variety of applications. These include different types of high power microwave (HPM) loads, laser heads to allow discharge pumping of appropriate laser medias, and e-beam producing loads.

Acknowledgment

This work was supported by the U.S. Air Force Phillips Laboratory, WSR, and U.S. Army Research Laboratory, PSD under contract DAAL01-95-K-3502.

[1] F. Davanloo , T.S. Bowen and C.B. Collins, Rev. Sci. Instrum. 58, 2103 (1987).

[2] F. Davanloo, J.J. Coogan, T.S. Bowen, R.K. Krause, and C.B. Collins, Rev. Sci. Instrum. 59, 2260 (1988).

[3] J. J. Coogan, F. Davanloo, and C.B. Collins, Rev. Sci. Instrum. 61, 1448 (1990).

[4] F. Davanloo, D.L. Borovina, J. D. Bhawalkar, C.B. Collins, F. J. Agee, and L. E. Kingsley, "High Power Repetitive Waveforms Generated by Compact Stacked Blumlein Pulsers," in Conference Record of the 1994 Twenty-First Power Modulator Symposium, 1994, pp. 201-205.

[5] C. Cachoncinlle, J.M. Pouvesle, F. Davanloo, J.J. Coogan, and C.B. Collins, J. Phys. D: Appl. Phys., 23, 984 (1990).

INDUCTIVE LINE ENERGY STORAGE GENERATOR

P. Choi

Laboratoire de Physique des Milieux Ionisés, Ecole Polytechnique

Palaiseau 91128 Cedex, France

ABSTRACT

Inductive energy storage (IES) generator has long been considered to be the most efficient system for energy usage in large pulsed power system in the MA level. A number of parameters govern the efficiency of energy transfer between the storage capacitors and the load, and the level of current deliverable to the load. For high power system, the energy storage capacitors are arranged as a Marx generator. The primary constraints are the inductances in the various parts of the circuit, in particular, the upstream inductance between the Marx and the POS, and the downstream inductance between the POS and the load. In this paper, we consider the effect of replacing part of the upstream inductance with a transmission line and introduce the new concept of an inductive line for energy storage (ILES). Extensive parametric scans have been carried out on circuit simulations to investigate the effect of this upstream transmission line. A model is developed to explain the operation of the ILES design based on the data obtained. Comparison with an existing IES generator shows that the ILES design offers a significant improvement in the maximum current and hence energy delivered to an inductive load.

IES Generator

The basic circuit of an idealized IES generator can be represented by the circuit in Fig.1. Initially, electrostatic energy is stored in the capacitor C_1, which would be disconnected from the rest of the circuit. At t=0, the circuit is connected, with the switch in the closed position, and a sinusoidal current begins to flow into L_1 through the switch. After a certain time the switch changes to a high impedance state and opens at a point when the current is I_c. Current now flows downstream of the switch into the load through an inductance L_2. Consider the case when the load is an inductive short circuit with negligible inductance $L_L << L_2$. If an ideal switch is assumed with zero impedance in the closed state and infinite impedance in the opened state, from a flux conservation argument, the new current is simply $I_0 = I_c * L_1/(L_1+L_2)$ and the total magnetic energy in the circuit is then $L_1/(L_1+L_2)$ of E_c, the energy stored in L_1 before the switch opens.

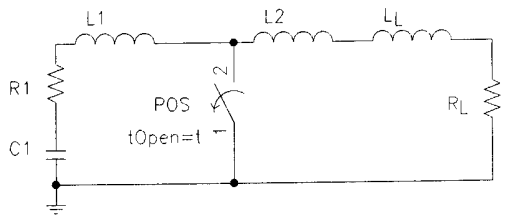

Fig.1 Equivalent circuit of an ideal IES generator

A typical plasma radiation source (PRS) load would fit in well with the above assumption of an inductive short circuit, with an initial inductance $L_L << 10$ nH for a high power system. During the course of energy delivery, the plasma structure will be compressed into a tight pinch with a corresponding increase in inductance. Both the kinetic energy of the compression and the magnetic energy in the current flowing will be converted to radiation upon stagnation. The compression can be characterized by an increase in inductance of $L_L = \Delta L$ associated with the kinetic energy, E_k. Assuming no losses and flux conservation, the fraction of energy delivered to the increased load is then given by $\Delta L/(L_1+L_2+\Delta L)$. In terms of the original

energy stored in L_1, the kinetic energy E_k is thus $E_c*[\Delta L/(L_1+L_2+\Delta L)*L_1/(L_1+L_2)]$. The current at the time of peak compression I_L is then given by $I_c*[L_1/(L_1+L_2+\Delta L)]$.

The power gain of the circuit is to a first approximation determined by the time compression, defined as the ratio of the conduction time when the switch is closed, to the time of energy delivery downstream. For a PRS load, the compression time is matched ideally to the current risetime. In a practical circuit, the rate of rise of current downstream is limited by the finite opening time of the switch, dR_s/dt, and by the ratio of the finite voltage at the switch when it opens to the downstream inductance V_s/L_2. For a resistive load R_L as in a diode, the energy delivery time is further limited by the inductive time constant, $(L_1+L_2)/R_L$.

Despite significant advancements in the understanding of the physics of opening switches, the primary constraint in an IES generator design is still considered to be the opening switch. The constraint of the switch exists in limiting the parameter range that an IES generator can function and thus the geometric configuration. This is particularly true for multi-TW systems, when a multi-module approach has to be adopted. However, the physical limits to the efficiency of the system are in fact in the inductive components in a practical generator. From the discussion in the last section, it would appear straight forward to reduce the downstream inductance L_2. This is in fact not feasible in a large system, where the power has to be fed from multiple modules. This sets the physical limit as to how close the opening switch can be from the load, and hence the minimum value of L_2.

The major limitation in the design of very large IES system is in fact in L_1, the upstream inductance. On the one hand, L_1 constitutes the energy storage inductance during the conduction phase. On the other hand, for a given bank capacitance, L_1 sets the quarter period when the initial current will rise to the maximum and hence determines the conduction time of the switch. It is necessary to examine which elements contribute in total to the value of L_1. The capacitor bank is composed of many individual capacitor units and closing switches, each possesses an elemental inductance. The interconnection between one capacitor and the next also represents an inductance.

Consider a given unit structure element of a capacitor connected through a switch with elemental capacitance C_n and inductance L_n. The quarter period of this structure into a short circuit is then given by $\pi/2(L_nC_n)^{1/2}$. For a bank composed of N such units, it is interesting to note that this value of the quarter period is unchanged irrespective of whether the capacitors are connected all in parallel, as in a classical capacitor bank, or all in series, as in a Marx circuit or any combination of series parallel units. However, the largest single part contributing to the upstream inductance is in the connection between the capacitor bank and the opening switch. The effect of this inductance L_c is to dictate a series connection of M units in a Marx configuration, with N/M Marx in parallel in the bank, such that $(M^2/N)*L_n >> L_c$ for the shortest possible quarter period. The limiting value of M is often set by the voltage breakdown constraint as the output voltage of the bank increases and by the desire to place a substantial part of the energy storage inductance inside vacuum, next to the opening switch.

As a practical example, consider the IES generator GIT-4.[1] The generator has a primary capacitive energy storage configured as 36 Marx units working in parallel. Each unit consists of 48 capacitors, connected as a 12 stages Marx circuit with 4 capacitors in parallel per stage, and has an output capacitance of 0.133 μF and an inductance of 1.8 μH. The 36 units are placed in four oil-filled tanks. The energy from the Marx generators is transferred to the vacuum insulator through four oil-insulated lines. This massively parallel design results in an

inductance L_M ~ 100 nH for the whole generator up to the vacuum insulator. The vacuum part of the inductive storage L_V, the plasma opening switch (POS), and the load are housed in a vertical vacuum section, located in the middle of the 4 Marx tanks. The POS is so located as to provide an effective upstream inductance $L_1=(L_M+L_V)$ of 220 nH and a downstream inductance L_2 of 70 nH. A large L_V reduces the voltage stress on the vacuum insulator when the switch opens. The capacitance of the primary store is C_1 = 4.8 μF and at 50 kV charging voltage the energy stored is 0.86 MJ. In operation, the POS conducts for 1.5 μs while the current builds up to the 2 MA level in the upstream inductance and opens in 150 ns, delivering 1.5 MA to a plasma load.

From the above discussion, the difficulties of reducing L_1 and L_2 appear to be intractable. Indeed, recent development work on several multi-megajoule class IES generators, like DECADE, ACE-4, GIT-16 has clearly demonstrated such problem. It is through an examination of this problem that a new solution has been derived, leading to a new design concept for inductive energy storage system which we call the Inductive Line Energy Storage - ILES - Generator. In the following, we will briefly present the methodology behind the concept and the principles of operation, together with results from circuit simulations.

ILES Generator

The problem with L_1 and L_2 could be examined in terms of reducible and irreducible elements. Irreducible elements are intrinsic to the component parts of the system associated with the capacitors, the closing switches and the construction of the Marx circuit. The junctions in the external connection are irreducible. The bulk of the external connections are considered reducible. It is obviously not possible to physically eliminate the reducible elements which contribute to the total inductance. What is proposed here is to convert them into distributed elements. In practice, this is achieved simply by adding a distributed capacitance to the structure to form a transmission line. Each transmission line is now characterized by a transit time τ and a characteristic impedance Z. The higher the capacitance added, the lower will be the impedance. The transit time is simply determined by the physical length of the structure and an equivalent inductance L_{eq} is defined by the product τZ.

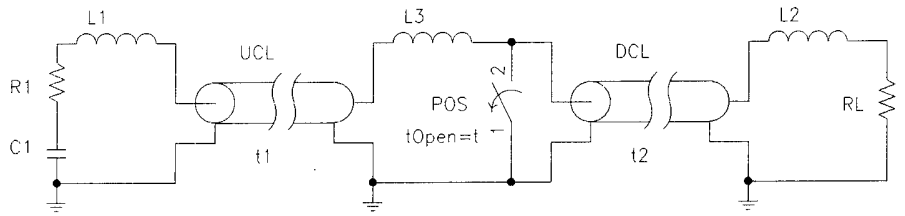

Fig.2 Equivalent circuit of an ILES generator showing the lumped and discrete components

An equivalent circuit of such a generator is shown in Fig.2. The components C_1, R_1 and L_1 represent the Marx circuit and the connection inside the Marx unit. A transmission line upstream of the switch, UCL (Upstream Coupling Line), connects the Marx to an inductance L_3, which represents the irreducible inductance at the junction between the vacuum interface and the plasma opening switch, POS. Downstream of the switch, another transmission line, DCL (Downstream Coupling Line), connects the switch to the load. The load is represented by an irreducible inductance L_2 and a resistance R_L. This simple circuit has been modelled on PSpice and extensive parameter scans have been carried out to review the effect of each

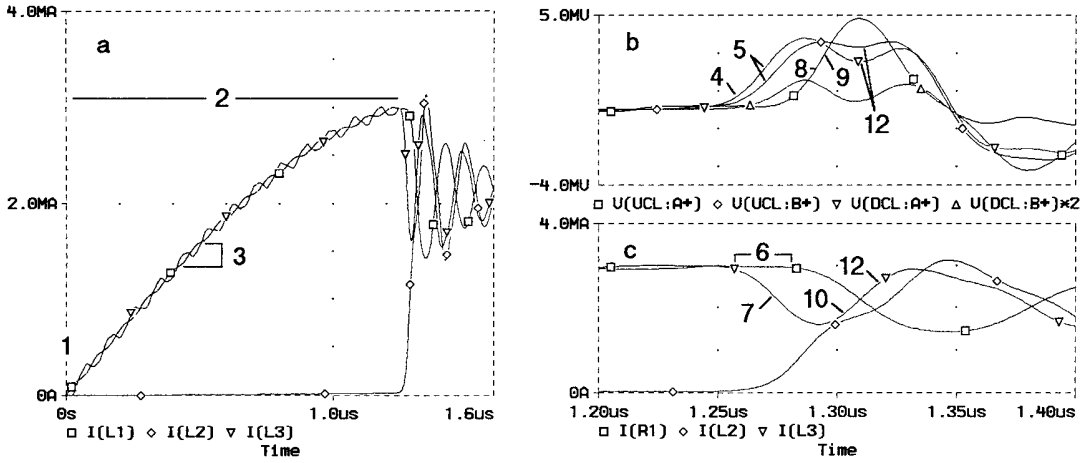

Fig.3 Voltage and current waveforms at different point in an ILES circuit, the numbering corresponds to different stages of operation. (a) currents through the inductances L_1, L_2 and L_3, (b) voltages at the input A+, and output B+ of the coupling lines UCL and DCL & (c) corresponding currents at an expanded time scale around the switch opening.

individual component. From these results, a unique operating regime for the ILES has been identified. The different stages of development in the circuit are outlined below with the help of the waveforms at the different points in the circuit, shown in Fig.3.

Before POS opens ($0 < t_{open} < t$)

1. Marx erects
2. Current flows from Marx to closed POS through UCL
   - *limiting value of current set by L_1 and UCL for a given Marx voltage and energy*
3. Current builds up in steps through successive reflections along UCL
   - *the size of each step and the duration depend on impedance and transit time of UCL*

After POS opens ($t_{open} > t$)

4. A voltage is developed across POS, $V_p = I * R_{POS}$, the POS resistance
5. This voltage V_p propagates away from the switch in both directions
   - *towards the load via DCL and towards the Marx through L_3 and UCL*
6. Within one transit time t_1 of UCL this change is not seen by the Marx
   - *the current through L_1 remains evolving (growing) as before*
7. Current in L_3 now decreases , essentially with time constant L_3 / R_{POS} if $R_{POS} < Z_{DCL}$
8. V_p reaches the end of UCL and sees the Marx
   - *the Marx current decreases at a rate depending on V_p*
9. V_p reflects from Marx as if open circuit if $L_1 > Z_{UCL} * t_1$
10. Current in L_3 begins to increase again
    - *roles of the DCL and load begin to come in*
11. The reflected voltage, V_L , from the load is inverted after a time L_2 / Z_{DCL}
12. V_L will be reflected at L_3 and so L_3 will have a $+V_p$ reflecting on the Marx side and a $-V_L$ reflecting on the load side
    - *current through L_3 is increased further and additional energy is extracted from UCL*
13. Step 8 to Step 12 are repeated while current is delivered to the load

A number of interesting points can be seen from the behaviour of the circuit. A couple of them will be discussed here. The maximum current during the conduction time is limited by the

irreducible inductance L_1 and the effective inductance L_{eq} of UCL. Recalling the definition of L_{eq}, it is obvious that while the transit time t_1 is limited by the geometrical distance between the Marx and the POS, the impedance Z_{UCL} can in fact be reduced to a point limited by breakdown constraints. This implies that a substantially lower upstream inductance can be obtained using a suitable UCL even if the Marx is situated at a large distance from the POS, compared with the normal method of connection. Fig.4 shows the conduction current in the Marx and that in the inductive load, obtained for the parameters of GIT-4, using (a) the IES circuit in Fig.1 and (b) the ILES circuit in Fig.2. The Marx is represented by a 4.8 μF capacitor charged to 600 kV at t=0. In the simulation, the POS opens from 1 mΩ to 8 Ω within 100 ns following a power law. The parameters for the DCL represent 70 nH equivalent

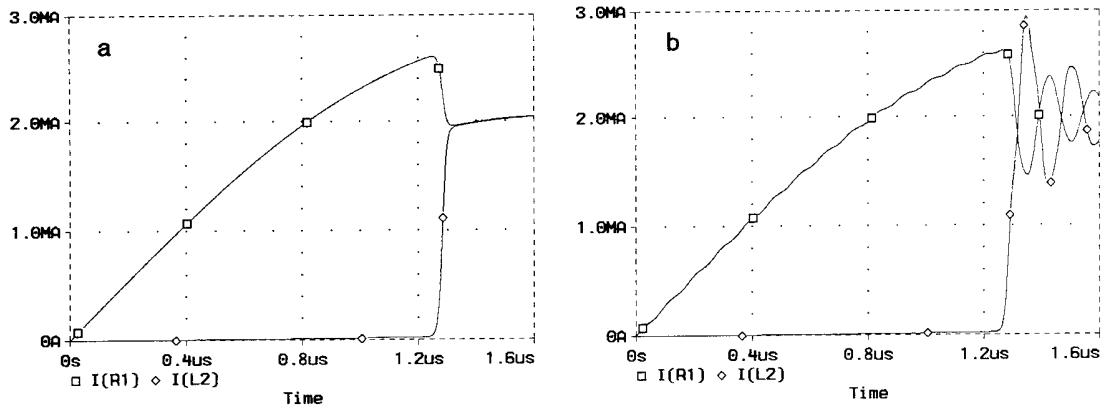

Fig.4 (a) Current in the Marx I_{R1} and in the inductive load I_{L2} for an IES circuit and (b) same quantities for an ILES circuit. For the IES circuit, L_1=220 nH, L_2=70 nH with a 12 nH load. For the ILES circuit, L_1=155 nH, Z_{UCL}=2.5 Ω, t_1=22 ns, L_3=10 nH, Z_{DCL}=5 Ω, t_2=14 ns, and a 12 nH load. R_1=1 mΩ.

as in the IES circuit. The parameters for UCL are quite reasonable for the geometry of GIT-4, being equivalent to four 10 Ω oil lines in parallel. What is unique is the current in the load. From a value of 1.95 MA rising in 80 ns in an IES circuit, the peak current in the ILES circuit rises to 2.94 MA in 83 ns, an increase of 51%. The unique effect of the UCL can be seen from the current delivered to the load, which is now higher than that originally flowing in the switch during the conduction phase.

It may seem intuitively that the smallest value of Z_{UCL} and the shortest line will give the lowest L_{eq} and the highest conduction current, and therefore the highest current into the load. This is in fact not the case. When the transit time of UCL is short compared with the scale time of the POS, the action of the inductive line is weak. At very short transit time, the circuit behaves like an IES circuit. Similarly, for a given UCL, lowering of L_1 should increase the load current. Indeed, reducing L_1 to 110 nH in the circuit above, a reasonable step with the GIT-4 design, increases the load current to 3.2 MA in 97 ns. However, continuous lowering of L_1 in fact leads to a point when the current into the load begins to decrease. The explanation lies in point 9 in the operation stages discussed above. This leads to the design criteria that it would be better to arrange the Marx unit into several modules in parallel, with a UCL connecting each module to a common POS. This effectively presents an increased L_1 to the UCL. In practice, the lowest value of Z_{UCL} that could be used would be limited by the voltage hold off capability of the line. This would then implies that the effective Z_{UCL} of a multi-module system would be lower as several lines will be used in parallel. In practice, even for a single module, multiple lines in parallel could be used to provide a sufficiently low impedance. This will further increase the current deliverable to the load.

The unique operation of the ILES circuit can also be seen from the energy budget in the different inductive elements. Fig.5 shows the evolution of magnetic energy in the three irreducible inductances for the conditions in Fig.4 but with L_1=110 nH. When the switch first opens, energy is extracted from L_3, part of it being delivered to the load L_2. The primary storage inductance within the Marx is isolated by the transit time of UCL. It is only until 2 transit times later, that the energy from L_1 arrives and the energy in L_3 begins to rise. A similar increase in energy in L_2 is seen after the transit time of DCL. It is important to note that the energy in L_3 in fact continues to rise to a point almost the same as that before the switch opens. With the parameters chosen, the peak energy delivered to the load inductor is 61 kJ, out of 864 kJ which is stored initially in the capacitor bank. If we were to use the IES circuit as in Fig.4, less than 25 kJ would be obtain in the same load.

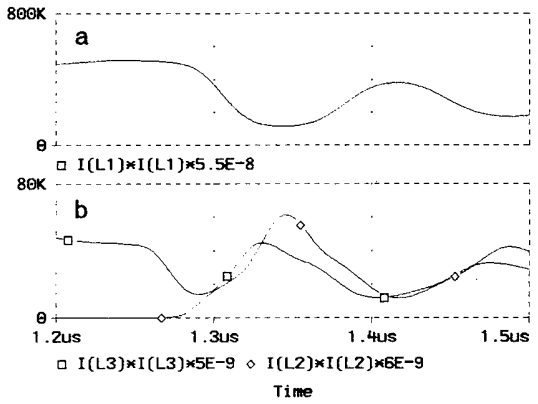

Fig.5 Magnetic energy stored in the inductors; (a) in L_1 and (b) in L_3 and L_2

A well known but seldom exploited fact about the IES generator is that it favours a highly inductive load. This can be seen from the energy efficiency expression derived at the beginning. The same efficiency is found in the ILES design though at a significantly higher value. Using the same circuit parameters in Fig.4 but increasing L_2 from 12 nH to 120 nH, the simulation shows that 316 kJ is extracted from the bank into this inductive load within 100 ns. This represents an energy efficiency of 37% from the bank, from a circuit which is not properly optimized for the ILES design criteria.

Conclusion

The ILES design presented here represents a uniquely different concept for pulsed power generators based on magnetic energy storage. The design overcomes several of the constraints limiting the ultimate performance of IES generators. While the model chosen for the circuit simulation is simple and the effect of a dynamic load is not included here, the results allow us to identify the unique stages of operation of the ILES generator. The Upstream Coupling Line provides energy storage during the conduction phase of the POS and participates in the energy transfer process during the opening phase. The high impedance allows a high voltage wave to be developed, while isolating the effect of the load inductance from the Marx, when the switch opens. This high voltage wave contributes to an increase in energy delivered to the load. The data presented for GIT-4 shows how an IES generator could be adapted into an ILES circuit with significant improvement in performance.

Acknowledgement

I would like to thank M. Krishnan of AASC, California, for an interesting discussion on the topic of opening switch circuits for inductive storage some years ago. His insight and prognosis on the limitations in very high power IES generator form the starting point of the present work. I would also like to thank A. Kim of the High Current Electronic Institute, Tomsk for many discussions on IES generators in general and GIT-4 in particular.

Reference

[1] S.P. Bugaev et al., IEEE Trans. Plasma Science, 18,(1990),p.115.

P-3-66

SCHEMES OF HIGH-POWER PULSED GENERATORS WITH INDUCTIVE STORAGES ON STEPPED LINES

V.S. Gordeev, V.S. Bossamykin

Russian Federal Nuclear Center, All-Russian Scientific Research Institute of Experimental Physics, 37Mira prosp.,607190 Sarov (Arzamas-16), Nizhni Novgorod region, Russia

Abstract

The paper describes some multistage pulse generator designs based upon homogeneous transmission lines of equal electrical length T_0, their impedance varied stepwise. The energy is initially stored as magnetic field by all the generator stages, while it is also stored by some of them as electrical energy. Upon triggering the switch connecting the high-voltage electrode of charged lines to the grounded generator frame, both magnetic and electrical energies would become wholly concentrated at the generator output due to wave effects. Ideally, for any number of stages, the resistive load connected in parallel to the current opening switch is where a square-shaped voltage pulse of $2T_0$ width would be generated, whose peak value may be considerably higher than the generator charging voltage.

Introduction

Most recently, there have been quite a big variety of design concepts for high-voltage pulse generators considered, which basically use homogeneous transmission lines of one and the same electrical length. These designs have the impedance varied stepwise from stage to stage, therefore we call them stepped-line generators. The energy initially stored by the many stages is to become concentrated at the generator output due to wave effects upon triggering the switch. With the line impedances being in specific proportion, the whole of the energy can be delivered to a matched resistive load with a square-shaped voltage pulse to be generated there. The output pulse width is independent of how many stages and overall dimensions the generator has, but it is only determined by the double electrical length of an individual stage. Simultaneously, there occurs the increase in voltage or current due to wave effects. Some concepts have been suggested which can provide a higher pulse power value. Theoretical and experimental studies on high-voltage nanosecond stepped-line generators carried out by RFNC-VNIIEF are summarized in refs. [1-5].

Like any other transmission - line generator reported, these devices may be two types - generators having initial energy stored capacitively and those with inductive energy storage, depending on whether the initial energy is stored only as magnetic or electrical field. Ref. [1] addresses two generator designs using stepped-line inductive storage with whatever number of stages. The magnetic field energy is made to build up through the generator's length by wave effects occurring upon triggering the input current opening switch. This is followed by significant current increase towards the generator output end. Ref. [3] describes a generator design, in which the stepped-line magnetic energy is brought up to the load as a result of square-shaped voltage pulse being supplied externally from a supplementary source. Wave effects are observed to cause substantial increase in the pulse voltage. This paper addresses just a few of the generator designs with inductive storage considered, the case specifically featured by initial energy being stored in the inner generator volume both magnetically and electrically at a time. Therefore, these devices can be referred to as combined energy storage generators. All the generator circuits are capable of increasing voltage.

Generator configurations

Fig. 1 (a, b, c) shows three stepped-line generator circuits based on combined energy storage. Generally, the generator is formed by "n" homogeneous transmission lines having the same electrical length T_0. The lines are numbered consecutively starting from the generator output, with their impedances Z_1, Z_2, Z_3 . . . , Z_n respectively. The total number of stages, "n", for the a, b and c cases shown may be at least 2, 3 and 4 respectively.

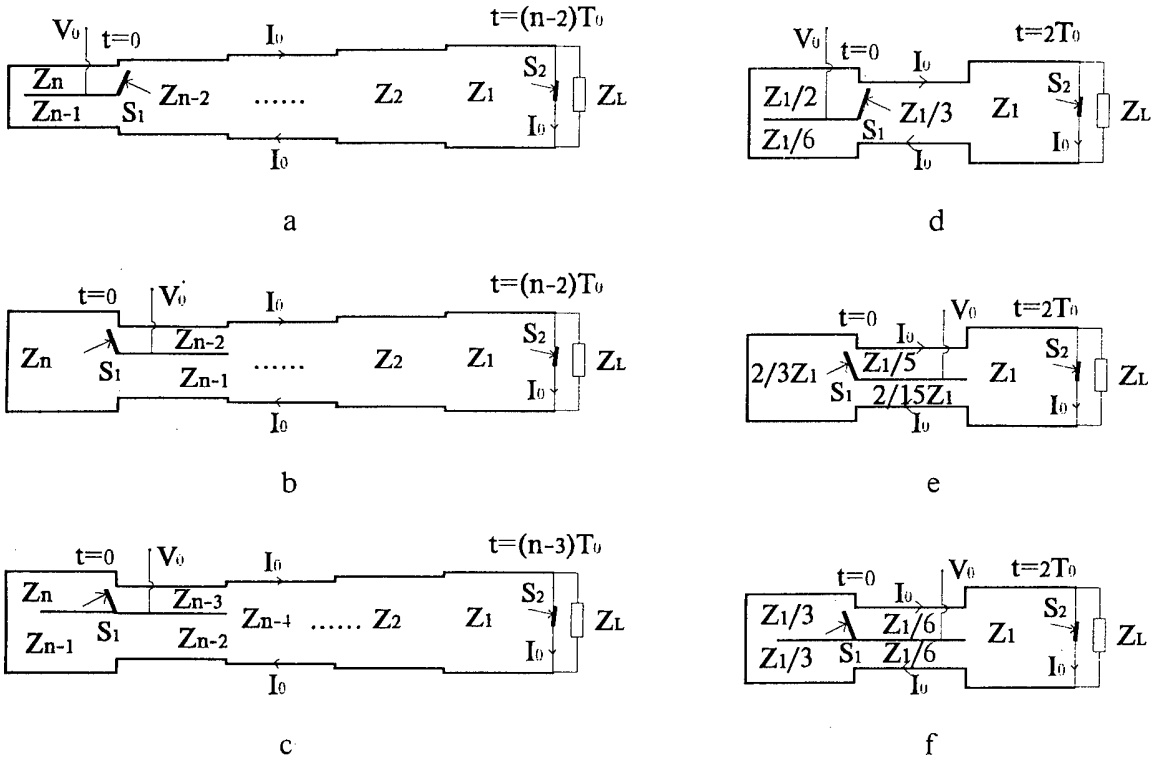

Fig. 1. Generator circuits.

The generators perform as follows. The closed circuit made up by the generator frame and the initially closed switch S_2 has I_0 current produced by the external power supply (not shown in fig. 1), and the energy is stored as magnetic field. Simultaneously, another external supply is to provide pulsed charging up to V_0 voltage of several generator lines with additional energy being stored as electrical field. The first and second cases each have two lines charged, their impedances Z_{n-1}, Z_n and Z_{n-2}, Z_{n-1}, respectively, and the third - four lines with Z_{n-3}, Z_{n-2}, Z_{n-1} and Z_n impedances. Following the initial energy storing process, there occurs triggering of the switch S_1 which is connecting the high-voltage electrode of charged lines to the grounded generator frame. The current I_0 direction and the charging voltage V_0 polarity are specified such that the first electromagnetic wave as it arrives would result in the current increasing at the generator output. Wave processes are what make both magnetic and electrical energies concentrated at the generator output. Along with this, the voltage is observed to achieve a several times higher peak value. The output switch S_2 that connects the resistive load Z_L to the generator output would become opened just when the first electromagnetic wave arrives

at it. Ideally, the matched load have a square-shaped voltage pulse of $2T_0$ width generated.

We can show that the following relationships must be satisfied to ensure that electromagnetic energy will be wholly transmitted to the matched load:

- 1st case $Z_i = Z_1 \dfrac{\alpha(\alpha+1)}{(\alpha+i-1)(\alpha+i)}$, where $i = 1,2,\ldots(n-1)$,

$$Z_n = Z_1 \frac{\alpha(\alpha+1)}{(\alpha+n-1)}, \quad V_0 = I_0 \cdot Z_n;$$

- 2nd case $Z_i = Z_1 \dfrac{\alpha(\alpha+1)}{(\alpha+i-1)(\alpha+i)}$, where $i = 1,2,\ldots(n-3)$,

$$Z_{n-2} = Z_1 \frac{\alpha(\alpha+1)}{(\alpha+n-3)(2\alpha+2n-5)}, \quad Z_{n-1} = Z_1 \frac{\alpha(\alpha+1)}{(\alpha+n-2)(2\alpha+2n-5)},$$

$$Z_n = Z_1 \frac{\alpha(\alpha+1)}{(\alpha+n-2)}, \quad V_0 = I_0 Z_1 \frac{\alpha(\alpha+1)}{(2\alpha+2n-5)};$$

-3rd case $Z_i = Z_1 \dfrac{\alpha(\alpha+1)}{(\alpha+i-1)(\alpha+i)}$, where $i = 1,2,\ldots(n-4)$,

$$Z_{n-3} = Z_{n-2} = Z_1 \frac{\alpha(\alpha+1)}{2(\alpha+n-3)(\alpha+n-4)}, \quad Z_{n-1} = Z_n = Z_1 \frac{\alpha(\alpha+1)}{2(\alpha+n-3)},$$

$$V_0 = I_0 \cdot Z_n.$$

We have used here α, the coefficient which is the ratio of electrical to magnetic energy as initially stored by the generator. If the above mentioned relationships are satisfied, the matched load voltage should be $0.5(\alpha+n-1)/\alpha$, $0.5(2\alpha+2n-5)/\alpha$ and $(\alpha+n-3)/\alpha$ times the charging voltage, respectively. Increasing the load voltage as compared with the charging voltage requires adding more stages and/or decreasing α value, i.e. making the electrical energy portion in the total energy input larger. Adding more stages would result in higher maximum-to-minimum impedance ratio of the stepped line, which is normally within 20 for coaxial lines, given the same dielectric material used throughout the generator. Note, that the impedance ratio grows with lower α values when the stages are fixed in number.

The most general case can be used to illustrate that closed inductive storage systems using stepped lines, must have with complete energy extraction the ratio of the matched load current to I_0, the initial current, equal to $(\alpha+1)/2$. Particularly, one may conclude the total energy stored by the generator would be $(\alpha+1)^2$ times the energy stored at the generator output stage as magnetic field.

The output switch opening can be provided by making use of the fact that at the arrival of the first electromagnetic wave the switch current would grow by a factor of $(\alpha+1)$ for all the circuits considered. This is of special importance in making several generators operate simultaneously as part of a multimodular system. It would be reasonable to ensure reliable triggering of the current opening switch by increasing the α value, i. e. the electrical energy portion in the total energy stored.

As an illustration, fig. 1 (d, e, f) gives the most suitable impedance rations for generators having the total electrical length of $3T_0$, given that equal energy values ($\alpha=1$) have been stored initially in electrical and magnetic fields. The first two cases (d, e) are where the generator includes four, and the third (f) case - five transmission lines, and the matched load voltages are 2, 2.5 and 3 times the charging voltage, respectively. With each stage added and the respective impedance and V_0/I_0 variations the voltage can be increased by $0.5V_0$ for the first circuit, and by V_0 for the second and third.

Triggering the switch S_1 produces electromagnetic waves. When the lines have transmitted the wave which is shown by the figures to travel initially to the left of the switch, their voltage becomes equal to zero. When the wave arrives at the point where different line impedances are connected, there occurs a reflected voltage wave. However, just at the same time there is another wave to come up to the same connection, which has been initially traveling to the right of the switch S_1. The generator circuit and line impedances are selected such that the superposition would result in the reflected wave having its net peak value of zero. This requirement is satisfied at any connection between different line impedances. Impedance ratios are selected so as to provide the same current value simultaneously for all the lines the wave in question has traveled through. While this current is the same in magnitude, its direction is opposite to the initial current I_0. Thus, there occurs not only complete lines discharging but also the magnetic field is made zero due to the superposition. Ideally, a square-shaped voltage pulse would be generated in the matched load as it is switched by opening the switch S_2 at the arrival of the first electromagnetic wave.

Conclusions

Some design concepts of multistage generators using stepped-line inductive storage have been discussed. What is distinctive of this approach is that initially the energy is to be stored by all the stages as magnetic field, but at the same time it is stored also as electrical field by some of them. Upon triggering the switch connecting between the high-voltage electrode of charged lines and the grounded generator frame, there are wave effects which make both magnetic and electrical energy concentrate wholly at the generator output. Ideally, given whatever number of stages, there would be a square-shaped pulse of $2T_0$ width generated in the resistive load, whose peak value may be substantially higher than the generator charging voltage.

The concepts discussed can be used as a basis to develop powerful high-voltage pulse generators including those to be incorporated in multimodular systems. Although the data described in this paper have not been tested experimentally, analytical and numerical studies they summarize involved techniques repeatedly verified by experiments on numerous stepped-line generators using capacitive energy storage. Anyway, selection of the generator circuit design and optimal requirements should be made individually for any specific application.

[1] Bossamykin V.S., Gordeev V.S., Pavlovskii A.I.. New schemes for high-voltage pulsed generators based on stepped transmission lines// 9-th International Conference on High-Power Particle Beams, BEAMS-92, Washington, DC, May 25-29, 1992 ; V. 1, PP. 511-516.
[2] Bossamykin V.S., Gordeev V.S., Pavlovskii A.I. et. al. Pulsed power electron accelerator with the forming systems based on stepped transmission lines// 9-th International Conference on High-Power Particle Beams, BEAMS-92, Washington, DC, May 25-29, 1992; V. 1, PP. 505-510.
[3] Bossamykin V.S., Gordeev V.S.. Stepped line conversion of pulsed voltage, current and electric power // 9th IEEE Internat. Pulsed Power Conf., Albuquerque, NM, June 21-23, 1993; V.2. PP. 918-921.
[4] Bossamykin V.S., Gordeev V.S., Pavlovskii A.I. et. al. STRAUS-2 electron pulsed accelerator // 9th IEEE Internat. Pulsed Power Conf., Albuquerque, NM, June 21-23, 1993; V.2. PP. 910-912.
[5] Bossamykin V.S., Gordeev V.S., Pavlovskii A.I. et. al. Linear induction accelerator LIA-10M// 9th IEEE Internat. Pulsed Power Conf., Albuquerque, NM, June 21-23, 1993; V.2. PP. 905-907.

P-3-67

The nanosecond generator RG-1 with near-rectangular pulse.

V.V.Bulan,E.V.Grabovsky,A.N.Gribov,V.G.Lujnov.

TRINITI, Moscow reg., Troitsk, 142092, Russia.

ABSTRACT.

The 300 kV, 17 Ohm generator RG-1 that can deliver the near-rectangular pulse with the pulse duration 80 ns FWHM is described in this paper. Polarity of output pulse can be changed by the simple switch. The fast capacities in the Marx generator are used instead the pulse forming line. The multispark gas switches have been developed to decrease the inductance of discharged circuit. The generator is supplied by the built-in high voltage source. The installed mini-computer controls its operation. It is used the power supply-line 220 V. The RG-1 can be used in different mode of operation: gas discharge, particle beam formation and so on.

INTRODUCTION.

The high voltage pulse generators are used for the various fields of science and technique. The conventional scheme of these generators is based on the combination of Marx generator and pulse forming line. The difference of the present generator is in the use of the fast capacities forming the near-rectangular pulse instead forming line. The application of these capacities reduced significantly the size (230x100x105 cm^3) and simplified its scheme. The photography of generator RG-1 with the open upper cover is shown in Fig.1.

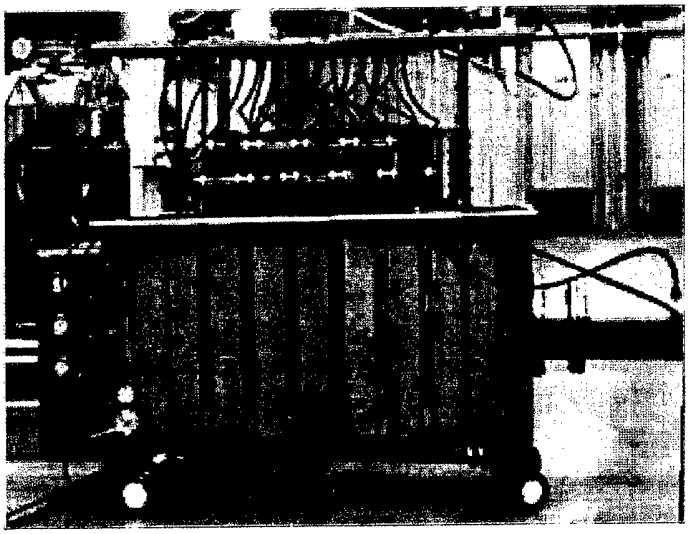

Fig.1. The photography of generator RG-1.

The output pulse amplitude on the matched 17 Ohm load can change from 100 to 300 kV. The polarity pulse is changed by the mechanical switch. The generator provides the 10 ns jitter of output pulse relatively the triggering pulse. The pulses repetition rate is one per minute for charging up to maximum voltage.

DESCRIPTION OF GENERATOR.

The generator RG-1(Fig.2) consists of the basic unit filled by oil, device unit and output unit. The Marx generator (MG), mechanical polarity switch (MPSW), high voltage source (HVS) and high voltage trigger generator (HVTG) are placed in the basic unit. The Marx generator has the form of loop. It is connected with the output unit through the polarity switch. The high voltage source provides the bipolar charging of Marx and the unipolar charging of trigger generator up to 40 kV. The high voltage trigger generator can deliver the pulse with amplitude up to 70 kV and the pulse rise time 50 ns that triggers some switches in Marx generator. The pulse with amplitude 4kV and the pulse rise time 50 ns from internal or external low voltage trigger generator (LVTG) triggers the HVTG.

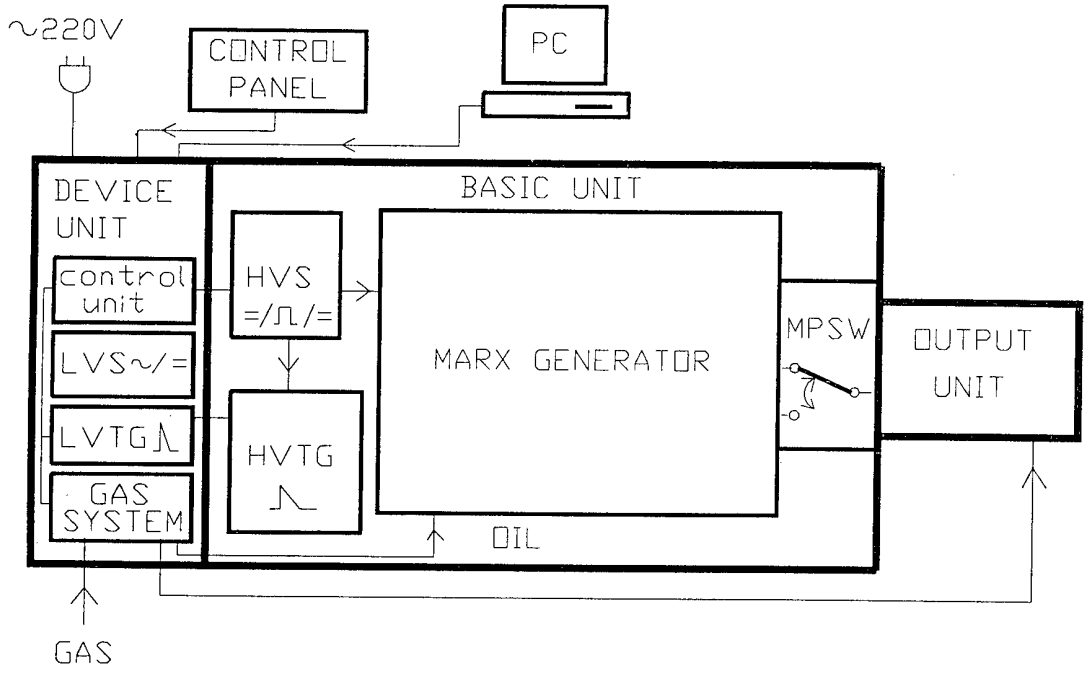

Fig.2 The scheme of generator.

The low voltage source (LVS), gas system, low voltage trigger generator and control unit is placed in the device unit. The control unit operates of the charge voltage and gas pressure in the switches and the gas volume of output unit and also delivers the triggering pulse. The gas system has the automatic and manual of operation control. The kind of gas can be different for the switches and the gas volume of output unit.

The output unit consists of the short line filled by oil and gas volume. The diameter of output unit is 25 cm and its length 42 cm. The load is placed in the gas volume.

The multichannel connector for connection with the control panel and PC is placed on the side wall of generator. The control panel was made in the separate block. It has the keyboard and display for control parameters of the generator.

MARX GENERATOR.

The electrical scheme of Marx generator is shown in Fig. 3. It consists of 10 condensers and 11 gas switches that is connected series in the loop. The closed loop in the center of generator is used to decrease the inductance of discharged circuit. The condensers are charged from the HVS through the water resistors R1-R16.

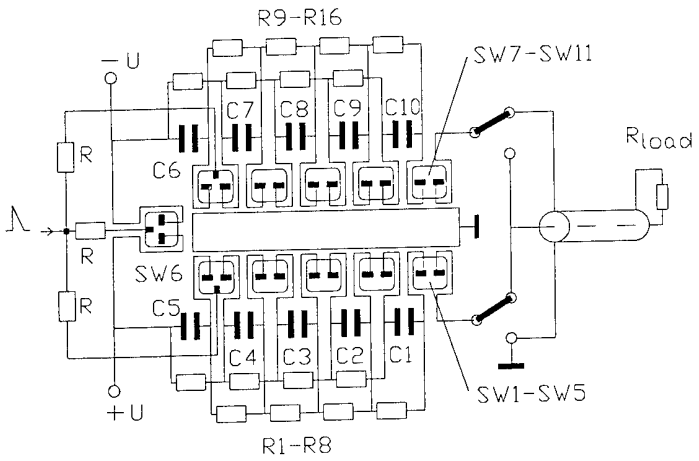

Fig.3 The electrical scheme of Marx generator.

The most switches (SW1-SW4,SW8-SW11) operates in the self-breakdown mode. Three switches (SW5-SW6) is triggered from the HVTG. The fast condensers have the capacity 28 nF and the size 30x12x13 cm^3. The maximum charging voltage of condensers for oil isolation is 100 kV. These condensers operate as the pulse forming lines with impedance 1.7 Ohm. The formed pulse has the pulse duration 80 ns FWHM and the long back front. Thus the Marx form the pulse equal the pulses sum from the separate capacities and its impedance is equal 17 Ohm. The multispark gas switches with the rail type electrodes have been developed. They have been tested on the self-breakdown voltage for the various pressures of nitrogen and SF_6/nitrogen mixture. The breakdown voltage for 4 ata of mixture is 80 kV. At least 2 channel breakdown of gap are observed by the switches with triggering electrode.

OUTPUT PULSE.

The measurements were made for the 10 and 30 Ohm load placed in the gas volume of output unit. The current and voltage monitors placed in the output unit were shown the stable work of generator. The voltage pulse on the 10 Ohm load for the charging voltage 30 kV is shown in Fig. 4. The output pulse has the pulse rise time of

7 ns, the pulse flat top of at least 50 ns with deviation less than 12 % from maximum voltage and the prepulse less than 1 % of peak voltage.

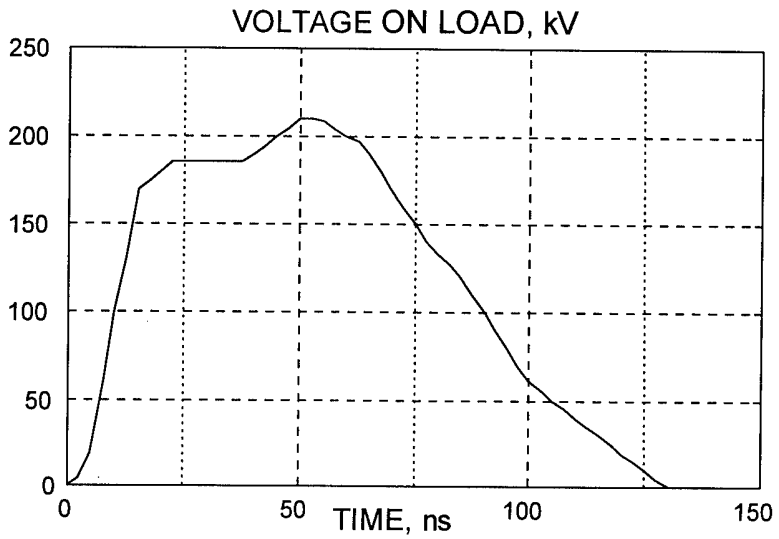

Fig.4. The voltage pulse on the 10 Ohm load

CONCLUSION.

The relatively small size, the use of built-in charge source and trigger generator and also simplicity in operation are the characteristic features of generator. The generator is designed for the investigation of high voltage discharge in gas. It can be used for trigger of the pulse power generators as Angara-5. The scheme on based this generator for producing the electron beam is developed now.

ACKNOWLEDGEMENT.

Authors thank Dr. V. Smirnov for trustful discussions. This project has been developed under contract of International Institute for Application Physics and High Technology, Moscow ,Russia. Authors thank prof. A. Blaugrund for trustful discussions.

REFERENCES.

1. Z.A.Albikov et al., Pulse thermonuclear facility Angara-5-1, Atomnaya Energiya.1990.-68,N1.-p.26-35.

2. V.V.Bulan et al., Electron beam generators at Angara-5 facility.Proc.9th.Int.Conf.on High-Power Particle Beams, Washington, 1992, p.425-430.

3. S.P. Bugaev, G.A. Mesyaz, The pulse discharge in dielectrics. Novosibirsk, Nauka, 1985.

P-3-68

PROTECTION OF CONTROL AND MONITORING EQUIPMENT FROM ELECTROMAGNETIC NOISE IN THE 67MJ, 50kV CAPACITOR BANK

I.V.Galakhov, A.S.Gasheev., I.A.Grusin., S.N.Gudov, Yu.P.Kuz'michev, V.M.Murugov, V.A.Osin, V.I.Pankratov and I.N.Pegoev

RFNC - VNIIEF, Sarov (Arzamas-16), Russia.

Abstract

A discharge of the 67MJ and 50kV capacitor bank used as a pulsed power system for flashlamp pumping of ISKRA-5's high-power iodine laser, involves control and diagnostic equipment being subjected to significant electromagnetic fields and electrical interference that will further develop through conductive circuits.

The paper describes and validates design approaches to the grounding system, signal carriage and decoupling circuits that would result in lower interference both for the capacitor bank's control and diagnostics systems. A summary is also given of the ten-years' practice in operating the control and diagnostics equipment during the facility experiments.

Introduction

Among engineering challenges of designing high-power physics research facilities with large power conditioning system, there is electromagnetic compatibility with the power units of control and diagnostics systems. Generally, the pulsed voltage existing with the capacitor bank discharge to the load and the voltage with diagnostic and control signal differ by a factor of more than 10^5, thereby showing the problem to be difficult and topical. These have been no standard provisions (necessary and sufficient) for electromagnetic compatibility reported to exist due to the unique nature of physics research facilities. However, it is also known that no actions taken toward electromagnetic compatibility in the design and development of facilities would lead to unreasonably increased costs and resources.

The physics research facility ISKRA-5 [1] has been designed and developed to study interaction between high-output laser beam and matter as part of laser fusion research program. Its installation was completed in 1988, and since 1989 the facility has been used by target experiments [2].

The facility is based on the iodine photodissociation laser having a light pulse, as generated by the master oscillator (MO), to be split in many and amplified by 12 identical amplification lines each including 5 stages. Total beam output has 30kJ energy in a pulse 0.25ns long.

Light sources to pump MO and laser amplifiers are supplied by a pulsed power (PP) system built around a capacitor bank with 67.2MJ of stored energy and 50kV operating voltage [3].

The PP system's capacitor banks have performance as described in Table 1 below.

The ISKRA-5 design included certain requirements to be developed for grounding, decoupling in power supply, techniques to carry control and diagnostic signals and for equipment shielding. Particularly, the designers showed that computer technologies can only be incorporated and operable in pulsed physics facilities provided they meet specific requirements, such as for interference suppression.

Table 1.

Performance of capacitor banks.

Parameter	CB-MO	CB-A1	CB-A2	CB-A2B	CB-A3	CB-A4	Overall capacitor bank
Stored energy, MJ	0.09	0.41	1.26	5.04	20.16	40.32	67.28
Peak discharge current, MA	1.4	7.2	7.2	9.6	42.2	84.5	152.1
Discharge half-time, μs	10	10	10	30	35	35	-
Modules	5	12	24	48	192	384	665

Technically, to identify what effort would be the more appropriate for interference suppression requires first of all that analysis should be done for interferences in terms of their origin and transmission by detection circuits for diagnostic and control signals, for unauthorised signals spectrum and the bandwidth requirements for the detectors. Note, however, that any effort would allow one or two orders of magnitude reduction in the interference signal at the most, this being normally less for larger bandwidth, and more for narrower one. With the differential input used by the detector the decrease up to 3 or 4 orders of magnitude may be achievable in the narrow bandwidth (within 0.1-1mhz). Therefore, it is only a package of simultaneous techniques that would allow the required 6 or 7 orders' reduction in interference signal for the above-mentioned signal ratio between the control and power discharge circuits.

The paper briefly summarizes major efforts carried out towards electromagnetic compatibility between the diagnostics and control systems and the power conditioning portion of ISKRA-5 physics facility.

Active interference suppression.

Basically, interferences are caused in ISKRA-5 facility by flashlamp discharge circuits and spark gaps triggering circuits. Therefore, there were steps taken to limit the energy going beyond discharge circuits. The ISKRA-5's capacitor bank has the energy from capacitors carried to the load by coaxial cables, with only one point in each discharge circuit (module) to be grounded, which is the "minus" terminal of capacitors. The amplifiers with flashlamps serving as discharge circuit loads have their frames insulated at 10kV from the building fittings and surrounding equipment (pumps, pipelines, etc.) and connected to ground only via outer coaxial cable conductors.

Thus, the energy delivered from capacitors to the load is confined within discharge circuits and made to have minimized effects upon the other facility systems.

Grounding system

Grounding arrangement is what also refers to active interference suppression, the techniques to decrease the interference signal value. The ISKRA-5 facility employs a three-line single-point grounding system.

The protective grounding line is intended for non-current carrier members (housing, shielding, frames, enclosures, etc.) of any equipment and control and diagnostics systems, whose pulsed spread currents are not high. The protection grounding line is made up by an

arrangement of frames with cables laid therein. Directly connected to this line are the building fittings and shielding of suitable rooms which accommodate computer hardware and diagnostics.

The process grounding line is intended for housing and units incorporated in power subsystems of the capacitor bank system. In order to avoid pulsed spread currents getting into the other grounding lines, the process grounding line is designed as steel buses of 50x4mm^4 size that are insulated at 1000V from the building fittings and connected to a single "common point" with specialized single-wire cables of at least 50mm^2 sectional area.

The system grounding line is used to connect electrically the frames and common buses of diagnostics units and computer hardware that have TTL signal exchange between each other. The system grounding line is laid into shielded frames having insulation at 1000V level, using wire of at least 16mm^2 sectional area to connect between the grounding system's "common point" and specialized rooms for diagnostic equipment.

The grounding system's "common point" is only where the three grounding lines are connected together. Spacially, these three grounding lines are altogether designed like a "tree", with each line branch originating from the "common point" and ending in the appropriate location.

Passive interference suppression

These are techniques to minimize interference signals getting into transmission lines for control and diagnostic signals. The ISKRA-5 control and diagnostic signals altogether have been conditionally categorized into 4 types as follows: high-level signals (all static and pulsed at above 1000V), medium-level 1 signals (all signals at 10-315V DC or AC, relay switched, and of commercial supply line 220V/50Hz), medium-level 2 signals (all pulsed signals at 10-500V generated by active and passive circuits) and low-level signals (signals within 1mV-10V, typically having spectrum up to 10kHz).

High-level signals are carried by coaxial cables laid either openly or in high-level enclosures which are insulated up to 1000V and grounded to the process grounding line. The three other signal categories are carried by braided cables that are laid in the respective medium-level 1, medium-level 2 and low-level frames, which provide a protective grounding line and, therefore, an additional shielding.

Local interference resistance

Local interference resistance is provided by a package of circuit and engineering design arrangements that suppress interfernce signals both between local systems and units and inside them - between functional components including printed circuit boards. Basically, the following arrangements may be used depending on specific features of local systems: two-wire signal transmission (with one wire necessarily for back transmission), transforming and optronic conductive isolators, electric filters, etc.

Conclusions

The ISKRA-5 laser facility has electromagnetic compatibility achieved between the power subsystem, which is the 67MJ, 50kV capacitor bank with a total discharge current of 150MA in 30μs, and its control and diagnostics systems, due to combined applications of three types of measures, such as procedures to minimize energy spread beyond power units, i.e. active interference suppression, procedures to minimize interference signals getting into the control and diagnostics communication lines and on to the detector inputs (passive interference suppression), and procedures to make the control and diagnostics equipment more

insensitive to interference signals (local interference resistance). It is with the integrated application of the above-mentioned measures that reliable operation of the facility's control and diagnostics equipment was ensured during ten years.

[1] Kirillov G.A., Murugov V.M., Punin V.T.,.Shemyakin V.I "High Power Laser System ISKRA-5" : International Conference SPIE, OE/LASE'90, Los Angeles, CA, USA, January 1990.
[2] Kirillov G.A., Murugov V.M., Punin V.T., Rogatchov V.G."ISKRA-5 Laser Experiments" : International Conference on Lasers'91, San Diego, CA, USA, December 1991.
[3] Bezuglov V.G., Galakhov I.V., Gasheev A.S., Gruzin I.A., Gudov S.N., Il'yn A.Yu., Kirillov G.A., Kuzmichev Yu.P., Kucherov A.I., Logutenko S.L., Murugov V.M., Osin V.A., Pegoev I.N., Petrakov V.N., Zolotovski V.I. "The 67MJ, 50kV Capacitor Bank for the High-Power Iodine Laser of the Facility ISKRA-5: Description and Experience." : 10th IEEE International Pulse Power Conference, Albuquerque, NM, USA, July 1995.

P-3-69

DIAGNOSTICS SYSTEM FOR THE 67MJ, 50kV PULSE POWER CAPACITOR BANK

I.V.Galakhov, A.S.Gasheyev, I.A Gruzin., S.N.Gudov, V.M.Murugov, V.A.Osin, V.I.Pankratov, I.N.Pegoev

RFNC-VNIIEF, Sarov (Arzamas-16), Russsia

Abstract

The diagnostics system described in the paper is for charging and discharging to the load of the large 67MJ and 50kV capacitor bank for the iodine laser pulse power of ISKRA-5 facility. Discharging diagnostics of the capacitor bank has used a technique to measure a sequence of times between representative discharge events for 665 discharge circuits of the bank. Benefits of the measurement techniques used are discussed.

Introduction

High-power laser facilities have been built in many countries for experimental research in laser fusion area. Among its subsystems every such facility has a pulse power system to supply flashlamps in the active medium pumping system of laser amplifiers. The pulse power system is built upon capacitor banks which are separated into individual modules. Each module is a bunch of capacitors which is discharged through a switched of the flashlamp an individual load.

High-power operating currents ($I_{max}\leq 300kA$) and voltage ($U_{ch}\leq 50kV$) are what predetermine failure probability for high-voltage components as $P_{fail}=10^{-4}$-10^{-5}per shot with the total number of component $N_c\geq 10^4$. There fore, in each physics experiments there may be any kind of failure in the pulse power system, which has to be detected and eliminated. This is what the capacitor bank diagnostics system is intended for.

There are some considerations that make the diagnostics system development a difficult problem. First, it is electromagnetic compatibility requirement between the capacitor bank and diagnostics equipment at the bank discharge and associated high interference pulses.

Next, it is requirement for multichannel measuring systems. Therefore, a measuring channel must have as simple design as possible to make equipment less expensive.

Finally, efficient diagnostic technique must be provided physical measure to allow maximum possible detection of pulse power system failures and failure prediction techniques to be developed.

The paper presents diagnostics techniques for charging and discharging events in the large 67MJ, 50kV, capacitor bank of ISKRA-5 facility.

Capacitor bank description

The ISKRA-5 capacitor bank [1] includes 665 capacitor modules. A module has its schematic diagram as shown in Fig.1. Its basic components are: a bunch of parallel-connected capacitors C_m, a spark gap Sw_m, cable connection lines K and series-parallel connected flashlamps L1-L4 as the load. Diagnostic signals during the module operation are to be produced by voltage dividers DV and pulse detectors D_{Sw}, $D_{L1,2}$.

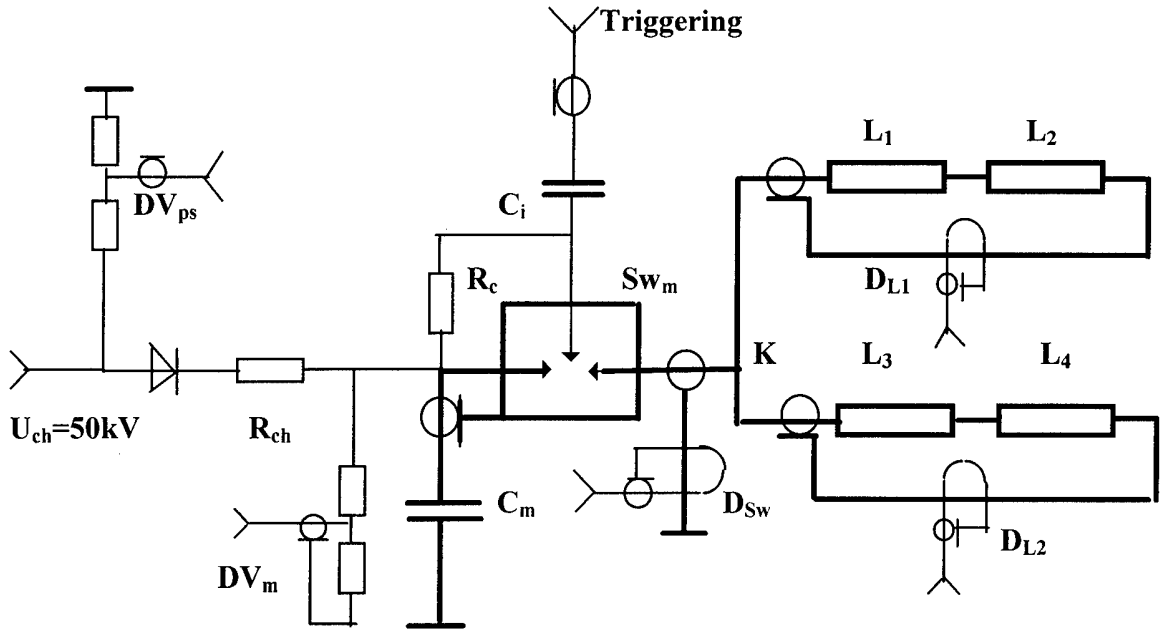

Fig.1 Schematic diagram of the ISKRA -5 capacitor bank module.

Diagnostics technique for module discharge to the load

Reportedly [2], there is a diagnostics technique for capacitor module discharge to the load, which measures peak value of the discharge current carried through the flashlamp and switch. When a high-voltage component is broken down, this would cause variations in the discharge circuit 's RLC parameters and thus make the experimental peak current measurement different from expected value.

However, this technique to measure peak current value offers the following disadvantage. It can only state the occurrence of a high-voltage component breakdown while providing no preliminary information on the failure possibility. However, as shown in practice, module components such as the switch and flashlamp have the probability of shot delays increasing with running time, which is due to these components having different breakdown conditions in their gas spark gaps because of wear. With shot delays in high-voltage module components, there would be no variations in the circuit RLC parameters, there fore, significant changes in the peak current value cannot be detected until the switch or flashlamp breakdown.

The diagnostics implemented at the ISKRA-5 facility [3] is pulse-time technique. The idea of the proposed technique is as follows. Experimentally, the initial and terminal times were determined for the following major discharge events of the module: switch and flashlamp shot delays, current onset and zero-crossing in the load, simultaneity in trigger generator shots. These are times when specific detectors are used to generate diagnostic signals with representative time intervals to be measured between them, and these measurements would serve for performance evaluation of module components.

Fig.2 shows a timing diagram for direction of transients involved in the bank discharge to the flashlamps, together with times measured between start-stop signals ($t_4=t_1+t_2+t_3\leq 50\mu s$).

The pulse-time diagnostics allows detection of delays, misfires and prefires of the module switch and triggering generators. It can be also efficiently used to detect discharge failures which involve variations in the discharge current RLC parameters. These are such failures as connection line breakdown between the switch and the load. As this takes place,

the discharge current half-period varies in duration, thus being just detected as decrease in the interval t_3.

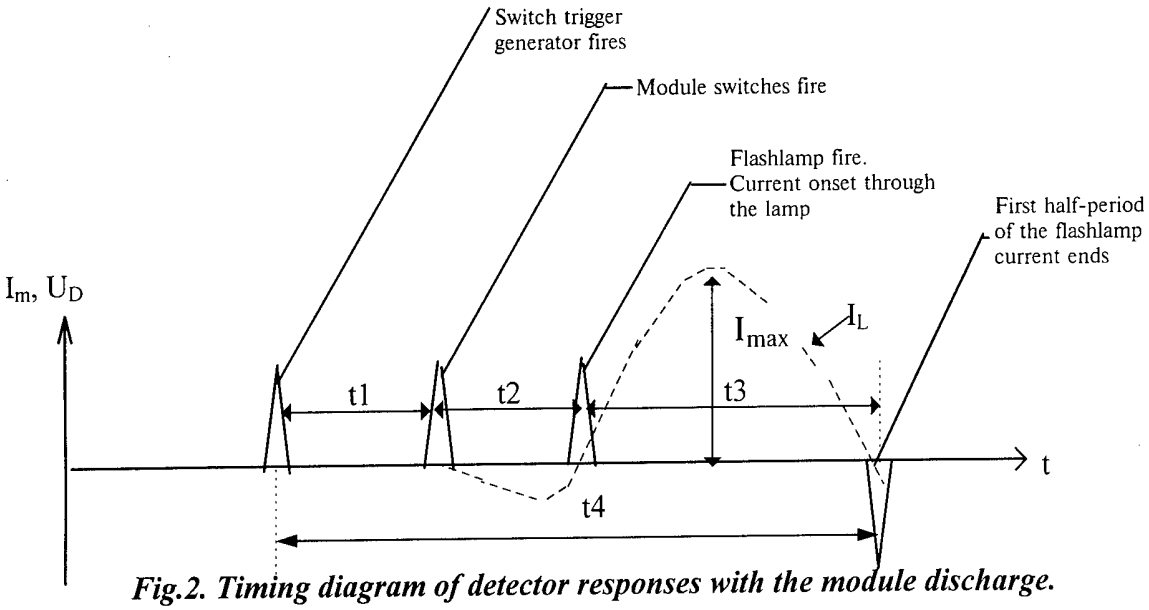

Fig.2. Timing diagram of detector responses with the module discharge.

Shot time measurements of high-voltage components provided an easy and efficient way to address major discharge diagnostics problems for the ISKRA-5 pulse power system.

The above-mentioned module discharge diagnostics is a technique that offers high interference immunity. This is primarily because detectors do not transmit analog signal to the diagnostics system, but a signal indicating the beginning or termination of any time interval, and thus requirement for nondistored signal transmission are not high. This allows efficient isolation between low-voltage diagnostics circuits and the high-voltage discharge circuit of the module.

This isolation is provided by using fast-response fiberoptic pulse communication units connected in between start-stop signal detectors and the equipment for time interval measurements.

With minimized number of measurements (one or two time intervals of a high-voltage components), the developments of diagnostics equipment was made much less expensive, while there was an opportunity to provide complete diagnostics for all the module components.

A great deal of data obtained from more than 10 000 experiments carried out on the ISKRA-5 facility during 1986-1996 proved the pulse-time diagnostics technique as highly efficient and important. During prelaunch adjustment operations, this technique allowed detection of about 5000 failure events of any kind in high-voltage module switches and trigger generations, and also application of performance prediction procedures for xenon flashlamps.

Similar diagnostics techniques may be designed into multiple pulse power systems operated with high-voltage modules having discharge events of microseconds duration.

Charge diagnostics of the capacitor bank module

For ISKRA-5 facility, the time to charge its 665 capacitor modules to 50kV voltage is 90-100s. During the whole of the capacitor bank charging cycle (fig.3), the module voltage is to be against the reference (at the power supply). Once a signal measurement goes beyond

±ΔV=0.5kV, the module is indicated to have failed and then withdrawn from the experiment. In this way, breakdowns in charging lines and capacitors and switch prefires can be detected.

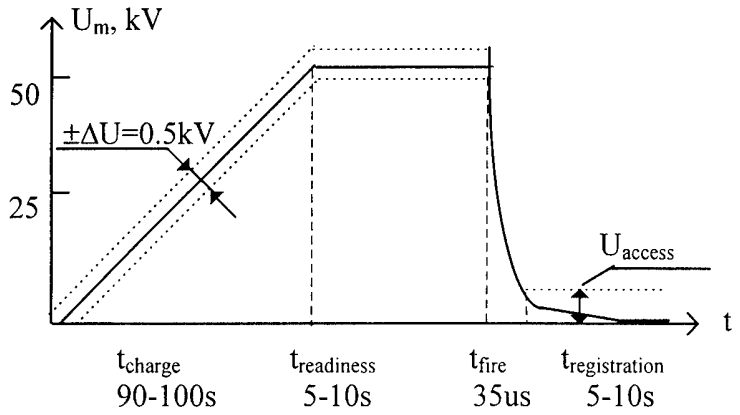

Fig.3. Charge diagnostics of the ISKRA-5 capacitor bank module.

For its detectors, the charge diagnostics system employs resistive voltage dividers with their interference immunity is achieved by no connection to exist between the "common points" of the module and the diagnostics system. For this purpose, the module has only a current control resistor with its signal to be transmitted via a cable (which is a shielded twisted pair, its shield and either wire connected only to the diagnostics "common point") to the diagnostics circuit where the lower divider port is located.

This approach ensures reliable performance of the diagnostics system.

Conclusions

For the purpose of diagnostics of the ISKRA-5 capacitor bank modules for their switching performance to the load, measurement techniques have been put into operational use to determine time intervals that account for discharging of circuit operating in oscillatory mode.

As compared with techniques to measure peak discharge current in a circuit, the pulse-time diagnostics helps predict switch and flashlamp failures.

[1] Bezuglov V.G., Galakhov I.V., Gasheev A.S., Gruzin I.A., Gudov S.N. et al. "The 67MJ, 50kV capacitor bank for the high-power iodine laser of the facility ISKRA-5: description and experience." : 10th IEEE Inter.Pulsed Power Conf.- Albuquerque, July 1995.

[2] Whitham K., Larson D., Merritt B.T., Christie D. "NOVA Pulse Power System: Design and Operational Experience" : UCRL-95051, 1987, Presented on SPIE Optoelectronics and Laser Applications, 1987.

[3] Antipov S.I., Galakhov I.V., Gasheev A.S., Gudov S.N., Il'in A.Yu., Kirillov G.A., Murugov V.M., Pankratov V.I., Pegoev I.N." System of pulse diagnostic for capacitor bank discharge." : Pribory i Technika Experimenta, N5, 1990.

P-3-70

PFN-MARX PULSERS FOR HPM TESTING APPLICATION

M. M. Kekez, National Research Council of Canada, M-51, Ottawa, Canada K1A 0R6

Abstract

This article deals with the development of fast compact systems applicable to the field of high power microwaves. Characteristics of a conventional Marx H.V. generator and two co-axial PFN-Marx pulser systems, operating up to 500 kV levels, are presented.

1. Conventional Marx: This type of generators are frequently used as the simulators of enhanced electromagnetic pulse effects. To drive HPM source, the voltage pulse should have a flat top of at least several 100 ns duration. At first glance, conventional Marx can meet this requirement. In zero order approximation, the output can be described as: $V=V_0e^{-t/\tau}$. Here, $\tau=RC$, R is the resistance of the load and C the erected capacitance (=capacitance of stage per number of stage). The energy delivered to the load as a function of time, t is:

$$\text{energy}= [V_0^2\tau/(2R)](1-e^{-2t/\tau})$$

If we allow a 10% drop in the voltage output (: i.e. $e^{-t/\tau}=0.9$), we have that $t/\tau =0.105$ and $e^{-2t/\tau}=0.81$. This suggests that for a 10% drop in the voltage, Marx generator has discharged only 19% of its energy. If at this instance, the system is short circuited by a crowbar switch, 81% of energy stored in the bank will be wasted. In some situation this is not important e.g. when one is developing high-power microwave sources where the width of the pulse is parameter in the investigation. This requires replacing a set of capacitors in the existing system with the set having longer time constant, τ to achieve the pulses of longer duration. An alternative way is to employ an LC circuit to compensate for Marx generator drop as described by Crumley *et al* [1]. An example of using a diverter (crowbar) switch to get "square" pulse is given in Fig. 1.

2. PFN-Rim-Fire: In this system, attention was paid to the rise time characteristics. To achieve the steep rise in the voltage pulse, twelve UV-coupled spark gap switches are employed per each stage. Each switch has a sphere-ring geometry that is placed in the vicinity of the return current path. All attempts are made to minimize the discontinuities in the internal structure of the coaxial arrangement. The main difference between the Rim-Fire and the system described in Ref. [2] is that, here we have employed 12 switches per stage. A single switch per stage was used in Ref. [2].

The Rim-Fire has 40 stages, hence 480 switches. As in Ref. [2] the first stage is activated by a 50 kV, 10 ns rise-time trigger pulse and all the remaining (468) spark gap are U.V. coupled and activated by overvoltage applied in a sequential manner as demonstrated in Ref. [2]. During the discharge circle, an impression is created as if the rim is on fire (hence the name for the system: "Rim Fire"). The brightness of the spark channel does not vary from a spark gap to a spark gap in both the azimuthal- and longitudinal directions. To evaluate the system, a 100 Ω transmission (diagnostic) line with its capacitive- and magnetic probes is attached to the output. To minimize the discontinuities, the peaking circuit described in Ref [2] was placed between the Rim-Fire and the 100 Ω line. When the system is pressurized to 7 psi of SF_6, the rise time is 150 to 300 ps, depending on the charging voltage.

The pulse width is governed by the capacitance in the stage and by the finite dimensions (inductance) of the connecting

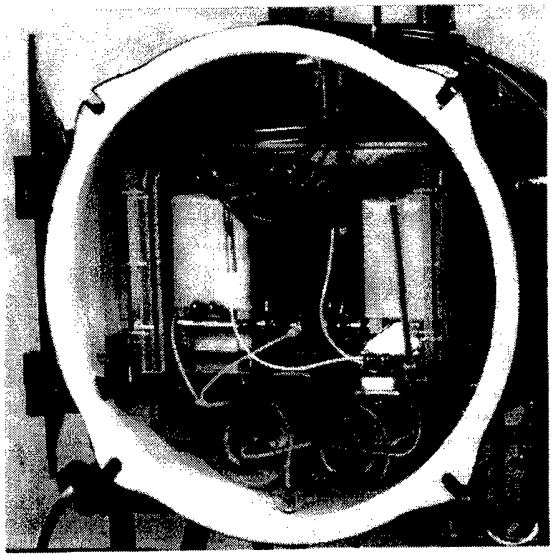

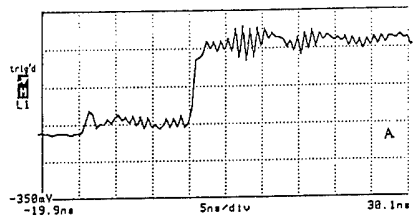

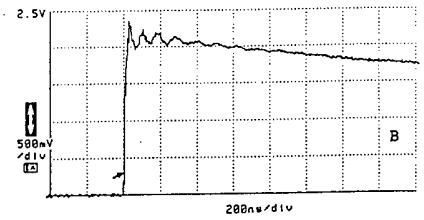

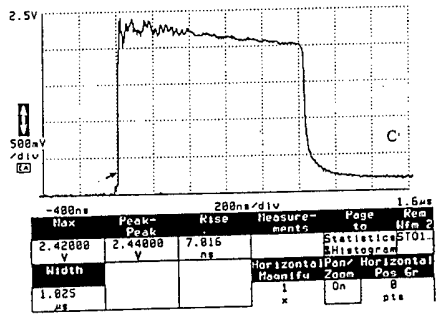

metallic plate (sandwiching six 2.7 nF, 40 kV Murata capacitors in each stage) withadjacent lead to the switch. Regardless how compact this geometrical combination is, the circuit can be represented by the LC section of the (co-axial) transmission line. L is the distributed inductance of all the leads, and C the lumped capacitance in the stage. We find that the duration of the pulse of 51 ns corresponds to $2(LC)^{1/2}$.

The reproducibility of output pulses is excellent, when viewed by both 602 A and 7250 digitizers (Fig. 2). The efficiency of the system defined as the ratio of the output voltage to 40 times the charging voltage (of 7 to 14 kV) is about 80 %. No attempt was made to minimize the rise-time characteristics. If this would be necessary, the system should be placed in a metallic enclosure, so that the pressure could be raised from current 7 psi to 50 plus psi'. We need only to follow the path used in the electrical switch gears in gas-insulated apparatus. It is believed that, this system should be superior in respect to the rise-time characteristics to the system given in Ref. [3]. In the current form, the system could be used to power a high-current relativistic magnetron (Brasile *et al* [4]) or Backward-Wave Oscillator (Schamiloglu *et al*, [5]).

3. PFN Marx: To broaden the width of the pulse, the lumped LC networks are employed in each stage of Marx. We have introduced purposely the inductance between the individual capacitor to get a PFN. Some other arrangements of PFN (e.g. Guillemin type "C" network) are discussed by Crovey *et al* [6]. In our case we have used ten 2.7 nF, 40 kV Murata capacitors separated by a small inductance in each stage. This facilitates the duration of the pulse of 373 ns duration (Fig. 3). If longer pulse is required more LC stages could be

Fig. 1. Top: Photograph of the conventional six stage-12 capacitors (0.09 µF, 75 kV, each) Marx generator. **A** is the waveform at the beginning of the load. With capacitive probe, the rise-time is 1 ns at 300 to 500 kV. If the load is placed in a coaxial enclosure the rise-time falls to 0.4 ns. **B** is the waveform obtained using two resistors of 400 and 300 Ω connected in series. With the resistive probe, the voltage, B is measured across a 300 Ω. The resistor ahead of the probe acts as an antenna (that radiates high frequency components of the pulse), therefore, the rise-time "rises" from 1 ns to 7-12 ns. The waveform **C** was obtained as in B, but with a triggered-crowbar switch activated at 1.025 µs. The crowbar action can be applied in programable steps from 400 ns to 1 µs. A trigger pulse of 200 kV and 20 ns duration was used.

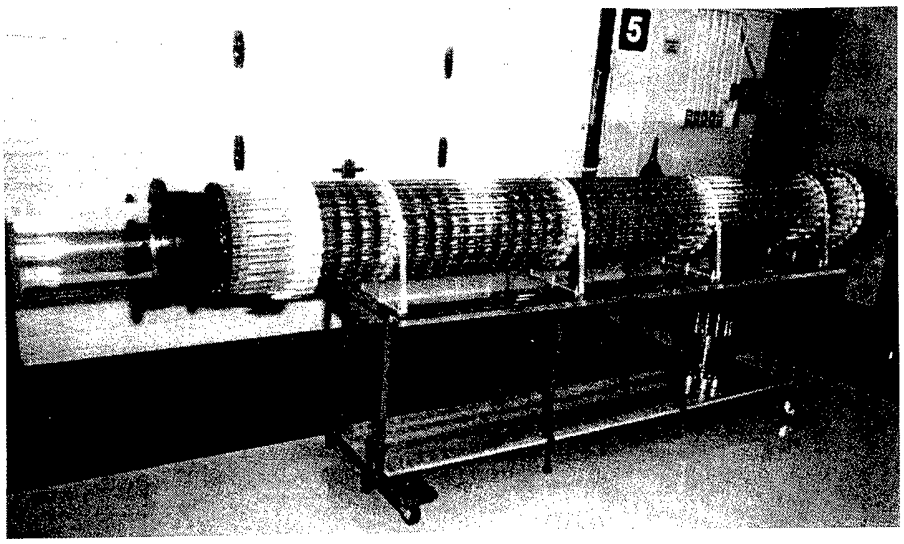

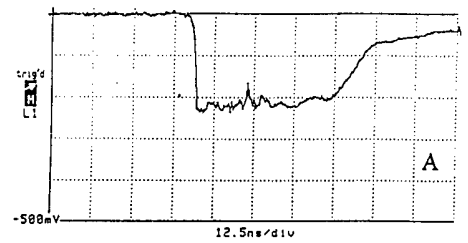

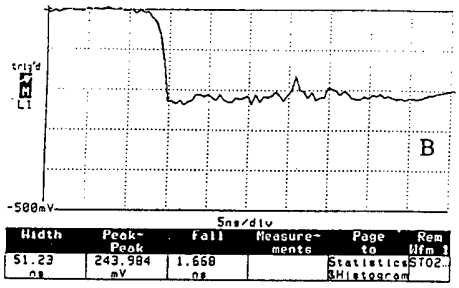

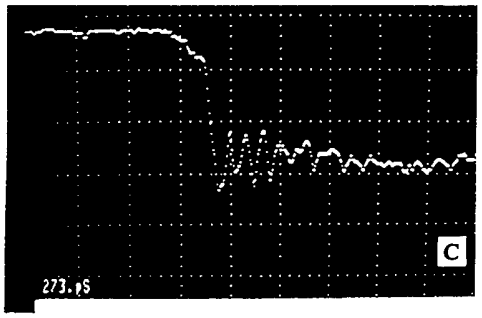

added. We find that the rise-time remains the same if more LC stages are added or if the PFN is reduced to a single stage.

The computer modelling of the performance of 8, 24 and 40-stage Marx generators were carried out using "PSpice" program. Internal PFN features: the characteristic impedance ($=(L/C)^{1/2}$) and the pulse width ($=2(LC)^{1/2}$) were considered. Also, we find that, the coupling capacitance between stages and switch characteristics must be taken into account in the computer simulation. The experimental results are well accounted for by a PSpice computer simulation as long as the experimental values of the formative time lag of the switch's breakdown were correctly observed. In zero order approximation, we get that, if the characteristic impedance of the stage is $Z_0=(L/C)^{1/2}$, then the output impedance of the system is nZ_0. The pulse width of the system, T is governed by a single stage: $T=(LC)^{1/2}$. "Smart gas mixture" used in the generator can contribute to minimizing the ripple at the flat portion of the pulse. However, this is a challenging task because: (a) it is rather difficult to produce a pure resistive load required to do the test covering the entire frequency range

Fig. 2. Top: Photograph of forty-stage Rim-Fire. The system is enclosed in a 11" diameter plexiglas tube. 24 copper rods of 1/4" diameter are enclosed in 1" diameter plexiglas tubes to provide the return current path.

Waveforms: A, B and C of Rim-Fire at low (400 kV) output voltage into a 100 Ω load. **A & B** recorded with 602A digitizer. **C** recorded with 7250 digitizer (2 ns/div; 273 ps rise-time). The dip on the flat portion of the pulse at around 15 ns is due to imperfection of the resistive termination.

from d.c. to giga-Hertz and (b) it is difficult to construct a H.V. resistive probe that could be as fast as the capacitive probes. To simplify the engineering task, a single switch per stage was used in Fig. 3 resulting in the rise-time of 4 ns.

In all systems an effort was made to reduce the size and weight and to make the systems portable. The co-axial structure offers the possibility of combining the Rim Fire technology with the classical LC networks in order to achieve an ultra fast rise-time and long duration pulses. With inductive charging, the pulse repetition frequency of 10 Hz can be accomplished.

Conclusions: Conventional- and PFN Marx are applicable to the "Super-Reltron" tube described by Miller *et al* [7]. It is frequently stated that this tube has an extended frequency coverage, excellent efficiency (due to good electron bunching and small energy spread of the electrons in the bunches), and convenient output configuration. We are interested to understand the onset characteristics in the tube's modulating cavity using our pulsers. We want to appreciate the importance of the observations by Scarpetti *et al* [8] that, a full space-charge limited current is fully established at 400 kV/cm for velvet (cloth fiber) cathodes and the emitted current can follow the nano-seconds rise time of the applied voltage pulse.

Acknowledgements: The author is deeply indebted to Dr C. Gardner and Dr. S. Kashyap of DREO for useful ideas and helpful discussions. Interest shown by Dr. A. L. VanKoughnett, NRC is appreciated.

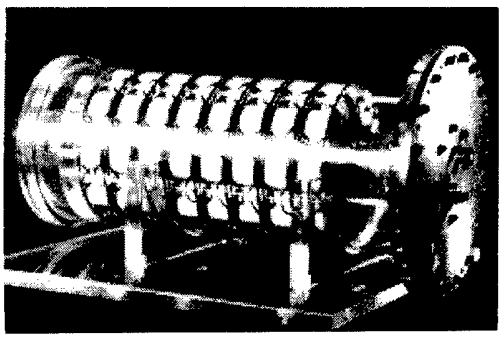

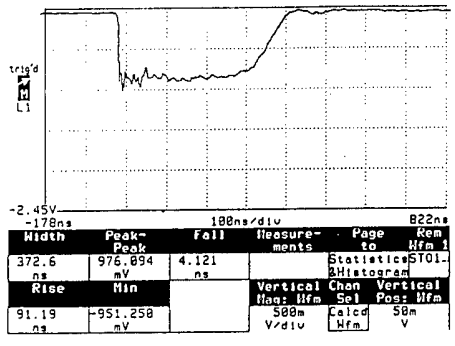

References:

[1] Crumley R. et al, 1989, "A long-pulse microwave driver", 7th IEEE Pulsed Power Conference, Monterey, CA, 120-122

[2] Kekez M. M. and Liu J. 1994, "A 60 Joule, 600 kV, 500 ps risetime, 60 ns pulse width Marx generator" Meas. Sci. Technol. **5**, 1389-1395

[3] Kekez M. M. 1991, "Simple sub-50-ps rise-time high voltage generator" Rev. Sci. Instrum. **62**, 2923-2930

[4] Brasile J. P. et al, 1994, "The Fier Test Facility: On-going works" AGARD-DRG Symposium, Ottawa, Canada, 2-5 May

[5] Schamiloglu E. et al, 1994, "High efficiency Backward-wave oscillator for HPM generation: Present status and Future" AGARD-DRG Symposium, Ottawa, Canada, 2-5 May

[6] Cravey W. R. et al, 1989, "Design of repetitive very H.V.-PFN of short duration" 7th IEEE Pulsed Power Conference, Monterey, CA, 116-119

[7] Miller R. B. et al, 1995, "Recent advances Super-Reltron source development" SPIE, **7**, 2557-01

[8] Scarpetti R. D. et al, 1987, "Electron emission from conductors subjected to intense short pulse electric fields" 6th IEEE Pulsed Power Conference, Arlington, VA, page 631-634

Fig. 3. Top: Photograph of 8-stage-PFN-Marx. The system is enclosed in a 11" diameter plexiglas tube. **Bottom**: The pulse width of the waveform is 372.6 ns and rise-time about 4.2 ns. Reproducibility of the pulse is excellent.

Controlled Multiple Channel Switch[1]

A.I.Kormilitsyn, V.S.Diyankov

Russian Federal Nuclear Center - Institute of technical Physics.
456770 Snezhinsk, Chelyabinsk region, box 245, Russia.

Abstract.

The method of the energy switching in the two-electrode sharpening discharged switch gap, when voltage pulse with variable rise velocity ($du/dt=10^{11}$-10^{14} V/s) is applied to the between switch electrodes, is concidered. The switch was set in the circuit with the inductive energy store and current switch (IGUR-3), that is used to switch of the energy to the accelerator tube. The switch gap change controlls the voltage (current) pulse front in the range 15-250 ns. The switching current amplitude is ~ 80 kA with voltage up to ~ 7 MV.

Introduction.

The different duration pulses formation essentially extends the possibility of the IGUR-3 accelerator to research. To obtain the required duration of the pulse front the sharpening discharger switch gap must be changed. The switch operation in the all range of the rise velocity of the voltage pulse is provided by the gap change in the range from 20 mm to 150 mm. In this case the number of the energy switching channels change in the range from 1 to 5 (7 switching. channels were obtained in the experiment with 5 high-voltage electrodes).

Experimental Setup and Results.

Circuits with the inductive energy store and the electrically exploding wires (EEW) switch of current is used to produce overvoltages and to form voltage pulse of required shape and duration. In the direct action IGUR-3 accelerator [1] the mentioned scheme (see fig.1) is

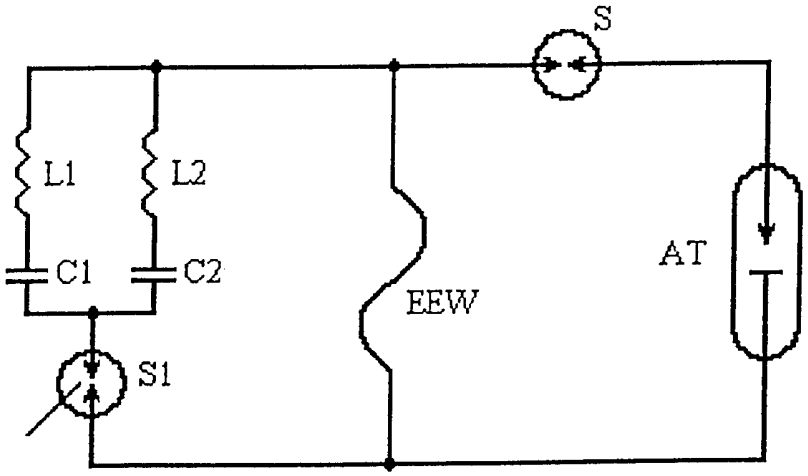

Fig.1
Simplified circuit of IGUR-3 accelerator
C1,C2-capasitor stores (Marx generator): L1,L2-inductive stores; EEW-exploding wires; AT-accelerator tube; S-sharpening discharged switch; S1-triggering discharged switch.

[1] The work was supported by ISTCprojekt #271

used for the production of voltages up to U = 7 MV with their subsequent switching to the

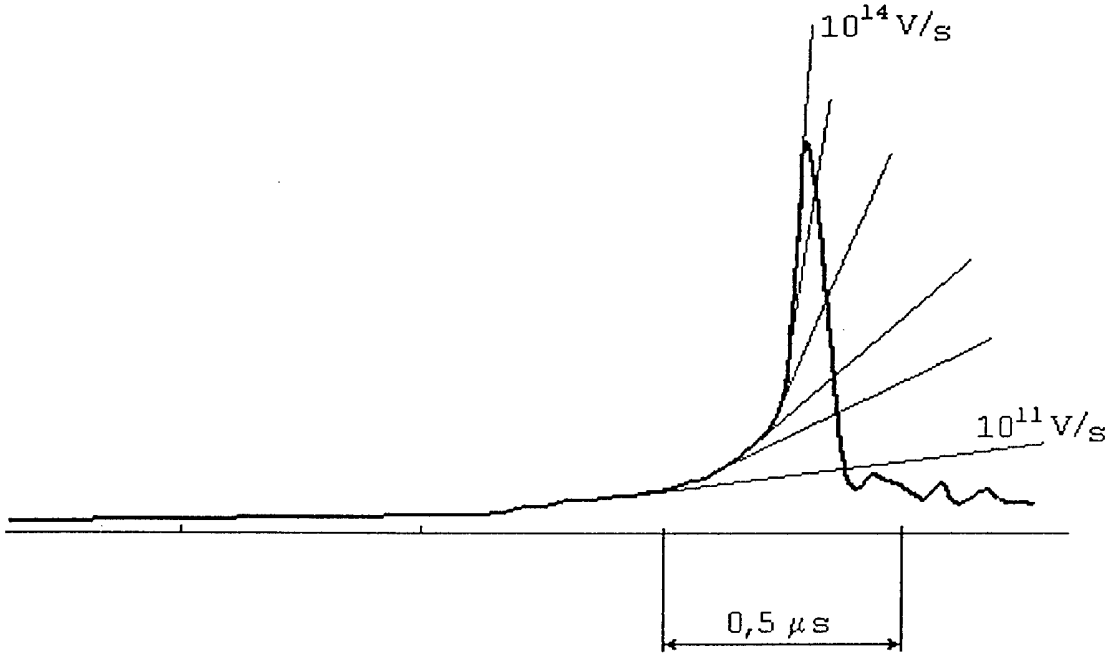

Fig. 2.
Typical voltage waveform for EEW of IGUR-3 accelerator.

acceleration tube (AT). The typical voltage waveform for EEW of IGUR-3 accelerator is represented in fig.2.

The characteristic peculiarity of such pulse is the presence of pre-pulse of ~ 1,7 μs duration

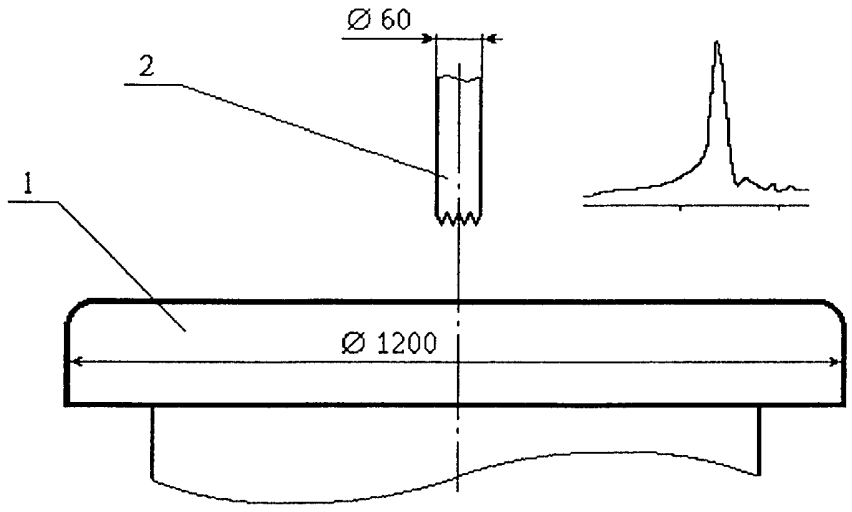

Fig. 3.
Schematic of the sharpenting discharged switch.
1-high-voltage electrode; 2-high-voltage flange of AT.

and main (working) pulse with variable rise velocity in the du/dt range between $1 \cdot 10^{11}$ and $1 \cdot 10^{14}$ V/s.

To switch the energy for loading at the IGUR-3 accelerator usage is made of the oil two-electrode sharpening discharged switch, which can operate, under the certain conditions, in the mode of "controlled" multiple channel switching of energy. The switch design is given in fig.3. High-voltage electrode consists of the cylinder 60 mm in diameter with the notch at its end. Second electrode is the plate high-voltage flange of acceleration tube. The electrodes are made of steel.

Conditions of the origin of the first discharge channels, the velocity of their propagation and the dynamics of overlapping by them of the oil discharge gap are essentially determined by the state of the surface of high-voltage electrode, by the value of electric field strength and by the voltage pulse rise velocity rise. Gap variation from 20 to 160 mm inside the switch allows its operation within the whole du/dt range. The increase of the gap in the switch leads to du/dt rise when switch comes into action and to realization of energy switching mode at a number of channels n>1. At increase of the gap (hp>30 mm) the velocity and the time of the development of primary channels don't permit to overlap the gap by one of them and the time of the process (t<3 ns) doesn't provide the conditions of primary channel transfer to leading one [2]. At significant du/dt rise, that leads to important increase of electric field strength at "the head" of the primary channels, the break-down along several channels takes place. With du/dt rise, a number of the energy switching channels in the switch gap increases. In fig.4 the dependence

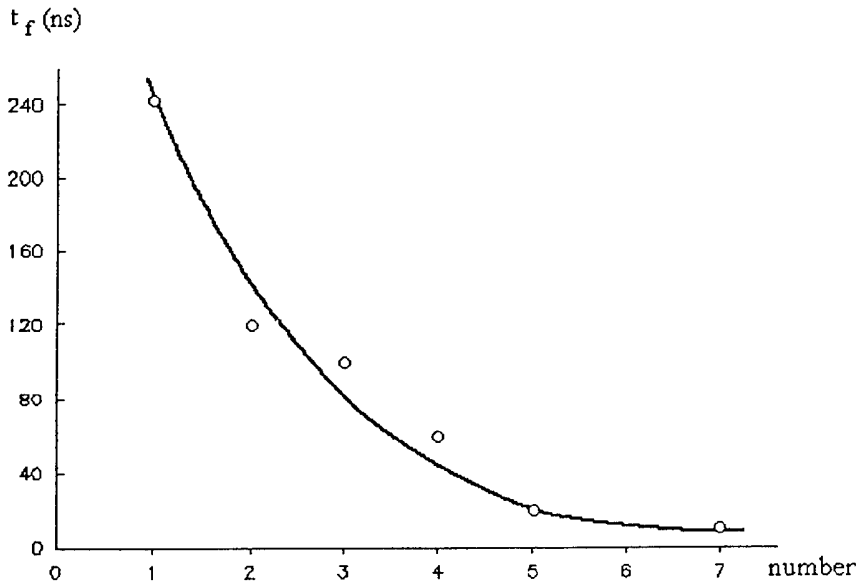

Fig. 4.
Voltage pulse front as a function of the number of switching channels.

of the front duration of voltage to AT on a number of switching channels is shown.

It is to note that the important role in the realization of multiple channel switching mode is played by the structure of high-voltage electrode surface. With polished electrode surface the mode of multiple channel switching isn't observed.

The conditions of the realization of "controlled" multiple channel switching mode are the following:

- voltage pulse with variable rise velocity (at $du/dt>10^{12}$ V/s) is passed to high-voltage electrode of the sharpening dischar ged switch;
- discharger switch has to come into action along all du/dt range of passed voltage pulse;
-multiple channel switching modes and the stability of the operation of pulse front reducing discharger in required mode is being achieved as a result of the forming of determined structure of high-voltage electrode surface.

Conclusion.

The proposed method of the pulses formation with the different front duration permites simply and without expense to control the pulses duration and one is widely used on IGUR-3 accelerator in carrying out of researches.

References

[1] V.S.Diyankov, A.I.Kormilitsyn, V.P.Kovalev Proc. of the 9th International Conference on High-Power Particle Beams, Washington, DC, May 25-29, (1992), p.455.
[2] V.Ya.Ushakov. Pulse Electric Break-Down of Liquid — Tomsk University Publication, Tomsk, (1975). (in Russian)

P-3-72

ENERGY CONCENTRATION ON S-300 PULSED POWER GENERATOR

Yu.Z. Bakshaev, A.S. Chernenko, V.D. Korolev, V.I. Mizhiritskiy, V.Y. Zazhivikhin

Russian Research Center "Kurchatov Institute" 123182 Moscow, Russia

Abstract.

Energy concentration in fast Z-pinch investigation experiments on 8-module 10 TW pulsed power S-300 generator (1.3 MV, 45 ns FWHM, 0.15 Ω) is realized by a 3-d vacuum energy concentrator. The concentrator was constructed on the basis of triplate MITLs connected parallelly at the central unit where Z-pinch is formed. At some start up experiments on 8-module installation version at 700 kV incident wave amplitude on concentrator for a gas puff load current of 4 MA with rise time of about 60 ns was obtained. The efficiency or current transfer from the concentrator input to the load for both a gas liner and a short-circuited case was practically the same.

Introduction.

For carrying out experiments on fast Z-pinch investigation in RRC "Kurchatov Institute" the 8-module pulsed power (10 TW) generator S-300 was constructed [1]. The S-300 Installation was designed for obtaining the output voltage pulse or 1.3 MV with 300 kJ of total energy at 0.15 Ω output impedance with 45 ns FWHM voltage pulse length.

In this paper we report experimental results on energy concentration at the output of S-300. Generator with a peak current of up to 4 MA with a rise time of 60 ns delivered to a liner load.

Experimental Results.

The energy transportation from the generator is accomplished by a vacuum 3-d energy concentrator (EC) [2]. A high-voltage pulse, created by the installation forming system, is transferred into the vacuum energy concentrator through a 1-m diameter insulator stack assembly (Fig. 1). The EC was constructed on the base of self magnetically - insulated transmission lines (MITLs). It consists of 16 homogeneous triplate MITLs of 20 cm length with a strip width of 8 cm connected electrically in parallel. At the EC input they are connected to the water pulse forming transmission lines, whereas on the EC output to 8 nonhomogeneous triplate MITLs (each homogeneous pair of MITLs is connected to one nonhomogeneous line. All these three lines are situated in the same vertical plane). Nonhomogeneous MITLs were connected to the central unit, where load is mounted. The central unit consist of two coaxial cylinders. Outside cylinder of 80 mm i.d. is a return current conductor whereas the inner one serves as a Z-pinch valve holder. The MITL's gap is equal to 1 cm. The total inductance of the output electrical circuit was ≈ 10 nH.

Optimization of EC was carried out on the basis of a model described the nonstationary processes in MITLs [3]. For calculation of S-300 output parameters the telegraph equations were used. At numerical simulation of wave processes in a MITL an

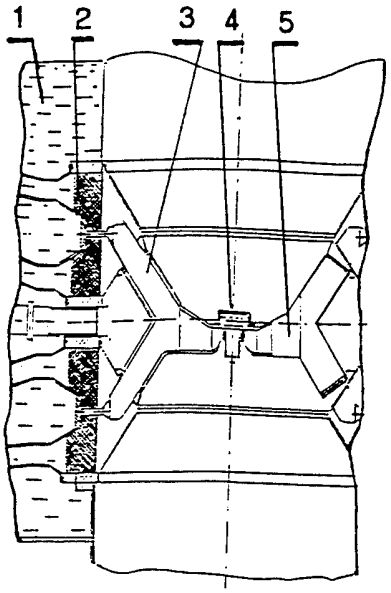

Fig. 1 The S-300 Installation output unit

1 - water transmission lines,
2 - insulator
3 - homogeneous MITLs
4 - gas valve
5 - nonhomogeneous MITLs.

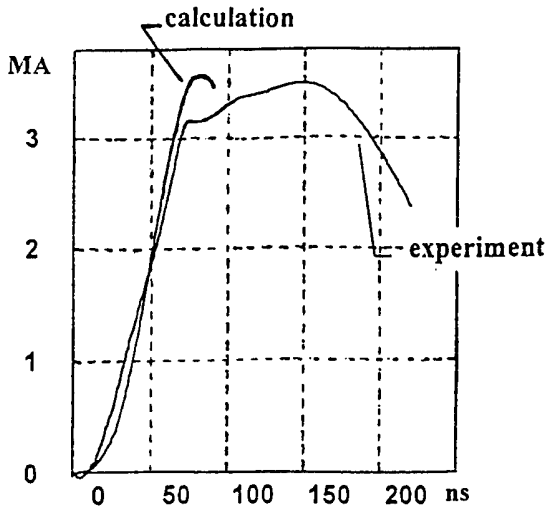

Fig. 2 Dependences of calculated and experimental currents vs time.

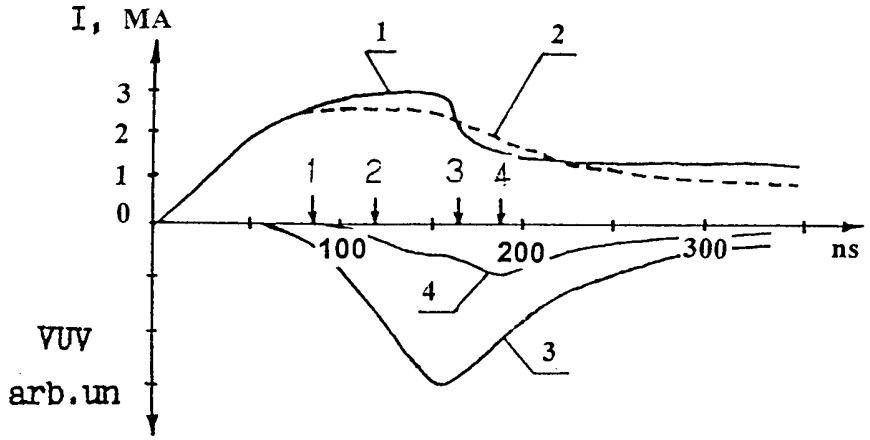

Fig.3 Experimental dependences or input current I_{in} (1) and output current I_{out} (2) vs time and VUV-XR diode unfiltered (3) and filtered (4) signals and visible light frames (10 ns exposures of the imploding plasma loads.

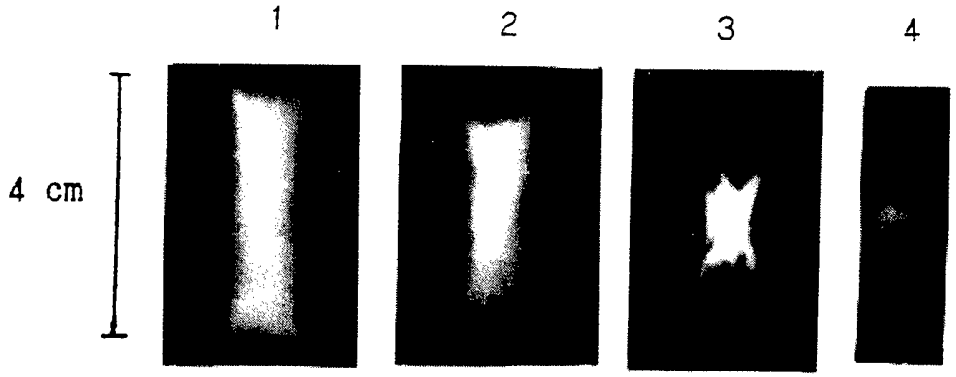

Fig. 4 10-ns time frames

electron leakage non-linear current was accounted. The liner motion was described by 0-D equation approximation. It is proposed that S-300 Installation consists of 8 water pulse forming lines which via gas switches were connected to a pair or water pulse transmission line. The output transmission lines are connected to the same electrode. At calculations each forming line was closed in its fixed moment. This permits to model the S-300 modules operation time spread.

The EC input and output current was measured using magnetic loops attached to the grounded electrodes of the homogeneous MITLs and to the load's outside cylinder. The output voltage was measured with a resistive divider. In experiments on S-300 Installation in 8-module version at 700 kV of incident wave amplitude for short-circuited EC regime up to 4 MA output current with rise time of about 60 ns was obtained (see Fig. 2). The efficiency of current transfer on EC to the inductive load ($L \leq 1$ nH) was more then 85 %. It should be pointed out that the measured current pulse length exceeds the calculated one. This can be explained that in numerical calculations are not fully accounted for the real processes of pulse forming and liner compression dynamics.

Fig. 3 presents some typical oscilloscope traces of the output current, VUV-XR diode signals and 6-frame image-converter photographs, obtained in experiments on gas implosion stability. In these investigations the current reached 4 MA with rise time or about 60 ns. The output voltage at the end of non-homogeneous MITLs exceeded 500 kV. In experiments on the gas liner stability investigation the efficiency of current transfer through the EC depends weakly on liner dynamics and was (85 ± 8) %. The divergence of input and output current tails was observed. The output current is more delayed. It can be explained by VUV radiation illumination or magnetic loops and EC's electrodes near the load as well. Several hundred joules of radiated energy in the VUV-range spectrum with the average 60 eV quanta energy will be enough for plasma formation on MITL's electrodes and loops [4].

Conclusions.

The 3-d vacuum energy S-300 Installation concentrator have been developed for experiments on gas puff liner implosions. This system is able to efficiently (>85 %) transport high peak (4 MA), fast risetime (60 ns) currents to the loads. Experimentally obtained current peak values are close to the calculated predictions.

References

[1] Rudakov L.I.: Kurchatov Institute Program of Soft X-ray Flash Generation for ICF study on the Base of Pulse Power Application. Seminar C.E.A./DAM - INSTITUTE KURCHATOV. Z-pinches et trés hautes pulssanges pulsées, Laboratoire de Physique des Milieux Ionisés. École Polytechnique (1993), 9

[2] Gordeev E.M., Korolev V.D., Liksonov V.I., Zazhivikhin V.V.: Proc. of XVI Intern. Symp. on Discharges Gas and Electrical Insulation in Vacuum. 23-30 May, 1994, Moscow-St. Peterburg, Russia. SPIE v. 2259 (1994), p. 283

[3] Bulan V.V., Zazhivikhin V.V.: Proc. of 8th Conf. on High Particle Beams, Novosibirsk, USSR, v. 2 (1991), p. 990.

[4] Gordeev E.M., Zazhivikhin V.V., Korolev V.D. et al.: Plasma Phys. v. 19 (9), (1993), p.574.

HIGH VOLTAGE NANOSECOND GENERATOR WITH PULSE REPETITION RATE OF UP TO 1,000 P.P.S.

V. P. Gubanov, S. D. Korovin, and A. S. Stepchenko

High Current Electronics Institute, Tomsk, RUSSIA

A compact high voltage nanosecond generator is described with pulse repetition rate of up to 1,000 p.p.s.. The generator includes a 30-Ohm coaxial forming line charged by a built-in Tesla transformer with high coupling coefficient, and a high voltage (N_2) gas gap switch with gas blowing between the electrodes. The maximum forming line charge voltage is 450 kV, the pulse duration is ~ 4 ns and its amplitude for a matched load is up to 200 kV.

The aim of present work was an attempt to create a compact high voltage nanosecond generator operating at possibly higher pulse repetition rate with high amplitude stability kept. Such generators [1-3] could be applied to create powerful sources of ultrawide band electromagnetic radiation [4], nanosecond microwave pulses [5], etc.

As a basis, a monopolar pulse generator diagram was chosen, with coaxial forming line and a Tesla transformer with high coupling coefficient [2]. The design of the generator is given in Fig. 1. The forming line (1) with the built-in Tesla transformer (5,6,7) is placed in a cylindrical case filled with transformer oil. The open ferromagnetic core (5) of the transformer serves simultaneously as the outer and the inner conductor of forming line. The primary winding (6) consists of single turn. The conic secondary winding (7) is placed on a cartoon framework and has 1,200 turns. The supporting insulators (4) made of Lucite provide high rigidity and electric strength of forming line.

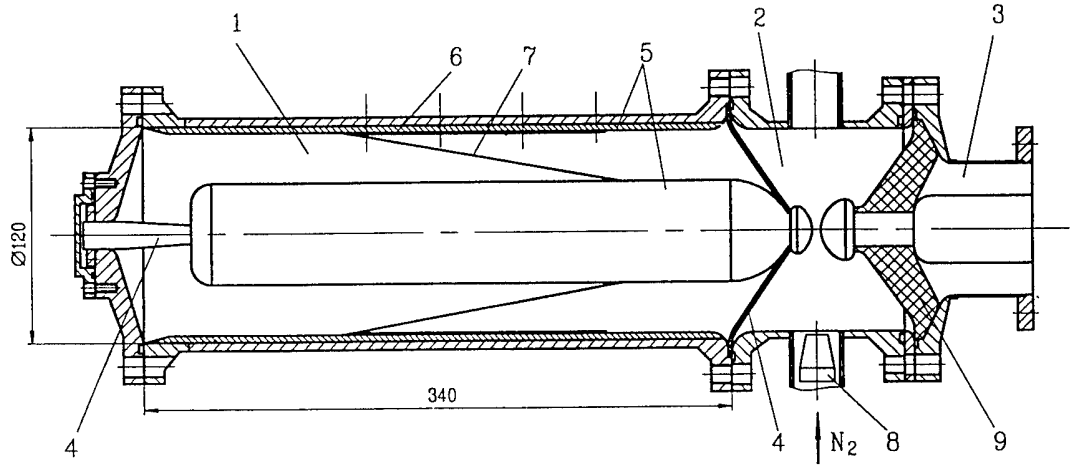

Fig. 1. Design of high voltage generator

The parameters of forming line are listed in Table 1. To discharge the forming line, a two-electrode gas switch (2) is used filled with nitrogen. The breakdown voltage (U_k) is varied by changing of gas pressure (0÷30 Atm) and electrode gap (0.5÷1.2 cm). At repetition rate over 10 p.p.s., the gas is blown across the gap. To form the gas flow, the collimator (8) is

used. The transmitting line (3) serves to deliver the generated high voltage pulse to the load. The active load was placed at the output of transmitting line to withdraw the energy from the system.

Length	34 cm
Outer diameter	12 cm
Insulation	transformer oil
Electric length	3,5 ns
Wave impedance	30 Ohm
Capacitance	70 pF
Maximum charge voltage - U_2^{max}	450 kV
Charge voltage at 200 p.p.s.	350 kV
Charging time for U_2^{max}	6 mks
Efficiency of Tesla transformer	50 %

Table 1.

One of the merits of the design is that rectified power network voltage is used in the primary of Tesla transformer without intermediate energy transformation. This allows to use thyristor switches in the primary circuit of store which possess extended live span and therefore provide operation at high repetition rate.

The power source is the rectifier of network voltage AC 220 V. Since the coupling coefficient between the contours of Tesla transformer is high ($k \sim 1$), the voltage across the forming line (U_2) follows the law [6]:

$$U_2 \approx U_1 \times \frac{N_2}{N_1} \times \frac{\alpha}{\alpha+1} \times [1-\cos(\pi \frac{t}{t_{ch}})]$$

where U_1-is the primary capacitor voltage, N_1, N_2 - are numbers of turns in the primary and secondary windings of Tesla transformer, respectively, α is the relative destining of contour self frequencies; t_{ch} is the moment of time at which $U_2 \approx U_2^{max}$. The high voltage gas switch is always tuned so that its breakdown occurs at $t_0 < t_{ch}$, and, consequently, $U_k < U_2^{max}$. This is necessary to avoid non-breakdowns of the switch and, consequently, the possibility of breakdown of forming line due to prolonged application of electric fields to its insulation. The energy is recuperated through the inductance after the gas switch operation. The time required for one operation cycle of generator is $\Delta t \sim 400$ mks.

In the experiments, the shape of generated high voltage pulses, their amplitude U_{max} and pulse-to-pulse instability σ have been monitored. In Fig. 2, typical trace of voltage pulse is shown obtained by high speed oscilloscope. The maximum voltage U_{max} was measured with the use of peak voltmeter [7]. The value σ has been determined as the relative mean-square deviation of U_{max} around its average. Usually, about 1000 consequent pulses have been used for averaging. In course of experiments, live span tests of generator has been made as well.

Measurements of σ for various blowing speed in dependence on pulse repetition rate (f_r) have been made in a wide range of gas pressure in the switch (P). The shapes of curves $\sigma(f_r)$ show that, at a given gas velocity, a limit value $f_{cr}(V)$ of repetition rate exists above that the instability rises steeply. Typical distributions of U_{max} show that, at $f > f_{cr}$ (2) the possibility

of switch breakdown at lower strength of electric field increases because the gas with decreased electric strength does not leave the discharge gap in time. In the experiments done, f_{cr} varied from 10^2 up to 10^3 p.p.s..

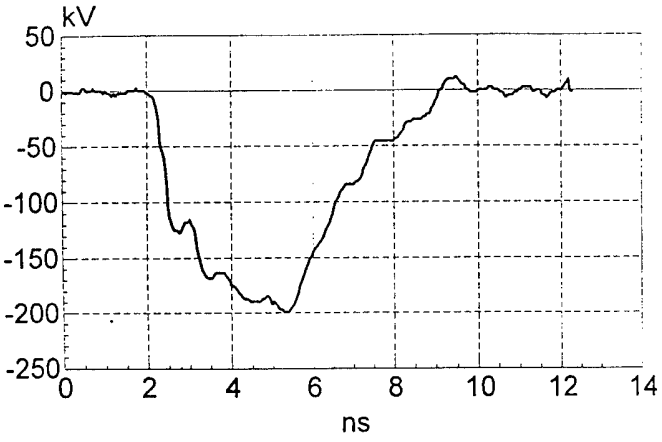

Fig. 2. Voltage pulse trase

The limit repetition rate of gas switch operation f_{cr} at a given gas velocity depends on its geometry and rises with decrease of electrode radii. The maximum gas velocity in the gap was not measured but is estimated to the pulses tend to be more unstable at higher gas pressure. As the experiments showed, significant change in instability occurs in the diapason of electric field in the gap from 300 to 500 kV/cm. Possibly, this is caused by effects of explosive emission excited on electrode surfaces on breakdown process. [9].

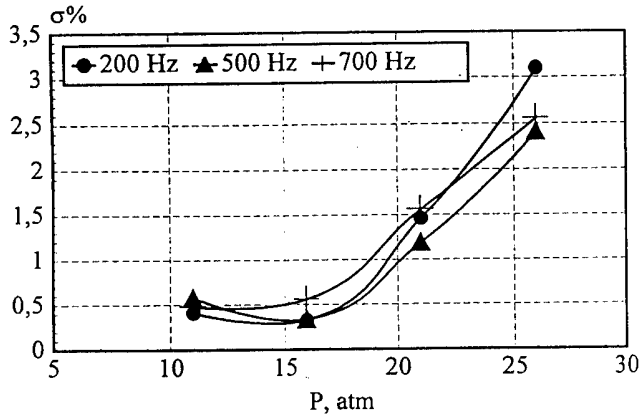

Fig. 3. Dependence of high voltage pulse amplitude instability on gas pressure, at optimum gas blowing speed

High electric strength of construction allowed to charge the forming line to ~450 kV at repetition rate of ~ 10 p.p.s.. The stored energy therewith was ~ 7 J, and the power in the load was ~1.5 GW. At repetition rate exceeding 10 p.p.s., the elements of primary circuit have been cooled as well as the gas within the switch, and the maximum charge voltage of forming line was decreased. The trials showed that the generator equipped by cooling system is able of continuous operation at charge voltage of ~350 kV and pulse repetition rate ~200 p.p.s.. In this case, the power of pulse is $P_p = U^2/R \sim 1$ GW, and the average power of generated pulses is $P_{av} \sim P_p \times \tau \times f \sim 1$ kW where τ is the pulse duration and R is the load resistance.

Since the forming line with the built-in Tesla transformer was not cooled, its heating took place in case of increased pulse repetition rate and prolonged operation. The maximum acceptable temperature at which no significant changes in mechanical strength of construction occur is estimated to 60°C. If the average power of pulses is

$$P_{av} > \frac{\eta}{1-\eta} \times \chi \times \Delta T_{cr},$$

(where χ is the heat conductivity of forming line, η - forming line charging efficiency), than the existence of temperature limitation leads to limitation of continuous work time of generator (Δt):

$$\Delta t \leq \frac{C}{\chi} \times \ln[1 - \frac{\eta}{1-\eta}(\chi \times \Delta T_{cr}/P_{av})]^{-1}$$

Here, C is the heat capacity of forming line, (C/χ) is the typical time to reach the steady-state regime. In our case, (C/χ) ~10 min, ΔT_{cr} ~40°C, η~0,5. The critical level of average power of pulses is $P_{av}^{cr} \sim \chi \times \Delta T_{cr}$ ~ 1 kW. At pulse repetition rate 1000 p.p.s. and $P_{av} \sim P_{av}^{cr}$, the maximum voltage in the load was ~90 kV. For P_{av} ~2 kW , U_{max} was ~120 kV, while the time to reach the maximum acceptable temperature was ~5 min. Continuous operation of generator at $P_{av} > P_{av}^{cr}$ can be realized by inputting additional cooling elements in the design.

REFERENCES

[1] *G.A. Mesyats.* Generation of powerful nanosecond pulses. Sovetskoye Radio, Moscow, 1974, 256 p.

[2] *A.S. Eltchaninov, F.Ya. Zagulov, S.D. Korovin, et al.* Relativistic high frequency electronics. Gorky, IAP AS USSR, 1981, p. 5.

[3] *V.V. Kremnev, G.A. Mesyats.* Methods of multiplication and transformation of pulses in high current electronics. Nauka, Novosibirsk, 1987, 226 p.

[4] *V.P. Gubanov, S.D. Korovin, I.V. Pegel, et al.* Generation of powerful electromagnetic pulses, Lett. Sov. J. Tech. Phys. 1994, v. 20, N 14, p. 89.

[5] *Roitman A.M., Korovin S.D., Polevin S.D., Rostov V.V., Moreland L.D. Schamiloglu E.* A high power microwave generator based on a relativistic BWO. Proc. SPIE's Int. Symp. on Optical Science Engineering and Instrumentation, 40th Annual Meeting San Diego, 1995, SPIE, Vol. 2557, pp. 422-433.

[6] *S.D. Korovin.* Tesla transformer in high current periodically-pulsed accelerators. Preprint N 47, TF SD AS USSR, 1988, 38 p.

[7] *V.P. Gubanov.* Peak voltmeter, Pribory i tehnika eksperimenta (Sov.), 1985, N 2, p. 137.

[8] *A.S. Eltchaninov, F.Ya. Zagulov, S.D. Korovin, G.A. Mesyats.* Electron beam accelerator with high pulse recurrence frequency, Proc. Of 3-rd Intern. Conf. On High Power Electron and Ion Beams. Novosibirsk, 1979, Vol. 1, p. 191-197.

[9] Yu.D. Korolev, G. A. Mesyats. Field emission and explosive emission processes in gas discharge. Nauka, Novosibirsk, 1982, 356 p.

High - Voltage many-pulses generator with inductive energy store and fuse.

V.P.Kovalev, V.S.Diyankov, A.I.Kormilitsin, B.N.Lavrentjev.

Russian Federal Nuclear Center - Institute of technical Physics.
456770 Snezhinsk, Chelyabinsk region, box 245. Russia

Abstract

The high-voltage generator with inductive energy store and fuses as opening switch that generated series of powerful pulses is considered. It differs from an ordinary generator with inductive store by different cross-section of series copper wires. The parameters of wires are chose from the empirical relations. The generation principle has been tested on the two high-voltage generators with characteristic impedance 2.2 ohm, 4 ohm and with output voltages 140 kV; 420 kV, respectively. Copper wires of diameter 0.1...0.23 mm have been used. Series from 2 to 5 pulses of 100...300 ns duration, 400...1000 kV amplitude and 1 - 10 GW power have been obtained. Pulses can be both the same and different.

Two successive bremsstrahlung radiation pulses have been obtained on devices EMIR-M and IGUR-3.

Series power megavolt pulses can be generated with power more 10^{11} W, pulses duration 10^{-3} ...10^{-6} s and time interval between them 10^{-7} ...10^{-5} s.

Introduction

The generator occupy intermediate position between mono - pulse generators and repetitive power generators. It creates series of powerful pulses $> 10^{10}$ W, when Marx generator or capacitor store is used as initial energy source. It differs from ordinary generator with inductive store by different cross - section of series copper wires.

Parameters of exploding wires are defined from relationships:

$$\sum_{i=1}^{n} K_i \cdot \rho \le \sum_{i=1}^{n} R_i < 2 \cdot \rho \qquad (1)$$

$$S_1 < S_2 < \ldots < S_i \le W/(\xi \cdot \rho), \qquad (2)$$

where R_L - initial resistance of i - series wires (ohm); n - amount of series wires;
W - power of store (J); ξ - matter constant (for copper $\xi = 2 \cdot 10^9$ $A^2/cm^4 \cdot s$);
s - cross-section of exploding wires (cm^2); ρ - characteristic impedance, $K_i \ge 0.03$.

Experimental configuration and results.

Generator has been investigated on two Marx generators with voltage U = 420 kV and U_1 = 140 kV and characteristic impedance 2.2 ohm and 4.4 ohm, respectively.

Scheme of experimental setup is showed on figure 1. Resistor divider and Rogovsky coil have been used for the measurement voltage and current. The generation principle has been investigated on two Marx generators with loads 13.5 ohm, 18 ohm, 27 ohm, 53 ohm, 106 ohm. Fig. 2 shows voltage pulse amplitudes as function of the load for series from three pulses. Wires with diameters 0.25 mm, 0.29 mm, 0.33 mm and lengths 0.5 m, 0.7 m, 0.9 m, respectively, have been used with 420 kV Marx generator. Such wire combination is marked as (∅ 0.25 mm × 0.5 m) + (∅ 0.29mm × 0.7 m) + (∅ 0.33 mm × 0.9 m). One can see, that strong decrease of pulse amplitudes is observed when load is less 50 ohm. Fig. 3 shows voltage pulse amplitudes as function of the load for series from four pulses with wire parameters (∅ 0.23 mm × 0.2 m) + (∅ 0.27 mm ×

0.2 m) + (∅ 0.29 mm × 0.25 m) + (∅ 0.31 mm × 0.35 m). Voltage pulses have equal amplitudes, therefore they flow together for equal loads. Analogous results have been turned in other combinations of diameter and length wires.

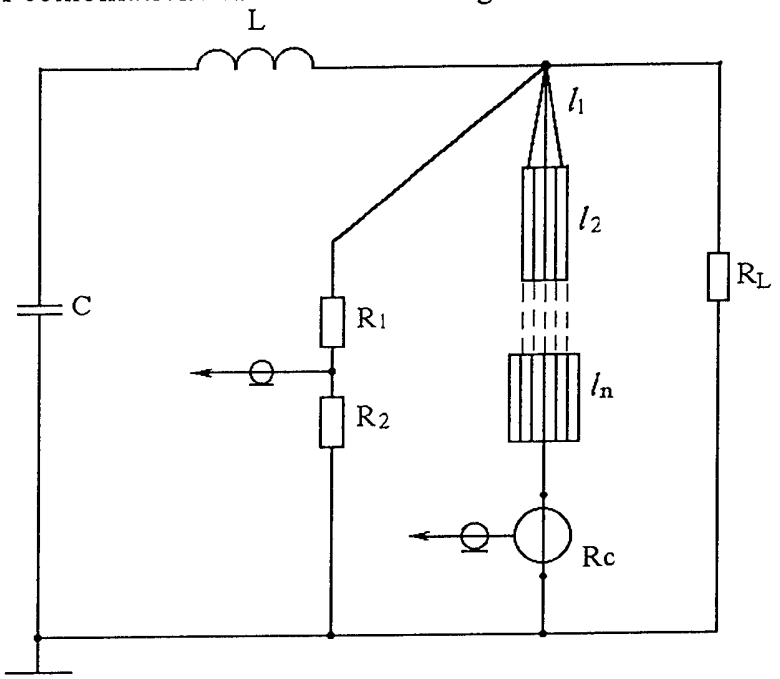

Fig. 1.
C - capacitor store; L - inductive store; (l_1 - l_n) - exploding wires; Rc - Rogovsky coil; R_L - load; (R_1 - R_2) - voltage divider.

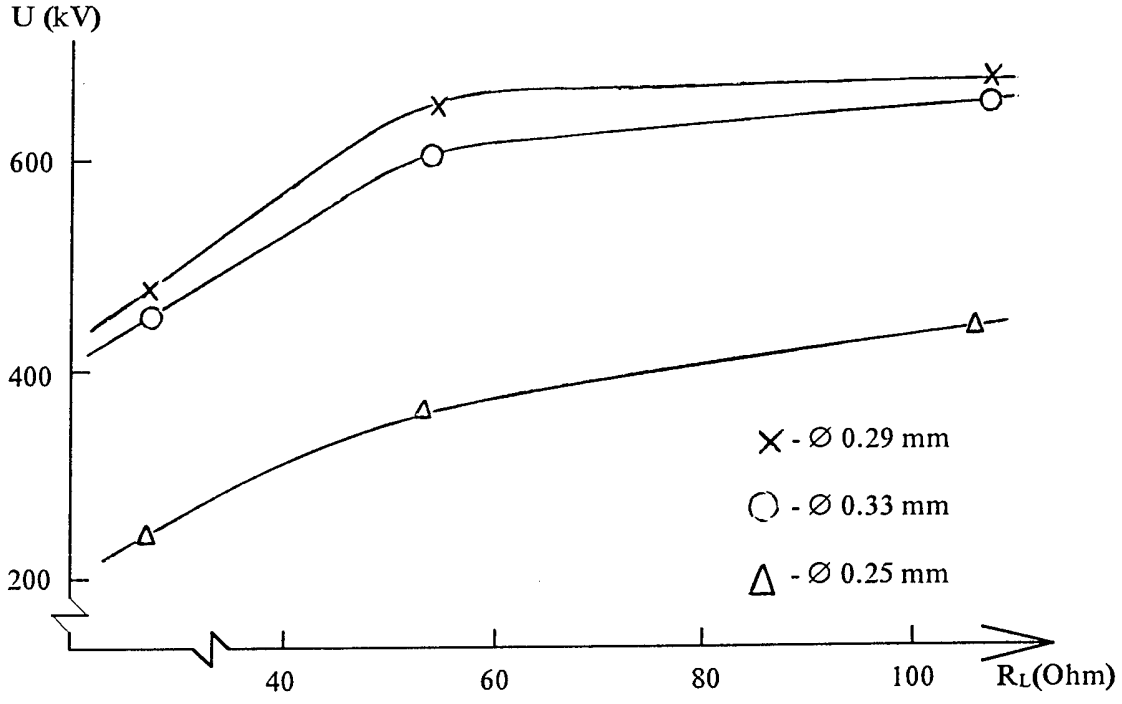

Fig. 2.
The voltage pulse amplitude as function of the load impedance under exploding wires with parameters (∅ 0.25 mm × 0.5 m)+(∅ 0.29 mm × 0.7 m)+(∅ 0.33 mm × 0.9 m).

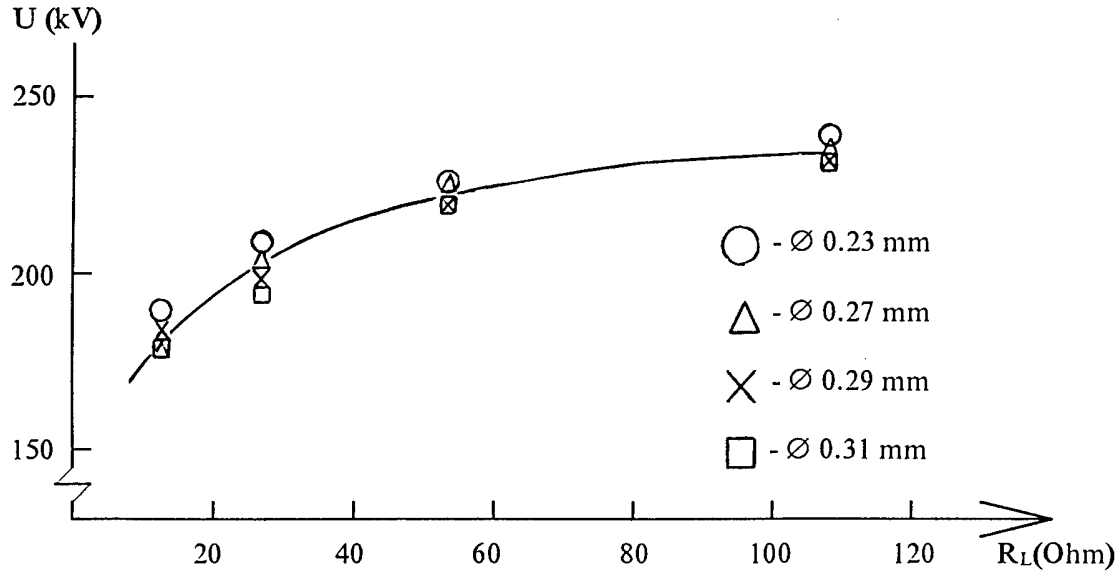

Fig. 3.
The voltage pulse amplitude as function of load impedance under exploding wires with parameters (∅ 0.23 mm × 0.2 m)+(∅ 0.27 mm × 0.2 m)+(∅ 0.29 mm × 0.25 m)+(∅ 0.31 × 0.35 m).

Fig. 5 (a, b) shows series from 3...4 high voltage pulses and exploding wires currents. One can see, that various durations, amplitudes, shapes of series pulses could be obtained.

The generation principle is tested also on devices EMIR-M [1] and IGUR-3 [2]. Two successive bremsstrahlung radiation pulses were obtained an device EMIR-M (fig. 4). Dose rate was $2...3 \cdot 10^8$ R/s on 1 meter from output window in every pulse. Two bremsstrahlung radiation pulses have been obtained on the IGUR-3 with duration 50...200 ns and dose rate about 10^{10} R/s near anode with time interval from 0.65 μs to 1.7 μs.

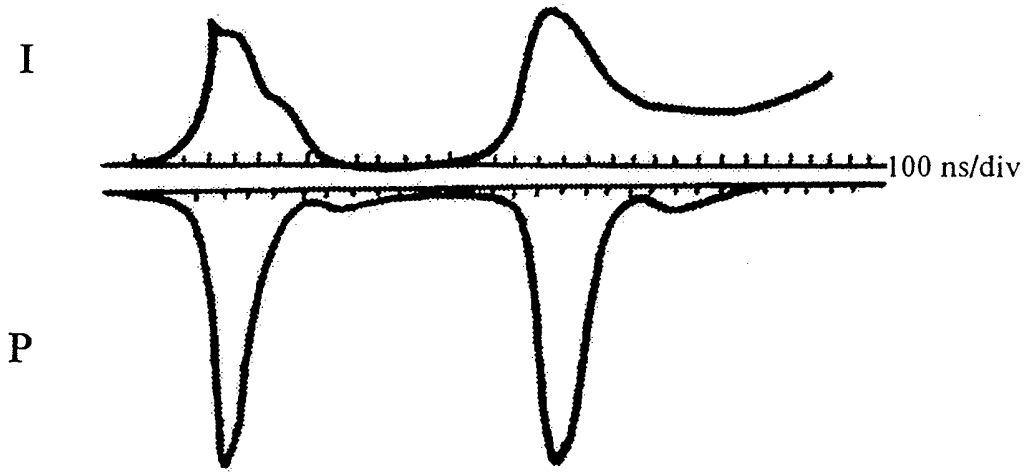

Fig. 4.
Scale M_I = 1.3 kA/mm; P = $3 \cdot 10^8$ R/s;

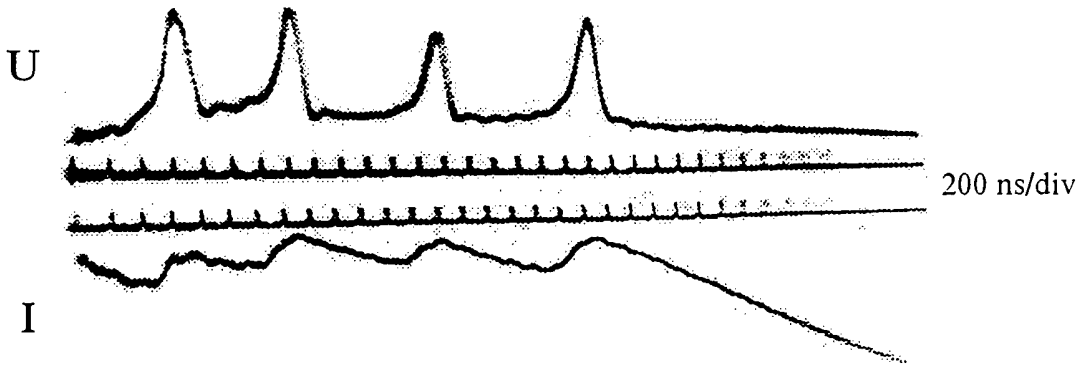

a) Scale: M_U= 38.6 kV/mm , M_I= 1.6 kA/mm.

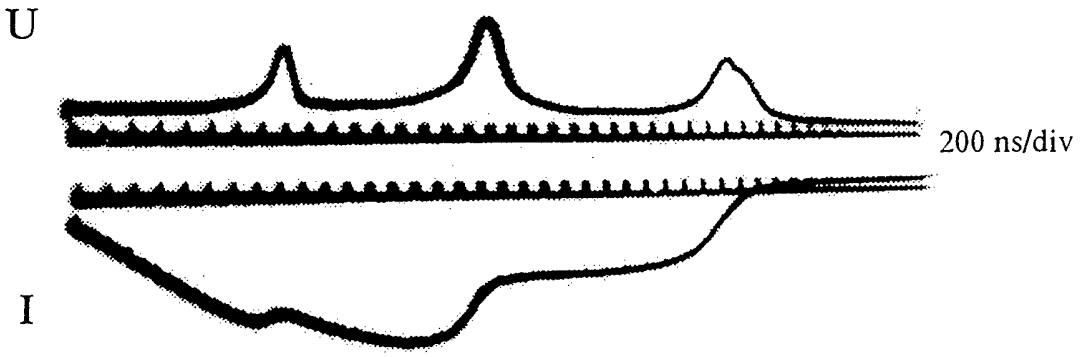

b) Scale: M_U= 55.2 kV/mm , M_I= 2.14 kA/mm.

Fig. 5.

Conclusion.

The generation principle had been investigated on two Marx generators and had been tested an working installations IGUR-3 and EMIR-M. It is showed efficiency with loads of type the vacuum diode and the constant resistor. Series high voltage pulses can be generated with power more 10^{10} W, duration 10^{-7} ...10^{-6} s and time interval between them 10^{-7}...10^{-5} s.

References

[1] Diyankov V.S., Lavrentyev B.N., et. al. Proc. of the 10th International Conference on High - Power Particle Beams. San Diego. Ca. (1994), p. 371.

[2] Diyankov V.S., Kovalev V.P., Kormilitsin A.I., Proc. of the 9th International Conference on High - Power Particle Beams, DC. May 25 - 29, (1992), p.455.

FUNCTIONING OF HIGH-T_C BULK SUPERCONDUCTOR LENSES (SUPERTRONS) FOR INTENSE ELECTRON BEAMS

H. Matsuzawa, A. Matsushita, Y. Ueda, H. Matsubara, and S. Suganomata

Faculty of Engineering, Yamanashi University, Kofu 400, Japan

Abstract

Self-magnetic fields of intense electron beams of nanosecond order (~340 keV, ~1 kA, ~10 ns) diffused through the walls of high-T_C Bi-based sintered superconductor tubes (Supertrons) with a velocity of ~10^4 m/s. The reaction to this slow viscous diffusion confines the electron beams to the bores of the tubes. The velocity will be one of criteria for applying sintered superconductors to high-frequency devices. The magnetic fields that were confined to the bores increased with lowering operation temperatures, being about 200 G at 90 K for a 3-mm-thick wall tube.

Introduction

Since the discovery of the high-T_C superconductor, we have proposed and developed a novel lens (Supertron) for charged particle beams. Despite many successful experimental results [1] including a high-T_C superconductor wiggler for free-electron lasers and an electron beam guide for induction linear accelerators, the principle of Supertrons was not confirmed and was expected to be as follows: When intense charged particle beams propagate through the bores of superconducting tubes (Supertrons), the self-magnetic fields of the beams will be confined to the bores because of the Meissner effect. The fields confined will be enhanced and accordingly focus the beams themselves. The tubes guid the beams along their axes even when the axes are curved [1] as laser light travels along optical fibers. In this paper, we tried to observe the magnetic fields that would diffuse through superconducting walls to know whether sintered superconductor tubes confine the self-magnetic fields of electron beams to the bores. The experimental results revealed that the magnetic fields diffuse through the walls with a slow diffusion velocity of ~10^4 m/s. The reaction to this slow velocity confines the fields and hence the electron beams to the bores of the tubes. These results confirm Roth's simulated results [2] that Supertrons will confine electron beams even when the self-magnetic fields diffuse through the walls of superconducting tubes.

Experimental apparatus

Figure 1 shows the experimental setup used. We prepared two Bi-based sintered superconductor lenses (critical temperature T_C = ~103 K),

which had 1.5- and 3-mm thick wall and hence inner diameters of 20 and 17 mm, respectively, with total axial lengths of 55 mm. The lenses, which were composed of four pipes, were glued onto the inner surface of a copper heat sink with electrically conducting silver-based epoxy resin. The heat sink was mounted on the top of cold head of a refrigerator. The sink and hence lenses played a role of anode of the beam diode which consisted of the cathode and the lens. Intense electron beams (~340 keV, ~1 kA, ~10 ns) were field emitted from the cathode and accelerated toward the lens. After being focused with the lens, the electron beams were detected with a Faraday cup which was placed downstream of a titanium foil of 20 μm thickness to absorb low-energy plasma electrons. To detect the magnetic fields that diffuse through the tube walls, two Rogowski coils of self-integrating type were mounted outside the lens tubes. Each coil detected such magnetic fields that propagated through a 1.5-mm-wide gap fabricated in the copper heat sink. Neon gases of 0.1 Torr order were introduced into the diode region and into the bores of the tubes to realize space-charge neutralization. Neon gas was chosen because it has the lowest thermal conductivity among the gases that do not liquefy at liquid nitrogen temperature.

Experimental results

Figure 2 shows the temporal behaviors of magnetic fields detected with the Rogowski coils. The first and second peaks correspond to the signals from the entrance and exit coils, respectively. The second peaks were delayed behind the first peaks by 410 ns. The tails of the waveforms go over the horizontal zero level because of excessively low values of the electrical resistors used for integrating the output of the coils. The long tails of the waveforms were caused by the after-glow produced with collisions between neon gases and electron beams. From Fig. 2, the diffusion velocities of magnetic fields through sintered superconducting walls were estimated to be ~10^4 m/s [3].

Figures 3 (a) and (b) shows the temperature dependences of electron currents detected with the Faraday cup and of magnetic fields detected with the Rogowski coils, for 1.5- and 3-mm-thick wall tubes. The Faraday-cup-detected currents were almost constant below the T_C, because all the electron currents that entered the tubes were focused for that temperature range and the current beams were focused thinner with decreasing temperatures [4]. We can say thus that the magnetic fields incident on the inner surface of the tube walls are constant below the T_C. On the contrary, the coil-detected magnetic fields decreased when the tubes were cooled below the T_C. This is because the superconducting tube walls shielded the self-magnetic fields of the electron beams. Therefore, the vertical differences between the broken lines originating from the top data for the Rogowski coils at T_C and each

datapoint mean the amplitudes of the magnetic fields shielded with the walls. These shielded fields are plotted in Fig. 4 as a function of operation temperatures. The 3-mm-thick wall tube shielded higher magnetic fields than the 1.5-mm thick tube.

Conclusions

Supertrons were revealed to function effectively by temporally confining the self-magnetic fields of electron currents to the bores of the superconducting tubes. The confining force results from a reaction to the slow, viscous diffusion of the self-magnetic fields with a velocity of ~10^4 m/s. The fields confined at 90 K were ~200 G for a 3-mm thick wall. Static magnetic fields, however, diffuse through grain boundaries of sintered superconductors. Therefore, for confining static fields, instead, we should use melt-processed materials that have little grain boundaries.

[1] For a review, see Matsuzawa, H., : J. Appl. Phys., 74 (1993) R111
[2] Roth, P., : J. Appl. Phys., 77 (1995) 4914
[3] Matsuzawa, H., Matsushita, A., Hayashi, Y., Suganomata, S., : Appl. Phys. Lett., 68 (1996) 2150
[4] Matsuzawa, H., Kobayashi, H., Mochizuki, H., Yoneyama, N., et al., : Jpn. J. Appl. Phys., 33 (1994) 2526

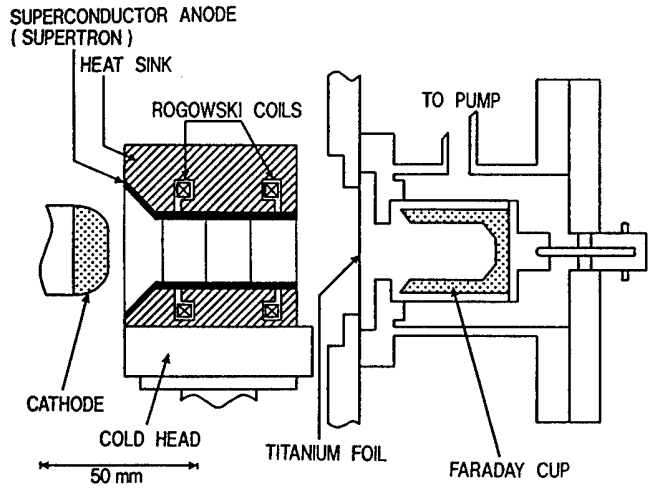

Fig. 1. Experimental apparatus.

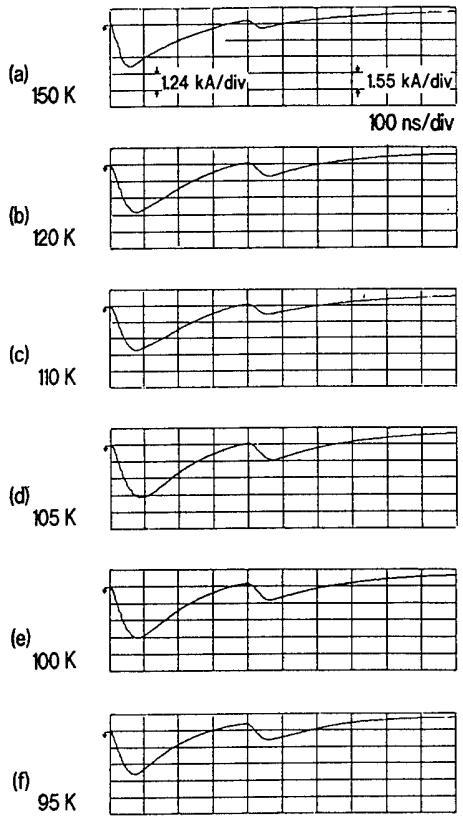

Fig. 2. Temporal behaviors of magnetic fields detected with Rogowski coils. 1st peaks: entrance coil. 2nd peaks: exit coil.

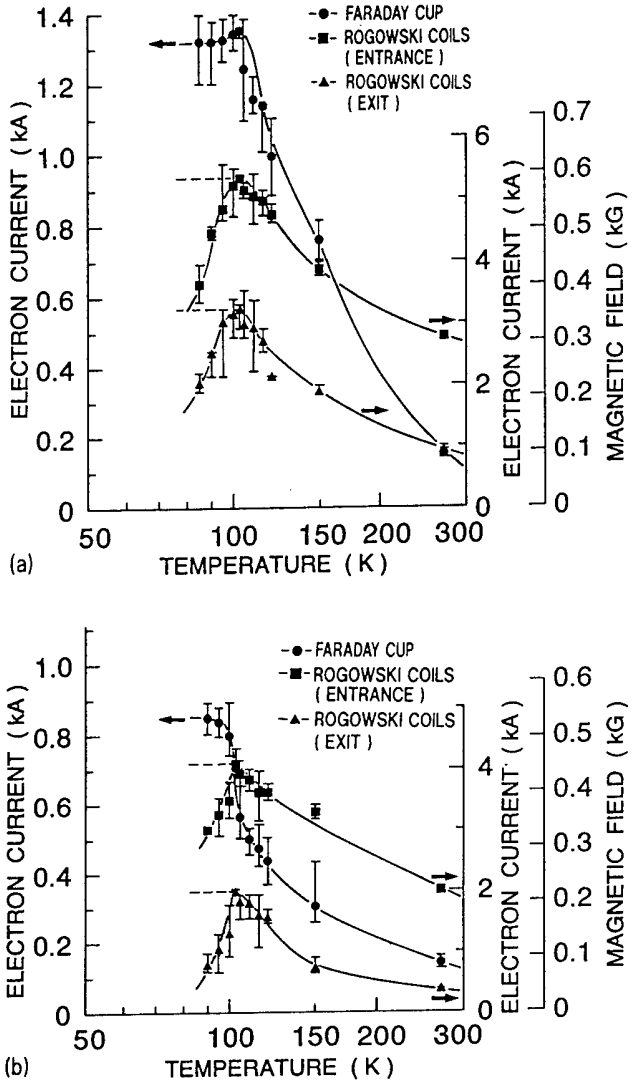

Fig. 3. Temperature dependences of electron currents detected with Faraday cup and of magnetic fields detected with Rogowski coils. (a) 1.5-mm- and (b) 3-mm-thick wall tubes.

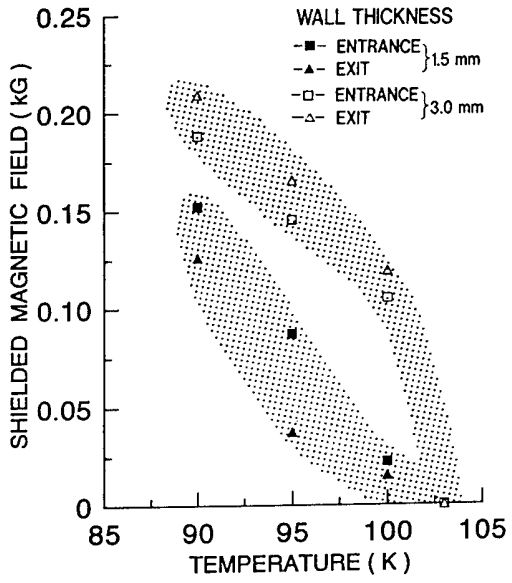

Fig. 4. Magnetic fields confined to tube bores *vs.* operation temperatures.

SYNCHRONIZATION OF 67MJ, 50KV PULSED POWER CAPACITOR BANKS OPERATION

V.G.Besuglov, I.V.Galakhov, A.S.Gasheev, I.A.Grusin, S.N.Gudov, G.A.Kirillov, V.M.Murugov, V.A.Osin, and V.N.Petrakov

RFNC - VNIIEF, Sarov (Arzamas - 16), Russia

Abstract

The paper describes a sync system for the 67MJ, 50kV pulse power capacitor bank of the ISKRA-5 facility's iodine laser. This system is to provide synchronism (a jitter within 0.3μs) in firing of 665 spark gaps, 476 electric discharge pumping sources and 513 flashlamps. The sync system is designed as series-voltage pulse generators to be fired at specifically predetermined times. Also, the system ensures switching of spark gaps in a sequence as required by the experiment and reliable operation of pumping sources. Procedures to maintain high interference immunity for the system are also addressed.

Introduction

ISKRA-5 facility includes a high-power 12-beam iodine laser whose design is based on multistage amplification approach[1]. In this way, each beam en route from the master oscillator to the final of the optical layout is made to go through 5 amplification stages consecutively, each stage, in turn, consists of modules each having a high-pressure spark-gap switch to discharge the capacitor bank energy to the light source (xenon flashlamp or electric-discharge source) [2]. The sync system's purpose is to provide simultaneous power delivery from modules to flashlamp by controlling the power module switches.

Table 1.

Amplification stage descriptions

Stage	A1	A2	A2B	A3	A4
Power modules in a channel	1	2	4	16	32
Power modules in the system	12	24	48	192	384
Light source	flashlamp	flashlamp	flashlamp	EDS	EDS
Discharge current half-period, μs	10	10	30	35	35

EDS - electric-discharge source

There is optimum amplification requirement, that the laser beam should be shaped by amplification stages with magnetic field in the active medium being at the minimum. This can be achieved by transmitting through amplification stages a single laser pulse at the termination of the first discharge current half-period in the light sources. The discharge current half-period varies from module to module in the range of 10 to 35μs.

Thus, it is the major purpose of the ISKRA-5 sync system to fire 665 high-pressure spark-gap switches and match in time the current zeroes at the first oscillation half-period termination in all the light sources (see diagram of fig.1). Also, the jitter for the current zero-crossing must be kept within ±1μs.

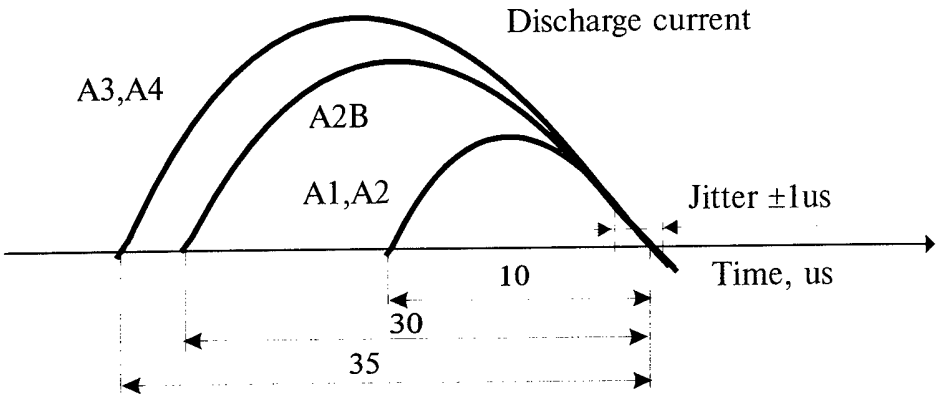

Fig.1. Matching current zeroes for different amplification stages.

Additionally, the sync system is intended to trigger electric-discharge sources (EDS). This is because the transient voltage that occurs with the module firing in the long switch to EDS line will be insufficient to make the breakdown of electric-discharge sources time-stabilised. The high-voltage pulse to trigger the EDS is to be sent simultaneously with the trigger pulse for switches.

Sync System Design Approaches

The design of a sync system for pulse capacitor banks is based on the following three considerations: trigger pulse characteristics for capacitor bank switches, the capacitor bank structure and performance algorithm.

There may be the following design options for the system:

- a trigger pulse generator individually for each switch,
- a single multichannel trigger generator for all the switches,
- a single multichannel trigger generator for a selected functional combination of switches.

The first option is generally used by sync systems at the facilities with switches having comparatively low-voltage (several kilovolts) triggering (ignitrons, thyristors, etc.). Trigger pulse generators in this case are normally represented by inexpensive thyristor circuits to be integrated into a low-voltage operated system. The second option is commonly used to design systems having relatively few switches. Reportedly, switches have the higher performance stability, the shorter the trigger voltage risetime.

When the channels are many (100 to 1000), there would be a physical limitation on signal shaping with shot voltage risetime, which is due to the generator's discharge circuit having high-voltage signals of the parasitic components, L_p and C_p. This is why it would be virtually impossible to design and develop a multichannel generator to trigger 100 to 1000 switches.

Therefore, what the ISKRA-5 pulse power system employs is the third option, i.e. where the capacitor is to be divided and considerably large sections, each having its switches to be triggered by one and the same generator of the sync system. The sync system is multistaged, each stage firing the consecutive on by turn. The whole of the sync system is triggered by a low-voltage pulse, therefore all shot delays as required for different generators are made at this level.

Sync System Configuration

The Sync System Structural Configuration of the ISKRA-5 capacitor bank is shown in fig.2. The sync system units can be altogether subdivided into two functions: basic sync equipment and channel sync equipment. Functions performed by the basic equipment are the same for all the channel and include shaping and timing of triggering pulses from the firing signal of the control system.

The basic equipment includes the following low-voltage units: sync system firing unit (SSFU) to convert the control system's trigger signal to the voltage pulse of about 150V, trigger pulse multiplier units (TPMU), and delay units as lines to delay the trigger pulse as specified before. High-voltage units are channel triggering generators (CTG) to fire the switches of modules A1 and A2 and switch trigger generators (TPG-S2B, TPG-S3, TPG-S4) for modules A2B, A3 and A4 in each channel. Together with trigger generators for electric-discharge sources (TPG-DS3, TPG-DS4), the latters make up the channel synchronisation function.

With this configuration, the sync system can provide the required delay between the module shots accounting for different amplification stages and match the current's zero-crossing times at the first discharge half-period termination.

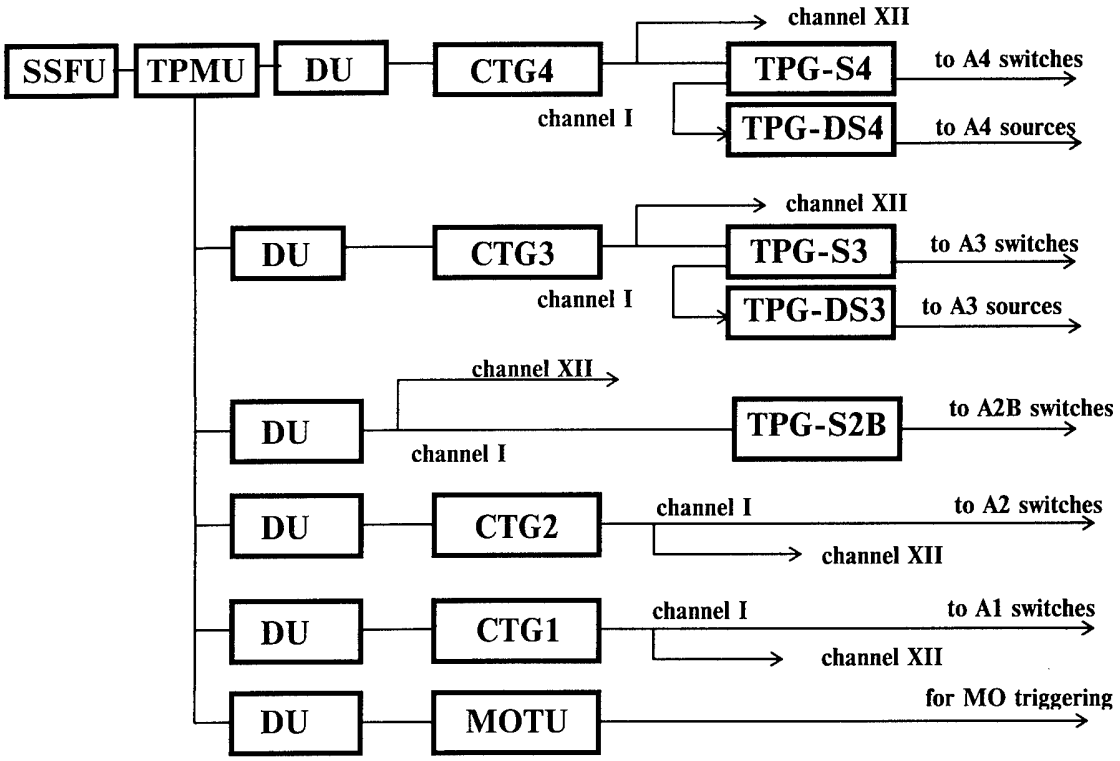

Fig.2. Schematic diagram of the ISKRA-5 sync system.

Notations in the schematic are: SSFU-sync system firing unit, TPMU - trigger pulse multiplier unit, DU-delay unit, CTG-channel trigger generator, TPG-S - trigger-pulse generator for switches, TPG-DS - trigger-pulse generator for discharge sources, MO-master oscillator, MOTU-master oscillator triggering unit.

Description of major system

The individual units and generators of the sync system have basic performance data as given in fig.2. The table includes averaged characteristics of the generators operated at the facility. All high-voltage generators are designed as required by the discharge circuit of a low-inductance capacitor to the input resistance of parallel-connected cables (12 to 32 cables per generator).

Table2.

Basic performance data of the ISKRA-5 sync system.

Unit	Input data		Output data		Output channels	Shot time	Jitter	Units in system
	U_m, V	τ^*, μs	U_m, V	τ^*, μs		μs	μs	
SSFU	30-200	0.1-0.3	150	0.15	1-12	0.3	0.03	3
DU, TPMU	≥100	0.1-0.5	120	0.15	2	0.3-100	0.03	5
CTG	≥50	0.1-0.5	120000	0.1-0.3	12	0.6	0.1	17
TPG-S	120000	0.1-0.2	120000	0.1-0.3	32	0.2	0.03	24
TPG-DS	120000	0.1-0.2	70000	0.15	32	0.2	0.03	24

τ^*- pulse risetime

Sync system reliability and interference immunity

Sync system units are subject to increased reliability and interference immunity requirements. Therefore, the emphasis in high-voltage sync generator developments was specifically laid on componentry. The generators have used tailor-made low-inductance capacitors. Also, high-pressure spark-gap switches have been specifically designed for 70kV operating voltage. Cable lines as long as 100m made of suitable high-voltage cable have been used to connect the sync system generators to the module switches and electric-discharge sources.

Particularly stringent requirements for interference immunity are set on low-voltage sync units. In order to meet these, additional provisions were made to arrange the grounding system, reduce parasitic connections and include isolations into low-voltage circuits.

Conclusion

The ISKRA-5 sync system is designed as series-parallel configuration, and thus allows experiments to be conducted with 665 spark-gap switches, 476 electric-discharge pumping sources, and 513 xenon flashlamps fired in a sequence as required. To date, there have been altogether about 5 thousand shots of the facility with at most 2 percent of these involving abnormal operations, thereby suggesting the effectiveness of the design approaches taken.

[1] Kirillov,G.A., Murugov,V.M., Punin,V.T., Shemyakin,V.I." High power laser system ISKRA V": Laser and Particle Beams (1990), vol.8, no.4, pp.827-831.

[2] Bezuglov,V.G., Galakhov,I.V., Gasheev,A.S., Gruzin,I.A., Gudov,S.N., et all. "The 67MJ, 50kV capacitor bank for the high-power iodine laser of the facility ISKRA-5: description and experience" : 10th IEEE Inter.Pulsed Power Conf.- Albuquerque, July 1995.

HIGH-POWER SEMICONDUCTOR RSD-BASED SWITCH

V.G.Bezuglov, I.V.Galakhov , I.A.Grusin, V.I.Zolotovsky, S.N.Gudov, S.L.Logutenko, V.M.Murugov, V.A.Osin, and V.N.Petrakov

RFNC - VNIIEF, Sarov (Arzamas - 16), Russia.

I.V.Grekhov and S.V.Korotkov

Phys. Techn. Inst., St. Peterburg, Russia.

V.I.Kovtun, V.A.Martynenko and G.D.Chumakov

Saransk, Russia.

Abstract

We describe the operating principle and test results for the high-power semiconductor RSD-based switch with the following operating parameters:

- operating voltage - 25kV,
- peak operating current - 200kA,
- maximum transferred charge - 70C.

The switch is intended for use by high-power capacitor banks in state-of-the-art research facilities. The switch is evaluated for its applicability in commercial pulsed systems. The possibility to increase the peak operating current to 500kA is shown.

Introduction

Addressing advanced research facilities in application to large-scale experimentation, switching of high current pulses poses a challenge. However, common switch types, i.e. ignitrons and spark gaps, as used earlier by these facilities, do not meet reliability and lifetime requirements set by designers with peak currents of 300-500kA and about 100C charge flowing through them. This is why it would be topical to explore new switch types, more importantly, those built upon semiconducting devices, because their long operation distinguishes them from the others.

In the early 1980s, Ioffe Physics and Technology Institute (St.-Petersburg, Russia) designed a new [1] semiconductor device they called reverse switched dinistor (RSD), whose capabilities of high current pulse switching would significantly surpass the most commonly used thyristors and make them well competitive against gas-discharge devices.

The concept the RSD current switching mechanism is based upon is that the thyristor-type device has its control electrode replaced by an areally uniform plasma layer. This helps produce a plasma channel, its area equal to that of the silicon plate, thereby resulting in substantially higher pulsed current values switchable by the device. What was found as the most suitable and power saving way to achieve this control plasma layer is reverse injection control, in which case the plasma layer would result from a short-term polarity change of the voltage applied to the device. Thus, reverse switched dinistors are anode-controlled two-electrode devices.

The RSD-switched current value is in proportion to the silicon plate operation area.

With the development of RSD having $50cm^2$ operation area, switched current values could be increased up to the range previously achievable by only gas-discharge devices. Thus, ref.[1] summarizes research on the assembly of three series-connected RSDs of $50cm^2$ operation area. The assembly had operating voltage up to 7.5kV and switched square current pulses of 100μs width and up to 300kA peak value.

A switch KRD-25 rated for 25kV operating voltage and up to 200kA operating current (the pulse about 500μs width) was developed for application in high-power capacitor banks to be designed into advanced Nd-glass laser systems (of several hundreds megajoule stored energy). This switch can be also used in commercial facilities where magnetic pulse technology is employed. The report is addressing this switch development.

RSD-switch design

The KRD-25 switch is designed as shown in fig.1. The switch is made up by 15 RSDs of $50cm^2$ operation area and 2kV lock voltage each. These 15 RSDs are designed as pellets, connected in series and enclosed in a common ceramic housing. Some provisions have been made for these designs to be in good contact one with another. This requires a substantial force of about 5 tons to be exerted to squeeze RSDs together in a stack. Specialized tie beams and dish springs are what serve to achieve this force. Fig.2 shows the exterior view of the KRD-25 switch.

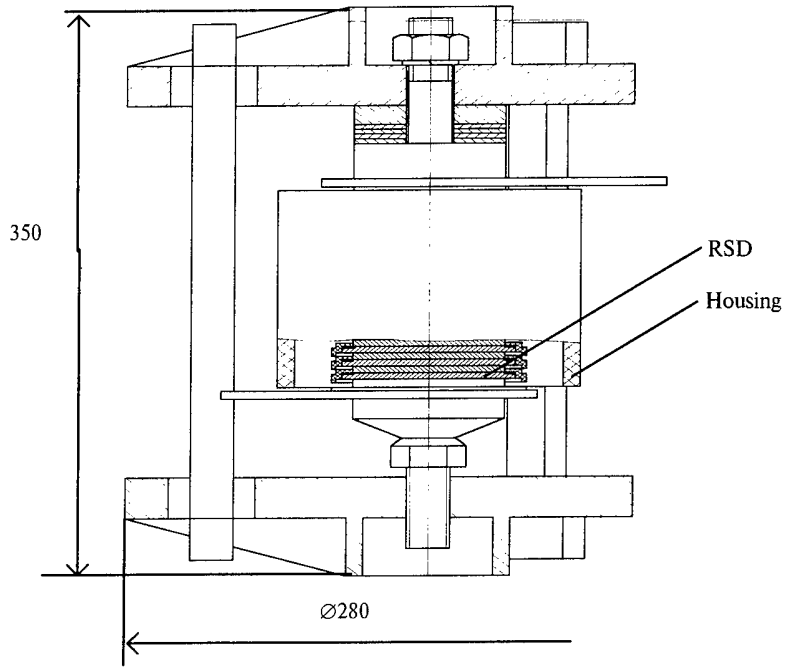

Fig.1. Schematic design of KRD-25 switch.

KRD-25 switch testing

The KRD-25 switch was tested using a dedicated test bed, whose circuit diagram is illustrated by Fig.3. The main discharge circuit is characterized as follows: U_0=+25kV, C_0=2600μF, Z_0=0.1Ohm, L_0=6.5μH. The triggering circuit characteristics are: U_t=-(5-10)kV, C_t=1.0μF, L_t=1.0μH. L_s is the saturated-core choke to isolate the fast triggering circuit from the lower main discharge circuit. Fig.4 shows a typical current shape the KRD-25 does switching for.

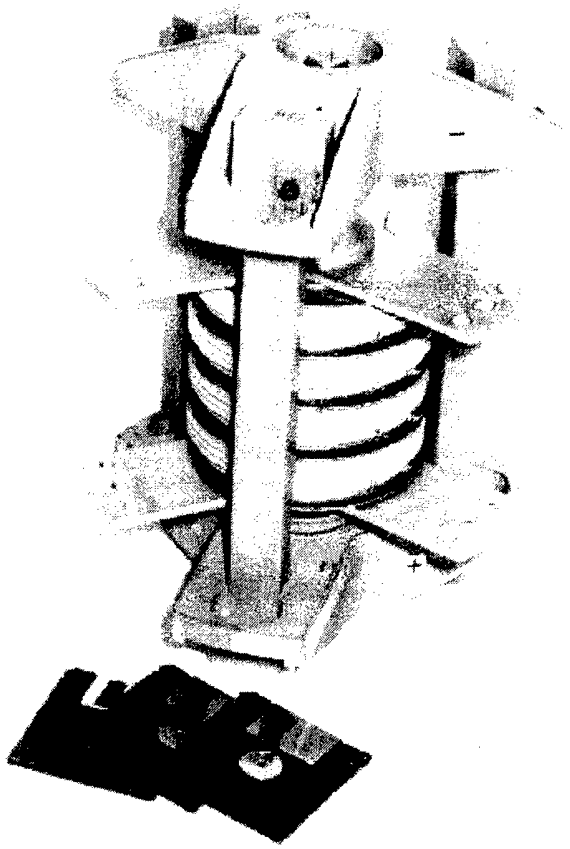

Fig.2. KRD-25 switch: general view.

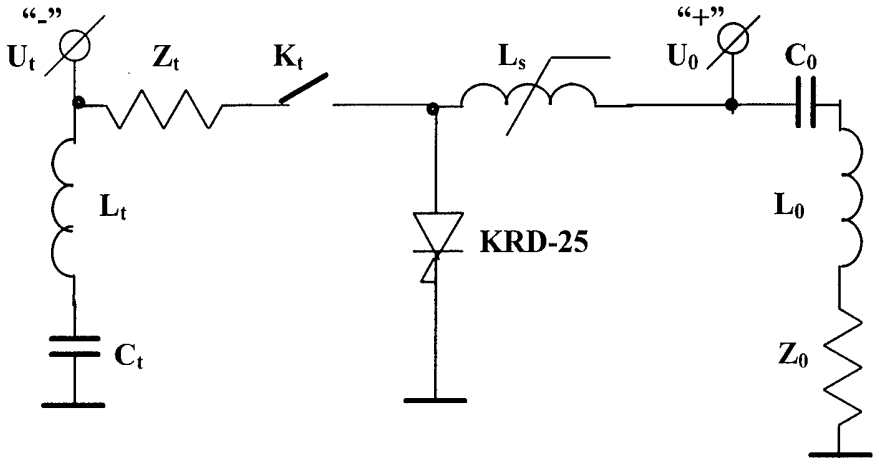

Fig.3. Circuit diagram for KRD-25 testing in single-shot operation.

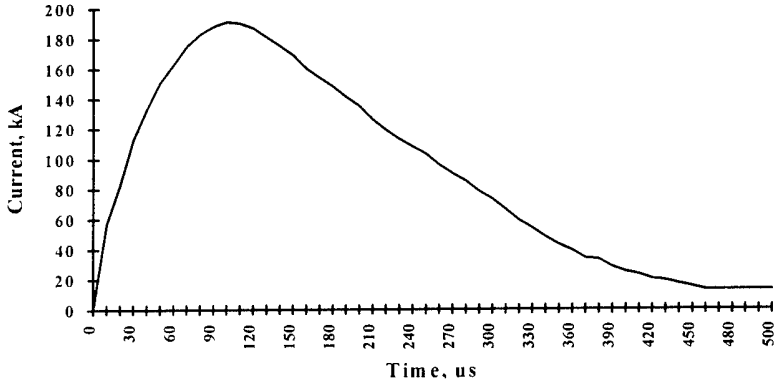

Fig.4. Typical oscilloscope trace of KRD-25 current during testing.

The authors established earlier [2], that 250±10kA would be the limit in the switched current peak value for RSD of 50cm^2 operation area having current pulses with their width at the base level about 500μs. Beyond this limit, there would occur an irreversible thermal breakdown in the RSD due to current contraction effect.

It has been shown by testing that KRD-25 switch can reliably switch the current up to 200kA and up to 70C charge. Testing was carried out in a single-shot mode, with one shot in 15 minutes.

As compared with common thyristors, RSD features the capability to switch oscillatory shaped current pulses, thus being particularly attractive for application in magnetic pulse commercial facilities.

There have been no experimental data on the RSD lifetime for the operational conditions as specified. However, one can assume it to be at least the same as the similar thyristor design's. While thyristor's lifetime depends to a significant extent on the wear of the narrow operation area around the control electrode, the RSD is free of this locally heavy-duty portion.

Conclusions

Testing has been carried out for a KRD-25 switch built around reverse switched dinistors (RSD) of 45 and 50cm^2 operation area. The tests involved switching of current pulses of 500μs width at the base and up to 250kA peak value. The tests have shown the KRD-25 switch to reliably switch 180-200kA current and up to 70C charge.

When they switch currents this high, the RSD would show no more than 20V voltage drop. This makes them quite promising for use in stacks of several units connected in parallel and may allow the switched current to be increased up to 400-500kA. Thus, RSD are attractive switch designs for pulsed power systems of advanced high-power lasers.

This switch type may also show promise as applied to electropulse commercial facilities and magnetic pulse technologies, in particular.

[1] Tuchkevich V.M., Grekhov I.V."New technique of high power switching by semiconductor devices" L.,"Nauka", 1988.

[2] Chumakov G.D., Galakhov I.V., Gudov S.N., Kirillov G.A., Kovtun V.I., Larson D., Martynenko V.A., Murugov V.M., Osin V.A., Zolotovski V.I. "Switching of High-Power Current Pulses up to 250kA and Submillisecond Duration using New Silicon Devices - Reverse Switched Dinistors." : 10th IEEE International Pulsed Power Conference, Albuquerque, NM, USA, July 1995.

NANOSECOND ELECTRON BEAMS COMPACT GENERATOR

D.V.Konkin, A.Ju.Nagovitsin, S.S.Pavlov, N.F.Popkov.

All-Russian Scientific Research Institute of Experimental Phisics, (VNIIEF) Sarov, Nizhni Novgorod region, 607190, Russia.

Abstract

In the report there is described a small-scale accelerator providing the storage energy of 40 J, electron energy of 200 keV, the released into the air beam current of 1 kA and the current pulse duration of 30-40 ns at the half-height. In the accelerator capacitive energy storage the multi-channel commutation is implemented ensuring the output current pulse front of 10 ns, while the inductiveness is 120 nH. The apparatus gross weight is approximately 100 kg.

Introduction

Now the radiation technologies find a wider industrial application, e.g. polymer coating solidification [1], gas exhaust and water waste purification [2,3], sterilization methods in medical and food industries [4].

Besides, to synchronize the physical processes there are required the sources with a highly stable shape pulse and operation delay also. Very often small-scale transportable electron accelerators are necessary for these purpose. So, the present effort has the above-mentioned directionality.

The accelerator described consists of the capacitive energy storage, vacuum diode, charging and initiation units and vacuum evacuation system.

The capacitive storage is assembled with ceramic capacitors of K15-10 type providing the unit working voltage of 31.5 kV. The storage includes three section connected in parallel, arranged according to Arkadiev-Marx scheme and operating on to the common load.

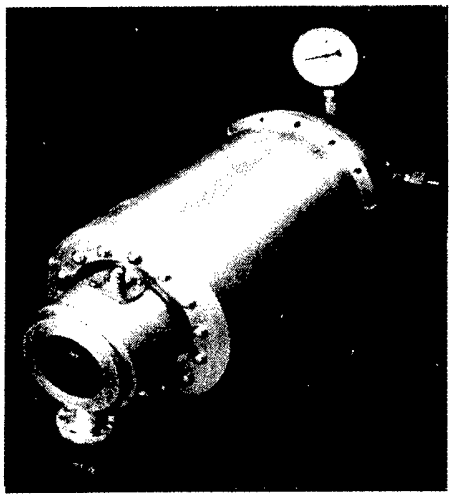

Fig.1. The small-scale accelerator

Each section incorporates 13 cascades charged up to the voltage of 25 kV. In each trigatron discharger the controlling electrode is placed on the one with zero potential. The discharger spark gap length is 1.7 mm. Control of all the storage dischargers is carried out synchronously, using the voltage pulses with the amplitude of 15 kV and front of 5 ns. The pulses are fed to each section through a separate high-voltage cable with the wave resistance of 75 Ohm. The lay-out of

the capacitive storage including the vacuum diode is shown in Fig. 2.

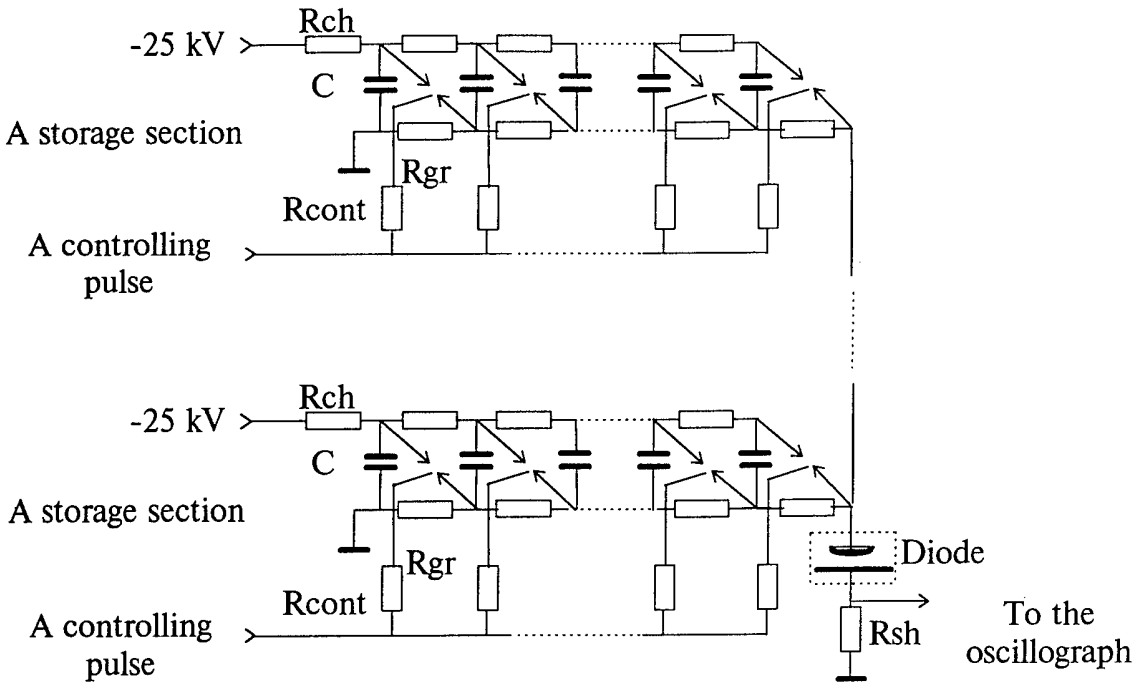

Fig.2. The accelerator principle lay-out, where Rch are the charge resistors, Rgr are the ground resistors, Rcont are control circuit resistors, Rsh is the shunt resistance.

The separated discharger gas volume is not envisioned in the design. So, the storage case is filled with Nitrogen/SF_6 mix. The mix provides (1) the conditions necessary for the discharger operation and (2) required electric strength.

Each storage section is arranged to ensure the lowest possible storage inductiveness and the optimal array of the discharges illuminating one another with the ultra-violet radiation in the course of the operation. In this case the legs with zero and high potentials are close and the minimum distance between them is defined based on only their geometric dimensions and electric strength considerations.

As a result of the above mentioned, all the diode electrodes are connected with the storage by short busbars of the same length minimizing the storage/diode system inductiveness.

In the experiment the said inductiveness was determined in the course of the diode operation in the short-circuiting mode.

Substituting into the Topmost formula $T=2\pi\sqrt{LC}$ the numbers T=60 ns and C_{imp}=0.76 nF, where T is the current oscillating period in the short-circuiting mode and C_{imp} is the storage capacitance in the moment of impact, the system capacitance may be derived, i.e. L=120 nH.

Based on the above mentioned, the characteristic resistance may be

calculated, i.e. $\rho=\sqrt{L/C_{imp}}=12.6$ Ohm.

The vacuum diode is placed on the capacitive storage case. Its overall dimensions are chosen to ensure the diode impedance equal to $2\sqrt{L/C_{imp}}$ at the maximum current.

The diode cathode is made of graphite. It is the planar disk with the diameter of 25 mm positioned an the stainless steel substrate connected with the capacitive storage high-voltage leg through basbar comprised by copper conductors. The anode is actually the grid pulled up on the frame and made of steel wire with the diameter of 0.1 mm. The anode/cathode gap is 3.2±0.2 mm. Behind the wire grid the electron outlet window is situated. In the window the membrane is installed separating the vacuum volume from the external environment. The membrane material is either some metal foil or polymer film, dependently on the task to accomplish. We used the aluminium foil with the thickness of 0.05 mm, as well as lavsan (or Darcon) one of the same thickness. The diameter of the outlet window is 51 mm.

In the diode the vacuum of ~ 10^{-4} mm Hg is being sustained.

The diode current pulses were picked up from the coaxial low-inductive shunt with the resistance R=0.065 Ohm placed between the anode and the capacitive storage grounded leg and registered by the oscillograph refered to the class of super-fast registrators. The current pulse front duration made 10±2 ns, while the duration at the half-height made 40±5 ns. The current pulse amplitude was 4±0.5 kA. The beam current was registered, using the Faradei Cylinder (FC). The beam current pulse duration at the half-height made 40±5 ns, the front duration made 10±2 ns. The maximum beam current pulse amplitude, using the aluminium foil outlet window, reached 0.73±0.08 kA. In case of the Darcon film outlet window application the maximum beam current pulse amplitude was 1.0±0.12 kA (Fig.3).

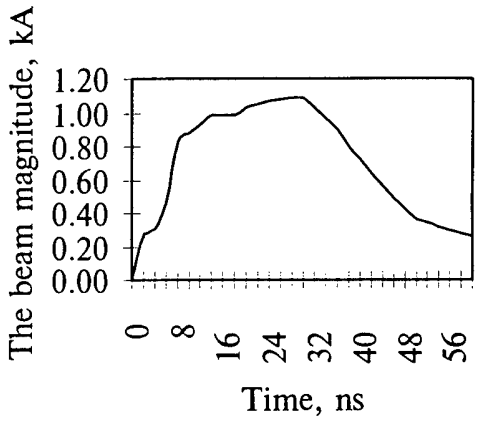

Fig.3. The electron beam pulse shape behind the Darcon outlet window at the distance of 1 cm from the latter

The beam current was registered at various distances and angles relatively to the diode outlet window. In Fig.4 there is shown the distribution of the experimental beam current numbers after crossing the foil outlet window.

The accelerator operation time diffference as regards the controlling pulse does not surpass ±1.5 ns.

Based on the registered experimental numbers of the beam run in the air, table numbers [5] and empirical formula describing the connection between the run and energy of electrons [6], $R=0.407T^{1.38}$ g/cm^2 for $0.15<T<0.8$ MeV, where R is the electron run, T is the kinetic

energy of electrons [6] there was defined the electron initial energy as much as 200±30 keV.

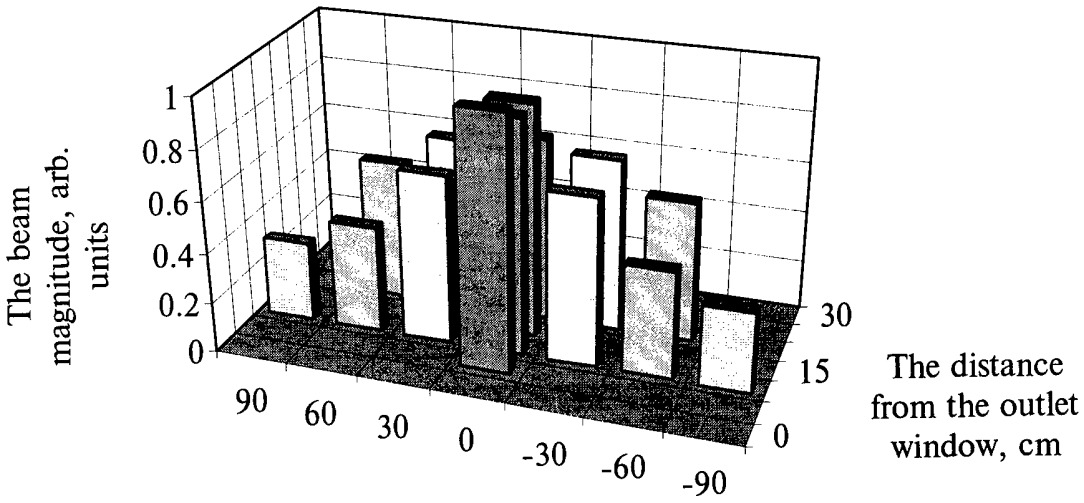

Fig.4. Electron beam distribution behind the outlet window

Conclusion

Here there is represented the accelerator providing the electron energy of 200 keV, released in the air beam current of 1 kA and current pulse duration at the half-height of 40 ns. In the accelerator capacitive storage the cascade multi-channel commutation is implemented facilitating the output voltage pulse front obtained of 10 ns, the apparatus inductiveness of 120 nH and the operation time difference relatively to the controlling pulse of not more than 1.5 ns. The accelerator meets the transportability requirements. Its weight without the auxiliary equipment (i.e. that of the capacitive storage and vacuum diode) is 35 kg, while including the auxiliary equipment it is as heavy as 100 kg.

[1] Abramyan E.A., Al'terkop B.A., Kuleshov G.D.: Intensivnye elektronnye puchki. M.: Energoatomizdat, 1984, p.1194

[2] Pikaev A.K.: Khimiya vysokikh energij, v.28, N1,1994, p.25

[3] Kunavin A.T. et al.: Khimiya vysokikh energij, v.28, N1,1994, p.21

[4] El'yash et al.: Atomnaya energiya, v.79, issue 6,1995, p.462

[5] Baranov V7F7:Dozimetriya elektronnogo izlucheniya. M: Atomizdat, 1974, p.192

[6] Mukhin K.N.: Experimental'naya yadernaya fizika, v.1. M: Energoatomizdat, 1983, p.278

Design And Analysis Of The PBFA-Z Vacuum Insulator Stack*

R.W. Shoup[1], F. Long, T. H. Martin, W.A. Stygar, H. Ives[2], R.B. Spielman, K.W. Struve[3], M. Mostrom[3], P. Corcoran[4], and I. Smith[4]

Sandia National Laboratories, Department 9573, MS-1194
Albuquerque, NM 87185-1194 USA

Abstract

Sandia is developing PBFA-Z, a 20-MA driver for z-pinch experiments by replacing the water lines, insulator stack, and MITLs on PBFA II with new hardware. The design of the vacuum insulator stack was dictated by the drive voltage, the electric field stress and grading requirements, the water line and MITL interface requirements, and the machine operations and maintenance requirements. The insulator stack will consist of four separate modules, each of a different design because of different voltage drive and hardware interface requirements. The shape of the components in each module, i.e., grading rings, insulator rings, flux excluders, anode and cathode conductors, and the design of the water line and MITL interfaces, were optimized by using the electrostatic analysis codes, ELECTRO and JASON. The time-dependent performance of the insulator stack was evaluated using IVORY, a 2-D PIC code. This paper will describe the insulator stack design and present the results of the ELECTRO and IVORY analyses.

Introduction

Figure 1 is a drawing of the PBFA II[1] accelerator. The accelerator is contained in two concentric tanks. The outer tank is the oil tank which includes thirty-six Marx generators as the prime power source.

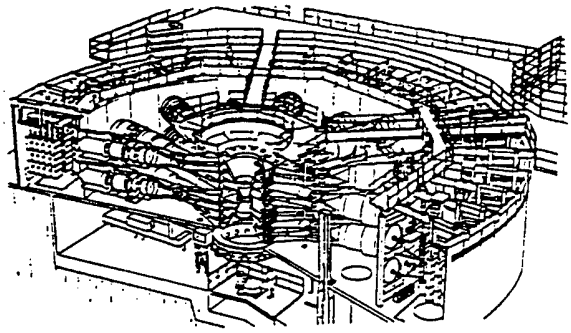

Fig. 1 PBFA II accelerator

The inner tank is filled with deionized water and contains the pulse compression and transmission network which provide the pulsed power to the vacuum insulator. The vacuum insulator on PBFA II contains the hardware needed to configure the machine for ion beam operation. In order to use the accelerator for magnetic implosions it is necessary to convert the electrical power flow to a low impedance, high current design. This is being accomplished by replacing the water lines, the vacuum insulator stack, and the magnetically insulated transmission lines on PBFA II with hardware of a new design. The reconfigured accelerator is identified as PBFA-Z[2]. The modified accelerator has been designed to deliver 20 MA of current to a 15-mg z-pinch load in

*This work was supported by the U.S. Department of Energy under Contract #DE-AC04-94AL85000.

[1]Field Command Defense Nuclear Agency, 1680 Texas Street S.E., Kirtland Air Force Base, NM 87117-5669 USA
[2]EG&G, 2501 Yale Blvd S.E., Albuquerque, NM 87106 USA
[3]Mission Research Corporation, 1720 Randolph Rd S.E., Albuquerque, NM 87106 USA
[4]Pulse Sciences, Inc., 600 McCormick Avenue, San Leandro, CA 94577 USA

100 ns. First shot is planned for late-July 1996.

Insulator Stack Design

The PBFA-Z insulator stack will be 340 cm in diameter and 172 cm high. The stack is subdivided into four levels, Level A through Level D. Each level will contain a set of Rexolite insulator rings and a set of aluminum grading rings. The bottom two levels, C and D, will be equipped with flux excluders to help grade the fields. A drawing of the PBFA-Z vacuum insulator stack, with the water line and MITL interface hardware, is shown in Figure 2.

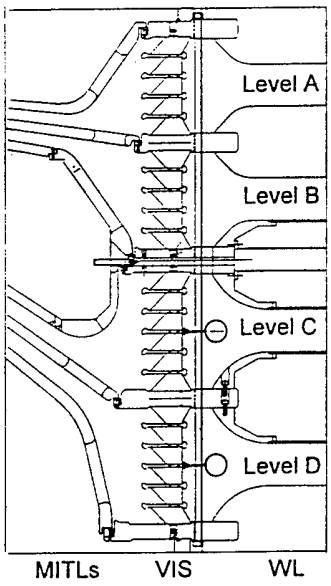

Fig. 2 PBFA-Z insulator stack

The stack grading rings were designed to keep the electric field stresses below 300 kV/cm on the vacuum side, below 250 kV/cm on the water side, and less than 30 kV/cm at the cathode triple points. The vacuum flares were designed to balance the peak fields on the grading rings. The number and shape of the grading rings, the radius of the water line-to-stack transition section, and the size and location of the flux excluders were selected to minimize field stresses and to keep the field grading below 10% in each module.

The PBFA-Z accelerator was modeled using circuit codes to determine the time-dependent voltage and current waveforms at the water lines, the insulator stack, and the MITLs. SCREAMER, a SNL-developed lumped element code was used to model the circuit from the Marx generators through the load and to optimize the Marx and water sections. TL code, a PSI transmission line code, was used to model the accelerator from the water transmission lines to the load, and to optimize the vacuum section design. The SCREAMER predictions of the stack voltages are presented in Figure 3.

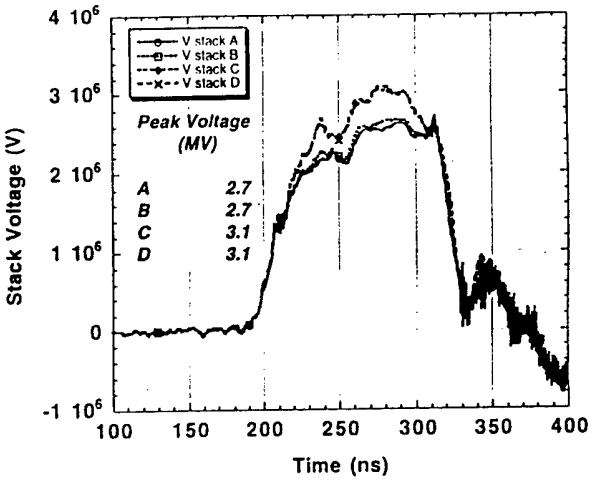

Fig. 3 Stack voltage predictions

Analysis Results

The electrostatic computer codes, ELECTRO[3] and JASON, were used to calculate the electric field stresses and the field grading during the various design iterations. The peak voltages predicted by SCREAMER and the TL code were used in the ELECTRO and JASON calculations. IVORY, a 2-D PIC code developed by MRC, was used to evaluate the time-dependent performance of the insulator stack.

Each level of the insulator stack was modeled separately. The geometry of the Level C model is shown in Figure 4. ELECTRO solves for the voltage and electric field distributions for specified geometries, media, media permittivities boundary conditions, and boundary elements.

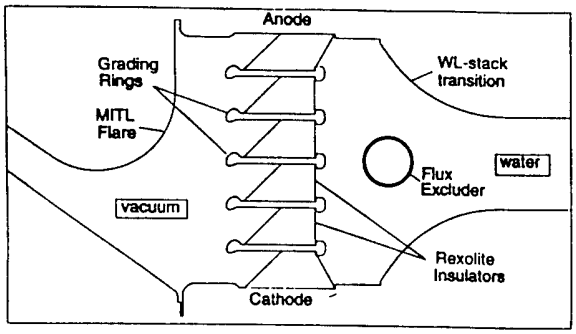

Fig. 4 Level C model

Figure 5 is a plot of the equipotential contours near the top grading ring on Level A. The shape of the grading ring edge was designed to follow the voltage contours, thereby minimizing the field stresses.

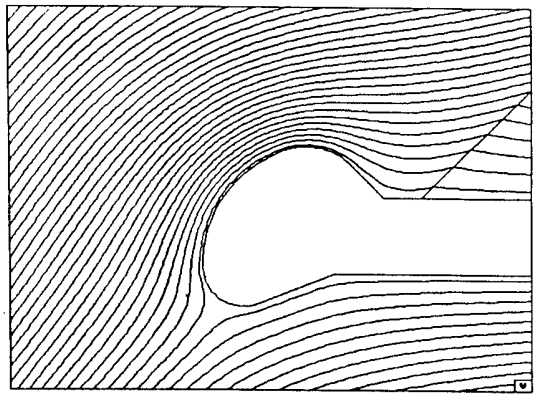

Fig. 5 Equipotential contour plot

The constant voltage contours for Level C of the PBFA-Z stack are plotted in Figure 6. The plot shows the grading to be uniform. Each insulator contains the same number of contour lines and the insulator voltages vary from -2.3% to +3.6% from the average.

The electric fields normal to the grading rings and the fields tangent to the insulator rings were plotted for each ring of the stack. Figure 7 presents the normal E-field plot for Grading Ring 3 on the vacuum side of Level C. Figure 8 presents the tangent E-field plot for Insulator Ring 1 on the vacuum side of Level C.

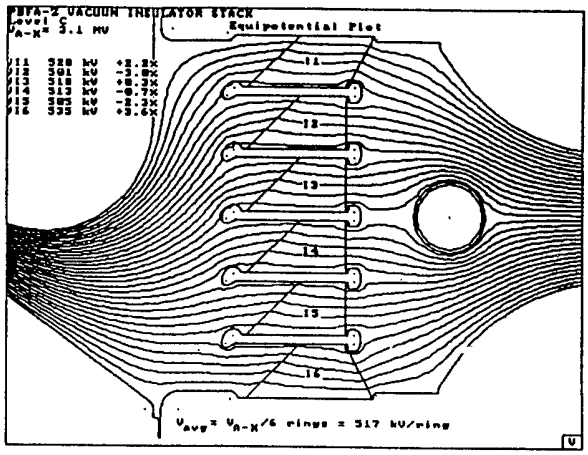

Fig. 6 Level C equipotential contours

IVORY was used in a 2-D mode to simulate the PBFA-Z insulator stack and MITL flares. The vacuum and dielectric interfaces and grading rings were centered in the simulation region. Figure 9 shows the IVORY stack model with grading ring emission.

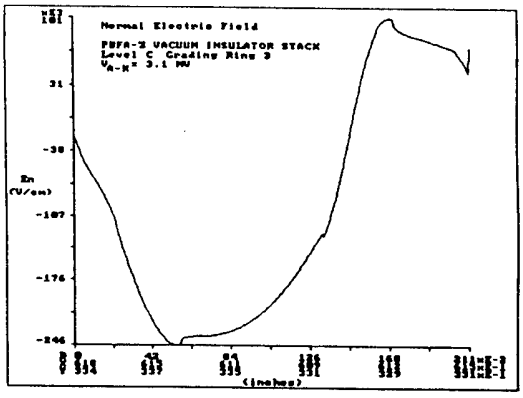

Fig. 7 Normal E-field plot

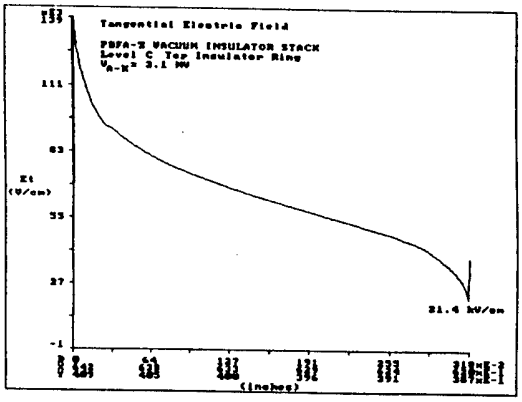

Fig. 8 Tangential E-field plot

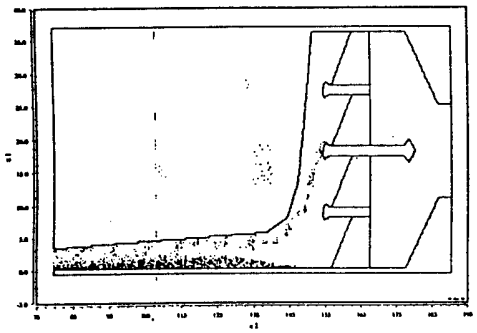

Fig. 9 IVORY insulator stack model

The grading calculations for the PBFA-Z stack are shown in Figure 10. The peak electric fields on Levels A and C are summarized in Figure 11. The peak fields on Levels B and D are comparable to those shown.

Insulator Ring	A - Level Va-k=2.7 MV Variation %	B - Level Va-k=2.7 MV Variation %	C - Level Va-k=3.1 MV Variation %	D - Level Va-k=3.1 MV Variation %
I1	+0.7	+3.2	+2.2	+2.9
I2	-5.6	-4.8	-3.0	-1.5
I3	+6.5	+6.3	+0.3	-1.0
I4	-4.6	-5.7	-0.7	0
I5	+3.0	+1.1	-2.3	-3.1
I6			+3.6	+2.3

Fig. 10 Grading Summary

Conclusions

Based on the results of the ELECTRO analysis, the peak electric fields on the grading rings are less than 260 kV/cm on the vacuum side and less than 200 kV/cm on the water side. The cathode triple point fields are less than 30 kV/cm. The grading of the baseline design is less than 6.5% on modules A and B and less than 3.7% on modules C and D. According to the results of the IVORY analysis, the voltage between rings on the baseline design can vary up to 10% without field emission and up to 19% with field emission. If the MITL gap is decreased by a factor of two, the voltage between rings can vary up to 50% from average and risk insulator breakdown.

References

[1.] B.N. Turman, et al., "PBFA II, A 100-TW Pulsed Power Driver for the Inertial Confinement Fusion Program," *Proc. 5th IEEE Pulsed Power Conference*, Arlington, VA, June 10-12, 1985, pp. 155-161, IEEE#85CH2121-2.

[2.] R.B. Spielman, et al., "PBFA II-Z: Conceptual Design Report," January 17, 1995, Sandia National Laboratories, Albuquerque, NM.

[3.] Integrated Engineering Software, Winnipeg, Manitoba, Canada R3H 0X4.

VIS Rings	A - Level Va-k=2.7 MV E-Normal (Vac Side)	A - Level Va-k=2.7 MV (kV/cm) (Water Side)	A - Level Va-k=2.7 MV E-Tangent (kV/cm) (CTP)	C - Level Va-k=3.1 MV E-Normal (Vac Side)	C - Level Va-k=3.1 MV (kV/cm) (Water Side)	C - Level Va-k=3.1 MV E-Tangent (kV/cm) (CTP)
I1			22.6			21.4
GR1	236	153		209	152	
I2			21.5			20.9
GR2	239	195		234	185	
I3			23.8			21.7
GR3	258	193		246	169	
I4			20.4			20.9
GR4	211	158		215	185	
I5			17.6			19.1
GR5				177	155	
I6						21.7

Fig.11 Peak electric fields on PBFA-Z Stack

Characterization of Diamond Film and Bare Metal photocathodes as a Function of Temperature and Surface Preparation

R.P. Shurter, D.C. Moir and D.J. Devlin

Los Alamos National Laboratory, Los Alamos NM 87545, USA

Abstract- **High current photocathodes using bare metal and polycrystalline diamond films illuminated by ultraviolet lasers are being developed at Los Alamos for use in a new generation of linear induction accelerators. These photocathodes must be able to produce multiple 60 ns pulses separated by several to tens of nanoseconds. The vacuum environment in which the photocathodes must operate is ~10-5 torr.**

I. Introduction

The DARHT (Dual Axis Radiographic HydroTest facility) will consist of two 20 MeV linear induction electron accelerators with each beam axis on the same plane, opposed by 90 degrees. The 4 kiloampere electron beams are focused to a minimum spot on a high Z target to generate intense bursts of bremsstrahlung radiation. The focused spot diameter is a key determinate in the image resolution of the radiographs produced by these machines. The emittance of the electron beam relates, by a power of four, to the minimum spot focus. The electron temperatures at the cathode of the electron beam injector is the dominant factor in the production of a low emittance beam.

The accelerator system architecture precludes the use of thermionic or thermo-dispenser type cathodes to produce the desired beam quality. The prototype injectors utilize velvet cold cathode emitters which inherently produce beams with electron temperatures >100eV.

In an effort to improve the beam quality the use of a photocathode is being investigated. The operating pressure of the diode will not permit the use of alkali metal compound or other photocathode surface preparations unstable in the presence of water vapor or other common vacuum background contaminants. Because of these constraints aluminum bare metal [1,2] and diamond film [3,4,5] photocathodes are being investigated. We report the work in progress of these investigations.

II Discussion

The photoelectric processes differ considerably between metals and wide band-gap semiconductors such as diamond.

In metals the photoelectron created by the photon within the solid has an energy above the other electrons at thermal equilibrium and is commonly referred to as a hot electron. Because of the abundance of free electrons in the metal, the photoelectron is likely to be scattered, elastically and inelastically, by other electrons and thus approach thermal equilibrium within a short distance. The scattering processes limit the emission to an escape depth of only a few atomic layers. By externally applying heat the escape probability of a photoelectron can be increased due to the increased mobility of the electrons by thermal

excitation.

The photoelectric process in a semiconductor take place when a photon is absorbed and converted into a free electron, i.e., raised from the valance band into the conduction band. Additionally, to escape to the vacuum level the electron must have sufficient energy to overcome the electron affinity. In semiconductors the electron scattering loss processes are negligible relative to losses by phonon scattering or interaction with the lattice. This process is much smaller than the electron scattering in metals.

III Experiment

A photocathode test stand (PCTS) (fig.1) was assembled to conduct scaled experiments on the subject photocathode materials. An ArF laser, 193 nm (photon energy 6.4eV) was selected to illuminate the photocathodes to achieve a reasonable quantum efficiency on a bare Al photocathode used as a baseline reference. The light beam. normal to the cathode surface, is able to be varied in intensity by over one order of magnitude through the use of multiple, thin quartz attenuating plates. The photocathode is able to be radiatively heated from ambient to 200C

The diode vacuum chamber is pumped with 1500 l/s cryopump. The planar diode (fig.2) is configured with an easily removable cathode. The anode is a >93% transparent W fine wire mesh screen. The tubular charge collector contains a defining aperture

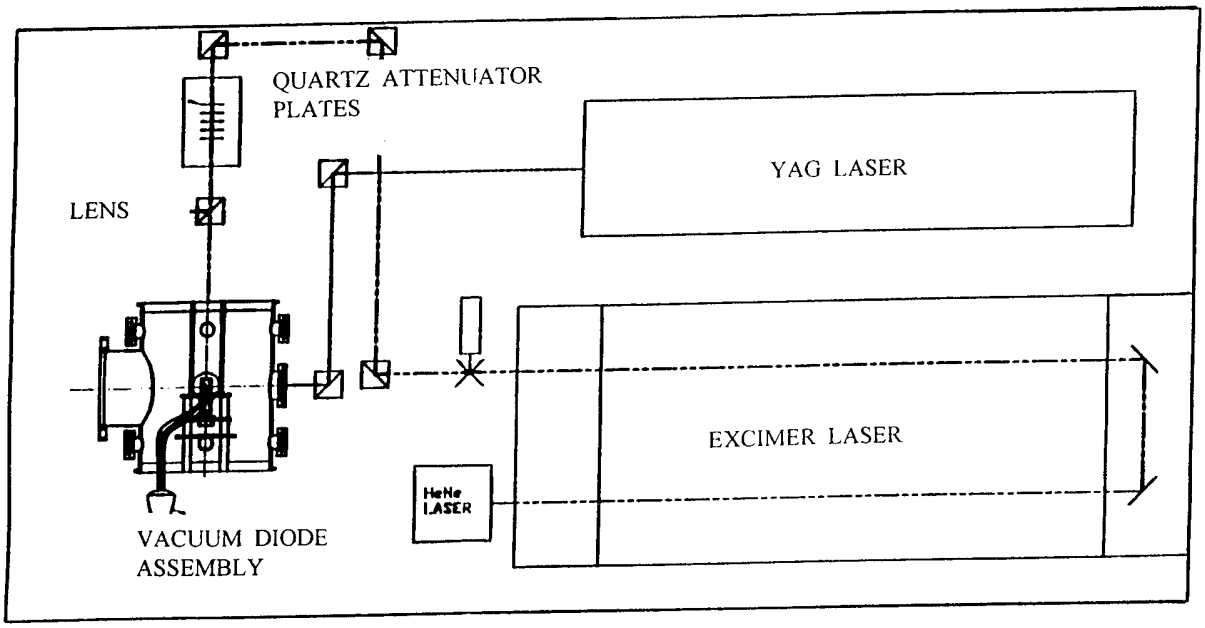

Fig.1

to size the illuminating laser beam and three UV transmissive fiberoptics, at the aperture, feeding a line filtered photodiode to sample each light pulse. The photodiode is calibrated to a laser energy meter with the cathode removed. The diode operates at 30kV d.c. and has an A-K gap of 6.7mm.

The selection of aluminum as the bare metal photocathode was made based on mechanical properties and work function. The cathode was diamond turned aluminum alloy with a 1 micron layer of pure aluminum vapor deposited on the emitting surface.

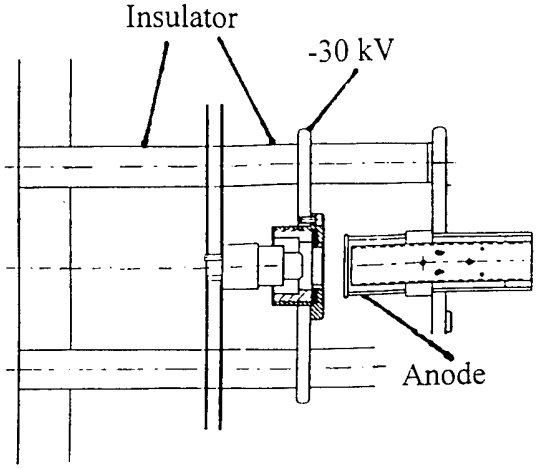

30 kV Planar Diode

Fig. 2

The diamond film samples were prepared by growing a polycrystalline diamond film on a Mo substrate with a microwave assisted CVD process [6,7,8]. The micrograph (fig.3) shows the crystal facet orientation of the diamond film surface.

Fig.3

The two diamond samples were uniformly (sub-optimum) boron doped with hydrogen terminated surfaces. The uniform doping profile inhibits the film conductivity and thereby limits the emission process. Multiple delta doping [9,10] (MDD) would result in a film conductance more than 20 times higher and is currently the focus of our materials technology research.

IV Calibration

Data obtained from the energy calibration of the photodiode consists of total laser energy measurements (Le) and a corresponding time resolved voltage trace from the photodiode. The photodiode voltage trace is integrated to obtain Volt-seconds (Vs). The calibration factor (Cal) is then given as:

$$Cal = Le / Vs.$$

The calibration factor can be used for converting integrated photodiode signal into energy or the unintegrated signal into power. A series of data is taken measuring the laser energy with a Scientec laser energy meter and obtaining the photodiode waveform. The laser attenuation is varied using quartz plates. The calibration factor as a function laser energy is shown in (Fig.4). The average value and rms deviation (5200+/- 300 V s) of the calibration is obtained from this series of measurements. The systematic deviation as a function of laser energy is within the 2rms uncertainty.

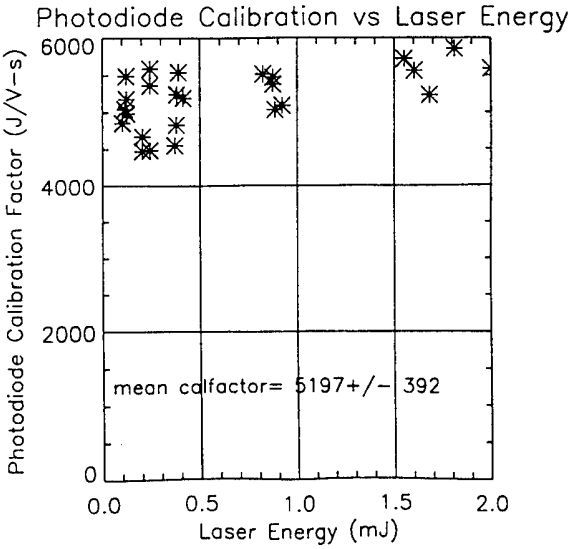

Fig. 4

V Data and Results

Typical photodiode and charge collector waveforms are shown in (Fig.5). The photodiode signal is converted to MW where the cathode area illuminated by the

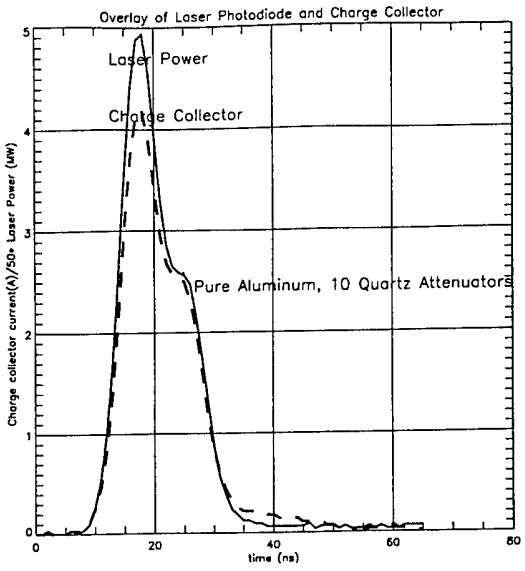

Fig.5

laser is 0.28 cm^2. The charge collector signal is presented in amperes and is obtained by dividing the voltage by the charge collector resistance of 3.8-ohms. In order to account for the digitzer impedance of 50-ohms, the signal is corrected upward in the analysis by 7.6%. Some electrons are transported through the laser entrance aperture in the charge collector. This effect also reduces the measured current. Transport calculations for a space charge limited beam indicate this effect is between 5-10% depending on beam energy. Finally, the grounded tungsten anode mesh is only 92% transmitting, resulting in another correction to the charge collector. The net average correction (k) for the charge collector is 1.25. The quantum efficiency (QE) is calculated by integrating both waveforms to obtain the total charge (k*Q) in Coulombs and laser energy (E) in Joules and using the following equation

$$QE = 6.4eV\ k*Q\ /\ E$$

where 6.4eV is the photon energy for 193nm photon produced by the ArF laser. The quantum efficiency as a function of laser energy for aluminum is shown in (Fig.8).The QE can also be obtained using the charge collector current (Icc) in amperes and laser power (P) in watts with the following relationship

$$QE = 6.4eV\ Icc\ /\ P$$

This relationship can be used at a single point (i.e., the peak) as shown in (Fig.6) or correlated at each time on a single pulse (Fig. 7).

For accelerator photocathode injector design, the most useful display is a plot of peak electron beam current density. This is shown in (Fig. 8). for aluminum at various temperatures. A comparison of diamond with uniform boron doping is compared with aluminum. This is shown in (Fig. 9).

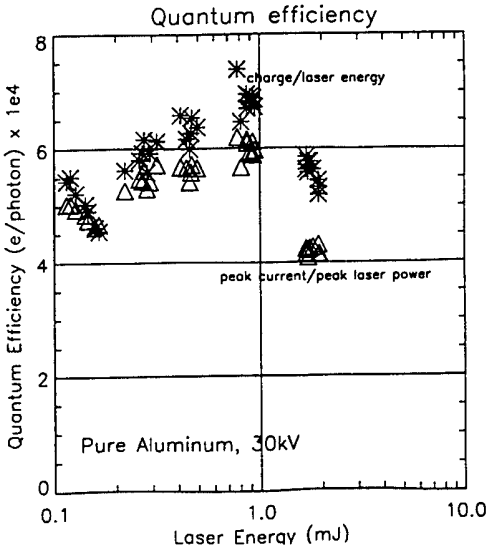

Fig.6

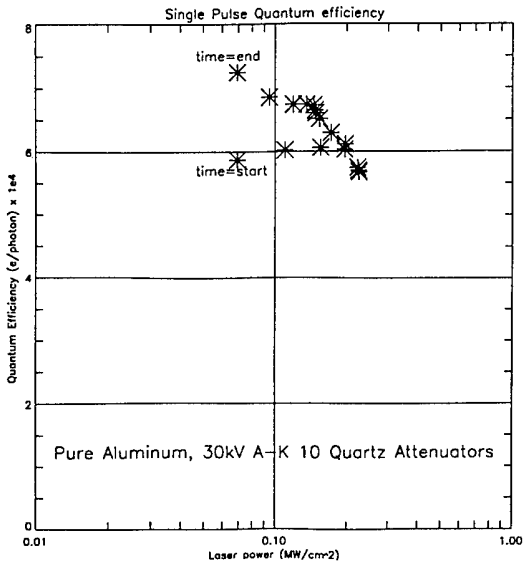

Fig. 7

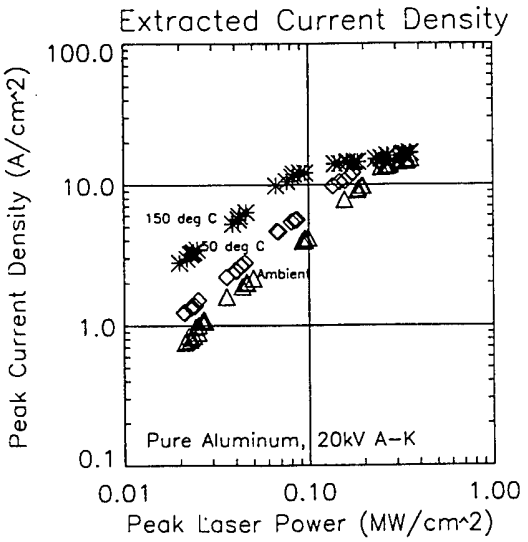

Fig.8

VI Conclusions

Aluminum as a photocathode material has been well characterized over the past several years at ambient temperature. Our experiments indicate that through thermal augmentation, the photoemission of pure aluminum may be stabilized and increased. The significant improvement in photoemission at moderate temperatures (150 C) suggest the possible application of a thermally augmented aluminum photocathode for use in the DARHT class high pressure electron beam injectors. Our results indicate the possibility of extracting a 4 kiloampere beam with less than 2 joules of incident ArF (193 nm) laser radiation.

The enhanced photoemission process is most likely based on the Fowler-DuBridge theory and would not lead to degradation of beam quality. The first follow-on experiments will include emittance measurements of a space charge limited beam from a heated, pure aluminum cathode.

Diamond film may be the ideal photocathode; it is robust, thermally conductive and chemically inert. The referenced literature indicates diamond film when MDD doped and with the proper surface termination can exhibit quantum efficiencies significantly higher than those achieved in the investigations we report. The designed growth of diamond films will be the focus of further investigations.

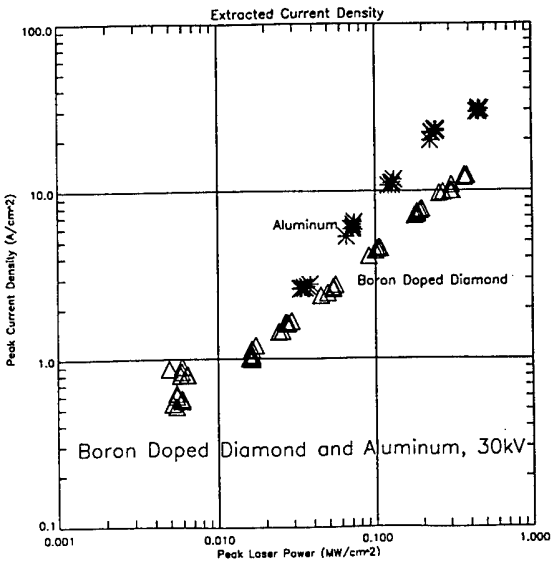

Fig. 9

As stated our investigations reported here do not show a high quantum yield for the diamond films tested. However the literature and outside sources suggest quantum efficiencies as high as 4% should be achievable.

Industrial applications have demonstrated large area diamond film growth in areas uniformly covering several tens of square centimeters.

Methods for diamond film growth other than the microwave assisted CVD process used for the samples tested are available. The most interesting alternative method considered at this point is an electron cyclotron resonance plasma (ECR) technique which is a relatively low temperature method that will allow film growth on ultraviolet transmissive substrates. This could lead to possible development of a semi-transparent or back illuminated photocathode.

ECR plasma growth of diamond films also allows the growth process to be tailored to be able to obtain preferential crystal facet orientation. The <111> facet has been demonstrated to exhibit the highest quantum efficiency.

This work was sponsored by the US Department of Energy under contract no. W-7405-ENG-36

VII References

1. Downey, L.A. Builta and D.C. Moir Appl. Phys Lett. **49** (15), 13 Oct. 1986
2. J. Kauppila, L.A. Builta J.K Crutcher, J.C. Elliott and D.C. Moir Proc IEEE Particle Accelerator Conf., Wash. DC Mar. 1987
3. Himpsel, JA. Knapp, J.A. VanVechten and D.E. Eastman Phys. Rev. B Vol 20 no.2 July 1979
4. Fischer, T. Srinivasan-Rao, T. Tsang and G. Brandes Nuc. Inst. and Meth. in Phys Research A 340 (1994) 190-194
5. Bandis, W. Chang, B.B. Pate, M.A. Plano M.D. Moyer and M.A. Moreno, proc. Third Int'l Conf. Applications of Diamond Films and Releated Materials, 1995
6. Okano, H. Naruki, Y. Akiba, T. Kurosu M. Ida and Y. Hirose Jpn. J. Appl. Phys. 27 (1988) L173
7. Mort, D Kuhman, M. Machonkin, M. Morgan, F. Jansen, K. Okumura, Y.M. Legrice and R.J. Nemanich Appl. Phys. Lett.,55 (11) (1989) 1121
8. Okano, H. Naruki, Y. Akiba, T. Kurosu, M. Lida, Y. Hirose and T. Nakamura, Jpn J. Appl. Phys. 28 (6) (1989) 1066
9. Kobayashi, T. Ariki, M. Iwabuchi, T. Maki, S Shikama and S. Suzuki J. Appl. Phys. 76 (3) 1994
10. W. Geis, D.D. Rathman, D.J. Ehrlich, R. A. Murphy and W.T. Lindley, IEEE Elec. Dev. Lett. EDL-8,341 (1987)

Development Status of Triggered Vacuum Switches at All-Russian Electrotechnical Institute and Prospects of Its Applications

D.F.Alferov, V.A.Vozdvijenskii, V.A.Sidorov

All-Russian Electrotechnical Institute (VEI)
12 Krasnokazarmennaja St., Moscow 111250, Russia

Introduction

The application of sealed-off triggered vacuum switches (TVS) for reliable and switching high-voltage high-capacity energy storages and power systems is rather perspective [1]. Such device is non-incandescence free three-electrode hermetically sealed one with pressure of residual gases not exceeding 10^{-4} Pa, capable under influence of a trigger pulse to be switched on with high rate (less than 1 μs) and to operate in wide of voltages and currents: U = (1 - 100) kV; I = (0,001 - 200) kA. TVS is distinguished by the high rate of electric strength recovery, compactness, noiselessness, fire and explosion proofness, ecological cleanness during manufacture and operation, reliability in a wide range of environment conditions.

Ability of a vacuum gap to withstand high voltages, as well as to recover dielectric property quickly attract for a long time attention of the designers of the switching apparatus [2]. The research and development of different type TVSs are carried out already more than 30 years in various research centers of the world not always very well. The parameters some of the available sealed-off TVSs, developed in foreign centers, are given in the table. As far as we know, there were manufactured only the experimental samples of such devices, which were used in laboratory and test facilities.

The development of such devices are carried out in VEI during last decade. As result, some of types of the sealed-off switches were developed and launched out into lot production at factories in Russia. Main parameters of such TVSs, possibilities of its application and prospect of further development are presented below.

Triggered vacuum switches, developed in VEI

The main parameters of sealed-off switches, developed in VEI, are presented in the table and in the references [7 - 9]. These TVSs use an erosion trigger system, which is triggered by means of an electric discharge over partly metallizes solid dielectric surface. The properties of an erosion trigger system is determined by two processes: deposition of metal vapor on dielectric surface owing to erosion of electrodes under action of an arc of the main discharge and evaporation of a metal film due to a trigger current. The use of an erosion trigger system has increased essentially the life of TVSs. The experience, obtained development during development and service of vacuum switches has allowed to determine the influence of an triggering gap arrangement. On starting characteristics of TVS and its resource. There was shown, that for given mode of operations of TVS it possible to reduce essentially switch-on delay time and to increase its resource by means of the choice of trigger pulse parameters, number of trigger gaps and an optimum orientation of a functional surface of the dielectric in rigger unit relatively main discharge gap.

The choice of the electrode system and of TVS depend on the mode of its use. There was used minified electrode system - TVS-40 [7] for switching high-voltage pulse power supply unit at currents up to hundreds of kiloamperes and the pulse duration to several milliseconds. Assembled electrode system represents a set of the alternated (in space) rods of opposite polarity at minimum distance between then ~ 8 mm. The trigger unit is placed in center of the basis of one (or two) electrodes. All electrodes are made from oxygen-free copper or chrome-copper composition.

Optimum range of switching currents of TVS-40 is 10-100 kA. The service life in this estimated through a summarized transferred charge ~ 10^6 A·s . At amplitudes of a

current more than 100 kA or transferred change more than 100 A·s the service life of TVS quickly decreases due to electrodynamics or thermal overloading electrodes. Recommended parameters of a trigger pulse in routine mode of operation - trigger voltage 5 kV, trigger current 1-2 kA at duration 10 μs.

The large voltage range and low voltage threshold of action permit to use TVS-40 in crowbar mode for getting of unipolar pulses on inductive load and protection of the electric equipment in the emergency operation. The delay time and jitter do not change practically in whole range of the operating voltage, that does such switches convenient in service.

Small switch-on delay jitter and large range operating voltage allow to switch on synchronously a lot of parallel TVSs across the load. Results of successful test of TVS-40 on test stand of MAXWELL Lab. for switch on of the capacitive storage at energy 250 kJ, voltage 11 kV, amplitude and duration of a current pulse 130 kA and 2,5 ms, respectively, are presented in the reference [6].

One of the distinctive peculiarities of TVSs is a valve ability, which becomes at apparent at certain combination of parameters of an electric circuit. For providing TVS-40 with valve properties the rate of the approach of current to zero should not exceed 200 A/μs. Valve properties of the switches permit to use its instead of the power thyristor units in those cases, when the operation resource is limited by the value $\leq 10^6$ A·s.

Moreover, in VEI there was developed other type switch TVS-3, which is intended to switch low inductive circuits at a rate of the current rise up to 10^{11} A/s and pulse duration to tens microseconds (see the table) [8]. The electrode system of this switch consists of two disk electrodes of specific shape, separated by the 5 mm gap. The trigger unit contains two series connected trigger gaps for reduction of the switch-on delay time and improvement of the starting characteristics. The switch has been tested in frequency-batch mode rate of the current pulses 500 Hz, voltage 30 kV, current amplitude 10 kA, duration of a half-cycle 30 μs and duration of continuous operation 3 s. Each of two tested switches has withstood 200000 pulses.

The switches TVS-3 are used in the laboratory impulse power equipment, supply units for power lasers and as switching elements in fast protection devices.

In VEI there was developed small-size switch TVS-7 for high frequency applications at relatively low currents up to 10 kA and maximum voltage 25 kV [9]. This switch used "cup-type" electrode system with double triggering. There were manufactured some experimental samples of such switch, the main parameters of which are given in the table. They have revealed high reliability of the start at low values of trigger current up to ~ 1 A. Required value of a trigger current for triggering on anode is equal to ~ 100 A at vacuum gap between main electrodes 3 mm. The use of trigger system has a rate of the discharge current rise > 10^{11} A/s without appreciable distortion of a current wave-front at value up to 10 kA and half-cycle duration ~ 200 ns. The switch has withstood more than 10^6 pulses without appreciable deterioration of the electric characteristics during testing in the frequency mode at 1 kHz, current 500 A, duration ~ 1 μs. The minimum trigger energy, required for maintenance of a steady mode of burning of the discharge at any polarity of main electrodes, is equal ~ 10 mJ.

Prospect of TVS improvement

The analysis of Russian and market of switching devices, as well as an experience of service of TVSs during 10 years, has allowed to reveal the ranges of parameters TVS, in which its have possess appreciable advantages over other types of devices: voltages 1-30 kV, currents 1-100 kA at transferred change in a pulse from fractions to A/s and repetition rate of pulses up to some kilohertz. The service life is estimated through a summarized transferred change 105 - 106 A/s. Further improvement of TVSs will allow to expand gradually these ranges in the direction, determined by the development of the pulse engineering. In particular, it must required, probably, an expansion of voltage range up to 50-100 kV for available pulse condensers on such voltages. There is the need of the increase of a limit current and a

Table

Main characteristics of the sealed-off TVS

	TVS-3	TVS-7	TVS-43	GPV-6313	ZR-7512	——	——	——
Designer	VEI, Russia	VEI, Russia	VEI, Russia	EGG, USA	MPD, USA	HRL, Japan	BREDRI, China	KEMA HPL, Netherlands
Operating voltage, kV	0,5-40	0,5-20	0,5-25	0,3-80	0,3-40	10	5-10	15
Maximum voltage, kV	50	25	40	——	55	——	——	100
Voltage drop, kV	——	0,02-0,05	0,15	——	——	——	——	——
Operating current, kA	0,2-60	0,02-10	10-200	60	50	120	3-8	0,5
Maximum current, kA	100	——	250	——	——	——	——	——
Maximum charge per pulse, A×s	1	0,1	100	0,5	0,7	——	——	——
Turn-on delay time, μs	0,1±0,02	0,05±0,01	2	< 1	< 1	——	0,02±0,005	0,1
Trigger voltage, kV	8	5	5	——	——	11-20	1	3-10
Trigger current min, A	20	10	1000	——	——	——	35	2
Trigger current length min, μs	0,2	0,05	5	——	——	——	——	——
Maximum current rate, A/s	10^{11}	$> 10^{11}$	$> 10^{9}$	——	——	——	——	——
Electric strength recovery time, μs	30	10	100	——	——	——	——	——
Frequency, Hz	500	1000	0,02	——	——	5	——	50
Service life (number of switches)	10^{6}	10^{8}	$2 \cdot 10^{4}$	——	——	10^{3}	——	——
Overall dimensions:								
diameter, mm	100	60	150	111	108	——	——	——
height, mm	190	100	203	187	216	——	——	——
Weight, kg	3,5	0,5	7	——	——	——	——	——
References	[8]	[9]	——	[6]	[6]	[5]	[3]	[4]

value of charge a pulse for the replacement of power ingitrons at currents up to 500 kA and a value of charge in a pulse up to 400 A/s. In case of need, there are possibilities of development of high-frequency TVSs.

The intensification of the introduction of TVSs on the market will be promoted by the essential increase of its service life and reliability as for high-current, so for high-frequency versions. Moreover, a rather important direction of the improvement of vacuum switches is the reduction of start losses at the initial stage of the formation of the conductive discharge channel, that it is essential for high-frequency switches. Other important problem is the increase of a recovery rate of an electric strength of TVS, determining probability of the multiple breakdown of the switch.

It should be done more detailed researches of physical processes of the initiated vacuum discharge development for resolution of all these problem. The results of associated researches, partially presented in the references [10-12], have contributed to more comprehensive understanding of the phenomena, restricted limit parameters of TVSs, and has allowed to outline the ways of increasing the service life and the switched charge value of the available types of TVSs at reduced mass-dimensional characteristics of a switch.

The researches have shown, that nowadays design possibilities of the improvement of an erosion trigger system are not completely settled. We succeeded in essential increasing the service life of TVS-40 up to complete wear of the main electrodes due to the modernization of a trigger unit design [13] .

The modernization of a trigger unit design, as well as the optimization of the main electrode system and application of to begin improvement of a high-current vacuum switch. As a result, there were developed, manufactured and tested experimental samples of TVS-43, which is capable to switch current pulses up to 200 kA at voltages up to 25 kV and switched charge value up to 120 A·s. The service life of the switch at a switching current ~ 150 kA (crest value) and rate of its rise ~ 10^9 A/s is estimated through a summarized transferred charge ~ 10^6 A·s. New switch has smaller metal consumption in comparison with TVS-40. Some modifications of TVS-43 at different cost for various modes of application were developed.

We do not see restrictions of principle the point of view of physics of the vacuum discharge for further increase of the limit values of a switching current up to 500 kA at a transferred charge > 100 A·s.

References

1 V.A.Vozdvijenskii, V.A. Sidorov, Proc. INTERELEKTRO, Sverdlovsk, 1990, pp. 2 - 11.
2 Vacuum Arcs. Theory and Application, J.M.Lafferty ed., Wiley, New Jork, 1980
3 Xu Bin-Yu, Lu Shu-Sen, Gu Wen-Chang, Proc. 8 th Int.Conf. on Gas Discharges and Their Applications, Oxford, Sept. 1985, pp. 413 - 415.
4 L.M.J.Vries, G.C.Damstra, IEEE Trans. Power Systems, 1986, v. 1, N 2, pp.75-80.
5 H.Arita, K.Suruki, Y.Kurosawa, IEEE Trans. Plasma Sci., 1992, v. 20, N 2, pp.76-79.
6 R.Dethlefsen, V.A.Sidorov, V.A.Vozdvijenskii, Proc. 8th Int. Pulsed Power Conf., San Diego, June 1991, pp. 511-514.
7 D.F.Alferov, V.A.Vozdvijenskii,I.O.Sibiriak, V.A.Sidorov, Instrum. Experim. Tech., . April 1991, pp. 1121-1125.
8 V.A.Vozdvijenskii, V.A.Sidorov, Prib. Tekh. Eksp. 1992, № 4, pp. 104-111.
9 D.F.Alferov, V.A.Vozdvijenskii, V.A.Sidorov, Instrum. Experim. Tech., 1995, v. 38, Part 1, pp. 62-69.
10 V.A.Vozdvijenskii, V.A.Sidorov, IEEE Trans. Plasma Sci., 1991, v. 19, N 5, pp. 778-781.
11 D.F.Alferov, N.I.Korobova,I.O.Sibiriak, 1993, Fisika Plasmy, v. 19. N 3, pp. 399-410.
12 D.F.Alferov, V.A.Vozdvijenskii, N.I.Korobova,I.O.Sibiriak, V.A.Sidorov, Zh.Tekh. Fiz., 1994, v. 64, N 2, pp. 180-188.
13 D.F.Alferov, V.A.Sidorov, Prib. Tekh. Eksp., 1996, N 3.

DECADE Design and Testing Status*

P. Sincerny, K. Childers, J. Goyer, D. Kortbawi, I. Roth, C. Stallings, J. Dempsey
Physics International Company
2700 Merced Street
San Leandro, CA 94577

L. Schlitt
Leland Schlitt Consulting Services
2725 Briarwood Drive
Livermore, CA 94550

Abstract

DECADE is a very high power generator that will be built at Arnold Engineering Development Center in Tullahoma, Tennessee by the Defense Special Weapons Agency. The full facility consists of 16 modules. Two full power modules (DM1 and DM2) have been built to verify the DECADE design at Physics International. Each module consists of a 570 kJ Marx generator that pulse charges a water transfer capacitor. The transfer capacitor discharges into a water output line through an array of 6 parallel triggered gas switches. The water output line then pulse charges the inductive store/opening switch pulse compression stage. When the opening switch opens, the inductive store discharges into an electron beam bremsstrahlung diode load.

The initial testing of the DM1 module has been completed. The electrical design of the module will be presented, including circuit modeling results. The test data from a module will be compared to the modeling results. This test data, including reproducibility and timing accuracy, was used to predict the output form the full system of 16 modules and a subset of 4 unit modules (DECADE Quad). One option under consideration is to deploy a DECADE Quad at the testing center in Tennessee prior to the full 16 module system. The design sketch of the DECADE Quad and the predicted output based on the modeling and the demonstrated module performance is included in this paper.

Introduction

The DECADE facility (Figure 1) will be the first high power x-ray simulator in the US to be built using inductive store/opening switch (IS/OS) technology for the final phase of pulse compression.[1] The advantage of using IS/OS technology is that the energy is stored magnetically at high density near the load providing for high power, short pulse discharge once the opening switch opens. The plasma opening switch (POS) has been used for pulse compression and power amplification in a variety of inductive energy storage systems with conduction times ranging from tens of nanoseconds to over one microsecond.[2-11] The use of IS/OS technology rather than the conventional capacitive storage technology becomes critical for large (>50 TW), short pulse (20 ns) electron beam (bremsstrahlung x-ray) generators.

DECADE Module (DM1) Description

A side view of the DECADE test module is shown in Figure 1. The principal components are the Marx generator, the transfer capacitor (TC), the triggered output switches, the water output line (OL), the vacuum insulator, the magnetically insulated transmission line (MITL) that serves as the inductive store, the plasma opening switch (POS), and the electron

* This work is supported by the Defense Special Weapons Agency. Review of this material does not imply Department of Defense endorsement of factual accuracy or opinion.

beam/bremsstrahlung diode load. Also shown in this figure is a sketch of the power or energy transfer from the Marx to the load. The discharge sequence begins by first command triggering the Marx generator, this results in pulse charging the transfer capacitor (TC). Output switches are then command triggered and the pulse is transported down the output line prior to charging the inductive store/POS stage in 250 ns. The final event is the opening of the POS, this discharges the inductive store as a current charged pulse forming line into the diode load.

Circuit Model and Output Performance

A circuit model has been developed over the last few years as a design tool for the DECADE system. Most of the circuit elements are modeled as transmission line segments. The computer code then simulates circuit performance by keeping track of transmission and reflection at the transmission line segment interfaces. The code runs quickly on an IBM-386 (or higher) PC, since no differential equations are solved. The circuit model for DM1 is shown in Figure 2. The model has been developed to attain excellent agreement with electrical performance of all components up to the conduction current into the POS. Due to the presence of plasma and electron beam between the POS and the diode there are presently no reliable electrical diagnostics to allow quantitative calibration of the model down stream of the POS.

The principal electrical diagnostics along the machine are Marx current monitors (current viewing resistors on each sub-Marx), capacitive voltage monitor on the TC, capacitive voltage monitor in the oil upstream of the tube, current monitors in oil and vacuum (B-dots) at the tube and in the anode upstream of the POS. The current monitors and the tube voltage monitor are calibrated to about ±5%. The voltage monitor on the TC has not been carefully calibrated.

The measured waveforms along the machine are compared to the model calculations for shot 1143 as shown in Figure 3. The model calculations agree within experimental error for the well calibrated monitors and the shape of the voltage on the TC agrees with the measurement.

The voltage produced by the opening action of the POS can be "measured" using the voltage measured at the tube, the current measured in the MITL, and the known impedance and length of the transmission line between the monitor and the POS location. A comparison of the "measured" voltage at the POS with the module calculations is shown in Figure 4(a). The agreement between the model calculations and the measured waveforms is attained by adjusting the assumed profiles for the diode and POS impedances. The final assumed profiles that achieved optimum agreement in both shape and amplitude are shown in Figure 4(b).

In addition to the electrical measurements discussed above, there are also x-ray radiation measurements including a filtered Si PIN that provides a measurement of the x-ray power pulse shape. An example of the measured x-ray power pulse shape from shot 1143 is shown in Figure 4(c). The timing jitter of this radiated power is critical to the analysis of the predicted performance of a multiple module system as discussed in the next section.

DECADE System Design - Bremsstrahlung Radiation Load

The planned DECADE machine is shown in Figure 1. This machine consists of 16 electrically independent modules similar to the DM1 module. Each of the 4 large Marx tanks contains 4 separate Marx modules. Each of the quads (large Marx tank plus 4 TCs and OLs) is mounted on tracks and is designed to move back to facilitate tube, MITL, and output switch maintenance. The diode array consists of 16 hexagonally close packed ten inch diameter pinched beam bremsstrahlung diodes. The radiation output from the machine provides a uniform (2 to 1 peak to valley), approximately 10,000 cm^2 test area 5 inches from the plane of the diodes. Notice each of the modules is operated independently from the Marx through the diode and can be fired separately or as the 16 module ensemble. The predicted dose pattern

for DECADE based on the single module (DM1 shot 1341) radiation measurement is shown in Figure 5.

The combination of the radiation output from the individual modules into a single composite 40 ns (FWHM) radiation pulse at the testing plane requires; low total timing jitter (≤10 ns command fire to peak x-ray power), a narrow 35 ns FWHM single module pulse width, and a method of adjusting timing differences between modules.

The x-ray power measured on a run of 16 shots on DM1 are shown in Figure 6. The 16 waveforms are shown overlaid as referenced to the initiation (t=0) of the command fire sequence. This is a method of simulating the expected radiation pulse shape from the 16 module system with one module. Adding up all of these 16 radiation waveforms produces the predicted composite DECADE radiation pulse shape also shown in Figure 6. Note the FWHM of the predicted radiated power on DECADE is 40 ns.

The last critical timing issue for the DECADE system is the ability to adjust timing differences among the individual modules. This timing difference should be small (<20 ns) since the Marx capacitance and Marx charge voltage will be carefully controlled among the modules. The DECADE system design includes two methods of adjusting the individual module's time to x-rays. First each module on DECADE has a separate command fire timing control on the TC output switches. The capability to adjust module timing over a 100 ns range has been demonstrated on DM1. The second method of timing control is to adjust the POS conduction time by changing the plasma density of the conducting plasma. The electrical parameter that is adjusted to change the POS plasma density is the POS plasma gun charge voltage. Each of the modules on DECADE will have a separate computer controlled voltage power supply for the POS guns. The capability to adjust the module timing over a 30 ns range by this method was also demonstrated on DM1. Either method can be used to eliminate the projected timing differences between modules on DECADE. The reason for providing both methods is that the peak power from individual modules may be optimized at different conduction times in which case the TC timing control would be used to eliminate timing differences.

Two full power test modules have been built at Physics International Company to verify the DECADE design before constructing the facility in Tennessee. The two modules can either be operated in separate test facilities or combined into a common load by opening a moveable shielding wall as shown in Figure 7. The front end of the second DECADE module (DM2) that was recently completed is shown in Figure 8. This new module is completely computer controlled and is the final demonstration system before constructing a radiation test facility in Tennessee.

DECADE Quad

One of the options under consideration is to initially deploy four modules or a quarter of the DECADE system in Tennessee. A drawing of a DECADE Quad in the bremsstrahlung load configuration is shown in Figure 9. Each of the four modules will have a separate ten inch diameter pinched-beam bremsstrahlung diode.

The DECADE Quad will also be capable of driving a plasma radiation source (PRS) load for producing soft x-rays from 1 to 8 keV. A conceptual sketch of one option for combining the output from all four modules into a single PRS load is shown in Figure 10. The design sketch shows the vacuum section of the Quad. The majority of the upstream vacuum MITL hardware is the same as for the bremsstrahlung load. The PRS MITL hardware, instead of terminating in a separate diode load, has a transition from coaxial geometry to triplate. The four triplate sections from each module would join a central triplate disc feed. The power from the triplate disc would be combined into the PRS load using a standard post hole convolute.

The PRS radiation output is predicted by first using the circuit model as shown in Figure 2 with modifications for a PRS load. The circuit model modifications consist of deleting the POS and bremsstrahlung load and adding a MITL section for combining the modules and an imploding plasma model for the PRS load. The peak predicted current for the DECADE Quad driving an imploding plasma load is 7.5 MA as shown in Figure 11(a). The second step in predicting the radiation output is to use the experimental scaling data from other machines to predict the Argon k-line radiation yield for 7.5 MA as shown in Figure 11(b). This scaling data suggests the DECADE Quad should be capable of producing at least 65 kJ of Argon radiation. One area requiring further development is the demonstration of stable PRS implosions when driven by 300-400 ns current pulses. Figure 11 shows the required implosion time on the DECADE Quad is 350 ns while the majority of the scaling data was taken on faster machines with less than 100 ns implosion times.

Conclusions

The final design verification tests of the 16 module DECADE machine are in progress on two full power modules, DM1 And DM2. The modular design for DECADE allows flexibility in the next phase of implementation in Tennessee. A design sketch of a four module DECADE Quad machine has been completed. This machine should be capable of producing 20 krad (Si) over 2200 cm^2 at 1.5 MV end point with a bremsstrahlung load and greater than 65 kJ of Argon k-line radiation.

References

1. P.S. Sincerny, S. Ashby, K. Childers, J.R. Goyer, D. Kortbawi, I. Roth, C. Stallings, J. Dempsey, L. Schlitt, 10th IEEE Pulsed Power Conference Proceedings, 1995, to be published.
2. R.A. Meger, R.J. Commisso, G. Cooperstein, and S.A. Goldstein, Appl. Phys. Lett. **42**, 943 (1983).
3. B.V. Weber, F.J. Commisso, G. Cooperstein, J.M. Grossmann, D.D. Hinshelwood, D. Mosher, J.M. Neri, P.F. Ottinger, and S.J. Stephanakis, IEEE Trans. Plasma Sci. **PS-15** (1987); see also Ref 6.
4. G.A. Mesyats, S. P. Bugaev, A.A. Kim, B.M. Koval'chuk, and V.A. Kokshenov, IEEE Trans. Plasma Sci. **PS-15** (1987).
5. C.W. Mendel, Jr., M.E, Savage, D.M. Zagar, W.W. Simpson, T.W. Grasser, and J.P. Quintenz, Appl. Phys. **71**, 3731 (1992).
6. R.J. Commisso, P.J. Goodrich, J.M. Grossmann, D.D. Hinshelwood, P.F. Ottinger, and B.V. Weber, Phys. Fluids B **4**, 2368 (1992).
7. J.R. Goyer, D. Kortbawi, P.S. Sincerny, D. Parks, and E. Waisman, J. Appl. Phys. **77** (6), 2309 (1995).
8. W. Rix, D. Parks, J. Shannon, J. Thompson, and E. Waisman, IEEE Trans. Plasma Sci. **19** (1991).
9. W.J. Summa, et al., "Advances in X-Ray Simulator Technology," 10th IEEE Pulsed Power Conference Proceedings, 1995, to be published.
10. B.V. Weber, et al., "The DECADE Performance Assessment Program", Beams 96 (June 1996).
11. K.D. Ware, et al., "Inductive-Energy Power Flow for X-Ray Sources", Beams 96 (June 1996).

Figures

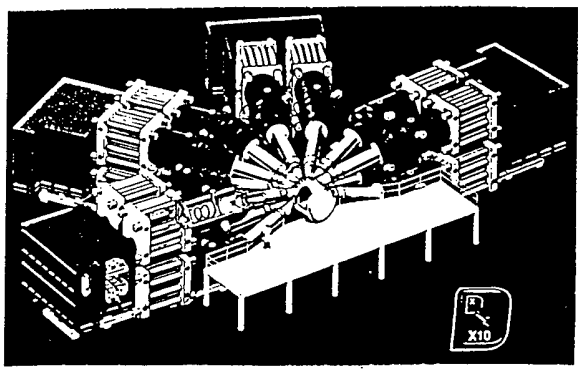

Figure 1. DECADE Simulator

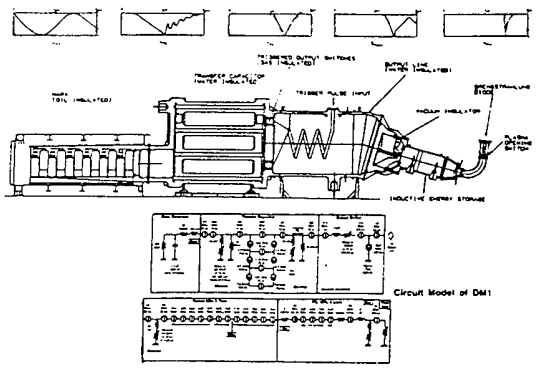

Figure 2. Side View and Circuit Model of a DECADE Module

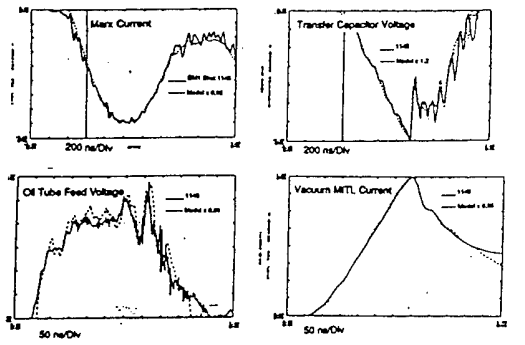

Figure 3. Electrical Measurement from DM1 on Shot 1143 Agrees Within 5% with the Circuit Model Results (Marx to the MITL)

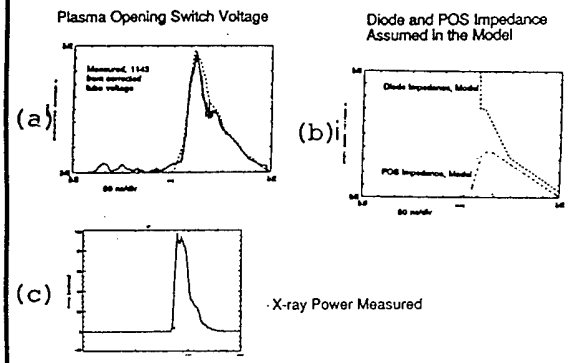

Figure 4. The Voltage Generated by the Plasma Opening Switch is 1.9 MV. The X-ray Radiation Produced in the Electron Beam Diode is Also Measured

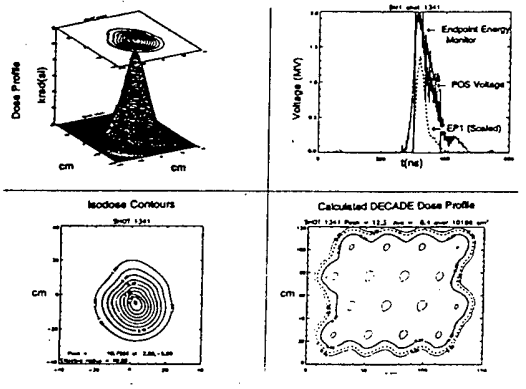

Figure 5. DM1 Radiation Measurements on Shot 1341

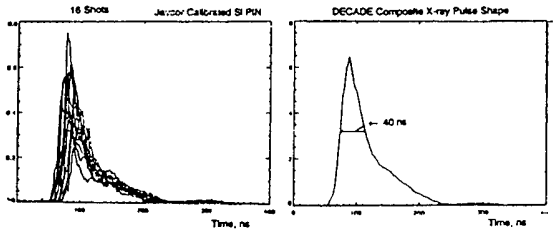

Figure 6. Composite DECADE Pulse Width from 16 Shots is 40 ns

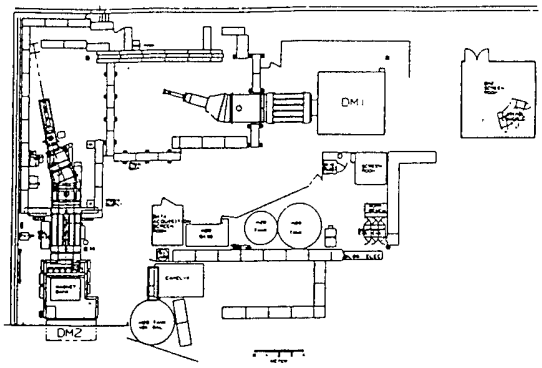

Figure 7. The DECADE Test Facilities

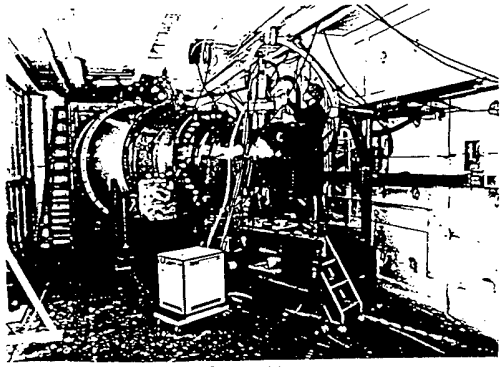

Figure 8. DM2 Output Line and Front-End

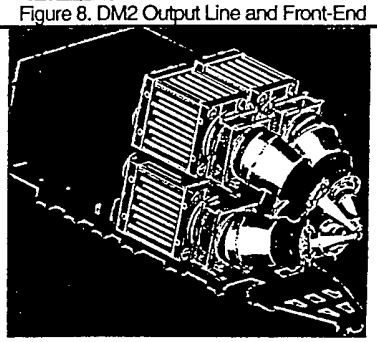

Figure 9. DECADE Quad Brems Configuration

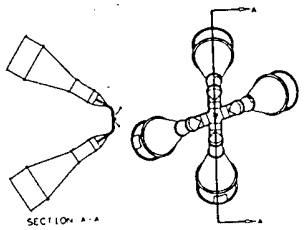

Figure 10. DECADE Quad Direct Drive PRS

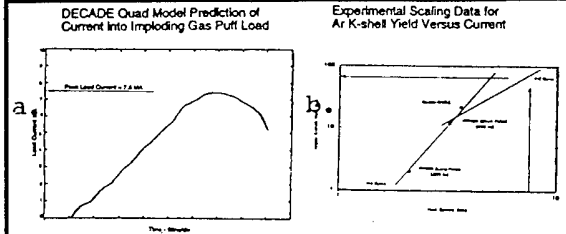

Figure 11. With Improved Stability at Longer Implosion Times the DECADE Quad will be Capable of 65 kJ of Argon K-line Radiation

P-3-83

EXPLOSIVE OPENING SWITCHES WITH CONTROLLED TIME OF CURRENT RISING IN THE LOAD

V.K. Chernyshev, G.I.Volkov, V.A.Ivanov, S.V.Pak, A.N.Skobelev

VNIIEF, Sarov, N.Novgorod region, Russia

When solving some physical problems, in particular, when studing the dynamic characteristics of solid liners accelerated by magnetic field, highpower magnetic energy sources with controlled time of current rising in the load are needed. The helical explosive-magnetic generators equipped with explosive opening switches are commonly used in our experiments. Such sources produce the energy of tens megajoules (1) and transmit it to the load in a matter of microseconds.

It is known that for the constant load and generator inductance the solution for the current commutation electrical circuit equipped with explosive opening switch is presented as follows:

$$I_l(t) = I_0(1-\exp(-\int \alpha R_p(t)dt) \quad \text{, where}$$

$I_l(t)$ is a current in the load,

I_0 is a current in the generator circuit at the instant the commutation is started up.

$R_p(t)$ is an opening switch resistance.

$$\alpha = (L_g + L_l) / L_g L_l \quad \text{, where}$$

L_g and L_l are generator and load inductance, respectively.

As seen from the solution, the time of current rising in the load, when L_l and L_g are specified, is defined by the integral $\int \alpha R_p(t).dt$. The time of energy transmission to the load may be controlled by varying Rp(t). In the studies performed earlier (2 and 3) the resitance of the length and thickness of the ruptured conductor. In this case the conductor was ruptured along the total length at a time due to the shell charge initiated simultaneously over the entire surface. A new metlod to change the resistance of opening switch due to detonation propagating in steps over the shell charge or to detonation

propagating in the mode of gliding shock wave was proposed and studied to extend the range for the time of current rising in the load.

In the first experiment performed with the helical explosive-magnetic denerator 160 mm in diameter and explosive dielectric jet opening switch (4) with the rupturing conductor 100 mm long, 1 mm thick and 300 mm wide, the detonation was initiated over the shell charge in the mode of gliding shock wave. The generator and load inductance was 25 nH. The current in generator and load circuits was 10 MA and 4.5 MA, respectively.

The recorded time of current rising in the load increased by a factor of 3 as compared with the earlier test when the simultaneous charge initiation was provided.

In the second experiment the helical explosive-magnetic generator 200 mm in diameter with explosive dielectric jet opening switch with the rupturing conductor 600 mm long, 2 mm thick and 600 mm wide was used. The generator and load inductance was 50 nH. The shell charge was initiated in successive steps along the way of current propagation with the delay of 1 μs every 100 mm. The ultimate generator current of 22 MA produced in the inductive load the current pulse with the amplitude of 22 MA and the leading edge rising of 10 μs. The time of current rising in the load increased by a factor of 2.8 as compared with the experiment when the whole shell charge was initiated at a time.

The obtained results indicate that there is a possibility to vary the time of current pulse rising in the load at the current level up to 10 MA due to the charge initiation provided at different times in the range between 2 and 10 μs.

References

[1] Chernyshev V.K., Volkov G.I., Ivanov V.A., Korchagin V.P., Pak S.V., Scobelev A.N., Strekin V.P.: Explosive Magnetic Source 30 MJ Stored Energy for Gas Ponderomotive Unit Power Supply. In: Megagauss Magnetic Field Generation and Pulse Power Applications, Nova Science Publishers, New York 1994, pp. 557-563

[2] Chernyshev V.K., Volkov G.I., Ivanov V.A., Vakhrushev V.V.: Study of Basic Regularities of Formation of Multi-MA-current Pulses with Short Risetime by EMG Circuit Interruption. In: Megagauss Physics and Technology, New York 1980, pp. 663-675

[3] Chernyshev V.K., Volkov G.I., Ivanov V.A., Mikhailov O.D.: Experimental Investigation of Explosive Opening SwitchOperation. In: Megagauss Magnetic Field Generation and Pulse Power Applications, Nova Science Publishers, New York 1994, pp. 731-732

[4] Chernyshev V.K., Andreevskikh L.A., Ivanov V.A., Mikhailov O.D., Novikov V.F.: Mechanical Conductor Disruption Character in Explosive Current Commutators. In: Megagauss Fields and Pulse Power Systems, Nova Science Publishers, New York 1990, pp. 533-536

P-3-84

DEVELOPMENT OF HIGHLY REPETITIVE PULSE POWER SYSTEM USING AMORPHOUS METALLIC CORES

Katsumi Masugata and Kiyoshi Yatsui,
Department of Electrical Engineering, Nagaoka University of Technology, Nagaoka, Niigata 940-21, Japan

Abstract

A new type of pulse power system has been developed to obtain an efficient, highly repetitive pulse-power generation. The system is constructed of a double pulse circuit (1st stage), step-up transformer and Blumlein pulse forming line (BL) and can generate high power pulse of 600 kV, 24 kA, 60 ns. In the system, discharge gap switches are replaced by magnetic switches. In addition, instead of Marx generator, step-up transformer is utilized to generate high voltage pulse. The system is tested under the double pulse mode where two 1st stage capacitors are connected in parallel and switched with a interval of T_d. The minimum value of T_d is limited by the recovery of 1st stage gap switches and at $T_d \geq 500$ μs (equivalent rep-rate of 2 kHz), the system is operated with good reproducibility. To enhance the recovery, magnetic switch is utilized, which enable the operation at $T_d \geq 30$ μs (equivalent rep-rate of 33 kHz).

1. Introduction

Pulsed power systems have been widely applied for the generation of high power particle beams, for the excitation of gas lasers, or for the strong radiation sources[1,2]. In those applications, it is very important to develop a highly repetitive system. Recently, magnetic switches have been utilized with thyristor or thyratron to obtain a highly repetitive operation and more than 5 kHz of repetition rate has been obtained[4]. However, due to the limitation of switching current in these switches, those combination seems to be applicable only for a small system.

A hydrogen gap switch on the other hand, has been found to have a fast recovery of breakdown voltage[5]. Since the upper limit of the switching

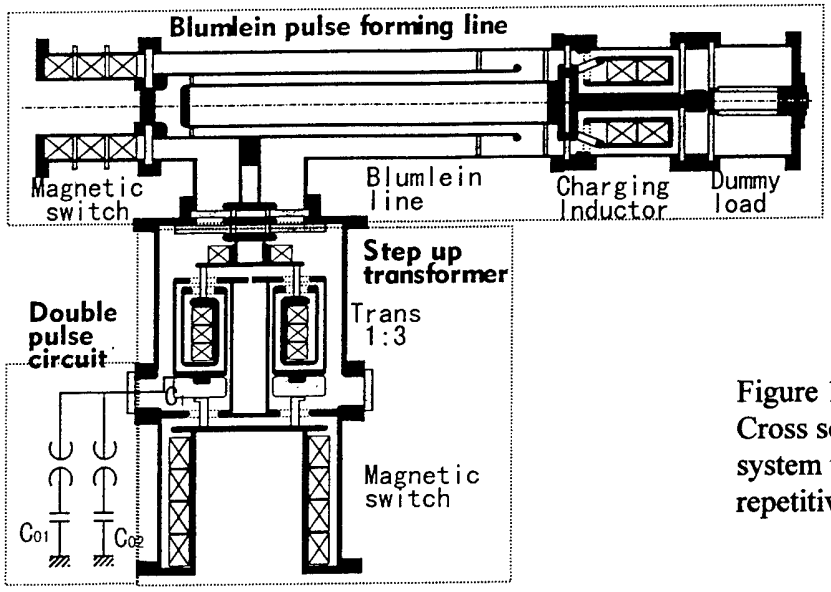

Figure 1.
Cross sectional view of the system to demonstrate highly repetitive operation.

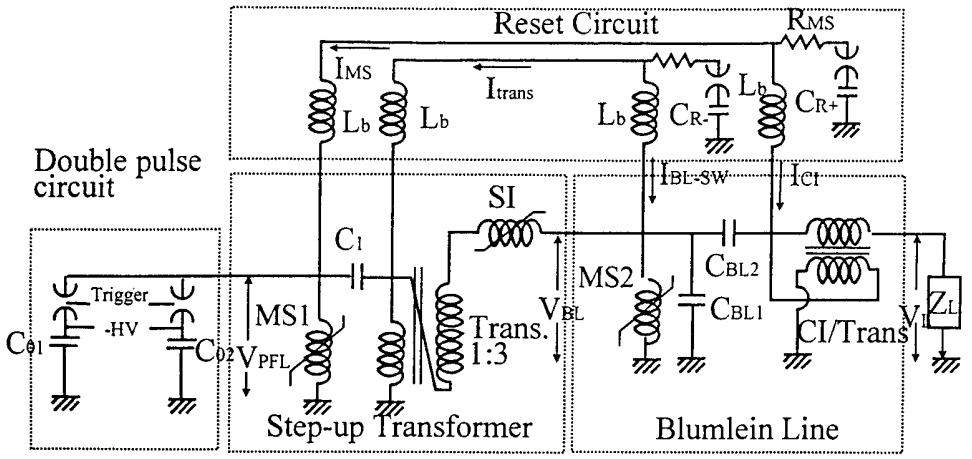

Figure 2. Equivalent circuit of the system.

current in the switch is very high, a combination of the hydrogen gap switch with magnetic pulse compressor is hopeful to develop high-power, high-repetition systems.

To develop a highly repetitive system, we have developed a new type of pulsed power system using magnetic pulse compressors with hydrogen gap switches. To demonstrate the performance, the system is tested on the double pulse mode.

2. Experimental system

Figure 1 shows the cross-sectional view of the experimental system. The system consists of a double pulse circuit, a step-up transformer[6] and a Blumlein pulse forming line[7] and has a output parameter of 600 kV, 24 kA, 60 ns. In the double pulse circuit, a pair of capacitors (C_{01}, C_{02}) with hydrogen gap switches are utilized to produce double pulse. The step up transformer consists of a 2nd stage capacitor (C_1), a magnetic switch of amorphous core (MS1), a step up transformer using amorphous core (Trans.), and a saturable inductor of amorphous core (SI) and the pulse is compressed and is stepped up in the circuit. In the Blumlein, magnetic switch (MS2) and saturable charging inductor (CI/Trans.) are utilized to obtain the efficiency and make possible the repetitive operation. The system is operated under the double pulse mode, where C_{01} and C_{02} are switched with an interval of T_d. In the system of using ferromagnetic cores, it is necessary to reset the cores to obtain the best performance and the reproducibly of the system. The reset of the core is done by applying bias current before operation. Since that the value of coercive forces (H_c) for amorphous metallic core is usually several A/m or less and corresponding current for the core of sub-meter diameter size is less than 10 A, it is possible to reset the core by a DC current. However, for repetitive operation, pulsed reset circuit is employed in the system to reset in the short time.

Figure 2 shows the equivalent circuit of the whole system used in the experiment. The double pulse circuit, the step-up transformer, and the pulse forming line are described with a reset circuit. As seen in the figure, a pair of capacitor banks (C_{R+}, C_{R-}, 80 μF, 3.5 kV each) are utilized in the circuit to reset the amorphous cores. Four inductors (L_b, 50 μH) are used to block the surge voltage produced by the main pulse of the system. To obtain unipolar (non oscillatory) wave forms, dumping resistors (R_d) of 1.6 Ω are inserted in each banks.

Figure 3 shows the waveforms of the reset current of the magnetic switch (I_{MS}), the transformer (I_{ST}), the Blumlein switch ($I_{BL\text{-}SW}$), and the charging inductor of the Blumlein (I_{CI}). The charging voltage of C_{R+} and C_{R-} in the shots are +1 kV and –kV, respectively. As seen in the figure, each currents have over dumped, unipolar waveform of rise time around 100 μs and peak current around 150 A. The values of H_c are less than 4 A/m for MS1, Trans, MS2, and less than 2 A/m for CI/Trans. and the current necessary to reset these cores are less than 10 A. Consequently, 150 A of reset current are one order of magnitude higher than the values, it seems to be sufficient to reset these cores.

The circuit parameter of the system in the test is listed in Table I. The experiment is done

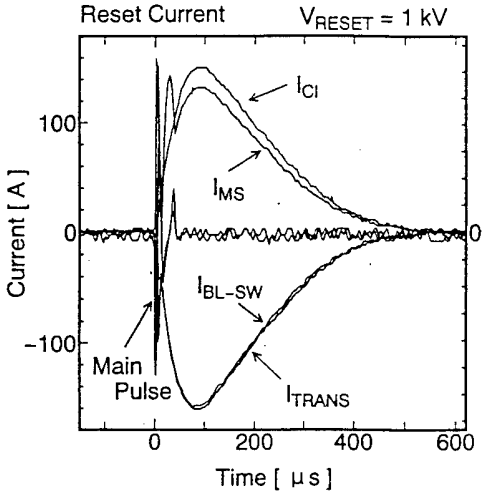

Figure 3. Typical waveforms of the reset current.

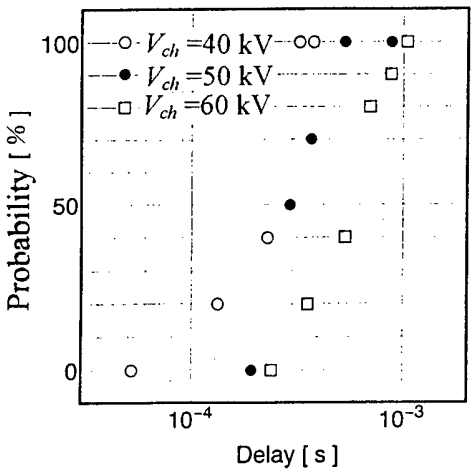

Figure 5. Probability of successful operations plotted against T_d.

Table I Circuit parameter in the experiment.

C_{01}, C_{02}	450 nF, 450 nF
C_{01}	240 nF
C_{BL1}, C_{BL1}	11 nF, 9 nF
Z_L	25 Ω
Output impedance of the line	24Ω
Hydrogen gap switches used in the double pulse circuit	gap length 8mm, filling pressure 10 atm, self breakdown voltage (V_{BS}) 100 kV

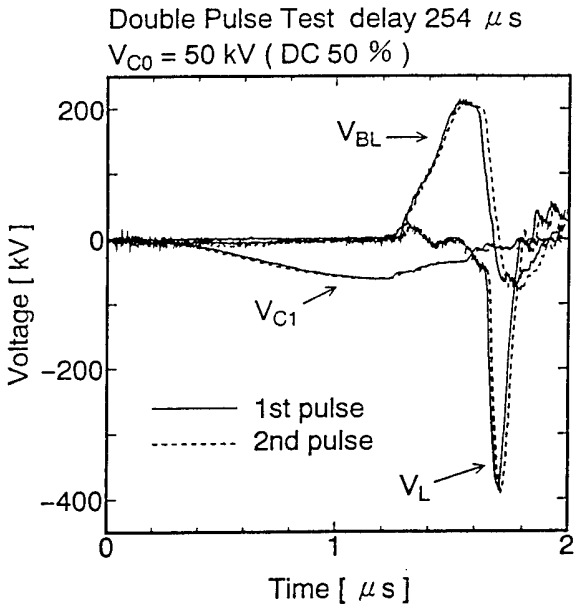

Figure 4. Typical waveforms obtained in the shot of T_d = 254 μs.

the sequence shown as follows.

1. Initial reset of the cores.
2. Charging of the 1st capacitors (C_{01}, C_{02}) and the reset circuits (C_{R1}, C_{R2}).
3. Trigger C_{01} and the reset circuits (C_{R1}, C_{R2}), simultaneously.
4. Trigger C_{02} with an interval of T_d after the trigger of C_{01}.

3. Results of the experiment

Figure 4 shows the typical waveforms of the charging voltage of C_1 (V_{C1}), the charging voltage of the line (V_{BL}), and the load voltage (V_L) obtained in the experiment in the shot of T_d = 254 μs and the charging voltage (V_{ch}) of 50 kV. Solid lines and dashed lines corresponds to the 1st and the 2nd shots, respectively. As seen in the figure, good correspondence has been obtained between the 1st and the 2nd shots. That is, the system is successfully operated at T_d = 254 μs as a result that hydrogen switch is recovered and sustain the charging voltage of C_{02}.

Figure 5 shows the probability of successful operation plotted against T_d as a parameter of charging voltage. Ten shots of operation is done for each T_d. As seen in the figure, when charging voltage is 50 % of the self breakdown voltage of the hydrogen switches (V_{BS}), probability of 100 % is obtained at T_d = 500 μs. That is, 2 kHz of equivalent repetition rate is obtained without miss-firing. In the case of 40% and 60 % of V_{BS}, the equivalent repetition rates are observed to be 3 kHz and 1 kHz, respectively.

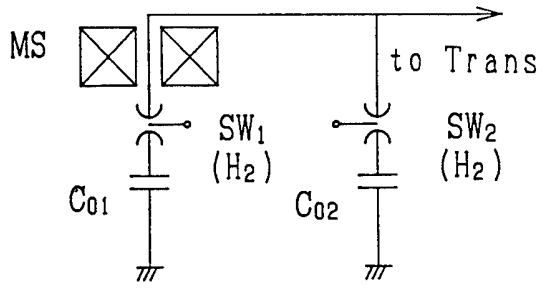

Figure 6. Circuit of 1st stage bank when MS is used to assist for the recovery of spark gap switch.

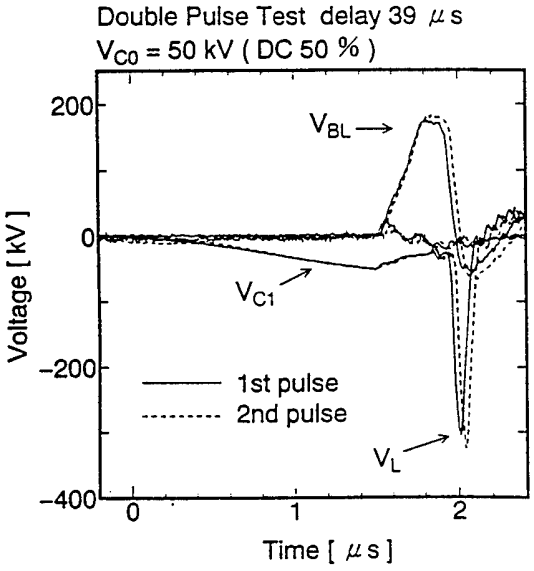

Figure 7. Typical waveforms obtained with magnetic assistance at $T_d = 39$ μs..

To obtain more high repetition rate, additional MS is used in the double pulse circuit. Figure 6 shows the circuit used in the experiment. The MS is the Fe based amorphous core of magnetic swing (ΔB) = 0.18 T and has a dimension of 250 mm (OD), 114 mm (ID) and 96 mm (W). The core with 4 turn of winding gives a $V\tau$ value of 0.049 (Vs). The MS is reset in the same direction as the current produced by C_{01}. As the $V\tau$ value produced by C_{02} is roughly estimated to be

$$\int_0^{\tau} V_{C02}\,dt \approx \frac{1}{2} V_{ch} \cdot \tau$$

where V_{C02} is the output voltage of C_{02}, τ is the charging time of C_1, and V_{ch} is the charging voltage of C_{02}. In case of V_{ch} is 50 kV, corresponding $V\tau$ value is 30 ms, the value is small enough compared to the $V\tau$ value obtained by MS. That is, the pulse voltage by C_{02} (2nd pulse) is sustained by MS. In the case, no time is necessary to recover SW_1 and T_d is limited only by the reset circuit.

The experiment is done at $V_{ch} = 50$ kV. To obtain fast rest of the cores, charging voltage of reset circuits are increased to 3 kV. The waveforms become stable when $T_d > 39$ μs.

Figure 7 shows the waveforms obtained by the circuit when $T_d = 39$ μs. In the case, the repetition rate is limited by the reset time and the result indicate that it takes about 39 μs to reset amorphous cores.

The energy transfer efficiency is estimated by comparing the charging energy of C_{01} with an output pulse energy obtained by integrating the product of a load voltage and load current. High value of 65 % is obtained, which is much better than the case of using SF_6 and operated in the single pulse mode (less than 50 %)[6], or the case that BL is operated with Marx generator (around 40 %).[7]

References

1) J. A. Nation: Particle Accelerators **10**, 1 (1979).
2) J C. Martin: Proceedings of IEEE **80**, 934 (1992).
3) M. T. Bertram, R. S. Clark: Particle beam fusion progress report SAND79-1944, 157 (1979).
4) D. S. Prono, D. Barren, D. L. Birx, J. K. Boydi, G. Caporaso, J. C. Clark, F. Coftield, F. Deadlock, J. Klingmann, W. Nexsen, Jr., M. A. Newton, D. Ravenscroft, L. Reginald. W. C. Turner. G. A. Westenscow, and K. Whitham: Proc. 7th Include Conf. on High-Power Particle Beams, Karlsruhe, vol. **I**, 214-220 (1988)
5) S. L. Moran and L. W. Hardesty: IEEE Transaction on Electron Device **38**, 726 (1991).
6) K. Masugata, H. Saitoh, H. Maekawa, and K. Yatsui: submitted.
7) K. Masugata, T. Tsuchida, H. Saitou, M. Shibata, K. Shigeta, Y. Sekimoto, and K. Yatsui: Proc. Int'l Conf. on High-Power Particle Beams, Washington DC, 485 (1992).

P-3-85

PRINTED BOARD DIPOLE TRIM MAGNET DESIGN FOR A 20 MEV LIA

Chengjun Liu, Wenjun Zhu, Kaizhi Zhang, Wenwei Zhang and Haijun Yu

Institute of Fluid Physics, CAEP, P.O.Box 523-56, Chengdu, 610003, P.R.China

Abstract

The printed board dipole trim magnet design for a 20MeV LIA is presented. The prototype dipole magnet with the sin/cos distributed windings has demonstrated more than 650 Gs-cm integrated dipole field and 1% integrated dipde field homogeneity within 5 cm in radius, which is about 40% of the magnet radius. Numerical modeling of two prototype magnet designs using the 3D magnetic field code SCMAG is presented as well as data from magnetic field measurements of the two magnets. The agreement between the calculations and measurements is accurate to 2-3%.

Introduction

The 20 MeV Linear Induction Accelerator (LIA) will produce a 3-kA, 20-MeV, 60-ns flattop high-brightness electron beam using a series of 250 -kV, ferrite-core induction cells, 8 of which construct an electron beam injector of 2-MV and the remaider is used as a post-accelerator. To transport the electron beam, each cell (except 4 of the injector)contains a solenoid magnet. An ideal solenoid would only produce a magnetic field along its axis. Real solenoid also produce transverse field component("error fields")which kick the beam off-axis, causing the chromatic oberration known as "corkscrew"[1] and enhancing the growth of the Beam Breakup instability (BBU).Both phenomena result in transverse oscillations and emittance growth of the beam .To meet the accelerator performance goals, the reduction of transverse error fields in these magnets is the principal design challenge. Our solenoid design features bifilar winding to reduce field errors due to winding geometry ,iron homogenizer rings within the solenoid to greatly reduce the effects of winding errors, and printed board dipole trim magnets inside the solenoids to correct any remaining field misalignment. These design considerations have been proved very effective[2],[3],[4].

Our two prototype dipole magnets are fabricated by photoetching 0.5mm thick copper sheet laminated to 0.2mm polymer film. Each dipole has two such layers, which are wrapped inside the solenoids and oriented 90° apart. Therefore, the dipole magnets can produce a dipole field of arbitrary phase angle to correct for solenoid installation errors.

In the following sections, the winding design and 3D field calculation, calculated and measured results, and conclusions are presented.

Winding design and 3D field calculation

It is important that the trim magnets must have a high enough dipole magnetic field and a good enough field homogeneity for the correction need, that maily depend on their winding distribution. For comparision, one designed two winding distributions for the prototype trim magnets, which are 12.6 cm in radius and 45 cm in length. One magnet has the sin/cos distributed windings of 30 turns in each half and its number of turns per degree at the circumference of the circular cross section is approximately proportional to the sin or cos of the phase angle. The other has the uniform distributed windings of only 6 turns in each half and its winding density is constant. For the two winding geometries, each turn is saddle-shaped as shown in Fig.1.

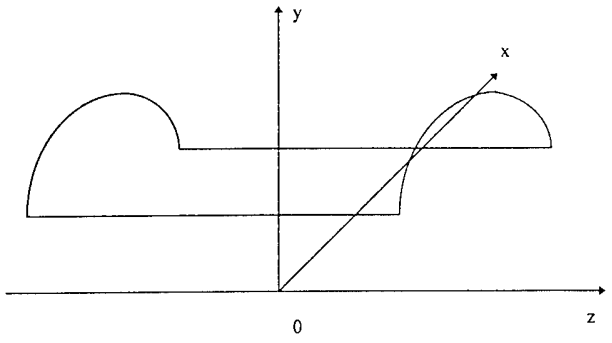

Fig.1. Saddle-shaped winding turn of the dipole magnets

The magnetic field in the trim magnet is calculated by the 3D magnetic field code SCMAG, in which the field at a point in space is obtained by integrating the Biot-Savart relation over the entire conductor path. Each turn conductor is represented by a straight section plus a circular arch for the end region. For field calculations each turn conductor is subdivided by 1-2 in thickness and 1-6 in width with each subdivision being approximated by a filament at its center.

Calculated and measured results

The normal dipole field, B_y, skew dipole field, B_x and axial field component, B_z in the two trim magnets were calculated. In calculations, the current per turn was 10A and 60A for the sin/cos distribution magnet and the uniform distribution one respectively. In this case, both magnets have nearly same electric consumed power. The 3D magnetic field measurements of the two magnets were completed by a Hall probe gaussmeter with 0.1 Gs sensitivity. Fig. 2 shows the calculated normal dipole field profiles both along the axial distance, Z and in the transverse cross sections, as well as the corresponding measured data. The calculated normal integrated dipole fields, $\int B_y dz$ at the various radius, r and phase angle, θ are shown in Fig.3.

as seen from Figs.2 and 3, the normal integrated dipole fields of the two magnets are nearly same and more than 650 Gs-cm, but the normal dipole field homogeneity for the sin/cos distribution magnet is much better than that for the uniform distribution one. The homogeneous field region with 1% homogeneity for the sin/cos distribution magnet is up to 5cm in radius, which is about 40% of the magnet radius, while that for the uniform distribution one only 2cm in radius. Furthermore, both calculations and measurements indicate that the skew dipole field , B_x and axial field component, B_z for the sin/cos

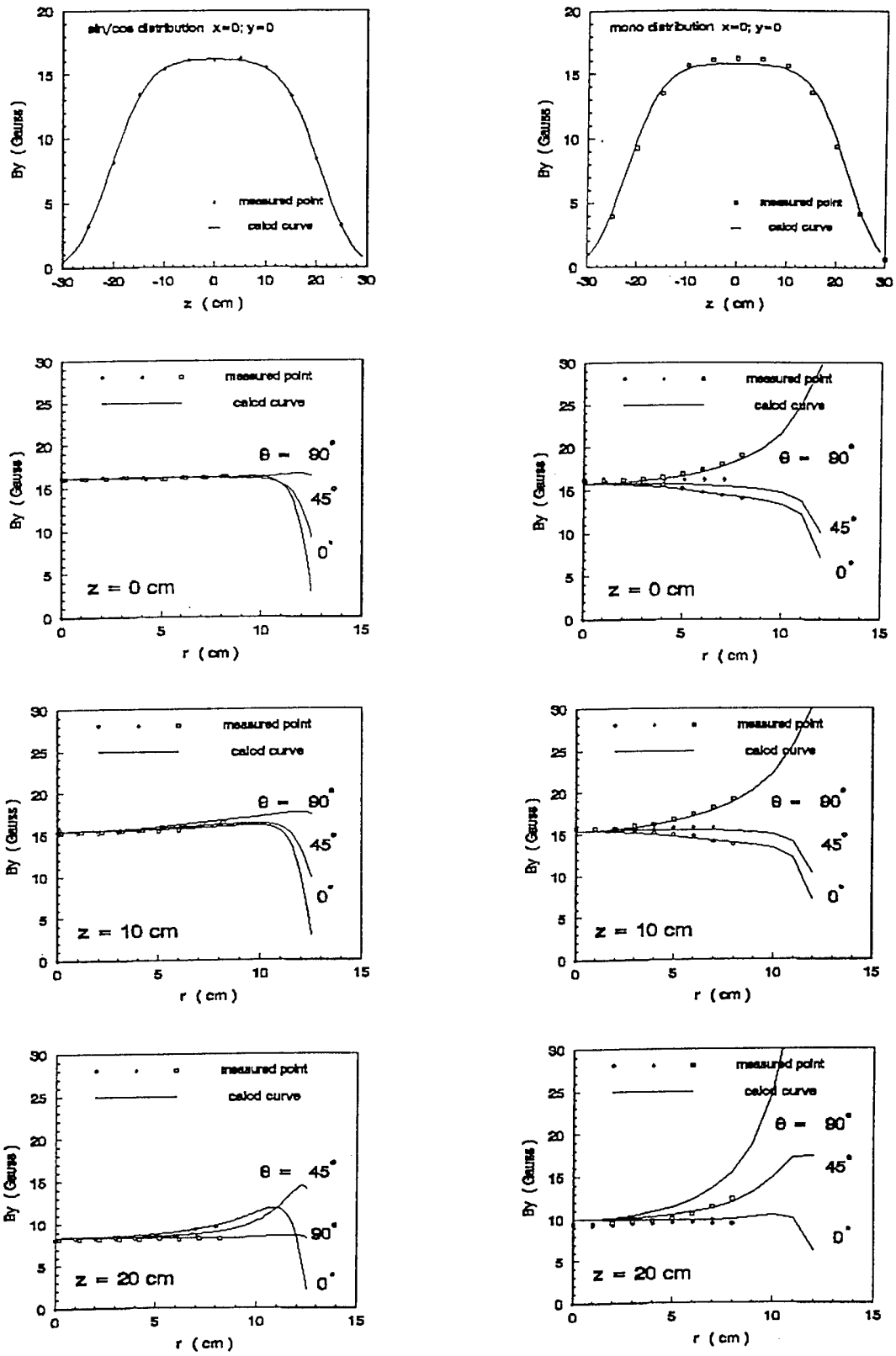

Fig. 2 Calculated and measured results for sin/cos distribution (left) and uniform distribution (right) : normal dipole field at axis, B_y (o) vs. axial position, Z(top), and B_y vs.radius, r at various phase angle, θ for various Z.

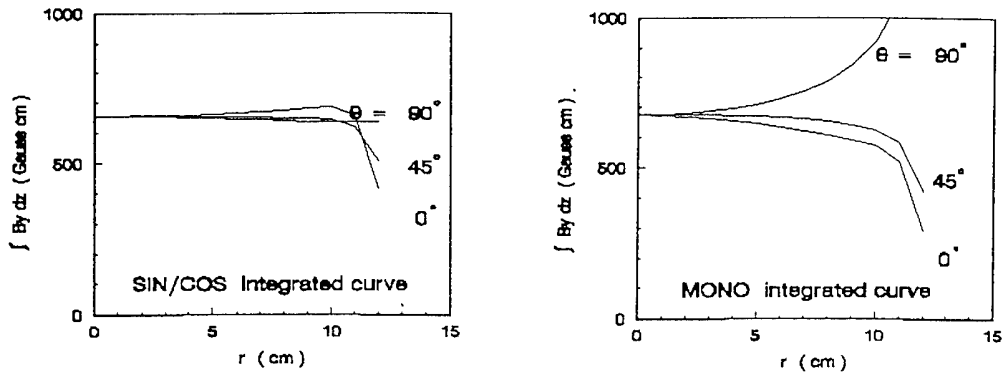

Fig.3 calculated normal integrated dipole fields, $\int B_y dz$ vs. radius, r at various phase angle, θ for sin/cos distribution (left) and uniform distribution (right).

distribution magnet are also less than that of the uniform distribution one. For the sin/cos distribution magnet, B_x/B_y within 5cm in radius and 40cm in axial length is less than 5%. Serious normal dipole field non-homogeneity and skew dipole field component can produce higher order field harmonics. For our trim magnets, the field harmonics in the end region are to be further examined.

It is also seen from Fig.2 that the agreement between the calculations and measurements is very good and accurate to 2-3%. this shows the SCMAG code did work very well.

Conclusions

Two prototype printed board dipole trim magnets with different distributed windings were designed and fabricated. Numerical modeling using the 3D magnetic field code SCMAG and measurements of the two magnets were completed. The results show the sin/cos distributed winding design is superior to the uniform distributed winding design in the field homogeneity. The magnet with the sin/cos distributed windings has demonstrated more than 650 Gs-cm integrated dipole field and 1% integrated dipole field homogeneity within a radius of 5cm which is about 40% of the magnet radius. The agreement between the numerical modeling and measurements is very good and accurate to 2-3%. The higher order field harmonics in the end region of the magnets are to be further studied.

[1] Chen,Y.J. , : Nucl. Inst. and Meth. in Phys.Res.A, **292** (1990) 455

[2] Feinberg, B., et al : Nucl. Inst. and Meth., **203** (1982) 81

[3] Burns, M.,et al: Conf.Proc. IEEE PAC, (1991) 2110

[4] Zentler, Jan-Mark, et al: Conf. Proc. LINAC, (1992)

P-3-86

HALO FORMATION IN RMS-MATCHED INTENSE ION BEAMS

C. Chen and Y. Fink
Plasma Fusion Center
Massachusetts Institute of Technology
Cambridge, MA 02139, USA

R. C. Davidson and Q. Qian
Plasma Physics Laboratory
Princeton University
Princeton, NJ 08543, USA

Halo formation is studied for ion beam propagation through an alternating-gradient focusing channel with root-mean-squared (RMS) matched envelopes in the space-charge-dominated regime. In particular, an earlier theoretical model [1] is generalized to describe halo formation observed recently in a potassium (K^+) beam in the 2-MV Heavy Ion Beam Injector Experiment at the LBNL [2], where the measured density profile shows a density depression on the beam axis. This generalization allows qualitative comparisons between the halo theory and the experimental measurements, which are found in good agreement.

1. INTRODUCTION

The problem of halo formation is a major concern in the design of advanced high-current, high-power particle accelerators with a wide range of applications such as heavy ion fusion, high-energy and nuclear physics research, tritium production, advanced radiation sources, and high-power, high-resolution radar, all of which require the production, acceleration, and transport of intense electron and/or ion beams. The consequences of halo formation range from emittance growth in the beam, to the buildup of radioactivity in the accelerator, to the meltdown of system components, depending on the applications.

For a space-charge-dominated beam which is root-mean-squared (RMS) matched into an alternating gradient focusing channel and whose density profile decreases parabolically from the beam axis, it has been previously shown [1] that nonlinearities in the beam self fields due to the charge density nonuniformity induce chaotic particle motion and cause a small fraction of particles to escape from the beam interior to form a halo. Recently, experimental evidence of halo formation has been observed in a space-charge-dominated potassium (K^+) beam in the 2-MV Heavy Ion Beam Injector Experiment at the Lawrence Berkeley National Laboratory (LBNL) [2], where the measured density profile shows a density depression on the beam axis. The aim of this paper is to generalize the halo theory [1] to allow the beam to have a density depression on the beam axis, so that qualitative comparisons can be made between the theory and the experimental observations.

2. THEORETICAL MODEL

We consider a thin, continuous, intense ion beam propagating with average velocity $\beta_b c\vec{e}_z$ through the periodic quadrupole magnetic field

$$\vec{B}^q(x,y,s) = B'_q(s)(y\vec{e}_x + x\vec{e}_y) = \vec{B}^q(x,y,s+S), \tag{1}$$

where (x,y) is the transverse displacement from the beam axis at $(x,y)=(0,0)$, $s=\beta_b ct$ is the axial distance, $B'_q(s) = (\partial B^q_x/\partial y)_0$ is the quadrupole field gradient, and S is the axial periodicity length of the quadrupole magnetic field.

In the present test-particle model for the beam, we assume that the beam density profile transverse to the propagation direction is given by

$$n_b(x,y,s) = \begin{cases} \hat{n}_b + \delta\hat{n}_b - 2\delta\hat{n}_b\left(\frac{x^2}{a^2}+\frac{y^2}{b^2}\right), & \text{for } \frac{x^2}{a^2}+\frac{y^2}{b^2} \le 1, \\ 0, & \text{otherwise.} \end{cases} \tag{2}$$

In Eq. (2), $N = \pi ab\hat{n}_b = \int n_b dxdy = \text{const.}$ is the number of ions per unit axial length. The parameter $\delta\hat{n}_b$ is a measure of the nonuniformity in the beam density and is allowed to be in the range $-\hat{n}_b < \delta\hat{n}_b \le 0$. Note that for $\delta\hat{n}_b < 0$, the density peaks at the elliptical beam envelope defined by $x^2/a^2 + y^2/b^2 = 1$.

In the paraxial approximation, the transverse equations of motion for an individual test particle can be expressed as [1]

$$\frac{d^2x}{ds^2} + \kappa_q(s)x + \frac{q}{\gamma_b^3\beta_b^2 mc^2}\frac{\partial}{\partial x}\phi(x,y,s) = 0, \tag{3}$$

$$\frac{d^2y}{ds^2} - \kappa_q(s)y + \frac{q}{\gamma_b^3\beta_b^2 mc^2}\frac{\partial}{\partial y}\phi(x,y,s) = 0. \tag{4}$$

In Eqs. (3) and (4), $\kappa_q(s) = qB'_q(s)/\gamma_b\beta_b mc^2$; q, m, and γ_b are the ion charge, rest mass, and relativistic mass factor, respectively; c is the speed of light in *vacuo*; and $\phi(x,y,s)$ and $\beta_b\phi(x,y,s)\vec{e}_z$ are the electrostatic and vector potentials associated with the space charge and current of the intense ion beam, which have been determined analytically [1] for the beam density profile defined in Eq. (2). For simplicity, we choose $\kappa_q(s)$ as the periodic step function defined by

$$\kappa_q(s) = \begin{cases} \kappa_{q0}, & \text{for } 0 \le s/S < \eta/4, \\ 0, & \text{for } \eta/4 \le s/S < (2-\eta)/4, \\ -\kappa_{q0}, & \text{for } (2-\eta)/4 \le s/S < (2+\eta)/4, \\ 0, & \text{for } 1-\eta/4 \le s/S < 1, \end{cases} \tag{5}$$

where $\kappa_q(s+S) = \kappa_q(s)$, and η is the filling factor.

Following Sacherer [3], the periodic envelope functions, $a(s+S) = a(s)$ and $b(s+S) = b(s)$, can be determined from

$$\frac{d^2a}{ds^2} + \kappa_q(s)a - \frac{2gK}{a+b} - \frac{(4g\epsilon_x)^2}{a^3} = 0, \tag{6}$$

$$\frac{d^2b}{ds^2} - \kappa_q(s)b - \frac{2gK}{a+b} - \frac{(4g\epsilon_y)^2}{b^3} = 0. \tag{7}$$

Here, $K = 2q^2N/\gamma_b^3\beta_b^2 mc^2$ is the normalized beam perveance, $g = (1-3\delta\hat{n}_b/\hat{n}_b)^{-1}$, $\epsilon_x = (\langle x^2\rangle\langle x'^2\rangle - \langle xx'\rangle^2)^{1/2}$ and $\epsilon_y = (\langle y^2\rangle\langle y'^2\rangle - \langle yy'\rangle^2)^{1/2}$ are the unnormalized RMS beam emittances in the x- and y-directions, respectively, and $x' = dx/ds$. Both ϵ_x and ϵ_y are taken to be constant in the model.

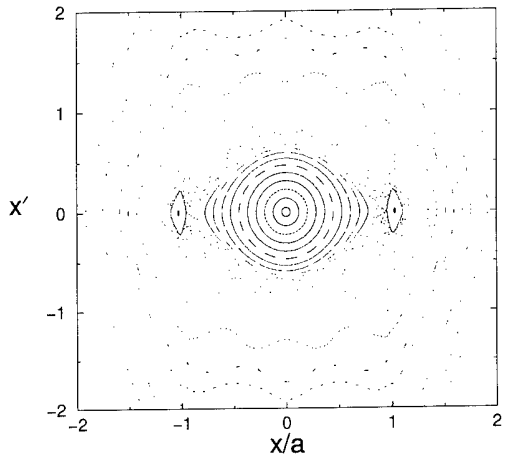

Figure 1: Poincaré surface-of-section plot in (x, x') phase space for 41 test particles in a nonuniform density beam. Here, the choice of system parameters corresponds to $\sigma_0 = 70°$, $\eta = 0.5$, $SK/4\epsilon_x = 16$, $\epsilon_x = \epsilon_y$, and $\delta\hat{n}_b/\hat{n}_b = -0.2$. The vertical axis is scaled by the dimensionless quantity $(S/4g\epsilon_x)^{1/2}$.

Finally, we specify the initial conditions for the test particles at $s = 0$ according to the distribution function

$$f_b(x, y, x', y', s = 0) = \frac{(N + \delta N)^2}{16\pi^2 g N \epsilon_x \epsilon_y}\delta(W - 1) - \frac{2\delta N}{\pi ab}\left(\frac{x^2}{a^2} + \frac{y^2}{b^2}\right) H\left(\frac{x^2}{a^2} + \frac{y^2}{b^2}\right)\delta(x')\delta(y'). \tag{8}$$

Here, $\delta N = \pi ab\delta\hat{n}_b$; $\delta(x)$ is the Dirac δ-function; $H(x)$ is defined by $H(x) = 1$, for $0 \leq x \leq 1$, and $H(x) = 0$ otherwise; and W is defined by

$$W = \frac{x^2}{a^2} + \frac{y^2}{b^2} + \frac{4g - 3}{16g^2}\left(\frac{a^2 x'^2}{\epsilon_x^2} + \frac{b^2 y'^2}{\epsilon_y^2}\right). \tag{9}$$

It is readily shown from Eq. (8) that $n_b(x, y, s = 0) = \int f_b dx' dy'$ is consistent with Eq. (2). Note that the maximum value of W for the test particles is equal to unity at $s = 0$ for the choice of distribution function f_b in Eq. (8).

3. RESULTS

It is evident that there is a large parameter space in which the beam dynamics can be investigated. The primary emphasis of this paper is to compare the present halo theory with recent experimental observations of halos around a space-charge-dominated potassium (K^+) beam in the 2-MV Heavy Ion Beam Injector Experiment at the LBNL. Because electrostatic quadrupoles are used to focus the beam transversely and to accelerate the beam longitudinally in the experiment, the comparisons below are meant to be qualitative.

Figure 1 shows the overall phase space structure as a Poincaré surface-of-section plot [4] in (x, x') phase space for a nonuniform density beam. The choice of system parameters in

Fig. 1 corresponds to vacuum phase advance $\sigma_0 = 70°$, $\eta = 0.5$, $SK/4\epsilon_x = 16$, $\epsilon_x = \epsilon_y$, and $\delta\hat{n}_b/\hat{n}_b = -0.2$, which is a good representative of the K^+ beam in the LBNL experiment [2]. In the experiment, the physical parameters are: $S \cong 0.8$ m, $\sigma_0 = 70°$, $I_b = 0.79$ A, and $4\gamma_b\beta_b\epsilon_x = 0.6 \times 10^{-6}$ m-rad; and the potassium ions are accelerated from 1 to 2 MeV with 4 electrostatic quaduroples (i.e., 2 lattice periods). Shown in Fig. 1 are the trajectories of 41 particles as they pass through the lattice points at $s = 0,\ S,\ 2S, \cdots, 400S$. The initial conditions for these particles are: $x(0)/a(0) = 0.1n$, $y(0) = 0$, and $x'(0) = y'(0) = 0$, where $n = 0, \pm 1, \cdots, \pm 20$. Note that for $y(0) = 0 = y'(0)$, the motion in (x, x') phase space is decoupled completely from that in (y, y') phase space. In Fig. 1, there are two stable period-one orbits near the edge of the beam at $(x, x') \cong (\pm a, 0)$. These stable period-one orbits are accompanied by two *unstable* period-one orbits located approximately at $(x, x') \cong (\pm 0.9a, 0)$. It is the chaotic separatrix associated with the unstable period-one orbits that is responsible for particle escape from the beam interior to form a halo.

For beam propagation through several lattice periods, the Kolmogorov-Arnold-Moser (KAM) surface [4] at $(x, 0) = (\pm 1.42a, 0)$ is expected to determine the halo size. Therefore, the halo size in the x-direction is estimated to be $x_{\rm halo} = 1.42a$, which is in good agreement with the measured halo size $x_{\rm halo} = 1.47a$ [2]. Detailed numerical studies of the beam dynamics with the initial distribution function defined in Eq. (8) show that a relatively small fraction (4%) of the particles in the beam become halo particles after five lattice periods, and the experimental measurements indicate that about 2% of the particles become halo particles in one lattice period.

4. CONCLUSIONS

It has been shown that charge density nonuniformities can cause halos to develop around intense ion beams propagating through a periodic quadrupole magnetic field. Halo formation has been attributed to chaotic particle motion induced by the nonlinearities in the self-electric and self-magnetic fields associated with the beam space-charge and current. For the parameter regime investigated, it is found that a halo develops once the beam has propagated through a few periods of the focusing lattice. Good agreement is found between the halo theory and the measurements of halos around a potassium (K^+) beam in the 2-MV Heavy Ion Beam Injector Experiment at the LBNL. Because only a small fraction of the beam particles become halo particles, this mechanism for halo formation is likely to persist even when the beam is RMS-matched into a periodic focusing channel.

5. ACKNOWLEDGMENTS

This work was supported by the U.S. Department of Energy, Grant No. DE-FG02-95ER40919 and Contract No. DE-AC02-76-CHO-3073.

[1] Q. Qian, R. C. Davidson, and C. Chen, *Phys. Plasmas* **2**, 2674 (1995).
[2] S. S. Yu, private communication.
[3] F. J. Sacherer, *IEEE Trans. Nucl. Sci.* NS-18, 1105 (1971).
[4] A. J. Lichtenberg and M. A. Lieberman, *Regular and Chaotic Dynamics*, 2nd Edition (Springer-Verlag, New York, 1992).

P-3-87

EQUIVALENT CIRCUIT MODELING OF SPACE CHARGE DOMINATED MAGNETICALLY INSULATED TRANSMISSION LINES

Kazuki HIRAOKA, Mitsuo NAKAJIMA and Kazuhiko HORIOKA
Department of Energy Sciences, Tokyo Institute of Technology
Nagatsuta 4259, Midoriku Yokohama, Japan 226

ABSTRACT

We have developed a new equivalent circuit model for space charge dominated MITLs(Magnetically Insulated Transmission Lines). MITLs under high power operation are dominated with space charge current flowing between anode and cathode. Conventinal equivalent circuit model does not account for space charge effects on power flow. To discuss the power transportation through the high power MITLs, we have modified the model. With this model, we can estimate the effects of space charge current on the power flow efficiency, without using complicated particle code simulations.

1. DEVELOPMENT OF THE MODEL

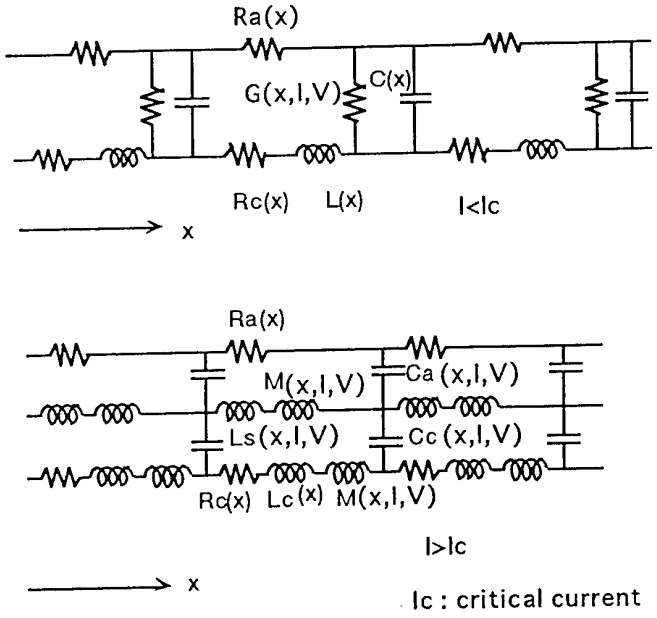

Fig.1 Modified Equivalent Circuit of MITL

In our modeling, as shown schematically in Fig.1, once magnetic insulation is established (I>Ic), the equivalent circuit is replaced by modified circuit that has space charge current path. Here, Ic is the critical current and G is the conductance of space charge limited current flows across the vacuum gap when the insulation is not achieved.

To determine Ic, L, M and C analytically, we use laminer flow theory of space charge flow[1]. It assumes that electrons move in straight trajectories normal to the electric and magnetic field and parallel to the axis. In this theory, solutions for potential, charge desity distribution, and fraction of the current carried by the space charge are obtained self-consistently as follows,

$$I = \frac{I_\alpha}{\ln\left(\frac{r_a}{r_c}\right)} \gamma_m \cdot \left\{ \ln\left(\gamma_m + \sqrt{\gamma_m^2 - 1}\right) + \frac{\gamma_0 - \gamma_m}{\sqrt{\gamma_m^2 - 1}} \right\} \tag{1}$$

$$I_b = \frac{I}{\gamma_m} \tag{2}$$

with

$$\gamma_{0,m} = 1 + \frac{eV_{0,m}}{m_0 c^2} \tag{3}$$

$$I_\alpha = \frac{m_0 c^2}{e}\frac{2\pi}{\mu_0 c} = 8500(A) \tag{4}$$

Here I is the total (anode) current, Vo is the anode potential, Vm is the potential at the edge of the electron sheath, and γ_m is the ratio of total (anode) current I and conduction (boundary) current Ib on the cathode. When the solutions for γ_m of equation (1) are not existing, we regard as the magnetic insulation is not achieved and the minimum value (for V) of right side of equation (1) is chosen for Ic.The distributing profile of space charge flow is assumed as,

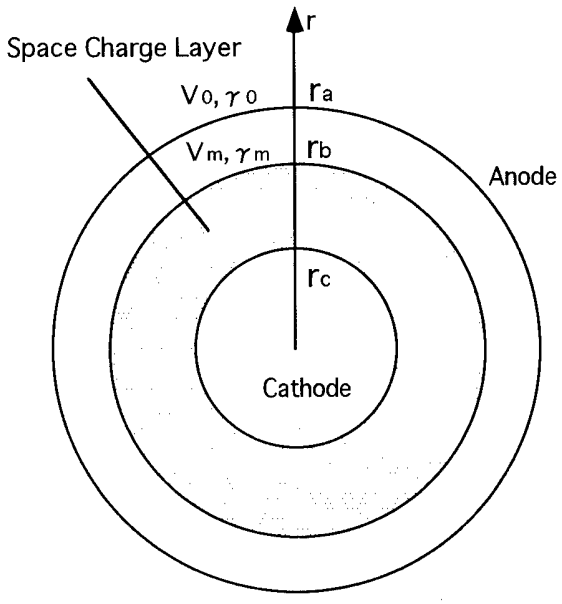

Fig.2 Cross section of cylindrical MITL

$$i(r) = \frac{I}{\gamma_m}\cosh\left(\frac{I}{I_\alpha \gamma_m}\ln\frac{r}{r_c}\right) \tag{5}$$

where r is coodinate of radial direction in the cylindrical MITL, rc and ra is radius of the cathode and anode(Fig.2), i(r) represents the current enclosed with the cylinder of radius r. The outer radius of space charge layer is expressed as

$$r_b = \exp\left(\ln r_a - \frac{\gamma_0 - \gamma_m}{\sqrt{\gamma_m^2 - 1}}\frac{I_\alpha \gamma_m}{I}\right) \tag{6}$$

With these functions, effective inductance Lc, Ls and mutual inductance M can be calculated analytically, as follows,

$$L_c = \frac{\mu_0 l}{2\pi}\ln\frac{r_a}{r_c} \tag{7}$$

$$L_s = \frac{\mu_0 l}{2\pi}\ln\frac{r_a}{r_b} + \frac{1}{I_s}\int_{r_c}^{r_b}\frac{i(r)-I_b}{I_s}\cdot\frac{\mu_0 l}{2\pi r}\cdot\frac{i(r)-I_b}{r}dr \tag{8}$$

$$M = \frac{\mu_0 l}{2\pi}\ln\frac{r_a}{r_b} + \int_{r_c}^{r_b}\frac{i(r)-I_b}{I_s}\cdot\frac{\mu_0 l}{2\pi r}dr \tag{9}$$

where, Is is the space charge current: Is = I - Ib = (1-1/γ_m)I, and l is the length of one unit of the equivalent circuit.

The calculation of effective capacitance Ca and Cc depends on some assumptions. At first, we must derive the expression for capasitance dC at radius r and gap distance dr,

$$dC = \frac{2\pi\varepsilon_0 l\, r}{dr} \tag{10}$$

If the currents flowing in the next unit are primed, the current flowing this capasitance is i(r)-i'(r). Using this current and an assumption of the square pulse, the voltage between the edge of electron sheath and the cathode surface is

$$V_m = \int_{r_c}^{r_b} \frac{1}{dC} \int_0^T \Big(i(r) - i'(r)\Big) dt \tag{11}$$

$$\approx \int_{r_c}^{r_b} \frac{1}{dC} \Big(i(r) - i'(r)\Big) T \tag{12}$$

$$= \int_{r_c}^{r_b} \frac{1}{2\pi\varepsilon_0 l} \cdot \frac{1}{r} \Big(i(r) - i'(r)\Big) T\, dr \tag{13}$$

For simplicity, we assume that the ratio i(r) and Ib is nearly equals that of i'(r) and I'b, and Cc is calculated from the next eq.

$$\frac{1}{C_c} = \frac{V_m}{(I_b - I_b')} \approx \int_{r_c}^{r_b} \frac{1}{2\pi\varepsilon_0 l} \cdot \frac{1}{r}\, i(r)\, dr \,/ I_b \tag{14}$$

The capasitance of the vacuum region is obtained by

$$C_a = \frac{2\pi\varepsilon_0 l}{\ln \dfrac{r_a}{r_b}} \tag{15}$$

The resistance R is electrode resistance when skin depth is about 10^{-5} m .
The conductance G of space charge limited current is usually the product of four functions(16). They are a space-charge-limited Langmuir-Child conductance G_{CL}which depends on voltage and geometry(17), an electric field dependent function f1 accounting for emission turn-on, a smooth function of current f2 which is 1 for zero current and drops to 0 when $I \geq I_c$, and correction function f3 for relativistic effects. Generally to say, the choice of these functions f is arbitrary. In this report, we chose f1, f3 = 1 for simplicity.

$$G = G_{CL} f_1 f_2 f_3 \tag{16}$$

$$G_{CL} = \frac{8\pi\, \varepsilon_0\, r_c}{9(r_a - r_c)^2} \sqrt{\frac{2eV}{m}} \tag{17}$$

2. RESULTS

Fig.3(a),(b)are comparisons of simulation results between the equivalent circuit calculation and the PIC simulation and the Flow Impedance model [2]. As shown in Fig.3(a), the effective impedance (V/I) is reduced to about 80% of wave impedance by taking account of space charge current[3] . Because the calculations of PIC and the Flow Impedance model are for positive polarity, they are not strict comparison, but qualitative characteristics are fairly expressed with our model. With some modifications, our model can treat positive polarity.

3. CONCLUDING REMARKS

We have developed a new equivalent circuit model of MITLs which includes space charge effects. Results obtained with this model are compared to those by PIC and Flow Impedane model simulations. The qualitative agreement between the simplified calculation and the results of PIC simulation is fairly good. The CPU time for the calculations is only one minute or so by an average level personal computer (with Power PC603 75MHz unit).

REFERENCES

[1] John M.Creedon, J.Appl.Phys. 46, p.2946 (1975).

[2] C. W. Mendel, Jr. and S. E. Rosenthal , Proc.10th Int.Conf.High Power Particle Beams, p276 (1994)

[3] K.Hiraoka,K.Horioka,M.Nakajima and T.Aoki , NIFS-PROC-24 (1996 now printing)

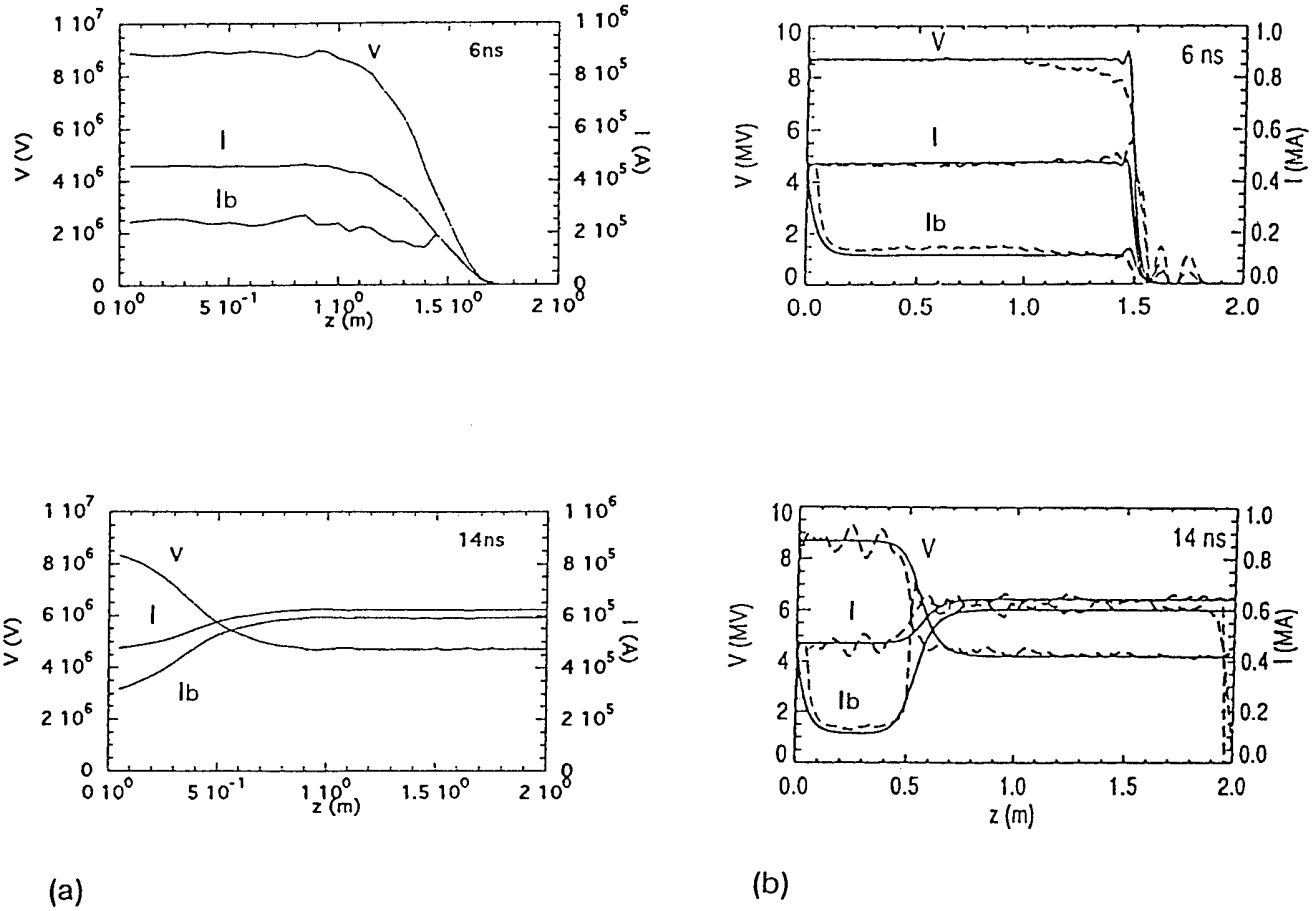

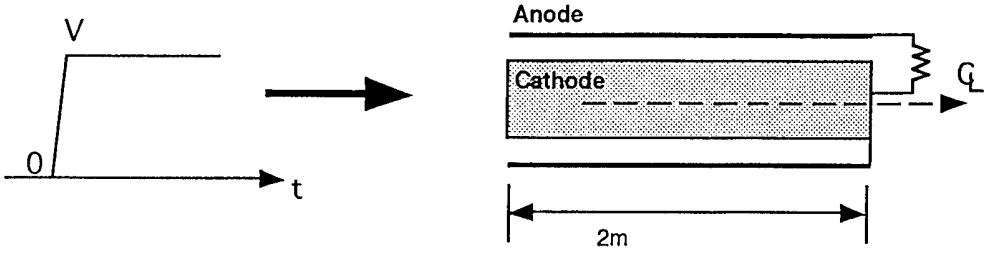

Fig.3 (a)The model and (b) PIC(dashed) and Flow Impedance model(solid) caluculations for a step voltage in a 24.3Ω, 2m long MITL.

CONTRIBUTED PAPERS P-4

Astrophysics

Beam and Plasma Diagnostics

Inertial Confinement Fusion

Ion Beam Physics

Ion Diodes

Ion Rings

Ion Sources

Plasma Opening Switches

Solid State Opening Switches

Targets

HIGH-VOLTAGE SPACE TETHER FOR PARTICLE SCATTERING IN EARTH'S RADIATION BELTS

V. V. Danilov
Krasnoyarsk State University, 660041 Krasnoyarsk, Russia
V. V. Mirnov[1], *D. Üçer*
Middle East Technical University, 06531, Ankara, Turkey

1 Introduction

New applications of space tethers are discussed in relation with the idea [1] of an active experiment, in the Earth's radiation belts. Two long (about 10 km long each) strings of radius $r_p \sim 1mm$ made from cevlar and coated with a highly conducting material are supposed to be tethered in opposite directions between the main satellite and two small subsatellites, flying through the ERB in equatorial plane. High potential difference $\phi_p \sim 1\ MV$ is applied between the tethers, by means of a compact high voltage generator carried by the main satellite. The tethers can effectively scatter the high energy particles into loss cone, providing a control of particle life time in ERB. This high-voltage satellite system can be used for precipitation of charge particles from man-made radiation belts, affecting the ozone layer depletion and other active experiments in space such as ARAKS, CRRES, *etc.*. Electrodynamic aspects of the tethers and technical requirements for the generator are the subject of the consideration below.

2 Structure of the sheath layer

The high energy particles are scattered due to the sheath layer formed around the tethers by relatively cold plasma ($n = 10^2\ cm^{-3}$, $T = 100\ eV$) existing in ERB. The problem of evaluation of the potential profile is quite similar to that studied in the standard double Langmuir probe theory [2]. Specific feature of our case is extremely high potential of the probe $p = e\phi_p/kT \sim 10^4$ and high aspect ratio $R = r_s/r_p \sim 10^8$, that strongly effects on the value of sheath radius r_s ($r_s \sim 0.5\ km$) and current collected by the tethers. Since this range of parameters is not widely discussed in publications, potential and current calculations are reproduced below by making use of some rough iteration technics.

With high voltage applied between the tethers two oppositely charged sheaths are formed around the strings. Positively charged string attracts the electrons and, correspondingly, the area around it is negatively charged, while the ions are attracted by another string, which is surrounded by positively charged layer. In stationary state electron and ion currents has to be equal to each other. Since the calculations related to ion and electron sheaths are quite similar, we will focus attention on the ion case only.

The typical ion velocity in the sheath area is $v_s = \sqrt{2e\phi_p/m_i} \sim 1.4\ 10^7\ m/sec$, transit (bounce) time $t_s = 2r_s/v_s \sim 10^{-4}\ sec$, Larmor radius is large enough, $r_{Li} \sim 100\ km$, that allows to neglect effect of magnetic field on particle motion. Electrostatic potential is, therefore, axisymmetric with respect to the tethers and with the assumption of an infinitely long string it varies along r only, where z axis of the cylindrical reference frame (r, α, z) is chosen to be along the strings. The particle dynamics is governed by the integrals of energy

[1]on leave from Budker Institute of Nuclear Physics, Novosibirsk, 630090, Russia

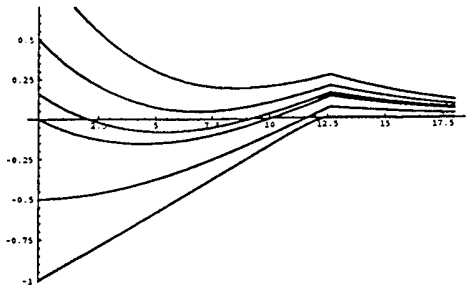

Figure 1: The graphs of $U_{eff}(M,r)$ (normalized to $e\phi_p$) versus $\ln r/r_p$ for a few values of M. The lower curve ($M = 0$) illustrates a typical behavior of electrostatic potential in sheath area

$E = m_i v^2/2 + e\phi(r)$ and angular momentum $M = mvr\sin\alpha$. With the help of conservation laws 3D problem of particle motion is reduced to 1D problem, which corresponds to the radial motion with effective potential energy $U_{eff}(M,r) = M^2/2mr^2 + e\phi(r)$. Analyzing graphs of U_{eff} illustrated in Fig.1, one can classify particles in accordance with their integral of motion into three main groups - locally trapped, absorbed and transit ions.

Ion distribution function is described by Vlasov-Maxwell equation with boundary condition at $r \to \infty$, implying that particles flying toward the string ($v_r < 0$) have a Maxwell distribution function: $f = f_m = n_\infty(m/2\pi kT)^{3/2}\exp(-mv^2/2kT)$, and boundary condition on the string surface ($r = r_p$) assuming that all particles reaching this surface become absorbed without any emission. Then, ion current density and ion density can be evaluated by integration of distribution function over the relevant region in velocity space.

The critical issue of ion density calculation is the distribution function of the locally trapped particles. If significant amount of these particles is accumulated and trapped in the sheath area, then electrostatic potential turns out to be shielded in the narrow vicinity of the string that strongly decreases scattering efficiency. Because of this reason some mechanism (AC current or other one) for removing and pumping of trapped particles has to be provided. In our further consideration we will analyze the most favorable case assuming that trapped particle distribution function equals to zero.

With the help of some simplifications based on the fact that the maximum of U_{eff} is well localized near the sheath boundary, $r_{max} \simeq r_s$ (see Fig.1), expression for ion density inside the sheath area can be written as follows:

$$n_i(r) = \frac{n_\infty}{\pi}\left[\int_{\alpha_1}^{\alpha_2} d\alpha \exp\left(-\frac{p\phi(r)\sin^2\alpha}{1-(r^2/r_s^2)\sin^2\alpha}\right) + \int_{\alpha_2}^{\pi} d\alpha \exp\left(\frac{p+p\phi(r)(r^2/r_p^2)\sin^2\alpha}{1-(r^2/r_p^2)\sin^2\alpha}\right)\right] \tag{1}$$

where $\alpha_1 = \arcsin[r_p/r]$, $\alpha_2 = arcsin[(r_s/r)\sqrt{1-\phi(r)(R^2-1)}\ ]$, $\phi(r)$ is a potential, normalized to ϕ_p. Since electrons are strongly repulsed by the negatively charged tether, their density is described by Boltzman distribution: $n_e(r) = n_\infty \exp[-p\phi(r)]$. Then, Poisson's equation has been treated numerically yielding potential profile. First approximation for $\phi(r)$ was found due to simplification that ion density is a *const*, $n_i(r) = n_\infty$. Making use of initial condition on the string surface, $\phi(r_p) = 1$, and varying initial slope at this point, the sheath radius r_s has been evaluated in the way allowing to satisfy with two other conditions, $\phi(r_s) = d\phi(r_s)/dr = 0$.

The profile obtained is then substituted into (1) to calculate corrected dependence $n_i(r)$. Corrected function turns out to be *const* ($n_i = n_\infty$) everywhere, except narrow vicinity of the string ($0 \le \ln(r/r_p) \le 5$), where ion density gradually decreases reaching value $n(r_p) = n_\infty/2$ on string surface. Since this area makes small contribution in r.h.s. of Poisson's equation, second iteration for $\phi(r)$ proved to be close to the first one, shown in Fig.1. With the accuracy needed for the treatment of the scattering problem this function

ϕ_p, MV	0.1	0.5	1.0	1.5	2.0	2.5	3.0
r_s, km	0.10	0.24	0.31	0.38	0,46	0.50	0.54
$J, 10^{-3}A$	1.4	3.2	4.5	5.5	6.4	7.2	7.8
P, kW	0.14	1.60	4.50	8.25	12.8	18.0	23.4

Table 1: The dependences of sheath radius r_s, collected current ($L = 10\ km$), and electrical power on applied potential difference ϕ_p

can be approximated as follows:

$$\phi(r) = \begin{cases} \phi_p\left[(\ln(r/r_p)/\ln R) - 1\right] & r \le r_s \\ 0 & r \ge r_s \end{cases} \tag{2}$$

Calculations of ion current density are not sensitive to the locally trapped particles. Evaluating corresponding integrals, one obtains:

$$j_r = n_\infty \left(\frac{2kT}{\pi m_i}\right)^{1/2} \frac{r_p}{r} \left(\exp p \int_{\sqrt{p}}^{\infty} x^2 \exp(-x^2)dx + R\int_0^{p/R} x^2\exp(-x^2)dx\right) \tag{3}$$

In the case of practical interest, $p \gg 1, R \gg 1$, expression (3) can be simplified yielding total current collected by the negative tether: $J_i = 2en_\infty r_p L(2e\phi_p/m_i)^{1/2}$. Similar expression for electron current is inversely proportional to $m_e^{1/2}$. Equating electron and ion currents yields potential of the strings with respect to infinity: $\phi_+ = \phi_p/(1 + m_i/m_e) \sim 500\ V, \phi_- = \phi_p/(1 + m_e/m_i) \sim \phi_p$, showing that only negative string can effectively scatter high energy component. The summary of the results related to electrical characteristics of the tethers is given in Table 1.

3 The scattering of high energy particles

Because the scattering angle of high energy particles caused by their collisions with the sheath layer is small, Fokker-Planck equation can be used for the treatment of particle losses from ERB. In the reference frame (x, y, z), z axis is supposed to be along magnetic field while the string is oriented along y axis. During a process of scattering the absolute value of perpendicular velocity, $\vec{v}_\perp = v_x\vec{e}_x + v_z\vec{e}_z$, and the value of v_y are conserved. Then, the increment of $\vec{v}_\perp$ is: $|\Delta\vec{v}_\perp| = 2v_\perp \sin(\alpha/2)$, where α is the scattering angle in xz plane. With the help of (2) α is found to be the following function of impact parameter ρ:

$$\alpha = \frac{2e|\phi_p|}{mv_\perp^2}\frac{1}{\ln R}\arctan\sqrt{r_s^2/\rho^2 - 1} \tag{4}$$

In order to find the rate of diffusion into the loss cone, θ component of velocity increment $\Delta v_\theta = 2\sin\frac{\alpha}{2}\cos\varphi$ is analyzed, where θ is a pitch angle, φ is azimuthal angle in a spherical reference frame. To evaluate average moment $< \Delta\theta^2 >=< \Delta v_\theta{}^2 > /v^2$, which defines the rate of losses, we take into account many microcollisions of test particle with the string, resulting from it's bounce motion along field lines and slow revolution of satellite in equatorial plane. Then, averaging can be done by means of integration over ρ ($-r_s \le \rho \le r_s$), while v, θ and $\sin\varphi = x/r_L$ are fixed, where x is a coordinate of guiding center, $r_L = mv\sin\theta/eB$ is

$H,\ km$	protons $A_{loss}(sec^{-1})$	protons E_0, MeV	protons $q_{total}(sec^{-1})$	electrons $A_{loss}\ (sec^{-1})$	electrons E_0, MeV	electrons $q_{total}(sec^{-1})$
2000	4.3×10^9	64.2	1.8×10^{15}	2.5×10^{17}	0.28	1.4×10^{18}
6000	9.9×10^{11}	17.7	3.1×10^{16}	1.2×10^{17}	0.22	3.7×10^{17}
10000	7.8×10^{15}	1.0	2.5×10^{21}	2.3×10^{16}	0.3	1.5×10^{17}
20000	1.9×10^{17}	0.25	8.0×10^{17}	9.1×10^{15}	0.57	2.5×10^{17}

Table 2: The characteristics of the distribution functions of loss-fluxes for the different radiation belts ($\phi_p = 1\ MV, L = 10\ km, r_s = 0.32\ km$)

a Larmor radius.

$$< \Delta\theta^2 >= 4(\pi - 2)\frac{Lr_s v}{2\pi r_L l\ (2\pi R_s)} \left(\frac{2e\phi_p}{mv^2 \ln R}\right)^2 \frac{1 - (x^2/r_L^2)}{\left(1 - (x^2/r_L^2)\sin^2\theta\right)^{3/2}} \tag{5}$$

Here l is a length of magnetic field line, R_s is a radius of satellite orbit.

Making use of Fokker-Planck equation the rate of particle losses from ERB has been evaluated. It results in the energy distributions of loss-fluxes, which represent the number of particles escaping from ERB per unit time and having energies greater than E. The fluxes are averaged over the time interval which is much longer then the period of satellite revolution over the Earth. They are also integrated over the area, thus, giving the rate of total amount of particles falling down to the Earth's surface. Using the experimental date obtained through the measurements of the fluxes of trapped particles in radiation belts, yields the tail of distribution function of escaping particles:

$$\frac{dN}{dt}(> E) = A_{loss}(E_0/E)^2 \exp(-E/E_0) \tag{6}$$

where factors E_0 and A_{loss} are given in Table.2. Note that in the case of proton belt localized at the altitude $H = 10000\ km$ the distribution function (6) turns out to be: $A_{loss}(E_0/E)^{5.5}$.

4 Conclusion

The above calculations show that the loss rate $dN(E)/dt$ depends on the distribution function of the trapped particles and applied potential difference. This allows to use the scattering center for the measurements of high energy particle distribution function. If potential difference can be varied in a wide range, both cold plasma and high energy particles' parameters can be measured with the same space tethers used as a diagnostic probe. For this purpose tunable high-voltage $0.1\ MV \leq \phi_p \leq 2\ MV$, low power $0.1\ KW \leq P \leq 10\ KW$, compact (weight $\leq 1\ T$) DC generator is needed. Some other opportunities appear in AC case.

References

[1] Vasilyev Yu. V., V. V. Danilov,*"Active experiment in space: man-made control of particle precipitation from the Earth's radiation belts using high-voltage string system"*, Dokl. RAN, (1995) **342**

[2] Swift J. D., M. J.Schwar, *Electrical Probes for Plasma Diagnostics*, New York: American Company, 1968.

ELECTRON BEAMS IN LARGE CORONAL LOOPS

M. Karlický[1], H. Aurass [2], G. Mann [2]

1 Astronomical Institute of the Academy of Sciences of the Czech Republic, 251 65 Ondřejov, Czech Republic

2 Astrophysikalisches Institut Potsdam, Observatorium für solare Radioastronomie, Telegrafenberg A31, 14473 Potsdam, Germany

Abstract

The type U(N) radio burst observed at February 23, 1993 is presented. Using a 1-D test particle model, this radio burst is modeled as an electron beam propagating in a large coronal loop. For modeling of transport processes Coulomb collisions, mirroring of electrons in the loop magnetic field, and scattering in zones of enhanced whistler wave turbulence are taken into account. In the model electrons are injected upwards along the loop axis in one leg. In the zone of whistler turbulence near the loop top the original beam is splitted up into two beams propagating from the top back and forward into both loop legs. It explains two widely separated radio sources observed during the descending branch of U burst spectra.

Introduction

During the flare process electron beams travel along open as well as along closed magnetic field lines and they generate type III or type U bursts in the radio spectra [1]. Type U bursts consist of a type III like rising branch that turns over into a descending (reverse drift) branch. Occasionally a type U burst is followed by a new rising branch, forming a burst spectrum reminding the letter "N". Such bursts are called type U(N) bursts [2]. All these radio bursts provide a diagnostic tool for studying particle acceleration, injection and propagation in the solar corona.

Observations of the February 23, 1993 U(N) type radio burst

Figure 1A shows the type U(N) burst spectrum (spectrometer of the Observatory of Solar Radioastronomy of the Astrophysikalisches Institut Potsdam in Tremsdorf) starting 18 min after a subflare in NOAA AR 7433 (N12 E40, Solar Geophysical Data). The main features of the radio source configuration are shown in the one-dimensional scans and the flux curves of the different subsources given in Figure 1B (Nançay multifrequency radio heliograph of the Paris-Meudon Observatory, NRH). The gross source site pattern confirms the model of an electron beam propagating in a closed coronal loop: a brightening at a given site (the leg into which the beam is injected) during the rising branch in the spectrum (U_{up} in Figure 1B) followed by a remote brightening during the descending branch in the spectrum (U_{down} in Figure 1B). The time difference between ascending and descending branches of the U burst at 236.6 MHz is 2.7 s. The N branch of the spectrum (N in Figure 1) occurs nearly at the site of the descending U branch source with 4.2 s time delay. Note that the N branch signature is more diffuse in comparison with the ascending

U branch. The burst sources are located near a large coronal soft X-ray loop rooted in NOAA AR 7433. For details and further examples see [7].

Looking more carefully to the details of Figure 1B some additional weak sources become visible just in the beginning of the brightening of the main U descending and N branch sources. These faint brightenings are situated definitely at the source site of the rising U burst branch, this means near the beam injection site.

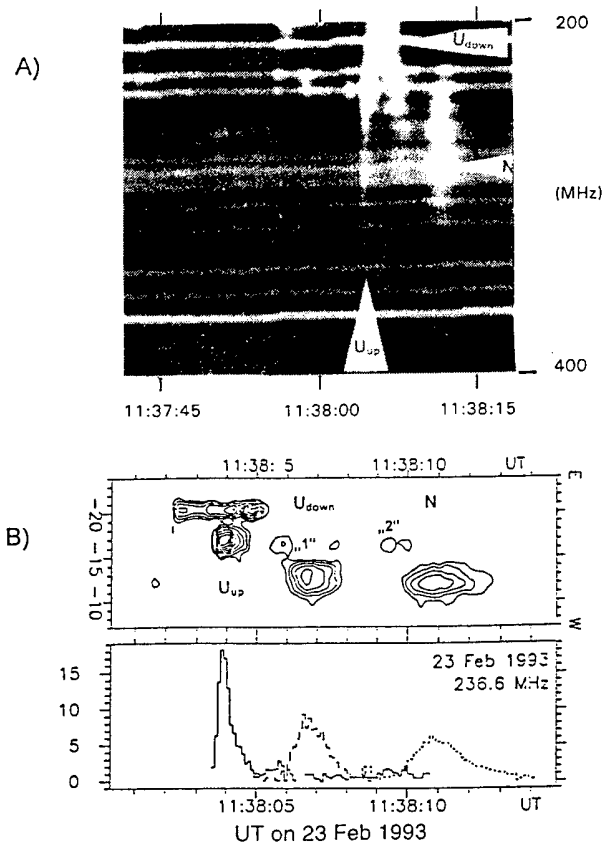

Figure 1. The type U(N) solar radio burst on February 23, 1993 as observed by the Tremsdorf spectrometer (Figure A) and by the Nançay multifrequency radio heliograph (Figure B, top one-dimensional scan at 236.6 MHz; bottom the flux of the subsources in arbitrary units (according to [7]). Continous line - ascending U burst branch; dashed line - descending U burst branch; dotted line - N burst branch).

Model

For modeling of this observations we use a 1-D test particle model [3], in which the trajectories of numerical electrons are computed in a large coronal loop. As concerns the energy losses and the pitch angle changes of individual electrons three effects are taken into consideration:

1. The energy losses and pitch angle scattering of electrons due to Coulomb collisions with the surrounding plasma are calculated by a Monte Carlo method as in [4].
2. Magnetic mirroring effects are included similarly as in [5] considering the conservation

of the electron magnetic moment.

3. Scattering at a zone of enhanced whistler turbulence was computed by Monte Carlo method as suggested in [6]. We compute the coefficients of Fokker-Plank equation in the following form:

$$D^w_{\mu\mu} = \left(\frac{\pi^2 e}{m_e c}\left(\frac{2n}{n+1}\right)\frac{W^{tot}_w}{B}\frac{1}{\gamma}\left(\frac{\beta\gamma}{1836\beta_a}\right)^{n-1}\right) \mid \mu \mid^{n-1} (1-\mu^2), \qquad (1)$$

$$D^w_{\mu} = \left(\frac{\pi^2 e}{m_e c}\left(\frac{2n}{n+1}\right)\frac{W^{tot}_w}{B}\frac{1}{\gamma}\left(\frac{\beta\gamma}{1836\beta_a}\right)^{n-1}\right) sign(\mu)((n-1)(1-\mu^2) \mid \mu \mid^{n-2} -2 \mid \mu \mid^{n}). \qquad (2)$$

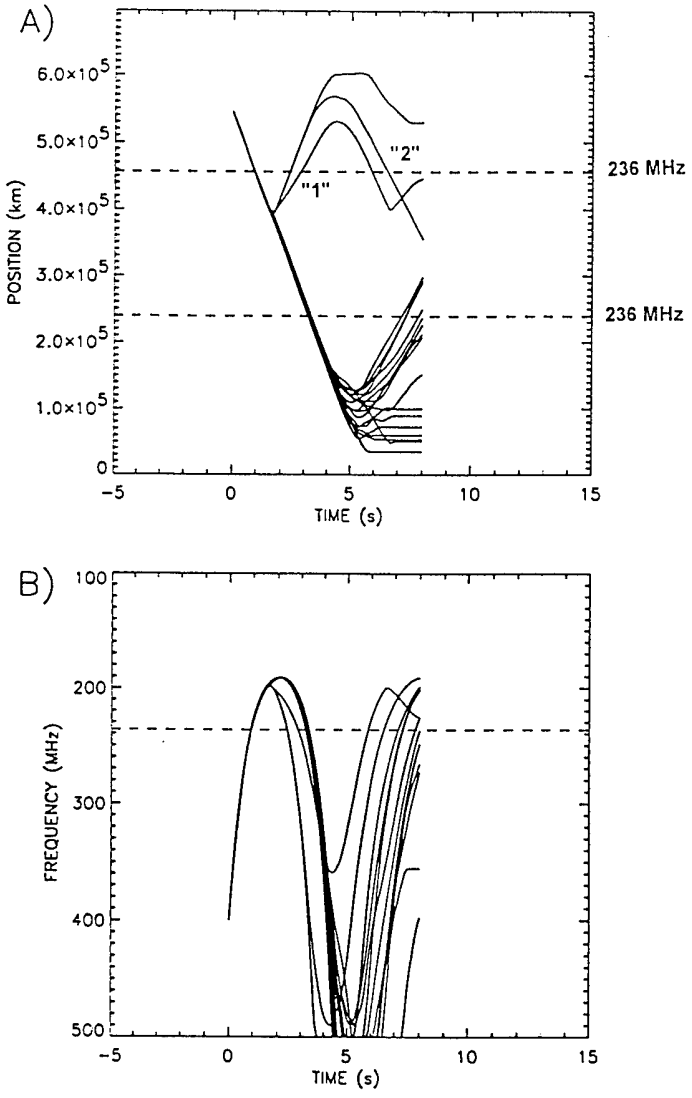

Figure 2. The numerical simulation of the February 23, 1993 U(N) burst. The trajectories of 20 numerical electrons in the distance vs time (A) and the frequency vs time (B) plots for the case when Coulomb collisions, mirroring and scattering of electrons at whistler turbulence zone near the loop top are considered.

Now, let us model the presented observation. The length of the semi-circular loop is estimated to about 1 solar radius from radio heliographic and YOHKOH observations. Assuming radio emission at the fundamental of the plasma frequency the density at the turning point of the loop has been determined from the U burst top frequency. Considering the geometrical and density aspects we build the density model. In varying the beam and the loop magnetic field parameters we fit the observed radio data (spectrogram, radio source site distribution, and timing) with our model. For an initial electron velocity of 10^{10} cm s^{-1}, and a plausible loop top magnetic field of B = 5 G the results shown in Figure 2 are derived. Figure 2A shows the trajectories of 20 representative numerical electrons. Most of these electrons are propagating along the loop and are reflected by the magnetic mirror on the opposite side of the loop. These trajectories correspond to the gross characterictics of the observed U(N) radio burst (Figure 1). For comparison with the observed radio spectrum (Figure 1A) see Figure 2B (the synthetic radio spectrum). To explain the 2 weak subsources observed after the rising U burst branch at the injection site of the loop (Figure 1B) we consider the whistler turbulence zone with an energy level $W_w^{tot} = 5 \times 10^{-6}$ erg cm^{-3}. In the present example, the whistler turbulence region must be near the loop top, but closer to the injection site as follows from the time sequence of the observed subsources (Figure 1B). As evidenced by Figure 2A, the zone of whistler turbulence backscatters some electrons. The backmoving electrons should form a faint reverse drift burst (the first weak subsource; "1" in Figures 1B and 2A), some of these electrons are mirrored in the injection leg of the loop and just form also a secondary faint N burst branch (the second weak subsource, "2" in Figures 1B and 2A). In the spectrum these faint additional N branches are covered by the stronger main U(N) burst spectral signature.

Conclusions

1. We successfully applied our model to the U(N) burst observed at February 23, 1993.
2. Scattering of beam electrons at a zone of enhanced whistler wave turbulence near the loop top is important for understanding the observations. Considering this scattering we can explain the remarkable spatial splitting of some type U burst radio sources.

Acknowledgements

We would like to acknowledge the support of Deutsche Forschungsgemeinschaft through Grant No. DFG - Au 106/6-1 and Academy of Sciences of the Czech Republic through Grant No. 303404.

[1] Suzuki, S., Dulk G.A.: Solar Radiophysics, Cambridge University Press (1985) 289
[2] Caroubalos C., Poquérusse M., Bougeret J. L., and Crépel R.: ApJ **319** (1987) 503
[3] Karlický M., Mann, G, Aurass, H.: A&A (1996) in press
[4] Karlický M.: Sol. Phys. **145** (1993) 137
[5] Karlický M., Hénoux J.C.: A&A **278** (1993) 627
[6] Miller J.A., Ramaty R.: ApJ **344** (1989) 973
[7] Aurass H., Klein K.-L.: A&A Suppl. (1996), in press

RELATIVISTIC ELECTRON BEAM DYNAMICS IN THE PULSAR MAGNETOSPHERE

O.V. Chedia, T.A. Kahniashvili, G.Z. Machabeli and
I. S. Nanobashvili

Department of Theoretical Astrophysics, Abastumani Astrophysical Observatory, A.Kazbegi ave.2[a], 380060 Tbilisi, Republic of Georgia

Abstract

The investigation of a relativistic electron beam dynamics in the pulsar magnetosphere is given. The equation of motion of the magnetospheric plasma particles is discussed. As it turned out, if the particle radial velocity $V_r > c/\sqrt{2}$ (where c is the speed of light), centrifugal acceleration changes its sign and the particle braking begins. Also the stability of the magnetospheric plasma with respect to the radially oriented potential perturbations is discussed and the possibility of the electrostatic field generation in the pulsar magnetosphere plasma along the magnetic field lines is shown.

Introduction

As it is well known, pulsar is a rotating neutron star with the extremely high magnetic field, about $10^{12} - 10^{13}$ G. We use the perpendicular rotator model of the pulsar magnetosphere. The magnetic field lines are frozen in the pulsar so they rotate together with it as a whole. Because of the rotation of the star together with its magnetic field the electric field is generated which has the nonzero component along the magnetic field lines. This electric field ejects the particles (most of scientists think that these particles are electrons) from the pulsar surface and accelerates them up to the relativistic velocities. The particles, moving along the curved magnetic field lines, radiate γ-quanta and when their energy ε_γ exceeds electron's doubled rest energy $2mc^2$ ($\varepsilon_\gamma > 2mc^2$), γ-quantum decays into an electron-positron pair. This pair is also accelerated in the electric field and γ-quanta appear again which also decay into the electron-positron pairs, etc. Because of this cascad process the relativistic electron-positron plasma is formed in the pulsar magnetosphere. This plasma in its turn screens the electric field generated by the pulsar rotation.

We assume that the magnetic field lines are located in the plane which is perpendicular to the pulsar rotation axis. We also assume that they are radial straight lines. This assumption is justified because we discuss the processes in the magnetospheric layer the thickness of which is much less than the curvature radius of the magnetic field lines.

As we have mentioned above, the particles move along the magnetic field lines which are frozen in the pulsar and rotate together with it, thus the "solid-body type" rotation (corotation) takes place in the pulsar magnetosphere. This is the reason of the strange dynamics of the plasma particles in the pulsar magnetosphere. In particular, as it turned out, if the plasma particle radial velocity $V_r > c/\sqrt{2}$, the centifugal force changes its sign and the particle braking begins. We show that because of the plasma particle braking the electrostatic field generation along the magnetic field is possible in the pulsar magnetosphere.

Main Consideration

The equation of the motion of the magnetospheric plasma particles was discussed in the paper [1]. We use the perpendicular rotator model of the pulsar magnetosphere and treat only the polar cap. The magnetic field lines are considered as radial straight lines located in the plane which is perpendicular to the pulsar rotation axis. This assumption is justified because we discuss the processes in the magnetospheric layer the thickness of which is much less than the curvature radius of the magnetic field lines. The magnetospheric plasma particles move along the pulsar magnetic field lines and also rotate together with them because the field lines are frozen in plasma. The electric field, generated by the pulsar rotation together with its magnetic field, is screened by the magnetospheric plasma.

It is convenient to begin the discussion of the plasma particle motion in the noninertial frame of a rotating magnetic field line,which is described by the metric

$$dS^2=-(1-\Omega^2r^2)dt^2+dr^2, \tag{1}$$

where Ω is the pulsar rotation frequency. Here and below we use so called geometric units $c=G=1$.

According to the Einstein principle of equivalence, we can not tell gravitation from noninertiality. Thus for the description of particle motion in the pulsar magnetosphere the 3+1 formalism can be used. This formalism is described in [2]. According to the 3+1 formalism, the equation of motion for the particle with the mass m and charge e has the following form [2]:

$$\frac{1}{\alpha}\frac{\partial\vec{p}}{\partial t}+(\vec{V}\vec{\nabla})\vec{p}=-\gamma\frac{\vec{\nabla}\alpha}{\alpha}+\frac{e}{m}(\vec{E}+[\vec{V}\vec{B}]), \tag{2}$$

where α is the so called "lapse function" and in our case $\alpha=\sqrt{1-\Omega^2r^2}$. Here and below we use the dimensionless momentum $\vec{p}$ ($\vec{p}$ is changed by $\vec{p}/m$). We can rewrite the equation (2) for the quantities defined in the rest inertial frame:

$$\frac{\partial\vec{p}}{\partial t}+(\vec{V}\vec{\nabla})\vec{p}=-\gamma\alpha\vec{\nabla}\alpha+\frac{e}{m}(\vec{E}+[\vec{V}\vec{B}]). \tag{3}$$

Now let us discuss the motion of the plasma particles in the zeroth approximation of the weak turbulence. In the limits of this approximation the quantities which are located in the equation of motion can be presented as:

$$\vec{E}=\vec{E_0}+\vec{E_1}, \qquad \vec{B}=\vec{B_0}+\vec{B_1}, \qquad \vec{p}=\vec{p_0}+\vec{p_1}, \tag{4}$$

where $\vec{E_0}$, $\vec{B_0}$ and $\vec{p_0}$ are the basic terms and $\vec{E_1}$, $\vec{B_1}$ and $\vec{p_1}$ are the perturbations in the first approximation of the expansion over the parameter of the weak turbulence. The small parameter in the approximation of the weak turbulence for the electron-positron plasma is

$$\frac{{E_1}^2}{mn\gamma}\ll 1. \tag{5}$$

From the equation of motion in the zeroth approximation for the radial acceleration one can obtain (see also [3]):

$$\frac{d^2r}{dt^2}=\frac{\Omega^2r}{1-\Omega^2r^2}\left[1-\Omega^2r^2-2\left(\frac{dr}{dt}\right)^2\right]. \tag{6}$$

The equation (6) can be solved exactly. Using Jacobian function, the solution can be presented in the form [3]:

$$r(t)=\frac{V_{0i}}{\Omega}\frac{Sn\Omega t}{dn\Omega t}, \tag{7}$$

where Sn and dn are the Jacobian elliptical sine and modulus respectively [4], V_{0i} is the particle initial velocity. From the equation (6) it follows that if the radial velocity $V_r > 1/\sqrt{2}$, the acceleration changes its sign and the particle is not accelerated but braked (see also [3]).

In the case $V_{0i} \rightarrow 1$, using the asymptotic expression for the Jacobian function one can find [3]:

$$r(t)=\frac{V_{0i}}{\Omega}sin\Omega t. \tag{8}$$

For the radial velocity we will obtain:

$$V_{0r}=V_{0i}cos\Omega t, \tag{9}$$

from which it follows that

$$V_0{}^2=(V_{0r})^2+(V_{0\varphi})^2=const \tag{10}$$

(because of the corotation $V_{0\varphi} = \Omega r$), i.e. no energy is expending on the particle braking along the field line, the radial energy transforms to the transversal one.

As it was shown above, the relativistic plasma particles are braked in the pulsar magnetosphere, if their radial velocity $V_r > 1/\sqrt{2}$. It is very interesting to discuss the stability of such a plasma with respect to the radial perturbations. In particular we discuss the potential perturbations oriented along the magnetic field lines. The initial stage of the perturbation development can be described by the equation which is easy to obtain from (3) by substituting in it the expansion (4). For the first order terms one can obtain:

$$\frac{\partial \vec{p_1}}{\partial t}+(\vec{V_0}\vec{\nabla})\vec{p_1}=(\vec{V_0}\vec{p_1})\Omega^2\vec{r}+e\vec{E_1}. \tag{11}$$

In order to eliminate the electric field $\vec{E_1}$ from the equation (11), we use the Poisson equation and the continuity equation in the first approximation of the weak turbulence. After this, making the spatial Fourier transformation one can obtain for the radial perturbations:

$$\left[\frac{\partial}{\partial t}+ik_rV_{0r}\right]^2 p_{1r}=\frac{\Omega {V_{0i}}^2}{2}\left[\frac{\partial}{\partial t}+ik_rV_{0r}\right]p_{1r}sin2\Omega t-\frac{{\omega_p}^2}{\gamma_0}p_{1r}sin^2\Omega t, \tag{12}$$

where ω_p is the plasma frequency. From the equation (12) we will obtain the dispersion relation (see in detail [5]):

$$\omega^2=\frac{{\omega_p}^2}{2\gamma_0}-\frac{{k_r}^2{V_{0i}}^2}{2}. \tag{13}$$

We know that $E_1 \sim exp(-i\omega t)$ so one can conclude that when the second term in the right hand side of (13) is larger than the first term the aperiodic instability is developing in the pulsar magnetosphere, i.e. the field E_1 is increasing exponentially along the magnetic field lines.

The condition of the aperiodic instability development can be written in the following form:

$$l_r < \frac{V_{0i}\sqrt{\gamma_0}}{\omega_p}, \tag{14}$$

where l_r is the charge separation scale in the magnetospheric plasma. For the typical parameters of the pulsar magnetosphere the charge separation scale at the light cylinder (the light cylinder is the surface on which the azimuthal velocity equals to the speed of light $V_\varphi = \Omega r = c$) is of the order $10^6 sm$.

Conclusion

At the end let us discuss the possible results of the instability. We can see that the plasma motion along the magnetic field lines and at the same time rotation together with them (i.e. corotation) causes the generation of the aperiodically increasing electrostatic field under the condition (14). On the other hand it is selfevident that the corotation can not take place on the arbitrary distances from the pulsar surface because on some distance the azimuthal velocity will reach the speed of light $V_\varphi = \Omega r = c$. So, the corotation must be removed. The instability which was discussed above can contribute to the process of the corotation removing, in particular the increasing electric field will cause the additional braking of the particles of one sort and the decreasing of the braking of the other sort. This fact will evidently cause the motion of the electrons and the positrons with respect to each other, i.e. the increasing current $\vec{j}$ will appeare. So, according to the Maxwell equation $4\pi\vec{j}=rot\vec{B}$, the magnetic field will be generated. The current will be directed along the pulsar magnetic field lines, therefore the generated magnetic field will have the azimuthal component B_φ. The particles move along the field lines so the corotation will be removed. The electric field, i.e. the current $\vec{j}$ will increase until the corotation law removal.

[1] O.V. Chedia, T.A. Kahniashvili, G.Z. Machabeli and I.S. Nanobashvili, Astrophys. Space Sci. (in press).

[2] "Black Holes: The Membrane Paradigm" eds. K.S. Thorne, R.H. Price, D.A. Macdonald (Yale University Press, New Haven and London), 1988.

[3] G.Z. Machabeli and A.D. Rogava, Phys.Rev. **50**, 98 (1994).

[4] "Handbook of Mathematical Functions", eds. M. Abramowitz and I.A. Stegun, 1964.

[5] T.A. Kahniashvili, G.Z. Machabeli and I.S. Nanobashvili, submitted to Phys. Plasmas.

ENERGETIC HIGH CURRENT DENSITY ELECTRON/ION BEAM GENERATION IN PLASMA OPENING SWITCHES

Ya.E.Krasik, R.Arad, A.Weingarten, and Y.Maron

Physics Department, Weizmann Institute of Science, 76100 Rehovot, Israel

In this paper we present experimental results on the generation of high energy ion/electron beams generation during operation of microsecond/nanosecond Plasma Opening Switch (POS). For the nanosecond POS, a coaxial configuration with negatively charged central electrode was used. For the microsecond POS, a strip-line geometry was investigated. Different arrays of magnetically insulated Collimated Faraday Cups (CFC) were used to observe energetic electron/ion flows towards the anode/cathode POS electrodes and towards the load. It was shown that in both nanosecond and microsecond cases, high-energy high current density axial ion flows are generated downstream towards the load at the load side edge of the plasma. The main axial ion acceleration occurs in the first few cm downstream with respect to the load side edge of the plasma at the beginning of the POS opening. Data observed by the anode CFC array show fast axial propagation of a radial electron flow along the anode electrode towards the load which is accompanied by an ion flow that first appears at the generator side of the plasma.

I. Introduction

The generation of high energy ion/electron beams during POS operation may substantially limit the efficiency of coupling inductively stored energy to a load. It was shown in previous research that during the POS operation an energetic ion flow is generated towards the cathode electrode[1]. In our previous study[2] we have shown that during the opening of the coaxial nanosecond POS (NPOS) with positively charged central electrode, a high energy proton flux is accelerated at the load side edge of the plasma towards the short-circuit end of the inductive load. Also, some preliminary data indicate the existence of an energetic ion flow downstream to the load during the opening of a microsecond POS[3] (MPOS). In this paper we present experimental results on energetic ion/electron emission from the plasma in a nanosecond NPOS with a negatively charged central electrode and a MPOS with a strip line electrode geometry.

II. Experimental setup

For the NPOS experiment we have used a coaxial anode and cathode with radii of 2 cm and 4.5 cm, respectively (see Fig. 1 a). To prefill the NPOS interelectrode gap by the plasma, a flashboard plasma source installed outside of the anode was used. The NPOS was powered by a 300 kV, 1 Ω, 90 ns generator with negative polarity output pulse. The NPOS upstream inductance was 70 nH and the load was a short coaxial line with an inductance of 20 nH.

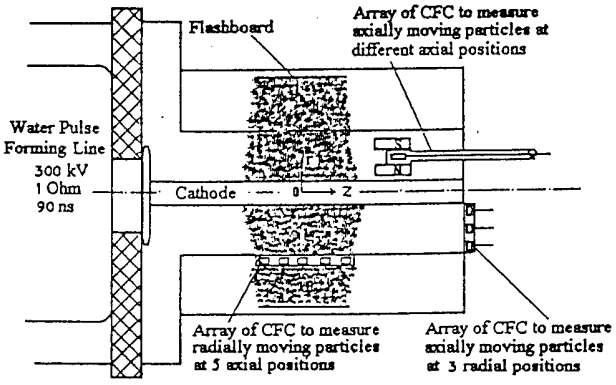

Fig. 1 a. Nanosecond POS experimental setup

The MPOS experiment was performed using a low inductance high current generator, C_g=2.8 μF, $\varphi_g \leq 45$ kV, L_g=25 nH. This generator supplies a current pulse with an amplitude of up to 200 kA and duration of 750 ns quarter period to a planar geometry MPOS (see Fig. 1 b). The MPOS consists of a strip line which has a 14 cm width and a 3.5 cm interelectrode gap. The plasma injection inside the MPOS interelectrode gap was implemented through the anode slots by the use of a flashboard plasma source placed 6 cm above the anode electrode. The upstream and downstream inductances were 60 nH and 50 nH, respectively.

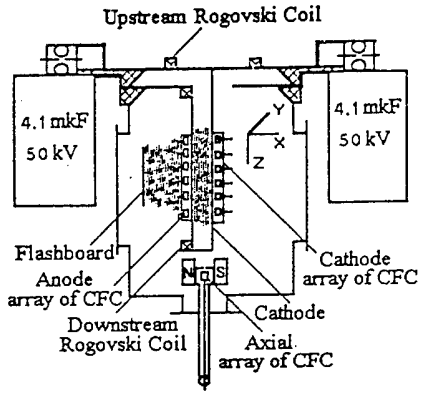

Fig. 1 b. The setup of the microsecond POS.

Electron/ion emission during both the NPOS and the MPOS operation was studied by several arrays of the CFC with 0.05 cm diameter of the entrance holes. To minimize plasma prefilling of the CFC, a 60% transparent mesh, placed 0.2 cm in front of collimating holes was used. To measure the ion current density of the ion flow propagating in the axial direction towards the load, 4 magnetically insulated CFC, azimuthally separated by 90°, were placed at the center of the interelectrode gap of the NPOS and at different distances from the plasma. To measure axial ion flow in the MPOS experiment we have used 3 movable arrays of magnetically insulated CFC. Each array consists of 4 CFC placed across the MPOS interelectrode gap with 0.7 cm distance between them. The distance between the arrays in the "Y" direction was 4.5 cm. Measurements of an electron/ion flow towards the anode electrode were done by arrays of 6 CFC (in the MPOS experiment) and 5 CFC (in the NPOS experiment). These CFC were separated in the axial direction from each other by 4 cm (MPOS case) and by 1.1 cm (NPOS case) and were placed instead of one of the anode strips.

III. Experimental data

3.1 Nanosecond POS

We have observed an axial flow of high energetic ions that propagates towards the short circuit end of the inductive load. The current density of this ion beam at a distance of ≈5 cm from the load side edge of the plasma reaches 1.5±0.5 kA/cm^2 with a pulse duration of 10±4 ns FWHM (see Fig. 2 a).

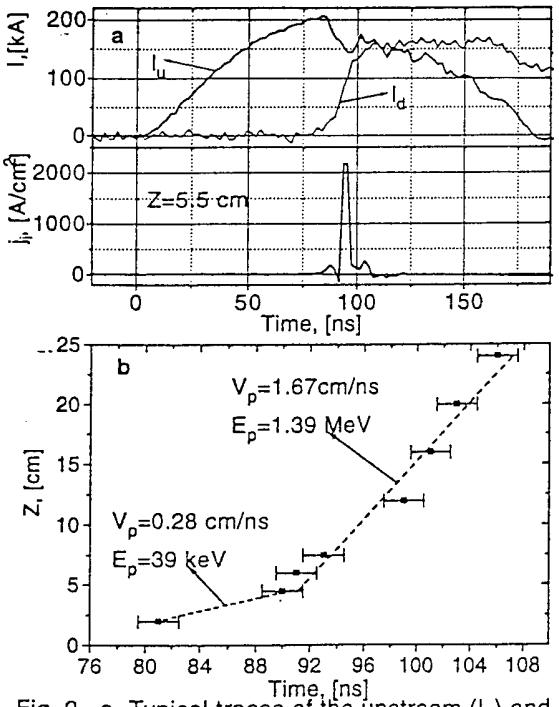

Fig. 2. a. Typical traces of the upstream (I_u) and the downstream (I_d) currents and the ion beam current density; b. TOF measurements of axially moving ions. Z=0 - the load side edge of the plasma.

It was shown by Time of Flight (TOF) measurements that the main axial ion acceleration occurs downstream the POS plasma within a few cm near the load side edge of the plasma at the beginning of the NPOS opening (see Fig. 2b). Further during their propagation ions propagate with almost the constant velocities.

This axial ion acceleration occurs over the entire cross-section of the POS interelectrode gap almost simultaneously (±3 ns) at all azimuthal and radial positions. Data obtained by CFC without magnets show that in front of this ion beam there is an electron beam with a duration of (8±3) ns at FWHM and current density of tens of A/cm^2. The short duration of the ion pulse and relatively small spread of the ion beam during its propagation, indicate that this ion beam is composed mostly of protons.

Data obtained by TOF measurements show that the energy of protons depends on the duration of the NPOS opening time (see Fig. 3). The shorter opening time, the higher is the ion energy observed. It was shown by the use of Al foils placed in front of the CFC collimating holes that the energy of part of protons exceeds 1.15 MeV but is less than 1.35 MeV, which is in good agreement with the TOF data. For POS opening times less than 15 ns almost all protons have energy E_p> 300 keV. The amount of protons with energy E_p>1.15 MeV does not exceed few percent of the total accelerated ions.

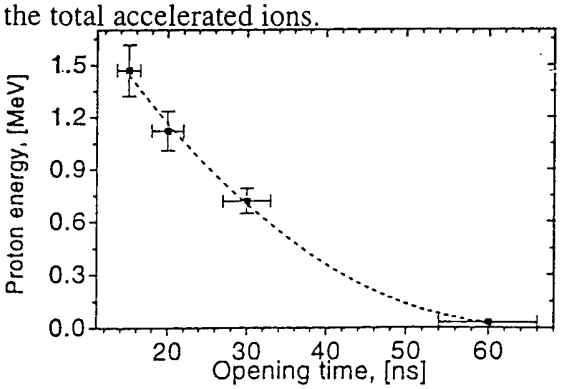

Fig. 3 Proton energy determined from TOF versus the POS opening time

The TOF measurements also show fast decrease of the ion current density with the axial distance that corresponds to an ion beam divergence of $\alpha/2=17.5^o$ at 5cm≤Z≤8 cm from the load side edge of the plasma (see Fig. 4).

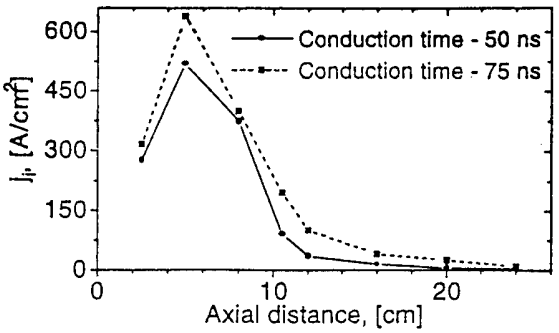

Fig. 4. Scaling of an average ion current density versus axial distance from the load side edge of the plasma.

Taking average ion current density at Z=8 cm from the load side edge of the plasma to be $j_i \approx$ 450 A/cm^2, the average proton energy to be ≈ 0.75 MeV, the pulse duration on FWHM to be ≈5 ns, and the ion beam cross-section to be 66 cm^2, one obtains a total ion current of ≈ 30 kA with energy ≈110 J and power density ≈ 0.34 GW/cm^2. The proton density in such an ion beam is ≈ 3×10^{12} cm^{-3} with a total amount of protons about 10^{13}.

Data observed by the anode array of CFC show fast (≈1.5×10^8 cm/s) axial penetration of a radial electron flow along the anode electrode in the direction towards the load. The shorter NPOS conduction time, the faster is the penetration velocity. The maximum radial electron current density was observed at the load side edge of the plasma (see Fig. 5).

The electron flow towards the anode electrode is followed by a radial ion flow. This radial ion emission is also moving towards the load side edge of the plasma with a velocity ≈1.5×10^8 cm/s. It was shown that ion current density increases towards the load and reaches several hundreds of A/cm^2, at the load side edge of the plasma.

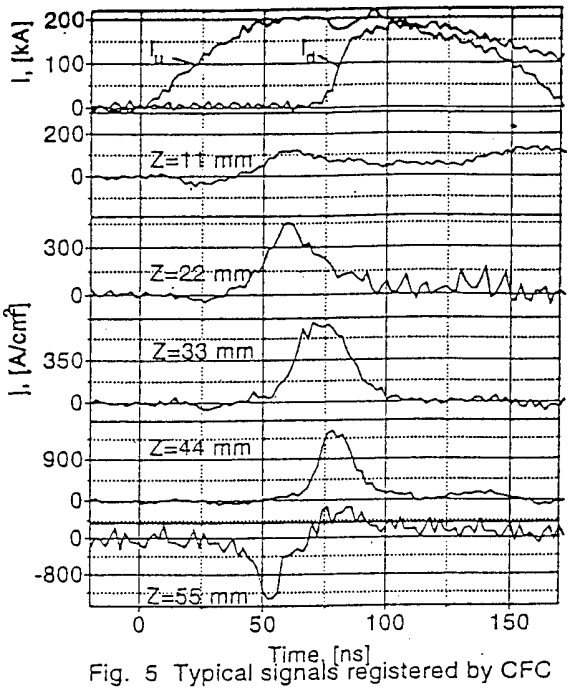

Fig. 5 Typical signals registered by CFC placed at different axial positions along the anode electrode. Here Z=0 is the generator side edge of the plasma.

3.2 Microsecond POS

Similarly to the case of the NPOS, a flow of fast ions in the axial direction towards the load was observed (see Fig. 6 a). The sharp rise of the downstream current begins only when this ion flow reaches the short circuit end of the load. This ion flow is generated simultaneously (± 15 ns) across the total strip line cross section. Data observed by CFC without magnets show that the ion flow is accompanied by co-moving electrons, and there is a short duration electron beam which precedes the ion flow. Also here, the main axial acceleration of ions takes place at the load side of the plasma (see Fig. 6 b). However, the velocity of the axially moving ions for MPOS conduction times > 350 ns was 3-4 times smaller than the ion axial velocity observed in the NPOS experiment. By varying the MPOS conduction time it was shown that the energy of the fast axially-moving ions increases with the decrease of the MPOS conduction time (see Fig. 7).

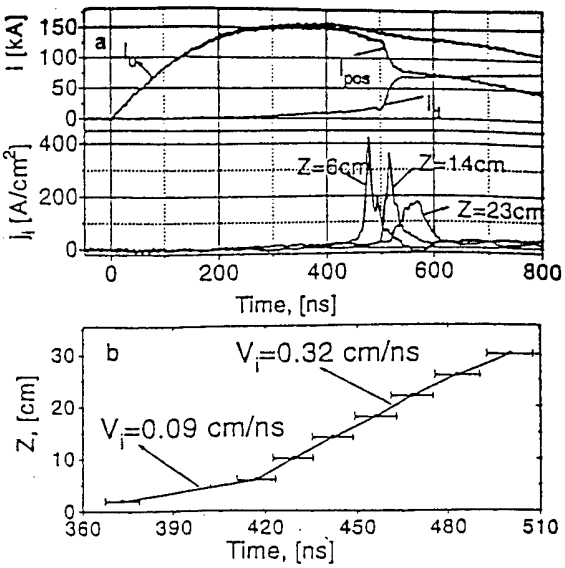

Fig. 6 a. Typical traces of upstream (Iu), downstream (Id) and MPOS (Ipos) currents and ion current density measured at different distances from the load side edge of the plasma; b. TOF measurements of an axially moving ions.

The ion current density and the pulse duration of this axial ion flow at Z=7±2 cm from the generator side edge of the plasma are up to 1 kA/cm^2 and 30±10 ns, respectively. We found out that this axial ion flow is focused during its propagation in the "Y" direction and has a maximum ion current density in the "X" direction in the middle of the MPOS interelectrode gap (see Fig. 8).

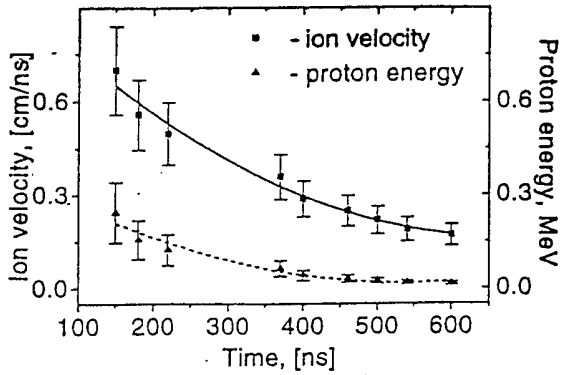

Fig. 7 Scaling of an ion velocity versus MPOS conduction time

The divergence of the ion beam in the "Y" and in the "X" directions are $\alpha_Y/2 \approx 11.5^o \pm 2.5^o$ and $\alpha_X/2 \approx 3.6^o \pm 1.2^o$, respectively.

The ion current density decreases by a factor 6 at a distance of 15 cm from the load side edge of the plasma which corresponds to an ion beam divergence of $\alpha/2 \approx 5^{o}$.

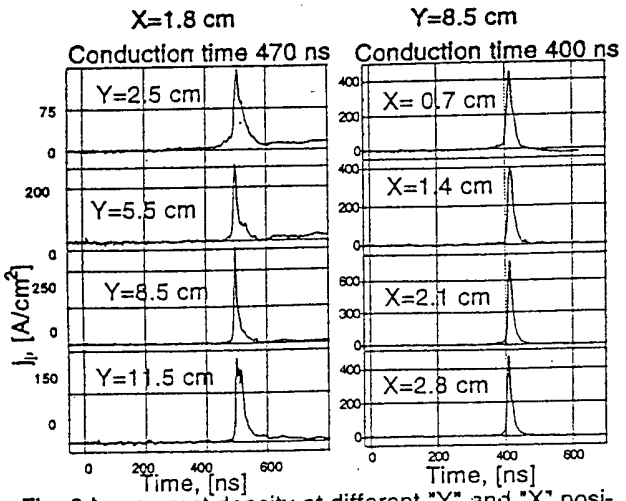

Fig. 8 Ion current density at different "Y" and "X" positions at Z=14 cm from the load side edge of the plasma.

As in the previous research[4] we have observed an ion flow towards the cathode electrode along the entire plasma length during the MPOS conduction and opening phases. The ion emission towards the cathode electrode began within 50 ns of the application of the upstream current pulse at the generator side edge of the plasma. The ion-emission-zone axial velocity was found to be $(5\pm1.5)\times10^{7}$ cm/s.

By placing the array of the magnetically insulated CFC inside the MPOS plasma at different axial positions we obtained a well defined ion flow inside the entire plasma. This ion flow propagates toward the load side edge of the plasma during the MPOS conduction (see Fig. 9). The velocity and duration of this flow is $\sim(6\pm1.5)\times10^{7}$ cm/s and 100 ns, respectively.

As for the NPOS case, data obtained by the anode array of CFC, show almost simultaneous appearance of an electron flow towards the anode electrode along the entire length of the plasma (see Fig. 10). This electron flow has a peak electron current density that propagates in the axial direction

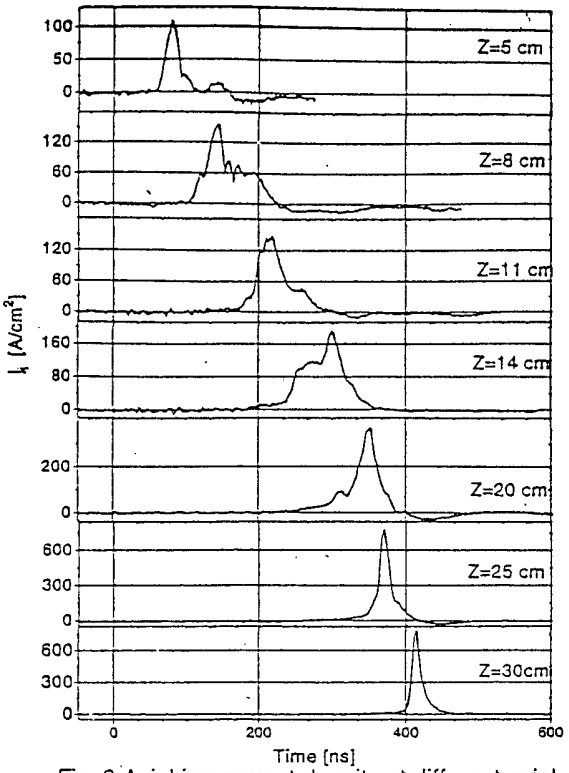

Fig. 9 Axial ion current density at different axial positions with respect to the generator side edge of the plasma. T=0 is the beginning of the I_u.

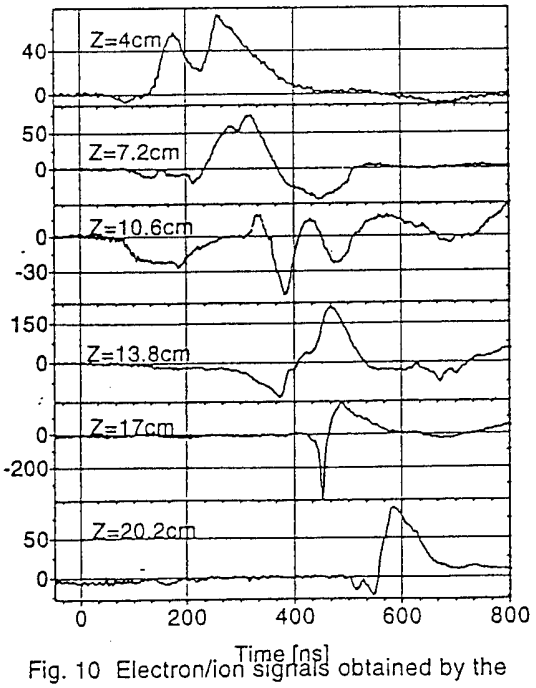

Fig. 10 Electron/ion signals obtained by the array of anode CFC. Conduction time - 500 ns. Z=0 is the generator edge side of the plasma.

with a velocity of ~5×10^7 cm/s, which is the same as that of the axially moving ions at this place. The peak of electron current density reaches a few hundreds of A/cm^2 at the load edge of the plasma at 20±5 ns prior to the beginning of the downstream current. The electron flow towards the anode electrode is followed by a radial ion flow that appears first at the generator side of the plasma. The axial propagation velocity of this ion flow is almost the same as the velocity of ions axially moving through the plasma.

IV. Discussion

Observed data show that similar phenomena occur during a nanosecond and a microsecond time scale POS, independent on its geometry and current pulse polarity[2] : 1. generation of axial fast ion beam moving towards the downstream load accompanied by co-moving electrons at time which corresponds to the POS opening; 2. Axial electron/ion flows towards the anode electrode during the POS conduction.

The phenomenon of an energetic ion flow generation at the load side edge of the plasma in the direction downstream of the POS is very similar to what was obtained in early studies of coaxial plasma accelerators[5]. These studies have showed that in the so-called "deflagration" regime, when the mean free path of electrons is larger than the plasma gun interelectrode gap, ion acceleration occurs at the load side edge of the plasma when the current front reaches this place. At this time sharp decrease of the discharge current and x-ray fluxes were also observed. The typical time scale and the plasma density used in these studies were ~ 10^{-6}s and ~ 10^{14}-10^{15} cm^{-3}, respectively. Flows of ions with a density about 10^{13} cm^{-3} and ion energy of E_i ≥50 keV were registered. A radial flow of energetic ions towards the anode electrode along the entire plasma length was also observed.

Several models[6] were suggested to explain the observed fast particles based on the Hall field development in the current sheath, on thermal expansion of the hot electron component of the plasma, and on certain plasma instabilities developed in the current sheath.

Recent experiments[7] on the Hawk generator have shown large energy losses between the load side edge of the plasma and the load. Similar results was obtained on the ACE 4 generator[8] where the authors suggested downstream motion of a current carrying dilute plasma to explain fast increase of the downstream inductance. The same results are predicted by numeric simulation of the POS operation[9] where Hall effect[10] was included. These simulations show the existence of an electron flow downstream towards the load and the anode electrode as the POS opens. Due to Hall fields associated with electron E× B drift, ions at the load side edge of the plasma are accelerated towards the load. The same simulations predict that during the POS conduction magnetic field penetrates into the plasma accompanied by an electron current flow. Large electrostatic fields develop inside the plasma behind the current channel. These electrostatic fields are responsible for the ion acceleration out of the plasma.

Data observed in the present experiments are in qualitative agreement with the results of numeric simulation described above. Indeed, we have observed well defined radial electron flow towards the anode electrode which propagates towards the load side edge of the plasma with a velocity about 1.5×10^8 cm/s and 0.5×10^8 cm/s for the NPOS and the MPOS, respectively. This radial electron flow may represent the electron part of the current flowing through the plasma in a form of a current channel which propagates axially towards the load side edge of the plasma. The maximum electron current density on the anode was observed at the load

side edge of the plasma, which is consistent with simulation results[9].

We have observed ion emission out of plasma during the MPOS operation in three directions: axially towards the load side edge of the plasma and towards the anode and cathode electrodes. We suggest that, the observed axially directed ion flow inside the plasma, which has the same axial velocity as that of the electron flow along the anode, results from the ion acceleration inside the current layer by Hall polarization fields.

We have shown that the electron flows towards the anode electrode are followed by radial ion emission which may occur from the positively charged plasma regions formed behind the current layer. The velocity of the radial-ion-emission propagation along the anode is consistent with the axial front velocity of the ion emission towards the cathode. We believe that these ion flows outside the plasma can significantly decrease the plasma density during the POS conduction expected to contribute to gap formation at the POS opening.

The generation of energetic ion flow in the axial direction, with the main acceleration occurring at the load side of the plasma, is also consistent with the results of early coaxial plasma gun studies and that was of numerical simulation. In fact, in both NPOS and MPOS cases, a low density plasma is present at the load side edge of the POS. Therefore, it is reasonable that when the current layer reaches this region, a high Hall electric field is developed, causing subsequent axial ion acceleration. This ion flow is accompanied by co-moving electrons and may be represented as a dilute plasma flow with a density about $3\times10^{12}cm^{-3}$ and $10^{13}cm^{-3}$ for the NPOS and the MPOS, respectively. We have observed that the sharp rise of the downstream current occurs only when the axial ion flow reaches the short circuit end of the load. This may indicate that in the region between the load side edge of the plasma and the short circuit end of the load, the current is flowing through this dilute plasma.

1. B.V.Weber, R.J.Commisso, P.J.Goodrich, D.D.Hinshelwood, W/P.Oliphant, P.F.Ottinger, and F.C.Young, Conf. Proc.of 7th Beams-88 (1988) p.1131.
2. M. Sarfaty, Y.Maron, Ya.E.Krasik, A.Weingarten, R.Arad, R.Shpitalnik, A Fruchtman, and S.Alexiou, Phys.Plasmas, **2**(6), (1995) p.2122.
3. P.S.Anan'in, V.B.Karpov, Ya.E.Krasik, I.V.Lisitsyn, A.V.Petrov, and V.G.Tolmacheva, Sov.Phys. Tech. Phys. **36**(8), (1991), p.894.
4. G.A.Mesyats, A.N.Didenko, E.N.Abdullin, V.M.Bystritskii, A.A.Kim, B.M.Koval'chuk, V.A.Kokshenev, Ya.E.Krasik, and A.A.Sinebryukhov, Sov.Phys.Dokl., **31**(7), (1986) p.557.
5. A.A.Kalmykov, A.D.Timofeev, and B.A.Shevchuk, Sov. Phys.-Techn. Phys., **15**(12) (1971), p.2002; and references therein.
6. N.A.Khizhnyak, Sov.Phys.-Techn.Phys. **14**(11), (1970), p.1534; V.I.Aref'ev and L.V.Leskov, Sov.Pys..-Tech.Phys. **17**(11), (1973), p.1822 and references therein.
7. B.V.Weber, P.F.Ottinger, J.R.Goyer, J.Tompson, J.E.Rowley, P.Filios, Conf. Proc. Beams-96, (1996).
8. J.Tompson, P.Coleman, C.Gilbert, D.Husovsky, A.R.Miller, J.Rauch, W.Rix, K.Robertson, and E.Waisman, Conf. Proc. Beams-94, (1994), p.12.
9. S. B.Swanekamp, J.M.Grossmann, P.F.Ottinger, R.J.Commisso, and J.R.Goyer, J.App.Phys **76**(5) (1994), p.2648.
10. A.S.Kingsep, Yu.V.Mokhov, and K.V.Chukbar, Sov.J.Plasma Phys. **10** (1984), p.854.

P-4-7

CO LASER INTERFEROMETER FOR REB-PLASMA EXPERIMENTS

V.S.Burmasov and E.P.Kruglyakov

Budker Institute of Nuclear Physics, Lavrentyeva av. 11, Novosibirsk, 630090, Russia

Abstract

The Michelson carbon oxide laser interferometer for measuring a plasma density in studies on REB-plasma interaction is described. A detail description of the interferometer and CO laser is presented. For a selection of a single wavelength laser operation the CaF_2 prism is applied. A Ge:Au photoconductor at 77^0 K is applied as a detector. The CO laser radiation at $\lambda = 5.34$ μm coincides with of the detector maximum sensitivity (of the order of 1000 V/W). This increases the interferometer sensitivity about ten times with respect to the He-Ne laser ($\lambda = 3.39$ μm) used as a source of light. The typical interferogram and time evolution of a plasma density obtained at GOL-M device are presented.

Introduction

An interferometry is the main diagnostic method of plasma density measurements in studies of the REB-plasma interaction. The range of the studies is wide enough: from $n_e \approx 10^{13}$ cm^{-3} up to $n_e \approx 3 \cdot 10^{15}$ cm^{-3}. The Michelson interferometers with He-Ne ($\lambda_1 = 1.15$ μm, $\lambda_2 = 3.39$ μm) and CO_2 ($\lambda = 10.6$ μm) lasers are used for a long time in both the target plasma density measurements and a study of diode plasma behaviour [1,2,3]. The CO_2 laser interferometer was mainly used at small phase shifts. Interferometers with He-Ne laser are applied for measurements of high plasma densities. The Ge:Au photoconductor cooled by liquid nitrogen was utilized as a detector in all those experiments.

An interferometer sensitivity is defined by a signal to noise ratio. At the first approximation, it is proportional to the maximum of the interference amplitude I_0 ($I = I_0 \cos^2(\varphi/2)$). I_0 is proportional to a laser output and to the detector spectral sensitivity. The Ge:Au photoconductor sensitivity is $\lesssim 10^3$ V/W at $\lambda = 3.39$ μm and ~ 1 V/W at $\lambda = 10.6$ μm.

In spite of the drop of the detector sensitivity at $\lambda = 10.6$ μm, in low density region we have obtained the interferometry maximum sensitivity ~ 10^{-4} of interference fringe using the powerful CO_2 laser. Unfortunately, the power of the typical He-Ne laser is less than 10 mW. As a result, the sensitivity of the interferometer with He-Ne laser was only of the order of 10^{-2} of interference fringe.

In this paper, a new interferometer with the carbon oxide (CO) laser ($\lambda \approx 5.34$ μm, P ~ 1 W) as a sours of light is described. A wavelength of the CO laser emission practically coincides with the maximum of the Ge:Au photoconductor sensitivity (~ 1000 V/W). It increases of the interferometer sensitivity by a factor of ten.

Arrangement

The interferometer applied for a measuring a plasma density at the GOL-M device [4]. A schematic of the interferometer and it arrangement relative to the solenoid are shown in Fig. 1. All the interferometer components are fixed on the massive dielectric frame. The beam splitter and windows of the plasma chamber are made of BaF_2. One of the splitter surfaces is covered with a dielectric layer which reflects about 50% of radiation.

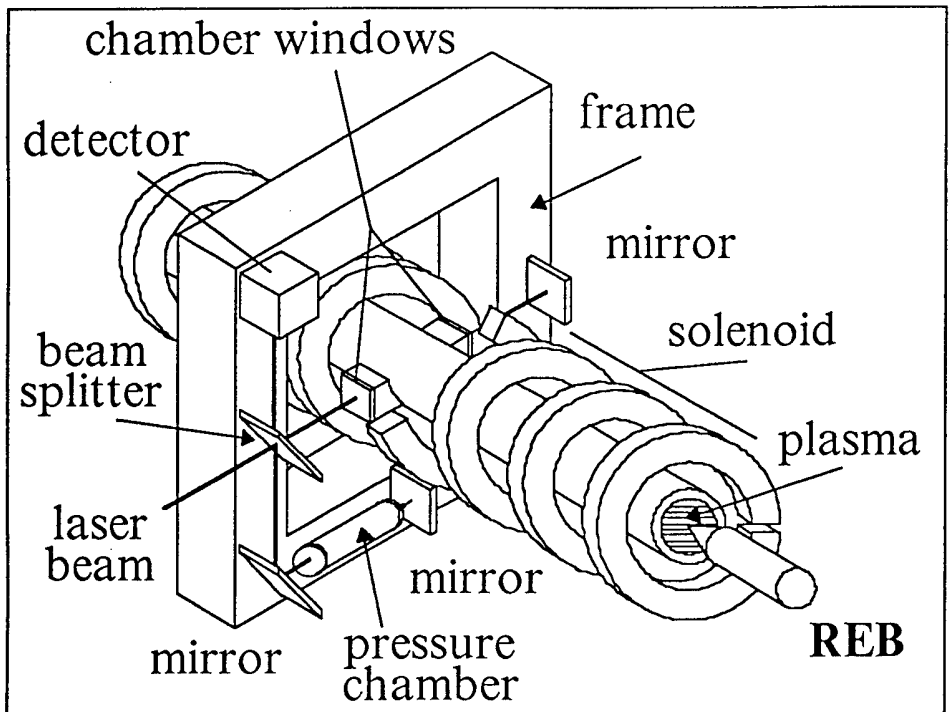

Fig. 1. The layout of the CO laser interferometer at the GOL-M device

Inside the reference arm, the pressure chamber is mounted to install the beginning phase of the interference signal. Windows of the chamber are also made of BaF_2.

A Ge:Au photoconductor at 77^0 is used as a detector. The photoconductor is mounted in the copper box for decreasing of electromagnetic stray pickup. As required, the box with the photoconductor is shielded with lead to reduce an influence of

X-ray radiation on the Ge:Au crystal. The lead shield thickness is about 5 cm. The photoconductor protection of this kind permit us to get interferograms practically without electric stray pickup. A frame vibration produced by a pulsed magnetic field is reduced to a minimum by the thorough mounting of the interferometer on the device.

We used a commercially available sealed CO laser. It is known that the carbon oxide laser emits a radiation within a broad spectral interval from 5.3 μm up to 6.1 μm [5]. Its coherence length $L = \lambda^2/\Delta\lambda$ = $4.6 \cdot 10^{-3}$ cm. It is very difficult to build at the large scale a massive interferometer (a length of arms about 1.5 m) whose arms would be equal one to another with accuracy within 10^{-3} cm. Consequently, prior to obtain the narrow spectrum the laser was upgraded.

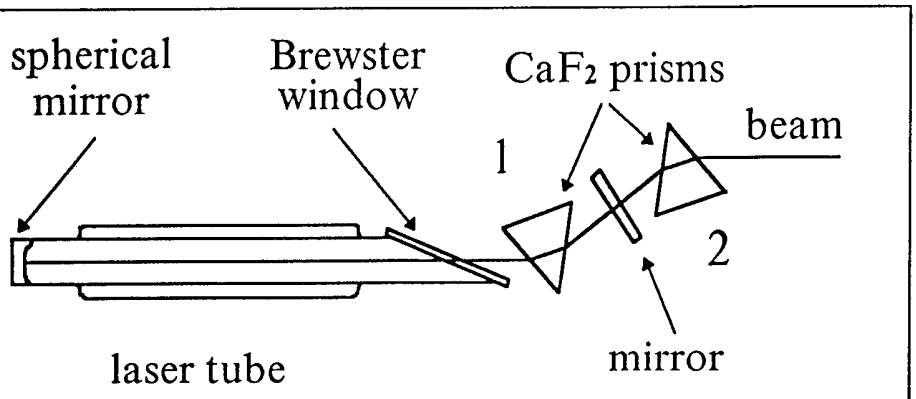

Fig. 2. Schematic diagram of the for the single wavelength laser operation

In order to select the single laser line a 70⁰ CaF_2 prism is mounted into the CO laser cavity (the prism No. 1 in Fig. 3). The prism No. 2 applied for straightening the laser beam to the initial direction. A single-wavelength operation of the laser is checked by the interferometer. The power of coherence of laser beam is $\gamma \sim 1$. An intensity of selected line (the transition $9 \rightarrow 8\ P(16)$, λ = 5.34 μm) is about 1 W.

The response time of the interferometer is determined by the Ge:Au detector, which is less than 100 ns. The interferometer can operate in the presence of significant pulse magnetic fields and hard X-ray radiation.

Results of measurements

The plasma density measurements by the interferometer is done at the GOL-M [4]. The main task of the device is to study an interaction of a powerful relativistic electron beam (REB) (700 keV, 2-3 kA, ∅ =1.7 cm, τ =200 ns). with a plasma in a strong magnetic field of the mirror type. The homogeneous magnetic field is B_{hom}=2.5 T and the mirror field is B_{mir}=4.5 T.

The target plasma ($n_e \sim 10^{15}$ cm^{-3}, $T_e \approx 1$ eV, $L_{plasma} = 250$ cm, $\varnothing = 8$ cm) is prepared by pulse discharge in hydrogen with pressure $P_{H_2} \approx 2$ Pa.

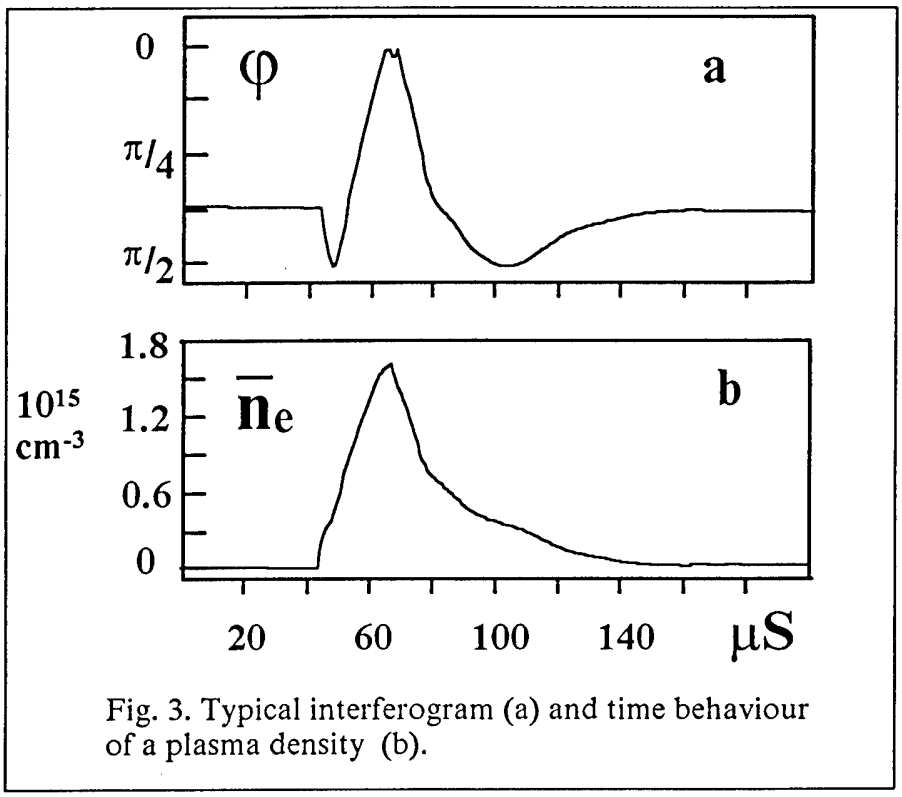

Fig. 3. Typical interferogram (a) and time behaviour of a plasma density (b).

The typical interferogram and a time evolution of a plasma density are shown in Fig. 3. To our estimation, the minimum recorded line integrated density is $\overline{n_e \ell} \lesssim 10^{13}$ cm^{-2}. It gives the interferometer sensitivity $\sim 10^{-3}$ of interference fringe.

Conclusion

Thus, the use of the carbon oxide laser with Ge:Au photoconductor improved the sensitivity of the interferometer more than ten times. The minimum recorded line integrated density is $\overline{n_e \ell} \sim 5 \cdot 10^{12}$ cm^{-2}. The response time of the interferometer is determined by the Ge:Au detector, which is less than 100 ns. The interferometer can be operated in the presence of substantial pulse magnetic fields and hard X-ray radiation.

[1] Arzhannikov A.V. et al. Proc. 3rd Int. Conf. on High Power Electron and Ion Beam Res. and Tech., Novosibirsk, **1**, (1979), 29.

[2] Burmasov V.S. et al. Fizika Plasmy, **12**, (1986), 435, (in Russian).

[3] Burmasov V.S. et al. IEEE Trans. Plasma Sci., **23**, (1995), 952.

[4] Burmasov V.S. et al. Questions of Atomic Science and Technology (Thermonuclear Fusion), No.2, (1987), 31, (in Russian).

[5] Masychev V.I., Sysoev V.K. Optics and Laser Technology, June (1984), 151.

P-4-9

MEASUREMENTS OF THE INITIAL DENSITY DISTRIBUTION OF GAS PUFF LINERS BY USING RAYLEIGH SCATTERING

Yu. G. Kalinin, A. Yu. Shashkov

Russian Research Centre "Kurchatov Institute", 123182, Kurchatov sq. 2, Moscow, Russia

Various optical techniques are available to measure distributions of the gas concentration in supersonic jet. The interferometry using two-dimensional interferograms seems to be the most informative one. Unfortunately, this method provides only the density values that are averaged along the probing beam. In the case of axially symmetrical jets one can determine the distribution of gas concentration after routine mathematical treatment of interferograms (solution of Abel equation). This treatment produces a tolerable error only in the case of the monotonic distribution of the density, i.e. without any inner spaces. Finally, the sensitivity of the two-dimensional image interferometer is very often not sufficient to investigate jets with low concentrations of particles. Objects of this kind require using of photoelectric interferometers. But great increase of sensitivity involves a rather complicated devices.

For measuring of initial density distribution of a gas-puff liner authors propose to use Rayleigh scattering of the laser beam in the gas jet. There is the fundamental difference of this diagnostic from abovementioned ones: the scattering provides the local measurements. Basic scheme of this method is presented below. The laser beam passes through the gas-liner along its diameter. The lens forms the image of the laser beam in the scattered light. The light intensity in the image is proportional to the gas concentration in the corresponding points. This technique is more sensitive, permits to measure the concentration at the point and makes possible to carry out an absolute calibration of all the system.

Let us compare the sensitivities of both methods.

1. Interferometry. For a plane layer with thickness L and absolute refractive index n, pass length difference δ may be written as

$$\delta = L(n-1) = k\lambda.$$

Here λ is wavelength, k - the order of interference. For example, for *XeCl* laser (λ = 308 nm) fringe shift k = 0.1 and layer thickness L = 1 cm

$$n - 1 = k\lambda / L \sim 3 \cdot 10^{-6}.$$

Using this value one can estimate the minimal detectable concentration of gases (see the table).

2. Rayleigh scattering. In the capacity of receiver it's profitable to use ICT. Its spatial resolution element dimensions are about 0.02 x 0.02 sq. cm. If the gain ICT is high enough, it's possible to fix each photoelectron radiated from the resolution unit. The number of photoelectrons is

$$I_{ph.e.} = \eta\, I_o\, \sigma\, N\, \Delta l\, \Omega\, \Delta h/h$$

Here $\eta \sim 10^{-1} - 5 \cdot 10^{-2}$ is quantum yield of the photocathode, I_o - the number of quanta of the incident beam, $\Omega < 4 \cdot 10^{-3}$ - the solid angle, h - the vertical dimension of the probing beam, Δl and Δh are the space resolution dimensions, N is the concentration and σ - the Rayleigh scattering cross-section related to the single molecule. The σ value may be presented by the following equation [1]:

$$\sigma = 32/3\, \pi^3\, (n-1)^2\, N_L^{-2}\, \lambda^{-4}$$

Here N_L is the Loschmidt number, λ - the wavelength. For our case

$$\sigma = 5 \cdot 10^{-19} (n-1)^2.$$

In order to obtain the accuracy about 10%, it's required to have $I_{ph.e.} = 10^2$ from the resolution unit. Thus,

$$N_{min} \sim 10^9\, (n-1)^{-2}.$$

The results of the estimation of the sensicivity are presented in the table.

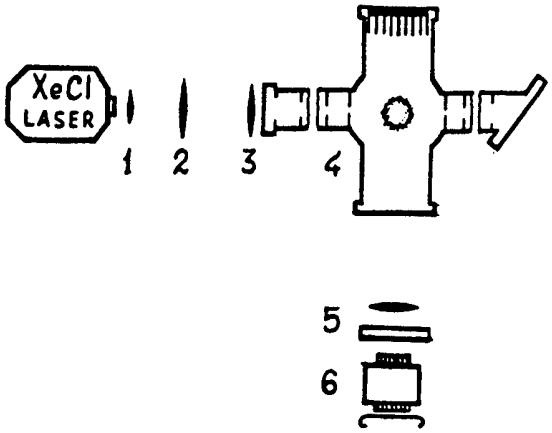

Fig. 1.

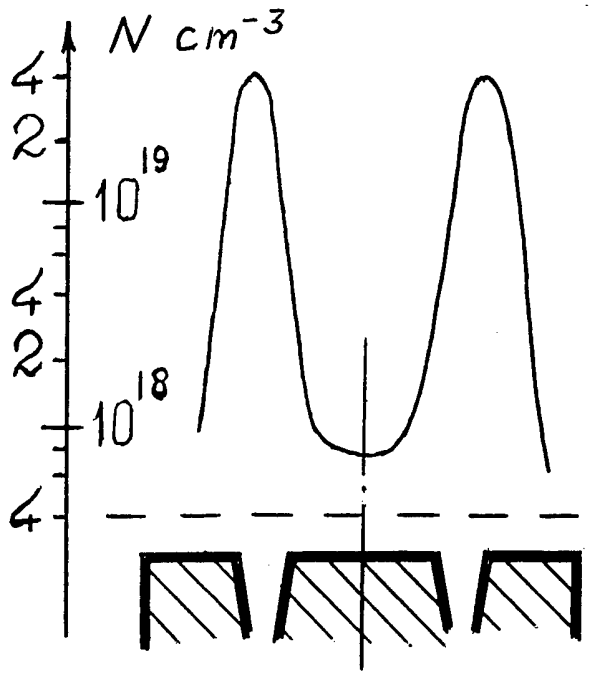

Fig. 4.

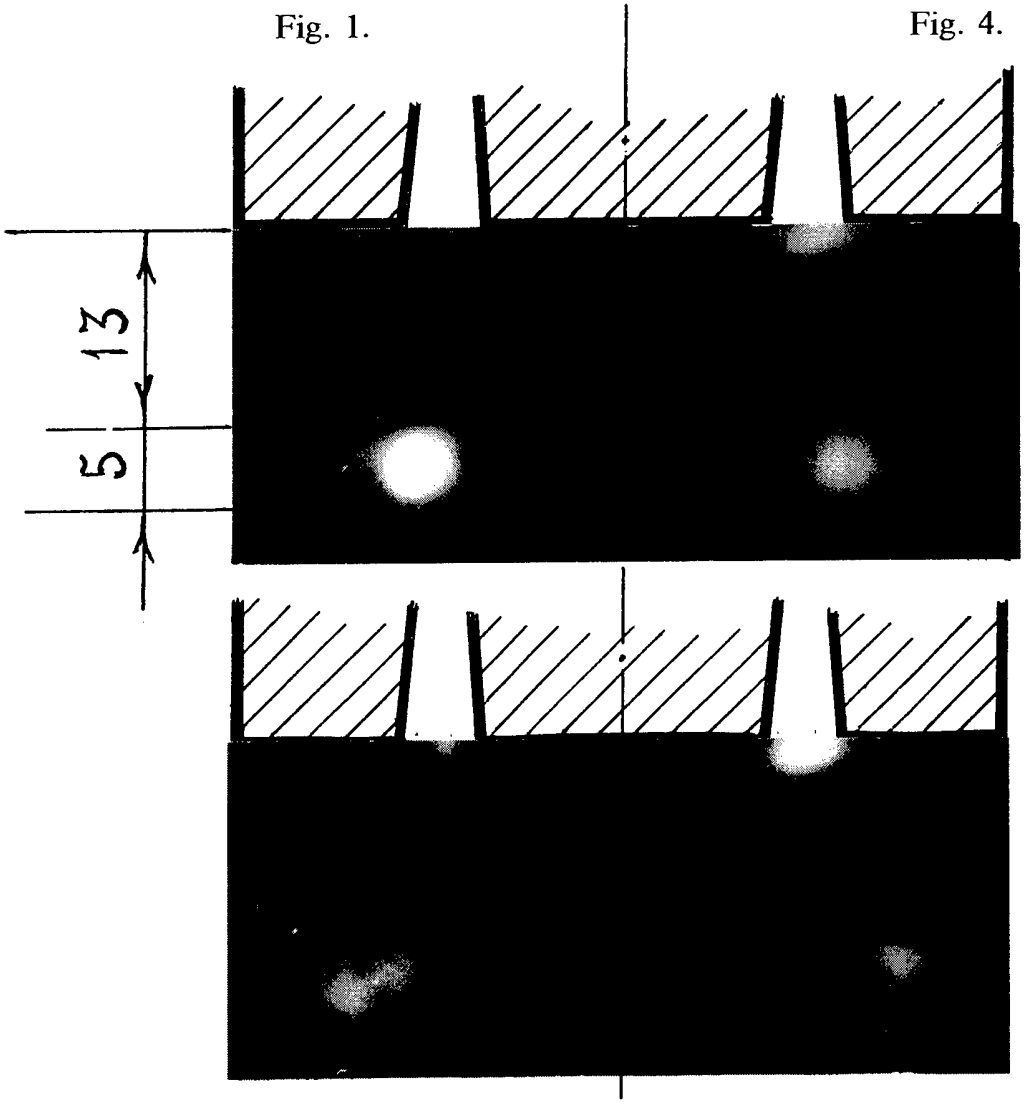

Fig. 2.

Fig. 3

Table.

Gas	$(n-1)$, 10^{-6}	N_{min}, 10^{18}	
		Interferometry	Rayleigh scattering
H_2	139	0.6	0.04
He	35	2.0	0.8
N_2	279	0.3	0.01

Raileigh scattering optical setup is shown in Fig. 1. The *XeCl* laser produced 70 mJ energy with pulse duration of 25 ns. Telescope 1, 2 and lens 3 formed the profile and guided the probing beam into the scattering chamber. The beam had a profile of a thin band with the cross-section 5 x 1 sq. mm in the region of gas jet. Chamber 4 was equiped by the input and output pipes with windows and a number of inner diaphragms. The light absorber was placed behind the gas jet and opposite to the pipe-hale window. It was done to minimize parasitic scattering of the probing beam. Images of the regions of crossing by the beam and gas-puff liner were formed by the lens with necessary filters 5 onto the MCP brightness amplifier photocathode 6. Solid angle of the lens was $3.5 \cdot 10^{-4}$.

Images of scattering objects are shown in Fig. 2 and Fig. 3. Liner axis is vertical. Top spots appear due to the parasitic scattering by the nozzle edge. Two low spots show scattering regions of the gas-puff liner.

Calibration of the scheme was carried out by filling up the chamber with a suitable gas at 100 or 50 torr pressure. Photofilms obtained were scaned photometrically and the gas jet concentrations were calculated (see Fig. 4).

By using this technique the gas jet stratification was detected in some cases (Fig. 3). One should note that it's impossible to detect similar stratification by using any interferometry.

The work was partially supported by Russian Foundation of Basic Researches (grant 96-02-18891) and C.E.A. of France.

[1] C.W.Allen, "Astrophysical quantities", 1973

P-4-10

REFRACTIVE INDEX GRADIENT DIAGNOSTICS: ANALYSIS OF DIFFERENT OPTICAL SYSTEMS AND APPLICATION TO COBRA ION DIODE

B.A. Knyazev[†], J.B. Greenly, D.A. Hammer, E.G. Krastelev[‡]

Laboratory of Plasma Studies, 369 Upson Hall, Cornell University, Ithaca, N.Y. 14853

M.E. Cuneo

SANDIA National Laboratories, Albuquerque, N.M. 87185-1193

Abstract

Different optical system variations for refractive index gradient diagnostics with a laser-beam probe have been analyzed. A "three-telescope" optical system which permits simultaneous measurement of both the laser-beam centroid deflection by a bi-cell photodiode and the spatial Fourier spectrum of the deflected beam by a streak camera has been implemented on the COBRA ion diode. The dynamics of the anode plasma layer has been studied with these techniques.

Introduction

The characteristics of the anode plasma of magnetically insulated high-voltage diodes critically affect the resulting ion-beam parameters (see, for example [1] and references therein). Refractive index gradient (RING) diagnostics is one method that can be used for investigation of the spatial distribution and composition of the anode plasma [2]. In order to have high sensitivity for the refractive index gradient measurement the laser beam deflection is measured using a bi-cell photodiode with a differential amplifier (see, for example, [2-4]). However, when the refractive index gradient changes rapidly across the probe-beam cross-section, the record of the cross-section of the beam passing through the anode plasma can give additional information [5]. We have analyzed the conventional optical schemes that have been used by previous authors and suggested and tested in the experiment a novel "three-telescope" optical system with simultaneous detection of the beam centroid deflection and the spatial Fourier spectrum of the deflected beam. Comparison of the main characteristics of these schemes is given in more detail in Ref. [6].

Measurement of the probe beam deflection

We have implemented an optical system for RING diagnostics (Fig. 1) with improved spatial resolution over earlier systems [2-4] and using both of the above-mentioned recording systems for study of the near-anode layer in the ion diode of the new ion-beam accelerator COBRA [7]. Because the anode of the accelerator has to be rebuilt after each pulse and the detectors must be located outside of a radiation zone, the optical system must be several meters long. According to the properties of Gaussian beams [6], to focus a laser beam to a small diameter spot, $2w$, one must initially expand the beam with a telescopic system. With an angular beam divergence $2\alpha_L$ for the laser, a magnification of the telescope $\kappa_1 = 6$ and a focal length of the lens L_{21} in Fig. 1 of $f_{21} = 120$ cm, we obtain (taking into account the shape of the caustic -

[†] Permanent address: Novosibirsk State University, 630090 Novosibirsk, Russia

[‡] Permanent address: P.N. Lebedev Physical Institute, Russian Academy of Science, Leninsky prospekt, 53, 117924 Moscow, Russia

see the inset to Fig. 1) the spatial resolution $2w=2\alpha_L f_{21}/\kappa_1 = 0.3$ mm, while the plasma is length $a = 95$ mm.

The probe beam passing the anode layer (see Fig. 1) is collimated by the lens L_{22} and split with a beam-splitter BS. The third telescope adjusts the diameter of the reflected portion of the beam to the size of the photodiode ($2r = 14$ mm). The refraction of the beam in the z-direction in the ion diode is then measured with a differential circuit and recorded with a digitizing oscilloscope. The value of deflection angle of the beam centroid can be found from the expression ($a<<f_{22}$)

$$\varphi = \frac{\kappa_1\kappa_2\pi w_{L0}}{2\sqrt{2}f_{22}}\frac{\Delta V}{V_L},$$

where w_{L0} is the initial laser beam radius, κ_2 the magnification of the second telescope consisting of L_{12}, and L_{22}, f_{22} is the focal length of the lens, f_{22}, and $\Delta V/V_L$ is the signal from the differential amplifier normalized to the signal if the laser falls entirely on one side of the bi-cell photodiode.

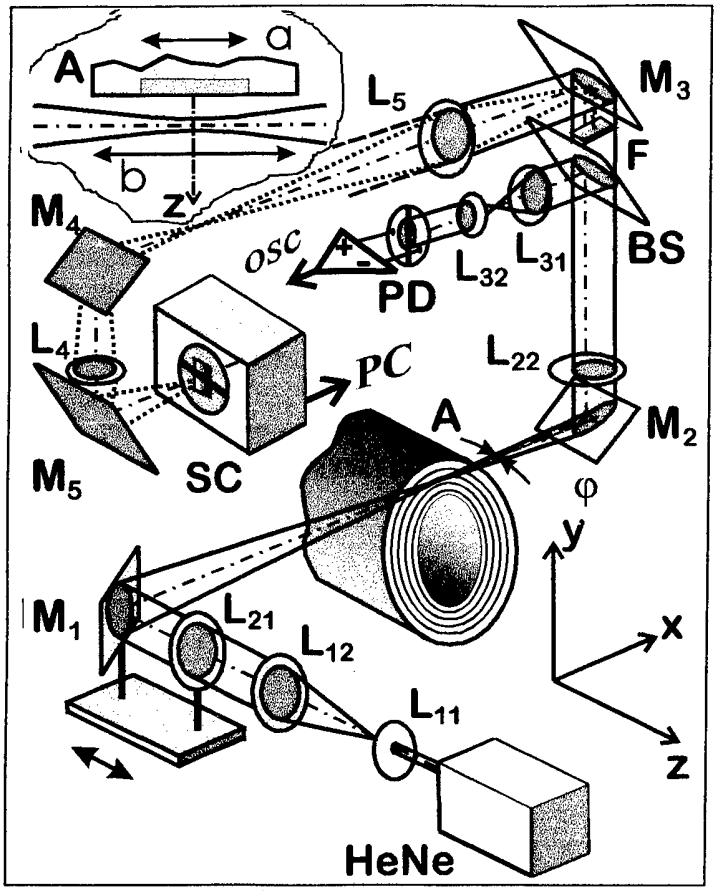

Fig. 1. Schematic of the experiment. Source - 20 mW HeNe laser. L_{mn} - lenses of the telescopic systems (κ_1 =6, κ_2=0.8, κ_3 =0.45); *PD* - bi-cell photodiode with differential amplifier; M_1 -M_4- - mirrors; *BS* - 50% beam-splitter; *F* - Fourier plane of lens L_{22} ; L_4, L_5 - achromatic lenses; *SC* - streak camera; *A* - annular Al anode; inset - geometry of the measurements.

The three-telescope system is very flexible and can be easily adapted to many experimental configurations. The arrangement of mirrors M_1 and M_2 as well as the installation of M_1 and L_{21} on a common platform enables moving the laser beam relative to the anode surface with the only other required re-adjustment being the photodiode position. To provide 10% linearity of the measurements, an additional restriction, $\kappa_1\kappa_2\kappa_3 < 2r/((2k + \pi)w_{L0})$ [6], has to be satisfied, where k is a constant that is about 0.4 [2]. Under the conditions of our experiments, the minimum detectable angle (less than 0.1 mrad) was determined by the level of electromagnetic noise.

A typical photodiode signal is shown in Fig. 2. The positive peak corresponds to a deflection of the laser beam away from the anode, as should be observed if an anode plasma layer is expanding away from the anode surface. The maximum positive deflection is observed at the end of the 80-ns diode voltage pulse (800 kV, 200 kA). The subsequent negative peak can be attributed to the arrival of desorbed gas, although other interpretations are possible. From a set of oscillograms such as that in Fig. 2 obtained for different distances between the laser beam and the anode, z, we obtain the function $\varphi(z;t)$. Integrating this function over z in order to obtain the profile of the refractive index gradient $\eta(z)$ near to the anode,

$$\eta(z) - 1 \cong \frac{1}{a}\int_{\infty}^{z}\varphi(z)dz.$$

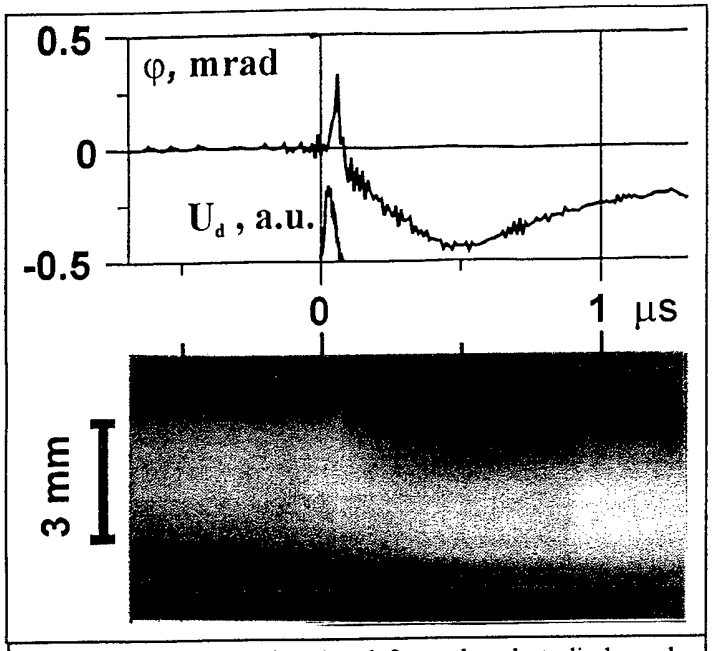

Fig. 2. Oscillogram of a signal from the photodiode and a scan of the intensity distribution of laser radiation in the Fourier-plane, recorded with the streak camera, recorded in one pulse. Distance of the beam axis from the anode was 0.45 mm; magnification factor of L_4 - L_5 optical system - 0.8; an effective slit width - 2 ns; U_d - a diode-voltage pulse.

the curves shown in Fig. 3 resulted. One can see that at the peak of the diode voltage ($t \sim 40$ ns) the thickness of the anode layer is less than 0.5 mm. Since the refractive index gradient is related to the densities of the individual components in the anode plasma layer by the expression

$$\eta - 1 = \sum_j K_j n_j ,$$

where

$K_e = -17.95 \cdot 10^{-23}$ cm^{-3} / electron for electrons and $K_H = +0.42 \cdot 10^{-23}$ cm^{-3} / atom for hydrogen [1], the path-length averaged electron density at a distance of 0.35 mm from the anode can be estimated to be a value of $3 \cdot 10^{15}$ cm^{-3}. If we assume that at the moment t = 300 ns the signal is determined only by neutral hydrogen, the gas density at the same distance (0.35 mm) is equal to $1 \cdot 10^{17}$ cm^{-3}

Study of the deflected probe beam with a Fourier transform optics

Measurement of the beam deflection with a bi-cell photodiode is a very sensitive method even by comparison with interferometry. However, when the refractive index gradient is sufficiently large, a Fourier transform optical system can be applied to obtain more information on the intensity distribution of the laser after it passes through the plasma layer. In our system the lens L_{22} performs a Fourier transform and gives the spatial frequency distribution of the probe beam at the back focal plane (F in Fig. 1). Lenses L_4 and L_5 image this plane with a variable magnification onto the input horizontal slit of a streak camera. A scan of this image is shown in Fig. 2. One can see that the spectrum of the spatial frequencies correlates well with the oscillogram. If we carry out a Taylor expansion of the refractive index $\eta(z)$ up to 2nd order, the intensity distribution in the Fourier plane is shifted as a whole but remains symmetric, namely

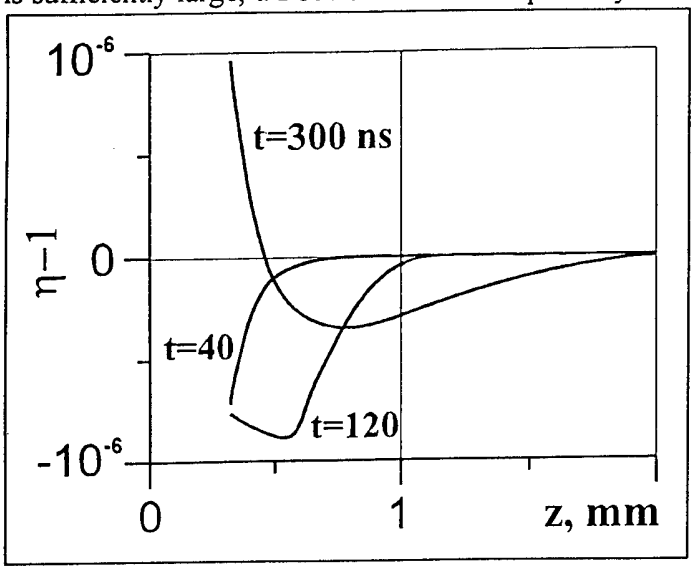

Fig. 3. The refractive index gradient vs. a distance for three moments, inferred from a series of twelve oscillograms.

$$\frac{dP(0,z)}{dz \cdot \Delta y} = \frac{P_o}{w_b^2 \gamma} \exp\left\{ - \frac{2(af_{22}\eta' - z)^2}{w_b^2 \gamma^2} \right\},$$

where $\gamma = (1 + k^2 a^2 \eta''^2 w^4 / 4)^{1/2}$, $w_b = 2f/kw$ is the Gaussian beam waist in the Fourier plane, and k is the wave number. In our case for the short distances between the laser beam and the anode, the profile of the deflected beam intensity in the Fourier plane is a little asymmetric. That means that the variation of $\eta(z)$ across the beam diameter is a higher order function of z.

The profile of $\eta(z)$ might be retrieved, in principle, from the recorded spatial frequency distributions by solving the inverse problem. However, an alternative way may be more fruitful. A RING optical system can be transformed to record simultaneously the intensity distributions in the front and back focal planes of the lens L_{22}. In this case the phase distribution of the beam passing through the layer can be retrieved by using an iteration procedure [8], at least for some profiles. If this method works, using a broad laser beam (and, perhaps, replacing spherical lenses with cylindrical ones), it may be possible to obtain the $\eta(z)$- profile in the whole gradient layer in a single pulse.

Conclusion

Theoretical analysis and experimental verification of the three-telescope RING diagnostic optical system with simultaneous measurement of the beam deflection and the spatial Fourier spectrum showed that this system is very convenient for a physically long optical system. First results obtained on the COBRA accelerator enabled us to estimate a thickness and an electron density for the anode plasma at the peak of ion beam generation and to observe the dynamics of the near-anode layer. Improvements to the system which will increase its capability are suggested.

Acknowledgments

This work was supported by Sandia National Laboratories Contract No. AF-1660. The authors thank F. Lindholm for assistance in the experiments, and H. Bluhm, P.I. Melnikov, A.N. Matveenko, and V.S. Cherkassky for useful discussions. Some aspects of the work were supported by grants from Russian State Committee on Higher Education and Ministry of Science.

[1] Sudan R.N., Longscope D.W., Phys. Fluids B: **5** (1993) 1614.
[2] Cuneo M.E., Lockner T.R., Tisone G.C., IEEE Trans. on Plasma Sci.: **19** (1991) 800.
[3] Enloe C.L., Gilgenbach R.M., Meachum J.S., Rev. Sci. Instrum.: **58** (1987) 1597.
[4] Bushujev I.M., Doroshkin A.A., Ivanov Art.A. et al., Proc. SPIE: **2619** (1995) 216.
[5] Dolgov-Savel'ev G.G., Knyazev B.A., Fokin E.P., Journal of applied spectroscopy: **20** (1974) 805 (in Russian).
[6] Knyazev B.A., Greenly J.B., Hammer D.A., Refractive index gradient diagnostics: Analysis of different optical systems and application to intense ion beam diode studies: Report of Laboratory of Plasma Studies LPS01-96, Cornell University, Ithaca, Jan. 1996.
[7] Smith D.L., Ingverson D., Bennet L.F. et al., Proc. IEEE: Pulsed Power Conference (1995) (to be published).
[8] Fienup J.R., Applied Optics: **21** (1982) 2758.

P-4-11

SPECTROSCOPIC DETERMINATION OF THE MAGNETIC FIELD DISTRIBUTION IN A GAS-PUFF Z-PINCH PLASMA

L. Gregorian, G. Davara, E. Kroupp, and Y. Maron

Department of Particle Physics, Weizmann Institute of Science, Rehovot 76100, Israel

Abstract

The time dependent radial distribution of the magnetic field in a gas-puff Z-pinch plasma has been determined by observing the Zeeman effect on emission lines, allowed for by polarization spectroscopy and high accuracy line-profile measurements. A modeling scheme, based on a 1-D magnetic diffusion equation, is used to fit the experimental data. The plasma conductivity inferred from the field distribution was found to be consistent with the Spitzer conductivity. The current density distribution and the time dependent plasma region in which the entire circuit current flows were determined.

I. Introduction

The interaction between magnetic fields and plasmas produced in cylindrical discharges such as the Z-pinch, capillary discharge, and vacuum spark has always been a fundamental problem in plasma physics research. In particular, the self generated azimuthal magnetic field in a Z-pinch strongly affects the plasma dynamics, its transport properties, and consequently the efficiency of the electromagnetic to thermal energy conversion.

In various theoretical models and simulations for the Z-pinch plasma [1,2] the time dependent magnetic field diffusion into the plasma is treated based on prescribed initial plasma conditions. In a recent study [3] the Faraday rotation technique has been used to measure the magnetic field within a radius of $\lesssim 0.5$ mm in a metallic wire explosion Z-pinch experiment. Here, we report on measurements of the magnetic field distribution during the implosion phase of a moderate density gas-puff Z-pinch plasma, using observations of the Zeeman effect on the line emission of oxygen ions. Also presented is a simulation scheme based on a 1-D magnetic diffusion equation, from which we determine the current density in the plasma and the electrical conductivity averaged across the plasma shell.

II. The Z-pinch Experiment

Detailed description of the experimental setup is given in Refs. [4] and [5]. The gas-puff Z-pinch is powered by a 25 kV, 320 kA, 1.6 μs high-voltage circuit, producing plasma pinch in $\simeq 620 \pm 20$ ns. We use CO_2 or argon as the source gas. A spectroscopic

system consisting of a 1.3 m, f#/9.1 spectrometer and a fast streak camera is used to obtain UV-visible spectra throughout the implosion, by observing the plasma along the axis, the diameter, and various chords. The spatial, temporal, and spectral resolutions achieved are 0.4 mm, 1 ns, and 0.05 Å, respectively. A half-wave plate is used for polarization-dependent measurements.

III. Magnetic Field Diffusion Modeling

The magnetic diffusion equation is obtained by combining the generalized Ohm's law (neglecting the Hall current term) and the Maxwell equations, and is given by:

$$\frac{\partial \vec{B}}{\partial t} = \vec{\nabla} \times \left(\vec{v} \times \vec{B}\right) - \frac{c^2}{4\pi}\vec{\nabla} \times \left(\frac{1}{\sigma}\vec{\nabla} \times \vec{B}\right) \tag{1}$$

Here, $\vec{v}$ is the particle velocity and σ is the plasma electrical conductivity. The boundary condition for this equation, assuming a cylindrical geometry of the plasma, is:

$$B_o(t) = B(r = R_o(t), t) = \frac{0.2I(t)}{R_o(t)}, \tag{2}$$

where R_o is the time dependent outer radius of the plasma and $I(t)$ is the total discharge current flowing through the plasma. Equation (1) can be solved numerically, given the prescribed radial distribution of the conductivity and the radial ion velocity distributions, and it is a subject currently being investigated in our laboratory. An analytical solution is obtained only by introducing various simplifying assumptions.

Here, we solve the equation in the frame of reference of the moving outer boundary of the plasma, neglecting the relative motion of the particles. In addition, planar geometry is assumed, which for most of the implosion phase is estimated to little affect the solution. The plasma conductivity is assumed to be uniform, so that an average value is used as a parameter. Based on these assumptions the diffusion equation can now be written as:

$$\frac{\partial B_\theta}{\partial t} = \frac{c^2}{4\pi\sigma}\frac{\partial^2 B_\theta}{\partial \xi^2} \tag{3}$$

$$B_\theta(\xi, 0) = 0, \quad B_\theta(\xi = 0, t) = B_o(t)$$

Here, we introduced a new spatial variable ξ, defined as $\xi = R_o(t) - r$. The boundary condition $B_o(t)$ used for the calculations is obtained from the results of a previous study [4], where we have determined the time dependent radial position of the outer boundary of the plasma, and measured the total discharge current $I(t)$ using a Rogowski loop. Both $R_o(t)$ and $B_o(t)$ are given in Fig. 1. For the solution of Eq. (3) we consider two cases: a semi-infinite geometry ($0 < \xi < \infty$), and a finite thickness

(slab) geometry ($0 < \xi < l$). For an arbitrary boundary condition $B_o(t)$ and constant conductivity, the semi-infinite geometry solution is given by [6]:

$$B(\xi,t) = \frac{\sqrt{\sigma}}{c} \int_0^t \frac{\xi B_o(\tau)}{(t-\tau)^{3/2}} \exp\{-\frac{\pi\sigma\xi^2}{c^2(t-\tau)}\} d\tau, \tag{4}$$

where t is the time of observation. The slab solution is given by [6]:

$$B(\xi,t) = \frac{\sqrt{\sigma}}{c} \int_0^t \frac{B_o(\tau)}{(t-\tau)^{3/2}} \sum_{n=-\infty}^{+\infty} \left\{ (\xi + 2nl) \exp\{\frac{\pi\sigma(\xi+2nl)^2}{c^2(t-\tau)}\} \right\} d\tau, \tag{5}$$

where l is the thickness of the plasma layer. We solved numerically both (4) and (5) for a fixed value of σ and different values of l and t, and a significant difference between the two solutions was observed only for $l \leq 0.5$ cm, which is less than the typical thickness of the plasma shell in our experiment (0.6-0.7 cm). As an example, in Fig. 2 we present the solutions of both (4) and (5) using the following parameters: $l = 0.7$ cm, $t = 530$ ns, and $\sigma = 2.4 \cdot 10^{14}$ s^{-1}. It is seen that the difference between the two profiles is negligible.

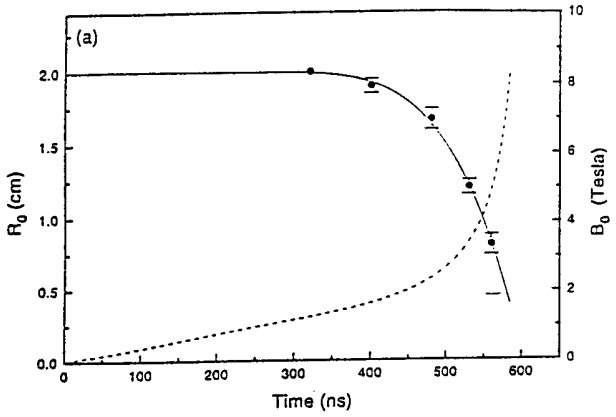

Fig. 1. Solid line : The oberved outer radius of the plasma R_0(t) (see text). Dashed line: The boundary field B_o(t) obtained using the measured total current in the plasma.

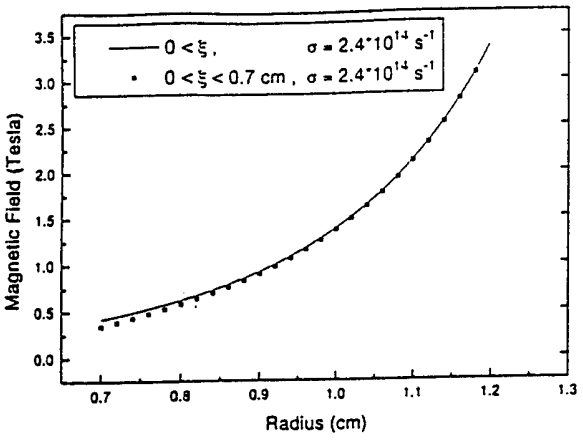

Fig. 2. Solutions of the magnetic diffusion equation, for $\sigma = 2.4 \cdot 10^{14}$ s^{-1}. Solid line: semi-infinite solution, $0 < \xi < \infty$ (see text). Dots: slab (planar, finite thickness) solution, $0 < \xi < 0.7$ cm.

IV. Experimental Results

The radial distribution of the magnetic field was determined from measurements parallel to the axis of line emission of **OIII-OV** ions (2700-3900 Å) [5]. These measurements were accomplished by the use of a half-wave plate which rotates the polarization plane of the collected radiation, thus enabling to observe the contribution of the $\Delta m = 0$ and the $\Delta m = \pm 1$ polarization components on the spectral profiles. For each radius and time we performed several discharges for each polarization, thus minimizing the effect of the shot-to-shot reproducibility. This gave an uncertainty of $\pm 2\%$ in the FWHM of the averaged profiles. The width difference between the spectral profiles of the same line, measured for the two polarizations at the same time and radius, was calculated, yielding the magnetic field strength, with an uncertainty of 15-20%.

Presented in Fig. 3 are the results of the magnetic field measurements at 530 ns (90 ns before the pinch). The data points are obtained from Zeeman splitting measurements for the line of **OIII** at $r = 0.85$ cm, of **OIV** at $r = 1.05$ cm, and of **OV** at $r = 1.2$ cm. The best-fitting curve for the data is obtained using the numerical simulation procedure described in the previous section. At 530 ns the planar-geometry assumption is justified, and the plasma conductivity for which this solution was obtained was $\sigma = 2.4 \pm 0.4 \cdot 10^{14}$ s^{-1}, which agrees with the Spitzer value, as estimated using our plasma parameters. The skin depth, defined as the e-fold decrease of the B field at the boundary, is 0.23 ± 0.02 cm, which is nearly half of the total thickness of the plasma shell. Also shown in Fig. 3 is the boundary field B_o, calculated using equation (2). It is seen that B_o agrees well with the spectroscopically measured boundary field, which indicates that at this time (90 ns before the pinch), within the error of the measurement, the entire circuit current flows through the plasma.

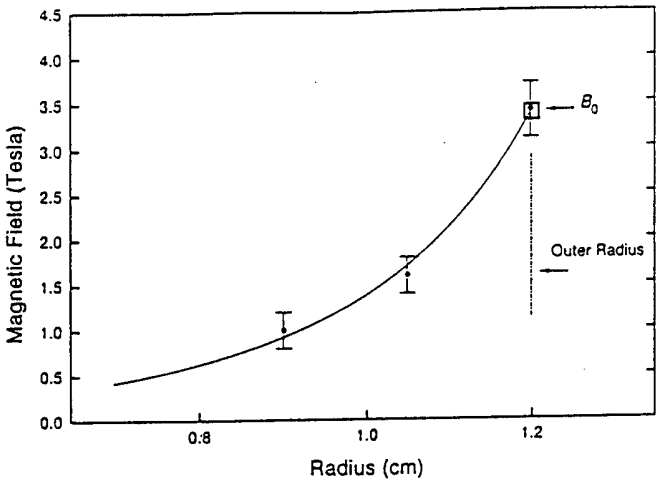

Fig. 3. The magnetic field distribution in the plasma at t = 530 ns. The curve is a best-fit solution of the magnetic field diffusion equation for $\sigma = 2.4 \cdot 10^{14}$ s^{-1}. The 1/e decrease of the magnetic field occurs at 0.22 cm from the outer plasma edge. B_o, represented by the square, is taken from Fig. 1.

The current density distribution is obtained from the magnetic field distribution given in Fig. 3. This allows the $J \times B$ forces in the plasma to be known, and to determine the relative contribution of these forces to the ion acceleration, as described in detail in Ref. [5]. The Joule heating is also calculated.

V. Conclusions

We have presented a simple scheme for modelling the magnetic field penetration into a cylindrical imploding plasma, to be used for fitting the experimental Zeeman splitting data recently obtained in our laboratory. The numerical scheme is based on the diffusion equation the boundary conditions of which are determined experimentally. From the best-fit solution the plasma conductivity and the current density are obtained, which in turn allow for the calculation of the $J \times B$ forces and the Joule heating in the plasma.

Acknowledgments

The authors are grateful to A. Fruchtman, A. Fisher, and V. Fisher for valuable discussions, and to P. Meiri for his considerable technical assistance.

References

[1] N. R. Pereira and J. Davis, J. Appl. Phys. **64**, R1 (1988).
[2] K. T. Lee, S. H. Kim, D. Kim, and T. N. Lee, Phys. Plasmas **3**, 1340 (1996).
[3] G. S. Sarkisov *et al*, JEPT **81**, 743 (1995).
[4] M. E. Foord *et al*, Phys. Rev. Lett. **72** (24), 3827 (1994).
[5] G. Davara, L. Gregorian, E. Kroupp, and Y. Maron, to be published.
[6] A. N. Tikhonov and A. A. Samarski, *Partial Differential Equations of Mathematical Physics* (Holden-Day, San Francisco, 1964).

SPECTROSCOPIC INVESTIGATION OF THE IMPLOSION DYNAMICS OF A GAS-PUFF Z-PINCH PLASMA

G. Davara, L. Gregorian, E. Kroupp, B. Peter, V. Fisher, and Y. Maron

Department of Particle Physics, Weizmann Institute of Science
Rehovot 76100, Israel

The time dependent properties of the imploding plasma produced in a gas-puff, 1.6 μs, 320 kA Z-pinch device are determined. Line emission of ions up to the sixth ionization stage is observed along various chords and in the axial direction. Measurements of radial ion velocity distributions from Doppler broadening and shifts, and of the radial charge state distribution across the plasma shell demonstrate the existence of an ionization front propagating radially inward with nearly constant velocity of $1 \cdot 10^7$ cm/s. Line intensity ratios and observed particle ionization times are used to determine the electron temperature. The electron density is obtained from Stark broadening and continuum radiation measurements. These measurements, combined with collisional-radiative calculations, yielded the absolute ion densities. The radial distribution of the magnetic field in the plasma is determined from Zeeman splitting using polarization spectroscopy. This gives the current density and the skin depth, yielding the Ohmic heating as a function of time and radius.

A pressure wave is observed to propagate ahead of the magnetic "piston". We show that the Joule heating due to the tail of the current channel sustains the radial propagation of an ionization front, moving ahead of the pressure wave. Quasistationary propagation of the ionization front is simulated by stationary MHD equations coupled with the equations of ionization kinetics.

The **JxB** forces and the plasma properties obtained from these measurements, combined with the previously determined ion radial velocity distributions, allow for experimentally-based calculations of all terms in the momentum and energy equations. Such a calculation demonstrates leading terms in both equations. It also provides a good check for comparing with the experimental data, and proves the applicability of the MHD considerations.

(The full text has not been supplied.)

P-4-14

APPLICATION OF CHARGE COUPLED DEVICES AS SPATIALLY-RESOLVED DETECTORS FOR X-RAY SPECTROGRAPH

S.Attelan-Langlet[1], B.Etlicher[1], V.O.Mishensky[2], Yu.V.Papazian[2], V.P.Smirnov[2], G.S.Volkov[2], V.I.Zaitsev[2]

[1]*Ecole Polytechnique, Palaiseau, 91128, France.*
[2]*Troitsk Institute for Thermonuclear and Innovation Investigations, Troitsk, 142092, Russia.*

Abstract

X-ray crystal spectrograph which contains CCD linear array as position-sensitive detector is described. Radiation detection is performed directly onto CCD.

Spectrograph has limit of sensitivity at about 2 J/(A·ster), spectral resolution ~1000 and dynamic range 100-120. The device operates on-line with IBM-PC based control system. Software of ones provides all the data acquisition and treatment. Output spectra are presented in absolute units.

The device was used during composite Z-pinch experiments at pulse-power installations «Angara-5-1» (TRINITI, Troitsk, Russia) and «GAEL» (Ecole Polytechnique, Palaiseau, France). Present day spectrograph is included into set of diagnostics of installation «Angara-5-1».

Some of spectra obtained are presented and discussed.

Introduction

Conventional X-ray spectroscopy has a lot of experience to employ X-ray films for spectra registration. One of the alternative techniques is utilizing the CCD as a spatially-resolved detector [1,2,3,4]. This method was considered in details in [5], where the model of interaction between X-ray radiation and CCD was supposed and quantitative measurements were performed. On this basis, linear CCD matrix (LCCD) was employed for spectra registration in X-ray spectrograph, which is described in present paper.

Spectrograph was used during composite Z-pinch experiments for X-ray measurements at two pulse-power installations, which have rather different radiation output. Some experimental results are presented and discussed.

Device construction

The spectrograph is of crystal type. The scheme of device is shown in fig. 1. MICA crystal ($2d = 19.9$ A) has a cylindrical shape ($2r\Phi = 5$ cm). MICA has high reflection features in several orders [6].

To sweep all the working spectral band from 4 up to 18 A (to obtain review spectra) the cassette with X-ray film can be installed. Cassette is placed coaxially with respect to the crystal. To investigate some spectral range in details LCCD is used. LCCD has linear array of 2048 cells with dimensions 15×15 μm^2, that corresponds to a range of about 4 A. LCCD characteristics in an quantum energy range 0.2÷50 keV are described in [5] in details.

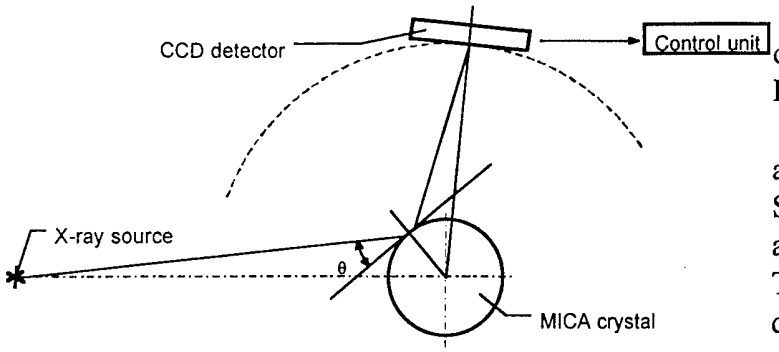

Fig. 1. The scheme of spectrograph. θ - Bragg angle.

The spectrograph dispersion is D~8 mm/A. Energy resolution is about $E/\Delta E \cong 10^3$. Spectral line FWHM is about 11 cells of LCCD. This means that detector does not diminish the device spectral resolution.

CCD control unit operation is synchronized with an experimental installation working cycle. Special precautions are undertaken to protect the unit against strong electromagnetic interference. (Unit case and all the cables have double screening, electronics scheme is grounded separately from installation grounding).

This device has on-line connection to computer (IBM-PC type), that allows to perform the express-analysis of results obtained. LCCD output analogous data by means of coaxial cable enter the special card installed into computer. This card, which contains ADC and RAM, is controlled by program.

The software, that governs the spectrograph, supports the following functions:

- data acquisition;
- preliminary processing of spectrum to gain data in absolute units (spectral density [J/A] vs. wavelength [A]);
- spectral lines intensities numerical simulation for given set of plasma parameters T_e, n_e, assuming some physical model of processes, which take place in Z-pinch;
- actual plasma parameters T_e, n_e determination, basing upon comparison of simulated and measured values of spectral lines intensities.

Applications

Spectrograph was used during composite Z-pinch experiments at two pulse-power installations, which have rather different radiation output: «Angara-5-1», TRINITI, Russia (I = 4 MA, τ = 90 ns [7]) and «GAEL», Ecole Polytechnique, France (I = 200 kA, τ = 50 ns [8]).

The load of «Angara-5-1» was hollow gas jet of Ar or C_3H_8 (linear mass 3 - 60 μg/cm, which was collapsed onto inner cylindrical column made of agar-agar foam (μ ~ 10^{-2} g/cm^3, d = 1 mm, 55 - 80 μg/cm). Some percentage of KCl (30 - 57% of mass) was added as diagnostics dopant. During the experiment intensive line radiation of H- and He-like ions of argon, potassium and chlorine was detected.

Fig. 2 presents line radiation spectra obtained in second reflection order of crystal. Soft X-ray radiation time behavior was monitored by means of detectors which time resolution capability is about ~1 ns. The typical oscilloscopic pattern for quanta of energy near 400-500 eV is presented in fig. 3.

Total radiation yields of resonant line of He-like chlorine have varied from 7 up to 20 J for several shots. For potassium this values were 3÷15 J, respectively. Total yield of potassium and chlorine line radiation was 18÷45 J from shot to shot.

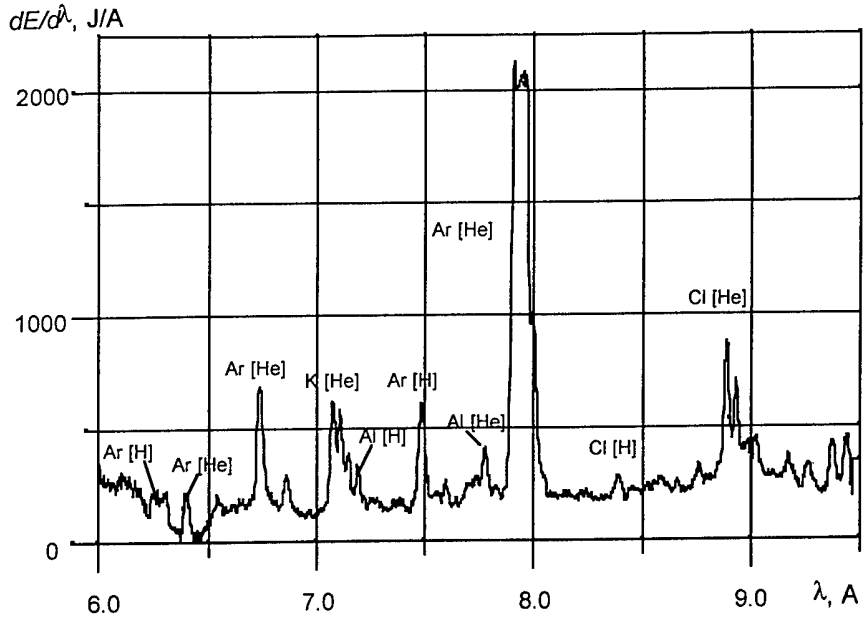

Fig. 2. Line X-ray radiation spectra of Ar, K and Cl, second reflection order of crystal. «Angara-5-1» installation. The outer shell is hollow Ar jet, the inner load is foam agar-agar cylinder (55 μg/cm) containing KCl dopant (30% of mass). An interfering radiation of cathod material ([H]- and [He]-Al, first reflection order) is observable.

Using time-integrated values of resonant H- and He-like transitions intensities, both with intercombination transition $1s2p(^3P_1)$-$1s^2(^1S_0)$ intensity one can estimate time- and space-averaged parameters T_e and n_e. Rather high intensity of He-like potassium ($h\nu = 3.51$ keV) and H-like chlorine ($h\nu = 2.95$ keV) prove the assumption, that inside pinch the hot ($T_e \sim 1$ keV) area (or areas) exists. Calculated values are: $T_e = 0.8 \div 1.2$ keV and $n_e \cong 2 \cdot 10^{21}$ cm^{-3}.

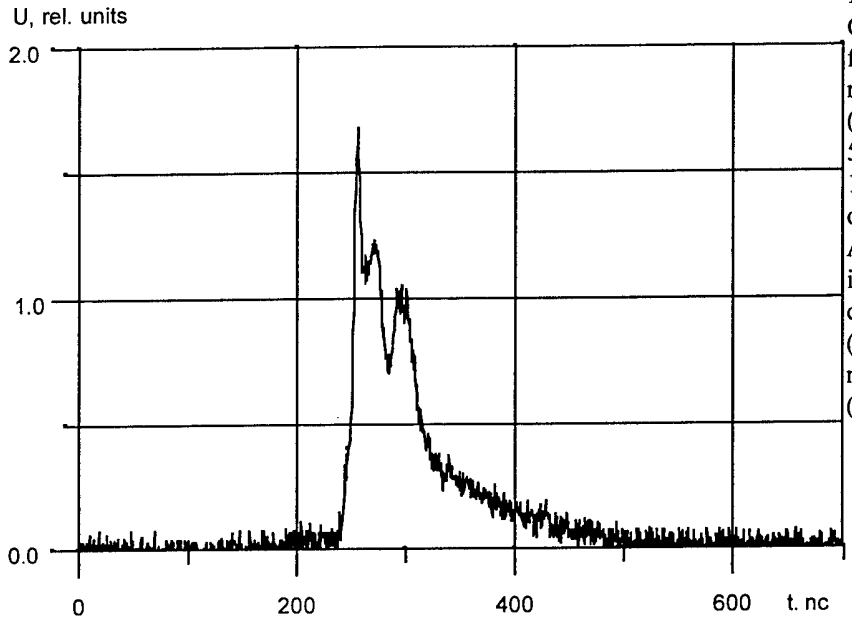

Fig. 3. Oscilloscope waveform of soft X-ray radiation vs. time (quanta energy 400-500 eV). «Angara-5-1» installation. The outer shell is hollow Ar jet, the inner load is foam agar-agar cylinder (60 μg/cm) containing KCl dopant (30% of mass).

The load of «GAEL» was hollow jet of Al plasma (linear mass 2-60 μg/cm, which was collapsed onto Al wire (d = 10-50 μm). The current transfer from outer shell of Z-pinch onto inner one was under investigation. An affect onto this phenomenon due to growth of instabi-

lity of mode m = 0 and hot spots formation near the axis of system were under interest too [9]. The line radiation detected was emitted from these hot spots. Total yield of line radiation was 0.2÷0.5 J. Typical hot spot plasma parameters were calculated as T_e = 350÷400 eV, $n_e = (2 \div 4) \cdot 10^{21}$ cm^{-3}.

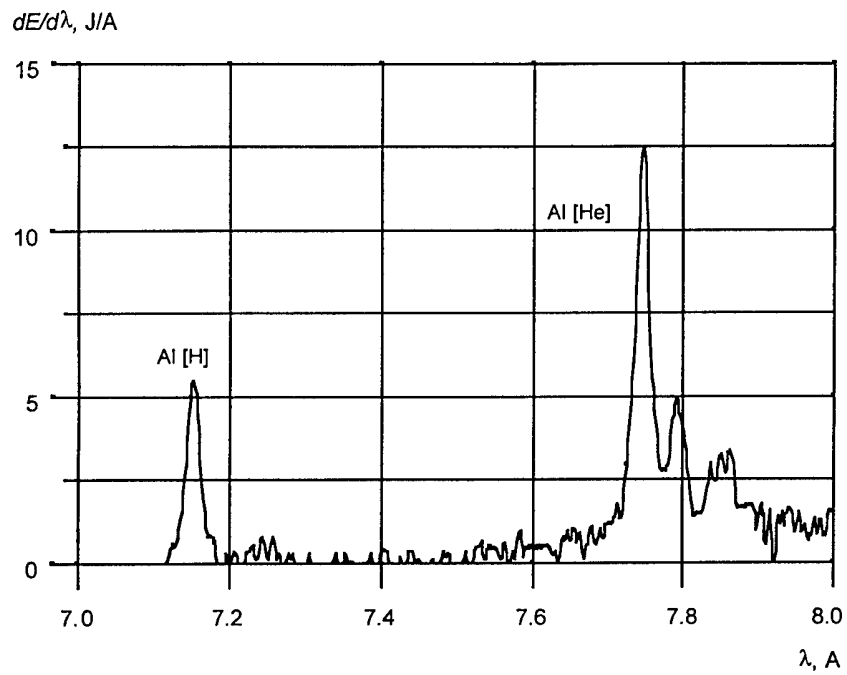

Fig. 4. Spectrum of Al, first reflection order of crystal. «GAEL» installation. The load is Al wire, d = 20 μm (8 μg/cm).

Discussion and Conclusions

CCDs have linear response with respect to the dose absorbed. That makes absolutely calibrated measurements much easier. Direct registration of X-ray onto CCD does not require complicated construction, optical schemes and high-voltage supplies. Quantitative interpretation of results obtained becomes more simple.

The spectrograph described offers good electromagnetic compatibility when used at pulse-power installations, which are strong interference sources.

The system is quite simple and reliable, that allowed to achieve totally automatic cycle of on-line plasma parameters acquisition. The Z-pinch parameters T_e and n_e are available immediately after each experimental run.

References

[1] S.Yu. Vorob'ev, V.I. Zaitsev, V.D. Korolev, I.V. Polyakov and A.S Chernenko, Vopr. Atom. Nauki Techn., Ser. Termoyad. Sintez, No.2(6), p. 38-41, 1980.

[2] J.R. Janesick, T.Elliot H.H. Marsh, S.Stewart, J.K. McCarthy. Potential of CCDs for UV and x-ray plasma diagnostics. Rev. Sci. Instrum. 56(5), pp. 796-801, May 1985.

[3] V.I. Korsh, V.E.Kuskov and V.Ya.Stenin, Instr. and Exp. Techn., No.3, 1982.

[4] A.V. Batunin, A.N. Bulatov, V.I. Zaitsev, Yu.N. Luzin et al., Instr. and Exp. Techn., No.4, 1992.

[5] G.S.Volkov, V.V.Zazhivikhin, V.I.Zaitsev, V.O.Mishensky. Charge-Coupled Devices as Position-Sensitive Detectors of X-ray radiation., Instr. and Exp. Techn., Vol. 39, No.3, 1996.

[6] B.L. Henke, P.A. Jaanimagi, Rev. Sci. Instrum. 56 (1985), No.8, pp. 1537-1552.

[7] E.P. Bol'shakov, E.P. Velikhov, V.P. Smirnov et. al., Atomnaja Energija, V.53, p.14, 1982.

[8] J.Delvaux, H.Lamain, C.Rouille, H.J.Doucet, J.M.Buzzi, M.Gazaix, B.Etlicher. High-power electron beam, 1981.

[9] F.J.Wessel, B.Etlicher, P.Choi. Demonstration of enhanced stability and energy transfer in an Aluminuim plasma embedded fibre Z-pinch. Phys. Rev. Letters, Feb. 1992.

P-4-15

CR-39 NUCLEAR TRACK DETECTOR APPLICATION FOR THE DIAGNOSTICS OF LOW ENERGY HIGH POWER ION BEAMS

M.S.Opekounov, S.A.Pechenkin, G.E.Remnev, *I.V.Ivonin

Nuclear Physics Institute, Lenin av. 2a, Tomsk, 634050, Russia
**Siberian Physical-Technical Institute, Revolution Square 1, Tomsk, 634050, Russia*

Abstract

This report presents the investigation results of spectral composition of ion beams generated by magneto-insulated ion diode of «MUK-M» and «TEMP» accelerators [1,2]. Energetical and mass characteristics of the accelerated ion beam were determinated by Thomson spectrometer with CR-39 plate detector (MOM-Atomki Nuclear Track Detector, Type MA-ND/p). Accelerated ion energy was from 40 up to 240 keV. Ion current density range is from 1 A/cm^2 up to 10 A/cm^2. Mass composition contained hydrogen, nitrogen, carbon and aluminum ions. The individual track analysis shows the track form, depth and diameter dependence on ion mass and energy.

Introduction

During last years we use CR-39 nuclear track detector (NTD) as a detector plate in Thomson spectrometer for the determination of accelerated ion beams' mass and energy spectra (Isakov et al., 1991, Matvienko et al., 1994) [1,2]. The ion energy, mass and atomic number of accelerated ion are determinated by the spectrometer construction.

Experiment

Research was carried with the ion beams generated by «TEMP» and «MUK-M» accelerators (Isakov et al., 1991)[1]. Ion beam composition is hydrogen, carbon, nitrogen and aluminum ions. Ion current range is from 1 A/cm^2 up to 100 A/cm^2. Ion energy is from 30 up to 300 keV/z. The mass and energy spectra of accelerated ion beam were determinated from the analysis of the common picture of NTD parabola tracks, determinated by Thomson spectrometer (fig.1). We used optical microscope for this research. Detector picture size was 1x1.5 cm.

Wide range of ion energy in the beam spectrum is defined by the particularities of the ions accelerating. Ion beam was collimated by two 50 μm diameter diaphragms. Into the Thomson spectrometer chamber, ion beam was separated and makes traces on detector surface as a system of parabolas, every one

corresponds to the certain kind of ions with equal A/z ratio, where A - atomic number of element, z - ion charge. After irradiation by the polycomponent ion beam, detector plate was etched by 6.28 N NaOH solution at t=60°C. Etching time was 1-6 hours.

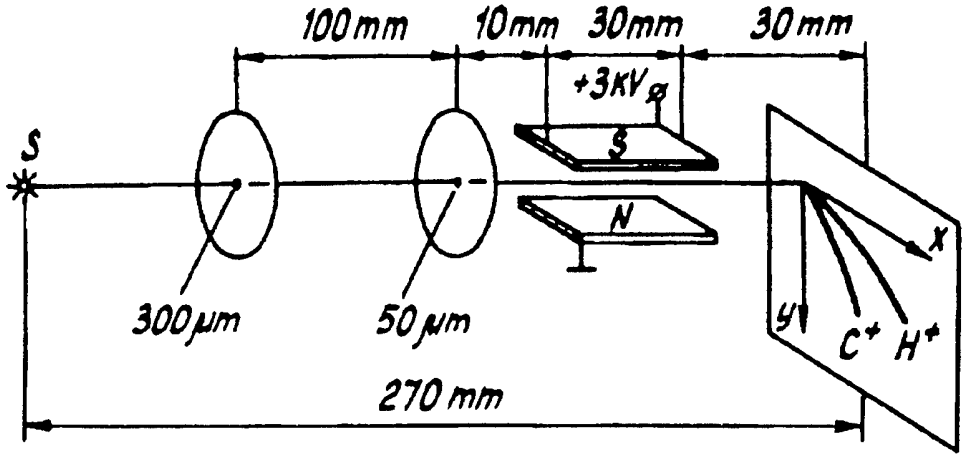

Fig.1. The principle of Thomson ion spectrometer.

The research of the individual ion track characteristics was carried in the electron microscope by investigation of carbon replica tracks on CR-39 detector plate, using the information about beam composition and ion energy. Fig.2 presents a typical photospectrogramm of CR-39 detector plate image and the electron photomicrographs of carbon replica profiles of ion tracks.

As a result of analysis of ion track after separation in Thomson spectrometer on detector plate, we have defined ion beam composition as a following: hydrogen ions (energy range is from 40 up to 120 keV) are 26 per cent, single and double charge carbon ions (energy range is from 80 up to 240 keV) - 70 per cent, nitrogen ions (energy range is from 60 up to 120 keV) is approximately 4 per cent. Wide range of ion energy in the beam spectrum is defined by the particularities of the ions accelerating. The low limit of the observed ion energy spectrum is limited by spectrometer construction. It is 30 keV. Individual ion tracks in the detector have almost regular form of the circle in the section, but depth is small. The ion track diameters depend on ion mass and ion energy. H^+, C^{+n} track diameters after 6 hours etching are 1-1.8 μm, track depths is from 0.13 up to 0.19 μm. This diameter dependence on energy is linear. The diameter dependence on mass is not observed distinctly. The track diameter and track depth from nitrogen ions are 2 times higher than analogous parameters for carbon and hydrogen ions in the same ion energy range. Obtained results are correspond to results (Sato et al., 1990)[3] and allow to make a conclusion about perspective using of this type detector for the low ion beams.

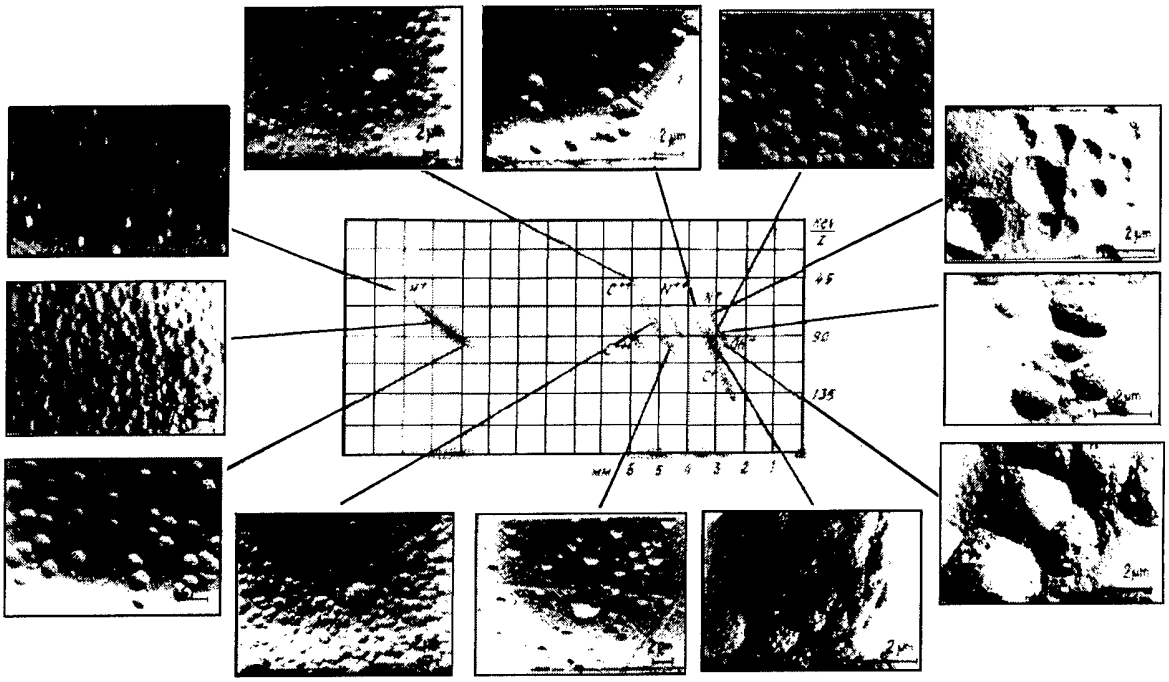

Fig.2. The typical photospectrogramm of CR-39 detector plate image and the electron photomicrographs of carbon replica profiles of ion tracks.

Conclusion

It is possible to use Thomson spectrometer with CR-39 NTD as a method for detector sensitive properties' calibration for different mass and energy ions. It is possible because processes of the detector etching, detector irradiation by different mass and energy ions and track identification are carried simultaneously[4,5].

[1] Isakov,I.F., V.N.Kolodii, M.S.Opekounov, V.M.Matvienko, S.A.Pechenkin, G.E.Remnev and Yu.P.Usov Sources of high power ion beams for technological application. Vacuum, **42** (1991),159-162.

[2] Matvienko,V.M., M.S.Opekounov, G.E.Remnev, V.V.Vasilyev, E.I.Luconin and E.G.Furman The short-pulse implanter. Proceeding of the 10-th Inter. Conf. **Beams'94** (1994).

[3] Sato M., Y.Hashimoto, M.Yatsuzuka and S.Nobuhara (1990). Self-crowbar switch operation in small milt. Proceedings of the 8-th Inter. Conf. **Beams'90, 2**, (1990) 1070-1075.

[4]Nuclear Track detector Application for the Diagnostics of Low Snergy High Power Ion Beams. G.E.Remnev, M.S.Opekunov, A.N.Grishin, I.V.Ivonin. Nuclear tracs in Solids, 17-th Int. Conf. Book of Abstracts, p.284, Dubna, 1994.

[5]CR-39 Nuclear Track detector Application for the Diagnostics of Low Snergy High Power Ion Beams. G.E.Remnev, M.S.Opekunov, A.N.Grishin, I.V.Ivonin. Radiation Measurements, Vol.25, Nos1-4, p.739-740, 1995.

VOLTMETER WITH COMPTON ELECTRONS

N. R. Pereira, S. G. Gorbics, and D. M. Weidenheimer

Berkeley Research Associates, PO Box 852, Springfield, VA 22152 USA

Abstract

We discuss a technique to measure bremsstrahlung's electron end point energy in the MV regime with only two detectors. One measures the total radiation. The other detector filters out all except the hardest photons by looking only at their Compton electrons, whose average energy is determined with a magnetic field.

Introduction

The voltage in a bremsstrahlung diode determines the hardness of the radiation. Harder radiation penetrates more easily, so that the voltage can be inferred from differential absorption behind increasingly thick filters of tungsten or other high atomic number materials. As always, the technique has limits and disadvantages. It does not work too well when most of the radiation is around 1 MeV, because in this regime the attenuation coefficients are roughly constant. The consequence is a practical upper limit to the voltage that is hard to get around even by adding more channels. One implementation uses 7 channels to cover up to 2 MV or so, a workable but inelegant way to get only a single number. Alternative approaches for measuring radiation hardness, e.g., the textbook technique of finding x-ray energy by looking at the Compton electron emerging from a thin foil in a specific direction, do not work well in a noisy pulse power environment because the signal strength is too low.

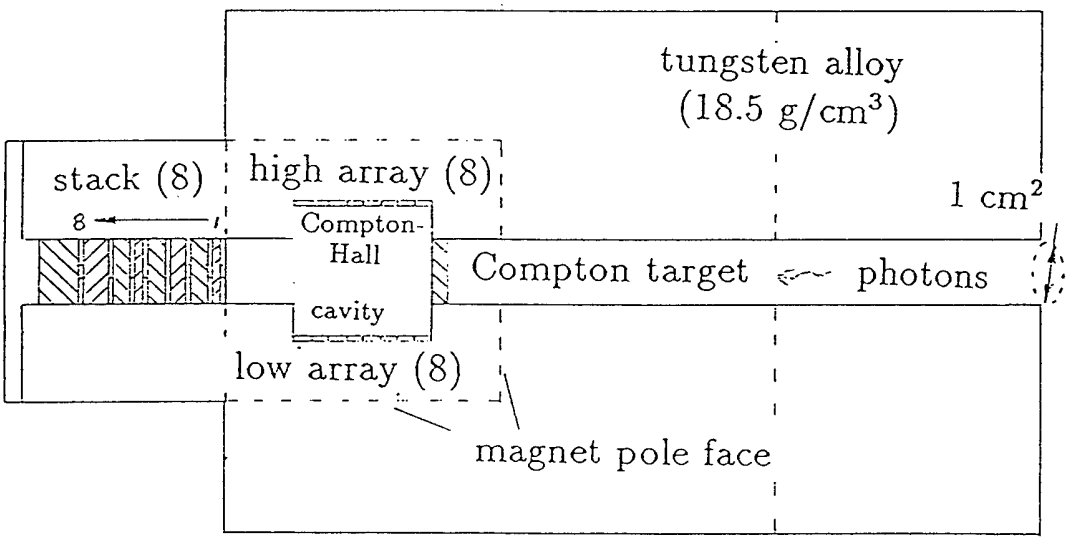

Figure 1. Design of the Compton-Hall voltmeter.

The voltmeter described here determines electron end point voltage with only two data channels. It uses the average energy of an entire spray of Compton electrons knocked out of a thick foil by the harder part of the x-ray spectrum. The electron's average energy is measured by their average curvature in a stationary magnetic field. This approach is a compromise between signal strength and energy resolution: its nomenclature, a Compton-Hall voltmeter, recognizes the two main processes.

In a bremsstrahlung diode the electrons are assumed to get a well-defined energy that is equal to the instantaneous voltage. When they hit the anode bremsstrahlung converter the electrons make x-rays, which travel to the instrument. Figure 1 is the voltmeter's geometry, which is identical to that of a hard x-ray spectrometer to be mentioned later. The radiation comes in from the right through a hole in a 10 cm thick tungsten collimator. On hitting the Compton target the x-rays make electrons. The target's thickness is about 1/3 of the CSDA range for the most energetic electrons, so that the electrons created at the front of the aluminum lose a substantial fraction of their energy. Comparatively little energy is lost in the air in between two permanent magnets, the Compton-Hall cavity. The $\sim$ 0.35 T strong magnetic field bends the Compton electrons over tens of mm toward the walls. The Compton current can be measured anywhere along the wall. The back contains many sensors as appropriate for a spectromeetr: only a single one is needed for a voltmeter.

The voltage is given by only two measurements, namely the current at some optimum point on the wall compared to one of the back sensors, or to a sensor at the Compton target (not shown).

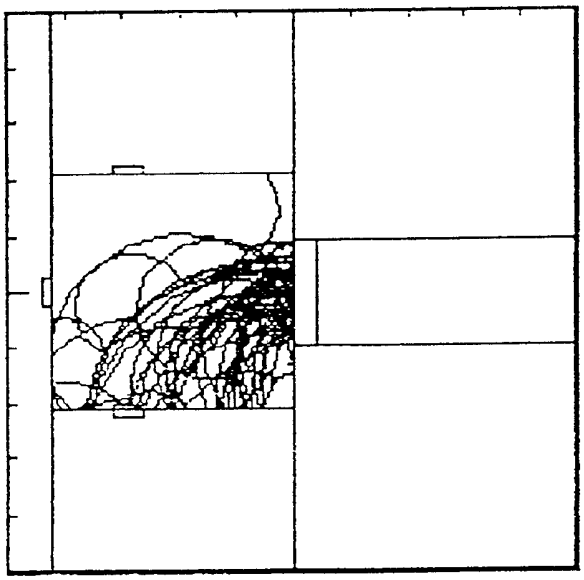

Figure 2. Electron motion in the Compton-Hall voltmeter.

Figure 2 illustrates the particle trajectories. A photon with 2 MeV comes in from the right. A spray of Compton electrons is bent down by the magnetic field: some electrons hit the top or bottom of the cavity, and turn backwards, but clearly most electrons end up in the Compton-Hall detector at the bottom. A background detector on top sees only photons that pass through the tungsten, scatter in the foil, or reach it some other way. The background can be subtracted, but it is better to suppress it with added shielding. Some Compton electrons reach the total dose detector straight behind the collimator, to the left. This detector gets most of its irradiation from photons that pass straight through the Compton target. An alternate position for the total radiation detector is in the collimator's throat, embedded in the Compton target.

All the various processes can be accounted for from first principles with a Monte Carlo code such as the ACCEPTM member of the ITS package.[1] Our computations

give a linear relation between diode voltage and the response of a sensor placed in a position appropriate to some specific voltage regime. However, a carefully computed bremsstrahlung spectrum from a full Monte Carlo run on an actual bremsstrahlung converter is not needed, because the Compton-Hall voltmeter looks only at the hardest part of the photon spectrum. This is adequately represented by a model spectrum that consists of a theoretical (Kramers) bremsstrahlung spectrum filtered with 2 cm thick aluminum. In the fully three-dimensional geometry of the instrument the Monte Carlo approach is essential for computing the Compton interactions in the thick target, slowing down of the electrons, and electron deflection in the magnetic field: for convenience the interaction with the detector is also done with ITS.

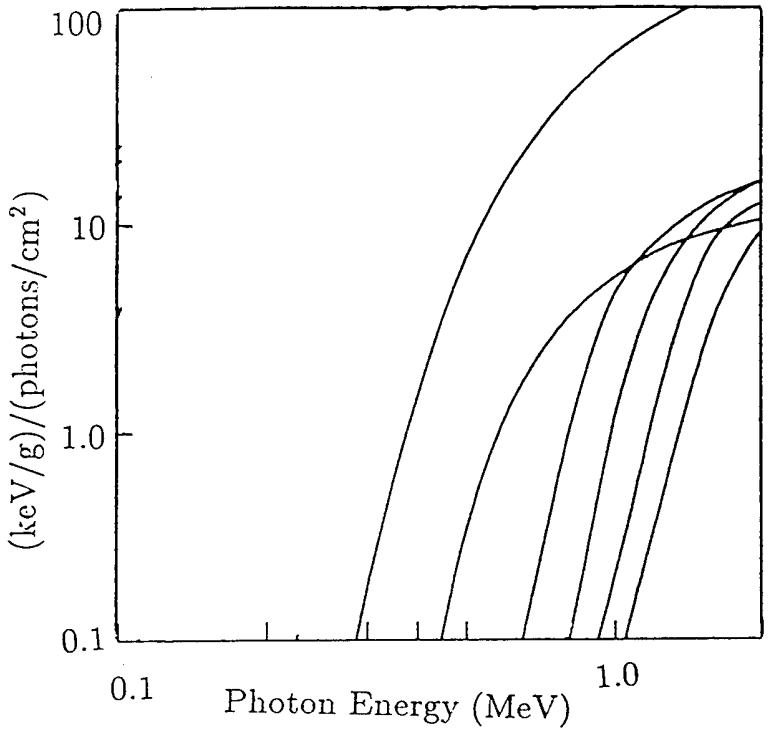

Figure 3. Response functions of Compton-Hall detectors compared to filtering.

The same geometry is suitable as a spectrometer for photon with energies exceeding 1 MeV. In this case you need the Compton current in various Compton-Hall detectors along the wall of the magnetic interaction region. For a time-integrated spectrometer the measurement can be done with thermoluminescent detectors (TLDs), which measure dose: dose rates are needed for a time-resolved spectrometer. Unfolding the spectrum from the dose (rates) requires the responses for each detector as function of photon energy.[2]

As an example, the solid lines in Figure 3 are the responses of Compton-Hall detectors located at different distance from the foil. The dashed line is the response of a detector behind a 6.35 mm thick tungsten.[2] All x-rays with energy $h\nu \lesssim$ 0.3 MeV are cut off by the tungsten filter. Likewise, the Compton-Hall detectors see no x-rays below a cutoff energy that is adjustable from about 0.7 MeV to 1.5 MeV. The maximum response behind the tungsten is one order of magnitude higher than that of the Compton-Hall sensors. Qualitatively, the response functions are similar: the Compton-Hall detectors behave as if they were filtered by a thick piece of material with

an adjustable atomic number in the hundreds.

The fourth Compton-Hall detector, at the arrow in Figure 3, has the appropriate cutoff to function as a voltmeter in the 1 to 2 MeV regime. Figure 4 compares the dose in a calcium fluoride TLD as measured on a van de Graaff electron accelerator with the computed response for this detector. Here the relative responses are normalized at 2 MeV: in the experiment the detector in the full radiation field was located at a different position than assumed in the computation. The dose in the Compton-Hall sensor is only a few percent of the dose in the full radiation field. Therefore, background radiation must be rigorously suppressed by excellent shielding all around the instrument.

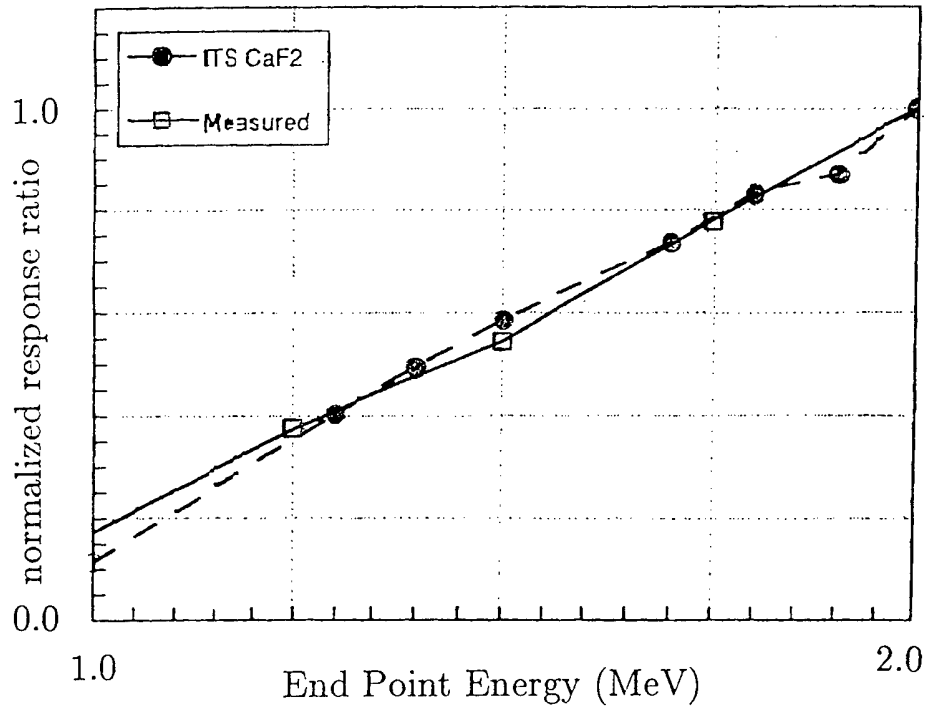

Figure 4. Relative response as function of electron energy.

The response of the Compton-Hall detector is linear with electron end point voltage, both in the computation and in the experiment. Although the absolute value of the voltage as inferred from this instrument remains to be absolutely calibrated, the linear response as function of voltage already makes the voltmeter usable for relative measurements. At this time the Compton-Hall voltmeter remains to be tested in a time-resolved mode, wherein the TLDs are replaced by dose rate detectors. Problems are not expected: suitable detectors are available from a time-resolved version of a differentially filtered spectrometer that also started in a simpler, time-integrated version.[2]

In conclusion, we would like to thank Dr. C. E. Dick (NIST) for his participation in the calibration using NIST's van de Graaff.

[1.] J. A. Halbleib, R. P. Kensek, T. A. Mehlhorn, S. M. Seltzer, M. J. Berger, *ITS Version 3.0, the Integrated TIGER Series* $\cdots$, SAND91-1634, 1992.

[2.] S. G. Gorbics and N. R. Pereira, *Differential absorption spectrometer for pulsed bremsstrahlung,* Rev. Sci. Instrum. **64**, 1835 (1993).

THE ROLE OF ELECTRON BEAMS AND NEW EXCITATION CHANNELS AND FOR DIELECTRONIC SATELLITES IN DENSE PLASMAS

F.B. Rosmej

Institut für Experimentalphysik V, Ruhr-Universität Bochum, Universitätsstr. 150, D-44780, Bochum, Germany

B.A. Bryunetkin, A.Ya. Faenov, I.Yu. Skobelev

MISDC, VNIIFTRI, Mendeleevo, Moscow region, 141570, Russia

M.P. Kalashnikov, P.V. Nickles, M. Schnuerer

Max-Born-Institut, Rudower Chaussee 6, D-12489 Berlin, Germany

New excitation channels for the explanation of the strong emission of Li-like and Be-like satellite transitions in numerous dense plasmas are proposed. These channels are based on the collisional innershell excitation from the excited states (ES-ISES) which are highly populated in the initial stage of plasma evolution:

Be-like satellites ES-ISES: $1s22xnz + e - 1s2x2ynz + e$

Li-like satellites ES-ISES: $1s2ny + e - 1s2xny + e$

In the case of Li-like satellites the ES-ISES channel predicts "Blue Satellites" of the He-like resonance line W = 1s2 - 1s2p 1P1 which are observed in the experiments.

Corresponding spectra simulations exploiting new calculated atomic dates for these mechanism are carried out. Experimental spectra of plasma, produced at intensities up to 10^{18} W/cm^2 and recorded by means of high resolution spherically bent mica crystal technique make possible a direct verification due to the low ion temperature in the heating phase. In dense pinching plasmas, the detailed satellite structure are smeared out due to rather high ion temperatures in the ionizing phase.

We investigate the role of energetic electrons on the satellite formation of Li-like and Be-like ions for all excitation channels and discuss the diagnostic properties.

(The full text has not been supplied.)

P-4-18

Visualisation of High-Current E-beams on Solid Surfaces

V.I.Solomonov, V.V.Osipov, S.G.Mikhailov, A.I.Lipchak

Institute of Electrophysics, Ural Division of Russian Academy of Sciences, Komsomolskaya 34, Ekaterinburg, Russia, 620219.

Up to day the visualizers of e-beams have essential disadvantages. They are rather complex, expensive, and/or average the recorded flux of electrons by surface. Therefore the task to find the new scintillators based on low cost, natural material for these purposes seems to be very important. To solve this task broad range minerals was examined. The natural specimens were investigated on high-current pulsed e-beam accelerators with the following parameters: current density from 10 to 1000 A/cm^2, energy from 100 to 300 keV, pulse duration from 2 to 50 ns [1,2]. It was found that high-intensive luminescence in visible spectral range with time duration to several tens of minutes is excited in such minerals as spodumen, calcite, apatite doped by Mn in the concentration range from 10^{-5} to 1 weight percents. The specimens with Mn concentration about 1 weight percentage appears to be the most suitable both by intensity and time of luminescence. The appearing of such luminescence allows one to observe the cross section of e-beam both during the action period and after it. The Fig. 1 presents the light "images" of e-beam on natural spodumen (Mn ~ 1 weight %) at the distance: 0 - (1), 5 - (2), and 10 - (3) mm from output foil of e-beam accelerator recorded after two minutes of e-beam action. The increase of dimensions of light "image" results from e-beam cross

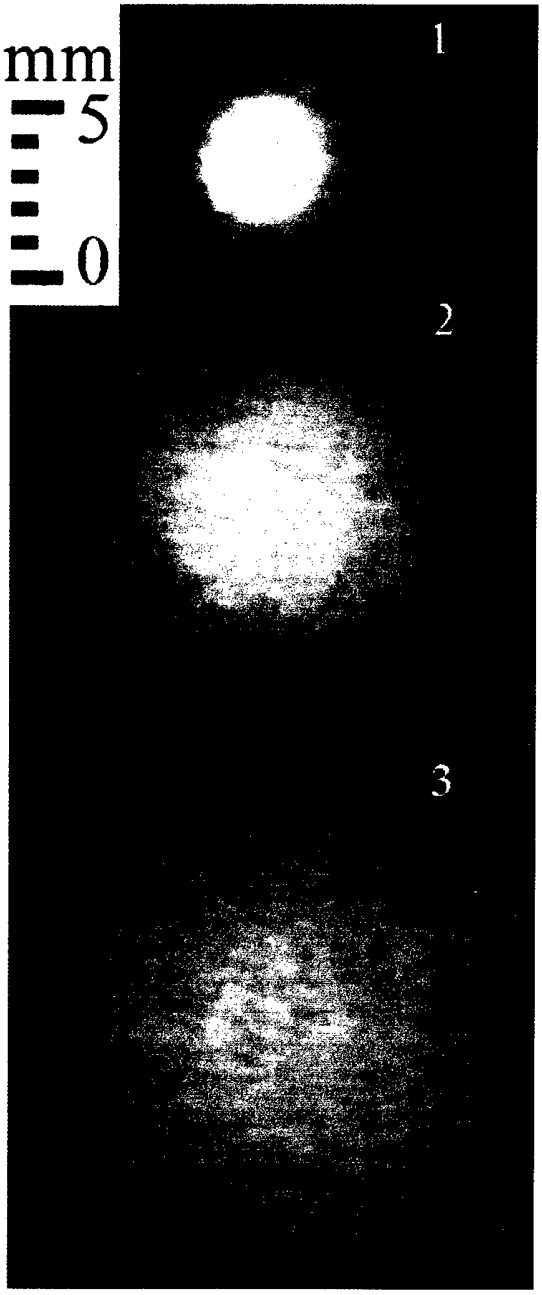

Fig. 1.

Light "images" of e-beam on natural crystal of spodumen

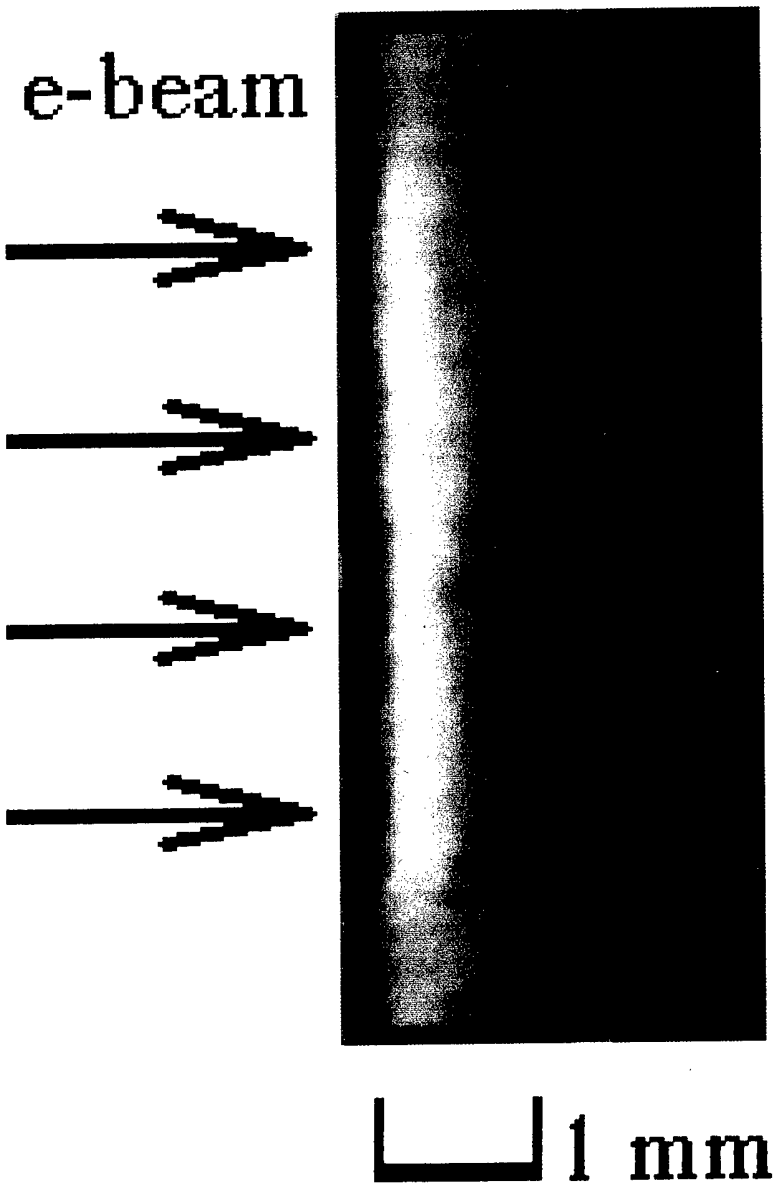

Fig. 2.

Section of the natural crystal of spodumen along longitudinal axis of e-beam

section expansion. The decrease of its intensity results from of current density decreasing. One can see that intensity of luminescence depends on current density and it is possible to record cross sections of e-beam at different distances from the foil. The Fig. 2 presents the section of the same specimen along the longitudinal axis of e-beam. The dimension of luminous layer depends on the run length of electrons in the specimen and is determined by energy of electrons. So it is possible to determine the last one by measurement of dimension of this layer.

The presented results let us to state that these natural materials may be utilised for visualisation of high-current pulsed e-beams both during its action period and after it. Every concrete crystal can be calibrated in absolute energy of electrons and current density values so it can be used as absolute transducer of these parameters. The proposed materials can solve the tasks of measurements of parameters of high-current pulsed e-beams such as electrons' energy and current density distribution. Such materials are widely spread in nature. They have low cost and they are not hydroscopic and are simple in manufacturing and using. Also techniques to grow these crystals are well developed now. These scincillators not only simplify the registration technique, but also low the cost of transducers of e-beams. So these materials seem to be very perspective.

References

[1] A.S. El'cheninov, F.J. Zagulov, S.D. Korovin et al. "High-current Nanosecond Accelerator of Electrons with High Repetition Frequency of Pulses". Voprosy atomtoj nuaki i tehniki. Elektrofizicheskaja apparatura.(Questions of atom science and technique. Electrophysical apparatus), (in Russian), 1987, #23, pp. 33-36.

[2] F.J. Zagulov, A.S.Kotov, V.G. Shpak et al. "RADAN - Compact High-current Pulse-Repetitive Accelerators of Electrons". Pribory Tehnika Eksperiment (in Russian), 1989, #2 pp. 146-149.

P-4-21

CHARACTERISTICS OF CHARGE COUPLED DEVICES OVER X-RAY SPECTRAL BAND

V.O.Mishensky, G.S.Volkov, V.I.Zaitsev, V.V.Zazhivikhin

Troitsk Institute for Thermonuclear and Innovation Investigations, Troitsk, 142092, Russia.

Abstract

The results of theoretical and experimental investigation of sensitivity and spatial resolution of charge coupled devices (CCD) been influenced by of X-ray quanta are reported. Both calculation model of interaction process between X-ray radiation and CCD-structure and experimental results of investigation of CCD characteristics are presented. The theoretical model of interaction between X-ray radiation and CCD is suggested.

In accordance with model described, the calculations of CCD sensitivity and spatial resolution, depending on X-ray radiation energy, are performed. The results of comparison of the calculation data and experimental data obtained for linear CCD (LCCD) are presented.

CCD has maximal sensitivity of ~$(1\text{-}2.5)\cdot 10^7$ V·cm^2/J for quanta of energies 0.5-8 keV. CCD spatial resolution varies from 15-20 μm (CCD gate size) for quanta of energies less then 4 keV and gets worse up to 150 μm for harder radiation (20-50 keV).

CCD usage as space-resolving detector for high-power installation diagnostics device is presented. Other fields of CCD application for X-ray detection are discussed. Advantage of CCD usage in comparison with traditional X-ray films is discussed from this point of view.

Introduction

Usually method X-ray picture measurements is film registration. In this case it is needed a lot of time for the obtaining of the final measurement results.

Present time, there is some experience of application of charge coupled devices (CCD) for direct X-ray registration [1, 2]. However the quantitative interpretation of the results obtained is difficult task because the lack of detailed information about CCD characteristics in X-ray region.

This paper contains the results of calculation and experimental investigation of CCD in X-ray region.

1. Experimental investigation of CCD characteristics.

For experimental investigation of CCD characteristics K_α lines of different materials were used (Cu,K_α = 8.04 keV, Mo,K_α = 17.45 keV, Sn,K_α = 25.04 keV).

As radiation source Marx-type generator was appreciated (I_{beam} = 0,5-2 kA, E_{beam} = 50-200 keV, T_{beam} = 60 ns). Fig.1 shows the experimental arrangement.

The linear CCD (LCCD) was used as X-ray detector. This LCCD is equipped with four sensitive areas. Each one consists of the linear array of 2048 cells. Cell size is 15×15 μm, that corresponds to total sensitive area length of 30.72 mm.

The value of X-ray flux influencing onto CCD was determined by absolutely calibrated semiconductor detector.

For the spatial resolution measurements the X-ray flux was collimated by means of slit of 25 μm aperture. The LCCD signal was compared with calibrating one obtained by means of X-ray film. The typical spatial profiles are shown in the fig.2.

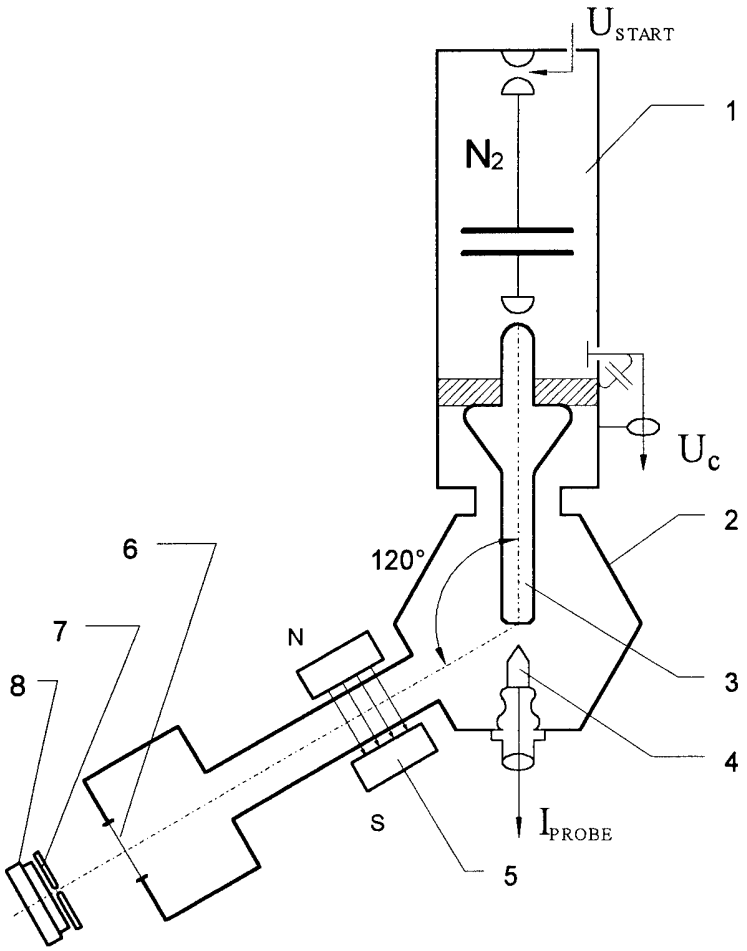

The Full Width at Half Magnitude (FWHW) of the profile obtained during the experiment depends on the effective spatial resolution of CCD

$$\Delta d^2 = (\delta d_{SLIT})^2 + (\delta d_{CCD})^2$$

where Δd is value of FWHM obtained by CCD, and δd_{SLIT} is actual value of FWHM obtained by means of film scanning. The experimental data for different X-ray energy quanta are presented in the Table 1.

Fig. 1. Experimental setup.
1- gas-filled Marx generator,
2- vacuum chamber,
3- anode, 4-cathode,
5-magnets, 6- outlet window,
7- slit-like aperture,
8- LCCD.

Table 1. Sensitivity and spatial resolution of CCD. Experimental data.

Quantum energy, keV	Sensitivity, V/(J/cm^2)	Resolution δd_{CCD}, μm
8.04	$1.5 \cdot 10^7$	71
17.4	$4.1 \cdot 10^6$	105
25.04	$1.86 \cdot 10^6$	110

2. CCD charge accumulation model. Computer simulation.

Charge accumulation model was developed under the following conditions:

- initial charge carriers distribution is produced by the absorption of X-ray quanta and actually is δ-function vs. time;
- electric field is totally concentrated immediately under insulator layer inside of thin potential minimum region beneath CCD gate;
- output signal is proportional to amount of charge which has been collected inside of potential minimum.

This charge consist of two parts:

- the first one is the charge which was born inside of region of potential minimum,
- the second one is charge which has diffused into this region from semiconductor substrate.

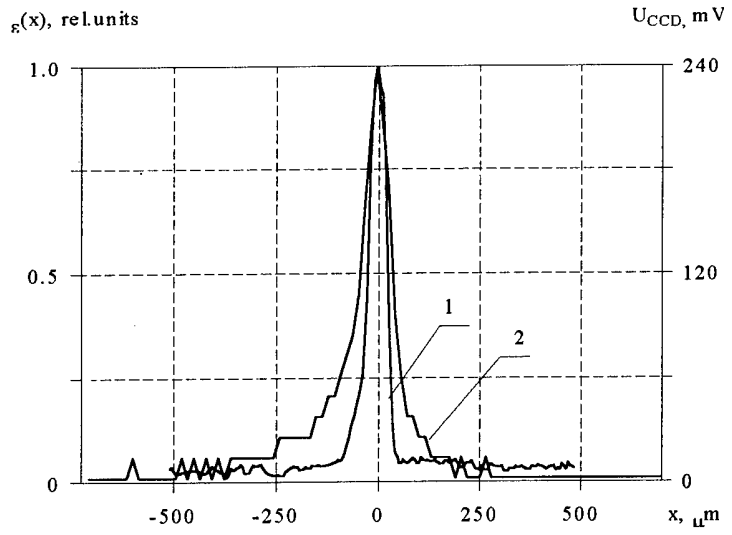

Fig. 2. Spatial profile of X-ray radiation flux $\varepsilon(x)$.
Slit-like aperture of width 25 μm was used.
Curve 1 corresponds to real spatial profile.
Curve 2 was detected by LCCD.

Using these assumptions was found the solution of diffusion equation. This solution depends on charge carriers diffusion length $L = \sqrt{D \cdot t_r}$, where D is diffusion coefficient, t_r is electron-hole recombination time.

The comparison between experimental data and calculations shows quite good coincidence for value $L = 150$ μm. CCD characteristics calculated for this L are shown in fig. 3.

For quanta of energy less then 3 keV, the spatial resolution is determined by size of CCD cells only. The device has sensitivity high enough (more, then 10^7 V·cm^2/J) in range 0.5 - 10 keV.

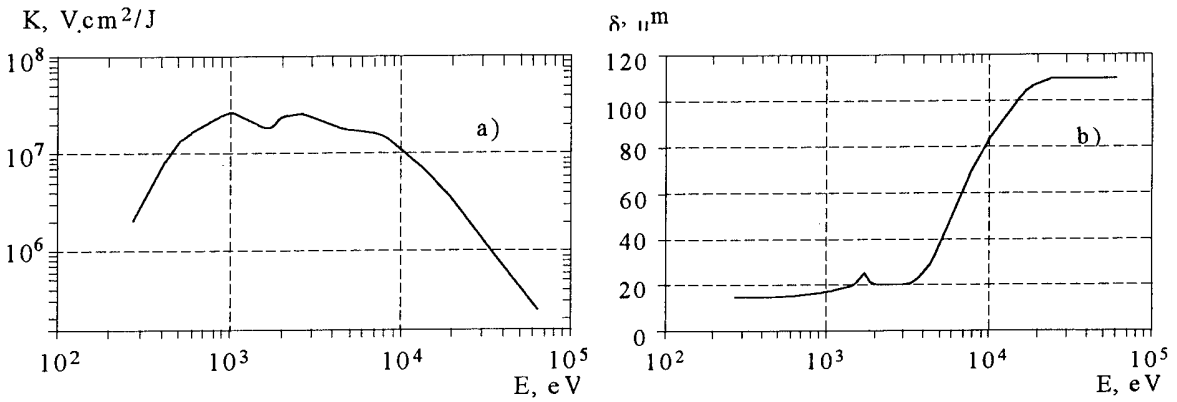

Fig.3. a) CCD sensitivity vs. quantum energy. b) CCD spatial resolution vs. quantum energy.

3. Applications.

The investigation of CCD characteristics shows that application of CCD as spatially-resolved detector of X-ray radiation is very hopeful. Some degradation of CCD which could be caused by radiation damage is negligible. Any distortion of device characteristics begins when dose absorbed is about 10^5 rad [3]. It allows to perform up to 10^6 measurement cycles per one CCD.

LCCD was used in X-ray crystal spectrograph. CCD signal was treated by analog-to-digit converter and then processed by computer (IBM-PC). This device was tested at pulse power installation ANGARA-5. Present time this spectrograph is included into permanent diagnostics set.

In the fig.4 X-ray spectrum of argon obtained during Z-pinch experiment (installation current 3.5 MA) is presented. One can see, that CCD detector provide quite enough possibility

to register spectra with spectrograph own resolution (in our case $E/\Delta E \sim 10^3$). Important advantage is rather short time of data acquisition and treatment (less then 30 sec).

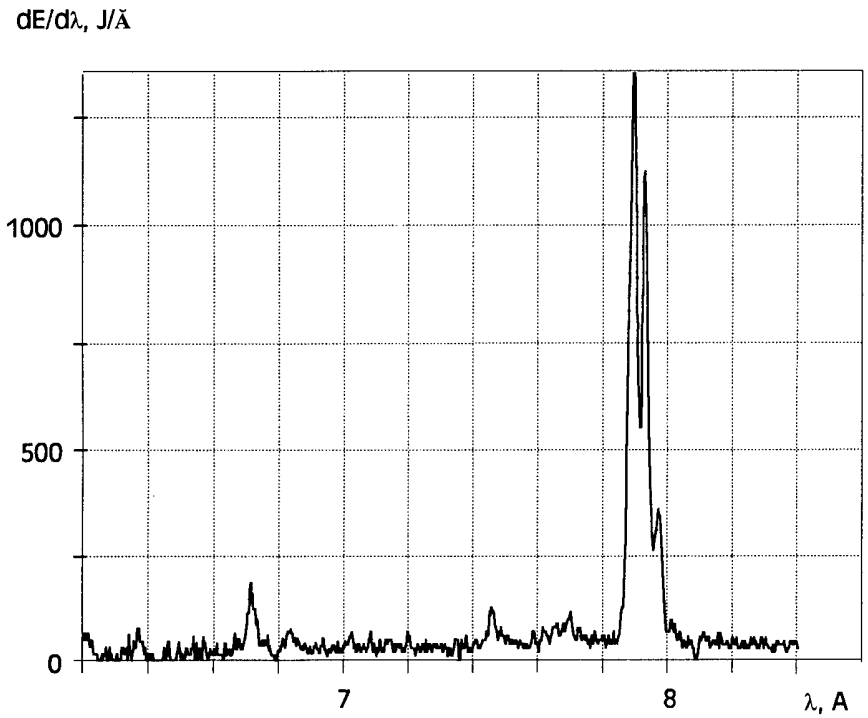

Fig. 4. X-ray spectrum registered by crystal spectrograph with CCD-detector. H-like and He-like emission of argon was registered in 2-nd crystal reflection order.

References.

[1] I. Matsushima, K.Koyama, M.T. Animoto, M.Yano, Rev. Sci. Instr., v.58, 144, pp.600-603, 1987.

[2] A.V. Batunin, A.N. Bulatov, V.I. Zaitsev, Yu.N. Luzin et al., Prib. Tekh. Eksp., 1992, No.4, p.165.

[3] V.I. Korsh, V.E. Kuskov, and V.Ya. Stenin., Prib. Tekh. Eksp., 1982, No.3, p.7.

P-4-24

STUDY OF PLASMA IN MAGO CHAMBER BY OWN NEUTRON RADIATION

O.M.Burenkov, S.F.Garanin, A.N.Demin, I.F.Dudin, V.P.Korchagin, I.V.Morozov, V.N.Mokhov, E.S.Pavlovsky, V.K.Chernyshev, V.B.Yakubov

Russian Federal Nuclear Center All Russian Scientific Research Institute of Experimental Physics, 607200, Arzamas - 16, Russia

1. INTRODUCTION

Paper [1] was the first to publish results of research into plasma heating in plasma chamber MAGO obtained in experiments using explosive magnetic generators (EMG). This paper presents results of experimental research into MAGO chamber operation using DT and DD - reaction neutron spectra measurement with the time-of-flight method. A possible interpretation of obtained new results is also given.

OBJECT: The MAGO chamber used for the experiments is a fairly compact device (Fig.1): a hollow copper thick-wall cylinder 200 mm in inner diameter and 165 mm in length with a central electrode 60 mm in thickness separating the internal chamber space into two compartments (25 and 80 mm in height) connecting to each other with a narrow annular nozzle whose minimum width was 12 mm.

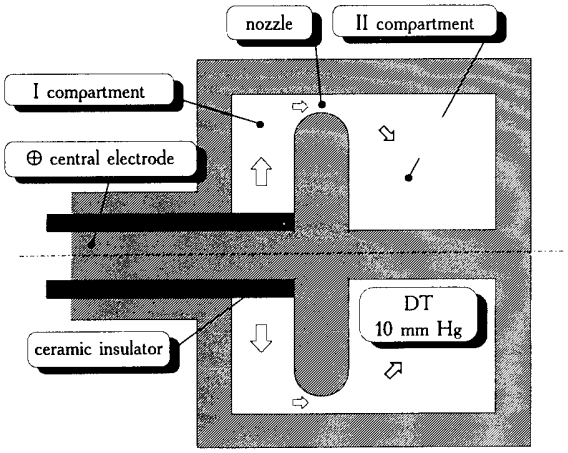

Fig. 1. Scheme of plasma chamber MAGO.

The vessel of the chamber with the central electrode constitutes a coaxial, short-circuited turn. The internal space of the chamber is filled with DT or DD - gas. At the chamber inlet the central electrode is separated from the vessel with ceramic insulator 20 mm in outer radius. Initial gas pressure in the chamber is 10-20 mm Hg. In the chamber initial magnetic field was preliminary created through gradual increase of electric current in the short-circuited turn up to 1.5 - 2.2 million amperes. Then the current abruptly, during 1-3 microseconds, increased up to 8-10 MA. Our experiments used explosive magnetic current sources with a current pulse generation unit (the stored energy is up to - 10 MJ).

During the abrupt current growth, according to the theoretic model, in the first chamber compartment where the insulator is located volume gas discharge occurs. Under action of ponderomotive forces low-temperature plasma begins to flow out of the first chamber compartment to the second through the narrow nozzle. At the nozzle outlet the plasma flow becomes supersonic and at the second chamber inlet a collisionless shock wave is generated. It is in this wave that kinetic energy of the plasma flux is converted to energy of chaotic ion movement. Later on the plasma which is already heated descends to the central electrode and is compressed with magnetic field and heavy insulator vapors which follow the DT plasma. In the hot plasma thermonuclear reactions take place and stop in some time by virtue of hot plasma mixing with cold plasma and insulator vapors. In the chamber specially designed for the above-described process scheme $5 \cdot 10^{13}$ neutrons are obtained in a pulse of - 2 μs duration.

In addition to these two parameters, the experimental data of the chamber involve information from current and light pickups, data of electron density obtained using

interferometry and data of plasma X radiation spectrum, there is the source image obtained in DT neutrons [1,2]. The neutron source is composed of two parts: 10% - the nozzle region; 90% - the central volume of the second chamber compartment. Mean energy of emitted neutrons in various directions is practically constant and close to 14.1 MeV.

2. RESEARCH TECHNIQUE

From the standpoint of plasma diagnostics, the MAGO chamber is not a very convenient device. The experiment is explosive, fragmental, the neutron source is voluminous, occupying practically the whole volume of the second chamber compartment; the neutron generation process duration, 2 μs, does not allow to use verified measuring techniques both for pulsed and continuous systems.

Under these conditions it was suggested that plasma ion temperature should be measured using the differences in DT and DD - reaction rate dependencies on ion temperature.

Deuterium-tritium mixture of 50/50% ratio as a most productive in the number of generated neutrons was usually used in the high-temperature plasma experiments. The dominant reaction in this mixture is the D and T nuclei reaction, D(T,n)He4+17.6 MeV. DD and TT type reactions concurrently proceed, however, on the background of TD they are practically insignificant. Among the reactions attended with neutron radiation the reaction D(D,n)He3+3.27 MeV is the closest by reaction rate.[1] When plasma ion temperature is 3 keV the DD reaction rate is 128 times less than the DT rate. Taking into consideration less detector sensitivity to DD neutrons, on the oscillograms for equicomponent DT plasma the DD pulse amplitude appears 850 times lower than from DT neutrons. At this ratio in the DT 50/50% experiments the DD pulse is completely lost in scattered neutrons from the DT reaction and is practically invisible.

To secure the possibility of measurements, it was suggested that the ratio of the number of nuclei in the D and T - mixture should be changed in order to obtain *equal amplitudes* of pulses from DD and DT neutron detectors. Simultaneous DD and DT recording was intended to be made with scintillation plastic detectors with neutron pulse separation by time of flight.

Oscillograms with three pulses of approximately equal amplitudes from gamma quanta and DT and DD neutrons were expected in the experiment . The principal experiment result should have been the measured ratio of DT and DD pulse areas appropriately recalculated to the reaction rate ratio and, eventually, to plasma temperature.

A feature of the reaction rate-temperature ratio dependence used is its nonuniqueness. With increasing temperature the ratio increases, reaches its maximum at 14 keV and then decreases. Thus, the experiment may result in ambiguity. For example, when the measured ratio is 120 the temperature may be both 3 and 35 keV.

3. EXPERIMENT RESULTS

Fig. 2 gives the oscillogram obtained in the experiment . The experiment was made on DT mixture with the ratio of the number of nuclei, T:D, 1:991. The ratio error was 0.15% .

On the oscillogram: the first pulse is gamma; the second is DT neutrons, energy 14.1 MeV; the third is DD neutrons, energy 2.45 MeV.

The measured integral ratio of DT and DD reaction rates was 139.

[1] Hereinafter by the DD reaction rate is meant $\langle\sigma v\rangle_{dd}$ for the neutron channel, by the DT reaction rate $\langle\sigma v\rangle_{dt}$

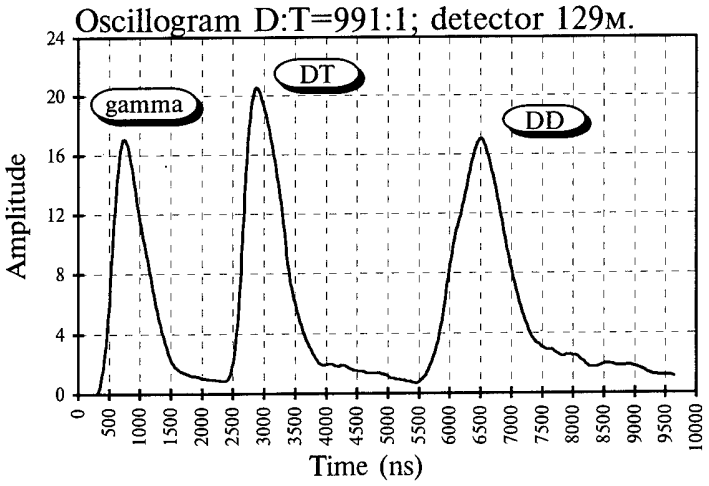

Fig. 2. Oscillogram obtained in the experiment with the nuclei ratio T:D of 1:991.

Neutron flux attenuation and scattering on the device elements, attenuation in air, spectral characteristics of the detectors were taken into account.

In the experiment DD pulse duration was considerably longer, this is noticeable even by eye. For temperature -3 keV we should have obtained practically identical 3 pulses. In effect we have three different pulses.

The first hypothesis is that the scattered radiation effect resulted in abrupt DD broadening. The hypothesis can be easily verified: transfer the gamma pulse to the time equal to the time of neutron delay relative to γ quanta on the base of 129 m and superpose this on the neutron pulse: the result of the superposition is given in Fig. 3.

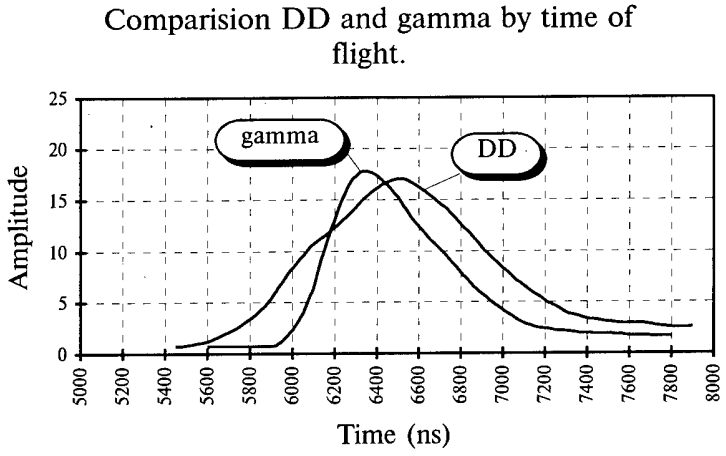

Fig. 3. Result of gamma pulse and DD-pulse superposition in time .

Scattered neutron radiation can only lag behind the primary. So, all the leading pulse elements can not result from scattering. It becomes fairly evident that we are dealing with more energetic ions than it seemed. An attempt to describe the observed DD pulse broadening with temperature dispersion results in the plasma temperature estimate of ~35 keV. This estimate is in good agreement with the measured reaction rate ratio. The ratio 139 approximately corresponds to 30 keV of plasma temperature .

Thus, we are brought as if into the second, descending half of the reaction rate-temperature rate ratio dependence, provided, of course, we try to retain the temperature notion itself. In the described experiment the direction to the detectors was 75 degrees to the chamber axis (almost perpendicular). This direction was not chosen premeditated. The question, that was occur just after first looking to results, is: what will we see along the axis of the chamber? It was the main goal of shot 2.

SHOT ¹2.

Fig. 4 gives the neutron pulse oscillogram in experiment ¹2 recorded by a detector 129 m off, located in the direction along the chamber axis. That time the experiment was made on pure deuterium.

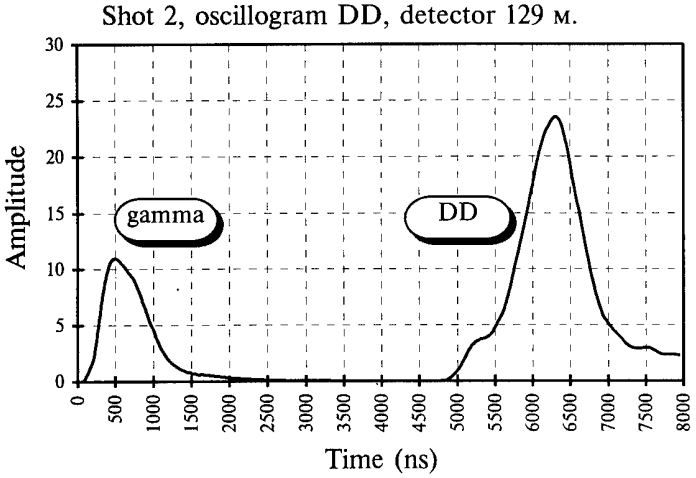

Fig. 4. Oscillogram obtained in the pure deuterium experiment .

The measured results were still more surprising. In Fig. 4 at the neutron pulse front a protruding "nose" of neutrons of considerably higher energy (3 MeV) is clearly seen. The quantitative estimate of the fraction of these neutrons is 10%. The estimate correlates with the 10%- estimate of the number of neutrons generated in the chamber nozzle by the results of neutron source image processing in the DT gas experiments [1]. It would be logical to relate the 3 MeV neutrons with the neutrons generated in the chamber nozzle. To generate a neutron of 3 MeV energy at collision with an immovable deuton, the deuton should be of 170 keV energy or the neutrons should be emitted in flow of material moving at a velocity of $2.3 \cdot 10^8$ cm/s.

Energetic dispersion for the bulk of the neutrons is the same as in the first experiment.

4. INTERPRETATION OF RESULTS

The obtained new results may be treated differently. There is no complete unanimity among the authors of this paper, but as one of possible options, the proposed interpretation of the results is admitted by everybody.

The DD pulse broadening found in the experiments, at first sight, is contradictory to theoretic representations and MHD computations of plasma chamber operation [1] where characteristic temperatures of ion plasma components are several keV. An important fact accounting for this contradiction is that the shock wave where plasma is heated is collislonless (CSW) and ion distribution in hot plasma is not necessarily Maxwellian when ion relaxation times are large (which is the case in our experiments, particularly for the fastest ions) Only for the Maxwellian distribution the distribution of relative ion velocities and the distribution of mass centers of colliding ions are independent, therefore, despite the fact that the principal contribution to the number of DD reactions is made by the most energetic ions, the mass center distribution determining the neutron spectrum broadening depends only on ion temperature. The situation changes if we have an ion spectrum with a larger fraction of fast ions as compared to the Maxwellian distribution. In this case the fastest ions making the main contribution to the DD reaction will also determine the neutron spectrum broadening. At equal mean ion energy the neutron spectrum can be broadened much more than for the Maxwellian spectrum.

Consider our plasma from this standpoint. In paper [3] ion distribution by relative velocities was obtained using numerical simulation for a perpendicular CSW with the Alfven-Mach number M=2.6 which may be considered as representative for CSW in our chamber. This distribution is given in Fig. 5. For comparison the same figure gives distributions by relative velocities for two particles obtained for one-particle Maxwellian distribution

$$\frac{df}{dv} \sim v^2 \exp\left(-\frac{v^2}{v_0^2}\right)$$

and for one-particle ion distribution reducing for high velocities according to the power law

$$\frac{df}{dv} \sim \begin{cases} \dfrac{v^2}{\left(1+\dfrac{v^2}{v_0^2}\right)^2}, & v < v_{max} \\ 0, & v > v_{max} \end{cases} \qquad (1)$$

where $\frac{m_i v_{max}^2}{2} = 2\bar{\varepsilon}$ ($\bar{\varepsilon}$ - mean ion energy equal for all three distributions; at the numerical simulation ion velocities had only two components perpendicular to the magnetic field) Comparison of these curves shows that the ion distribution obtained at the numerical simulation severely differs from the Maxwellian, contains a "tail" of fast ions and is fairly well described using distribution (1)

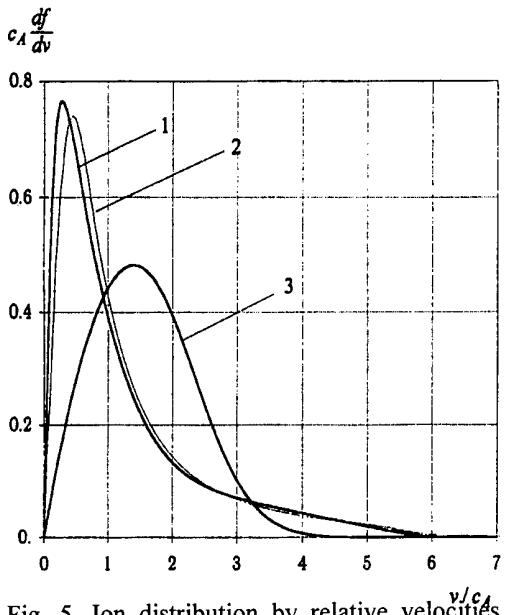

Fig. 5. Ion distribution by relative velocities v behind the front of the perpendicular CSW with the Alfven-Mach number M=2.6 (c_a- Alfven sound speed). 1-distribution obtained in numerical simulation [3], 2 - distribution for power law (1), 3-Maxwellian distribution.

In order to find out if distribution (1) with reasonable temperature values (since distribution (1) is not Maxwellian, by temperature we mean the measure of average energy, i.e. for the velocity distribution isotropic in space $T \equiv 2/3\bar{\varepsilon}$) can lead to the DD pulse broadening observed in the experiments, numerical computations of DD neutron yield at a given ion distribution type were made. In doing so the following effects were taken into consideration: actual dependence of the DD reaction cross section on energy [4], impact on energy of neutrons emitted in various directions, velocities of mass centers of colliding ions and their relative velocities, and device smearing of neutron pulses detector.

As for the "nose" in the second experiment, to account for this, one is forced to assume presence of a small amount of plasma moving along the axis z at a velocity of $-2 \cdot 10^8$ cm/s. We suggested that these neutrons are generated in the nozzle region in plasma flowing at large velocities near the internal electrode-anode (where, according to our calculations, plasma is rarefied and, hence, moves at a high velocity which can also be promoted by the Hall effect [6]) This plasma is heated due to friction on the electrode and/or due to development of turbulence resulting from the Kelvin- Helmholtz instability caused by large velocity difference across the nozzle. Thus, it was believed that some small fraction of neutrons, α, at the forward pulse front is generated in plasma moving at a velocity of u from collision of ions which have isotropically distributed velocities u relative to the plasma with cold ions of the main flow. An explanation for existence of such large plasma flow velocities is not provided in the MHD- computations of plasma chamber operation. One of possible hypotheses which might lead to so large velocities suggests presence of low-density residual deuterium plasma which remains in the first compartment after outflow of the bulk of the plasma and flows after the bulk of the plasma at higher velocities.

Taking into consideration all of the above, we assumed that in both the experiments α=0.06, u=2.2·10^8 cm/s, maximum ion "temperature is 5.5 keV, ion distribution for the main pulse, 1-α==0.94, is described with distribution (1) , and the time history of temperature for both the experiments is shown in Fig.6. (for comparison the figures also present the initial non- broadened neutron distributions vs the times of DD- neutron arrival at the pickups).

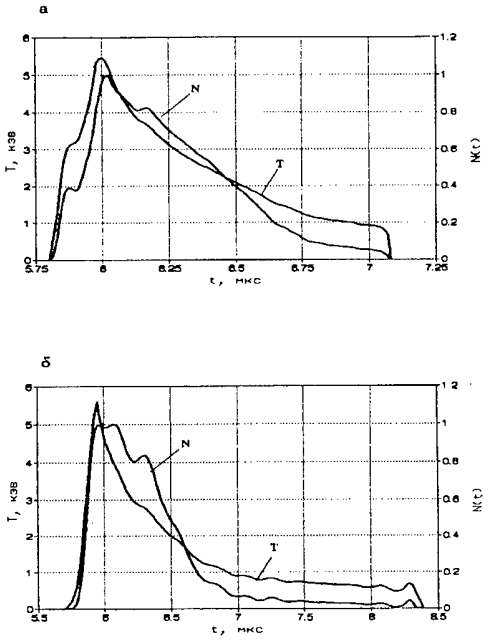

Fig. 6. Ion "temperature" T vs time in experiments No.1(a),No.2(b). Initial non-broadened neutron distributions Ntt vs times of DD-neutron arrival at the pickup are also given.

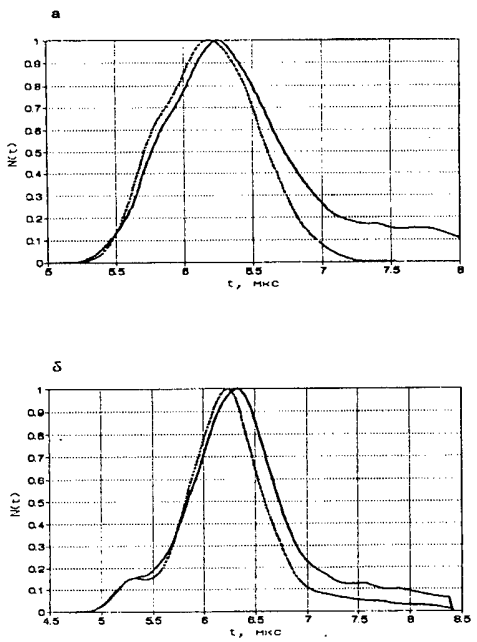

Fig. 7. DD-pulses vs time in the experiments (solid line) and computations (dotted line), (a) experiment No.l, (b) - experiment No.2.

The obtained time dependence of DD-pulses is shown in Fig.7., for comparison the same figures give the experimental curves of DD-pulses. From the figures it is seen that the forward fronts of the obtained pulses are in good agreement with the experiment.

CONCLUSION

Using the time-of-flight technique for the MAGO chamber, even though the generated neutron pulse is of large duration, is still worthwhile on DD and, possibly, on DT. Using this technique proved surprisingly productive. The obtained neutron pulse dispersion was an order of magnitude superior to the expected values. A certain fraction of neutrons of pronounced energy anisotropy was also detected. About 10% of neutrons escaping ahead, along the chamber axis have a considerable excess in energy. Unfortunately, it was yet impossible to verify that the anisotropy fact is not coincidental for the two above-described experiments. To confirm this, an experiment is required with simultaneous measurement of spectra along the chamber axis and in the perpendicular direction.

The obtained results provide a basis for planning special diagnostic experiments on neutron spectra recording with the time-of-flight method. Evident therewith becomes the need of separate study of the nozzle region and the central chamber region In two perpendicular directions. It is possible to separate temporal processes from dispersive only using a great number of detectors on flight bases of 50-300 m.

The measured results for spectra of neutrons generated in DT and DD reactions may be basically explained if one assumes that the ion plasma component produced in a CSW in the MAGO chamber has the non- Maxwellian distribution by velocities at characteristic mean ion energies on the order of several keV.

The obtained results provide information about ion distribution behind the front of the perpendicular CSW with the characteristic Alfven-Mach numbers of M~3.

REFERENCES

1. A.M.Buyko, G.l.Volkov, S.F.Garanin, V.A.Demidov, Yu.N.Dolin, V.V.Zmushko, V.A.Ivanov, V.P.Korchagin, M.V.Lartsev, V.l.Mamyshev, l.V.Morozov, V.N.Mokhov, N.N.Moskvichev, A.P.Mochalov, E.S.Pavlovsky, S.V.Pak, S.V.Trusillo, V.K.Chernyshev, and V.B.Yakubov. "Feasibility study of thermonuclear magnetized plasma generation in magnetic implosion system MAGO", 3d Zababakhln Scientific Readings, Kyshtym, Russia, January 1992. Digest of Technical Papers: Proc. IX IEEE International pulsed Power Conf., edited by K. Prestwich and w. Baker, Institute of Electrical and Electronics Engineers, New York, V. I, pp. 156-162, 1993. DAN, v.344, No.3, p.323-327, 1995.

2. R. Lindemuth, R. E. Reinovsky, R. E. Chrien, J. M. Christian, C. A. Ekdahl, J. H. Goforth, R. C. Haight, G. ldzorek, N. S. King, R. C. Kirkpatrick, R. E. Larson, G. L. Morgan, B. W. Olinger, H. Oona, P. T. Sheehey, J. S. Shlachter, R. C. Smith, L. R. Veeser, B. J. Warthen, S. M. Younger, V. K. Chernyshev, V. N. Mokhov, A. N. Demin, Y. N. Dolin, S. F. Garanin, V. A. Ivanov, S. V. Pak, E. S. Pavlovskii, N. Y. Seleznev, A. N. Skobelev, G. I. Volkov and V. B. Yakubov, "Target plasma formation for Magnetic Compression/Magnetized Target Fusion (MAGO/MTF)", Phys. Rev. Lett.. V. 75, No. 10, p. 1953, 1995.

3. S.F.Garanin and A.l.Golubev. "Study of transverse shock waves in collisionless magnetized plasma", VANT. Ser.Teor.i Prikl.Fizika, No.l, p.18-25, 1985.

4.B.N.Kozlov, "Thermonuclear reaction rates", Atomnaya Energiya.v.12, p.238-240, 1962.

5. H. Yoon, "Quasilinear evolution of Alfven-ion-cyclotron and mirror instabilities driven by ion temperature anisotropy", Phys. Fluids B, V. 4, No. 11, pp. 3627- 3637, 1992.

6. S. F. Garanin and V. I. Mamyshev, "Detaching near-anode flows of magnetized plasma", Fizika Plazmy, v.16, p.1218-1225, 1990.

FOUCUSED PROTON BEAMS PROPAGATING IN REACTOR OF FUSION POWER PLANT

K. Niu
Teikyo Heisei University, Uruido, Ichihara, Chiba 290-01, Japan

One of the difficulties of light ion beam fusion is to propagate the beam in the reactor cavity and to focus the beam on the target. The light ion beam has some local divergence angle because there are several causes for divergence at the diode. The electrostatic force induced at the leading edge causes the beam divergence during propagation. To confine the beam in a small radius during propagation, the magnetic field must play a role. Here electron beam is proposed to be launched simultaneously with the launch of proton beam. If the electron beam has the excess current, the beam induces the magnetic field in the negative azimuthal direction, which confines the ion beam in a small radius by the electrostatic field as well as the electron beam by the Lorentz force. The metal guide around the beam path helps the beam confinement, and reduces the total amount of magnetic field energy induced by the electron current.

1. INTRODUCTION

PBFA-II in Sandia National Laboratory has started to be used for the experiment of beam-target interaction[1,2].

Here proton beam is chosen as energy driver[3]. The optimum particle energy of a proton for ICF is 4MeV[4]. In order to launch a large amount of beam energy such as 12MJ to the target, the beam current becomes strong, and the local divergence angle remains not small. Sandia shows that the limiter set in the diode decreases the electron current along the cathode surface of the diode, which suppresses an instability in the diode and reduces the local divergence angle of the lithium beam[5]. Even with the smaller emittance of the beam, however, it is difficult to launch the beam for several meters in the reactor cavity from the diode to the target with the ballistic way. It seems to be inevitable to utilize magnetic field in order to propagate LIB confined in a small radius.

General talks including research history were given for transport and focusing of LIB6, 7). NRL tried to propagate proton beam in a plasma channel[8]. A strong current flowed in the plasma channel. Thus the channel had the strong magnetic field in the azimuthal direction in order to confine the proton beam in the plasma channel.

Sandia and NRL tried to propagate light ion beam around a wire, in which a current flowed to produce a magnetic field in the azimuthal direction[9].

The group of University of California Irvine investigated theoretically the plasmoid which can propagate across magnetic fields in vacuum and maintain both charge and current neutrality[10,11], Other work on collective focussing was reported[12]. and experimentally verified[13].

The ion charge at the leading edge produces the electrostatic field, causing the beam divergence[14].

It seems to be only one way in order to delete the ion charge at the leading edge of propagating beam is the simultaneous launching of electron beam with the launching of ion beam. The number density of electron beam is equal to that of ion beam, and the speed of electron beam exceeds a little that of ion beam. Then the ion charge at the leading edge always is neutralized by the electrons launched simultaneously. The excess electron current induces not only the magnetic field in the negative azimuthal direction but also the electrostatic field in the negative radial direction. The Lorentz force by the excess electron current and negative azimuthal magnetic field confines the propagating electron beam in a small radius. The pinched electron beam induces the negative radial electric field which confines the ion beam in a small radius, too.

2. PROPAGATION OF PROTON BEAM WITH ELECTRON BEAM

A proton beam is extracted form a diode. In order to delete the proton charge at the leading edge of the beam, and to obtain the electric current which induces the azimuthal magnetic field to confine the beam in a small radius by the Lorentz force, the electron beam is extracted simultaneously from a triode. The speed of electron beam must exceed that of proton beam, too, to produce a net negative current.

Inside the reactor cavity, the radius of the metal guide is 6mm. The beam combined with proton and electron is confined in a radius of r_b = 5mm. The proton beam current is I_p = 16.6MA and its mean propagation velocity is 2.768×10^7m/s. The mean number density is $n_p = 4.766 \times 10^{17}\mathrm{m}^{-3}$. The number density of electron beam is equal to that of proton, ie $n_e = 4.766 \times 10^{17}\mathrm{m}^{-3}$, and the charge neutrality of combined beam retains. The excess electron are scattered out to the metal guide. Because the electron beam launched from the triode has a little faster propagation velocity $v_e = 2.851 \times 10^7$ m/s, the electron beam current is $I_e = -17.1$MA. This excess electron current -500kA of the combined beam produces the azimuthal magnetic field $B_\theta = -20$T at r = 5mm and -10T at r = 2.5mm. This magnetic field in the azimuthal direction confines the propagating combined beam in a radius of 5mm. The electron plasma frequency of the combined beam is $\omega_e = 3.894 \times 10^{10}$rad/s. On the other hand, the mean cyclotron frequency of electron is $\omega_{ce} = 1.76 \times 10^{11}$rad/s, and of proton is $\omega_{cp} = 0.96 \times 10^8$rad/s. The mean gyroradius of electron is $\rho_{re} = 1.621 \times 10^{-6}$m, and of proton is $\rho_{rp} = 2.891 \times 10^{-3}$ m. When the beam propagates across the atimuthal magnetic field, the radial electric field is induced. In our case, the mean intensity of the radial electric field is $E_r = 2.771 \times 10^8$V/m. The energy of these atimuthal magnetic field and the radial electric field is supplied by the kinetic energy of electron beam. The metal guide restricts the space volume of these induced fields. The small volume inside the metal guide limits the reduction in the electron propagation velocity.

The electrons have the much smaller gyroradius in comparison with the beam radius except the neighborhood of axis where no magnetic field exists. Thus the majority of electrons propagates with the drift velocity $v_e = E_r/B_\theta = 2.851 \times 10^7$m/s. The protons have the comparable gyroradius with the beam radius. The gyroradius of a proton changes its radial position. According to this, the proton propagation velocity does not follow the drift velocity across the magnetic field and protons are retarded after electrons. In such a way, the net current -500kA due to the excess electron propagation velocity maintains in the combined beam.

At the leading edge of the beam, electrons become dominant along the axis whose distance is $d_{zr} = 1 \times 10^{-6}$m, because of their excess velocity. The mean electron number density there is $n_{er} = 1 \times 10^{22}\mathrm{m}^{-3}$. They produce the electric field E_z in the negative axial direction and E_r in the negative axial direction. The order of magnitude of these electric fields are $E_z = E_r = -2 \times 10^6$V/m. By the action of B_θ and E_z, electrons drift with the velocity of $v_{mr} = 2 \times 10^5$m/s to the outward radial direction at the leading edge of the beam. At last, electrons are absorbed in the metal guide.

It is clear that our combined beam just forms the z-pinch plasma, if we observe this phenomenon in the moving flame with the proton propagation velocity. Surely the combined beam pinches to a small radius, provided that no instability occurs.

3. SIMULATION

The governing equations in order to numerically simulate the motions of propagating ions and electrons are the Maxwell equations for the scaler potential ϕ and vector potential $\mathbf{A}$,

$$\phi_j(\mathbf{r}_j, t) = \frac{1}{4\pi\epsilon} \sum_i \frac{Q_i(\mathbf{r}_i, t)}{|\,\mathbf{r}_j - \mathbf{r}_i\,|} \qquad (1) \qquad \mathbf{A}_j(\mathbf{r}_j, t) = \frac{\mu}{4\pi} \sum_i \frac{Q_i \mathbf{v}_i(\mathbf{r}_i, t)}{|\,\mathbf{r}_j - \mathbf{r}_i\,|} \qquad (2)$$

The relations between electromagnetic fields and potentials are

$$\mathbf{E}_j(\mathbf{r}_j, t) = -\frac{\partial \mathbf{A}_j(\mathbf{r}_j, t)}{\partial t} - \nabla_j \phi_j(\mathbf{r}_j, t) \qquad (3)$$

$$\mathbf{B}_j(\mathbf{r}_j, t) = \nabla_j \times \mathbf{A}_j(\mathbf{r}_j, t) \qquad (4)$$

In these equations, $\mathbf{r}$ is the space vector, t the time, μ the magnetic permeability in the vacuum, Q the charge, $\mathbf{v}$ the velocity vector, ϵ the dielectric constant in the vacuum, $\mathbf{E}$ the electric field and $\mathbf{B}$ the magnetic flux density. The suffix i indicates the particle (ion or electron) number. In these equations, retarded effect on potentials is not taken into account. The equation of motion for ion or electron is

$$m_j \frac{d^2\mathbf{r}_j}{dt^2} = Q_j(\mathbf{E}_j + \mathbf{v}_j \times \mathbf{B}_j) \tag{5}$$

where m is the particle mass.

Equation (5) for an ion which is summed up by that for an electron gives

$$M_j \frac{d^2\mathbf{R}_j}{dt^2} = \mathbf{J}_j \times \mathbf{B}_j \tag{5'}$$

where the pair particles M_j, the velocity $\mathbf{V}_j$of pair particles, and the current $\mathbf{J}j$ of pair particles are defined by

$$M_j = m_{ij} + m_{ej} \quad (6) \quad R_j = \frac{m_{ij}r_{ij} + m_{ej}r_{ej}}{M_j} \quad (7) \quad \mathbf{J}_j = Q_j(\mathbf{v}_{ij} - \mathbf{v}_{ej}) \quad (8)$$

In eq. (5'), the dependent variables are $\mathbf{R}_j$ and $\mathbf{J}_j$ in stead of $\mathbf{v}_{ij}$ and $\mathbf{v}_{ej}$ in eq. (5). Because $m_{ij} >> m_{ej}$, $\mathbf{v}_{ij}$ in eq. (8) is substituted by $\mathbf{V}_j = d\mathbf{R}_j/dt$. To stabilize numerical results, it is required to delete the unreal electron thermal velocity occurring by the too strong interactions between super particles which have too large charges. Even with a large thermal velocity, electron Larmor radii is very small in comparison with the beam radius ($r_b = 5$ mm), except the neighborhood of axis. Therefore the electron velocity $\mathbf{v}_{ej}$ in eq. (8) is approximated by the drift velocity $\mathbf{v}_{ej} = \mathbf{E}_j \times \mathbf{B}_j/B_j^2$, except the neighborhood of axis where electron velocity $\mathbf{v}_{ej}$ is constant. Thus eq. (8) reduces to

$$\mathbf{J}_j = Q_j(\mathbf{V}_j - \frac{\mathbf{E}_j \times \mathbf{B}_j}{B_j^2}) \tag{8'}$$

The electric field $\mathbf{E}_j$ is derived to

$$\mathbf{E}_j = \frac{1}{Q_j}(\int \nabla_j \times \frac{\mathbf{B}_j}{\mu} dV) \times \mathbf{B}_j - \mathbf{V}_j \times \mathbf{B}_j \tag{9}$$

Of course, the electric field $\mathbf{E}_j$ derived by eq. (9) includes the electrostatic component. In this system of equations, the scaler potential ϕ does not appear explicitly, which makes simulation simple.

The axial magnetic field will stabilizes the beam propagation[15], as the Tokamak plasma is stabilized by the toroidal field. The axial magnetic field can be applied by the electron azimuthal current. The beam propagations obtained by simulations are given in Figs.1—2.

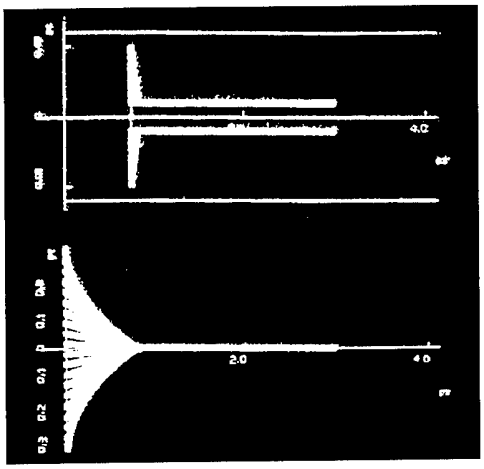

Fig.1. Ion pathes.

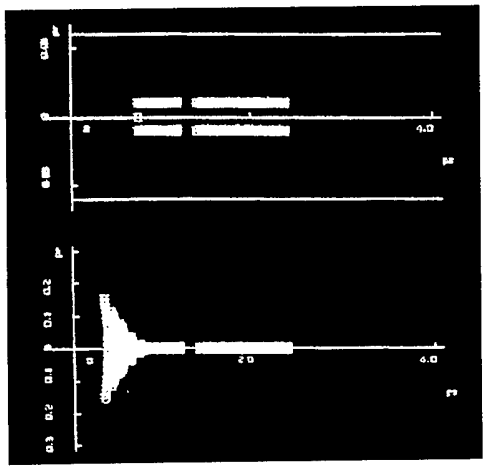

Fig.2. Ion positions.

These two types of simulation indicate that proton beam with the excess electron current is confined in the metal guide and can propagate to the target without contact with the wall of metal guide.

4. DISCUSSION

Here a super particle is assumed to occupy)Equation (9) for $\mathbf{E}_j$ comes from Notwithstanding these difficulties, simulations show that the charge-neutral beam which consists of proton and electron with an excess electron current confines the propagating beam in the metal guide. The electron net current induces the azimuthal magnetic field, whose intensity is stronger with the increasing radius in the metal guide. This azimuthal magnetic field confine the beam electrons well in a small radius. The pinched electrons produces the electric field in the negative radial direction, which confines the beam ions in the metal guide.

When the electron has a small velocity component in the azimuthal direction around the axis, this negative azimuthal current induces an axial magnetic field, which is stronger with the smaller radius in the metal guide. The axial magnetic field similar to the toroidal field in Tokamak is expected to stabilizes the particle propagation.

The number density of the background plasma in the metal guide should be small. Otherwise, electrons in the background plasma cancels out the excess electron current in the beam. The number density of the background plasma in the metal guide must be less than 10^{21} particles per cubic meter, because the beam number density is 5×10^{22} particles per cubic meter.

When the trailing edge of the proton beam is on the diode surface, the triode can supply the excess electron current to the beam. How is the excess electron current supplied after the trailing edge of the proton beam leaves the diode surface? The energetic electrons cannot be transported in the vacuum between the triode and the trailing edge of the proton beam. One idea to solve this problem is to elongate the pulse width of proton beam, although the useless excess energy of proton beam is required.

REFERENCES

1) Mehlhorn, T. A. 1993 Laser Interaction and Related Plasma Phenomena **10**, 553.
2) Cook, D. L. 1993 Book of Abstracts; International Symposium on Heavy Ion Inertial Fusion 68.
3) Niu, K. 1994 Laser Part. Beams **12** 85.
4) Niu, K. 1993 Laser Part. Beams **11** 97.
5) Quintenz, J. P. et al. 1992 Proceedings of the IAEA Technical Committee Meeting on Drivers for Inertial Confinement Fusion (Osaka), 67.
6) Ottinger, P. F. et al. 1992 Proceedings of 9th International Conference on High-Power Particle Beams (Washington,DC) Vol. **1**, 60.
7) Olson, C. L. et al. 1994 Book of Abstracts on Beams' 94, 3-1.
8) Ottinger, P. F. Goldstein S. A. & Mosher, D. 1982 NRL Memorandom Report 4989.
9) Watrous, J. J. et al. 1991 J. Appl. Phys. **69** 639.
10) Peter, W. & Rostoker, N. 1982 Phys. Fluids **25** 730.
11) Wessel, F. J. et al. 1990 Phys. Fluid **B2**, 1467.
12) Robertson, S. 1983 Phys. Fluids **26** 1129.
13) Kraft, R., Kusse, B. & Moschella, J. 1986 Phys. Fluids 245.
14) Niu, K. Mulser, P. & Drska, L. 1991 Laser & Part. Beams **9**, 149.
15) Aoki, T. & Niu, K. 1988 Laser & Part. Beams **6** 737.
Fusion (Frascati), 68.

ENERGY LOSS OF HEAVY ION BEAMS IN PLASMA

T.Okada and T.Hotta

Faculty of Technology, Tokyo University of Agriculture and Technology, 2-24-16 Naka-machi, Koganei-shi, Tokyo 184, Japan

Abstract

The energy loss of heavy-ion beams (HIB) is studied by means of Vlasov theory and Particle-in-Cell (PIC) simulations in a plasma. The interaction of HIB with a plasma is of central importance for inertial confinemant fusion (ICF). A number of studies on the HIB interaction with target plasma are found in the literature [1-4]. It is important for heavy-ion stopping that the effects of the non-linear interaction of HIB within the Vlasov theory are included. Reported are results of a numerical study of nonlinear effects to the stopping power for HIB in plasma. It is shown that the PIC simulations of collective effects of stopping power are good agreement of the Vlasov theory.

Introduction

The energy loss of HIB is usually studied within the linear and nonlinear theory of collisions. On the other hand, there exists some waves in a plasma. Therefore, interest arises in studying the influence of waves in the stopping power of the target plasma. In this paper we present results on the study of the collective phenomena in HIB and plasma interaction.

The projectile energy loss due to cillisions is obtained by performing the average, using the known velocity distribution and integrating over the impact parameter for the collisions [5]:

$$\frac{dE}{dx} = -\frac{4\pi Z^2 e^4 V_p^2}{3k_B T} \int dv_e \frac{f(v_e)}{v_e} \int \frac{bdb}{b^2 + (Ze^2/mv_e^2)^2} \tag{1}$$

$$f(v_e) = n\left(\frac{m}{2\pi k_B T}\right)^{3/2} exp\left(-\frac{mv_e^2}{2\pi k_B T}\right) \tag{2}$$

where k_B is the Bolzmann constant, V_p is ion beam velocity, v_e is plasma electron velocity and T is temperature.

In the limit $V_p \ll v_{th}$, the stopping power:

$$\frac{dE}{dx} = -\frac{16\pi^{1/2} n Z^2 e^4 m^{1/2} V_p}{3(2k_B T)^{3/2}} \int \frac{db}{b} \tag{3}$$

which is the energy loss per unit of tragectory length in the plasma. One can cut off the impact parameter at some value b_{min}, which is:

$$b_{min} \cong \frac{Ze^2}{2k_BT} \tag{4}$$

One can introduce another cut off at a maximum impact parameter b_{max}:

$$b_{max} \approx \frac{v_{th}}{\omega_p} \tag{5}$$

where ω_p is the plasma frequency:

$$\omega_p = (4\pi ne^2/m)^{1/2} \tag{6}$$

Inserting Equations (5) and (6) as the lower and upper limits of the integration in Equation (3), we get

$$\frac{dE}{dx} = -\frac{16\pi^{1/2}nZ^2e^4m^{1/2}V_p}{3(2k_BT)^{3/2}} ln\Lambda \tag{7}$$

$$ln\Lambda = ln\frac{b_{max}}{b_{min}} = ln\frac{v_{th}/\omega}{Ze^2/2k_BT} \tag{8}$$

$ln\Lambda$ is the Coulomb logarithm of the collisions.

We next examine the opposite extreme limit, $V_p \gg v_{th}$. The energy loss of the ion in a Coulomb collision characterized by an impact parameter b is then:

$$\Delta E(b) = \frac{2Z^2e^4}{mv^2} \frac{1}{b^2 + (Ze^2/mv^2)^2} \tag{9}$$

Integrating Equation over all impact parameters yields:

$$\frac{dE}{dx} = \frac{2\pi nZ^2e^4}{mV_p^2} ln\left(1 + \left(\frac{mV_p^2 b_{max}}{Ze^2}\right)^2\right) \tag{10}$$

There are two contributions to the stopping of the projectile. At distances smaller than the Debye length, energy is transfered by Coulomb collisions with the electrons, we have:

$$b_{min} = \frac{Ze^2}{mV_p^2} \quad : \quad b_{max} \approx \frac{v_{th}}{\omega_p} \tag{11}$$

$$\left(\frac{dE}{dx}\right)_{collisions} = -\frac{4\pi nZ^2e^4}{mV_p^2} ln\frac{v_{th}/\omega_p}{Ze^2/mV_p^2} \tag{12}$$

To this we have to add the energy loss due to the force exerted on the projectile by the field. This was found by Pines and Bohm to be approximately

$$\left(\frac{dE}{dx}\right)_{collective} \cong -\frac{2\pi nZe^4}{mV_p^2} ln\left(1 + \frac{2V_p^2}{< v_{th}^2 >}\right) \tag{13}$$

PIC simulation

In order to simulate the energy loss of HIB, we perform a numerical calculation using PIC code for the beam-plasma system. The code is two-dimensional in space and velocity, respectively.

The distribution of the projectile and plasma particle is determined by the Vlasov-Maxwell equations:

$$\begin{aligned} \nabla \times \mathbf{E}(\mathbf{x},t) &= -\tfrac{\partial}{\partial t}\mathbf{B}(\mathbf{x},t) \\ \nabla \times \mathbf{E}(\mathbf{x},t) &= \mu_0(\varepsilon_0 \tfrac{\partial}{\partial t}\mathbf{E}(\mathbf{x},t) + \mathbf{j}(\mathbf{x},t)) \\ \varepsilon_0 \nabla \cdot \mathbf{E}(\mathbf{x},t) &= \rho(\mathbf{x},t) \\ \nabla \cdot \mathbf{B}(\mathbf{x},t) &= 0 \end{aligned} \tag{14}$$

The normalization units are shown in table 1, and the initial conditions are shown in table 2.

Table 1: Normalization units

space	c/ω_p	charge	q
velocity	c	current	$4\pi n_0 qc$
time	ω_p^{-1}	electric field	$(4\pi n_0 m_e c^2)^{1/2}$
dencity	n_0	magnetic field	$(4\pi n_0 m_e c^2)^{1/2}$
mass	m_e	energy	$n_0(c/\omega_p)^2 mc^2/2$

Table 2: Initial condisions

heavy-ion beam		*target*	
species	Bi	speces	Li
atomic number	83	atomic number	3
continue time	10 [ns]	plasma density	1.0×10^{22}[piece/cm^3]
beam density	3.0×10^{15}[piece/cm^3]	plasma temperature	1000 [eV]
energy of one particle	30 [MeV]	lengh of one range	3.0×10^{-7}[cm]

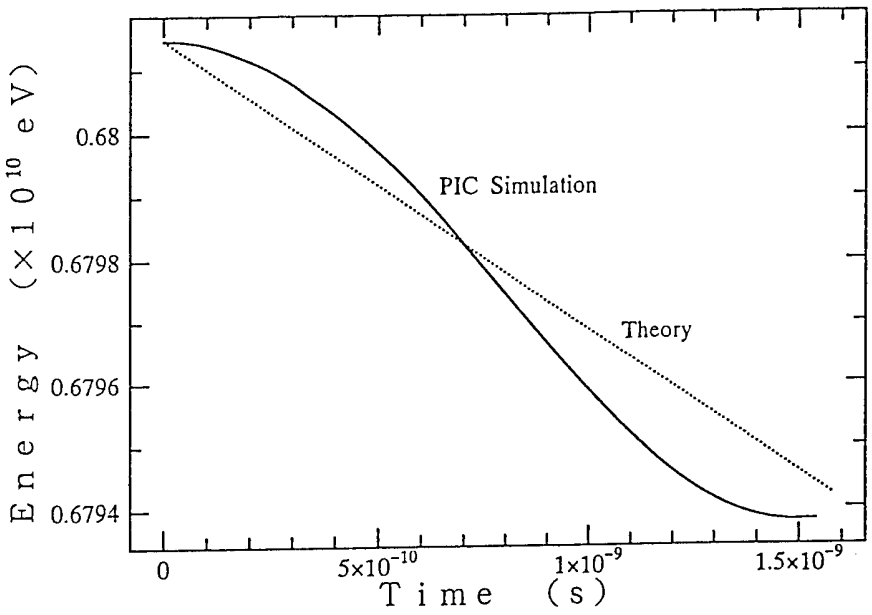

Fig. 1 Beam kinetic energy versus time

Conclusion

The theory of HIB stopping power in plasma is developed on the basis of the Vlasov-Maxwell equations. In the interaction of HIB with a plasma, there exists some waves in a heated plasma. The stopping power is expressed in the collision dominant part and collective part.

It is shown that the PIC simulation of collective effects of stopping power are good agreement of the Vlasov theory.

[1] Nardi.E, Peleg.E and Zinamon.Z : Phy. Fluids 21 (1978) 574.
[2] Nardi.E, Zinamon.Z : Phys. Rev. Lett. 49 (1982) 1251.
[3] Peter.Th and Meyer-ter-Vehn.J : Phys. Rev. A43 (1991) 1998.
[4] Peter.Th and Meyer-ter-Vehn.J : Phys. Rev. A43 (1991) 2015.
[5] Zinamon.Z : Nuclear Fusion by Inertial Confinement Chap.5 (1993) 119.

STABLE PROPAGATION OF LIGHT-ION BEAM IN INERTIAL CONFINEMENT FUSION

T.Okada and H.Murakami

Faculty of Technology, Tokyo University of Agriculture and Technology, 2-24-16 Naka-machi, Koganei-shi, Tokyo 184, Japan

Abstract

The stabilization mechanism of the filamentation instability for a light ion beam (LIB) penetrating plasma is investigated. For the stabilization of the filamentation instability, an external magnetic field which is parallel to the direction of the light ion beam propagation is applied. From a dispersion relation, linear growth rates of filamentation instabilities are obtained in a light ion beam-plasma system with an external magnetic field. Numerical simulations are carried out using a particle-in-cell (PIC) method. The stabilizing mechanism of the filamentation instability is described. The theory and simulation comparisons illustrate the results.

Introduction

In the investigation of the inertial confinement fusion by LIB[1-3], it is the central problem to propagate the beam stably through the plasma. There are many investigations of numerous instabilities in relativistic electron beam, heavy ion beam and light ion beam propagations[3,4]. Filamentation instability[5] is one of the instabilities which is deleterious in the stable propagation of the beam through the plasma. Recently, the application of the external magnetic field, which is induced by the rotating light ion beams[6] or generated by using an intense laser beam[7], has been proposed for stable propagation of the beam. In this paper, we report on numerical studies of the stabilization of filamentation instability in a light ion beam-plasma system with an external magnetic field which is parallel to the direction of the light ion beam propagation. We only consider the model of spatially infinite collisionless, charge, and current neutral system with light ion beam propagation velocity $\boldsymbol{V}_{zb}$ and background plasma at $\boldsymbol{V}_{zs}$ of species $s = e$ (plasma electrons) or i (plasma ions) along $\boldsymbol{B}_0^z$ which is an external magnetic field in the z-direction. We only consider electromagnetic modes with wavenumber $\boldsymbol{k}_\perp$ normal to $\boldsymbol{V}_{zb}$, induced electric fields $\delta\boldsymbol{E}$ parallel to $\boldsymbol{V}_{zb}$ and induced magnetic fields $\delta\boldsymbol{B}$ normal to both $\boldsymbol{V}_{zb}$ and $\delta\boldsymbol{E}$.

The Dispersion Relation for the Filamentation Instability

The dispersion relation for the filamentation instability has been investigated for a beam-plasma system with external magnetic field. For a monoenergetic beam with Maxwellian thermal spread v_{Tb} of transverse velocities, and a background plasma with a Maxwellian thermal spread v_{Ts} (s=e,i), assuming that the ion beam density n_b is smaller than the background electron density n_e, the relativistic linear dispersion relation for the filamentation instability is given by[8,9]

$$\omega^2 = c^2 k_\perp^2 + \sum_{j=b,e,i} \omega_{pj}^2 + \sum_{j=b,e,i} \omega_{pj}^2 \frac{\beta_j^2 c^2 k_\perp^2}{(\omega - l\omega_{rj})^2 - (\Omega_{rj}^+ - \Omega_{rj}^-)^2} \tag{1}$$

where

$$\omega_{rj} = -\frac{\varepsilon_j \omega_{cj}}{2} \left(1 - \left(1 + \frac{2\omega_{pj}^2}{\omega_{cj}^2} \beta_j^2 (1 - f_m) \right)^{1/2} \right), \tag{2}$$

$$(\Omega_{rj}^+ - \Omega_{rj}^-)^2 = \omega_{cj}^2 \left(1 + \frac{2\omega_{pj}^2}{\omega_{cj}^2} \beta_j^2 (1 - f_m) \right), \tag{3}$$

$$f_m = -(\sum_{k=e,i} n_k e_k \beta_k)/(n_b e_b \beta_b), \quad \omega_{pj}^2 = \frac{4\pi n_j e_j^2}{m_j}. \tag{4}$$

In equations (1),(2),(3) and (4), l is the azimuthal harmonic number, m_j the mass, $\varepsilon_j = \mathrm{sgn}(e_j)$, $\omega_{cj} = |e_j| B_0^z / m_j c$, $\beta_j c = V_{zj}$ and f_m is the fractional current neutralization by the background plasma for a charge neutralized system. From equation (1), we expect that the maximum growth rate of the filamentation instability is stabilized by the external magnetic field and the beams can propagate without triggerring the filamentation instability or with having sufficiently slow filamentation growth.

PIC Simulations

In order to simulate a filamentation instability, we perform a numerical calculation using an electromagnetic particle in-cell code[10] for the beam-plasma system. The code is two-dimensional in space and velocity, respectively. The external magnetic field B_0^z is in the z-direction and the induced electric and magnetic fields are respectively indicated by $E = (0, 0, E_z)$ and $B = (B_x, B_y, 0)$. The simulation is performed under the conditions that the grid spacing is $0.2c/\omega_{pe}$, the time step is $0.1\omega_{pe}^{-1}$, the length of simulation range is $3.2c/\omega_{pe}$, the number of ion beam simulation particles is 2500, the number of plasma electron simulation particles is 7500, and the number of plasma ion simulation particles is 5000. We choose the following parameters (ensuring current neutrality); $v_{Tb} = \sqrt{T_b/m_b} = 0.001c$, $v_{Tj} = \sqrt{T_j/m_j} = 0.01c$ $(j = e, i)$, $V_{zb} = 0.1c$, $V_{ze} = 1/30c$ and $V_{zi} = 0$. As periodic boundary conditions are used at the ends of the simulation region, the results do not depend on the choice of the simulation range which is small in comparison with the

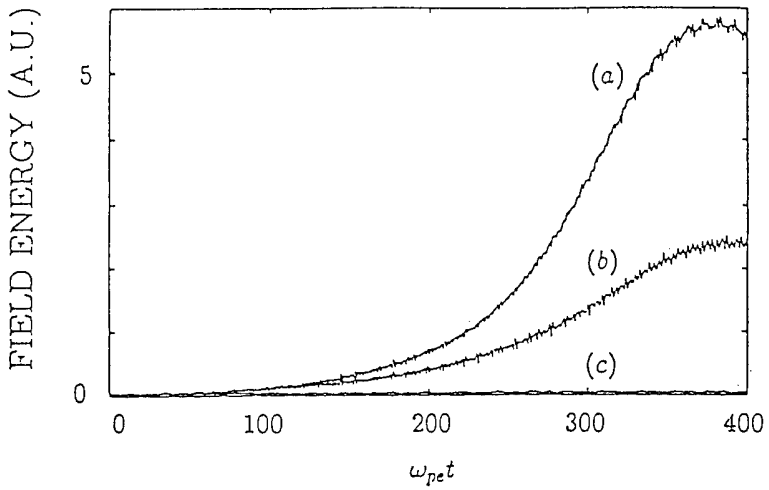

Fig. 1. Energies of induced magnetic fields at the linear stage with (a) $B_0^z/(4\pi n_e m_e c^2)^{1/2}$ =0, (b) $B_0^z/(4\pi n_e m_e c^2)^{1/2}$ =0.02 and (c) $B_0^z/(4\pi n_e m_e c^2)^{1/2}$ =0.2.

Table 1. Maximum growth rates of the filamentation instability γ_S are the maximum growth rates by using PIC code and γ_t are these by the theory.

$B_0^z(\sqrt{4\pi n_0 m_e c^2})$	$\gamma_s(\omega_{pe})$	$\gamma_t(\omega_{pe})$
0.00	7.07×10^{-3}	2.041×10^{-3}
0.01	6.99×10^{-3}	1.910×10^{-3}
0.02	5.60×10^{-3}	1.127×10^{-3}
0.03	1.67×10^{-3}	0.000
0.04	1.67×10^{-3}	0.000
0.05	1.43×10^{-3}	0.000
0.06	1.06×10^{-3}	0.000
0.07	1.06×10^{-3}	0.000
0.08	3.34×10^{-4}	0.000
0.09	3.61×10^{-4}	0.000
0.10	2.13×10^{-4}	0.000

beam radius. The wavelength of the most unstable mode in the simulations and from the analytic theory is smaller than the beam radius.

Induced magnetic fields for $B_0^z/(4\pi n_e m_e c^2)^{1/2}$ =0, 0.02 and 0.2 at the early stage are plotted in Fig.1. In Table 1, the maximum growth rates γ_S, which are obtained by using the PIC code, and γ_t, which are obtained from equation (1), are shown at the external magnetic field B_0^z. The maximum growth rates from the simulations are about $2 \sim 3$ times more than these from the theory in Table 1. There is a discrepancy between the growth rates in the theory and simulations because the theory is in cylindrical symmetric coordinates and simulation is in cartesian coordinates, as well as the current neutralization is not complete in the simulations. If we take the effect of fractional current neutralization into account, the growth rate in the theory start decrease[8] and the theory will be consistent with the simulations. From these results, the filamentation instability is stabilized by the external magnetic fields. If we assume the magnetic field is a result from the beam rotation, we must treat the beam as rotating and investigate the focusing of the rotating beam. The three dimensional PIC simulations including the effects of the beam rotation will be reported in a future work.

Conclusion

We will discuss the results for an expected experiment, i.e. for a typical beam of 5MeV (V_b=0.1c) protons,well-pinched ion current of 0.5MA ($n_b = 10^{15} cm^{-3}$) and 40nsec beam duration τ. If we apply an external magnetic field B_0^z=$0.2\sqrt{4\pi n_e m_e c^2} \approx$ 3.5tesla (n_e=$3\times10^{15} cm^{-3}$) to the beam-plasma system, the maximum growth rates of the filamentation instability become γ_S=$8.0\times10^{-6}\omega_{pe} \approx 2.5 \times 10^7 sec^{-1}$. The largest growth will appear at the tailend of the beam, we estimate the effect at the tailend to be the value of $\gamma_S\tau$. Consequently, the beams can propagate stably through the plasma by the external magnetic fields with a small growth rate since $\gamma_S\tau$=0.98 which is small e-foldings. Consequently, the filamentation instability may be stabilized by the external magnetic field.

[1] J.P.VanDevender and D.L.Cook : Science **232** (1986) 831.

[2] D.L.Cook : Bull. of American Phys. Soc. **36** (1991) 2480.

[3] P.F.Ottinger, D.Mosher and S.A.Goldstein : Phys. of Fluids **24** (1981) 164.

[4] T.Okada and W.Schmidt : J. Plasma Physics **37** (1987) 373.

[5] C.L.Olson : (private communication).

[6] K.Niu : Laser and Particle Beams **12** (1994) 85.

[7] W.Bauer, W.Höbel, A.Ludmirsky, E.Stein and T.Westermann : "A Contribution to the Magnetic Focusing in an Applied-B-Extractor Ion Diode by a Laser Pulse Driven Solenoid" *in Proceeding of the Conference on 10th Int. Conf. on High Power Particle Beams* 1 (1994) 83.

[8] T.Okada and K.Niu : Laser and Particle Beams **6** (1988) 699.

[9] R.C.Davidson : *Basic Plasma Physics* **2**, Amsterdam, North-Holland Publishing, edited by A.A.Galeev and R.N.Sudan, ch.9 (1984) 789.

[10] R.L.Morse : *Method of Computational Physics* **9**, New York, Academic Press (1970) 213.

THE INTERACTION PHYSICS OF THE FAST IGNITOR CONCEPT

C. Deutsch* , H. Furukawa, K. Mima, M. Murakami and K. Nishihara

Institute for Laser Engineering, Osaka University, Suita 565,

OSAKA, Japan

Since its inception [1] in 1994, the so-called Fast Ignitor Scenario (FIS) proposed to ease the indirect drive approach to inertial confinement fusion [2] of hollow pellet containing the thermonuclear fuel deuterium + tritium (DT) has been the object of many intensive investigations.

Most of them, conducted through numerical simulations [3-5], have already addressed basic issues concerning the capability of ultrafast lasers with irradiance $I \geq I_{18} \equiv \frac{10^{18}}{cm^2}$, to bore a channel in the corona of the precompressed target fuel. The latter is expected to be prepared through powerful lasers [2] or intense heavy ion beams [6] suitably synchronized. This novel and time segmented scenario [1], has to be appreciated as the latest sophistication elaborating upon the already overexploited disparity between the cheap compression cost ($\sim n^{2/3} \sim 1.1 \times 10^7$ J/g) of strongly degenerate Fermi electrons and the high toll requested for plasma heating ($\sim 6 \times 10^8$ J/g).

Our main concern in the present work is the efficiency of the relativistic electron beams (REB) in the MeV energy produced by the ultrafast lasers currently under development [7]. More specifically, we intend to critically investigate the REB capabilities to igniting hot spots well localized within the overall supercompressed DT.

---

* Permanent address: LPGP (URA 073 CNRS), Bât. 212, Université Paris XI, 91405 ORSAY, France

Following recent numerical simulations [3-5], we take it for granted that the REB propagation may be approximated in a cylindrical geometry on an acceleration distance ~ 200 μm through a very steep density gradient [8]. Nonetheless, we shall work our model in a homogeneous approximation with a fixed beam density n_b and a target plasma density n_p.

FIS prescriptions [1] recommend a 3 kJ REB energy at 1 MeV for hot spot ignition. This amounts to a current ~ 3×10^8 Amp. Considering a compressed core radius $\sigma \cong 50\mu m$ a plausible channel radius $a = \frac{\sigma}{4}$ yields an average beam density $n_b \sim 1.3\times10^{22}$ e-cm^{-3}. It should also be noticed that a 300 g/cc DT core at the usual 5 keV temperature [2] appears as a fully ionized and weakly couplet ($\Lambda \sim 5\times10^{-3}$) hydrogenic plasma with $n_p \sim 10^{26}$ e-cm^{-3}.

The ratio $\frac{n_b}{n_p} \leq 10^{-4}$ demonstrates that in spite of its huge current the REB should be taken dilute in the overcompressed target with a mean electron interdistance larger by a good order of magnitude compared to that in the target. The REB-target interaction is then reducible to that of a linear superposition of isolated charges. Focussing attention on the most significant stopping mechanisms, we include binary electron-electron collisions through a plasma-adapted Møller expression

$$-\frac{dE}{dx} = \frac{2\pi n_p e^4}{m_e \beta^2 c^2} \times \left[\ell n \frac{1}{2\tau_{min}} + 0.125 \left(\frac{\tau}{\tau+1} \right)^2 - \frac{(2\tau+1)}{(\tau+1)^2} + 1 - \ell n 2 \right] \quad ,$$

with τ_{min} = ratio of projectile electron wavelength $\lambda\!\!\!^{-}_e$ to target Debye length λ_D, $\tau = \gamma - 1$ in terms of the usual Lorentz parameters $\beta = \frac{V}{c}$, $\gamma = \left(1-\beta^2\right)^{-1/2}$, and the excitation of Langmuir collective modes

$$-\frac{dE}{dx} = \frac{2\pi n_p e^4}{m_e \beta^2 c^2} \times \ell n \left[\frac{V}{\omega_p \lambda_D} \times \left(\frac{2}{3} \right)^{1/2} \right]^2 \quad ,$$

in terms of the target electron plasma frequency ω_p.

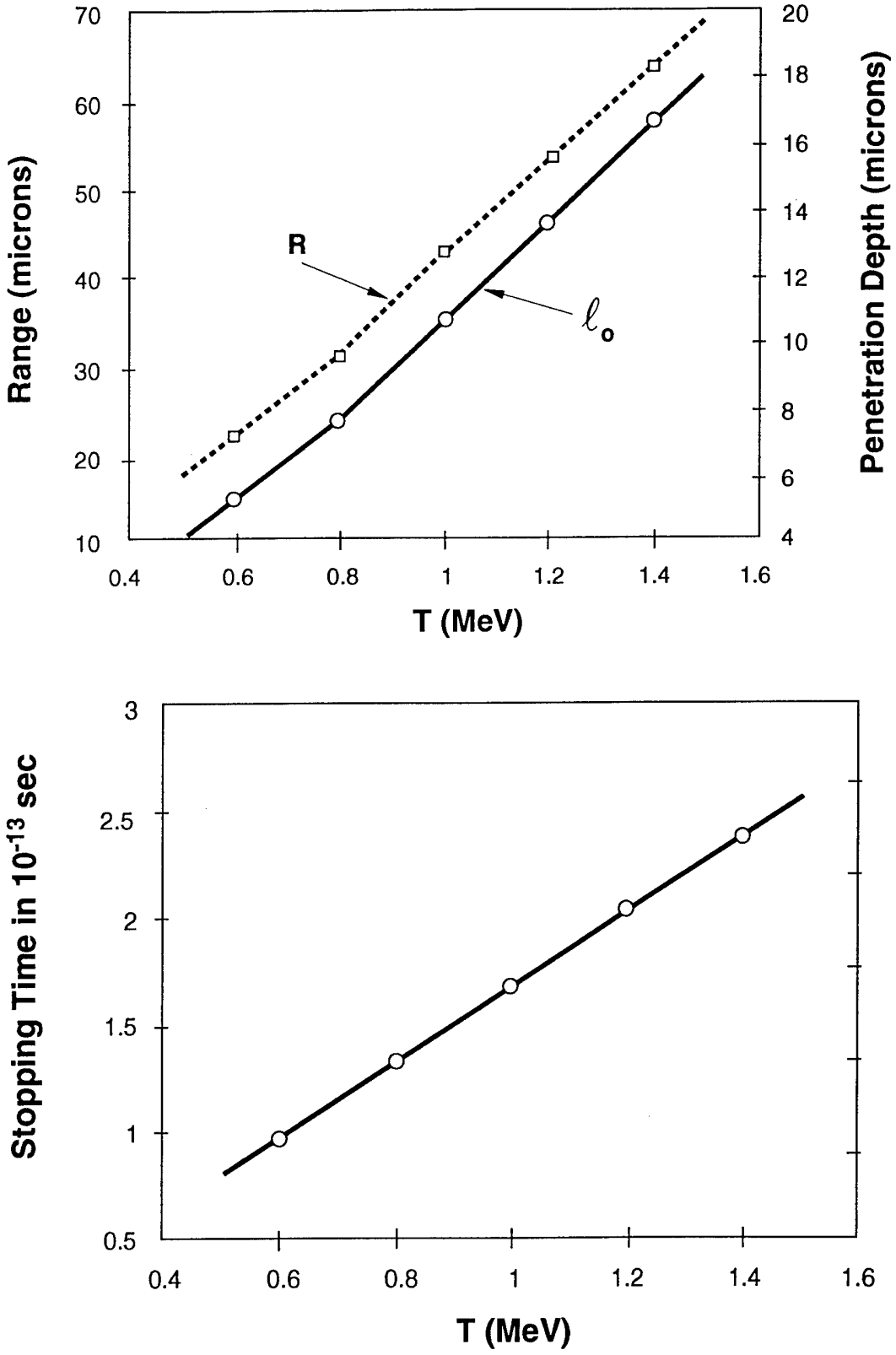

Figure 1- (a) REB range R (μm) and maximum penetration depth ℓ_0 (cm) in a 300 g/cc DT target at 5 keV and $0.5 \leq T\ (MeV) \leq 1.5$; (b) corresponding stopping time t_{stop}.

We are entitled to restrict to a continuous slowing down approximation because large and sudden energy losses are likely to happen very rarely. However, in contradistinction to the simpler ion stopping case we have to give up the straight line approximation for the projectile trajectory. Due attention has now to be paid to the quasielastic and highly erratic motion of the relativistic electrons experiencing multiples scattering on target ions. Such a process is essentially quantified by the square average deflection per unit path length (Z=1, A=2) .

Energy lost to target electrons is treated through binary collisions and Langmuir wave excitation. The overall penetration depth is determined by quasielastic and multiple scattering on target ions (see Figs. 1). It thus appears possible to ignite efficient hot spots in a target with density larger than 300 g/cc.

REFERENCES

[1] M. Tabak, I. Hammer, M.E. Glinsky, W.L. Kmer, S.C. Wilks, J. Woodworth, E.M. Campbell, M.D. Peny and R.J. Mason, *Phys. Plasmas*, **1**, 1626 (1994)

[2] J. Lindl, *Phys. Plasmas*, **2**, 3933 (1995)

[3] G. Bonnaud and E. Lefebvre, *Phys. Rev. Lett.*, **74**, 200 (1995)

[4] M. Busquet, *Chocs*, **13**, 57 (1995)

[5] A. Pukhov and J. Meyer-Ter-Vehn, *Proceedings LIRPP'95 Conference*, Ile Osaka, April 1985 (to appear)

[6] C. Deutsch, *Ann. Phys. Fr.*, **11**, 1 (1986)

[7] S. Sakabe, *Private Communication* (september 1995)

[8] M. Busquet, *Private Communication* (november 1995)

INVESTIGATION OF THE COMPOSITION OF AN ION BEAM PRODUCED USING A MULTI ARC ION SOURCE

V. Engelko*, H. Giese, M. Mischin+, S. Schalk, O.Y. Tsibin+

Forschungszentrum Karlsruhe, INR, Postfach 3640, D-76021 Karlsruhe, Germany
**Efremov Institute of Electrophysical Apparatus, 189631, St. Petersburg, Russia*
+St. Petersburg State Technical University, 194064, St. Petersburg, Russia

Complementing the diode and beam transport optimization studies currently performed in FZK/Karlsruhe on the proton-beam-facility PROFA [1,2], side investigations were run at the St. Petersburg State University which focused on ion beam divergence and composition measurements using TOF techniques. To ensure direct transferability of the results to the PROFA facility, these measurements were made on a scaled down replica of the PROFA diode, comprising an array of small polyethylene flash-over plasma sources and a grid extraction system. Presented here are only the results of the beam composition measurements, which allow the following conclusions: (i) The ion beam contains H and C ions and heavier constituents that still have to be identified. (ii) The beam composition changes significantly with the total number of shots: While in the start phase of the experiments H^+ ions predominated, heavier components outweighed these later on in the experiments, supposedly due to hydrogen depletion of the surface layer of the anode polyethylene units. (iii) Reconditioning of the polyethylene units seems possible by running the diode at higher currents (self cleaning) or by cutting off a surface layer.

1. INTRODUCTION

One of the ITER-related topics presently studied at FZK/Karlsuhe is the feasibility of the production and focusing of an intense (~ 1 kA), pulsed (≥ 10μs), low kinetic energy (10-30 keV) proton beam, suitable for the investigation of ITER divertor erosion under plasma disruption conditions. As part of these studies the proton beam facility PROFA was built, serving for the development and optimization of suitable methods for proton beam production and focusing. Optimal results were accomplished when the proton beam was produced using a multi arc ion source, in which the source plasma is generated by synchronous ignition of an array of flash-over discharges across 6 mm diameter polyethylene (PE) plugs and a grid extraction system. Although it is generally known that PE flash-over discharges produce a hydrogen-rich plasma, and it has therefore become common practice to employ this type of plasma source in pulsed proton beam facilities, the majority of these operate in the hundred nanosecond range [3]. Since in PROFA the details of the surface discharges and the pulse duration differ significantly from these earlier applications, it was considered prudent to perform detailed measurements of the beam composition. These were conducted on a scaled down replica of the PROFA diode with attached TOF analyzer at the St. Petersburg State Technical University.

2. EXPERIMENTAL SETUP

A scheme of the test-facility is shown in Fig. 1. The diode part is composed of a multi arc ion source comprising an array of cylindrical polyethylene discharge units (PE) with central needle electrodes (NE), which are embedded in a common discharge electrode (DE). Plasma production was achieved by applying a positive high voltage pulse U_{diode} of 10-30 kV amplitude and ≈ 100μs duration to the discharge electrode. While R_0 and C_a control the diode ignition, R_a controls the total discharge current. R_a and C_a were chosen to create an anode plasma density corresponding to that of PROFA. Once the plasma has reached the anode grid (AG) it is under the influence of the electrical field, and ions are ex-

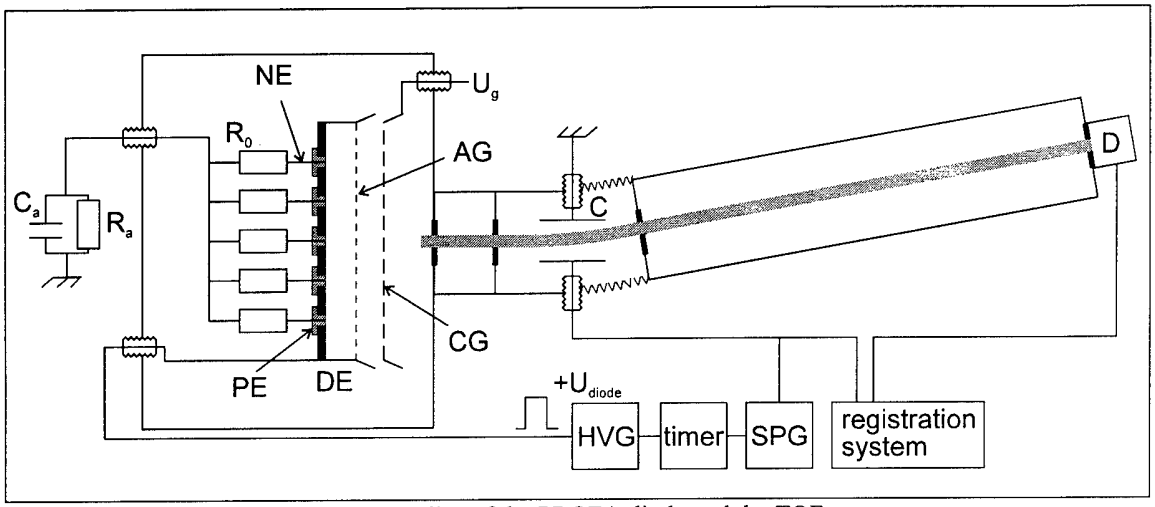

Fig. 1: Schematic of the scaled down replica of the PROFA diode and the TOF setup.

tracted and accelerated towards the cathode grid (CG).

The time of flight spectrometer consists of two articulated channels with a set of diaphragms, a beam deflector (C) and a detector (D). A fraction of the beam enters the channel through the first diaphragm. The orientation of the flight channel is chosen, such that ions can pass into the flight channel and reach the detector only during the front edge of the pulsed deflection voltage. A timer network allows to delay the instant at which the strobe pulse generator (SPG) applies the deflection voltage relative to the diode high voltage pulse by a time span Δt and thus to take beam samples at different times.

The relatively small signals produced by the extracted fraction of the ion beam are presently recorded using a secondary electron multiplier. Since the secondary electron emission coefficients for the different types of ions are not precisely known, the results presented hereafter are still of a qualitative nature. It is therefore planned to repeat part of the measurements using a biased collector with a high sensitivity transimpedance amplifier.

Different ion types were identified by the time delays t_i of the individual peaks on the detector signal according to the relation $M_i = k(\Delta t) \cdot U_o \cdot t_i^2$, where M_i is the ion mass/charge state and $k(\Delta t)$ is the coefficient of the relative sensitivity depending on the time delay Δt between the beginning of the diode voltage pulse U_{diode} and the front edge of the strobe pulse. This coefficient also depends on M_i because of two reasons: a) dependence of the time of flight of the particles through the diaphragm window in the transverse direction ($\sqrt{M_i}$) and b) dependence of the secondary emission coefficient on ion mass.

While the majority of the measurements was made using the same high voltage supply for anode plasma production and ion acceleration, part of the experiments was repeated using a separate supply for ion acceleration. This allowed to use an acceleration voltage of only a few 100 V and thus to spread the TOF spectrum leading to improved peak resolution.

3. RESULTS

Starting off the measurements with new PE plugs, these were progressively aged by producing 1 pulse per 5 seconds.

It was found that the beam composition depends on the following factors:

- sampling time relative to the onset of the diode voltage pulse (this point is not further discussed in the present context).
- total number of pulses for ageing
- magnitude of the anode discharge current
- condition of the plug surface

A typical mass spectrum obtained for new plugs, the surface of which had been cleaned with alcohol is given in Fig. 2. One can clearly distinguish groups of light and

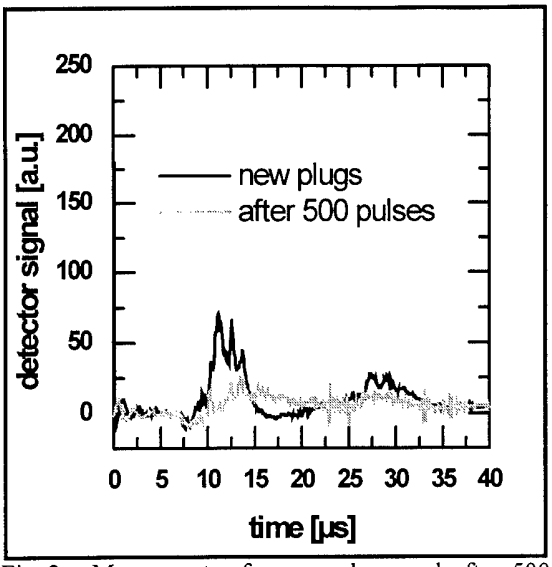

Fig. 2: Mass spectra for new plugs and after 500 pulses.

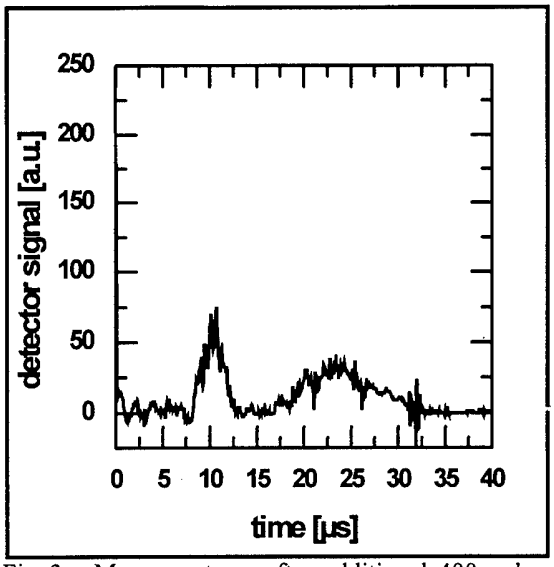

Fig. 3: Mass spectrum after additional 400 pulses with 3x higher discharge current.

heavy ions, the former being dominant. After 500 pulses the amplitudes of both light and heavy components decreased significantly. Operating the source in a higher current regime leads to partial restoration of the mass spectrum and to a slower ageing, which is illustrated in Fig. 3. Here the mass spectrum acquired after additional 400 pulses with a three times higher discharge current is shown.

To recondition the PE plugs, a surface layer of 0.1 and 0.5 mm was cut off. While in the first case no visible improvement of the mass-spectrum was observed, in the second case a pronounced light ion peak corresponding to ions with mass numbers 1, 2 and 4 was obtained directly after treatment (see Fig. 4).

The evolution of the spectrum with the number of pulses depends on diode operation details. If the diode operates without breakdowns, the amplitude of the light components decreases progressively and the stability of the spectrum deteriorates after 50-70 pulses. On the other hand an increase of the light components takes place after a breakdown occurred. This effect is displayed in Fig. 5 in which the spectra ob-

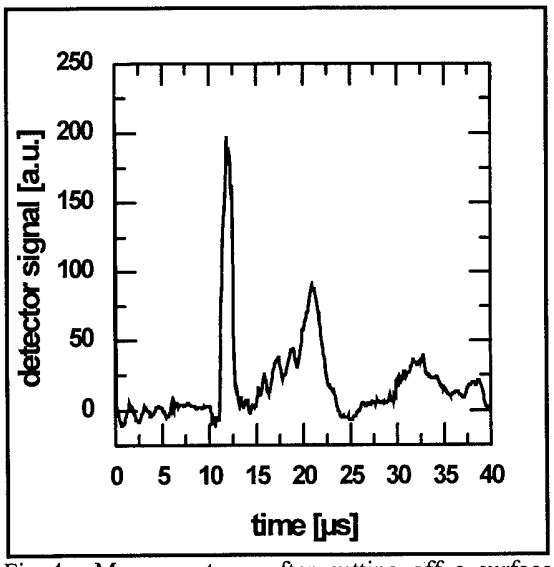

Fig. 4: Mass spectrum after cutting off a surface layer of 0.5mm.

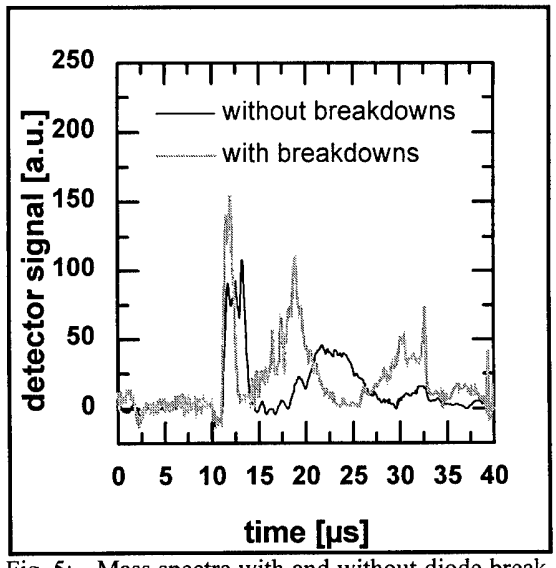

Fig. 5: Mass spectra with and without diode breakdowns during operation.

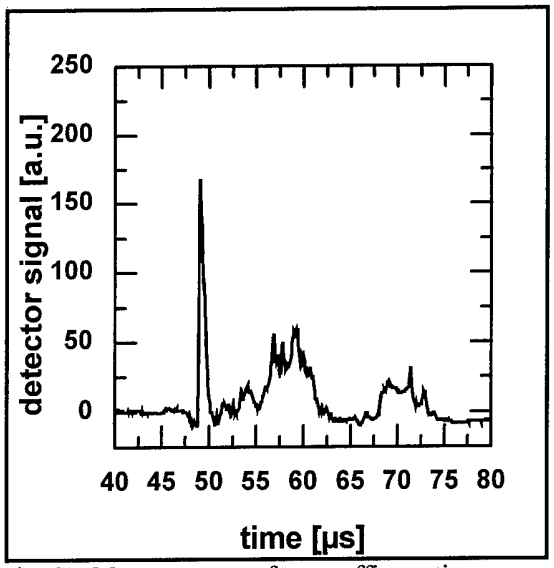

Fig. 6: Mass spectrum after paraffin coating

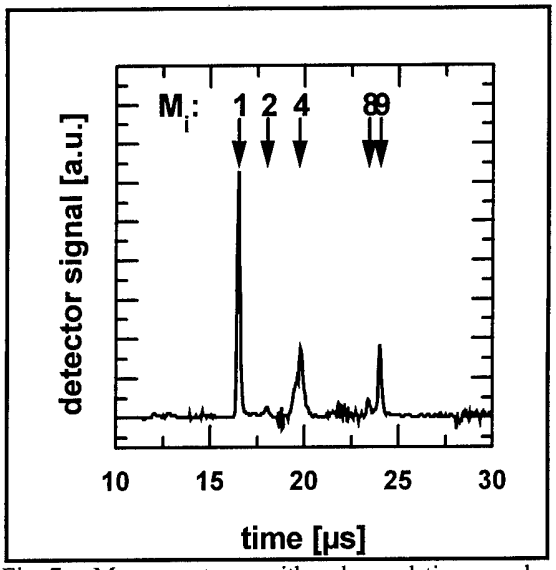

Fig. 7: Mass spectrum with enhanced time resolution.

tained after 70 pulses without breakdowns and after 130 pulses with breakdowns are shown.

As an alternative method for the restoration of the PE surface properties, repetitive coating of the surface with a suitable hydrogen-rich material was tested. Since up to now no easy to handle solvent was found for PE, these tests were made using molten paraffin. Fig. 6 shows that immediately after paraffin coating, the light ion content is substantially increased[1]. Unfortunately, this improvement of the mass-spectrum lasts only for about 20 pulses, after which the number and amplitude of heavy components increases. Fast evaporation of the paraffin could be the reason for this short lived improvement.

The results presented in Fig. 2-6 were obtained using the same high voltage supply for plasma production and ion acceleration. The ion kinetic energy thus ranged from 10 ÷ 30 keV. As mentioned before, part of the measurements were repeated using a separate low voltage power supply for ion acceleration. An example of the mass spectra obtained with this set-up for $U_a = 400\,V$ is shown in Fig. 7. This result was obtained after conditioning of new, untreated polyethylene plugs by several shots. It is clearly seen that protons represent the predominant beam component.

4. CONCLUSIONS

The composition of an ion beam, produced using a multi-arc-type ion source was studied. It was found that protons can be the predominant beam component if certain conditions are fulfilled:

- at the beginning and periodically after 50 ÷ 100 pulses the polyethylene plugs should be mechanically cleaned by cutting off a surface layer of around 0.5 mm thickness;
- the discharge current for one plug should exceed a certain value (e.g. 5A);
- repetitive coating of the plug surface with molten hydrogen rich material could prove beneficial, but for practical application of this method, it is necessary to find a suitable material and coating procedure.

5. REFERENCES

[1] V. Engelko et al; 'Measurement of extent of intense ion beam charge neutralization'.

[2] V. Engelko et al; 'Formation of an intense proton beam of microsecond duration'. Both this conference.

[3] A.A. Kolomensky, et al, Proceedings of the 6th International Conference on High Power Particle Beams, Kobe, Japan, 1986, pp. 208-210.

[1] Prior to covering of the plugs they were under operation for 250 pulses.

MEASUREMENT OF EXTENT OF INTENSE ION BEAM CHARGE NEUTRALIZATION

V. Engelko*, H. Giese, S. Schalk

Forschungszentrum Karlsruhe, INR, Postfach 3640, D-76021 Karlsruhe, Germany
**Efremov Institute of Electrophysical Apparatus, 189631, St. Petersburg, Russia*

Various diagnostic tools were employed to study and to optimize the extent of space charge neutralization in the pulsed intense proton beam facility PROFA. (see papers to this conference [1,2]), comprising Langmuir probes, capacitive probes and a novel type of three electrode collector. The latter does not only allow to measure ion and electron beam current densities in a high magn. field environment, but also to deduce the density spectrum of the beam electrons. Appropriate operating conditions were identified to attain complete space charge neutralisation.

1. INTRODUCTION

One of the tasks presently pursued at FZK/Karlsruhe is the possibility of simulating ITER divertor erosion under plasma disruption conditions by exposing divertor candidate materials to an intense (~ 1 kA), pulsed (≥ 10μs), low kinetic energy (10-30 keV) proton beam with a power density of up to 10 MW/cm^2 [3, 4]. As a first step towards the realization of a facility capable of producing such a beam, the PROFA facility was built in 1994 [1]. Representing a scaled down version of the projected machine, PROFA was conceived for a max. beam current of ~ 150A and serves as a test-bed for vacuum diode development and beam transport optimization. Beam focusing, an essential necessity to reach the required current density, is performed in two stages: Ballistic focusing and subsequent compression in an increasing magnetic field.

Numerical simulations have shown that the two stage focusing is successful only under certain conditions. One of these is a high degree of space charge neutralization. This paper presents some results of the investigation and optimization of the beam space charge neutralization in the focusing channel of the PROFA facility.

2. EXPERIMENTAL SETUP

Fig. 1 shows the principal layout of the PROFA facility and illustrates its focusing scheme. The proton beam emerging from the concave anode extractor grid surface with a focal distance of 60cm passes through two cathode grids (G1, G2) before it enters the focusing channel. The magnetic compression system symbolized in Fig.1 by a set of coils, produces an induction of 6 mT at the entrance of the focusing channel, and of 4 T at the target position, located 60cm below the ball. focus. The magnitude of the magnetic induction at the target was chosen to meet typical ITER conditions. Electrons, neutralizing the space charge of the ion beam, are produced on the cathode grids as a result of ion induced secondary electron emission.

Three types of diagnostic tools were employed in the reported investigations:

(i) Langmuir probe (LP): Measurements of the radial distribution of the space charge in the ballistic region.

(ii) Capacitive probe (CP): Measurements of the beam potential in the ballistic and target region.

(iii) Three Electrode Collector (TEC): Since the high magnetic induction at the target precludes the use of magnetically insulated faraday cups for measurements of the ion current density in this location, this novel type of detector was employed. As indicated in the bottom of Fig.1, the TEC is a cylindrical detector, consisting of 3 mutually insulated concentric components: A usually grounded outer screen electrode 'OE', an intermediate electrode 'IE' and a collector 'cup'. Entrance aperture diameters of OE and IE ranged from ~1mm to ~1cm.

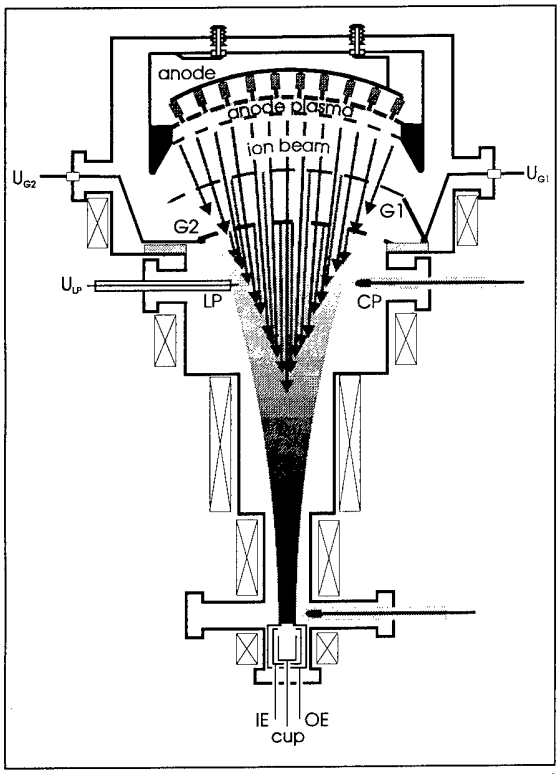

Fig. 1: Scheme of the beam focusing and neutralization at PROFA.

Large apertures were covered with a high transparency stainless steel cloth to homogenize the inter-electrode electric field. Adequate biasing of the IE and cup allowed to measure the following parameters:

Ion current density j_i:

IE negatively biased with $|eU_{IE}|$ exceeding the longitudinal energy of the electrons accompanying the ions. Cup positively biased with $|eU_{cup}|$ exceeding the kinetic energy of the secondary emission electrons from the cup. The correct bias voltages are found by increasing the respective bias until I_{cup} saturates. The ion current density j_i is obtained as the sum of IE and cup current divided by the effective TEC entrance aperture.

Electron current density j_e:

IE grounded. Cup positively biased as before. Since beam electrons are no longer repelled by U_{IE}, I_{cup} is the sum of ion and electron current. Subtraction of the previously obtained j_i gives j_e.

Electron density n_e:

The measured dependence $I_{cup}(U_{IE})$ is differentiated. Since j_i does not depend on U_{IE} it follows

$$\frac{1}{A_{OE,eff}}\frac{dI_{cup}}{dU_{IE}} = \frac{dj_e}{dU_{IE}} \qquad (1)$$

with $A_{OE,eff}$ being the effective OE aperture area. Considering the relations $j_e = ev_{\|}n_e$ and $v_{\|} = \sqrt{2eU_{IE}/m}$ one obtains:

$$\frac{dn_e}{dU_{IE}} = \frac{1}{e}\sqrt{\frac{m}{2eU_{IE}}}\frac{dj_e}{dU_{IE}} \qquad (2)$$

Integration of (2) leads to the density of the electrons accompanying the ions at the aperture of the OE.

Apart from the above mentioned diagnostics, Rogowski coils were used to monitor all system currents, i.e.: total diode current (I_D), cathode grid currents (I_{G1}, I_{G2}), current to the focusing channel wall (I_{CH}).

3. RESULTS

Fig. 2 shows an example of the results obtained in the course of the TEC measurements in the compression channel. Shown here is spectrum of electron longitudinal energies. One can see that these energies are smaller than would correspond to the second cathode grid bias voltage of -300 V.

Fig. 3 demonstrates the dynamics of the beam current neutralisation. One ob-

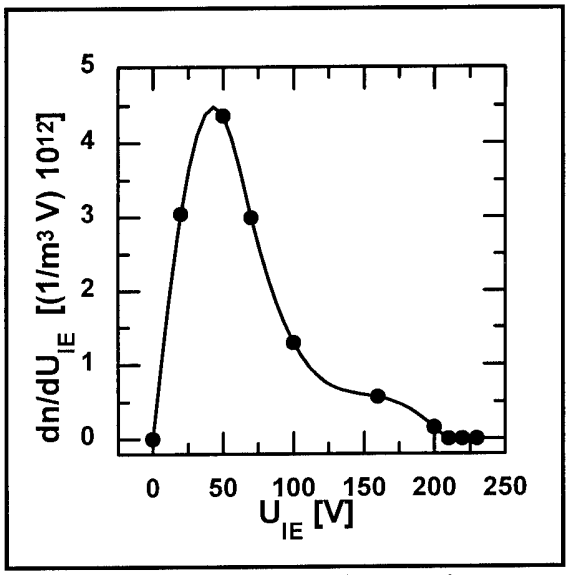

Fig. 2: Density spectrum of beam electrons

serves that full neutralisation occurs only after about 7 μs counted from the start of the diode pulse. After that time the electron current exceeds that of the ions, a behaviour that is typical for all operation regimes of the facility.The degree of neutralisation is not homogeneous across the beam cross section, but shows an oscillatory behaviour. Since the radial distribution of the ion current density shows a Gaussian profile, the reason for this particular behaviour, which has so far not yet been fully understood, has to be attributed to the electrons.

Fig. 4 gives an example of the results obtained in the CP-measurements. Shown are the diode voltage and current U_D and I_D, the cathode grid currents I_{G1}, I_{G2} and the signal from the CP in the ballistic region.

It was experimentally determined that all secondary emission electrons are injected into the focusing channel, if the grids are biased according to: $-U_{G1} \le -1\text{kV}$ and $U_{G2} = -100 \div -300\text{V}$. From the magnitudes of the grid currents in the presence of the magnetic field one can derive that the secondary emission coefficients for the first and second cathode grids are $\kappa_1 = 1.4$ and $\kappa_2 = 1.6$ respectively. The electron current entering the focusing channel is

$$I_e = I_D\left[(1-\alpha_1)\kappa_1 + \alpha_1(1-\alpha_2)\kappa_2\right] = 0.62 \cdot I_D$$

where $\alpha_1 = 0.71$ and $\alpha_2 = 0.8$ are the cathode grid transparencies. Note that 64% of I_e

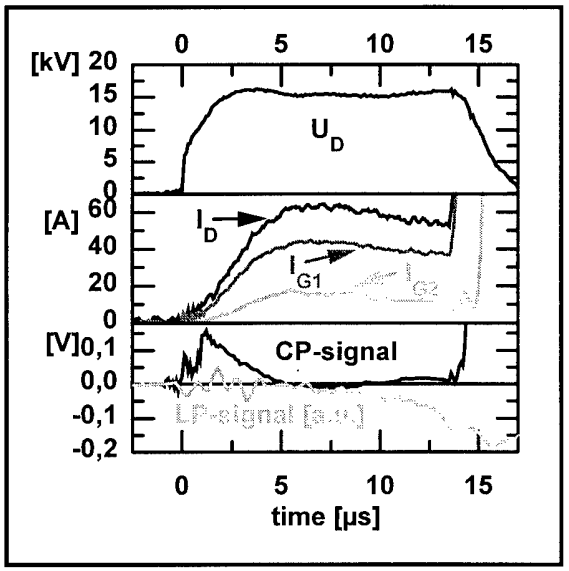

Fig. 4: A typical pulse at PROFA.

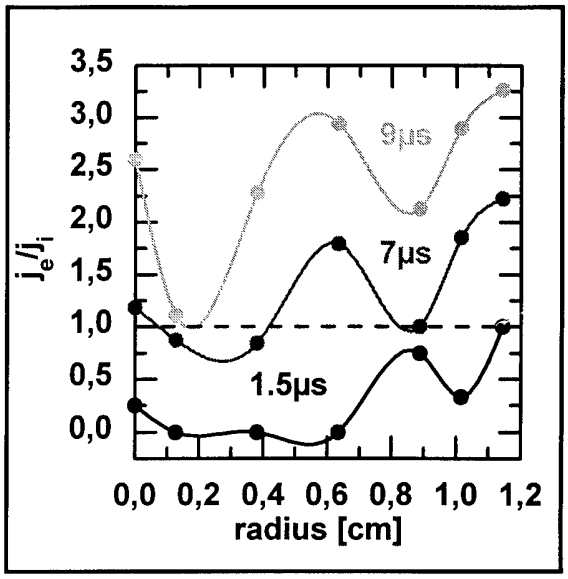

Fig. 3: Extent of neutralization

is provided by the first cathode grid.

The ion current passing into the focusing channel (I_i) is equal to $I_i = \alpha_1\alpha_2 I_D = 0.58 \cdot I_D$. Since $I_e > I_i$, secondary electron emission from the cathode grids supplies in principle enough electrons to fully neutralize the ion beam space charge. The time, which is necessary to reach equality of electron and ion charge in the focusing channel is approximated by

$$t_n = \frac{I_i L}{v_i I_e} \le 1\mu\text{s} \qquad (3)$$

where L is the length of the focusing channel and v_i the ion velocity. In contrast the

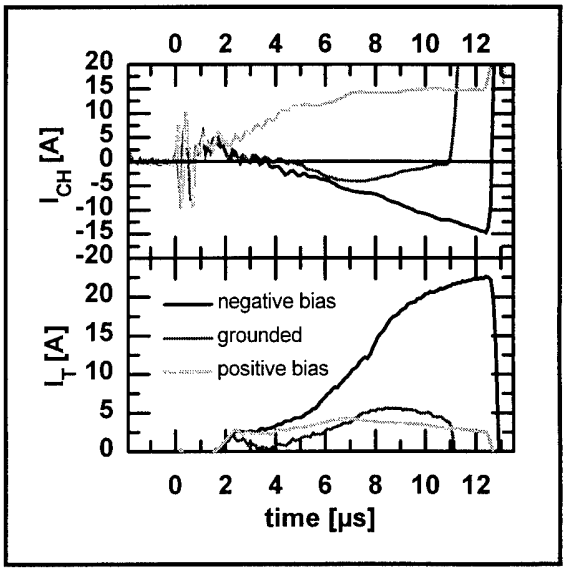

Fig. 5: I_{CH} and I_T vs. time

capacitive probe signal shows that the beam potential drops to zero (or negative) voltage only after 5μs[1]. Thus full space charge compensation (or even overcompensation) does not build up immediately, but is governed by the expansion time of the electron cloud from cathode grids to the target through the strongly inhomogeneous magnetic compression field. In the measurements discussed here, an insulated metal disk was installed in the target position, on which beam impingement also produced secondary electrons. It seems, however, that for establishing the neutralization process these are of subordinate importance, since CP and LP signals are hardly influenced by the target bias.

On the other hand, the target potential was found to have a substantial influence on the current to the focusing channel wall. Fig. 3 compares I_{CH} and I_T for different target biasing situations. Here I_T is the sum of ion and electron beam current. Since in all target biasing situations discussed here, sec. emission electrons emerging from the target were reflected by the cathode grids back to the target and could thus not contribute to I_T, the electron current originates mainly from the cathode grids.

(i) Grounded target: In the initial phase of the pulse ($t \leq 2\,\mu s$) an ion current flows to the wall. Later I_{CH} drops to zero and I_T appears. After $5\,\mu s$ I_{CH} becomes negative.

(ii) Negative bias $U_T=U_{G2}$: In the initial phase ($t<2\text{-}2.5\,\mu s$), I_{CH} exhibits the same behaviour as with grounded target. But other than with grounded target it goes negative already after $3\,\mu s$ and increases with time, as does the target current.

(iii) Positive bias $U_T=U_{G2}$: Part of the ion current flows to the channel wall during the entire pulse.

Langmuir probe measurements in the ballistic focusing region showed that electrons appear near the beam axis after $2 \div 2.5\,\mu s$, while at the beam periphery they appear after $5 \div 7\,\mu s$. The density of the negative space charge is significantly higher near the beam axis than at its outer boundary. The kinetic energy of the electrons is of some hundreds of eV, which means that most of them originate from the cathode grids. The ion beam radius coincides with the radius of the magnetic force line passing through the outer edge of the ion emitting surface.

4. CONCLUSION

In the pulsed proton beam facility PROFA, the ion beam space charge neutralisation is provided predominantly by secondary emission electrons from the cathode grids. Close to the beam axis electrons expand over the full length of the focusing channel within $2 \div 2.5\,\mu s$, creating an electric field of sufficient strength to confine protons inside the focusing channel and to transport a major fraction of the beam to the target. Full neutralisation of the beam space charge occurs within $5\,\mu s$. After this time the potential of the focusing channel volume becomes negative, which leads to the appearance of an electron current to the wall of the focusing channel. Negative biasing of the target with $U_T=U_{G2}$ only slightly influences on the potential of the focusing channel volume, but leads to a significant increase of the electron current to its wall.

For efficient neutralisation of the proton beam space charge, both cathode grids should be biased negatively with $-U_{G1} \leq -1kV$ and $-U_{G2}=-100 \div -300V$. The target should be grounded or negatively biased.

5. REFERENCES

[1] V. Engelko et al; 'Formation of an intense proton beam of microsecond duration', this conference.

[2] V. Engelko et al; 'Investigation of the composition of an ion beam produced using a multi arc ion source', this conference.

[3] V. Engelko et al; 'Compression of intense proton beams', Proc. Beams '94,San Diego 1994

[4] V. Engelko et al; 'Pulse intense proton beam facility for ITER disruption simulations', Proc. Beams '94, San Diego 1994

[1] In the absence of the magn. field, the CP shows a residual positive beam potential, due to the finite kinetic energy of the compensating electrons.

CHARGE NEUTRALIZATION OF SMALL ION BEAM CLUMPS*

Dale R. Welch
Mission Research Corporation, 1720 Randolph Road SE, Albuquerque, NM 87106, USA

C. L. Olson and D. L. Hanson
Sandia National Laboratories, P.O. Box 5800, Albuquerque, NM 87185, USA

Abstract

The mega-ampere currents associated with light ion fusion (LIF) require excellent charge neutralization to prevent divergence growth. As the size and space-charge potential of a beam clump or "beamlet" become small (submillimeter size and kilovolt potentials), the neutralization becomes increasingly difficult. Linear theory predicts that plasma electrons cannot neutralize potentials $< \phi_{crit} = 1/2\ m_e v_i^2/e$, where m_e is the electron mass and v_i is the ion beam velocity. A non-uniform beam would, therefore, have regions with potentials sufficient to add divergence to beam clumps. The neutralization of small beamlets produced on the SABRE accelerator and in numerical simulation has supported the theory, showing a plateau in divergence growths as the potential in the beamlet exceeds ϕ_{crit}.

I. Introduction

The neutralization of an ion beam to the order of millimeter scale lengths has been simulated with many particle-in-cell (PIC) simulation codes and shown to be quite good. As the size and potential of beam nonuniformities become small (submillimeter size and kV potentials), C. L. Olson[1,2] has shown that the neutralization becomes increasingly difficult. At some point, the clump potential is too small to drag a neutralizing electron along with it. The theory states that an electron cannot neutralize potentials $< \phi_{crit} = 1/2\ m_e v_i^2/e$, where v_i is the ion beam velocity. A clumpy beam would, therefore, have many regions with electric potentials sufficient to add divergence to the clumps of the order of $\theta_m = (Z\ m_e/m_i)^{1/2}$, where m_e, m_i and Z are the electron mass, ion mass and ion charge state. This divergence hinders the focusing of an ion beam down to a centimeter-sized target for light-ion fusion (LIF).

To model the neutralization of beam clumps, we have experimentally produced small ion beamlets. A 5-10 mrad divergence proton beam was created with the SABRE accelerator[3] by allowing the beam to expand in vacuum for 115 cm. Small beamlets of varying potentials were then produced as the beam passed through a plate with pinholes of several different radii. The beamlets then drifted in a 29-cm long region filled with helium or argon gas and are imaged on radiachromic film. A similar configuration was simulated using the particle-in-cell code IPROP.[4] In both experiment and theory, we find for the vacuum case (actually pressure < 1 mtorr) that, as the potential increases, the inferred beamlet divergence approaches but does not exceed θ_m. The simulations show that electrons emitted from the pinhole plate continue to prevent the unneutralized potential from exceeding ϕ_{crit} as the beamlet current increases. As the gas pressure is increased, the divergence growth drops rapidly above 6 mtorr argon and 30 mtorr helium indicating plasma shielding.

*Work supported by Sandia National Laboratories.

II. Scaling of Pinhole Image Thickness with Beamlet Potential

In the expanding beam configuration, the SABRE diode produces a 75 kA, 4 MV proton beam of 20-30 mrad divergence. The beam, which has a significant carbon component, strikes an aluminum foil which is range thick to 4 MV carbon ions, leaving a fairly pure proton beam. The foil provides a good source of electrons for neutralization well outside the diode magnetic fields. Beyond the foil, the beam is well charge neutralized and drifts nearly ballistically for 115 cm. Assuming uniform emission from the diode and ballistic transport, the maximum proton divergence exiting a pinhole of radius r_p after drifting length L is $\theta_\mu = ((r_o - r_i)/2 + r_p)/L$, where for SABRE the inner radius $r_i = 4.5$ cm and the outer radius $r_o = 6.5$ cm. After the SABRE beam passes through the various pinholes of 0.5-10 mm radii, the resulting 0.075-2.5 keV potential (0.3-100 amp) beamlets expand from a combination this incoming divergence and the divergence resulting from any unneutralized space charge. The beam then produces an image on radiochromic film 29 cm from the pinhole plate.

In Figure 1, we plot the full thickness (inner to outer edge) of the image from the pinholes as a function of pinhole radius for the vacuum case, 0.1 and 1 torr argon pressure (in the region behind the pinholes). The estimated error in the image thickness measurement is 1 mm. To interpret the data, we have also plotted reference lines calculated using IPROP assuming cylindrical symmetry and initial divergence θ_μ. The simulation lines correspond to image thickness produced from pure ballistic transport, from unneutralized 2.5 keV potential (10 amp) proton beams and from the full unneutralized potential corresponding to r_p. We see that for vacuum transport, as r_p increases, the data thicknesses follow the θ_μ only curve. This behavior is due to the very low potential of the small r_p beamlets which add very little additional divergence. At roughly r_p = 4 mm, the data moves to the 10-amp curve and remains there. This behavior suggests that electrons, likely emitted from the pinhole plate, prevent unneutralized space charge of > 2.5 keV in good agreement with the theory. As expected for significant argon pressures, the beam picks up little additional divergence and expands ballistically. This is due to the effective plasma shielding of the dense plasma produced by impact ionization of the beam.

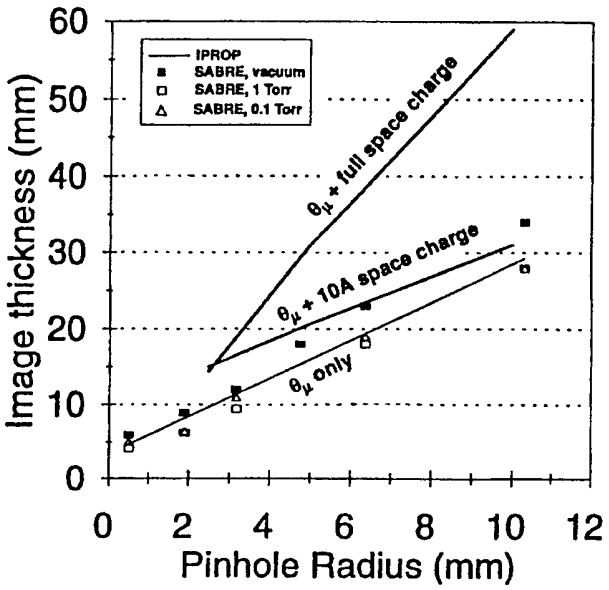

Figure 1. The edge-to-edge image thickness of protons measured 29 cm from a pinhole of various radii is plotted. IPROP reference lines for a ballistic beam, 2.5-keV potential beam and a full space charge beam are also plotted.

III. Plasma Shielding of Beam Potential in a Background Gas

A 4-MeV proton is an effective ionizer of a background gas. The fraction of electron to beam density, where the electrons are produced via impact ionization (3.8×10^{-16} cm^2 ionization cross section in argon), is $f_e = 0.04\ t\ p$, where t is the time into the beam pulse in nanoseconds and

p is the argon pressure in mtorr. For a roughly 30 ns SABRE pulse, we can expect f_e to increase from unity to 10 as the argon pressure increases from 1 to 10 mtorr. The unneutralized potential discussed should decrease with increasing f_e because the amount of unneutralized space charge decreases with Debye length squared. To explore this effect, we have both in experiment and simulations propagated beamlets in a range of pressures and calculated the image thickness from a 4.8-mm radius pinhole. This particular pinhole was chosen because it produces a beam with potential roughly twice ϕ_{crit}. Instead of using the image edges which will actually vary in time as the beam becomes increasingly neutralized due to the gas ionization, we used the full-width-half-maximum (FWHM) as the figure of merit.

The IPROP simulations in this case were run in three-dimensions to better approximate the experiment. We assumed that the beam was emitted from the anode with $r_i = 4.5$ cm and $r_o = 6.5$ cm and with a 40 mrad divergence. The protons were then ballistically transported to the pinhole plate where the actual simulations began. The region behind the plate was filled with a uniform argon density. Space-charge limited emission was permitted from the pinhole plate only, the outer 3-cm wall (the actual outer wall radius was 15 cm) did not emit. The gas ionization was accomplished in Monte-Carlo fashion with all electrons followed kinetically as particles. Gas interactions included impact ionization of the gas by protons and secondary electrons and elastic scattering of charged particles off gas neutrals. The model contrasts with the usual hybrid model in IPROP in which the plasma electron distribution is split into thermal-fluid and kinetic-particle components. The pure kinetic approach assures a highly accurate calculation of the charge neutralization, however, the maximum electron density is limited to roughly 100 n_b or 10^{13} cm^{-3} due to the resolution of the plasma frequency.

In the table, the FWHM from the experiment and simulation are plotted for the argon pressure scan. Again the experimental uncertainty is ±1 mm. As expected, we see that the FWHM are largest at small pressure. Both SABRE and IPROP give a roughly 15 mm FWHM for the vacuum case. The transition to smaller FWHM occurs at roughly 5 mtorr although the data exhibits some scatter probably due to shot-to-shot current density fluctuations. At 10 mtorr, the IPROP values continue to shrink down to 9 mm versus 11 mm in the experiment. The thickness does not change much at higher pressures in the experiment with the image remaining at or above 11 mm as the pressure is increased. In the table, complete neut. refers to the IPROP simulation with zero field values, i.e. complete charge and current neutralization. In this case, IPROP calculates 7.3 mm FWHM. The reason for this difference is uncertain. The most likely explanation is film saturation which would become more apparent at the higher pressures where image intensities are greatest. This effect needs further study.

Again, to interpret the meaning of the data we must examine the charge neutralization calculated by IPROP. In Figure 2, the space charge potential at $z = 15$ cm and 1.6 cm radius is plotted for the vacuum and 10 mtorr argon cases. We see the potential approaches the critical potential of 2.5 keV at early times for both cases, but as f_e increases to roughly 10 in the 10-mtorr case, the potential drops by roughly the same magnitude. Thus, plasma shielding is quite effective and is responsible for roughly a 40% drop in the image thickness.

Table 1. Summary of the 4.8-mm pinhole image FWHM from SABRE and IPROP.

Shot	Argon Pressure (mtorr)	SABRE FWHM (mm)	IPROP FWHM (mm)
1318	0	15±1	14.8
1319	0.8	12±1	
1322	1.2	13±1	14.7
1326	3.5	11±1	
1320	5.3	13±1	11.5
1323	6.5	12±1	
1321	10.5	11±1	9.2
1325	30	11±1	
1324	100	12±1	
Complete neut.			7.3

IV. Conclusions

The data and theory suggest a minimum potential in vacuum to which a beam clump or beamlet can be neutralized. At this potential, a neutralizing electron cannot keep up with the moving clump. This behavior adds divergence to the cold beamlets produced in the SABRE experiment leading to a larger pinhole image. In vacuum, the electrons drawn in from surfaces cannot reach a density greater than that of the ion beam; in a background gas, the density can be orders of magnitude larger. The pinhole images show a transition near 5 mtorr argon where the FWHM is reduced from 15 to 11 cm. The IPROP simulations confirm this transition and show that it is the result of the presence of the dense plasma produced mainly by proton impact ionization. The unneutralized space charge decreases with increasing density.

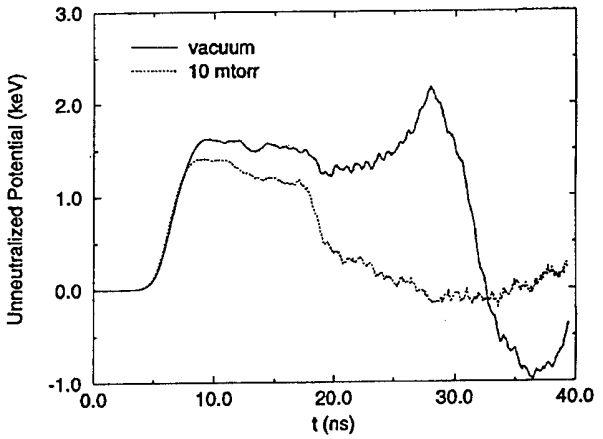

Figure 2. The unneutralized space charge calculated at z = 15 cm and 1.6 cm radius is plotted versus time for a beamlet emerging from a 4.8-mm pinhole in vacuum and 10-mtorr argon.

[1] C. L. Olson, and J. W. Poukey, Proceedings of IX International Conference High Power Particle Beams, Washington D.C., **72**, 897 (1993).

[2] C. L. Olson, Standoff Meeting Series on Ion Beam Uniformity, Sandia National Laboratories, 1995.

[3] D. L. Hanson, *et al.*, Bull. Am. Phys. Soc. **40**, 1800 (1995).

[4] D. R. Welch, C. L. Olson and T. W. L. Sanford, Phys. Plasmas **1**, 1994.

Ne beam-Kr target interaction

V.E.Fortov, V.V.Kostin, V.S.Vorob'ev

High Energy Density Research Center of RAS, Izhorskaya 13/19, Moscow, 127412, Russia

M.I.Kulish, V.B.Mintsev

Institute of Chemical Physics of RAS, 142432, Moskovskaya obl, Chernogolovka, Russia

D.Hoffman

GSI-Darmstadt, Postfach 110552, 6100 Darmstadt, Germany

Energetic heavy ions of Ne - crystal Kr target interaction is investigated both: experimentally and with help 2-D computer code. Dynamics of the target matter heating, expansion and destruction are described. It was obtained end tested the new equation of state for Kr in wide range of parameters.

The interaction of energetic charged particle beams with materials of different composition, density, temperature etc. is an active field of research [1-6].

This work deals with the interaction of the Ne beam with the Crystal Kr target. The study was carried out both: theoretically (with help of the computer simulation) and experimentally. The computer simulation was provided by the two-D Lagrangian computer code, which allows to take into account: ion beam absorption, hydrodynamics motion of the matter, elasto-plastic properties and destruction of the target matter. The experiments were carried out on the GSI (Darmstadt,Germany) facility.

The parameters of the ion beam were the following: ions energy E=300 MeV/amu, Ne charge equals to 10, total number of beam particles was order of 10^{10}, spot size diameter of the beam equals to D=1.5 mm. The pulse consists of the four bunches, each of them has the duration 80 ns with the interval between them 270 ns. Total pulse energy equals to 1.5 J. The Kr target thickness varies in 10-40 mm diapason and has the density of the order of 3.05 g/cm^2. The initial target matter temperature equals to 30^0 K.

As a result of these investigations were obtained the evolution of damage process, spatial distribution of the stresses, density and mass velocities. The target matter motion has an essential two-D character in these conditions.

Computer code

The interaction of the ion beam with target is strongly dependent on the local temperature and degree of ionization in the plasma. The deposition of the beam, the hydrodynamic evolution and atomic physics of the plasma must be calculated self-consistently.

The total stopping cross-section of ions in matter is divided into two parts: the interaction of the ion with the target electrons (called electronic stopping) and with the target nuclei (called nuclear stopping). The nuclear stopping component can be separated because the heavy recoiling target nucleus can be considered to be unconnected to its lattice during the passage of the ion, and the interaction can be treated simply as the kinetic scattering of two screened particles. The electronic stopping of the ion in the target is treated within the local density approximation, wherein each infinitesimal volume element of the solid is considered to be an independent plasma; that's , the ion-target interaction can be treated as that of a particle with a density averaged free electron gas [5].

The calculation of a non-stationary behavior of a condensed matter under shock loading was made with using of the three conservation equations (of mass, momentum and energy) in integral form [7]. An elastic-plastic behavior of the matter is included in the code .The stress-tensor components are split into a hydrostatic equation of state and the elastic-plastic constitutive model. Hook solid law binds the deviatoric stress and strain components. A linear-elastic evolution of the solid is used in the Von Mises yield condition to find the limit value at which the material starts to yield and exhibits plastic behavior [6]. The yield strength depends on pressure and plastic deformation [8]. The dependence of the yield strength and shear modulus from temperature is neglected.

The dynamic fracture of a sample induced by shock loading commonly called by spallation in this work is described by relation proposed by Kanel [9]. The stress relaxation on the cracks was took into account due to correction of the yield strength and shear modulus.

Correction of the volume of the finite-difference mesh cells was also accomplished. In the equation of state the compact volume components (without voids volume) are used:

It was used the equation of state of the target matter in Mie-Grunaisen form. It consist of two parts: first describes the cool behavior of the matter, the second one corresponds to the thermal component:

$$P = P_1 - P_0,$$

$$P_0 = const\frac{\sum_{i=1}^{5} a_i x^{i-1}}{\sum_{i=1}^{5} b_i x^{i-1}},$$

$$P_1 = \frac{RT}{\mu v}\left(3D\left(\frac{\theta(v)}{T}\right)\frac{\gamma + L/3}{1+L} - C_l\right)$$

$$C_l = \begin{cases} 0, \ldots\ldots solid_state \\ \frac{Sv_{0l}}{v}, \ldots liquid_state \end{cases}$$

$$L = \frac{hT^{1/2}}{(2\pi m k_b)^{1/2}(g_a m v)^{1/3}\theta_d(v)},$$

$$\theta_d(v) = \frac{Const}{v^2}, \quad \theta(v) = \theta_d(v)(1+L),$$

$$\gamma(v) = \sum_{i=1}^{6} i c_i (\ln v)^{i-1},$$

where: v is a specific volume of the target matter, $x=v/v_{0s}-1$, . v_{0s} , v_{0l} are the specific volumes of the solid and liquid at $T=0^0$ K, γ is the Gruneisen coefficient, R is the universal gas constant, μ is the atomic weight, T is the temperature, θ_d, θ are the Debye and effective Debye temperatures, k_b is the Bolzmann constant, h is the Plank constant, m is the atomic mass, L is the generalized Lindemann parameter, dimensionless parameter s (the residual entropy) is order of unity, constant g_a equals to unity too for Kr, D(x) is the Debye function and constants a_i, b_i, c_i are the empirical constants.

The cold curves for a liquid are similar to the cold curves for a solid, but they are characterized by a somewhat higher value of v_{0l}. The density of the liquid, extrapolated to zero temperatures, is somewhat lower than the corresponding density of a solid [10]. The heat of vaporization is proportional to the number of bonds (coordination number) that must be broken in order to remove an atom from the condensed state and form a vacancy. In the crystalline state this number is, as a rule, larger than in a liquid.

Fig.1,2 illustrates the cold curves (liquid and solid) and dependents $\rho=f(T)$ with the solid-liquid, liquid-gas and other transition regions for Kr.

Results and discussion

Obtained numerical simulation data were compared with experimental for the pulse parameters: ion energy 300 MeV/amu, total number of charged particles in the beam equals to 10^{10}. Target width varies in diapason 10-30 mm. Results are showed on Fig. 1,2. Target geometry obtained experimentally for time t=2,18 mks is showed on Fig.1.

Maximum of the mass velocities is located at the free surfaces of the target and in the Brag's peak area. A small decreasing of the density while transition to the back surface of the target is connected with the energy deposition.

Due to the tensile stress action, which arises after refraction of the compressive pulse from a free surface, the matter can be destroyed in the area. Existence of the destroyed area may be explained by the tensile stress action, since the target matter can be treated in these regions as a solid. While heating of the target it can be evaporated not only in the irradiated areas. These illustrations allows to draw a conclusion that the matter starts failure at the early stages after the beam action and this failure is connected not with the evaporation of the matter but with the spallation processes.

The case with target thickness is showed on Fig. 2, which illustrates the spatial distribution of radius mass velocity for time t=2,18 mks. Maximal value of the velocity corresponds to the Brag's peak area. Comparison of these data with the experimental one was provided for the target geometry. The target geometry was obtained experimentally with help of high velocity streak camera for the same time moments. There is the good agreement between these results not only in general (maximal target expansion corresponds to the Brag's peak area in both cases). The comparison of the radius mass velocities in the Brag's peak area both cases shows that maximum of this parameter equals to value 340 m/s in simulation data and 270 m/s in experiment. The difference is very small and may be explained by the not enough accuracy of the equation of state and due to action of the thermoconductivity of both types: radiative and electron.

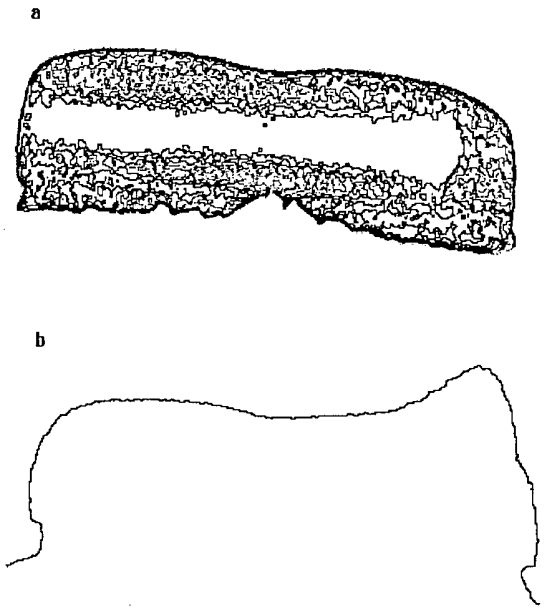

Fig.1 Target geometry for time t=2 (a), 18 (b) mks.

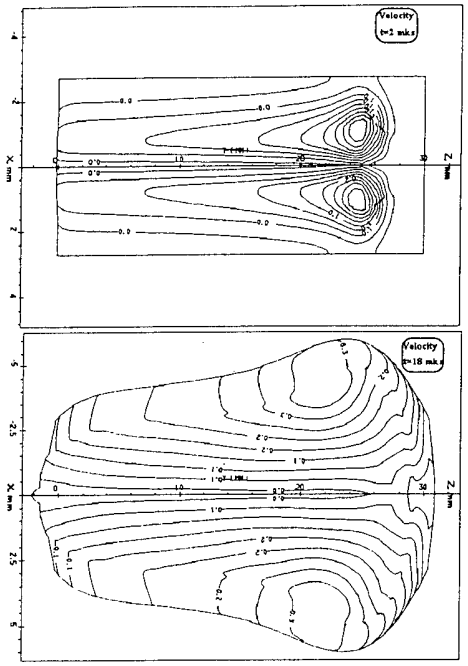

Fig.2 Spatial distribution of target mass velocity for the same time.

Summary

Obtained results allow to draw a conclusion about a good agreement between the simulation data and the experimental one. The numerical code and the presented equation of state of the Kr target describes the investigated phenomena with a good accuracy (difference in radial mass velocities is of the order of 20 %). Target failure takes place not only in consequence of matter melting and evaporation, but due to spallation phenomena too.

Literature:

1. J.E. Rogerson, R.W.Clark, J.Davis. Ion-beam deposition, heating and radiation from an aluminum plasma // Phys.Rev.A- **31**- 5- pp.3323-3331 (1985).
2. A.Fernandez, A.Barrero. Ion beam fusion plasmas. Ablation and heating regimes // Plasma Phys. and Controlled Fusion- **28**- 7- pp.989-1007 (1986).
3. A.Ng, A.R.Piriz. Ultrahigh-pressure generation using light-ion beams // Phys.Rev.A- **40**- 4- pp. 1993-1998 (1989).
4. N.K.Gupta, C.D.Munz, B.Goel. An efficient chock capturing scheme for ion beam target simulation // Laser and Particle Beams- **8**- 4- pp. 807-825 (1990)
5. J.F.Ziegler. Stopping cross-sections for energetic ions in all elements. Pergamon Press, v.2 (1980).
6. V.E.Fortov, V.V.Kostin, V.A.Skvortsov. Mathematical modeling of the solid targets destruction by the ion beams. // Sov. J. High Temperature- **31**- 6- pp. 897- 902 (1993).
7. V.E.Fortov, V.V.Kostin, S.Eliezer. Spallation of metals under laser irradiation // J.Appl.Phys.- **70**- 8- pp. 4524-4531 (1991).
8. V.V. Fiodorov. Failure and Destruction Kinetics of Solids. Tashkent (1985).
9. G.I.Kanel, V.E.Fortov // Adv.Mech- **10**- 3 (1987).
10. V.S.Vorob'ev. Thermodynamic model of a liquid // JETP Lett., **62**, 7, pp. 574-579 (1995).

RECENT RESULTS FROM EXPERIMENTAL AND NUMERICAL INVESTIGATIONS OF THE SELFMAGNETICALLY B_Θ-INSULATED ION DIODE

W. Bauer, P. Hoppé, H. Bachmann, H. Bluhm, L. Buth, H. Massier, D. Rusch, E. Stein
O. Stoltz, W. Väth

Forschungszentrum Karlsruhe GmbH, Postfach 3640, 76021 Karlsruhe, Germany

and

T. Westermann

Fachhochschule Karlsruhe, Moltkestraße 4, 76133, Karlsruhe, Germany

Abstract.
The comparison of measured to calculated data of foil acceleration experiments on KALIF showed discrepancies which made a reinvestigation of the beam characteristics produced by the B_Θ-Diode necessary. It was shown that the peak power density achieved in the focus is only 0.15 TW/cm^2 rather than the 0.25 TW/cm^2 quoted earlier. In addition a most likely time history of the proton power density with a FWHM pulse duration of 60 ns in the focus is derived. The experiments led to a new description of the operating principle of this diode which has been confirmed by particle-in-cell-simulations. As a result of these considerations suggestions for a new design of the diode are derived and investigated by simulations.

Introduction.
In foil acceleration experiments performed at the high power pulse generator KALIF the light ion beam produced in an ion diode impacts on a thin foil target placed in the focal plane of the diode [1]. For the interpretation of this type of experiment theoretical models are under development which need the ion beam characteristics as input data. Due to unexpected large differences between calculated and measured acceleration data [2] also the beam characteristics were considered as a possible error source. These differences were found to be especially pronounced in acceleration experiments carried out with the B_Θ diode (Fig.1). Therefore the characteristics of the beam produced by this diode type were reinvestigated in a set of new experiments. This paper describes the results of these experiments and their consequences for the understanding of the diode's operating principle.

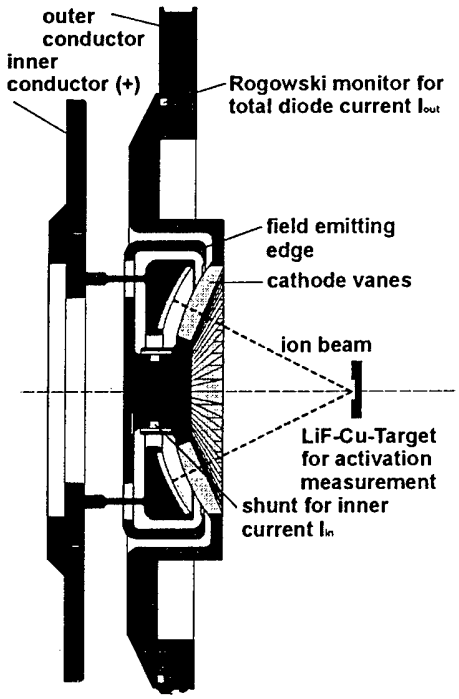

Fig. 1: Cross section of the B_Θ-diode

Measurement of the focused beam properties.
1. The peak proton power density $p_{p,p}$ in the focus is determined by

$$p_{p,p} = \frac{1}{A_t} \cdot \langle I_p \rangle \cdot f_r \cdot f_t \cdot V_{d,p} \qquad (1)$$

where $\langle I_p \rangle$ is the mean proton current calculated from the count rates of an activation target of an area A_t placed in the focal plane. In the energy range of KALIF

lithium fluoride on copper or - outside the focus - also carbon are used. The coefficient f_r accounts for the radial distribution measured in nuclear reaction experiments on boron foils, while the coefficient f_t describes the time evolution of the current, i. e. the ratio of the current in the diode at peak power to the mean diode current (=mean current weighted with the yield-function of LiF-Cu-activation). The voltage $V_{d,p}$ is the diode voltage at the mid radius of the diode at the moment the electrical power in the diode reaches its maximum and is determined by applying inductive correction terms to the voltage measured at the water/vacuum interface or to the voltage measured by a vacuum voltage monitor. The main result of 16 activation measurements, which are described in detail in [3] is that the peak proton power density in the focus ranges from 0.1 to 0.19 TW/cm^2 with a most probable value of (0.15 ± 0.05) TW/cm^2 only instead of the 0.25 TW/cm^2 quoted earlier [4]. This reduction is mainly caused by sensitivity differences in different batches of LiF-targets.

2. Since foil accelerating experiments and LiF/Cu activation measurements cannot be carried out at the same shot attempts were made to relate the LiF/Cu activation results to the measured voltage or current at the diode. The electrical signals measured near the diode are consistent with all other diagnostics of the KALIF generator and are also in agreement with transmission line calculations. Therefore they are considered as reliable. But there is a lack of a clear relation between the peak proton power density found in activation experiments and all other diagnostics (Fig. 2).

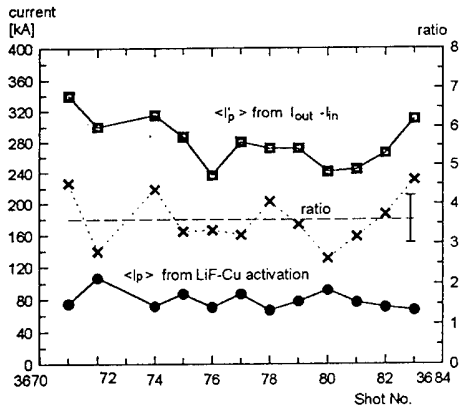

Fig. 2: Comparison of the mean currents from activation and electrical measurements

The fraction of the mean proton current collected in the activation target was between 22% and 33% of the mean diode current $\langle I_{out} \rangle$ and from 36% to 63% of the mean ion current $\langle I_{out} - I_{in} \rangle$. This means that only about a third of the total electrical energy flowing into the diode is transferred to protons with energies above the 500 keV activation threshold of LiF and that most of the diode current I_{out} is due to either protons of lower energies or heavier ion species or to electron losses. The even larger spread in the fraction of the mean ion current might indicate that in addition also the focusing properties - described by the coefficient f_r - do not remain constant. This is clearly demonstrated by quite different peak proton power densities measured in experiments with very similar electrical characteristics and vice versa. All these observations mean that for a shot showing „normal" electrical signals no possibility exists to reduce the experimental uncertainty of the peak proton power density achieved in the focus.

3. Time history and composition of the beam.
With the observations described above a precise and reliable time history of the proton power density in the focus cannot be established on basis of the measured currents and the voltage at the diode. Therefore the curve achieved by scaling the peak proton power density from activation measurements of 0.15 TW/cm^2 to the peak of the ion power in the focal plane should be considered as a best estimate only (Fig. 3).The fast rising leading edge is due to 'bunching' of the protons: lower energy protons start earlier in time and reach the target together with protons born later but accelerated to higher energies. This sharp rise was also observed by the foil accelerating experiments [1]. The steep increase also can be seen by magnetically insulated Faraday cups placed on different radial positions behind the cathode (Fig. 4). The delay of 11ns in the cup signals from different radii is related to the turn on characteristics of this diode.

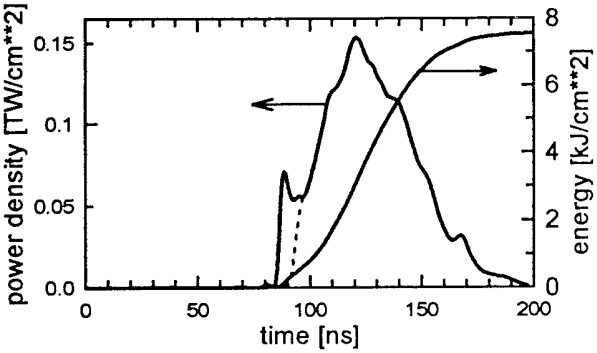

Fig. 3. Proton power density and energy in the focus, estimated from electrical signals

Indications on the composition of the ion beam were achieved from experiments where 6 μm thick aluminum foils were placed some millimeters in front of the Faraday cups. The signals of unfiltered and filtered Faraday cups show no significant difference for most of the time. This indicates that the ion beam does not contain a significant fraction of carbon ions. This result, which is also confirmed by time-of-flight methods may be due to the dense plasma between the vanes, where carbon ions may have been absorbed.

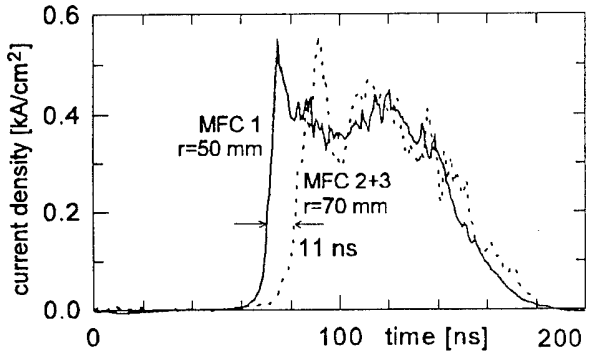

Fig. 4. Averaged signals of Faraday cups at different radial positions

With the focused power density reduced to 0.15 TW/cm^2 and the spread of ± 0.05 TW/cm^2 a much better agreement was achieved between calculated and measured foil acceleration data [5]. However the pulse length is certainly not below 60 ns and could not be reduced to half as suggested in [2], which in [5] is now accepted by theory. The rather large experimental uncertainty in the determination of the peak proton power density is limiting the verification of impact target codes as well as the determination of e.g. equation of state data used in these codes. It seems to be not possible to generate ion beams with better reproducibility with this B_Θ-diode. The following paragraph tries to give an explanation for this and gives hints to improve the situation.

Operating principle of the present B_Θ-diode.

In addition to the measurements reported so far the sum of the operating experience with this diode includes the following observations: The diode operates best if the voltage pulse starts with a 60 ns long precursor of 100 kV before rising to its final value of 1.0 to 1.6 MV. During this precursor no ion emission is observed; ions are only emitted after a voltage of 1 MV is achieved. The ion emission starts first at the inner part of the anode as shown by Faraday cup results and confirmed by an enhanced erosion at the inner edge of the anode, and due to the observed damage pattern most of the electron losses occur at one side of the 6 posts at the back side of the anode. Combining these results the diode's operation can be described in four phases:

First, electron emission starts on all surfaces where the field strength is sufficient during the voltage 'foot'; electrons from the vanes impact on the plastic anode inlay and start to produce an anode plasma; plasma formation starts also at the rear side of the anode. Second, while the voltage rises electron losses increase, especially at the anode support posts, where the insulating B_Θ -field is partly balanced by the current flowing through the posts. These posts act as 6 electron diodes. In the third phase the current of the 6 electron diodes generates the B_Θ-field that insulates the front ion diode. Ion current is produced for about 60 ns. Neutralizing electrons are taken from the plasma at the vanes. Finally expanding plasmas in the 6 electron diodes as well as the ion diode short out the gaps; the ion emission stops. The magnetic energy decays according to its L/R time constant - completely decoupled from the KALIF-generator.

In this process the field emission edge is not essential because most of the electrons come from the vanes and are lost in the 6 electron diodes. Therefore the field emission edge (Fig. 1) was removed in three consecutive steps with no decrease of the diode performance.

Particle-in-cell-simulations and a new design of the B_Θ - Diode.

Simulations using the two dimensional, stationary code BFCPIC2D [6] reported earlier supported the assumption, that most of the electrons emerge from the field emission edge, since it was the area of the highest electric field. The vanes appeared as flat surface with much less field. The 6 posts could not be modeled in two dimensions; however the current flowing through them was treated correctly. Fig. 5 shows the electron current density distribution. Omitting the field emission edge enhanced the electron emission at other parts of the surface, especially at the vanes. But the diode maintains its function as Fig. 6 shows. The values for electron and ion current obtained by the simulations do not show detailed agreement with the measured numbers, but they show, that omitting the field emission edge does not drastically change the properties of the diode. Since the 6 posts acting as electron diodes suffer the most serious damage and moreover, can be treated only with tricks in the PIC-code a design was suggested (Fig. 7), where these posts are replaced by a solid ring, while their task - providing the B_Θ - field - is maintained by a specifically designed electron diode placed in the back of the diode close to the axis, where the damage is less serious and replacement of parts is easier. This has also the advantage, that two parameters can be adjusted separately: The geometry, especially the gap distance of the electron diode adjusts the insulating B_Θ-field, while the gap between anode and vanes adjusts the ion current. Experiments on this diode are under way.

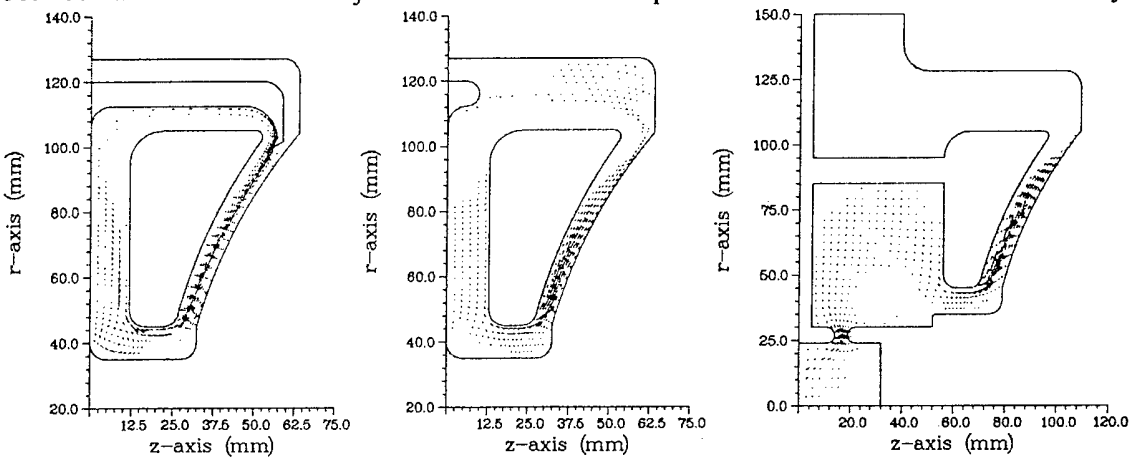

BFCPIC2D-simulation results: electron current density

Fig. 5: present diode Fig. 6: FE-edge omitted Fig. 7: New design

References:

[1] K. Baumung, H. Bluhm, P. Hoppé, S.V. Razorenov, D. Rusch, J. Singer, O. Stoltz, A.V. Utkin, this conference, Session 22

[2] O. Vorobjev, A. Ni, B. Goel, KfK-Bericht 5299, 1994, unpublished

[3] P. Hoppé, H. Bachmann, W. Bauer, H. Bluhm, L. Buth, H. Massier, D. Rusch, O. Stoltz, W. Väth, FZKA 5590, 1995, p. 52, unpublished

[4] W. Bauer, H. Bachmann, H. Bluhm, P. Hoppé, H. Karow, H. Lotz, D. Rusch, C. Schultheiss, E. Stein, O. Stoltz, T. Westermann, Proc. 9th Int. Conf. High Power Particle Beams, Eds. D. Mosher, G.Cooperstein, Wash. DC. 1992, Vol 2, p 735

[5] B. Goel, O. Vorobjev, in ref. [3], p. 109, and Laser and Particle Beams, to be published

[6] T. Westermann, Nucl. Instr. Meth. **A 263**, (1988), p. 271

ION DIODE DIAGNOSTICS TO RESOLVE BEAM QUALITY ISSUES

H. Bluhm, A.Arzhannikov, L.Buth, P. Hoppé, V. Licht, A. Matveenko, D.Rusch, O. Stoltz, J. Singer, C. Singleton, A.Tauschwitz, W.Väth, S. Yoo*

Forschungszentrum Karlsruhe, Institut für Neutronenphysik und Reaktortechnik
Postfach 3640, 76021 Karlsruhe
**Permanent address: Institute of Nuclear Physics, Novosibirsk, 630090*

Abstract

Various diagnostic methods and instruments are under development at FZK to measure important physical quantities in the accelerating gap of high power ion diodes on KALIF with high spatial and temporal resolution. These methods include optical spectroscopy, refractive index measurements, dispersion interferometry, and high resolution ion energy analysis. The paper describes the set-up of these diagnostics and first results obtained for applied and selfmagnetically insulated diodes.

Introduction

Beam quality is the main issue of intense light ion beam production and focusing. Beam quality does not only comprise divergence but also ion energy spread, purity, uniformity, ion canonical angular momentum, etc. Beam quality is tightly connected to diode operational stability. Most of the effects that influence beam quality have their origin inside the diode gap. Although substantial progress has been made, both theoretically and experimentally to understand the sources of beam imperfections, many important details remain unknown. Especially, the dynamics of the anode plasma and the electron sheath in high power diodes is not well understood.

Optical diagnostics - spectroscopic, interferometric, deflection- can yield detailed information on the electromagnetic fields and particle distributions in the electrode plasmas as well as in the diode gap. Therefore, we have begun to set-up a diagnostic effort to measure some of the main quantities with high spatial and temporal resolution. This includes ion spectroscopy, dispersive interferometry, refractive index gradient measurements, and high resolution ion energy analysis.

In this paper we report on the status of these developments and present first results.

Ion spectroscopy

The characteristics of the diode have been described elsewhere [1] and will not be repeated here. The spectroscopic system consists of two Cserny-Turner spectrographs with 1 and 0.5 m focal length respectively. An intensified gated diode array of 750 active elements is used as the detector at the exit of the 0.5 m system. A similar detector system or an array of 15 photomultipliers can be used with the 1 m system. The photomultipliers are coupled to the spectrograph via a quartz fiber bundle consisting of 15 columns with 40 fibers each. A spatial resolution of less than 0.5 mm and a temporal resolution of 10 ns for the diode array and of 2 ns for the photomultiplier array can thus be realized. A spectral resolution of 0.5 Å was obtained.

Since we tried to exploit the natural contaminants of our anode plasma the the major hindrance to the measurements became intensity. The intensity of most lines was insufficient to extend the measurements far into the gap. It turned out that doping of the anode surface either locally or globally changes the diode characteristics too much and therefore is of limited value.

Thus, mainly carbon (C I 2479 Å, C II 6578 Å, C III 2297 Å, C III 4647 Å, C IV 5802 Å) and hydrogen (H_α, H_β) lines are used to determine n_i, n_e, T_e, as well as the particle flux, the B-field, and the ion trajectory deflection.

The general structure of the C II - C IV line intensity evolution in the anode plasma is presented in fig. 1. Here the line of sight was 0.25 mm from the solid surface and the spatial resolution was 0.5 mm. Synchronously to H_α, the C II line is created during the initial phase of the sliding discharge across the Pd covered TiH film on the anode surface[2]. It is assumed that the origin of these carbon ions are surface contaminants released during the early heating of the metal films. After the beginning of ion

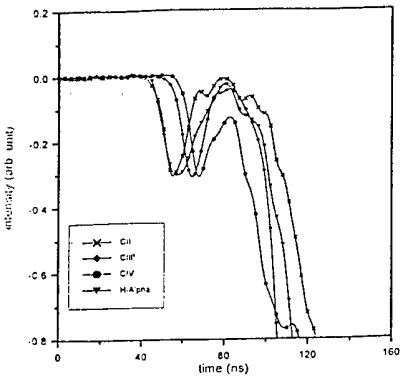

Fig.1 Time evolution of the emission intensity of C II, CIII, C IV, and H_α lines

current extraction the return current continues to heat the plasma and a transition from C II to CIV occurs. At the same time, the H_α line disappears, indicating complete ionization of the plasma. Since we observe a more rapid decay in space of the line intensities in the diode gap than expected from a space charge limited current density distribution we must conclude that the electric field is shielded by a hydrogen plasma in front of the carbon plasma. Shifting the line of sight of the spectrometer into the gap shows that the visible component of the anode plasma does not expand more than 1 mm into the gap during the whole pulse. This is confirmed by the refractive index diagnostics (see below).

Nonlinear dispersion interferometer

The main purpose of the dispersion interferometer is to measure the electron density in the ion diode acceleration gap. For a mean cord length of 3 cm through the ring shaped ion emitting area, the line density (n•l) is expected to be around 10^{14} cm^{-2} . This line density will cause a very small fringe shift of less than 1/100 wavelength and therefore a very sensitive interferometer is needed. Besides sensitivity, stability and simplicity are desirable in the hostile environment of the accelerator. The dispersion interferometer first proposed in [3] comes close to these requirements.

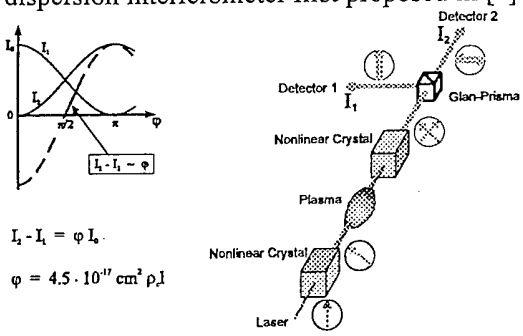

Fig.2 Set-up of the nonlinear dispersion interferometer system

An important property of the dispersion interferometer is that its two probe beams use the same optical path through the object which makes it rather insensitive to mechanical vibrations of its optical elements. Thus additional measures for stabilization are unnecessary. The general set-up of the interferometer is shown in fig. 2. Both the fundamental wave of a Nd:YAG laser and its second harmonic are transmitted through the plasma. After exiting from the plasma the infrared beam is frequency doubled a second time. Both green beams are polarized perpendicular to each other. Their relative phase shift is determined by the wavelength dependance of the optical pathlength. For a plasma this is proportional to the pathintegral of the electron density with a high degree of accuracy if the wavelengths are far away from any ionic or atomic resonances. A Glan polarizer whose transmission axis is fixed at 45° with respect to both beam polarizations splits the beams with equal intensities into both polarization directions. Thus the split beams can interfere at the position of the two detectors. However, the relative phase shift in both interference patterns is π. Thus subtracting the detector signals from each other can lead to complete cancelation of the difference signal. Using a Soleil-Babinet compensator in the beam path, this phase shift can be adjusted before the experiment, i.e., without the object.

On the other hand, there are special requirements to the laser system of the interferometer. The intensity must be high enough for frequency conversion, and single frequency operation is needed to get a smooth intensity profile on a ns time scale.

At present, a seeded, pulsed Nd:YAG laser with a pulsewidth of 10 ns and a pulse energy of about 100 mJ is used. As the short pulses give no complete measurement of the KALIF shot, the interference image must be compared to a reference measurement similar to a holographic method. This limits the sensitivity to about 30 mrad corresponding to $d(r_e l) \sim 7 \times 10^{14}$ cm^{-2} because of small drifts from pulse to pulse.

Presently an alternative single frequency cw laser system is under consideration. To achieve an intensity sufficient for frequency conversion the laser beam must be transmitted through several amplifiers. With the resulting quasistationary beam the complete KALIF pulse can be analyzed in one shot, and the sensitivity of the dispersion interferometer can be improved by one to two orders of magnitude. First results with the short pulse laser system in the immediate neighbourhood of the anode showed that late in

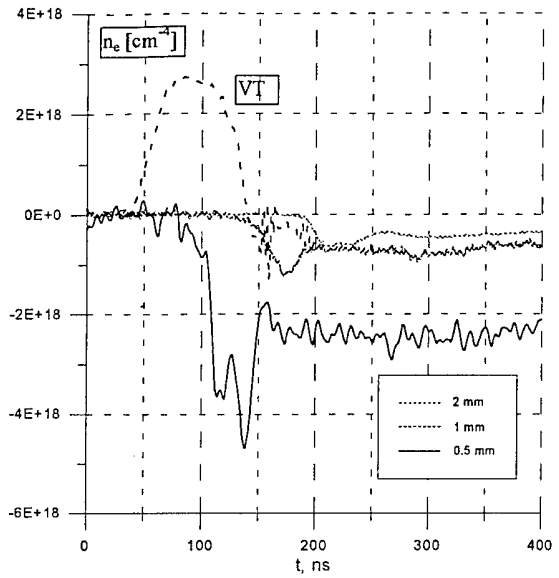

Fig.3 Electron density gradient at different lines of sight, 0.5, 1, and 2 mm from the anode. VT is the generator voltage

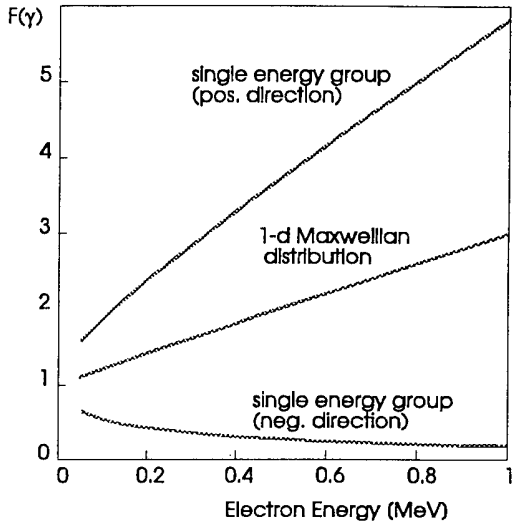

Fig.4 F(γ), the relativistic factor describing the phase shift multiplier for different electron energy distributions

the KALIF pulse an electron density of more than 10^{16} cm^{-3} is reached. Measurements at earlier times could not yet been made.

RING-diagnostic

A Refractive INdex Gradient (RING)-diagnostic permits to measure the gradient of electron and neutral densities in a plasma. It has been used previously by other authors [4,5]. It is based on the deflection of a laser beam transmitted through a plasma with density gradients. The angle of deflection is given by the following equation

$$\delta\phi = \frac{1}{\tilde{n}_0} \cdot \left| \int ds \cdot \nabla_\perp \tilde{n} \right|,$$

where $\tilde{n} = 1 + K_i n_i$ and $\tilde{n}_0$ are the perturbed and unperturbed indexes of refraction respectively. The integration has to be carried out along the laser beam path. The K_i are constants representing the different particle species. Their values range from $0.5 \cdot 10^{-23}$ to $50 \cdot 10^{-23}$ cm^3.

The basic scheme of the diagnostic set-up on KALIF is as follows: After passing through the plasma the cw laser beam is focused onto two glass fibres positioned next to each other. The use of fibres is the main difference compared to previous set-ups [4,5]. The advantage of our arrangement is that much faster photodiodes can be used and the time resolution can almost be increased 10 times compared to bi-cell detectors [4,5]. However, the sensitivity is somewhat reduced. We expect temporal and spatial resolutions of $\tau \approx 2$ ns and $\delta x \approx 0.2$ mm. The sensitivity of our instrument is $\nabla n l_{min} \approx 3 \cdot 10^{16}$ cm^{-3}.

Fig. 3 shows the time evolution of the electron density gradient at different distances from the anode.It is observed that the electron density gradient diminishes by more than one order of magnitude on a scale length of less than 0.5 mm. Also, as expected, the maximum gradient steadily decreases if the line of observation is shifted away from the anode. However, the plasma front does not reach farther than 1 mm into the gap before the end of the pulse.

Phase shift of a laser beam passing through a cloud of relativistic electrons

Applying interferometric and refractive index diagnostics to high power ion diodes containing relativistic electron clouds requires a careful consideration of the effect of these electrons on the measurements. We assume that the incident laser beam propagates parallel to the magnetic field lines which are considered to be so strong that the electrons move along these lines too.

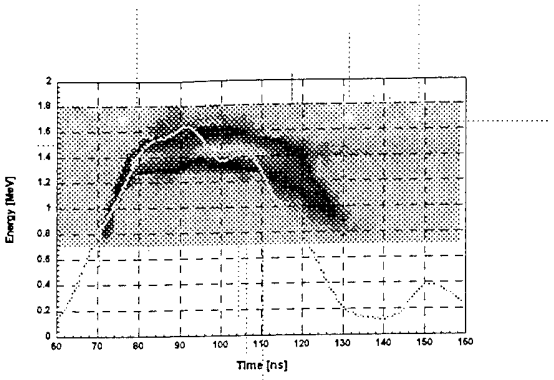

Fig. 5 Ion energy distribution measured with the magnetic energy analyzer (contour plot) compared to the voltage curve derived from the electrical (capacitive) monitor.The result shown was obtained for selfmagnetically insulated B_θ-diode

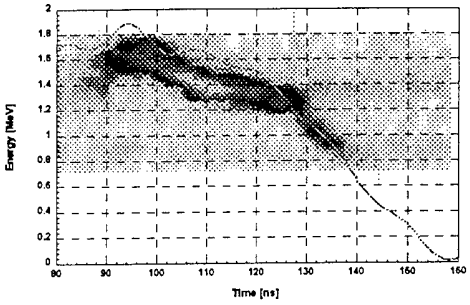

Fig.6 Same as fig. 5, but result obtained for the B_{appl}-diode.

The fringe shift of the wave is proportional to the path integral of the refractive index and in case of a single energy group of electrons may be written in the following form$\delta\Phi(\gamma) = F(\gamma)\delta\Phi_0$, where $\delta\Phi_0$ is the fringe shift for the case of nonrelativistic electrons. $F(\gamma)$ is an additional coefficient that depends on the relativistic factor γ of the electrons. $F(\gamma) = \gamma(1+\beta)$ for a movement of the electrons into the direction of wave propagation (positive direction) and $F(\gamma) = 1/\gamma \ (1+\beta)$ for the opposite movement (negative direction). For the case of an ion diode the relativistic factor has to be calculated in accordance with the electrical potential at the position under consideration: $\gamma = 1 + e\,(\varphi - \varphi c\,) / m\ c^{**}2$.
The results show that in the presence of relativistic electrons the fringe shift, measured e.g. with the RING diagnostic, does not only depend on the electron density but also on their relative movement with respect to the laser beam path.

Magnetic Energy Analyzer

A high resolution magnetic energy analyzer has been built to measure the ion energy distribution. It consists of a circular permanent magnet system with a diameter of 0.22 m and a field strength of 0.76 T. An array of 16 1 mm² pin diodes is used to register the ion energy as a function of time. A 3000 Å thick gold layer deposited on a 1.5 µm mylar foil positioned at the beam focus is used to Rutherford scatter the protons through the collimator infront of the magnet. The energy resolution of the system is better than 30 keV for the ion energy range below 2 MeV. The energy of the pin-diode channels was calibrated on a Van De Graaff generator. Results are shown in fig.5 and 6 for the B_θ and the B_{appl} diode respectively. Although certain differences appear between the electrically measured voltage pulse shape and the ion energy behaviour, there is no clear indication of ion energies greater than the applied voltage. However the width of the energy distribution is typically between 10 and 20% of the mean energy, i.e. between 100 and 200 keV. It is somewhat larger for the selfmagnetically insulated diode. Systematic errors in the derived voltage curves become visible during the rising part of the curve in case of the B_{appl} diode and during the falling part in case of the $B_\theta$diode. These are probably due to the LdI/dt correction which can be erroneous, especially in the case of the B_{appl} diode because of the use of plasma opening switches in the power feed.

References

1. H. Bluhm, P. Hoppé, H. Laqua, D. Rusch, Proc. IEEE, Vol. 80, NO. 6, (1992), p. 995
2. H. Laqua, H. Bluhm, L. Buth, P. Hoppé, J. Appl. Phys. 77, (1995), p. 5545
3. P.A. Bagryanskii, V.P. Drachev, Yu. I. Krasnikov, Sov. J. Plasma Phys. 18(2), (1992), p.138
4. M. E. Cuneo, T.R.Lockner,G.C.Tisone, IEEE Trans. on Plasma Sci. 19, (1991), p. 800
5. B. A. Knyazev, J.B. Greenly, D.A. Hammer, E.G. Krastelev, and M.Cuneo, paper p4-10, Beams 96, Prague, June 10-14, 1996

ELECTRON INERTIA EFFECTS FOR AN ELECTRON FLUID MODEL BY THE APPLIED-B ION DIODE

A.V.Gordeev, S.V. Levchenko

Nuclear Fusion Institute, Russian Research Center "Kurchatov Institute", Kurchatov Square 1, Moscow, 123182, Russia

ABSTRACT

In the framework of the one-dimensional vortex-like electron fluid model in applied-B ion diodes (see [1]) the numerical calculations are presented, where the electron inertia effects are taken into account. The existence of the additional relation between the magnetic field and the electric potential gives a possibility to reduce the ion diode problem to the system of the algebraic equations for the constants introduced. The ion current density in an ion diode is determined only by the magnetic flux cut out by the virtual cathode. As an illustration, the ion diode impedance for the KALIF device is calculated.

1 INTRODUCTION

The last computer simulations of the applied-B ion diodes [2, 3] show that the electron density profile in the ion diode gap between the anode and the virtual cathode has a maximum value near the anode. This effect has a simple interpretation within the frame of a new applied-B ion diode model [4, 5], where the electron mixing and screening processes are taken into account. At present time a new theory of an applied-B ion diode is developed [1], where electron inertia effects are taken into account. For the case when magnetic Debye length $r_B = B/4\pi e n_e$ is of the order of the electron collision depth c/ω_{pe}, the mixing processes result in smoothing-out of the Lagrange invariant $I = \Omega/n_e$ ($\Omega = B - (c/e)[\nabla \times \vec{p}]_z$ - the electron vorticity) over the entire diode gap and building-up of the electric field screening at the size scale r_B. In addition, the magnetic Debye length r_B is constant all over the anode gap and has only a slight time dependence. From the definition of the magnetic Debye length it is clear that the magnetic flux conservation in the diode gap results in decreasing of the magnetic Debye length by the increasing of number of electrons in the diode gap.

Thus, in contrast with the state $n_e =$ const postulated in [6] an adiabatic law $B/n_e =$ const there arises.

2 REDUCTION OF THE ION DIODE PROBLEM TO ALGEBRAIC EQUATIONS

In according with the paper [1] the ion diode is governed by the system of equa-

tions

$$\frac{db}{dx} = -\nu g, \qquad (1)$$

$$\gamma^3 \frac{dg}{dx} = \nu \frac{\Lambda}{\beta} - b, \qquad (2)$$

where for the dimensionless density ν there exists the available expression

$$\nu = \frac{J\gamma^3/\sqrt{1-\varphi} + \beta b^2}{\gamma + \Lambda b}. \qquad (3)$$

Here are introduced the normalized functions

$$b = \frac{B}{B_a}, \quad \nu = \frac{n}{n_0}, \quad \varphi = \frac{\Phi}{U},$$

and the normalized coordinate $x\omega_0/c \Rightarrow x$, where B_a –the anode surface magnetic field,

$$\omega_0^2 = \frac{4\pi e^2 n_0}{m_e}, \Lambda = \frac{IB_a}{4\pi m_e c^2},$$

$$\beta = \frac{B_a^2}{4\pi n_0 m_e c^2}, J = \frac{j_i}{en_0\sqrt{2ZeU/m_i}}.$$

The arbitrary constant n_0 is introduced for convenience and not enters in the final results.

One can see that near the anode the electron density has an integrable singularity. Here the coordinate x is measured from the anode surface ($x = 0$) to the virtual cathode surface ($x = d$), after which the electric field becomes zero.

Of course, the drift equation for the electron motion

$$E_x + \frac{1}{c} v_y B_z = 0 \qquad (4)$$

is valid also, but $I' = B/n_e$ is no longer equal to a constant value.

Later on the dimensionless counterpart of equation (4) will be very useful

$$\frac{d\varphi}{dx} = -\alpha\beta bg, \qquad (5)$$

where

$$\varphi - 1 = \alpha\left[\gamma - 1 + \Lambda(b-1)\right]$$

is the dimensionless electric potential and $\alpha = m_e c^2/eU$.

From the equations (1) and (5) it follows the integral relation

$$\frac{\Lambda}{1+\Lambda} b = s \frac{1 + a - \sqrt{1+a}}{a}, \qquad (6)$$

where

$$a(s) \equiv -1 + \Lambda^2 - 4\Lambda^2 \bar{J} \sqrt{\frac{1+\Lambda}{\alpha}} \sqrt{1-s}.$$

In this case the eigenvalue problem for the second order system can be reduced to algebraic equations for the finding-out of the constants introduced.

Eq.(6) permits to obtain the following expression for γ

$$\gamma = \frac{\Lambda b}{\sqrt{1+a}}. \qquad (7)$$

The ion current density j_i

$$j_i \equiv \frac{\bar{J}\Lambda^2}{\sqrt{\alpha}} \sqrt{\frac{2Zm_e}{m_i}} \frac{m_e c^3}{4\pi e r_0^2}, \qquad (8)$$

($r_0 \equiv |I|/4\pi e$ – the magnetic Debye length), depends on the dimensionless constants $\bar{J}, \Lambda$ and α. These constants must be calculated starting from the additional conditions. The equilibrium condition inside the ion gap gives the following relation among the constants

$$\Lambda^2\left(1 - \frac{4\bar{J}}{\alpha}\right) = \Lambda_0^2, \qquad \Lambda_0 = \frac{IB_0}{4\pi m_e c^2}. \qquad (9)$$

In addition, from the equilibrium condition at the virtual cathode one can obtain

$$\gamma|_{vc} = \frac{1 + \Lambda - 1/\alpha}{1 + \Lambda_0}. \qquad (10)$$

Besides, there exists conservation law of the vorticity flux that can be presented in the form

$$\Pi = \frac{1}{\alpha} \int_0^d \frac{\gamma}{\sqrt{\gamma^2 - 1}} d\varphi \qquad (11)$$

and the integral conservation of the electric neutrality

$$\Pi = \frac{\Lambda \bar{J}}{\alpha} \int_0^d \frac{\gamma}{b\sqrt{\gamma^2 - 1}\sqrt{1 - \varphi}} d\varphi. \qquad (12)$$

Here the equality $\Pi = \text{const}$ for the dimensionless magnetic flux between the anode and the virtual cathode can be considered as an initial condition.

3 CALCULATION OF THE ION CURRENT DENSITY FOR THE DIODE

The simple transformation of the integral expression (11) by the account of (12) leads to the conclusion that

$$\gamma|_{vc} = 1. \qquad (13)$$

It means that the δ-function electron layer at the virtual cathode is absent in the model presented. This gives a possibility to exclude the constants $\bar{J}$ and Λ with the help of Eqs. (9), (10) and (13). So, from the relation (11) one can obtain the functional dependence $\alpha = \alpha(\Lambda_0)$, where α has a minimum as a function of Λ_0. By the conservation of the magnetic flux Π in a experimental device one can consider that the experimental dependence $U = U(t)$ coinsides with the calculated dependence $\alpha^{-1}(\Lambda_0)$ by the appropriate choice of $\Lambda_0 = \Lambda_0(t)$.

Making use the time dependence of Λ_0 obtained one can calculate the electron number N_e related to the unit area in the plane (x, y)

$$N_e = \frac{\Pi B_0}{4\pi e \Lambda_0}. \qquad (14)$$

As an illustration, further on the experimental results on the KALIF device are analyzed within the framework of the theory presented. By using the experimental oscillogram for the shot number 3947 one can calculate the ion current density from the formula

$$j_i = \sqrt{\alpha} \frac{2\lambda + 1}{4\lambda^2} \sqrt{\frac{2Zm_e}{m_i}} \frac{eB_0}{4\pi m_e c}, \qquad (15)$$

where the dimensional parameter $\lambda = \alpha\Lambda_0$ is introduced. Given $\alpha(t)$ and for the known function $\alpha(\Lambda_0)$ the calculated ion current density is plotted on Fig. 1.

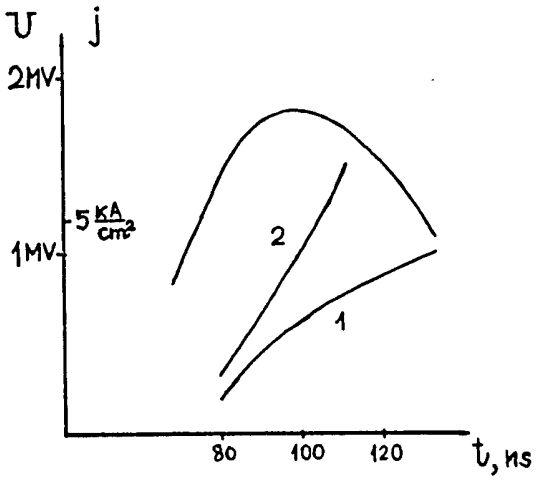

Figure 1: The experimental (1) and

the calculated (2) ion current densities for the given voltage by KALIF device.

Of course, the model presented not takes into account, for example, the electron motion along the magnetic field. On the other hand, the discrepancy between the predicted and experimental values can be assigned to the possible magnetic flux losses in the real experiment. The additional calculations show that by the decreasing of Π with time the discrepancy between the predicted and experimental values are reduced. Also, it is well to bear in mind that the theory presented is primarily related to the "barrel diode" geometry.

Fig. 2 shows the appropriate N_e accumulation, where the characteristic value $n_e \simeq N_e/d$ is in accordance with the numerical simulations [3].

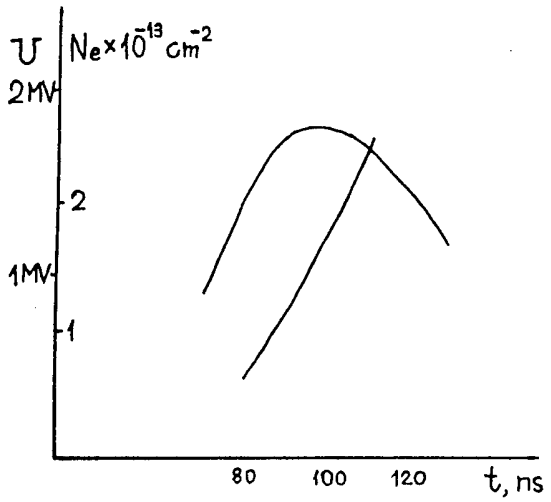

Figure 2: The calculated accumulation of the electron number N_e per unit area in the plane (x, y).

4 CONCLUSION

The model presented is developed in the framework of the cold relativistic electron fluid. The main feature of such a fluid model for the case $\vec{B}\nabla = 0$ is the conservation of the electron vorticity

$$\frac{\partial \Omega}{\partial t} + \nabla(\Omega v_e) = 0, \qquad \Omega \equiv \Omega_z, \quad (16)$$

which together with the electron continuity equation give the Lagrange invariant $I = \Omega/n_e$. The diffusion smoothing-out of the value I leads to the simplified equations, which can be reduced to algebraic eqations, containing only two experimental parameters: the total magnetic flux and the initial magnetic field. This permits to calculate the ion current density for a given voltage plot $U(t)$.

5 ACKNOLEDGMENTS

We wish to thank Dr.H.Bluhm (FZK, Germany) for interest in this investigation.

References

[1] A.V.Gordeev *In: Proceeding of the BEAM'96 Conference, Prague,1996.*

[2] T. Westermann and R. Schuldt, *Phys.Fluids B 5, 4408 (1993).*

[3] T.D. Pointon, M.P. Desjarlais, D.B. Seidel et. al., *Phys. Plasmas 1, 429 (1994).*

[4] A.V. Gordeev, A.V.Grechikha, *Preprint IAE-5742 RRC, Moscow,1994*

[5] A.V. Gordeev and A.V.Grechikha, *JETP Lett., v. 61, 196 (1995).*

[6] M.P. Desjarlais, *Phys.Rev.Lett. v.59, 2295 (1987); Phys.Fluids B 1, 8 (1989).*

THE VORTEX-LIKE SELF-CONSISTENT ELECTRON FLUID MODEL BY THE APPLIED-B ION DIODE: EQUILIBRIUM AND INSTABILITY

A.V.Gordeev

Nuclear Fusion Institute, Russian Research Center "Kurchatov Institute", Kurchatov Square 1, Moscow, 123182, Russia

ABSTRACT

The electron inertia effects in the one-dimensional model of the applied-B ion diode for the relativistic diode potential $eU/m_ec^2 \geq 1$ are investigated, when the magnetic Debye length r_B is of the order of the collisionless electron skin depth c/ω_{pe}. For this, an analytical relation between the magnetic field and the electric potential is discovered that makes it possible to reduce the second order eigenvalue problem to the system of algebraic equations. Instabilities inside the vacuum gap and in the near-anode emitting plasma are considered. In the near-anode Hall plasma the instability with two ion species is obtained that can give contribution to the ion angle divergence.

1 INTRODUCTION

Ion diodes are used to generate high-power ion beams to be focused on targets for inertial confinement fusion [1]. The electron magnetic insulation in an applied-B ion diode makes it possible an essential increasing of the ion current [2] . The last computer simulations give new insight into the physical processes in the applied-B ion diodes [3, 4]. A maximum value of the electron density obtained in simulation near the anode has a simple interpretation within the frame of a new applied-B ion diode model [5], where for the first time was formulated an idea about electron mixing and screening processes in ion diodes. Such processes result in smoothing-out of the Lagrange invariant $I' = B/n_e$, (B - is z-component of the magnetic field) over the entire diode gap and building-up of the electric field screening at the magnetic Debye length $r_B = B/4\pi en_e$.

In the present paper a modified electron fluid model is proposed, where a new Lagrange invariant $I \equiv \Omega/n_e$ is introduced [6] ($\Omega \equiv B - (c/e)\mathrm{curl}_z\vec{p}$ - the electron vorticity, $\vec{p}$ - the relativistic electron momentum). Besides, as it was shown in [6], the ion diode turbulence results in a diffusion smoothing-out of the Lagrange invariant by the following diffusion equation

$$\partial L/\partial t + (\vec{v}_0 + \langle n_1\vec{v}_1\rangle/n)\nabla L =$$

$$= (1/n)\nabla(n\hat{D}\nabla L), \qquad (1)$$

where $\hat{D}$ is a turbulent diffusion tensor.

Thus, a new equilibrium $n_e \sim \Omega$ arises.

Also, the EMHD instabilities in the ion diode gap and in the near-anode plasma are considered, which can give rise to the ion divergence.

2 SELF-CONSISTENT MODEL OF ELECTRON FLUID IN AN APPLIED-B ION DIODE

The relativistic electron fluid is described by the equation

$$\frac{\partial \vec{p}}{\partial t} + \nabla \gamma mc^2 = -e\vec{E} - \frac{e}{c}[\vec{v}, \vec{\Omega}]. \quad (2)$$

Here $\vec{\Omega} = \vec{B} - (c/e)\mathrm{curl}\vec{p}$, $\vec{p} = \gamma m\vec{v}$, $\vec{v}$ – the electron velocity, $\gamma = 1/\sqrt{1 - \vec{v}^2/c^2}$.

From Eq. (2) it follows for the one-component magnetic field and by $\partial/\partial z = 0$ the following equation

$$\frac{\partial \Omega}{\partial t} + \nabla(\Omega v_e) = 0, \qquad \Omega \equiv \Omega_z, \quad (3)$$

which together with the electron continuity equation gives the Lagrange type equation for the quantity $I = \Omega/n_e$.

From Eqs. (2) and (3), taking into account the Poisson equation and the Amper law one can obtain for a stationary case after simple transformations the system of equations

$$\frac{db}{dx} = -\nu g, \quad (4)$$

$$\gamma^3 \frac{dg}{dx} = \nu \frac{\Lambda}{\beta} - b, \quad (5)$$

where for the dimensionless density ν there exists the available expression

$$\nu = \frac{J\gamma^3/\sqrt{1-\varphi} + \beta b^2}{\gamma + \Lambda b} \quad (6)$$

Here are introduced the normalized functions

$$b = \frac{B}{B_a}, \quad \nu = \frac{n}{n_0}, \quad \varphi = \frac{\Phi}{U},$$

and the normalized coordinate $x\omega_0/c \Rightarrow x$, where B_a –the anode surface magnetic field,

$$\omega_0^2 = \frac{4\pi e^2 n_0}{m_e}, \Lambda = \frac{IB_a}{4\pi m_e c^2},$$

$$\beta = \frac{B_a^2}{4\pi n_0 m_e c^2}, J = \frac{j_i}{en_0\sqrt{2ZeU/m_i}}.$$

The arbitrary constant n_0 is introduced for convenience and not enters in the final results.

The coordinate x is measured from the anode surface ($x = 0$) to the virtual cathode surface ($x = d$), after which the electric field becomes zero.

The dimensionless counterpart of the electron drift equation

$$E_x + \frac{1}{c} v_y B_z = 0 \quad (7)$$

may be represented as

$$\frac{d\varphi}{dx} = -\alpha\beta bg, \quad (8)$$

where

$$\varphi - 1 = \alpha\,[\gamma - 1 + \Lambda(b-1)]$$

is the dimensionless electric potential and $\alpha = m_e c^2/eU$.

Dividing Eq.(4) by Eq.(8) and introducing a new "potential" $\psi = \sqrt{1-\varphi}$, one can obtain the equation, which can be integrated analytically. The result is [7]

$$\frac{\Lambda}{1+\Lambda} b = s\,\frac{1 + a - \sqrt{1+a}}{a}, \quad (9)$$

where

$$a(s) \equiv -1 + \Lambda^2 - 4\Lambda^2 \bar{J} \sqrt{\frac{1+\Lambda}{\alpha}} \sqrt{1-s},$$

$\bar{J} \equiv J/\beta$, $s = 1 - \psi^2/\alpha(1+\Lambda)$,

The ion current density j_i

$$j_i \equiv \frac{\bar{J}\Lambda^2}{\sqrt{\alpha}} \sqrt{\frac{2Zm_e}{m_i}} \frac{m_e c^3}{4\pi e r_0^2}, \qquad (10)$$

($r_0 \equiv |I|/4\pi e$ - the magnetic Debye length), depends on the dimensionless constants $\bar{J}, \Lambda$ and α, which can be calculated starting from additional conditions.

The equilibrium condition in the ion diode takes the form

$$\Lambda^2 (1 - \frac{4\bar{J}}{\alpha}) = \Lambda_0^2, \qquad \Lambda_0 = \frac{IB_0}{4\pi m_e c^2}. \qquad (11)$$

Besides, the vorticity flux conservation

$$\int_0^d \Omega \, dx = \text{const}$$

and the integral neutrality of the ion diode

$$N_e = ZN_i \qquad (12)$$

must be taken into account. Here N_e and N_i – the particle number, related to the unit area in the (x, y) plane.

An additional investigations show that for this model the δ -function electron layer at the virtual cathode is absent and the electric and the magnetic fields are continiuous.

3 EMHD INSTABILITIES IN AN APPLIED-B ION DIODE

The investigations of the ion diode instability have a big history. The successive progress in this region results in the understanding that the slow instabilities are the most dangerous ones. The paper [8] seems to confirm a real instability, which discovered in recent numerical calculations. One must bear in mind that ions and electrons inside the ion diode can be considered as a plasma-like medium with the electric field screened at the magnetic Debye scale r_B. The characteristic parameters of this plasma lie in the EMHD region [9]

$$4\pi n_e m_e c^2 \ll B^2 \ll 4\pi n_i m_i c^2 \qquad (13).$$

The instability frequencies of the applied-B ion diode have an abrupt change in some point of the diode operation. In the first half of the voltage pulse there exist the fast disturbances, which apparently connected with the electron diffusion in the diode gap. Such instabilities prevent the inclination from the condition $I = \text{const}$ (or $I' = \text{const}$). The corresponding dispersion equation in the quasiclassical limit is equal [10]

$$-\bar{\omega}^3 + \kappa\bar{\omega}^2 \left(\kappa^2 + 1 + \frac{d\ln n_{e0}}{d\ln B_0} \right) = \kappa^3 \Pi_i. \qquad (14)$$

Here

$$\bar{\omega} = \frac{\omega \delta_B}{c}, \Pi_i = \frac{4\pi e^2 Z^2 n_{i0} \delta_B^2}{m_i c^2}, \delta_B = \left| \frac{B_0}{B_0'} \right|,$$

$\kappa = k\delta_B$, ω and k – the frequency and the wave vector of the disturbances, $n_0(x)$ – the equilibrium density, $B_0(x)$ – the magnetic field, $B_0' \equiv dB_0/dx$.

From Eq.(14) one can see that for $\kappa \sim 1$ and $d\ln n_{e0}/d\ln B_0 < 0$ the instability can exist that leads to the smoothing-out of the I'.

In the second stage of the voltage pulse the slow disturbances are usually developed, which are give contribution to the ion divergence. Below such an instability will be considered, which arises in the near-anode Hall plasma by the account of two ion species: hydrogen and carbon. The basic assumptions will be: 1) the neglecting of the electron inertia; 2) the magnetized electrons; 3) the neglecting of the heavy component (carbon) velocity; 4) unmagnetized ions (protons). Within a framework of this approximations the main equations will be the following ones: Ohm's law

$$0 = -en_e\vec{E} - (en_e/c)[\vec{v}_e \times \vec{B}] - \alpha_e\vec{j}, \quad (15)$$

the proton motion equation

$$n_i m_i d\vec{v}_i/dt = \xi_H \nabla B^2/8\pi - \alpha_{12}\vec{v}_i, \quad (16)$$

and proton continuity equation

$$\partial n_i/\partial t + \nabla(n_i\vec{v}_i) = 0. \quad (17)$$

Calculations give the following dispertion equation for the frequency ω

$$i\omega^2 = \left(\frac{cB}{4\pi en}\right)^2 \frac{\xi_H}{\xi_C}\frac{k^3}{a\delta_B}, \xi_\alpha = \frac{Z_\alpha n_\alpha}{n_e}. \quad (18)$$

Estimate for the KALIF device emitter gives the increment value

$$\mathrm{Im}\omega < 10^9 s^{-1}. \quad (19)$$

4 CONCLUSION

Thus, the turbulent mixing processes result in the smoothing-out of the value I and the establishing of the unique magnetic Debye length r_B over the entire volume of the diode gap. The electric field screening at the lengh r_B leads to the decreasing of the effective diode gap ("voltage decay") and also to the decreasing of the phase velocity of the disturbances in an applied-B ion diode.

5 ACKNOWLEDGMENTS

I wish to thank Dr. H.J.Bluhm (FZK, Germany) for interest in this investigations.

References

[1] J.P.VanDevender and D.L.Cook, *Science v.232, 831 (1986).*

[2] M.P. Desjarlais, *Phys.Rev.Lett. v.59, 2295 (1987); Phys.Fluids B 1, 8 (1989).*

[3] T. Westermann and R. Schuldt, *Phys.Fluids B 5, 4408 (1993).*

[4] T.D. Pointon, M.P. Desjarlais, D.B. Seidel et. al., *Phys. Plasmas 1, 429 (1994).*

[5] A.V. Gordeev and A.V.Grechikha, *JETP Lett., v. 61, 196 (1995).*

[6] A.V. Gordeev, *Preprint IAE-5884/6, RRC, Moscow, 1995.*

[7] A.V.Gordeev, *Preprint IAE - 5962/6, RRC, Moscow, 1996.*

[8] R.W.Lemke and S.A.Slutz, *Phys. Plasmas 1995, v.2, p 549.*

[9] A.V. Gordeev, A.S. Kingsep, L.I. Rudakov, *Physics Report, 1994, v.243, n.5.*

[10] A.V. Gordeev, A.V.Grechikha *Primarbericht, KFK, Karlsruhe, 1993 (unpublished).*

ELECTRON SHEATH COLLAPSE IN AN APPLIED-B ION DIODE

A.Grechikha

Forschungszentrum Karlsruhe, Institut für Neutronenphysik und Reaktortechnik
Postfach 3640, 76021 Karlsruhe, Germany

Abstract

The effect of the electron sheath collapse in an applied-B ion diode due to the presence of the resistive anode plasma layer is found. It is more damaging at higher diode voltages and it may be responsible for the parasitic load effect observed in the experiments.

Introduction

Applied-B ion diodes are used for the generation and focusing of intense ion beams in the Inertial Confinement Fusion Program. The basic effort has been to increase the energy and improve the quality of the beams. Experiments show that there are many obstacles to this, and the unstable behavior of the magnetized electrons is among them. Describing the electron component is one of the basic problems in the theory of ion diodes. The reason is that, in contrast with a classical Child-Langmuir diode, in which the electrons are freely accelerating between the electrodes, an ion diode requires magnetic insulation of the electrons, which would otherwise carry most of the current. Magnetic insulation, however, makes the behavior of the electrons extremely complicated.

The basic goal of the present work is to investigate the role of the anode plasma in the problem of stability of the electron sheath in the diode. Both analytic and numerical approaches are used. It is shown analytically that the infinitely thin electron sheath is generally speaking unstable in the presence of a resistive anode plasma and the threshold thickness of the plasma layer is less, the greater the ion current enhancement is. The numerical part of the work is to study the role of finite electron gyroradii which are assumed to be zero in the theory. The main result is that low-voltage diodes exhibit better stability due to the limiting effect of larger gyroradii.

Theory

Let us consider an infinitely thin electron sheath in the diode (Fig. 1), the position of which is determined by the balance [1] between electrostatic attraction to the anode and resulting
magnetic pressure defined by the extent of the compression of the magnetic flux captured in the gap and the extent of the expansion of the magnetic flux captured in the charge-neutral region

$$B_{gap}^2/8\pi - E_{gap}^2/8\pi = B_{cn}^2/8\pi \ . \qquad (1)$$

Here the left side represents the net force acting on the sheath from the anode and the right side represents pressure of the magnetic flux captured in the charge-neutral region of the diode. The presence of the anode plasma results in a different scaling for the two forces: the magnetic one and the electrostatic one. The pressure of the magnetic flux captured to the diode gap is proportional to the inverse square of the distance from the sheath to the anode, while the electrostatic force for the given voltage is proportional to the inverse square of the

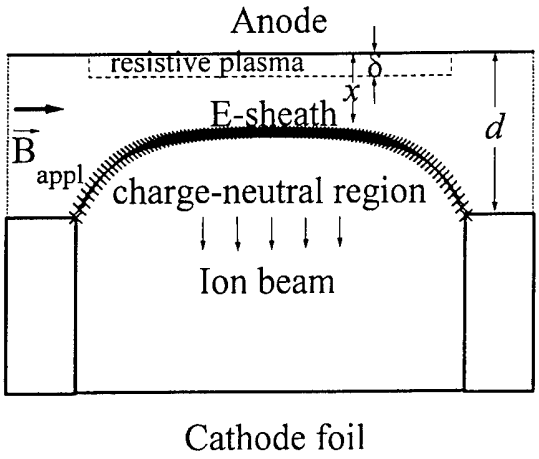

Fig. 1. Geometry of the model.

distance from the sheath to the boundary of the plasma layer (we assume here, for this simple argument, the skin time for the magnetic field penetrating into plasma to be small compared with the pulse duration). If both forces are large enough compared with the pressure of the magnetic flux captured in the charge-neutral region (the case of the large current enhancement), the stability of the electron sheath is impossible as the electrostatic force (directed to the anode) rises faster than the magnetic one (having the opposite direction) when the sheath position is shifting towards the anode. The theory provides the expression

$$1-\frac{\tanh\sqrt{\gamma\tau}}{\sqrt{\gamma\tau}}=\frac{1-qx/\delta}{1-q} \qquad (2)$$

for the growth rate γ where $\tau=4\pi\sigma\delta^2/c^2$ is the plasma skin time and $q=(\frac{x(L-d)}{d(L-x)})^2\frac{L-\delta}{L-x}$. One can find that $\gamma>0$ at

$$\delta > d(\frac{x(L-d)}{d(L-x)})^3\frac{L}{L-d}/(1+(\frac{x(L-d)}{d(L-x)})^3\frac{d}{L-d}). \qquad (3)$$

If $L >> d$, one can neglect the change in the pressure of the magnetic flux in the charge-neutral region and the condition of instability simplifies to:

$$\delta > d(\frac{x}{d})^3. \qquad (4)$$

This means that at the large enhancement ($x << d$) a smaller plasma layer is sufficient to cause the electron sheath instability. The physical meaning of the threshold is that the spatial derivative of the force F acting on the unit square of the electron sheath, where

$$F=B_{gap}^2/8\pi-E_{gap}^2/8\pi-B_{cn}^2/8\pi \qquad (5)$$

changes its sign from negative to positive and instead of returning the sheath to the equilibrium position, the force F acts to increase the deviation from equilibrium. One can

show that the unequality (3) is equvivalent to the condition $dF/dx > 0$.

Simulations: The Model

Simulations using the 2D PIC code KARAT [2] were carried out in order to clarify the nonlinear stage of the instability, its sensitivity to the physical parameters, and its possible effect on the ion diode behavior. A simple model for the simulations was chosen: the resistive plasma was modelled by a region with constant resistivity; the ion beam was absent. This simple model is more preferable than an exact one in the sense that it cuts off all the features which are not related to the studied effect, such as the two-fluids electron-ion instabilities as well as by the instability of the plasma surface due to the ion beam emission. (See the Discussion also.) The only quantitative consequence of the absence of ions in the simulations is that the voltage and electric field in the gap are related by the factor $\alpha = 1$ rather than $\alpha = 0.75$ as it would be in the case of a Child-Langmuir diode.

Results

Figure 2 exhibits the pattern of the sheath instability for the high-voltage case $U = 100MV$ which is closer to the theory's assumptions as the electron gyroradii are small and the approximation of an infinitely thin electron sheath works well enough. One can see that the instability results in spot-like regions where the electron sheath penetrates into the resistive plasma. Figure 3 exhibits the same case with half the anode width along the magnetic field. Only one spot develops.Figure 4 exhibits a lower voltage case with $U = 10MV$. One spot develops, but it is much more diffuse. The depth of the electron sheath penetration into the plasma is much less.

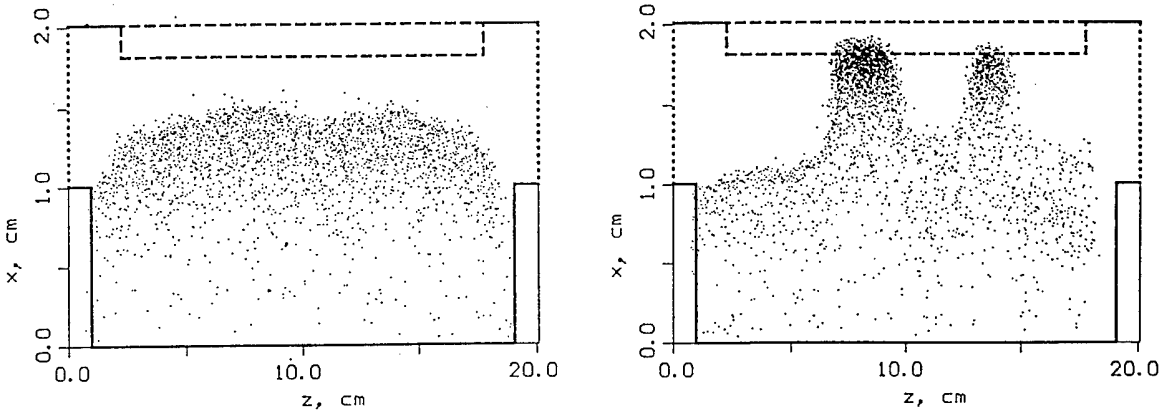

Fig. 2. Instability at $U = 100MV$ for $t = 9.0ns$ and $t = 10.3ns$.

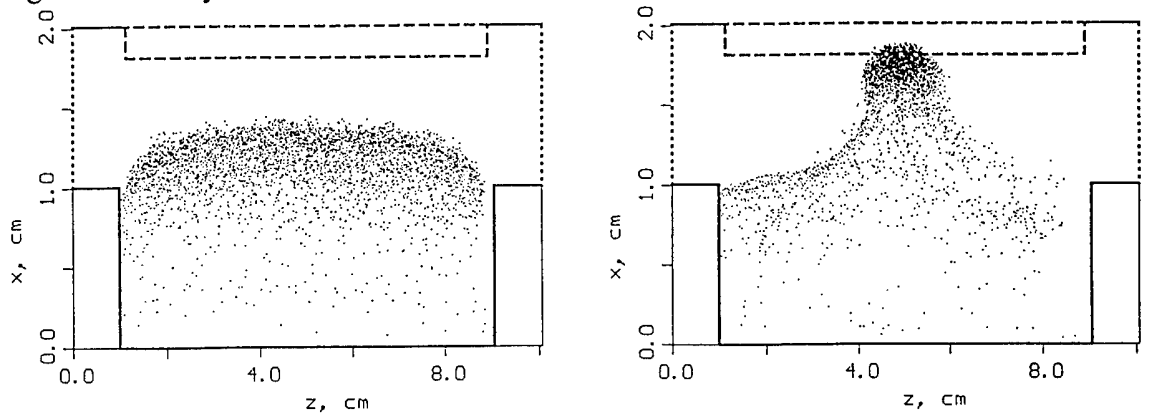

Fig. 3. Instability at the same voltage and an anode that is half as wide in the direction of the magnetic field for $t = 3.0ns$ and $t = 3.8ns$.

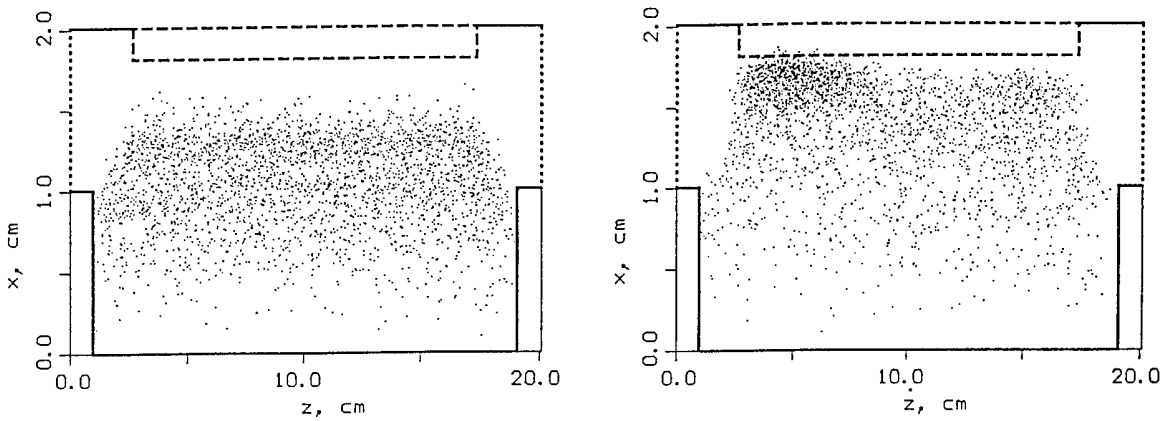

Fig. 4. Instability at $U = 10MV$ for $t = 21.5ns$ and $t = 25ns$.

Discussion

It has been shown that in the case of higher voltages, the instability is more damaging in the sense of the electron sheath uniformity and insulation. Better performance of the diode is expected at lower voltages due to the stabilizing effect of the relatively larger electron gyroradius, which obeys the scaling

$$r_L/d \sim m_e c^2/U. \qquad (6)$$

The simulations with the low voltage $U = 1MV$ did not exhibit any significant effect of the instability at all. This conclusion, however, may be too optimistic because in the real 3D electron dynamics their gyroradii could be less due to the possibility of energy transfer from gyrorotation to other degrees of freedom - e.g. to ion beam. The described effect may be responsible for the parasitic load effect both because of the breakdown of the electron insulation at the spots and the enhancement in ion current emitted from the spots; theion beam from the spots would not contribute to the focussable beam because of strong local defocussing.

This instability due to the presence of the anode plasma is not the only one. It can be shown that the ion emission from the plasma leads to instability of the plasma boundary, with a growth rate provided by the dispersion relationship

$$\omega^2 = 1.81...i|k|Bj_i/c\rho \qquad (7)$$

which is consistent with the observed time dependence of the anode plasma layer broadening. Here ρ is the mass density of the plasma and the wavenumber k is directed across the magnetic field. The physical meaning of this instability is that rippling of the plasma surface leads to the modulation of the emitted ion current density which is larger at the tops of the ripples, and this, in turn, causes modulation of the magnetic pressure acting on the plasma surface which results in the further development of the ripples. This instability may also significantly limit the ion beam quality, but its detailed description is beyond the scope of the present paper.

[1] M.P.Desjarlais, Phys.Fluids B **1**, 8 (1989).
[2] Ignatov A.M., Tarakanov V.P., *Phys.Plasmas*, **1**, *741 (1994).*

Ion Diode Optics: Measurement of Divergence and Aiming of Beams for Transport to Light-Ion ICF Targets*.

E. Krastelev, B. N. Kniazev, F. Lindholm, D. A. Hammer, B. R. Kusse, J. B. Greenly

Laboratory of Plasma Studies, Cornell University,Ithaca NY 14853 USA

Abstract

Diagnostic development for measurments of anode plasma structure and ion beam local aiming and microdivergence are being developed on the COBRA accelerator at Cornell University. Results of streaked-scintillator and tracer target beam diagnostics, and streaked anode light imaging are described.

Successful development of transport and focusing systems for light-ion beam ICF drivers requires accurate characterization of the ion diode as the first element in a particle beam optics system. Considerable effort has been devoted to this characterization and optimization in the radial geometry of PBFAII at Sandia National Laboratories, and in axial ("extraction") geometry on KALIF at Forschungszentrum Karlsruhe, generally using the beam focus as the diagnostic of beam optics. Local beam diagnostics for microdivergence and aiming as a function of time and position in the diode are now being investigated on the Cornell Beam Research Accelerator (COBRA). COBRA has recently been completed as a four-cavity linear inductive voltage adder for 4 MV, 20Ω, 40 ns. The experiments described here were done before completion,with a single cavity, using a passive epoxy-filled groove anode plasma source in the LION extraction applied-B diode [1]. We describe here first results with new diagnostics using streaked light emission from the anode plasma, and streaked scintillator shadow box targets. These measurements begin to characterize the time-dependent optics of the ion beam, and the diode dynamics responsible for these observed optics.

Figure 1a gives a diagram of the radial structure of the anode surface, and a radial image across this surface, produced by a lens on a radially aligned linear fiber optic array. Untreated aluminum surfaces between the epoxy-filled grooves are much more reflective than the grooves, as seen in this image, for which the anode was uniformly illuminated by an external light source. The aluminum (Al) surfaces which were blackened as indicated on the diagram exhibit greatly reduced reflection. Figure 1b shows a streak photograph of anode plasma light during a diode shot, seen through this radial slit. There is nearly uniform light intensity across the grooves separated by untreated Al, while the grooves separated by blackened Al show much greater intensity over the grooves than over the Al. If the plasma light intensity were uniform in radius, the high reflectivity of the untreated Al would give observed intensity higher than the grooves, as in Fig.1a. Since the observed intensity is instead nearly uniform, and the intensity over the blackened Al is greatly reduced, we conclude that most of the plasma light emission is over the grooves and not over the aluminum. It is remarkable that this persists for the entire duration of the diode pulse, implying that the plasma remains localized in radius over the millimeter scale length of the grooves.

Figure 2 shows a series of streak photos from the anode plasma light diagnostic (without blackened Al) with varied magnetic insulation strength. With low B/Bcrit (a) anode plasma light appears earliest at the outer radius, with medium B/Bcrit (b) light appears almost simultaneously at all radii, and with high B/Bcrit (c) light appears first at the inner radius. The magnetic configuration in these shots was chosen to make the ion current density uniform over the radius in (b); current density peaked at the outer radius in (a), and at the inner radius in (c). Thus initial turn-on of the anode plasma is correlated to the shape

of the virtual cathode electron layer which also determines the radial distribution of ion current density during the pulse, and these are both controlled by the magnetic field strength and shape. We believe this anode plasma light diagnostic will give further useful information in clarifying the underlying diode dynamics that influence beam optics, by correlating the anode plasma structure with beam optics diagnostics.

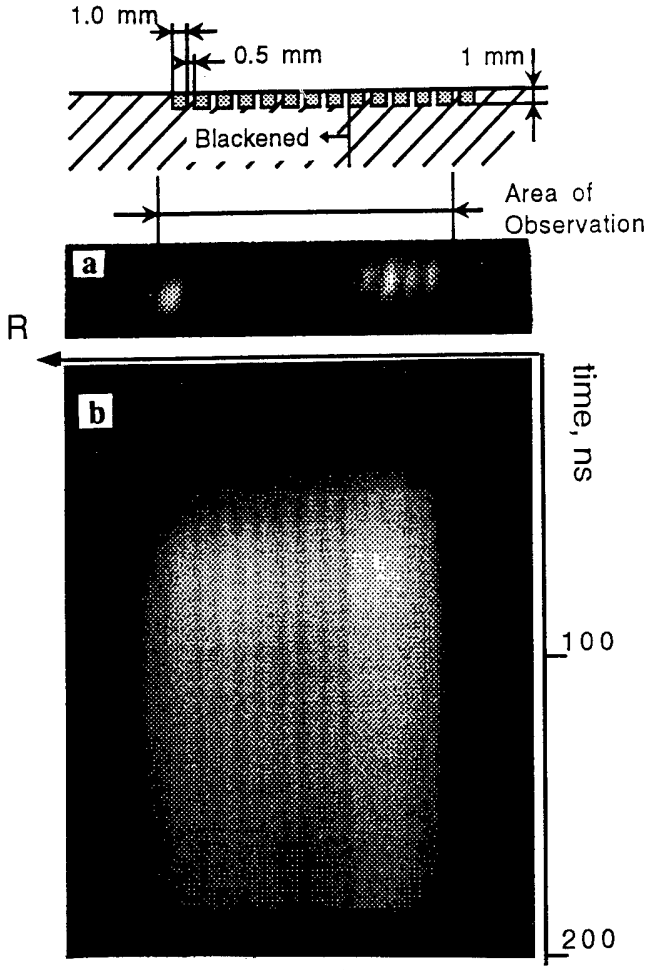

Figure 1.

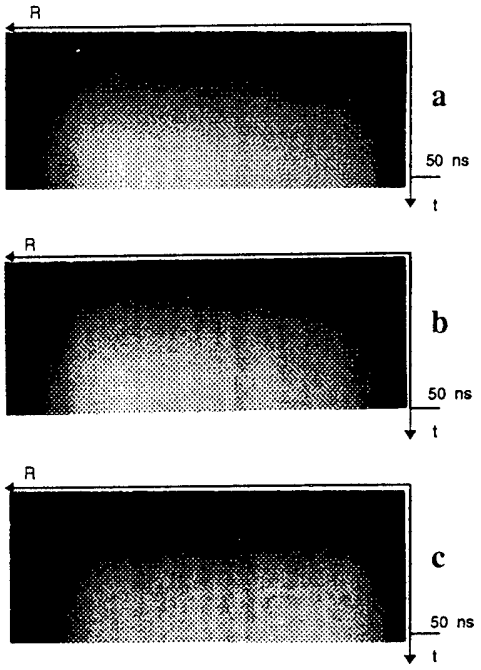

Figure 2.

Figure 3 presents results of the streaked-scintillator beam optics diagnostic. Fig. 3a is a diagram of the LION magnetically-insulated extraction ion diode used on COBRA for these experiments (REF.1). Figure 3b is a streak photo of the scintillation produced by two beamlets defined by a pair of slits as shown in the diagram. The diode voltage and current waveforms are shown in Fig.3c. The streak shows initial low microdivergence of 55mrad, which rapidly increases after 32ns in the pulse to 86mrad. The average deflection from straight axial propagation of the beamlet at 84 mm radius is comparable to the microdivergence, but the beamlet at 70 mm shows large initial inward angle of 140mrad, which decreases strongly during the pulse. This shot was into vacuum, with no gas cell in the diode. We believe the initial deflection of the inner beamlet is due to space potential in the beam propagation volume. The beamlet aiming was also investigated using a time-integrated tracer target oriented nearly parallel to the axial beam propagation, so that the beamlets defined by slits impacted the target at a grazing angle. The resulting damage traces are shown schematically in Figure 4, which also gives the result of measurement of the angles of these traces as a function of radius for two different magnetic field strengths.

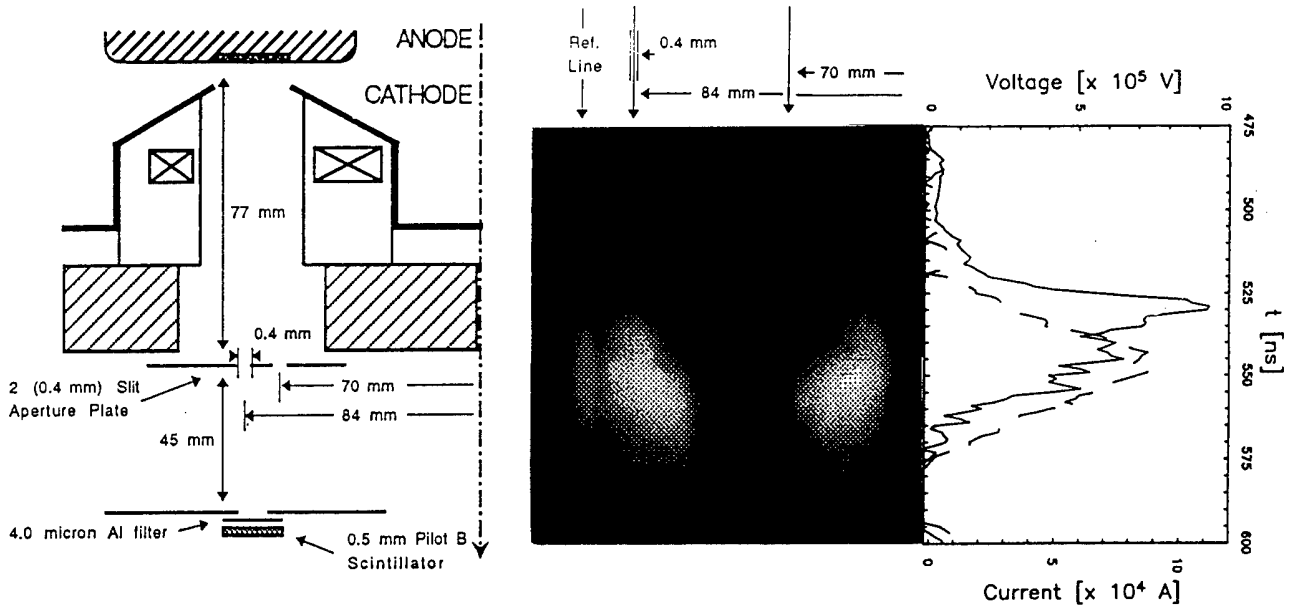

Figure 3.

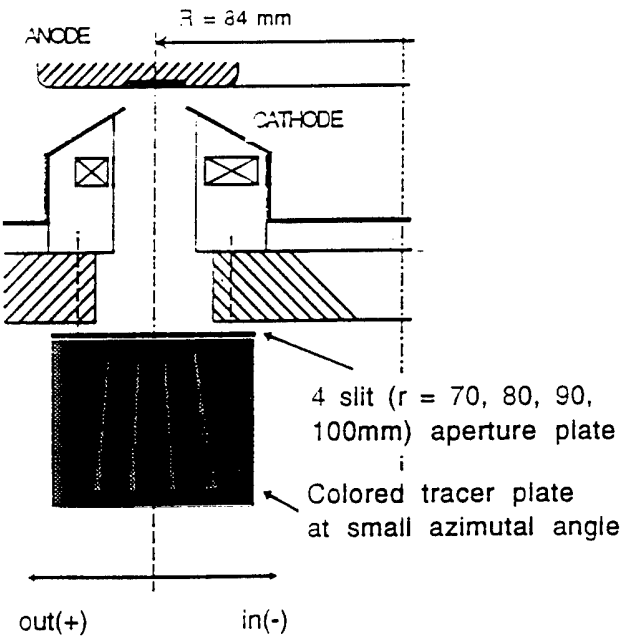

Figure 4.

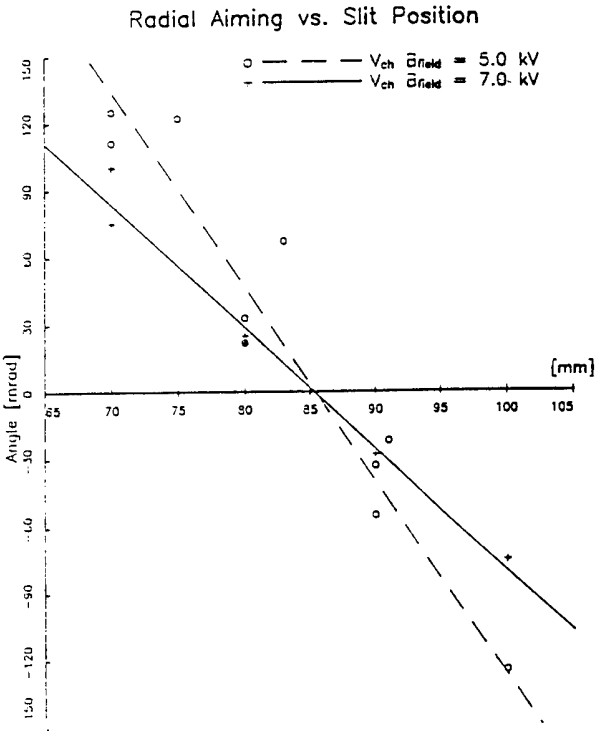

When a neutralizing gas cell was used (not shown) the angles decreased to zero within measurement uncertainty, implying that space potential was largely responsible for the inward (outward) deflection of the inner (outer) beamlets. Since the aiming angles in vacuum propagation were decreasing with time, the strong increase in microdivergence of the individual beamlets seen in Fig. 3 is thus unlikely to be due to space charge, and probably is due to diode gap dynamics. Since the plasma structure (Figs. 1 and 2) seems relatively constant, fluctuations caused by gap instabilities seem the most likely mechanism.

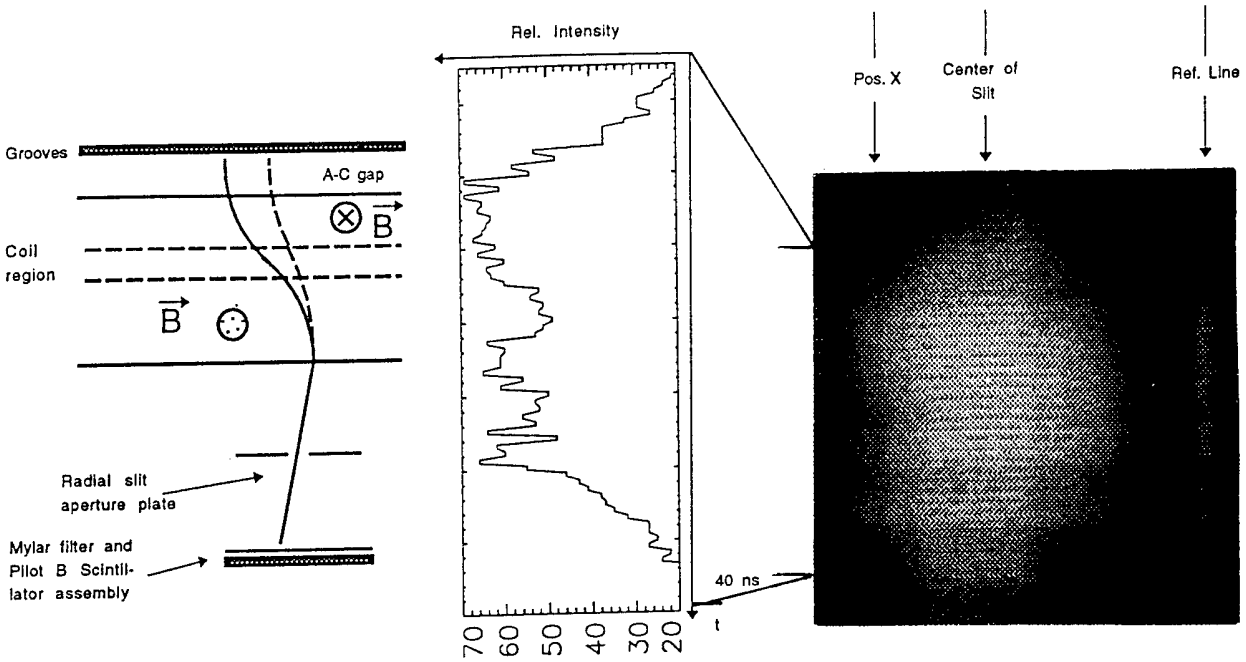

Figure 5.

Figure 5 shows a streaked scintillator viewing a beamlet defined by a radial slit. As indicated by the diagram, the effect of the decreasing voltage during the pulse and the consequent increasing azimuthal deflection of the beam in the applied magnetic field is to sweep the azimuthal position on the anode from which the beamlet viewed by the scintillator originates. The result is that the time axis of the streak corresponds to beam intensity as a convoluted function (nonlinear) of anode azimuthal position and time. This intensity is modulated, as seen in the figure, and may imply a fairly coherent azimuthal beam structure with several-millimeter scale length. The origin of this structure is unknown, and may be the result of diode instability. The diagnostics shown here rely upon aperture definition of beamlets, and will become unreliable due to aperture ablation with beams much more intense than the 500-800 A/cm2 in these experiments. It is hoped that apertures may be replaced by intentional structuring of, or local introduction of tracer particles of different ion species into, the anode plasma, to eliminate the need for apertures in diagnosing optics of more intense beams. These diagnostics will be pursued in experiments now beginning on the full four-cavity COBRA.

*Work supported by Sandia National Laboratories.

Reference:

1. J. B. Greenly, R.K. Appartaim, J.C. Olson and L. Brissette, *Proc. 10th Intl. Conf. on High Power Particle Beams*, June 1994, San Diego, p. 398.

MODIFICATION OF DIODE CHARACTERISTICS BY ELECTRON BACK-SCATTER FROM HIGH-ATOMIC-NUMBER ANODES*

D. Mosher, G. Cooperstein, D.V. Rose+, and S.B. Swanekamp+

Plasma Physics Division, Naval Research Laboratory, Washington, DC, 20375, USA

In high-power vacuum diodes with high-atomic-number anodes, back-scattered electrons alter the vacuum space charge and resulting electron and ion currents. Here, electron multiple back-scattering is studied through equilibrium solutions of the Poisson Equation for 1-dimensional, bipolar diodes in order to predict their early-time behavior. Before ion turn-on, back-scattered electrons from high-Z anodes suppress the diode current by about 10%. After ion turn-on in the same diodes, electron back-scatter leads to substantial enhancements of both the electron and ion currents above the Child-Langmuir values. Current enhancements with ion flow from low-Z anodes are small.

In high-power vacuum diodes with high-atomic-number (high-Z) anodes, a large fraction of the electrons are back-scattered, thereby altering the space charge in the vacuum gap and the resulting electron and ion currents from their conventional values. This process may contribute to observed differences in the early-time behavior of pinched-beam diodes (PBDs) with low-Z and high-Z anodes in NRL Gamble II experiments.[1] Here, electron multiple back-scattering is studied through equilibrium solutions of the Poisson Equation for 1-dimensional (1D), bipolar diodes in order to model behavior prior to pinching. The treatment builds on a model developed by Pereira.[2] An analytic approximation to the back-scattered distribution described by electron-current and -energy parameters provides a first integral of the Poisson Equation that is solved numerically to determine how the diode currents are modified for various assumed back-scatter coefficients. A Monte-Carlo code calculates the back-scattered electron distributions for various incident electron distributions and anode materials. The back-scatter parameters used in the Poisson analysis are then evaluated from the Monte-Carlo results to determine the back-scatter-modified diode currents.

The starting point is the nonrelativistic Poisson Equation in 1D in which cold electrons are emitted from the cathode at $z = 0$, accelerated across the diode with potential variation $\phi(z)$, and enter the anode at $z = d$ and $\phi = V$. A fraction α of the incident electron current is isotropically back-scattered with energy reduced from the incident value eV to βeV. Since $\beta < 1$, back-scattered electrons are returned to the anode by the diode electric field, and the back-scattering process is assumed to repeat ad infinitum with the same values of α and β. With these assumptions, the Poisson Equation can be integrated analytically to yield

$$B\left(\frac{d\Phi}{d\xi}\right)^2 = \Phi^{1/2} - \left(\frac{M}{m}\right)^{1/2}\left(\frac{J_i}{J_e}\right)\left(1-\sqrt{1-\Phi}\right) + \frac{4}{3}\sum_{n=1}^{\Phi>1-\beta^n}\left(\frac{\alpha}{\beta}\right)^n\left(\Phi-1+\beta^n\right)^{3/2} \qquad (1)$$

where $B = (2eV/m)^{1/2}V/4\varepsilon_0 J_e d^2$, m and M are the electron and ion mass, $\xi = z/d$, $\Phi = \phi/V$, and J_e and J_i are the magnitudes of the electron and ion current densities traversing the diode. The boundary conditions $\Phi(0) = \Phi'(0) = 0$, and $\Phi(1) = 1$ have been employed in Eq. (1).

* Work supported by the Office of Naval Research, USA.

+ JAYCOR, Vienna, VA

The first two terms on the right-hand-side are the familiar forms that follow from conservation of energy and current in 1D for cold, laminar electron and ion flows with zero electron energy at the cathode and zero ion energy at the anode.[3] The last term follows for multiple, isotropic back-scattering of monoenergetic electrons.[2] This 1D formalism approximates early-time charged-particle flow in Gamble II PBD experiments before the electron beam pinches radially.[1]

Before ion turn-on, $J_i = 0$ in Eq. (1), and J_e is determined from the value of B that permits the two boundary conditions on Φ to be satisfied when the equation is integrated numerically for various α and β values. Figure 1 plots the variation of J_e/J_{cl} for these calculations, where J_{cl} is the usual Child-Langmuir current density (B = 9/4). The results indicate that back-scattering suppresses the current by 5 - 20% for values of α and β associated with high-atomic-number anodes (0.3 - 0.7 for tantalum depending on incident energy and angle[4]). For low-atomic-number anodes such as aluminum or carbon, α and β are of order 0.1 and suppression is negligible. The equivalent relativistic calculations show little difference from Fig. 1 for diode voltages in the 1-MeV range of interest. The nonrelativistic treatment is therefore employed since the results are then not voltage dependent. The weak suppression predicted for moderate α and β values arises because β close to 1 is required for a substantial back-scattered-electron contribution to space charge near the cathode.

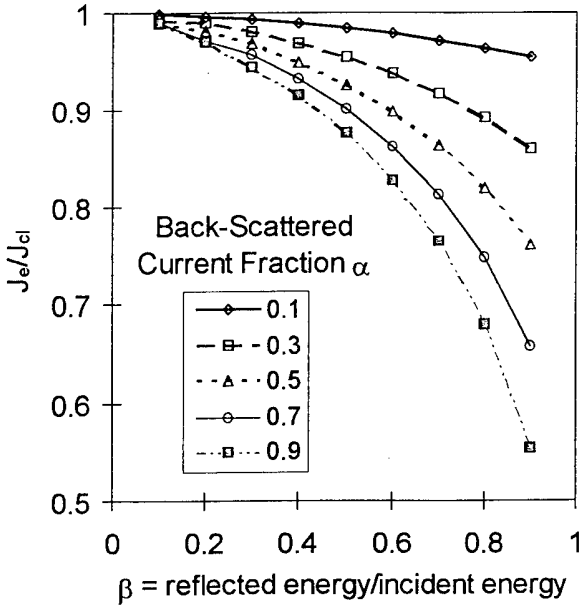

FIG. 1. Suppression of electron current with back-scattering parameters in the absence of ions.

When ion emission is included in the analysis, the ion-to-electron current ratio is determined by space-charge-limited flow at the anode: $\Phi'(1) = 0$. Substituting this condition into Eq. (1) leads to

$$\left(\frac{M}{m}\right)^{1/2}\frac{J_i}{J_e} = \frac{1+\alpha\beta^{1/2}/3}{1-\alpha\beta^{1/2}} \quad ; \quad \frac{J_i}{J_{cl}} = \frac{J_i}{J_e}\frac{J_e}{J_{cl}} \tag{2}$$

where the converging infinite series has been evaluated analytically. The current ratio from Eq. (2) is substituted into Eq. (1) to determine the value of B as above, and the results are shown in Fig. 2. For small values of α, electron and ion currents are enhanced by a factor of 1.86 as expected for 1D, bipolar flow.[3] For α and β values of high-atomic-number anodes, large enhancements in both electron and ion current are predicted. In this regime, back-scattered-electron space charge near the anode enhances ion emission which, in turn, enhances cathode electron emission. This boot-strap process causes enhancement to increase dramatically with small increases in α near β =0.5 . Further small increases in α cause the enhancement to approach infinity, beyond which no equilibrium solutions to Eq. (1) exist that satisfy the boundary conditions. Mathematically, the no-solution regime corresponds to potential distributions with an extremum in the vacuum gap so that the dependence of charge

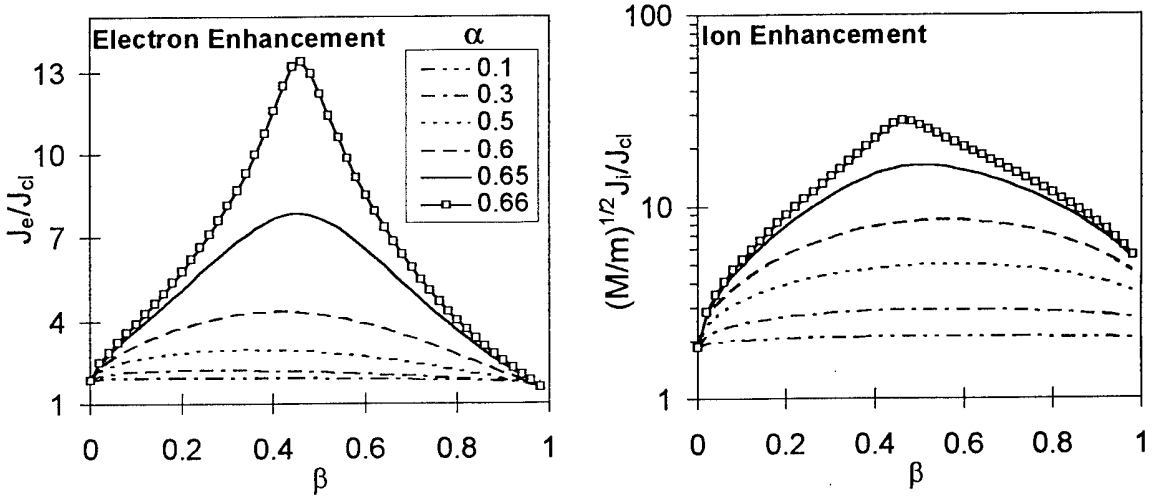

FIG. 2. Enhancement of bipolar electron and ion current with back-scattering parameters.

density on Φ is no longer valid. Physically, this regime may correspond to inherently time-dependent flows[5] that describe a low-impedance phase observed in PBDs.[6] The no-solution regime, shown in Fig. 3, has been calculated by determining the portion of (α,β) space for which $\Phi'(\xi) = 0$ somewhere between the electrodes.

Having calculated how the charged-particle flow depends on monoenergetic, isotropic back-scatter parameters, it remains to compare this assumed electron distribution with computed, more realistic forms. The Integrated TIGER Series of Monte Carlo electron/photon transport codes[7] was used to determine the back-scattered-electron distributions for various incident-electron energies, angles and anode materials. A sample result of TIGER calculations is shown in Fig. 4 for electrons with $E_0 = 1$ MeV incident on Ta at $\theta_0 = 60°$. Here, R is the number fraction of incident electrons that are back-scattered, E is their energy, θ is the angle from the normal at which they emerge, and $d\Omega$ is a solid-angle increment. With $f(E,\theta) = d^2R/dEd\Omega$, $R = \int f dEd\Omega$, and $RE_0\langle\beta\rangle = \int f E dEd\Omega$. These calculations show that R and $\langle\beta\rangle$ depend weakly on E_0 over the range 0.2 - 2 MeV so that the assumption of constant back-scatter coefficients during multiple

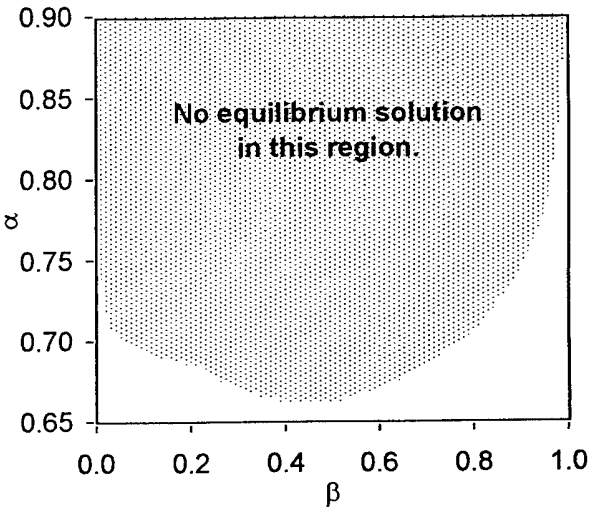

FIG. 3. Back-scatter parameters without equilibrium solutions.

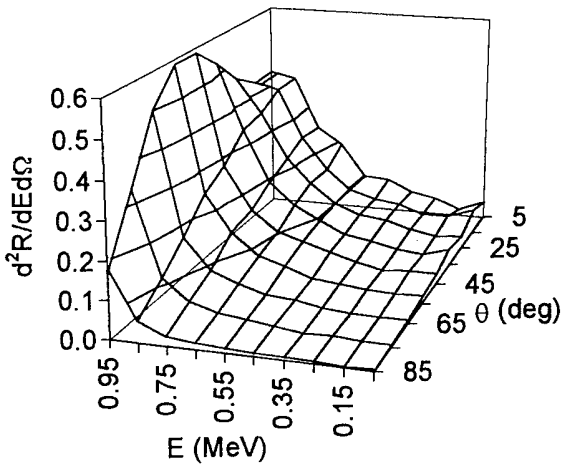

FIG. 4. Back-scattered electron distribution for 1-MeV electrons incident on Ta at 60 degrees.

scattering is reasonable. For 1 MeV electrons incident on Ta, R and $<\beta>$ vary from 0.46 to 0.64 and 0.32 to 0.5 as θ_0 varies from 0 to 60°.

In order to determine $<\alpha>$ and compare the TIGER results to the model of Eq. (1), the data exemplified by Fig. 4 is collapsed to an axial-velocity distribution. The plotted points represent the number-fractions ΔR_{ij} of electrons scattered into energy increments ΔE =0.1 MeV about E_i and into solid-angle increments $\Delta\Omega_j = 2\pi sin\theta_j\Delta\theta$ with $\Delta\theta$ = 10°. Each ΔR_{ij} has a relativistic axial velocity v_z determined from E_i and $cos\theta_j$. These are sorted in v_z and summed in $\Delta v_z = 0.1v_0$ bins, where v_0 is the incident electron speed. The results are shown in Fig. 5 for 1-MeV electrons incident on Ta. For comparison with the model used in Eq. (1), the axial velocity has been normalized by $w = v_z/v_0$, and the distribution $g(w) = (1/R)dR/dw$ is used so that the integral over w is unity. Poor statistics in Δw bins results from the coarse TIGER ΔE and $\Delta\theta$ gridding. The isotropic/monoenergetic distributions use the TIGER $<\beta>$ values and display constant dR/dw up to $w = <\beta>^{1/2}$ since $d\Omega \sim sin\theta d\theta \sim d(<\beta>cos\theta) = dw$.

The TIGER w-distributions determine $<\alpha>$, the ratio of back-scattered to incident current, using $<\alpha> = R<w>/cos\theta_0$, where $<w> = \int g(w)wdw \approx 0.6$. For 1-MeV electrons incident on Ta, $<\alpha>$ varies from about 0.3 to 0.75 as θ_0 varies from 0 to 60°. Since ion turn-on usually occurs when the anode is heated by electrons magnetically deflected to steep incident angles, the large corresponding values of $<\alpha>$ and $<\beta>$ and Fig. 2 indicate large current enhancements. This results will be mediated by differences between the realistic TIGER back-scattered distributions and the nonrelativistic, isotropic model used in Eq. (1). Figure 5 shows that the model overestimates the contribution by electrons with low w and underestimates those with large w. Excess low-w electrons increase the electron space charge near the anode, thereby enhancing ion emission. Insufficient high-w electrons reduce the electron space charge near the cathode, thereby increasing electron emission. Both effects indicate that more realistic, back-scattered-electron distributions will reduce the enhancements determined from the solution of Eq. (1) bringing them closer to Pereira's values.[2] For the future, it is desired to combine a particle-in-cell (PIC) code with a Monte-Carlo treatment to examine time-dependent diode behavior in the no-solution regime.

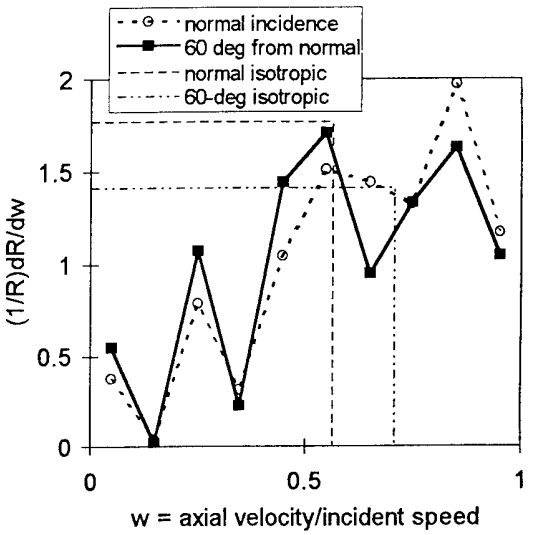

FIG. 5. Normalized axial-velocity distributions for 1-MeV electrons incident on Ta.

The authors acknowledge helpful discussions with M. Desjarlais.

[1] G. Cooperstein, *et al.*, these Proc. See D.J. Johnson and S.A. Goldstein, J. Appl. Phys. **48**, 2280(1977).

[2] N.R. Pereira, J. Appl. Phys. **54**, 6307(1983).

[3] L. Langmuir, Phys. Rev. **33**, 954(1929).

[4] A. Pregenzer and J.E. Morel, J. Appl. Phys. **57**, 4849(1985).

[5] H. Derfler and R. Holmstrom, J. Appl. Phys. **37**, 4189(1966).

[6] Cooperstein, *et al.*, Bull. Am. Phys. Soc. **23**, 800(1978).

[7] J.A. Halbleib, R.P. Kensek, G.D. Valdez, S.M. Seltzer, and M.J. Berger, IEEE Trans. Nucl. Sci. **39**, 1025(1992).

EXPERIMENTAL OBSERVATIONS OF ELECTRON-BACKSCATTER EFFECTS FROM HIGH-ATOMIC-NUMBER ANODES IN LARGE-ASPECT-RATIO, ELECTRON-BEAM DIODES*

G. Cooperstein, D. Mosher, S.J. Stephanakis, S.B. Swanekamp+, B.V. Weber, and F.C. Young

Plasma Physics Division, Naval Research Laboratory, Washington, DC, 20375, USA

Backscattered electrons from anodes with high-atomic-number substrates cause early-time anode-plasma formation from the surface layer leading to faster, more intense electron beam pinching, and lower diode impedance. A simple derivation of Child-Langmuir current from a thin hollow cathode shows the same dependence on the diode aspect ratio as critical current. Using this fact, it is shown that the diode voltage and current follow relativistic Child-Langmuir theory until the anode plasma is formed, and then follows critical current after the beam pinches. With thin hollow cathodes, electron beam pinching can be suppressed at low voltages (<800 kV) even for high currents and high-atomic-number anodes. Electron beam pinching can also be suppressed at high voltages for low-atomic-number anodes as long as the electron current densities remain below the plasma turn-on threshold.

Previous experiments have shown the important role that anode ions play in electron beam pinch-formation processes [1]. These ions originate from a thin anode plasma surface layer produced from thermal desorption of absorbed gases and their avalanche breakdown. Although electron backscattering from the anode substrate was known to play a role, emphasis was placed on the properties of this surface layer and its role on the collapse velocities of hollow electron beams emitted from hollow cathodes. Here, we concentrate on the role of electron backscattering from the anode substrate and its subsequent effect on the total diode impedance time history in large-aspect-ratio (R >>D) hollow electron beam diodes. R is the cathode radius and D is the anode cathode (A-K) gap spacing. Early in time, before the onset of anode ions or self-pinching, electrons hit the anode at normal incidence, and back-scattered electrons from high-atomic-number (high-Z) anodes can increase diode impedance through space-charge enhancement [2]. This early time backscattering can also promote abrupt impedance decrease through bipolar flow due to enhanced anode heating and plasma production. This enhanced heating is due to backscattered electrons re-entering the anode when reflected by the diode electric field. For thin hollow cathodes (cathode thickness < A-K gap, see Fig. 1), this early production of ions from high-Z anodes at radii larger than the cathode appears to affect the critical current or diode impedance long after the onset of self-pinching. This results in pinched-beam diodes with high-Z anodes exhibiting a lower impedance or higher critical current than identical-geometry diodes with low-Z anodes. This is true for the full pulse duration even after the effect of different A-K gap closure ve-

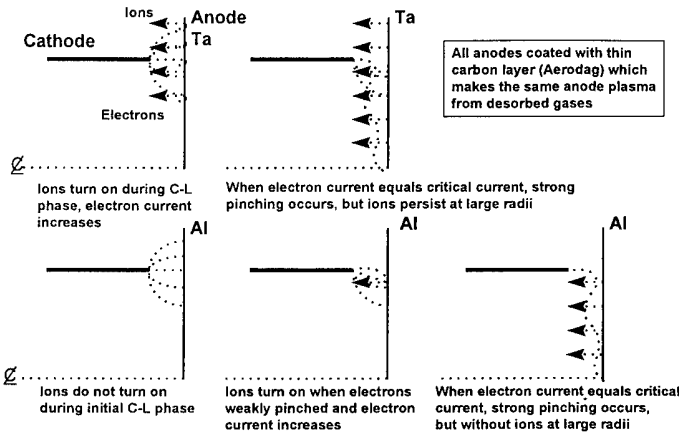

Fig. 1 Backscatter from high-Z anode substrates initiates anode plasma at early times and effects electron flow from thin hollow cathodes.

locities (due to different anode plasma onset times) is taken into account. It is speculated that ions from low-Z anodes are not produced opposite the cathode but only inside the cathode's inner diameter where the electrons first hit the anode at grazing incidence and heating is enhanced above normal incidence. (see Fig. 1)

The experimental arrangement used on Gamble II is illustrated in Fig. 2. For the data presented in this paper, all the cathodes were hollow and all anodes were coated with a thin (~10 μm) carbon layer (Aerodag). The same results were obtained with or without a carbon beam stop placed just behind the anode to prevent reflexing.

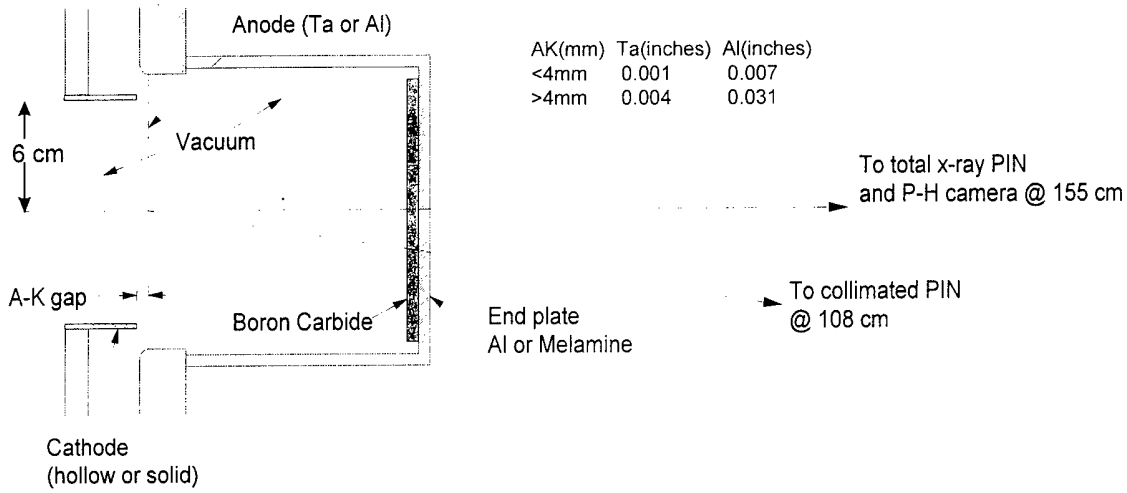

Fig. 2. Experimental arrangement on Gamble II.

An example of the differences observed between Al and Ta anodes is illustrated in Fig. 3. Current, voltage, total and collimated x-ray PIN diode signals, impedance, and x-ray pinhole photos are compared for Ta and Al anodes. For the Ta anode, the impedance abruptly falls at 30 ns and remains less than the Al anode impedance for the duration of the pulse. The Ta x-ray image shows a stronger pinch with less emission opposite the cathode.

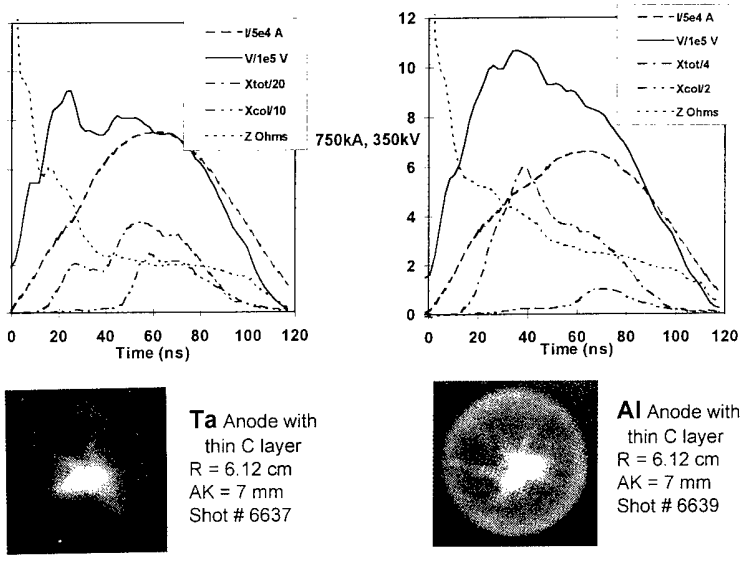

Fig. 3. Ta and Al anodes compared.

It is easier to quantitatively interpret these data if current is plotted against voltage in a way that allows the transition from Child-Langmuir (C-L) flow to pinched-beam flow to be easily seen. This is accomplished by noting that a simple derivation of C-L current from a thin hollow cathode shows the same linear dependence on diode aspect ratio, R/D, as the critical current. Assume that the relativistic C-L (R C-L) current can be approximated over the range of 0.1 to 3 MV by $I_{clrel}=2\times10^3\ V^{4/3}\ A/D^2$ where I is in amperes, V is in MV, D is in cm, and A is the area. For this case, the area

A=(2πR) (2 Kcl D) because the beam spreads out a distance Kcl D on either side of the cathode (see Fig. 4). Experimental data suggest that the proportionality constant Kcl ≈ 0.9 if anode ions are not present. Then, $I_{clrel} = 8\pi x 10^3 \, K_{cl} \, V^{4/3} \, (R/D)$. The critical diode current (Larmor radius ~ D) is $I_{crit} = 8500 \, K_{cr} \, (\gamma^2-1)^{1/2} \, (R/D)$ where $\gamma = 1+V/0.511$. Data suggests that the proportionality constant Kcr ≈ 1.6.

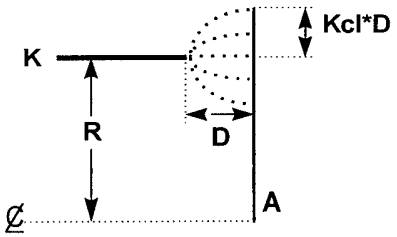

Fig. 4. Anode-cathode geometry.

Because both Iclrel and Icrit are proportional to R/D, they can be plotted together as in Fig. 5. When comparing these curves to experimental data, it is assumed that D is corrected for gap closure by subtracting vt where $v = v_K + v_A$ is the sum of the cathode and anode closure velocities. For the case Kcr = 1.6 and Kcl = 0.9, critical current or pinching is not achieved until about 2.5 MV. However, as soon as anode ions turn on, the electron current is increased through bipolar flow by 1.86 so that Kcl ≈ 1.7. In that case, critical current is achieved at about 0.8 MV. For this reason, we speculate that electron beams from thin hollow cathodes will not pinch when V < 800 kV.

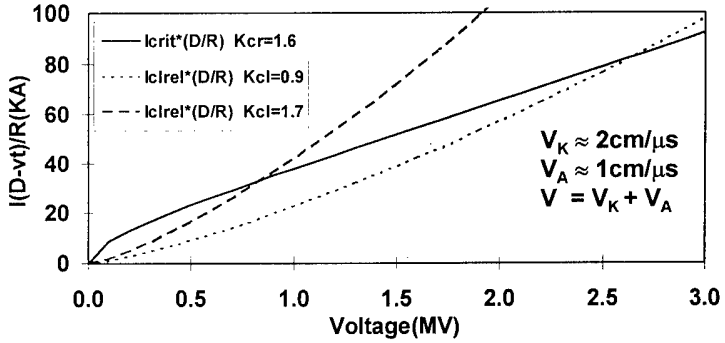

Fig. 5 Icrit and Iclrel normalized by (D-vt)/R for hollow cathode

The data from Fig. 3 are replotted at the top of Fig. 6 using the format from Fig. 5. The data are plotted every 2 ns from 10 to 100 ns. For the Ta anode, the data follows R C-L until about 25 ns when it starts to transition to critical current. At this time, we assume that the anode plasma turns on and we add the anode plasma velocity of 1 cm/μs to the cathode plasma velocity of 2 cm/μs. By 50 ns, when the pinch has appeared on axis (see Fig. 3.), the data follows the critical current for the duration of the pulse. For the Al anode, the data follows R C-L until about 40 ns when it starts to transition to critical current. Again, after about 50 ns, when the pinch has appeared on axis, the data follows critical current for the duration of the pulse. Here Kcr = 1.3 rather than the value of 1.6 for Ta. At the bottom of Fig. 6, the data is replotted to illustrate what the A-K gap spacing might be as a function of

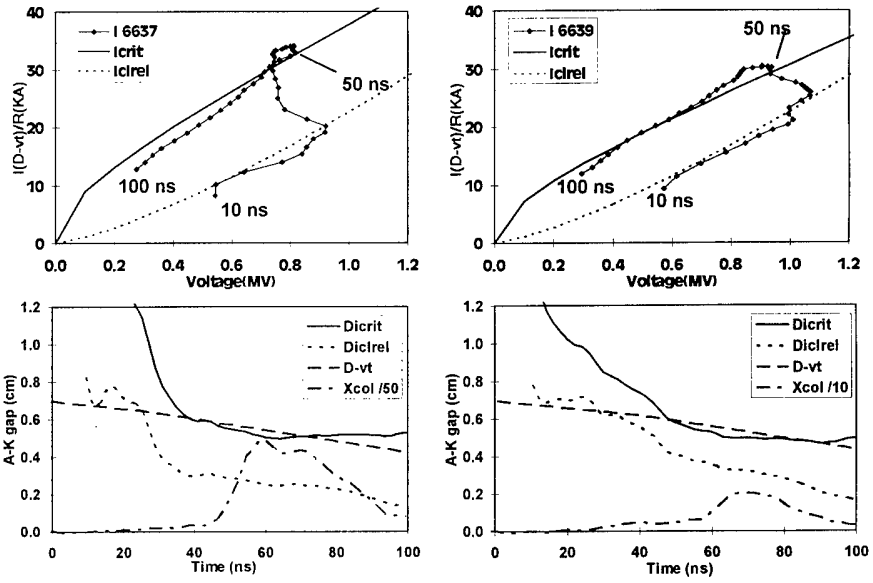

Fig. 6. Shots 6637, Ta anode, and 6639, Al anode, from Fig. 3.

time if the data followed either R C-L or critical current. The heavy dashed line, D-vt, shown for illustrative purpose, starts at the measured A-K gap of 7 mm and falls at 2 cm/μs until anode plasma turn-on, and then falls at 3 cm/μs. Note that, early in time, D-vt agrees with Diclrel and then agrees with Dicrit at the onset of pinching.

The same diode operated at higher voltages and currents (Fig. 7) continues to exhibit the same qualitative behavior. For the Ta anode, the transition occurs at 25 ns with critical current achieved by 45 ns. For the Al anode, the transition occurs at 30 ns with critical current achieved by 50 ns. For both cases, Kcr = 1.6 and Kcl = 0.9.

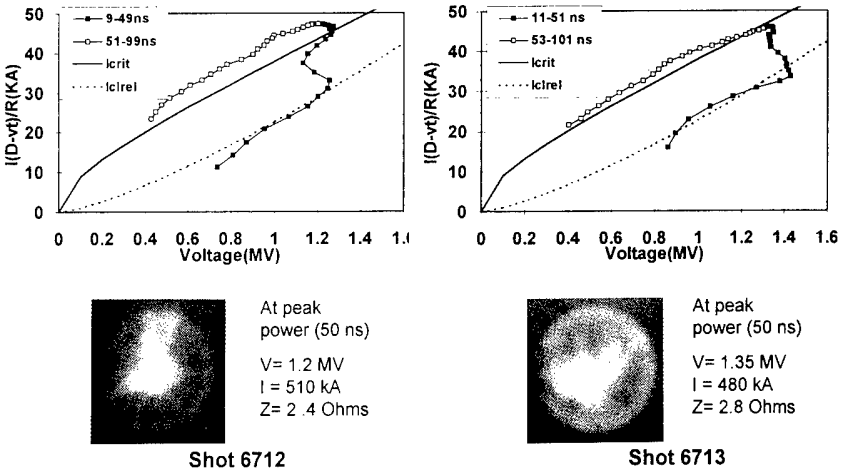

Fig. 7. Shot 6712 used a Ta and 6713 an Al anode with 7 mm A-K gap.

Another prediction of the theory is that intense electron beam pinching can be suppressed from thin-hollow-cathode diodes independent of diode current, aspect ratio, or anode material if the diode voltage is held below about 800 kV. This is consistent with the data shown in Fig. 8 for shot 6649. Because of the high current density, it was assumed that the anode plasma turned on at early times with a velocity of 1.5 cm/μs and Kcl ≈ 2. A final prediction of the theory is that electron beam pinching can also be suppressed at high voltages for low-atomic-number anodes as long as the electron current densities remain below the plasma turn-on threshold. This behavior is illustrated in shot 6715. Late time pinching is observed.

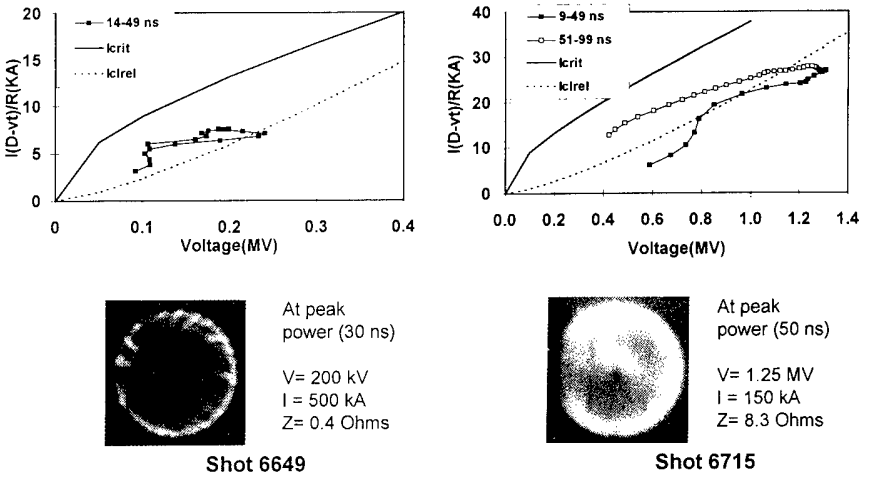

Fig. 8. Shot 6649 used a Ta anode with a 2 mm A-K gap. Shot 6715 used an Al anode with a 12 mm A-K gap.

* Work partially supported by the Office of Naval Research, USA, and Defense Nuclear Agency.

\+ JAYCOR, Vienna, VA.

References

[1] A.E. Blaugrund, G. Cooperstein and S.A. Goldstein, Phys. Fluids, 20, 1185 (1977)

[2] D. Mosher, G. Cooperstein, D.V. Rose, and S.B. Swanekamp, these Proceedings.

SELF-PINCH FOCUSING EXPERIMENTS PERFORMED ON THE KALIF ACCELERATOR USING THE B_{appl} DIODE

P. Hoppé, Y. Nakagawa, W. Bauer, H. Bluhm, L. Buth, H. Guth, A. Hellmann H. Massier, D. Rusch, O. Stoltz, A. Tauschwitz, W. Väth

Forschungszentrum Karlsruhe GmbH, Postfach 3640, 76021 Karlsruhe, Germany

Abstract

Experiments using the B_{appl} diode with a subdivided beam drift section were performed on the KALIF accelerator with the objective to investigate the generation of net currents and their influence on the focusing properties of the extracted proton beam. The generation of net currents up to 50% of the diode current was observed for argon gas pressures below 0.1 mbar in the second drift section. The differences in the time histories of various net current monitors might be related to a radial dependency of the net current densities in the beam. A comparison of the focusing properties investigated in shots with and without current neutralization showed only small differences. No enhancement of the power density related to self-pinch effects was found. However, the possibility to propagate the beam over a short vacuum distance allows the use of a backlighter target required for laser absorption spectroscopy.

Introduction

On the KALIF accelerator a proton power density of up to 1 TW/cm^2 was reached in the focal plane of the B_{appl} diode [1]. Considering the emission of an annular proton beam (limited by the angles α_1 and α_2) from a spherical anode surface, a beam of constant brightness B will produce an even higher power density $P = \pi B (\sin^2\alpha_1 - \sin^2\alpha_2)$ if the incident angle $\alpha = (\alpha_2 - \alpha_1)$ to the focal plane can be increased. This can be achieved by the generation of a B_Θ field (induced by the non-current neutralized beam itself) in the drift section upstream of the focal plane of an extractor diode. The reduction of the focal length depends on the net current produced by the beam and on the distance the beam has to propagate non-neutralized. This distance is rather limited for the KALIF B_{appl} diode. The beam has to be maintained current neutralized in regions where it propagates through the return flux of the strong insulating B_{appl} field. Therefore the beam drift section for self pinch experiments was subdivided by a second foil into 2 independent sections which can be held at different gas pressures. In the first section an argon pressure of 5 mbar is needed in areas where the beam crosses the return flux of the B_{appl} field. In the second section, a sufficiently low gas pressure for the generation of a net current must be established.

With the DRIFTPIC code available at Karlsruhe [2], simulations for this self-field focusing scheme could not be performed because this problem needs a self consistent treatment of current neutralization. Based on the calculation of single particle orbits, a reduction of the focal length of about 2 mm was estimated for a net current of 200 kA in the beam.

Experimental arrangements and diagnostics

The drift section routinely used is formed between the Mylar foil No.1 (1.7μm thick, placed as close as possible to the cathode side of the acceleration gap), the walls of the B_{appl} field coils and the walls of the drift tube (Fig.1). With foil No.2 (also 1.7μm thick), this drift

section was subdivided into a first section, always held at the argon pressure of 5 mbar used normally in the entire drift section, and a second section including the beam focus. In this second section the argon pressure could be varied independently from the pressure in the first section.

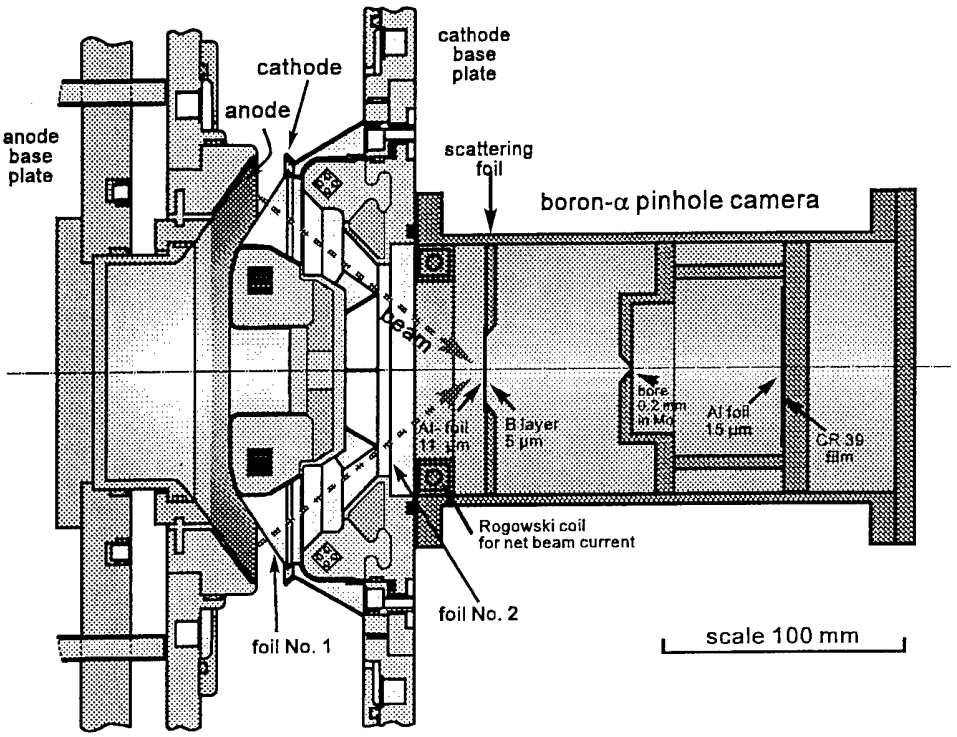

Fig.1: Cross section of the B_{appl} diode with two drift sections and the Bα diagnostics

The radial profile of a high power proton beam at a given axial position can be measured by placing at this position a boron scattering foil normal to the beam. The beam protons are scattered isotropically on this boron foil (about 5 µm thick) and the emitted α particles from the reaction p (^{11}B,2α) α are imaged on an ion sensitve film (CR39) placed in a pin hole camera [3]. The thickness of the aluminum filter foils in front of the boron foil (11µm) and the CR39 film (15 µm) were chosen such that only protons with energies above 1.5 MV can be the origin of tracks due to α particles on the CR39 film. Rutherford scattered protons with energies below 1.7 MV.cannot track the film.

The tracks on the CR39 films were counted using an automatic computer system [4]. In order to avoid misinterpretations the track density on the CR39 should not exceed about 300 to 400 for a sample area of 250 by 250 µm. A separation between proton- and α-particle impacts on the film was not possible.

For the measurement of the beam net current, an integrating Rogowski coil was placed in the drift tube just behind the rear surface of the support plate of the B_{appl} field coils. In this position the entire beam must penetrate through the inner surface of the Rogowski coil (Fig.1). For comparison with the signal of the Rogowski coil, a shunt type current monitor was used to measure the net current delivered to a metal cylinder (5 or 10 mm in diameter) or to a LiF target with a diameter of 50 mm.

Experiments and results

In all shots the diode and KALIF parameters remained unchanged. The KALIF Marx was always charged to 85 kV.

Argon gas pressures of below 0.1 mbar in the second drift section had a strong influence on the generation of net currents. Net currents up to 50% of the diode current were measured by the Rogowski coil with vacuum in this second drift section. The time-of-flight corrected net-current time histories (Fig. 2), measured by the Rogowski coil and the shunt monitor supporting a LiF target, showed 3 different phases. In phase 1 no net current was measured for the time interval of about 10 ns following the onset of the diode current. This means that during this time the beam remained current neutralized. In phase 2 the net current increased within about 20 ns (shunt monitor) and about 40 ns (Rogowski coil) to a final value. The gas pressure in the second drift section had a strong influence on this final value but not on the net current onset characteristics (Fig.3). In all shots the final values seen by the Rogowski coil were higher when compared with the shunt monitor. During phase 3 the mean signals of both monitors remained about constant. For pressures of 0.014 mbar and below, oscillations with a frequency around 80 MHz were observed during this phase. When replacing the LiF target on top of the shunt monitor by a metal rod (10 mm diam., 35 mm long), the phase 1 was reduced to about 5 ns and the final values reached for the same gas pressure were lower. A reduction of the diameter of the rod to 5 mm did not modify the shunt signal.

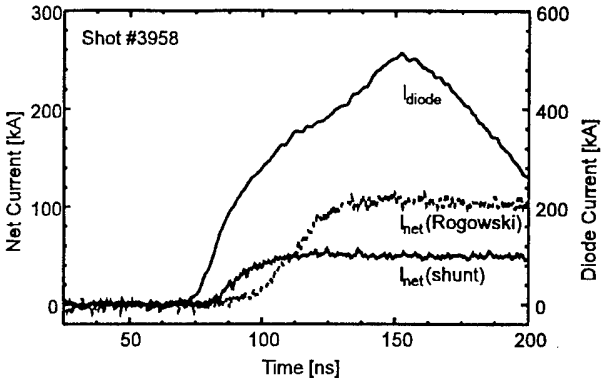

Fig. 2: Time histories of the net currents

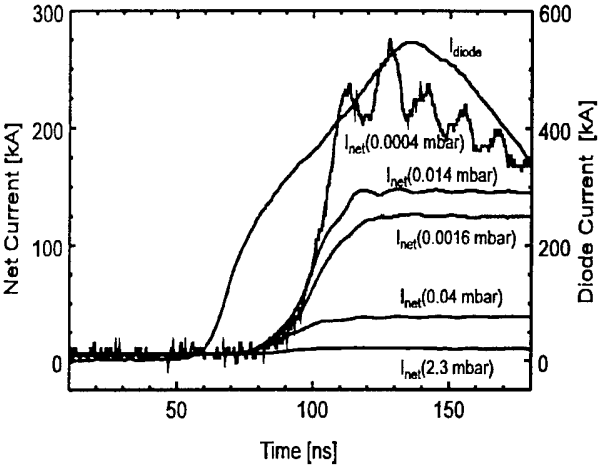

Fig.3: Time histories of the net currents for various argon gas pressures

In order to determine the axial position of the focal plane for the standard drift section arrangement (filled with argon gas of 5 mbar), the boron foil was moved axially in steps of 5 mm from 15 mm before to 20 mm behind the nominal focal plane. This series proved that the focal plane of the beam is as expected assuming ballistic beam propagation (27 mm referred to the rear side of the B_{appl} coil support plate). The position of the focus is well reproducible (less than +/- 2mm) and the FWHM of the radial beam profile is typically 7 to 8 mm (Fig. 4, upper part, and Fig. 5 curve A). An increase of the beam width and ring type patterns corresponding to estimates based on ballistic beam propagation were found on the CR39 films when placing the boron foil before and behind the nominal focal plane (Fig 4, lower part). Azimuthal inhomogeneities were more pronounced on images from boron foils placed axially closer to the B_{appl} coil. Obstacles in the path of the beam became visible. CR39 films from a similar set of experiments performed with vacuum in the second drift section showed the following differences. The minimum of the FWHM moved axially about 5 mm

upstream and slightly increased to about 9 mm (Fig. 5, curve B). These results indicate that net currents of up to 280 kA, acting over a distance of about 5 cm on the beam, may slightly influence the focusing properties of the beam. However, no enhancement of the focused power density was observed. This also means that the beam can be propagated over a short vacuum section outside the B_{appl} field. Thus a backlighter source for the measurement of the target temperature by absorption spectroscopy can be installed. With vacuum in the entire drift section, but keeping foil No.1 in place, only ringshaped radial distributions were observed. The minimum ring diameter was found in the nominal focal plane (Fig. 5, curve C). If, in addition, the foil No.1 was also ommitted the focus disappeared (Fig. 5, curve D).

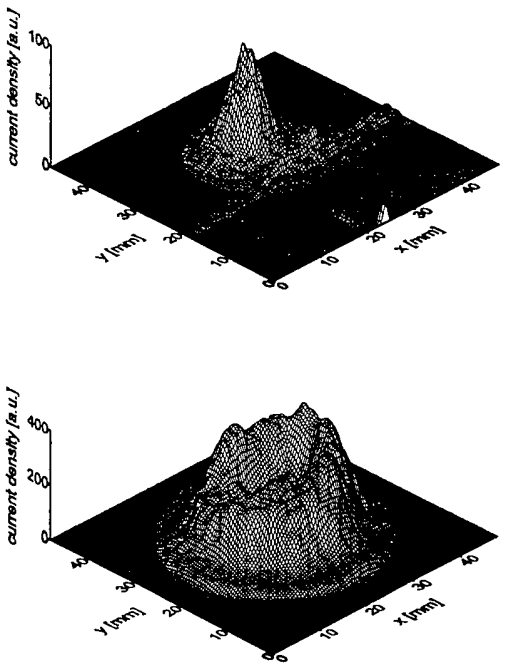

Fig. 4: Current density distribution at the nominal focus (upper) and 15 mm behind (lower)

Conclusions and outlook

The time histories of the net currents and the differences between their amplitudes are not yet well understood. An inhomogeneous radial current distribution that develops when the beam propagates through the second drift section might explain this. Depending on time, the number of electrons required for the neutralization of the inner beam regions cannot be supplied either by the low density back ground gas or by the neighboring surfaces. This assumption needs to be verified by adequate modeling and numerical simulations. The self-induced net currents did not increase the power density of the beam. This result seems to be unrelated to any problems with the sensitivity of the Bα diagnostics or to insufficient shot to shot reproducibility.

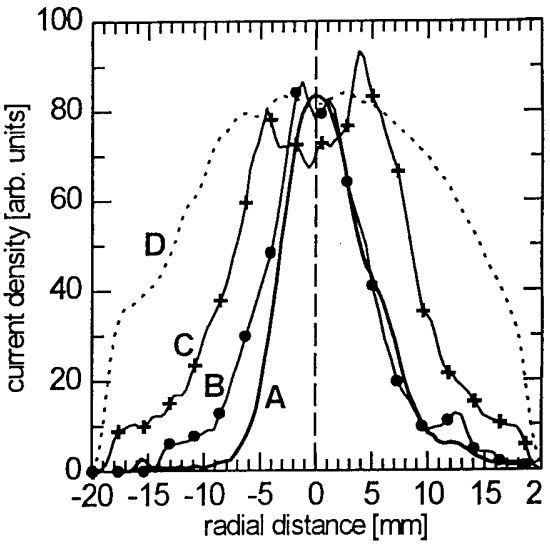

Fig. 5: Radial beam profiles of 4 shots with various neutralization conditions

References

[1] H. Bluhm et al., Proc. 9th Int. Conf. on High Power Particle Beams, (1993)
[2] L. Feher et al., KfK Bericht 5207, Karlsruhe, (1993)
[3] A. Klumpp, H. Bluhm, KfK Bericht 4130, Karlsruhe, (1986)
[4] H. Guth, A. Hellmann, FZKA Bericht 5523, Karlsruhe, (1995)

Ion Diode Simulation with a Finite-Volume PIC Approach for the Numerical Solution of the Maxwell-Lorentz System

C.-D. Munz, R. Schneider, E. Stein, U. Voß, T. Westermann [2], M. Krauß [3]

Forschungszentrum Karlsruhe — Technik und Umwelt,
Institut für Neutronenphysik und Reaktortechnik,
Postfach 3640, D-76021 Karlsruhe

The numerical concept realized in the the Karlsruhe Diode Code KADI2D is briefly reviewed. Several new aspects concerning the Maxwell field solver based on high resolution finite-volume methods are presented. A new approach maintaining charge conservation numerically for the Maxwell-Lorentz equations is shortly summarized.

1. Introduction

For experiments with the object of optimization as well as for further developments of ion diodes it is very important to get a deep physical understanding of the fundamental time-dependent phenomena occuring inside those diodes. Elaborate computer simulations are an effective and ideal tool to enhance the knowledge about the complex ion diode physics and, additionally, could force time and reduce costs of further developments. The basic physical observations are modelled mathematically by the Maxwell-Vlasov equations. However, for numerical calculations it is more convenient to replace the Vlasov equation by its characteristic equations resulting in the Maxwell-Lorentz system.

Solving numerically the Maxwell field equations it is important to have an adequate computational grid which covers the relevant diode domain in an appropriate manner. Therefore, we adopt a grid model based on boundary-fitted coordinates (BFC) [10] resulting in quadrilateral meshes with regular data structure. The numerical solution of the Lorentz and stationary Maxwell equations for BFC based grid concepts is realized with the simulation program BFCPIC [12] which has been developed at the Forschungszentrum Karlsruhe during the last years. However, important time-dependent phenomena such as the origin and consequences of electromagnetic instabilities inside the ion diode gap cannot be investigated with BFCPIC code. For that purpose, the Karlsruhe Diode code KADI2D has been developed solving numerically the full nonstationary Maxwell equation together with the Lorentz equations [4]. Attacking the nonstationary field equations, modern numerical techniques based on finite-volume (FV) methods are employed in KADI2D . The application of FV methods for the numerical solution of the Maxwell equations is a new approach in self-consistent particle simulation which is inherently very robust even when strong gradients occur.

2. The Numerical Model

The particle-in-cell (PIC) method [2, 5] is an attractive computational tool for studying kinetic phenomena, in particular in plasma physics where, for example, the self-consistent numerical solution of the Maxwell-Lorentz equations have to be computed. This means, that the orbits of electrically charged particles have to be determined with respect to externally applied as well as (in the case of ion diodes strong) self-generated electromagnetic fields. The basic idea of the PIC method can be summarized as follows.

Suppose the sum external and the self-consistent charge and current density ρ and $\mathbf{j}$, respectively, is given at the time level $t = t_{n-1/2}$. Solving the Maxwell equations

$$\partial_t \mathbf{E} - c^2 \nabla \times \mathbf{B} = -\frac{1}{\epsilon_0}\mathbf{j} \quad , \quad \partial_t \mathbf{B} + \nabla \times \mathbf{E} = 0 \, , \tag{2.1}$$

$$\nabla \cdot \mathbf{E} = \frac{1}{\epsilon_0}\rho \quad , \quad \nabla \cdot \mathbf{B} = 0 \, , \tag{2.2}$$

for instance, numerically with a FV field solver, we obtain the electric field $\mathbf{E}$ and magnetic induction $\mathbf{B}$ at the new time level $t = t_n$ at the barycenters of the computational grid zones. Afterwards, the

[2]Fachbereich Naturwissenschaften, FH Karlsruhe, Postfach 2440, D-76012 Karlsruhe

[3]Forschungszentrum Karlsruhe, Hauptabteilung Informations- und Kommunikationstechnik, Postfach 3640, D-76021 Karlsruhe

electromagnetic fields have to be interpolated to the actual charged particle positions $\mathbf{x}_k(t_n)$, where the index k runs over all particles inside the computational domain. The used interpolation scheme is an extension of the standard area-weighting method to arbitrary quadrilateral BFC grid zones [11]. The electromagnetic fields at the particle position set up the Lorentz force

$$\mathbf{F}_k(t) = q_k \left[\mathbf{E}(\mathbf{x}_k, t_n) + \mathbf{v}_k \times \mathbf{E}(\mathbf{x}_k, t_n)\right] , \tag{2.3}$$

which is responsible for the redistribution of the charges q_k within the domain of interest. The new phase space coordinates $(\mathbf{v}_k, \mathbf{x}_k)$ are determined by solving the relativistic (electrons) and non-relativistic (ions) Lorentz equations:

$$\frac{d\mathbf{U}_k(t)}{dt} = \frac{\mathbf{F}_k(t)}{m_k}, \quad \mathbf{U}_0 = \mathbf{U}_k(t_{n-1/2}) ; \qquad \frac{d\mathbf{x}_k(t)}{dt} = \mathbf{v}_k(t), \quad \mathbf{x}_0 = \mathbf{x}_k(t_n), \tag{2.4}$$

where m_k and $\mathbf{U}_k = \gamma_k \mathbf{v}_k$ denotes the mass and relativistic velocity, respectively, of the k-th charged particle. The particle-pushing according to the Lorentz equations (2.4) is numerically performed by applying the second-order time-centered leapfrog-scheme. In order to obtain the new density distributions due to the movement, the particles have to be located with respect to the computational grid [11]. The resulting interpolation weights for the four barycenter corners surrounding the new particle position $\mathbf{x}_k(t_{n+1})$ are calculated, necessary for the assignment of the contribution of the k-th particle to the self-consistent charge and current density at the new time level $t = t_{n+1/2}$ [4].

Now, the iteration cycle is closed and the electromagnetic fields used for the next cycle have to be determined from the solution of the nonstationary Maxwell equations (2.1). By considering the linked interplay of Maxwell and Lorentz equations the self-consistent solution of this non-linear system is obtained.

3. The Finite-Volume Maxwell Solver

Solving Maxwell equations numerically we use in the KADI2D code high resolution FV methods [7] which are from the point of construction very evident and known to be very robust and able to resolve strong gradients without generating spurious oscillations. Usually, numerical algorithms in time domain only approximate the Maxwell equations (2.1) and (2.2). These equations may be recast in conservation form [4]

$$\partial_t u + \partial_{x_1} f_1(u) + \partial_{x_2} f_2(u) = q . \tag{3.1}$$

Here, we restricted ourselves to two space dimensions and assume that the vector of the electric field and magnetic induction $u = (E_1, E_2, E_3, B_1, B_2, B_3)^T$ does not depend on x_3. The new aspect in this formulation is that the differential operator is no longer the curl, but rather the divergence applied to the fluxes $f_i(u) = \mathsf{K}_i\, u$, $i = 1, 2$, where the K_i are constant 6×6 matrices. The vector of the source terms q essentially contains the current densities of equation (2.1).

We assume that the physical domain is covered by a structured boundary-fitted grid composed by quadrilateral zones V_{ij} with the area $|V_{ij}|$. A FV scheme is obtained integrating the conservation equations (3.1) component-by-component over the space-time volume $V_{ij} \times [t_n, t_{n+1}]$. With the average of u over the grid cell V_{ij} at time $t = t_n$ we get the explicit FV scheme in conservation form

$$u_{ij}^{n+1} = u_{ij}^n - \frac{\Delta t}{|V_{ij}|} \sum_{\beta=1}^{4} G_{ij,\beta}^n + \Delta t q_{ij}^n , \tag{3.2}$$

where the vector q_{ij}^n approximates the source terms averaged over V_{ij} and the time interval $\Delta t = t_{n+1} - t_n$. The so-called numerical flux $G_{ij,\beta}^n$ has to be an appropriate approximation of the physical flux through the edges $S_{ij,\beta}$ of V_{ij}. FV schemes are completely defined if the numerical fluxes are specified. The suitable calculation of these fluxes from averaged quantities at the time level $t = t_n$ is the main task in the context of FV methods.

One possibility of flux estimation is based on the solution of the so-called Riemann problem (RP) [4, 8], which can be solved exactly in the present case of linear hyperpolic equations. By the use of the RP solution the local structure of wave propagation is directly incorporated into the numerical approximation, responsible for the inherent robustness of these schemes. The simplest numerical flux approximation based on the RP solution is only first-order accurate in both space and time and, in general, hardly applicable for most practical purposes. To get higher-order schemes it is sufficient to improve the order of the numerical flux calculation [8]: Applying the MUSCL approach [6] a second-order

space and time accurate TVD FV upwind-scheme is obtained [4], which is implemented as the standard Maxwell field solver in the KADI2D program system.

4. Numerical Results

The contour plots shown in Fig. 1 are recorded at $t = 90$ ns and $t = 180$ ns and give an impression of the spatial distribution of the E_3 field component for a typical TM problem, where two wave trains are excited in each direction [8]. The numerical results (lower pictures) are obtained for a quadratic computational domain parallel to the axis but the grid lines inside the domain are strongly disturbed according to a sine curve. The comparison with the exact solution (upper pictures) plotted at the same computational grid convincingly shows the quality of the approximation.

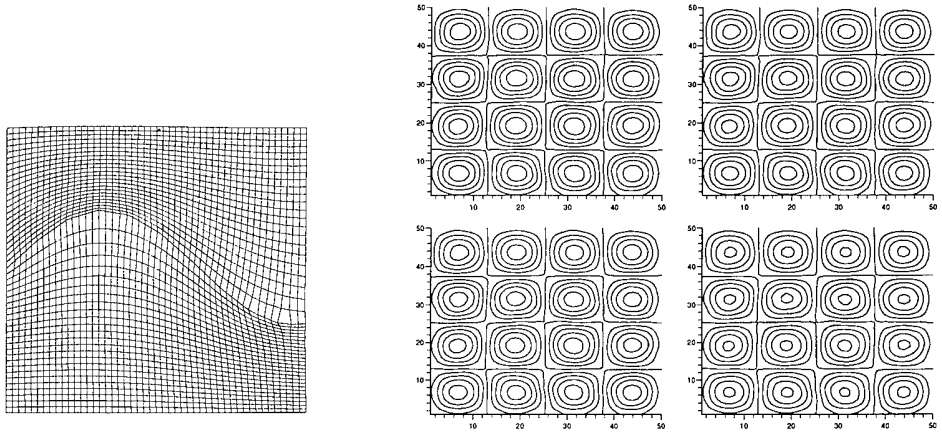

FIGURE 1. Spatial distribution of the E_3 field of a TM calculation on a strongly disturbed grid inside the depicted computational domain at $t = 90$ and $t = 180$ ns. The inspection reveal that the numerical obtained (lower plots) are in nearly perfect agreement with the exact (upper plots) solution.

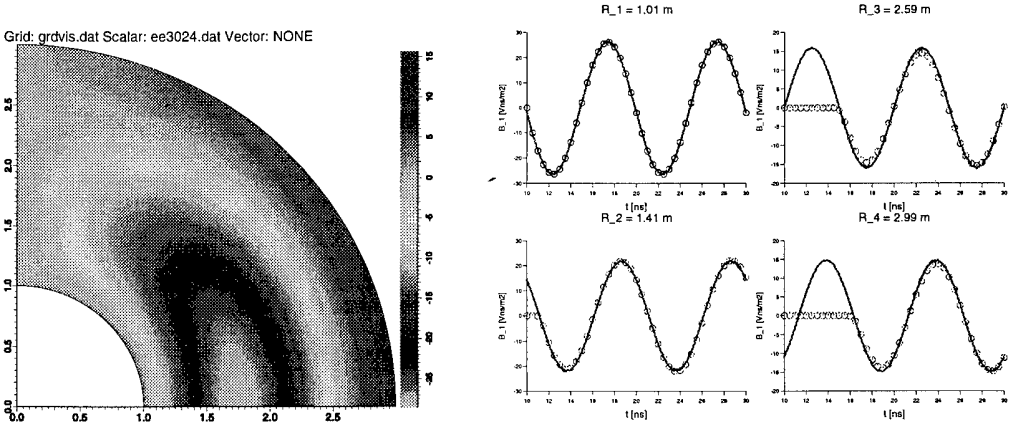

FIGURE 2. Contour plot of the spatial distribution of the exact (upper part) and numerically obtained (lower part) of the B_2 dipol field at $t = 30$ ns. A quantitative comparison between the closed-form solution (solid lines) and the numerical result (open circles) of the B_1 field component at four different fixed points is monitored in the right plot.

The Maxwell equations form a system of hyperbolic equations and hence boundary conditions and their implementation are only well-posed if they take into account the wave propagation as given by the theory of characteristics. For the used FV based approach it is comprehensively shown in [8], that the numerical realization of both physically and computationally motivated boundary conditions is founded within the framework of RP. In Fig. 2 the finite-sized domain is seen, consisting of a quarter ring with an inner and outer radius R_i and R_o, respectively. At R_i the closed-form solution of an oscillating 2d-dipol is irradiated into the domain while open boundary conditions are imposed at R_o and symmetric considerations are necessary at the axis. The contour plot depicted in Fig. 2 is a snapshot of the numerically obtained B_2 dipol field distribution at $t = 30$ ns, clearly indicating that no visible wave reflection occur at the truncated numerical domain at R_o. By scanning the time variation of the B_1 field component at four fixed points in space lying at the bisector of the angle of the first quadrant the exact solution (solid lines) and numerical approximation (open circles) reveal the high quality and accuracy of the applied methods. We investigated and implemented in addition to the second-order TVD upwind-scheme modern higher order ENO extensions of FV methods [9, 3] as a further optional Maxwell field solver for KADI2D. To achieve consistent numerical accuracy in time Runge-Kutta schemes are used to solve numerically a semi-discretized formulation of FV schemes in conservation form [8]. It is found out [8] that the number of grid points could be considerable reduced using sophisticated ENO implementations and, hence, these schemes seems to be very attractive for extension of the KADI2D code up to three dimensions in space.

5. A new Approach to Improve Charge Conservation

As it is outlined in Sec. 2, the Maxwell field solver is applied as one part in the self-consistent charged particle simulation. However, each step of the PIC approach introduces numerical errors and a discrete analogue of the charge conservation does not hold exactly or even with a defect of a certain order. Since only current density is used for the numerical field calculation, the consistency of $\epsilon_0 \nabla \cdot \mathbf{E}$ with charge density ρ may be lost. For practical purposes the correction of the electrical field is much more important than those of the **B**-field, hence, we restrict ourselves only to the **E**-field correction. Similar to Assous et al. [1] we introducing the Lagrangean multiplier φ, which may be considered as a potential correcting the actual electric field. Additionally, we modify the system of interest by introducing the term $\frac{1}{\beta^2}\partial_t\varphi$ and study the constraint, strictly hyperbolic problem [8]:

$$\partial_t \mathbf{E} - c^2 \nabla \times \mathbf{B} + c^2 \nabla \varphi = -\mathbf{j}/\epsilon_0 \,, \tag{5.1}$$

$$\frac{1}{\beta^2}\partial_t \varphi + \nabla \cdot \mathbf{E} = \rho/\epsilon_0 \,. \tag{5.2}$$

Here, β denotes the magnitude of the yet unknown parameter, which has to be estimated numerically. Obviously, this purely hyperbolic approach posseses the property that the information of correction or equivalent the errors due to Gauß law propagates with a finite velocity βc.

References

[1] F. Assous, P. Degond, E. Heintze, P. Raviart, and J. Segre, *On a finite-element method for solving the three-dimensional Maxwell quations*, J. Comput. Phys., 109 (1993), pp. 222–237.

[2] C. Birdsall and A. Langdon, *Plasma Physics via Computer Simulation*, McGraw-Hill, New York, 1985.

[3] S. Chakravarthy, B. Engquist, A. Harten, and S. Osher, *Uniformly high-order accurate nonoscillatory schemes III*, SIAM J. Numer. Anal., 24 (1987), pp. 279–309.

[4] E. Halter, M. Krauss, C.-D. Munz, R. Schneider, E. Stein, U. Voss, and T. Westermann, *A concept for the numerical solution of the Maxwell-Vlasov system*, Forschungszentrum Karlsruhe – Umwelt und Technik, **FZKA 5654**, (1995).

[5] R. Hockney and J. Eastwood, *Computer Simulation using Particles*, McGraw-Hill, New York, 1981.

[6] B. Leer, *Towards the ultimative conservative difference scheme V. A second order sequel to Godunov's method*, J. Comput. Phys., 32 (1979), p. 101.

[7] R. LeVeque, *Numerical Methods for Conservation Laws*, Birkhäuser, Basel, 1990.

[8] C.-D. Munz, R. Schneider, and U. Voss, *A finite-volume method for Maxwell equations in time domain*, submitted, (1996).

[9] C.-W. Shu and S. Osher, *Implementation of essentially non-oscillatory shock capturing schems I*, J. Comput. Phys., 77 (1988), pp. 439–471.

[10] J. Thompson, Z. Warsi, and C. Mastin, *Boundary-fitted coordinate systems for numerical solution of partial differential equations - A review*, J. Comput. Phys., 47 (1982), p. 1.

[11] T. Westermann, *Localization schemes in 2D boundary-fitted grids*, J. Comput. Phys., 101 (1992), p. 307.

[12] ———, *Numerical modelling of the stationary Maxwell-Lorentz system in technical devices*, Int. J. Num. Mod., 7 (1994), p. 43.

CHARACTERISTICS OF MAGNETICALLY INSULATED DIODE IN A MULTI-SHOT OPERATION

E. Chishiro, K. Masugata, and K. Yatsui
Laboratory of Beam Technology, Nagaoka University of Technology
Nagaoka, Niigata 940-21, Japan

We have evaluated beam characteristics in a multi-shot operation. The MID utilizes in the experiment is a racetrack type diode, where flat electrodes of anode and cathode are utilized. On the anode, polyethylene sheet of 1 mm thickness is attached as an ion source. The MID is successively operated without breaking the vacuum. An ion current density (J_i) of 350 A/cm^2 is observed at the first shot when diode gap is 5 mm. The value decreases with increasing the number of shot and at 7th shot J_i is decreased to be less than 150 A/cm^2. After 7 shots, the surface of anode is observed and is found to be covered with sticked matter of metallic materials such as Zn, Al, Fe, Cu. These matelials seem to be produced by the ablation of the MID electrode. By eliminating the sticked matter form the surface, J_i is recovered to the initial value. The decrease of J_i is due to that the anode is covered with the sticked matter, which prevent the growth of anode plasma.

1. Introduction

An intense, pulsed, light-ion beam (LIB) is considered as a hopeful candidate for an energy driver of inertial-confinement fusion.[1] Furthermore, it has been successfully demonstrated to be applied for materials science.[2-4]

A magnetically insulated diode (MID) has been used to generate LIB. In the MID, a magnetic field is applied parallel to the surface of electrodes to inhibit electron flow to the anode. Thereby the anode has rare damage, which enable the multi-shot operate without replacing anode. However, when the MID is successively operated without breaking the vacuum, an ion current density (J_i) decreases with increasing number of shot.

In this study, J_i is measured in the successive operation. The effects of deterioration of ion source (polyethylene), backstreaming oil of vacuum pumps and sticked matter deposited on ion source are evaluated.

2. Experimental setup

Figure 1 shows the schematic of the experimental setup. The MID is a racetrack type diode,[5] where flat electrodes of anode and cathode are utilized. In the MID, an insulating magnetic field is produced by an externally applied current flow through the cathode which acts as a one-turn coil. In the beam extraction side of the cathode, brass vanes are installed. Inside the cathode, aluminum anode is placed, which is connected to an output of pulse-power sys-

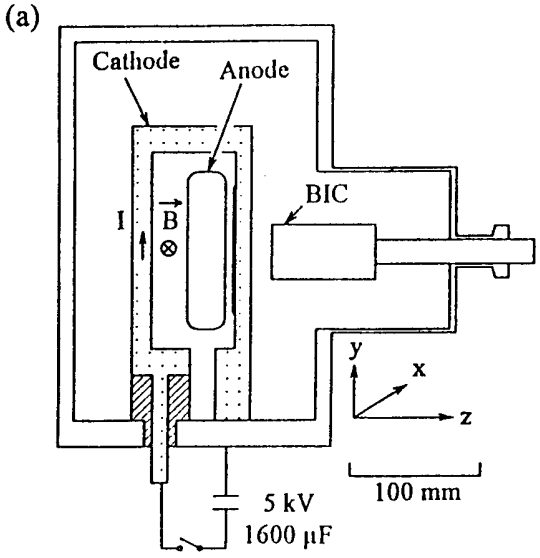

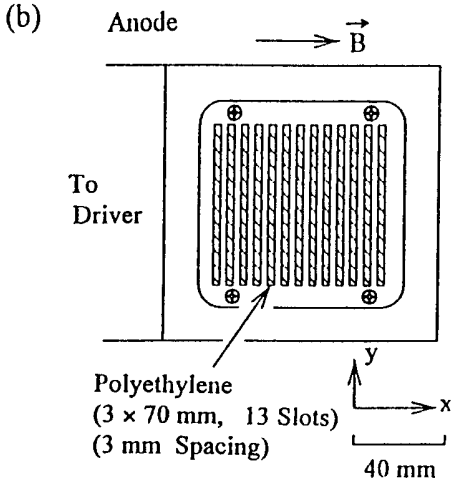

Fig. 1 (a) Schematic diagram of MID
(b) Frontal diagram of anode.

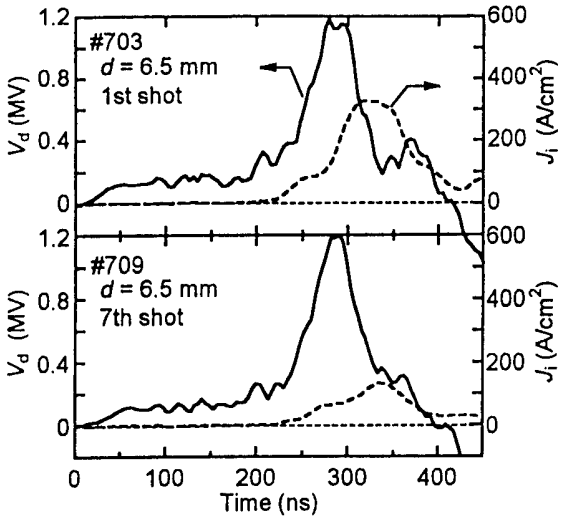

Fig. 2 Typical waveforms of diode voltage (V_d) and ion current density (J_i).

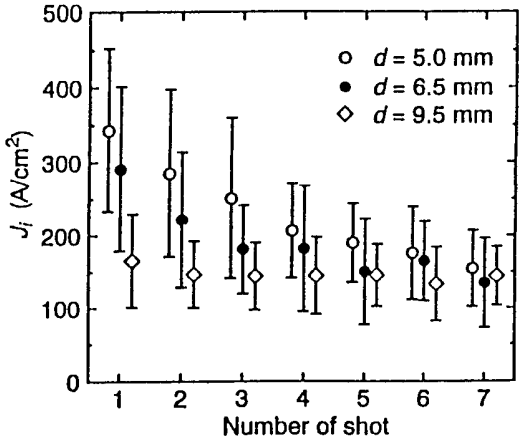

Fig. 3 Dependence of J_i on number of shot.

tem "ETIGO-II".[6] As an ion source, the anode has thirteen of polyethylene-filled, 70-mm-long grooves on an active anode area.

An inductively corrected diode voltage (V_d) is monitored by a capacitive divider. For the measurement of J_i, a BIC which has four apertures is used to measurement the average value. As shown in Fig.1, the measured points are center area on the active ion source. The BIC is made from copper and is located at 34-37 mm downstream from the anode surface.

The process of the successive operation is as follows: First shot is operated at 90 minutes after the start of evacuation. After the 1st shot, successive shots are done with an interval of 15 minutes. After the shots, vacuum is broken to replace the anode. The pressure in the operation is 10^{-2} Pa.

3. Successive operation characteristics

The decrease of J_i in successive operation is evaluated under several diode gap (d) conditions. For the all condition of d, a ratio of insulating magnetic field for critical insulating field [7] is set in 1.1-1.2.

Figure 2 shows typical waveforms of V_d and J_i when d is 6.5 mm. As seen in the

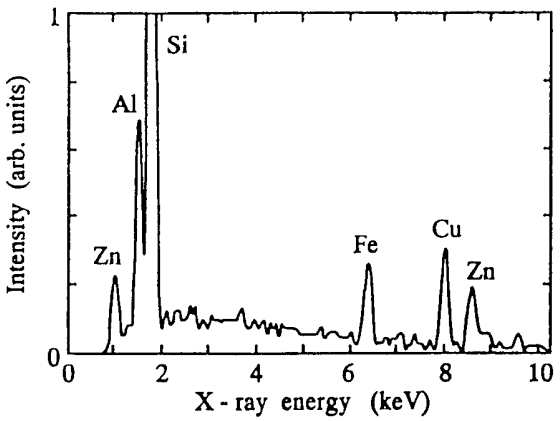

Fig. 4 Mass spectrum of Si substrate after 7 shot.

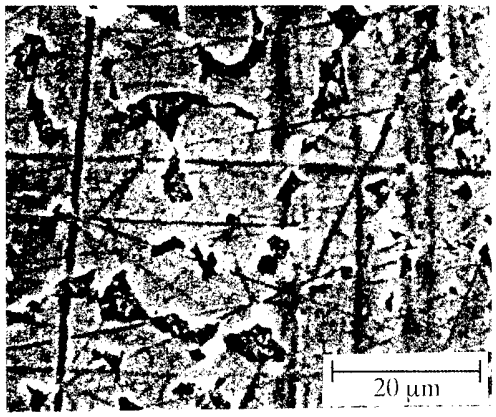

Fig. 5 Microscope image of surface of ion source.

figure, J_i rises at about 30 ns after the main voltage pulse. Through all shots, this delay time is in the range of 20-50 ns and it is independent on d or the number of shot. A peak value of J_i is 330 A/cm^2 at 1st shot (Fig.2 (a)), and after 7 shots, the value decreases up to 150 A/cm^2 (Fig.2 (b)).

Figure 3 shows dependence of J_i on the number of shot. Series of the successive operation are repeated for 8-11 times for each gap length. Dots and error bars indicate averages and deviations of peak value of J_i, respectively. In 1st shot the larger value of J_i =350 A/cm^2 is observed at d = 5 mm. The value of J_i decrease with increasing the number of shot, and at 7th shot J_i decrease up to ≈150 A/cm^2.

4. Effect of sticked matter on LIB generation

When MID is successively operated, sticked matter is stacked on the ion source surface.

To analyze the composition of the matter, Si substrate is attached on the center of the active anode. After shots the substrate is removed and the mass spectrum of the surface of the sample is analyzed by an X-ray fluorescence analyzer, the result of which is shown in Fig. 5. The surface consists of Al, Zn, Fe and Cu, which seems to be produced by the ablation of the electrodes by the irradiation of ion beam or electron beam.

Figure 6 shows the scanning electron microscope image of the surface of ion source after 7 shots. As seen in the figure, the full surface of the ion source is covered with the sticked matter.

To evaluate the effect of the sticked matter on the generation of ion beam, change of J_i is observed on the following procedure.

(a) Operate 6 shots.
(b) Break the vacuum and exhaust again. (non-elimination)
(c) Operate 3 shots.
(d) Break the vacuum, eliminate the matter by wiping the surface and exhaust again. (elimination)
(e) Operate 5 shots.
(f) Switch to rotary pumps from diffusion pumps, keep the MID in low vacuum of 10 Pa for 20 minutes and after that, exhaust again.
(g) Operate 1 shot.

Above procedure is repeated for 5 times, and

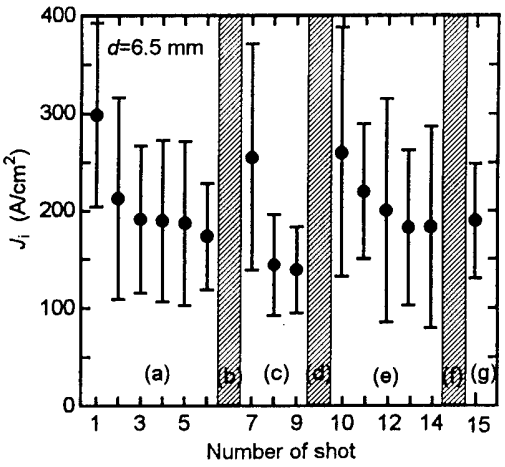

Fig. 6 Dependence of J_i on elimination or non-elimination of sticked matter.

obtained the statistics of the data (Fig.7). On the process (c), high value of J_i is obtained only at the first shot, and after the 2nd shot J_i became low. On the other hand, on the process (e), J_i of 300 A/cm^2 is obtained at the first shot and it gradually decreases with increasing number of shot. This characteristics is almost similar to the process (a). From the experiment, we see that the anode is refreshed by eliminating the sticked matter.

In oily exhausting system, 0.5% of residual gas in a vacuum chamber is generally backstreaming oil molecules.[8] The backstreaming oil is expected to be enhanced in the process (f) and it may affect the production of ion beam. However, on the process (g), clear change of J_i is not observed, which shows that backstreaming oil in the vacuum dose not strongly affect the characteristics of ion source.

In the process (d) we see the change of the color of the surface of polyethylene from translucent to white, which seems to be due to the deterioration of the surface by the irradiation of the anode plasma. However, we found that the deterioration dose not affects the successive characteristics.

5. Conclusion

Successively operation characteristic has been evaluated experimentally. An ion current density (J_i) of 350 A/cm^2 is observed at the first shot when diode gap is 5 mm. The value decreases with increasing the number of shot and at 7th shot J_i decreases to be less than 150 A/cm^2. After 7 shots, the surface of anode is observed and is found that it is covered with sticked matter of metallic materials such as Zn, Al, Fe, Cu, and it seems to be produced by the ablation of the electrode. By eliminating the sticked matter form the surface, J_i is recovered to the initial value.

Reference

[1] T. H. Johnson: *Proc. of the IEEE*, **72**, 547 (1984).
[2] K. Yatsui: *Laser & Particle Beams*, **7**, 733 (1989).
[3] K. Yatsui, X. Kang, T. Sonegawa, T. Matsuoka, K. Masugata, Y. Shimotori, T. Satoh, S. Furuuchi, Y. Ohuchi, T. Takeshita and H. Yamamoto: *Phys. Plasmas*, **1**, 1730 (1994).
[4] E. L. Neau: *IEEE Trans. on Plasma Sci.*, **22**, 2 (1994).
[5] K. Yatsui, A. Tokuchi, T. Tanaka, H. Ishizuka, A. Kawai, E. Sai, K. Masugata, M. Ito and M. Matsui: *Laser & Particle Beams*, **3**, 119 (1985).
[6] K. Yatsui, Y Arai, k. Masugata, M. Maruyama, M. Ito, E. Sai, M. Ikeda, Y. Shimotori, A. Takahashi and T. Tanabe: Proc. of 6th Int'l conf. On High-Power Particle Beams, Kobe, Japan, 329 (1986).
[7] R. N. Sudan and R. V. Lovelace: *Phys. Rev. Lett.*, **31**, 1174 (1973).
[8] L. Maurice, P. Duval and G. Gorinas: *J. Vac. Sci.*, **16**, 741 (1979).

EVALUATION OF THE EFFECT OF ANODE GROOVE PITCH TO ION BEAM FOCUSIBILITY ON SPHERICAL PLASMA FOCUS DIODE

K.Imanari, W.Jiang[+], K.Masugata[+], and K.Yatsui[+]
Dep. of Elec. Eng., Oyama Nat. Col. of Tech., Oyama, Tochigi 323, Japan
[+]Lab. of Beam Tech., Nagaoka Univ. of Tech., Nagaoka, Niigata 940-21, Japan

ABSTRACT

To evaluate the effect of anode plasma ununiformity on LIB focusibility, we have developed a new PIC simulation code. Inducing anode grooves in the code, we have represented the anode plasma ununiformity. On the experiment conditions, groove pitch ~ 2.2 mm and groove width = 1.0 mm, simulation results is in good agreement with the those of the experiments. At the groove pitch = 2.4 mm, local divergence was very small, although focus length was very long. Therefore, we have recognized that the focusibility of SPFD would be determined by the z-deflection angle rather than the local divergence angle. To get higher power density on focus point, it may be effective to modify the anode curvature.

§1. Introduction

To obtain intense, pulsed, light-ion beam (LIB), we have developed Spherical Plasma Focus Diode (SPFD). Figure 1 shows the schematic of the SPFD. It is three-dimensionally focused, self-magnetically insulated diode. Its features are given below, 1) very simple and compact structure, 2) large solid angle of focusing, and 3) axial symmetry [1,2].

On experiment, the LIB focusing size has been evaluated to be 6.0 mm × 4.5 mm$^{\phi}$ by using Rutherford scattering camera. Since the average deflection angle measured by shadow box is only 1~7 degrees in the elevation angle of ψ, it is considered that the LIB seems to have large local divergence [3]. The local divergence will be caused by nonuniformity of anode plasma and electric field disturbance along the anode surface. To evaluate the effect of anode plasma ununiformity on

LIB focusibility, we have developed a new PIC simulation code.

§2. Simulation Results

Table 1 shows the specifications of PIC code. We have considered the anode grooves in the code. It is expected that the ununiformity of anode plasma and disturbance of electric equi-potential surface would be produced.

Figure 2 shows the waveforms of diode voltage(V_d) and current(I_d), in case of experimental anode groove condition (pitch ~ 2.2 mm, width = 1.0 mm). Their peaks are V_d~940 kV and I_d~160 kA respectively. The diode impedance estimated to be 5.9 Ω. They are well matched with the experimental results.

Figure 3 shows the typical ions map and equi-potential lines at t=4.5 ns, associated with Fig. 2. It is proved that the equi-potential lines was disturbed along the ion density alternation. Moreover, ions locus have curved in the acceleration gap. It is considered that they will cause the large local divergence and deflection.

To estimate the effect of the potential disturbance on the LIB focusing, we have evaluated the ion beam local divergence. Figure 4 shows the local divergence angle dependency on anode groove pitch. It was calculated from the FWHM of ion profile accumulated on z axis, and averaged in the elevation angle of ϕ. Fig. 4 gives the minimum of 41 mrad at anode groove pitch = 2.4 mm and maximum of 60 mrad at 3.0 mm.

Figure 5 shows the local z-deflection angle averaged in the elevation direction of ϕ. The deflection angle seems to be increase with the groove pitch. At anode groove pitch = 2.4 mm, z-deflection angle of 114 mrad is in good agreement with the experimental result.

Figure 6 shows the ion focus length observed on the diode axis of z. At anode groove pitch = 2.2 mm, where the local divergence angle is small, the focus length has the peak of 6.6 mm. Putting these results together, we have recognized that the focusibility of SPFD would be determined by the z-deflection angle rather than the local divergence angle. To get higher power density on focus point, it may be effective to modify the anode curvature.

§3. Conclusion

1) We have developed a new PIC Simulation code. It is including the

anode groove to evaluate the ion beam focusibility.

2) On experiment anode conditions, simulation results is in good agreement with the experimental results.

3) The focusibility of SPFD would be determined by the z-deflection angle rather than the local divergence angle.

References

[1] K. Yatsui, et al., Proc. 12th Int'l Conf. on Plasma Phys. and Controlled Nucl. Fusion Res., IAEA, 3, 153(1989).

[2] W. Jiang, et al., Physics of Plasmas, 2, 325(1995).

[3] W. Jiang, et al., Laser and Particle Beams, 13, 343(1995).

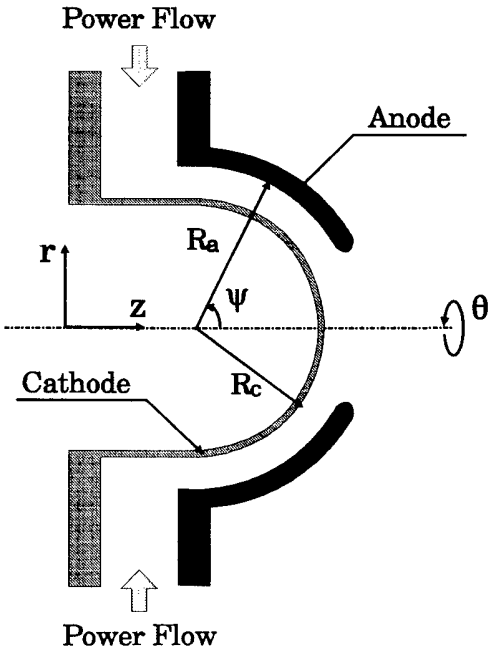

Figure 1 Schematic of the SPFD

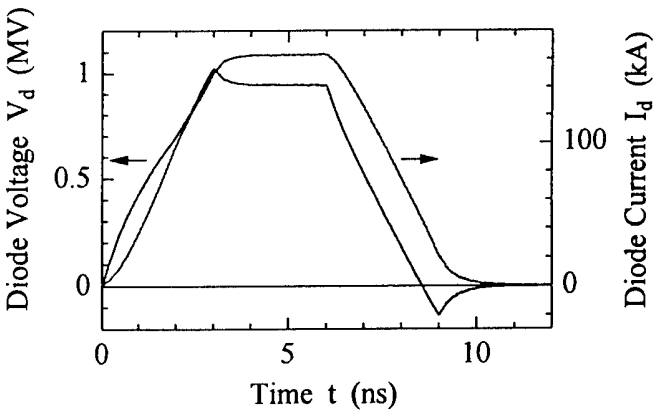

Figure 2 Waveforms of diode voltage(V_d) and current(I_d)

Table 1 Specification of Simulation Code

PIC Code	
Treatment	: Electro-Magnetic and Relativistic (only ion)
Dimension	: 2.5
Mesh Size	: 0.02 cm square
Time Resolution	: 0.3 ps

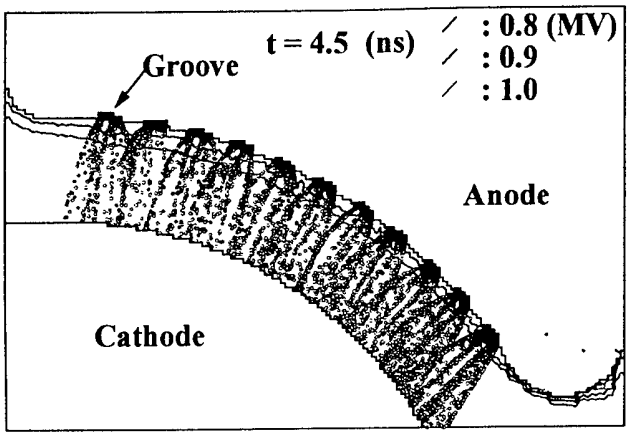

Figure 3 Ions map and equi-potential lines

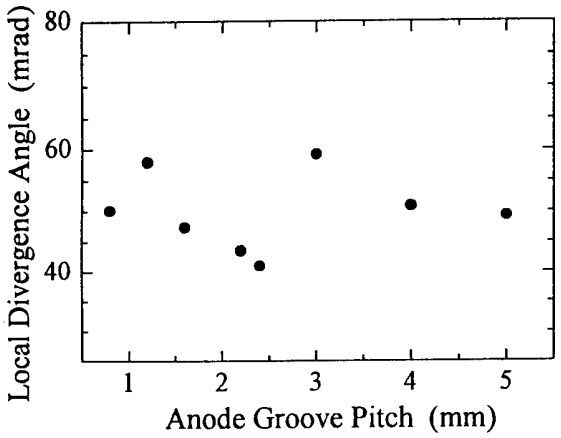

Figure 4 Local divergence angle dependency on groove pitch

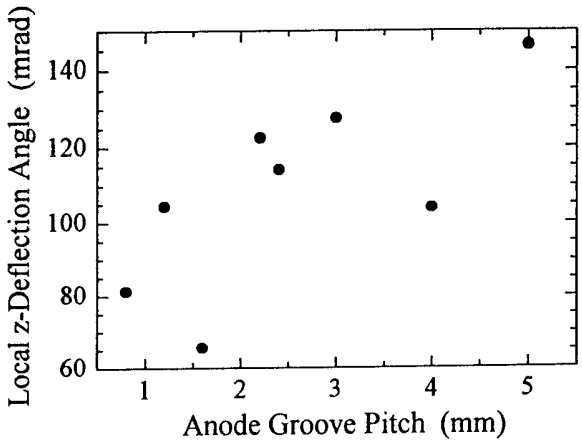

Figure 5 Local z-deflection angle dependency on groove pitch

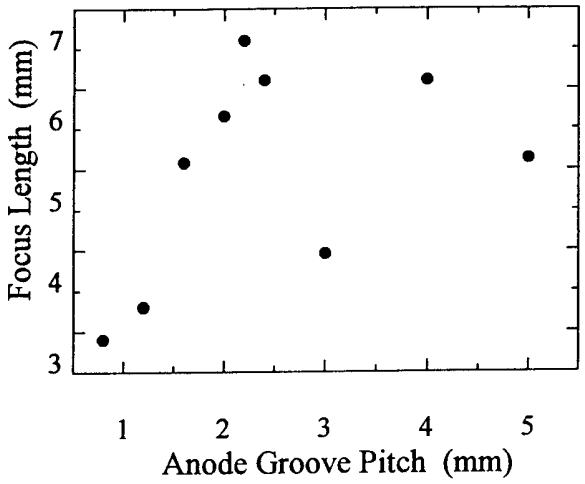

Figure 6 Focus length observed on the diode axis

The Cornell Field-Reversed Ion Ring Experiment FIREX: Experimental Design and First Results*

W.J. Podulka, J.B. Greenly, D.E. Anderson, S.C. Glidden,
D.A. Hammer, Yu.A. Omelchenko and R.N. Sudan

Laboratory of Plasma Studies, Cornell University, Ithaca, NY 14853 USA

Abstract

The goal of FIREX (Field-reversed Ion Ring EXperiment) is to produce a fully field-reversed ring with 1 MeV protons. Such a ring requires about $2\text{–}3\times10^{17}$ protons, or 30–50 mC of charge. This charge is to be injected as an annular proton beam through a suitable magnetic cusp configuration to produce a compact ring. We describe here the critical design issues for the ion beam accelerator. First experimental results of ion diode operation indicate that the design is capable of producing the required beam parameters.

I. Introduction

The new FIREX (Field-reversed Ion Ring EXperiment) accelerator is a 1.2 MV, 800 kA, 150 ns pulsed power source constructed at Cornell for driving a magnetically-insulated ion diode. This diode, based on designs developed at Cornell over the last decade, generates a proton beam in a magnetic field system designed to form ion rings. FIREX is intended as a major step toward the realization of a field-reversed ion ring or ion ring/FRC reactor in which a significant fraction of the azimuthal current is carried by large orbit ions that provide MHD stability to a high-β field-reversed configuration (see companion paper [1]). The goal of FIREX is to produce a fully field-reversed ring with 1 MeV protons, which requires $\gtrsim$ 30 mC protons in the ring and $\gtrsim$ 400 kA proton current from the diode [1]. The basic experimental approach follows that of our earlier experiments: an annular proton beam is injected through a magnetic cusp into a solenoidal field, thereby converting up to 90% of the proton kinetic energy into rotation. On the FIREX experiment, the cusp is very compact axially ($\lesssim$ 12 cm), and the solenoid is a gradual ramp, rising from 6 to 9 kG over 2 meters of axial length. Due to this axial gradient, the circulating beam particles are slowed down axially and eventually are reflected by the mirror effect.

II. FIREX Pulser

In designing the pulsed power driver, the need to limit costs and meet space restrictions while at the same time provide the large amount of charge required to achieve field reversal led to a design that reuses existing tanks and gas switches from the LION pulser [1] but adds new high energy-density capacitors and triaxial pulse shaping lines. A bipolar Marx generator of 24 3.0 μF, 100 kV capacitors charges a 50 nF triaxial water dielectric intermediate storage capacitor (ISC). The ISC is composed of three concentric coaxial cylinders, with the outer- and inner-most cylinders nominally at ground potential (see Figure 1). The outside diameter of the outer cylinder was limited by the dimensions of the existing water tank (2 m). The diameters of the intermediate and inner cylinders were then determined by limiting the electric field on the intermediate conductor to 75% of the positive breakdown strength of water.

After an ISC charging time of approximately 1.2 μs, a self-break SF_6 gas switch closes, charging the pulse-forming line (PFL). In an effort to decrease the overall diameter of the PFL and increase the length-to-circumference ratio, as well as operate with relaxed electric field values on the conductors, the PFL is split into two nested lines. After the main gas switch closes, the

PFL is charged as two lines of 2.5 Ω and 3.2 Ω in series. After the main water switch closes, the lines discharge in parallel as a 1.4 Ω, 60 ns pulseline.

The main water switch is a six electrode self-break switch that connects the PFL to a 1.4 Ω, 20 ns coaxial output line. Inside the output line is a 14 Ω, 80 ns (one way) transit-time isolator used to feed power and signals to and from anode potential. Between the output line and the 60 nH vacuum interface is an 8 electrode prepulse water switch. The diode load sits at the end of a short (~ 65 cm long) 10 Ω magnetically insulated vacuum transmission line attached to the vacuum interface.

The downstream portions of the PFL conductors, output line, and the vacuum insulator outer conductor are all fabricated using perforated stainless steel to allow for shock wave pressure relief when the water switches fire.

In the results reported in this paper, an epoxy groove anode has been used. To achieve a greater proton fraction in the beam, an evaporating metal foil anode plasma source (EMFAPS) anode [2] will later be installed. A new approach will be tried on FIREX to divert a portion of the main pulse energy to drive the EMFAPS foil. Previously, on the LION accelerator, a plasma opening switch was used to transfer a small fraction of the main pulse to drive the anode plasma source. LION data indicate that a 10 ns, 100 kA current pulse that arrives 5 to 10 ns before the main pulse is required to evaporate the metal foil and establish the proper plasma parameters. To avoid the reliability problems of an opening switch, on FIREX a portion of the high-voltage pulse energy is being capacitively coupled to the EMFAPS driver. Electrodes have been placed on the water side of the vacuum insulator inner conductor in close proximity to the grounded water switch midplane. The electrode spacing, as well as the radial position, can be adjusted to change the timing and amplitude of the signal. The signal is carried to the anode foil using a 4 Ω transmission line located inside the inner conductor of the vacuum line. Pspice [3] circuit analysis was used to model the FIREX pulser. Output from the Pspice model was incorporated in PIC simulations during the design phase of the FIREX experiment.

III. FIREX Ion Diode

The central component of the FIREX ion accelerator is an applied-B magnetically-insulated ion diode of a type first employed at Cornell for ion ring generation in 1978. The first critical feature in the diode design is the magnetic field and electrode configuration of the diode, which determines the diode efficiency, distribution of ion current density and the diode impedance. The FIREX design is developed directly from the optimized diode used since 1992 on LION [4]. For FIREX, the voltage and current density are nearly the same as for the LION diode, but the total diode area is a factor of five larger, and the pulse length is three times longer. The FIREX diode and magnetic field configuration are shown in Figure 2. The field is the result of the superposition of the external solenoid driven by a 3 s pulse that penetrates all diode structures, and the diode coil, driven by a 0.5 ms pulse that is excluded by selected components in the structure to shape the magnetic field. The field in the diode gap is designed to produce an ion current density uniform across the diode radius, and to have only a small spread in canonical angular momentum for beam particles at different radii. These conditions are optimized experimentally by adjusting the ratio between the solenoid field and the diode field. Variation of 5% in this ratio changes the magnetic flux surface tilt in the gap enough to significantly change the diode operation. Figure 3 shows diode voltage and total current waveforms, and proton current density measured by filtered magnetically insulated faraday cups at 70% marx charge (64 kV). Figure 4 shows experimental diode current and voltage waveforms from Fig. 3, as well as waveforms from a shot with 20% lower magnetic insulation, compared to the results of Pspice simulations at 100% marx charge. (The simulated current trace is proton current only, and should be multiplied by 1.33 to obtain diode current.) The ion diode impedance profile used in the simulations was constructed from LION diode data, extrapolated to the FIREX pulse length using information

about plasma motion and impedance collapse from LION diagnostics [4]. In the experimental result, the initial voltage rise is slower than the simulation, and the droop in voltage is more rapid in the second half of the pulse. The current waveform shape is similar, but the amplitude is about half of that simulated at full marx charge and the modeled diode coupling. The diode is presently insulated to $V_{crit} = 1.3$ MV (V_{crit} is the critical voltage for magnetic insulation), at the outer anode radius. The design of the diode and cusp fields allows for up to twice this V_{crit}, with the solenoid field matched for optimal ring formation. The two experimental waveforms in Fig. 4 show strong improvement in voltage pulse shape with the 20% increase in V_{crit}. We believe that the initial voltage rise is still limited by marginal insulation of the diode at early time, and anticipate that the voltage rise will be further sharpened as V_{crit} is increased. A faster voltage rise and higher early voltage peak should allow a faster rise in the ion current enhancement, and bring the initial current rise up toward the simulation. We also believe that the late voltage droop will be further lessened by stronger insulation, based on LION data. Turn-on of the present passive anode may limit the allowable increase in V_{crit} to achieve these goals, but the EMFAPS anode should relax this limitation as well as provide a much higher proton fraction than the presently inferred $\sim$ 60% of the beam. The FIREX diode is designed with an area of 500 cm^2, so that the required ion current density is limited to below 1.5 kA/cm^2, to avoid severe "parasitic load" regimes in which ion current is diverted to undesired ion species, and diode impedance collapses rapidly.

The FIREX pulser design process used the diode model and ring generation requirements in a much more detailed and interactive way than previous pulsed power generator designs, in that calculated beam pulses from the accelerator (diode and pulser) were used extensively in ring formation simulations to iteratively optimize the design of both the pulser and the magnetic system. The early results we have shown give promise that FIREX, when optimized at full pulser energy, will be able to provide the beam required for field-reversed ring formation during the next year.

*Work supported by US DOE Grant No. DE-FG02-93ER54221.

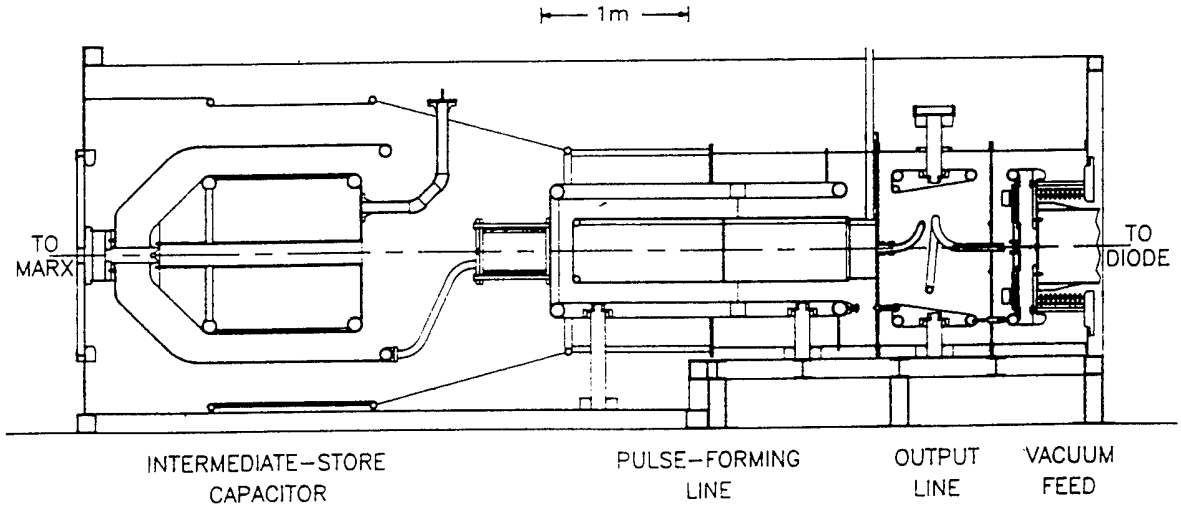

Figure 1: Water section of the FIREX pulser.

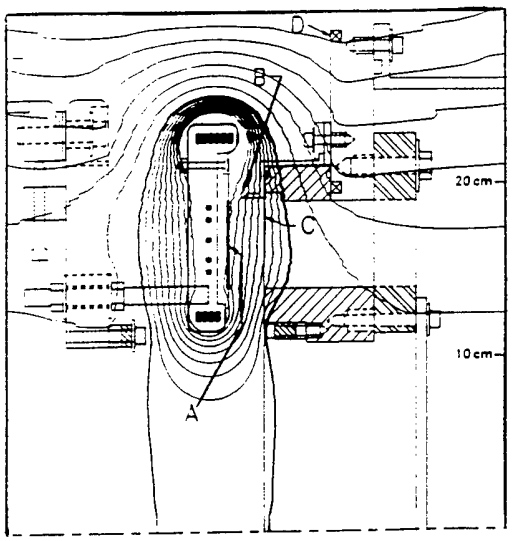

Figure 2: FIREX diode. (A) Anode;
(B) Cathode; (C) Diode Foil;
(D) Diode Current Monitor.
Field lines are plotted less frequently
outside the separatrix for clarity.

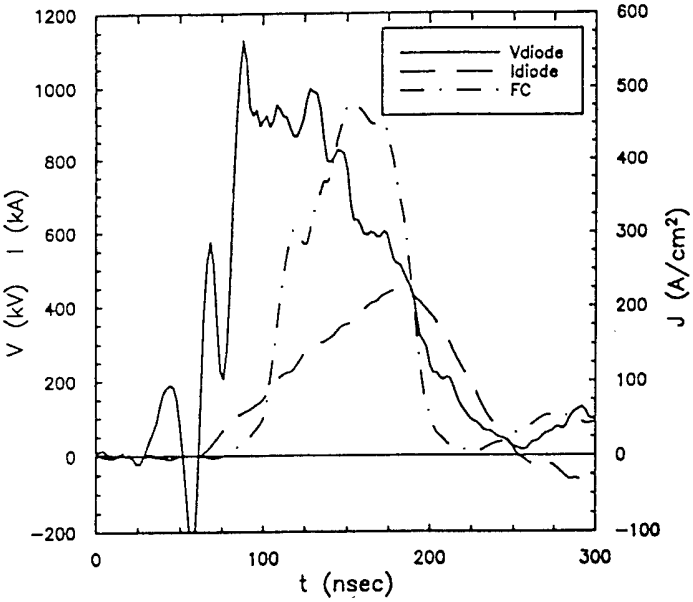

Figure 3: FIREX diode traces.

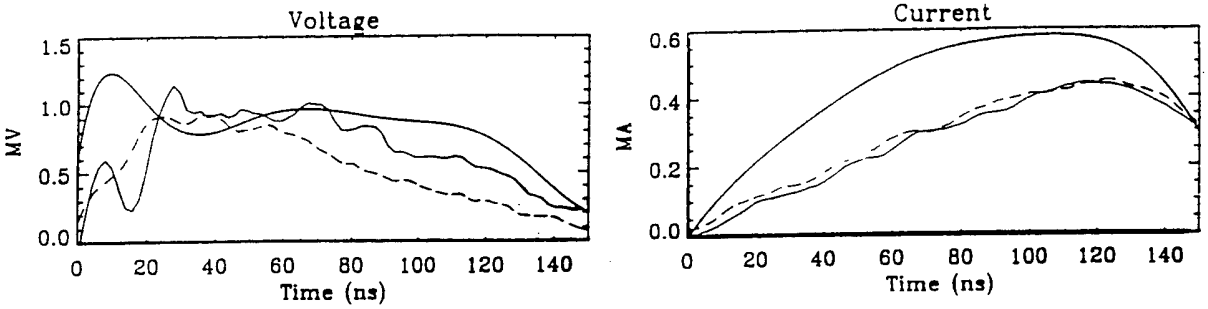

Figure 4: Simulated (solid) and experimental (solid – 1.3 MV V_{crit}, dashed – 1.06 MV V_{crit}) waveforms.

References

[1] R.N. Sudan, J.B. Greenly, D.A. Hammer, Yu.A. Omelchenko, and W.J. Podulka, BEAMS 96 Conference.

[2] G.D. Rondeau, *Studies Of An Extractor Geometry Magnetically Insulated Ion Diode With An Exploding Metal Film Anode Plasma Source*, Ph.D. Thesis, Cornell University (1988).

[3] Pspice Version 5.0, MicroSim Corporation.

[4] J.B. Greenly, R.K. Appartaim, J.C. Olson and L. Brissette, *Proc. 10th Intl. Conf. on High Power Particle Beams*, June 1994, San Diego, p. 398.

3-D Studies of the Formation and Stability of Strong Ion Rings

Yu.A. Omelchenko and *R.N. Sudan*
Laboratory of Plasma Studies, Cornell University, Ithaca, N.Y. 14853

Abstract

We are engaged in conducting complex, 3-D simulations in support of the on-going experimental program, FIREX (Field-Reversed Ion Ring Experiment) launched at the Cornell University to produce an ion ring magnetic field-reversed configuration by injecting an intense annular proton beam across a plasma-filled magnetic cusp region into a neutral gas immersed in a ramped solenoidal magnetic field. Our previous axisymmetric PIC simulations performed with the FIRE code have demonstrated that strong ion rings (with a self-magnetic field large enough to reverse the applied field on axis) can be created using this technique on the equipment designed and assembled at Cornell. We have created a new, parallel, object-oriented, 3-D, hybrid, PIC code, FLAME to study questions of extreme importance to the success of the FIREX program, namely, the 3-D injection of a powerful ion beam into a strongly magnetized plasma, formation of a field-reversed ring, and the stability and equilibrium of such rings to toroidal perturbations. Using FLAME we have investigated the stability of the ring formation during the injection phase and at later times when the ring is virtually stopped and the applied magnetic field is nearly reversed. Our simulations have revealed the effect of toroidal aberrations in the axially ramped magnetic field on the ion ring formation.

1. Introduction

Ion rings [1] consist of energetic ions with gyroradii of order the plasma major radius, and carry enough azimuthal current to generate a self-magnetic field to maintain a self-consistent equilibrium [2].. The project FIREX is currently underway at Cornell to experimentally create an ion ring with large field reversal factor $\zeta = \delta B/B > 1$ (δB is the diamagnetic self-field on axis and B is the external magnetic field). When ζ exceeds unity the resultant field at the axis of the ring is opposite in direction to the external field. Such a configuration is called a Field Reversed Configuration (FRC) (Fig. 1) and has good properties for plasma confinement. In FIREX ion rings are produced by injecting a strong proton beam (with the number of particles $N_b \sim (2 \div 5) \times 10^{17}$) through a magnetic cusp followed by a ramped solenoidal field (Fig. 2).

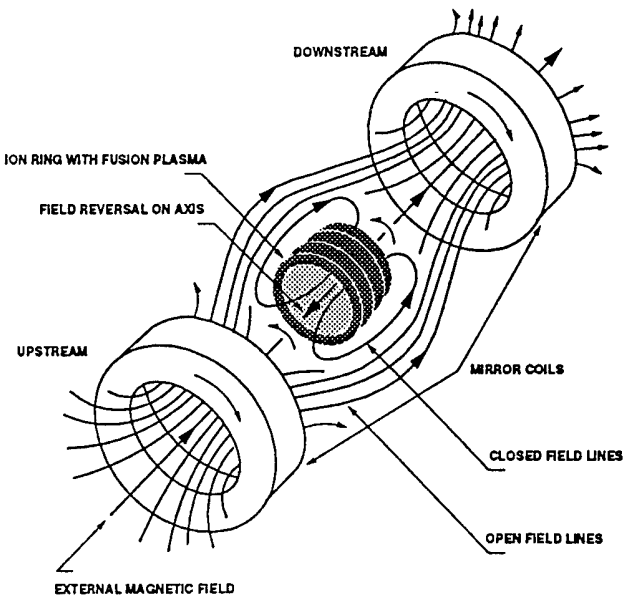

Figure 1: Schematic drawing of ion ring magnetic field reversed configuration.

The effect of the radial component of the cusp magnetic field acting on the particles results in the conversion of a substantial fraction of their axial energy (initially $\sim$ 1 MeV) into the az-

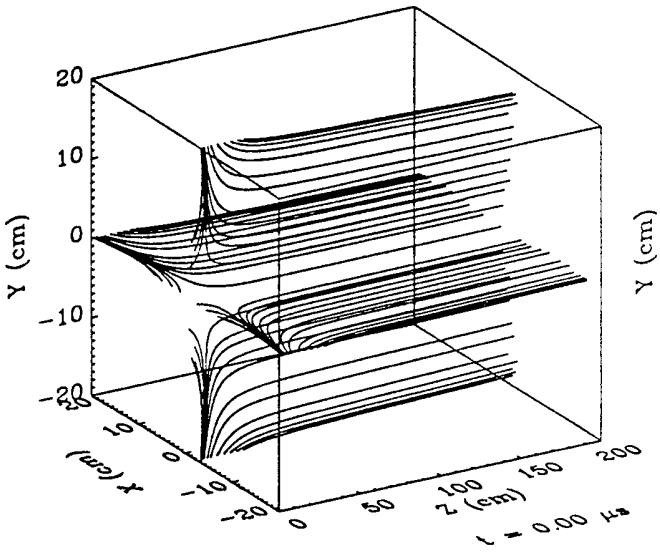

Figure 2: Applied magnetic field structure (field lines are plotted at the poloidal planes, $\theta = 0, \pi/2, \pi, 3\pi/2$).

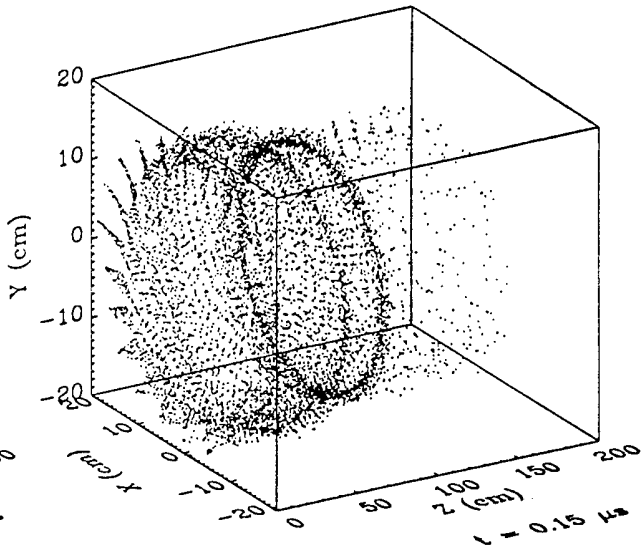

Figure 3: 3-D (Cartesian) snapshot of the rotating ion beam; spikes indicate particle positions on the injection surface.

imuthal energy of particle gyration around the center axis with radii $R \simeq 15$ cm, leading to the formation of a cylindrical layer of rotating ions advancing into the solenoidal field (Fig. 3).

The formation of FRC's by an energetic proton beam, and their long-time stability are the primary issues for analytical and computational research in support of FIREX. Two particle-in-cell (PIC) codes have been developed to study these problems.

The $2\frac{1}{2}$-D (axisymmetric), hybrid, PIC code, FIRE was developed at an early stage of the experimental program, and provided a deep insight [3] into the dynamics of the formation of a strong magnetic field reversed ion ring. Particularly, it was found that:

- the ion beam is trapped and bunched into a ring on a fast timescale (of the order of several ion cyclotron periods) by the self-generated magnetic compressional waves propagating predominantly in the radial direction;
- the ring has a compact form and may contain up to 70% of the total number of injected particles;
- the field reversal on axis (with $\zeta > 1.5$) occurs on the collisional diffusion timescale of several microseconds;
- once closed lines of force are formed the ring and the background plasma act as a collective entity with the result that the energetic ion momentum is shared with plasma ions. Thus the ring is significantly decelerated on reflection in the ramped solenoidal field compared to free particle motion, which gives enough time to switch an upstream mirror to trap the ring.

2. Computational Model

A new 3-D, hybrid, PIC code, FLAME has been created recently to simulate plasma phenomena in the 3-D, cylindrical (r, θ, z) geometry. It is based on the same principles of physics as the $2\frac{1}{2}$-D FIRE code, i.e. it follows low-frequency, quasi-neutral plasma motions described by the Maxwell equations with displacement current totally neglected:

$$\nabla \times \mathrm{B} = \frac{4\pi}{c}(\mathrm{j}_e + \mathrm{j}_i), \qquad (1)$$

$$\frac{\partial \mathbf{B}}{\partial t} = -c\nabla \times \mathbf{E}, \qquad (2)$$

where $\mathbf{j}_e, \mathbf{j}_i$ are the electron and total ion current densities. The multiple ion species are represented by macro-particles (whose motion is governed by the Newton-Lorentz equations), and the electrons are modeled as a cold massless fluid obeying a generalized Ohm's law:

$$\mathbf{E} = \frac{1}{\sigma}\mathbf{j}_e + \frac{\mathbf{j}_e \times \mathbf{B}}{en_e c}, \quad \sigma = \frac{\omega_{pe}^2}{4\pi(\nu_{ei} + \nu_{en})}. \qquad (3)$$

In (3) ω_{pe} and n_e are the electron plasma frequency and number density; ν_{ei} and ν_{en} are the characteristic frequencies of elastic electron collisions with background ions and neutrals, respectively. We use a finite-difference representation to discretize all spatial operators in the poloidal plane (r,z), and exploit the periodic nature of the toroidal, θ-direction by representing all physical quantities as finite Fourier series and using a fast Fourier transform (FFT) algorithm to switch between the cylindrical mode and configuration spaces. The magnetic field $\mathbf{B}$ components are defined on the staggered poloidal grid mesh (commonly known as the Yee lattice) to ensure the conservative form of a discrete divergence analog, $\nabla \cdot \mathbf{B}$. The electric field, $\mathbf{E}$ in our model is not advanced in time as it is normally done in fully electromagnetic codes, but instead is found from its relation to the electron density and current (3). To avoid significant numerical errors that can result from nonlocal operations performed in spatial regions with large plasma density gradients we introduced two grid vector fields, corresponding to the physical electric field, $\mathbf{E}$. The *primary* field is computed via Ohm's law and defined along with the quantities describing plasma response (the ion and electron charge, ρ_e, ρ_i, and current, $\mathbf{j}_e$, $\mathbf{j}_i$ densities) on the Yee E_θ-grid. The *secondary* electric field is constructed by a spatial averaging of the primary field, and defined together with a discrete curl operator, $\nabla \times \mathbf{B}$ at standard Yee's vertices. Thus, the resulting spatial finite-difference operators are accurate to the second order of mesh spacing, conserve $\nabla \cdot \mathbf{B}$ identically (with computer arithmetics precision) and provide an explicit algorithm for computing the self-consistent, low-frequency, electromagnetic field.

Boundary conditions for $\mathbf{E}, \mathbf{B}$ on axis are satisfied in m-mode space by taking advantage of the known asymptotic behavior of each particular mode. The electric field, $\mathbf{E}$ and the normal component of the magnetic field, $\mathbf{B}$ are assumed to vanish at all conducting surfaces (the shorting out of the normal component of $\mathbf{E}$ can be validated either through the assumption of surface charge quasineutrality at the plasma-metal interface due to an "infinite" electron supply by the conducting wall at high magnitudes of the electric field that could result under experimental conditions, or by assuming infinite permittivity of the wall material, ϵ). The tangential component of the magnetic field then suffers a discontinuity across plasma boundaries (it vanishes inside conductors). Particle boundary conditions absorb (beam species) or reflect (background ions) particles at all rigid boundaries.

FLAME has been designed to run on massively parallel facilities. The parallel computing is achieved, as usual, by partitioning the global computation domain into subdomains, assigning grid and particle data to each subdomain, and processing them concurrently [4]. The numerical algorithm alternates the time advances of the magnetic field and particle positions as well as the particle charge deposition with acts of transfering grid and (if necessary) particle data between the neigbouring subdomains. The partitioning of the global computation region is done only in the poloidal plane so that FFT's are always local to processors. The general (object-oriented) communication algorithm we have developed assigns an arbitrary number of subdomains to any particular processor and makes possible the transfer of grid and particle data across the processors using similar (in spirit) techniques.

3 Results

We have applied FLAME to study the 3-D stability of ion beam injection and ring formation phase. The important point of this study was to

determine whether the presence of toroidal fluctuations in the beam density and current, caused by static toroidal aberrations of the ramped applied magnetic field, $m \neq 0$ may amplify perturbations to such an extent that they have a disruptive effect on a ring trapping and the formation of a field-reversed configuration.

The results hint the good toroidal stability properties of the rings previously observed in the axisymmetric ($2\frac{1}{2}$-D) simulations. In particular, we have studied the "quiet" injection (Fig. 3) of an unperturbed ion beam into a ramped applied magnetic field distorted by static dipole ($m = 2$) radial and toroidal harmonics of the order of several percent of the radial component of the axisymmetric solenoidal field at the characteristic beam injection radius.

We have found that this symmetry-breaking factor does not significantly interfere with the beam trapping and ring formation mechanisms previously studied under the assumption of axisymmetric evolution of the beam-plasma system. The beam is trapped by the self-field on the same spatial and temporal scales previously derived from the axisymmetric studies (Fig. 4). However, the 3-D simulation reveals that the beam modulation at $m = 2$ (which develops during the ring formation and disappears later on due to the phase mixing of the large-orbit beam particles), results in an increase in the radial beam temperature and an additional radial beam spread compared to the axisymmetric case.

We have discovered that the maximum toroidal perturbations of the ring-generated magnetic field are of the order of 20% of the averaged self-field strength at the ring location after 1 μsec. However, the self-field that diffuses to the axis remains much more uniform throughout the simulation. The temporal evolution of the maximum field-reversal factor follows very closely the time history during the axisymmetric formation of the ring (obtained in $2\frac{1}{2}$-D simulations), and even speeds up thereafter due to the closer proximity of the ring to the axis.

We intend to verify further these important issues through a thorough investigation of the stability of a stationary, field-reversed ring with respect to the tilt and precession modes. The results of our research are expected to provide further insight into the general theory of equilibrium and stability of field-reversed configurations.

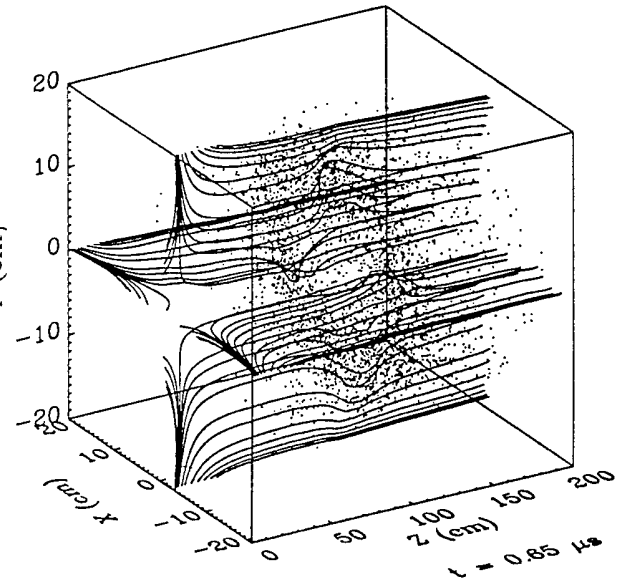

Figure 4: Superimposed 3-D simulation snapshots of the total magnetic field and the ion ring.

This work was supported by U.S. DOE Contract No. DE-FG02-93ER54221, and was done using the IBM SP2 system of the Cornell Theory Center.

References

[1] R.N. Sudan. "Particle Ring Fusion". In B. Brunelli and G.G. Geotta, editors, *Unconventional Approaches to Fusion*, page 311. Plenum. Publ. Corp., New York, 1982.

[2] J. Finn and R.N. Sudan, Nucl. Fusion **22**, 1443 (1982).

[3] Yu.A. Omelchenko and R.N. Sudan, Physics of Plasmas **2**, 2773 (1995).

[4] P.C. Liewer and V.K. Decyk, J. Comp. Phys. **85**, 302 (1989).

HIGH CURRENT ION INJECTORS FOR LONG-PULSE INDUCTION ACCELERATORS

J. Hasegawa, H. Nakai, H. Iwasaki, M. Nakajima, K. Horioka, and S. Kawasaki*

Department of Energy Sciences, Tokyo Institute of Technology, Nagatsuta 4259, Midori-ku, Yokohama, 226, Japan.
**Department of Physics, Saitama University, Urawa, 338, Japan.*

Abstract

This paper presents results of our recent study on reproducibility of ion beams extracted from a grid-controlled vacuum arc ion source. Mass-spectroscopy measurements showed that the vacuum arc discharge plasma sometimes contains large amount of impurities. We found that these impurities change a space-charge-limited current value of the extraction gap and degrade the reproducibility of the extracted ion beams. We also found that the production of impurities can be suppressed with a liquid-N_2 trap installed near the arc electrode.

Introduction

The goal of our study is to develop high-current ion injectors for long-pulse induction accelerators. Requirements for such ion injectors include the following: high brightness, good reproducibility, and high repetition rate. Moreover, they must supply adequate ions for more than μs pulse duration. As a candidate of the ion sources that can meet such severe requirements, we developed a vacuum arc ion source.

Until now, many scientists have estimated the capability of vacuum arc ion sources as ion injectors[1]. One of the major problems is that the ion beams extracted from the vacuum arc ion sources have large beam noise and poor reproducibility. This is because the vacuum arc plasma usually has strong flux variations, which makes it difficult to keep the perveance matching at the extraction gap during the pulse. To solve this problem, Humphries *et al.* originally proposed and developed a grid-controlled extractor, which decouples the beam optics from the source fluctuation[2]. Since this extractor operates in a space-charge-limited mode and the virtual anode in the extraction gap maintains the ion beam current density at a Child-Langmuir(CL) value, it can reduce the beam noise and improve reproducibility of the extracted ion beams.

We adopted the grid-controlled extractor for our vacuum arc ion source and tested its basic operations in the previous experiments[3]. From the previous results, we confirmed that the grid-controlled structure is effective for noise reduction and control of ion beam waveforms. However, we also found that the waveforms of the ion beams often become very noisy and lose their reproducibility. In such a situation, the ion beam current density increases beyond the calculated CL value. This seems to imply that the effective CL value of the gap is enhanced by lighter ions or higher stripped ions in the source plasma. To confirm it experimentally, we have performed mass spectroscopy of the extracted ion beams. In this paper, we report

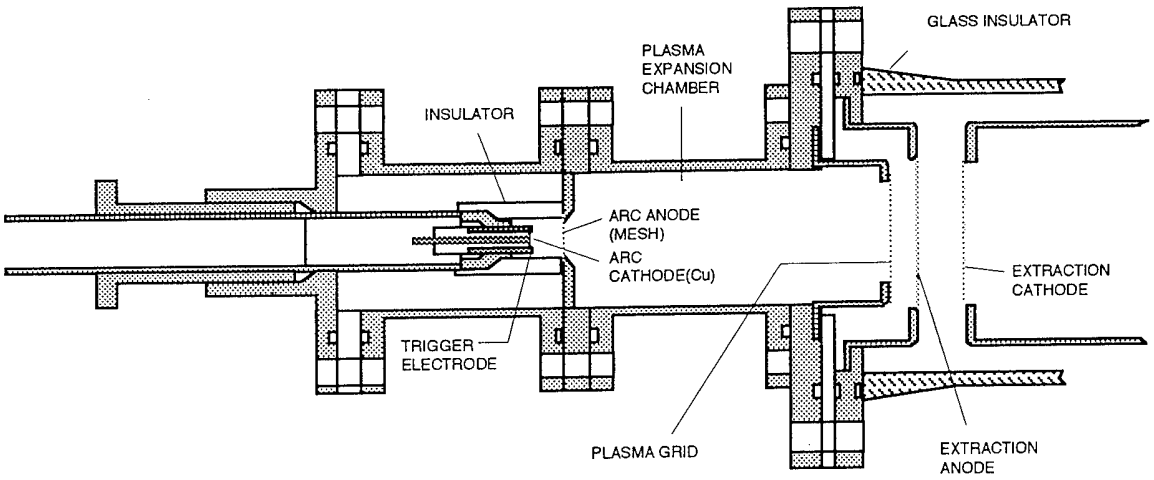

Fig. 1 Schematic drawing of vacuum arc ion source

the results of the mass spectroscopy and discuss the operation of the grid controlled extractor in case the source plasma has the charge-to-mass distribution.

Experimental Setup

A schematic drawing of the vacuum arc ion source is shown in Fig.1. The arc cathode is surrounded by the ceramic insulator and the cylindrical trigger electrode of stainless steel. The arc anode consists of a stainless-steel mesh. The mesh anode can stabilize the source plasma supply because it assures almost uniform electric field over the cathode surface. The driving circuit of the vacuum arc discharge is a 5Ω-100μs pulse forming network and the arc discharge current is typically set to 100-200A. The grid-controlled extractor consists of three grid electrodes of tungsten mesh(100mesh/inch, ϕ0.02). The anode is biased at about -90V with respect to the plasma potential to confine the source plasma electrons in the expansion chamber. The dc extraction voltage(1-10kV) is applied with a 0.25μF capacitor. The pressure of the chamber is maintained at 10^{-6}-10^{-5}Torr by turbo-molecular pumps and in some measurements liquid-N2 cryo-pumping is additionally used to achieve lower background pressure.

To perform mass-spectroscopy measurements, a mass-selection magnet is directly connected to the vacuum arc ion source. A Faraday cup installed downstream detects the signal of the ion beams whose directions are bent by 30 degrees by the magnet.

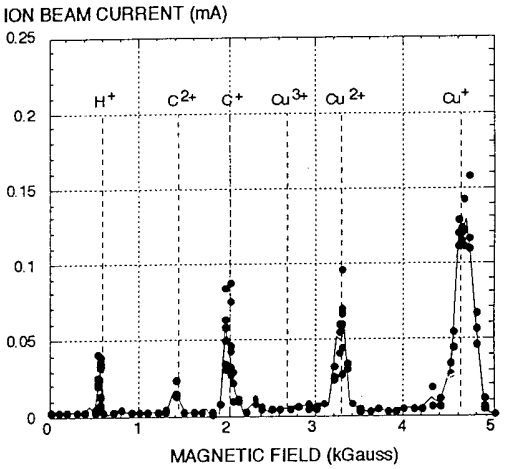

Fig. 2 Charge-to-mass distribution of vacuum arc ion beams. Cu cathode, Extraction voltage : 10kV

Results and Discussions

The result of mass spectroscopy of the ion beams produced with the copper cathode is shown in Fig.2. Figure 2 reveals that the source plasma clearly contains carbon ions and protons as ingredients. Particularly, the amount of the carbon plasma is comparable to the amount of the copper plasma.

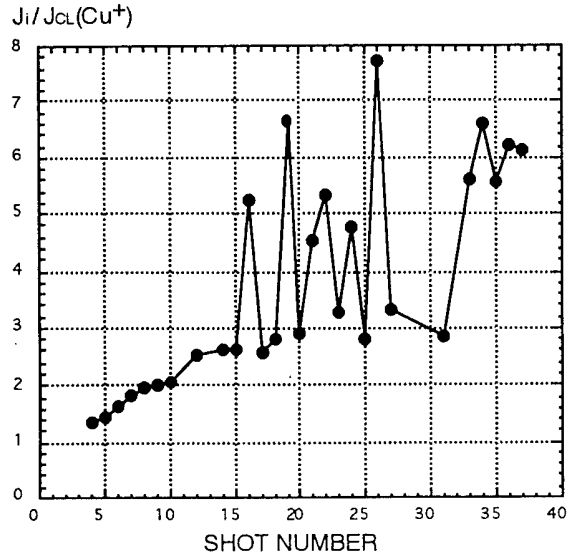

Fig. 3 Dependence of averaged current density on total shot number. Copper cathode.

Therefore, the existence of these lighter plasma component leads to enhancement of the CL value.

We observed that averaged ion current increased with operations. Figure 3 and 4 show the dependence of the beam current enhancement on the total number of shots. In Fig.3, the current density of each shot is averaged over 100μs, and normalized to the CL value for Cu^+. When we successively operate the ion source, typically three types of current waveforms are observed. Each shot number corresponds to the shot number in Fig.3.

As shown in Fig.4(a), at the beginning of the serial operation, the ion source operates fairly well. The current density is constant during the whole pulselength and almost equal to the CL value except for the initial and final peaks. The cause of large initial peak is probably hydrogen plasma produced by the trigger discharge and the initial arc discharge. The final one can be explained by the increase of the CL value caused by the fall off of the virtual anode potential.

The current density increases with increasing number of total shots. In Fig.4(b), although the waveform has almost flat top

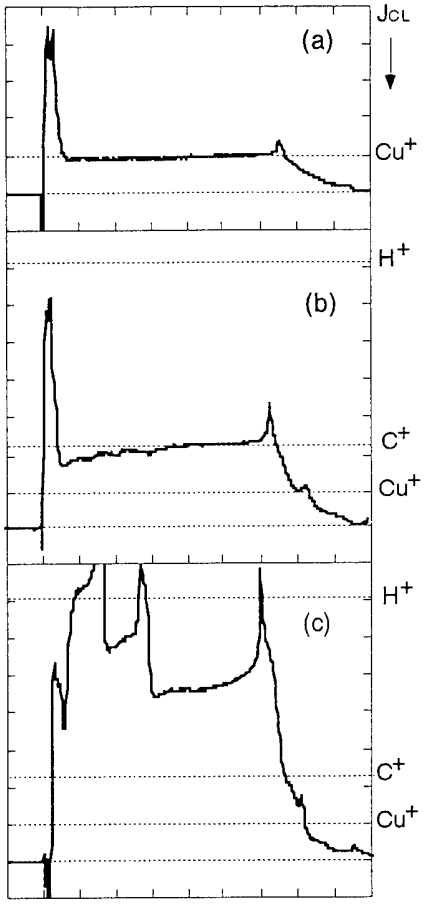

Fig. 4 Typical waveforms of ion beam at different shot number. Shot number is (a) 4 (b) 15 (c) 34 H:20μs/div V: 0.28mA/cm^2/div

between the two peaks, the normalized current density becomes close to the CL value for C^+.

When the total number of shots exceed about twenty(Fig.4(c)), the current density fluctuates considerably between the shots and then there is no reproducibility at all. In this situation, the waveform of ion beam current sometimes has several spikes. The peak value often exceeds the CL value for protons. We think that the leakage of the plasma electrons occurs in addition to the enhancement of the effective CL value.

From these results, we can make the following two remarks: first, the source of impurity is probably hydrocarbonic compounds around the vacuum arc region. Second, the vacuum arc discharges tend to pollute the cathode surface still more. In fact,

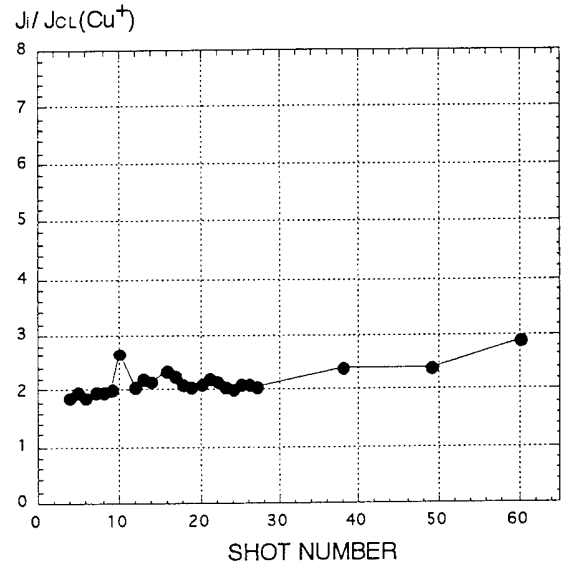

Fig. 5 Dependence of ion beam current density on total shot number with liquid N2 trap.
Background pressure: $3x10^{-6}$Torr.

we observed that the edge of the cathode became dirty after several tens of shots.

To perform the plasma production at cleaner cathode surface conditions, we installed a liquid N_2 trap near the arc cathode. The background pressure was decreased down to $3x10^{-6}$Torr.

As shown in Fig.5, the enhancement of the ion beam current density is considerably suppressed by the use of the liquid-N_2 trap. After 60 shots, its enhancement factor is less than 1.5.

The above results indicate that elimination of the impurities around the arc discharge region improve the reproducibility of the ion source.

Concluding remarks

We explored the effects of impurities on the operation of the grid-controlled vacuum arc ion source, which becomes a severe problem when we applied the source to accelerator injection. From the mass spectroscopy measurements, we found that the copper plasma produced in our source contain large amount of carbon plasma as impurity. The existence of lighter impurities leads to the enhancement of the ion beams. Moreover, the strong flux variations of impurities leads to the beam noise and degrades the reproducibility of the waveforms of the ion beams

References

[1] B. H. Wolf, H. Emig, D. Rück and P. Spädtke, : Rev. Sci. Instrum. **65**(1994), p3091

[2] S. Humphries, Jr. et al., : J. Appl. Phys., **59** (1986), no. 6, p1790.

[3] J. Hasegawa, M. Nakajima and K. Horioka, NIFS-PROC-**23** (1995), p35.

MICROSTRUCTURED LIQUID METAL ELECTRON AND ION SOURCES (MILMES/MILMIS)

J. Mitterauer

Technische Universität Wien, Institut für Allgemeine Elektrotechnik und Elektronik
Gusshausstrasse 27-29, A-1040 Wien, Austria

Abstract

Ion or electron beams can be emitted from liquid metal wetted needles, or from capillaries or slits into which the liquid metal is allowed to flow. Large-area liquid metal field emission sources have been proposed recently, using either two-dimensional, regular arrays of cones or capillaries, or even a substrate with an intrinsically microstructured surface covered by a liquid metal film. This latter concept has been realized in a pilot experiment by *in situ* wicking and wetting of a porous sintered metal disc. Microstructured liquid metal ion or electron sources are capable to operate in a pulsed mode at a current level which is orders of magnitude above that for steady-state operation.

Introduction

In a liquid metal field emission source (i.e., a liquid metal ion source (LMIS) or a liquid metal electron source (LMES), depending on the polarity of the applied voltage) the ions or electrons, respectively, are generated directly at the surface, or are emitted directly from the surface of a liquid metal exposed to vacuum by means of a high electric field resulting from suitable voltages applied to an emitting electrode geometry. When the surface of a liquid metal is subjected to a high electric field, it is distorted into a cone or a series of cones which protrude more and more from the surface with increasing field strength. With increasing applied voltage, the radius of curvature at the apex of these cones becomes smaller and smaller, and therefore, the local electric field at the tip becomes larger and larger. When the local field reaches values of the order of 10^9 V m^{-1}, atoms of the metal tip are ionized either by field evaporation and/or field ionization. With the proper polarity, the free electrons are rejected into the bulk of the liquid metal, while the ions are accelerated and expelled from the emitter by the same electric field which has ionized them. The ionization process is accompanied by a faint luminous glow surrounding the apex region of each cone. The brightness of this glow increases with growing emission current. Because the radius of curvature at the apex of such a cone is about 10^{-7} m, for interelectrode spacings of some 10^{-3} m applied voltages of some 10^3 V are sufficient to obtain the required high electric fields.

The static forces involved in the formation of the cones are polarity independent; therefore, in principle, simply by reversing the polarity of the applied voltage, a LMIS can operate as a liquid metal electron source (LMES) and may be utilized for a hybrid emitter with a single gun assembly.

Comparatively few experiments have been performed with LMES. Swanson and Schwind [1] investigated a Ga-LMES but found only high current nanosecond length pulsed emission, believed to be due to a periodically occuring explosive destruction of the liquid cone.They conclude that DC electron emission from a field stabilized cone is simply not possible regardless of the substrate radius. Later on, using a Ga- and In-LMES, Rao et al.[2] stated that it is possible to obtain DC electron emission if sufficiently sharp needle substrates and low extraction voltages are used. They explained that in such cases the emission is not from a field stabilized liquid metal cone, but rather it is normal field electron emission, as would be expected from such a solid emitter coated with a liquid metal film. Mitterauer [3] has reported DC electron emission from a Cs-LMES with rather blunt emitter tips. However, emission in the field emission (FE) mode has been restricted to a voltage range below the onset voltage of the field ion (FI) mode. Oscillations superimposed on the DC current presumably indicate the ocurrence of microinstabilities similar to micro-cathode spots. Just recently, Hata et al.[4] observed on a sharp needle of a Ga-In-Sn alloy LMES the formation of a seemingly field stabilized microcone during DC electron emission by means of a high voltage transmission electron microscope. The formation site of this microcone is localized and the radius of the base is much smaller than that of the cone in the FI mode operation of the source. When the thickness of the liquid film was increased by inserting the needle into the liquid metal reservoir again, pulsed explosive emission ocurred.

Microstructured liquid metal field emission sources

Microstructured liquid metal ion or electron sources (MILMIS/MILMES) show both an intrinsic and an induced microstructure of the liquid metal surface. The intrinsic microstructure is determined by the geometry and shape of the solid substrate which supports the liquid metal. The induced microstructure primarily is determined by the electrohydrodynamic instabilities induced by the applied electric field. For a single-point LMIS/LMES, the supporting solid substrate is either a needle or a capillary tube. Assuming an uniform wetting of the substrate, there results a single emitting cone or cusp with rotational symmetry. This type of LMIS nearly exclusively has been used within the ample field of focused liquid metal ion beam technology. Equally, almost all LMES-experiments hitherto have been performed with this source type (e.g., [1]-[4]).

In the case of a linear array MILMIS/MILMES, the supporting solid substrate is either a linear array of stacked needles, or a capillary elongated to a long slit of nearly rectangular cross section, therefore allowing the occurrence of a linear array of emitting cones. In the first case, the uniform distance between the emission sites strictly is determined by the intrinsic microstructure, i.e., the equidistant needle tip array. In the second case, the equidistant spacing of emission sites primarily depends on the induced microstructure, i.e., the dependence of the wavelength of a stable mode of the surface capillary wave on the applied field.

Entirely different to the case of single-point LMIS/LMES, there exist only some examples of linear array MILMIS. At the European Space Research and Technology Centre (ESTEC), a field emission electric propulsion (FEEP) system based on the LMIS-principle, with cesium as the propellant, progressively has been developed and evolved from a single-pin emitter, through linear arrays of stacked needles, to the presently favored slit emitter module [5]. Homogeneous high current ion emission from a micron-sized slit has been demonstrated successfully [6], allowing the occurrence of a linear series of equally spaced emitting sites with a distance of less than 10^{-5} m and a linear current density of more than 5×10^{-1} A m^{-1}.

An alternative concept of a linear array type source is the impregnated-electrode-type LMIS with porous ion emission tips made of a refractory metal [7]. Typically, a porous tip is formed by sintering tungsten powder; this porous material is machinable and it is easy to fabricate multiple ion-emission points. Using this approach, germanium ion currents of about $4\text{x}10^{-3}$ A were obtained from a source equipped with a linear array of eight ion emission points equally spaced at a distance of 1.4×10^{-3} m. The corresponding linear current density of about 4×10^{-1} A m^{-1} is comparable with the results for a slit emitter using Cs as liquid metal [6].

Finally, for a two-dimensional array MILMIS, the solid substrate in the most elementary case is a planar surface parallel to a planar counter-electrode. The surface of the liquid will distort into a two-dimensional array of cusplike structures. Theoretically each cusp should be a potential emission site, contributing therefore to a broad ion beam [8]. At Sandia National Laboratories, there was a major effort underway to develop a lithium ion source for inertial confinement fusion (ICF) research on the Particle Beam Fusion Accelerator II (PBFA II) [9]. One of the most promising ion sources under investigation is a two-dimensional array LMIS. This approach involved a large-area (800 cm^2), barrel-shaped, vertical surface made of porous or fritted material in order to provide wicking and wetting from a Li reservoir. The LMIS is located on the anode surface of the accelerator diode, where the high voltage power pulse ($U = 3\times10^7$ V, $I = 4\times10^6$ A, $P = 1.2\times10^{14}$ W, $t < 5\times10^{-8}$ s) from the accelerator should be converted into a beam of energetic Li ions.

Unfortunately, this very first attempt to realize a large-area, two-dimensional array LMIS did not work properly and did not meet the requirements for ICF. Obviously, the main reason for this failure was the use of an intrinsic microstructured, rough solid substrate (made of sintered Inconel 600 with an average grain density of 4×10^4 cm^{-2}) instead of a plane, smooth substrate; therefore, an undisturbed pattern of surface waves with a submicron wavelength never could be attained.

Pilot experiment on a cesium MILMIS/MILMES

By far the most simple method to realize an irregular array structure covered with liquid metal is *in situ* wicking and wetting of a porous sintered metal from a liquid metal reservoir. The similarity of this concept to the impregnated-electrode-type LMIS is obvious; the only difference is in using the intrinsically

roughness of the sintered metal surface instead of machined points as potential emission sites. In order to prove the applicability of this concept of MILMIS or MILMES to cesium (Cs), which is the liquid metal exclusively used with the FEEP-slit emitter [5], Mitterauer [10] has performed an pilot experiment with a gridded Cs-MILMIS/MILMES. A sectional view of the emitter-accelerator configuration of the source is shown in Fig.1. A porous metal disk (1) of 5 mm diameter and 2 mm thickness, made of sintered Inconel 600 (that is the same material being used as the substrate in the PBFA II Li-MILMIS) with a grain size between 10 and 50 µm and an average grain density of about 4×10^4 cm^{-2}, is pressed tightly into the stainless steel emitter body (2). Fig.3a shows a circular image area of this Cs wetted porous microstructure without emission at artificial illumination. Cs is supplied to the reservoir (3) on the rear of the porous metal insert by a totally closed Cs feeding system involving capillary forces. The accelerator electrode is a stainless steel plate (4) with a tapered aperture; on the rear there is stretched a stainless steel grid (5) with a mesh width of 2 mm. The interelectrode distance (the grid to the porous emitter surface) is 2 mm.

The electric circuit is shown in Fig.2. The ion or electron beam is collected by a liquid nitrogen cooled cold shroud CS on ground potential; the emitter E and accelerator ACC are connected to the potentials $\pm U_E$ and $\pm U_{ACC}$, respectively, versus common ground. In order to test the capability of the MILMIS/MILMES to operate in a high current pulsed mode, a low-inductive high voltage capacitor C = 2000 pF is connected between emitter and cold shroud. The impulse current is recorded by the voltage drop on a low-inductance shunt $R_S = 0.1\ \Omega$ with a Tektronix 519 oscilloscope. With applied DC-voltages $U_E = 10$ kV and $U_{ACC} = 2$ kV, characteristic values of the emission current were $I_E = 3\times10^{-5}$ A for the MILMIS and $I_E = 5\times10^{-5}$ A for the MILMES, respectively. The individual emission sites on the emitter surface of the MILMIS are characterized by a more or less bright glow. An analysis of the photomicrograph Fig.3b with an image field of 0.5 mm diameter shows approximately 50 self-luminous emission sites at a total emission current level of about 1×10^{-4} A. Therefore, for the total emitter surface with 5 mm diameter results an average number of about 5000 individual emission sites with a mean emission current of 2×10^{-8} A/site.

Pulse operation of the MILMIS/MILMES is obtained by applying a negative/positive high voltage pulse to the accelerator, while the emitter is connected to the capacitor C at a charging voltage U_E of ±10 - 12 kV. The steady-state emitter current is about $(1\text{-}3)\times10^{-5}$ A. The high voltage pulse is supplied by a coaxial cable pulse generator; the pulse voltage U_{ACC} is ±5 - 15 kV, the pulse width is 6×10^{-8} s with a rise time of 1×10^{-8} s. The resulting high current pulse discharge shows a damped oscillation with a frequency of approximately 4.2 MHz and a duration of about $(6\text{-}8)\times10^{-7}$ s. Depending on both the charging voltage U_E and the pulse voltage U_{ACC}, the measured maximum peak current is between 9×10^2 A for the MILMIS and 1.4×10^3 A for the MILMES, with a maximum increase of 1.7×10^{10} A s^{-1}. After such a pulsed discharge, the MILMIS/MILMES operates obviously without any damage in the low-current regime. These results prove the principal capability of this gated MILMIS and MILMES to operate in a pulsed mode at a current level which is orders of magnitude above that for a steady-state DC mode.

Conclusions

In principle, MILMIS and MILMES are indestructible, regenerative sources of high current, large-area ion or electron beams. This is possible at least by combining both an intrinsic microstructure of a solid substrate and an induced microstructure of a liquid metal.

Prospective appplications of MILMIS's are broad ion beam technologies, e.g., material processing and electric space propulsion. However, the most interesting and spectacular applications of pulsed MILMIS's will be light-ion inertial confinement fusion and fundamental research of matter under unusual conditions. The most promising application of MILMES's is switching in pulsed power technology. This technology normally incorporates the use of capacitive storage of electrical energy that is rapidly delivered to a load by means of a fast closing switch such as a spark gap. There is, however, considerable interest in the use of inductive energy storage primarily because of the order-of-magnitude improvement in stored energy density. One key problem is the lack of a fast, reliable repetitive opening switch. A number of techniques are being investigated for the development of such switches, e.g., electron beam controlled dicharge devices and plasma erosion opening switches. Considering the free-running self-pulsed mode of a single site LMES [1], there exist encouraging prospects for an arrayed, large-area MILMES to be a candidate for such a high current opening switch.

[1] Swanson, L.W. and Schwind, G.A., J.Appl.Phys. 49 (1978) 5655
[2] Rao, K.A., Bell, A.E., Schwind, G.A., and Swanson, L.W., J.Vac.Sci.Technol. B7 (1989) 1793
[3] Mitterauer, J., J. Phys.(Paris) 45, Suppl.12 (1984) C9-185
[4] Hata, K., Saito, Y., Oshita, A., Takeda, M., Morita, C., and Noda, T., Appl.Surf.Sci. 76/77 (1994) 36
[5] Bartoli, C., von Rohden, H., Thompson, S.P., and Blommers, J., J.Phys.D:Appl.Phys. 17 (1984) 2473
[6] Mitterauer, J., IEEE-Trans.Plasma Sci. PS-15 (1987) 593
[7] Ishikawa, J., Gotoh, Y., Fukayama, N., Ogata,.Y., Yoshida, K., and Tsuji, H., Vacuum 44 (1993) 357
[8] Pregenzer, A., Rev.Sci.Instrum. 61 (1990) 571
[9] Gerber, R.A., Bieg, K.W., Dreike, P.L., McKay, P.F., Pregenzer, A.L., Tisone, G.L., and Woodworth, J.R., Rev.Sci.Instrum. 61 (1990) 511
[10] Mitterauer, J., J.Vac.Sci.Technol. B13 (1995) 625

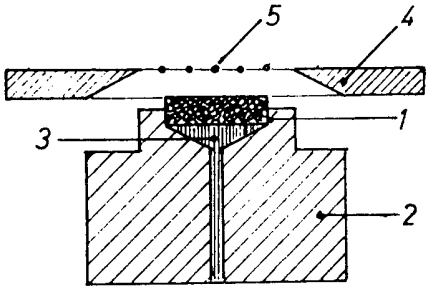

Fig.1. Schematic sectional view of the emitter-accelerator configuration of the Cs-MILMIS/ MILMES. (1) porous metal disc; (2) emitter body; (3) cesium reservoir; (4) accelerator electrode; (5) accelerator grid.

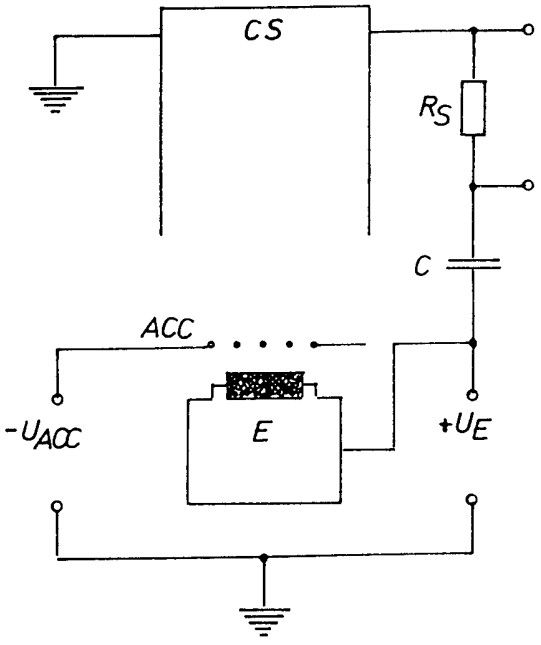

Fig.2. Schematic view of the electric circuit of the Cs-MILMIS/MILMES. ACC, accelerator; E, emitter; CS, cold shroud; C, high voltage capacitor; R_S, low-inductance shunt; U_E, emitter voltage; U_{ACC}, accelerator voltage

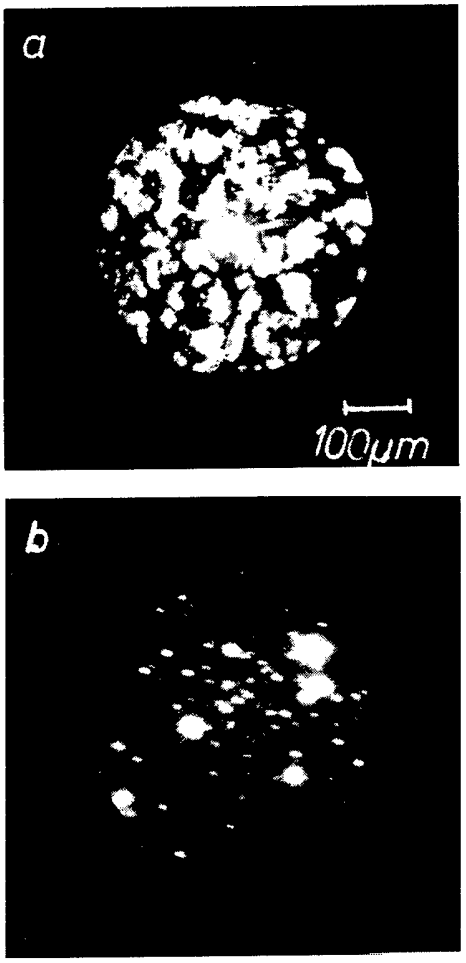

Fig.3. Identical circular image areas (diameter 0,5mm) of the porous emitting surface of the Cs-MILMIS/MILMES. (a) Cs wetted porous micro-structure without emission; artificial ligth exposure. (b) Self-luminous ion emission sites without artificial illumination; exposure time 12 minutes.

GENERATION OF HIGH INTENSIVE AND HIGH POWER METAL IONS BY VACUUM ARC *TAMEK* SOURCES

Alexander M. Tolopa

Applied Physics Institute, P.O.Box 561, Sumy, 244024 Ukraine.
TAMEK HiTech Inc., 1001 Fourth Avenue Plaza, Suite 3200, Seattle, WA, 98154, USA

Abstract

This paper presents a review of vacuum arc facilities to be as injectors for metal ion accelerators. A vacuum arc in different modes: 1). Arc current I_{arc}=2-50 A, pulse duration t_p=10 μs to 20 ms; 2). I_{arc}=20-100 A, t_p=50-1000 μs; 3). I_{arc}=100-2000 A, t_p=100-2000 μs; 4). I_{arc}=10-100 kA, t_p=1-10 μs were investigated as metal ion injectors. The metal flows generated by cathode spots are expanded for diameters of 10-50 cm, and then, or deposited on the grounded target, or post accelerated between grids at U_{accel}=10-120 kV. On the basis of such injectors the series of TAMEK sources were investigated with metal ion current from I_i> 0.01 A, pulse duration up to 20 ms, up to I_i<5 kA, t_p=1-5 μs.

Introduction

Ion beam modification of metals, composite materials, ceramics, glass, polymers is used to improve surface properties such as wear, corrosion and friction resistance, hardness, electrical conductivity, wettability, etc., [1]. In 1984 the authors of Refs.[2-8] started to develop vacuum arc metal ion sources for surface modification technologies. The development was made by designing Technological Accelerator of Metal Ion and Electron Kit (TAMEK sources) which were capable of generating both high-energy metal ion beams and low-energy plasma from the same cathode material, thus providing high-dose (intensive) metal ion implantation (HDI), ion deposition, ion mixing and ion beam assisted deposition (IBAD).

1. Versatile TAMEK source

TAMEK is a vapour vacuum arc source of multiply charged ions (from Me^{+2} up to Ta^{+6}, W^{+6}) emitted from any hard cold electroconductive cathodes (fig. 1). The alternation of HDI and low-energy ion deposition (fig. 2a) was proposed [5]. In the pulsed mode (f<100 Hz) both ion implantation at E_i<200 keV, U_{accel}<100 kV, the dose accumulation rate on the grounded target $dD_i/dt<10^{16}$ ion/cm^2/min, and deposition of the same ions at E_i<100 eV, coating growth rate dH/dt=50-200 nm/min, are implemented during each pulse.

As the accelerating voltage polarity is reversed, the source generates an electron beam with E_e<100 keV, I_e<5 A.

Modular design of the TAMEK source (fig.3) permits us to install it on a vacuum chamber. It is easier to adapt the TAMEK sources for generation of ion beams with the spot size of 2000 cm^2. For this purpose it is only necessary to replace the conical anode and the extracting grids by new ones of corresponding diameter, as the plasma and ion flows from the vacuum arc cathode spots are expanded forward at angles of 60-120 degrees for different cathode materials. We have lengthened the electrodes to obtain the diameter of 50 cm.

The TAMEK sources can efficiently generate high-melting metal (e.g., W, Ta) ions which are hardly available with other types of sources. To obtain mixed ion beams we used cathodes

made from alloys and composites such as TiB_2, TiC, TiSiC, TiMoSi, SiC, MoS, CuMoSi, CuSiC, AlBW, NiCrAlY.

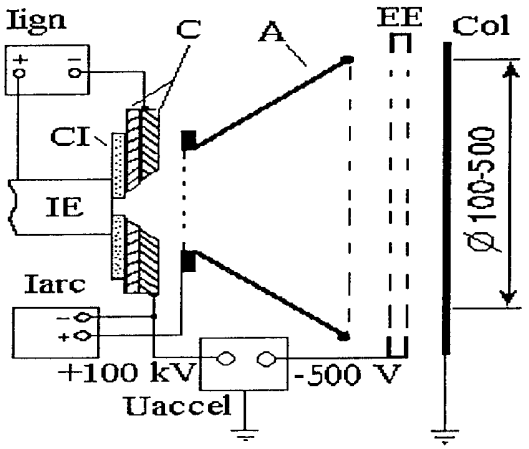

Fig. 1. Scheme of the TAMEK source. A-anode, C-replaceable disk cathodes, IE-igniting electrode, CI- ceramic insulator, EE-grid extracting electrode, Col-grounded collector.

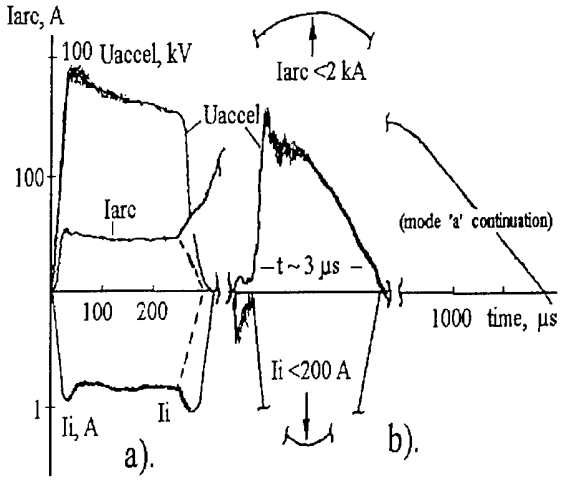

Fig. 2. Signals of TAMEK source operational modes. a), IBAD mode with HDI; b), IBAD mode with HPIB. U_{accel}, accelerating voltage; I_{arc}, vacuum arc discharge current; I_i, ion current. Dashed lines indicate I_i and I_{arc} in the HDI mode without ion deposition.

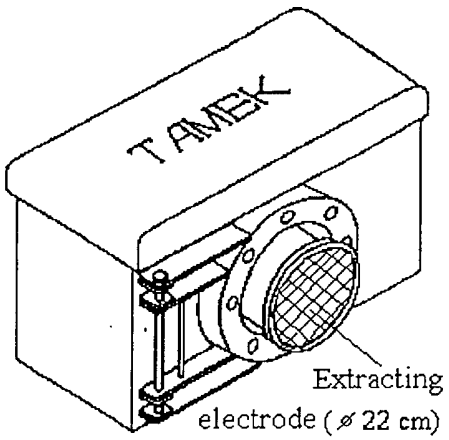

Fig. 3. TAMEK source picture. High-voltage power supplies and an ion gun are located in the space of 70x40x25 cm^3.

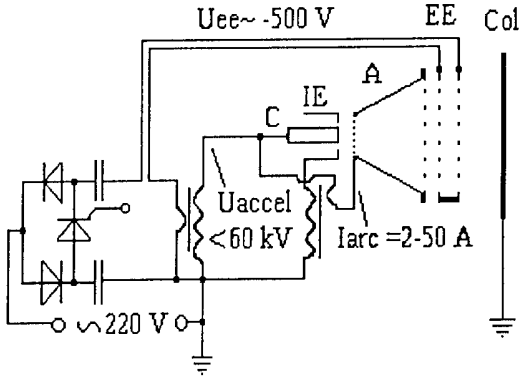

Fig. 4. Scheme of the source with low current vacuum arc.

2. Low current millisecond duration vacuum arc source

Special scheme (fig. 4) was proposed [6] for realization of both an extra low current and long pulse duration vacuum arcs. This scheme automatically reignites the arc for all accelerating voltage. A low current vacuum arc can be produced with the single emitting center in the cathode spot, e.g., a sequence (up to 20 ms) of single short pulses was generated at a current I_{arc}=2-4 A for copper cathode, and I_{arc}=8-10 A for tungsten cathode. At higher arc current the source operates more stable and generates low intensity metal ion beams of time duration determined only by the power supply transformers. Such low current vacuum arc mode generates more highly stripped metal ions due to more less de-ionization of metal ions in the low density near surface cathode plasma.

3. TAMEK-M sources of microsecond duration high power metal ion beams

At a high current vacuum arc it is possible to use only one discharge gap without triggering for microsecond duration metal HPIB generation [7]. The direct capacitance discharge (fig. 5) is used for metal plasma generation after ignition of Marx generator.

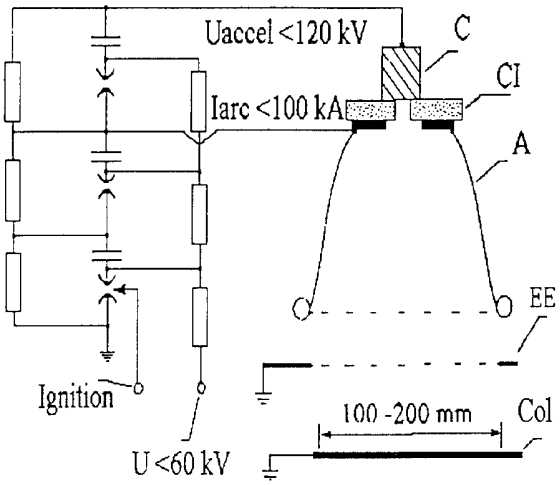

Fig. 5. Scheme of TAMEK-M source.

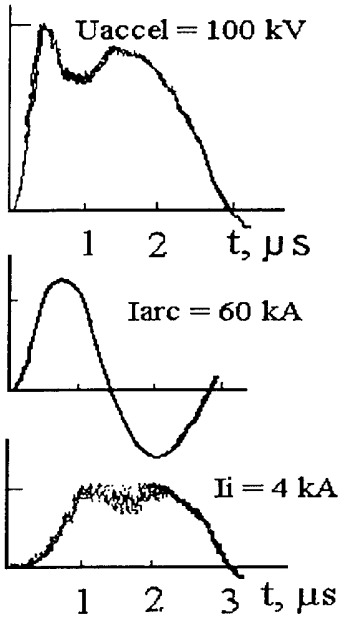

Fig. 6. Typical pulses for TAMEK-M source (fig. 5).

Source on fig. 7 uses Archimedes spiral type path of the anode -AM for creation of a magnetic field for electron insulating. At the beginning of a pulse the electrode -AM has a floating potential, that lead to the surface flashover on the insulator -CI and cathode sports formation on the road part of the anode. Simultaneously, the magnetic field from this electrode increases the anode plasma ionization. At I_{arc}<100 kA (fig. 6) such sources generate metal ion current I_i<5 kA, t_p=0.5-10 μs. For a shorter pulse duration it is difficult to achieve a low inductance of a vacuum arc discharge circuit, to take also into account the rather big capacitance which is necessary to generate a high arc current. Upper limit for pulse duration is restricted by necessity to adjust the accelerating gap with Child-Langmuir limit for the ion current density and closing the accelerating gap by an explosive cathode plasma. Due to high speed of vacuum arc anode plasma motion and its erosion during a pulse for vacuum arc ion sources it is possible to use accelerating gaps up to 10 cm. Parameters received: U_{accel}<120 kV, I_i<5 kA, t_p=1-5 μs are enough for successful metal surface modification with the surface energy input of dW=0.5-5 J/cm^2 [4,9,10,13].

In the reversed mode such sources generate electron beams with current of I_e<50 kA.

4. Plasma immersion metal ion implantation

A combination of conventional metal vacuum arc PVD method and plasma immersion metal ion implantation (PIII) are proposed [8]. Fig. 8 presents the scheme of the combination of PVD and PIII. Unlike the other authors [11], we have come to the conclusion that PVD and surface modification by HPIB is a promising combination. We make use of metal plasma density of $D_p=10^{12}$-10^{13} cm^{-3} generated by a vacuum arc at I_{arc}=100-2000 A, and a low induction power source with U_{accel}<60 kV which is periodically (one pulse in 0.5-3 min) switched on between the target and the plasma source. HPIB generation with I_i<200 A, t=1-3 μs takes place through alternation of HPIB and PVD, and vice versa without a time break (fig. 2b).

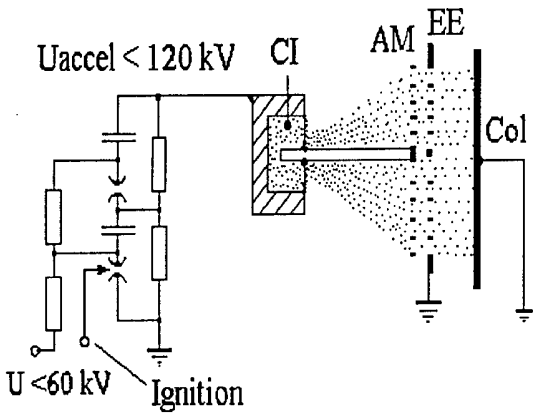

Fig. 7. Scheme of the HPIB source with self-generation of an anode plasma and insulated magnetic field.

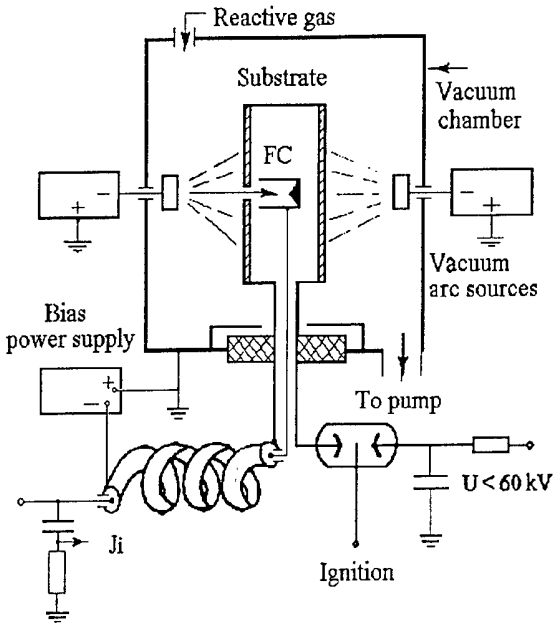

Fig. 8. Scheme of the source for combination of PVD and metal PIII by a high power metal ion beam.

Conclusions

This short review has demonstrated that using unique properties of vacuum arc to generate metal ions it is possible to construct metal ion accelerators with broad range of parameters. Improved coating adhesion with easy sample preparation and modular design of the TAMEK sources make they convenient for industry applications. Vacuum units can thus become versatile and capable to implement surface modifications by HDI, IBAD, HPIB and metal PIII, or electron irradiation.

TAMEK sources can be used successfully in conventional application fields of ion implantation and physical vapour deposition, e.g., in textile, paper, plastics, food, aeronautics and space industries, medical sector, etc. As a rule, service time of treated parts is increased by 2-15 times, but it is much longer for parts whose service time depends on corrosion and wear resistance, such as notching dies, disk milling cutters, trimming knives, blades of aviamotors, valves from a cryogenic and other compressors, relay and other contacts. The most attractive examples here are tools used for shaping, cutting, and piercing of plastics, papers, synthetic fibers, soft tissues and similar materials [1,4,9,10,12,13]. So, it seems that vacuum arc sources such as TAMEK can occupy an important position on the technological market of devices for surface modifications by ion, plasma and electron beams.

References

[1]. Proc. Intern. Conf. on Surface Modification of Metals by Ion Beams, Japan, Kanazawa, 1993. Surface and Coating Technology, volms 65 and 66 (1994)
[2]. A.I.Aksenov, N.G.Pankovetz, and A.M.Tolopa, Prib. Tekn. Eksp. 3(1987)139.
[3]. A.M.Tolopa, Rev.Sci.Instrum., 65(4)(1994) 1322.
[4]. A.M.Tolopa, Rev.Sci.Instrum., 65(10)(1994) 3134.
[5]. A.I.Aksenov, S.A.Lukovnikova and A.M.Tolopa, Patent USSR (Certificate) # 1457446 from 2.12.1986.
[6]. A.I.Aksenov, D.A.Noskov and A.M.Tolopa, Patent USSR (Author Certificate) # 1419495 from 2.12.1986.
[7]. G.S.Kazmin, L.N.Orlikov and A.M.Tolopa, Patent USSR (Author Certificate) # 1494835 from 27.02.1987.
[8]. D.A.Noskov and A.M.Tolopa, Patent USSR (Author Certificate), # 1517376 from 10.04.1987
[9]. A.D.Pogrebnjak and A.M.Tolopa, Nucl.Instrum. and Methods. B52 (1990) 25.
[10]. A.M.Tolopa, Mat.Res.Soc.Symp.Proc., 316 (1993)1059.
[11]. Abstract of Intern. Workshop on Plasma Immersion ion implantation, Australia, 12-15 February, 1995.
[12]. S.M.Duvanov, A.P.Kobzev and A.M.Tolopa, Nucl.Instrum. and Methods., B85 (1994) 264.
[13]. A.M.Tolopa, in Ion Beam Modification of Materials, J.S.Williams, R.G.Elliman, M.C.Ridgway, (eds.), Elsevier Science B.V. (1996)1102.

EXPERIMENTS ON ION SPACE-CHARGE NEUTRALIZATION WITH PULSED ELECTRON BEAMS

U. Herleb and H. Riege

CERN LHC-Division, CH-1211 Geneva 23, Switzerland

Abstract

The method of space-charge neutralization of heavy ion beams with electron beam pulses generated with electron guns incorporating ferroelectric cathodes [1] has been experimentally investigated. Several experiments are described, the results of which prove that the intensity of selected ion beam parts with defined charge states generated in a laser ion source can be increased by one order of magnitude. For elevated charge states the intensity amplification is more significant and may reach a factor 4 for highly charged ions from an Al target.

Introduction

A new method of neutralizing heavy ion (HI) beams with pulsed electron beams has been proposed in reference [1]. This scheme leads to some sort of alternating gradient focusing of the HI beam by the space-charge forces of the focusing electron pulses and the defocusing forces of the HI space charge, when not neutralized by electrons. This papers gives a more detailed experimental data complementing reference [1].

Experimental Set-up and Results

The experimental set-up consists of two main parts: The electron gun and a laser-ion-source (LIS). To understand each component it was necessary to do the initial experiments in separate set-ups.

Figure 1 shows the electron gun. A ferroelectric cathode (FE) is used as an electron emitting source. It consists of a PLZT (lead-lanthanum-zirconium-titanate) ceramic disk with a diameter of 16 mm and a thickness of approximately 0.5 to 0.8 mm. On both sides silver electrodes are screen printed: on the rear side (RE) a full ring electrode, on the front side an annular grid electrode (GE). In order to excite electron emission a fast negative voltage pulse is applied to the RE while the GE is grounded. This causes a fast spontaneous polarization change which leads to a high charge density on the free surface of the GE and electron emission. See also [2,3].

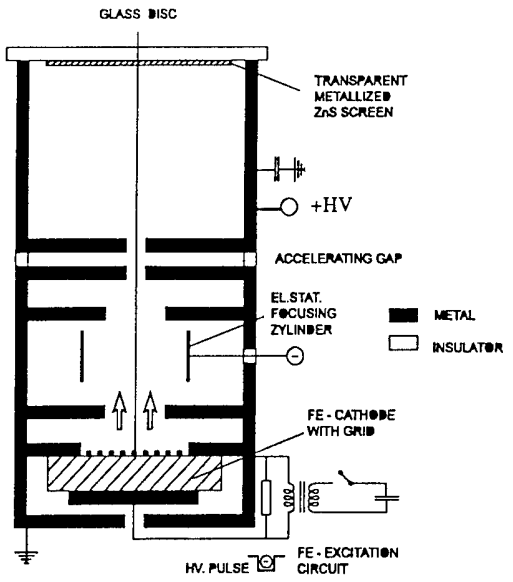

Figure 1: electron gun

An electrostatic lens for focusing the electron beam is installed followed by an acceleration gap. To detect the electron beam a metalized glass disk with a ZnS layer is used. For measuring the emitted charge and current a similar gun set-up with a Faraday-cup (FC) above the GE of the sample is available. Figure 2 shows the emitted current of a PLZT 2/95/5 electrode. The current amplitude 100 mA, the length of the electron pulse is 190 ns (FWHM). A high voltage pulse with a maximum amplitude of 3.1 kV was applied to the RE.

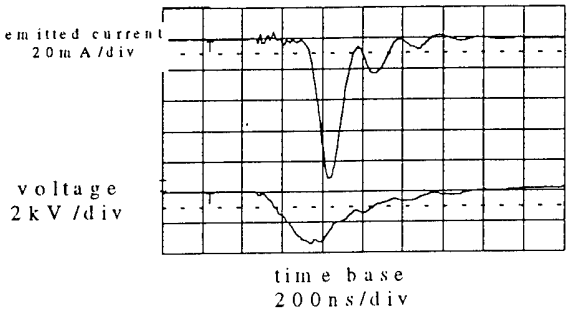

Figure 2: emitted current obtained from a PLZT sample

The laser-ion-source (LIS) consists of a small evacuated expansion chamber, an ion acceleration system and a Nd:YAG laser. The maximum output energy of the laser is 0.8 J whilst the pulse length is 5 ns (FWHM). Focusing the laser beam on the target leads to a maximum power density of $6 \cdot 10^{10}$ W/cm^2. All metals could be used as a target. The experiments which are described below were made with an aluminium target.

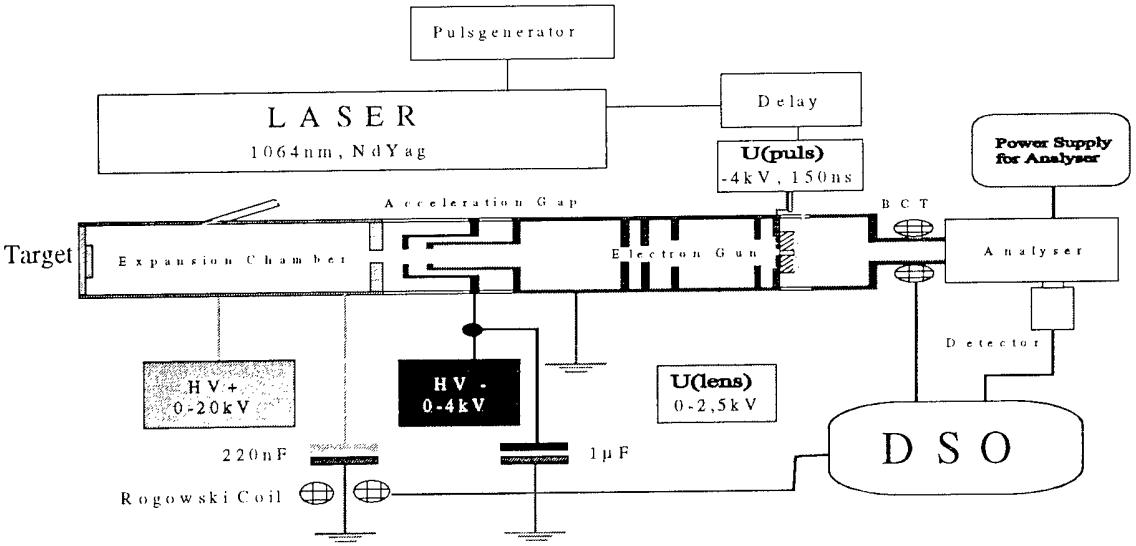

Figure 2: experimental set-up

The main experimental set-up is shown in Fig. 2. At expansion chamber high voltage up to 20 kV can be applied. After a drift distance of 250 mm the plasma reaches the acceleration gap which consists of three electrodes. The first one is connected to the expansion chamber, on the second electrode a negative voltage between 0 and -4 kV could be applied whilst the third one is grounded. Between the acceleration gap and the electron gun is a drift tube installed. For current experiments the acceleration gap of the electron gun is not installed. The installed ferroelectric cathodes have a 3 mm centre hole through which the ion beam must pass. The beam diagnostics comprise a beam current transformer which is installed near the ferroelectric cathode, and an electrostatic ion analyser (EIA). Either a FC or a secondary electron multiplier (SEM) could be used for detecting the ions. A current transformer (BCT) is used to control the total current which is leaving the LIS and for detecting, if there are any breakdowns in the acceleration gap.

Figure 3 shows the field distribution of the acceleration gap. It was calculated for an ion beam current of 15 mA which is leaving the target. One can clearly see the blow up of the beam caused by the space charge of the ion beam. In this calculation a neutral plasma enters the acceleration gap from the left side. On the high voltage side (left) a potential of 15 kV is applied, on the middle electrode -2.5 kV, whilst the left electrode is at zero potential. The used design is the same as the one used in the LIS. The units at the axis are in arbitrary units. The x-axis cuts the extraction system into two halves. An aperture of 12 mm is used for the high voltage electrode and of 10 mm for the two other electrodes.

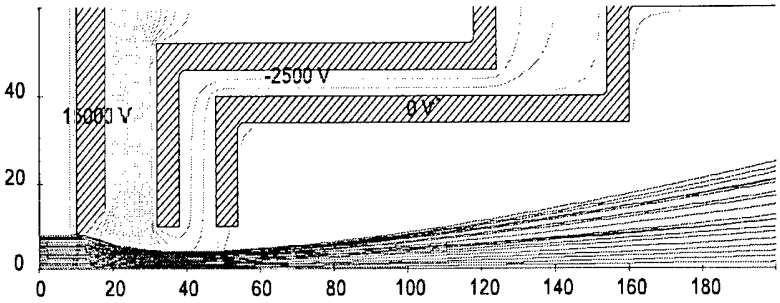

Figure 3: extraction system field distribution

Figure 4 shows a FC signal. During these measurements the FC was installed instead of the EIA which made it possible to detect the total ion current which is passing through the hole in the FE. These measurements were done without space charge neutralization. The plotted ion current shows a maximum amplitude of 2 mA. The applied accelerating voltage was 15 kV. The lower trace shows the total current which is leaving the expansion chamber. The maximum current is 20 mA whereas electrons which are flowing to the expansion chamber have also to be taken into consideration (approximately 5 to 10%). The noise at the time zero is due to the laser switching. With the EIA installed the different charge states could be well separated. Depending on the amplitude of the voltage applied to the deflection plates of the EIA, ions with corresponding energies were be observed.

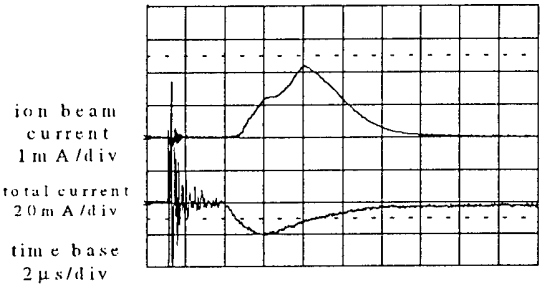

Figure 4: total current (see text)

Figure 5 shows the SEM signal at an ion energy of 15.6 keV/z. This experiment was made without space charge neutralization, too. On the very right, one can identify charge state plus one. Higher charge states arrive earlier at the SEM. On the very left of the spectrum the peak of seven times charged aluminium ions is visible (see arrow).

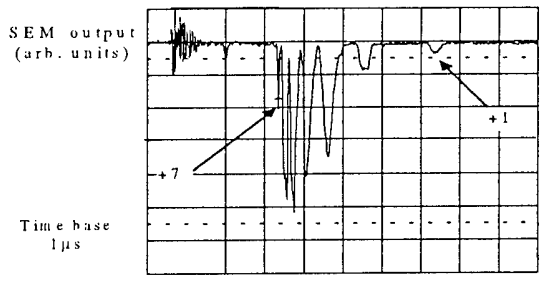

Figure 5: time of flight spectrum for aluminium ions, energy: 15.6 keV/z

In figure 6 the aluminium +7 energy distribution is shown. On the x-axis the time of flight between the target and the SEM is printed, on the y-axis the measured pulse height in arbitrary

units. The synchronisation between laser pulse and electron beam pulse was adjusted such, that the ion beam and the electron beam meet between the last aperture of the electron gun and the grounded electrode of the acceleration system. The ions with the shortest time of flight have the highest energy. This was with 15 kV extraction voltage 15.8 keV/z. The energy spread is small, the ions with the longest time of flight have an energy of 15.0 keV/z. Is the electron gun working, one can clearly identify an increase of the total current by a factor of 2. The enhancement of the charge is given by a factor 4. An increase of the current of every charge state could be observed with this electron beam timing. In figure 7 the enhancement factors for different charge states of Al ions are given. The enhancement for charge state plus one is the largest with a factor of 2.5. The factors for the charge states which are not listed have to be confirmed.

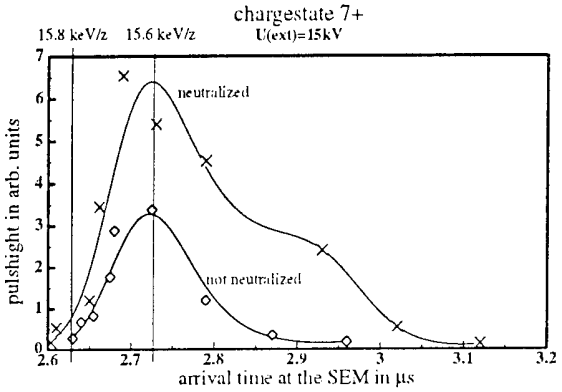

Figure 6: peak of aluminium +7 with and without space charge neutralization

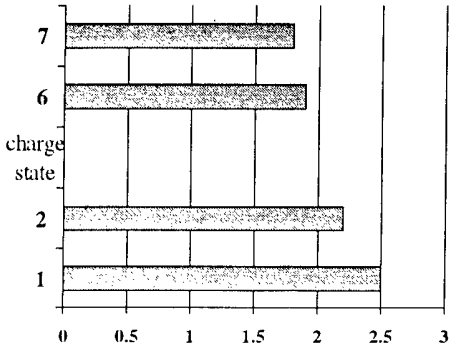

Figure 7: enhancement factor of different charge states with space charge neutralization

Outlook

The experimental results presented in this paper are preliminary. The next steps to be taken are more quantitative studies of the neutralization technique. These depend strongly on parameters, such as electron beam intensity, pulse length, beam shape at the regions of encounter with the ion beam part to be neutralized. Also synchronization times with the extracted ion beam, and maximum charge state of the ion beam have to be taken into consideration. It is foreseen to do the space charge neutralization with multiple electron bunches at different locations in the complete system in order to achieve an efficient and stronger current enhancement of the highly charged ion beam [1].

[1] U. Herleb, H.. Riege, *Ion beam Neutralization with Ferroelectrically Generated Electron Beasms,* talk 0-1-8 presented at this Conference.
[2] H.Gundel, H.Riege, Appl. Phys. Lett. 56 (16) (1990) 1532
[3] H. Riege, Nucl. Instrum. Methods A 340 (1994) 80

PHOTORESONANCE ANODE PLASMA PRODUCTION BY KrF LASERS

B.A. Knyazev, P.I. Melnikov[1], A.A. Doroshkin, A.N. Matveenko
Novosibirsk State University, 630090 Novosibirsk, Russia

H. Bluhm
Institut für Neutronenphysik und Reaktortechnik, Forschungszentrum Karlsruhe Postfach 3640, D-76021 Karlsruhe, Germany

Abstract

The interaction of an intense KrF laser pulse with vapor clouds of different elemental composition has been studied experimentally. The clouds were produced by evaporation of solid targets with a ruby laser. Ionization of the expanding clouds by a KrF laser was observed for clouds containing tantalum atoms.

Photo-resonance ionization

Anode plasma sources with a specified elemental composition a required to generate ion beams for various applications. Practically all elements of the periodic table are used in industrial accelerators and plasma ion implantators. The future development of ICF is also expected to be based on high-power lithium, boron, or carbon ion accelerators [1]. A critical problem of beam production is the formation of a near-anodde plasma layer containing the desired ions. However, for many ion species proper ion sources are too complicated or not available. So called "laser ion sources" generate a hot plasma with multiple-charged ions, and their efficiency is low. A dense plasma of low temperature can be produced by the LIBORS (**L**aser **I**onization **B**ased **O**n **R**esonance **S**aturation) technique [2].

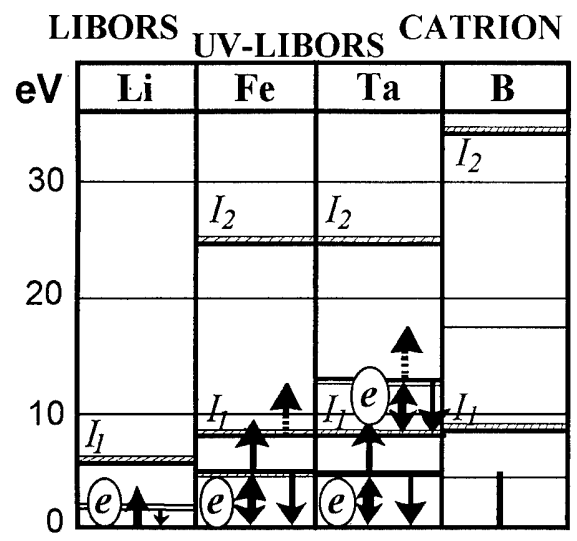

Fig. 1. Schematics of the photo-resonance processes. Encircled **e's** identify transitions participating in super-elastic collisions

Briefly, the LIBORS process consists of several stages: generation of a saturated population of an atomic resonance transition by laser radiation, heating of seed electrons through super-elastic electron-atom collisions, collisional population of the of the upper levels, and eventually, rapid ionization of the gas. Obviously, such a chain of processes can occur only for a sufficiently high gas density. The LIBORS ion source based on a dye-laser as the radiation source has been used to obtain a near-anode lithium plasma in the magnetically-insulated diode of the PBFA-II accelerator [3]. However, this method is not universal (especially for repetitive industrial ion sources) due to the low robustness of dye lasers. Another serious problem is the absence of dye lasers in the UV range, whereas the resonance transitions of most elements lie in this range.

[1] Permanent address: G.I. Budker Institute of Nuclear Physics, 63090 Novosibirsk, Russia

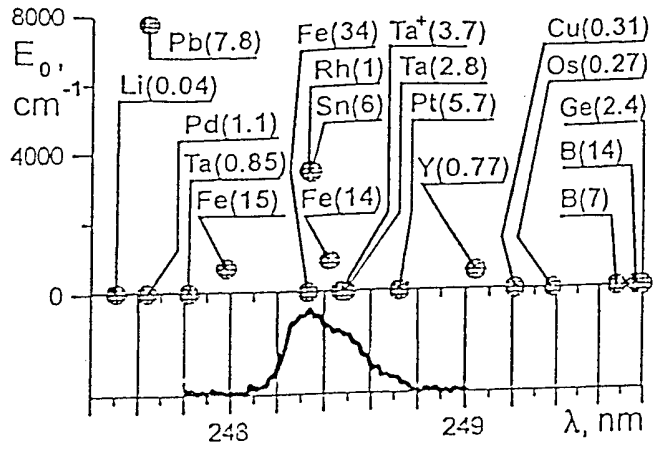

Fia. 2. The lasing spectrum of the KrF laser and wavelengths of atomic resonance transitions versus energy at the lower state. The numbers in brackets are spontaneous emission probabilities g_a in units of 10^8 s^{-1}.

However for a number of elements resonance transitions do occasionally overlap with the generation band of excimer lasers [4]. These elements (including As, Fe, Pt, Al, U, ...) can be ionized by the UV-LIBORS technique with the use of a robust repetitive excimer laser. An advantage of this method in comparison with the conventional LIBORS method is its possibility of direct photo-ionization of an excited atom by the excimer laser radiation. Further extension of this technique, suggested in Ref. [5], makes it possible, in principle, - to obtain the ions of every element by the production of multi-component clouds, containing the above mentioned elements as an admixture and by using the UV-LIBORS technique to ionize such clouds. During the first stage a "resonant" element drives this process without being changed itself, similar to a catalyst in a chemical reaction. Because of this property, we call the modified LIBORS process "**CAT**alytic **R**esonance **ION**ization" (CATRION). This term is especially correct for tantalum (KrF laser) and uranium (XeF laser) atoms as "catalysts", because both the atom and the singly-charged ion of these elements can be excited with the same laser. All of the above mentioned processes are schematically shown in Fig. 1.

Experimental setup

The experiments have been performed with the CATRION setup (Fig. 3) at Novosibirsk State University. The setup consist of a vacuum chamber, three powerful laser systems, and a variety of different diagnostics. It is described in more detail in Ref. [6]. To form a gas cloud, a ruby laser beam was focused onto a mono- or multi-component target positioned in the vacuum chamber. The catalysts to be excited by the KrF laser (Sn, Fe, Ta, Fe-B) as well as the working atoms (B, Ti, Mo) were constituents of the targets. The experiments have shown that there is a range of ruby-laser intensities F, at which one can obtain a practically non-ionized gas cloud. This range appears to be rather narrow and it is specific for each target composition. The vapour cloud density, estimated from optical spectroscopy and from refractive index gradient (RING) diagnostics [6], depends on the value of F and can become sufficiently high (10^{16}-10^{18} cm^{-3}) to enable gas ionization by the: LIBORS process. Expansion velocities are close to the expected thermal velocities. A density peak of the

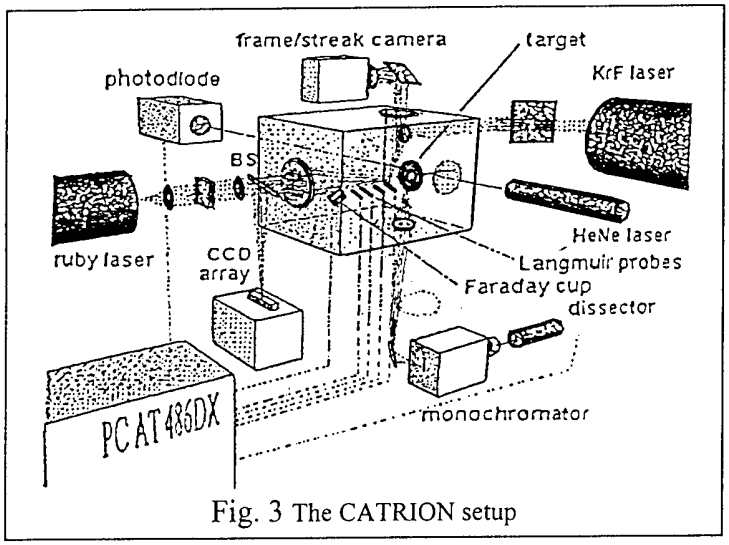

Fig. 3 The CATRION setup

expanding cloud moves away form the target, probably due to release of atoms from the surface. The ratio of longitudinal and transverse velocities varies from 1 to 2 for different targets [6]. The density of the expanding cloud, which has been measured for titanium by a resonance fluorescence technique, decreases extremely fast and the cloud front even if the cloudless are produced with a microsecond dye laser. For this reason, laser-produced vapor layers seem to be very promising for anode plasma production.

Interaction of KrF-laser radiation with the vapor clouds

According to Ref. [4,5] saturation of the resonance transition in a tantalum atom occurs at F = 150 kW/cm^2·nm. Therefore, the intensity of the resonance radiation has to exceed this value. The other requirement for the LIBORS process is a high density of the cloud to provide during the short KrF laser pulse a sufficiently large number of electron-atom collisions. In the experiments, the expanding vapor clouds were irradiated with a wide (1 cm dia.) KrF laser beam at a maximum power density of F = 500 kW/cm^2·nm. Ion saturation signals of Langmuir probes positioned at different distances from the target, as well as spectral line intensities, and spectral line broadening were recorded in each shot. The luminosity of the cloud in the visible range was recorded with a streak/framing camera. One can see from Fig. 4 that an evaporated hot gas cloud radiates for about 1-2 μs. T his self-luminosity of the cloud is observed for every target composition. According to the Langmuir probe measurements, the initial vapor cloud is a low-ionized gas with some thermal electrons. These electrons, obviously, will play the role of seed electrons in the further evolution of photo-resonance ionization. A continuum is observed in the gas spectrum during the ruby laser pulse, whereas later only atomic and singly-ionized ion lines are detected. A wide single-peak pulse is recorded by the Langmuir probes [6].

When the cloud is irradiated with the KrF laser beam, the sequence of events remains absolutely the same for materials whose atoms are not resonant to the radiation. However, for those clouds containing the catalyst atoms, the performance changes dramatically. Immediately after a KrF laser pulse the whole cloud flashes (see Fig. 4) and the light decays after 100-200 ns.

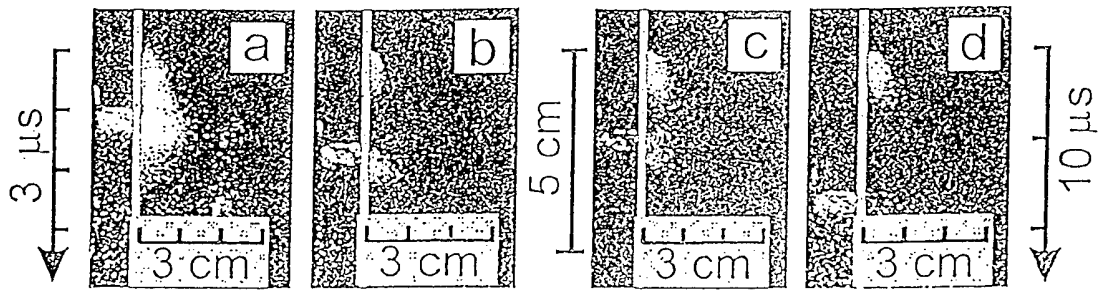

Fig. 4. Framing camera photographs of the luminosity (visible spectral range) of an expanding Ta cloud at the KrF laser irradiation. The frames were sweeping during the exposure time along the target surface (see the time axes). The surface position is marked with a light line. The delay of the KrF laser pulse relative to the ruby laser pulse is clearly seen by a glare "behind" the target (at the left).

Spectroscopic diagnostics (in the visible range) show the appearance of a continuum that rapidly disappears after the laser pulse. In the UV range, intense lines from singly and doubly-ionized atoms are observed. An additional ion peak appears on the falling slope of the Langmuir probe signal in such situations (see ocillograms in Ref. [6]). The intensity of the cloud flash decreases with increasing delay of the KrF laser pulse, and the flash does not appear at all for a delay more than 7 μs. The other signals also return to their usual form. All

data suggest that the most probable explanation of the results is UV photo-resonance ionization by the LIBOR mechanism.

To verify the results we have performed measurements with a HeNe-laser beam deflection (RING) diagnostics [7] for a tantalum cloud irradiated with a KrF laser beam. A 100 ns, 40 mJ KrF laser was used in this experiment. The HeNe laser probe beam was focused by a lens to a spot of 0.3 mm diameter and transmitted parallel to the target surface at a distance of 1 mm. The beam deflection was measured with a bi-cell photodiode and a differential amplifier. 'The resulting oscillograms (thin lines) together with the smoothing curves (thick lines) are given in Fig. 5. Taking into account that the oscillograms show the dynamics of a refractive index gradient and remembering that the refractive index gradient is positive for the electrons and negative for the other species, one can see that the results confirm previous conclusions about the cloud ionization. Immediately after begin of the ruby laser pulse, the negative deflection indicates the appearance of an expanding gas cloud. After a short time interval a thermally ionized component of the cloud comes to the probe beam and a short positive peak superposes on the negative one. The next positive peak is observed after begin of the KrF laser pulse and corresponds to the photo-resonance gas ionization. The signal is maximum (maximum gradient) for a delay of the KrF laser pulse close to 1.5 μs. The low value of the signal at later times can be interpreted as the arrival of the maximum cloud density (zero gradient) at the probe beam.

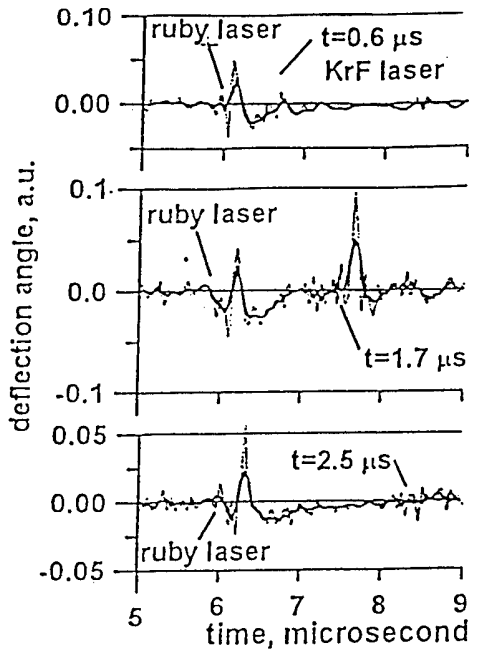

Fig. 5 RING diagnostics for a Ta cloud. The distance between the probe beam and the target is 1 mm. The beam diameter is 0.3 mm

Acknowledgements

This work was supported by Forschungszentrum Karlsruhe, a grant from the Russian Ministry of Science (# 06-06), a grant from the Russian State Committee on Higher Education (95-05.2-185), and by the program "Russian University". The authors thank G. Kessler for his support to this work, and I.A. Bushuiev and A.A. Ivanov for their assistance in the experiments.

References

[1] Cook D.L., J. Fusion Energy: **11** (1992) 69.
[2] Measures R., Cardinal P., Phys. Rev. A: **23** (1981) 804.
[3] Bieg K.V., Tisone G.C., Lockner T.R. et al., Proc. 8th Internat. Conf. on High-Power Particle Beams, Novosibirsk. 199), World Scientific: **V.2** (1990) 993.
[4] B.A., Melnikov P.I., Bluhm H., Preprint of G.I.Budker Institute of Nuclear Physics, Novosibirsk: **94-8** (1991); Physics of Intense Light Ion Beams and Production of High Energy Density in Matter, Forschungszentrum Karlsruhe: Annual Report 1994 (1995) 36.
[5] Knyazev B.A., Melnikov P.I., Bluhm H., Proc. I0th Int. Conf. on High Power Particle Beams, San Diego 1994 (1994) 451.
[6] Bushuev I.M., Doroshkin A.A., Ivanov Art.A. et al., Proc. SPIE: **2619** (1995) 216.
[7] Knyazev B.A., Greenly J.B., Hammer D.A. et al., see a paper in this Proceedings.

INTERACTION OF A FAST MAGNETIC FIELD WITH NON-MAGNETIZED PLASMA FOR THE PLASMA OPENING SWITCH CASE

A.S.Chuvatin, L.I.Rudakov*, and B.Etlicher

Laboratoire de Physique des Milieux Ionisés, Laboratoire du C.N.R.S., Ecole Polytechnique, 91128 Palaiseau, France
**Russian Scientific Center "I.V.Kurchatov Institute", 123182, Moscow, Russia*

Abstract

We discuss the problem of the magnetic field penetration into a plasma and plasma acceleration by a magnetic field in the particular case of the Plasma Opening Switch. Resent experiments lead to the formulation of a new type of shocks, the Hall plasma shock-waves, and a basic description of such shock-waves is given. The discussion presented in this paper allows simple estimation of the POS conduction time and new estimation of the opening time.

Introduction

Physics of the Plasma Opening Switch (POS) [1] is being studied intensively today. The POS phenomenon consists of an abrupt increase of the plasma resistance at the end of the time t_c. This allows penetration of the current into the load region during the times $t_s << t_c$. At plasma densities of $n_i \sim 10^{15}$-10^{16} cm^{-3} the magnetic field from the generator current propagates throughout the injection region during $t_c = 0.5$-1 μs ("μs regime"). In classical statement of the problem, the rapidly rising magnetic field generates shock-waves and accelerates the plasma in the POS.

For a weakly-collisional plasma the theory of strong MHD shock-waves was developed earlier by Sagdeev [2] and experimental research of the phenomenon was actively carried out in 60-70-s specifically in the θ-pinch geometry [3]. Later it was shown that for small-scale ($\Lambda < \delta_i$, Λ denotes the characteristic plasma size, $\delta_i = c/\omega_{pi}$ is the collisionless ion skin-depth) short-duration ($t < \omega_{ci}^{-1}$) processes the plasma dynamics had to be described in frames of the MHD with the Hall term [4]. Earlier publications from the *Kurchatov Institute* demonstrated a possibility of existence of another type of shock-waves, when the magnetic field could penetrate the plasma with the velocities substantially higher than the Alfvén velocity, v_A [5]. In the framework of this approach the ions are considered to be stationary and the equation of frozenness of the magnetic field into electron fluid is

$$\frac{\partial \mathbf{B}}{\partial t} = \mathrm{rot}[\mathbf{v}_e,\mathbf{B}] + D\Delta\mathbf{B} \qquad (1)$$

where $\mathbf{v}_e = -c\times\mathrm{rot}\mathbf{B}/4\pi en$. If one introduce a current as $I = crB/2$, Eqn. (1) can be rewritten in cylindrical geometry as follows

$$\frac{\partial \mathbf{B}}{\partial t} + \frac{1}{2\pi ce}\left[\nabla I^2 \times \nabla\left(\frac{1}{nr^2}\right)\right] = -\mathrm{rot}\,(D\,\mathrm{rot}\mathbf{B}) \qquad (2)$$

and has a shock-wave solution (the KMC-shock) with the velocity which was found first in [6]

$$u_f = -\frac{cB}{8\pi e} r^2 \nabla_r\left(\frac{1}{nr^2}\right) \qquad (3)$$

This approach, which is commonly called now Electron Magnetohydrodynamics (EMH) [7] should be used for description of the plasma dynamics in POS [8], Z-pinches [9-11], semiconductors [12], or, for example, in magnetosphere [13].

Formation of the Hall MHD shock-wave

The density shock observed in the experiment [14] had a wedge-like shape instead of being a plow-shaped as predicted by the "pure" MHD consideration (v_A was a monotonic function with the maximum at the cathode). In addition, instead of being behind, the magnetic

field traveled ahead of the plasma density perturbation. The fastest plasma density jump propagation with the velocity ~ 10^7 cm/s was registered almost in the midgap, the shock front width being of the order of $\delta_f \sim 1$ cm. Typical value of the plasma density increase over the initial value was measured to be $n_1/n_0 = 2\text{-}3$. Interesting peculiarity of this experiment was simultaneous existence of three regions in the interelectrode gap, MHD, EMH, and the intermediate one (see Fig. 5 in [14]). The conduction phase was controlled by the region with $v_A \sim u_f$.

The KMC solution (3) exists if $v_A < u_f$. In the "pure" EMH, $v_A << u_f$, the magnetic field shock occurs on the background of motionless ions and the density jump is absent [5]. At the same time the ions can be accelerated at the front of the magnetic field shock wave [15, 16]. One can estimate the change of the ion momentum and ion density as follows

$$n_0 M v_i \approx \nabla\left(\frac{B^2}{8\pi}\right)\frac{\delta_f}{u_f} \tag{4}$$

$$\frac{n_1 - n_0}{n_1} \approx \frac{v_i^2}{u_f^2} \tag{5}$$

where δ_f is the width of the shock front, n_0 and n_1 are the ion densities in front of, and behind the shock respectively. As $\nabla \sim 1/\delta_f$, the ion velocity is of the order of

$$v_i \approx \frac{v_A^2}{2u_f} \tag{6}$$

It is important that both v_A and u_f are determined by the initial plasma density. Eqn. (5, 6) yield both spatial profile and the maximum value of v_i close to that in the discussed experiment. The force affecting the ions can be ascribed, in fact, to the electric field of charge separation which arises at the penetration front (Hall field). Important feature of this ion acceleration process is that EMH requirements are still satisfied at the penetration front ($v_e > u_f, >> v_i$). Therefore, the width of the shock front and its spatial profile may be determined in the EMH framework. For example, the magnetic field front widening due to the electron-ion friction [5] can be found using the Spitzer conductivity, σ_{sp}

$$\delta_f^{sp} = \frac{c^2}{4\pi\sigma_{sp}u_f} \tag{7}$$

On the other hand, unlike in the "pure" MHD shock-wave, the density redistribution defined by Eqn. (6) lags behind the magnetic field shock, as shown schematically in Fig. 1.

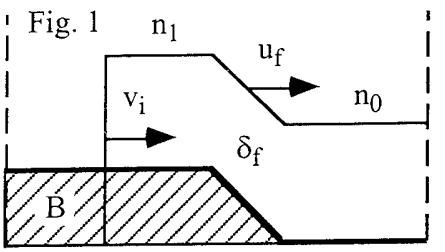

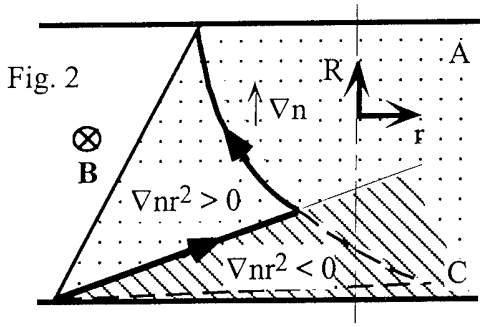

Fig. 1. Qualitative 1D picture of the magnetic field and plasma density profiles in the Hall shock-wave. Magnetic field is ahead of the piston ($u_f > v_i$).

Fig. 2. Qualitative 2D presentation of the current flowing in the experimental geometry [14]. A - anode, C - cathode. Prohibited ($\nabla nr^2 < 0$) and allowed ($\nabla nr^2 > 0$) for penetration regions are showed.

It is possible to distinguish this phenomenon from both EMH and MHD shocks and to define it as a Hall-effect-driven density shock, or Hall shock-wave (HSW). The magnetic field evolution in the HSW is substantially faster than the ion motion at the leading edge of the penetration. In its turn, the ion motion is not negligible behind the front of the magnetic field shock and is responsible for the plasma density dynamics.

Eqn. (2) predicts that a stationary quasineutral current flow without dissipation conserves the so-called Hall potential, $U_H = B^2/8\pi en$. Therefore, in a non-stationary case and cylindrical geometry the magnetic field can penetrate initially only the plasma region where $\nabla nr^2 > 0$. Let us give an illustration of electron trajectories for the experiment in Ref. [14]. In the experiment under consideration the measured plasma density does not changes as fast as $1/r^2$ at a given cross-section of the plasma column, Fig. 2. Due to the curvature of the magnetic field lines electron trajectories along the cathode correspond to $\nabla nr^2 < 0$ and are prohibited. Therefore, electrons would choose a path which is inclined to the normal of the cathode in order not to enter the prohibited region.

Theoretical scalings of the conduction and opening times

Successful operation of an inductive storage generator depends on the POS coupling with the primary energy storage on one hand (t_c) and with the load on the other hand (t_s) [1]. The table compares characteristics of high-density plasma switches in those experiments where the initial plasma density was known.

POS	HY-Tech [18]	EYESS [19]	SINAPS-500 [20]	Hawk [21]	GIT-8 [22]	ACE-4 [23]
I_{max} (MA)	0.13	0.5	0.5	0.7	1.6	2
r (cm)	2	12	4	6.5	8	6
Δ_{AK} (cm)	2.5	5	2.7	2.5	3	2
L_p (cm)	5	17	17	8	15	20
n_e (cm^{-3})	5×10^{15}	4×10^{13}	1.2×10^{15}	5×10^{15}	2.3×10^{15}	4×10^{15}
Z_{eff}	2	2	1	2	1	1
t_c^{exp} (μs)	0.7	0.5	1	0.9	0.75	1
t_c (μs), Eqn. (8)	0.87	0.41	1.06	0.84	0.81	0.86
t_s^{exp} (ns)	100	120	100	50	100	50
t_s (ns), Eqn. (9)	96	161	100	58	65	38

Conduction time we evaluate here as a time of the piston displacement during the HSW propagation along the plasma length, L_p, given by Eqn. (6) in the limiting case $v_i \sim u_f$. This corresponds to $v_i \sim v_A/\sqrt{2}$ and yields

$$t_c \approx \frac{\sqrt{2}L_p}{v_A} \approx 6.5\times10^{-11}\frac{rL_p}{I_{max}}\sqrt{\mu n_i} \qquad (8)$$

where $v_A = v_A^{max}/2$ is calculated with initial n_i and is roughly averaged over the conduction time. We used CGS units, except I_{max} is in Amperes; r is the radius of the opening and $\mu = 12$ for a carbon plasma. The radius r is taken as a radius of the local interelectrode maximum of $v_A(r)$.

Therefore, the approach presented in this paper suggests the following scenario of the high-density POS dynamics, i.e. when initially $L_p > \delta_i$. The shock-wave piston (6) propagates locally along the z-axis and pushes the plasma towards the electrodes. At the end of the conduction time, when the plasma length which remains ahead the leading edge of the piston is small, $\Delta z < c/\omega_{pi}$, the magnetic field starts to penetrate rapidly in front of the plasma piston and arrives to the load. The characteristic time of this process can be estimated by putting $\nabla_r \sim 1/\delta_i$ in Eqn. (3)

$$t_s = \frac{\delta_i}{u_f} \approx 1.1\times10^{-3}\,\frac{\mu}{Z}\,\frac{r}{I_{max}} \qquad (9)$$

where Z denotes the ion charge which is not experimentally determined and represents the only free parameter. For the minimum time of the $C^{+}\rightarrow^{2+}$ ionization, when $\langle\sigma_i v_e\rangle_{max} \sim 10^8$ cm^3/s [17], one can find $\tau_i \sim (n_1\langle\sigma_i v_e\rangle)^{-1} \sim 50$ ns $\leq t_s$. This means that we are indeed in the frontier situation, and Z = 1 or Z = 2 may be chosen (see the table).

Conclusion

One should note that t_s given by Eqn. (9) can be less than the experimental rise-time of the load current, t_s^{exp}, because of the decay in a real inductive load. Then, a better estimate of u_f requires more information on the plasma density gradient function, $\nabla_r(n_0)$. With this remarque, one can see a good agreement with the experiment for all the considered microsecond-conduction-time plasma switches. Finally, in this work we pointed out some new important features of the Hall shock-wave formation in POS plasmas. The model allows better understanding of the experiment [14], as well as of some other experiments with high-density POS. This work is partially supported by DRET under the contract #92.134 and by ETCA/CEG under the contract #420/115/01.

[1] IEEE Trans. Plasma Sci. (special issue) PS-15, No. 6 (1987).
[2] R.Z.Sagdeev, in *Reviews of Plasma Physics*, edited by M.A.Leontovich (Consultants Bureau, New York, 1966), Vol. 4, p.23.
[3] M.V.Babykin, P.P.Gavrin, E.K.Zavoisky, L.I.Rudakov, and V.A.Scorjupin, *Sov. Phys. JETP* **43**, (411)1962.
[4] A.V.Gordeev and L.I.Rudakov, *Sov. Phys. JETP* **55**, (2310)1968.
[5] A.S.Kingsep, Yu.V.Mokhov, and K.V.Chukbar, *Sov.J.Plasma Phys.* **10**(4), 495 (1984).
[6] A.S.Kingsep, K.V.Chukbar, and V.V.Yan'kov, in *Reviews of Plasma Physics*, edited by B.B.Kadomtsev (Consultants Bureau, New York, 1990), Vol. 16, p.209.
[7] A.V.Gordeev, A.S.Kingsep, and L.I.Rudakov, *Physics Reports* **243**, 215 (1994)
[8] K.V.Chukbar and V.V.Yan'kov, *Sov. Phys. Tech. Phys.* **33**, 1293 (1988).
[9] L.I.Rudakov, in *Proc. Second Int. Conf. on Dense Z-pinches*, edited by N.R.Pereira, J.Davis, and N.Rostoker (AIP, Laguna Beach, 1989), p.290.
[10] V.V.Yan'kov, *Sov. J. Plasma Phys.* **17**, 305(1991).
[11] A.S.Chuvatin, P.Choi, and B.Etlicher, *Phys. Rev. Lett.* **76**, 2282 (1996).
[12] V.N.Kopylov, *Sov. Phys. JETP* **78**, 198(1980).
[13] J.D.Huba, P.A.Bernhardt, and J.G.Lyon, *J. Geophys. Res.* **97**, 11 (1992).
[14] A.S.Chuvatin and B.Etlicher, *Phys. Rev. Lett.* **74**, 2965 (1995).
[15] A.S.Chuvatin, *Ph.D. thesis*, PMI-2874, Ecole Polytechnique, 1993.
[16] A.Fruchtman, L.I.Rudakov, *Phys. Rev. Lett.* **69**, 2070(1992).
[17] Ya.B.Zel'dovich, Yu.P.Raizer, *Physics of Shock Waves and High-Temperature Hydrodynamic Phenomena*, Academic Press, NY and London, 1967.
[18] G.G.Spanjers, E.J.Yadlowsky, R.C.Hazelton, and J.J.Moschella, *J. Appl. Phys.* **77**, 3657 (1995), Fig. 4.
[19] J.R.Goyer, in *Proceedings of the Eighth IEEE Int. Pulsed-Power Conf.*, San Diego, 1991, p. 520; D.Kortbawi, F.K.Childers, J.M.Greedon, J.R.Goyer, R.R.Prasad, J.C.Riordan, and P.S.Sincerny, ibid, p. 680, Fig. 4b.
[20] B.Cassany and P.Grua, *J. Appl. Phys.* **78**, 67 (1995), Fig. 8b.
[21] D.Hinshelwood, B.V.Weber, J.M.Grossmann, and R.J.Commisso, Phys. Rev. Lett. 68, 3567(1992), Fig. 2.
[22] this conference, paper P-4-64, Fig. 3.
[23] J.Thompson, P.Coleman, R.Crumley, C.Gilbert, D.Husovsky, P.Melcher, W.Rix, K.Robertson, R.Ingermanson, D.Parks, and E.Salberta, "Downstream Power Flow of Microsecond Conduction Time Plasma Opening Switch on ACE-4", in *Proceedings of the 10th Int. Pulsed Power Conference*, Albuquerque, NM, 1995, Fig. 3.

EXPERIMENTAL CHARACTERIZATION OF GIT-8 PLASMA OPENING SWITCH

A.Chuvatin, C.Rouillé, B.Etlicher, F.Bayol*, A.Morell*, A.Kim†, S.Loginov†, V.Kokshenev†, and B.Kovalchuk†

Laboratoire de Physique des Milieux Ionisés, Laboratoire du CNRS, Ecole Polytechnique, 91128 Palaiseau, France
** Centre d'Etudes de Gramat, 45600 Gramat, France*
† High Current Electronics Institute, 631055 Tomsk, Russia

Abstract

High-current Plasma Opening Switch was experimentally studied on GIT-8 inductive generator. Cordial laser interferometry allowed to register the line-integrated POS plasma density dynamics during the switch operation. Recording of the axially distributed Bremsstrahlung radiation from the plasma region was used to determine the axial position where the opening started. New experimental result was the registration of fast plasma density oscillations with the characteristic frequency of $\omega \sim 5\times10^7$-10^8 rad/s prior and during the opening. Special study confirmed these oscillations to appear due to a plasma process. The oscillation frequency depended on the mean electron density as $\omega \sim n_e^{-0.5}$.

Experimental setup

The GIT-8 Plasma Opening Switch (POS) is capable to operate at the conduction current as high as 5 MA [1]. In the described series of experiments the switch was operating at 2 MA current with the conduction and opening times of 1 μs and 100-150 ns accordingly. GIT-8 primary energy storage consisted of 72 oil-insulated small Marxes combined in 8 modular Marx tanks. Total erected capacitance of the system was 9.6 μF. At 40 kV charging voltage (1.1 MJ total stored energy) the Marxes provided a 480 kV peak voltage, 3 MA peak current pulse into the storage inductance and POS. The plasma injection section of GIT-8 is shown schematically in Fig. 1. This section represented a coaxial vacuum line with the anode and cathode radii of 10 cm and 8 cm respectively (200/160 configuration). The plasma was injected by 32 cable plasma guns in axial direction towards the generator. The plasma gun power supply consisted of 4 capacitors (3 μF, 16 guns/cap) charged up to 40 kV. The capacitors provided approximately 10 kA peak current in each gun with the time period of 4.7 μs. The load represented a short-circuit with the inductance of about 50 nH.

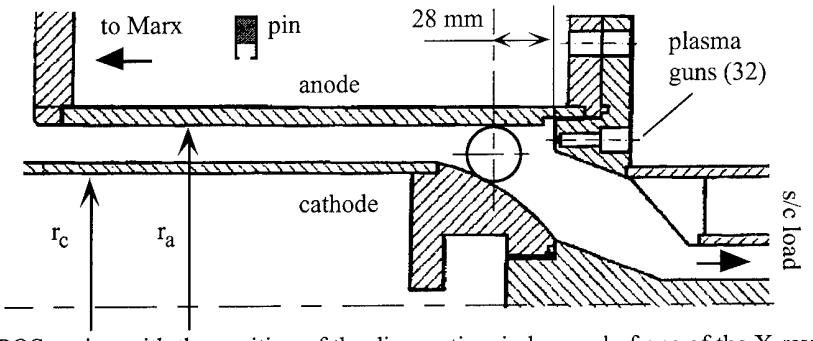

Fig. 1. GIT-8 POS region with the position of the diagnostic window and of one of the X-ray diodes (PIN).

Plasma density was measured with the help of interferometer described in [2]. The scene beam crossed from shot to shot the GIT-8 POS plasma along different chords at 28 mm from the plasma injection plane and at different radial positions of the diagnostic window, $\Delta = r - r_c$ (see Fig. 1). The interelectrode gap was equal to 3 cm at this plasma axial cross-section.

The time delay between the guns firing and the generator shot, τ, was chosen to be 3.5 μs. Statistical dispersion around this fixed value provided some variation of the initial POS plasma density. A 60 mW He-Ne laser with the instability of the beam power < 1% allowed to measure the minimum linear plasma densities of approximately 5×10^{14} cm^{-2}. Spatial and temporal resolutions were better than 2 mm and 20 ns accordingly. At each beam position the initial plasma density was evaluated for 2-3 guns firing without pulsed-power. Separate series with pulsed-power was dedicated to investigation and elimination of the following possible sources of noise: plasma luminosity, electromagnetic noise, electro-optical effect [3], fluorescence in fiber optics, influence of high-energy quanta on the photodiode signal. Consequent modifications of the optical scheme excluded all the above-listed sources of non-plasma contribution to the measured signal. Refraction effect which also could influence our plasma density measurements was studied according to the following procedure. The probe beam passed through the plasma and hit the optical fiber (see Ref. [2]) without recombination with the reference beam. The fiber input was collimated with a 400 μ diameter pin-hole, (Fig. 2a).

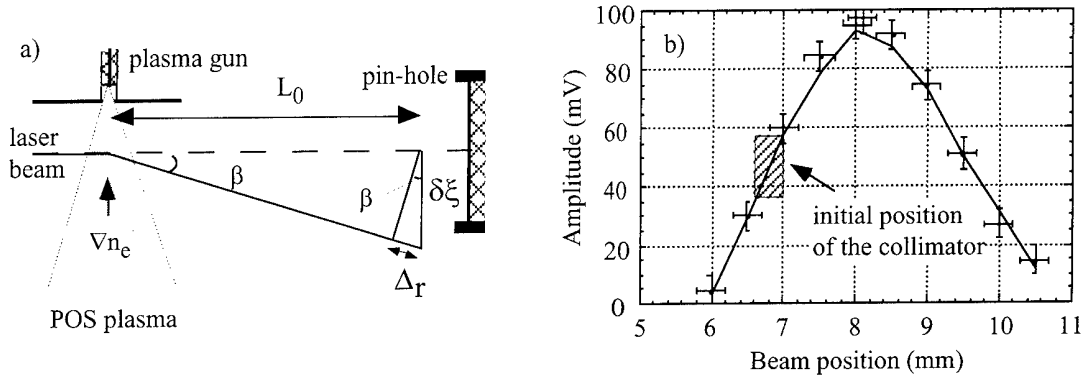

Fig. 2. (a) measurements of the probe beam deflection angle in the plasma, (b) determination of the laser beam profile for the density gradient estimation.

Before each shot the beam intensity profile was determined by displacing the registration cell in two directions corresponding to axial or radial plasma density gradients. The result of such calibration is represented in Fig. 2b. After this simple procedure the pin-hole was installed on the slope (axial and radial) of the intensity distribution, where a sensitivity to the beam deviation was maximum. Mechanical vibrations did not infringe considerably the initial adjustment. The average value of the electron density gradient, $\langle \partial n_e/\partial \xi \rangle$, over the optical path in the plasma length, L_p, is connected with the beam deviation angle, $ß \approx \delta\xi/L_0$, by the following formula [4]:

$$\frac{\partial n_e}{\partial \xi} = - 2.80\times10^{21}\frac{\beta}{L_p} \qquad (1)$$

for λ = 633 nm and we took into account the double laser beam path through the plasma. Therefore, the "false" linear plasma density induced into the signal due to the refraction effect can be estimated as follows

$$\langle n_e L_p \rangle_r \approx 2.8\times10^{21}\,\beta^2 L_0 \qquad (2)$$

where $L_0 \approx 300$ cm in our experiment.

Bremsstrahlung radiation produced by fast electron leakages during the POS operation was registered with the help of 8 X-ray diodes. These detectors were installed at different axial positions along the injection and downstream regions, perpendicularly to the generator axis (see Fig. 1). They were collimated on approximately 5×5 cm^2 of the anode surface and were sensitive to the photon energies above 200 keV.

Experimental results

Typical time history of the line integrated density during the POS operation is shown in Fig. 3 (a, b). Estimated plasma length (assuming cylindrical symmetry), L_p, was approximately 8 cm for both radial beam positions of this figure. Until the current starts to flow through the plasma channel and during 300-500 ns after the upstream current beginning, the line-integrated plasma density, $\langle n_e L_p \rangle$, follows the one measured during the gun firing only with the accuracy better than 30%. Then, the density increases over the guns-only density (region 1 in Fig. 3a) and drops abruptly (region 2). This fact can be an indication of the passage of a shock-wave through the point of measurements [5]. Then, the linear plasma density rests almost at the same level as when the upstream current starts. It worth noting that the time interval between I_0 beginning and the density drop was practically the same for all radial positions of the beam, i.e. the shock process front was almost plane. The most interesting peculiarity of the plasma density behavior was an appearance of fast density oscillations with the characteristic frequency $\omega \sim 5\times10^7$-10^8 rad/s, prior and during the opening (region 3). These oscillations were typical for shots with $\tau = 3.5$ μs, at practically all radial position in the first window. One should also note that the amplitude of these oscillations was weaker near the electrodes. Fig. 3b allows estimation of the refraction effect contribution in the plasma density measurements. The same fast oscillations are seen in this shot. All the other physical sources of noise provided finally negligible signal with respect to the interferometer response. The measured deviation of the scene beam was deduced into a "false" line density upon Eqns. (1, 2). Fig. 3b convincingly shows that the density gradient could interfere the useful signal only during and after the opening and that the earlier fast oscillations were produced by a real plasma process. The effect of the fast gradient increase can be explained by disruption of the plasma during the opening.

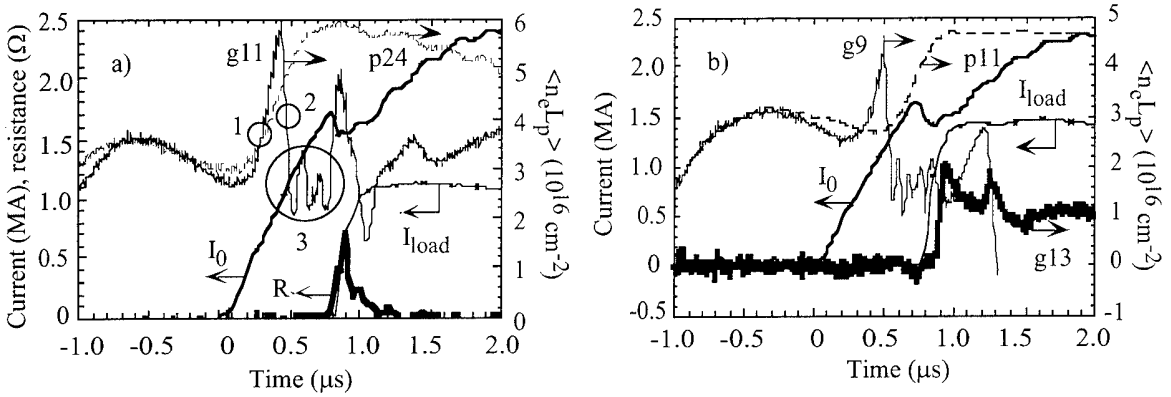

Fig. 3. (a) Typical plasma density behavior at $\Delta = 21.5$ mm with the GIT-8 current (g11) and during the plasma guns firing only (p24). R denotes the POS resistance estimated as $V/(I_0-I_{load})$; (b) comparison of the measured line plasma density at $\Delta = 6.5$ mm with a "false" line density (bold curve) induced by refraction in the plasma. Interferometer and refractometer shots were identical within 10% for t_c, t_s, I_0 and I_{load} amplitudes, and they were synchronized with respect to the load current start.

The timing of X-ray radiation showed that the earliest X-ray arrival corresponded to the same axial position as where the line-integrated plasma density measurements were accomplished. Then the radiation propagated both towards the generator (with small amplitudes of the signals) and to the load ("strong" X-ray production). Later "strong" X-ray source displacement towards the load represented most probably an electron leakages limiting the final effective POS impedance [6]. On the other hand, simultaneous signal displacement backward to the generator could correspond to the residual electron current at established high POS voltage. Therefore, it is reasonable to suppose that the opening process (first appearance of the local POS impedance) did start in the region of the plasma density measurements and that the registered fast oscillation reflected some feature characterizing the opening process.

Statistical dispersion of the delay τ did not allow direct shot-to-shot comparison and further reconstruction of the radial plasma density profile. However, one can estimate some mean plasma density along each chord as $n_e = \langle n_e L_p \rangle / L_p$. Here n_e denotes the averaged plasma density at the moment of time when it becomes to differ from the plasma guns only density. Fig. 4 demonstrates that the registered plasma oscillations strongly depend on the mean density. The function which fits the experimental data with the minimum absolute dispersion is approximately $\omega \sim n_e^{-0.5}$. Most probably, the measured oscillations were a result of hydrodynamic plasma instability having characteristic frequency equal to v_A/λ, where v_A is the Alfvén velocity, and the instability wavelength $\lambda \sim 0.5$ cm yields already an absolute value of frequency close to the experimentally measured.

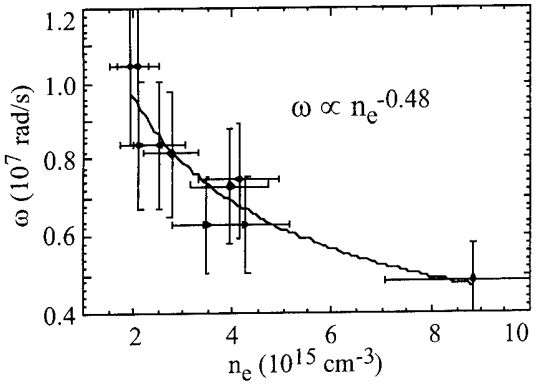

Fig. 4

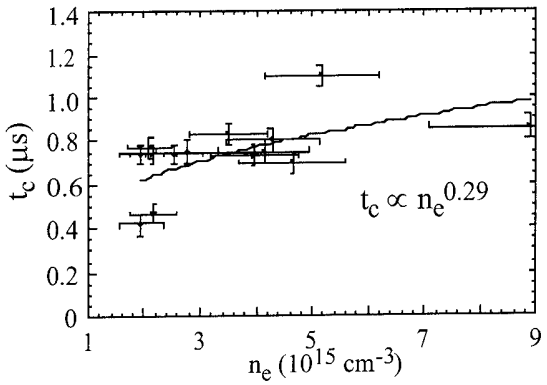

Fig. 5

Fig. 4. Variation of the measured plasma density oscillation frequency with the averaged plasma density.
Fig. 5. Dependence of the conduction time on the averaged plasma density.

It is interesting to compare existing scalings of the conduction time with those obtained in the described experiment. In the most part of approaches theoretical relations predict the dependence $t_c \sim n_e^{0.25}$ (see, e.g., Refs. [3, 7]). Fig. 5 summarizes statistics of the experimental data. It is seen that the power of the fitting function correlates well with the theoretically predicted coefficient.

Conclusion

The main result of the described experiment is the observation of the fast plasma density oscillations in the Plasma Opening Switch prior to the current interruption. These oscillations were proved to be a result of some plasma process, presumably MHD macro-instability of the plasma. The instability can result in plasma inhomogeneities formation at the end of the conduction phase. The frequency of the plasma oscillations was found to depend on the mean density in the interelectrode gap as $\omega \sim n_e^{-0.5}$. This work is partially supported by DRET under the contract #92.134 and by ETCA/CEG under the contract #420/115/01.

[1] A.Kim, "Microsecond POS research at HCEI in Tomsk", internal report HCEI-LPMI, 1995.
[2] A.S.Chuvatin, B.Etlicher, N.S.Edison, C.Rouillé, *Rev. Sci. Instrum.*, **64**, 2267 (1993).
[3] D.Hinshelwood, B.Weber, J.M.Grossmann, and R.J.Commisso, *Phys. Rev. Lett.* **68**, 3567 (1992).
[4] F.C.Jahoda and G.A.Sawyer, in *Methods of Experimental Physics*, Vol. 9, Part B, edited by R.H.Lovberg and H.R.Griem (Academic Press, N.Y., 1971), p. 1.
[5] this conference, paper P-4-63.
[6] L.E.Aranchuk, A.S.Chuvatin, A.V.Gordeev, Model for calculation of output characteristics of nanosecond REB generator with Plasma Opening Switch, *Eighth Int. Conf. on High-Power Particle Beams*, Novosibirsk, USSR, July 2-5, 1990.
[7] A.S.Chuvatin, B.Etlicher, F.Douieb, V.Frolov, C.Rouillé, H.Lamain, and P.Auvray, Long-conduction-time Plasma Opening Switch development for a new high-power generator. *EUROEM 94 Int. Symposium on Electromagnetic Environments and Consequences,* Bordeaux, France, May 30 - June 4, 1994.

ANOMALOUS RESISTIVITY IN THE PLASMA OPENING SWITCH

G.I.Dolgachev, L.P.Zakatov, Yu.G.Kalinin,
A.S.Kingsep, M.S.Nitishinski, A.G.Ushakov

Applied Physics Division, Russian Research Center "Kurchatov Institute", 123182, Moscow, Russia

Abstract

Experimental studies and modelling together with analytical consideration of the plasma opening switch (POS) anomalous resistivity are being pursued to improve the understanding of the physical mechanism of the POS conduction phase. Experiments have been undertaken for a "microsecond" POS of coaxial geometry. Measurements of Stark broadening of H_α line allowed to find turbulent oscillations in plasma at the stage of conductivity. A comparison with the modelling including low-frequency (ion-acoustic) turbulence and Doppler broadening (neutral gas temperature 1-3 eV) allowed to estimate the value of electric field 10-30 kV/cm. The turbulent field increased toward the cathode up to 50 kV/cm in the near-cathode layer.

Introduction

In the paper authors point out the well known effects of anomalous resistivity of plasma and turbulent heating [1-3] to be applicable to POS performance and which, it seems, are being beyond the discussion on POS performance mechanism.

Considering theoretical models to be adequate reflection of POS dynamics a special attention should be paid on electron magneto hydrodynamics (EHD, [4], [5]). First the basic effect - a convective wave of magnetic field - has been registered experimentally [6]. Second, the effective POS impedance [7] is in the correspondence with EHD predictions. Third, as shown in [8], [9], EHD explains the one of the most important effects in the POS - charge limit for charge comes through the POS up to the switching moment [10].

This correspondence it seemed constitutes an opportunity to make a correct scaling when bringing the existing results to the machines sufficiently larger scale. We want to point out that this similarity (both in theory and experiment) could be violated if not considering a new effect playing a sufficient role - anomalous resistivity.

Anomalous resistivity.

The possibility of anomalous resistivity to be a key effect in POS dynamics is shown in [11]. Resistive effects are important if the typical scale of the electron flow (field distribution) exceeds the geometric scale of the device a, i.e. $a < \frac{mc^2}{T} r_{De}$, where $r_{De}=(T/4\pi ne^2)^{1/2}$ - Debye radius. For example for T=10 eV, n=10^{13} cm^{-3}, we get a<30 cm, which is not a straight limit at all. The value of anomalous resistivity for experimental conditions can be estimated using Sagdeev formula for conductivity : $\sigma_{ef}=(4\pi)^{-1}\omega_{pe}\, v_{Te}/u$; having $v_{Te}/u \approx \omega_{pe}/\nu_{ef} = nT/W$, $W=E_\sim^2/4\pi$, we obtain

$$\sigma=(4\pi e^2/m)^{1/2}(n^{3/2}T/E_\sim^2).$$

For E=10 kV/cm and typical POS dimensions: width along the axis 10 cm, interelectrode gap 12.5 cm, we obtain R ~ 1 Ohm. This corresponds with experimental estimates [7] giving 0.2-0.4 Ohm at a conduction phase.

Experimental data and low-frequency turbulence estimation.

Experimental determination of low-frequency electric field strength and turbulence degree of POS plasma using Stark broadening of H_α line is a continuation of early experiments [12]. Experimental data were obtained at "Taina" pulsed power generator [7] for current pulse amplitude 200 kA with 2.0 μs quarter period. Plasma guns for POS were made as 36 spark gaps placed at the circle 30 cm diameter with the inner electrode (cathode) diameter 5 cm. The radial gap is greater than longitudinal dimension used by spark gaps which is different from those used in another POS diagnostic experiments [13] but is characteristic for experiments with high voltage multiplication.

Crossed dispersion scheme [12] (spectrograph with Fabri-Perot interferometer) was used for observation with a subsequent registration using streak camera. Such a scheme allowed to gather information with spectral resolution in a direction perpendicular to the streak direction. Each part of the spectral line is formed by the light come from some part of the POS interelectrode gap. The resolution for the experiment is - 0.4 A, and- 10 ns. Observing line contours one can suppose that their formation was determined due to Stark effect as broadening takes 1-3 A, at the same time Zeeman broadening due to drive current magnetic field could not exceed 0.2 A.

The characteristic line contours can be divided into three types (with space and time ranges as shown at FIG.1b):

1 - relatively narrow contour with wings was found at 500-600 ns after drive current beginning at the centre of POS and near the anode; it was observed within 400-500 ns.

2 - broken contour with several equidistant peaks was observed near the anode at the switching moment.

3- contour with 2 satellite symmetrically placed peaks at the middle of the gap and near anode was found at 900-1100 ns after current beginning; it was observed within 300-400 ns.

This contours testify of presence of quasistatic, high-frequency and quasi-constant electric fields correspondingly. In this paper we consider type 1 contours which could be provoked by low-frequency oscillations in the plasma. Line contour (FIG.2) is formed by the light from approx. 2.5 cm of interelectrode gap. One can suggest that this form is provoked by a combination of Doppler and low-frequency turbulence effects. The simulation of the profile was fulfilled using approach from [14]. Supposed that turbulent field distribution is isotropic and could be approximated by Gauss function with square mean of turbulent electric field strength E_0. Holzmark broadening is suggested negligible. Besides that a sufficient Doppler broadening could be observed which could be estimated as: $I(\omega)=I_0\exp\{-(\Delta\omega/\Delta\omega_D)^2\}$, where $\Delta\omega_D=\omega_0 V_T/c$, $V_T=(2kT/M)^{1/2}$, for Maxwell distribution only. The resulting intensity is:

$$I(\omega) = I_{01}\cdot\exp\left\{-\left(\frac{\omega-\omega_0}{\Delta\omega_D}\right)^2\right\}+\frac{3}{2}\sqrt{\frac{6}{\pi}}I_{02}\sum_{s\neq 0}\left(\frac{1}{3}\beta_{s\pi}+\frac{2}{3}\beta_{s\sigma}\right)\times\frac{1}{|s|gE_0}\int_{-\infty}^{+\infty}\left(\frac{\omega_1-\omega_0}{sgE_0}\right)^2\times$$

$$\times\exp\left\{-\left(\frac{\omega_1-\omega}{\Delta\omega_D}\right)^2-\left(\frac{\omega_1-\omega_0}{sgE_0}\right)^2\right\}d\omega_1$$

$I_{01}=\dfrac{2\beta_{0\sigma}}{3\sqrt{\pi}\cdot\Delta\omega_D}$, $I_{02}=\dfrac{1}{\sqrt{\pi}\cdot\Delta\omega_D}$ and $\int_{-\infty}^{+\infty}I(\omega)d\omega=1$, where $\beta_{s\pi}$, $\beta_{s\sigma}$ - weight of Stark component, s - its number (for H_α line $-8<s<8$), $\Delta\omega=\omega-\omega_0$, $g=3ea_0/2\hbar$, a_0 - Bohr radius.

This equation was used to obtain model line profile (FIG.3). Comparing with experimental profile it is possible to estimate the filed strength as 10-30 kV/cm near the

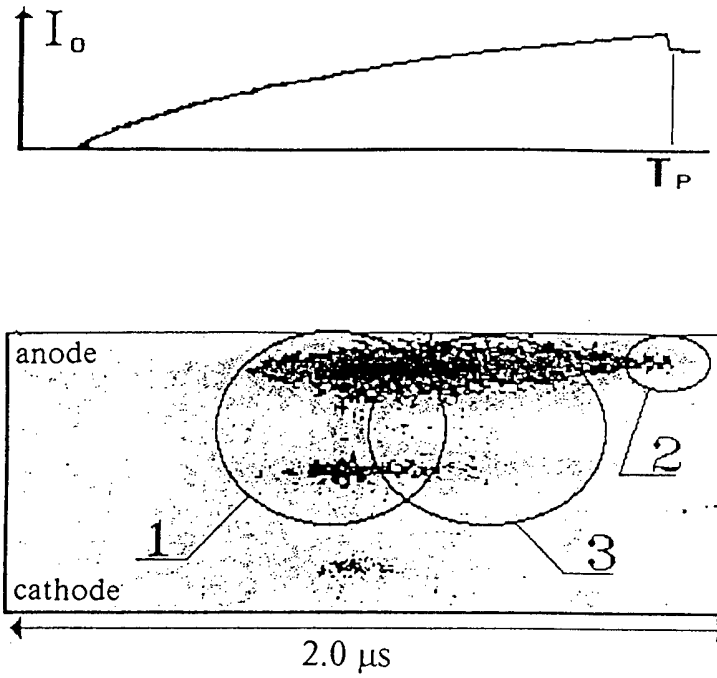

FIG.1 (a) upstream current for "Taina" shot; (b) a scheme of spectrogram streak of H_α line luminescence (3 interference orders); darkening is proportional to intensity, anode-cathode gap is 12.5 cm. Regions with different types of broadening are marked.

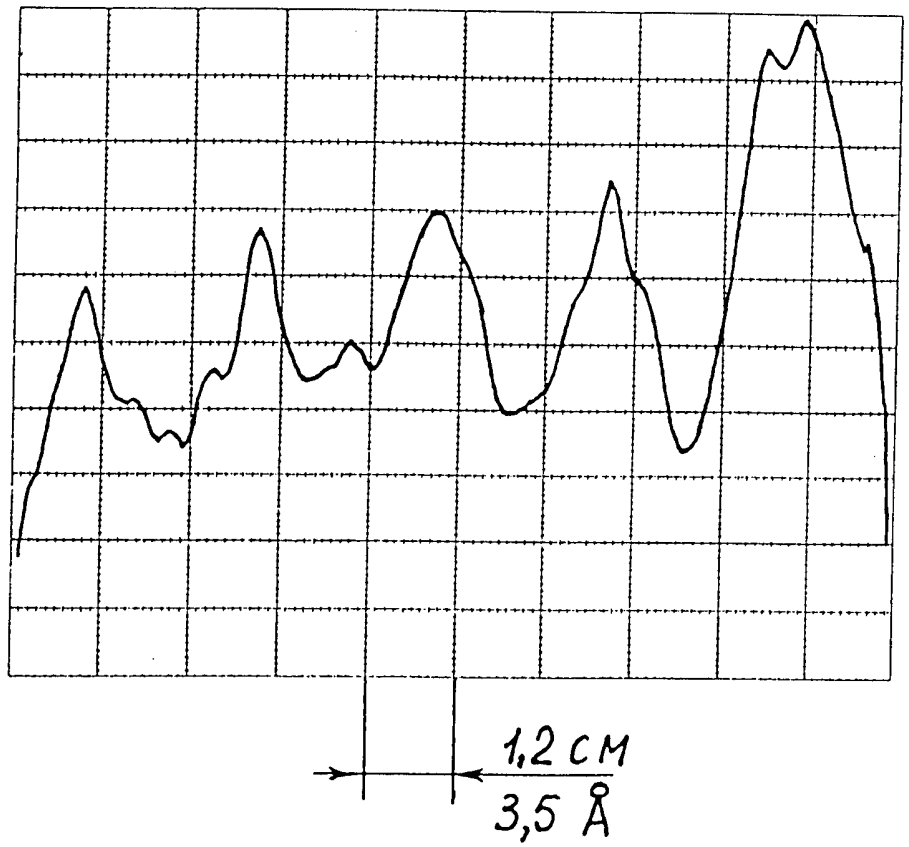

FIG.2 The line contours for 5 interference orders of H_α line. The horizontal axis is corresponding to the gap size (1.2 cm/div ; cathode is on the left, anode - on the right) and to the spectral shift (3.5 A/div). On the vertical axis is intensity (rel.units). Data are given for 1.0 μs after current beginning.

anode for neutral gas temperature 1-3 eV. Turbulent field increases toward the cathode up to 50 kV/cm as the distance between the side peculiarities of the profile increases.

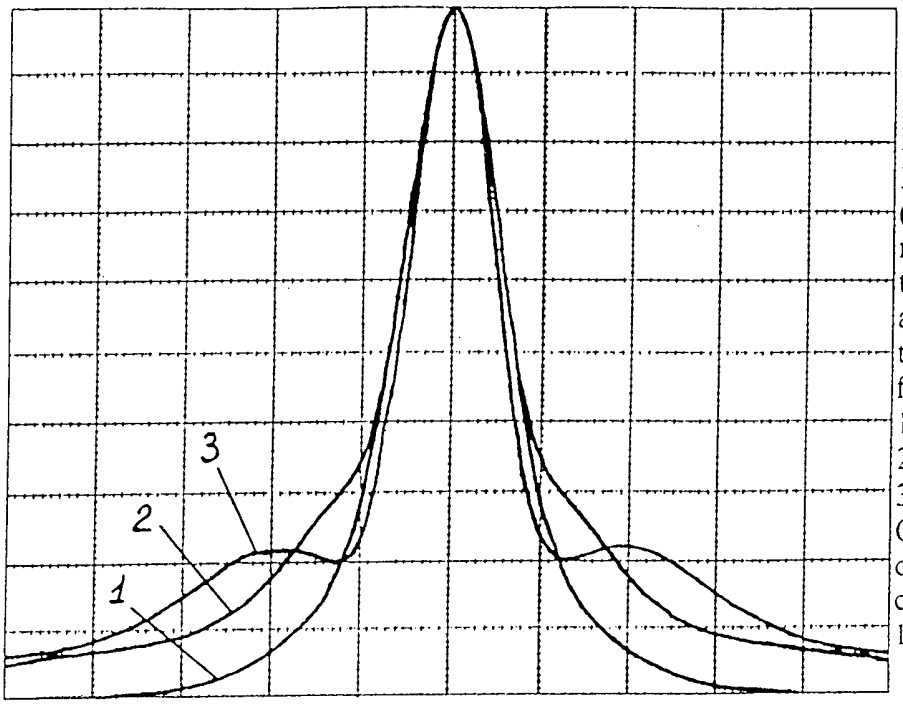

FIG.3 Calculated H_α line contours (rel. units) for neutral gas temperature 4.5 eV and different turbulent electric field strength:
1- E_0= 10 kV/cm,
2- E_0= 30 kV/cm,
3- E_0= 50 kV/cm.
One horizontal division is corresponding to 1 A.

Conclusion.

The paper stresses the sufficiency of anomalous plasma resistance in the dynamics of the plasma opening switch. Turbulent noises in the POS were registered in experiments on Stark broadening investigations of neutral hydrogen H_α at the conduction phase. The simulation allowed to estimate turbulent field strength. One can suppose that if with scaling of experimental POS-based machines the scale of electron flow will exceed the geometric scale then today's similarity laws will not be used.

This work was supported by the Russian Foundation of Fundamental Research - grants No. 94-02-04431-a, 94-02-03059-a and ISF- grant **N8X000**.

References.

[1]. *A.A. Galeev, R.Z. Sagdeev .//* in the Sov. "Problems of Plasma Theory"/ Edited by M.A. Leontovich, is. 7, p.3, Moscow, Atomizdat Publishers, 1973.
[2]. *Bychenkov V.Yu., Silin V.P., Uryupin S.A. //* Phys.Reports, 1988, vol.164, p.119.
[3]. *A.S. Kingsep //* Sov. J.Plasma Physics 'Fizika Plazmy', 1991, **17**, p.582.
[4]. *A.S. Kingsep, K.V. Chuckbar, V.V. Yan'kov //* in the Sov. "Problems of Plasma Theory" / Edited by B.B. Kadomtsev, is. 16, p.209, Mosocw, Energoatomizdat Publishers, 1987.
[5]. *Gordeev A.V., Kingsep A.S., Rudakov L.I. //* Phys. Reports, 1994, vol. 243, N5, p.215.
[6]. *Weber B.V., Colombath D.G., Commisso R.J.* et al *//* Proc. VI Int. Conf. on High-Power Particle Beams BEAMS'86, 1986, Kobe, p.882.
[7]. *G.I. Dolgachev, L.P. Zakatov, A.G.Ushakov //*Sov. J.Plasma Physics, 1991, **17**(10), pp.1171-82.
[8]. *A.V. Gordeev, A.V. Grechikha, A.V. Gulin, O.M. Drozdova //* Sov. J.Plasma Phys, 1991, **17**, p.650.
[9]. *L.I. Rudakov. //* Sov. J.Plasma Physics 'Fizika Plazmy', 1993, vol.19, p.835.
[10]. *Yu.P. Golovanov, G.I. Dolgachev* et al. *//* Sov. VANT, Ser. 'Termonucl. Fusion', 1987 (4), p.30.
[11]. *A.Kingsep, A.Munier//* These Proceedings.
[12]. *Yu.P. Golovanov, G.I. Dolgachev, L.P. Zakatov* et al. *//* Sov. J.Plasma Physics, 1991, **17**(7), p.799.
[13]. *Hinshelwood D., Weber B.V., Grossmann J.M., Commisso R.J.//* Phys.Rev.Lett., 1992, Vol.68, p.3567.
[14]. *A.B. Berezin, B.V.Lyiblin, D.G.Yakovlev //* Preprint K-0609. Leningrad, NIIEFA Publishers, 1983.

INVESTIGATION OF A STRIP-LINE LONG-CONDUCTION-TIME PLASMA OPENING SWITCH ON MAG-1'

V.Frolov, A.Chuvatin, S.Semushin, and B.Etlicher,

Laboratoire de Physique des Milieux Ionisés, Ecole Polytechnique, 91128, Palaiseau, France

Abstract

Experimental results of the long-conduction-time Plasma Opening Switch (POS) operation in a strip-line geometry of electrodes are presented. Considerable plasma motion and plasma pinching during the conduction time were registered. Diminishing of the plasma asymmetry with the help of electrode "wings" allowed visible improvement of the POS operation. Operation of the plasma guns used in this experiment was specially studied. Synchronization of two plasma switches with the help of a low-inductive upstream electrical connection is efficient only in the case of initially big difference in their conduction times. Computer simulations with the use of new numerical method of adaptive mesh refinement are compared with the experiment.

Experimental setup

Experiments were carried out on MAG-1' two-module inductive storage generator operating in plane geometry of electrodes. For each module the plasma was initially injected through the anode rods of a 40 cm wide strip-line with the interelectrode gap of 4 cm (Fig. 1). From 10 to 20 plasma guns (PG) [1] per module were installed in a line along the strip width. Each plasma gun was individually connected with the common capacitor bank through a 2 m cable. The gun represented a 15-20 cm length, 6 mm diameter rigid copper cable with polytetrafluorethylen insulator. No additional covering of the dielectric surface [1] was used. The load was a short-circuit installed at 30 cm downstream of the plasma injection region. A low-inductance capacitor bank (C_S = 8.48 μF, Fig. 2) provided a 250 kA upstream current with the quarter-period of 1.5 μs. Anode current density was registered by 15 B probes per each module. The probes were installed on the anode in 5 rows parallel to that of the plasma guns, both in the upstream and downstream regions. This diagnostic was coupled with the Faraday cup technique and visible streak camera.

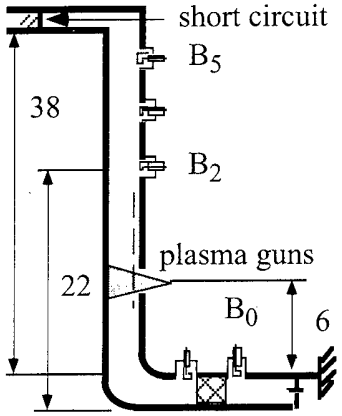

Fig. 1

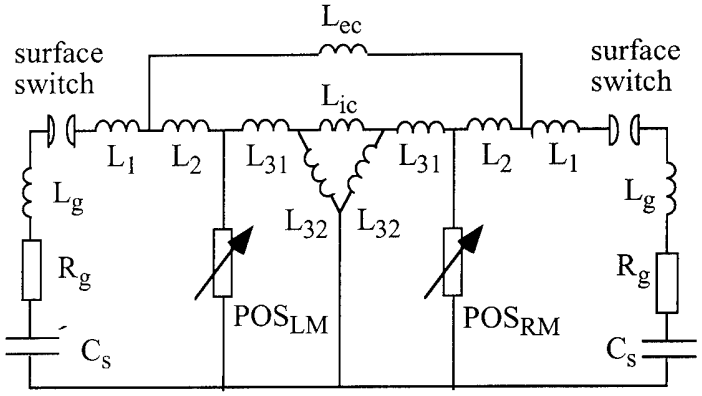

Fig. 2

Fig. 1. General design of one MAG-1' strip-line module (side view).
Fig. 2. Equivalent electrical circuit of the generator. External synchronizing connection between two modules, L_{ec}, is also shown.

Operation of plasma guns

The plasma produced by PG was studied with the help of Faraday cups (FC). After a long usage of the gun (about 50 shots), the FC peaks had a shot-to-shot scattering of 150-180 ns in their time of arrival and of 30% in their amplitudes. The average time positions of the FC peaks

from different guns could differ also by 200 ns that corresponded to a 15% difference in the density-velocity product. New guns were well reproducible in time between approximately the 20th and the 40th shot. The FC measurements allowed also estimation of the lower ion density limit which was typically equal to 5×10^{13} cm^{-3} for the 25 kV gun charging voltage. For three investigated gun charging voltages (10, 18 and 25 kV) the maximum FC signals were obtained for 18 kV. However, the resulting dependence of velocity on the charging voltage was very weak.

Typical FC signal consisted of several separated groups corresponding to the gun current oscillations. The first group, shown in Fig. 3 had normally two peaks. The time-of flight measurements showed that these two peaks had different velocities (4.6 and 6.2 cm/μs in the figure) and thus, corresponded to two groups of ions. These groups were formed at different stages of the first current half-period: in the beginning and near the maximum of the gun current rise.

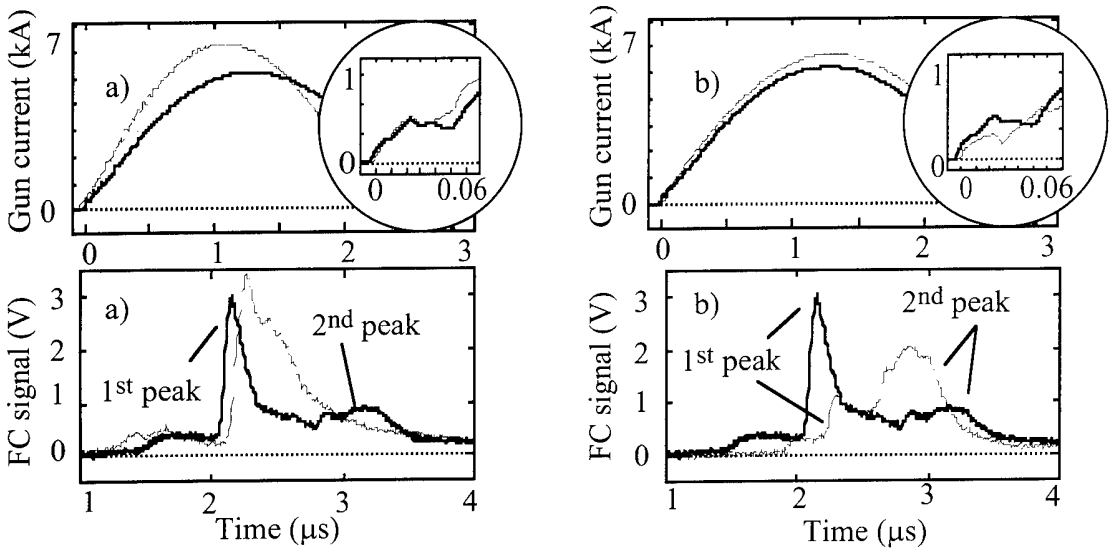

Fig. 3. Plasma gun currents and corresponding FC signal traces in two cases. (a) Different amplitudes at quarter-period of the current oscillations, but identical behavior of the current signals during the first 20-30 ns. (b) Close current amplitudes at t = T/4 but different current time behavior in the beginning.

The difference in origin of two ion peaks was demonstrated in a separate experiment. The same gun was connected with the powering capacitor through different cables that allowed to change the gun current amplitude, Fig. 3. This modification changed drastically the second ion peak amplitude. However, when the current waveforms were close to each other during the first 20-30 ns, the velocity and amplitude of the first ion peak did not change. And vice versa, different time behavior of the gun current in the beginning yielded scattering in the amplitude and time of the first fast ion peak. Therefore, one can suppose formation of the plasma injection front during the first 20-30 ns of the gun current rise-time.

Streak-camera images confirmed this supposition. Several gun puffs were in a good correlation with the current oscillations. The second puff was always brighter than the first one. Streak photos confirmed existence of several groups of particles created during first current halfperiod. The light at the cathode always started at the moment of arrival of the fastest ions to the cathode surface (first FC peak). At the same time, the maximum increase of the cathode brightness was close in time to the second peak of FC signal. The distribution of plasma luminosity at different points of the gap was also used for estimation of the plasma velocity. The mean plasma velocity corresponding to the ions created during the first half-period of the gun current was about 4.7 cm/μS, i.e. close to the value obtained from FC signals.

POS operation

Let us consider first operation of one module. In the initial strip-line configuration the POS plasma was created by 16 plasma guns . Generator charging voltage of 30 kV yielded the

maximum conduction current I_{0max} = 250 kA, conduction time t_c = 700-800 ns and the opening time not less than t_s = 150-200 ns (Fig. 4a). Plasma current losses after the opening were as high as 10-20% of I_{0max}. In this configuration one should note very particular time behavior of the signal of the downstream B-probe situated it the middle of the row closest to the plasma injection region, j_2 (B_2 in Fig. 1). The current density obtained with the center B-probe always showed a negative peak in the beginning. This negative signal was sharper for higher currents, longer conduction times and appeared sometimes in the center of the next row, closer to the short-circuit, j_5 (B_5). Besides, the signal of the central probe lagged behind the traces of all the other downstream B-probes. This time delay could be explained by the so-called "crow-bar" of the probe covered by the plasma during its motion. One can conclude that, probably due to initial inhomogeneity of the plasma density and magnetic field, this motion had different velocities in the center and at the borders of the strip-line.

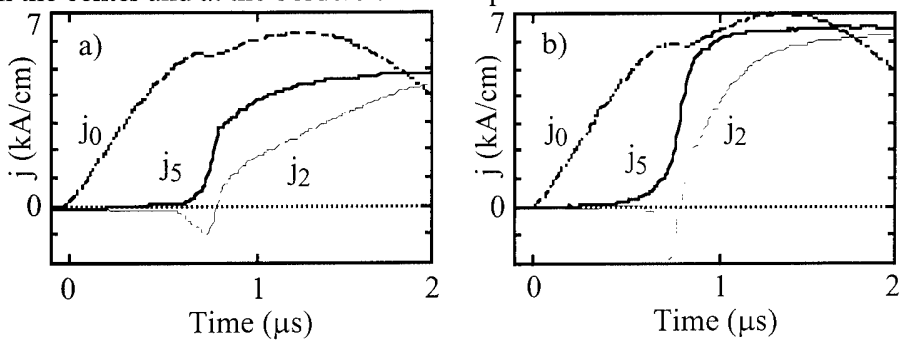

Fig. 4. Upstream and downstream current densities measured in the center of the anode for two cases: (a) initial configuration without the anode "wings", 16 guns, and (b) with the "wings", 10 guns.

Therefore, relatively long opening time could be a result of asymmetry of our plasma system. To verify this hypothesis, we installed two additional anode "wings" in the plasma injection region. These electrode "wings" partially closed the opened strip-line borders and prevented the plasma to exit from the interelectrode gap. For this new configuration with the "wings", the optimized number of plasma guns was found to be equal to 10. The plasma guns were distributed uniformly along 40 cm of the electrode width. The best shots were characterized by disappearance of the difference in B-probe signals at the borders and in the center. The negative peak appeared now simultaneously on all three B-probes of the row closest to the plasma. Finally, the opening became faster (Fig. 4b) and the plasma current losses became smaller. From our point of view, this fact confirms the influence of the initial plasma density homogeneity on the "quality" of the opening.

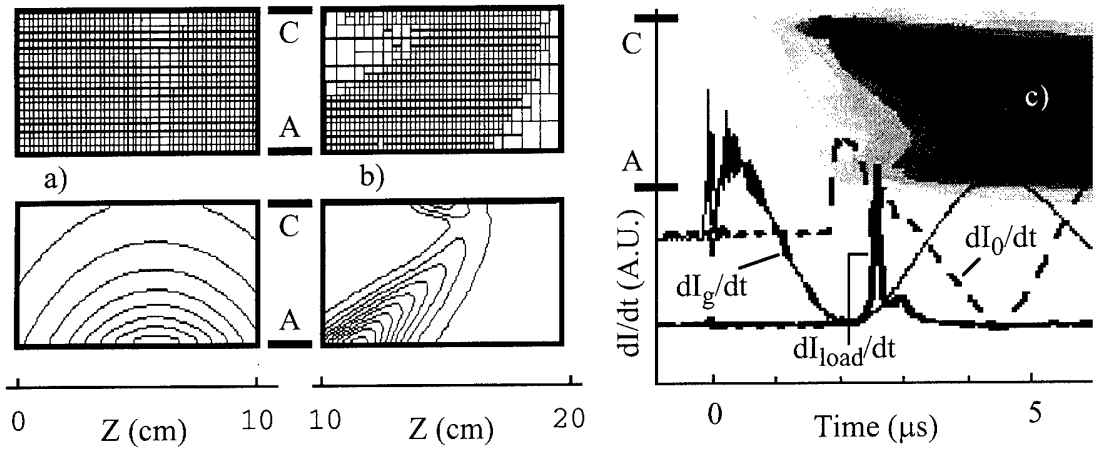

Fig. 5. (a) Initial mesh density (upper) and initial plasma distribution in the gap (lower) in AMR numerical simulations. (b) Mesh density and plasma density at the moment of the POS opening. A - anode, C - cathode.(c) Streak-camera image synchronized with the current derivatives: dI_g/dt - plasma guns, dI_0/dt - upstream current, dI_{load}/dt - downstream current.

Computer simulations of the POS operation were carried out with the help of a new numerical method of adaptive mesh refinement (AMR) [2]. This method allowed considerable reduction of the computer run-time for this kind of problems. The results shown in Fig. 5 (a, b) were obtained by using the one-fluid MHD model with modifies Spitzer conductivity. No secondary plasma creation was supposed in the present calculations. The initial plasma density was chosen to correspond to that estimated with the FC technique (5×10^{13} cm^{-3} on the cathode surface with 1/r-like density distribution, where r is the distance from the plasma guns plane). Numerically simulated pictures confirmed considerable plasma motion during the conduction phase. The opening occurred through rarefaction of the midgap plasma.

At the same time, experimental results showed importance of the electrode phenomena in the POS dynamics. Fig. 5 (c) represents the image obtained during the POS shot with the help of a streak camera. The slit was situated to visualize the entire interelectrode gap from the load side of the installation. It was perpendicular to the electrode surface, so that the visible light from the plasma passed along the strip-line and entered the optical system of the streak-camera through a hole in the anode near the short-circuit (see Fig. 1). The cathode radiation started at the moment when the plasma arrived to the cathode surface and created a secondary electrode plasma. During the generator current rise-time this plasma rapidly filled the entire gap in. Dynamic range of our diagnostic did not allow to resolve the midgap plasma rarefaction. Therefore, inclusion of the secondary plasma dynamics could be important in our numerical modeling and will represent a subject for the future work.

Synchronization of two POS modules

Synchronization of two modules with the help of a low-inductive upstream connection between them [3] was verified experimentally (see Fig. 2). The connection L_{ec} consisted of thirty 50 Ohm, 1.5 m length parallel cables. The cables were distributed homogeneously along the strip-line width, before the vacuum chamber insulator. Two-module MAG-1' installation allowed direct comparison of the shots with and without synchronization. This part of the experiment included two series of shots.

In the first series the initial plasma density differed considerably for the right (RM) and the left (LM) modules. In this case the optimum injection delays for LM and RM were also different. Without synchronization, this resulted in a difference of the conduction times bigger than the opening time value for one module, $t_{c(RM)} - t_{c(LM)} > t_s$. When the left POS approached its optimum operation, the right one did not interrupt the current any more. The synchronization was tested for the conduction time difference changing from 200 to 500 ns. In this case the rise-time for the sum of both load currents was shorter than in absence of the connection between the modules.

Second series of experiments was performed when the initial plasma density was approximately the same for both modules. Therefore, separate modules had already close values of the conduction times even without additional connection between them. The result of this series was opposite to that of the first series. If $\Delta t_c < t_s$, the external upstream connection often made Δt_c even bigger. Therefore, one can conclude that the procedure of synchronization proposed in [3] was efficient only in the case when the difference of the conduction times of two plasma switches was bigger than the opening time of one POS .

Acknowledgments

The authors would like to thank K.Koshelev, P.Choi and D.Kouznetsov for the discussion of the experiments; Ya.Krasik for the participation in MAG1' installation; H.Lamain, P.Auvray and C.Rouillé for the technical support. This work is partially supported by DRET under the contract #92.134 and by ETCA/CEG under the contract #420/115/01.

References

[1] C.W.Mendel et. al, *Rev. Sci. Instrum.* **51** (12), 1641 (1980).

[2] Semushin S.A., Adaptive Mesh Refinement approach for MHD and gas dynamical problems, Preprint LPMI, Ecole Polytechnique, 1996.

[3] G.I. Dolgachev et al., *Sov. J. Plasma Phys.* **17** (10), 1171 (1991).

THEORETICAL MODELLING OF THE MAGNETIC-FIELD-PENETRATION IN A PLASMA OPENING SWITCH EXPERIMENT

K. Gomberoff, R. Shpitalnik[†], A. Weingarten, Y. Krasik and Y. Maron

Department of Particle Physics, Weizmann Institute of Science, Rehovot 76100, Israel

[†]*Plasma group, NRC, Yavne, 81800*

Abstract

Fast magnetic field penetration into a positive-polarity plasma-opening-switch (POS) of 100 ns duration time has been recently measured. The measurements provide the temporal and spatial evolution of the magnetic field in the plasma. We present theoretical results for the magnetic field evolution based on the Hall model for fast magnetic field penetration into a cylindrical plasma of inhomogeneous density [1], and compare them with the experiment. This model allows for magnetic field penetration into most of the plasma for both positive and negative switch polarities as long as fast magnetic field penetration along the electrodes occurs. The evolution of the magnetic field depends on various parameters. These parameters are the switch polarity, the plasma density profile and the time-varying field values in the vicinity of the electrodes and at the plasma-vacuum boundaries. The magnetic field near the electrodes is unknown experimentally. We assume its shape and time dependence based on previous theoretical models and numerical simulations. The other parameters, namely the plasma density profile and the field values at the plasma-vacuum boundaries, are taken from the measurements. The model yields an analytical solution under some simplifications that are possibly valid for this experiment. The theoretical results appear to fit well the spatial and temporal magnetic field values obtained experimentally, and provide an explanation for the fast magnetic field penetration.

[l] K. Gomberoff and A. Fruchtman, Phys. Fluids B, 5 (8), 2841 (1993)

(The full text has not been supplied.)

P-4-69

SPECTROSCOPIC INVESTIGATION OF THE TIME DEPENDENT MAGNETIC FIELD DISTRIBUTION IN A PLASMA OPENING SWITCH

R.R. Shpitalnik[1], A. Weingarten, K. Gomberoff, Ya.E. Krasik, R. Arad, M. Sarfaty[2], and Y. Maron.

Department of Particle Physics, Weizmann Institute of Science, Rehovot 76100, Israel

[1]*Plasma group, NRC, Yavne, 81800*

[2]*University of Wisconsin, Madison*

Observation of the MF distribution in short duration plasmas is of major importance. This work presents time-dependent, spatially resolved, non-intrusive measurements of the Magnetic Field (MF) penetration into a Plasma Opening Switch (POS) experiment using observations of Zeeman splitting. In this experiment, a positive voltage pulse is applied to the inner conductor of a shorted coaxial POS, giving a peak current of 135 ± 10 kA with a quarter period of 90 ns. The interelectrode gap is 2.5 cm. In the measurements, the spectral profiles of the π and σ components of the line emission from the same volume element are observed in a single discharge, using two spectroscopic systems. It allows for unfolding the Doppler broadening from the Zeeman splitting. To obtain local measurements, the plasma is seeded with BaII ions, giving spatial resolution of ~ 1 cm. Measurements of Stark broadening and line intensity time histories are used to verify that the seeded plasma does not affect the POS properties.

The MF distribution is observed as a function of time throughout the pulse, starting at t = 10 ns after the generator current is applied. At t = 20 - 25 ns, the MF is found to reach the axial center of the plasma. At this period, the current (determined from the MF gradients) is found to flow through a channel in the plasma ~ 1 cm wide in the axial direction. At t = 30 - 35 ns, the MF is observed at the load side of the plasma, showing there higher values than in the center of the plasma. At later times, t = 60 ns, most of the current is observed to flow in the load side of the plasma and between the plasma and the load. The average axial velocity of the MF penetration is $v = (1.0 \pm 0.35) \cdot 10^8$ cm/s. A simulation, based on field penetration due to the Hall effect, is developed. The model that combines the effects of the cylindrical geometry and the non-homogeneous plasma density, gives results that are consistent with the experimental results. The high MF values observed at the load side at t = 30 - 35 ns can be explained by fast MF penetration along the cathode.

(The full text has not been supplied.)

EXPERIMENTAL INVESTIGATION OF THE ION CURRENT DISTRIBUTION IN MICROSECOND PLASMA OPENING SWITCH

V.Bystritskii, S. Grigor'ev, A. Kharlov, A.Sinebryukhov,

Institute of Electrophysics RAS, Academy ave.4, Tomsk 634055, RUSSIA

Abstract This paper is devoted to the investigations of the microsecond plasma opening switch properties (MPOS) as an ion beam source for surface modification. Two plasma sources have been investigated : flashboard and cable guns. The detailed measurements of axial and azimuthal distributions of ion current density in the switch have been performed. It was shown that the azimuthal unhomogeneity of the ion beam increases from the beginning to the end of MPOS. The advantages and problems of this approach are considered.

Introduction

It was shown recently [1] that microsecond plasma opening switch (MPOS) can be used as an ion beam source for material surface modification. The advantages of MPOS are following: large area of ion beam cross-section (500-1000 cm^2); wide range of ion current density (10-150 A/cm^2); high efficiency of ion beam generation. Nevertheless, the first experiments have showed that there are several serious problems that should be solved for more successful application of MPOS to modification:

- The problem of uniformity and controlling of power density for the ion beam;
- Requirement for high reproducibility of ion beam parameters from shot to shot;
- The requirement of the long operation for the plasma source ($\geq$ 100 shots).
- The formation of microcraters on the sample surface under ion beam action.

The solving of these problems requires a better understanding of the POS operation and ion beam-matter interaction physics. To make more precise this understanding we have performed the detailed measurements of axial and azimuthal distributions of ion current density in the switch. This report is devoted to the MPOS properties as an ion source for the modification of the materials. The questions of the surface modification for various steels are discussed in other our report presented on this conference also.

Experimental setup and diagnostics

The experiments were carried out on the "MARINA" generator. The setup schematic is given at fig.1. The generator-POS parameters were following: the POS inner and outer electrodes diameter were equals to 55 and 200 mm correspondingly, output generator voltage - 480 kV, upstream and downstream POS inductances 1.8 and 0.8 μH, short circuit current 220 kA, current rise time 1.3 μs. In the main part of the experiments the plasma gun source was used. The plasma guns of coaxial type were installed on the outer electrode (the number of plasma guns was equal to either 8 or 16). The generator was operated in the negative polarity regime. The investigated samples and diagnostic equipment were installed behind the cathode splits. The capacitive and resistive voltage probes placed in the oil tank near the interface and two: upstream and downstream POS current monitors were used. The ion current density in the POS region was measured

by collimated Faraday cups with transverse magnetic field. The field was produced by permanent magnets and has a strength of 0.15 T. In some shots the carbon targets were placed inside the mylar films with mass thickness of 0.3 - 2 mg/cm to determine the ion energy spectrum. In order to measure total proton number the nuclear activation technique on the reaction $^{12}C(p,\gamma)^{13N} \rightarrow \beta^+$ with threshold of 460 keV was used.

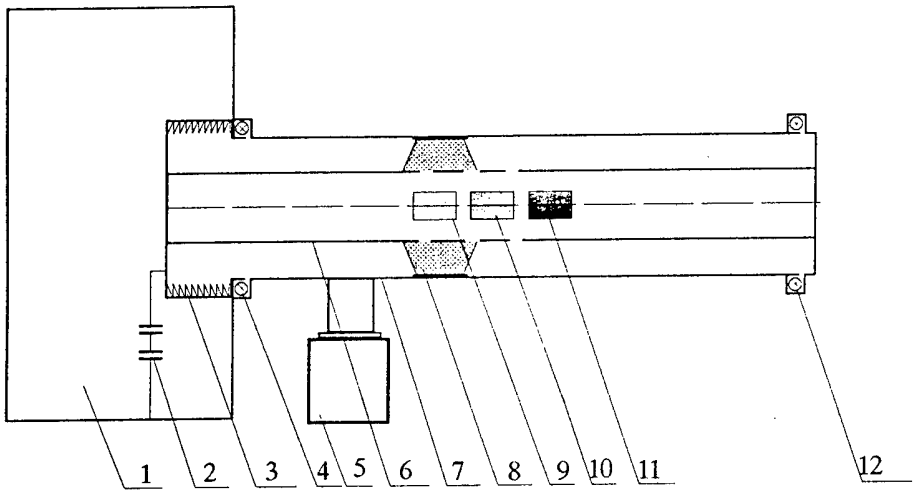

Figure 1: Experimental setup and diagnostics.
1 - Marx, 2 - capacitive voltage monitor, 3 - oil-vacuum interface, 4, 12 - Rogovsky coils, 5 - vacuum pump, 6 - cathode, 7 - anode, 8 - plasma source, 9 - collimated Faraday cup, 10 - carbon target, 11 - irradiated sample.

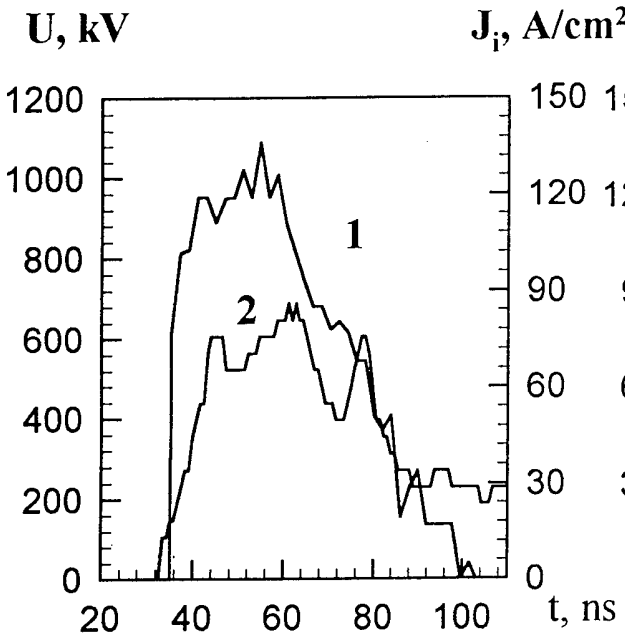

Figure 2: Characteristic waveforms of the switch voltage (curve 1) and ion current density (curve 2).

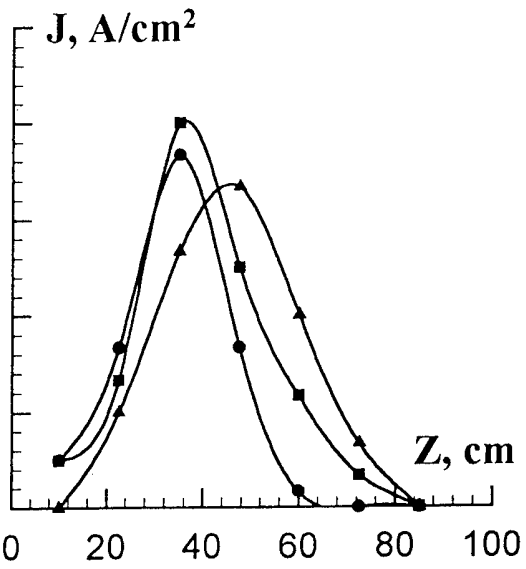

Figure 3: Axial distribution of the ion current density for various time delays. □ - 800 ns, △ - 1000 ns, + - 1200 ns.

Plasma source and POS regimes

It was shown in our experiments that the lifetime for the flashboard source is much less than for the cable gun source ($N_s \sim 50$ and $N_s \geq 200$ shots correspondingly). By this reason the cable gun source was chosen for the our experiments on modification of the materials. This source produced plasma flow with density of $5 \cdot 10^{13}\, cm^{-3}$ and velocity of $10^7\, cm/s$ when it was powered from 3 μF capacitor bank with 30 kV charging voltage. With this plasma source the POS operation regimes were stable and reproducible. The optimal time delay between POS and generator firings, providing the best regimes of POS operation, is equal to 0.9-1 μs. Switch voltage was equal to $0.8 \div 1$ MV and the pulse length was equal $50 \div 70$ ns. The operation regimes coincide in general for the 8 and 16 plasma guns but the ion beam uniformity is higher for 16 plasma guns. The plasma density in the anode-cathode gap was measured without firing of the generator using negatively biased collimated Faraday cups (CFC), which operated in the saturated regime of plasma probe. The plasma density nonuniformity in azimuthal direction was nearly 40 % for 8 plasma guns and 25 % for 16 ones.

Investigation of the ion current density distributions

The typical waveforms of switch voltage and CFC signal are given in fig.2. When the cathode in switch region was made in "squirrel cage" form, the ion beam uniformity and repeoducibility were bad: the ion current densities measured by CFC at the center and at the border of the split were differed in 2-3 times. To eliminate this effect the cathode splits were covered by stainless steel grid with cells dimensions of 1 mm. In this case this difference was not more than 20 %. The axial ion current distribution for various time delays between POS and generator firings is presented in fig.3 (total ion current, measured by CFC with magnetic field) and fig.4 (proton current, measured by nuclear activation technique). Integrating the axial distributions, we obtained 40 kA of the proton current (with ion energy higher than 440 keV) and 60-70 kA of the total ion current in POS. The efficiency of the ion beam generation is equal to 35-40 %. The ion beam particle energy and composition measurements with Thomson parabola showed that the ion beam consists mainly from protons and carbon ions with charge state of 1-3. The ion energy corresponds roughly to POS voltage, that is confirmed in activation measurements with mylar films. The ion beam composition is not homogeneous along the POS cathode: protons are removed in the load direction.

The azimuthal uniformity of the ion beam was investigated by nuclear activation technique also. Eight identical graphite plates 1x5 cm were installed behind the cathode splits (cathode splits are distributed over 45 degree in azimuth) in several axial positions (in one shot). The dispersion of the activation results in azimuthal direction increased significantly from the beginning to the end of POS. It can be seen in fig.2. As it was shown earlier [2], the divergency of the ion beam is increased to the POS end also. So, we can conclude, it is preferable for the modification to place samples in the first half of the switch length.

Conclusion

This experimental run showed that for the effective work of the MPOS as an ion source for the materials modification the next conditions are needed:

1. To install the samples inside the cathode tube.
2. The cathode splits have to be covered by the gird with small cell.
3. The samples have to be installed in the first half of the switch. If these conditions are satiesfied, the ion source on the base of MPOS can be very convinient for the material surface modification.

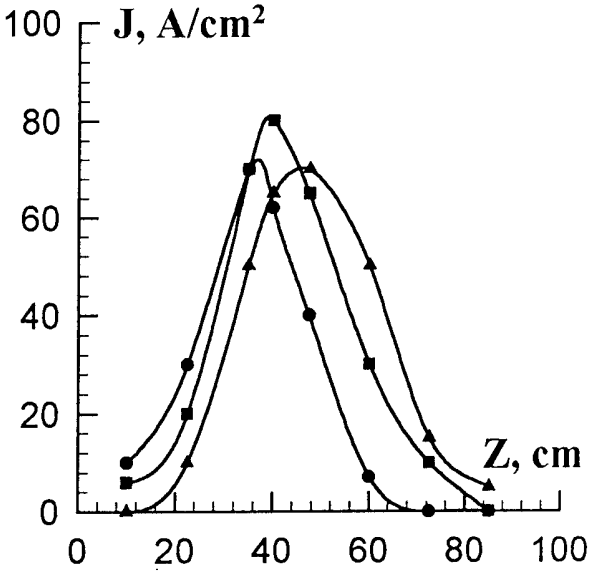

Figure 4: Ion current density measured by activation for various time delays. □ - 800 ns, △ - 1000 ns, + - 1200 ns.

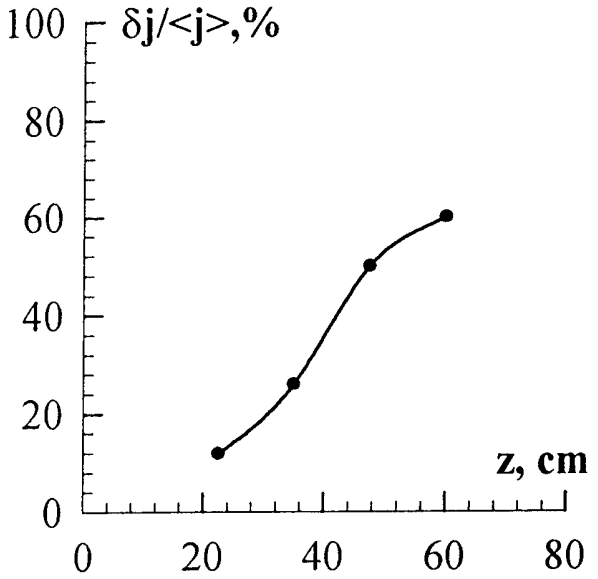

Figure 5: Azimuthal unhomogeneity of ion current density along the switch.

References

[1] V.M. Bystritskii, S.V. Grigor'ev et al., Use of Microsecond Plasma Opening Switch for Material Surface Modification. In Book : Proceedings of the 9th International Pulsed Power Conference, 1993, Albuquerque, New Mexico.

[2] V.M. Bystritskii, I.V. Lisitsyn et al., Investigation of Ion and Electron Flows in the Switching Phase of the Microsecond Plasma Opening Switch with Power Level of 0.2 TW, Fizika Plasmy (Journal of Plasma Physics in Russian), 1991, v.17, no. 1.

EXPERIMENTAL INVESTIGATION OF THE MATERIAL SURFACE MODIFICATION IN MICROSECOND PLASMA OPENING SWITCH

V.Bystritskii[1], S. Grigor'ev[1], A. Kharlov[1], A.Sinebryukhov[1], P.Burkov[2], V. Grigor'ev[3], T. Koval[3]

[1]*Institute of Electrophysics RAS, Academy ave.4, Tomsk 634055, RUSSIA*
[2]*Institute of Strength Physics and Material Control RAS, Academy ave.8, Tomsk 634055,RUSSIA*
[3]*Institute of Nuclear Physics, 2A Lenin ave, Tomsk 634050, RUSSIA.*

Abstract This paper is devoted to the investigations of the material surface modification by high power ion beam generated in microsecond plasma opening switch properties (MPOS). The various types of steels have been investigated : stainless steel 17-4PH, carbon steel C1020, pure iron. For all these materials the optimal regimes for irradiation were defined. The significant increasing in microhardness was obtained for these materials ($1.5 \div 2$ times). The numerical calculations and theoretical estimations of the ion beam-matter interaction have been performed also. The advantages and problems of this approach are considered.

Introduction

It was shown recently [1] that microsecond plasma opening switch (MPOS) can be used as an ion beam source for material surface modification. The advantages of MPOS are following: large area of ion beam cross-section (500-1000 cm^2); wide range of ion current density (10-150 A/cm^2); high efficiency of ion beam generation. The questions of the MPOS properties as an ion source for modification are discussed in other our report presented on this conference also. This paper is devoted to the investigations of the material surface modification by high power ion beam generated in microsecond plasma opening switch properties (MPOS). There is no theoretical model explaining the physico-chemical and mechanical changes, which occur in near surface layer of solids after high power ion beam irradiation. To make more precise the understanding of these phenomena we have performed the detailed investigations of the surface modification for various steels. The numerical calculations of the ion beam- solid matter interaction have been performed also.

Experimental setup

The experiments were carried out on the "MARINA" generator [2]. The generator-POS parameters were following: the POS inner and outer electrodes diameter were equals to 55 and 200 mm correspondingly, output generator voltage - 480 kV, upstream and downstream POS inductances 1.8 and 0.8 μH, short circuit current 220 kA, current rise time 1.3 μs. In the main part of the experiments on modification the plasma gun source was used. The plasma guns of coaxial type were installed on the outer electrode . Switch voltage was equal to $0.8 \div 0.9$ MV and the pulse length was equal 60 ns. The ion beam particle energy corresponds to POS voltage. Ion current density can be varied within 10-100 A/cm^2. The investigated samples and diagnostic equipment were installed behind the cathode splits.

Investigation of the surface modification

Varying the parameters of irradiation it is possible to form in the near surface layers the structure and phase states having a necessary properties. The purpose of this experiment was to investigate the properties of phase composition change and overall features of the steels and iron after high power ion beam action. Irradiated samples were of rectangular shape with dimensions 50x17x2 mm. Samples were tested by metallographic analysis and microhardness measurements. All samples were cut for microhardness measurement in depth. Metallographic analysis was made with optical microscope NEOPHOT-21 and raster-type electron microscope REM-200. Microhardness measurements were carried out with PMT-3 device for m=20,50,100,200 g. The measurement accuracy lies within 20 kg/mm^2. The study performed shows that surface power density and number of shots play the main role in the formation of phase composition and steel properties. According to metallographic data, within the chosen range of irradiation parameters the melting of a thin near surface layer occurs. The microcraters formation is observed for all irradiated samples. The threshold for the microcrater formation for all investigated steels and iron lies on the level $30 \div 40 A/cm^2$. When the current density is equal 100 A/cm^2 or more, even in single pulse irradiation the complete surface melting with intensive material evaporation occurs resulting in specific wave-like surface relief. The results of the microhardness measurements for the stainless steel 17-4PH are given at Fig. 1,2.

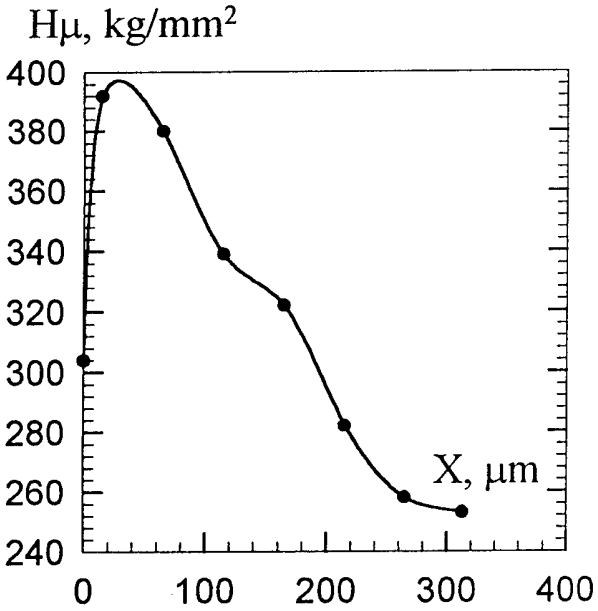

Figure 1: Microhardness for 17-4PH stainless steel (j= 40 A/cm^2, 5 shots).

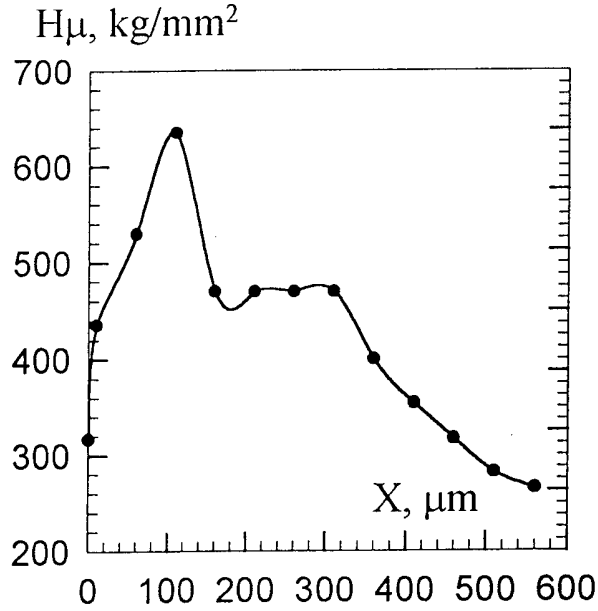

Figure 2: Microhardness for 17-4PH stainless steel (j= 60 A/cm^2, 5 shots).

The ion beam treatment, as it can be seen from the microhardness measurements, brings to the formation of the surface layer with enhanced hardness. The depth of this layer varies between 200-400 μm for various regimes. For corrosion testing of 17-4PH we have performed anodic polarization in a 1 weight percent HCl solution. The width of the passivation region increases on 20-30 percent in comparison with nonirradiated samples. The results of the microhardness measurements for the carbon steel C1020 are given at

Fig. 3,4 and for pure iron at fig. 5,6. It is need to remark that both for C1020 and pure iron the optimal treatment regime is nearly 30 A/cm^2 (two times less than for 17-4PH).

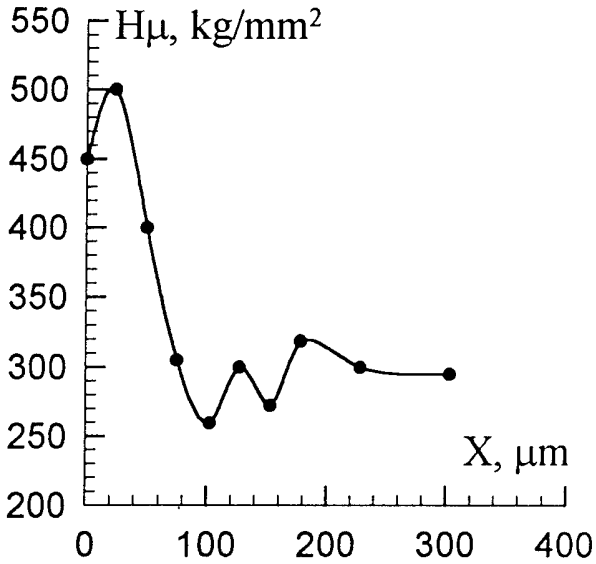

Figure 3: Microhardness for C1020 carbon steel (j= 60 A/cm^2, 5 shots).

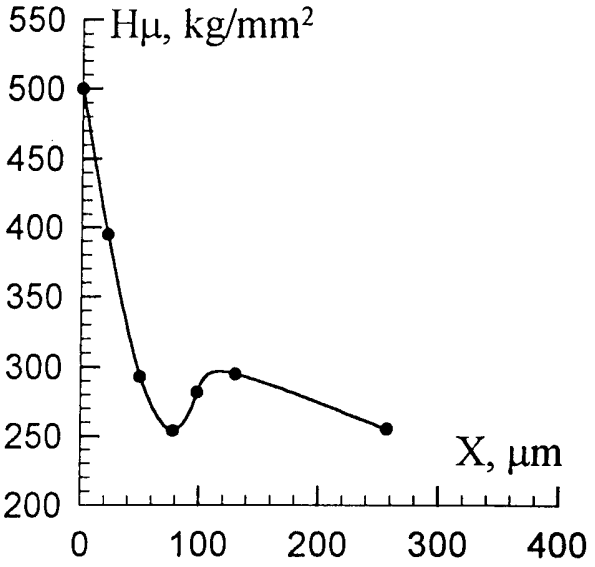

Figure 4: Microhardness for C1020 stainless steel (j= 30 A/cm^2, 5 shots).

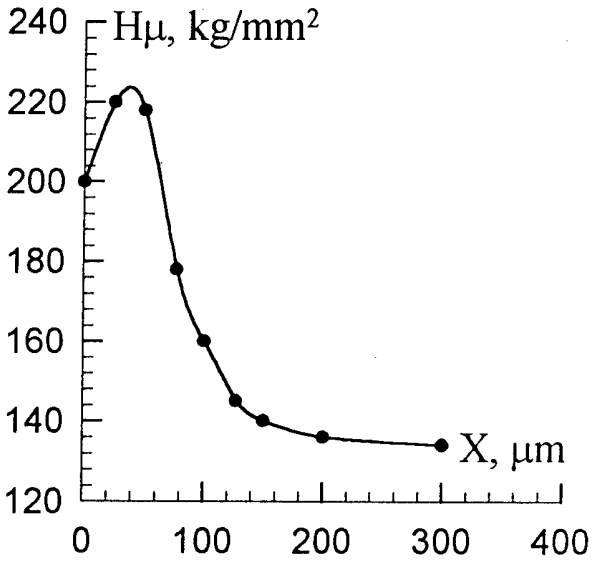

Figure 5: Microhardness for pure iron (j= 60 A/cm^2, 5 shots).

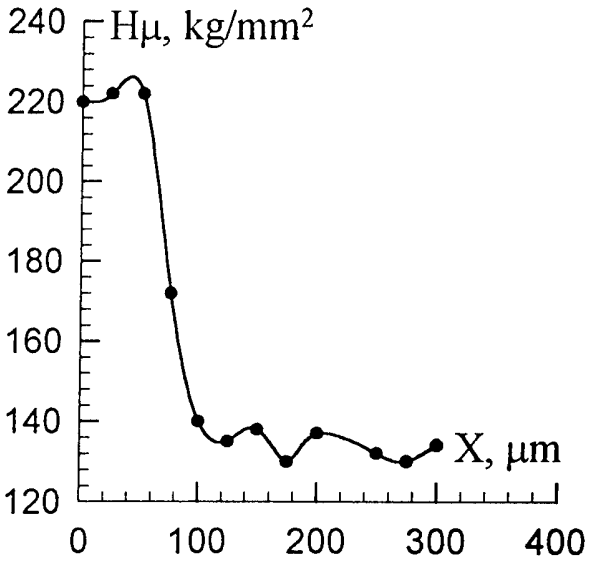

Figure 6: Microhardness for pure iron (j= 30 A/cm^2, 10 shots).

Numerical modeling of the ion beam-matter interaction

The numerical simulation have been performed with using the "BETAIN" code [?]. For the description of the matter behavior the elastic-plastic model is used in this model. It allows to describe with help of the state equations both the process in the energy deposition zone, where the matter can be melted and evaporated and outside this zone. For the correlation

between the thermodynamical plasma parameters the wide-range equations of state are used. These equations take into account the phase transitions and the charge state plasma changes. The temperature field for various ion current densities is given at fig. 5 (at the pulse end). The high temperature gradient is explained by the carbon ions contamination in the ion beam. The maximal pressure values vs depth are given at fig. 6 (sign "-" is corresponding to the compressing wave).

Conclusion

These experimental results show that the depth of modification lies between 100÷400 μm. This value is nearly two orders higher than the ion range. The temperature action region cannot be more than 2 ÷ 3 ion ranges. The pressure wave amplitude is not sufficient for the material hardening. For the explanation of this phenomenon further experimental investigations and theoretical efforts are needed.

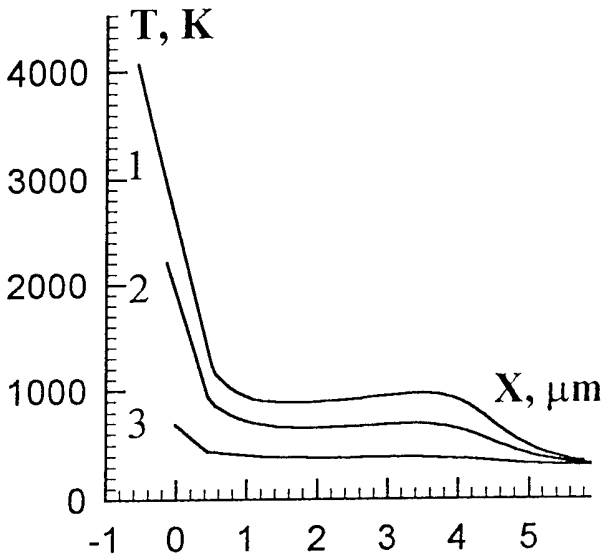

Figure 7: Temperature distribution at the pulse end (1- j =100 A/cm^2, 2 - 50 A/cm^2, 3 - 100 A/cm^2)

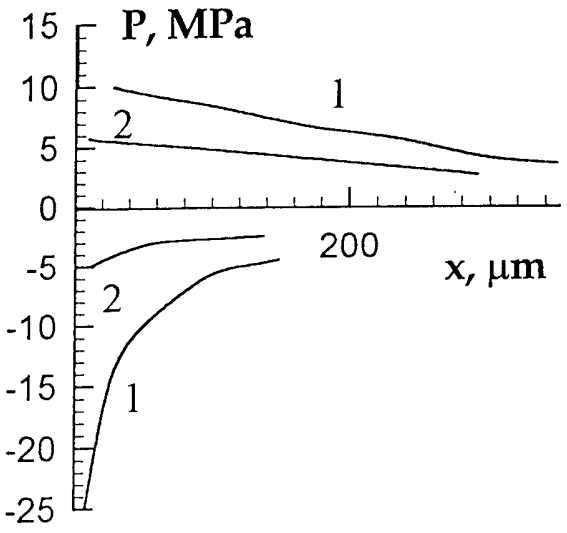

Figure 8: Maximal pressure values vs depth (1 - j = 100 A/cm^2, 2- 50 A/cm^2).

References

[1] V.M. Bystritskii, S.V. Grigor`ev et al., Use of Microsecond Plasma Opening Switch for Material Surface Modification. In Book: Proceedings of the 9th International Pulsed Power Conference, 1993, Albuquerque, New Mexico.

[2] V.M. Bystritskii, A.V. Kharlov et al., Experimental Investigation of Ion Current Distributions in the Microsecond Plasma Opening Switch. (These Proceedings, p. 1217)

[3] V.V. Valchuk, S.V. Khalikov, A.P. Yalovetc. The Modeling of the High Power Charged Particle Flows Interaction with the Multilayered Targets. Matematicheskoe modelirovanie (in Russian), 1992, v. 4, No. 10, p. 111.-123.

EFFECT OF ANOMALOUS RESISTIVITY ON THE DYNAMICS OF PLASMA SWITCHING

A.Kingsep*, A.Munier**
** Russian Research Center "Kurchatov Institute", 123182, Moscow, Russia*
*** Centre d'Etudes Limeil – Valenton, BP 27, 94195, Villeneuve – St. Georges Cedex, France*

Abstract. The paper reminds some of the conditions for electron MHD, and shows how this leads to anomalous resistivity which may play an important role in the dynamics of POS. It has been shown that not only the order of value of the resistance of the plasma–filled diode but rather basic scalings have to be changed in the regime of essential anomalous resistivity.

Anomalous resistance. One of the features of the plasma switching scenario lies in the large importance of a conduction phase (see, e.g., [1,2]) conditioned by the regime of the electron magnetohydrodynamics (EMHD) [3–4]. The window of parameters of EMHD is conditioned by the following chain of inequalities:

$$V_{Te}, V_{Ae} \gg j/ne \gg V_A, c_S, \tag{1}$$

$$\omega_{Be}, \omega_{pe} \gg \tau^{-1} \gg \omega_{Bi}, \omega_{pi}, \tag{2}$$

$$c/\omega_{pe}, \rho_{Be} \ll a \ll c/\omega_{pi}, \rho_{Bi}. \tag{3}$$

Here τ and a are, respectively, space and time scales of the problem, other terms are conventional. However, just in the same range of parameters (1)–(3) the ion–acoustic current instability can be excited and, hence, anomalous resistivity, see, e.g., [5–7]. This regime has been already considered in application to the POS physics [5,8,9]. Our goal is to show in this paper that not only the efficient resistance of the POS diode but rather its scaling turns out to be determined by the anomalous resistivity. That, in principle, could revise all the experimental scalings known at present moment if we will deal with essentially greater machines.

In all the references, [5,6,8,9], the ion–acoustic turbulent scenario was considered as the most efficient in respect of the anomalous resistivity. In principle, it is not the only possibility, see, e.g., [10]. If, however, the following inequality is true: $\omega_{Be} < \omega_{pe}$ or, what is the same, $B^2 < 4\pi nmc^2$, ion–acoustic mechanism looks to be predominating one. The reason of that is ion–acoustic wave being a "heavy quantum", $\omega < \omega_{pi}$, $k_{max} > r_{De}^{-1}$. The way to construct correctly the resistive scenario is well known, see, e.g., [11]. We have to balance the momentum transfered by the electrons from the electric field to the plasma waves

$$ne\mathbf{E} = \int \gamma_{\mathbf{k}}^e N_{\mathbf{k}} \mathbf{k} d\mathbf{k}, \quad N_{\mathbf{k}} \equiv W_{\mathbf{k}}/\omega_{\mathbf{k}}, \tag{4}$$

and the momentum transfered from the electric field to the waves by ions,

$$Zn_i e\mathbf{E} = -\int \gamma^i_{bfk} N_{\mathbf{k}} \mathbf{k} d\mathbf{k}. \tag{5}$$

In these relations, $\gamma^{e,i}_{\mathbf{k}}$ are the growth rates and $W_{\mathbf{k}}$ the spectral density of oscillations. It is obvious from (4,5) that we need just as heavy quantum as possible to obtain the efficient momentum transfer. Hence, the competition of unstable modes providing the anomalous resistivity is not only the competition of thresholds and growth rates of all the possible instabilities but first of all it means comparison of their properties as the momentum carriers. The ion sound wins this competition if it remains non–magnetized. The main condition of the non–magnetization of this mode is $k\rho_{Be} > 1$, which for the typical unstable waves, $k \sim r_{De}^{-1}$, results just in the relation mentioned above, $\omega_{Be} < \omega_{pe}$.

The scenario of instability has to be essentially nonlinear. In the case of POS, not $\mathbf{E}$ but the current value is determined by the outer circuit, that means the overwhelming role of nonlinearity. To wit, the nonlinear stimulated scattering of plasmons by ions provides the ion input into the momentum transfer while the predominating process in the electron dynamics is the Cherenkov resonant coupling with the same waves. The resulting order of value of the resistivity is well known [11,7]. In the non–adiabatic regime, i.e., with essential plasma cooling, the nonlinear Ohm's law looks like

$$j \simeq nec_s (MT_i/mT_e)^{1/2} (E^2/8\pi nT_e)^{1/4}. \tag{6}$$

Let us take into account that the ratio T_e/T_i is not so crucial parameter and to keep it in our estimates would be, generally speaking, above their accuracy. Thus, we can reduce (6) to the well–known Sagdeev formula:

$$\sigma \simeq (\omega_{pe}/4\pi)(nev_{Te}/j). \tag{7}$$

EMHD resistance. It is essential that even if anomalous resistivity joins the game, the whole resistance of the diode, in a broad range of parameters, remains the same. This is a feature of the electron magnetohydrodynamics (see details in [3]) that typical resistance of the plasma–filled diode does not depend upon the efficient collisional frequency:

$$R_{eff} \simeq j/nec^2 = 30\,\frac{j}{nec}\ \text{Ohm}\ . \tag{8}$$

This estimate is true with the accuracy of some dimensionless geometrical factor. It turns to be universal unless the conditions (1)–(3) break. Let us take the generalized Ohm's law in form

$$ne\mathbf{E} = ne\frac{\mathbf{j}}{\sigma} + \frac{1}{c}[\mathbf{j}, \mathbf{B}]$$

and then its tangent projection onto the plasma–anode boundary,
$E_{\|(\text{plasma})} = E_{\|(\text{electrode})} = 0 \Longrightarrow -j_\|/\sigma + j_\perp B/nec = 0.$

This reduced equation leads to the very simple and obvious result:

$$\theta = \frac{j_\|}{j_\perp} \sim \frac{nec}{\sigma B} = (\omega_{Be}\tau_{ei})^{-1} \ll 1, \tag{9}$$

since the Hall parameter obeys $(\omega_{Be}\tau_{ei})^{-1} \gg 1$ in all the media that satisfy the EMHD description (hence in metals as well). The less is the resistivity, the less is the angle of the current flow line crossing the electrode surface. In a result, the whole resistance of the diode turns out to be universal. In other terms, EMHD resistance may be presented as universal value of the voltage drop on the Hall plasma–filled diode [3,4]: $U_H \simeq B^2/8\pi ne$.

This situation reminds for example of an ordinary shock wave, completely conditioned by the dissipation (look, e.g., at the Hugoniot adiabate) but whose basic parameters do not depend on the dissipation rate. However, the structure of the shock front does, and our case is similar. To wit, only providing the proper geometrical relations we could thereby provide the universal result (8). If it breaks, the non-universal anomalous resistivity joins the game.

Broken scaling. Perhaps, one of the most important and obvious results of EMHD is that concerning a non–diffusive penetration of the magnetic field into the depth of a conducting medium . Within the frames of the simple model (2-d geometry, permanent conductivity σ, non-zero component of the density gradient along the boundary) one can obtain (see, e.g., [3,4]):

$$B(z,t) = B_0\{1 - tanh[(z - ut)/\Delta]\} \tag{10}$$

where $u = (cB_0/8\pi e)|\partial n^{-1}/\partial x|$ and $\Delta = (4ec/\sigma B_0)|\partial n^{-1}/\partial x|^{-1}$. Another possibility is the magnetic field locked near the boundary (despite the problem is time–depended), nevertheless, the typical space scale, that is the depth of the current layer, remains the same, i.e., Δ. After all, if the magnetic field (current) has already been penetrated into the diode gap in the conduction phase of the POS operation, the stationary space scale of the current distribution turns out to be equal to Δ again. Just this universal estimate provides the universal resistance (8) of any plasma–filled diode in the EMHD regime. On the other hand, just this scale seems to be crucial in the problem of validity of (8). Indeed, if the typical space scale of the diode gap $a \leq \Delta$, we hardly can expect that (8) is true. [Importance of the inter–gap geometry of the plasma filling is not less obvious from (9)].

If, however, we substitute convential Coulomb resistivity in Δ and also use the typical parameters of POS plasmas, condition $a \geq \Delta$ remains always true. It can be violated only by using anomalous conductivity (9) instead of classical one. Starting from the basic EMHD equations [3,4] one can obtain the following 1–d equation which describes the field penetration into the plasma depth:

$$\partial_t B + \kappa B \partial_z B = (c^2/4\pi)\partial_z(\sigma^{-1}\partial_z B),$$

where $\kappa = \partial_x(c/4\pi ne) \simeq c/4\pi ane$ with $a \equiv n/|\nabla n|$. If $\sigma =$ const, this is simply Burgers' equation, but if we use Sagdeev formula (9) as a model, it results in

$$\partial_t B + \kappa B \partial_z B = -\lambda \partial_z (\partial_z B)^2, \tag{11}$$

where $\lambda = mc^3/(4\pi)^{3/2} ne^2 (nT)^{1/2}$. We have obtained solutions of (11) as steady as similar to (10) with and without taking into account the plasma heating etc. There is no use, however, to take the space scale Δ from these solutions, it is quite enough to present (11) in the dimensionless form which results in the following space scale: $\Delta = (\lambda/\kappa)^{1/2}$.

Let us take L to be the typical space scale of the diode. If $L < \Delta$ or, what is the same;

$$L^2 < \frac{mc^2 a}{e(4\pi nT)^{1/2}} \quad \text{or} \quad L^2 < \frac{mc^2}{T} r_{De} a, \tag{12}$$

not the universal scaling (8) but much more complicated resulting from the turbulent scenario becomes true. Meanwhile, nowadays (8) turns out to be in rather good agreement with the experimental data, hence, experimental scalings known up-to-date, could break as well if the dimensions of a diode are not large enough. Thus, in all the scaling predictions for the next generation machines using POS'es, we have to pay especial attention to the conditions relative to (12).

[1] Mason,R.J., Auer,P., Sudan,R.N., et al. : Proc. 8-th IEEE Pulsed Power Conf., San Diego, Calif., Cat. No 91 Ch 3052-8, (1991), 529

[2] Mason,R.J., Auer,P., Sudan,R.N. : LA-UR-92-1409, LASL, (1992); Phys Fluids B, (1993)

[3] Kingsep,A.S., Chukbar,K.V., Yan'kov,V.V. : Reviews of Plasma Phys., B.B.Kadomtsev, Ed., Consultants Bureau, NY, **16**, (1990)

[4] Gordeev,A.V., Kingsep,A.S., Rudakov,L.I. : Phys.Reports, **243**, (1994), 215

[5] Kalda,J.L., Kingsep,A.S. : Sov.Journ.Plasma Phys. **15**, (1989), 981

[6] Kalda,J.L., Kingsep,A.S., Sevastianov,A.A. : Proc.of 17-th EPS Conf.on Contr. Fusion and Plasma Physics, J27, Amsterdam, **14B**,part IV, (1990), 1820

[7] Kingsep, A.S. : Sov.Journ.Plasma Phys., **17**, (1991), 582

[8] Kulsrud,R.M., Ottinger,P.F., Grossmann,J.M. : Phys. Fluids, **31(6)**, (1988)

[9] Sudan,R.N., Similon,P.L. : BEAMS'88, Karlsruhe, Conf. Proc., (1988), 416

[10] Sasorov,P.V. : Fizika Plazmy (Plasma Phys. Reports), **18**, (1992), 275

[11] Galeev,A.A., Sagdeev,R.Z. : Reviews of Plasma Physics, M.A.Leontovich, Ed., Consultants Bureau, NY, **7**, (1979)

ENERGETIC ION EMISSION IN A POSITIVE POLARITY NANOSECOND PLASMA OPENING SWITCH

M.Sarfaty*, Ya.E.Krasik, A.Weingarten, A.Fruchtman, and Y.Maron

Department of Physics, Weizmann Institute of Science, Rehovot 76100, Israel

Abstract

We studied the emission of energetic ions from the plasma in a coaxial Plasma Opening Switch (POS) powered by a 300 kV, 15 kA, 90 ns positive polarity pulse. Fluxes lasting 2 - 3 ns of ions flowing radially onto the cathode were seen to occur at all axial locations of the switch plasma within 5 ns of the beginning of the upstream POS current. It is suggested the termination of this ion flux results from the formation of a cathode plasma that is consistent with our spectroscopic measurements. Later in the pulse, longer duration (100 ns) ion fluxes were observed radially, first appearing in the generator side of the switch plasma. Fluxes, 30 - 40 ns long of ions flowing axially towards the POS load at velocities $(2\pm1)\times10^8$cm/s were also seen. The dependence of the start time of the axial ion flow, of the ion velocities, and of the ion flux on the POS operation parameters were studied.

I. Introduction

Experimental studies of coaxial POS operated with a negative polarity for the central electrode showed a large increase of the ion current density at the cathode both in the nanosecond[1] and microsecond[2] regimes. The total ion current flow in the radial direction toward the cathode was measured to be ~(10-20)% and ~ 30% of the total POS current in the nanosecond and in the microsecond time scales, respectively. This residual ion current limits the rise in the POS resistance. Therefore, the investigation of the ion dynamics, especially of energetic ions, is extremely important for the improvement of the POS performance.

II. The Experimental Setup

The POS experimental setup is shown in Fig. 1. The plasma was injected radially outward through a 75% transparent anode by a gaseous (CH_4) plasma gun[3]. An LC-water-line generator with a positive polarity output pulse was used to deliver a 90-ns quarter period pulse with a peak current of (135±10) kA. An upstream vacuum inductance, 120 nH, was made by two aluminum tubes with outer and inner diameters 10 cm and 5 cm, respectively. A short-circuit coaxial inductance, 25 nH, served as the POS load. The POS upstream and downstream currents were measured by two Rogovskii coils.

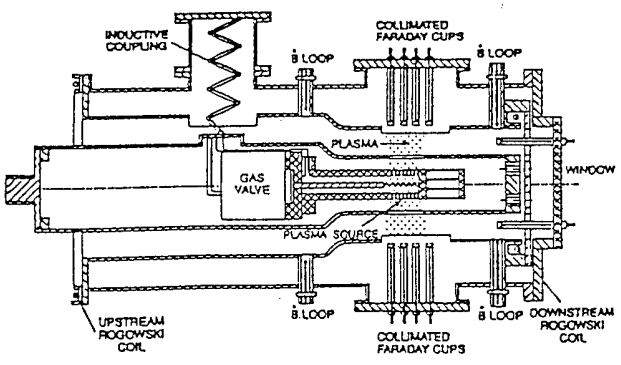

Fig. 1. The POS experimental setup

---

*University of Wisconsin, Madison, USA

The plasma electron density prior to the generator pulse was determined to be $(1.3\pm 0.5)10^{14}cm^{-3}$ at 0.5 cm from the anode surface from Stark broadening of H_α and H_β. The plasma average flow velocity, determined by Doppler shift of several ion species, was found to be $(1.5\pm0.5)10^6$cm/s. The electron density was found to be uniform in the azimuthal direction and over the 4-cm axial direction within 15%.

Varying the POS conduction times was achieved by changing the time delay, τ_d, between the discharge of plasma source and the generator. Typical waveforms of the upstream and downstream currents, and the POS current are shown in Fig. 2. The slow rise of the downstream current pulse was also observed in the previous studies[4] of a coaxial positive polarity POS.

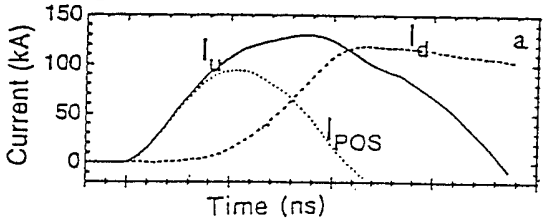

Fig. 2. Typical waveforms of the upstream (I_u), the downstream (I_d) and the POS (I_{POS}) currents.

The ion current density distribution in the radial direction at several axial positions along the POS axis was measured by two arrays of 4 Collimated Faraday Cups (CFC) with a transverse magnetic field. The CFC were placed in front of 1.4 cm wide slots in the cathode, at two opposite sides of the POS, and at axial distances of 1.7 cm from one another. The CFC could be radially translated to yield the ion radial velocities from Time of Flight (TOF) measurements. The current density and velocities of ions flowing in the axial towards the load were measured by four magnetically insulated CFC, azimuthally separated by 90°, and placed at the radial center of the POS interelectrode gap at various distances from the load side edge of the plasma.

III. Measurements and Data Analysis

3.1. Radial ion flow

The CFC signals in the two sides of the POS were similar to within the ±30% shot-to-shot irreproducibility. Based on these observations we assume in the estimates below azimuthally symmetric CFC signals over the entire plasma in the switch region. At distance of 1.5 cm from the cathode slots the signal exhibit two peaks, shown in Fig. 3. A short duration ion pulse, 2-3 ns long, appeared in almost all CFC within 5 ns from the beginning of the upstream current. The amplitude of these ion current spikes reached 40 A/cm^2. The decrease of the plasma density near the CFC by reducing the time delay τ_d, or by reducing the cathode slot width to 0.2 cm, resulted in the disappearance of the early ion spike, with less significant effect on the longer duration late ion signal.

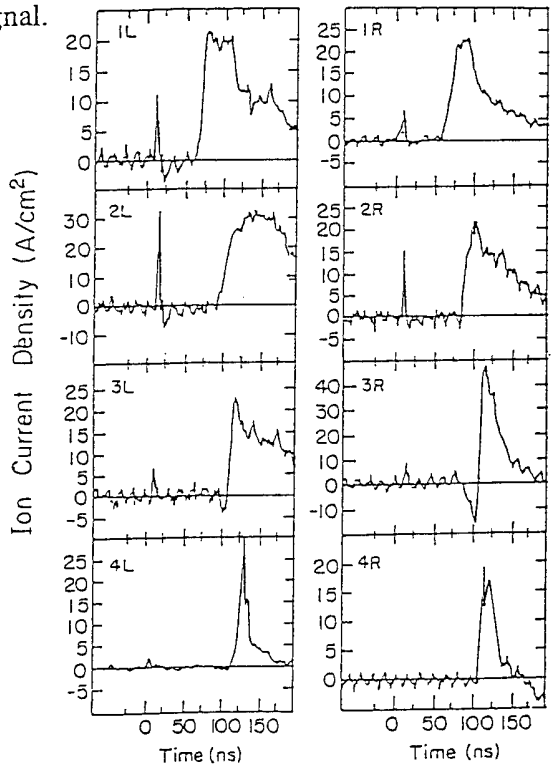

Fig. 3. The ion current density measured by two arrays of CFC at 4 axial locations and in both oppositive sides of the POS.

The start time of the longer-duration ion current was found to depend on the CFC axial position (see Fig. 4). This ion pulse began first

at the generator side and later at the load side of the plasma. The axial propagation velocity of the ion-ejection zone during pulse are found to be $(8\pm1.5)10^7$cm/s and $(9.5\pm 1.5)10^7$cm/s for the longer and shorter conduction times, respectively.

At 1.4 cm from the cathode slot the ion late signals has a relatively short time duration, while at larger distances the ion current was lower and lasted up to a few microseconds. The increase in the ion pulse

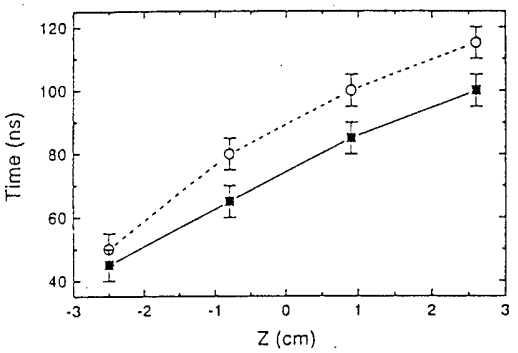

Fig. 4. The appearance time of the fastest ions, emitted in the radial direction for two operation regimes of the POS: 50 ns conduction time (solid) and 80 ns conduction time (dashed). The zero axial position correspond to the axial center of the POS plasma.

duration results from the differences in the ion velocities due to their different mass and charge. The radial velocity of the fastest ion component, averaged over 20 experiments for the same τ_d, was $(2.3\pm0.5)10^8$cm/s. Our spectroscopic investigations[3] of the plasma source showed that the plasma, formed from CH_4, consists of C and H atoms, protons, and CII-CIV ions. The fastest ion component is thus probably protons with energies (28±11) keV that is consistent with the POS voltage. The estimated total radial ion current rises in time to a maximum level of 5 kA, which is ≈ 5% of the current flowing through the POS.

3.2 Axial ion flow

In the upper half of Fig. 5 we present the current density of the ion flow propagated in the axial direction towards the shorts circuit end of the load. The reproducibility of the ion current density and the ion pulse duration was ±50% and ±30%, respectively. The flow of electrons co-moving with the ions was observed by the CFC without magnets and using a bias voltage of 100 V (see the lower half of Fig. 5). The ion axial velocity obtained from these TOF measurements was found to be similar in all axial locations, $(1.8\pm0.5)10^8$cm/s for the cases where the conduction times were ≤80 ns. The average peak density was (55 ± 20)A/cm^2, with a pulse FWHM of (30±10) ns. For longer conduction times, the ion axial velocity was found to be smaller, $(8\pm2)10^7$cm/s, and the signal duration increased with the axial distance. Based on the TOF data the time at which the ions left the load side of the plasma was found to be (60±15) ns when the POS conduction time was about 50 ns, which coincides with the rise of the downstream current.

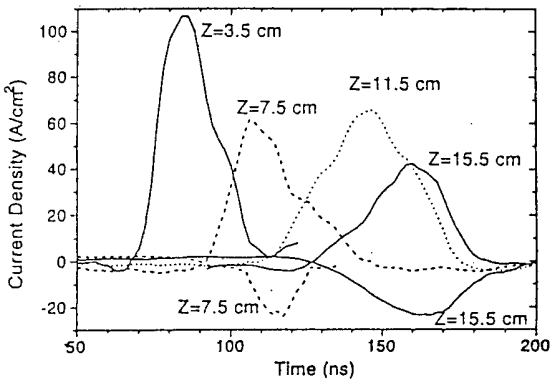

Fig. 5. Ion current density traces measured in a single discharge by 4 axially separated magnetically insulated CFC. The CFC are positioned between the plasma and the load.

IV. Discussion

Let us describe the process we believe is responsible for the short duration ion pulse collected at the CFC screen box. The same process is expected to occur near the cathode because it electrically is connected by plasma to the CFC screen boxes.

When a voltage is applied between the cathode and the anode, plasma electrons are drawn to the anode. As a result, electrons are

drained from the vicinity of the cathode, and rising voltage falls mainly on the electron-free gap near the cathode. The ions in this region are drawn by the electric field to the cathode, and within an ion plasma period a space charge limited flow is established. At a certain intensity of the electric field, explosive emission occurs at the cathode, which forms plasma that serves as a source of electrons. This results in a space-charge limited bipolar flow with a low voltage drop that is characterized by a negligible ion flow.

The ion charge per unit are collected by the cathode during first 5 ns of the pulse is $Q_i=\int j_i(t)dt\approx 0.6$ nC/cm^2. The electron density near the cathode surface is $n_e\approx 4\times10^{13}$ cm^{-3} and the radial size of the region free of electrons at this time is estimated by $d=Q_i/en_e \approx 100$ μm. This electric field is sufficient to cause explosive emission at the cathode surface.

The formation of an electrode plasma was shown by our spectroscopic observations[3]. These measurements showed line emission of surface adsorbents (Si, O, C, H) and of electrode material (Al) within 50 ns after the beginning of the upstream current at 0.1 cm from the cathode surface (see Fig. 6). The electrode plasma radial velocity was determined

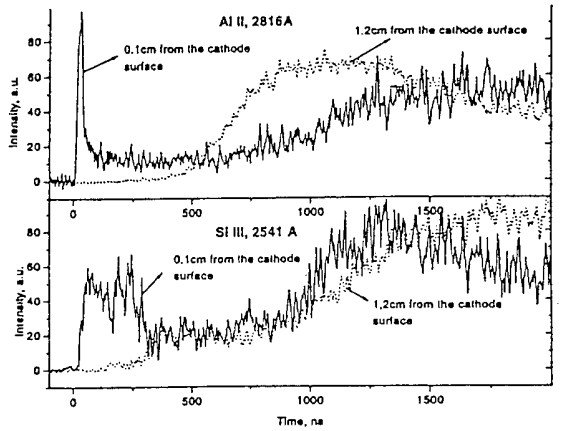

Fig. 6. Relative line intensities of AlII and SiIII ions at different radii from the cathode surface.

by the time interval between the appearance of the light at the different radii, $V_{pl}\approx(1.5\pm 0.5)10^6$cm/s. This suggests that this plasma was formed at the first few ns relative to the start of the upstream current.

The long duration ion current observed later in the pulse shows current densities that are higher that the plasma ion saturation current. Such long duration ion pulses were seen in nanosecond and microsecond POS experiments. Here, the long duration ion pulses were observed to be delayed with respect to the beginning of the upstream current. The delay time was found to depend on the axial position along the cathode with the axial propagation velocity being $\approx10^8$cm/s, which can be interpreted as the propagation velocity of the ion emitting sheath[5].

The energetic ion flow in the axial direction towards the short circuit load is explained on the basis of the magnetic field evolution in the plasma[3]. The measurements described there showed a fast magnetic field penetration into the plasma and a formation of a narrow current layer at the load edge of the plasma. Only then the ion axial velocities become substantial.

These observations showed Z/M scaling for the ion velocities that allows us to conclude that the proton velocity at the load side edge of the plasma are $(1.5\pm0.4)10^8$cm/s, at t=75 ns. The proton velocity, presently obtained, is in agreement with this value.

[1] B.Weber, R.J.Commisso, P.J.Goodrich, D.D.Hinshelwood, W.F.Oliphant, P.F.Ottinger, and F.C.Young, Conf.Proc. Beams-88, (1988) p.1131.

[2] G.A.Mesyats, A.N.Didenko, E.N.Abdullin, V.M.Bystritskii, A.A.Kim, B.M.Koval'chuk, V.A.Kokshenev, Ya.E.Krasik, and A.A.Sinebryukhov, Sov.Phys.Dokl., **31**(7), (1986) p.557.

[3] M.Sarfaty, Y.Maron, Ya.E.Krasik, A.Weingarten, R.Arad, R.Shpitalnik, A.Fruchtman, and S.Alexiou, Phys.Plasmas, **2**(6), (1995) p.2122.

[4] V.M.Bystritskii, A.N.Didenko, S.N.Volkov, I.B.Ivanov, Ya.E.Krasik, and A.V.Petrov, Sov.Plasma Phys.,**12** (1986), p.679.

[5] P.F.Ottinger, S.A. Goldstein, and R.A.Meger, J.Appl.Phys. **56** (1984), p.774.

PRELIMINARY STUDIES ON A PLASMA FOCUS OPENING SWITCH

C.S. Wong, P. Choi*, S.P. Moo and J. Singh

Plasma Research Laboratory, Physics Department, University of Malaya
50603 Kuala Lumpur, Malaysia

**Laboratoire de Physique des Milieux Ionisés, Ecole Polytechnique*
Palaiseau 91128, France

ABSTRACT

The small plasma focus device UNU/ICTP PFF has been modified to assess the operation of a plasma focus based long conduction (> 2 μs) opening switch, with a plasma filled diode as the load. The UNU/ICTP PFF is a Mather type plasma focus device powered by a single 15 kV, 30 μF capacitor delivering a peak current of 150 kA when discharged at 15 kV. The device has been optimised for reproducible focusing in various gases including deuterium, argon, carbon dioxide, helium as well as in air. In particular, the optimum operating pressure for air is between 0.5 to 1.1 mbar, whereas for argon it is between 0.3 to 3 mbar. For the operation of the UNU/ICTP PFF as an opening switch, the electrodes geometry is modified to redirect the plasma motion at the end of the axial rundown phase to avoid the normal plasma focus action, and the operating regime is shifted to low pressure to favour plasma opening switch action. With air as the working gas, pressure as low as 10^{-3} mbar has been tested. At such a low pressure, a set of twelve plasma injection cable guns is used to initiate breakdown of the discharge. The design and operating principle is presented and some preliminary results obtained on the operational characteristics of this device are discussed

Introduction

Inductive energy storage (IES) is a principle which promises the realization of compact, cost effective and efficient high voltage pulsed power system. In a typical system, energy initially stored in a capacitor bank is discharged through the circuit inductance into the opening switch, which is in the closed state and provides full conduction. After some time, when the current reaches maximum, the switch is to open from a low impedance to a high impedance state. Thus the current that was flowing in the circuit up to that point will be transferred to the load, which is connected across the switch. The key component is the opening switch element, the performance of which sets a limit to the power gain and voltage gain obtainable from an IES generator. The power gain is a measurement of the conduction time versus the opening time, while the voltage gain is limited by the physical resistance of the switch in the opened state. On the one hand, the switch is required to conduct for a relatively long time until current reaches maximum. On the other hand, the switch has to turn high impedance in as short a time as possible when it opens. An extensive discussion on the various opening switch technology for IES can be found in [1] and the physics of the different switches in [2]. For most high power applications, the plasma erosion opening switch is chosen as the switch element. The conduction time for such switches is at best below 1 μs. For longer conduction time, some form of plasma motion has to be considered during the conduction period and devices like plasma flow switch can be used.[3] The long conduction period, however, is associated with a slower opening. In this paper, we present an opening switch design based on a modified

plasma focus geometry. This plasma focus opening switch combines the action of the plasma flow switch during the several μs long conduction phase with an opening action analogous to the erosion switch in tens of ns. Preliminary measurements demonstrate the validity of the design.

Long Conduction Opening Switch

The plasma flow switch is primarily a coaxial plasma gun, not dissimilar from that of a plasma focus in the Mather geometry. The major difference of the plasma flow switch is in the use of a plasma discharge initiated in vacuum from exploding a set of wires or foils, rather than a uniform gas prefill as in a plasma focus. Otherwise, the operation is similar, with a long axial run down phase after discharge initiation. This is shown schematically in Fig.1, which highlights the three different stages of plasma evolution in a conventional plasma focus. At the end of the coaxial electrode, the main plasma bulk is expelled off the end of the electrode and compressed radially inward, toward the load region, convecting the stored magnetic energy. In this way, current is transferred to the coaxial load on axis, when the switch plasma stagnates onto the load and the switching time is primarily governed by the flow characteristics of the switch plasma.

In the modified plasma focus opening switch (MPFOS), the main current carrying plasma in the closed state of the switch is also carried by a low density plasma in a modified plasma focus geometry. The device is operated with a low pressure prefill. The initial plasma is created from gas breakdown along the insulator under the control of additional plasma injection from an array of small plasma guns. This plasma injection method allows a uniform current sheath to be formed along the insulator initially. This is followed by a long axial run down phase, when the current in the primary circuit is building up and the sheath is snow-ploughing forward. It is arranged that the current sheath shall reach the end of the coaxial electrode structure just before the current reaches maximum. At this point, the current sheath continues to move forward and outward at the same time as the central electrode geometry changes and the device is operating like an inverse pinch. The plasma continues to expand laterally while under the inverse pinch effect and this lowers the plasma density in the current layer. Switching occurs during this period and current is transferred to a load, which is connected to the end of the switch electrodes. These stages are illustrated in the schematic as shown in Fig.2.

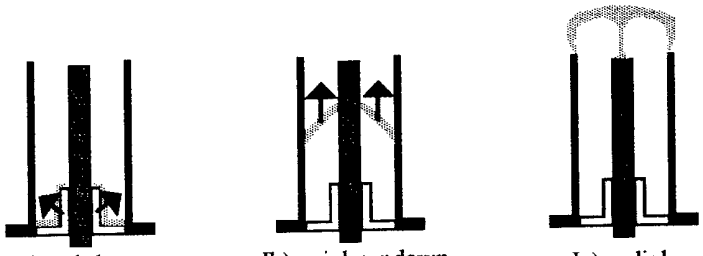

Fig.1 Schematic showing 3 stages of the evolution of a plasma focus

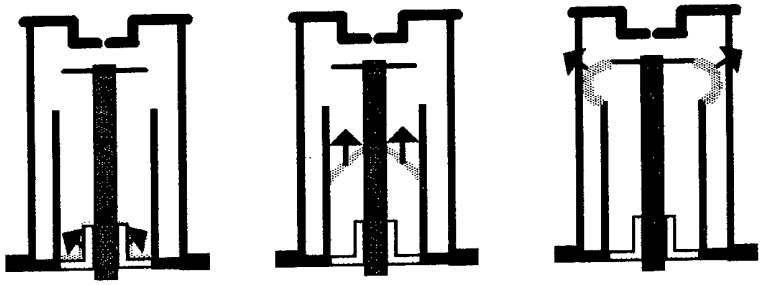

Fig.2 Schematic showing the 3 stages of evolution of a modified plasma focus opening switch

The dense plasma focus has been proposed as an opening switch utilizing the rapid change of impedance of the plasma during the final stage of the radial collapse phase.[4] The advantage of such opening switch design for repetitive operation was high-lighted. It should be pointed out that the scheme proposed here operates in totally different regimes compared with a plasma focus during the opening, while retaining the same advantage of a long conduction configuration under repetitive operation. In an MPFOS, the physics of the opening relies on the development of a high resistivity regime in a low density plasma with rapid magnetic field penetration during the inverse pinch phase, rather than the rapid pinching of a high density plasma as in a dense plasma focus.

Experimental Apparatus

An experiment has been carried out to assess the validity of the action of the modified plasma focus opening switch. A small plasma focus device, UNU/ICTP PFF, is modified to operate as a long conduction (> 2 μs) opening switch, with a plasma filled diode as the load. The UNU/ICTP PFF is a Mather type plasma focus device powered by a single 15 kV, 30 μF capacitor delivering a peak current of 150 kA when discharged at 15 kV.[4] As a plasma focus, the device has been optimized for reproducible focusing in various gases including deuterium, argon, carbon dioxide, helium as well as in air. In particular, the optimum operating pressure for air is between 0.5 to 1.1 mbar.

For the operation of the UNU/ICTP PFF as an opening switch, the electrodes geometry is modified to redirect the plasma motion to avoid the normal plasma focus action, and the operating regime is shifted to below 10^{-1} mbar to enhance plasma opening switch action. At such a low pressure, a set of twelve injection cable guns is used to initiate breakdown of the discharge. These guns are mounted near the back-wall of the focus tube and provide the initial ionization path for discharge formation. They are powered by the main capacitor discharge via standard 50 Ω cables. The length of the cables are such that the guns are initiated about 80 ns after voltage is established across the focus electrodes. For the present experiment, a diode structure is arranged to sit directly on top of the switch to act as the load. The diode is plasma filled by allowing a small portion of the switch plasma to pass from the switch section into the diode section through a series of apertures. A picture of the modified system is shown in Fig. 3.

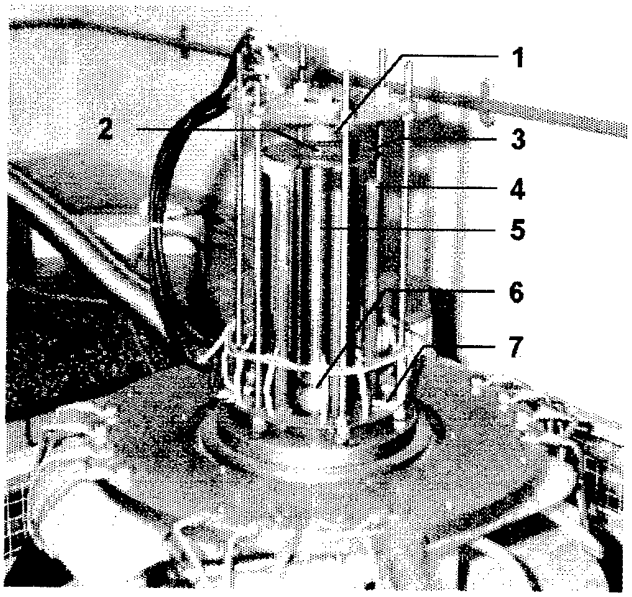

Fig.3 The modified plasma focus opening switch, showing 1) diode cathode, 2) diode anode, 3) expansion plate, 4) switch cathode, 5) switch anode, 6) breakdown insulator, and 7) plasma guns

Results

Preliminary results have been obtained from the modified plasma focus opening switch using

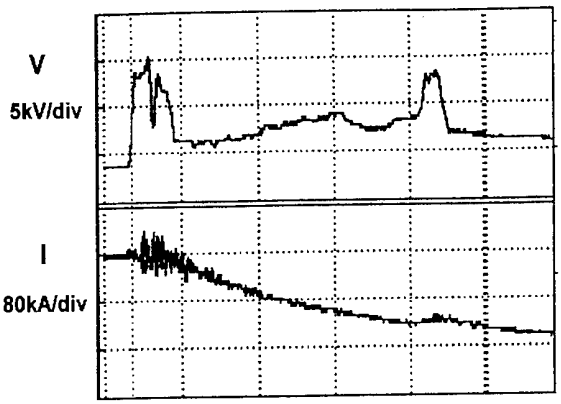

Fig.4 Voltage and current signal measured outside the chamber, showing the operation of the MPFOS; horizontal scale 500 ns/div.

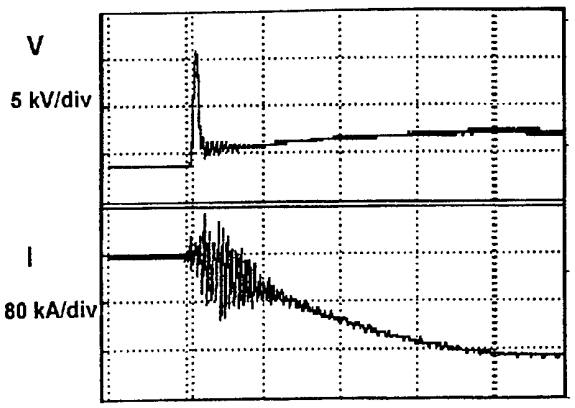

Fig.5 Voltage and current signal measured outside the chamber when opening action is not operative; horizontal scale 500 ns/div.

air as the low pressure fill gas. The opening action has been established for certain pressures. Fig. 4 shows the voltage and current signal obtained from a discharge with 0.01 mbar at 14 kV charging. The initial breakdown was under the control of the plasma guns, delayed from the start of the voltage by 80 ns. After a conduction period of 1.9 μs, the voltage is observed to rise sharply within a time < 50 ns and is maintained for over 100 ns. As this voltage was measured outside the chamber at the base of the electrodes, the exact value at the opening has not been obtained, though measurements from hard X-ray signal indicate a value higher than that shown by the voltage monitor. The opening action has been measured down to a pressure of below 0.002 mbar. In contrast, when the pressure is increased to 0.5 mbar, the voltage signal no longer shows an opening action, as shown in Fig. 5. At this pressure, the initial breakdown occurs before the action of the plasma guns. The rapid change of impedance as the plasma reaches the end of the axial run down is no longer observed.

Conclusion

The MFPOS design presented here is shown to exhibit several of the the necessary qualities of an ideal long conduction plasma opening switch The novel feature in the MFPOS is to couple the axial run down phase of the plasma focus with an inverse pinch phase where the proper plasma parameters for plasma opening switch action can be prepared. This overcomes some of the limitation imposed on other long conduction opening switches like the plasma flow switch or the plasma focus, while retaining the inherent long conduction feature. While the device is far from optimized and the data are necessarily preliminary, the switch is capable of conducting for over 2 μs and opening in 50 ns. Work is going on to quantify the current transfer efficiency and to qualify the proper regime of operation.

Acknowledgements

The collaboration has been supported partially by an ICTP Visiting Scholar Programme

Reference

[1] K.H. Schoenbach, M. Kristiansen and G. Schaefer, Proc. IEEE, 72(1984)p.1019

[2] Special issue on fast opening vacuum switches, IEEE Trans. Plasma Sci., Vol.6, 1987.

[3] P.J. Turchi et al., IEEE Trans. Plasma Sci., 6(1987)p.747.

[4] S. Lee et al, Am. J. Phys. 56, 62 (1988).

TWO DIMENSIONAL HALL MHD MODELING OF A PLASMA OPENING SWITCH WITH DENSITY INHOMOGENEITIES

O.Zabaidullin*, A.Chuvatin, and B.Etlicher

Laboratoire de Physique des Milieux Ionisés, Laboratoire du C.N.R.S., Ecole Polytechnique, 91128 Palaiseau, France

** Institute for Nuclear Fusion, Russian Scientific Center "I.V.Kurchatov Institute", 123182 Moscow, Russia*

Abstract

The results of two-dimensional numerical modeling of the Plasma Opening Switch in the MHD framework with Hall effect are presented. In the simulations we used enhanced Hall diffusion coefficient. Recent experiments justify application of this approach. The result of the modeling also correlates better with the experiment than in the case of classical diffusion coefficient. Numerically generated pictures propose a switching scenario in which the translation between conduction and opening phases can be explained by an abrupt "switching on" and further domination of the Hall effect at the end of the conduction phase.

Introduction

Engineering development of a new Inductive Energy Storage (IES) generator with the Plasma Opening Switch (POS) requires both reliable scalings for the conduction and opening times [1] and numerical modeling of the POS plasma behavior. For this purpose, we used a two-fluid MHD code [2] incorporating phenomena related to the Hall effect in plasmas [3]. Recent experimental results on GIT-8 IES show that at the moment of opening the POS plasma has an inhomogeneous density, presumably due to hydromagnetic plasma instability [4]. Previously it was shown that the combined influence of the Hall effect and micro inhomogeneities leads to the enhanced magnetic field diffusion coefficient [5]. In our simulations we used both classical and Hall diffusion coefficients.

Basic equations

The system of the MHD equations with Hall affect is solved in 2D cylindrical geometry (r, z) and contains the following equations:

a) equation of the plasma density conservation

$$\frac{\partial n}{\partial t} + \mathrm{div}(n\mathbf{V}) = 0 \qquad (1)$$

b) and c) are the equations for the plasma velocity components, $\mathbf{V} = (V_r, V_z)$

$$\frac{\partial n m_i V_r}{\partial t} = -\frac{B_\varphi}{4\pi}\frac{\partial r B_\varphi}{r\partial r} - \frac{\partial r n m_i V_r^2}{r\partial r} - \frac{\partial n m_i V_r V_z}{\partial z} - 2\frac{\partial nT}{\partial r} \qquad (2)$$

$$\frac{\partial n m_i V_z}{\partial t} = -\frac{1}{8\pi}\frac{\partial B_\varphi^2}{\partial z} - \frac{\partial r n m_i V_z^2}{\partial z} - \frac{\partial r n m_i V_r V_z}{r\partial r} - 2\frac{\partial nT}{\partial z} \qquad (3)$$

d) equation for the plasma temperature, T

$$3\frac{\partial nT}{\partial t} = -3\mathrm{div}(nT\mathbf{V}) - 2nT\mathrm{div}(\mathbf{V}) \qquad (4)$$

e) equation of the magnetic field, B_φ, dynamics

$$\frac{\partial B_\varphi}{\partial t} = \nabla\times(\mathbf{V}\times\mathbf{B}) - \nabla\times(D(\mathbf{V}\times\mathbf{B})) - \nabla\times(\frac{\mathbf{B}}{4\pi en}\times(\nabla\times\mathbf{B})) \qquad (5)$$

where D is the coefficient of magnetic field diffusion.

g) Maxwell equation for the current density, **j**:

$$\mathbf{j} = \frac{c}{4\pi}(\nabla \times \mathbf{B}) \tag{6}$$

h) equation of the external electrical circuit:

$$U_0 = \frac{1}{C_g}\int_0^t I_g dt + L_g\frac{dI_g}{dt} + \frac{1}{c}\frac{\partial}{\partial t}\iint B_\varphi dS + \frac{1}{I_g}\iiint\frac{j^2}{\sigma}dV \tag{7}$$

In Eqn. (7) C_g is the capacity of the primary energy store, U_0 is the initial voltage of the generator battery, L_g is the storage inductance, I_g is the generator current and S is the cross-section of the POS discharge chamber. Therefore, the circuit represents a classical POS scheme [6] with an inductive load.

The system of equations (1-7) can be solved for two cases: 1) with the classical coefficient of the magnetic field diffusion, $D_\sigma = c^2/(4\pi\sigma)$, σ is the Spitzer conductivity. 2) with the Hall diffusion coefficient in the form, $D_{Hall} = cB/(32\pi en)$ [5]. In the second case the Hall effect manifests itself twice in the equation (5): in the Hall term (the third term), and in the diffusional term (the second term). Both these terms serve to describe the influence of the plasma density perturbation on the enhanced magnetic field diffusion. Finally, in comparison with the previous 2D POS simulations (see i.g. the review [3] and references therein) the present one is coupled with the external circuit and includes plasma density inhomogeneities.

Boundary conditions

The system (1-7) is solved in the region between two coaxial cylinders: the outer anode of the radius R_a and the inner cathode of the radius R_c ($R_c \le r \le R_a$) (Fig. 1a). The discharge chamber is limited by a dielectric-vacuum interface at $z = 0$ and by the short-circuit load at $z = Z_0$, i.e. $0 \le z \le Z_0$. The boundary conditions for equations (2) and (3) represent the fact that the plasma is confined by the vacuum chamber walls

$$V_r\,(r = R_c,\ r = R_a) = V_z\,(z = 0,\ z = Z_0) = 0$$

As the electrodes are considered to be superconductive, the boundary conditions for equation (5) can be written as follows

$$E_z = \frac{c}{4\pi en}((\nabla \times \mathbf{B}) \times \mathbf{B}) - \frac{c}{4\pi\sigma}(\nabla \times \mathbf{B}) = 0$$

At the vacuum interface surface the value of the magnetic field can be found from the solution $I_g(t)$ of the equation (7)

$$B_\varphi(r, 0, t) = \frac{2I_g(t)}{cr}$$

Initial conditions

For the initial conditions we took the following test parameters: $Ig = 0$, $V_0 = 3\times10^4$ V, $C_g = 4.6$ μF, $R_a = 15$ cm, $R_c = 10$ cm, $Z_0 = 45$ cm and $L_g = 80$ nH. The distribution of the plasma density n(r, z), at the initial moment of time, is shown in Fig. 1a. The mean plasma density changes from 10^{16} cm^{-3} at the anode to 10^{15} cm^{-3} at the cathode. Initial plasma density profile has a conical shape with the angle $\varphi \approx 45^0$ and satisfies in the overall anode-cathode gap the condition of high-density plasma switch [1], $L_p > c/\omega_{pi}$, where L_p is the axial plasma length.

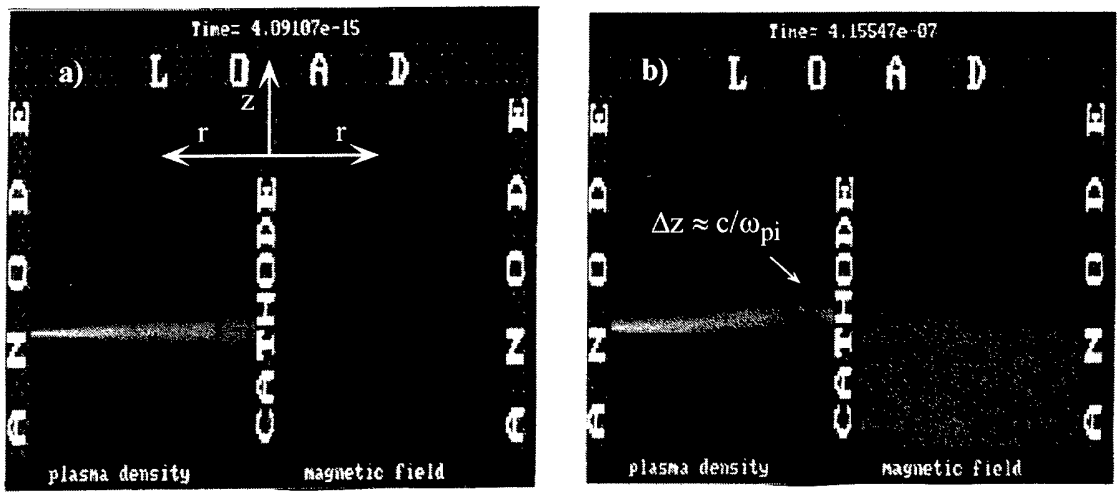

Fig. 1. Conduction phase and beginning of the opening phase.

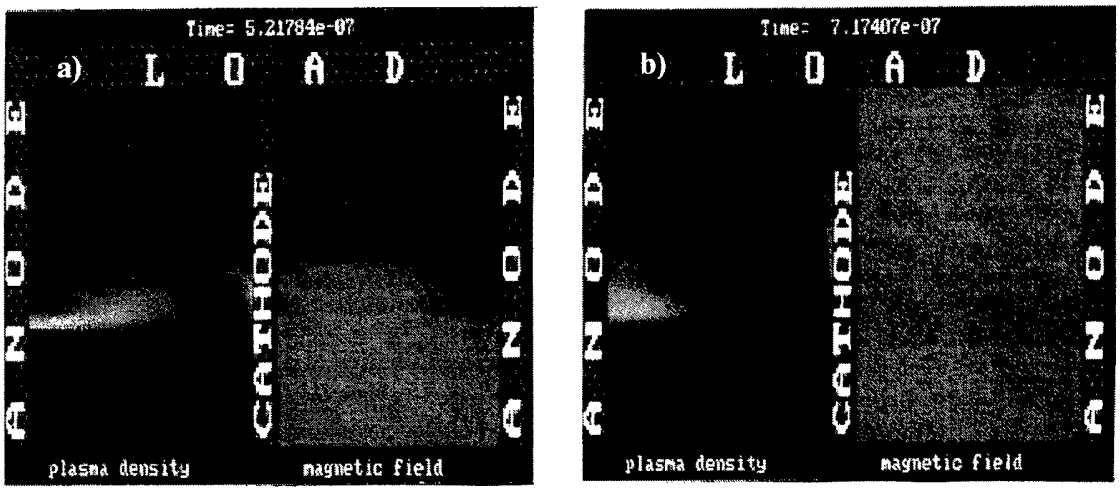

Fig. 2. Opening phase and beginning of the final phase.

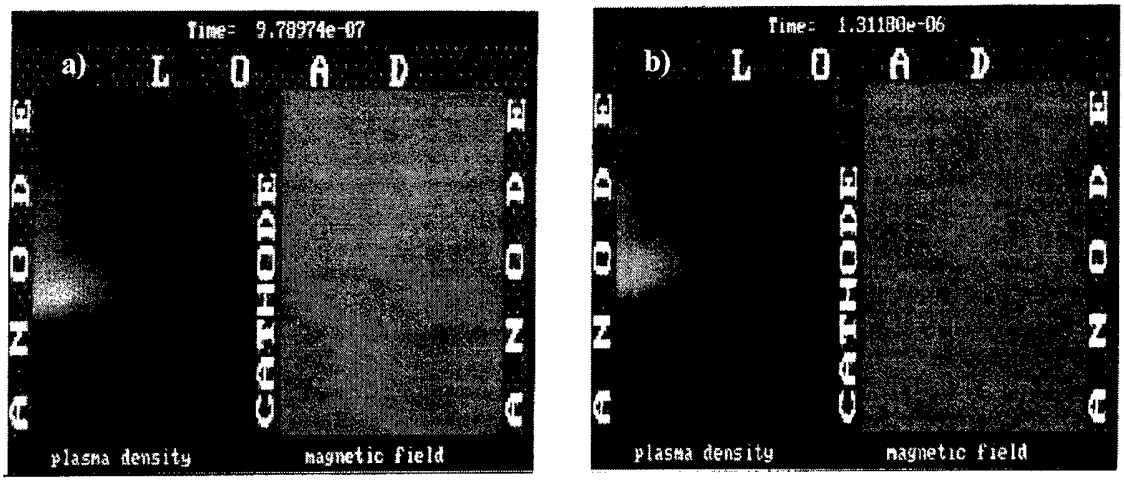

Fig. 3. The final phase.

Distribution of the initial plasma temperature is reconstructed as

$$T(r, z, 0) = T_0 \times \left(\frac{n(r, z, 0)}{n_c}\right)^{2/3}$$

where $T_0 = 3$ eV is the characteristic temperature of the plasma near the cathode. For the sake of simplicity, dynamics of the POS is studied for a plasma containing mostly H^+ ions.

Results of the POS modeling

Distribution of the plasma density and of the magnetic field at the initial moment of time are shown in Fig. 1a. The brightness scale (from black to white) corresponds to the increase of value by a factor of 1.2. The time history of $n(r, z)$ and $B_\varphi(r, z)$ is given by Fig. 1-3 for six moments of time. This result corresponds to the modeling with enhanced diffusion coefficient, D_{Hall}. One can clearly distinguish three phases in this figure: conduction phase, opening phase, and appearance of the so-called "crowbar" phenomenon.

During the conduction phase (Fig. 1) the magnetic field rises inside the interface-plasma volume. Axial plasma translation due to the plasma pushing by the magnetic pressure leads to gradual thinning of the leading plasma edge. This dynamics can be interpreted as a formation of the so-called Hall shock-wave described in [1]. In our simulations, due to rather sharp density gradient chosen initially, the maximum plasma density perturbation starts from the near-cathode region. The simulation confirms that the conduction phase is terminated when the axial thickness of the plasma leading edge, Δz, becomes smaller than the value c/ω_{pi}, where ω_{pi} is the ion plasma frequency. Therefore, transition to the opening is determined simply by the condition $\Delta z < c/\omega_{pi}$ [1]. During the opening phase (Fig. 2) the magnetic field propagates rapidly through the plasma neck Δz and fills in the load volume during the time $t_s \sim 150$ ns (typical opening time value for a μs POS). This propagation is governed by the Hall terms in Eqn. (5) which now dominate. Therefore, the plasma neck can be further described in the framework of Electron Magnetohydrodynamics (EMH) [3]. The final phase (Fig. 3) is characterized by the enhanced diffusion of the magnetic field throughout the plasma bulk (see Fig. 2b). The gap of rarefied plasma recloses under its own thermal pressure that manifests itself as a "crowbar" of the load current. Analogous simulations but with classical diffusion coefficient D_σ showed the gap of rarefied plasma density maintained by the magnetic pressure. Therefore, the rapid switch reclosure observed in many experiments [6] is a specific feature of the D_{Hall} modeling.

Conclusion

Finally, in our simulations the combined influence of the Hall effect and plasma density inhomogeneities on the magnetic field dynamics provide good agreement with typical experimental results and qualitatively explain the switch reclosure. The transition from the conduction phase to the opening phase can be interpreted as a transition towards the so-called Hall plasma in which the Hall effect and magnetic field convection dominate. This MHD-EMH transition occurs due to the thinning of the plasma channel during its motion and seems to be a common feature for all high-density plasma switches with the initial plasma length $L_p > c/\omega_{pi}$.

This work is partially supported by DRET under the contract #92.134 and by ETCA/CEG under the contract #420/115/01.

[1] this conference, paper P-4-63.
[2] V.Vikhrev, O.Zabaidullin, and A.Terentiev, *Plasma Phys. Reports* **21**, 20 (1995).
[3] A.Gordeev, A.Kingsep, and L.Rudakov, *Physics Reports* **243**, 215 (1994).
[4] this conference, paper P-4-64.
[5] O.Zabaidullin and V.Vikhrev, *Proceedings of the 22th EPS conference on Controlled Fusion*, Bournemouth, UK, 1995, Part III, p. 197.
[6] *IEEE Trans. Plasma Sci.* (special issue) **PS-15**, No. 6 (1987).

THEORETICAL MODEL OF THE SOS EFFECT

S.A.Darznek, G.A.Mesyats, S.N.Rukin, S.N.Tsiranov

Institute of Electrophysics
Russian Academy of Sciences, Ural Division
34, Komsomolskaya Str., Ekaterinburg, 620219, Russia

Abstract

This paper describes physical principles underlying operation of semiconductor opening switches (SOS). The SOS effect occurs at a current density of up to 60 kA/cm^2 in silicon p^+-p-n-n^+ structures filled with residual electron-hole plasma [1]. Using a theoretical model developed for plasma dynamic calculations, the mechanism by which current passes through the structure at the stage of high conduction and the processes that take place at the stage of current interruption were analyzed. The dynamics of the processes taking place in the structure was calculated with allowance for both diffusive and drift mechanisms of carrier transport. In addition, two recombination types, viz., recombination via impurities and impact Auger recombination, were at the basis of the model. The effect of the structure on the pumping-circuit current and voltage was also taken into account. The real distribution of the doped impurity in the structure and the avalanche mechanism of carriers multiplication were considered. The results of calculations of a typical SOS are presented. The dynamics of the electron-hole plasma is analyzed. It is shown that the SOS effect represents a qualitatively new mechanism of current interruption in semiconductor structures.

Theoretical Model

The equation of a quasineutral plasma for an inhomogeneously doped semiconductor is at the root of the theoretical model describing the dynamics of the electron-hole plasma in a semiconductor p^+-p-n-n^+ structure (Fig. 1). For the holes in the n-region of the structure the equation is of the form

$$\dot{p} = D_a(p,N,E)\cdot p'' - V_a(p,N,E)\cdot p' + Q_p(p,N,E)\cdot p + G(p,n,E), \qquad (1)$$

where p and n stand for the concentration of holes and electrons respectively,

$$D_a = \frac{n\cdot V_n'\cdot D_p + p\cdot V_p'\cdot D_n}{n\cdot V_n' + p\cdot V_p'} \qquad (2)$$

is the ambipolar diffusion coefficient,

$$V_a = \frac{n\cdot V_n'\cdot V_p - p\cdot V_p'\cdot V_n}{n\cdot V_n' + p\cdot V_p'} \qquad (3)$$

the ambipolar drift velocity, and

$$Q_p = \frac{V_p'\cdot (D_n\cdot N'' + V_n\cdot N')}{n\cdot V_n' + p\cdot V_p'} \qquad (4)$$

the parameter, which has dimensions of the frequency and allows for the effect of doping inhomogeneity on the plasma movement (D_n and D_p being diffusion coefficients of electrons and holes; $V_n(E)$ and $V_p(E)$ the carrier drift velocities allowing for saturation in a strong electric field E [2]; $N(x)$ the difference between the concentration of donors $N_D(x)$ and acceptors $N_A(x)$; x the coordinate along the structure axis.

In the p-region to the left of the p-n junction the minor carriers are electrons, for which an equation similar to (1) can be derived:

$$\dot{n} = D_a(n, N, E) \cdot n'' - V_a(n, N, E) \cdot n' + Q_n(n, N, E) \cdot n + G(p, n, E), \tag{5}$$

where D_a and V_a are ambipolar coefficients (2) and (3) in eqn (1), while

$$Q_n = \frac{V_n' \cdot (-D_p \cdot N'' + V_p \cdot N')}{n \cdot V_n' + p \cdot V_p'} \tag{6}$$

and has the same meaning as Q_p in the equation for holes.

The carrier generation rate $G(p,n,E)$ allows for the following elementary processes: the Shockley-Read-Hall recombination via deep impurities [3]; the Auger recombination [4]; ionization processes in a strong field [5] taking into account the effect of free carriers on the ionization coefficient [6].

The approximation of the ohmic contact at the structure boundaries was used as the boundary conditions for eqns (1) and (2). The electric field was determined using the continuity equation for the current density allowing for the displacement current. To take proper account of the mutual effect of the pumping circuit and the SOS, the set of equations (1) — (2) was solved simultaneously with Kirchhoff's set of equations.

Plasma Dynamics under the SOS-Effect Regime and the Current Interruption Mechanism

Below we present results of calculations of a typical SOS, which comprises 196 series-connected p^+-p-n-n^+ structures with the cross-sectional area of 0.24 cm^2, connected in a two-loop pumping circuit [1] having the following parameters under the short-citcuit regime: charging voltage = 100 kV; forward pumping time = 490 ns; forward-pumping current amplitude = 0.47 kA; reverse pumping time = 125 ns; reverse-pumping current amplitude = 1.8 kA.

The general time dependence of the current flowing through the SOS and the voltage across the SOS is shown in Fig. 2. During forward pumping, when the p-n junction is conducting forward, the electric field makes the holes drift from the p-region to the base of the diode and then to the high-doped n^+-region, while the electrons move in the opposite direction from the n-region and gradually occupy the p-region of the structure. Consequently, two plasma waves propagate in opposite directions from the p-n junction. Given equal conditions, the speed of the electrons is an order of magnitude higher than that of the holes and the electron wave reaches the outer boundary of the structure in ~300 ns, while the holes do not manage to pass the n^+-region of the diode (see Fig. 3).

During forward pumping the basic contribution to the total resistance of the diode is due to the base region of the p^+-p-n-n^+ structure, because the concentration of charge carriers is at a minimum there. At the initial stage of pumping the density of current flowing in the diode grows faster than the base resistance drops. As a result, a positive voltage peak arises at the switch (see Fig. 2) and a region of a strong electric field is formed in the base. After the diode resistance becomes lower than the impedance of the circuit and the load resistance and up to

the moment of current interruption the SOS operates as a current generator. Note that after the base is occupied with carriers, the plasma moves counter to the electric field in the base.

At the end of forward pumping most of the plasma is concentrated in high-doped regions of the diode (Fig. 3). As soon as the flow of current through the switch is reversed, plasma starts returning to the p-n junction plane. Note that the major part of the plasma moves slower than the plasma front. As a result, the plasma profile fronts become sharper first in the p-region and then in the n-region of the structure. After sharp fronts are formed in the spatial distribution of the plasma the regions of the p^+-p-n-n^+ structure behind the fronts turn out to be almost free of injected charge carriers. In these regions current is transferred solely by major carriers whose concentration is minimum on the outer side of the plasma fronts and the particles move at the saturation speed of ~100 μm/ns.

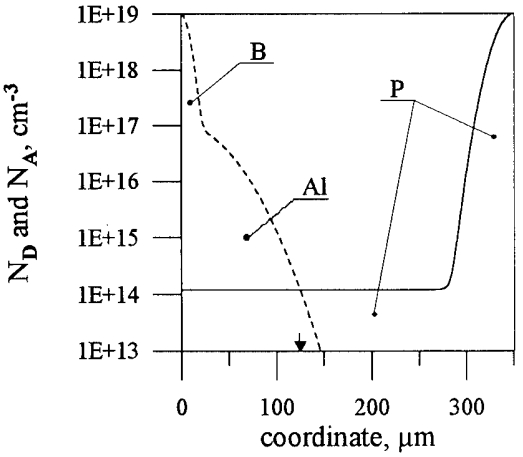

Fig.1. The doping profile of a typical semiconductor p^+-p-n-n^+ structure. Solid line — distribution of donors; dashed line — distribution of acceptors. The vertical errror indicates position of the p-n junction.

When the plasma front comes to the region where major carriers cannot transfer current through the switch, a strong field arises near the plasma front (Fig. 4), leading to an intensive impact ionization of the semiconductor. This encourages formation of additional free carriers, which transfer current through the structure. At the given stage a high-resistance region appears in the high-doped region of the diode. As a result, current is interrupted in and voltage grows across the switch. Note that the beginning of the current interruption is in no way connected with the principle according to which the charge introduced in the structure during forward pumping must be equal to the charge removed from the structure during reverse pumping. This is of principal importance for, e.g., drift step-recovery diodes (DSRD) [7].

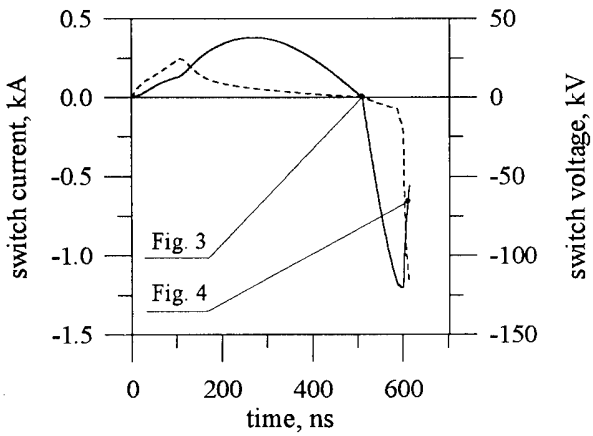

Fig.2. Time dependence of the current in the interrupter (solid line) and the voltage across the interrupter (dashed line).

At the stage of current interruption a characteristic region of a strong electric field with clearly defined boundaries appears in the p^+-p-n-n^+ structure (Fig. 4). The left-hand boundary of the distribution $E(x)$ changes its position little if at all, while the right-hand boundary moves towards the p-n junction. The increase in the size of the field is the physical reason for the growth of voltage across the switch. The volume charge comparable in value with the concentration of major carriers is formed only in narrow regions with high gradients of $E(x)$.

Conclusion

The analysis of the dynamics of the electron-hole plasma in a semiconductor structure, which was performed at current densities and pumping pulse time characteristic of the SOS effect, suggests the following:

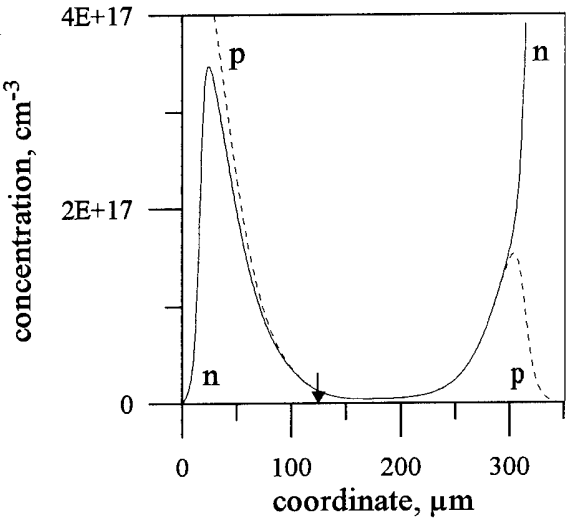

Fig.3. Distribution of electron (solid line) and hole (dashed line) concentrations at t = 509 ns.

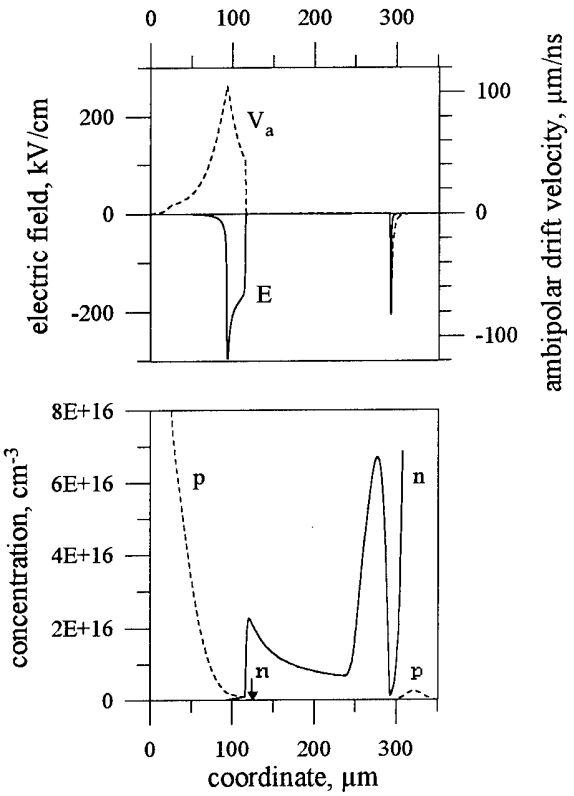

Fig.4. Distribution of electron (solid line) and hole (dashed line) concentrations, the electric field profile (solid line) and the ambipolar velocity of plasma movement (dashed line) at t = 611 ns.

1. Removal of all residual plasma from the structure is not a mandatory condition for sharp interruption of reverse current. By the beginning of current interruption the central portion of the base still contains an electron-hole plasma whose concentration is nearly two orders of magnitude higher than the level of the base doping (see Fig. 4). The beginning of current interruption is independent of the principle of the equality of the charge introduced in the structure during forward pumping and that removed from the structure during reverse pumping.

2. Current interruption depends on the processes taking place in narrow high-doped regions of the p^+-p-n-n^+ structure. It has a dynamic character and can be independent of the formation of a spatially expansive volume charge owing to an intensive avalanche multiplication of carriers in a strong electric field.

So, the SOS effect differs qualitatively from other principles of current switching in semiconductor devices: the process of current interruption develops not in the base of the structure but in narrow sections located in high-doped regions. The base of the structure remains to be filled with a dense residual plasma. It is this factor that allows combining a high density of the interrupted current and nanosecond cut-off time.

References

[1] Rukin S.N., Kotov Yu.A., Mesyats G.A. et al. Proc. 10th Int. Conf. on High Power Particle Beams, San Diego, CA, USA. 1994. Vol. 1. P. 33 — 36.

[2] Landolt-Börnstein. Numerical Data and Functional Relationships in Science and Technology. Vol. 17, Subvolume a. Physics of Group IV Elements and III-V Compounds. Berlin, Springer-Verlag, 1982.

[3] Bonch-Bruyevich V.L., Kalashnikov S.G. Physics of Semiconductors. M.: Nauka, 1990. (in Russian).

[4] Tugov N.M., Glebov B.A., Charykov N.A. Semiconductor Devices. M.: Energoatomizdat, 1990 (in Russian).

[5] Grekhov I.V., Serezhkin Yu.N. Avalanche Breakdown of the p-n Junction in Semiconductors. L.: Energiya, 1980 (in Russian).

[6] Ghosh R., Roy S.K. Effect of Electron-Electron Interactions on the Ionization Rate of Charge Carriers in Semiconductors. Solid State Electr., 1975, v.18, p. 945.

[7] Tuchkevich V.M., Grekhov I.V. New Principles of Switching High Powers by Semiconductor Devices. L.: Nauka, 1988 (in Russian).

INHOMOGENEOUS MIXING EFFECT OF D AND T FUELS ON ICF PELLET IMPLOSION

S. Kawata, K.Kurawaki, A.Tuyuki and K.Hirota

Department of Electrical Engineering, Nagaoka University of Technology, Nagaoka 940-21, Japan
e-mail: kawata@voscc.nagaokaut.ac.jp

Abstract

This paper shows that a 5 $\sim$ 15% mixing inhomogeneity of the deuterium (D) and tritium (T) concentrations in a D-T pellet still gives a sufficient fusion energy output in D-T inertial confinement fusion (ICF). Numerical and analytical studies support this new result as long as the D and T total amounts are equal and the implosion process is stable. This result means that fusion energy output and burn process are rather insensitive to the initial inhomogeneous fuel mixing in the D-T ICF pellet.

Introduction

In deuterium(D)-tritium(T) inertial confinement fusion (ICF) a fuel pellet is compressed to about a thousand times the solid density. The fuel compression ratio is extremely high. Therefore, the requirement for implosion uniformity is quite stringent [1]: the tolerable nonuniformity during the implosion is only a few percent. The nonuniformity arises from the driver energy illumination nonuniformity, the pellet structure nonuniformity and the Rayleigh-Taylor (R-T) instability. In addition, other causes may be the imbalance of the contents of the D and T fuels [2], and also the inhomogeneous mixing of the initial D-T fuel concentrations [3]. The fuel-content imbalance in the D-T pellets has already been studied (2): a 30 % content imbalance still gives sufficient fusion energy output.

In this paper, we study the effect of inhomogeneous mixing (Fig.1) of the D-T fuel concentrations on the fusion energy output. In a D-T pellet, we may have the inhomogeneously-mixed frozen D-T fuel in a pellet fabrication process, although the total amounts of D and T are equal. The inhomogeneous mixing of D and T fuels may influence the DT burn and the fusion energy output, and induces the mass-density nonuniformity. In this paper we study on the inhomogeneous mixing effect on the fusion energy output. The mass-density nonuniformity is discussed briefly at the end of this paper. A one-dimensional numerical simulation presents that a 40 % mixing inhomogeneity of the D and T concentrations still gives a sufficient fusion energy output, as long as the total amounts of the D and T are equal. However an estimation for nonuniform implosion suggests that the tolerable mixing inhomogeneity of the deuterium (D) and tritium (T) is 5 $\sim$ 15%. This result means that fusion energy output and burn process are rather insensitive to the inhomogeneous fuel mixing in the D-T ICF pellet.

Inhomogeneously-mixed D and T Fuels

In order to study the effect of inhomogeneous mixing of the D and T concentrations (Fig.1) on fusion energy output, we performed a one-dimensional computer simulation which includes the equations for the D-T, D-D and D-H_e^3 reactions [2]. In the simulation,

the three-temperature fluid model[4] is employed and the fuel-burn process is computed [5]. The diffusion equation is solved for alpha particle transport, and neutrons escape freely. Electron and radiation heat conductions [4,6] are also included by the flux-limited diffusion model. The SESAME library is used for the equation of state. As the initial condition for the zeroth-order unperturbed profile, we employ the constant-pressure model [7], in which the temperature of the inner hot spot is 10 keV, that of the outer part is 3.33keV, the density n_{0h} is 333 times the solid density at the hot spot, and the density n_{0out} is 1,000 times the solid density at the outer part. In our simulation, the initial ρR for the hot spot is 0.5g/cm^2 and is fixed, when the total ρR value is changed in the parameter studies. Our D-T pellet has no tamper. The density perturbations for the D and T are imposed to the zeroth-order density profile $n_0(r)$, so that the D and T total amounts are equal:

$$n_D = n_0(r)/2 + \delta\{n_{0out}/2\}P_N(r/r_{out}), \tag{1}$$

$$n_T = n_0(r)/2 - \delta\{n_{0out}/2\}P_N(r/r_{out}). \tag{2}$$

Here δ is the perturbation amplitude, $N = 2n + 2, (n = 1, 2, 3, ...)$, and $P_N(R)$ is the Legendre function which satisfies the following equation: $\int_0^1 R^2 P_N(R)dR = 0$ Because of this property of the Legendre function, we can guarantee that the D and T total amounts are equal. This initial density profile may be obtained during the implosion process, in which we may have some instabilities. During a D-T-pellet fabrication, a pellet may have the inhomogeneous mixing of the D and T fuels, although the D and T total amounts can be controlled to be equal. As a result of some instabilities and implosion nonuniformities, the pellet may have the mixing inhomogeneities. Our initial condition is an example of the inhomogeneities.

Figure 1 presents the relations between the normalized fusion energy output and δ for ρR= 3 g/cm^2. Figure 1 shows that a 40 % mixing inhomogeneity of the D and T concentrations in the D-T pellet still gives a sufficient fusion energy output.

In order to estimate the inhomogeneous mixing effect of the D and T concentrations on fusion energy output, we employ the following simplified reaction equations for the D and T:

$$\begin{aligned} dn_T/dt &\simeq -n_D n_T < \sigma v >_{DT} + n_D^2 < \sigma v >_{DD} /4 \\ &\simeq n_T^2(- < \sigma v >_{DT} + < \sigma v >_{DD} /4) \end{aligned} \tag{3}$$

$$\begin{aligned} dn_D/dt &\simeq -n_D n_T < \sigma v >_{DT} - n_D^2 < \sigma v >_{DD} \\ &\simeq -n_D^2(< \sigma v >_{DT} + < \sigma v >_{DD}) \end{aligned} \tag{4}$$

Here $< \sigma v >$ shows the fusion reaction rate and t the time. In this analysis, we assume that the temperature is constant in time and $\delta << n_{0out}$. For simplicity of analysis, the density profile is assumed to be constant (n_{0out}) in space. Then we can estimate the fusion energy output E_f as follows:

$$\begin{aligned} E_f &\simeq \int dt \int dr 4\pi r^2 e_f n_D n_T < \sigma v >_{DT} \\ &\simeq 4\pi\tau e_f < \sigma v >_{DT} \int dr r^2 n_D n_T \\ &\propto \int dr r^2 n_D n_T \end{aligned} \tag{5}$$

Here e_f is the fusion energy by one D-T reaction, and τ the confinement time. A further calculation gives us the following expression:

$$\int dr r^2 n_D n_T \simeq \int dr \frac{r^2}{F_1}\left(\frac{n_{0out}^2}{4}\right)\left[1+\Delta F_2-\Delta^2\left(\frac{F_3}{F_1}\right)\right] \quad (6)$$

Here $\Delta = \delta \times P_N(r/r_{out})$, $F_1 = AB$,
$A = 1 + (n_{0out}\tau/2)\left(< \sigma v >_{DT} - < \sigma v >_{DD}/4\right)$,
$B = 1 + (n_{0out}\tau/2)\left(< \sigma v >_{DT} + < \sigma v >_{DD}\right)$,
$F_2 = (n_{0out}\tau/2)(< \sigma v >_{DT} - < \sigma v >_{DD}/4)/A - (n_{0out}\tau/2)(< \sigma v >_{DT} + < \sigma v >_{DD})/B$, and $F_3 = (n_{0out}^2\tau^2/4)(< \sigma v >_{DT} - < \sigma v >_{DD}/4)(< \sigma v >_{DT} + < \sigma v >_{DD})/F_1$. The first term of the righthand side of Eq.(4) comes from the D-T reaction by the zeroth-order of the D-T density(n_{0out}). From the relation of $\int_0^1 R^2 P_N(R)dR = 0$, $N = 2n+2, (n = 1,2,3,...)$, the second term of the righthand side of Eq.(4) vanishes approximately, if we assume that the reaction rate $< \sigma v >$ does not depend on r. This estimation result shows that the second order of the mixing inhomogeneity δ influences the fusion energy output, as long as the D and T total amounts are equal. Therefore, the fusion energy output is insensitive to $\delta(<< 1)$, and the decrease in the fusion energy output is expected to be small.

Discussions

In this paper, we presented a numerical and analytical study of the effect of inhomogeneous mixing of the D and T concentrations on fusion energy output in a DT-ICF fuel pellet. We found that a 40% mixing inhomogeneity of the D-T fuel concentrations in a D-T fuel pellet can still give a sufficient fusion energy comparable to that of a pellet which contains deuterium and tritium homogeneously. This means that the D-T fusion energy output is rather insensitive to mixing inhomogeneities of the D-T fuel concentrations, as long as the total D and T amounts are equal in the D-T pellet. This result comes from the following fact: during the burn, only a fraction of the fuel is burned and the remainder, usually about 60 to 70%, remains inert. Consequently, the fusion energy output and the burn process seem to be insensitive to the inhomogeneous mixing of the D and T concentrations.

In our one-dimensional analyses, we did not include instability effects on the energy output. If the pellet has mixing inhomogeneities during implosion and burn phases, the pellet has a mass-density fluctuation, and may suffer the *R-T* and other instabilities. This should be studied in detail in the near future. Here we discuss on this point briefly. When a DT pellet has the initial DT mixing inhomogeneity

$$n_D = \{n_0/2\}(1+\Delta), n_T = \{n_0/2\}(1-\Delta), \quad (7)$$

the pellet has the following mass-density nonuniformity:

$$\rho = \rho_0[1 + \{m_D - m_T\}/\{m_D + m_T\}\Delta] = \rho_0[1 - \Delta/5] \quad (8)$$

The tolerable nonuniformity may be a few percent [1]. If we impose this nonuniformity requirement, the tolerable DT mixing inhomogeneity may be about 5 times a few percent, that is, $5 \sim 15\%$.

[1] Lindl, J. D., McCrory, R. L. and Campbell, E. M., *Phys. Today* **9**(1992)32; Kawata, S. & Niu, K., *J. Phys. Soc. Jpn.* **53**(1984)3416.
[2] Kawata, S. and Nakashima, H., *Laser and Particle Beams* **10**(1992)479.

[3] Kawata, S., *Laser and Particle Beams*, 13(1995)383.
[4] Tahir, N.A. et al., *J. Appl. Phys.* 60(1986)898.
[5] Fraley, G.S., et al., *Phys. Fluids* 17(1974)474.
[6] Zel'Dovich, Ya.B. & Raizer, Y.P., "*Physics of Schock Wave and High Temperature Hydrodynamic Phenomena*", New York: Academic Press,1966.
[7] Meyer-ter-Vehn, J., *Nuclear Fusion* 22(1982)56.

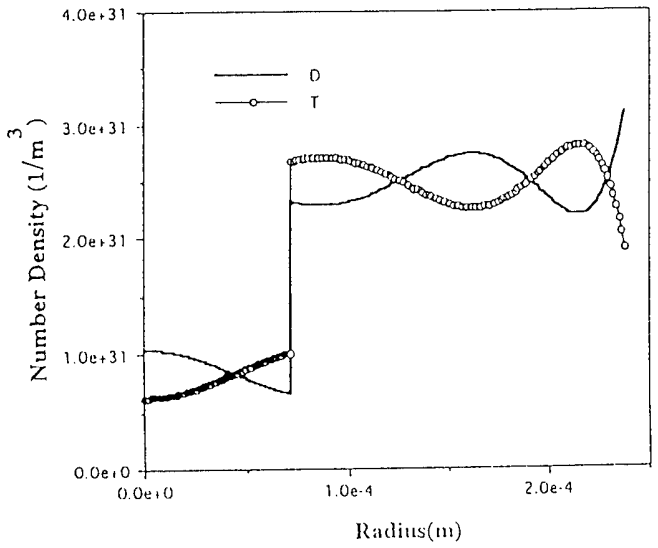

Fig.1 The initial density profiles for D and T with the perturbation for ρR=4g/cm^2, δ=0.3 and the mode N=8.

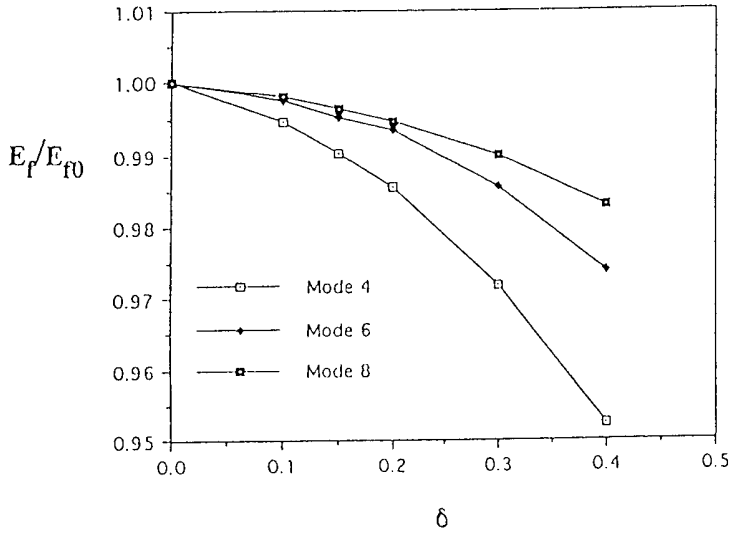

Fig.2 The relation between the normalized fusion energy output and δ for ρR= 3g/cm^2.

LARGE-SIZE PELLET IN ION-BEAM ICF

S. Kawata, K.Kurawaki, A.Tuyuki and K.Hirota

Department of Electrical Engineering, Nagaoka University of Technology
Nagaoka 940-21, Japan
e-mail: kawata@voscc.nagaokaut.ac.jp

Abstract

In this paper we discuss a concept of a large-size-pellet ion-beam inertial confinement fusion(ICF) in which a DT fuel pellet is more than several tens mg. In the large-size-pellet ICF the fuel is compressed to less than 1000 times the solid density, for example about 100 times the solid density in order to realize $\rho R > 1 \sim 3g/cm^2$. Because of the low compression ratio, constraints required for the uniform fuel implosion are relaxed compared with those for a high-compression implosion of a small pellet. This concept of the large-size-pellet implosion may present another approach to ICF. In this paper we present a simple estimation for the concept and one-dimensional numerical analyses for the large-size-pellet implosion. A simple linear estimation for the Rayleigh-Taylor instability presents that the fuel pellet may not be destroyed by the instability.

Introduction

A large number of studies for inertial confinement fusion (ICF) have been performed.[1-4] The researches have been concentrated on a small-size-pellet DT ICF. The small pellet is compressed to about 1000 times the solid density in order to extract the fusion energy in a short time with a high burn rate and to save the input driver energy. The requirement for uniform compression of the small pellet is quite stringent:[1-3] it is well known that the nonuniformity should be suppressed less than a few % in order to attain the high compression. One of other approaches to ICF may be a low-compression one, which is presented and discussed in this paper. In the low-compression scheme, a fuel should contain a larger DT mass compared with that in a high-compression pellet in order to attain $\rho R > 1 \sim 3g/cm^2$. Because of the low compression ratio and the large size of pellet, the low-compression scheme relaxes the uniformity requirement and the driver-energy-focusing one, which is quite severe especially in Light-Ion-Beam ICF approaches.

The purpose of this paper is to point out that a large pellet is robust against the nonuniform implosion compared with the small pellet, and that sufficient fusion energy output may be obtained in the large-pellet impact ICF.

Concept of Large-Size-Pellet ICF

One of the main objectives in the large-size-pellet ICF is to reduce the fuel density compression ratio. Because of the low compression, the uniformity requirement can be relaxed.

The input energy being required to compress and heat the fuel is estimated by the sum of the heating energy $W_h = 38.3 M_{DTh} T_i$ J and the energy (pressure work) to compress the fuel. Here M_{DTh} is a fraction of the fuel (M_{DT} mg) heated up to T_i eV by the input energy, and its radius is assumed to be 3 times the radius at which a produced

α particle stops. In the calculation for the pressure work, electrons are assumed to be in the perfect-degenerate gas state. The pressure work is $W_P = 114(\kappa^{2/3} - 1)M_{DT}$ J, where κ is the density compression ratio. In this section we employ the following typical parameter values in DT ICF: $\rho R = 3g/cm^2$, the implosion efficiency is 5%, η_d =20%, M =1.1, f_a =0.1, T_i = 5keV and η_t =45%. Finally we obtain the relation between the compression ratio and the input energy, as shown in Fig.1; the numerical values beside the line denote the total DT mass. For the large pellet containing about 1 gram of the DT, the required density compression ratio is rather low and is less than 100.

The implosion-uniformity requirement can be estimated as follows: first the nonuniformity of implosion speed δv_{imp} is estimated. From the approximate relations of $R_0 = v_{imp}t_f$ and $\delta R = \delta v_{imp}t_f$, $\delta v_{imp}/v_{imp} = \delta R/R_0 = (\delta R/R)(R/R_0) = (\delta R/R)\kappa^{-1/3}$. Here R_0 is the initial radius, R the final radius of the pellet and κ the volume compression ratio. On the other hand ρR is proportional to R^{-2}, and $\delta(\rho R)/(\rho R) = (1 + \delta R/R)^{-2}$. Then $\delta R/R = \{\delta(\rho R)/(\rho R)\}^{-1/2} - 1$. Combining these relations, we obtain $\Delta = \delta v_{imp}/v_{imp} = \{\{\delta(\rho R)/(\rho R)\}^{-1/2} - 1\}/\kappa^{1/3}$. From this result $\Delta_{low-\rho}/\Delta_{high-\rho} = (\kappa_{high-\rho}/\kappa_{low-\rho})^{1/3}$. Here $\Delta_{high-\rho}$ shows the nonuniformity in the conventional high-compression scheme and $\Delta_{low-\rho}$ presents one in the large-pellet ICF, for the fixed allowable $\delta(\rho R)/(\rho R)$. For the high-compression scheme the volume compression ratio $\kappa_{high-\rho}$ is about 10000, and for the large-pellet ICF $\kappa_{low-\rho}$ may be a few hundreds to 500 in our pellet employed in this paper. Therefore the factor of $\Delta_{low-\rho}/\Delta_{high-\rho}$ is about 2.7$\sim$4. Consequently the nonuniformity tolerance in the large-size-pellet ICF is 2.7$\sim$4 times larger than that in the high-compression ICF. The nonuniformity of about 5$\sim$8% may still give sufficient fusion energy output in the large-pellet ICF. This result confirmed that the large pellet is rather stable against the nonuniformity compared with the conventional small pellet.

Simulation Results and Stability

Our simulation was performed by a one-dimensional hydrodynamic Lagrangian code. In order to simulate the large-size pellet we employ the three-temperature model.

Figure 2 shows a fuel pellet structure employed in this study. The numerical simulation is started at the instant when the ion-beam-deriven-accelerated projectile impacts on the pellet surface. A DT gas is located at the pellet center. The projectile is made of the solid Pb and is accelerated to 120 km/s.

Table 1 shows the parameter values employed in the simulation and a part of the results obtained. Figure 3 presents the radius-time diagram. By the initial shock wave, first the inner DT gas reacts slightly at about 34 nsec. At this time the main DT is not yet ignited(see Fig.6). After the further compression, the DT gas is ignited and burned at the time($\sim$67 nsec) of the maximum compression. The main DT fuel is also heated up by the alpha particles produced in the DT gas. Then the main DT fuel is ignited and burned in a manner of a volume-compression scheme. In this particular case the implosion efficiency is about 3.5%. The maximum ρR is 6.84g/cm^2. The peak DT number density is 383 times the solid density. The fusion energy output is 64.2GJ and the pellet gain is 428. The burn-up ratio is 76.2% in this case. This high burn ratio is consistent with the high ρR and the long burn time. The burn time duration is longer than 2 nsec (see Fig.8), that is rather long compared with that in a conventional small pellet.

Based on the numerical results presented above, we also performed a simple linear estimation for the R-T instability growth.[4] In order to evaluate the growth, we computed $\gamma\tau$, which can be estimated by the following integral: $\gamma\tau \simeq \int_0^t dt\sqrt{Agk}$ Here A is the

Atwood number, g the acceleration which is obtained by the simulation result, τ the time interval during which the R-T instability takes place, and k the wave number which is estimated by 2π/(the thickness of the layer concerned). In our simulation the interface between the solid DT and the pusher is in danger of the R-T instability. The histories of the growth rate γ and the growth factor $\gamma\tau$ are presented in Fig.4. The instability is found during the deceleration phase by the reflected strong shock wave (mode 1) and the stagnation phase (mode 2). (At the very beginning of the implosion we have another unstable mode (mode 0). However $\gamma\tau < 1$ for the mode 0, because of the small k and γ.) $\gamma\tau_s$ is about 3.8 during the stagnation phase (mode 2) for the interface. $\gamma\tau_d$ is about 2.0 during the deceleration phase (mode 1) by the reflected shock. We believe that these values are not too large in the large-pellet ICF.

These estimation results present that the large-size pellet may not be destroyed by the R-T instability.

Conclusions and Discussions

In this paper we proposed the concept of the large-pellet ICF, and discussed about it based on the hydrodynamic computer simulations and the simple estimations. The results of this work demonstrate that the large-pellet ICF scheme may supply sufficient fusion energy output. The results of the researches also show that the large pellet may be robust against the nonuniformity compared with the small pellet. We also performed the linear estimation for the R-T instability growth based on the one-dimensional simulation results. The linear analyses present that the large-pellet implosion may be rather stable.

[1] J.J.Duderstadtand G.A.Moses, "Inertial Confinement Fusion",(John Wiley and Sons, New York, 1981).

[2] J.D.Lindl, R.L.McCrory and E.M.Campbell, Phys. Today, **9**(1992)32.

[3] S.Kawata and K.Niu, Jpn.J.Appl.Phys., **53**(1984)3416.

[4] F.Hattori, H.Takabe and K.Mima, Phys. Fluids, **29**(1986)1719.

Table 1. Parameter values employed and Results

PARAMETER	VALUE
DT gas layer radius	5.00 [mm]
(DT gas density)/(DT solid density)	1/10000
DT solid layer thickness	2.43 [mm]
Total DT fuel mass	0.250 [g]
Pusher thickness	0.500 [mm]
Pb projectile thickness	1.86 [mm]
Pb projectile speed	120 [km/s]
Input energy	150 [MJ]
Maximum DT ion temperature	11.6 [keV]
Maximum ρR	6.84 [g/cm^2]
Maximum compression ratio of the DT fuel	383
Fusion energy output	64.2 [GJ]
Pellet gain	428

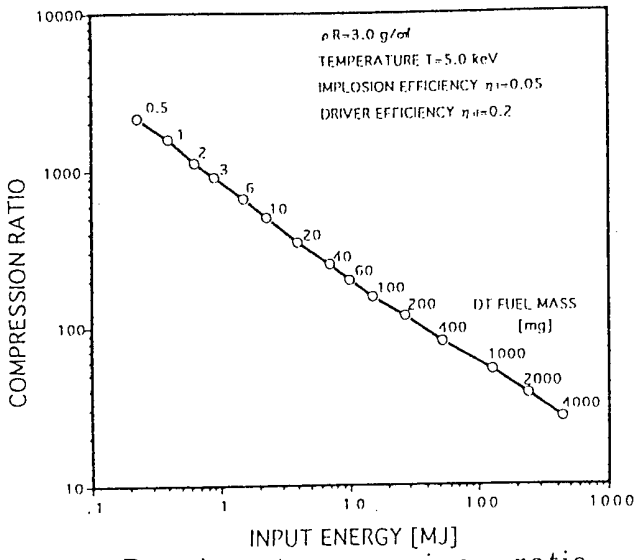

Fig.1 Density compression ratio versus the input energy.

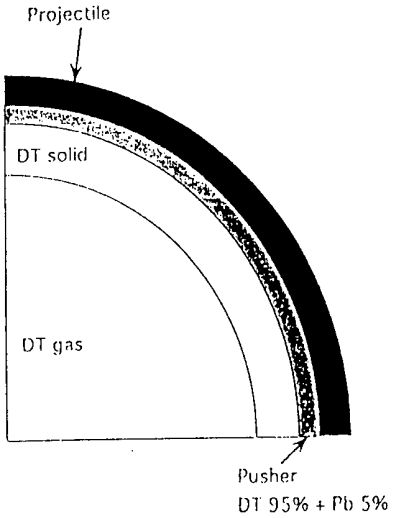

Fig.2 Pellet structure and the projectile.

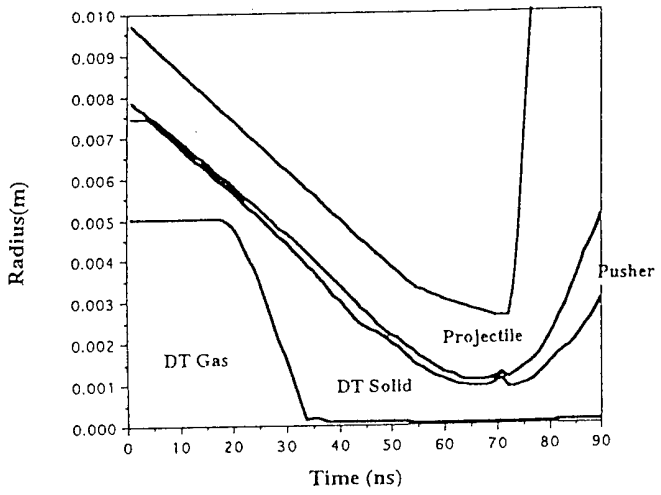

Fig.3 Radius-time diagram in the one-dimensional simulation.

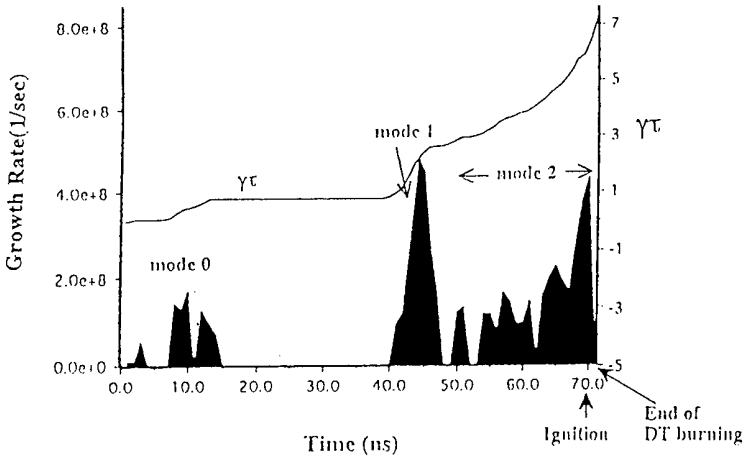

Fig.4 Histories of the growth rate γ and γτ of the R-T instability. In the estimation for γ we used the instant acceleration and the instant pusher thickness at every moment.

SLOWING DOWN OF AN ABLATIVELY ACCELERATED FOIL AFTER IMPACT ON A STATIONARY TARGET

H. Marten, B. Goel, W. Höbel
Forschungszentrum Karlsruhe, Institut für Neutronenphysik und Reaktortechnik
Postfach 3640, D-76021 Karlsruhe, FRG

Recently, Baumung et al. (1995) observed a nontrivial slowing down of an ablatively accelerated aluminum foil striking a non-moving LiF crystal. We analyze these experiments using a radiation-hydrodynamic code. Isolating different involved phenomena we conclude that the behaviour observed in the experiment is caused by the radiative transport of heat energy from the hot ablated plasma into the cold accelerated aluminum flyer.

1. Introduction

In foil acceleration experiments performed with the high-voltage pulsed power generator KALIF, intense proton beams generated in the ion diode are used to irradiate thin foils, thus generating ultrahigh pressures of up to 60 GPa in condensed matter. Once the proton beam starts depositing energy inside the foil, a part of the matter is ablated and heated to high temperatures. The high pressure of this plasma then drives a compression wave into the remaining solid and cold part. At the rear surface of the target (interface between solid state and vacuum, the so-called "free surface") the compression wave is reflected as a release wave running back into the target, the release wave is reflected at the ablation-plasma boundary as a pressure wave, and so on. Experiments as well as numerical simulations show that these wave reverberations in the condensed part of the foil lead to a stepwise increase of the targets rear-surface velocity, and ablatively driven velocities of up to 12 km/s have been measured in these experiments.

Recently, Baumung et al. (1995) presented velocity measurements of an ablatively accelerated aluminum foil striking a stationary target. In these experiments, a laser-Doppler interferometer records the rear-surface velocity of the Al-foil of 71 μm initial thickness through a non-moving LiF-window (thickness about 5 mm) initially placed at a pre-defined distance behind the Al-foil. The collision of the Al-flyer with the LiF-foil generates two compression waves propagating into both materials and leads to a typical velocity signal as shown in Fig. 1 at about 55 ns. Because of the nearly identical dynamic properties of the two materials the flyer velocity first drops to about one half of its impact velocity, remains almost constant until the pressure wave generated in the flyer reaches the ablation-plasma interface, and finally starts to drop. The dashed curve shown in Fig. 1 is a simplified model of a collision of two "cold" targets, i.e. the collision of two cold foils with an impact velocity taken from the experiment and a flyer thickness of 48.5 μm (= initial thickness minus range of 1.5 MeV-protons). Compared to the experimental results of Fig. 1, two remarkable differences are noticed: In the experiment the "velocity plateau" after the impact is shorter and the decrease of the "velocity tail" is less steep than expected from the cold-target estimates. In the following sections, these differences are examined in more detail by numerical simulations performed with the hydrodynamic code KATACO (Goel et al. 1993).

2. Model Calculations

Since the wave reverberation inside the cold part of the Al-foil is a quasi-periodic phenomenon with the period slightly changing in time due to changes of the target thickness, one may define a phase of the pressure wave, Φ, starting with $\Phi = 0$ at that time when the pressure wave just reaches the targets free surface. Numerical simulations have shown that the "velocity plateau"

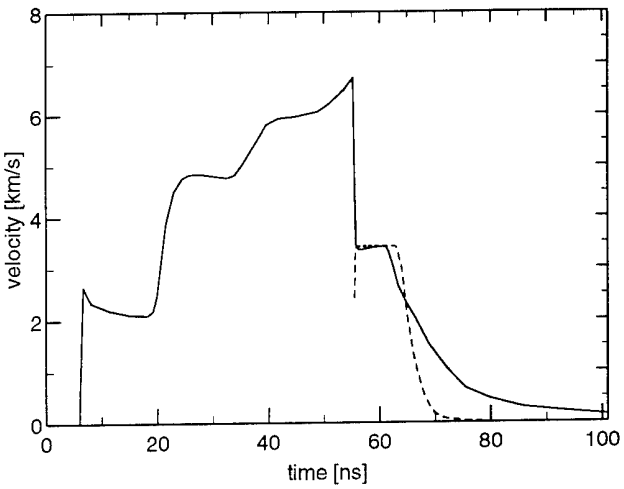

Figure 1: Measured velocity of an ablatively accelerated Al-foil striking a stationary target at about 55 ns (Baumung et al. 1995). The dashed curve is a simplified theoretical model for the impact of two cold foils (see text).

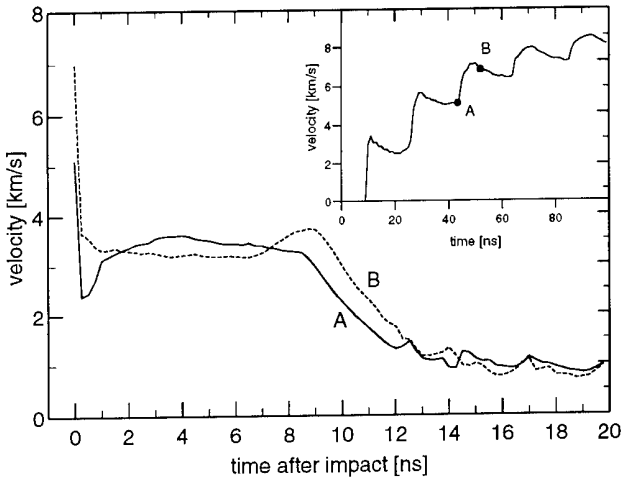

Figure 2: Simulated velocity evolution of the LiF-Al interface after the impact at two different phases of the pressure wave (A: $\Phi = 0$; B: $\Phi = \pi$). In the inlet, the moments of impact for the two models are shown within the velocity curve of a free flying target.

after the target impact is in general not as flat as found in the experiment, but shows a structure which depends on Φ at the time of impact. Fig. 2 shows two computed velocity signals after the impact at two different phases. In model A (impact at $\Phi = 0$), the rear-surface velocity of the flyer drops to about one half of the initial value but soon increases by about 1 km/s due to acceleration by the just arriving pressure wave. In model B (impact at $\Phi = \pi$) the arrival of the pressure wave at the rear surface is seen as a velocity hump near the end of the plateau. Also, the length of the plateau is somewhat increased in this case. In an experiment it is difficult to control the phase of impact. Nevertheless, from our simulations we can estimate that in the experiment shown in Fig. 1 the impact took place at about $\Phi = 0.1 \cdot 2\pi$.

A shorter velocity plateau after impact can in principle be achieved when the thickness of the remaining solid Al-foil is reduced by additional evaporation of matter beyond the proton range, e.g. by thermal conduction. In order to correctly consider the thermal conductivity in solids, new thermal conduction coefficients according to Bespalov & Polishchuk (1989) have been implemeted in KATACO, with an additive correction accounting for the measured value

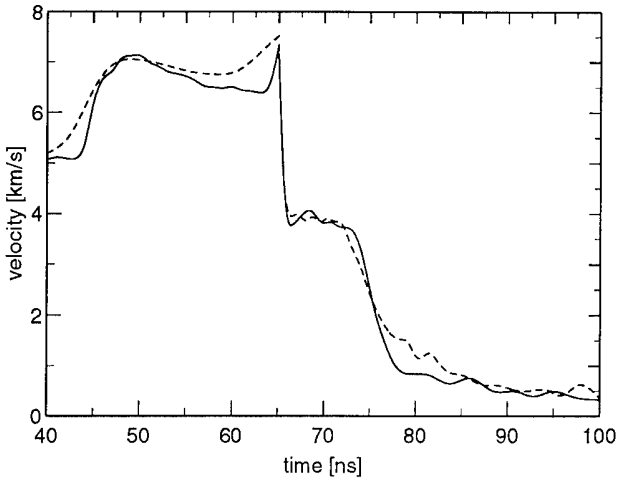

Figure 3: Computed target velocity as a function of time (impact at $t = 65$ ns) including radiative transfer (dashed) and without radiative transfer (straight line).

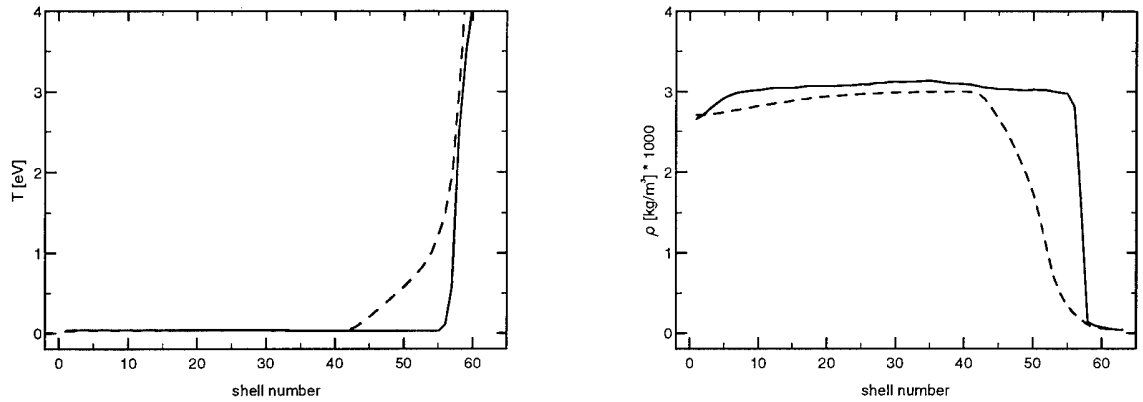

Figure 4: Temperature and density structure of models with (dashed) and without radiative transfer (straight lines) at the time of impact ($t = 65$ ns).

of $\kappa_{Al} = 223$ W/Km at normal density. Nevertheless, a comparison of impact calculations with and without thermal conduction has shown that this process is not responsible for the observed reduction of the final target thickness. Thermal conduction is only of minor importance in these experiments.

A second process that can reduce the thickness of the cold Al-foil by additional evaporation is due to heat transport by radiation. KATACO contains a formalism for multi-angle, multi-frequency radiative transfer. In these calculations we used 2 angular directions and 10 frequency intervals, with Planck-mean emission and absorption coefficients calculated with the code EOSOPC (Ping Wang 1993). In Fig. 3, the resultant velocities are compared for simulations with and without radiative transfer, the corresponding model structures at the time of impact ($t = 65$ ns) are shown in Fig. 4. Indeed, the additional transport of energy by radiation from the hot plasma to the cold region leads to an additional evaporation (increasing in time) seen in the temperature structure of Fig. 4. This results in an earlier reflection of the pressure wave generated at impact and thus in a shorter plateau of the rear-surface velocity (Fig. 3). The additional pressure of the evaporation zone retards the slowing down of the aluminum foil and leads to a less steep decrease of the velocity tail ($t < 72$ ns in Fig. 3), as observed in the

experiment. Furthermore, the pressure of the evaporation zone reduces the density gradient at the ablation boundary so that any reflection of a compression or a release wave becomes less definit. As a result, the steps in the target velocity already become rounded before the impact takes place (Fig. 3). This behaviour is observed in the experiments as well (c.f. Fig. 1).

3. Conclusions

The impact experiments depend on the phase of the pressure wave inside the solid part of the flyer *at* the time of impact. Since the latter is a complicated function of the initial distance d between the flyer and the impactor, as well as of the targets velocity evolution which in turn is influenced by the targets equation of state (Goel & Vorobiev 1996), impact experiments at a definite phase are difficult to perform and the corresponding necessary initial distance d can only be found either by trial and error or by previous numerical simulations.

While thermal conduction was found to be unimportant for these experiments, radiative effects are not negligible. This is somewhat surprising at a first glance. The usual argument for neglecting radiation in numerical simulations comes from a comparison of the *local* radiation energy with the *local* thermal energy content. In the hot plasma generated by the KALIF-B_Θ diode, the radiation energy is about 7 % of the thermal energy content, and it might be enticing to neglect this "small fraction". However, radiation has always to do with *transport* of energy, here resulting in a net energy-flux from a hot plasma into solid and cold matter. The resulting local excess of radiation energy heats up these cold regions until a new local thermodynamical equilibrium is reached, and it is this non-equilibrium effect which significantly reduces the final thickness of the solid flyer in these experiments. A more detailed study of radiative processes with higher numbers of angluar directions and frequency intervals as well as numerical computations with different equations of state are just under development (Goel et al. 1996).

References

Baumung K., Rusch D., Singer J., Razorenov S.V., Utkin A.V., Kanel G.I., 1995, Hydrodynamic Beam-Target Experiments on KALIF. in: H.-J. Bluhm (ed.) Physics of Intense Light Ion Beams and Production of High Energy Density in Matter, Annual Report 1994, Forschungszentrum Karlsruhe FZKA 5590, p. 73

Bespalov I.M., Polishchuk A.Ya., 1989, Sov.Tech.Phys.Lett. 15, 39

Goel B., Vorobiev O.Yu., 1996, Equation of State Information from Beam-Target Interaction Experiments at KALIF, Laser and Particle Beams, accepted for publication

Goel B., Höbel W., Marten H., Vorobiev O.Yu., Lomonosov I.V., Gryaznov V.K., 1996, Status of Equation of State for Aluminum in the Light of Beam-Target Interaction Experiments at KALIF, these proceedings

Goel B., Höbel W., Würz H., 1993, Numerical Simulation of Radiation Transport on Supercomputers. in: H. Küsters (ed.) Proc. of the Joint Internat. Conf. on Mathematical Methods and Supercomputing in Nuclear Applications, Karlsruhe, April 19-23, 1993 Vol. 2, p.63

Ping Wang, 1993, EOSOPC - A code for computing the equations of state and opacities of plasma with detailed atomic model, Interner Bericht Forschungszentrum Karlsruhe

TEMPERATURE DIAGNOSTICS OF KALIF TARGETS BY SOFT X-RAY SPECTROSCOPY

G. Meisel, H. Bluhm, L. Buth, P. Hoppé, R. Hüttner, D. Rusch, E. Saenger, T. Schön, J. Singer, O. Stoltz

Forschungszentrum Karlsruhe, Institut für Neutronenphysik und Reaktortechnik, P. O. Box 3640, D-76021 Karlruhe, Germany.

Abstract

The K_α radiation emitted by Al and Mg targets when bombarded with the KALIF proton beam was spectroscopically investigated. From the time integrated spectra peak temperatures of ≈13 eV and ≈23 eV are estimated for the B_Θ diode and the B_{appl} diode, respectively. For time resolved absorption experiments a laser system was set up to generate soft x-rays to be used as backlighter. The system and its properties are described. Results of laser induced x-ray backlighter spectra are given.

Introduction

The high specific power deposition of 50 to 200 TW/g [1] as obtained in the focus of the KALIF proton beam allows one to generate a dense plasma in the kT = 10 .... 25 eV range [2]. The temperature thus obtained can be determined by measuring high resolution K_α x-ray spectra of low Z elements contained in the plasma [3]. The temperature information essentially is contained in the K_α satellite pattern. Thin foils with subrange thickness were bombarded by the KALIF proton beam. Both spectroscopic alternatives, emission as well as absorption, are applied [4]. Emission gives time averaged temperature information whereas the absorption scheme will allow us to perform time resolved experiments.

Emission Spectroscopy

The x-ray spectrometer is equipped with two flat crystals that can be rotated independently. Cleaved RAP and KAP crystals [5] were used for λ = 0.8 to 1.6 nm. The spectra were recorded on Kodak DEF-2 x-ray film [6]. A 2 µm thick mylar foil with 0.05 µm Al coatings on both sides (Type B(10 HH) by Alexander Vacuum Research Inc.) was used as spectrometer entrance window. The films were scanned by a microdensitometer which outputs a film optical density = ^{10}log (1/film transmission) which is roughly proportional to the x-ray flux at the film position [6].

The quality of the spectrometer crystals was tested by recording soft x-ray spectra emitted from a laser induced plasma (see below). The crystals were found to be similar in reflectivity and resolution. The resolution was determined to be about 1000 for the RAP and KAP crystals used.

Emission spectra were taken with the B_Θ diode for Al, Mg, and NaF targets. With the B_{appl} diode spectra were recorded for Al and Mg. The x-ray emission for NaF targets with thickness up to 12 µm was found to be too weak to be recorded with the present equipment.

The spectra obtained for 6 µm thick Al targets as obtained with the two different KALIF diodes are given in fig. 1. Both spectra show a strong low energy component which is emitted by weakly ionized Al atoms as is deduced from calculations [7]. The higher energy

components are emitted by higher ionized Al as indicated in figure 1. Obviously, the B_{appl} diode produces stronger high ionization states indicating that the plasma reaches a higher temperature for this diode.

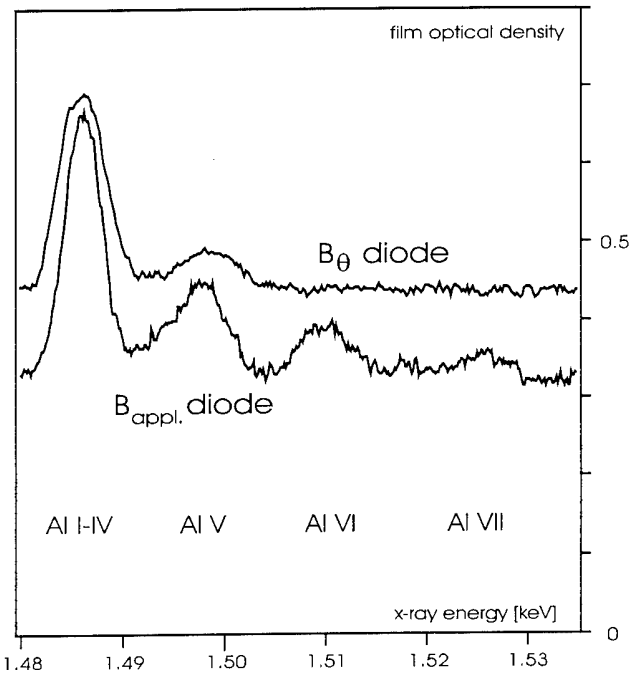

Fig. 1: K_α emission spectra for Al targets of 6 µm thickness as obtained with the two different KALIF diode types. The background results from film fog and from the unshielded part of the hard x-rays.

A more detailed discussion of the observed spectra required a corresponding full calculation for different temperatures, also including the appropriate temporal and spatial averaging corresponding to our experimental conditions. Such full calculations are not available at present. There are, however, results for fixed temperatures [8] without averaging which nevertheless allow some conclusions concerning the peak temperatures: The highest ionization states appearing in the two experimental spectra are Al V for the B_Θ diode and Al VII for the B_{appl} diode. From a visual comparison with the results of the above mentioned calculates spectra we estimate that the peak temperatures reached for the two diodes are ≈13 eV and ≈23 eV for B_Θ and B_{appl}, respectively.

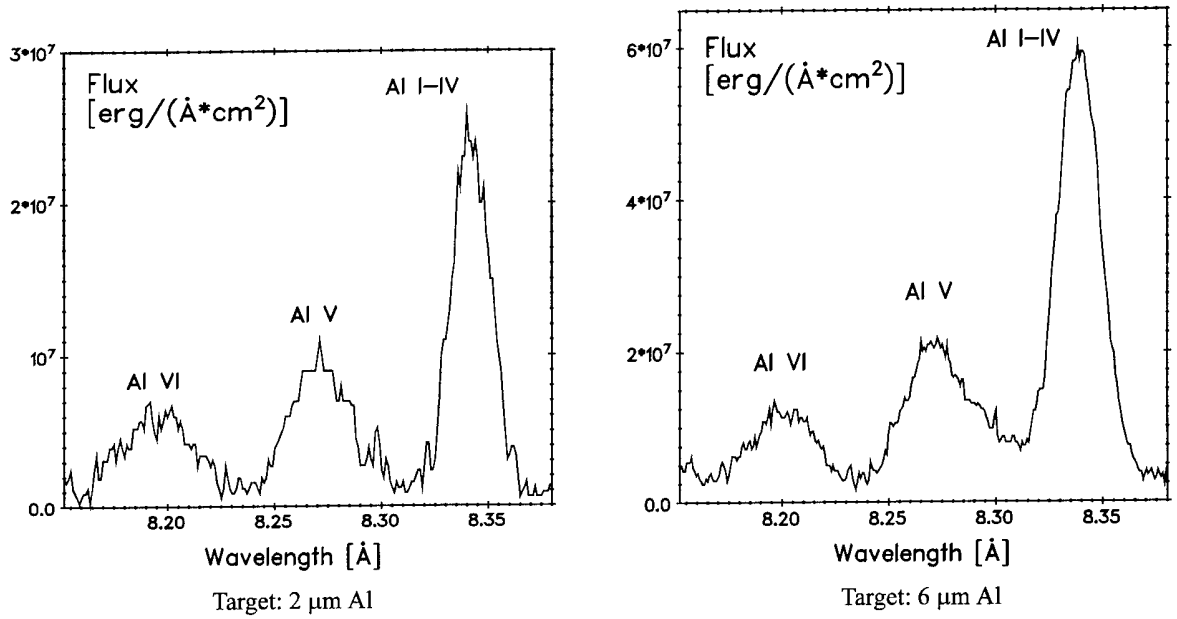

Fig. 2: K_α emission spectra for Al targets of 2 µm (left) and 6 µm (right) thickness as obtained with the B_{appl} diode. Note that the ordinates differ by a factor of 2 for the two curves.

We have also investigated the influence of the target thickness on the shape of the Al spectra. Fig. 2 gives a comparison of the results for 2 µm and 6 µm thickness. It demonstrates that the emission intensity is doubled for a threefold target thickness, i.e. there is some self

absorption, though it is not extremely strong. The shape of the spectra is about the same showing that the self absorption for the different ionization groups changes only little under our experimental conditions.

The Mg K_α emission spectra are weaker by about a factor of two as compared to Al. This is in fair agreement with a rough theoretical estimate [9]. Comparative calculations for Al and Na [7] predict slightly lower x-ray fluxes for Na resulting in a signal on the film that is down by a factor of 3. If we assume an additional overall uncertainty factor of two, the Na signal might be just barely visible with our present instrumentation. Further investigations are required to clarify the reason why no Na emission signals were observed.

Absorption Spectroscopy

The absorption scheme requires a backlighter source that emits a soft x-ray continuum in the respective K_α region. A laser generated plasma is used for this purpose. The laser system has a Q switched Nd:YAG oscillator which is injection seeded from a single mode cw Nd:YVO_4 laser. Its output is an almost diffraction limited pulse of 200 mJ with 7 ns duration. The oscillator output is amplified in three Nd:Glass stages to 10...15 J and frequency doubled to 4...8 J at 532 nm.

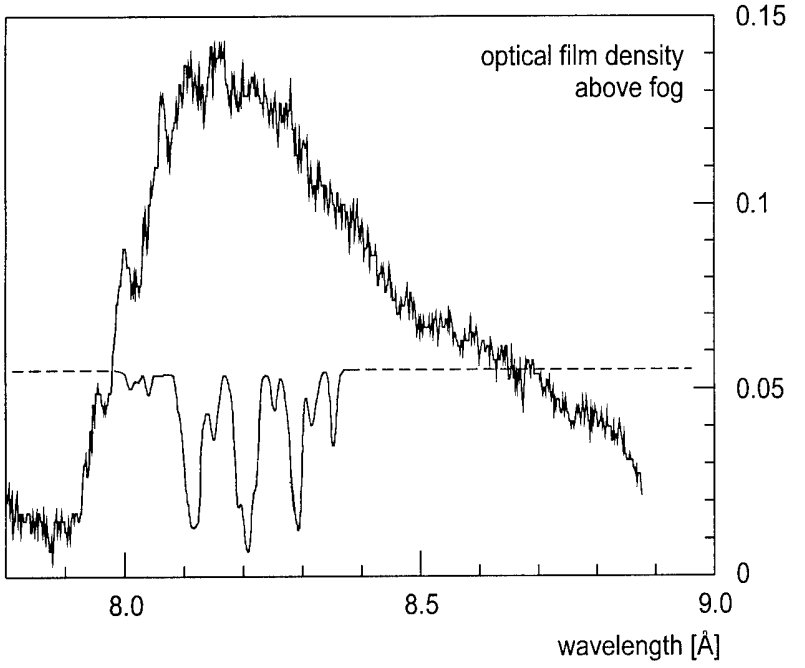

Fig. 3: Laser induced Dy M x-ray spectrum (upper noisy trace). Lower trace: Calculated [7] Al absorption lines.

The output beam is focused onto different rare earth targets to generate an x-ray emitting plasma. As an example, fig. 3 gives the M spectrum for a Dy metal target. Some calculated K_α absorption features of Al [7] are included as inset.

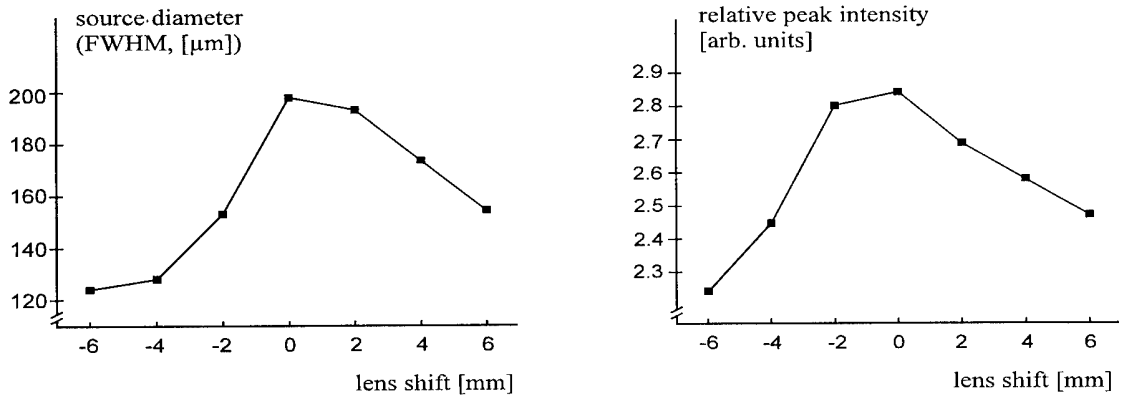

Fig. 4: The effect of laser defocusing on the backlighter source diameter and on the x-ray intensity as obtained from pinhole images. Lens focal length was 500 mm.

An important parameter of the backlighter is its source diameter since it can be a resolution limiting factor. Pinhole camera images were taken to determine the source size and how critical it depends on the focusing. It was found (cf fig. 4) that tighter focusing leads to higher x-ray intensities, but the source diameter increases, too. However, for the diameters observed for tightly focused laser pulses the source size allows for sufficient resolution.

Photodiode arrays as soft x-ray detectors

The x-ray film material used so far has two essential drawbacks: The film fog causes an optical density of about 0.2 which increases with storage duration. Thus the minimum detectable intensity is limited, which resulted, e. g., in the negative Na results (see above). On the other hand, the highest useful ("saturation") optical density is about 3. The saturation to background ratio is only about 15 which limits the detection dynamic range considerably.

A photodiode array has the potential to extend the detection range by its lower background and its higher saturation to background ratio. We therefore also use self-scanning linear photodiode arrays such as model RL1024SAU-811 by EG & G Reticon with a reduced protective silicon oxide layer thickness as soft x-ray detectors. A copper L_α spectrum taken with this diode array is shown in fig. 5; it demonstrates a signal-to-noise ratio superior to the corresponding film record.

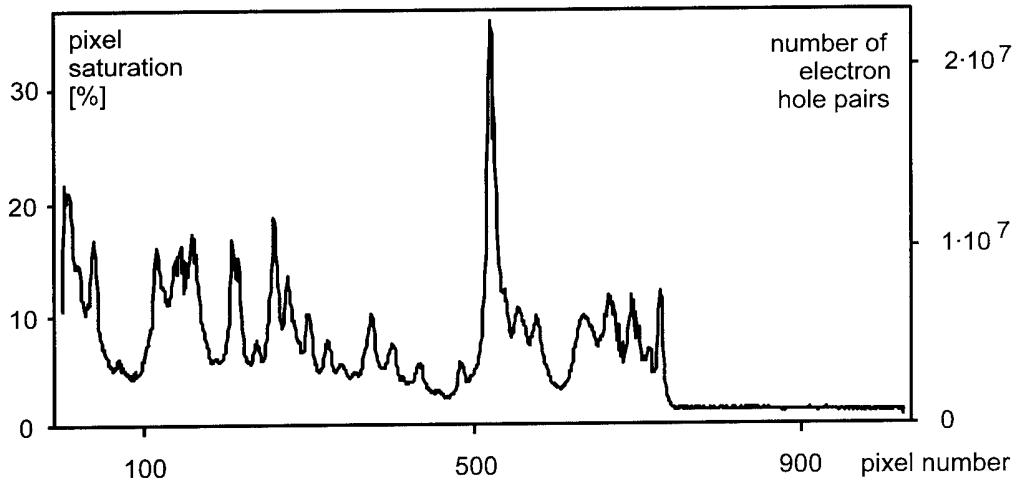

Fig. 5: X-ray spectrum from a laser generated Cu plasma as recorded by a linear photodiode array. The photon energy is about 1 keV.

[1] H. Bluhm, G. Keßler: Report FZKA 5590 (1995) 1
[2] B. Goel, W. Höbel, A. Ludmirski, J. J. MacFarlane, and P. Wang: Report FZKA 5590 (1995) 99
[3] E. Nardi and Z. Zinamon: J. Appl. Phys. **53** (1981) 7075
[4] G. Meisel, A. Ludmirski, J. Singer, H. Bluhm, and T. Schön: Report FZKA 5590 (1995) 95
[5] B. L. Henke, P. Lee, T. J. Tanaka, R. L. Shimabukuro, and B. K. Fujikawa: Atomic Data and Nuclear Data Tables **27** (1982) 1
[6] B. L. Henke, J. Y. Uejio, G. F. Stone, C. H. Dittmore, F. G. Fujiwara: J. Opt. Soc. **B3** (1986) 1540
[7] J. J. MacFarlane and P. Wang: "Numerical Simulation of High Energy Density Plasmas in KALIF Beam-Target Interaction Experiments", Fusion Power Associates Report FPA-95-3 (December 1995)
[8] B. Goel: private communication (1996)
[9] J. J. MacFarlane: private communication (1995)

STABILITY OF BURNING WAVE IN PRACTICAL SIZE OF TARGET

K. Niu

Teikyo Heisei University, Uruido, Ichihara, Chiba 290-01, Japan

Two dimensional simulations show that the radiation gap with the thickness of 2 mm plays the radiation mixture which leads the uniform temperature profile along the surface of inner shell of the indirect driven target. Non-symmetric structure of the pusher or fuel layer, for example, have the possibility to induce the spherically non-symmetric implosion motion. As the momentum of imploding fuel gives the vital role to ignite and to burn the fuel, the paper check the implosion and the burning of the fuel by using two dimensional hydrodynamic code.

1. INTRODUCTION

PBFA-II in Sandia National Laboratory has started to be used for the experiment of beam-target interaction[1,2].

On the other hand, the theories have been given for targets irradiated by ion beams.[3-7]. Targets irradiated by ion beams analyzed in these papers are indirect driven ones.

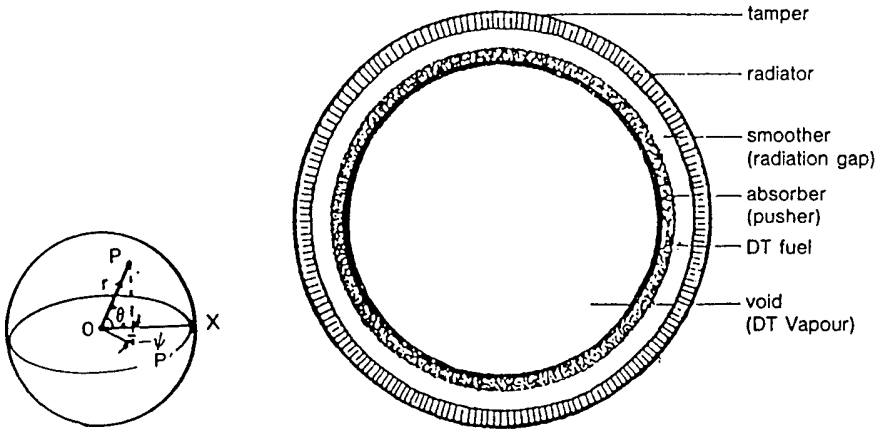

Figure 1. Indirect driven target

Many of them, however, are for rather small targets by using one dimensional simulation codes. Our practical size of indirect driven target is given in Fig.1 and its parameters are indicate in Table 1. A practical target which releases 3GJ fusion thermal energy has the deuterium-tritium (DT) fuel of 23 mg. The outer radius of the fuel layer 5.5 mm and the thickness of it is 286 μm. If the fuel layer is pushed toward the center by the pusher pressure of 10^{12}Pa, the implosion velocity reaches at last 5×10^5m/s, Whose Mach number is 12. Although the pusher pressure is not so large, the fuel layer increases the implosion velocity in the central void, and the core pressure of the fuel after the collision at the center arrives at 10^{18} Pa. The momentum of imploding motion of the fuel leads to a high density and a high temperature, which ignite and burn fuel. In this paper, the hydrodynamic motion of fuel and the propagation of burning wave are analyzed by using two dimensional simulation code.

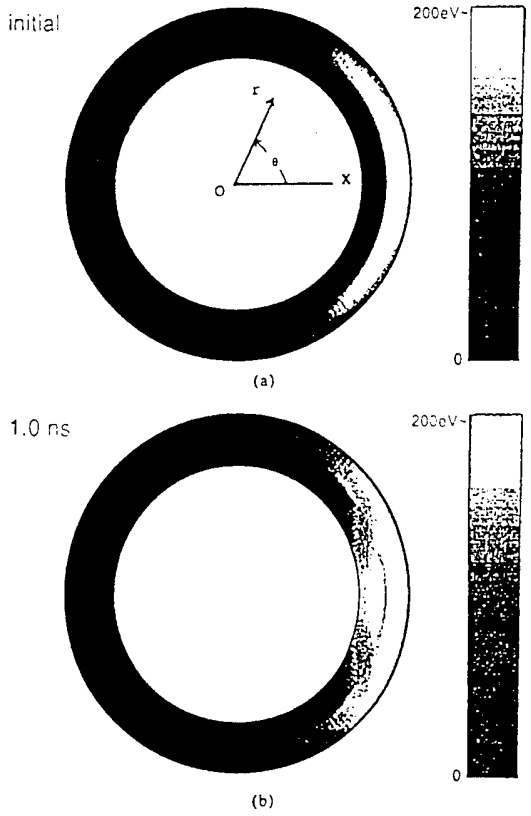

Figure 2. Profiles of temperature in the direct driven target

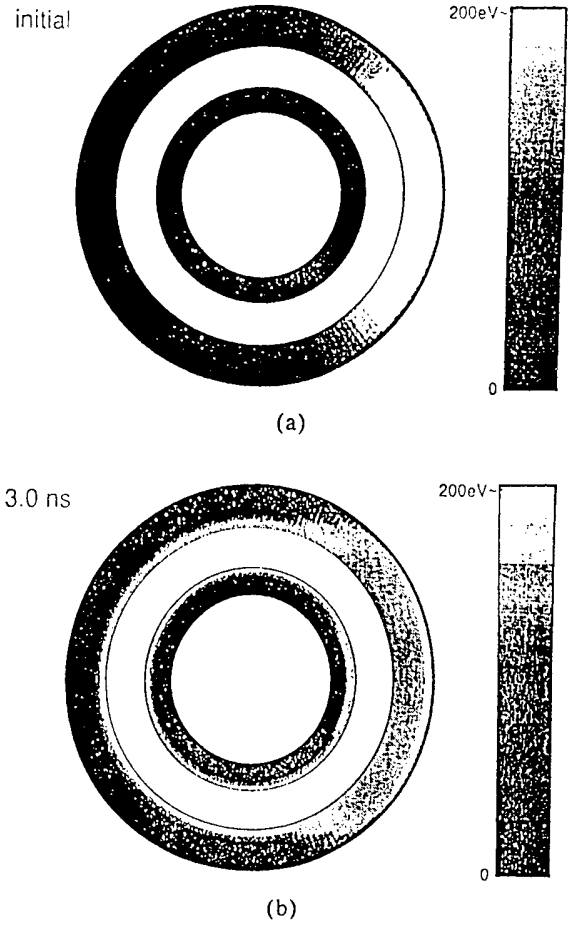

Figure 3. Profiles of temperature in the indirect driven target

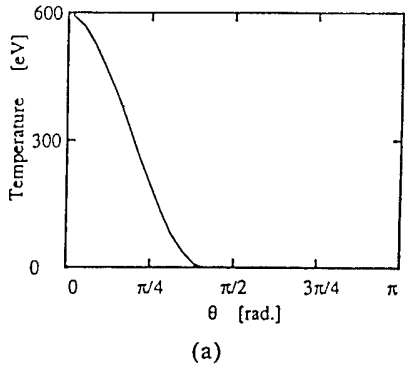

Figure 4. Initial profile of temperature on the inner surface of the radiator layer.

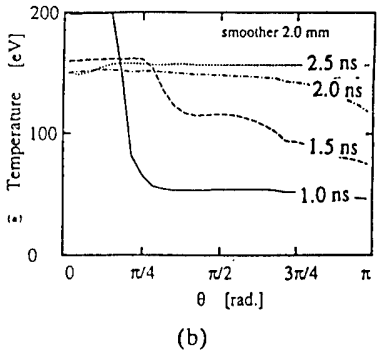

Figure 5. Distributions of temperature on the outer surface of the pusher layer.

2. ROLE OF RADIATION GAP

The role of radiation gap in the indirect driven target is investigated by using the two dimensional code of

radiation transport[8]. Hydrodynamic motions are out of consideration. Figure 2 shows the direct driven target. The pusher layer is irradiated by a ion beam. Soon the fuel layer is heated with an spherically non-symmetric way. While Fig. 3 shows a indirect driven target. The temperature distribution of the inner surface of outer layer soon after the beam irradiation, is drawn along the azimuthal direction in Fig.4. Figure 5 indicates that the temperature distribution of the outer surface of the inner layer approaches the uniform after 2.5 ns. Radiation gap, whose thickness is 2 mm, makes uniform the radiation intensity in it.

3. HYDRODYNAMIC MOTION AND BURNING

Here for simplicity the Lagrangean motion of fuel layer is analyzed. The fundamental equations are eqnation of motion and equation of energy as follows.

$$\rho\frac{\partial \mathbf{v}}{\partial t} = -\nabla p + \mu\Delta\mathbf{v} \qquad (1)$$

$$\rho\frac{\partial e}{\partial t} = -p\nabla\cdot\mathbf{v} + \nabla\cdot\mathbf{J} + S \qquad (2)$$

The limited free flux

$$|\,\mathbf{J}\,| = f(\frac{3mT}{2k})^{1/2}e \qquad (3)$$

is used for thermal flux $\mathbf{J}$. For the released fusion energy S,

$$S = \frac{E_a}{4}(\frac{\rho}{m})^2 < \sigma v > \qquad (4)$$

is used, where the collision cross-section $< \sigma v >$ is given by

$$< \sigma v >= 3.68 \times 10^{-12}(1.16 \times 10^7/T)^{-2/3} exp[-19.94(1.16 \times 10^7/T)^{-1/3}] \qquad (5)$$

For state equations among the internal energy e, pressure p, density ρ and temperature T, the table of Sesame Library is used. The fundamental equations are expressed by the polar coordinate (r, θ, ϕ), and the simplification of two dimension $\partial/\partial\phi = 0$ is utilized.

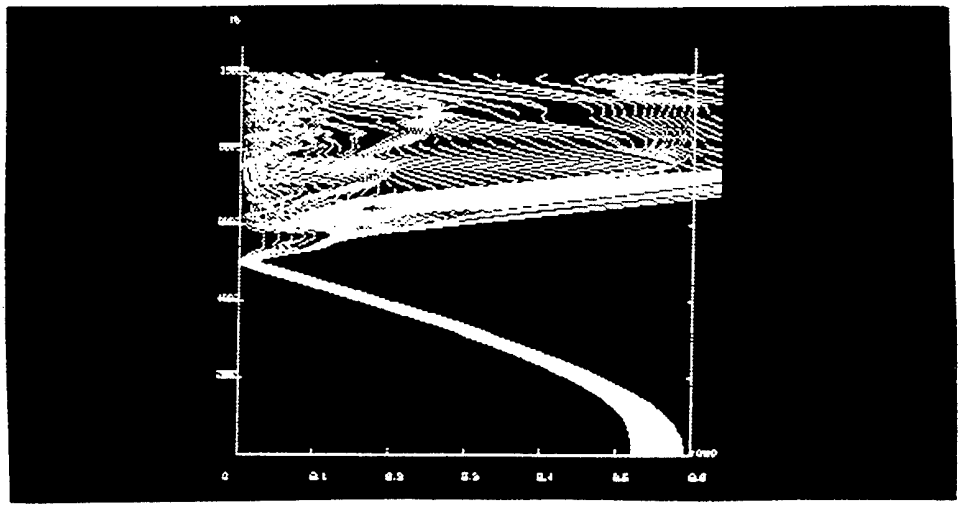

Figure 6. Stream lines of fuel layer.

The spherically non-symmetric effects are given for the pusher pressure p on the outer surface of the fuel layer and the thickness d_{th} of the initial fuel layer as follows.

$$p = p_o(1 + c_p \cos a\theta) \qquad (6)$$

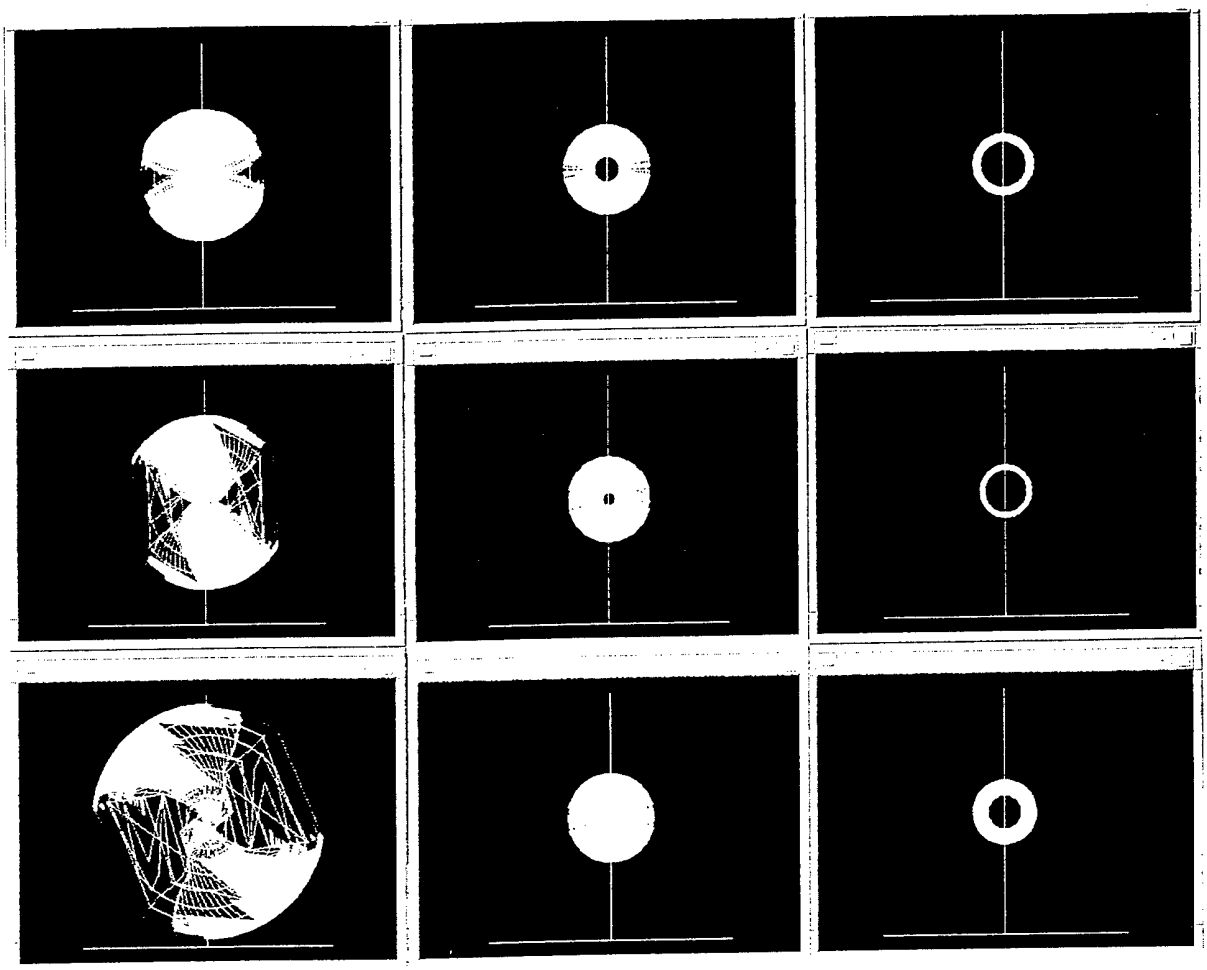

Figure 7. Ignition in the fuel layer

$$d_{th} = dr_o(1 + c_{th}\cos b\theta) \tag{7}$$

We can chose modification factors c_p and c_{th}, and mode numbers a and b.
A simulation result is given in Fig.6 and 7 for $c_p = 0$ and $c_{th} = 0$.

4. Summary

As stream lines in Fig.6 shows, the burning occurs soon after the fuel collides with each other at the center. But the place where ignition occurs depends the implosion motion. Some time ignition occurs at the center while another time ignition occurs at the boundary. At present the effect of non-symmetric parameters on fuel burning is not clear. More detailed investigation will be continued.

REFERENCES

1) Melhorn, T. A. 1993 Laser Interaction and Related Plasma Phenomena **10**, 553.
2) Cook, D. L. 1993 International Symposium on Heavy Ion Inertial Fusion (Frascati) 68.
3) Murakami, M & Meyer-ter-Vehn, J: 1991a Nucl. Fusion **31**, 1315.
4) Murakami, M. & Meyer-ter-Vehn, J. 1991b Nucl. Fusion **31**, 1331.
5) Tahir, N. A. & Arnolds, R. C. 1991 Phys. Fluids **B3**, 1717.
6) Tahir, N. A. & Deutsch, C. 1991 International Workshop on Laser Interaction and Related Plasma Phenomena (Monterey), 71.
7) Niu, K., Aoki, T., Sasagawa, T. & Tanaka, Y. 1990 Laser Part. Beams **12**, 85.

PLASMA-BEAM INTERACTION EXPERIMENTS AT TIT

M.Ogawa, U.Neuner, T.Endou, S.Yamauchi, M.Nakajima, K.Horioka and Y.Oguri
Department of Energy Sciences, Tokyo Institute of Technology,
4259 Nagatsuta, Midori-ku, Yokohama 226 Japan

1. Introduction

Interaction of heavy-ion beams with dense plasma is important as a fundamental process for heavy-ion inertial confinement fusion. It is a key issue to study an energy deposit rate of heavy-ion driver beams in a fuel pellet, which turns to a state of hot plasma. Theoretical works show a stopping power of $-dE/dx \propto (Z)^2$ where the equilibrium charge state Z of the projectile is governed by a balance of ionization and recombination. Theory predicts an enhancement of the equilibrium charge state Z, compared to cold matter, for the plasma with electron density of up to $10^{19}cm^{-3}$. The equilibrium charge state turns to decrease for the denser plasma with the electron density of $n_e > 10^{19}cm^{-3}$ because dielectronic recombination becomes significant [1]. On the other hand, the stopping power depends on energy of the projectile heavy ions in a low-energy region below MeV/u. The strong dependence on energy appears in the energy region where the velocity of projectile is close to the velocity of valence electron. So it is interesting to perform the interaction experiments for the dense plasma of $n_e > 10^{19}cm^{-3}$ and for the low-energy beam of E<< MeV/u.

Enhancement of energy loss in plasma has been first observed for an intense deuteron beam impinging on the plasma formed by the incident beam itself [2]. Further interaction experiments with heavy-ion beams have been extended by GSI and Orsay groups [3,4]. The GSI group has observed a significant enhancement of energy loss for heavy ions of $\approx$ MeV/u energy with a z-pinch discharge plasma target. The electron density of the z-pinch target ranges up to $1x10^{19}$ cm^{-3} [5]. Evolution of charge state of the projectile heavy ions has been also observed [6]. The Orsay group has studied the beam-plasma interaction for an expanding plasma formed by laser irradiation. Jacoby has revealed a dramatic enhancement of the stopping power for 45 keV/u Ar ions in discharge hydrogen plasma [7]. A precise plasma effect has been examined for a 1 MeV proton beam by ITEP group [8].

The 1.7 MV tandem at TIT generates various heavy ion beams suitable for the experiments of low-energy region. A laser plasma target is developed for the tandem beams. The laser plasma has potential as an effective charge stripper for intense heavy ions. We report our present status of the charge stripper experiments with the laser plasma.

2. Laser plasma target

A TEA CO_2 laser generates IR pulses of λ=10 μm with energy of 3 J. The laser pulse is composed of a fast component with a 0.2 μs width and a slow component with a decay time of 3 μs. Laser plasma is formed by irradiation of a polyethylene plate. The λ=10 μm light has a cutoff density of $1.1x10^{19}cm^{-3}$. Visible light from the plasma is detected by a photo diode to monitor the intensity of laser shots. The ablation rate is estimated by weighing the polyethylene plate after 200 and 400 shots. The number of ablating CH_2 molecules is determined as $9x10^{17}$ per pulse. This number is comparable with the order of $8x10^{17}$ atoms$\cdot cm^{-2}$ of a carbon stripper foil of 10 $\mu g cm^{-2}$. A spatial distribution of visible light is measured as a function of time using a

streak camera. Fig.1 shows an example of contour plots of light intensity at t= 0.4 μs after laser incidence. The figure indicates an expansion to a distance of more than 10 mm from the polyethylene surface. The electron density of the plasma is obtained by measuring Stark broadening of H_α and H_β lines as a function of time and space. The plasma emission is analyzed with a monochrometer of 25 cm focal length. The photo diode serves as a monitor of laser energy because the laser energy per pulse fluctuates shot by shot. This is because the TEA CO_2 laser is based on a high voltage discharge. Photomultiplyer signals of the monochrometer are normalized with the photo diode output intensities. The wavelength is selected in a step of 1 nm in the vicinity of H_α and H_β peaks and in a step of 2 nm in the region of tails.

Fig.2 shows spatial dependencies of the electron densities at t=1 μs. The abscissa z is a distance from the polyethylene surface and the parameter R is a radial distance from the laser axis. The electron density decreases as a power function of distance z between z=1 and z=10 mm for the data of off-axis R≠0. The curve for R=0 shows a similar decay with the curves for R≠0 between z=1mm and z=6 mm. It is noteworthy that the density keeps a constant level of 3 x 10^{16} cm^{-3} in the distance range of 9 mm to 30 mm for the R=0 case, i.e., on the laser axis. This fact suggests that the ablating matter is ionized by post-irradiation of the laser. The maximum density observed in the vicinity of the polyethylene surface is consistent with the cutoff density. Fig.3 indicates time dependencies of the electron densities along the laser axis for the different distances from the polyethylene surface. The time dependence of the density is weak between 1 and 4.6 μs compared to the spatial dependencies shown in fig.2. The long duration of light emission suggests that the dense plasma remains even at the tail of laser irradiation. Temperature of the plasma is evaluated from a ratio of peak to continuum for the H_α and H_β lines. The temperature exceeds 10 eV for the region of z<2 mm and decreases to several eV for the area distant from the laser focal point.

3. Experiments with the tandem beams

The 1.7 MV tandem at TIT is a 5SDH2 model of NEC. The plasma target is first tested as a charge stripper for heavy ions. Fig.4 depicts a layout of experimental setup. A Li^+ beam of 0.9 MeV is transported to a target chamber. The beam has a spot size of 3 mm in diameter. A typical beam current is 10 nA, which gives 6x10^4 incident ions in a time window of 1 μs. The laser light is guided to the polyethylene plate by a mirror and a focusing lens of f = 50 cm.The mirror acts as a steerer of the laser light. The lens is mounted on a linear motion base to adjust the distance between the ion beam and the polyethylene surface. A carbon foil and a beam viewer plate of Desmarquest are attached to the target assembly. The assembly is mounted on a rotary and linear drive for vacuum. The drive is used for fine position setting of the plate and for selection of the carbon foil and the viewer. The target chamber is evacuated to the vacuum of 10^{-7} Torr.

The outgoing ions from the plasma are analyzed with a magnet of ρ=25 cm. The charge stripped ions of Li^{++} and Li^{+++} deflected to an angle of 30 degree are detected with a plastic scintillator of 2 ns decay time. The scintillator is coated with an aluminum layer to shield the direct plasma light. Visible light from the expanding plasma is monitored with a photo diode. Signals of the scintillator and the photo diode are simultaneously recorded with a fast digital oscilloscope. The relative enhancement of charge stripping is to be estimated by comparing the stripping yields between the plasma and the carbon foils.

4. Conclusions

The electron density decreases as a power function of the distance from the polyethylene surface. Along the laser axis, the electron density is independent of the distance between z=9 and z=30 mm. This region is a good candidate for uniform plasma although the density is as low as $3x10^{16}$ cm^{-3}. The ions of Li^- from a sputter ion source must be intensified to improve the counting statistics. The present plasma contains a considerable amount of carbon ions in low-charge states. These not-fully ionized carbon ions interact with the incident ion beam nearly as neutral atoms. The problem of low degree of ionization can be solved by forming laser plasma of lithium or solid hydrogen instead of the polyethylene.

References

1 T.Peter and J.Meyer-ter-Vehn, Phys. Rev. A43 (1991) 1998-2030
2 F.C.Young et. al., Phys.Rev. Lett. 49 (1982) 549-553
3 D.H.H.Hoffmann et. al., Nucl. Instr. and Meth., B90 (1994) 1-9
4 C.Couillaud et. al., Phys. Rev. E49 (1994) 1545-1562
5 D.H.H.Hoffmann et. al., Particle Acc., 37&38 (1992) 371-384
6 J.Jacoby et. al., GSI-96-02 Report, 7 (1996)
M.Engelbrecht et. al., GSI-96-02 Report, 8 (1996)
7 J.Jacoby et. al., Phys. Rev. Lett. 74 (1995) 1550-1553
8 G.Belyaev et. al., Int. Symp. on Heavy Ion Inertial Fusion, Princeton, USA, 1995

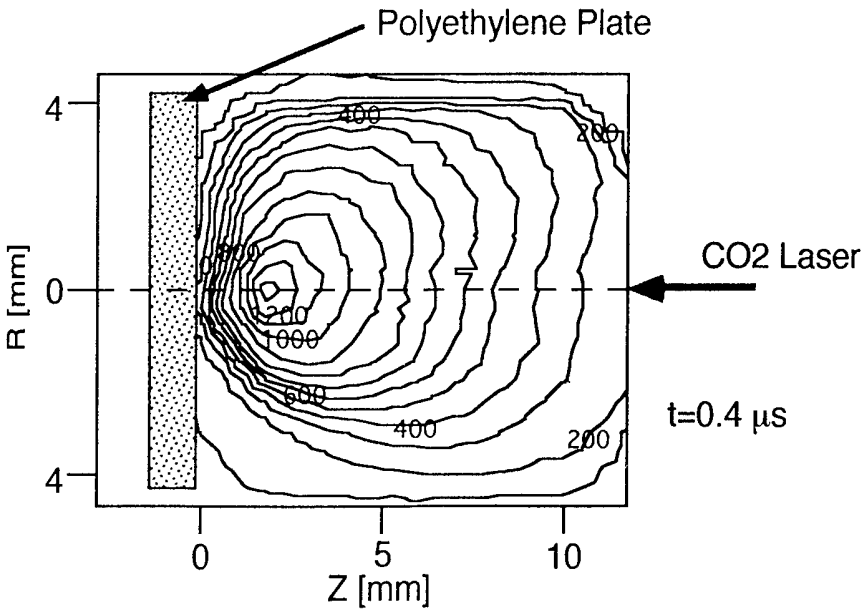

Fig.1 Contour plot of emitted visible light from plasma.

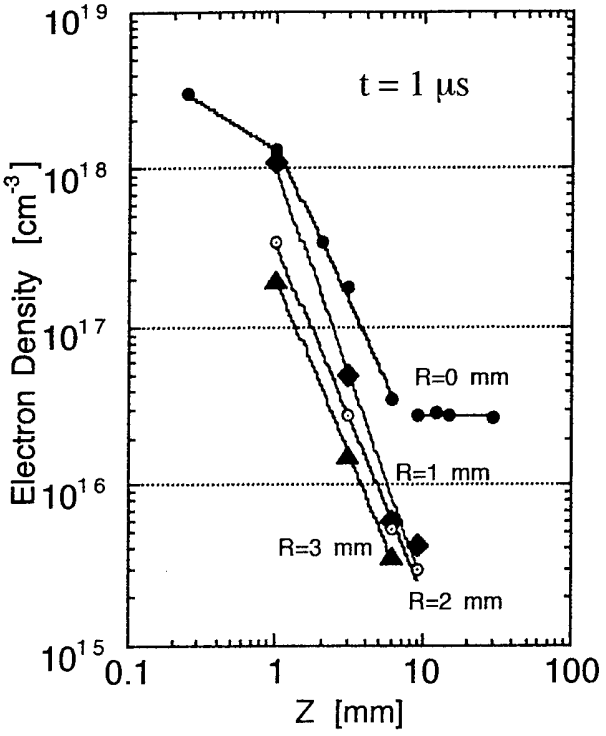

Fig.2 Spatial distribution of electron densities 1 μs after laser incidence.

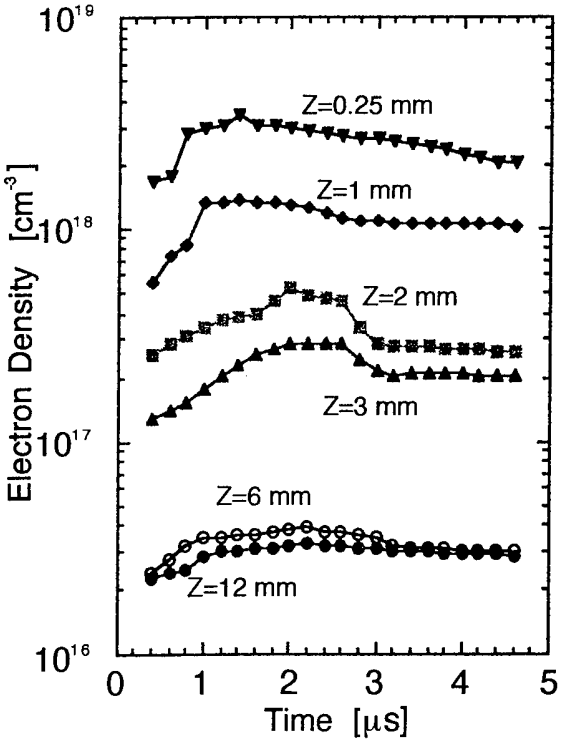

Fig.3 Time dependence of electron density for different distances from polyethylene surface.

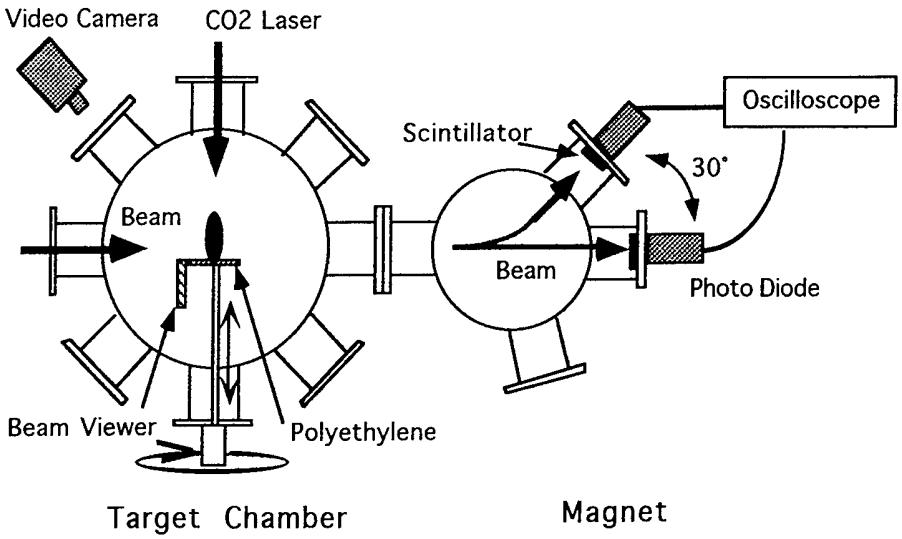

Fig.4 A schematic layout for charge stripping experiment.

THEORETICAL AND EXPERIMENTAL INVESTIGATION OF REB INTERACTION WITH AEROGEL TARGETS

V.P.Efremov,V.E.Fortov - *HEDRC RAN 127412, Moscow*
B.A.Demidov, I.A.Ivonin - *RRC Kurchatov Institute 123182, Moscow*
O.Yu.Vorobiev - *Institute of Chemical Physics 142432, Chernogolovka, Russia*
N.Keeler- *KAMAN Diversities Technologies Corporation, USA*

Abstract

In the present work recent results of luminosity measurements of aerogel targets (with density about 0.36 g/cc) irradiated with "KALMAR" beam are reported. The beam current was varied in the range 10-20 kA, the pulse duration was 80-120 ns and the electron energy was from 200 keV to 290 keV. Absorbed energy distribution in the deposition zone has been compared with results of calculations.

INTRODUCTION

Relativistic Electron Beams (REB) are widely used for investigation of thermodynamic properties of matter under pulse volume energy deposition. Among their advantages, compared to laser and heavy ion beams, is a relatively large and good predictable range of electrons in a hot material. That makes the theoretical analysis of such experiments more simple. The main advantages of aerogel targets compared to other materials are small density (large range of electrons) and the transparent material [1]. The first point makes it possible to eliminate the influence of rarefaction waves coming from irradiated surface. The second one allows to measure the luminosity distribution along the energy deposition zone placing the recording device perpendicularly to the beam direction.

EXPERIMENTAL TECHNIQUE

The experiments were carried out on the KALMAR accelerator [2]. The samples of porous transparent dialectrical material with a low density (SiO2 -aerogel, ρ=0.36 g/cc) were irradiated by the electron beam. The light luminosity from the energy deposition zone was recorded after passing through an optical system (Fig.1)

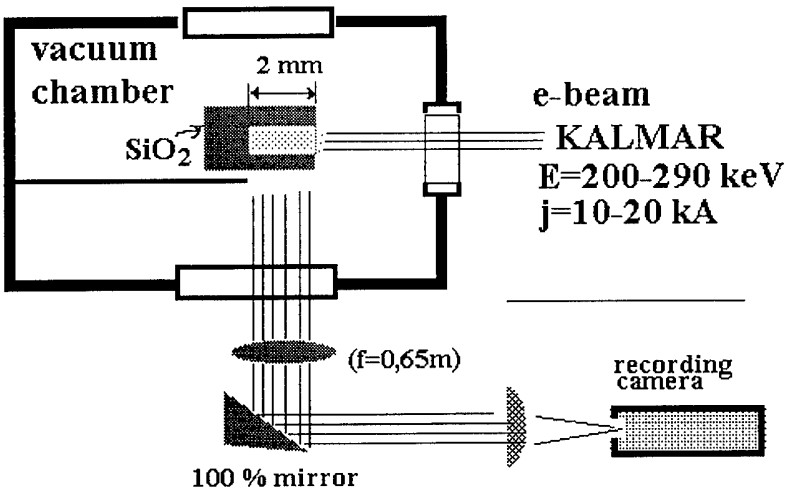

FIG. 1. Scheme of experiment

The beam radius was about 10 mm. That ensures a plane exposition of the sample.

RESULTS AND DISCUSSIONS

The results of experiments for two different regimes of the beam are shown in Fig.2-3. It is seen that the size of the energy deposition zone increases in time in accordance with the growth of the beam voltage and decreases after 60-90 ns when accelerating voltage falls down. In the case of break down regime shown in Fig.3 the drop of the beam current (when the time equals 60 ns) leads to corresponding decrease in luminosity. It has been found that the shape of the measured intensity curve does not depend on the size of the aerogel sample. Therefore one can neglect the scattering of the photons in the sample. The location of the maximum of the light intensity depends on the value of maximal voltage. The depth corresponding to the maximum intensity equals to 0.6 mm for V=290 kV and to 0.35 mm for V=240 kV.

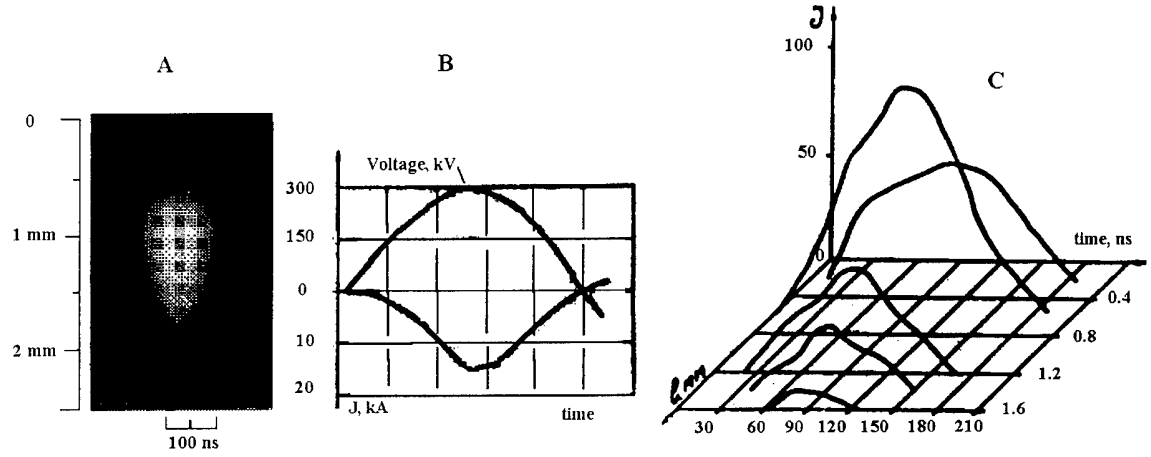

FIG. 2. Camera recording (**A**), oscillographs of current and voltage of electron beam pulse (**B**) and the measured intensity profiles (**C**) for usual regime.

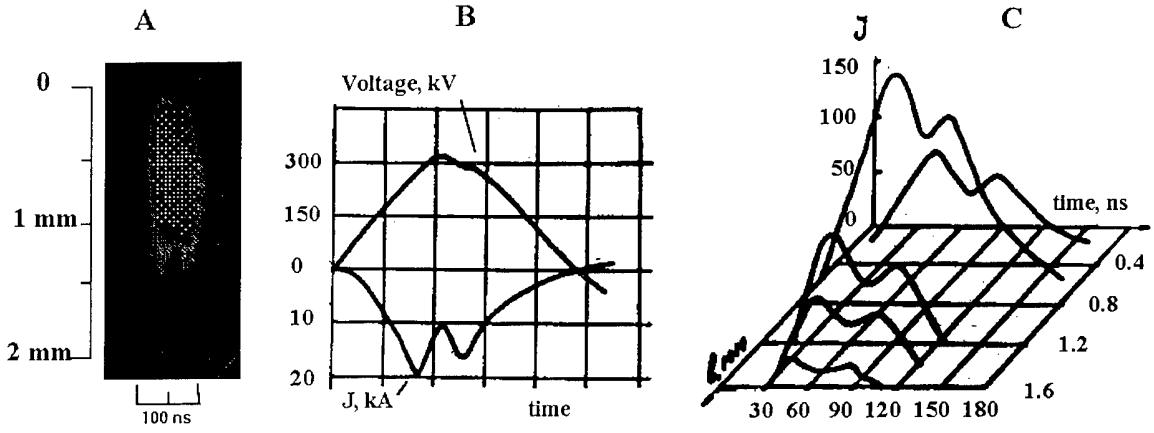

FIG. 3. Camera recording (**A**), oscillographs of current and voltage of electron beam pulse (**B**) and the measured intensity profiles (**C**) for break down regime.

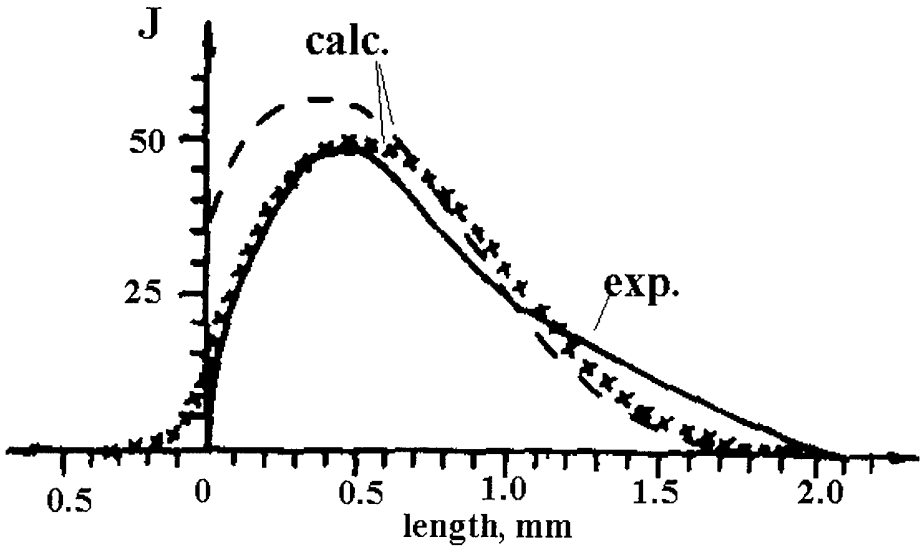

FIG. 4 Calculated energy deposition distribution inside aerogel sample together with the measured distribution of the light radiation intensity (solid line).

Figure 4 shows the comparison of the experimental measurements of radiation intensity with calculations of the beam energy deposition. The dashed line gives the distribution of a monoenergetic beam with 290 keV electrons calculated using semiempirical formula [3]. The crosses are the result of Monte-Carlo simulation of the beam energy distributed inside the target [4]. Both calculated curves give rather close values of maximum. One can conclude from this comparison that there exists a direct correlation between the distributions of the deposited beam energy and the light radiation intensity

CONCLUSIONS

1) The light radiation intensity of aerogel is proportional to the current of the electron beam in all investigated regimes.
2) The measured light radiation distribution along the energy deposition zone shows a good agreement with the predicted one based on the energy deposition curves.

These experiments may be used both as a beam diagnostics tool and so for the investigation of the response of a dense nonideal plasma to bulk energy depositions.

REFERENCES

[1] Burchell M., Thomson R. Bul. of the Amer.Phys.Soc, **40**(6)(1995) 1409
[2] V.E.Fortov, V.P.Efremov et al. Shock compression of condensed matter 1991, Elsevier Science Publishers (1992) 833
[3] T.Tabata and R. Ito, Nucl.Sci.Eng.**53** (1974) 226
[4] A.F.Akkerman, M.M.Basko, B.A.Demidov et. al Application of high--current charged particle beams in dynamic high-pressure physics IChPhCh Preprint 1986, Chernogolovka

PANEL DISCUSSION, June 14, 1996

Contributions by Gerald Cooperstein, Hans Bluhm, Hans Karow, Jeff Quintenz, Dmitri Ryutov, Gennady Mesyats, Valentin Smirnov, Ravi Sudan

Minutes taken by the Conference Chairman Karel Jungwirth

Panel Discussion

Karel Jungwirth:

Ladies and gentlemen, dear colleagues. Before we start the panel discussion I would like to propose the idea that each of the parnelists will stress some most important from his point of view points connected with this conference or, may be, also in a broader sense. Each of them will have five minutes, seven minutes at maximum, and then if anybody from the audience would like to comment or feel that there is something important to say to the conference he or she will be entitled to do so.

To begin with, I would like to ask our colleague Gerry Cooperstein to give us a brief summary of his feelings about this conference as a whole, in comparison to the previous conferences. Please.

Gerald Cooperstein:

Dear colleagues, I have the great pleasure of being asked to compare this conference to previous BEAMS conferences. Because I am one of the people fortunate enough to have attended all the BEAMS meetings, starting with the 1975 meeting in Albuquerque, then four more in the U.S., two in Novosibirsk, and one each in France, Japan and Germany, I am in a good position to comment on how well this meeting has held up to the tradition of all the previous BEAMS meetings.

I must admit that during BEAMS92, when Pavel Sunka and Karel Jungwirth proposed having the Institute of Plasma Physics sponsor BEAMS96 in Prague, several members of the BEAMS International Advisory Committee had concerns. We were unsure of the political stability of the then Czechoslovakia, and we were unsure if the Institute of Plasma Physics had the resources to maintain the fine tradition of the BEAMS meetings.

Fortunately, the attractiveness of Prague as a location, and the confidence of Karel Jungwirth overcame our concerns. In retrospect, we are now all very happy that we accepted the offer of the Institute of Plasma Physics. First, the new Czech Republic is clearly at the forefront of all the former Eastern Block countries in leading the way to democracy. Prague, besides being a very beautiful city, is an exciting places to visit at this point of history. The BEAMS community is fortunate to be part of this new revival. Second, the Institute of Plasma Physics, through the leadership of the conference co-chairman, Jiri Ullschmied, has done an extraordinary job of making BEAMS96 one of the most memorable and successful conferences of the series. In addition to offering us an excellent first class technical program, I want to make particular note of the fact that they have brought our meeting into the modern world through the extensive use of e-mail, FTP and a home page on the World Wide Web. I am sure that every participant appreciated the ability to have up-todate information, to be able to submit their abstracts electronically, and to get very quick feedback on the make up of the final program. Even more incredible was their ability to put all of the abstracts up on the Internet long before the conference, even those abstracts that were not submitted electronically but were submitted by regular mail. It was very useful to all of us attending here to see the abstracts ahead of time.

Jiri Ullschmied has prepared for me some statistics *(see page 1289 of this Proceedings)* about the meeting, to share with you. First, if we look at the total attendance of the last five BEAMS meetings from 88 to 96, excluding BEAMS92 which had a very large number of people attending from the Washington area, we see that BEAMS96 had a larger attendance (308 people and 435 abstracts) than four of the previous five meetings. In fact, the slope of the

attendance curve is positive. This fact is very encouraging, because most of us perceive that the funding in our field is diminishing. Second, if you look at the detailed attendance breakdown, we note that almost twice as many of our colleagues from the former Soviet Union attended BEAMS96, than attended any of the previous BEAMS meetings that were outside of their country. In fact, almost many have attended BEAMS96 as attended the BEAMS90 meeting in Novosibirsk. (104 at BEAMS96 and 150 at BEAMS90). We must thank our Czech colleagues for encouraging this FSU participation.

Before allowing my distinguished colleagues to present their impressions about the technical content of the meeting in each of their areas of expertise, I must take this opportunity to make some general comments in areas in which I am particularly concerned. I believe that some of the most exciting new results were presented in the z-pinch area, especially the recent Sandia results using a very large number of wires. In the ICF area, there has been a major increase in understanding diode physics. I must remind you that, even though ions still have a long way to go and z-pinches are already achieving exciting hohlraum temperatures, only ion beams offer the promise of stand-off that is required for an ICF reactor. In both areas, the diagnostics have become more and more sophisticated, leading to improved understanding of both the ultimate potential and the problems in achieving that potential.

I am also happy that there are still major machine-building programs at Sandia, at the Defense Nuclear Agency supported laboratories, at the French laboratories, and in the FSU. I am especially pleased that there is a growing number of application papers presented at this conference. Both of these facts are good signs for the future of our field and the continuing success of the BEAMS meetings. Thank you.

Thank you very much Jerry and now I would suggest that the panelists speak briefly, five minutes, six minutes at most, in the alphabetic order to support the new image of the Czech Republic as a democratic country. So, please, our colleague Bluhm first.

Hans Bluhm:

Before I start my summary in two of the fields that have been covered by this conference I would like to add some more general remarks to those which Jerry just made. These remarks which I want to make are somewhat more skeptical than his ones, but this is my personal view. My impression is that the BEAMS conference is now a well established conference, where I meet friends that I know already since more than fifteen years, but unfortunately I do not meet too many new faces here. Also my impression is that the enthusiasm that was carrying previous conferences has somewhat decayed. This became also obvious in the audience which in some of the oral sessions broke apart. I did not find too many exciting new ideas, and I think this development is becoming especially visible in the field that I am now going to report on first: in the field of intense light ion beam production.

All major programmes that have been contributing to this field got cutbacks. At Sandia we see a reduction of the light ion beam programme and this has also occurred in Germany and at ILE Osaka in Japan. This may raise the question whether light ions are still a serious candidate for a high-gain ignition facility. We should ask ourselves the question, why did these changes occur and how can we reverse this trend. Are we a victim of the general budget constraints, or is it a result of our attempt to overrun unresolved fundamental physical problems in the field by ever larger machines, or did we meet any general physical limitation that prevents or slows down further progress? I think each of these three possible explanations is correct to a certain degree.

This conference, however, has also shown that by going back to work on the basics of intense ion beam production, that means to work on the source and divergence problems, as

well as on the operational stability of our diodes, and to attack the transport of intense ion beams, can advance the field again. Important steps have been made into these directions, I think, in all labs. I would like to mention especially the experimental achievements that have been obtained at Sandia by Alex Filuk and others, but also at Cornell University by John Greenly and others, which rely on better diagnostics, and these diagnostics to a large degree have been stimulated by Yitzhak Maron and his group, who also during this conference made some very good contributions.

The achievements in our understanding of the basic physics of light ion diodes are also based on the theoretical progress that we have made. And I would like to mention especially the analytic theories that have been developed by Mike Desjarlais and also by Alexei Gretchikha. Many of you know that the light ion beam programme is given another period of about two or three years. As I understand this is true for our programme in Germany, but it is obviously also true for the programme in the United States. And the question is, is this time really sufficient, will we be able to improve our knowledge enough to give definite answers to all these problems? And the second question: is this time enough to investigate those ideas which came up rather late - I mean two-stage diodes and self-pinch transport which just have been started to be investigated.

The second subject I would like to report on are the beam-matter-interaction experiments. I think the presentations of Kurt Baumung, Balbir Goel, and Holger Marten, but also of Professor Fortov and the Sandia group show that intense ion beams can even with their present performance contribute to our understanding of non-ideal plasma. However, we are in competition with other methods here, and the question is what can light ions or soft x-ray sources do better or cheaper than already established techniques like lasers, gas guns, wire explosions and so on. And the second question that we should try to answer is, who are our customers, i.e. who is interested in these results and who needs them.

Although I observed a certain decay in intense light ion beam research a new field has come to light: Especially during this conference a large number of contributions dealt with ion and electron beam applications. In 1988, when we in Karlsruhe hosted this conference, there were nearly zero percent of the papers addressing this area. During this conference about 20 % of the papers were in this field. Many of the applications were with electron beams, this may be because it is easier to produce large-area electron beams than ion beams, and I would like to mention the contributions here from Efremov Institute, from Tomsk, and from Karlsruhe, too. Ion beam surface treatments are already approaching industrialization. We have heard that a company has been founded, and Dr. Neau and others from Sandia and from this company - Quantum Manufacturing - have reported on their ideas.

I would like to suggest that if this field shall become an important established new field in the BEAMS conferences, then we must also attract solid state physicists and material scientists, and I propose that the organizers of the next conference invite well known experts from this field to begin the dialogue. Of course we all know that commercialization of these ideas needs inexpensive, efficient, reliable and small-size generators. And the key component in these generators is always the switch. Magnetic switches may be O.K. for short pulses, but for long pulses they may become too large. And, therefore, I think the semiconductor opening switch that is being developed in Ekaterinburg and was presented here by Dr. Rukin from Professor Mesyats group is a promising candidate for a switch in such a facility.

O.K., I think this is all what I would like to add to the conference summary.

Thank you Hans for your introspective and sometimes also a bit alarming ideas. I am sure that self satisfaction would be the worst approach we could apply to our own field. And

now, I would like to ask Hans Karow who is perhaps going to say us a few more optimistic ideas or even mention perspective possibilities concerning the future of our fields of interest.

Hans Karow

Thank you, Chairman.

The future prospects of the research areas of the 'BEAMS Community' as present at this conference is a most pressing question, and I would like to contribute to this discussion not only from my view point as a member of the 'Beams Community' but also from my European view point as a Secretary of the European Science Foundation.

The present scope of the BEAMS conference series comprises, as I understand, science, research and applications in the areas of nuclear fusion processes - in particular civilian research on the ultimate goal of controlled inertial confinement fusion for electric power generation by means of pulsed particle beams or electromagnetic pulsed power devices. Besides that, the Beams conferences are a forum for pulsed power research for medium energy density applications.

With regard to the goal of inertial confinement fusion, the R&D community was split in the past decades into civilian R&D laboratories and military-driven laboratories. At least the civilian R&D community suffered rather heavily from this divided situation and the classification practised on the side of military R&D on inertial fusion.

It was a tremendous development when in December '93, after the end of the cold war, there came the official declassification act from the US government concerning R&D on inertial confinement fusion for civilian application.

Consequently, in May of this year, the European Science and Technology Assembly (ESTA) in Brussels, (consisting of 100 senior representatives from all fields of science and industry in Europe), which is an advisory body to the European Commission installed an ESTA Working Group of which I was the Secretary to analyse the situation and to report to the Assembly. The main recommendation of this report was to implement within the European fusion programme a component on inertial confinement fusion which, at its starting phase, should cover approximately one tenth of the total programme's financial volume. The main reasons for a substantial onset of ICF research in Europe were stated to be: (i) the scientific status and prospects of ICF are at a comparable level with magnetic confinement fusion; both approaches are still in a science & research phase - not in a technical phase, and the question cannot yet be answered which concept(s) may succeed in the long term; (ii) international collaboration, the *sine qua non* of large R&D projects, now is no longer impeded by classification. These were the main points in ESTA's report and recommendations forwarded to the European Commission which is co-ordinating controlled nuclear fusion research in Europe.

The ESTA report and recommendations raised very strong responses and even reverberations in the European scene of fusion research and R&D policy.

First, at the European level, the European Commission appointed (for the second time) a review panel with the task of reviewing the status and prospects of the current European R&D programme on controlled nuclear fusion. In addition, for the first time the European Commission installed for the first time a co-ordination committee for research into inertial confinement fusion research. The European Science Foundation, in conjunction with the ESTA recommendations, intends to undertake an exploratory ESF Workshop in order to discuss and formulate the possible R&D content of a first phase of an ICF programme co-ordinated at the European level. At the national level in various European countries, research

councils and governmental administrations are at present intensely debating the issues of controlled nuclear fusion research.

Secondly, in recent weeks there has been a strong echo in the scientific press - in NATURE and other upper journals - as well as in the public media, with many positive comments on the ESTA approach.

Thirdly, there is an increasing response to the ESTA recommendations from the science and research communities in Europe - inside and outside nuclear fusion. Besides agreeing statements, one experiences some strong resistance to ESTA's endorsement of ICF from parts of the MCF communities, in particular from representatives of the ITER project. These critics deny ESTA's statement that (laser-) ICF and MCF are equally advanced along the route towards an ignited and self-burning fusion plasma (as measured by the triple product of density, temperature and confinement time). This argument, I think, can be ruled out on scientific grounds. However, the critics against ICF research still maintain the old policy argument that any onset of ICF research in Europe would still be impeded by the fact that no official declassification of ICF research has been declared in Europe. Also this claim has been ruled out by reality as proved by the publications on formerly classified ICF subjects by European authors in recent years - also at the BEAMS '96 conference. However, a formal declassification statement from the UK and French government, equivalent to the one by the US government in 1993, could indeed be most helpful to terminate such formal debate.

However, also within the fields of ICF research itself and due to the limited funding resources, we see fierce competition at the national level between the different driver communities.

This brings me back to the initial question of the prospects of the 'Beams Community'. We have just heard from senior conference observers that, at first glance, the outcome of BEAMS '96 could lead us to be optimistic but not too much so. The 'BEAMS community' should undergo realistic self-critics when self-evaluating its own R&D progress so far achieved.

With regard to the ambitious and far-ranging goals of controlled inertial confinement fusion, we have to realise that the high-power particle beams community (with its various ion beam disciplines) is in continuing and heavy competition with the high-power laser community and its various disciplines. I also share the opinion of my colleague Hans Bluhm on this panel: the particle beams community will have to try much harder in the race towards achieving R&D milestones. These are in the near-term: feasible and cost-efficient schemes and proof-of-principle experiments for the repetitive generation, transport and focusing of particle beams (ion beams), and for the deposition of such beams of high power density and pulse energy on target; economising of experimental facilities and work; feasible concepts for ICF reactor schemes; demonstration of valuable spin-off of ICF research for other fields and for technical applications.

In trying harder, we should recognise the fact that the comfortable times of strategic fusion research on its own are over. Under today's financial constraints for science and research at the national and international scene, both magnetic fusion research as well as inertial fusion research are subject to open and heavy competition with the whole spectrum of medium or large R&D projects in the physical sciences and energy research. Hereby we face the fact that research councils and governments are increasingly worried by the 'difficult dimensions' of nuclear fusion which is considered to be complex, big, long-term, expensive, high-risk R&D, needing international collaboration and co-ordination, and aiming at nuclear energy generation. Fusion research is therewith subject not only to the 'usual' risks of ambitious and complex R&D subjects but also to political uncertainties. To win this battle

will need all the skills, 'pulsed power', and energy of the 'BEAMS Community' and, last but not least, its coherence and solidarity.

Thank you, Chairman.

Thank you Hans for your interesting information and also for your fighting in the interests of this community. I think that your words were so stimulating that when coming home everybody, after relaxing here in Prague, will start to make everything to increase the chances of winning the battle. Thank you. And now I would like to ask Jeff Quintenz to - actually I am really glad that at the very final moments of the conference the audience hall is almost as full as it was during the opening ceremony, so taht we can perhaps afford now to hear several words about hohlraums.

Jeff Quintenz:

Yes, thank you. Professor Jungwirth asked me to share five or ten minutes worth of wisdom on hohlraum heating. I agree to confine myself to five or ten minutes, but am not sure I have enough wisdom to fill the time slot. I will try it in any case.

As you heard earlier in this conference, both ion beams and z-pinches have now been used to heat hohlraums. Using light ion beams, we have achieved greater than 60 eV in a rather large hohlraum, producing approximately 1 TW of x-rays. I confine myself to talking about using pulsed power drivers to heat hohlraums. Hans Bluhm has already mentioned the progress in ion beam driver development, and Valentin Smirnov will talk about the developments in z-pinch drivers. The results of these ion beam experiments have been, to my belief, to establish the proof-of-principle of using intense light ion beams to heat hohlraums, with no surprises in the interaction of those beams with matter. The intensity, however, of these beams is limiting the experiments that we can perform with these sources today. And so more progress will be required in focusing and transporting light ion beams before we can make much more progress in utilizing these beams to heat hohlraums and drive capsules. That is not to say, however, that they are not useful today to do ICF relevant experiments. In particular, we heard at this conference about some beautiful experiments using intense light ion beams to drive shock waves in matter, for equation of state studies.

In the area of z-pinch driven hohlraums, the achievement of 85 TW and greater than 400 kJ of x-rays from a z-pinch and then putting these sources within a hohlraum and heating the hohlraum to somewhat in excess of 85 eV, I believe, is a break through. The application of these z-pinch driven hohlraums is immediate. In the ICF programme we are using these hohlraums as very well characterized sources for x-ray driven materials studies, materials that are being selected for fusion capsules today, and I think that the diagnostics which are developed in parallel with these source developments are actually putting the field of pulsed power research in a very favorable position for continued rapid progress. The unique contribution of these sources, the fact that we can today heat very large volume hohlraums for very long times, has put us, for the first time, in a good position in the healthy competition between pulsed power and lasers for inertial fusion. We now have a driver, that is actually the driver of choice for many experiments in ICF. This is a first. We are no longer just tolerated by our laser friends, we actually have a source that they find valuable in the science of inertial fusion. So I believe personally that we are on the verge of something very significant. I don't share my colleague Hans Bluhm's pessimism today. I think the future is very bright and I look forward to new facilities around the world, in particular close to my home, the PBFA-Z accelerator, which will be fired for the first time this summer, promises to extend the power and energy in x-rays to unprecedented levels. We already have the most power in x-rays ever generated in the laboratory and we look to extend it significantly in a very near future. So, for

ICF, I think, the application of our field is going to be a growing one, with very significant events in the near future.

If I move on very briefly to more general comments, I need to address the issues of break-throughs and budgets. Everyone has talked about budgets, some have talked about break-throughs. As I said, I think this is a very exciting time, but our excitement must be tempered with the realization and reality that we live in, that budgets are constrained and unlikely to get less constrained in the near future. This forces us to think differently. First, we must recycle. We are recycling our facilities: PBFA is being used to drive z- pinches and ion beams. There are other examples of facilities which have been modified for multiple applications. Second, we must innovate. The new ideas like fast Marxes and inductive energy store to produce more capable pulsed power facilities at lower cost, are necessary to continue the rate of progress. And third, we must team. Teaming is a requirement, it is not a luxury. And I see at this conference, in particular, many papers from multiple institutions, and in fact from multiple countries - and that is a very positive development - and I think it in large measure has contributed to our success to date.

So, the technical progress to me has been very exciting in many areas of our field. I think the future is bright. I am personally very excited, and I think that we are entering an era where the capabilities of our experimental facilities are advancing rapidly; the diagnostics we have are advancing in precision and capability - for the first time we are able to look with great spatial and time resolution, inside these very extreme environments; we are benchmarking our ever evolving computer codes. We have in the near term, very powerful computers coming on line on which to run our 3-D simulations, and to close the cycle, to develop simple models which, I think, will ultimately demonstrate our understanding of these complex processes. I see all that advancing very well and, again, I look forward to a very bright future.

Thank you Jeff. And now let me say a few personal words: During the last six years a lot of things changed. The importance of declassification was already mentioned by Hans Karow and I believe that we are going the right way also in other aspects. Many people whom I knew ten years ago only by their names from publications are now my personal friends, as are those I have known from the very old times when we all were extremely young. One of them is my old friend Mitia Ryutov and I am glad that I can ask him now to say several words and add some comments.

Dmitri Ryutov:

According to instructions given to me by our Chairman, Dr. Jungwirth, I will discuss the studies of beam-plasma interaction, experiments on plasma heating by E-beams, the issues of the microwave generation and, at the end, will make some comments on liner stability.

Beam-plasma interactions have always been one of the key elements of basic plasma physics. It is very good that our community contributes to these studies in a significant way: this underlines an importance of our research in a broader context of plasma physics, physics of non-linear phenomena, and physics (and astrophysics) in general. These studies appeal to wider circles of the physics community, they show a high intellectual potential of our field of research, raise feeling of respect, if you wish.

At this conference, there have been several papers describing beam-plasma interactions: from Kanazawa, from Novosibirsk, and, finally, very nice papers from our host Institute - Institute of Plasma Physics at Prague. What was remarkable in these papers compared to the earlier ones, was a high quality of optical diagnostics used for the measurements of microturbulence. The general environment of these experiments, with their

intense electromagnetic noises and high level of x-ray background, is very hostile to fine measurements. Still, the ways have been found to circumvent these problems and optical methods of studying plasma microturbulence are now in a wide use, producing information in an almost textbook fashion. I probably should mention here the name of Dr. Kruglyakov from Novosibirsk, who contributed a lot to the development of these techniques.

And, no surprise, some puzzles that did confuse researchers for many years, in particular, that of a Langmuir collapse in a magnetic field, were solved in these measurements. I think that the same techniques might probably be employed also for the measurements of electromagnetic fields in microwave generators; at least the techniques based on the spectral measurements can be used for these purposes.

Then, directly related to this basic science research, are the works dealing with the plasma heating by E-beams in solenoids. Again, these works have been done in Novosibirsk, in Prague, and in Kanazawa. The main accomplishment is that, at least in one experiment (Novosibirsk), they have reached the level of 300 kJ of the injected beam energy and have not noticed any degradation of the efficiency of plasma heating (Dr. Koidan's talk). In fact, the efficiency increased and it is now probably 25%; the corresponding plasma parameters are quite impressive.

Fashions change in fusion research, but I think that this approach still has some fusion potential and we will see what happens within coming few years. But it is also interesting that this research has important spin-offs. In particular the Novosibirsk facility GOL-3 can be used as a UV generator, both as a flash lamp, and as a laser; the work on the heating source for the GOL-3 facility gave rise to the development of high power, high quality ribbon beams that can be applied for microwave generation; GOL-3 is intensely used for tokamak disruption simulations.

Now I switch to the issues of microwave generation. What impressed me here most was the progress in relativistic klystron research, as reflected in the paper by Dr. Friedman, including very high efficiency reaching 50%. The other important development was a better understanding of the pulse-shortening problem - some order has been finally brought into it, as was very nicely presented here by Dr. Benford. Then, we saw that a number of concepts and variety of configurations used in pulsed microwave experiments has grown considerably. The configurations include cylindrical and annular beams, with singly and multiply connected structures, plasma annuli enclosing E-beams, ribbon beams, and many others. All of them have a promising future. Of some concern, I think, is that there are not too many customers, at least to my knowledge, so it would be very important to try to better identify who are these customers, and may be to look for new applications. Otherwise, the lack of customers may become a major problem on the way of development of these systems.

A few comments about the Rayleigh-Taylor instability and the liner instabilities in general. I would like to emphasize that one can expect a very strong stabilizing effect of rotation and of shear flow on Rayleigh-Taylor instability of imploding liners. And, what is more important, there exists a very flexible technique allowing one to generate rotation and/or shear flows. And what is probably even more important than that, is that even if the system is unstable with respect to the Kelvin-Helmholtz modes (shear flow modes), still the shear flow may produce a considerable slowing-down of mixing caused by the Rayleigh-Taylor instability. The reason for this is that the perturbations generated in these two instabilities have very different structure.

The Rayleigh-Taylor instability produces familiar bubble and spike perturbations, strongly stretched in the direction of the effective gravity force. Perturbations produced by the Kelvin-Helmholtz instability are the vortices with much more rounded shape. They may

effectively destroy the rapidly growing spikes. Also important is that the width of the mix layer between the heavy and the light fluid in the Rayleigh-Taylor case asymptotically grows as the time square, while in the Kelvin-Helmholtz instability the mix layer between two fluids with different tangential velocities grows only linearly with time. All this is just a reflection of the fact that these two instabilities are very different in their nature. It may well happen that the pre-existing Kelvin-Helmholtz instability excited near the liner surfaces will be beneficial for the better performance of the pinch.

Although futurology is a very risky endeavor, I take a risk of making one prediction: in the coming two years we will be witnessing a great progress in the understanding of liner performance, including very difficult issues of stability and mix. The basis for my optimism is, first, the existence of a large number of experimental devices complementing each other in terms of the information provided and, second, creation - in the course of years - a rather detailed piece-wise description of the processes involved. I have a feeling that these pieces of theoretical understanding, together with experimental results, will very soon get together to create a comprehensive picture of the liner implosion.

The other thing that I should mention here is that rotating liners and/or the liners with shear flows can be used for simulating some astrophysical phenomena, like turbulent momentum transport in rotating imploding stars, or turbulent generation of magnetic field. Maybe, we should look more closely on what we can suggest in this direction, again, with the idea of establishing closer links with a broader community of physicists.

Then, my final comment: I have heard suggestions that at the future conferences parallel sessions should be established. I think that it is in fact good that we do not have these parallel sessions, because this brings a spirit of unity to our group, and if we separated the microwave people from the ion beam people, and those from the Z-pinch people and so on, and so forth - well, it would work, because the separate conferences for each of these areas of research already exist, but this particular, BEAMS, conference would lose much of its charm. The opportunity of cross-fertilization provided by the BEAMS conferences is a very valuable asset of our community and we should preserve it.

Thank you very much.

Thank you Dmitri. And now allow me to ask our colleague Mesyats to say several words.

Gennady Mesyats

I would like to say a few words about high-power microwaves. During this conference, we listened to many interesting new results in high power microwave area. First results to be mentioned are, may be, the soft radiation from very short electron beam, a few highly elliptical circular beam investigations of Ekaterinburg and Nizhny Novgorod, and very interesting results using ribbon electron beam of microsecond duration for high power microwave radiation in Novosibirsk Nuclear Institute - Dr. Arzhannikov, and may be one of interesting results from All-Russian Electrotechnical Institute from Moscow - Dr. Zavyalov - continuous microwave radiation using low energy electron beam and plasma-filled diode. And many interesting results have bee reported on high power microwave hundred-nanosecond radiation from New Mexico University, Texas Technical University and so on. According to my opinion, this area of investigation at our conference is very good, too.

Furhter, may be a few words about industrial applications. Industrial application of ion beam and electron beam for modification of materials, for modification of metal, dielectric and so on - investigation from Sandia, Los Alamos, Ural, Siberia and so on.

Finally, I would like to add a few comments about collaboration. Very interesting: In this Book of Abstracts we can see many articles, many papers with authors from different

laboratories from several countries. Evidently, in all countries, separate laboratories have just limited money for investigation, and for investigation of high power particle beams in particular, and they are forced to collaborate. As a result of this collaboration, many reports at this conference are joined investigations from former Soviet Union Republics, from France, United States, China, and so on.

At the end of my talk I would like to express my thanks to the Local Organizing Committee. The Russian delegation was very big, the biggest delegation at the conference - more than hundred people - and the Local Committee and the International Committee did a lot to support our group. This conference, I think, was organized very well. Thank you very much, Karel, and many thanks to all our colleagues from the Academy of Sciences of the Czech Republic.

Thank you very much. Now allow me to introduce our colleague Valya Smirnov.

Valentin Smirnov:

Thank you very much Karel. I recall first BEAMS conferences were completely devoted to pulsed power for beams production, beams physics, microwave generation and beam-matter interactions. Now we have met a different situation. Z-pinches started to be a very important part of our activity. In some the present name of the conference is in contradiction with its content.

I think at this conference z-pinches as an ICF relevant source and source for basic application is formulated finally. And in this sense I would like to congratulate my colleagues from Sandia with bright results on very powerful soft X-ray radiation from multiwire arrays. During this conference we got some new results of previous scheme of z-pinch using for ICF and for other application. I mean the double liner implosion scheme developed in TRINITI, I mean very interesting results of complex z-pinch presented for instance today by Bernard Etlicher, and I mean the new ideas and new developments of scheme of Rudakov from Kurchatov Institute.

Also, there are some interesting papers about small-scale z-pinches, which we could see here - for instance some new results of small pinches given us by paper of Dr. Kubes - the development of neck instability. I think that all results give us very good optimism in the future development of z-pinches as drivers for different basic and science applications. Personally I have been impressed by the picture shown by professor Chernyschev, with quasi-spherical liner compression. This example proves we have more ideas that we could really test on our devices. The idea of using of quasi-spherical implosion is very attractive. We know that such experiment in the microsecond time scale has been done on Shiva-Star facility. It would be extremely interesting to develop this approach for nanosecond scale implosion of dense spherical plasma.

Very impressive results reported in this direction need further improving of theory and technology. I think that everybody agree with remark of Ravi Sudan that when going into the so high energetics z-pinches we should start a new physics of z-pinch. During this conference, we heard several ideas about stability of implosion, which just now have been mentioned by professor Ryutov. Clearly, further progress in the theory and code development is needed. Also, there is a lot of things that we should do in the experiment. I mean the production of very uniform, very controllable annular plasma shell for implosion, necessary for getting good results. So, for me field of Z-pinch physics is inexhaustible up to now, but following to the present fashion or present challenge we have to look for some industrial applications. I should mention that we do not see many papers in this direction. But it is known that z-pinch like discharge has a large potential for different kind of applications. Let me remind you some of

them. First of all, it is production of nanosized powder of metals and oxides. In this direction team of professor Mesyats made a lot. Just now this development started in Karlsruhe. In Fortov team some interesting phase transitions in solid were observed in Z-pinch discharge. In Russia several laboratories try to use wire explosion to modify the inner surface of the metal tubes for industrial applications. In our laboratory - Troitsk - one team is involved in the hardening of metal surface by implosion of gas-puff. They have also got some interesting results.

So, you see, Z-pinches are quite promising for many directions of basic research and application, and I think that during our next meetings we will meet new bright results. Thank you very much.

Thank you. An now, as you all probably feel, we are going to interconnect the both ends of this conference together. At the opening session there were four Czechs sitting here at the table, three of us were genuine Czechs and the fourth was - if you allow me to say it that way - a honorary Czech, and at the same time doyen of our community. It's a pleasure for me to express deep gratitude for the support of Ravi Sudan of our work here in Prague during all the decades. And I am very very very glad that I have the honour to introduce him as the last speaker of this panel discussion. Please.

Ravi Sudan

I have been given the singular privilege by Dr. Jungwirth to have the last word on the subject. But he qualified that by demanding that I speak about the future. Speaking about the future is very hazardous and my only comment is that the future is not a passive state waiting to happen, but is determined by the present. Therefore it is our enthusiasm or lack thereof for the things we do, that will determine the future.

Our field, or at least the fields represented in this conference, were nurtured by the needs of the cold war. The end of the cold war has had strong impact on these fields; some for good, and some not so good. For example, in the U.S. Department of Energy, the Office of Magnetic Fusion got its budget cut from 340 million dollars a year to somewhere round 240-million in one year. But every dark cloud has a silver lining. The silver lining in this case was that it initiated a strong re-examination of what we were doing. Many of the things that you took for granted have been brought under scrutiny; that is what is happening to the tokamak programme at the present time. The next step - ITER - is being brought under increasing scrutiny in the United States. The silver lining is that the science aspect of energy research has moved up by a notch. Through this process, we have gained a little at Cornell because we have got funding for an idea that has been around for a long time but was never really funded at a level to accomplish anything. So, that explains my enthusiasm and the enthusiasm of the Cornell team that is dedicated to ion ring research, of which I spoke at the very first BEAMS Conference and now at the eleventh Conference. So we, our little group, is very enthusiastic and I am sure other little groups pursuing other ideas would be extremely enthusiastic and the outcome of these studies may form the basis for future fusion research.

Now to get serious funding we must answer the needs of society. Although the cold war has ended, nuclear weapons have not disappeared, and they will still provide the momentum for a lot of work for a long time. People in this conference have realized that they also have to branch out into commercial applications, and several groups are looking into that, including professor Yatsui's, who is making a very strong thrust in that direction in Japan.

The other areas are energy and environment. Concern with energy is not shared by society as a whole, at least in the United States. They think - there are no energy problems. So, energy research in the United States is being maintained by the enthusiasm of scientists, not so

much by the perception of the public. Environment is another matter, there is a lot of enthusiasm from the public. And, therefore, that is an area we must explore. I was particularly impressed by Dr. Bowman's talk on transmutation technology which may have an application for environmental good. But the only point at which I would differ with him is that while I would accept the RF linac as a means for providing neutrons for the present, I think our community can come up with choices for accelerators that may be more economic in the future. This is just the sort of thing that we, as a community, should be addressing: to seek the possibility of cheaper, less costly accelerators, to do what the RF linac would accomplish.

Back to the energy area; in ICF I would like to be an iconoclast. I would like to ask questions now, that I might have asked thirty years ago. I share the enthusiasm for z-pinches, and they would perhaps be part of the solution for the nuclear weapon problem. But for energy, in ICF there is a stand-off problem that Jeff mentioned. And that is where you would need ions. Now, for ions there are two communities: there is the light ion community and the heavy ion community. And I personally don't see any reason for this division. There is a whole range of ions between hydrogen and uranium, and why should we concentrate on one or the other. The actual reason is that accelerators were available in these two limits. The heavy ion accelerator existed before any thought of ICF and the pulsed power technology provided light ions. But I think the optimum ion mass is somewhere in between. This is another area where we can show some imagination, to come up with accelerator ideas for ions in the region of Calcium, for instance. The currents required would not be as large as those required for lithium ions nor I guess, would the cost, perhaps, be as great as that for a heavy ion accelerator. That is an area where young people ought to be doing some serious thinking.

Then, there is a question of transport of energy to the pellet. For the laser people, there is no problem of transport. Zero charge photons can be focused easily. Actually they focus too easily and have to be smeared out to obtain uniformity over the pellet. We have assumed that charged particles should be focused the same way as photons, namely by lenses, and by free propagation. It may not be the way to focus at all. There may be another way of transferring energy in high ion beam currents to the DT pellet. That's an iconoclastic thought that the younger section of this audience may well ponder over. Why should a charged particle be following the same trajectory as a photon, because they have quite different properties.

So, there are fundamental questions still to be answered in our field, there are major needs of society that we could address. I have great confidence in the ingenuity of the people assembled here and I also hope that you can attract younger people to this field in the future.

Thank you.

Karel Jungwirth:

Thank you, thank you all dear colleagues. And everybody can check that it's precisely noon, precisely the time at which our conference is to be ended. I will thank, therefore, to all our panelists and I would like to ask my colleague Shiloh to join me here, and then also my co-chairman Ullschmied who did the most work and helped me for two years, to help me also with the closing ceremony. Thank you very much.

CLOSING CEREMONY

Karel Jungwirth

Dear colleagues, first of all allow me, please, to thank all of you for the hard work you have done in your laboratories when getting the new results and preparing the reports to this conference. I hope and believe that everybody has given us his manuscript so that we will be able to send you in time also the proceedings of this conference. Allow me, please, to thank, to express also our thanks to the stuff of this congress centre and especially to Mrs. Hanousková for the excellent job they did during the whole week. I haven't heard any complaints about services. And allow me to express my thanks also at least to the responsible persons from the Guarant Agency, the co-organizer of this conference - to Miss Benešová and Miss Podhorská.

And now I would like to have a few extra minutes to express my deepest gratitude to all the sponsors which have contributed to the success of this conference. Without their help we wouldn't be able to do it, and to prepare it as it was done and prepared including publishing and mailing you the proceedings of this conference. To have an idea about the total amount of money we got from the sponsors, imagine that it represents more than one third of the whole budget of this conference. Therefore, let me name the sponsors now:

I thank the **Sandia National Laboratory** - thank you Don Cook; I thank the **Office of Naval Research** - thank you Chuck Roberson; I thank the **European Science Foundation** - thank you Hans Karow; I thank the **Naval Research Laboratory** - thank you Tim Coffey; I thank the **Physics International** - thank you Charles Stallings; I thank the **Maxwell Laboratory** - thank you Roger White; I thank the **US Air Force European Office of Aerospace Research and Development** - thank you Vicky Cox.

And let me to mention explicitely that we have also our domestic Czech sponsors since it tells something about the new shape of the economy of this young new born state. I thank the **ČEZ,** which means the Czech Energetics Enterprises - thank you Peter Karas, I thank the **Energoprojekt Praha** - the Prague Projects of Energy - thank you Jaroslav Knotek, and I thank the **Škoda Jaderné Inženýrství** - Škoda Nuclear Machinery - thank you Vladimír Lobovský.

As our French colleagues used to say „Le roi est mort, vive le roi!" In this connection I have to tell you a few words. In addition to all these plenary and poster meetings there were three meetings of the International Advisory Committee and we had to make decisions about the future of these conferences. It was by far not an easy task, and I will start with the information about the last conference of this century, of this millennium. We had serious offers of two candidates, both very very attractive. Finally, after long discussions and by far not unanimously, we have decided that the last conference of this millennium will be held in France, that means the conference BEAMS'2000.

The situation with the next conference taking place in two years was much easier to decide. Here we were completely unanimous and so I am happy to be able now to give over all the burden to my colleague Shiloh who is going to invite us to come to Haifa in June 1998.

Please.

Joseph Shiloh:

Thank you Karl. I must tell you that when I heard Jerry Cooperstein give the statistics before and when I watched the success of this conference I got really worried because I feel the responsibility to top it or at least to be able to be equal.

Basically, what Jerry said were three criteria to the success of the conference: One is the number of people which we saw on the graph and then are the innovations, the technical and scientific innovations, and the beauty and the history of the location of the conference.

I am not going to ask you for help on the last issue I think we can have it done quite well in Israel, but I am asking you for help on the first two issues. And I'd like everyone of you to make a resolution to be innovative to send us an abstract and to come to Israel in two years.

Thank you.

Karel Jungwirth:

Thank you very much and what we can promise you is that we will give you all the help we can and all the experience and data.

And now I wish to everybody who will stay all this weekend in Prague to have still a good nice weather. To all of you I wish safe flights home, much success in your professional life, and happiness in your private life.

Good luck.

Jeff Quintenz:

Before we all stand up to leave harbor, I have been asked by the International Committee to express our very sincere gratitude for the hard work that professor Jungwirth, doctor Ullschmied, professor Sunka, the entire Local Organizing Committee has put forward to make this a truly outstanding conference. And I wish that we would all stand and give a grand applause to these fine organizers.

BEAMS STATISTICS

Jiří Ullschmied

The 11th International Conference on High-Power Particle Beams was held in the Congress Centre Prague from June 10 to June 14, 1996, and was hosted by the Institute of Plasma Physics, Academy of Sciences of the Czech Republic. From 568 pre-registrants just 309 participants from 23 countries actually attended the conference. This number is still rather encouraging, if compared with the attendance of five previous conferences held in Kobe (1986), Karlsruhe (1988), Novosibirsk (1990), Washington, D.C. (1992), and San Diego (1994) - see Fig. 1.

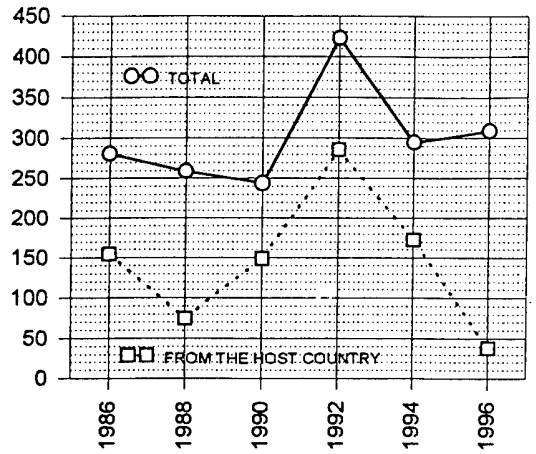

Fig.1
Number of participants of the last six BEAMS conferences

The distribution of BEAMS'96 attendees by country was the following: Australia (1), Austria (1), Belarus (3), Canada (1), Chile (2), Czech Republic (38), France (19), Georgia (2), Germany (25), Israel (12), Italy (2), Japan (17), P.R. China (5), Poland (4), Romania (2), Russia (105), S. Korea (1), Switzerland (2), Turkey (1), Ukraine (3), United Kingdom (3), USA (60).

As seen from the following table, the distribution of BEAMS attendees by country depends to a great extent on the geographical location of the conference, and it is positively influenced by the changing political climate in the last period as well.

Table - Number of participants from several selected countries at the last six BEAMS conferences

	USA	Japan	Russia (+ other FSU countries)	Germany	France	Israel	others	**TOTAL**	host country
1986	77	155	17	5	8	5	14	**281**	*155*
1988	99	19	16	75	21	8	21	**259**	*75*
1990	52	14	149	10	6	0	13	**244**	*149*
1992	286	15	64 (+ 1)	10	13	12	22	**423**	*286*
1994	173	19	56 (+ 2)	13	10	12	10	**295**	*173*
1996	60	17	105 (+ 8)	25	19	12	63	**309**	*38*

The BEAMS'96 international Programme Committee considered about 430 submitted paper abstracts. 422 papers were accepted for presentation, from which 303 have been really delivered to the conference. Sixty papers were presented orally in eight oral sessions, the other as posters in four poster sessions.

The distribution of papers among the main topical groups was roughly the following: Imploding liners, z-pinches, plasma foci (53), pulsed power technology and its applications (39), high-power microwaves, FELs (38), ion beams, ion diodes (25), electron beams, beam-plasma systems (24), radiation sources other than microwave (23), ion beam applications, BDTT (20), ICF, targets (16), electron beam applications (16), POSs, SOSs (14), diagnostics (14), vacuum and plasma discharges (9), accelerators (7), other (5). Consequently, there is a clear tendency: the 'non-beam' papers begin to prevail at the 'BEAMS' conferences!

This Proceedings contain the full texts of 289 papers, and 14 abstracts of the papers the full texts of which were not available even three months after the conference.

From the BEAMS Pre-history

Regrettable enough, the 11th International Conference on High Power Particle Beams is over. It belongs already to the 22 years' old history of the BEAMS conferences, the roots of which can be traced even to the end of the sixties. Some people might still remember that in 1996 it was not the first time the 'hundred-spired golden Prague' hosted the world beam community in its ancient surroundings. In fact Prague may be considered as the site of pre-history of all international BEAMS conferences.

Already in 1967 Miloš Seidl, former head of the Beam-Plasma Department of the Institute of Plasma Physics of the Czechoslovak Academy of Sciences, organized in Prague enthusiastically the First International Symposium on Beam-Plasma Interaction.

Milos's boys in 1965
Upper row (from left): J. Pohanka, A. Rajský, M. Seidl, P. Šunka
Lower row: A. Stupka, L. Hyttych, J. Jancarik, P. Jarošová, V. Piffl, J. Ullschmied

Among its 125 participants from 16 countries there were such outstanding personalities as A. Bers (MIT), F. Botiglioni (CEA Fontenay), M. Brambilla (Saclay), H. Bremmer (FOM), N.S. Buchelnikova (INP Novosibirsk), T. Consoli (Saclay), F.W. Crawford (Stanford), Ya.B. Fainberg and V.D. Fedorchenko (FTI Kharkov), G. von Gierke (IPP Garching), R.W. Gould (CALTECH), S.M. Hamberger (Culham), W. Herrmann (IPP Garching), H.J. Hopman (FOM), F. Magistrelli (Frascati), G. Müller (IPP Garching), A.A. Rukhadze (FIAN), S.A. Self (Stanford), L.D. Smullin (MIT), C.B. Wharton (GD San Diego), E.K. Zavoyskiy (Kurchatov Inst.), and many others (cf. IPPCZ-91, October 1967).

Some of them, still active in the field, might have recognized in the white-bearded BEAMS'96 chairman the very young secretary of that Symposium. That time Karel Jungwirth shared his responsibility for the scientific programme with Pavel Šunka, who is now director of the BEAMS´96 host organization - the Institute of Plasma Physics of the Czech Academy of Sciences.

In the second half of sixties Milos Seidl and his group concentrated their efforts on the study of high-frequency beam-plasma instabilities. He and his co-workers contributed substantially to the understanding of the mechanism of plasma heating by non-relativistic electron beams. Milos's dream was to build a beam-plasma machine, in which the plasma density and temperature could be easily adjusted by two corresponding control knobs only. In that pioneer times it seemed that to heat plasma by electron beams up to the thermonuclear temperatures is a relatively easy task, that it is just a question of proper increasing the injected beam energy.

The idea to built a high current relativistic electron accelerator in the Prague Institute of Plasma Physics arose shortly after the first Beam-Plasma Symposium. Unfortunately, Milos did not manage to realize it himself any more, as he - very providentially - left the country in August 1968, just one day before the invasion troops entered Czechoslovakia.

Milos and his 'boys' in 1996
From left: M. Seidl, P. Šunka, K. Jungwirth, J. Ullschmied, and V. Piffl

The paths of life of Milos and his 'boys' became separated for long 22 years, something which was hard to imagine in 1968. In 1969 Milos joined Stevens Institute of Technology in Hoboken, NJ, as Professor of Physics and director of the Plasma Physics Laboratory. After four years of his US stay any official contacts with his native Institute in Prague were strictly cut off from the Institute's side, and just rare unofficial private contacts with his former collaborators - kept well in secret, of course - continued without any interruption up to the 'velvet revolution' in November 1989.

In 1990 Milos Seidl was elected an honorary member of the newly established Scientific Council of the Prague Institute of Plasma Physics. It was a great pleasure for all Milos's former colleagues, and for the Prague REB team in particular, to meet their former 'boss', the distinguished Professor Emeritus of Physics and Engineering Physics Milos Seidl, in Prague again at the occasion of the BEAMS'96 conference, which he was invited to attend as an honorary conference quest. It was by far not just a chance that the Academy of Sciences of the Czech Republic used this very occasion to award him for his merits in physical sciences by the Golden Medal of Ernst Mach.

We wish Professor Milos Seidl much health, success and happiness, and many next fruitful years.

BEAMS'96 organizers

LIST OF PARTICIPANTS

1.	**AFONIN** Vasiliy I.	*Russian Federal Nuclear Center, Institute of Technical Physics (VNIITF)* *P.O. Box 245, Snezhinsk, 456 770, Chelyabinsk Reg.*	**RUSSIA**	Phone 7 (35171) 395 10 Fax 7 (35171) 309 79	E-mail: ovd@dep26.ch70.chel.su
2.	**AGEE** Forrest J.	*Phillips Laboratory, WSP,* *3550 Aberdeen Ave., S.E., Albuquerque, Kirtland AFB, 87117-5776, NM*	**USA**	Phone (505) 846 2824 Fax (505) 846 1278	E-mail: ageef@plk.af.mil
3.	**ANFINOGENTOV** Vasiliy G.	*Saratov State University,College of Applied Science* *83 Astrakhanskaya, Saratov, 410 071,*	**RUSSIA**	Phone. 7 (8452) 514 294 Fax 7 (8452) 240 298	E-mail. vga@ccollege.saratov.su
4.	**ANTHOUARD** Philippe	*C.E.A. - CESTA,* *B.P. 2, Le Barp, F-33114,*	**FRANCE**	Phone: 33 (5) 668 4089 Fax: 33 (5) 771 5440	E-mail:
5.	**ARKHIPOV** Alexander V.	*St. Petersburg Technical University, Dept. of Physical Electronics* *Politechnicheskaya 29, St. Petersburg, 195 251,*	**RUSSIA**	Phone: 7 (812) 552 6127 Fax: 7 (812) 552 7954	E-mail: e-beams@phtf.hop.stu.neva.ru
6.	**ARZHANNIKOV** Andrei V.	*Budker Institute of Nuclear Physics, SD RAS,* *Lavrentyev Avenue 11, Novosibirsk, 630090,*	**RUSSIA**	Phone: 7 (3832) 359 912 Fax: 7 (3832) 352 163	E-mail: A.V.Arzhannikov@inp.nsk.su
7.	**BABICKÝ** Václav	*Institute of Plasma Physics AS CR, Pulsed Plasma Systems Dept.* *P.O. Box 17, Prague 8, 182 00,*	**CZECH REPUBLIC**	Phone 42 (2) 6605 3244 Fax 42 (2) 858 6389	E-mail: babicky@ipp.cas.cz
8.	**BADALEC** Jan	*Institute of Plasma Physics AS CR, Tokamak Dept.* *P.O. Box 17, Prague 8, 182 00,*	**CZECH REPUBLIC**	Phone 42 (2) 6605 2947 Fax 42 (2) 858 6389	E-mail: badalec@ipp.cas.cz
9.	**BAILEY** Vernon	*Pulse Sciences, Inc.,* *600 McCormick St., San Leandro, 94577, CA*	**USA**	Phone: (510) 632 5100 Fax (510) 632 5300	E-mail:
10.	**BAKSHAEV** Yuryi	*Russian Res. Centre "Kurchatov Institute",* *Kurchatov Sq., 1, Moscow, 123182,*	**RUSSIA**	Phone. 7 (095) 196 9509 Fax.	E-mail:
11.	**BARANOWSKI** Jaroslaw	*Soltan Institute for Nuclear Studies,* *Swierk-Otwock, 05-400,*	**POLAND**	Phone. 48 (22) 779 9673 Fax 48 (22) 779 3481	E-mail: p05msa@cx1.cyf.gov.pl
12.	**BAUER** Walter H.	*Forschungszentrum Karlsruhe, INR* *Postfach 3640, Karlsruhe, D-76021,*	**GERMANY**	Phone. 49 (7247) 823 869 Fax: 49 (7247) 822 823	E-mail: bauer@inr.fzk.de
13.	**BAUMUNG** Kurt	*Forschungszentrum Karlsruhe, INR* *Postfach 3640, Karlsruhe, D-76021,*	**GERMANY**	Phone: 49 (7247) 824 675 Fax. 49 (7247) 825 987	E-mail: baumung@inr.fzk.de
14.	**BELENKI** Georgi S.	*Russian Res. Centre "Kurchatov Institute", Institute of Nuclear Fusion* *Kurchatov Sq., 1, Moscow, 123182,*	**RUSSIA**	Phone: 7 (095) 196 9874 Fax. 7 (095) 196 9874	E-mail: king@rec.msk.su
15.	**BENATTAR** René	*École Polytechnique,* *Lab. PMI, Palaiseau, F-91128,*	**FRANCE**	Phone: 33 (1) 6333 4116 Fax: 33 (1) 6933 3023	E-mail. benattar@lpmi.polytechnique.fr
16.	**BENFORD** James	*Microwave Sciences,* *1041 Los Arabis Lane, Lafayette, 94549, CA*	**USA**	Phone. (510) 283 8454 Fax: (510) 283 8487	E-mail: jnbenford@earthlink.net
17.	**BLAHA** Milan	*Berkeley Scholars, Inc.,* *5532 Hempstead Way, Springfield, 22150, VA*	**USA**	Phone: (301) 552 3266 Fax:	E-mail:
18.	**BLAUGRUND** Abraham E.	*Weizmann Institute of Science, Dept. of Nuclear Physics* *P.O. Box 26, Rehovot, 76100,*	**ISRAEL**	Phone: 972 (8) 934 3458 Fax: 972 (8) 934 4182	E-mail. FNBLA@weizmann.weizmann.ac.il
19.	**BLUHM** Hansjoachim	*Forschungszentrum Karlsruhe, INR* *Postfach 3640, Karlsruhe 1, D-76021,*	**GERMANY**	Phone: 49 (7247) 822 438 Fax: 49 (7247) 822 823	E-mail: bluhm@inr.fzk.de
20.	**BOWMAN** Charles D.	*Los Alamos National Laboratory,* *P.O. Box 1663, Los Alamos, 87545, NM*	**USA**	Phone: (505) 665 6922 Fax: (505) 665 6927	E-mail: bowman@atdiv.lanl.gov

21.	**BRADU** Pascal	*D.R.E.T./S.T.R.D.T./Groupe 3,* *26, Boulevard Victor, Paris-Armees, F-00460,*	**FRANCE**	Phone 33 4552 4737 Fax 33 4552 6520	E-mail
22.	**BRAIDWOOD** Sean	*D.S.T.O., Bldg 77* *P.O. Box 1500, Salisbury 5108, South Australia*	**AUSTRALIA**	Phone 61 (8) 259 7076 Fax 61 (8) 259 5938	E-mail staines#m#_geoff@macitd2.dsto.gov.au
23.	**CARLSON** Randolph L.	*Los Alamos National Laboratory, Dynamic Experimentation Division* *114 La Vista Dr., Los Alamos, 87544, NM*	**USA**	Phone (505) 667 9754 Fax (505) 665 3359	E-mail carlson_rl@lanl.gov
24.	**CARMEL** Yuval	*University of Maryland,* *Institute for Plasma Research, College Park, 20742-3511, MD*	**USA**	Phone (301) 405 4976 Fax (301) 314 9437	E-mail carmel@plasma.umd.edu
25.	**CARYOTAKIS** George	*Stanford Linear Accelerator Center, Kly/Micro* *2575 Sand Hill Rd., Menlo Park, 94025, CA*	**USA**	Phone. (415) 926 4446 Fax (415) 926 3654	E-mail: caryo@slac.stanford.edu
26.	**CHEN** Chiping	*Massachusetts Institute of Technology, Plasma Fusion Center* *167 Albany Street, Cambridge, 02139, MA*	**USA**	Phone. (617) 253 8506 Fax: (617) 253 6078	E-mail: chenc@pfc.mit.edu
27.	**CHERNENKO** Andrei S.	*Russian Res. Centre "Kurchatov Institute",* *Kurchatov Sq., 1, Moscow, 123182,*	**RUSSIA**	Phone. 7 (095) 196 7746 Fax 7 (095) 196 9874	E-mail potap@potap.msk.su
28.	**CHERNYSHEV** Vladimir K.	*All-Russian Research Institute of Exp. Physics,* *Pr. Mira 37, Sarov (Arzamas-16), 607 190, Nizhnyi Novgorod Reg.*	**RUSSIA**	Phone 7 (83130) 4 5738 Fax. 7 (83130) 54 565	E-mail: vcher_1763@rfnc.nnov.su
29.	**CHESTERFIELD** Stewart R.	*British Aerospace Defence, Dynamics Division,* *P.O. Box 5, Bristol, BS12 7QW, Avon*	**UK**	Phone: 44 (117) 931 6558 Fax 44 (117) 931 8928	E-mail CHESTER@awc.dyn.bae.co.uk
30.	**CHLENOV** Alexander	*Res. Inst. of Sci. Instruments, Min. of Atomic Energy,* *Turaevo, Lytkarino, 140 061, Moscow Region*	**RUSSIA**	Phone 7 (095) 552 3911 Fax: 7 (095) 552 3911	E-mail
31.	**CHOI** Peter	*École Polytechnique,* *Lab. PMI, Palaiseau, F-91128,*	**FRANCE**	Phone 33 (1) 6933 3416 Fax: 33 (1) 6933 3023	E-mail pchoi@lpmi.polytechnique.fr
32.	**CHRÁSKA** Pavel	*Institute of Plasma Physics AS CR,* *P.O. Box 17, Prague 8, 182 00,*	**CZECH REPUBLIC**	Phone 42 (2) 6641 3030 Fax 42 (2) 858 6389	E-mail: chraska@ipp.cas.cz
33.	**CHUVATIN** Alexander	*École Polytechnique,* *Lab. PMI, Palaiseau, F-91128,*	**FRANCE**	Phone 33 (1) 6933 4115 Fax: 33 (1) 6933 3023	E-mail. chuvatin@lpmi.polytechnique.fr
34.	**ČLUPEK** Martin	*Institute of Plasma Physics AS CR, Pulsed Plasma Systems Dept.* *P.O. Box 17, Prague 8, 182 00,*	**CZECH REPUBLIC**	Phone 42 (2) 6605 3234 Fax: 42 (2) 858 6389	E-mail: clupek@ipp.cas.cz
35.	**COFFEY** Timothy	*Naval Research Laboratory,* *4555 Overlook Ave., S.W., Washington, 20375-5360, DC*	**USA**	Phone: (202) 767 3301 Fax: (202) 404 8110	E-mail. nrl_1001@utopia.nrl.navy.mil
36.	**COHN** Daniel	*Massachusetts Institute of Technology, Plasma Fusion Center, NW16-172* *167 Albany Street, Cambridge, 02139, MA*	**USA**	Phone (617) 253 5524 Fax: (617) 253 0700	E-mail: cohn@pfc.mit.edu
37.	**COOPERSTEIN** Gerald	*Naval Research Laboratory,Code 6770, Plasma Physics Division* *4555 Overlook Ave., S.W., Washington, 20375-5346, DC*	**USA**	Phone. (202) 767 2290 Fax: (202) 767 0436	E-mail: cooperstein@ppd.nrl.navy.mil
38.	**COX** Victoria	*European Office of Aerospace R&D, Edison House* *223/231 Old Marylebone Rd., London NW1, 5TH,*	**UK**	Phone: 44 (171) 514 443 Fax: 44 (171) 514 4960	E-mail. vcox@eoard.af.mil
39.	**DAN'KO** Sergei	*Russian Res. Centre "Kurchatov Institute",* *Kurchatov Sq., 1, Moscow, 123182,*	**RUSSIA**	Phone: 7 (095) 196 9672 Fax: 7 (095) 196 9874	E-mail:
40.	**DANILOV** Valentin V.	*Krasnoyarsk State University,Research Lab. "Cosmophysics"* *Svobodny 79, Krasnoyarsk, 660 041,*	**RUSSIA**	Phone. ? Fax: 7 (3912) 44 86 25	E-mail: danilov@phys.kgu.krasnoyarsk.su
41.	**DARZNEK** S.A.	*Institute of Electrophysics, UD RAS,* *Komsomolskaya 34, Ekaterinburg, 620 219,*	**RUSSIA**	Phone 7 (3432) 493 444 Fax: 7 (3432) 445 051	E-mail: rukin@ief.intec.ru

42.	**DAVIS** Harold A.	*Los Alamos National Laboratory, P-1, MS-E526* *P.O. Box 1663, M.S. E526, Los Alamos, 87545, NM*	**USA**	Phone (505) 665 8373 Fax (505) 667 3552	E-mail davis@lanl.gov
43.	**DELVILLE** Jean-Christophe	*C.E.A. Bruyeres-le-Chatel,* *B.P. 12, Bruyeres-le-Chatel, 91580,*	**FRANCE**	Phone 33 (1) 6926 7752 Fax 33 (1) 6926 7015	E-mail
44.	**DEMIN** Anatoly	*Russian Federal Nuclear Center (VNIIEF),* *Pr. Mira 38, Sarov (Arzamas-16), 607 190, Nizhnyi Novgorod Reg.*	**RUSSIA**	Phone 7 (83130) 457 38 Fax 7 (83130) 545 65	E-mail vcher_1763@rfnc.nnov.su
45.	**DESJARLAIS** Michael P.	*Sandia National Laboratories, Org. 1241,* *P.O. Box 5800, MS 1186, Albuquerque, 87185-1186, NM*	**USA**	Phone (505) 845 7273 Fax (505) 845 7890	E-mail: mpdesja@sandia.gov
46.	**DEUTSCH** Claude	*Université de Paris XI, Centre Universitaire d'Orsay, Lab. de Physique des Gaz et des Plasmas* *Bat. 212, Orsay, F-91405,*	**FRANCE**	Phone 33 (1) 6941 7605 Fax 33 (1) 6941 7844	E-mail deut@psisun.u-psud.fr
47.	**DIYANKOV** Oleg V.	*Russian Federal Nuclear Center - VNIITF,* *P.O. Box 245, Snezhinsk, 456 770, Chelyabinsk Reg.*	**RUSSIA**	Phone 7 (35172) 3 2993 Fax 7 (35172) 3 0979	E-mail ovd@dep26.ch70.chel.su
48.	**DIYANKOV** Vladimir S.	*Russian Federal Nuclear Center - VNIITF,* *P.O. Box 245, Snezhinsk, 456 770, Chelyabinsk Reg.*	**RUSSIA**	Phone 7 (35172) 3 2993 Fax 7 (35172) 3 0979	E-mail: ovd@dep26.ch70.chel.su
49.	**DRŠKA** Ladislav	*Fac. of Nucl. Sci. and Physical Engineering, CTU, Dept. of Physical Electronics* *V Holešovičkách 2, Prague 8, Troja, 180 00,*	**CZECH REPUBLIC**	Phone 42 (2) 8576 2276 Fax 42 (2) 232 0861	E-mail drska@lilit.fjfi.cvut.cz
50.	**DUMISTRESCU-ZOITA** C.	*École Polytechnique,* *Lab. PMI, Palaiseau, F-91128,*	**FRANCE**	Phone 33 (1) 6933 3416 Fax 33 (1) 6933 3023	E-mail czoita@lpmi.polytechnique.fr
51.	**DYABILIN** Konstantin S.	*Institute for High Temperatures, RAS (IVTAN), High Energy Density Research Center* *Izhorskaya 13/19, Moscow, 127412,*	**RUSSIA**	Phone 7 (095) 485 7988 Fax 7 (095) 485 7990	E-mail: ksd@hedric.msk.su
52.	**EIZENHÖFER** Harald	*Dornier Medizintechnik GmbH,* *Industriestr. 15 / Postfach 1128, Germering, D-82101,*	**GERMANY**	Phone Fax 49 (89) 8410 8770	E-mail.
53.	**ENGELKO** Vladimir	*Efremov Institute of Electrophysical Apparatus,* *Metallostroy, Sovetskii-1, St. Petersburg, 189631,*	**RUSSIA**	Phone 7 (812) 4627 845 Fax 7 (812) 314 3360	E-mail. engelko@sirius.niiefa.spb.su
54.	**ETLICHER** Bernard	*École Polytechnique,Lab. de Physique des Milieux Ionises* *B.P. 27, Palaiseau, F-91128,*	**FRANCE**	Phone 33 (1) 6933 3259 Fax 33 (1) 6933 3023	E-mail: etlicher@lpmi.polytechnique.fr
55.	**FAEHL** Rickey J.	*Los Alamos National Laboratory,* *P.O. Box 1663, MS B259, Los Alamos, 87545, CA*	**USA**	Phone (505) 667 2806 Fax (505) 665 7725	E-mail: rjf@lanl.gov
56.	**FAVRE** Mario	*Pontificia Universidad Catolica de Chile, Facultad De Fisica* *Casilla 306, Vicuna Mackenna 4860, Santiago-22, ,*	**CHILE**	Phone 56 (2) 686 4472 Fax. 56 (2) 686 4365	E-mail: mfavre@lascar.puc.cl
57.	**FIALA** Jaroslav	*ŠKODA Výzkum s.r.o.,* *Tylova 57, Plzeň, 316 00,*	**CZECH REPUBLIC**	Phone 42 (19) 722 7114 Fax: 42 (19) 722 7118	E-mail:
58.	**FILATOV** Alexandr L.	*Institute of Electrophysics, UD RAS,* *Komsomolskaya 34, Ekaterinburg, 620 219,*	**RUSSIA**	Phone 7 (3432) 493 320 Fax. 7 (3432) 445 051	E-mail: filatov@ief.intec.ru
59.	**FILATOVA** Irina I.	*Inst. of Molecular and Atomic Physics, BAS,* *F. Skaryna Ave. 70, Minsk, 22 0072,*	**BELARUS**	Phone 375 (172) 684 436 Fax: 375 (172) 393 064	E-mail: imafbel@bas05.basnet.minsk.by
60.	**FILUK** Alex B.	*Sandia National Laboratories,* *P.O. Box 5800, MS 1187, Albuquerque, 87185-1187, NM*	**USA**	Phone: (505) 845 7385 Fax: (505) 845 7890	E-mail: abfiluk@sandia.gov
61.	**FISHER** Amnon	*Naval Research Laboratory,Code 6790* *4555 Overlook Ave., S.W., Washington, 20375-5000, DC*	**USA**	Phone: (202) 767 3708 Fax: (202) 767 3950	E-mail:
62.	**FORTOV** Vladimir E.	*High Energy Density Research Centre, RAS (IVTAN),* *Izhorskaya 13/19, Moscow, 127412,*	**RUSSIA**	Phone. 7 (095) 485 7988 Fax. 7 (095) 938 1870	E-mail: fortov@rfbr.ru fortov@hedric.msk.su

63.	**FRIEDMAN** Moshe	*Naval Research Laboratory, Code 6732* *4555 Overlook Ave., S.W., Washington, 20375-5000, DC*	**USA**	Phone: Fax:	(202) 767 3145 (202) 404 8181	E-mail:
64.	**FROLOV** Vladimir	*École Polytechnique,* *Lab. PMI, Palaiseau, F-91128,*	**FRANCE**	Phone: Fax:	33 (1) 6933 3275 33 (1) 6933 3023	E-mail: frolov@lpmi.polytechnique.fr
65.	**FUCHS** Michael	*Institute of Applied Physics, RAS,* *46, Ulyanov St., Nizhnyi Novgorod, 603600,*	**RUSSIA**	Phone: Fax:	7 (8312) 384347 7 (8312) 362 061	E-mail: fuchs@appl.sci-nnov.ru
66.	**GALAKHOV** Igor V.	*Russian Federal Nuclear Center (VNIIEF),* *Pr. Mira 37, Sarov (Arzamas-16), 607 190, Nizhnyi Novgorod Reg.*	**RUSSIA**	Phone: Fax:	7 (83130) 56 646 7 (83130) 54 565	E-mail: galakhov_2566@rfnc.nnov.su
67.	**GARANIN** Sergey F.	*All-Russian Research Institute of Exp. Physics,* *Pr. Mira 37, Sarov (Arzamas-16), 607 190, Nizhnyi Novgorod Reg.*	**RUSSIA**	Phone: Fax:	7 (83130) 136 65 7 (83130) 54 565	E-mail: mvn_072e@spd.rfnc.nnov.su
68.	**GEORGESCU** Nicolae	*Institute of Physics and Technology of Radiation Devices, Plasma Phys. & Nucl. Fusion Lab.* *P.O. Box 5206, Bucharest-Magurele, R-76900,*	**ROMANIA**	Phone: Fax:	40 (1) 780 4290 40 (1) 420 9391	E-mail: ngeorge@roifa.ifa.ro
69.	**GERASIMOV** Anatolyi	*Russian Federal Nuclear Center (VNIIEF),* *Pr. Mira 37, Sarov (Arzamas-16), 608 190, Nizhnyi Novgorod Reg.*	**RUSSIA**	Phone: Fax:	7 (83130) 432 56 7 (83130) 582 69	E-mail: otd4@expd.rfnc.nnov.su
70.	**GIESE** Harald	*Forschungszentrum Karlsruhe, INR* *Postfach 3640, Karlsruhe, D-76021,*	**GERMANY**	Phone: Fax:	49 (7247) 824 695 49 (7247) 824 874	E-mail: giese@inr.fzk.de
71.	**GILAD** Pinchas	*RAFAEL,* *P.O. Box 2250, Dept. 24, Haifa, 31021,*	**ISRAEL**	Phone: Fax:	? 972 (4) 879 5289	E-mail:
72.	**GILGENBACH** Ronald	*University of Michigan, Nuclear Engineering & Rad. Sci. Dept.* *2355 Bonisteel Blvd., Cooley Bldg., Ann Arbor, 48109-2104, MI*	**USA**	Phone: Fax:	(313) 763 1261 (313) 763 4540	E-mail: rongilg@engin.umich.edu
73.	**GIMZBURG** Albert	*RAFAEL,* *P.O. Box 2250, Haifa, 31021,*	**ISRAEL**	Phone: Fax:		E-mail
74.	**GINZBURG** Naum S.	*Institute of Applied Physics, RAS,* *46, Ulyanov St., Nizhnyi Novgorod, 603600,*	**RUSSIA**	Phone: Fax:	7 (8312) 384 552 7 (8312) 362 061	E-mail: ginzburg@appl.sci-nnov.ru
75.	**GLAZYRIN** Igor V.	*Russian Federal Nuclear Center - VNIITF,* *P.O. Box 245, Snezhinsk, 456 770, Chelyabinsk Reg.*	**RUSSIA**	Phone: Fax:	7 (35172) 32 993 7 (35172) 30 979	E-mail: ovd@dep26.ch70.chel.su
76.	**GOEL** Balbir	*Forschungszentrum Karlsruhe, INR* *Postfach 3640, Karlsruhe, D-76021,*	**GERMANY**	Phone: Fax:	49 (7247) 822 445 49 (7247) 824 874	E-mail: Balbir.Goel@inr.fzk.de
77.	**GOFMAN** Yury	*Kharkiv State University, Dept. of Physics and Technology* *4 Svobody Sq., Kharkov, 310 077,*	**UKRAINE**	Phone: Fax:	380 (572) 352 566 380 (572) 353 977	E-mail: tovstiak@pem.kharkov.ua (Subj: for Gofman)
78.	**GOMBEROFF** Katia	*RAFAEL,* *P.O. Box 2250, Dept. 24, Haifa, 31021,*	**ISRAEL**	Phone: Fax:	? ?	E-mail: fngomber@weizmann.weizmann.ac.il
79.	**GORDEEV** Alexander V.	*Russian Res. Centre "Kurchatov Institute", Institute of Nuclear Fusion* *Kurchatov Sq., 1, Moscow, 123182,*	**RUSSIA**	Phone: Fax:	7 (095) 196 7345 7 (095) 196 9874	E-mail: gordeev@rec.msk.su
80.	**GORDEEV** Vyacheslav S.	*Russian Federal Nuclear Center (VNIIEF),* *Pr. Mira 37, Sarov (Arzamas-16), 607 190, Nizhnyi Novgorod Reg.*	**RUSSIA**	Phone: Fax:	7 (83130) 623 88 7 (83130) 582 69	E-mail: otd4@expd.rfnc.nnov.su
81.	**GORELOVA** Svetlana V.	*Russian Federal Nuclear Center (VNIIEF),* *Pr. Mira 38, Sarov (Arzamas-16), 607 190, Nizhnyi Novgorod Reg.*	**RUSSIA**	Phone: Fax:	7 (83130) 613 86 7 (83130) 545 65	E-mail: popkov_3001@spd.rfnc.nnov.su
82.	**GRABOVSKIY** Evgeniy V.	*Troitsk Inst. for Innov. & Thermonucl. Investigation, TRINITI* *Centralnaya St. 3-19, Troitsk, 142092, Moscow Region*	**RUSSIA**	Phone: Fax:	7 (095) 334 5614 7 (095) 334 5614	E-mail: angara@fly.triniti.troitsk.ru
83.	**GRECHIKHA** Alexei V.	*Forschungszentrum Karlsruhe, INR* *Postfach 3640, B630, Karlsruhe, D-76021,*	**GERMANY**	Phone: Fax	49 (7247) 824 668	E-mail: gretchik@inr.fzk.de

84.	**GREENLY** John B.	*LPS, Cornell University,* *369 Upson Hall, Ithaca, 14853, NY*	**USA**	Phone: (607) 255 7379 Fax: (607) 255 3004	E-mail: johng@lps.cornell.edu
85.	**GRIBOV** Alexander N.	*Troitsk Inst. for Innov. & Thermonucl. Investigation, TRINITI* *Pushkova, Troitsk, 142092, Moscow Region*	**RUSSIA**	Phone: 7 (095) 334 5614 Fax: 7 (095) 334 5614	E-mail: angara@fly.triniti.troitsk.ru
86.	**GRINEVICH** Boris Ye.	*All-Russian Research Institute of Exp. Physics,* *Pr. Mira 37, Sarov (Arzamas-16), 607 190, Nizhnyi Novgorod Reg.*	**RUSSIA**	Phone: 7 (83130) 4 5738 Fax 7 (83130) 54 565	E-mail: vcher_1763@rfnc.nnov.su
87.	**GRUSIN** Igor A.	*Russian Federal Nuclear Center (VNIIEF),* *Pr. Mira 37, Sarov (Arzamas-16), 607 190, Nizhnyi Novgorod Reg.*	**RUSSIA**	Phone: 7 (83130) 56 646 Fax: 7 (83130) 54 565	E-mail: grusin_2566@rfnc.nnov.su
88.	**GUDOV** Sergei N.	*Russian Federal Nuclear Center (VNIIEF),* *Pr. Mira 37, Sarov (Arzamas-16), 607 190, Nizhnyi Novgorod Reg.*	**RUSSIA**	Phone 7 (83130) 56 646 Fax: 7 (83130) 54 565	E-mail: gudov_2566@rfnc.nnov.su
89.	**GÜNZEL** Reinhard	*Forschungszentrum Rossendorf,* *Glasewaldt Str. 21, Dresden, D-01277,*	**GERMANY**	Phone: 49 (351) 260 2462 Fax: 49 (351) 260 2703	E-mail: guenzel@fz-rossendorf.de
90.	**HAMMER** David	*LPS, Cornell University,* *369 Upson Hall, Ithaca, 14853, NY*	**USA**	Phone: (607) 255 3916 Fax: (607) 255 3004	E-mail hammer@lps.cornell.edu
91.	**HARADA** Nobuhiro	*Nagaoka University of Technology, Dept. of Electrical Engineering* *1603-1 Kamitomioka, Nagaoka-city, 940-21, Niigata*	**JAPAN**	Phone: 81 (258) 46 6000 Fax: 81 (258) 46 6506	E-mail: nob@voscc.nagaokaut.ac.jp
92.	**HASEGAWA** Jun	*Tokyo Institute of Technology, Dept. of Energy Sciences* *4259 Nagatsuta, Midori-ku, Yokohama, J-226, Kanagawa*	**JAPAN**	Phone: 81 (45) 924 5665 Fax: 81 (45) 921 1318	E-mail: jhasegaw@es.titech.ac.jp
93.	**HEINE** Frank	*Universität Erlangen-Nurnberg, Physics Dept. I* *Erwin Rommel Str. 1, Erlangen, D-91058,*	**GERMANY**	Phone: 49 (9131) 85 7265 Fax: 49 (9131) 15 249	E-mail: heine@kassandra.physik.uni-erlangen.de
94.	**HEMELÍK** Stanislav	*Energoprojekt Praha a.s.,* *Bubenská 1, Praha, 170 05,*	**CZECH REPUBLIC**	Phone: 42 (2) 870 708 Fax: 42 (2) 6671 1120	E-mail:
95.	**HERLEB** Ulrich	*CERN, LHC Division,* *LHC Division, Geneve, CH-1211,*	**SWITZERLAND**	Phone: 41 (22) 767 2028 Fax:	E-mail: u.herleb@cern.ch
96.	**HINSHELWOOD** David D.	*Naval Research Laboratory, c/o Code 6773* *4555 Overlook Ave., S.W., Washington, 20375-5000, DC*	**USA**	Phone: (202) 767 8486 Fax: (202) 767 2012	E-mail: ddh@suzie.nrl.navy.mil
97.	**HIRAOKA** Kazuki	*Tokyo Institute of Technology, Dept. of Energy Sciences* *4259 Nagatsuta, Midori-ku, Yokohama, J-226, Kanagawa*	**JAPAN**	Phone: 81 (45) 924 5665 Fax: 81 (45) 921 1318	E-mail: khiraoka@energy.es.titech.ac.jp
98.	**HOPPÉ** Peter	*Forschungszentrum Karlsruhe, INR* *Postfach 3640, Karlsruhe, D-76021,*	**GERMANY**	Phone: 49 (7247) 824 674 Fax: 49 (7247) 822 823	E-mail: hoppe@inr.fzk.de
99.	**HORIOKA** Kazuhiko	*Tokyo Institute of Technology, Dept. of Energy Sciences* *4259 Nagatsuta, Midori-ku, Yokohama, J-226, Kanagawa*	**JAPAN**	Phone: 81 (45) 924 5661 Fax: 81 (45) 921 1318	E-mail: khorioka@es.titech.ac.jp
100.	**HOSOKAI** Tomonao	*Tokyo Institute of Technology, Dept. of Energy Sciences* *4259 Nagatsuta, Midori-ku, Yokohama, J-226, Kanagawa*	**JAPAN**	Phone: 81 (45) 924 5665 Fax: 81 (45) 921 1318	E-mail: thosokai@energy.es.titech.ac.jp
101.	**JACQUET** Laurent	*C.E.A. - FRANCE,* *60 Avenue Daumesnil, Paris, 75012,*	**FRANCE**	Phone: 33 (1) 4342 1637 Fax: 33 (1) 4386 7429	E-mail:
102.	**JANCARIK** Jiri	*Lawrence Livermore National Laboratory,* *7000 East Avenue, Livermore, 94550, CA*	**USA**	Phone: (510) 423 1982 Fax: (510) 422 3165	E-mail: jancarik1@llnl.gov
103.	**JENIŠTA** Jiří	*Institute of Plasma Physics AS CR,* *P.O. Box 17, Prague 8, 182 00,*	**CZECH REPUBLIC**	Phone: 42 (2) 6605 2852 Fax: 42 (2) 858 6389	E-mail: jenista@ipp.cas.cz
104.	**JUNGWIRTH** Karel	*Institute of Plasma Physics AS CR, Academy of Sciences of CR* *P.O. Box 17, Prague 8, 182 00,*	**CZECH REPUBLIC**	Phone: 42 (2) 242 40 536 Fax: 42 (2) 242 20 944	E-mail: jungwirt@lorien.site.cas.cz

105.	**KALININ** Yuri G.	*Russian Res. Centre "Kurchatov Institute", Institute of Nuclear Fusion* *Kurchatov Sq., 1, Moscow, 123182,*	**RUSSIA**	Phone Fax	7 (095) 196 9672 7 (095) 196 9874	E-mail
106.	**KALYNOV** Yuri K.	*Institute of Applied Physics, RAS,* *46, Ulyanov St., Nizhnyi Novgorod, 603600,*	**RUSSIA**	Phone Fax	7 (8312) 384347 7 (8312) 362 061	E-mail: kalynov@appl.sci-nnov.ru
107.	**KAMADA** Keiichi	*Kanazawa University, Faculty of Science,* *Kakuma-machi, Kanazawa, 920-11, Ishikawa*	**JAPAN**	Phone: Fax:	81 (762) 64 5671 81 (762) 64 5739	E-mail: kkamada@plasma.s.kanazawa-u.ac.jp
108.	**KANDAUROV** Igor V.	*Budker Institute of Nuclear Physics, SD RAS,* *Lavrentyev Avenue 11, Novosibirsk, 630090,*	**RUSSIA**	Phone Fax	7 (3832) 359 589 7 (3832) 352 163	E-mail: KANDAUROV@inp.nsk.su
109.	**KARGIN** Victor	*Russian Federal Nuclear Center (VNIIEF),* *Pr. Mira 37, Sarov (Arzamas-16), 607 190, Nizhnyi Novgorod Reg.*	**RUSSIA**	Phone Fax	7 (83130) 613 86 7 (83130) 545 65	E-mail: popkov_3001@spd.rfnc.nnov.su
110.	**KARLICKÝ** Marian	*Astronomical Institute AS CR,* *Observatory Ondrejov 266, Ondřejov, 251 65,*	**CZECH REPUBLIC**	Phone: Fax:	42 (2) 881 611 42 (2) 881 611	E-mail: karlicky@asu.cas.cz
111.	**KARLYKHANOV** Nikolai G.	*Russian Federal Nuclear Center, Institute of Technical Physics (VNIITF)* *P.O. Box 245, Snezhinsk, 456 770, Chelyabinsk Reg.*	**RUSSIA**	Phone: Fax:	7 (35172) 329 93	E-mail: ovd@dep26.ch70.chel.su
112.	**KAROW** Hans	*European Science Foundation,* *1 Quay Lezay Marnesia, Strasbourg, F-67080,*	**FRANCE**	Phone Fax	33 (88) 767 128 33 (88) 370 532	E-mail: hkarow@esf.org
113.	**KASUYA** Koichi	*Tokyo Institute of Technology, Dept. of Energy Sciences* *4259 Nagatsuta, Midori-ku, Yokohama, J-226, Kanagawa*	**JAPAN**	Phone Fax	81 (45) 924 5662 81 (45) 921 1318	E-mail: kkasuya@es.titech.ac.jp
114.	**KAWATA** Shigeo	*Nagaoka University of Technology, Dept. of Electrical Engineering* *1603-1 Kamitomioka, Nagaoka-city, 940-21, Niigata*	**JAPAN**	Phone Fax:	81 (258) 46 6000 81 (258) 46 6506	E-mail: kawata@voscc.nagaokaut.ac.jp
115.	**KEKEZ** Mladen M.	*National Research Council of Canada, Electrical Engineering Division* *Montreal Rd., Ottawa, K1A OR6, Ontario*	**CANADA**	Phone Fax	(613) 993 0427 (613) 941 6982	E-mail
116.	**KESSLER** Günther	*Forschungszentrum Karlsruhe, INR* *Postfach 3640, Karlsruhe, D-76021,*	**GERMANY**	Phone Fax:	49 (7247) 822 440 49 (7247) 824 874	E-mail: Christine.Kastner@inr.kfk.fzk.d400.de
117.	**KINGSEP** Alexander	*Russian Res. Centre "Kurchatov Institute", Institute of Nuclear Fusion* *Kurchatov Sq., 1, Moscow, 123182,*	**RUSSIA**	Phone Fax	7 (095) 196 7345 7 (095) 196 1635	E-mail: king@rec.msk.su
118.	**KIUTTU** Gerald	*Phillips Laboratory,High Energy Sources Division* *3550 Aberdeen Ave., S.E., Albuquerque, Kirtland AFB, 87117-5776, NM*	**USA**	Phone: Fax	(505) 846 0683 (505) 846 9853	E-mail: kiuttu@plk.af.mil
119.	**KLIMA** Richard	*Institute of Plasma Physics AS CR, Theoretical Dept.* *P.O. Box 17, Prague 8, 182 00,*	**CZECH REPUBLIC**	Phone Fax:	42 (2) 6605 2326 42 (2) 858 6389	E-mail: klima@ipp.cas.cz
120.	**KNYAZEV** Boris A.	*Novosibirsk State University, Dept. of General Physics* *Pirogova St. 2, Novosibirsk, 630090,*	**RUSSIA**	Phone: Fax	7 (3832) 370 770 7 (3832) 355 237	E-mail: knyazev@phys.nsu.ru
121.	**KOGUCHI** Harukisa	*Kanazawa University, Faculty of Science,* *Kakuma-machi, Kanazawa, 920-11, Ishikawa*	**JAPAN**	Phone Fax:	81 (762) 64 5917 81 (762) 64 5739	E-mail: koguchi@plasma.s.kanazawa-u.ac.jp
122.	**KOIDAN** Vasili S.	*Budker Institute of Nuclear Physics, SD RAS,* *Lavrentyev Avenue 11, Novosibirsk, 630090,*	**RUSSIA**	Phone: Fax:	7 (3832) 359 589 7 (3832) 352 163	E-mail: koidan@inp.nsk.su
123.	**KOLÁČEK** Karel	*Institute of Plasma Physics AS CR, Pulsed Plasma Systems Dept.* *P.O. Box 17, Prague 8, 182 00,*	**CZECH REPUBLIC**	Phone Fax:	42 (2) 886 980 42 (2) 858 6389	E-mail: kolacek@ipp.cas.cz
124.	**KOLPIN** Marc	*Physics International Company,* *2700 Merced St., San Leandro, 94577-0599, CA*	**USA**	Phone: Fax:	(510) 577 7208 (510) 577 7287	E-mail: MAKOLPIN@corp.olin.com
125.	**KONDYURIN** Alexei	*Institute of Technical Chemistry, RAS,* *13 Lenin Str., Perm, 614 000,*	**RUSSIA**	Phone Fax	7 (3422) 391 323 7 (3422) 324 375	E-mail: kond@icmm.perm.su

126.	**KORCHAGIN** Victor	*Russian Federal Nuclear Center (VNIIEF),* *Pr. Mira 37, Sarov (Arzamas-16), 607 190, Nizhnyi Novgorod Reg.*	**RUSSIA**	Phone 7 (83130) 457 38 Fax 7 (83130) 545 65	E-mail vcher_1763@rfnc.nnov.su
127.	**KORENEV** Sergey A.	*Joint Institute for Nuclear Research, Laboratory of Particle Physics* *P.O. Box 79, Dubna, 141980, Moscow Region*	**RUSSIA**	Phone 7 (09621) 652 66 Fax 7 (09621) 658 91	E-mail korenev@lshe17.jinr.dubna.su
128.	**KORMILITSYN** Alexei I.	*Russian Federal Nuclear Center (VNIITF),* *P.O. Box 245, Snezhinsk, 456 770, Chelyabinsk Reg.*	**RUSSIA**	Phone 7 (35172) 329 93 Fax 7 (35172) 309 79	E-mail: ovd@dep26.ch70.chel.su
129.	**KOROLEV** Valeri	*Russian Res. Centre "Kurchatov Institute", Applied Physics Division* *Kurchatov Sq., 1, Moscow, 123182,*	**RUSSIA**	Phone 7 (095) 196 9075 Fax 7 (095) 196 9874	E-mail
130.	**KOROVIN** Sergei D.	*High Current Electronics Institute, SD RAS,* *4, Akademicheski Avenue, Tomsk, 634055,*	**RUSSIA**	Phone 7 (3822) 258 706 Fax: 7 (3822) 259 134	E-mail korovin@hcei.tomsk.su
131.	**KOSHELEV** Vladimir I.	*High Current Electronics Institute, SD RAS,* *4, Akademicheski Avenue, Tomsk, 634055,*	**RUSSIA**	Phone: 7 (3822) 258 915 Fax 7 (3822) 259 410	E-mail. koshelev@lhfe.hcei.tomsk.su
132.	**KOZHUNOV** Yuri	*Russian Federation Research Institute of Pulse Technique* *Luganskaya 9, 115 304 Moscow,*	**RUSSIA**	Phone 7 (095) 321 3501 Fax 7 (095) 321 4855	E-mail:
133.	**KRČMA** František	*Institute of Plasma Physics AS CR,* *P.O. Box 17, Prague 8, 182 00,*	**CZECH REPUBLIC**	Phone 42 (2) 6605 3243 Fax: 42 (2) 858 6389	E-mail: krcma@ipp.cas.cz
134.	**KRASIK** Yakov E.	*Weizmann Institute of Science, Dept. of Particle Physics* *Herzl St., P.O. Box 26, Rehovot, 76100,*	**ISRAEL**	Phone 972 (8) 934 2049 Fax 972 (8) 934 4106	E-mail fnkrasik@weizmann.weizmann.ac.il
135.	**KRAVÁRIK** Josef	*Fac.of Elect. Engin., Czech Technical University, Dept. of Physics* *Technická 2, Prague 6, Dejvice, 166 27,*	**CZECH REPUBLIC**	Phone. 42 (2) 2435 3336 Fax. 42 (2) 311 1786	E-mail. kubes@feld.cvut.cz
136.	**KREJČÍ** Aleš	*World Trend,* *Na Hřebenkách 65, Prague 6, 150 00,*	**CZECH REPUBLIC**	Phone: 42 (2) 521 375 Fax: 42 (2) 627 4152	E-mail.
137.	**KRISTIANSEN** Magne	*Texas Technical University, Dept. of Electrical Engineering* *79409-3102, TX*	**USA**	Phone (806) 742 2224 Fax: (806) 742 1281	E-mail. nukrs@ttacsl.ttu.edu
138.	**KROUSKÝ** Eduard	*Institute of Physics, AS CR,* *Na Slovance 2, Prague 8, 180 40,*	**CZECH REPUBLIC**	Phone: 42 (2) 6606 2792 Fax: 42 (2) 6605 2107	E-mail: krousky@fzu.cz
139.	**KRUGLYAKOV** Eduard P.	*Budker Institute of Nuclear Physics, SD RAS,* *Lavrentyev Avenue 11, Novosibirsk, 630090,*	**RUSSIA**	Phone: 7 (3832) 359 323 Fax: 7 (3832) 352 163	E-mail: E.KRUGLYAKOV@inp.nsk.su
140.	**KUBEŠ** Pavel	*Fac.of Elect. Engin., Czech Technical University, Dept. of Physics* *Technická 2, Prague 6, Dejvice, 166 27,*	**CZECH REPUBLIC**	Phone: 42 (2) 2435 2330 Fax: 42 (2) 311 1786	E-mail: kubes@feld.cvut.cz
141.	**KUROPATKIN** Yurii P.	*Russian Federal Nuclear Center (VNIIEF),* *Pr. Mira 37, Sarov (Arzamas-16), 607 190, Nizhnyi Novgorod Reg.*	**RUSSIA**	Phone: 7 (83130) 546 38 Fax: 7 (83130) 545 65	E-mail: popkov_3001@spd.rfnc.nnov.su
142.	**KUSSE** Bruce R.	*LPS, Cornell University,* *369 Upson Hall, Ithaca, 14853, NY*	**USA**	Phone: (607) 255 4127 Fax: (607) 255 3004	E-mail: kusse@lps.cornell.edu
143.	**KUZYAEV** Anatoliy I.	*All-Russian Research Institute of Exp. Physics,* *Pr. Mira 37, Sarov (Arzamas-16), 607 190, Nizhnyi Novgorod Reg.*	**RUSSIA**	Phone: 7 (83130) 457 38 Fax: 7 (83130) 545 65	E-mail: vcher_1763@rfnc.nnov.su
144.	**L'EPLATTENIER** Pierre	*École Polytechnique,* *Lab. PMI, Palaiseau, F-91128,*	**FRANCE**	Phone: 33 (1) 6933 3572 Fax: 33 (1) 6933 3023	E-mail: pierrel@lpmi.polytechnique.fr
145.	**LÁSKA** Leoš	*Institute of Physics, AS CR,* *Na Slovance 2, Prague 8, 180 40,*	**CZECH REPUBLIC**	Phone: 42 (2) 6606 2792 Fax: 42 (2) 6605 2107	E-mail. laska@fzu.cz
146.	**LAŠTOVIČKA** Zdeněk	*Energoprojekt,* *Bubenská 1, Prague 7, 170 05,*	**CZECH REPUBLIC**	Phone: 42 (2) 870 708 Fax: 42 (2) 6671 1120	E-mail:

147.	**LAROUR** Jean	*École Polytechnique,* *Lab. PMI, Palaiseau, F-91128,*	**FRANCE**	Phone 33 (1) 6933 3280 Fax 33 (1) 6933 3023	E-mail larour@lpmi.polytechnique.fr
148.	**LAWSON** Wesley G.	*University of Maryland,* *Electrical Engineering Dept., College Park, 20742, MD*	**USA**	Phone (301) 405 4972 Fax (301) 314 9437	E-mail. lawson@eng.umd.edu
149.	**LEE** Cha-Yeol	*Kanazawa University, Faculty of Science,* *Kakuma-machi, Kanazawa, 920-11, Ishikawa*	**JAPAN**	Phone 81 (762) 64 5917 Fax 81 (762) 64 5739	E-mail lee@plasma.s.kanazawa-u.ac.jp
150.	**LEEPER** Ramon J.	*Sandia National Laboratories, Diag. & Target Exp. Dept-9577* *P.O. Box 5800, MS 1196, Albuquerque, 87185-1196, NM*	**USA**	Phone (505) 845 7185 Fax (505) 845 7820	E-mail rjleepe@sandia.gov
151.	**LIGACHEV** Alexandre E.	*Gagarinskiy per. 16, ap. 25a* *Moscow, 121 002,*	**RUSSIA**	Phone 7 (095) 930 4505 Fax 7 (095) 241 3049	E-mail: IBEAM@rinet.ru
152.	**LINHART** Jirka G.	*University of Ferrara,Dipartimento di Fisica* *12 Via del Paradiso, Ferrara, I-44100,*	**ITALY**	Phone 39 (532) 781 811 Fax 39 (532) 781 810	E-mail: bortolotti@ferrara.infn.it
153.	**LIU** Chengjun	*Institute of Fluid Physics, CAEP,* *P.O. Box 523-56, Chengdu, 610003, Sichuan*	**P.R. CHINA**	Phone 86 (816) 248 4138 Fax 86 (816) 227 2695	E-mail: DINGBN@sun.ihep.ac.cn
154.	**LU** Mingfang	*Chinese Academy of Sciences, Institute of Physics, P.O. Box 603* *Nan San Jie 8, Zhong Guan Cun, Beijing, 100080,*	**P.R. CHINA**	Phone 86 (10) 255 1489 Fax 86 (10) 256 2605	E-mail: mflu@aphy02.iphy.ac.cn
155.	**LUBOMIRSKIY** Alexander	*Russian Federal Nuclear Center (VNIIEF),* *Pr. Mira 37, Sarov (Arzamas-16), 607 190, Nizhnyi Novgorod Reg.*	**RUSSIA**	Phone 7 (83130) 546 38 Fax 7 (83130) 545 65	E-mail popkov_3001@spd.rfnc.nnov.su
156.	**LUDMIRSKY** Ariold	*NRC Soreq.Plasma Group* *Yavne, 81800,*	**ISRAEL**	Phone 972 (8) 943 4753 Fax 972 (8) 943 4775	E-mail: ariold@ndc.soreq.gov.il
157.	**MACH** Rostislav	*Nuclear Physics Institute, AS CR,* *Řež u Prahy, 250 68,*	**CZECH REPUBLIC**	Phone 42 (2) 6641 5261 Fax 42 (2) 685 7003	E-mail: mach@vax.ujf.cas.cz
158.	**MAGDA** Igor I.	*NSC Kharkov Institute of Physics and Technology,* *Akademicheskaya St. 1, Kharkov, 310108,*	**UKRAINE**	Phone 7 (0572) 40 44 64 Fax 7 (0572) 35 17 38	E-mail. magda@kfti.kharkov.ua
159.	**MAKO** Frederick	*FM Technologies,* *10529-B Braddock Road, Fairfax, 22 032, VA*	**USA**	Phone (703) 425 5111 Fax. (703) 425 3539	E-mail:
160.	**MANDELBAUM** Benjamin	*RAFAEL,* *P.O. Box 2250, Dept. 21, Haifa, 31021,*	**ISRAEL**	Phone: 972 (4) 795 233 Fax: 972 (4) 792 212	E-mail:
161.	**MANUILOV** Vladimir N.	*Institute of Applied Physics, RAS,* *46, Ulyanov St., Nizhnyi Novgorod, 603600,*	**RUSSIA**	Phone: 7 (8312) 384 571 Fax: 7 (8312) 362061	E-mail: manuilov@appl.sci-nnov.ru
162.	**MARKOVITS** Meir	*RAFAEL,* *P.O. Box 2250, Dept. 24, Haifa, 31021,*	**ISRAEL**	Phone 972 (4) 879 2563 Fax 972 (4) 879 5289	E-mail: zviam@mofet.macam98.ac.il
163.	**MARON** Yitzhak	*Weizmann Institute of Science, Faculty of Physics* *P.O. Box 26, Rehovot, 76100,*	**ISRAEL**	Phone: 972 (8) 934 4055 Fax: 972 (8) 466 966	E-mail: fnmaron@weizmann.weizmann.ac.il
164.	**MARSHALL** Thomas C.	*Columbia University, Dept. of Applied Physics* *Room 213, S.W. Mudd Building, New York City, 10027, NY*	**USA**	Phone (212) 854 3116 Fax: (212) 854 8257	E-mail: tcm2@columbia.edu
165.	**MARTEN** Holger	*Forschungszentrum Karlsruhe, INR* *Postfach 3640, Karlsruhe, D-76021,*	**GERMANY**	Phone: 49 (7247) 82 2444 Fax: 49 (7247) 82 3824	E-mail: hmarten@inrrisc5.fzk.de
166.	**MASUZAKI** Masaru	*Kanazawa University, Faculty of Science, Dept. of Physics* *Kakuma-machi, Kanazawa, 920-11, Ishikawa*	**JAPAN**	Phone: 81 (762) 64 5672 Fax: 81 (762) 64 5739	E-mail: masuzaki@plasma.s.kanazawa-u.ac.jp
167.	**MATSUZAWA** Hidenori	*Yamanashi University, Faculty of Engineering* *Takeda 4-3-11, Kofu, J-400, Yamanshi*	**JAPAN**	Phone 81 (552) 20 8477 Fax 81 (552) 20 8477	E-mail:

168.	**MEISEL** Gert	*Forschungszentrum Karlsruhe, INR* *Postfach 3640, Karlsruhe 1, D-76021,*	**GERMANY**	Phone Fax	49 (7247) 823 437 49 (7247) 822 823	E-mail: bauer@inr.fzk.de
169.	**MENDEL, Jr.** Clifford W.	*5119 Sunningdale N.E.* *Albuquerque, 87110-5851, NM*	**USA**	Phone Fax	(505) 265 3840 (505) 265-3840	E-mail: mendel@swcp.com
170.	**MESYATS** Gennady A.	*Russian Academy of Sciences,* *14 Leninskiy Prospect, Moscow, 117 924,*	**RUSSIA**	Phone Fax	7 (095) 938 1858 7 (095) 938 2211	E-mail: mesyats@ief.intec.ru
171.	**MIRNOV** Vladimir V.	*Middle East Technical University, Dept. of Physics* *Ankara, 6531,*	**TURKEY**	Phone: Fax:	90 (312) 210 5047 90 (312) 210 1281	E-mail: vladimir@rorqual.cc.metu.edu.tr
172.	**MIRONYCHEV** Peter	*Russian Federal Nuclear Center (VNIIEF),* *Pr. Mira 37, Sarov (Arzamas-16), 607 190, Nizhnyi Novgorod Reg.*	**RUSSIA**	Phone Fax:	7 (83130) 613 86 7 (83130) 54 565	E-mail: popkov_3001@spd.rfnc.nnov.su
173.	**MITTERAUER** Johannes	*Institut für Allgemeine Elektrotechnik und Elektronik,* *Gusshausstrasse 27-29, Vienna, A-1040,*	**AUSTRIA**	Phone Fax:	43 (1) 58801 3682 43 (1) 504 2477	E-mail:
174.	**MIZHIRITSKI** Valeri	*Russian Res. Centre "Kurchatov Institute",* *Kurchatov Sq., 1, Moscow, 123182,*	**RUSSIA**	Phone Fax	7 (095) 196 9254 7 (095) 196 1635	E-mail: rudakov@rec.msk.su
175.	**MORAVEC** Jaroslav	*Institute of Plasma Physics AS CR, Pulsed Plasma Systems Dept.* *P.O. Box 17, Prague 8, 182 00,*	**CZECH REPUBLIC**	Phone Fax	42 (2) 6605 2940 42 (2) 858 6389	E-mail: moravec@ipp.cas.cz
176.	**MOROZOV** Ivan V.	*All-Russian Research Institute of Exp. Physics,* *Pr. Mira 37, Sarov (Arzamas-16), 607 190, Nizhnyi Novgorod Reg.*	**RUSSIA**	Phone Fax	7 (83130) 4 5738 7 (83130) 54 565	E-mail: vcher_1763@rfnc.nnov.su
177.	**MUELLER** Georg	*Forschungszentrum Karlsruhe, INR* *Postfach 3640, Karlsruhe, D-76021,*	**GERMANY**	Phone Fax	49 (7247) 824 302 49 (7247) 825 987	E-mail: mueller@inr.fzk.de
178.	**MUNIER** Alain	*C.E.A. - FRANCE,* *2 rue des Jardiniers, Marolles-en-Brie, F-94440,*	**FRANCE**	Phone Fax:	33 (1) 4598 1097 33 (1) 4386 7429	E-mail:
179.	**MUNZ** Claus-Dieter	*Forschungszentrum Karlsruhe, INR* *Postfach 3640, Karlsruhe, D-76021,*	**GERMANY**	Phone Fax	49 (7247) 822 449 49 (7247) 824 874	E-mail: Claus-Dieter.Munz@inr.fzk.de
180.	**MURUGOV** Vasilii M.	*Russian Federal Nuclear Center (VNIIEF),* *Pr. Mira 37, Sarov (Arzamas-16), 607 190, Nizhnyi Novgorod Reg.*	**RUSSIA**	Phone Fax	7 (83130) 56 646 7 (83130) 54 565	E-mail: murugov_2566@rfnc.nnov.su
181.	**NAGOVITSIN** Alexander Yu.	*Russian Federal Nuclear Center (VNIIEF),* *Pr. Mira 37, Sarov (Arzamas-16), 607 190, Nizhnyi Novgorod Reg.*	**RUSSIA**	Phone Fax	7 (83130) 61 386 7 (83130) 54 565	E-mail: popkov_3001@spd.rfnc.nnov.su
182.	**NANOBASHVILI** Irakli S.	*Abastumani Astrophysical Observatory, GAS,* *A. Kazbegi Ave 2a, Tbilisi, 380 060,*	**REP. GEORGIA**	Phone Fax:	995 (8832) 383510 995 (32) 398 783	E-mail: inanob@dtapha.kheta.georgia.su
183.	**NANOBASHVILI** Sulkhan	*Institute of Physics, Academy of Sciences Georgia,* *Tamarashvili 6, Tbilisi, 380077,*	**REP. GEORGIA**	Phone Fax:	995 (32) 398 783 995 (32) 398 783	E-mail: snanob@physics.iberiapeac.ge
184.	**NEAU** Eugene	*Quantum Manufacturing, Inc., Bldg. 3, Suite 210* *2201 San Pedro Dr. N.E., Albuquerque, 87 110, NM*	**USA**	Phone: Fax:	(505) 881 4121 (505) 880 0727	E-mail: elneau@RT66.com elneau@QMInc.com
185.	**NESTEROV** Eugene V.	*High Energy Density Research Center, RAS (IVTAN),* *Izhorskaya 13/19, Moscow, 127412,*	**RUSSIA**	Phone Fax:	7 (095) 484 1877 7 (095) 484 1877	E-mail: NST@nictiv.ivtan.msk.su
186.	**NEY** Philippe	*École Polytechnique, Lab. de Physique des Milieux Ionises* *B.P. 27, Palaiseau, F-91128,*	**FRANCE**	Phone Fax.	33 (1) 6933 3668 33 (1) 6933 3023	E-mail: ney@lpmi.polytechnique.fr
187.	**NITISHINSKY** Mikhail S.	*Russian Res. Centre "Kurchatov Institute", Applied Physics Division* *Kurchatov Sq., 1, Moscow, 123182,*	**RUSSIA**	Phone Fax	7 (095) 196 9185 7 (095) 196 9874	E-mail: potap@potap.msk.su
188.	**NIU** Keishiro	*Teikyo Heisei University, Dept. of Information System* *2289-23 Ohtani, Uruido, Ichihara, 290-01, Chiba*	**JAPAN**	Phone Fax:	81 (436) 74 5511 81 (436) 74 3659	E-mail:

189.	**NOVOMEYSKAYA** Diana	*Institute of Nuclear Physics of Tomsk PTU,* *Prospekt Lenina 2A, P.O. Box 25, Tomsk, 634 050,*	**RUSSIA**	Phone 7 (3822) 440 097 Fax 7 (3822) 440 812	E-mail remnev@ifc.tiasur.tomsk.su
190.	**OGAWA** Masao	*Tokyo Institute of Technology ,Dept. of Energy Sciences* *4259 Nagatsuta, Midori-ku, Yokohoma, J-226,*	**JAPAN**	Phone 81 (45) 924 5612 Fax: 81 (45) 924 5695	E-mail mogawa@energy.es.titech.ac.jp
191.	**OKADA** Toshio	*Tokyo University of Agriculture & Technology,* *2-24-16 Naka-machi Koganei-shi, Tokyo, 184,*	**JAPAN**	Phone 81 (423) 88 7116 Fax: 81 (423) 85 6255	E-mail: okada@cc.tuat.ac.jp
192.	**OLEINIK** Georgiy M.	*Troitsk Inst. for Innov. & Thermonucl. Investigation, TRINITI* *reg. "B", 3-159, Troitsk, 142092, Moscow Region*	**RUSSIA**	Phone. 7 (095) 334 5614 Fax: 7 (095) 334 5614	E-mail angara@fly.triniti.troitsk.ru
193.	**OPEKOUNOV** M. S.	*Institute of Nuclear Physics of Tomsk PTU,* *Prospekt Lenina 2A, P.O. Box 25, Tomsk, 634 050,*	**RUSSIA**	Phone 7 (3822) 440 097 Fax: 7 (3822) 440 812	E-mail: remnev@ifc.tiasur.tomsk.su
194.	**OSIPOV** Vladimir V.	*Institute of Electrophysics, UD RAS,* *Komsomolskaya 34, Ekaterinburg, 634 049,*	**RUSSIA**	Phone: 7 (3422) 445 174 Fax: 7 (3422) 445 051	E-mail: plasma@intec.ru
195.	**OSSAKOW** Sidney	*Naval Research Laboratory, Code 6700* *4555 Overlook Ave., S.W., Washington, 20375-5346, DC*	**USA**	Phone: (202) 767 2723 Fax: (202) 767 1607	E-mail: OSSAKOW@ccf.nrl.navy.mil
196.	**OZUR** Grigory E.	*High Current Electronics Institute, SD RAS,* *4, Akademicheski Avenue, Tomsk, 634055,*	**RUSSIA**	Phone 7 (3822) 259 709 Fax: 7 (3822) 259 410	E-mail: ozur@lve.hcei.tomsk.su
197.	**PALDY** Lester G.	*State University of New York and Stony Brook,* *Center for Sci.&Tech. Education, Stony Brook, 11974-3733, NY*	**USA**	Phone: (516) 632 7075 Fax: (516) 632 7220	E-mail: lpaldy@ccmail.sunysb.edu
198.	**PANESH** Anatoly M.	*L. Karpov Institute of Physical Chemistry,* *10 Vorontsovo pole, Moscow, 103 064,*	**RUSSIA**	Phone: 7 (095) 975 2450 Fax: 7 (095) 975 2450	E-mail: panesh@nifhi.rc.ac.ru
199.	**PATRAN** Alin	*Institute of Physics and Technology of Radiation Devices, Plasma Phys. & Nucl. Fusion Lab.* *P.O. Box 5206, Bucharest-Magurele, R-76900,*	**ROMANIA**	Phone 40 (1) 780 4290 Fax 40 (1) 420 9391	E-mail patran@roifa.ifa.ro
200.	**PAVLO** Pavel	*Institute of Plasma Physics AS CR, Theoretical Dept.* *P.O. Box 17, Prague 8, 182 00,*	**CZECH REPUBLIC**	Phone: 42 (2) 6605 2506 Fax 42 (2) 858 6389	E-mail pavlo@ipp.cas.cz
201.	**PEREIRA** Nino R.	*Berkeley Research Associates, Inc.,* *P.O. Box 852, Springfield, 22150-0852, VA*	**USA**	Phone. (703) 750 3434 Fax: (703) 750 3106	E-mail: pereira@bra4a.nrl.navy.mil
202.	**PESKOV** Nikolai Yu.	*Institute of Applied Physics, RAS,* *46, Ulyanov St., Nizhnyi Novgorod, 603600,*	**RUSSIA**	Phone. 7 (8312) 384 575 Fax. 7 (8312) 362 061	E-mail peskov@appl.sci-nnov.ru
203.	**PETERSON** Gus G.	*Naval Research Laboratory, NRC Research Associate, Code 6770, Plasma Physics Division* *4555 Overlook Ave., S.W., Washington, 20375, DC*	**USA**	Phone. (202) 767 3066 Fax: (202) 767 2012	E-mail: peterson@suzie.nrl.navy.mil
204.	**PETR** Jan	*Energoprojekt,* *Bubenská 1, Prague 7, 170 05,*	**CZECH REPUBLIC**	Phone: 42 (2) 870 708 Fax: 42 (2) 6671 1120	E-mail
205.	**PETRŽÍLKA** Jan	*Institute of Plasma Physics AS CR, Tokamak Dept.* *P.O. Box 17, Prague 8, 182 00,*	**CZECH REPUBLIC**	Phone: 42 (2) 6605 2944 Fax 42 (2) 858 6389	E-mail: jape@ipp.cas.cz
206.	**PIERRE** Joan Ma	*Defense Nuclear Agency,* *6801 Telegraph Road, Alexandria, 22310-3398, VA*	**USA**	Phone: (703) 325 7302 Fax: (703) 325 2959	E-mail: pierre@hq.dna.mil
207.	**PIFFL** Vojtěch	*Institute of Plasma Physics AS CR, Pulsed Plasma Systems Dept.* *P.O. Box 17, Prague 8, 18200,*	**CZECH REPUBLIC**	Phone: 42 (2) 6605 3223 Fax 42 (2) 858 6389	E-mail piffl@ipp.cas.cz
208.	**PIKAR'** Alexander	*Russian Federal Nuclear Center (VNIIEF),* *Pr. Mira 37, Sarov (Arzamas-16), 607 190, Nizhnyi Novgorod Reg.*	**RUSSIA**	Phone: 7 (83130) 61 386 Fax. 7 (83130) 54 565	E-mail pikar_3001@spd.rfnc.nnov.su
209.	**POGREBNJAK** Alexander D.	*Sumy Institute for Surface Modification,* *Av. Shevchenko 17, P.O. Box 163, Sumy, 244030,*	**UKRAINE**	Phone: 7 (0542) 220 338 Fax. 7 (0542) 275 002	E-mail simp@demex.sumy.ua

210.	**POPKOV** Nicolai F.	*Russian Federal Nuclear Center (VNIIEF),* *Pr. Mira 37, Sarov (Arzamas-16), 607 190, Nizhnyi Novgorod Reg.*	**RUSSIA**	Phone: 7 (83130) 61 386 Fax: 7 (83130) 54 565	E-mail: popkov_3001@spd.rfnc.nnov.su
211.	**PORNET** Jacqueline	*C.E.A. - FRANCE.* *59/E Rue Edmont Vaillant, Athis.Mons, 91200,*	**FRANCE**	Phone: 33 6938 8515 Fax:	E-mail:
212.	**POTAPOV** Anatoliy	*Russian Federal Nuclear Center (VNIITF), Institute of Technical Physics (VNIITF)* *P.O. Box 245, Snezhinsk, 456 770, Chelyabinsk Reg.*	**RUSSIA**	Phone: Fax: 7 (35172) 320 77	E-mail:
213.	**PROSKUROVSKY** D. I.	*High Current Electronics Institute, SD RAS,* *4, Akademicheski Avenue, Tomsk, 634055,*	**RUSSIA**	Phone: 7 (3822) 259 709 Fax: 7 (3822) 259 410	E-mail: pdi@lve.hcei.tomsk.su
214.	**PRUCKER** Udo	*University of Erlangen-Nurnberg,* *Erwin-Rommel Str. 1, Erlangen, D-91058,*	**GERMANY**	Phone: 49 (9131) 85 7118 Fax: 49 (9131) 15 249	E-mail: prucker@circe.physik.uni-erlangen.de
215.	**PUTNAM** Sidney D.	*Pulse Sciences, Inc.,* *600 McCormick St., San Leandro, 94577, CA*	**USA**	Phone: (510) 632 5100 Fax: (510) 632 5300	E-mail: sputnam@titan.com
216.	**QUINTENZ** Jeffery P.	*Sandia National Laboratories,* *P.O. Box 5800, MS 1195, Albuquerque, 87185-1195, NM*	**USA**	Phone: (505) 845 7245 Fax: (505) 845 7464	E-mail: jpquint@sandia.gov
217.	**ŘÍPA** Milan	*Institute of Plasma Physics AS CR,Pulsed Plasma Systems Dept.* *P.O. Box 17, Prague 8, 182 00,*	**CZECH REPUBLIC**	Phone 42 (2) 6605 3243 Fax: 42 (2) 858 6389	E-mail: ripa@ipp.cas.cz
218.	**RAACKE** Jens	*Heinrich Heine Universität, Institut für Experimentalphysik* *Universitätsstraße 1/25.42, Düsseldorf, D-40225,*	**GERMANY**	Phone: 49 (211) 811 3106 Fax: 49 (211) 811 3116	E-mail: raacke@bennett.exphy.uni-duesseldorf.de
219.	**RADJUK** Elena	*Radiation Physics & Chemistry Problems Institute, BAS,* *Minsk-Sosny, 220 109,*	**BELARUS**	Phone. 375 (172) 467 494 Fax: 375 (172) 467 317	E-mail: goulo%bas06.basnet.minsk.by@demos.su
220.	**REISER** Martin	*University of Maryland,Institute for Plasma Research* *Energy Research Building, College Park, 20742-3511, MD*	**USA**	Phone (301) 405 4960 Fax (301) 314 9437	E-mail: mreiser@glue.umd.edu
221.	**REMNEV** Gennady E.	*Institute of Nuclear Physics of Tomsk PTU,* *Prospekt Lenina 2A, P.O. Box 25, Tomsk, 634 050,*	**RUSSIA**	Phone. 7 (3822) 440 097 Fax: 7 (3822) 440 812	E-mail: remnev@ifc.tiasur.tomsk.su
222.	**RIEGE** Hans	*CERN,LHC Division* *Geneve 23, CH-1211,*	**SWITZERLAND**	Phone 41 (22) 767 3579 Fax: 41 (22) 767 9155	E-mail: riege@cernvm.cern.ch
223.	**ROBERSON** Charles	*Office of Naval Research, Physics Division, Code 1112* *800 North Quincy Street, Arlington, 22217-5660, VA*	**USA**	Phone: (703) 696 4222 Fax: (703) 696 3945	E-mail: robersc@onrhq.onr.navy.mil
224.	**RÖWEKAMP** Peter	*Heinrich Heine Universität, Institut für Experimental Physik* *Universitätsstraße 1/25.42, Düsseldorf, D-40225,*	**GERMANY**	Phone 49 (211) 811 2322 Fax 49 (211) 811 3116	E-mail: roewe@bennett.exphy.uni-duesseldorf.de
225.	**ROHLENA** Karel	*Institute of Physics, AS CR,* *Na Slovance 2, Prague 8, 180 40,*	**CZECH REPUBLIC**	Phone: 42 (2) 6606 2792 Fax: 42 (2) 821 227	E-mail: rohlena@fzu.cz
226.	**ROMANOV** Igor G.	*Nizhegorodskiy Branch of the Inst. for Machine Science, RAS,* *Belinskiy 85, Nizhniy Novgorod, 603 600,*	**RUSSIA**	Phone: 7 (8312) 320 179 Fax: 7 (8312) 320 301	E-mail:
227.	**ROMANOVA** Vera	*P.N. Lebedev Physical Institute, RAS,* *Leninskiy Prospekt 53, Moscow, 117924,*	**RUSSIA**	Phone 7 (095) 135 7995 Fax: 7 (095) 135 7880	E-mail: romanova@sci.lpi.ac.ru
228.	**ROMARY** Philippe	*C.E.A. - CESTA, Service de Physique Experimentale* *B.P. 2, Le Barp, F-33114,*	**FRANCE**	Phone. 33 5 668 4912 Fax: 33 5 771 5439	E-mail:
229.	**ROSENBERG** Avner	*RAFAEL,* *P.O. Box 2250, Haifa, 31021,*	**ISRAEL**	Phone. 972 (4) 879 5018 Fax: 972 (4) 879 5315	E-mail.
230.	**ROSENBLUM** Moshe	*Atomic Energy Commission,* *P.O. Box 7061, Tel Aviv, 61070,*	**ISRAEL**	Phone. 972 (3) 646 2010 Fax: 972 (3) 646 2974	E-mail:

231.	**ROTH** Peter	*Gerstenstr. 1, Pfaffenhofen, D-85276,*	**GERMANY**	Phone: 49 (8441) 76989 Fax: ?	E-mail
232.	**RUDAKOV** Leonid I.	*Russian Res. Centre "Kurchatov Institute", Institute of Nuclear Fusion.* *Kurchatov Sq., 1, Moscow, 123182,*	**RUSSIA**	Phone: 7 (095) 196 9685 Fax: 7 (095) 196 1635	E-mail: rudakov@rec.msk.su
233.	**RUKHADZE** Anri A.	*General Physics Institute, RAS,* *Vavilova 38, Moscow, 117942.*	**RUSSIA**	Phone: 7 (095) 135 0247 Fax: 7 (095) 135 8011	E-mail: loza@fp7.gpi.ru
234.	**RUKIN** Sergei N.	*Institute of Electrophysics, UD RAS,* *Komsomolskaya 34, Ekaterinburg, 620 219,*	**RUSSIA**	Phone: 7 (3432) 493 444 Fax: 7 (3432) 445 051	E-mail: rukin@ief.intec.ru
235.	**RŮŽIČKA** Tomáš	*Czech Academy of Sciences,* *Narodni 3, Prague 1, 110 00,*	**CZECH REPUBLIC**	Phone: 42 (2) 242 40 567 Fax: 42 (2) 242 20 944	E-mail: natsci@lorien.site.cas.cz
236.	**RYASLOV** Eugenei A.	*Russian Federal Nuclear Center (VNIIEF),* *Pr. Mira 37, Sarov (Arzamas-16), 607 190, Nizhnyi Novgorod Reg.*	**RUSSIA**	Phone: 7 (83130) 54 638 Fax: 7 (83130) 54 565	E-mail: raslov_otd4@expd.rfnc.nnov.su
237.	**RYUTOV** Dmitri D.	*Lawrence Livermore National Laboratory,* *7000 East Avenue, L-630, Livermore, 94 551, CA*	**USA**	Phone: (510) 422 9832 Fax: (510) 423 3484	E-mail: ryutov@moonshine.llnl.gov
238.	**RYZHKOV** Vladislav	*Institute of Nuclear Physics of Tomsk PTU,* *Prospekt Lenina 2A, P.O. Box 25, Tomsk, 634050,*	**RUSSIA**	Phone: 7 (3822) 440 621 Fax: 7 (3822) 440 812	E-mail: remnev@ifc.tiasur.tomsk.su
239.	**SADOWSKI** Marek	*Soltan Institute for Nuclear Studies,* *Swierk-Otwock, 05-400,*	**POLAND**	Phone: 48 (22) 779 8678 Fax: 48 (22) 779 3481	E-mail p05msa@cx1.cyf.gov.pl
240.	**ŠALANSKÝ** Jan	*Institute of Plasma Physics AS CR, Pulsed Plasma Systems Dept.* *P.O. Box 17, Prague 8, 182 00,*	**CZECH REPUBLIC**	Phone: 42 (2) 6605 3242 Fax: 42 (2) 858 6389	E-mail: maxwell@ipp.cas.cz
241.	**SALNIKOV** Leonard .I.	*Radiation Physics & Chemistry Problems Institute, BAS,* *Minsk-Sosny, 220 109,*	**BELARUS**	Phone: 375 (172) 467 050 Fax: 375 (172) 467 317	E-mail: goulo%bas06.basnet.minsk.by@demos.su
242.	**SANFORD** Thomas W.L.	*Sandia National Laboratories, Org. 1231, Intense Ion Beam Research Dept. 9531* *P.O. Box 5800, MS 1193, Albuquerque, 87185-1193, NM*	**USA**	Phone: (505) 845 7816 Fax: (505) 845 7864	E-mail: twsanfo@sandia.gov
243.	**SAVELIEV** Yuri M.	*University of St. Andrews, School of Physics and Astronomy* *North Haugh, St. Andrews, KY16 9SS, Fife*	**UK**	Phone: 44 (1334) 476 161 Fax: 44 (1334) 463 104	E-mail yms@st-andrews.ac.uk
244.	**SCHAMILOGLU** Edl	*University of New Mexico, Dept. of Electrical and Computer Eng.* *323C EECE Building, Albuquerque, 87131, NM*	**USA**	Phone: (505) 277 4423 Fax: (505) 277 1439	E-mail: edl@eece.unm.edu
245.	**SCHNEIDER** Ralph	*Defense Nuclear Agency, EST, Simulation and Test Division* *6801 Telegraph Road, Alexandria, 22310-3398, VA*	**USA**	Phone: (703) 325 1142 Fax: (703) 325 0249	E-mail: schneider@hqg.dna.mil
246.	**SEIDL** Milos	*Stevens Institute of Technology, Physics Dept.* *Castle Point on the Hudson, Hoboken, 07030, NJ*	**USA**	Phone: (201) 216 5665 Fax: (201) 216 5638	E-mail: M.SEIDL@vaxa.stevens-tech.edu
247.	**SEMUSHIN** Sergei	*École Polytechnique,* *Lab. PMI, Palaiseau, F-91128,*	**FRANCE**	Phone: 33 (1) 6933 3248 Fax: 33 (1) 6933 3023	E-mail: sem@lpmi.polytechnique.fr
248.	**SERLIN** Victor	*Naval Research Laboratory, Code 6754* *4555 Overlook Ave., S.W., Washington, 20375-5000, DC*	**USA**	Phone: (202) 767 0678 Fax: (202) 767 0046	E-mail: serlin@ppd.nrl.navy.mil
249.	**SHAPIRO** Alexander	*All-Russian Electrotechnical Institute (VEI),* *Krasnokazarmennaya 12, Moscow, 111250,*	**RUSSIA**	Phone: 7 (095) 361 9453 Fax: 7 (095) 362 5617	E-mail: kozlov@dir.vei.msk.su
250.	**SHASHKOV** Andrei	*Russian Res. Centre "Kurchatov Institute",* *Kurchatov Sq., 1, Moscow, 123182,*	**RUSSIA**	Phone: 7 (095) 196 9672 Fax: 7 (095) 196 9874	E-mail:
251.	**SHCHERBAK** Anatoliy F.	*Ministry of Sci. & Technol. Policy of Rus. Fed., Dept. of Basic Research* *Tverskaya St. 11, Moscow, 103905,*	**RUSSIA**	Phone: 7 (095) 229 4046 Fax: 7 (095) 230 2823	E-mail:

252.	**SHILOH** Joseph	*FM Technologies,* *10529-B Braddock Road, Fairfax, 22 003, VA*	**USA**	Phone (703) 425 2973 Fax (703) 425 3539	E-mail jshiloh@gmu.edu
253.	**SHLAPAKOVSKII** Anatoli S.	*Institute of Nuclear Physics of Tomsk PTU,* *Prospekt Lenina 2A, P.O. Box 25, Tomsk, 634050,*	**RUSSIA**	Phone 7 (3822) 440 726 Fax 7 (3822) 440 812	E-mail shl@tsinph.tomsk.su
254.	**SHOUP** Roy W.	*Field Command Defense Nuclear Agency,* *1680 Texas St. S.E., Kirtland AFB, 87117-5669, NM*	**USA**	Phone (505) 845 3652 Fax (505) 845 7841	E-mail shoup@fc.dna.mil
255.	**SHPAK** Valery G.	*Institute of Electrophysics, UD RAS,* *Komsomolskaya 34, Ekaterinburg, 620 049,*	**RUSSIA**	Phone 7 (3432) 499 085 Fax 7 (3432) 445051	E-mail radan@ief.intec.ru
256.	**SHPITALNIK** Reuven R.	*NRC Soreq, Plasma Group* *Dept. 27, Yavne, 81 800,*	**ISRAEL**	Phone 972 (8) 434 760 Fax 972 (8) 434 775	E-mail reuven@ndc.soreq.gov.il
257.	**SHULOV** Vyacheslav A.	*Moscow Aviation Institute,* *Volokolamskoe Shosse 4, Moscow, 125 871,*	**RUSSIA**	Phone 7 (095) 158 4424 Fax 7 (095) 158 2977	E-mail surface@k208.mainet.msk.su
258.	**SHUNAILOV** Sergei A.	*Institute of Electrophysics, UD RAS,* *Komsomolskaya 34, Ekaterinburg, 620049,*	**RUSSIA**	Phone 7 (3432) 499 085 Fax 7 (3432) 445051	E-mail radan@ief.intec.ru
259.	**SHURTER** Roger P.	*Los Alamos National Laboratory,* *P.O. Box 1663, M.S. P942, Los Alamos, 87545, NM*	**USA**	Phone (505) 667 4408 Fax (505) 665 4396	E-mail shurter@lanl.gov
260.	**SINCERNY** Peter	*Physics International Company, P.O. Box 5010, Division 7000* *2700 Merced St., San Leandro, 94577, CA*	**USA**	Phone (510) 577 7138 Fax (510) 577 7247	E-mail slgreen@corp.olin.com
261.	**SINEBRYUKHOV** Andrei A.	*Institute of Electrophysics, RAS, Tomsk Branch* *Akademicheskaya St. 4, Tomsk, 634055,*	**RUSSIA**	Phone 7 (3822) 259 040 Fax 7 (3822) 259410	E-mail aasin@ief.tomsk.su
262.	**SINITSKY** Stanislav L.	*Budker Institute of Nuclear Physics, SD RAS,* *Lavrentyev Avenue 11, Novosibirsk, 630 090,*	**RUSSIA**	Phone 7 (3832) 359 924 Fax 7 (3832) 352 163	E-mail sinitsky@inp.nsk.su
263.	**SKLADNIK-SADOWSKA** E.	*Soltan Institute for Nuclear Studies,* *Swierk-Otwock, 05-400,*	**POLAND**	Phone 48 (22) 779 8678 Fax 48 (22) 779 3481	E-mail p05msa@cx1.cyf.gov.pl
264.	**SKVORTSOV** Vladimir A.	*High Energy Density Research Center, RAS (IVTAN),* *Izhorskaya 13/19, Moscow, 127412,*	**RUSSIA**	Phone 7 (095) 485 7988 Fax 7 (095) 485 7990	E-mail skv@hedric.msk.su
265.	**SMIRNOV** Valentine P.	*Troitsk Inst. for Innov. & Thermonucl. Investigation, TRINITI* *Novikova, 3-19, Troitsk, 123 098, Moscow Region*	**RUSSIA**	Phone 7 (095) 334 5614 Fax 7 (095) 334 5614	E-mail smirnov@dir.iiapp.msk.su
266.	**SOKOLOWSKI** Waldemar	*Spectroscopy&Imaging GmbH,* *Bruno-Walter-St. 7, Berlin, D-12247,*	**GERMANY**	Phone 49 (30) 771 6644 Fax 49 (30) 771 6645	E-mail:
267.	**SOKOVNIN** Sergei Yu.	*Institute of Electrophysics, UD RAS,* *Komsomolskaya 34, Ekaterinburg, 620 219,*	**RUSSIA**	Phone 7 (3422) 493 320 Fax 7 (3422) 445 051	E-mail razrad@ief.e-burg.su
268.	**SOTO** Leopoldo	*Comision Chilena de Energia Nuclear,* *Casilla 188-D, Santiago,*	**CHILE**	Phone 56 (2) 273 8723 Fax 56 (2) 273 8723	E-mail l_soto@reina.lreina.cchen.cl
269.	**SPASSOVSKY** Ivan P.	*Korea Atomic Energy Research Institute,* *P.O. Box 105, Yusong, Daejon, 305-600,*	**SOUTH KOREA**	Phone 82 (42) 868 200 1 Fax 82 (42) 868 2702	E-mail ipspass@nanum.kaeri.re.kr
270.	**SPIELMAN** Rick B.	*Sandia National Laboratories, Dept. 9573* *P.O. Box 5800, Albuquerque, 87185-1194, NM*	**USA**	Phone (505) 845 7470 Fax (505) 845 7864	E-mail rbspiel@sandia.gov
271.	**STALLINGS** Charles	*Physics International Company, P.O. Box 5010, Division 7000* *2700 Merced St., San Leandro, 94577, CA*	**USA**	Phone (510) 577 7121 Fax (510) 577 7108	E-mail chstallings@corp.olin.com
272.	**STANISLAWSKI** Jacek	*Soltan Institute for Nuclear Studies,Dept. of Thermonuclear Research* *Swierk-Otwock, 05-400,*	**POLAND**	Phone 48 (22) 779 8613 Fax 48 (22) 779 3841	E-mail p05msa@cx1.cyf.gov.pl

273.	**STINNETT** Regan W.	*Quantum Manufacturing, Inc., San Pedro Office Park, Bldg. 3* *1033 Tramway Lane N.E., Albuquerque, 87122, NM*	**USA**	Phone: Fax:	(505) 856 5070 (505) 880 0727	E-mail: RWStinn@rt66.com
274.	**STÖCKEL** Jan	*Institute of Plasma Physics AS CR, Tokamak Dept.* *P.O. Box 17, Prague 8, 182 00,*	**CZECH REPUBLIC**	Phone Fax	42 (2) 6605 3944 42 (2) 858 6389	E-mail: stockel@ipp.cas.cz
275.	**STRAUSS** Dirk	*Forschungszentrum Karlsruhe, INR* *Postfach 3640, Karlsruhe, D-76021,*	**GERMANY**	Phone: Fax:	49 (7247) 824 695 49 (7247) 825 987	E-mail:
276.	**STRELKOV** Pavel S.	*General Physics Institute, RAS,* *Vavilova 38, Moscow, 117942,*	**RUSSIA**	Phone: Fax:	7 (095) 132 8216 7 (095) 135 8011	E-mail: loza@fp7.gpi.msk.su
277.	**STROGANOV** Vadim A.	*High Energy Density Research Center, RAS (IVTAN),* *Izhorskaya 13/19, Moscow, 127412,*	**RUSSIA**	Phone: Fax:	7 (095) 484 4474 7 (095) 484 1877	E-mail: NST@nictiv.ivtan.msk.su
278.	**SUDAN** Ravindranath N.	*LPS, Cornell University,* *369 Upson Hall, Ithaca, 14853, NY*	**USA**	Phone Fax:	(607) 255 7392 (607) 255 3004	E-mail: sudan@lps.cornell.edu
279.	**ŠUNKA** Pavel	*Institute of Plasma Physics AS CR,* *P.O. Box 17, Prague 8, 182 00,*	**CZECH REPUBLIC**	Phone: Fax:	42 (2) 688 3030 42 (2) 858 6389	E-mail: sunka@ipp.cas.cz
280.	**SVOBODA** Vojtěch	*Institute of Plasma Physics AS CR, Tokamak Dept.* *P.O. Box 17, Prague 8, 182 00,*	**CZECH REPUBLIC**	Phone: Fax:	42 (2) 6605 3947 42 (2) 858 6389	E-mail: svoboda@ipp.cas.cz
281.	**TARAKANOV** Vladimir P.	*Institute for High Temperatures, RAS (IVTAN), High Energy Density Research Center* *Izhorskaya 13/19, Moscow, 127412,*	**RUSSIA**	Phone: Fax:	7 (095) 183 8626 7 (095) 485 7990	E-mail: KARAT@tarak.msk.su
282.	**TAUSCHWITZ** Andreas	*University of Erlangen,INR* *Erwin Rommel Str. 1, Erlangen, D-91058,*	**GERMANY**	Phone. Fax:	49 (7247) 822 453 49 (7247) 822 823	E-mail: Andreas.Tauschwitz@inr.fzk.de
283.	**TICHÝ** Milan	*Faculty of Mathematics and Physics, Charles University, Dept. of Electronics and Vacuum Physics* *V Holešovičkách 2, Prague 8, 170 00,*	**CZECH REPUBLIC**	Phone: Fax:	42 (2) 8576 2332 42 (2) 8576 2350	E-mail: tichy@mff.cuni.cz
284.	**TINKA** Ivan	*Energoprojekt,* *Bubenská 1, Prague 7, 170 05,*	**CZECH REPUBLIC**	Phone: Fax.	42 (2) 870 708 42 (2) 6671 1120	E-mail:
285.	**TOLOPA** Alexander	*Research Center Rossendorf, Inc.,Inst. for Ion Beam Physics (FWIM)* *P.O. Box 510119, Dresden, D-01314,*	**GERMANY**	Phone. Fax:		E-mail: tolopa@hera.fz-rossendorf.de
286.	**TOULISOV** Evgenyi	*Res. Inst. of Sci. Instruments, Min. of Atomic Energy,* *Turaevo, Lytkarino, 140 061, Moscow Region*	**RUSSIA**	Phone. Fax:	7 (095) 552 3911 7 (095) 552 3911	E-mail:
287.	**ULLSCHMIED** Jiří	*Institute of Plasma Physics AS CR, Pulsed Plasma Systems Dept.* *P.O. Box 17, Prague 8, 182 00,*	**CZECH REPUBLIC**	Phone: Fax:	42 (2) 887 963 42 (2) 858 6389	E-mail: ullsch@ipp.cas.cz
288.	**USHAKOV** Andrey G.	*Russian Res. Centre "Kurchatov Institute", Applied Physics Division* *Kurchatov Sq., 1, Moscow, 123182,*	**RUSSIA**	Phone: Fax:	7 (095) 196 9185 7 (095) 196 9874	E-mail: krash@kiae.su
289.	**VÄTH** Walter	*Forschungszentrum Karlsruhe, INR* *Postfach 3640, Karlsruhe 1, D-76021,*	**GERMANY**	Phone: Fax:	49 (7247) 823 445 49 (7247) 825 987	E-mail:
290.	**VALENTA** Václav	*ŠKODA, Nuclear Machinery, Plzeň, Ltd.,* *Orlik 266, Plzeň, 316 06,*	**CZECH REPUBLIC**	Phone: Fax:	42 (19) 704 2824 42 (19) 722 7118	E-mail:
291.	**VECCHI** Marcello	*ENEA,* *via Martiri di Monte Sole, 4, Bologna, 40 129,*	**ITALY**	Phone: Fax:	39 (51) 609 8718 39 (51) 609 8738	E-mail: vecchi@rin365.arcoveggio.enea.it
292.	**VITKOVITSKY** Ihor	*Logicon RDA,* *2100 Washington Blvd., Arlington, 22204-5706, VA*	**USA**	Phone: Fax:	(703) 486 3566 (703) 920 4710	E-mail
293.	**VOGEL** Nadja	*University of Technology Chemnitz-Zwickau, Optical Spectroscopy & Molecule Physics* *Dept. of Physics, 13303, Chemnitz, D-09107,*	**GERMANY**	Phone: Fax:	49 (371) 531 3037 49 (371) 531 3060	E-mail: n.vogel@physik.tu-chemnitz.de

294.	**VOLKOV** Gennady I.	*All-Russian Research Institute of Exp. Physics,* *Pr. Mira 37, Sarov (Arzamas-16), 607 190, Nizhnyi Novgorod Reg.*	**RUSSIA**	Phone 7 (83130) 4 5738 Fax: 7 (83130) 54 565	E-mail: vcher_1763@spd.rfnc.nnov.su
295.	**VRBA** Pavel	*Institute of Plasma Physics AS CR, Theoretical Dept.* *P.O. Box 17, Prague 8, 182 00,*	**CZECH REPUBLIC**	Phone 42 (2) 6605 2521 Fax 42 (2) 858 6389	E-mail: vrba@ipp.cas.cz
296.	**WARE** Kenneth D.	*Defense Nuclear Agency,* *6801 Telegraph Road, Alexandria, 92310-3398, VA*	**USA**	Phone: (703) 325 6734 Fax: (703) 325 0249	E-mail: wareke@hqg.dna.mil
297.	**WEBER** Bruce V.	*Naval Research Laboratory,* *4555 Overlook Ave., S.W., Washington, 20375-5320, DC*	**USA**	Phone (202) 767 8313 Fax: (202) 767 2012	E-mail: weber@suzie.nrl.navy.mil
298.	**WOOLVERTON** Kevin	*Texas Technical University, Dept. of Electrical Engineering* *P.O. Box 43102, Lubbock, 79409-3102, TX*	**USA**	Phone: (806) 742 3468 Fax: (806) 742 1281	E-mail: NUS69@ttacs.ttu.edu
299.	**YALANDIN** Michael I.	*Institute of Electrophysics, UD RAS,* *Komsomolskaya 34, Ekaterinburg, 620 049,*	**RUSSIA**	Phone: 7 (3432) 499 085 Fax: 7 (3432) 445051	E-mail: radan@ief.intec.ru
300.	**YATSUI** Kiyoshi	*Nagaoka University of Technology, Laboratory of Beam Technology* *Kamitomioka 1603-1, Nagaoka, 940-21, Niigata*	**JAPAN**	Phone: 81 (258) 46 6105 Fax: 81 (258) 46 6506	E-mail: yatsui@voscc.nagaokaut.ac.jp
301.	**YATSUZUKA** Mitsuyasu	*Himeji Institute of Technology, Dept. of Electrical Engineering* *2167 Shosha, Himeji, 671-22, Hyogo*	**JAPAN**	Phone: 81 (792) 674 862 Fax: 81 (792) 674 862	E-mail: yatuzuka@elct.eng.himeji-tech.ac.jp
302.	**ŽÁČEK** František	*Institute of Plasma Physics AS CR, Tokamak Dept.* *P.O. Box 17, Prague 8, 182 00,*	**CZECH REPUBLIC**	Phone 42 (2) 688 3028 Fax 42 (2) 858 6389	E-mail: zacek@ipp.cas.cz
303.	**ZAVIALOV** Michael	*All-Russian Electrotechnical Institute (VEI)* *Krasnokazarmennaya 12, Moscow, 111250,*	**RUSSIA**	Phone 7 (095) 361 9453 Fax: 7 (095) 362 5617	E-mail: kozlov@dir.vei.msk.su
304.	**ZHANG** Jiang-de	*The National University of Defense Technology, Applied Physics Dept.* *Changsha, 410 073, Hunan*	**P.R. CHINA**	Phone: 86 (731) 451 8307 Fax: 86 (731) 451 8307	E-mail:
305.	**ZHARINOV** Evstafii I.	*All-Russian Research Institute of Exp. Physics,* *Pr. Mira 37, Sarov (Arzamas-16), 607 190, Nizhnyi Novgorod Reg.*	**RUSSIA**	Phone 7 (83130) 45 738 Fax: 7 (83130) 54 565	E-mail: vcher_1763@spd.rfnc.nnov.su
306.	**ZHONG** Hui-huang	*The National University of Defense Technology, Applied Physics Dept.* *Changsha, 410 073, Hunan*	**P.R. CHINA**	Phone: 86 (731) 451 8307 Fax: 86 (731) 451 8307	E-mail:
307.	**ZHU** Wenjun	*Institute of Fluid Physics, CAEP, Accelerator Laboratory* *P.O. Box 523-56, Chengdu, 610 003, Sichuan*	**P.R. CHINA**	Phone: 86 (816) 222 5695 Fax: 87 (816) 222 5695	E-mail:
308.	**ZINCHENKO** Vladimir	*Res. Inst. of Sci. Instruments, Min. of Atomic Energy,* *Turaevo, Lytkarino, 140 061, Moscow Region*	**RUSSIA**	Phone: 7 (095) 552 3911 Fax: 7 (095) 552 3911	E-mail:
309.	**ZOTOVA** Irina V.	*Institute of Applied Physics, RAS,* *46, Ulyanov St., Nizhnyi Novgorod, 603600,*	**RUSSIA**	Phone: 7 (8312) 384 316 Fax: 7 (8312) 362 061	E-mail: zotova@appl.sci-nnov.ru

AUTHOR INDEX

NNNN - First Author
NNNN - Presenting Author
NNNN - Co-author 1-48

Abdallah Jr., J. **687**
Abdallah, C.T. 433
Abubakirov, E.B. **410**
Adachi, T. 52
Adams, R.G. 1 48
Afonin, V.I. **691** **697** **701**
Agafonov, M.A. **182** **213**
Agalakov, V.P. **301**
Agee, F.J. 928
Alberts, T.E. 37
Alfverov, D.F. **999**
Aliaga-Rossel, R. 762
Alley, W.E. 753
Allshouse, G.A. 37
Allshouse, G.O. 146
Anderson, D.E. 1171
Anderson, J. 238
Ando, R. 331 339 351 393
Andreev, A. 267 793 809
Andronov, A.N. **485**
Anfinogentov, V.G. **381**
Anthouard, P. **628**
Aoki, T. 501
Appartaim, R.K. 111
Apruzese, J.P. 146 749
Arad, R. 41 1039 1216
Aranchuk, L. 276
Arkhipov, A.V. 319 **371** **789**
Arzhannikov, A.V. 182 213 **367** 1127
Astrelin, V.T. 182
Attelan-Langlet, S. **1064**
Aubert, J.H. 37
Aurass, H. 1031
Auvray, P. 276
Averchenkov, V.Ya. 296 619 640
Avrillaud, G. 276
Azharonok, V.V. **797**
Babineau, M.A. 121
Baca, P. 37
Baca, P.M. 37
Bachmann, H. 1123
Bailey, J.E. 1 37 48
Bailey, V.L. 60
Bakshaev, Yu.L. **962**
Baksht, R.B. **522**
Balakirev, V.A. 426 **611**
Bangerter, R.O. 91
Baranowski, J. 737
Barber, T.L. 37
Bardy, J. 628
Barinov, N.U. 301
Barnard, J.J. 91
Bauer, W. **1123** 1155
Baumung, K. **72**
Bayol, F. 276 1203
Belenki, G.S. 301
Benattar, R. **771**
Benford, G. 217
Benford, J. **217**
Berntien, U. 659
Bezuglov, V.G. **977** **981**
Blaha, M. 709
Bliokh, Yu.P. 229
Bloomquist, D.D. 1
Bluhm, H. 72 1123 **1127** 1155 1195 1257
Bobashev, S.V. 174
Bobylev, A.V. 182
Bogdanov, L.Yu. **319**
Boller, J.R. 115
Bondarenko, G.G. **840**
Bonnafond, C. 628
Borisov, V.V. 526
Borovina, D.L. 928
Borovkov, V.V. 296
Bossamykin, V.S. **619** **640** 938
Bowman, C.D. **139**
Branitski, A.V. **140** **292** **526** **530** **534** **542**
Bratman, Vl.L. **401**
Breeze, S.F. 150
Breeze, S.P. 37
Bruns, C. 753
Bryunetkin, B.A. 1075
Brzosko, J.S. 131
Bugaev, S.P. **905**
Bulan, V.V. **942**
Bulgakov, T. **917**
Burdakov, A.V. 182
Burenkov, O.M. **1084**
Burkov, P.V. 1221
Burmasov, V.S. **335** **1046**
Butenko, V.I. 64
Buth, L. 1123 1127 1155 1257
Buzin, V.N. 538 558
Bystrickii, Vit. **127** 917 **1217** **1221**
Bystricky, V. 917
Bystruckii, V.M. **886**
Campbell, M.M. 882
Carlson, A.L. 37 48
Carlson, R.L. **188**
Carmel, Y. 405
Caryotakis, G. **406**
Cassany, B. 276
Castle, M. 238
Cengher, M. **599**
Chagin, M.N. 182
Chaikovski, S. 917
Chamdani, E.P.A. 898
Chandler, G.A. 1 37
Chedia, O.V. **1035**
Chen, Ch. **1018**
Cheng, D. 924
Cheng, J. 238
Chernenko, A.S. **154** 962
Chernikov, E.V. 873
Chernykh, E.V. **457**
Chernyshev, V.K. 7 538 **558** **1008** 1084
Chernyshev, V.V. 158
Chigrinov, S. **921**
Childers, K. 1003
Ching, C.H. 48
Chishiro, E. 27 **1163**
Chittenden, J.P. 741
Chlenov, A.M. 671 675
Chmielewski, A.G. 824
Cho, S.O. 453
Choi, P. 276 **305** 505 509 **566** 570
574 679 **932** 1233
Christiansen, J. 603
Chuaqui, F. 505
Chuaqui, H. 305 566 570 574 **679** 762
Chubrik, N.I. 797
Chumakov, G.D. 981
Chuvatin, A.S. 276 **1199** **1203** 1211 1237
Clark, R.E.H. 687
Coates, D.M. 263
Coats, R.S. 1 101
Cochran, F.L. **705**
Coffey, S.K. 131 158

Cohn, D. **249**
Collier, J. 271
Collins, C.B. 928
Colombant, D. 206
Commisso, R.J. 121 749
Cook, D.L. 1 37
Cooperstein, G. 115 1147 **1151**
Corcoran, P. 150 989
Csanak, G. 687
Cuneo, M.E. 1 101 1054
Dan'ko, S. 550
Danilenko, K.N. 292
Danilenko, K.V. 140
Danilov, V.V. **1027**
Darznek, S.A. **1241**
Datsko, I.M. 522
Davanloo, F. **928**
Davara, G. 41 1058 **1063**
Davidson, R.C. 1018
Davis, H.A. **263** 890 894
Davis, J. 705 **709** 757
Davlatjan, T.A. **832** **836**
De Groot, J.S. 721 753
De Mascureau, J. 628
Decker, G. 174 659
Deeney, C. 1 150
Degnan, J.H. 131 158 558
DeGroot, J.S. 146
Deichuly, M.F. **221**
Delsart, P. 628
Demidov, B.A. 1269
Demin, A.N. 1084
Dempsey, J. 1003
Denisenko, P.V. 182
Denisov, Yu.A. 817
Deniz, A.V. 627
Deryugin, Yu.N. **192**
Derzon, M.S. 1 37
Desjarlais, M.P 1 48 **101**
Destler, W.W 405
Deulin, Yu.I. 182
Deutsch, C. **1103**
Devin, A. 628
Devlin, D.J. 993
Didenko, A.N. **445** **449**
Diyankov, O.V. 697 **713** 717 725 **775**
Diyankov, V.S. **309** 958 969
Dolgachev, G.I. 301 **1207**
Doroshkin, A.A. 1195
Douglas, M.R. 37 146 150
Dudin, I.F. 1084
Dukart, R.J. 1 37
Dumitrescu-Zoita, C. 276 305 574 679
Dyabilin, K.E. 140
Dyabilin, K.S. 292 **632** **653**
Ebine, T. 52
Eddleman, J.L. 146 721 753
Efremov, V.P. **1269**
Emic, J. 753
Emlin, D.R. 844
Endou, T. 1265
Engelko, V. **95** 267 **793** 809 **1107** **1111**
Ermakov, A.E. 473
Etlicher, B. **276** 758 1064 1199 1203 1211
1237
Eyharts, P. 628
Eyl, P. 628
Eylon, S. 91
Faehl, R.J. 275 **636**
Faenov, A.Ya. 683 687 1075
Fainberg, Ya.B. 229
Farny, J. 271
Favre, M. 305 **505** 566 570 **574** 679
762
Fedotkin, A.S. 640
Fedulov, M.V. 140 542
Fedyunin, A.V. 522
Fehl, D.L. 37
Fernsler, R. 206
Fessenden, T.J. 91
Filatov, A.L. **909**
Filatova, I.I. 797
Filios, P.G. 121 284
Filipowicz, M. 917
Filuk, A.B. 1 **48** 1115
Fink, Y. 1018
Fisher, A. 749
Fisher, R.C. 115
Fisher, V. 1063
Foerster, E. 733
Fortov, V.E. 140 292 449 457 632 653
1119 1269
Frank, K. 603
Frescaline, L. 276
Friart, D. 550
Friedman, M. **206**
Frolov, I.N. 140 526 534 542
Frolov, V. 276 **1211**
Fruchtman, A. 1229
Fuchs, M.I. 410
Funatsu, M. 52
Furukawa, H. 1103
Gahl, J.M. 433
Galakhov, I.V. **946** **950** 977 981
Gale, D.G. 131
Garafov, A.M. 691
Garanin, S.F. 558 1084
Gasheev, A.S. 946 950 977
Gasque, A.M. **550**
Gass, V.G. 473
Gavrilov, N.W. **844**
Georgescu, N. **582** **591**
Gerasimov, A.I. 619 640
Gerber, K.A. 627
Gerusov, A.V. 140
Giese, H. 95 1107 1111
Gilgenbach, R. **347**
Gilliland, T.L. 37 146 753
Ginzburg, N.S. 213 **242** **245** **496**
Girka, I.O. 323
Girka, V.O. **323**
Giuliani Jr., J.L. 709 **757**
Glazyrin, I.V. 697 713 **717** 725 775
Glidden, S.C. 1171
Goel, B. **23** 1253
Goertler, A. 603
Gofman, Yu.I. **801** **805**
Gogolewski, P. 737
Golubev, A. 271
Gomberoff, K. **1215** 1216
Gondarenko, N.A. **745**
Gonzales, A. 886
Gorbachev, K.V 445 449 457
Gorbics, S.G. 1071
Gorbulin, Yu.M. 154 550
Gordeev, A.V **1131** **1135**
Gordeev, V.S. 619 640 **938**
Goyer, J.R. 121 1003

Grabovskii, E.V. 140 292 526 534 542 546
632 653 942
Grabowski, C.T. 433
Graham, J.D. 131
Granatstein, V.L. 238 405
Grebenyuk, V. 917
Grechikha, A.V. **1139**
Greenly, J.B. 81 **111** 263 1054 1143 1171
Greenly, J.M. 115
Gregorian, L. 41 **1058** 1063
Grekhov, I.V. 981
Gribov, A.N. 942
Grigor'ev, S.V. 1217 1221
Grigoriu, C. 27 **898**
Grigoryev, V.P. 1221
Grinevich, B.Ye. **538** 558
Grishin, A.V. 619 640
Gritsina, V.P. 640
Grua, P. 550
Grushin, I.I. 869 873
Grusin, I.A. 946 950 977 981
Gryaznov, V.K. 23
Gubanov, V.P. **965**
Gudov, S.N. 946 950 977 981
Guilhelm, D. 628
Gula, A. 917
Gullickson, R.L. 284
Gurashvili, V.A. 797
Gurin, V.E. 158
Gurko, V.F. 327
Guth, H. 1155
Haill, T.A. 1
Hakoda, M. 355
Hammer, D.A. 81 683 687 1054 1143 1171
Hammer, J.H. 146 **178** **554** 721 753
Han, M. 578
Hanamori, S. 355
Hanson, D.L. 1 1115
Hasegawa, D. 351
Hasegawa, J. **1179**
Haseroth, H. 271
Hashimoto, Y. **848**
Hatfield, L.L. 469 607
Hebert, M.P. 284
Hebron, D.E. 37
Heine, F. **603**
Hellmann, A 1155
Henins, I. 275
Herleb, U. **68** **1191**
Hernandez, J. 753
Hinshelwood, D.D. **115**
Hiraoka, K. **1022**
Hirota, K. 1245 1249
Hochman, J.M. 347
Hoebel, W. 23 1253
Hoffman, D. 1119
Hoffman, D.H.H. 603
Hogan, B. 238
Holmberg, C.D. 131
Hoppé, P. 72 1123 1127 **1155** 1257
Horioka, K. 501 1022 1179 1265
Hosokai, T. **501**
Hotta, T. 1095
Hubbard, R. 206
Huetner, R 1257
Hunt, J.W. 263
Hurst, M.J. 37
Hussey, T.W 558
Ido, D 52

Igarashi, H. 351
Ikeda, A. 339
Ilyin, V.N. 485
Imada, G. 27
Imanari, K. 27 **1167**
Ionov, A.I. 558
Ishihara, O. 481
Ivanov, B.I. 64
Ivanov, V.A. 1008
Ivanov, Yu.F. 873
Ives, H. 989
Ivonin, I.A. 1269
Ivonin, I.V. 1068
Iwasaki, H. 1179
Jacquet, L. 550
Jayness, R. 347
Jeong, Y.-U. 453
Jiang, W. 27 **477** **890** 894 1167
Jobe, D.O. 37 146 150 753
Johan, A. 276
Johnson, D.J. 1 37 101
Jones, T.G. 115
Jongewaard, E. 406
Kahniashvili, T.A. 1035
Kalachnikov, V.V. 832 836
Kalashnikov, M.P. 1075
Kalinin, Yu.G. 154 550 **1050** 1207
Kalynov, Yu.K. 401
Kamada, K. 331 339 **351** 393
Kaminski, A.A. 245
Kaminski, A.K. 245
Kamiya, T. 52
Kandaurov, I.V. 327 335
Kanel, G.I. 72
Kargin, V.I. 158 192 296 644 656 663
667
Karlický, M. **1031**
Karlykhanov, N.G. 717 **725** 775
Karmanov, F.I. 623
Karpova, I.G. 844
Kasuya, K. **52**
Kataev, V.N. 158
Kato, S. 355
Kaufman, Y. **509**
Kawada, M. 339
Kawakita, Y. 355
Kawasaki, S. 1179
Kawata, S. 355 **781** **1245** **1249**
Kazakova, I.F. 192
Keeler, N. 1269
Keinigs, R.K. 636
Kekez, M.M. **954**
Kellogg, J.C. 749
Kellogg, J.W. 37
Kharlov, A.V. **1217** 1221
Khilchenko, A.D. 182
Khmara, V.A. 485
Khryapov, P.A. 905
Kiefer, M.L. 1
Kies, W. 174 659
Kievitskaya, A. 921
Kim, A.A. 127 276 1203
Kingsep, A.S. 154 550 **729** 1207 **1225**
Kingsley, L.E. 928
Kirillov, G.A. 977
Kiuttu, G.F. **131** 158 558
Klyachkin, Yu. **852** **853**
Knyazev, B.A. **1054** 1143 **1195**
Koba, Yu.V. 154

Kobayashi, S. 405
Koguchi, H. **331** 351
Kogutnitskii, A.E. 445
Koidan, V.S. 182
Kokhanenko, A.P. 817
Kokshenev, V.A. 127 1203
Koláček, K. 162 343
Kolganov, N.G. 401
Komarov, O. 267 793
Kondyurin, A. 852 853
Konkin, D.V. **985**
Konoplev, I.V. 242
Konyukhov, V.V. 182
Korchagin, V.P. 1084
Korenev, A.S. 854
Korenev, A.S. 854
Korenev, S.A. **615** **785** **854**
Korioth, J.L. 928
Kormilitsin, A.I. 309 **958** 969
Korobeinikov, A.Yu. 473
Korolev, P.V. 158
Korolev, V.D. 154 962
Korostelev, A.M. 426
Korotaev, A.G. 817
Korotkov, S.V. 981
Korovin, S.D. 965
Kortbawi, D. 121 1003
Korzhenevskii, S.R. 909
Koshelev, A.S. 619
Koshelev, S.V. 697 713 717
Koshelev, V.I. 221
Kostin, V.V. 1119
Kotel'nikov, D.V. 663 667
Kotlyarevskii, G.I. 492
Kotov, Yu.A. 828 909
Kovack, F. 276
Koval'chuk, B.M. 127 276 1203
Koval, T. 1221
Kovalev, N.F. 410
Kovalev, V. 793 809
Kovalev, V.P. 309 691 **969**
Kovtun, V.I. 981
Králíková, B. 271
Krása, J. 271
Krasik, Ya.E. 41 **1039** 1215 1216 1229
Krasilnikov, M.A. **431**
Krastelev, E.G. 1054 **1143**
Krause, R.K. 928
Krauss, M. 1159
Kravárik, J. 162 737
Kreh, B.B. 131
Krejčí, A. 162 733
Kristiansen, M. 469 607
Kroupp, E. 41 1058 1063
Krouský, E. 733
Kruglov, V.S. 832 836
Kruglyakov, E.P. 327 335 1046
Krukovkii, A.Yu. 140
Kubeš, P. **162** **737**
Kudelkin, I.D. 558
Kuftin, A.N. **414** 485
Kulish, M.I. 1119
Kurawaki, K. 1245 1249
Kuropatkin, Yu.P. 649
Kusse, B.R. 1143
Kusunoki, T. 351
Kuvshinov, V.A. 905
Kuz'michev, Yu.P. 946
Kuzelev, M.V. **225** 431
Kuzmin, V.N. 797
Kuznetsov, D.V. 140 542
Kvashnin, A.N. 182
Kwan, J. 91
Láska, L. 271
Labetsky, A.Yu. 522
Labrouche, J. 628
Lackner, H. 60
Lake, P. 48
Lampe, M. 206
Langbein, K. 271
Langner, J. **860**
Larour, J. 305 582 587
Lash, J.S. 347
Lassalle, F. 276
Latysheva, L.N. 623
Lau, Y.Y. 347
Launspach, J. 628
Lavrentiev, B.N. 309 969
Lawson, W. **238**
Lazarchuk, V.P. 691
Lazarev, S.A. 296 619 640
Lebedev, M.E. 140 292 632 653
Lee, B.-Ch. 453
Lee, C.Y. 339 351 **393**
Lee, J. 453
Lee, O.A. 182
Leemans, W. 91
Leeper, R.J. 1 **37**
Lehecka, T. 627
Lemke, R.W. 101
Leon, J.F. 276
Levchenko, S.V. 1131
Li, Ch. 924
Licht, V. 1127
Lidestri, J. 60
Ligachev, A.E. 844
Ligacheva, E.A. 844
Lindholm, F. 1143
Linhart, J. **741**
Lipchak, A.I. 1076
Lisichkin, A.L. **461**
Lisitsyn, I.V. 127
Liu, Ch. **1014**
Liu, Y. 924
Liu, Y.-H. **397**
Lockner, T.R. 1 101
Loginov, S.V. 1203
Logunov, G.I. 158
Logutenko, S.L. 981
Lomonosov, I.V. 23
Long, F. 150 989
Louksha, O.I. **418** 485
Lovberg, R.H. 263
Loza, O.T. 225
Lozovskii, A.D. 864
Lu, M. **578**
Lucas, B. 174
Luchinsky, A. 917
Luginsland, J. 347
Luhmann Jr., N.C. 406
Luzhnov, V.G. 942
Lyabutin, S.K. **135**
Lyakshev, A.N. 489 492
Lygin, V.K. **385** 485
Lyublin, B. 793
Lyubomirskii, A.G. 656
Mašek, K. 271 275
Machabeli, G.Z. 1035

Maenchen, J.E 882
Magda, I.I. **422**
Mahrin, V. 917
Makarov, A,G. 182
Makartsev, G.F. 158 296
Mako, F. 437
Mankowski, J. **607**
Mann, G. 1031
Manuilov, V.N. 385 401 485
Marder, B.M. 1 146 753
Markov, P.I. 426
Maron, Y. **41** 48 146 1039 1058 1063
1215 1216 1229
Marshall, T.C. 397
Marten, H. 23 **1253**
Martin, T.H. 150 989
Martinez, C. 37
Martynenko, V.A. 981
Maslov, G.N. 619
Massier, H. 1123 1155
Masuda, W. 27
Masugata, K. 27 477 898 **1010** 1163 1167
Masuzaki, M. **196** 331 **339** 351 393
Matsubara, H. 973
Matsushita, A. 973
Matsuzawa, H. **973**
Matveenko, A.N. 1195 1127
Matvienko, V.M. 873
Matzen, M.K. 1 37 150
Maxon, S. 753
McDaniel, D.H. 1 37 150
McGuire, E.J. 1 37 48
McGurn, J.S. 37 146 150 753
McNamara, W.F. 37
Medovshikov, S.F. 542
Mehlhorn, T.A. 1 37 48 101
Meisel, G. **1257**
Mekler, K.I. 182
Melkozerov, A.V. 663 667
Melnikov, G.V. 489
Melnikov, P.I. 182 1195
Mendel Jr., C.W. 1 **56**
Menge, P.R. 1
Merle, E. 628
Meshkov, O.I. 327 335
Messina, G. 453
Mesyats, G.A. 135 828 909 917 1241
Meyers, J.W. 131
Mikhailov, S.G. 1076
Mikhailov, V.M. 445
Milyavskii, V.V. **389**
Mima, K. 1103
Mintsev, V.B. 1119
Mirnov, V.V. 1027
Mironenko, V.D. 649
Mironychev, P.V. 158 192
Mischin, M. 1107
Mishenski, V.O. 140 542 1064 **1080**
Mitchell, I. 762
Mitin, L.A. **229** 430
Mitterauer, J. **1183**
Miu, D. 898
Miyamoto, S. 52
Mizhiritskii, V.I. 154 962
Moats, A.R. 37
Mocek, T. 271
Mock, R.C. 146 753
Moir, D.C. 993
Mokhov, V.N. 558 1084
Monjaux, P 276
Moo, S.P 1233
Morell, A. 1203
Moreno, J. 305 505
Mori, M **355**
Morozov, I.V. 1084
Mosher, D. 115 146 749 753 **1147** 1151
Mostrom, M. 150 989
Motovilov, V.A. 909
Moya, S.S. 188
Mróz, W. 271
Mueller, G. **267** **809**
Munier, A. 1225
Munz, C.-D. **1159**
Murakami, H. 1099
Murakami, M. 1103
Muron, D.J. 37
Murugov, V.M. 701 946 950 977 981
Nagovitsin, A.Yu. 985
Naito, K. 355
Nakagawa, Y. 1155
Nakai, H. 1179
Nakai, S. 52
Nakajima, M. 501 1022 1179 1265
Nakayama, M. 481
Nanobashvili, I.S. 1035
Nash, T.J. 37 146 146 150 753
Nastasi, M. 275
Nazarenko, S.T. 158 296
Nazarov, D.S. 359
Neau, E. **255**
Nedoseev, S.L. 140 534 542 546
Neri, J.M. 115
Nesterov, E.V. 445 449 457 461
Neuner, U. 1265
Ney, P. 771
Nichipor, H. 824
Nickles, P.V. 1075
Niimi, G. 52
Nikiforov, A.F. 140
Nikiforov, V.G. 140
Nikolaev, V.S. 182
Nikolov, N.A. 453
Nishigori, K. 52
Nishihara, K. 1103
Nishimoto, H. 60
Nishiyama, S. 355
Nitishinski, M.S. 1207
Niu, K. **1091** **1261**
Noack, D.D. 37
Nobuhara, S. 465 481
Nochovnaya, N.A. **813** 844 878
Noonan, W.A. 115
Nudikov, V.N. 158
Obenschein, S.P. 627
Odintsov, Yu.M. 619
Ofitserov, M.M. 401
Ogawa, M. 501 **1265**
Ognivenko, V.V. 64
Oguri, Y. 1265
Okada, T. **1095** **1099**
Okayama, H. 52
Oleinik, G.M. 140 526 530 534 542 546
Oliver, B.V. 115
Olsen, R.W. 37
Olson, C.L. 115 1115
Olson, J.C. 111 263 890 894
Olson, R.E. 37
Olson, T. 886

Omelchenko, Yu.A. 81 1171 **1175**
Onishchenko, I.N. 64 **426**
Opekounov, M.S. 817 **1068**
Osin, V.A. 946 950 977 981
Osipov, V.V. 1076
Ostashev, V.I. 691
Otochin, A.A. 140
Ottinger, P.F. 115 121
Oucherenko, D.A. 817
Outten, C.A. 131
Ozur, G.E. 259 **359**
Paduch, M. 162 737
Pak, S.V. 1008
Panesh, A.M. **864**
Pankratov, V.I. 946 950
Papazian, Yu.V. 1064
Paraschiv, I. 595
Parys, P. 271
Parzhitskii, S. 917
Patran, A. 587
Pavlov, S.S. 985
Pavlov, V.S. 158
Pavlovskii, A.P. **649**
Pavlovsky, E.S. 1084
Pawley, C.J. 627
Pechenkin, S.A. 1068
Pegel, I.V. 913
Pegoev, I.N. 946 950
Peng, X. 924
Pereira, N.R. 745 **1071**
Perevodchikov, V.I. 229 430
Perin, S.S. 182
Persiansev, I.V. 292
Peskov, N.Yu. 213 245
Peter, B. 1063
Peter, W. 437
Peters, C. 91
Peterson, D.L. 146 150
Peterson, G.G. **749**
Petkun, A.A. 221
Petlytski, V. 921
Petrakov, V.N. 977 981
Petrov, S.I. 691
Petrukhin, A.A. 538
Pfeifer, M. 271 733
Phillips, R. 406
Pichugin, V.E. 140 542 546
Picon, J.C. 628
Piekoszewski, J. 860
Pikar', A.S. 158 192 296 644 656 663
667
Pikuz, S.A. **683** 687
Pikuz, T.A. 683
Podulka, W.J. 81 **1171**
Pogue, E.W. 636
Pointon, T.D. 48 101
Ponomarev, A.V. 225
Ponomarev, S.V. 701
Popkov, N.F. **158** 192 **296** **644** **656** **663**
667 985
Pornet, J. 550
Porter, J.L. 37 150
Postnikova, A.S. 485
Postupaev, V.V. 182
Potarov, A.V. 691
Potyomkin, A.V. 873
Presura, R. 591 **595** 599
Price, D. 217
Prishchepov, V.P. 64
Prokopenko, Yu.V. 422
Proskurovsky, D.I. **259** 359 813
Prucker, U. 603
Pshenichnov, I.A. 623
Puchkarev, V. 886
Pulsifer, P.E. 146
Putnam, S.D. **60**
Puzynin, I.V. 615 785 854
Qian, Q. 1018
Qiu, A.C. 301
Quintenz, J.P. **1** 37
Raacke, J. **659**
Radjuk, E. 824
Ratakhin, N. 917
Razilov, R.V. 182
Razinkova, T.J. 140
Razorenov, S.V. 72
Reass, W.A. 263
Reed, K.W. 255
Reginato, L. 91
Reiser, M. 238
Rej, D.J. **275** 894
Remnev, G.E. 817 869 **873** 878 **902** 1068
Renk, T.J. 1 882
Renner, O. **733**
Ridlon, R.N. 188
Riege, H. 68 1191
Rintamaki, J.I. 347
Řípa, M. 343
Robozerov, S.V. 485
Rodgers, J. 405
Roewekamp, P. **174** 659
Rogerson, J. 709 757
Rohlena, K. **271**
Romanov, I.G. **821**
Romanova, G.M. 821
Romanova, V.M. 683 687
Romary, P. 550
Roques, A. 628
Roschupkin, S.A. 445 449
Rose, D.V. 115 1147
Rosenthal, S.E. 1
Rosmej, F.B. **1075**
Rosocha, I. 886
Roth, I. 1003
Roth, P. **363**
Rothstein, V.P. 813 259
Rouille, C. 276 758 1203
Rous, J. 305
Rousskikh, A.G. 522
Rovenskikh, A.F. 182
Rowley, J.E. 121 284
Rudakov, L.I. 154 729 **776** **780** 1199
Ruden, E.L. 131
Ruggles, L.E. 37 150
Ruiz, C.L. 1 37
Rukhadze, A.A. 225 431
Rukin, S.N. 135 1241
Rusch, D. 72 1123 1127 1155 1257
Russkov, A.S. 158
Rutkovskaia, K. 921
Ryaslov, E.A. 158 192 296 644 656 663
667
Ryutov, D.D. 178 554
Ryzhackova, E.G. 192
Ryzhkov, V.A. **869** 873
Saavedra, R. 679 762
Sabirov, B. 917
Sadowski, M. **170**

Saenger, E. 1257
Sajer, J.M. 550
Salnikov, L.I. **824**
Samoilov, V.N. 615 785 854
Samsonov, S.V. 401
Sanford, T.W.L. 1 **146** 150 **753**
Sanin, A.L. 327 335
Saraph, G. 238
Saratov, A.F. 158
Sarfaty, M. 41 1216 **1229**
Sasorov, P.V. 140 542
Sawyer, P.S. 37
Schalk, S. 95 1107 1111
Schamiloglu, E. **433**
Schegolikhin, N. 267
Scheitrum, G. 406
Scheuer, J.T. 275
Schleinitz, H.M. 263
Schlitt, L. 1003
Schmitz, F. 174
Schneider, L.X. 255
Schneider, Ralph F. 284 757
Schneider, Rud. 1159
Schnuerer, M. 1075
Schoen, T. 1257
Schumacher, G. 267 809
Schwandner, A. 603
Scotnikov, V.A. 909
Seamen, J.F. 1 37 146 150 753
Sedykh, S.N. 245
Seidel, D.B. 1
Seitz, G.J. 188
Semenov, E.P. 182
Semushin, S. 276 **758** 1211
Semyonov, S.I. 158
Senikh, A.V. 701
Sergeev, A.P. 245
Sergeev, A.S. 242 245 496
Serlin, V. 206 **627**
Sevastianov, A.A. 776
Shaidullin, V.Sh. 558
Shapiro, A.L. 229 430
Sharkov, B. 271
Sharp, W.M. 91
Shashkov, A.Yu. 1050
Shelkovenko, T.A. 683 687
Shen, Zh.K. 301
Shijan, V.D. 671 675
Shiloh, J. **437**
Shimanovich, V.D. 797
Shkvarunets, A.G. 225 **405**
Shlapakovskii, A. S. **441**
Shlenov, Yu.V. 840
Shoup, R.W. 150 **989**
Shpak, V.G. 242 **473** **913**
Shpitalnik, R.R. 41 1215 **1216**
Shulov, V.A. 813 **878**
Shumilin, V.P. 445 449 457 461
Shumshurov, A. 271
Shunailov, S.A. 242 473 913
Shurter, R.P. 188 **993**
Sidel'nikov, G.L. 611
Sidorenko, D.Yu. 426
Sidorov, V.A. 999
Silva, P. 566 **570** 574
Simanovskii, D.M. 174
Šimek, M. 343
Sincerny, P. **1003**
Sinebryukhov, A.A. 127 917 1217 1221
Sinebryukhov, V.A. 127 917
Singer, J. 72 1127 1257
Singh, J.P. 1233
Singleton, C. 1127
Sinitsky, S.L. 182 213 367
Sissakian, A.N. 615 785 854
Skála, J. 271
Skladnik-Sadowska, E. 737
Skobelev, A.N. 1008
Skobelev, I.Yu. 1075
Skvortsov, V.A. 389 **513**
Slavnov, Yu.K. 526
Slinker, S. 206
Slovikovskii, B.G. 135
Slutz, S.A. 1 101
Smirnov, V.P. 140 292 526 534 542 546
632 653 1064
Smith, I. 60 150 989
Sochugov, N.S. 905
Sokolova, O.V. 558
Sokovnin, S.Yu. **828**
Solomonov, V.I. **1076**
Sominski, G.G. 319 371 418 789 485
Sonegawa, T. 27
Sorokin, S. 917
Sotnikov, G.V. 426
Soto, L. 679 **762**
Spassovski, I.P. **453**
Spencer, T.A. 347
Spielman, R.B. 1 37 146 **150** 753 989
Springer, P.T. 753
Stallings, C. 1003
Stambulchik, E. 48
Stanislawski, J. 860
Stark, M.A. 37
Stein, E. 1123 1159
Stepchenko, A.S. 965
Stephanakis, S.J. 115 749 1151
Stinnett, R.W. **882**
Stoltz, O. 72 1123 1127 1155 1257
Stolupin, V. 917
Straka, P. 271
Strauss, D. 267 809
Strelkov, P.S. 225
Stroganov, V.A. 445 449 457 461
Struts, V.K. 902
Struve, K.W. 146 150 753 882 989
Stygar, W.A. 1 146 150 989
Sudan, R.N. **81** 780 1171 1175
Suganomata, S. 973
Summa, W.J. 158 284
Sun, F.J. 301
Sunami, H. 52
Suvorov, V.N. 649
Swanekamp, S.B. 1147 1151
Sweeney, M.A. 1
Tabak, M. 721
Takahata, S. 331
Tantawi, S. 406
Tarakanov, V.P. 913
Tarasov, A.D. 640
Tarasov, A.V. 182 213
Tauschwitz, A. **91** 1127 1155
Tereshatova, E. 853
Thevenot, M. 628
Thoe, R.S. 753
Thomas, J. 60
Thompson, J. 121
Thornhill, J.W. 146 709 749

Tikhonov, A.N 840
Tisone, G.C 1
Tkotz, R 603
Toda, K. 331
Tokarev, A.S. 832 836
Tolopa, A.M. **1187**
Tomaszewski, K 162 737
Toor, A. 721
Torres, J A 37 150
Toulisov, E V 675
Toyosugi, N. 393
Tsareva, I.N. 821
Tsibin, O Y 1107
Tsimring, Sh E 385 485
Tsiranov, S.N. 1241
Tstvetkov, V.I 492
Turkin, N.G. 797
Turov, A.M. 135
Tuyuki, A. 1245 1249
Ucer, D 1027
Uchida, H. 848
Ueda, Y. 973
Ullschmied, J. **343** **766**
Ulmaskulov, M.R. 242 473 913
Ulyanov, D.K. 225
Ushakov, A.G. 1207
Usov, Yu.K. 526
Utkin, A.V. 72
Vaeth, W. 1123 1127 1155
VanDevalde, D.M. 37
Vargas, M. 37 146 753
Vaselenok, A.A. 797
Vdovin, S.V. 182
Vecchi, M. **623**
Velikhov, E.P. 140
Velikovich, A.L. 705
Villate, D. 628
Vitkovitsky, I.M. 284
Vogel, N.I. 513 **518**
Voisin, L 628
Voitsekhovskii, A.V **817**
Volkov, A.B. 401
Volkov, G.I 1008
Volkov, G.S. 140 1064 1080
Volkov, S.N. 886
Vorob'ev, V.S. 1119
Vorobiev, O.Yu. 23 292 1269
Voronov, B.F. 701
Vorontsov, V.I. 663 667 158
Voss, U. 1159
Vozdvijenskii, V.A. 999
Vrba, P. **375**
Vyacheslavov, L.N. **327** 335
Waganaar, W.J. 894
Wakisaka, T. **465**
Walter, K.C. 275
Wang, X.H. 301
Ware, K.D. 131 158 **284**
Watanabe, M. 52
Weaver, J. 405
Weber, B.V. **121** 749 1151
Webster, W. 627
Weidenheimer, D.M. 1071
Weingarten, A. 41 1039 1215 1216 1229
Welch, D.R. 115 753 **1115**
Wenger, D.F. 37
Wessel, F. 886
Westermann, T. 1123 1159
Whitney, K.G. 146
Wolovski, J. 271
Wong, C.S. 305 **1233**
Wood, B.P 275
Woolverton, K. **469**
Woryna, E. 271
Wozniak, J. 917
Wu, C. 52
Wyndham, E. 305 505 566 570 574 679
762
Xu, R. 301
Yakubov, V.B. 1084
Yakunkin, M.M 840
Yakusheva, D 853
Yalandin, M.I. 242 473 913
Yamasaki, T. 848
Yamauchi, S. 1265
Yang, S. 578
Yang, T. 578
Yankelevich, Y. 886
Yasuike, K. 52
Yatsui, K. **27** 477 890 **894** 898 1010
1163 1167
Yatsuzuka, M. 465 **481** 848
Yegorov, A.M. **64**
Yegorychev, B.T. 558
Yerichev, V.N. 558
Yoo, S. 1127
Yoshida, H. 339 393
Yoshikawa, M. 331
Young, D. 481
Young, F.C. 115 749 1151
Yovchev, I.G. 453
Yu, H. 1014
Yu, S.S. 91
Zabaidullin, O. **1237**
Zagar, D.M. 37 150
Zaitsev, V.I. 140 542 1064 1080
Zakatov, L.P. 301 1207
Zakharov, A.E. 292 701
Zakharov, S.V. 140 526 534 542
Zakoutaev, A.N. 873
Zambra, M. 305 505
Zapevalov, V.E. 414 485
Zavyalov, M.A. 229 **430**
Zazhivikhin, V.V. 140 546 962 1080
Zelenskii, D.K. 192
Zeng, J.T. 301
Zenhter, P. 550
Zenkov, D.I. 649
Zhakov, S.V. 473
Zhang, J. **924**
Zhang, K. 1014
Zhang, W. 1014
Zharinov, E.I. 538 558
Zharov, V.F. 327
Zherlitsyn, A.G. **489** **492**
Zhong, H. 924
Zhu, W. 1014
Ziethen, G. 174
Zimakov, S.D. 558
Zimek, Z. 824
Zimmerman, G.B. 721 753
Zinchenko, Vl. **671** **675**
Zoita, V. 582 **587** 591 595 599
Zolotovsky, V.I. 981
Zotkin, R.P. 182
Zotova, I.V. 242 496
Zubov, A.D. 775
Zurin, M.V. 140 526 534 542

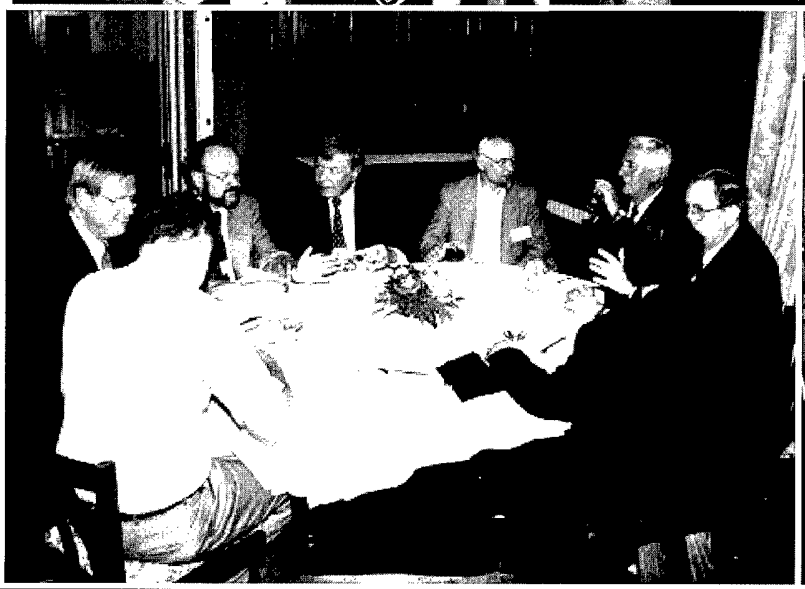

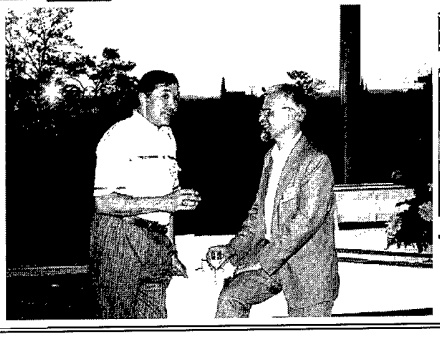

Invitation to the next conference

Welcome to Haifa
ברוכים הבאים לחיפה

We look forward to the continued success of the BEAMS meetings at

BEAMS'98

in Haifa, Israel.

Conference date: **June 8-12, 1998**
Host organization: **Rafael, Haifa**

For more information please contact

Dr. Joseph Shiloh, Conference Chair
Dept. 23, Rafael
Haifa, ISRAEL
E-mail: beams98@plasma-gate.weizmann.ac.il
jshiloh@rafael.co.il *or* shilo@eng.tau.ac.il

WWW home page BEAMS'98:
http://plasma-gate.weizmann.ac.il/~peter/beams98.html